Table of Contents

No.	Description of Paper	Page No.
1	**Solid-Liquid Extraction Kinetics of Total Phenolic Compounds from Red Dates** *(Paper 2CE01)* Chen Yen Leng, Chua Bee Lin	1
2	**Drying Kinetics and Optimisation of Pectin Extraction from Banana Peels via Response Surface Methodology** *(Paper 2CE02)* Chong Yek Cze, Chua Bee Lin	15
3	**Characteristics Study of Photovoltaic Thermal System with Emphasis on Energy Efficiency** *(Paper 2CE03)* Chuah Yee Yong, Mohammad Taghi Hajibeigy	29
4	**Synthesis of a Sustainable Sago-Based Value Chain via Fuzzy Optimisation Approach** *(Paper 2CE04)* Jeffrey Chong Hong Seng, Yoke Kin Wan, Viknesh Andiappan	39
5	**Optimisation of Process Parameters for Devulcanisation of Natural Rubber Utilising Deep Eutectic Solvent (DES)** *(Paper 2CE05)* Kishen Kunju, Rashmi G. Walvekar, Mohammad Khalid Siddiqui	56
6	**Design of Biomass Combined Heat and Power (CHP) Systems based on Economic Risk using Minimax Regret Criterion** *(Paper 2CE06)* Ling Wen Choong, Wan Yoke Kin, Viknesh Andiappan	90
7	**Amine Based Devulcanization of Waste Tire Rubber** *(Paper 2CE07)* Mohammad Afiq Bin Zulkefly, Suganti Ramarad, Rashmi Walvekar	106
8	**Removal of Dye in Wastewater by Adsorption-Coagulation Combined System with *Hibiscus Sabdariffa* as the Coagulant** *(Paper 2CE08)* Nicholas Ho Jian Hoong, Nurhazwani Ismail	123
9	**Potential of Hibiscus Sabdariffa and Jatropha Curcas as Natural Coagulants in the Treatment of Pharmaceutical Wastewater** *(Paper 2CE09)* Sheena Sibartie, Nurhazwani Binti Ismail	138
10	**Synthesis and Optimisation of A Sustainable Wastewater Treatment Plant via Material Flow Cost Account (MFCA)-based Approach** *(Paper 2CE10)* Run Ting Siew, Yoke Kin Wan	153
11	**Preliminary Study on Effect of Chemical Composition Alteration on Elastic Recovery and Stress Recovery of Nitrile Gloves** *(Paper 2CE11)* Kai Yang Tan, Siew Wei Phang, Chee Kin Phang, Jing Lang Choh	171
12	**Process Debottlenecking and Retrofit for Design of Palm Oil Milling Process via Inoperability Input-Output Modelling** *(Paper 2CE12)* May May Tan, Viknesh Andiappan, Yoke Kin Wan	184

13 **Coagulant Dipping Time and Temperature Optimisation for Latex Glove Uneven Coating Investigation** *(Paper 2CE13)* 202
Loong Than, Siew Wei Phang, Kim Nam Ho

14 **Assessment of Natural Deep Eutectic Solvent (NADES) Pretreatment on Sugar Production from Lignocellulosic Biomass** *(Paper 2CE14)* 219
Yuen Jun Mun

15 **The Application of Image Processing to Solve Occlusion Issue in Object Tracking** (*Paper 2EE01)* 239
Cheong Yun Zhe, Chew Wei Jen

16 **Comparative Study between Planar and Bent Antenna Characterization** 251
(Paper 2EE02)
Lau Zheng Tung, Ghafour Amouzed Mahdiraji

17 **Inertial Sensing of Cyclists to Predict the Next Move** *(Paper 2EE03)* 265
Mahesh A/L V.Nagarrettinam, Dr. Mohsen Nabi Poor

18 **A New Type Of Electrical Bike Using Dual Rotor Permanent Magnet Machine** *(Paper 2EE04)* 280
Mohd Izzat Bin Zainuddin, Aravind C.V

19 **Electromagnetic Braking with DC Field Excited Configuration for Train Traction Systems** *(Paper 2EE05)* 297
Preshant A/L Krishna, Aravind C.V, Aminath Saadha

20 **Energy Recovery through Phase Layered Heat Removal using Sustainable Materials** *(Paper 2EE06)* 311
Rikesh Ramsurn, Aravind CV, Mohammad Taghi Hajibeigy

21 **Vertical Wind Energy Configuration for Low Velocity Regime** *(Paper 2EE07)* 323
Teow Wei Wei, Aravind CV, Charles R. Sarimuthu

22 **Traffic Monitoring Using Bluetooth** *(Paper 2EE08)* 335
Neow Way Shyun, Edwin Chung Chin Yau

23 **Suppression of Ground Borne Vibration Induced by High-Speed Lines** 357
(Paper 2ME01)
Ali Mohamed Rathiu, Mohammad Hosseini Fouladi, Satesh Narayana Namasivayam

24 **Numerical Analysis and Geometry Optimisation of Vertical Vane of Room Air-conditioner** *(Paper 2ME02)* 375
Chan Wei Yin, Abdulkareem Sh. Mahdi Al-Obaidi, Felicia Wong Yen Myan, Yap Kim Haw

25 **The Fabrication of Non-Implant 3D Printed Nose** *(Paper 2ME03)* 391
Elliot Andrews, Yong Leng Chuan

26 **Assessing Bioinspired Topographies for Their Antifouling Potential Control Using Computational Fluid Dynamics (CFD)** *(Paper 2ME04)* 404
Jacky Ling, Felicia Wong Yen Myan

27 **Design and Optimisation of Home Scale Greywater Recycling Package** 415
(Paper 2ME05)
Kalaichelvan a/l Arugam, Azadeh Ghadimi, LH Chang

28 **Mechanical Characterization of Zirconia Ceramic Composite** *(Paper 2ME06)* 430
K. Dickson, W. J. Kelvin Chew, S. Ramesh

29 **Preparation and Characterization of Durian Husk Fiber Filled Polylactic Acid Biocomposites** *(Paper 2ME07)* 441
Man Chee Lee, Seong Chun Koay, Ming Meng Pang, Kim Yeow Tsai

30 **Operational Research on Design and Process Optimization of Ozone Water Application in Kitchen** *(Paper 2ME08)* 452
Lee Chun Jing

31 **Stabilising an Inverted Pendulum with PID Controller** *(Paper 2ME09)* 468
Lim Yon Yaw, Hoo Choon Lih, Felicia Wong

32 **Evaluation of SIPIC01 and SIPIC02 on Motor Speed Control** *(Paper 2ME10)* 484
Wei Sheng Loh, Mohd Hardie Hidayat Mohyi, Choon Lih Hoo

33 **Design and Analysis of a Mechanical Regenerative Braking System** *(Paper 2ME11)* 499
Matthew Toh Xiang Wen, Douglas Tong Kum Tien

34 **Sintered Properties of Stainless Steel-doped Y-TZP Ceramics** *(Paper 2ME12)* 515
M. M. Mervyn Marlon, W. J. Kelvin Chew, S. Ramesh

35 **Design and Fabrication of Collapsible Scissor Bridge** *(Paper 2ME13)* 532
Mohamad Nabil Aklif bin Bero, Noor Zafirah binti Abu Bakar

36 **Comparisons of Flow Patterns over a Hierarchical and a Non-hierarchical Surface in Relation to Biofouling Control** *(Paper 2ME14)* 554
Mohammed Ridha Bin Ahmad Fawzan, Felicia Wong Yen Myan

37 **Modelling and Simulation of Rail Vehicle Ride Quality** *(Paper 2ME15)* 572
Nigel Lopez Michael, Mohd Farid Bin Aladdin

38 **The Enhancement of Pre-Storage Filtration Efficiency for The Rainwater Harvesting System in Malay** *(Paper 2ME16)* 594
Yoong Sion Ong, Ken Sim Ong, Y.K. Tan, Azadeh Ghadimi

39 **Simulation of thermal performance on bicycle helmet** *(Paper 2ME17)* 610
Chris Carl Rosette, Noor Zafirah Abu Bakar, Mohd Hardie Hidayat Mohyi

40 **Fabrication of Non-Implant 3D Printed Skin** *(Paper 2ME18)* 625
Shivani Amish Kumar Pandya, Yong Leng Chuan

41 **Lift and Drag of Non-conventional Wings at Subsonic Speeds and Zero Angle of Attack – an Experimental Investigation** *(Paper 2ME19)* 637
Ting Chern Wei, Abdulkareem Shafiq Mahdi Al-Obaidi

42 **The Study of Seating Comfort in Passenger Vehicles** *(Paper 2ME20)* 653
Umi Salmah Binti Seraj, Mohd. Farid Aladdin, Douglas Tong Kum Tien

43 **Preparation and Characterization of Plastic Wood Composite Made Up of Durian Husk Fiber and Recycled Polystyrene Foam** *(Paper 2ME21)* 668
Varnesh Subramaniam, Koay Seong Chun, Pang Ming Meng, Albert Tsai

44 **Development of a PID Controlled Arduino-Based Stabiliser** *(Paper 2ME22)* 679
Wah Yee Lyn, Felicia Wong Yen Myan, Tai Jun Jet, Hoo Choon Lih

45 **Electrical Energy Harvesting From Cooker's Wasted Heat With Using Conduction Cooling** *(Paper 2ME23)* 693
Wincent, Ghafour Amouzard Mahdiraji

46 **Anti-windup PI controller, SIPIC For Motor Position Control Application** 703
(Paper 2ME24)
Kah Kit Wong, Choon Lih Hoo, Mohd Hardie Hidayat Mohyi

47 **Design and Fabrication of Small Vertical-Take-Off-Landing Unmanned Aerial Vehicle** *(Paper 2ME25)* 718
Yasir Ashraf Bin Abd Rahman, Mohammad Taghi Hajibeigy

48 **Design and Analysis of an Eddy Current Braking System** *(Paper 2ME26)* 738
Yeoh Joe Han, Douglas Tong Kum Tien

49 **A Gesture Detection Algorithm for a Game Console** *(Paper 2ME27)* 755
Edmund Tan Ee Loon, Mohsen Nabi Poor

50 **Design and Implementation of a GSM-Based, Seismic Activities Monitoring and Warning System Using Fuzzy Logic Algorithm** 780
(Paper EUG01)
Kenneth C. Lopez, Sydney Girl C. Panganiban, Orland Jos R. Parducho, Gian Miguel M. Reyes, Glofett T. Velasco[1],Johnrenz R. Villegas, Favis Joseph C. Balinado, Rio A. Aguilar

51 **Development of an Android – Based Home Illumination System** 787
(Paper EUG02)
Derrick J. Castillo, Carlo C. Medina, Avigail Anne T. Sanchez, Neil P. Balba, Rio B. Aguilar

52 **Quadcopter Flight Controller with Four Degrees of Freedom and Data Acquisition Capability using Fuzzy Logic** *(Paper EUG03)* 796
Kaye Cristine Tolentino, Josephine Suelto, Alvyn Ramos, Rina Quiatchon, Ralph Laurence Visaya, Favis Joseph Balinado

53 **GSM – Based Flood Monitoring System and Data Acquisition using Smoothing Average Technique** *(Paper EUG04)* 812
Princess Joy V. Natividad, Adrian F. Cardenas, Joselito P. De Castro, Frances Camil C. Ilagan, Juns Jaurigue, Kaye Cristine M. Tolentino, Favis Joseph Balinado, Rio B. Aguilar

54 **GSM Based Energy Consumption Monitoring with Control: A Prototype** *(Paper EUG05)* 825
Eufila Gerdaleen Legaspi, Kenneth Agra, Jother Amutan, Kim Roylan Bundalian, Favis Joseph Balinado, Rio Aguilar

55 **GSM Based Fire Notification and Data Acquisition System Using Kalman Filtering Technique** *(Paper EUG06)* 838
Carlene Joy A. Breganza, John Carlo U. Ancheta, Edmar M. Atienza, Kevin L. Domingsil, Sidney Wyne R. Solas, Favis Joseph C. Balinado, Arvin Dela Roca

56 **Maximization of Machine Capacity Utilization Using Overall Equipment Effectiveness** *(Paper EUG09)* 847
Carmina A. Flores, Reniel S. Malabuyoc, Angela Rose R. Mijares, Ryan Jeffrey P. Curbano

57 **Microcontroller-based 6-DOF Bolted Aluminum for Independent Gait Humanoid** *(Paper EUG10)* 857
Wena Rose Magpantay, Pamela B. Mandanas, Arjay Manzolim, John Paul S. Endaya, Favis Joseph C. Balinado, Arvin P. Dela Roca

58 **Design and Implementation of Microcontroller-Based Gesture Controlled Robot Head Applying Three Degrees of Freedom** *(Paper EUG11)* 866
Andaya T. Leonardo , Joselito P. De Castro Jr, Jan Vincent D. Banzuela , Adriel Nichol F. Malabanan, Arvin P. Dela Roca

59 **Weather Adaptive Automotive Headlights Using Arduino Microcontroller** *(Paper EUG14)* 876
Kevin L. Domingsil, Frances Camil C. Ilagan, Glofett T. Velasco, Princess Joy V. Natividad, Carlene Joy A. Breganza, Arvin P. Dela Roca

60 **A Wired PID-Based Altitude Controlled Remotely Operated Underwater Vehicle with Data Acquisition** *(Paper EUG15)* 886
Frances Camil C. Ilagan, Christian Jay B. Carabio, Marie Thalia Grace M. Amutan, Vanna Kaori S. Lustre, Kevin L. Domingsil, Carlene Joy. Breganza, Princess Joy V. Natividad, Arvin P. Dela Roca

61 **SGO and Tsallis Entropy Assisted Segmentation of Abnormal Regions from Brain MRI** *(Paper EUG16)* 898
K. Suresh manic, Nawf Al Shibli, Rahma Al Sulaimi and Deepti Suresh

62 **A Novel Image Processing Scheme to Evaluate Breast Thermal Images** *(Paper EUG17)* 910
N. Sri Madhava Raja, Deepti Suresh, A. Kirthini Godweena

63 **Kapur/Tsallis Entropy guided Segmentation of Plasmodium Species from Thin Blood Smear Images** *(Paper EUG18)* 920
Deepti Suresh, Sri Madhava Raja.N, Kirthini Godweena.A

64 **Performance Evaluation for High Transmission Rate of 40GB/S with Intensity Modulation in WDM based Long Haul SMF** *(Paper EUG19)* 929
MD Shahrukh Adnan Khan, Sharsad Kara Kuni, Md. Masum Howlader, Md. Moshiur Rahman, Aravind CV

65 **Design of a Fully Automated Ventilation System for Vehicles Subjected to direct sunlight** *(Paper EUG20)* 937
Ahmed Medani Mohamed, Ahmed Abdalla Omer, Obai Younis, Dania Ahmed

66 **PCM Based Thermal Energy Storage System Integrated with Solar Parabolic Through Collector** *(Paper EUG21)* 955
S.Raja, S.Prakash, R.Gokulnath, A.Krishnamoorthy, J.Lillymercy

67 **Analysis of Carbon Reinforced Metal Matrix Composite for IC Engine Valves** *(Paper EUG22)* 968
P. Sivashankari, A. Krishnamoorthy, S. Prakash, S. Raja, S. Venkatesh

68 **X-ray Diffraction Analysis of *Scomberomorus Guttatus*-derived hydroxyapatite and montmorillonite on polylactic acid biocomposite** *(Paper EUG23)* 979
Hon-Meng Ng, Soo-Tueen Bee, Lee Tin Sin, Ratnam, C. T., A. R. Rahmat

69 **Performance Analysis of Duobinary Modulation for 40gb/s N-channel WDM in EDFA Based Standard Single Mode Fibre** *(Paper EUG24)* 996
MD Shahrukh Adnan khan, Md. Moshiur Rahman, Manobendu Sarker, Aravind CV

70 **The ORPOC Star: Five Characteristics that Define an Optimal Motorcycling Riding Posture** *(Paper EUG25)* 1008
S. Suresh, M. I. N. Ma'arof, H. Husain and N. Senin

71 **Investigation of Ethylene Octene Copolymer Effects on Polypropylene Wood Composite** *(Paper EUG26)* 1022
Chun Ming Ng, Soo Tueen Bee, Chong-Yu Low , Lee Tin Sin

72 **A Numerical Investigation on the Performance of Wind Turbine Airfoils with Gurney Flaps and Airfoil Shape Alteration** *(Paper EUG27)* 1033
Abubker Fadl, Mohammed Abbasher , Obai Younis Taha, Ali El Seory

73 **Analysis of Taper Width Variations in Linear Reluctance Machine** *(Paper PG01)* 1041
Aminath Saadha, Aravind CV, Preshant Krishna, F.Azhar

74 **The Impact of Hybrid Photovoltaic Thermal Systems to Ecotourism in Malaysia** *(Paper PG02)* 1051
Mohammad Taghi Hajibeigy, Aravind CV, Rashmi W

75 **Linking Liberatory Pedagogy to Engineering and Sustainable Development** *(Paper PG03)* 1072
Jayasubamani Arvi S.Moganakrishnan,Satesh Narayana Namasivayam

Solid-Liquid Extraction Kinetics of Total Phenolic Compounds from Red Dates

Chen Yen Leng*, Chua Bee Lin
School of Engineering, Taylor's University, Malaysia

**chenyenleng@gmail.com*

Abstract
Red dates are one of the most famous herbal plants in making traditional Chinese medicine. They contain large amount of bioactive compounds. The objectives of this research were to optimise the crude extract yield and total phenolic compounds (TPC) yield from red dates using response surface methodology (RSM) and model the extraction kinetics of TPC yield from red dates. Date fruits were dried in an oven under temperatures 50°C, 60°C, 70°C and 80°C until a constant weight was obtained. The optimum drying temperature was 60°C as it gave the highest crude extract yield and TPC yield. Besides that, single factor experiments were used to determine the optimum range of four extraction parameters which were: liquid-solid ratio (10-30 ml/g); ultrasonic power (70-90%); extraction temperature (50-70°C); and extraction time (40-60min). The optimum range of the four parameters were further optimised using the Box-Behken Design (BBD) of RSM. The extraction conditions that gave the highest crude extract yield and TPC yield were chosen. The optimum value for liquid-solid ratio, ultrasonic power, extraction temperature and extraction time were 30ml/g, 70%, 60°C and 60 min respectively. The two equations generated from RSM were reliable and can be used to predict the crude extract yield and TPC yield. The higher the extraction temperature, liquid-solid ratio, and extraction time and lower ultrasonic power, the higher the crude extract and TPC yield. Finally, the results of TPC yield versus time based on the optimum extraction parameters from RSM optimisation were fitted into three extraction kinetic models (Peleg's model, Page's model and Ponomaryov's model). It was found that the most suitable kinetic model to represent the extraction process of TPC from red dates was Page's model due to its coefficient of determination (R^2) was the closest to unity, 0.9663 while its root mean square error (RMSE) was the closest to zero, 0.001534.

Keywords: Red dates, total phenolic compound (TPC), response surface methodology (RSM), extraction kinetic models

1. Introduction

Medical plants have similar properties as pharmaceutical drugs. They can be used for medical purposes as they contain chemical compounds which help humans with their health and prevent diseases. There are 21,000 plants around the world can be used for medical purposes due to their high nutritional values according to World Health Organization [1].

Red dates are described as 'the king of nuts' [2]. They are one of the most famous and useful herbal plants in making traditional Chinese medicine. Red dates contain a high level of Vitamin C which can help improve insomnia, protect the liver and reduce cholesterol [3]. In addition, red dates also contain a large amount of total phenolic compounds (TPC) that increases their antioxidant activity by removing free radicals which cause cancer and other diseases [4].

For an accurate analysis, the optimisation of extraction process is needed. Response Surface Methodology (RSM) is a useful tool to optimise extraction process. It helps to lower the cost of the process and it gives better understanding of the extraction process [5]. RSM has been applied successfully for *Macadamia tetraphylla* and other herbal plants but no article is available regarding the optimisation of crude extract yield and TPC yield of red dates [6].

From an engineering perspective, it is very helpful to do a mathematical modeling of extraction processes. It is used to model the experiment, relate the consumption of energy, time, solvent and other parameters to the extraction kinetics [7]. The widely used extraction kinetic models of antioxidant compounds included Peleg's model, Page's model and Ponomaryoc's model. To find the best fitted model of the extraction process, the correlation coefficient (R^2) and root mean square error (RMSE) were calculated. The closer the R^2 and RMSE to unity and zero respectively, the higher the fit of predicted kinetic models to the experimental data.

To the best of author's knowledge, the optimisation of crude extract yield, TPC yield from red dates was not widely developed. The reported findings regarding the antioxidant activity of TPC yield were inconsistent. There were also three commonly used models were not widely used to describe the process of extraction of TPC from red dates. They were Peleg's model, Page's model and Ponomaryov's model.

One of the objectives of this research was to optimise the crude extract yield and TPC yield of red dates using response surface methodology (RSM). Box-Behnken Design (BBD) with three central points of RSM was used due to its high efficiency and less number of experiments were required thus lowering the total cost [8]. Another objective was to model the extraction kinetics of crude extract yield from red dates. Among the mentioned three kinetic models (Peleg's model, Page's model and Ponomaryov's model), the best fitted extraction kinetic model was chosen to predict the output of extraction process of TPC from red dates.

2. Methodology

The methodology conducted to achieve the objectives of this research was discussed in this section. Also, the analysis and justification of all tasks were included.

2.1 Ultrasonic Extraction of Total Phenolic Compounds from Red Dates

50 g of date fruits with no seeds were washed with tap water and dried in an oven at 50, 60, 70 and 80ºC respectively until constant weight was obtained. The dried fruit was grinded to powder using blender. 11g of red dates powder was extracted for 60 min with 165ml of pure ethanol as extraction solvent in an ultrasonic bath under 60°C. The ultrasonic bath was operated at 70% of input power and 37kW. After 60 min, the mixture was placed in a rotary evaporator under 40 °C until crude extract was observed. The crude extract was weighted to determine the crude extract yield.

2.2 Quantification of Total Phenolic Compound Yield from Red Dates

The quantification of TPC yield from red dates was carried out by using gallic acid as a standard [4]. 0.1g of crude extract was dissolved in 1.5ml of distilled water. 5ml of 10 % of Folin-Ciocalteu phenol reagent, 4ml of 7 % of Na_2CO_3 and 1ml of extract were mixed together. After 1 hour, the mixture was poured into 96-well plate. The first row of the 96 well plate was filled with 0.2 ml of pure ethanol to act as blank solution. The 96-well plate was then placed into microplate spectrophotometer to measure its absorbance at 765 nm. The amount of gallic acid from red dates were determined by referring to the calibration curve of gallic acid plotted. Concentration of TPC was calculated using Eq. (1).

$$\text{Concentration of TPC } \left(\frac{\text{g GAE}}{\text{g extract}}\right) = \frac{C_t V_t}{W_1} \times 10^{-6} \quad (1)$$

where C_t is the concentration of gallic acid in sample extract (μg/ml), V_t is the total volume of the sample extract (ml), W_1 is the dry weight of extract (g).

2.3 Selection of Best Drying Temperature and Single Factor Experiments

The best drying temperature of red dates among four different drying temperatures (50, 60, 70 and 80°C) was determined. The drying temperature that gave the highest crude extract and TPC yield was selected as the optimum drying temperature.

Single factor experiments were used to study the four parameters (liquid-solid ratio, ultrasonic power, extraction temperature and extraction time) individually and determine the optimum range of four parameters for RSM. Crude extract yield and TPC yield of red dates were obtained by following the experimental design which was created by varying one factor and others were kept at their midpoint.

2.4 Optimisation of Extraction Conditions

Box-Behken Design (BBD) of response surface methodology was used to optimise extraction conditions based on the optimum ranges determined from single factor experiments. The experiments were carried out by referring to the Design of

Experiment (DOE) of BBD which was created using Design Expert software 7.0. The crude extract yield and TPC yield of TPC were determined by following the DOE created. The experiments were repeated for three times. Their average values were used to compare to determine the optimum combination of each parameter. The extraction conditions that give the highest results are chosen as the optimum extraction conditions. Besides that, the validations of optimum extraction conditions were achieved as the difference between the crude extract and TPC yield based on the optimum extraction conditions and the calculated results from the two equations provided from RSM were less than 10 %.

2.5 Mathematical Modeling of Extraction Kinetic Model for Red Dates

Three widely used extraction kinetic models, Peleg's model, Page's model and Ponomaryov's model were used to describe the process of extraction of TPC from red dates mathematically. The equation of Peleg's model, Page's model and Ponomaryov's model were showed in Eq. (2), (3) and (4) respectively. The results of TPC yield under optimum extraction conditions were fitted to the three extraction kinetic models respectively. The constants' values of each models and the coefficient value of R^2 and RMSE were determined using Matlab Curve Fitting Tool 2017. Based on the values of R^2 and RMSE obtained, the best fitted extraction kinetic model to the experiment was chosen. Furthermore, the results of TPC yield of three samples at different time were substituted into the best fitted extraction kinetic models. The validation of the best kinetic model was achieved as the difference of TPC yield calculated using the best fitted model and experimental value was less than 10%.

Peleg's model: $C(t) = \mathrm{C}_0 + \frac{t}{\mathrm{K}_1 + \mathrm{K}_2 t}$ (2)

Page's model: $C(t) = e^{-\mathrm{k}t^{\mathrm{n}}}$ (3)

Ponomaryov's model: $1 - \frac{C_t}{C_e} = \mathrm{b} + \mathrm{k}_3 t$ (4)

Where $C(t)$ is the concentration of TPC at time t (mg/g_{powder}), C_0 is the initial concentration of TPC (mg/g_{powder}), K_1 is Peleg's rate constant (min g_{powder}/mg), K_2 is Peleg's capacity constant (g_{powder}/mg), k and n are Page's constant, C_e is the equilibrium concentration of TPC in the plants (mg/g_{powder}), b is washing coefficient and k_3 is slow extraction coefficient (min^{-1}).

3. Results and Discussions

Based on the methodology described, discussions of results are separated into four sessions, which are determination of the optimum drying temperature, analysis of single factor experiments, analysis of response surface methodology and fitting the extraction kinetic models of red dates. The data was expressed as the average of three replicates ± standard deviation.

3.1 Determination of the Optimum Drying Temperature

Red dates were dried under four different drying temperatures, which were 50, 60, 70 and 80°C. The effects of drying temperature on crude extract and TPC yield of red dates were listed in Table 1. Based on Table 1, the crude extract and TPC yield of red dates increased with higher drying temperature up to 60°C. The heating affects the bioavailability of total phenolic compounds [9]. The heat energy provided during drying process may break the connections between phenolic compounds and the fibre of red dates which is insoluble. Hence, the releasing of phenolic compounds throughout drying process has showed that the bioavailability of total phenolic compounds is increased by heating. Thus, the crude extract and TPC yield increased together with high drying temperature up to 60°C.

However, at drying temperature of 70 and 80°C, the crude extract and TPC yield of red dates started to decrease. The possible reason may be the thermal degradation of total phenolic compounds started from high drying temperature 70°C [10]. Similar to the results of previous findings, in this research, the optimum drying temperature was 60°C as the highest crude extract and TPC yield were obtained under drying temperature of 60°C [11].

Table 1. Effects of drying temperature on crude extract and TPC yield

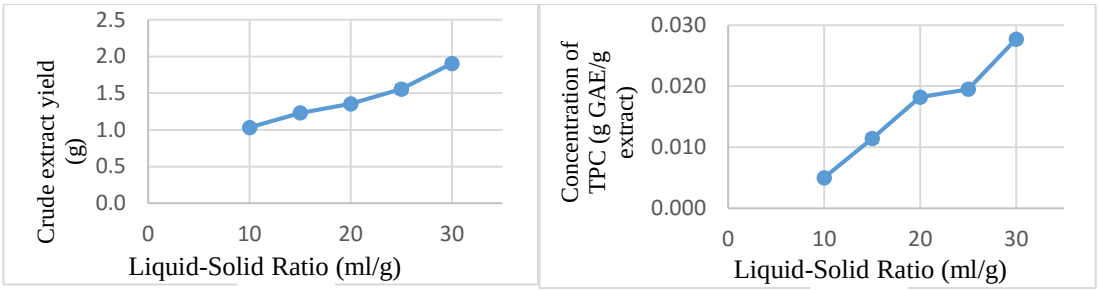
Temperature (°C)	Crude extract yield (g)	TPC yield (g GAE/g extract)
50	4.44±0.067	0.022±0.00006
60	4.56±0.089	0.023±0.00009
70	4.41±0.022	0.022±0.00004
80	4.37±0.038	0.021±0.00001

3.2 Analysis of Single Factor Experiments

Single factor experiments were conducted to determine the optimum range of each factor for RSM. The four factors involved were liquid-solid ratio, ultrasonic power, extraction temperature and extraction time. The effects of each factor on crude extract and TPC yield were further discussed in section 3.3.1 to 3.3.4.

3.2.1 Effect of Liquid-Solid Ratio on Crude Extract and TPC Yield

Based on Fig. 1, the concentration of TPC increased together with liquid-solid ratio. The concentration of TPC increased from 0.005±0.0001 to 0.0277±0.0007g GAE/g extract and the crude extract yield increased from 1.032±0.0009 to 1.905±0.053 g when the liquid-solid ratio increased from 10 to 30 ml/g. The two graphs are having similar trend. This was because more solutes can be dissolved into solvent as the volume of solvent was larger and the contact area of solute and solvent increased [5]. At the same time, as the contact area of solute and solvent increased, the rate of mass transfer of total phenolic compounds from cell into solvent increased, thus resulting higher TPC yield. Hence, the optimum range of liquid-solid ratio for RSM was 10 to 30 ml/g as they gave the three highest concentration of TPC.



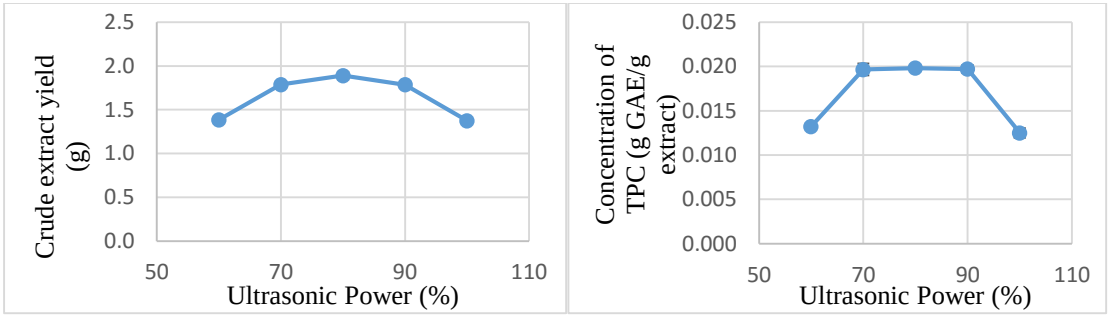
1a. 1b.

Figure 1. Effects of liquid-solid ratio on crude extract yield (1a) and TPC yield (1b).

3.2.2 Effect of Ultrasonic Power on Crude Extract and TPC Yield

Ultrasonic power is another factor that affects TPC and crude extract yield. Based on Fig. 2, the TPC and crude extract yield were having the similar trend. The concentration of TPC increased from 0.0132±0.0001 to 0.0198±0.00004 g GAE/ g extract and the crude extract yield increased from 1.385±0.023 to 1.889±0.0429 g with higher ultrasonic power up to 80%. This may due to the cavitation shear stress created by ultrasound to break the cell wall of red dates increased, thus, more TPC was able to diffuse out from the cell wall into solvent [12]. As reported from previous research, TPC is having higher stability at higher ultrasonic power [13]. Thus, more TPC was found in the solvent and the crude extract was heavier after removing the solvent.

However, under ultrasonic power of 90%, the concentration of TPC was slightly decreased from 0.0198±0.00004 to 0.0197±0.0005 g GAE/ g extract while the crude extract yield decreased from 1.889±0.0429 to 1.785±0.0247g. The small decrement of the two responses might due to the TPC yield has become saturated as the phenolic compounds have been dissolved into the solvent. Besides that, at 100% of ultrasonic power, a large decrement of concentration can be seen in Fig. 2. The concentration of TPC decreased might due to the degradation of TPC [14]. Hence, the optimum range of ultrasonic power for RSM was 70 to 90%.



2a. 2b.

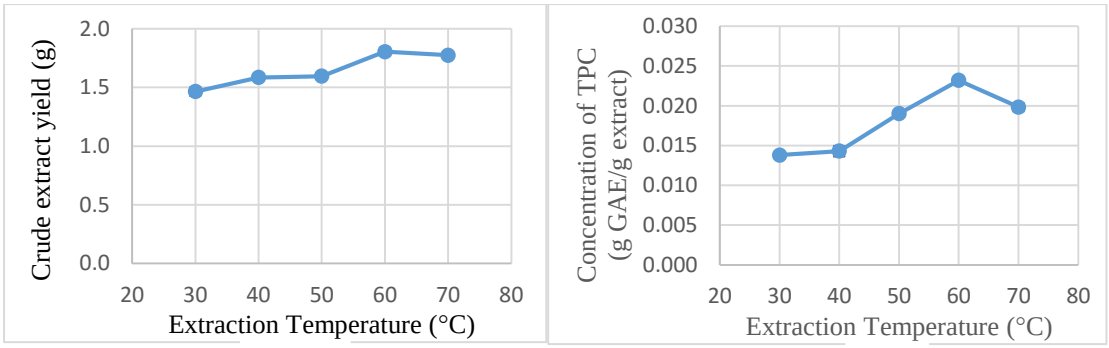
Figure 2. Effects of ultrasonic power on crude extract yield (2a) and TPC yield (2b).

3.2.3 Effect of Extraction Temperature on Crude Extract and TPC Yield

Based on Fig. 3, the crude extract yield increased rapidly from 1.465±0.0365 to 1.805±0.0337g and the concentration of TPC increased from 0.0138±0.0003 to 0.0232±0.0003 g GAE/g extract as the extraction temperature was getting higher up to 60°C. The positive effects of extraction temperature on the responses could be due to

the molecules gained the energy provided by heating up the extract in the ultrasonic bath. The molecules vibrated violently when they gained the energy and broke the connections between the cell wall and TPC. Thus, TPC was able to diffuse into the solvent more easily. TPC is also readily stable under higher extraction temperature up to 60°C [15]. Apart from that, the solubility of molecules in red dates increased together with extraction temperature [16].

From Fig. 3, the crude extract yield and concentration of TPC dropped from 1.805±0.0337 to 1.775±0.0266g and 0.0232±0.0004 to 0.0198±0.0001 g GAE/g extract respectively when the extraction temperature increased to 70°C. It could be due to the decreasing of cavitation effect by ultrasonic with the increasing of extraction temperature. It caused lesser cavitation bubbles to collapse at the surface of red dates and thus, lesser TPC was extracted. Furthermore, TPC was proved to be thermo-sensitive and they underwent degradation at temperatures beyond 60°C [5]. Thus, the optimum range of extraction temperature for RSM was 50 to 70°C.



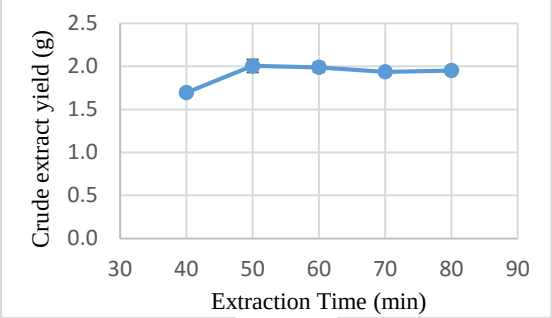
3a. 3b.

Figure 3. Effects of extraction temp. on crude extract yield (3a) and TPC yield (3b).

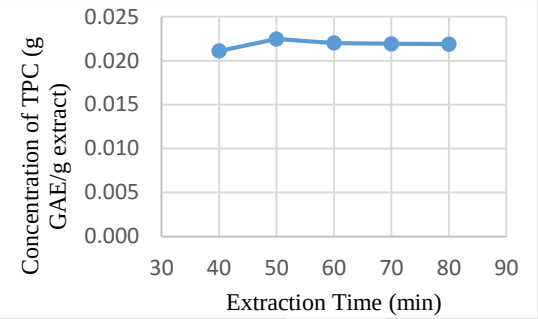
3.2.4 Effect of Extraction Time on Crude Extract and TPC Yield

Based on Fig. 4, it can be seen that the concentration of TPC increased from 0.0211±0.0004 to 0.0225±0.0002 g GAE/g extract at the beginning but started to decrease from 0.0225±0.0002 to 0.0219±0.0001 g GAE/g extract when extraction time exceeded 50 min. The crude extract yield increased from 1.695±0.0365 to 2.007±0.0744 g for extraction time below 50 min and decreased from 2.007±0.0744 to 1.953±0.0126 g for extraction time more than 50 min.

At extraction time of 40 min, the TPC and crude extract yield and were lower because there wasn't sufficient time for the extraction process to reach equilibrium. The rate of mass transfer of total phenolic compounds from red dates into solvent increased significantly with extraction time until 50 min. The concentration of TPC has reached equilibrium state at extraction time of 50 min as it gave the highest TPC yield. For extraction time longer than 50 min, the TPC yield decreased rapidly. It could be due to the total phenolic compounds were not stable and they started to decompose [17]. Another reason might be more impurities were extracted from red dates by cavitation effect and affected the purity of TPC. Hence, the optimum range of extraction time for RSM was 40 to 60 min.



4a.



4b.

Figure 4. Effects of extraction time on crude extract yield (4a) and TPC yield (4b).

3.3 Analysis of Response Surface Methodology

Based on the results obtained from single factor experiments, the range of liquid-solid ratio (A), ultrasonic power (B), extraction temperature (C) and extraction time (D) were 20-30ml/g, 70-90%, 50-70°C and 40-60min respectively. The range of parameters were then used to create design of experiments using Design Expert software 7.0 and the experimental results were listed in Table 2. The results were expressed in the average of three runs ± standard deviation.

Table 2. Experimental crude extract and TPC yield for RSM

Run	A	B	C	D	Crude extract yield (g)	TPC yield (g GAE/g extract)
1	25	70	50	50	2.045±0.032	0.0224±0.0002
2	20	80	70	50	1.755±0.014	0.0195±0.0002
3	20	80	60	60	1.855±0.011	0.0298±0.0006
4	25	70	70	50	2.175±0.074	0.0245±0.0001
5	30	90	60	50	2.025±0.051	0.0302±0.0008
6	20	80	50	50	1.315±0.020	0.0265±0.0002
7	25	80	60	50	1.875±0.024	0.0285±0.0001
8	30	80	70	50	2.065±0.083	0.0187±0.0001
9	25	70	60	40	1.715±0.021	0.0269±0.0006
10	30	80	60	60	2.175±0.022	0.0298±0.0009
11	25	90	60	40	1.625±0.008	0.0273±0.0006
12	25	80	60	50	1.945±0.017	0.0278±0.0003
13	30	80	60	40	1.865±0.026	0.0272±0.0003
14	25	90	50	50	1.545±0.009	0.0258±0.0004
15	25	80	70	60	1.785±0.013	0.0155±0.0003
16	20	80	60	40	1.585±0.016	0.0269±0.0002
17	30	80	50	50	1.745±0.007	0.027±0.0007
18	30	70	60	50	2.065±0.002	0.0299±0.0008
19	25	90	70	50	2.045±0.044	0.0165±0.0004
20	20	70	60	50	1.635±0.059	0.0281±0.0004
21	25	80	60	50	2.075±0.006	0.0277±0.0006
22	25	90	60	60	1.875±0.033	0.032±0.0001
23	25	70	60	60	1.845±0.041	0.0317±0.0001
24	20	90	60	50	1.855±0.005	0.0244±0.0001

25	25	80	60	50	2.075±0.052	0.0286±0.0003
26	25	80	70	40	2.015±0.093	0.0184±0.0006
27	25	80	50	60	1.715±0.021	0.0259±0.0002
28	25	80	50	40	0.845±0.015	0.0194±0.0003

Based on Table 2, the range of crude extract yield was 0.845-2.175g, TPC yield was 0.0165-0.032 g GAE/g extract. However, the experiment with highest TPC yield did not give the highest crude extract yield. Thus, for this research, optimising TPC yield of red dates was the main objective. The optimised conditions determined were 30ml/g of liquid-solid ratio, 70% of ultrasonic power, 60°C of extraction temperature and 60min of extraction time. The validation was achieved as the difference between experimental and predicted TPC yield was 9.45% which was less than 10%.

3.3.1 ANOVA for Crude Extract Yield

ANOVA is a statistical method to analyse the significance of parameters. The parameter is considered significant with P-value less than 0.05. Based on Table 3, liquid-solid ratio (A), extraction temperature (C), extraction time (D) and the interaction of extraction temperature and time (CD) affected the crude extract yield significantly. Ultrasonic power (B) and all the interactions of the four parameters were not significant due to their large P-value. Furthermore, the quadratic model can be used to explain the responses of crude extract yield due to its low p-value 0.0029 ($p < 0.05$). In addition, the p-value of lack of fit ($P = 0.1939$) indicated the lack of fit for this model was not significant. In other words, the quadratic model was highly fitted to the experimental data of crude extract yield.

Table 3.ANOVA for crude extract yield

Source	Sum of squares	df	Mean square	F value	P-value
Model	1.82	14	0.13	5.08	0.0029
A	0.31	1	0.31	12.27	0.0039
B	0.022	1	0.022	0.85	0.3739
C	0.58	1	0.58	22.55	0.0004
D	0.21	1	0.21	8.35	0.0127
AB	0.017	1	0.017	0.66	0.4308
AC	0.0036	1	0.0036	0.14	0.7135
AD	0.0004	1	0.0004	0.016	0.9024
BC	0.034	1	0.034	1.34	0.2680
BD	0.0036	1	0.0036	0.14	0.7135
CD	0.30	1	0.30	11.84	0.0044
A^2	0.017	1	0.017	0.65	0.4356
B^2	0.0007594	1	0.0007594	0.030	0.8658
C^2	0.16	1	0.16	6.29	0.0261
D^2	0.20	1	0.20	7.82	0.0151
Residual	0.33	13	0.026		
Lack of Fit	0.30	10	0.03	3.06	0.1939
Pure Error	0.030	3	0.00982		
Cor Total	2.15	27			

The relationships of linear, interaction and quadratic effects of each parameters were expressed in a quadratic equation, Eq.(5). Eq.(5) can also be used to predict the crude extract yield under different extraction conditions.

$$\text{Crude extract yield} = \begin{aligned} &-17.3675 + 0.26733A - 0.0603B + 0.29692C \\ &+ 0.33183D - 0.0013AB - 0.0006AC + 0.0002AD \\ &+ 0.000925BC + 0.00003BD - 0.00275CD - 0.0021A^2 \\ &+ 0.00001125B^2 - 0.0016375C^2 - 0.001825D^2 \end{aligned} \quad (5)$$

To simplify the quadratic equation created using Design Expert Software Version 7.0, the non-significant (P > 0.05) factors and interactions were removed. The simplified equation, Eq (6) was showed below:

$$\text{Crude extract yield} = \begin{aligned} &-19.0265 + 0.0323A + 0.3460C \\ &+ 0.3526D - 0.00275CD - 0.001555C^2 - 0.001743D^2 \end{aligned} \quad (6)$$

The correlation coefficient (R^2) of Eq.(6) was 0.7987 while the R^2 of Eq.(5) was 0.8455. The R^2 of Eq.(5) was higher than Eq.(6). It can be said that the predicted responses value from Eq.(5) were closer to the fitted regression line compared to Eq.(6). Thus, Eq.(5) was suitable to be used to predict crude extract yield instead of Eq.(6).

The parameters with positive coefficient from Eq.(5) gave positive effects to crude extract yield while the parameters with negative coefficient gave negative effects to crude extract yield. Based on Eq.(5), the coefficients of liquid-solid ratio, extraction temperature and time were positive. Thus, the crude extract yield increases together with liquid-solid ratio, extraction temperature and time.

3.3.2 ANOVA for TPC Yield

Based on Table 4, extraction temperature (C), extraction time (D), the interaction of ultrasonic power and extraction temperature (BC), ultrasonic power and extraction time (BD) and quadratic term of extraction temperature (C^2) were significant in affecting TPC yield due to their low p-values (P < 0.05). The other parameters and interactions of the four parameters were not significant as their p-values were more than 0.05. In addition, the p-value of quadratic model for TPC yield was 0.0016. The experimental results were highly fitted to the quadratic model due to its low p-value. The lack of fit of the model was also calculated using Design Expert Software Version 7.0 to analyse the error in the model. The value of lack of fit of this quadratic model was 0.5342, which was less than 0.05. It can be said that the quadratic model was very close to the responses of experimental TPC yield.

Table 4. ANOVA for TPC yield

Source	Sum of squares	df	Mean square	F value	p-value
Model	0.0004675	14	0.00003339	5.78	0.0016
A	0.000003715	1	0.000003715	0.64	0.4370
B	0.000003203	1	0.000003203	0.55	0.4697
C	0.00007489	1	0.00007489	12.96	0.0032
D	0.00003571	1	0.00003571	6.18	0.0273
AB	0.000004	1	0.000004	0.69	0.4204

AC	8.327×10^{-8}	1	8.327×10^{-8}	0.014	0.9063
AD	0.000001823	1	0.000001823	0.32	0.5839
BC	0.00002704	1	0.00002704	4.68	0.0497
BD	2.5×10^{-9}	1	2.5×10^{-9}	0.0006891	0.9795
CD	0.00000484	1	0.00000484	0.84	0.3767
A^2	0.000007066	1	0.000007066	1.22	0.2888
B^2	0.000006551	1	0.000006551	1.13	0.3063
C^2	0.0002364	1	0.0002364	40.92	< 0.0001
D^2	2.226×10^{-7}	1	2.226×10^{-7}	0.039	0.8474
Residual	0.0000751	13	0.00000577		
Lack of Fit	0.00005885	10	0.000005885	1.09	0.5342
Pure Error	0.00001625	3	0.000005417		
Cor Total	0.0005426	27			

A quadratic equation, Eq.(7) was formed to predict the TPC yield under different conditions. The coefficients of extraction temperature and time were positive while the coefficient of liquid-solid ratio ultrasonic power were negative. Hence, the TPC yield increases if lower liquid-solid ratio, lower ultrasonic power, extraction temperature and time are used.

$$\begin{aligned} TPC\ yield = {} & -0.19853 - 0.00451A - 0.000663B + 0.00984C \\ & + 0.000688D + 2\times10^{-5}AB - 2.886\times10^{-6}AC + 1.35\times10^{-5}AD \\ & - 2.6\times10^{-5}BC - 2.5\times10^{-7}BD - 1.1\times10^{-5}CD \\ & + 4.34\times10^{-5}A^2 + 1.05\times10^{-5}B^2 - 6.27\times10^{-5}C^2 - 1.93\times10^{-6}D^2 \end{aligned} \quad (7)$$

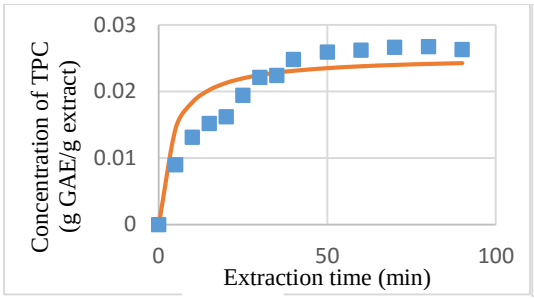
By removing the non-significant factors and interaction, Eq.(7) was simplified to Eq.(8).

$$TPC\ yield = 0.028 - 0.002498C + 0.001725D - 0.0026BC - 0.0066C^2 \quad (8)$$

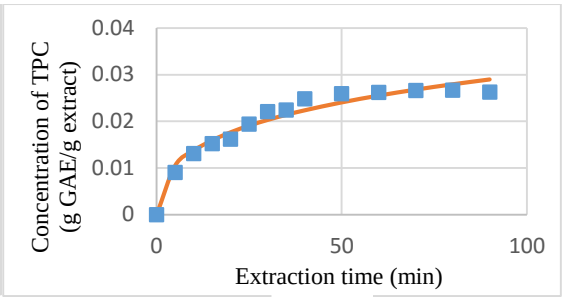
The correlation coefficients (R^2) of Eq.(7) and Eq.(8) were 0.9173 and 0.8042 respectively. The R^2 of Eq.(7) dropped from 0.9173 to 0.8042 after simplifying. By considering more factors and interactions, the predicted values determined using Eq.(7) were closer to the regression line. Thus, Eq. (7) was highly suitable to be used to predict the TPC yield due to its high R^2 value, 0.9173.

3.4 Fitting the Extraction Kinetic Models of Red Dates

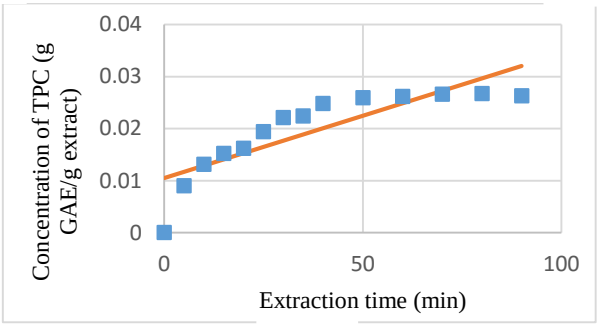
In this research, the experimental data was compared with the predicted data using three kinetic models (Peleg's model, Page's model, Ponomaryov's model). Fig. 5-7 show the comparison graphs of experimental data and the three mentioned kinetic models respectively. The results are showed in Table 5.



5a.



5b.



5c.

Figure 5. Fittings of Peleg's model (5a), Page's (5b) and Ponomaryov's model (5c)

Table 5 Root mean square error (RMSE), coefficient of determination (R^2) and models' constants of kinetic models

Model	Model's constants	R^2	RMSE
Peleg's model	K_1=148.1, K_2=39.65	0.824	0.003506
Page's model	k=5.241, n=-0.08715	0.9663	0.001534
Ponomaryov's model	k_3=0.02623, b=2.157, C_e=-0.009102	0.716	0.004652

The calculated models' constants were showed in Table 5. As shown in Fig. 5, the line of predicted data calculated using Page's model passed through the most experimental data points compared to the rest of kinetic models. In addition, R^2 and RMSE of each model were calculated using Matlab Curve Fitting Tool 2017. The experimental data is highly fitted to the kinetic model if the value of R^2 is close to unity while RMSE is close to zero. Based on Table 5, the model with the highest R^2, 0.9663 and lowest RMSE, 0.001534 was Page's model. Therefore, Page's model was the most suitable to describe the extraction process of TPC from red dates among the mentioned models. The fittings of the mentioned models were in order of: Page's model > Peleg's model > Ponomaryov model.

Validation of extraction kinetic model was carried out to ensure that the most suitable kinetic model (Page's model) to describe the extraction process of TPC from red dates is reliable. The experimental results of TPC yield under optimum extractions at 45 min, 65 min and 85 min were compared with the predicted data calculated using Page's model, Eq. (9). The differences of experimental and predicted data are showed in Table 6.

Page's model: $C(t) = e^{-(5.241 \times t^{-0.08715})}$ (9)

Table 6. Difference of experimental and predicted TPC yield

Extraction time (min)	TPC yield (g GAE/g extract)		Difference (%)
	Experimental	Predicted	
45	0.0253±0.0002	0.0233	8.20
65	0.0250±0.0004	0.0262	4.83
85	0.0259±0.0002	0.0285	9.97

Based on Table 6, the differences between experimental and predicted TPC yield at extraction time 45, 65 and 85 min were 8.2%, 4.83% and 9.97% respectively. The validation of extraction kinetic model was achieved as the differences between experimental and predicted TPC yield were less than 10%. Therefore, Page's model was most reliable and most suitable to be used to predict the TPC yield of red dates at different extraction times.

4. Conclusion

In this research, the optimised conditions to extract total phenolic compounds from red dates were determined using response surface methodology. The optimum value for liquid-solid ratio, ultrasonic power, extraction temperature and extraction time were 30ml/g, 70%, 60°C and 60 min respectively. Besides that, among three extraction kinetic models, Page's model is the most suitable to be used to describe the extraction kinetics of total phenolic compounds of red dates due to its coefficient of determination (R^2) was the closest to unity, 0.9663 while its root mean square error (RMSE) was the closest to zero, 0.001534.

Acknowledgement

The author would like to express her gratitude to her supervisor, Dr. Chua Bee Lin for her support, guidance and encouragement. The author also would like to give appreciation to lab assistants from Taylor's University for their advices.

References

[1] B. Valdivia-Correa, C. Gómez-Gutiérrez, M. Uribe, and N. Méndez-Sánchez, "Herbal medicine in Mexico: A cause of hepatotoxicity. A critical review," *Int. J. Mol. Sci.*, vol. 17, no. 2, pp. 48–49, 2016.

[2] B. A. S. Norhasidah S, Z.Farahniza, A.G. Maaruf, E.U. Engku Hanisah, "Antioxidative properties of edible bird's nest mincroparticulates incorporated into red dates drink," pp. 4–6, 2014.

[3] S. Yao, "Past , Present , and Future of Jujubes — Chinese Dates in the United States," *HortScience*, vol. 48, no. 6, pp. 672–680, 2013.

[4] S. S. Al Harthi, A. Mavazhe, H. Al Mahroqi, and S. A. Khan, "Quantification of phenolic compounds, evaluation of physicochemical properties and antioxidant activity of four date (Phoenix dactylifera L.) varieties of Oman," *J. Taibah Univ. Med. Sci.*, vol. 10, no. 3, pp. 346–352, 2015.

[5] Y. C. Yang, M. C. Wei, T. C. Huang, S. Z. Lee, and S. S. Lin, "Comparison of modified ultrasound-assisted and traditional extraction methods for the extraction of baicalin and baicalein from Radix Scutellariae," *Ind. Crops Prod.*,

vol. 45, pp. 182–190, 2013.

[6] A. Dailey and Q. Vuong, "Optimum Conditions for Microwave Assisted Extraction for Recovery of Phenolic Compounds and Antioxidant Capacity from Macadamia (Macadamia tetraphylla) Skin Waste Using Water," *Processes*, vol. 4, no. 1, p. 2, 2015.

[7] S. Jokic, D. Velic, M. Bilic, Ana Bucic-Kojic, M. Planinic, and S. Tomasa, "Modelling of the process of solid-liquid extraction of total polyphenols from soybeans," *Czech J. Food Sci.*, vol. 28, no. 3, pp. 206–212, 2010.

[8] N. Anuar, A. F. Mohd Adnan, N. Saat, N. Aziz, and R. Mat Taha, "Optimization of extraction parameters by using response surface methodology, purification, and identification of anthocyanin pigments in melastoma malabathricum fruit," *Sci. World J.*, vol. 2013, 2013.

[9] H. S. Kim and K. B. Chin, "Effects of Drying Temperature on Antioxidant Activities of Tomato Powder and Storage Stability of Pork Patties," *Korean J. Food Sci. Anim. Resour.*, vol. 36, no. 1, pp. 51–60, 2016.

[10] J. A. Larrauri, P. Rupérez, and F. Saura-Calixto, "Effect of drying temperature on the stability of polyphenols and antioxidant activity of red grape pomace peels.," *J. Agric. Food Chem.*, vol. 45, pp. 1390–1393, 1997.

[11] M. Planinić, "Influence of Temperature and Drying Time on Extraction Yield of Phenolic Compounds from Grape Pomace Variety 'Portogizac,'" *Chem. Biochem. Eng. Q.*, vol. 29, no. 3, pp. 343–350, 2015.

[12] B. Karki, "Use of high-power ultrasound during soy protein production and study of its effect on functional properties of soy protein isolate," 2009.

[13] F. F. S.Rodrigues, *Advances in Fruit Processing Technologies*. New York: Taylor & Francis Group, 2012.

[14] A. E. Ince, S. Şahin, and S. G. Şümnü, "Extraction of phenolic compounds from melissa using microwave and ultrasound," *Turkish J. Agric. For.*, vol. 37, no. 1, pp. 69–75, 2013.

[15] N. Ruenroengklin, J. Zhong, X. Duan, B. Yang, J. Li, and Y. Jiang, "Effects of various temperatures and pH values on the extraction yield of phenolics from litchi fruit pericarp tissue and the antioxidant activity of the extracted anthocyanins," *Int. J. Mol. Sci.*, vol. 9, no. 7, pp. 1333–1341, 2008.

[16] W. Qu, Z. Pan, and H. Ma, "Extraction modeling and activities of antioxidants from pomegranate marc," *J. Food Eng.*, vol. 99, no. 1, pp. 16–23, 2010.

[17] U. K. Ibrahim, E. A. Austin, and R. Mohd Salleh, "Effect of Drying Temperature and Time on Antioxidant and Total Phenolic Content in <i>Garcinia mangostana</i> Pericarp," *Adv. Mater. Res.*, vol. 1113, pp. 279–284, 2015.

Drying Kinetics and Optimisation of Pectin Extraction from Banana Peels via Response Surface Methodology

Chong Yek Cze*, Chua Bee Lin

School of Engineering, Taylor's University, Malaysia.

*yekcze.chong@sd.taylors.edu.my

Abstract

Banana peels which are the waste in abundance, are used to extract valuable pectin. The gelling ability of the pectin has gained attention in food and pharmaceutical industries. This research aims to select the best drying kinetic model for banana peels and also optimize the ultrasound extraction process of pectin using Box-Behnken response surface design (BBD). Determination of gelling mechanism of pectin using degree of esterification (DE) is also focused in this research. In this study, oven drying with temperature 50°C was chosen as the best drying temperature as it gave the highest extraction yield. Furthermore, The new model, Page-Two-term model was selected as the best model to describe the drying kinetics of banana peels due to highest R^2 value (0.9991) and lowest RMSE value (0.001). BBD was also used to optimise the extraction temperature, extraction time and solid-liquid ratio (SLR) to obtain the highest pectin yield. The optimal conditions were 75°C extraction temperature, 23 min extraction time and 1:33.3 g/ml SLR with maximum predicted pectin yield of 6.19%. The actual pectin yield extracted using the optimal conditions were $6.08 \pm 0.2\%$ which was in close agreement with the predicted value with only small error percentage of 1.78%. Likewise, the DE for both pectins extracted using unoptimised and optimised conditions were $71.92 \pm 1.38\%$ and $76.1 \pm 2.07\%$ respectively. Both of the pectins were classified as high-methoxyl pectins as the DE of both pectins were above 50%. Besides that, the pectin with higher DE also indicated that the rate of gel formation is higher. According to the results, it can be concluded that the pectin did not degraded yet the pectin yield and gelling time has successfully improved after optimised the pectin extraction process using BBD. From this study, banana peel revealed as a potential alternative pectin source due to the comprising results.

Keywords: Banana peels, Pectin, Drying kinetics, RSM, Degree of esterification.

1. Introduction

Banana (*Musa*) is one of the popular food crops that can found in the world market. Banana is generally processed into value-added product such as chips and jam. Because of the high demands of banana products, abundant of banana peels are produced every day and it has reported that about 39000 tons of banana peels are generated annually in U.S [1]. Hence, many scientists tend to find out the application of the banana peels to reduce the industrial waste and a valuable compound, pectin is found in the banana peels [2].

Pectin is a polysaccharide that consists of ∝-(1,4) galacturonic acid [1]. It is widely used as gelling agent for puree and jelly preparation [1]. Pectin is also proved to have wound healing and cholesterol-lowering effects [3]. Pectin is categorized based on the gelling mechanism using degree of esterification (DE) [2]. Pectin can be divided into low-methoxyl (LM) pectin (DE < 50%) and high-methoxyl (HM) pectin (DE > 50%). LM pectin forms gels under divalent ions whereas HM pectin form gels under high sugar concentration solution [4]. Likewise, the gel formation rate of pectin can be determined by DE. Pectin is classified as slow gelling (DE 58-65%) or fast gelling (DE > 72%) [2]. It is important to analyze the esterification degree of pectin because it is used to determine the suitability of end products [2].

Drying is the primary process prior to pectin extraction process. It is normally performed using natural sunlight or artificial dryer such as oven [5]. Drying is used to preserve the quality and extend the shelf life of the foodstuffs by reducing the moisture content to desired level [6]. Sun drying is the conventional method to preserve foodstuffs as it is renewable and low in cost. Yet, large-scale production is not always preferred to use sun drying [7]. Hence, artificial dryer is the alternative to provide uniform and fast drying process. With regards to this, both methods were studied in this research.

Thin-layer drying kinetic models are the mathematical modelling that used to predict the drying behaviour and time of food products [6]. Many popular drying models such as Page, Logarithmic, Henderson and Pabis models have successfully described the drying kinetics of various plants [5], [8, 9]. Besides, some new models have developed to improve the accuracy [5], [10]. For instances, a new model which combined the Page and Two-term drying models has proved to give a promising results for cocoa beans [5]. These two models are chosen because both of them give favourable fitting in many applications according to past experience [5]. Yet, this new model, Page-two-term model has only been used in cocoa beans [5]. Regarding to this, this model was performed in this research to study the potential of this new model applies on banana peels and also compared with the Page and Two-term models.

Extraction of pectin can be achieved using acid, ultrasound-assisted (UAE) and microwave-assisted extraction (MAE) [11]. However, UAE which used the acoustic energy to break the cell wall, has gained a lot of attention these years [12]. This is because UAE reduces the extraction time and increases the extraction yield with lower energy consumption [12]. With this respect, UAE was selected to extract the pectin from banana peels in this research.

To the best of author's knowledge, no research has been conducted to study both drying kinetics and optimisation of pectin extraction from banana peels using RSM together [13, 14]. Hence, the present study is carried out with the objectives as follows:

1. To select the best drying models to describe the drying process of banana peels.
2. To optimise the pectin yield with different extraction parameters (extraction temperature, extraction time and solid-liquid ratio) using Box-Behnken response surface design (BBD).
3. To determine the gelling mechanism of pectin based on degree of esterification using titrimetric method of Food Chemical Codex 1981.

2. Methodology

This section discusses about the methods that carried out in this research in order to accomplish the objectives.

2.1 Pre-treatment of Banana Peels

Ripened banana peels were collected from a commercial fruit juice store in Taylor's University, Subang Jaya, Selangor, Malaysia. 100 g of banana peels were washed with distilled water to remove dirt on the surface before cutting into slices.

2.2 Drying of Banana Peels

In this research, the oven drying was compared with the conventional method which is sun drying. The drying method that produced the highest pectin yield was selected for modelling. The initial moisture content of the samples was measured using moisture analyser (Model XM50, Precisa Gravimetrics AG, Switzerland) to estimate the bone-dry weight before drying. All the samples were spread evenly in single layer on an aluminium tray to avoid any overlapping.

For sun drying, the samples were dried under the sun from 9 a.m. to 5 p.m. and tempered from 5 p.m. to 9 a.m. until it reached constant weight [6]. Weighing balance (Model TX423L, Shimadzu, Japan) was used to measure the weight of the samples. The surrounding temperature (32°C), humidity (79.7%) and wind velocity (2.6 m/s) were measured using HVAC datalogger (Model DO2003, Delta OHM, Italy). For oven drying, The peels were dried in an oven (Model UN75, Memmert, Germany) with different temperature 40°C, 50°C, 60°C and 70°C until the weight of samples reached constant.

After drying, the dried banana peels were grinded into powder using a grinder (Model BL-1525 BG OEM, China). The powdered peels were kept in polyethylene bag at room temperature for further analysis.

2.3 Mathematical Modeling and Statistical Analysis

The optimum drying method and temperature that produced the highest pectin yield was used to study the drying kinetic models. 100g of pre-treated banana peels were dried using the optimum drying method/temperature and the weight loss of the banana peels was measured every 5 minutes until constant weight was obtained. The moisture content (MC) and moisture ratio (MR) of banana peels were calculated using Eq. (1) and Eq. (2) [5], [15].

$$MC \text{ (dry basis)} = \frac{w_i - w_{db}}{w_i} \quad (1)$$

where, w_i is the initial weight of the sample (g) and w_{db} is the bone-dry weight (g).

$$MR = \frac{M - M_e}{M_o - M_e} \quad (2)$$

where, M_o is the initial moisture content, M is the moisture content at time and $M_e$is the moisture content at equilibrium.

The experimental data were fitted into the three drying kinetic models as shown in Table 1. Microsoft Excel SOLVER 2016 was used for non-linear regression analysis [5]. In non-linear regression analysis, statistical indicators, coefficient of determination (R^2) and root mean square error (RMSE) were used to determine the fitting goodness [5], [15]. The formula of R^2 and RMSE are as follow.

$$R^2 = 1 - \frac{\sum_{i=1}^{N}(MR_{Exp.i} - MR_{Pred.i})^2}{\sum_{i=1}^{N}(MR_{Exp.i} - \overline{MR_{Pred.i}})^2} \quad (3)$$

$$\text{RMSE} = \sqrt{\frac{1}{N}\sum_{i=1}^{N}(MR_{Exp.i} - MR_{Pred.i})^2} \quad (4)$$

where, z is the constant number, N is the data number has run, $MR_{exp,i}$ and $MR_{pred,i}$ are the experimental and predicted moisture ratio value respectively.

Table 1. Drying kinetic models

No.	Model	Equation	Ref.
1	Page	$MR = e^{-kt^n}$	[17]
2	Two-term	$MR = ae^{-kt} + ce^{-gt}$	[5]
3	Page-Two-term	$MR = ae^{-kt^n} + ce^{-gt^n}$	[5]

2.4 Ultrasound-assisted Extraction (UAE) of Pectin

The UAE process was conducted based on publication with minor modification [11, 12]. Four gram of powdered banana peels was added into 0.1 M of citric acid with pH 1.5 and SLR 1:30 g/ml. The mixture was then placed in the ultrasonic water bath (Elmasonic P120H, Elma, Germany) with temperature 80˚C and sonicated for 60 min. The power and frequency of sonicator are set to 80 W and 37 kHz respectively. The mixture was left to cool down and then filtered out using a vacuum filtration. The

filtrate was precipitated using 95% of ethanol with ethanol-to-filtrate ratio 2:1 v/v. The precipitate and filtrate were then separated using a centrifuge (Scanspeed 1236MG, LaboGene, Denmark) at 6000 RPM for about 30 min. The precipitated pectin was rinsed with 95% ethanol thrice to remove impurities and then dried in the oven with temperature 50 ˚C for 12 hours. The pectin yield based on the total peels used for extraction was calculated using Eq. (5).

$$\text{Pectin yield } (\%) = \frac{\text{weight of dried pectin (g)}}{\text{initial weight of dried banana peel powder (g)}} \times 100 \quad (5)$$

2.5 Experimental Design using RSM

Box-Behnken Design (BBD) in Design Expert 7.0 Software was used to optimize the pectin extraction conditions from banana peels. Three independent variables (X_1: extraction temperature, X_2: extraction time and X_3: solid-liquid ratio) were employed as these factors were found to be important in affecting the pectin yield based on previous study from publication [18]. For each factor, the level of the factor was chosen by taking the reference from previous work [18]. The three variables with their corresponding coded and actual values is shown in Table 2. By inserting the parameters and levels into BBD, 17 sets of experiment with different extraction conditions were developed as shown in Table 6. The variables in different level combination arranged by the BBD were used for pectin extraction using UAE method as mentioned in Section 2.4.

Table 2. Extraction parameters and levels

Extraction Parameters	**Code**	**Levels**		
		-1	**0**	**1**
Extraction temperature (°C)	X_1	60	70	80
Extraction time (min)	X_2	20	40	60
Solid-liquid ratio (w/v)	X_3	1:20	1:30	1:40

2.6 Statistical Analysis and Validation of Optimal Conditions

Design Expert Statistical 7.0 Software was used to study the experimental data with regression analysis. F-test at P-value (0.05) was used to assess the significance of regression coefficients [7]. The regression model adequacy was evaluated by coefficient of determination, R^2 and adjusted R^2 [7]. Besides that, the significant independent variables in the model were assessed using ANOVA with confidence level 95%. Response surface graphs were then generated using the regression coefficients.

The optimum extraction conditions that obtained from BBD were carried out an experiment. Experimental and predicted values were compared to validate the model and error of less than 5% between both values indicates a good fit [15].

2.7 Determination of Degree of Esterification (DE)

The esterification degree (DE) of the sample was determined using titration method with a little modification from publication of [4]. 2 ml of ethanol was added to 0.2 g of dried pectin and the mixture was then dissolved in 20ml of distilled water. The mixture was stirred continuously until the pectin was completely dissolved. 3 drops of phenolphthalein were added to the mixture and 0.1M of NaOH was used to titrate the mixture until it turned into pale pink. The titration volume (V_1) was recorded. Next, the mixture was added with 10ml of 0.1M NaOH and stirred continuously for an hour. 10ml of 0.1M HCl was added and the mixture was shaken until the colour of pale pink disappeared. 3 drops of phenolphthalein were added and 0.1M NaOH was used to titrate the mixture until it turned into pale pink. The titration volume (V_2) is recorded. The experiment was repeated for three times. The DE was calculated using Eq. (6).

$$\mathrm{DE}(\%) = \frac{V_1}{V_2+V_1} \times 100 \quad (6)$$

3. Results and Discussion

3.1 Selection of Drying Process and Drying Temperature

Sun drying (conventional method) and oven drying were compared to select the suitable drying method for banana peels. The drying method was selected based on the highest pectin yield. Since the temperature in the oven can be adjusted, different temperature (40°C, 50°C, 60°C and 70°C) were also tested to select the optimum temperature based on the extraction yield. The pectin yield obtained from sun drying and oven drying was tabulated in the following Table 3. According to the results, oven drying with temperature of 50°C was selected as it gave a highest pectin yield.

Table 3. Pectin yield at different drying process

Method	Temperature (°C)	Pectin Yield (%)
Sun drying	32	1.38±0.07
Oven drying	40	2.84±0.12
	50	2.88±0.07
	60	1.92±0.09
	70	1.78±0.08

Sun drying gave the lowest pectin yield (1.38±0.07%) due to rainy season on September 2017. The drying process became less effective as the average daytime temperature was only about 32°C with low wind velocity of 2.6 m/s and high humidity of 79.7%. These conditions increased the enzymatic degradation since the moisture in the peels could not be removed as soon as possible and this activated the microbiological activity, leading to spoilage of the peels [19]. Thus, the cell structure had destroyed by microbiological activity and this resulted in low pectin yield. The limitation of sun drying is the samples could only dry at day time with sunlight whereas oven drying does not have this limitation. Hence, the samples were able to dehydrate faster than sun drying to prevent microbiological spoilage to produce higher pectin.

For oven drying, results showed that the pectin yield increased from 40°C to 50°C and started to decrease after 50°C. Temperature of 50°C gave the highest pectin yield (2.88±0.07%) while 70°C gave the lowest pectin yield (1.78±0.08%). This could be explained as at low temperature, the heat energy was not strong enough to eliminate the moisture as soon as possible and this led to samples spoilage due to microbiological activity [19]. Yet, high temperature dried and harden the peels surface, blocking the moisture to escape [20]. This is also called as "case hardening" [20]. In other words, high temperature dried the food outside but inside still remained moist. This caused the moisture inside the peels could not be evaporated and the trapped moisture caused bacteria growth and spoilage, resulting in low pectin yield [20].

3.2 Drying Kinetics and Modeling

The initial moisture content of the banana peels before drying was measured as 92.15%. It is normal to have high initial moisture content because most of the fruits contain more than 90% of water [21]. It is important to measure the initial moisture content because it is used to estimate the bone-dry weight of the sample. The collected moisture content data was converted to moisture ratio and then plotted in graph as shown in Figure 1. Referring to Figure 1, moisture ratio decreased continuously with time and remained constant after 1400 min. The exponential decreasing curve also shows that internal mass transfer had governed by diffusion [15]. The constant zero moisture ratio at the later phase of the process indicated that the moisture of the samples were fully removed. The moisture ratio data was then fitted to the drying models and the following table 4 shows the goodness of fit of each drying model.

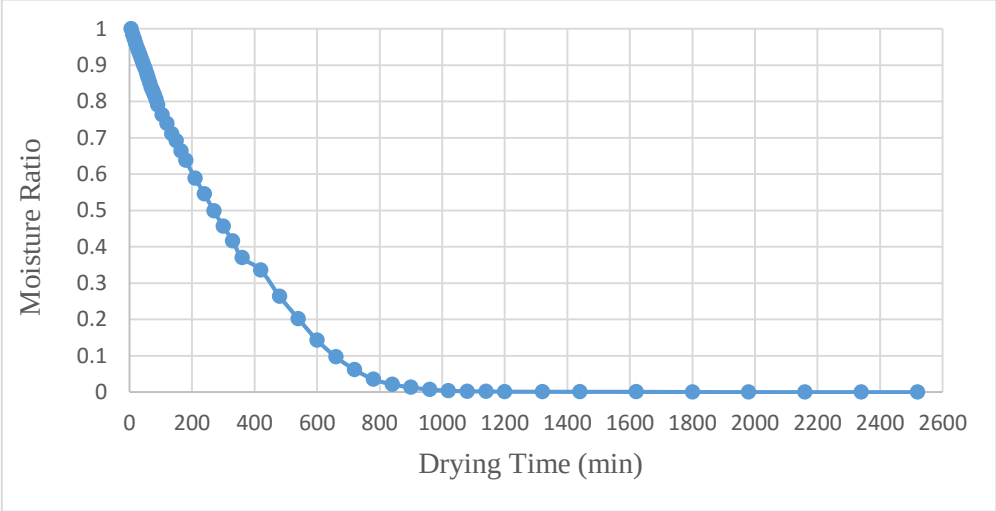


Figure 1. Graph of moisture ratio against drying time

Table 4. The fitness of different models at 50°C drying temperature

No.	Model name	Coefficients and Constants	R^2	RMSE
1	Page	n = 1.164, k = 0.001098	0.9975	0.0026
2	Two-term	a = 0.0181, k = 1.4819, c = 1.0359, g = 0.00297	0.9947	0.0056

3	Page-Two-term	a = 0.09, k = 0.00405, c = 0.9012, g =0.000207, n = 1.4221	0.9991	0.001

According to Table 4, the fitting goodness of the models according to the statistical indicators (R^2 and RMSE) were in the order of: Page-Two-term > Page > Two-term. Page-two-term was selected as the best-fitted drying model to describe the drying process of banana peels as it gave the highest R^2 value (0.9991) and lowest RMSE value (0.001). Similar result has been obtained in cocoa beans plant in previous study [5]. Since Page-Two-term model is the new model that specially developed to describe the drying kinetics of cocoa beans, it can be concluded that this new model is also applicable in banana peels according to the satisfactory results.

3.3 Experimental Design and Regression Analysis

17 experiments were conducted according to the conditions arranged by BBD as shown in Table 5. The experimental results showed the pectin yield ranging from 2.75% to 6.03%. Experiment 17 (X_1= 70°C, X_2 = 20 min and X_3 = 1:20) gave the maximum pectin yield (6.03%$\pm$0.11%) whereas experiment 1 (X_1= 60°C, X_2 = 40 min and X_3 = 1:20) gave the minimum pectin yield with only 2.75%$\pm$0.13%. The influence of extraction parameters on pectin yield was discussed in details in Section 3.4.

Table 5. Box-Behnken design with experimental and predicted pectin yield

Std	Run	Temp, X_1 (°C)	Time, X_2 (min)	SLR, X_3 (g/ml)	Pectin Yield, Y (%)	
					Experimental	Predicted
5	1	60	40	1:20	2.75$\pm$0.13	2.725
1	2	60	20	1:30	4.50$\pm$0.15	4.278
8	3	80	40	1:40	4.50$\pm$0.10	4.525
16	4	70	40	1:30	6.00$\pm$0.14	5.540
12	5	70	60	1:40	3.75$\pm$0.18	3.503
14	6	70	40	1:30	5.20$\pm$0.09	5.540
11	7	70	20	1:40	5.75$\pm$0.28	5.804
3	8	60	60	1:30	3.50$\pm$0.13	3.578
17	9	70	40	1:30	5.50$\pm$0.08	5.540
6	10	80	40	1:20	4.85$\pm$0.13	4.682
7	11	60	40	1:40	3.00$\pm$0.10	3.167
4	12	80	60	1:30	5.00$\pm$0.22	5.221
10	13	70	60	1:20	5.00$\pm$0.15	4.946
13	14	70	40	1:30	5.60$\pm$0.13	5.540
9	15	70	20	1:20	3.83$\pm$0.15	4.076
15	16	70	40	1:30	5.40$\pm$0.17	5.540
2	17	80	20	1:30	6.03$\pm$0.11	5.951

In addition, Table 6 below shows the regression analysis based on the experimental results. ANOVA was used to study the model adequacy and the significant of corresponding variables. Based on rule of thumb, high F-value and p-value lower than 0.05 indicate the model and variable are significant. Referring to the results, quadratic model fitted adequately to the experimental results due to large F-

value (19.45) and small p-value (0.004). Likewise, R^2 and adjusted R^2 are used to check for the model adequacy and suitability. The experimental and predicted values showed a good correlation due to high value of R^2 (0.9616) and adjusted R^2 (0.9121) [1]. Besides, adequate precision measures the error related to the predicted response and the desirable value is above 4 [1]. The results showed that the model's adequate precision value was 13.839 which denoted that the model can be used inside the operation region [1].

Likewise, the significant of the corresponding variables on pectin yield (Y) can also be determined by F-value and p-value in Table 6 as shown as below. The higher the F-value and the smaller the p-value, the more significant the variable is. Linear term of extraction temperature (X_1) had the largest effect because of highest F-value and smallest p-value, followed by the quadratic term of extraction temperature ($X_1{}^2$) and SLR ($X_3{}^2$) and the interaction term of X_2X_3 whilst extraction time (X_2) showed the least significant influence on the pectin yield. However, the results revealed that linear term of SLR (X_3), quadratic effect of extraction time ($X_2{}^2$) and interaction effect of X_1X_2 and X_2X_3 did not have significant effects due to p-values more than 0.05. The following Eq. (7) is the polynomial equation that formulated by the surface model to describe the relationship between the extraction parameters and pectin yield.

$$Y\ (\%) = -55.405 + 1.24237X_1 + 0.10112X_2 + 0.85263X_3 - 0.0000375X_1X_2 - 0.0015X_1X_3 - 0.0039625X_2X_3 - 0.00795X_1{}^2 + 0.00003125X_2{}^2 - 0.0097X_3{}^2 \quad (7)$$

Referring to Eq. (7), the coefficient with higher value indicates it has higher impact on the response. Linear variables (X_1, X_2 and X_3) and quadratic variable ($X_2{}^2$) had positive effect on the pectin yield due to positive coefficients in the equation. Positive coefficient indicated the variable was directly proportional to the response value. Oppositely, negative coefficients of interactions (X_1X_2, X_1X_3 and X_2X_3) and quadratic variables ($X_1{}^2$ and $X_3{}^2$) indicated negative effect on the pectin yield. Negative coefficient showed a curvilinear relationship between the variable and response [23]. Curvilinear relationship means the response increases with the variables (negative coefficient) only up to certain point and starts to decrease after that.

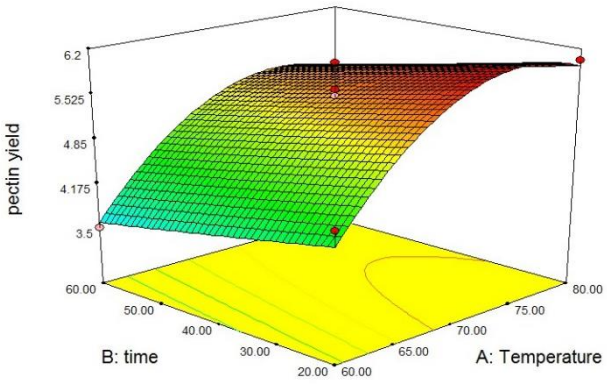
Table 6. Variance analysis for quadratic model of response surface

Source	DF	Sum of Square	Mean Square	F-value	p-value
Model	9	16.18	1.80	19.45	0.0004
X_1	1	5.49	5.49	59.47	0.0001
X_2	1	1.02	1.02	11.07	0.0126
X_3	1	0.041	0.041	0.44	0.5285
X_1X_2	1	2.25×10^{-4}	2.25×10^{-4}	2.435×10^{-3}	0.9620
X_1X_3	1	0.090	0.090	0.97	0.3565
X_2X_3	1	2.51	2.51	27.19	0.0012
$X_1{}^2$	1	2.66	2.66	28.80	0.0010
$X_2{}^2$	1	6.579×10^{-4}	6.579×10^{-4}	7.12110^{-3}	0.9351
$X_3{}^2$	1	3.96	3.96	42.88	0.0003

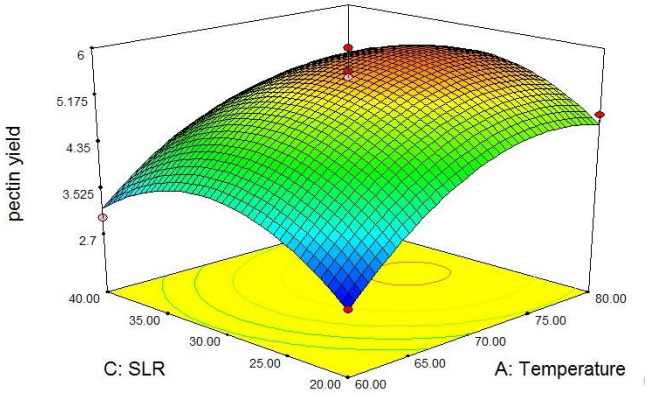
Residual	7	0.65	0.092		
Lack of Fit	3	0.29	0.098	1.12	0.4412
Pure Error	4	0.35	0.088		
Cor Total	16	16.82			
Std. Dev.	0.30				
Mean	4.72				
R^2	0.9616				
Adj-R^2	0.9121				
Adeq Precision	13.839				

3.4 Effect of Extraction Parameters

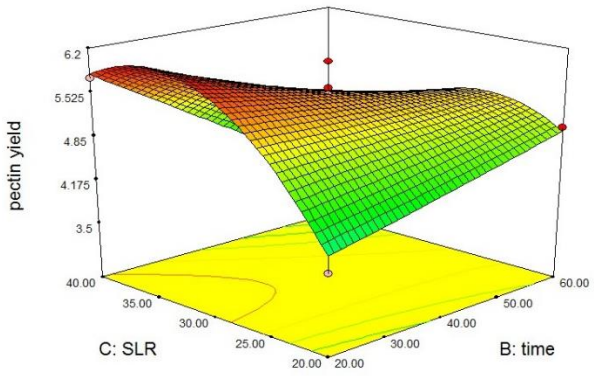
The relationship between the extraction variable was studied with the help of three-dimensional (3-D) response surface graphs in Figure 2 and the influence of extraction variables on response was discussed in Section 3.4.1 to 3.4.3.



(a)



(b)



(c)

Figure 2. Influence of extraction variables on pectin yield. (a) Time vs temperature at 1:30 g/m SLR. (b) SLR vs temperature at 40 minutes. (c) SLR vs time at 70°C temperature.

3.4.1 Effect of Extraction Temperature on Pectin Yield

Fig. 2 shows that pectin yield increased significantly with temperature. The pectin yield decreased slowly after reaching the temperature of 76°C. Similar results has been obtained from previous study of [14]. Increasing temperature disrupt the hydrogen bonds and ester linkages, enhancing the solvent penetration to cause higher extraction yield [12]. However, further increasing the temperature decreases the viscosity and surface tension of the extraction solvent [14]. This reduces the cavitation effects and mass transfer intensity, leading to low pectin yield [14]. Moreover, previous study has also reported that high temperature caused thermal degradation of pectin and this resulted in low pectin yield [24].

3.4.2 Effect of Solid to Liquid Ratio (SLR) on Pectin Yield

Pectin yield was found to increase with SLR until approximately 1:30 g/ml and further increase the solvent volume results in low extraction yield even though SLR was not the significant influence factor according to ANOVA. Similar trend has been found in previous work of [14]. Other than that, 1:30 g/ml of SLR has also been found to produce maximum pectin yield in previous research of [18]. This can be explained as increasing the volume of extraction solvent enhanced the driving force for mass transfer during extraction, leading to higher pectin released into the surrounding solvent [25]. Yet, excess amount of solvent decreased the pectin yield because the solvent was saturated with the solute and this reduced the penetration and mass transfer rate of the pectin into the extraction solvent [26].

3.4.3 Effect of Extraction Time on Pectin Yield

Based on the ANOVA results in Table 7 and Fig. 2c, the extraction time and SLR had significant relationship. At low SLR, the pectin yield increased with extraction time whilst the pectin yield decreased with time at high SLR. This can be explained as at low SLR, the driving force is low due to less amount of extraction solvent hence, more reaction time is required for the mass transfer of pectin to the solution [25]. Nonetheless, the pectin yield decreased with longer sonication time at high SLR because the structure of pectin side chain was destructed and decomposed after prolonged exposure of excessive ultrasound waves [24]. Other than that, as mentioned in Section 3.4.2, high SLR saturated the extraction solvent and this reduced the mass transfer between the pectin and the solvent. Therefore, longer extraction time at high SLR resulted in low extraction yield.

3.5 Determination and Validation of Optimal Extraction Conditions

The optimum extraction conditions (extraction temperature, extraction time and SLR) generated by the Design Expert 7.0 Software were 74.34°C, 22.73 min and 1:33.3 g/ml respectively with the predicted pectin yield of 6.19%. By considering the

operability and limitation of apparatus in real process, the optimal extraction temperature and extraction time were round off to 75°C and 23 min respectively. The suitability of optimized conditions was validated experimentally. The experimental pectin yield obtained was 6.08%±0.2% while the error percentage based on the predicted value was only 1.78 %. The small deviation between the experimental and predicted value might due to the decimal place of the extraction conditions value was round off for operability. Using the unoptimised conditions, only 5% of pectin yield was obtained but the yield had successfully improved by 21.66% after optimisation.

3.6 Esterification Degree of Pectin Before and After Optimisation

The degree of esterification (DE) of the pectin before and after optimisation were compared to determine the gelling mechanism. The DE of the pectin before and optimisation were found as 71.92%±1.38% and 76.1%±2.07% respectively. Both of the DE values were acceptable because the tissue pectin is usually in the range of 60 to 90% [2]. However, the DE of pectin after optimisation was slightly higher than the pectin before optimisation because of lower temperature was used in optimised conditions. Previous research has reported that DE values reduced with higher temperature because the methly esterified carboxyl groups that presented in the pectin chains could be destroyed at high temperature [27].

Since both DE values were above 50%, the pectins were classified as high methoxyl (HM) pectins which can form gel with high sugar concentration. In food industry, HM pectin is suitable to process into high sugar jam and canned food [30]. Besides, the pectins were also classified as fast gelling pectins as the DE values were more than 71% [28]. Since the setting rate increased with DE values, the optimized pectin could form gels faster than the pectin before optimisation due to higher DE value [29]. Based on the results, it can be concluded that, the type of gel formation remained unchanged after optimisation yet the gelling speed had improved.

4. Conclusion

In this study, oven drying with 50°C was suggested as the optimum drying temperature for banana peels because it provided the highest pectin yield. Among three drying models (Page, Two-term and Page-Two-term), Page-Two-term Model was selected as the most suitable model to describe the drying kinetic of banana peels with 0.9991 R^2 value and 0.001 RMSE. Three extraction conditions of pectin extraction from banana peels were optimized using Box-Behnken Design and the optimal conditions were 75°C of extraction temperature, 23 min of extraction time and 1:33.3 g/ml of SLR. Using the optimal conditions, the experimental pectin yield was found as 6.08±0.2% which was not much different with the predicted yield of 6.19%. After optimised the extraction process, the isolated pectin was still remained as high-methoxyl pectin (DE>50%) yet the extraction yield and gelling time had successfully improved.

Acknowledgement

The corresponding author was grateful to the guidance and assistance by Dr.

Chua Bee Lin throughout the whole research process. The author was also appreciated for the financial support from the School of Engineering, Taylor's University, Malaysia.

References

[1] G. J. Swamy and K. Muthukumarappan, "Optimization of continuous and intermittent microwave extraction of pectin from banana peels," *Food Chem.*, vol. 220, pp. 108–114, 2017.

[2] K. A. T. Castillo-Israel, S. F. Baguio, M. D. B. Diasanta, R. C. M. Lizardo, E. I. Dizon, and M. I. F. Mejico, "Extraction and characterization of pectin from Saba banana [Musa 'saba'(Musa acuminata x Musa balbisiana)] peel wastes: A preliminary study," *Int. Food Res. J.*, vol. 22, no. 1, pp. 202–207, 2015.

[3] C. Freitas de Oliveira, D. Giordani, R. Lutckemier, P. D. Gurak, F. Cladera-Olivera, and L. D. Ferreira Marczak, "Extraction of pectin from passion fruit peel assisted by ultrasound," *LWT - Food Sci. Technol.*, vol. 71, pp. 110–115, 2016.

[4] S. Q. Liew, N. L. Chin, and Y. A. Yusof, "Extraction and Characterization of Pectin from Passion Fruit Peels," *Agric. Agric. Sci. Procedia*, vol. 2, pp. 231–236, 2014.

[5] C. L. Hii, C. L. Law, and M. Cloke, "Modeling using a new thin layer drying model and product quality of cocoa," *J. Food Eng.*, vol. 90, no. 2, pp. 191–198, 2009.

[6] P. Khawas, A. J. Das, K. K. Dash, and S. C. Deka, "Thin-layer drying characteristics of Kachkal banana peel (Musa ABB) of Assam, India," *Int. Food Res. J.*, vol. 21, no. 3, pp. 975–982, 2014.

[7] I. T. Toĝrul and D. Pehlivan, "Modelling of thin layer drying kinetics of some fruits under open-air sun drying process," *J. Food Eng.*, vol. 65, no. 3, pp. 413–425, 2004.

[8] D. I. Onwude, N. Hashim, R. B. Janius, N. M. Nawi, and K. Abdan, "Modeling the Thin-Layer Drying of Fruits and Vegetables: A Review," *Compr. Rev. Food Sci. Food Saf.*, vol. 15, no. 3, pp. 599–618, 2016.

[9] C. Ertekin and M. Z. Firat, "A comprehensive review of thin-layer drying models used in agricultural products," *Crit. Rev. Food Sci. Nutr.*, vol. 57, no. 4, pp. 701–717, 2017.

[10] J. A. K. M. Fernando and A. D. U. S. Amarasinghe, "Drying kinetics and mathematical modeling of hot air drying of coconut coir pith.," *Springerplus*, vol. 5, no. 1, p. 807, 2016.

[11] H. Bagherian, F. Zokaee Ashtiani, A. Fouladitajar, and M. Mohtashamy, "Comparisons between conventional, microwave- and ultrasound-assisted methods for extraction of pectin from grapefruit," *Chem. Eng. Process. Process Intensif.*, vol. 50, no. 11–12, pp. 1237–1243, 2011.

[12] R. Minjares-Fuentes, A. Femenia, M. C. Garau, J. A. Meza-Velázquez, S. Simal, and C. Rosselló, "Ultrasound-assisted extraction of pectins from grape pomace using citric acid: A response surface methodology approach," *Carbohydr. Polym.*, vol. 106, no. 1, pp. 179–189, 2014.

[13] C. L. Hii, C. L. Law, and M. Cloke, "Modelling of Thin Layer Drying Kinetics of Cocoa Beans During Artificial and Natural Drying," *J. Food Eng.*, vol. 3, no.

1, pp. 1–10, 2008.
[14] I. G. Moorthy, J. P. Maran, S. M. Surya, S. Naganyashree, and C. S. Shivamathi, "Response surface optimization of ultrasound assisted extraction of pectin from pomegranate peel," *Int. J. Biol. Macromol.*, vol. 72, pp. 1323–1328, 2015.
[15] S. k Kumar, "Drying Kinetics of Banana Peel," *J. Food Process. Technol.*, vol. 6, no. 11, pp. 10–12, 2015.
[16] H. Darvishi, A. R. Asl, A. Asghari, M. Azadbakht, G. Najafi, and J. Khodaei, "Study of the drying kinetics of pepper," *J. Saudi Soc. Agric. Sci.*, vol. 13, no. 2, pp. 130–138, 2014.
[17] W. P. da Silva, C. M. D. P. S. e Silva, F. J. a. Gama, and J. P. Gomes, "Mathematical models to describe thin-layer drying and to determine drying rate of whole bananas," *J. Saudi Soc. Agric. Sci.*, vol. 13, no. 1, pp. 67–74, 2014.
[18] KulkarniS.G. and P. Vijayanand, "Effect of extraction conditions on the quality characteristics of pectin from passion fruit peel (Passiflora edulis f. flavicarpa L.)," *LWT - Food Sci. Technol.*, vol. 43, no. 7, pp. 1026–1031, 2010.
[19] K. Manjarres-Pinzon, M. Cortes-Rodriguez, and E. Rodríguez-Sandoval, "Effect of drying conditions on the physical properties of impregnated orange peel," *Brazilian J. Chem. Eng.*, vol. 30, no. 3, pp. 667–676, Sep. 2013.
[20] S. Marianski and A. Marianski, *The Art of Making Fermented Sausages*. 2009.
[21] *Food Analysis: Theory and Practice - Yeshajahu Pomeranz, Clifton E. Meloan - Google Books*. .
[22] T. Gunhan, V. Demir, E. Hancioglu, and A. Hepbasli, "Mathematical modelling of drying of bay leaves," *Energy Convers. Manag.*, vol. 46, no. 11–12, pp. 1667–1679, 2005.
[23] W. C. Lee, S. Yusof, N. S. A. Hamid, and B. S. Baharin, "Optimizing conditions for enzymatic clarification of banana juice using response surface methodology (RSM)," *J. Food Eng.*, vol. 73, no. 1, pp. 55–63, 2006.
[24] Y. Xu *et al.*, "Effects of ultrasound and/or heating on the extraction of pectin from grapefruit peel," *J. Food Eng.*, vol. 126, pp. 72–81, 2014.
[25] E. Chaharbaghi, F. Khodaiyan, and S. S. Hosseini, "Optimization of pectin extraction from pistachio green hull as a new source," *Carbohydr. Polym.*, vol. 173, pp. 107–113, 2017.
[26] J. Prakash Maran, V. Sivakumar, K. Thirugnanasambandham, and R. Sridhar, "Optimization of microwave assisted extraction of pectin from orange peel," *Carbohydr. Polym.*, vol. 97, no. 2, pp. 703–709, 2013.
[27] X. Huang, D. Li, and L. jun Wang, "Characterization of pectin extracted from sugar beet pulp under different drying conditions," *J. Food Eng.*, vol. 211, pp. 1–6, 2017.
[28] B. R. Sharma, L. Naresh, N. C. Dhuldhoya, S. U. Merchant, and U. C. Merchant, "An Overview on Pectins," *Times food Process. J.*, vol. 51, no. June-July, pp. 44–51, 2006.
[29] R. Guidetti *et al.*, "Extraction and Characterization of Pectin from Citric Waste," *Chem. Eng. Trans.*, vol. 44, no. 3, pp. 1–7, 2015.
[30] CP Kelco, *GENU® pectin*. A HUBER COMPANY, pp. 1-36, 2010.

Characteristics Study of Photovoltaic Thermal System with Emphasis on Energy Efficiency

Chuah Yee Yong[1*], Mohammad Taghi Hajibeigy[2]

Taylor's University Lakeside Campus, Subang Jaya, Selangor, Malaysia

[*]yeeyong0911@gmail.com

Abstract

Solar energy is typically collected through photovoltaic (PV) to generate electricity or through thermal collectors as heat energy, they are generally utilised separately. This project is done with the purpose of integrating the two systems to improve the energy efficiency. The idea of this photovoltaic-thermal (PVT) setup design is to simultaneously cool the PV panel so it can operate at a lower temperature thus higher electrical efficiency and also store the thermal energy. The experimental data shows that the PVT setup increased the electrical efficiency of the standard PV setup from 1.64% to 2.15%. The integration of the thermal collector also allowed 37.25% of solar energy to be stored as thermal energy. The standard PV setup harnessed only 1.64% of the solar energy whereas the PVT setup achieved 39.4%. Different flowrates were tested to determine its effects on the PVT setup's electrical and thermal efficiency. The various flowrate does not significantly impact the electrical efficiency since it did not significantly impact the cooling of the panel. The various flowrates resulted in fluctuating thermal efficiencies, the relation between the two is inconclusive in this project.

Keywords**:** Photovoltaic (PV), Photovoltaic-thermal (PVT), Electrical Efficiency, Thermal Efficiency

1. Introduction

Current world energy demand is largely fulfilled by fossil fuel. Fossil fuel has the advantages over renewable energy that it is well documented and has much more developed technology to harness the energy it provides. However, there are many reasons for us to move on to renewable energies such as solar, wind, geothermal and so on. Conventional coal-fired plants is the top generator all around the world but the process comes with large amounts of greenhouse gases and are unsustainable with the sources depleting. Figure 1 below shows the 2016 statistics of power generation and the methods used.

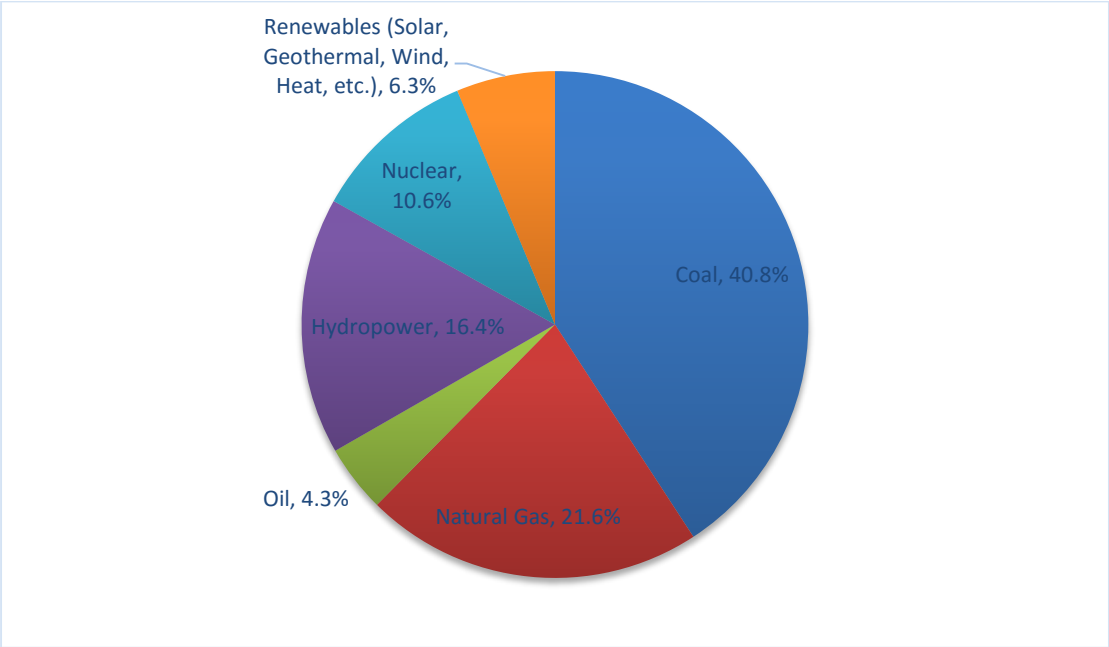


Figure 6: Sources of Global Electricity Generation[1]

With cutting down the usage of fossil fuel to generate power as a target, this project approaches it through attempting to improve current methods of harnessing solar energy. Present methods of collecting solar energy falls to two categories, photovoltaic (PV) and thermal energy. Photovoltaics uses semiconducting materials which are capable of converting light into electricity, whereas thermal collectors are self-explanatory, where a collector is used to collect heat radiated from the light source.

Only a small amount of the solar energy can be harnessed by the PV panels, which are due to factors such as the current limitations of the technology. Standard monocrystalline panels can operate at roughly 15%-20% efficiency where the remaining solar energy are converted into thermal energy and are wasted.

The proposed method to increase solar energy harnessed is to retrofit a thermal system to a standard monocrystalline panel, where the integrated system is expected to operate at a higher efficiency. The design is to attach a heat sink to the back of the solar panel with thermal compound in between to allow heat to transfer from the panel to the heat sink. The heat sink is submerged into a body of water where it transfers the heat to a water storage tank through a copper tube. The idea of this design is to simultaneously cool the panel which improves operating efficiency and harness the thermal energy.

2. Methodology

2.1 Setup Design and Fabrication

Solar panels generally are sold in the market without any heat dissipation modifications, where the panels are usually installed individually. That meant the fabrication of heat sinks to suitable specifications are required, SEMS Sdn. Bhd. agreed to arrange a heat sink in the desired dimensions. Due to limited budget, it is not viable to fabricate a custom heat sink from scratch. Figure 2 shows the solar panel with the heat sink attached to the underside of the monocrystalline panel.



Figure 2: PVT Panel Setup

To avoid short circuit of the wirings, the wiring housing are sealed with silicone glue which are water proof. The space between the panel and the heat sink are filled with thermal compound Kafuter K-5211, that prevents air pockets which reduces the effectiveness of heat transfer between the two layers.

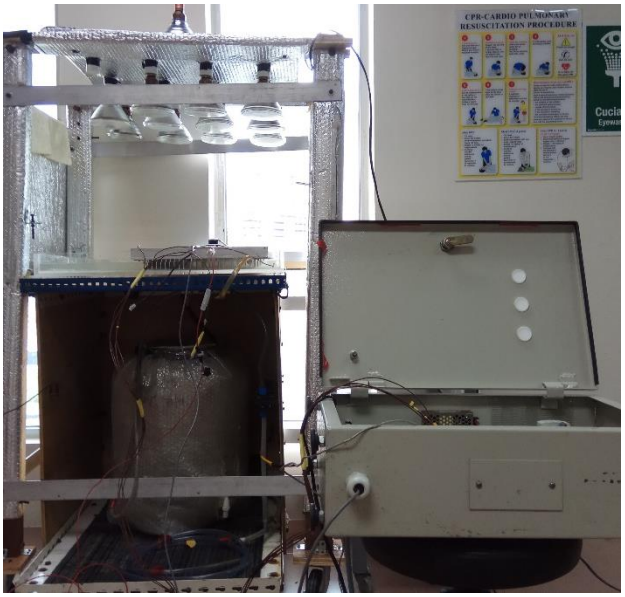


Figure 7: Overall Experimental Setup

The experiment will be done indoors to keep factors such as ambient temperature, fluctuating solar energy as consistent as possible. The overall setup can be seen in Figure 3 above, where the lightbulbs are placed directly above the panel that are used to provided consistent light energy. The heat sink is submerged in water within a Perspex container that has water being cycled through a water storage tank. The metal box on the right of the water storage tank holds the electronics such as the pyranometer and the data-logger.

2.2 Experimental Procedures

The steps below were taken to obtain the electrical and thermal performance:

i. Adjust the power supplied to the water pump at 12V.
ii. Switch on the lights.
iii. Start the data-logger.
iv. Start the EpSolar Monitoring Software.
v. Allow the setup to continue for 10 minutes.
vi. Collect data and switch off water pump and lights.
vii. Experiment is repeated at different water pump power supply after water storage tank return to ambient temperature.

The panel temperature is observed throughout the experiment to ensure it does not exceed 70°C as it can cause permanent damage to the panel which reduces its operating efficiency.

2.3 Electrical Efficiency

The electrical efficiency of the solar panel was calculated using the equation below:

$$\eta_{elec} = \frac{V_m I_m}{AR}$$

Where η_{elec} = *electrical efficiency*

V_m = *maximum power point voltage, V*

I_m = *maximum power point current, A*

A = *panel area,* m^2

R = *solar radiation,* W/m^2

2.4 Thermal Efficiency

At steady state, the PVT thermal performance can be calculated using the equation below:

$$\eta_T = \frac{\text{thermal energy collected}}{\text{total amount of solar energy}}$$

$$\eta_T = \frac{mC_p(T_o - T_i)}{ARt}$$

Where η_T = *thermal efficiency*

m = *water mass, kg*

C_p = *specific heat capacity, kJ/kg.K*

T_o = *outlet temperature, K*

T_i = *inlet temperature, K*

A = *panel area,* m^2

R = *direct solar radiation,* W/m^2

t = *time, s*

3. Results

3.1 Electrical Efficiency

3.1.1 Difference in Standard PV and PVT Setup

The difference between a standard monocrystalline PV setup and the novel PVT setup fabricated for this project is observed. The factors for both setups such as ambient temperature, distance of panel to lightbulbs and more are kept as consistent as possible. The power generated are recorded using EpSolar Monitoring Software. Figure 4 below shows the irradiance and the power generated by the PV setup throughout the experiment. At the peak of the power generated by the solar panel, the PV setup achieved a 3.77% electrical efficiency. This setup recorded an average efficiency of 1.64%.

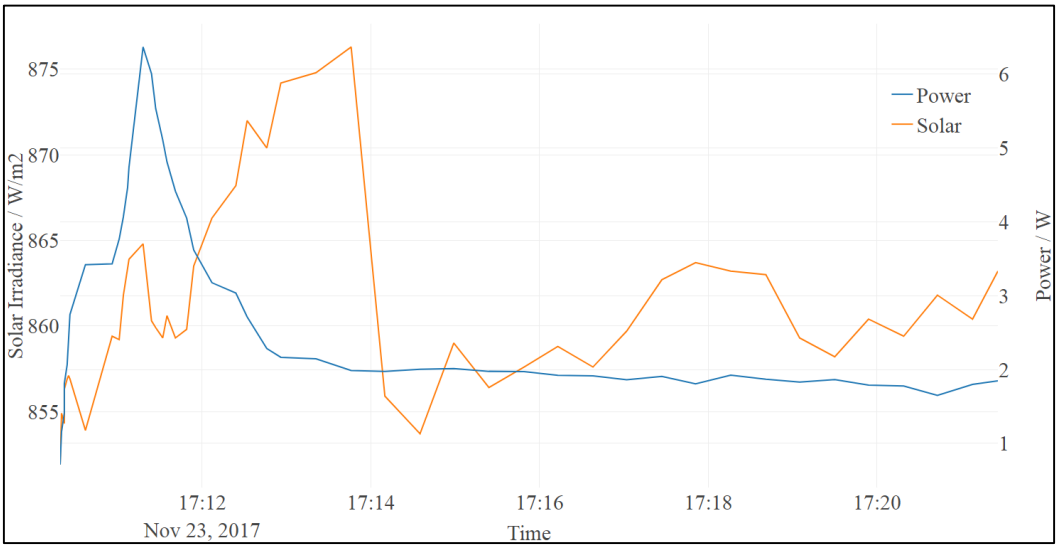


Figure 4: Real Time Power Graph of PV Panel

Figure 5 below shows the results of the PVT setup, with the water pump running at 8.4 L/min. It is measured at 4.62% maximum electrical efficiency and 2.15% average electrical efficiency.

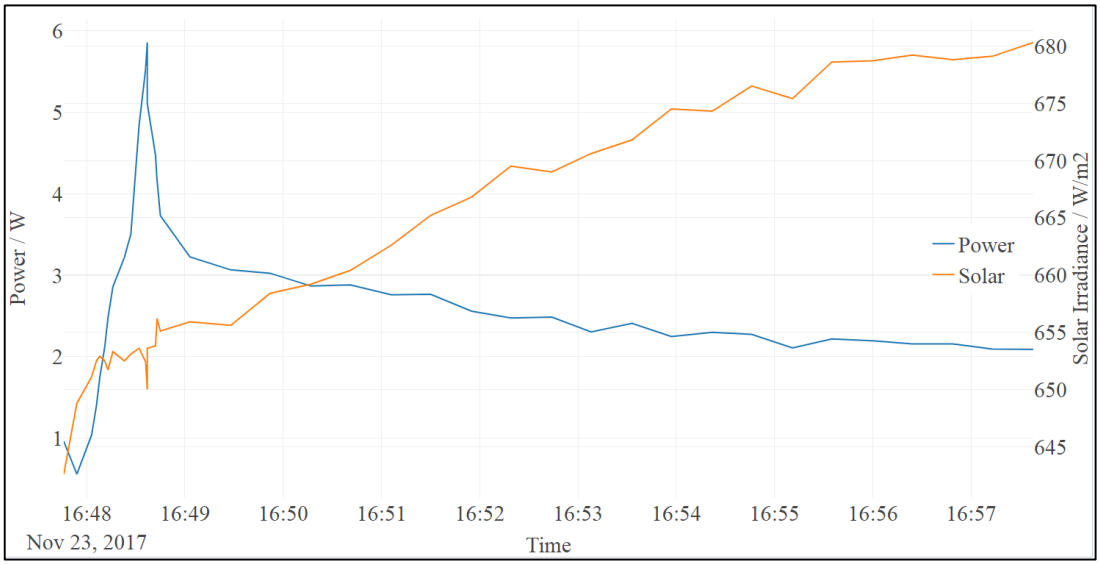


Figure 5: Real Time Power Graph of PVT Setup

3.1.2 **Difference in Flowrate of PVT Setup**

By using an adjustable AC/DC converter, the flowrate flowing into the Perspex container are set to 3.9 L/min, 5.3 L/min, 6.4 L/min and 8.4 L/min. The flowrates are respectively due to the voltage fed to the water pump being 6V, 7.5V, 9V and 12V.

Table 1: Water Pump Flow Rate at the Corresponding Voltages

Voltage Supplied	Flow Rate (L/min)
6.0V	3.9
7.5V	5.3
9.0V	6.4
12.0V	8.4

The electrical power generated between the four experiments are recorded and graphed together to be compared in Figure 6 below.

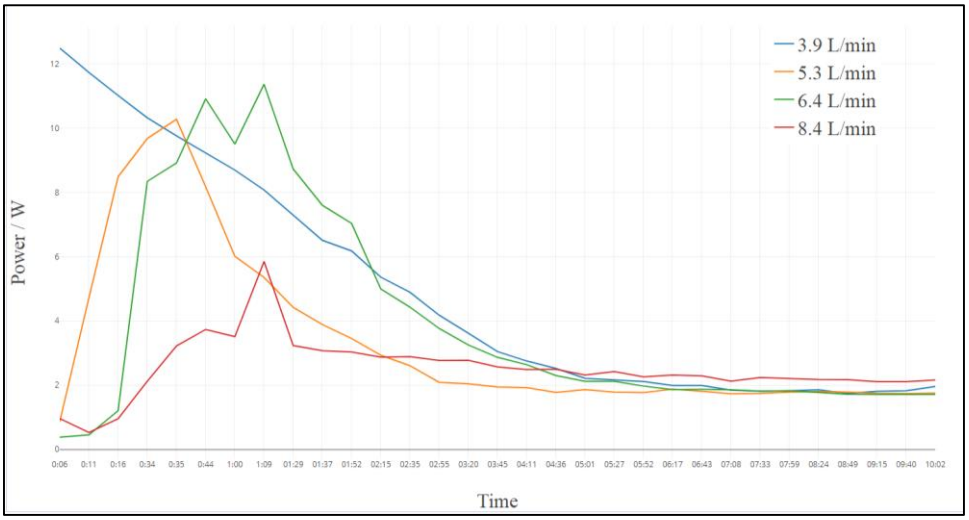


Figure 6: Real Time Power Graph at Different Flow Rates

Figure 6 shows that after the electrical generation stops fluctuating around two minutes into the experiment, the flowrate does not significantly impact the electrical power generated by the panel.

3.2 Thermal Efficiency

The same experimental procedures are used to determine the thermal performance of the PVT setup. The temperature of the water in the storage tank is recorded and the difference between the beginning and the end of the experiment is tabulated as below.

Table 7: Difference of Water Temperature

Water Flowrate	**Temperature Difference (°C)**
3.9 L/min	1.9
5.3 L/min	1.1
6.4 L/min	2.3
8.4 L/min	1.4

By using the formulae mentioned in subsection 2.4, the thermal efficiency of the setup can be calculated. The heat capacity of water is assumed to be at 4184 J/kgK. Table 3 below shows the resulting thermal efficiency of the PVT setup at various flowrates.

Table 3: Different Flowrates and the Corresponding Thermal Performance

Experiment	**Water Flowrate**	**Average Irradiance**	**Thermal Efficiency**
1	3.9 L/min	704.10	48.25%
2	5.3 L/min	705.57	27.88%
3	6.4 L/min	715.77	57.46%
4	8.4 L/min	672.01	37.25%

3.3 Combined Efficiency

The combined efficiency of the standard PV setup and the fabricated PVT setup are compared. Combined efficiency refers to the sum of both thermal efficiency and the electrical efficiency. It is used to compare whether the integration of thermal collector to the standard PV panel will yield an improvement in harnessing solar energy.

The combined efficiency of the PVT system resulted in 39.4% efficiency while the standard PV setup can only harness electrical energy, thus only operates at 1.64% efficiency in harnessing solar energy.

4. Conclusion

The integration of a thermal system which simultaneously cools the panel and collect thermal energy allowed the solar panel to operate at a higher efficiency. The standard PV setup is rated at 1.64% electrical efficiency while the PVT setup is rated at 2.15%. The decreasing power generated over time can be attributed to the increasing temperature of the panel, illustrated in Figure 7 below where the PVT setup is shown dissipating heat better than the standard PV setup.

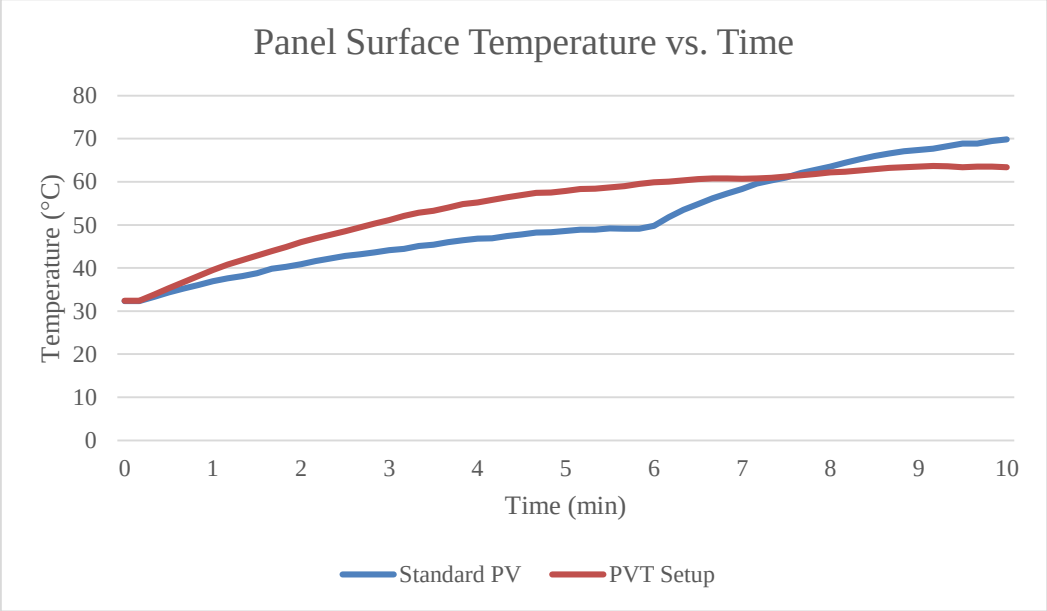


Figure 7: Temperature of PV Panel Surface Over Time

The PVT setup boasts a much improved combined efficiency in harnessing solar energy, from 1.64% to 39.4% of solar energy collected which deems that integration of thermal system to an existing PV setup successful in terms of improving energy efficiency.

The effects on how the flowrate affect the electrical efficiency and thermal efficiency are also studied in this project. It seems that the flow rate does not significantly impact the electrical efficiency. Whereas the thermal efficiency of the PVT setup fluctuates and the relationship between the two could not be defined.

However, it should be noted that the solar panels provided could be unreliable as typical monocrystalline panels operates at roughly 15% efficiency, while the panels used only operated around 2%.

References

[1] International Energy Agency, "Key world energy statistics," *Statistics (Ber).*, p. 80, 2016.

[2] I. L. Alboteanu, F. Ravigan, and S. Degeratu, "Methods for Increasing Energy Efficiency of Photovoltaic Systems," *Int. J. Power Renew. Energy Syst.*, vol. 1, pp. 51–61, 2014.

[3] H. Bahaidarah, A. Subhan, P. Gandhidasan, and S. Rehman, "Performance evaluation of a PV (photovoltaic) module by back surface water cooling for hot climatic conditions," *Energy*, vol. 59, pp. 445–453, 2013.

[4] R. Mazón-Hernández, J. R.García-Cascales, F. Vera-García, A. S. Káiser, and B. Zamora, "Improving the Electrical Parameters of a Photovoltaic Panel by Means of an Induced or Forced Air Stream," vol. 2013, 2013.

[5] J. K. Tonui and Y. Tripanagnostopoulos, "Air-cooled PV/T solar collectors with low cost performance improvements," *Sol. Energy*, vol. 81, no. 4, pp. 498–511, 2007.

[6] C. G. Popovici, S. V. Hudişteanu, T. D. Mateescu, and N.-C. Cherecheş, "Efficiency Improvement of Photovoltaic Panels by Using Air Cooled Heat Sinks," *Energy Procedia*, vol. 85, no. November 2015, pp. 425–432, 2016.

[7] A. Hasan, S. J. McCormack, M. J. Huang, and B. Norton, "Evaluation of phase change materials for thermal regulation enhancement of building integrated photovoltaics," *Sol. Energy*, vol. 84, no. 9, pp. 1601–1612, 2010.

[8] K. A. Moharram, M. S. Abd-Elhady, H. A. Kandil, and H. El-Sherif, "Enhancing the performance of photovoltaic panels by water cooling," *Ain Shams Eng. J.*, vol. 4, no. 4, pp. 869–877, 2013.

[9] R. Prasher and C.-P. Chiu, "Thermal Interface Materials," in *Materials for Advanced Packaging*, D. Lu and C. P. Wong, Eds. Cham: Springer International Publishing, 2017, pp. 511–535.

[10] D. L. Saums, "Advances in Thermal Interface Materials for Power LED Applications," in *Thermal Management for LED Applications*, C. J. M. Lasance and A. Poppe, Eds. New York, NY: Springer New York, 2014, pp. 299–346.

[11] J. H. Kim, S. H. Park, J. G. Kang, and J. T. Kim, "Experimental performance of heating system with buildingintegrated PVT (BIPVT) collector," *Energy Procedia*, vol. 48, pp. 1374–1381, 2014.

[12] M. A. Hasan and K. Sumathy, "Photovoltaic thermal module concepts and their performance analysis: A review," *Renew. Sustain. Energy Rev.*, vol. 14, no. 7, pp. 1845–1859, 2010.

[13] J. H. Kim and J. T. Kim, "Comparison of electrical and thermal performances of glazed and unglazed PVT collectors," *Int. J. Photoenergy*, vol. 2012, 2012.

[14] N. Aste, C. Del Pero, and F. Leonforte, "Water PVT Collectors Performance Comparison," *Energy Procedia*, vol. 105, pp. 961–966, 2017.

[15] U. Qureshi, "Performance Assessment of Standalone PV / T Collector under Hybrid Cooling Condition with Different air Flow Rate," vol. 3, no. 1, pp. 4058–4060, 2016.

[16] M. Meral and F. Din, "Critical Factors that Affecting Efficiency of Solar Cells," *Smart Grid Renew. Energy*, vol. 1, no. 1, p. 47, 2010.

[17] M. Mattei, G. Notton, C. Cristofari, M. Muselli, and P. Poggi, “Calculation of the polycrystalline PV module temperature using a simple method of energy balance,” *Renew. Energy*, vol. 31, no. 4, pp. 553–567, 2006.

[18] B. P. Rand, J. Genoe, P. Heremans, and J. Poortmans, “Solar Cells Utilizing Small Molecular Weight Organic Semiconductors,” *Prog. Photovolt Res. Appl.*, vol. 15, no. February 2013, pp. 659–676, 2007.

Synthesis of a Sustainable Sago-Based Value Chain via Fuzzy Optimisation Approach

Jeffrey Chong Hong Seng[1*], Yoke Kin Wan[1], Viknesh Andiappan[2]

[1]*School of Engineering, Faculty of Built Environment, Engineering, Technology & Design, Taylor's university, Lakeside Campus.*

[2]*Department of Chemical Engineering, The University of Bath, Claverton Down, BA2 7AY, Bath, United Kingdom Bath,*

jeffreychong940123@gmail.com, YokeKin.Wan@taylors.edu.my, vamr6103@gmail.com

Abstract

Sago palm (Metroxylan Sagu) is one of the underutilised crops that can potentially produce staple food for human, especially in Asia's Region. Sago starch, which can be obtained from the trunks of sago balm contains high carbohydrates. Sago starch can be produced via sago starch extraction process (SSEP). During the SSEP, several types of sago wastes are generated such as sago fiber (SF), sago bark (SB) and sago wastewater (SW). With the increase in production of existing factories and sago mills, the sago industrial practice in waste disposal management is gaining more attention, thus implementation of effective waste management is vital. One of the promising ways to have effective waste management is to create value out of the sago wastes. In a recent study, the feasibility of a sago-based refinery, which is a facility to convert sago wastes into value-added products (e.g., bio-ethanol and energy). The study found that it is feasible to have a sago-based refinery in sago industry. The introduction of other product alternatives (e.g., bio-butanol and bio-hydrogen) towards utilisation of sago wastes to create value added products while considering the environmental impact has not been considered for sago value chain. Hence, an optimum sago value chain, which involved conversion activities of sago wastes into value-added products, is aimed to be synthesised in this work. The optimum sago value chain will be evaluated based on profit and carbon emissions using fuzzy-based optimisation approach via a commercial optimisation software, Lingo 16.0. To illustrate the application of the developed approach, an industrial case study has been solved. As results, the optimum pathway for bioconversion of sago waste is to produce bio-ethanol through fermentation and power through CHP system.

Keywords: Sago Industry, Waste-to-Wealth, Optimisation, Process Synthesis

1. Introduction

Sago palm (*Metroxylan Sagu*) is one of the underutilised crops that can potentially produce staple food for human, especially in Asia's Region. The sago palm produces sago starch which contains high carbohydrates that can be obtained from the trunks of sago palm. Such palm is an excellent crop for sustainable agriculture due to its ability to thrive in most soil conditions and it requires only one time planting that has the ability of self-sustain by producing its young tree, also known as suckers or tillers [1]. It can also be served as an income for poverty alleviation as it is commonly planted in rural areas [2].

Karim et al. [3] states that, under optimal farming practices, up to 25 metric tonnes of sago starch per hectare annually can be achieved, which is roughly 3 - 4 times the starch yield of staple crops such as rice (6 tonnes/ha/yr) or wheat (5 tonnes/ha/yr) [2], [4]. Sago starch can be produced via sago starch extraction process (SSEP) as shown in Figure 1. As shown, there are several types of sago wastes that are generated during the process, namely sago fiber (SF), sago bark (SB) and sago wastewater (SW)[4].

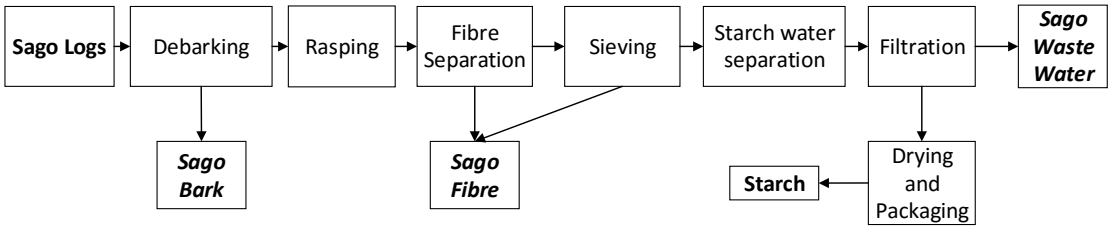


Figure 8: Block Flow Diagram of SSEP

In current industrial practices, SB is used as timber fuel for firing or will be disposed around the mills to be used as flooring material [4]. SF is used as animal feed, otherwise, it will be released into nearby streams along with SW. According to Adeni et al. [5], SW, combined with SF, represents high organic materials, chemical oxygen demand (COD) and biochemical oxygen demand (BOD), which does not comply to the discharged regulations set in Environmental Quality Act, 1974. The installation of pollution control devices can be costly, approximately 20-50% of the total investment for a large scale production mill, which is not preferred by producers in this relatively low value commodity industry [5]. SF and SB, which are lignocellulosic waste (LCW), contains residue starch which can be converted into value added products such as glucose, which can be further refined to higher value product such as bio-fuels.

To address the aforementioned issues, a viable alternative is to create value out of the sago wastes to improve the current performance of sago value chain. As mentioned, SF and SB could be utilised for the production of value added products (i.e., ethanol, organic acids, enzymes and others)[6]. However, the idea of converting sago wastes into valuable products is still in its infancy. In most recently, Wan et al. [7] studied the feasibility of a sago-based refinery, which is a facility to convert sago wastes into value-added products (e.g., bio-ethanol and energy). The study results showed that it is feasible to convert sago wastes (SB and SF) into bioethanol and energy in sago-based refinery. In addition, Wan and her co-authors [8] also conducted a value chain

analysis for sago industry to determine the optimum value chain pathway for sago industry. Value chain is a set of activities that are done to design, produce, market, deliver and support the product created by a party [9]. First proposed by Michael Porter, value chain divides break down a chain of activities into individual parts to scrutinise the dynamics of activities in order to reveal its strength and weaknesses, thus identifying value creation opportunities. Application of value chain in the sago industry has been pioneered by a study done by Wan et al. [8], whom developed a value chain to improve the sustainability of the industry to identify value creation opportunities. However, the conversion of sago wastes into value-added products had not been considered in the sago value chain. Therefore, in order to further improve the economic and environmental performance of the sago value chain, this study aims to expand the previous work done by Wan et al [8], by introducing alternatives towards utilisation of sago wastes to create value added products while considering the environmental impact done to the sago value chain. **Error! Reference source not found.** showed the sago value chain done by Wan et al. [9] and the sago value chain has been expanded in this work by considering value added product conversion technologies (i.e., technology 1, intermediates products, technology 2, and value-added products).

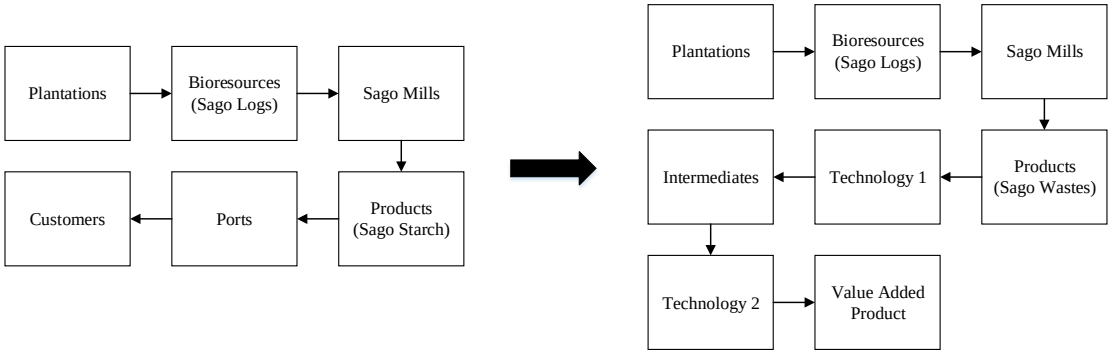


Figure 9: Proposed Value Chain of Sago Industry in this Study

Douglas et al. [10] adapted fuzzy-based optimisation approach based on 'max-min' aggregation to synthesis of a sustainable integrated bio-refinery. The author's study did not identify the optimal value chain in the sago industry. However, the author has proven that fuzzy-based optimisation approach can be used to obtain an optimal pathway from a superstructure, while considering the economic and environmental impact. Therefore, in order to further improve the economic and environmental performance of the sago value chain, this study aims to expand the previous work done by Wan et al. [11], by introducing alternatives towards utilisation of sago wastes to create value added products to maximise profit, while minimising environmental impact done of the sago value chain. To determine the optimum pathway in this, a fuzzy-based optimisation approach will be developed in this work to find an optimal solution to the multi-objective model in this study. To illustrate the application of proposed model, a real industrial case study has been solved.

2. Methodology

Error! Reference source not found.3 illustrates the methodology using the fuzzy-based optimisation approach. First step is to determine the superstructure based on the layers of activities from the proposed value chain in this study. Then, the

objectives of the study have to be set and relevant data needs to be collected based on the objective set. In this study, the objective of maximising profit and minimising CFP of the sago value chain is set for synthesis of an optimal value chain for sago waste conversion. Profit and CFP objectives are contradictory. Therefore, a fuzzy-based optimisation approach has to be developed. Douglas et al. [10] Following the fuzzy-based optimization approach, the mass balance has to be formulated, as well as the formulation of equations necessary for all objective functions, which in this case, is the profit and CFP equations. The developed formulations are then solved using a commercial optimization software Lingo V.16.

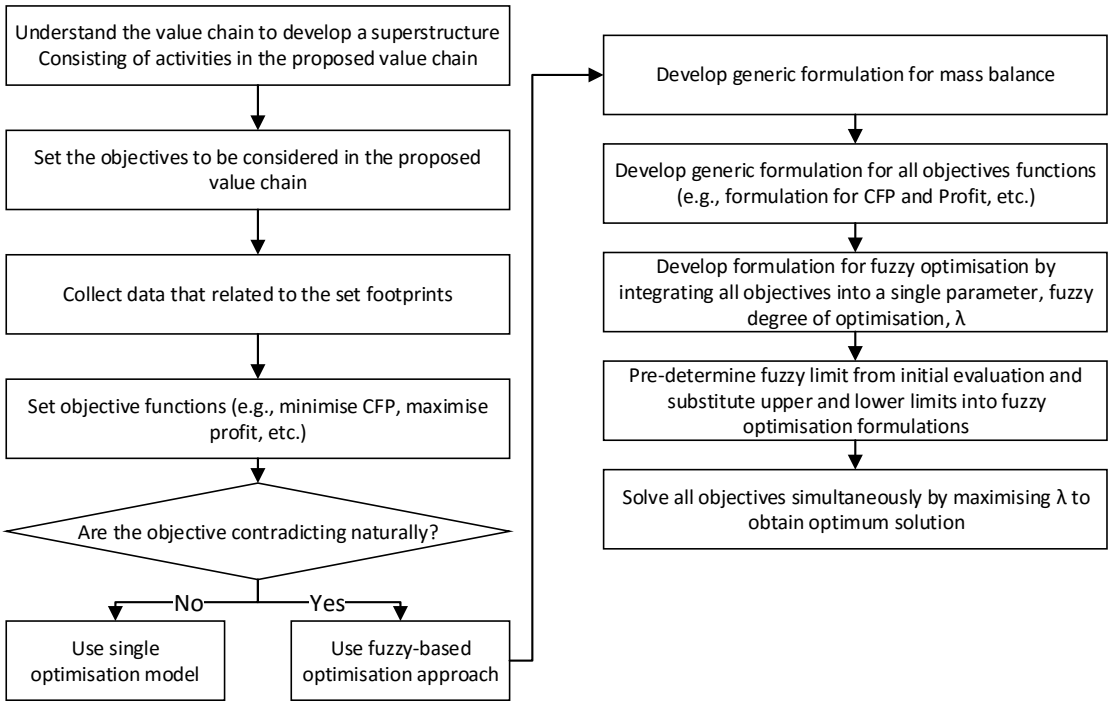


Figure 10 : Methodology Flow Chart for Fuzzy-Based Optimisation Approach

To illustrate the alternatives stages of the value chain, superstructure is first developed. As shown in Figure 4, the superstructure illustrates the seven layers of activities that is considered in the value chain proposed in this study. With reference to the approach used by Wan et al. [8], the activity starts from the harvesting palms from a set of plantation $g \in G$ with annual available palm F_g^{av}, processed and converted to a set of bio-resource $m \in M$, which is limited to only sago logs in this study. The sago logs are then sent to a set of sago mill $f \in F$ with starch production capability $F_f^{starch.lim}$. The sago mill *f* turns the bio-resource *m* into a set product $p \in P$ based on the amount of starch produced from the sago mill, which in the case of this study, represents the sago wastes. In the study of Wan et al.[8], the product considered in the author's study is just sago starch in the product *p* layer. However, in this study, sago starch would not be focused, unlike as shown in the works of Wan et al. [8]. Sago wastes (e.g., SB, SF, SW) will be considered in this study instead.

The sago waste is then sent to a set of conversion technologies 1 $c \in C$ to produce a set of Intermediate product $d \in D$. Intermediate product d is then sent for further processing in a set of technology 2 $e \in E$ to produce a set of end product $z \in Z$. To model this superstructure, mathematical equations have been formulated in following sections.

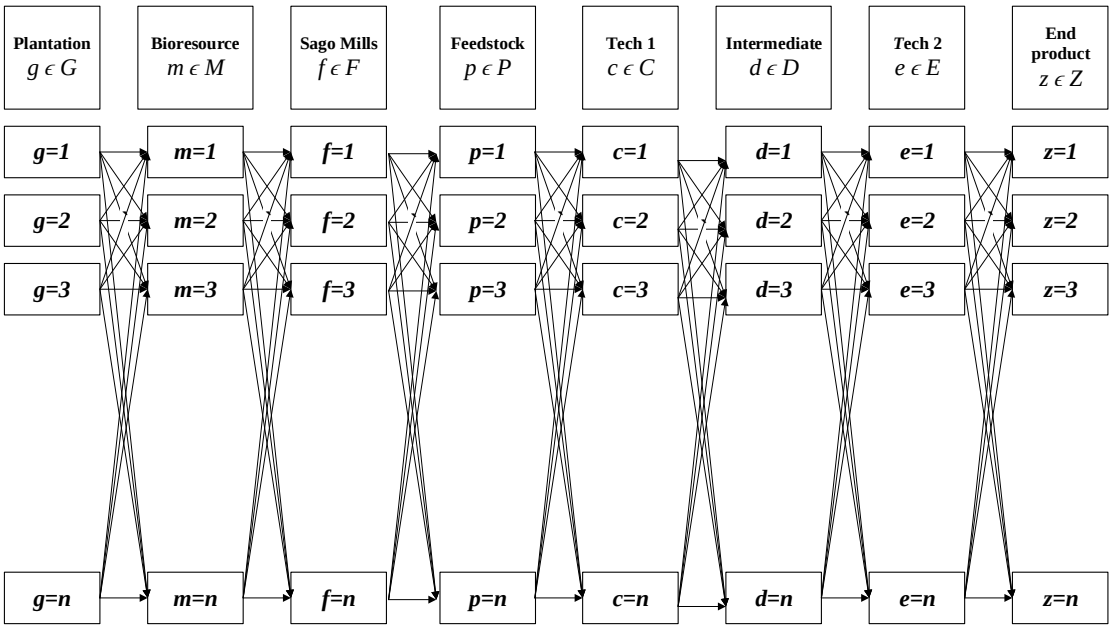


Figure 11: Generic Superstructure

2.1 Mass Balance Equations

The mass balance for the first four layers of activities illustrated by the value chain in this study is adopted from the work done by Wan et al [8]. The total number of palms harvested F_g^{out} (palm/y) from plantation g has to be less than available palms to ensure a sustainable harvesting process, as:

$$F_g^{av} > F_g^{out} \qquad \forall g \qquad (1)$$

Harvested sago palms from plantation g are then converted into bio-resource m before its sent to sago mill f. Currently, the only bio-resource m sent to sago mills are sago logs. Therefore, given the conversion of palms to sago logs $X_{g,\log}$, the total amount of sago logs sent to sago mill f, $F_{g,\log}^{in}$ (log/y) can be determined via:

$$F_{g,\log,f}^{in} = F_{g,f}^{out} X_{g,\log} \qquad \forall g \qquad (2)$$

The total sago logs transported to sago mill f is the determined via:

$$F_f^{in} = \sum_{g=1}^{G} F_{g,\log,f}^{in} \qquad \forall f \qquad (3)$$

It is noted that sago logs can be transported via roads or river. However, only road transportation is considered in this study, similar to the study done by Wan et al.[8]. Given a lorry capacity $C_{\text{weightlim}}^{\text{lorry}}$ (t/trip) and weight per log $W_{\log}$ (t/log), the number of trips

needed to transport the sago logs from plantation *g* to sago mill *f* $n_{g,f}^{trip}$ (trip) is determined via

$$n_{g,f}^{trip} \geq \frac{F_{g,\log,f}^{in} W_{\log}}{C_{weight\,\lim}^{lorry}} \qquad \forall g \forall f \qquad (4)$$

In sago mill *f*, the sago logs are converted into sago starch, producing sago wastes as by-products, labelled as product *p* in this study. To calculate the amount of starch produced from sago mill *f* $Starch^f$ (t/y), Equation (5) is formulated.

$$Starch^f = \sum_{g=1}^{G} F_{g,\log,f}^{in} X_{g,\log,starch} \qquad \forall f \qquad (5)$$

Given that each sago mill *f* has a production capacity F_{Starch}^{av} (t/y) which cannot be exceeded, hence, the equation below is included in the model

$$Starch^f < F_{Starch}^{av} \qquad \forall f \qquad (6)$$

To satisfy sago demand, *StarchDemand* (t/y) which is set at 32,000 t/y in this study, the Equation (7) is added into the model.

$$StarchDemand = \sum_{f=1}^{F} starch^f \qquad (7)$$

The amount of product *p* produced from sago mill *f* from SSEP $F_{f,p}^{out}$ is calculated via:

$$F_{f,p}^{out} = Starch^f X_{starch,p} \qquad \forall f \forall p \qquad (8)$$

Hence, the amount of product *p* produced F_p^{in} (t/y) from all sago mills is calculated as:

$$F_p^{in} = \sum_{f=1}^{F} F_{f,p}^{out} \qquad \forall p \qquad (9)$$

Product *p* is then sent to technology 1 *c* to be converted into intermediate *d*. The amount of product *p* sent to technology 1 *c* F_c^{in} (t/y) is as

$$F_c^{in} = \sum_{p=1}^{P} F_{p,c}^{in} \qquad \forall c \qquad (10)$$

In technology 1, the amount of intermediate *d* produced from product *p* is dependent on the conversion $X_{p,b}^{c}$, as:

$$F_{c,d}^{out} = F_c^{in} X_{p,d}^{c} \qquad \forall c \forall d \qquad (11)$$

Given the conversion $X_{p,b}^{c}$, the amount of intermediate *d* produced F_d^{in} (t/y) can be calculated via:

$$F_d^{in} = \sum_{c=1}^{C} F_{c,d}^{out} \qquad \forall d \qquad (12)$$

Next, intermediate *d* is the distributed to technology 2 *e* via:

$$F_d^{out} = \sum_{e=1}^{E} F_{d,e}^{out} \qquad \forall d \qquad (13)$$

Between these 2 layers of activities, conversion of Intermediate *d* into suitable unit for Technology 2 *e* $X_{d,e}^{unit}$ might be needed (e.g., conversion of syngas to power unit GJ in for CHP in technology 2 *e*). Therefore, the flow into technology 2 *e* is calculated via:

$$F_{d,e}^{in} = F_{d,e}^{out} \; X_{d,e}^{unit} \qquad \forall d \forall e \qquad (14)$$

Hence, the amount received in technology 2 *e* F_e^{in} (unit/y)can be calculated via:

$$F_e^{in} = \sum_{d=1}^{D} F_{d,e}^{in} \qquad \forall e \qquad (15)$$

Similar to technology 1 *c*, the amount produced from technology 2 *e* is dependent on the conversion $X_{d,z}^{e}$

$$F_{e,z}^{out} = F_{e,z}^{out} \; X_{d,z}^{e} \qquad \forall e \forall z \qquad (16)$$

Given the conversion $X_{d,z}^{e}$, the amount of end product *z* produced F_z^{in} (unit/y) can be calculated via:

$$F_z^{in} = \sum_{e=1}^{E} F_{e,z}^{out} \qquad \forall d \qquad (17)$$

2.2 Economic Performance Evaluation Equations

The economics performance of each activities is evaluated to determine the economic performance of the proposed value chain as a whole. In this study, the economic performance is defined as the difference between revenue obtained from production of end product *z* and the cost associated with the production of end product *z*. Similar to mass balance formulation at section 2.4, the economic performance of the first four layers of activities in the value chain is formulated with reference to the approach taken by Wan et al in [8]. At plantation *g*, the cost considered is the harvesting cost, as well as the transportation of bio resource *m* (sago logs) to sago mill *f*. the total cost of harvesting $Tot\cos t_g^{Harvest}$ (USD/y), as well as total cost of transportation $Tot\cos t^{Transportation}$ (USD/y) is calculated via:

$$Tot\cos t_g^{Harvest} = \sum_{g=1}^{G} U\cos t_g^{Harvest} F_g^{out} \qquad (18)$$

$$Tot\cos t^{Transportation} = \sum_{f=1}^{F}\sum_{g=1}^{G} U\cos t^{km} d_{g,f}^{trip} n_{g,f}^{trip} \qquad (19)$$

Where $U\cos t_g^{Harvest}$ is the cost of harvesting at plantation *g*, $U\cos t^{km}$ (USD/palm) is cost of transportation per km USD/km) and $d_{g,f}^{trip}$ (km) is the distance between plantation *g* and sago mill *f*. Hence the total cost incurred by all plantations $Tot\cos t^{Plantation}$ (USD/y) is as:

$$Tot\cos t^{Plantation} = Tot\cos t_g^{Harvest} + Tot\cos t_g^{Transportation} \qquad (20)$$

In sago mill *f*, the cost considered is the cost of process $Tot\cos t_f^{Process}$ (e.g., electricity, water consumption) as well as raw material cost $Tot\cos t_f^{Material}$ for the

production of sago starch. In this study, sago wastes are assumed to be produced from SSEP without cost. The cost of transportation to refinery site for conversion via technology 1 *c* is also not considered in this study. Therefore, the total cost of the sago mill is calculated by summing the cost of process and raw materials as showed in Equations (21) – (23):

$$Tot\cos t_f^{Material} = \sum_{f=1}^{F} U\cos t_f^{Material} Starch^f \quad (21)$$

$$Tot\cos t_f^{Process} = \sum_{f=1}^{F} U\cos t_f^{Process} Starch^f \quad (22)$$

$$Tot\cos t^{mill} = Tot\cos t^{material} + Tot\cos t^{process} \quad (23)$$

where $U\cos t_f^{Material}$ (USD/t) and $U\cos t_f^{Process}$ (USD/t) is the process and raw material unit cost to produce one tonne of sago starch in sago mill *f*. The total cost of production $Tot\cos t^{Prod}$ (USD/y) is the calculated via:

$$Tot\cos t^{Prod} = Tot\cos t^{plantation} + Tot\cos t^{mill} \quad (24)$$

Next, the cost of the product *p* $Tot\cos t_p$ (USD/y) is considered in this study via:

$$Tot\cos t_p = \sum_{p=1}^{P} \mathrm{UCost_p} F_p^{in} \quad (25)$$

where $\mathrm{UCost_p}$ is unit cost of product *p* (USD/t). In order to produce intermediate *d* from Technology 1 *c*, there will be cost associated, which is calculated via:

$$Tot\cos t_b = \sum_{b=1}^{B} \mathrm{UCost}_b F_b^{out} \quad (26)$$

where UCost_b (USD/t) is the unit cost of converting product *p* to intermediate *d*. Similarly, the cost to produce end product *z* via Technology 2 *e* is calculated via:

$$Tot\cos t_e = \sum_{e=1}^{E}\sum_{z=1}^{Z} \mathrm{UCost}_e F_e^{in} \quad (27)$$

where UCost_e (USD/t) is the unit cost of converting Intermediate *d* into End Product Z via technology 2 *e*. Lastly, the total cost of the value chain $Tot\mathrm{Cost}^{Overall}$ (USD/y) is calculated via:

$$Tot\mathrm{Cost}^{Overall} = Tot\cos t_{production} + Tot\cos t_b + Tot\cos t_c + Tot\cos t_d + Tot\cos t_e \quad (28)$$

Next, the revenue from the proposed value chain $Tot\,\mathrm{Rev}_z$ (USD/y) can be calculated via:

$$Tot\,\mathrm{Rev}_z = \sum_{z=1}^{Z} \mathrm{Price}_z F_z^{in} \quad (29)$$

where Price_z is the unit price for the End Product *z* produced. Therefore, in order to evaluate the economic performance of the proposed value chain, the overall profit $Tot\,\mathrm{Profit}^{Overall}$ (USD/y) is calculated via:

$$Tot\,\mathrm{Pr}ofit^{Overall} = Tot\,\mathrm{Re}v_z - Tot\,\mathrm{Cos}t^{Overall} \quad (30)$$

2.3 Carbon Footprint (CFP) Computation Equations

The formulation of CFP is done with reference to CFP formulation done by Wan et al. [8]. The author considered the land use change (LUC) emission from the commercialisation of land for plantation. Given that the yearly emission per metre square from LUC $UCFP_g^{LUC}$ (kg/m^2.y) is 2.33 as reported by Fargione et al. [11]. The total land use change carbon footprint from plantation g $TotCFP^{LUC}$ (kg CO^2/y) can be calculated via:

$$TotCFP_{plantation}^{LUC} = \sum_{g=1}^{G} A_g UCFP_g^{LUC} \quad (31)$$

$$TotCFP_{plantation}^{Fuel} = \sum_{f=1}^{F} UCFP_{km}^{fuel} n_{g,f}^{trip} d_{g,f}^{trip} \quad (32)$$

$$TotCFP_{plantation}^{total} = TotCFP_{plantation}^{LUC} + TotCFP_{plantation}^{Fuel} \quad (33)$$

Next, the total amount of power and fuel consumed in sago mill f is determined in order to calculate the CFP emission from sago mill f. The CFP from power consumption and fuel consumption is calculated via:

$$TotCFP_{mill} = \sum_{f=1}^{F} UCFP_{KWh}^{Power} E_{f,starch} Starch^f \quad (34)$$

Thus the total CFP emission from production process can be calculated via:

$$TotCFP^{\mathrm{Pr}oduction} = TotCFP_{mill}^{Power} + TotCFP_{plantation}^{total} \quad (35)$$

Considering that product p in this study represents the sago waste produced from SSEP, the CFP emission for production of product p is assumed to be zero. However, the CFP emission from conversion of product p to intermediate d via technology c is considered in this study as:

$$TotCFP_b^{Total} = \sum_{b=1}^{B} UCFP_b F_b^{out} \quad (36)$$

Next, the CFP emission from conversion of intermediate d to end product z via technology 2 e is the sum of the base CFP emission from processing intermediate d and also the specific power consumption of producing end product z via technology 2 e.

$$TotCFP_e^{Base} = \sum_{e=1}^{E} UCFP_e^{base} F_e^{in} \quad (37)$$

$$TotCFP_e^{Specific} = \sum_{z=1}^{Z} \sum_{e=1}^{E} UCFP_{e,z}^{specific} F_{e,z}^{out} \quad (38)$$

$$TotCFP_e^{Total} = TotCFP_e^{Base} + TotCFP_e^{Specific} \quad (39)$$

The total overall CFP $TotCFP^{Overall}$ (kg CO^2/y) is calculated via:

$$TotCFP^{Overall} = TotCFP^{total}_{plantation} + TotCFP_{mill} + TotCFP^{Total}_{b} + TotCFP^{Total}_{e} \quad (40)$$

2.4 Fuzzy-Based Optimization Approach Equations

Cost and Environmental objectives are often contradictory, a fuzzy-based optimisation approach is adopted in this study to select the optimum pathway for conversion of sago waste to value –added products. Using the 'min-max' aggregation concept in fuzzy optimisation, the optimum pathway can be obtained by maximising the least satisfied constraints. Fuzzy optimisation combines multiple objectives into a single variable, λ, having a range of 0 to 1. In this study, the objectives are integrated into λ as shown in the equations below:

$$\frac{CFP^{UL} - TotCFP}{CFP^{UL} - CFP^{LL}} \geq \lambda \quad (41)$$

$$\frac{Tot\,\mathrm{Pr}ofit - \mathrm{Pr}ofit^{LL}}{\mathrm{Pr}ofit^{UL} - \mathrm{Pr}ofit^{LL}} \geq \lambda \quad (42)$$

where $TotCFP$ and $Tot\,\mathrm{Pr}ofit$, are the carbon footprint and profit generated by utilizing the optimum pathway for conversion of sago wastes. Meanwhile, CFP^{LL} and CFP^{UL} are the pre-determined lower and upper limit of the carbon footprint generated, same goes for $\mathrm{Pr}ofit^{UL}$ and $\mathrm{Pr}ofit^{LL}$ for profit generated. These upper and lower limit are determined by extracting data from evaluation results of the model at different objectives.

It is noted that each objective has a predetermined fuzzy range, represented by a linear function within the lower and upper limit, as shown in Figure 12. Figure 12 (a) illustrates the maximization case, where λ approaches 1 when the objective, $Tot\,\mathrm{Pr}ofit$ approaches the upper limit, $\mathrm{Pr}ofit^{UL}$ of the fuzzy approach. On the contrary, Figure 12 (b) demonstrates the minimization case, where λ approaches 1 when the objective, $TotCFP$ approaches the lower limit, CFP^{UL}.

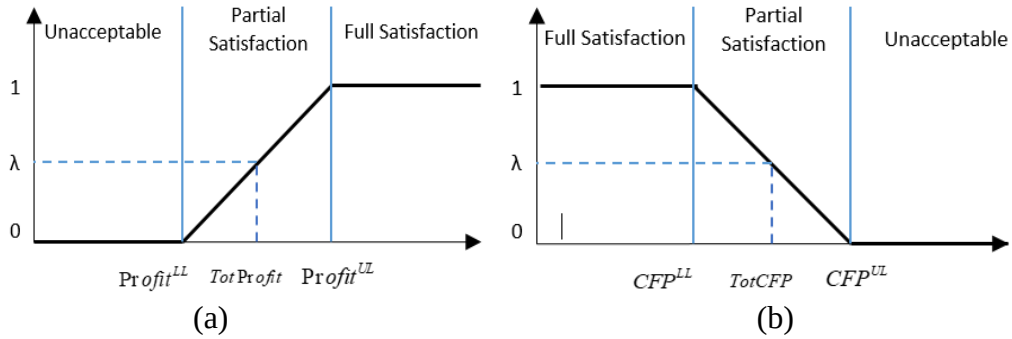


Figure 12: The Concept of Fuzzy

In order to generate an optimum pathway for the conversion of sago waste while maximizing profit and minimizing carbon footprint, Eq. (40) and (41) are included in the optimization model, and solved simultaneously by maximising the degree of

satisfaction, λ. This mixed integer linear programming (MILP) model is solved via Lingo v17.0 in a Lenovo Ideapad 700 with Intel Core i7-6700HQ (2.6 GHz) and 8GB ram running on 64-bit operating system.

3. Case Study

Figure 13 shows the case study superstructure that with all the possible pathways of activities from the proposed value chain in this study. In this case study, plantations from Mukah, Dalat, Saratok and Betong are considered, with sago logs as the only bio-resource produced from the considered sago plantations. The sago mills considered in this study are the ones located around the plantations.

The sago mills products considered in this study are the sago fibers, sago wastes, and sago wastewater, which are produced simultaneously in the sago mill during SSEP. In this study, eight different conversion technology are considered in technology 1 that produces primarily four different intermediates, which will be sent to technology 2 considered in this study. The end product considered in this study consists of high value product from agriculture biomass that has been intensively studied recently. Data from superstructure, such as amount of palms available annually, capacities of sago mill and distance between sago mill and plantation can be found is taken from data reported by Wan et al. [8]. For this study, the conversion rate of palm to sago log $X_{g,log}$ are taken as 10 logs/palm, the weight of log W_{log} is taken as 0.05t/log. Different plantation g produces palms with different starch content due to different soil conditions, which can also be found in [8]. To determine the economic and environmental performance of the value chain proposed in this study, unit costs and CFP emission of producing intermediate *d* and end product *z* via technology 1 *c* and technology 2 *e* are estimated from literature and summarized in

Table 8. The data used in conversion of feed to product at each layer, as well as the economic and environmental impact of the technologies are shown in

Table 8 obtained from [12]–[18]. Data is collected from various literature on biomass conversion technologies.

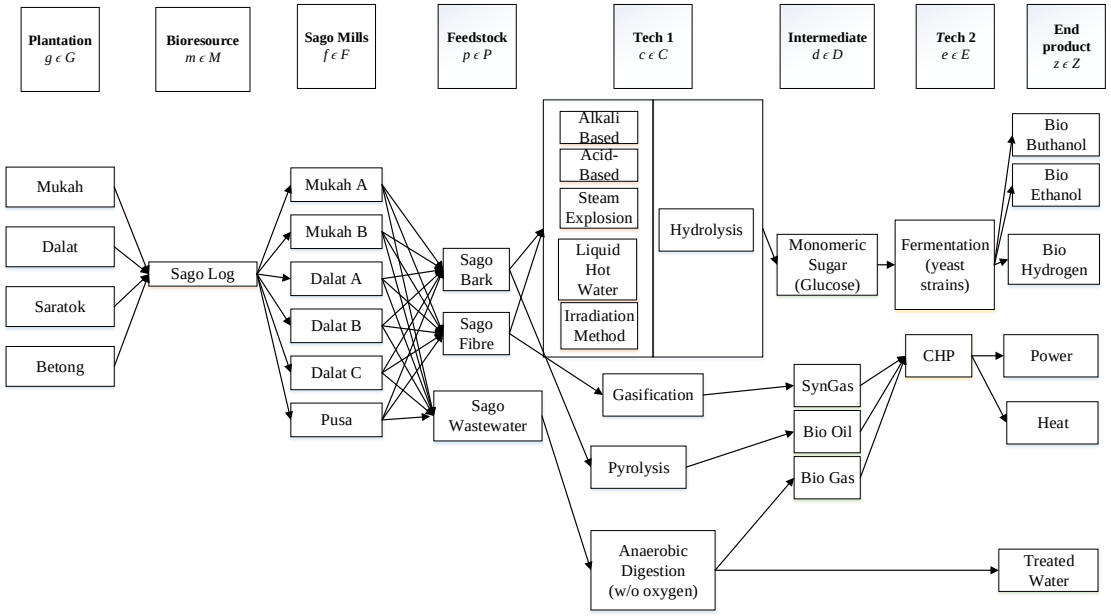


Figure 13: Case Study Superstructure

Table 8: Conversion, Cost and CFP data

	Feed Type	Product Type	Conversion (product/feed)	Cost (USD/Tonne Product)	CFP (kg CO_2/tonne Product)
Alkali Based	Sago Fiber	Glucose	0.4828	650	467.48
	Sago Bark	Glucose	0.16401		
Acid Based	Sago Fiber	Glucose	0.5440	420	503.44
	Sago Bark	Glucose	0.1848		
Steam Explosion	Sago Fiber	Glucose	0.6120	430	521.42
	Sago Bark	Glucose	0.2079		
Liquid Hot Water	Sago Fiber	Glucose	0.6120	790	467.48
	Sago Bark	Glucose	0.2079		
Irradiation Method	Sago Fiber	Glucose	0.2244	370.58	317.15
	Sago Bark	Glucose	0.0762		
Gasification	Sago Fiber	Syngas	0.2271	45,200	2,200
	Sago Bark	Syngas	0.2220		
Pyrolysis	Sago Fiber	Bio-Oil	0.3200	89,630	1,727
	Sago Bark	Bio-Oil	0.3200		
Anaerobic Digestion	Sago Waste Water	Bio Gas	1.7250	4,400	0
Fermentation	Glucose	Butanol	0.0857	1,370	12,652.53
	Glucose	Ethanol	0.2910	874.52	5,977.79
	Glucose	Hydrogen	0.0111	5400	13,055.82
CHP	GJ	Power(GJ)	0.2222	1.55	0
	GJ	Heat(GJ)	0.8000	16.95	0

3.1 Results and Discussion

To solve the case study, the upper and lower fuzzy limit is pre-determined by solving the objectives individually (e.g., maximize profit, minimize CFP emission) without mutual interaction between objectives. The single objective optimization results are shown in Table 9. Based on the results on Table 9, the upper and lower fuzzy limits is coded into the model and solved via Lingo 16.0 in a Lenovo Ideapad 700 with Intel Core i7-6700HQ (2.6 GHz) and 8GB ram running on 64-bit operating system. The CPU time to obtain the maximum global optimal solution for degree of satisfaction λ is approximately within 5s. In addition, Table 3-6 illustrate the flow rate between layers at different objectives.

Table 9: Total Profit and CFP in multiple objectives

Objective Functions	Total Profit (Million USD/y)	Total CFP (tonne CO2/y)
Max Total Profit	342.90	779,803.00
Min Total CFP	-4.30	768,777.90

Table 10: Mass Flowrates of logs from plantations to sago mills with objective function minimize $TotCFP^{Overall}$, maximize $Tot\,\mathrm{Pr}ofit^{Overall}$ and maximize λ.

Flow Rate from sago plantation to sago mill (log/y)						
	minimize $TotCFP^{Overall}$					
	Mukah A	Mukah B	Dalat A	Dalat B	Dalat C	Pusa
Mukah	0	375,000	0	0	200	0
Dalat	0	0	302,400	317,400	204,600	0
Saratok	0	0	0	0	0	220,000
Betong	0	0	0	0	0	0
	maximize $Tot\,\mathrm{Pr}ofit^{Overall}$					
	Mukah A	Mukah B	Dalat A	Dalat B	Dalat C	Pusa
Mukah	0	374,200	0	0	0	0
Dalat	0	600	302,400	343,600	178,800	0
Saratok	0	0	0	0	0	220,000
Betong	0	0	0	0	0	0
	maximize λ					
	Mukah A	Mukah B	Dalat A	Dalat B	Dalat C	Pusa
Mukah	0	0	0	0	0	0
Dalat	200	343,600	302,400	343,600	343,600	0
Saratok	0	0	0	0	0	0
Betong	0	0	0	0	0	0

Table 11: Mass Flow Rate of Sago Wastes from sago mills with objective function minimize $TotCFP^{Overall}$, maximize $Tot\,\mathrm{Pr}ofit^{Overall}$ and maximize λ.

Production of Sago wastes from Sago mills.

Objectives	minimize $TotCFP^{Overall}$			maximize $Tot\,\mathrm{Pr}ofit^{Overall}$			maximize λ		
	SF	SB	SW	SF	SB	SW	SF	SB	SW
Mukah A	0	0	0	0	0	0	4.8	19.2	96
Mukah B	8,250	33,000	165,000	8,246	32,987	164,936	9,246	32,985	164,928
Dalat A	7,257	29,030	145,152	7,257	29,030	145,152	7,257	29030	145,152
Dalat B	7,617	30,470	152,352	8,246	32,985	164,928	8,246	3,295	164,928
Dalat C	4,914	19,659	98,296	4,291	17,164	85,824	8,246	3,295	164,928
Pusa	3,960	15840	79,200	3,960	1,584	79,200	0	0	0

Table 12: Mass Flow Rate of intermediate *d* into technology 1 with objective function minimize $TotCFP^{Overall}$, maximize $Tot\,\mathrm{Pr}ofit^{Overall}$ and maximize λ.

	minimize $TotCFP^{Overall}$			**maximize** $Tot\,\mathrm{Pr}ofit^{Overall}$			**maximize** λ		
	SF	SB	SW	SF	SB	SW	SF	SB	SW
Irradiation Method	0	128,000	0	0	0	0	0	128,006	0
Gasification	0	0	0	0	0	0	3,068	0	0
Pyrolysis	32,000	0	0	32,002	128,008	0	28,933	0	0
Anerobic Digestion	0	0	640,000	0	0	640,040	0	0	640,032

Table 13: Amount of Intermediate *d* and End Product *z* produced

	minimize $TotCFP^{Overall}$	**maximize** $Tot\,\mathrm{Pr}ofit^{Overall}$	**maximize** λ
Butanol	0	0	0
Ethanol	2,839	0	2,839.
Hydrogen	0	0	0
Power	8,480,067	8,716,897	8,523,204
Heat	0	0	0

An optimum sustainable sago value chain with degree of satisfaction, λ of 0.8596, a total profit of 294.2 million USD/y and CFP emission of 770.32 ton CO_2/y is obtained as shown in Table 14. Furthermore, Table 14 also shows the flow rate between activities in the optimum sago value chain at optimised solution.

Based on the optimised result, only palms from Dalat is harvested, which is first processed into sago logs before sending into sago mill Dalat A, Dalat B, Dalat C and Pusa SSEP process. The SSEP process then produces sago waste SF, SB and SW. SF is then sent into gasification and pyrolysis to produce syngas and bio-oil respectively, while SB is sent for microwave irradiation pre-treatment, followed by hydrolysis to produce monomeric sugars such as glucose. SW is sent to for anaerobic digestion to produce biogas. The intermediates are then sent for further processing. Glucose undergoes fermentation to produce ethanol, while syngas, bio-oil and bio gas are sent to CHP to generate power. The amount of final products produced in this optimised sago value chain is 2,839.611 t/y of ethanol and 8,523,204 GJ/y of power.

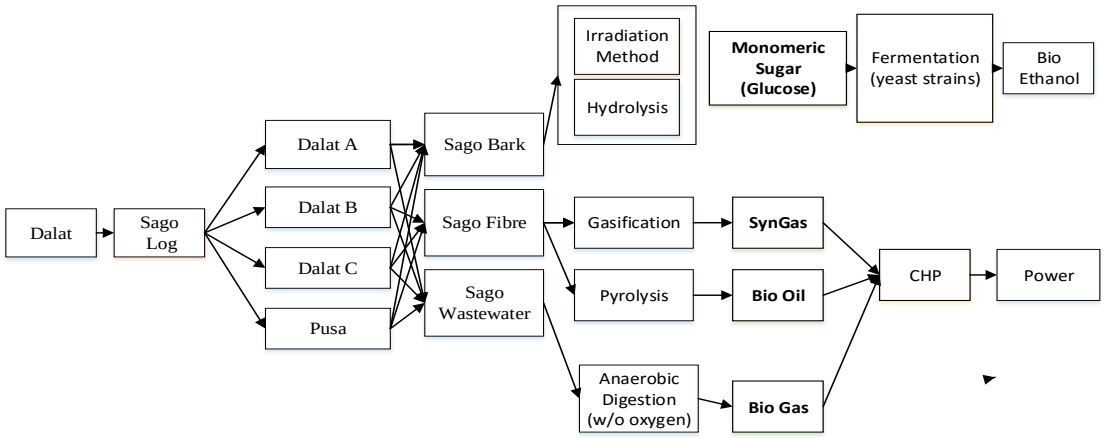


Figure 14: Optimized Sago Value Chain

Table 14: Mass Flow Rate of Optimized Sago Value chain

Pathways	*Amount*	*Pathways*	*Amount*
Dalat - Sago Log	133,340	SF- Gasification	3,068
Sago Log - Dalat A	343,600	SF - Pyrolysis	28,933
Sago Log - Dalat B	302,400	SB- Irradiation Method	128,005
Sago Log - Dalat C	343,600	SW- Anaerobic Digestion	640,032
Sago Log - Pusa	343,600	Irradiation Method - Glucose	9,758
Dalat A - SF	8,246	Gasification - Syngas	696

Table 15: Mass Flow Rate of Optimized Sago Value chain (Continued)

Pathways	*Amount*	*Pathways*	*Amount*
Dalat A - SB	32,985	Pyrolysis - Bio Oil	9,258
Dalat A - SW	164,928	Anaerobic Digestion - Bio Gas	1,104,055
Dalat B - SF	7,257	Glucose - Fermentation	9,758
Dalat B - SB	29,030	Syngas - CHP	696

Dalat B - SW	145,152	Bio Oil - CHP	9,258
Dalat C - SF	8,246	Bio Gas - CHP	1,104,055
Dalat C - SB	32,985	Fermentation - Bio Ethanol	2,839
Dalat C - SW	164,928	CHP - Power	8,523,204
Pusa - SF	8,246		
Pusa - SB	32,985	Total CFP	770,324,800
Pusa - SW	164,928	Total Profit	294,206,200

4. Conclusion

A fuzzy-based optimisation model approach that considers economic and environmental performance of the proposed sago value chain simultaneously is developed in this study. This model can be used as an analysis tool that aids decision making in selecting the most optimal pathway for conversion of sago waste to value added product while considering the environmental and economic impacts.

This model developed in this study is requires intensive data and is customized for sago industry in this study; however, with some modification, it can be applied in different agriculture industry to evaluate conversion pathways of agriculture biomass into value-added products. Note that data such as yield, cost and CFP of crops might not be readily available and is subjected to the magnitude of attention and research on that specific agriculture industry. Sensitivity to uncertainties or changes in data is not considered in this study via robust optimization, which can be considered in the future. The limitation of this study is that it only considers the sago wastes produced from the SSEP process in the sago mill, which can also be considered in future researches.

Acknowledgement

The author would like extend his upmost gratitude to Dr.Wan Yoke Kin and Dr. Viknesh Andiappan for their kind support and guidance in supporting him throughout the process of completing this study.

References

[1] M. Flach, “Sago palm,” *Diversity*, p. 76, 1997.

[2] FAO, “Expert consultation on the establishment of a sago network for Asia and the Pacific,” no. March, pp. 1–83, 2013.

[3] A. A. Karim, A. P. L. Tie, D. M. A. Manan, and I. S. M. Zaidul, “Starch from the sago (Metroxylon sagu) palm tree - Properties, prospects, and challenges as a new industrial source for food and other uses,” *Comprehensive Reviews in Food Science and Food Safety*, vol. 7, no. 3. pp. 215–228, 2008.

[4] D. S. Awg-Adeni, S. Abd-Aziz, K. Bujang, and M. A. Hassan, “Bioconversion of sago residue into value added products,” *African J. Biotechnol.*, vol. 9, no. 14, pp. 2016–2021, 2010.

[5] D. S. Awg-Adeni, K. B. Bujang, S. Abd-Aziz, and M. A. Hassan, "Recovery of Glucose from Residual Starch of Sago Hampas for Bioethanol Production," vol. 2013, 2013.

[6] M. Machines, "Chapter 1," pp. 1–11, 1995.

[7] Y. K. Wan, J. Sadhukhan, and D. K. S. Ng, "Techno-economic evaluations for feasibility of sago-based biorefinery, Part 2: Integrated bioethanol production and energy systems," *Chem. Eng. Res. Des.*, vol. 107, pp. 102–116, 2016.

[8] Y. K. Wan, R. T. L. Ng, D. K. S. Ng, K. B. Aviso, and R. R. Tan, "Fuzzy multi-footprint optimisation (FMFO) for synthesis of a sustainable value chain: Malaysian sago industry," *J. Clean. Prod.*, vol. 128, pp. 62–76, 2016.

[9] T. Koc and E. Bozdag, "Measuring the degree of novelty of innovation based on Porter's value chain approach," *Eur. J. Oper. Res.*, vol. 257, no. 2, pp. 559–567, 2017.

[10] D. H. S. Tay, D. K. S. Ng, N. E. Sammons, and M. R. Eden, "Fuzzy optimization approach for the synthesis of a sustainable integrated biorefinery," *Ind. Eng. Chem. Res.*, vol. 50, no. 3, pp. 1652–1665, 2011.

[11] J. Fargione, J. Hill, D. Tilman, S. Polasky, and P. Hawthorne, "Land clearing and the biofuel carbon debt.," *Science*, vol. 319, no. 5867, pp. 1235–8, 2008.

[12] N. Nahar, D. Ripplinger, and S. W. Pryor, "Process yield and economic trade-offs for enzymatic hydrolysis of alkaline pretreated corn stover," *Biomass and Bioenergy*, vol. 99, pp. 97–105, 2017.

[13] T. Eggeman and R. T. Elander, "Process and economic analysis of pretreatment technologies," *Bioresour. Technol.*, vol. 96, no. 18 SPEC. ISS., pp. 2019–2025, 2005.

[14] T. S. Kannan, A. S. Ahmed, and F. N. Ani, "Energy Efficient Microwave Irradiation of Sago Bark Waste (SBW) for Bioethanol Production," *Adv. Mater. Res.*, vol. 701, no. April, pp. 249–253, 2013.

[15] T. Pielhop, J. Amgarten, P. R. von Rohr, and M. H. Studer, "Steam explosion pretreatment of softwood: the effect of the explosive decompression on enzymatic digestibility," *Biotechnol. Biofuels*, vol. 9, no. 1, p. 152, 2016.

[16] P. Noparat, P. Prasertsan, S. O-Thong, and X. Pan, "Dilute Acid Pretreatment of Oil Palm Trunk Biomass at High Temperature for Enzymatic Hydrolysis," in *Energy Procedia*, 2015, vol. 79, pp. 924–929.

[17] D. Kumar and G. S. Murthy, "Impact of pretreatment and downstream processing technologies on economics and energy in cellulosic ethanol production," *Biotechnol. Biofuels*, vol. 4, no. 1, p. 27, 2011.

[18] P. Elaiyaraju and N. Partha, "Biogas Production from Sago (Tapioca) Wastewater Using Anaerobic Batch Reactor," *Energy Environ.*, vol. 23, no. 4, pp. 631–645, 2012.

Optimisation of Process Parameters for Devulcanisation of Natural Rubber Utilising Deep Eutectic Solvent (DES)

Kishen Kunju, Rashmi G. Walvekar, Mohammad Khalid Siddiqui

kishen.kunju@sd.taylors.edu.my
rashmi.walvekar@gmail.com
khalidchem@gmail.com

Abstract

Waste rubber is a polymeric material containing 50 % of rubber and is generally referred to as waste tyre rubber. The main purpose of this research is to study ultrasonic devulcanisation of waste rubber utilising deep eutectic solvent (DES) of $ZnCl_2$: Urea by improving process parameters such as sonication time, reaction temperature and rubber: DES mass ratio by effectively cleaving cross-link sulphur bonds. DES was created and prepared by mixing $ZnCl_2$ with urea at 2:7 and 1:4 molar ratio respectively. Physicochemical properties of the prepared DES was measured using DSC, KFT and TGA analysis to find the freezing point, moisture content and degradation temperature, whereby their freezing point below 60℃, moisture content lower than 3.0 wt.% and 200℃ degradation temperature average. Rubber to DES mass ratio was varied at 1:20, 1:30 and 1:40 and sonicated for 15 minutes inside ultrasonic water-bath. Samples were placed onto hot plate whereby heating temperature was varied at room temperature, 130℃, 150℃, and 180℃ for 15 minutes. Samples were filtered, washed with distilled water and dried in oven for 24 hours. Once dried, samples were taken for analysis using TGA, EDX, FESEM, FTIR and Gel content. Under TGA analysis, most samples have an average degradation temperature of 200℃, hence justifying a successful devulcanisation .EDX analysis shows two occurrence during devulcanisation process which is bond reformation and cleavage .Furthermore, it is determined that heating temperature of 130℃ is an important parameter as it is the optimum temperature for $ZnCl_2$: urea. Under FTIR analysis, it shows that disulphide bond, S-S is the only bond that is being broken while the rest still remains the same. Gel content analysis showed that samples has a lower soluble fraction after devulcanisation process. Finally, FESEM proves that at 130℃ and 15 minutes is the optimum temperature and time which is illustrated by the smooth curve at that particular point.

Keywords: Cross-link Sulphur Bonds, devulcanisation, Deep Eutectic Solvent (DES), cleaving, ultrasonic

1. Introduction

Rubber is a form of elastic and flexible substance which is able to elastically deform through a certain applied force. It mainly composed of polymers exhibiting a long-chain carbon bond, rotating around its axis and twisting the chains into different combinations. Main source of rubber originates from rubber tree known as ***Hevea brasiliensis*** [1] which grows sufficiently well under cultivation.

Oil, fillers and antioxidants are compounded together with raw rubber to increase the tensile strength of the rubber and life cycle. In order to utilize raw rubber, it needs to be vulcanised first in order to increase the rubber's strength and life as well as reducing manufacturing cost. And only after that, vulcanisation rubber process is carried out as shown in Fig 1.1.1. It is an irreversible process in which rubber molecules is cross-linked to the sulphur compound, resulting in tires being elastic and strong resistant to bio-degradation and high temperature [2].

In the manufacturing sector, rubber is considered to be the largest component in composing a tire to where it is broadly applied .Throughout the years, demand for rubber has been ever increasing globally from household applications to industrial fields such as gloves, shoes, insulators and especially on tyres. And with the increasing demand of tyres, the number of vehicles on the road has been increasing drastically. This leads to the around 800 million tires being disposed annually and it is said to increase by 2 % every year [3]. 1.3 billion tires are produced globally which is equivalent to nearly 17 million tonnes per year of used tires as reported by Sienkiewicz et al. [4] which will ultimately lead the wastage of rubber tyres.

Waste rubber is a polymeric material containing 50 % of rubber in tyres and is generally referred to as waste tyre rubber [5]. There is a large amount of vulcanized residue that comes from the production of rubber materials and it considered to be a major problem. Less efforts were taken into recycling them even after their life cycle has ended, resulting in these tyres being wasted to a point where it becomes a pollution source. This is due to the fact that the rubber tyre has a complex microstructure of a three dimensional cross-linking bonds which makes the material not so easily decomposed and insoluble [5].

Therefore to reduce wastage of rubber tyres, different methods of devulcanisation has been introduced. Devulcanisation method is one of the ways to reduce the impact risks on environment by transforming tyres back into virgin rubber or original rubber that can be used for re-vulcanisation purposes. Rubber with a complex structure of three dimensional network arrangement has carbon-sulphur (C-S) bond and sulphur-sulphur (S-S) bond attached to it. This C-S bond are longer compared to C-C bond as sulphur is much larger than carbon. During the devulcanisation process, C-S and S-S bonds are broken down resulting in a three dimensional structure to obtain plasticity. As shown in Figure 2, C-S bond is broken down under the presence of high

temperature, where it gains enough energy to in order to break the C-S bond. It is then re-vulcanised again by heating to 120-150℃ to form better products.

Some of the currently available methods used for devulcanisation are microwave heating [7], continuous ultrasonic [8], microbial action [9], and many other methods. These methods used are definitely capable for devulcanisation of rubber material, however up to a certain limit. This is due to the fact that few of the solvents used before this are not suitable as it is costly and hazardous. In addition to that, end product from using from those methods mentioned has a poor mechanical strength which is not ideal for re-vulcanisation process.

Recent study carried out by [11] shows experimental analysis where ionic liquid (IL) was used as a solvent for devulcanisation of rubber through microwave irradiation method and it showed positive results. Devulcanisation of rubber tyre was carried out with the combination of microwave radiation and IL which achieved to 50% removal of sulphur. However, further research found that ionic liquids was not very convenient to be used due to its limitations whereby it has high toxicity level, poor degradability, combustible material and not to mention highly cost. Therefore, these limitations can be avoided by finding a more suitable candidate to replace ILs.

One of the emerging alternative solvent which shows similar properties to ILs is known to be Deep Eutectic Solvent (DES). It's been proven that ILs is able to devulcanise waste tyre rubber and with that justifies DES is an excellent alternative to IL which can devulcanise the waste tyre rubber whilst avoiding all the limitations and problems encountered. It is a mixture of two or more components having a lower melting point than each individual component. By mixing ammonium halide salt which is a hydrogen bond acceptor (HBA) and hydrogen bond donor (HBD) molecule, DES is obtained, resulting in significant decrease in freezing point. Since it has similar properties to ILs such as easy regeneration and non-flammable, it shares similar advantages as well in terms of low vapour pressure, biodegradability, chemical stability, cheap material and easily obtained [13]. Thus, DES is considered as a green solvent in being an important alternative to volatile organic solvents

Similar research area [12] has been done within the petrochemical industry whereby for desulphurisation process, DES was used to remove sulphur from petrochemical products such as oil. Based on the research done by Wang, Liu, Li et al. [10] , it was found that the removal efficiency of sulphur is as high as 99.48% which further proves that DES is a suitable solvent in removing sulphur and it can be used for devulcanisation process.

Many different combinations of HBA and HBD have been performed since the first experimental analysis of DES was reported. One of the common combination is with choline chloride, ChCl and zinc chloride, $ZnCl_2$ salt with other types of HBDs such as urea. ChCl salt is commonly picked because it is low in cost and toxicity,

biodegradable, and its biocompatibility [10]. On the other hand, zinc chloride, $ZnCl_2$ is chosen due to its biocompatibility and biodegradability of the salt [10].

Hence, currently new approach for devulcanisation process using the DES alongside with ultrasonic treatment under controlled condition of temperature and sonication of water bath was introduced. With the use of DES as a cheaper and greener solvent, this can help reduce energy consumption during the devulcanisation process as well improving its recovery process. Thus, for the interest of the study, the chosen DES used alongside ultrasonic devulcanisation of rubber samples is $ZnCl_2$: Urea at various molar ratios of 1:4 and 2:7.

The key objectives on proposing this project which is based upon research study consists of the following:-

a) To synthesize and characterize $ZnCl_2$: Urea as a deep eutectic solvents (DESs) of a various molar ratio
b) To optimise the sonication time, heating temperature and rubber : DES mass ratio on devulcanisation of the waste rubber

2. Methodology

Based on the research project that will be carried out, quantitative study will be used throughout the entire project to which the justification would be made based on the removal amount of sulphur from waste tyre rubber sample during devulcanisation process.

2.1 DES preparation samples

The selection and synthesis process for two types of DESs solvent chosen was carried out. The selection of DES is made based on boiling point of DES whereby it must be higher than the temperature of devulcanisation which is about 180℃. Based on thesis done by Ricky et al. [39], it was determined that zinc chloride: urea and choline chloride: urea is the best selection for DES synthesis to be carried out. Table 3.2.1 depict the factors of the selected DES that later will be used for devulcanisation process.

In order to prepare DES, zinc chloride (salt) as the hydrogen bond acceptor and urea as the hydrogen bond donor was ordered and purchased under Sigma Aldrich Sdn.Bhd. Preparation of DES was made based on 1:4 and 2:7 molar ratio of $ZnCl_2$: Urea. By following the steps to prepare DES based on a research from [14], mass of $ZnCl_2$ and urea were weighed accordingly and both compounds were added into a 100 ml Schott bottle alongside a magnetic stirrer. The bottle was sealed with a parafilm to ensure minimum moisture content. This is to prevent the crystallization of DES from occuring. It was then placed onto a hot plate placed inside fume hood running at 300 rpm and at 130-170℃, in order to synthesize DESs solvent. The solvent is left

approximately for 2-4 hours. It is considered successful if the solution obtained is a homogeneous and if it's not, then the process has to be repeated [13]. The reason for the DES samples to be conducted in a fume hood and sealing the cap with parafilm is to ensure entire moisture goes into solvent. Table 6 depicts the molar ratio used for $ZnCl_2$: Urea solvent.

Table 1: Preparation of DES molar ratio

Ammonium/Halide salt	*HBDs*	*Molar ratio*	*Freezing Point (K)*
$ZnCl_2$	Urea	1:4	278.15
$ZnCl_2$	Urea	2:7	275.15

.

2.2 Physiochemical Properties of DES

In order to determine whether the DES prepared is suited to be used as a devulcanising agent, Karl-Fischer Titration, Differential Scanning Calorimetric (DSC), Thermogravimetric Analysis (TGA) will be performed upon the prepared DES samples.

2.2.1 Karl-Fischer Titration

The moisture content of the prepared DES sample is done through KFT analysis whereby the moisture must not exceed 3 wt % as said by [16]. To find out the accuracy and precision of the analysis instrument, 1.00 mg/g of Hydranal water standard was utilised whereby it was purchased and ordered from Sigma-Aldrich Malaysia.

2.2.2 Differential Scanning Calorimetric Analysis

Freezing point of the synthesized DES is determined using the DSC available at Taylor's University School of Bioscience, where it will be carried out in nitrogen surrounding. Before conducting the experiment, the equipment is calibrated correctly to the standards values so that the accuracy of the readings obtained will be high. A portion of DES sample was extracted out and weighed between 5-10 mg in a small pan. The small pan was then placed onto Perkin Elmer – DSC 8000 instrument analysis. The sample was first heated from 30℃ to 60℃ at a rate of 10 K/min, then cooled from 60℃ to -70℃ at a rate of 5 K/min and finally heated from -70℃ to 0℃ at rate of 5 K/min. The suitable freezing point of the synthesized DES should lower than the constituent components and also, the preferred melting point of DES should be below 60℃ [12].

2.2.3 Thermogravimetric Analysis

The degradation temperature is determined through TGA analysis. The experiment is conducted at temperature of 180℃. A portion of synthesized DES sample was extracted out and weighed between 5-10 mg into a small pan. The small pan was then

placed onto Perkin Elmer – TGA 8000 instrument analysis allowing the analysis to be carried out from ambient temperature to 500℃, with 10℃ increment every minute under constant nitrogen purge gas of 40 ml/min environment [15]. The amount of liquid is measured as a temperature function.

2.3 Rubber: DES Sample Preparation

Once physiochemical properties of DES sample were measured and gave good results, devulcanisation of rubber samples were carried out next. Under this process, 4 variables were fixed which consist of sonication time, sonication frequency, DES molar ratios and heating time. Apart from that, 2 variables were varied which are heating temperature and rubber: DES mass ratio.

DES samples as shown in Table 6 were selected for the fact that they are amine-based DES which are suitable for desulphurization process [28] and thus, it is considered to be the same condition for devulcanisation process. Rubber: DES mass ratio was varied at 1:20, 1:30 and 1:40 whereby the total mass of the rubber and DES should be equivalent to 50 grams. These ratios are specifically picked as to avoid sluggish mixture being formed which could render the devulcanisation process during ultrasonic treatment [3]. Rubber and DES was weighed accordingly to mass ratio and inserted inside the Schott bottle where it will be mixed thoroughly.

2.4 Ultrasonic Devulcanisation & Heating Treatment

Once it is mixed thoroughly, the rubber sample mixtures were placed inside the ultrasonic water bath to undergo ultrasonic treatment at sonication time of 15 minutes at 37 kHz [17]. During treatment, rubber: DES samples experienced and received the ultrasonic frequency wave in all possible directions. With the rubber and DES being exposed to ultrasonic wave, the cross-link bonds are overstressed which allows the sulphur-sulphur bonds as well cross-link bonds to become detached. Thus, penetration of DES is easier which leads to cleavage of cross-link bonds [3]. Through sonication, it is predicted that small fragment of the cross-links bond is broken. Therefore to further improve recovery, rubber: DES samples are subjected to heating treatment at 4 different temperatures for each sample after ultrasonic treatment.

Under this treatment, samples mixtures are transferred onto conical flask. It is then proceeded by heating on hot plate in a fume hood environment at room temperature, 130℃, 150℃ and 180℃ for 15 minutes. Heating temperatures was selected based on the flash point of rubber which is nearly 205℃ [18-20]. Thus, heating temperature is recommended to be below the flash point temperature for safety aspects. A controlled sample was used to which it does not undergo ultrasonic water bath treatment and heating

As soon as the heating process is completed, the rubber mixture sample was filtered out using a tea bag instead of a filter paper. This is due to the DES high viscosity which makes it very difficult for the rubber to be filtered out. The rubber mixture which was filtered was washed thoroughly with distilled water [18] to ensure there is no contamination of DES in the rubber mixture samples. Finally, the samples was placed inside the oven for approximately 24 hours at 70℃ for it to dry.

Therefore, the total number of samples required for two different molar ratios, three different rubber: DES mass ratio as well four different heating temperatures is 30. The following Table 2 and 3 depicts the formulation and experimentation of the samples of various molar ratio.

Table 2: The formulation and experimentation of the sample 2:7 molar ratio.

DES Molar ratio	Rubber:DES	Sonication time / min	Heating	Experimental Run
2:7	1:20 (2.38 g : 47.62 g)	15	30	**1A**
			130	**2A**
			150	**3A**
			180	**4A**
		Controlled Sample		**5A**
	1:30 (1.61g : 48.39 g)	15	30	**6A**
			130	**7A**
			150	**8A**
			180	**9A**
		Controlled Sample		**10A**
	1:40 (1.22g : 48.78 g)	15	30	**11A**
			130	**12A**
			150	**13A**
			180	**14A**
		Controlled Sample		**15A**

Table 3: The formulation and experimentation of the sample 1:4 molar ratio.

DES Molar ratio	Rubber:DES	Sonication time / min	Heating	Experimental Run
1:4	1:20 (2.38 g :47.62 g)	15	30	**1B**
			130	**2B**
			150	**3B**
			180	**4B**
		Controlled Sample		**5B**
	1:30 (1.61 g : 48.39 g)	15	30	**6B**
			130	**7B**
			150	**8B**
			180	**9B**
		Controlled Sample		**10B**
	1:40 (1.22g : 48.78 g)	15	30	**11B**
			130	**12B**
			150	**13B**
			180	**14B**
		Controlled Sample		**15B**

2.5 Sample Analysis

Analysis on the rubber sample mixture can be carried out once the rubber is completely dry after being left in the oven for 24 hours. Fourier Transform Infrared Spectroscopy (FTIR) will performed on the rubber sample mixture since it revolves around the presence of the carbon-sulphur bonds.

2.5.1 Fourier Transform Infrared Spectroscopy

The FTIR method used for this particular research study is the FTIR-ATR Spectrum 100. To make further confirmation, FTIR equipment allows the user to determine the specific bond that is broken down after devulcanisation process. This is done by analysing the spectrum generated from FTIR based on before and after data results of the rubber sample mixtures. In order to understand spectrum generated from FTIR, it is best to refer to journal by Garcia and co-workers et al.[13] so that the spectrum can be determined as to which compound it corresponds to specifically. Through this analysis, it is expected that there will be decrease in the intensity of the spectrum based on sulphur cross-link bonds during devulcanisation process. It is also expected that C-S and S-S bonds will decrease after the completion of devulcanisation process.

2.5.2 Thermogravimetric Analysis

Thermogravimetric analysis (TGA) analysis was carried out in with Shimadzu system form Japan. As reported by Medhat M [21], it is heated within a certain temperature range, ranging from 20℃-600℃, with an increment of 10℃ per minute. The entire analysis was carried out in a nitrogen controlled environment. Through this analysis, degradation temperature of the rubber samples can be determined.

Experiment is carried out at temperature of 180℃, in which small amount of DES is inserted into TGA tool. Analysis is carried out from ambient temperature to 500℃, having an increment of 10℃ per minute under a controlled nitrogen environment. Based on the TGA curve obtained from [35], a decreasing slope produced indicates there is a sudden drop in mass. This point at which it has a sudden drop is the degradation temperature of the rubber sample.

3. Results and Discussion

The data obtained was analysed carefully and comparison was made based on previous research carried out on this topic. Results of the analysis will consist of DES characterization, FTIR and TGA results on the rubber sample mixtures.

3.1 DES Analysis of Physiochemical Properties

In order to prepare DES, zinc chloride (salt) as the hydrogen bond acceptor and urea as the hydrogen bond donor was ordered and purchased Sigma Aldrich Sdn.Bhd. Preparation of DES was made based on 1:4 and 2:7 molar ratio of $ZnCl_2$: Urea. A homogeneous solution is obtained which has a very high viscosity at ambient temperature. Based on these, its physiochemical properties of the prepared DES samples such as moisture content, freezing point and degradation temperature is measured and determined.

The moisture content present inside the prepared DES samples must not exceed more than 3 wt % as it will affect and change its properties which could lead to crystallisation during devulcanisation process [22]. Thus 2 batches of different molar ratio of DES consisting of 1:4 and 2:7 was used to determine its respective moisture content. Based on Table 5, it can be seen that the moisture content for both the DES molar ratio does not exceed than the maximum allowable moisture content, thus they are suited to be used as a devulcanising agent.

Table 4: Moisture content of the prepared DES sample

DES Molar Ratio	*Sample Abbreviation*	*Moisture Content (wt. %)*
1:4	DES 1	3.0000
2:7	DES 2	0.07166

Freezing point is another important physiochemical properties to be measured off from the prepared DES samples in order to show the liquidity range of the solvent and is ensured to be less than 60℃ so that it can be applicable in industrial fields. By looking at the freezing point of DES obtained, its freezing point is below than its constituent component depicted in Table 5. This confirms a successful prepared synthesis of DES. Another confirmation of a successful synthesis of DES is the experimental freezing point obtained from the DSC analysis is compared with the literature value from [13, 21], whereby it will show a small percentage error between the readings obtained.

Table 5: Freezing point of the prepared DES sample

Salt	*HBD*	*Molar ratio*	*Freezing point , K*		*Percentage Error, %*
			Literature	Experimental	
$ZnCl_2$	Urea	1:4	278.15	288.15	3.47
$ZnCl_2$	Urea	2:7	275.15	278.81	1.31

Degradation temperature of the prepared DES sample is an important requirement to be known so that DES prepared earlier does not degrade at 180℃ which is operating temperature of devulcanisation. The measurement is carried out accordingly as mentioned in sub-section 2.2.3. The following two figures below depicts the weight loss of $ZnCl_2$: urea for two different molar ratio vs. temperature.

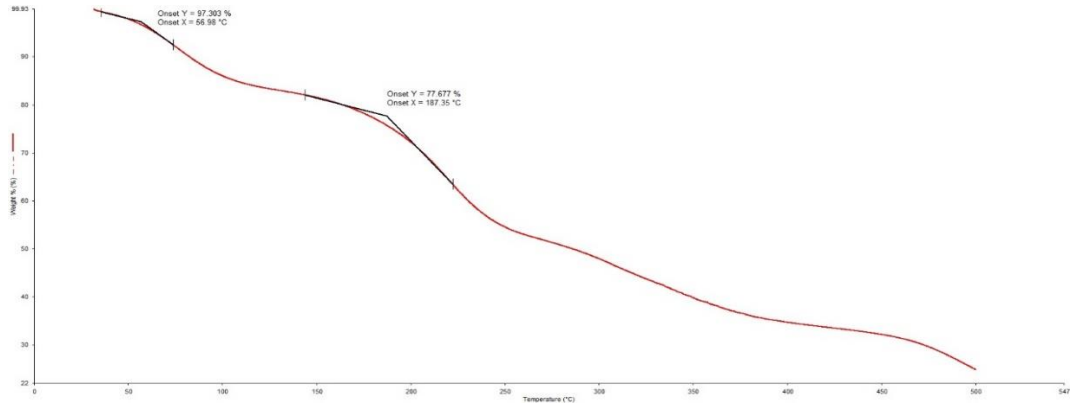


Figure 1. TGA analysis for DES molar ratio of 2:7

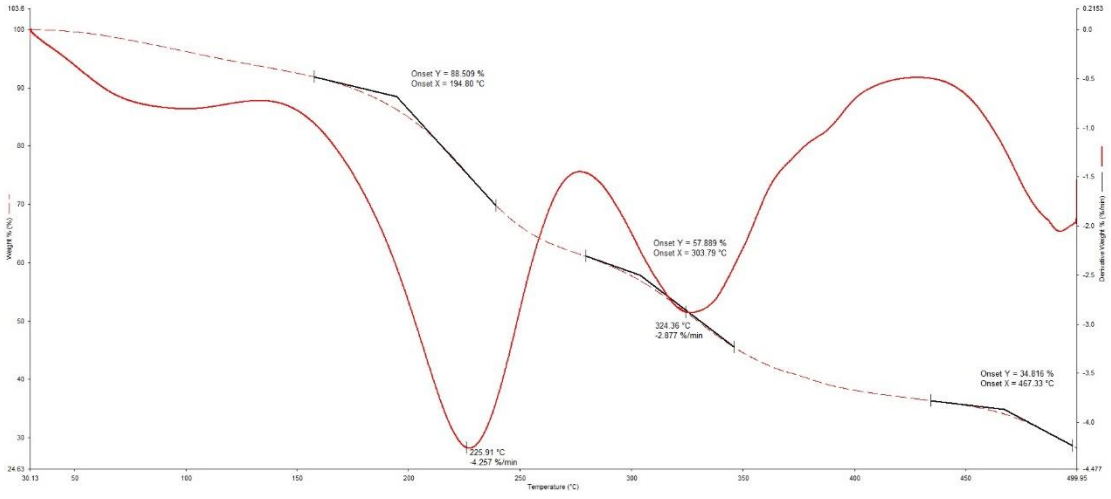


Figure 2. TGA analysis for DES molar ratio of 1:4

Based on the TGA curve obtained from [15], a decreasing slope produced indicates there is a sudden drop in mass. This point at which it has a sudden drop is the

degradation temperature of the DES .Referring to Figure 1 and 2, it can be seen that the degradation temperature was found to be at 187.35℃ and 324.36℃ respectively for 2:7 and 1:4 molar ratio. The values obtained clearly states that devulcanisation temperature must not be allowed to reach to the degradation temperature to avoid the DES degradation. Therefore, the prepared DES samples is suited to be used for this particular devulcanisation research study. In addition to that, the operating temperature of the devulcanisation used is below the DES degradation temperature, making it a suitable operating temperature for devulcanisation process.

3.2 Analysis of Devulcanised Rubber

Analysis is performed on the devulcanised rubber mixture samples on its structural bonds and temperature degradation using FTIR and TGA respectively.

3.2.1 Fourier Transform Infrared Spectroscopy Analysis

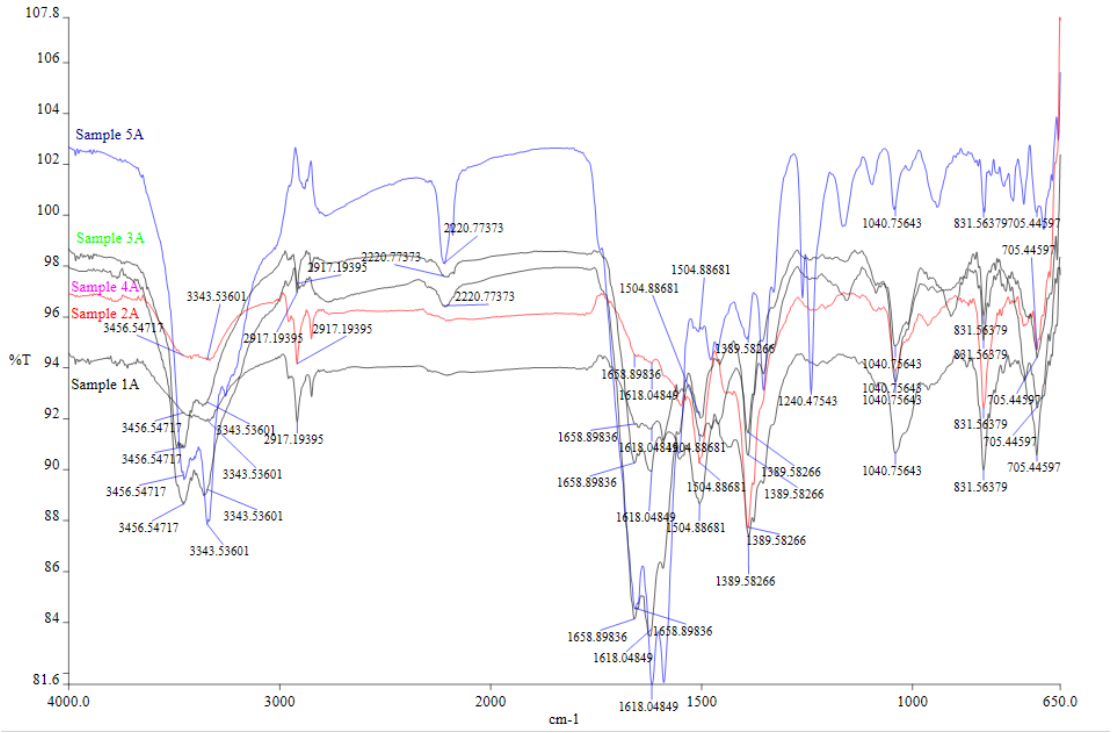


Figure 3. FTIR analysis for rubber: DES mass ratio at 1:20

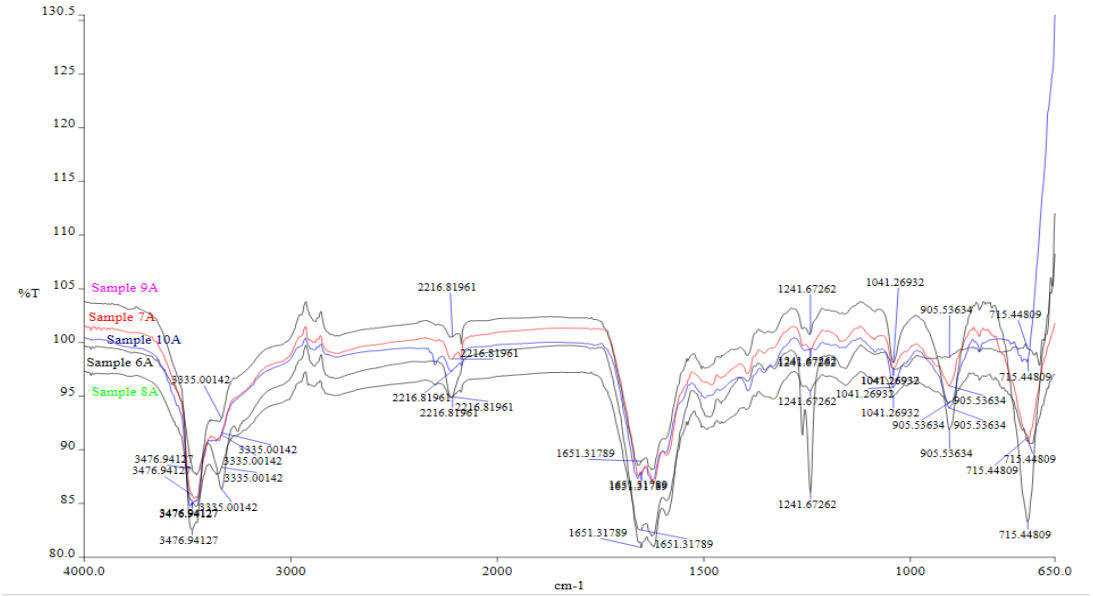


Figure 4. FTIR analysis for rubber: DES mass ratio at 1:30

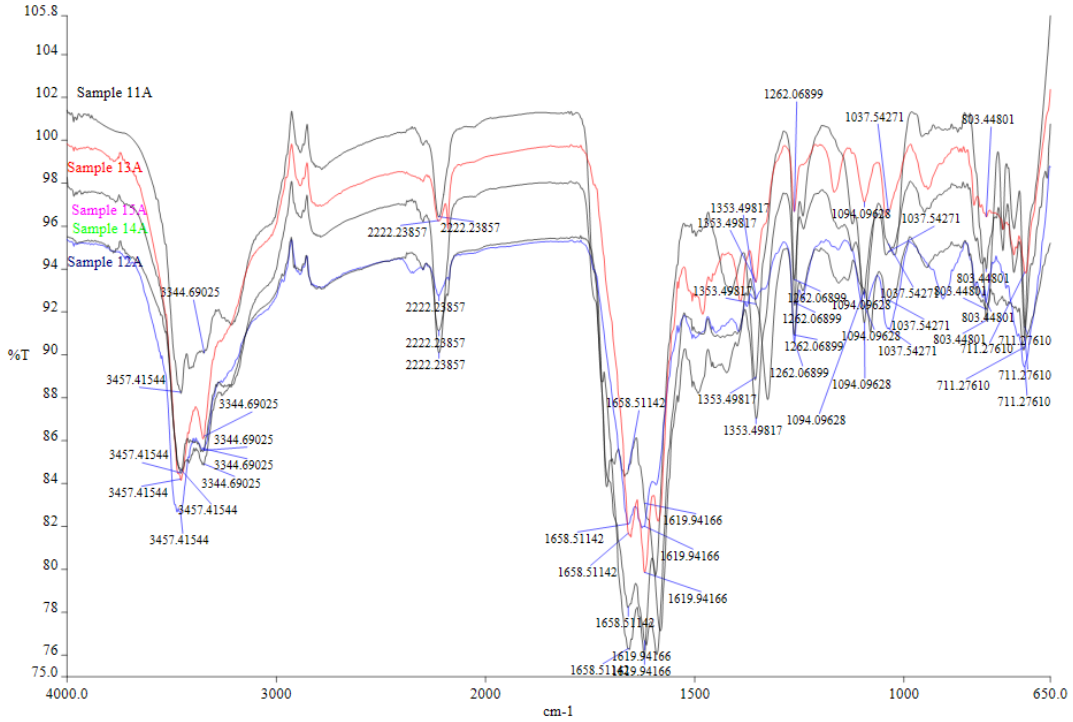


Figure 5. FTIR analysis for rubber: DES mass ratio at 1:40

Referring to Figure 3, it can be seen that above 3550 cm^{-1}, there is an appearance of a broad peak especially for Sample 1A and 2A, which indicates that the presence of O-H group. This also indicates water presence which might still remain in the sample. Presence of water is due to the fact the rubber sample mixture was washed previously with distilled water so droplets of water might still be present. Thus, it can be said that there is a low amount of rubber degradation happening.

In Figure 3 and 5, wavelength for CH_3 functional group makes an appearance in the region of 1389.58266 cm^{-1} and 1353.49817 cm^{-1} respectively for all of the samples. However, for rubber: DES mass ratio at 1:20 in Figure 4, there was no presence of CH_3 functional group, in other words there is no structural change. Aside from that, functional group of CH appears at the region of 2917.19395 cm^{-1} for mass ratio at 1:20 as shown in Figure 3. Despite that, there was no peak appearance of the functional group CH for mass ratio at 1:30 and 1:40.

–S-S functional group or bond was analysed at wavelength between 700-550 cm^{-1} and it can be identified that sample 1A, 2A, 3A, 4A, 6A, 7A, 8A, 9A, 11A, 12A, 13A, and 14A have a peak appearance indicating bond reformation is occurring. On the other hand, sample 5A, 10A and 15A does not a peak appearance since it is a controlled sample, therefore there is no reformation occurring. Another bond that was analysed is the –C-S- bond for which it falls in the wavelength region of 700-520 cm^{-1}. Since there is still peak appearance in Figure 3, 4 and 5 for all the samples, hence it can be said that

bonds have not been broken down. Thus, it can be concluded that ultrasonic treatment was unable to break the bond which has a higher bond energy than –S-S- bond.

Another analysis was made based on bonds through FTIR analysis as shown in Figure 6, 7 and 8 for devulcanisation process of $ZnCl_2$: urea for 2:7 molar ratio at different mass ratio.

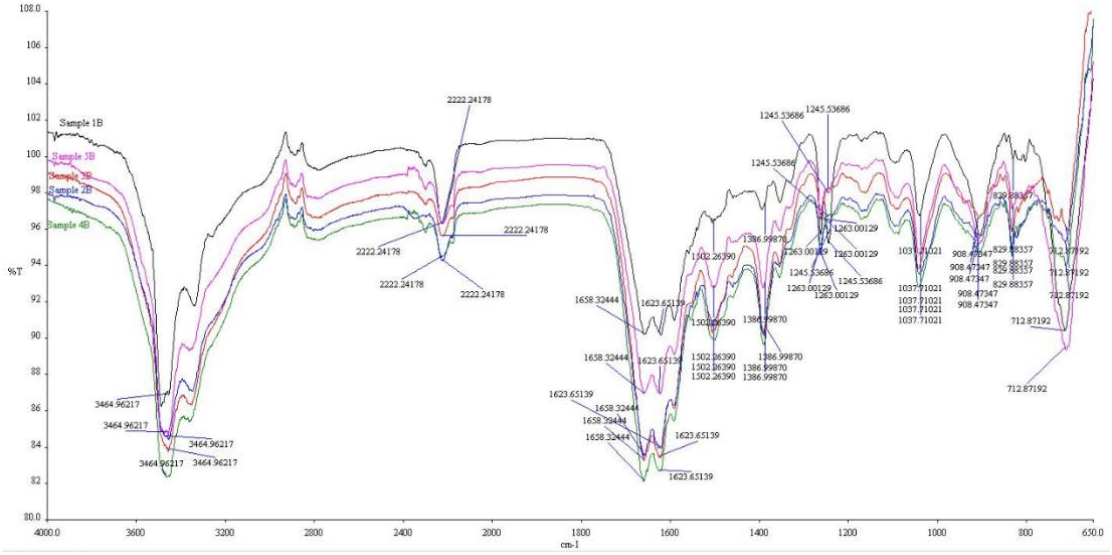


Figure 6. FTIR analysis for Samples 1B, 2B, 3B, 4B, 5B at mass ratio 1:20

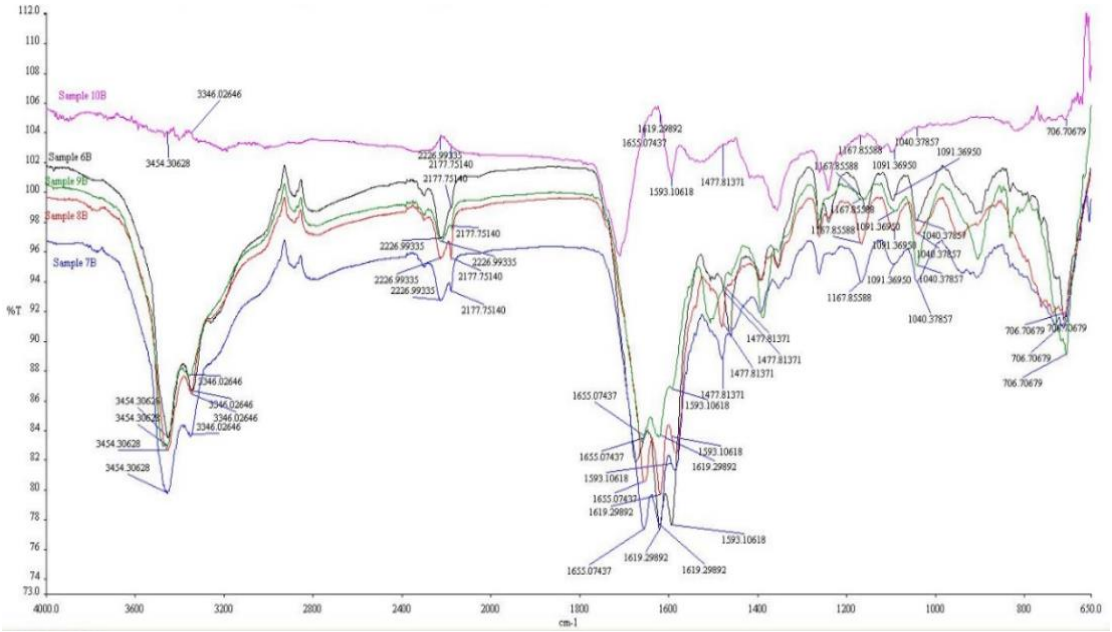


Figure 7. FTIR analysis for Samples 6B, 7B, 8B, 9B, 10B at mass ratio 1:30

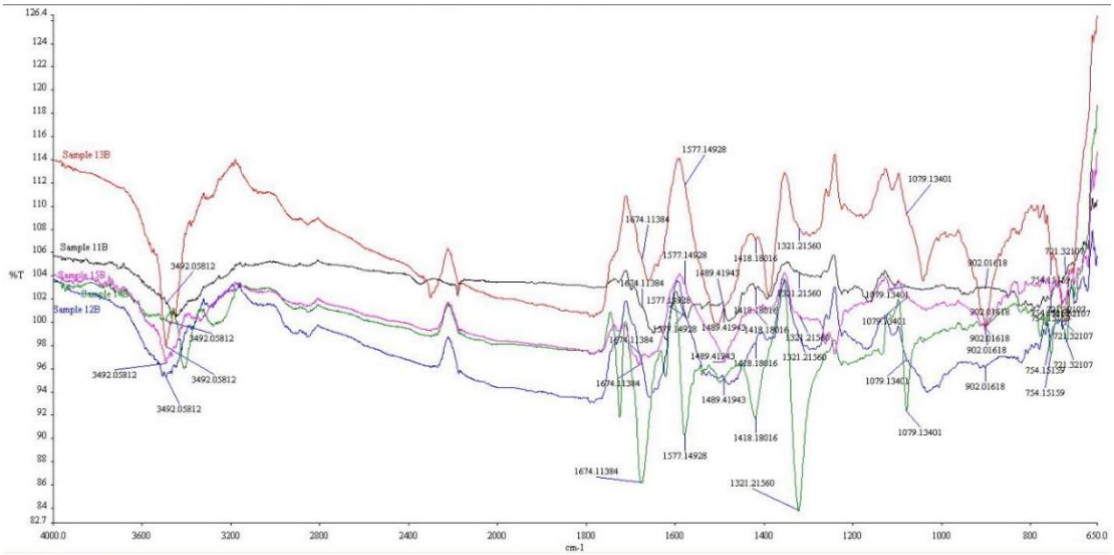


Figure 8. FTIR analysis for Samples 11B, 12B, 13B, 14B, 15B at mass ratio 1:40

Based on FTIR curve plotted from Figure 6, 7 and 8, line I stands for –S-S- bond region whereas line II stands for –C-S- bond region. Based upon the overall chart figure, it can be analysed that for mass ratio of 1:30, there is disappearance of –S-S- peak whereas for mass ratio of 1:20 and 1:40, there is an appearance of –S-S- peak. Carbon-sulphur bond for this particular treatment is also not broken down since it has a low supply of energy, resulting in zero cleavage of sulphur cross-link bond. From Figure 5.2.3.5, it also can be seen that there is a disappearance of S-S peak for sample 8B. This occurs because of the uneven dispersion particles of rubber or rubber mixture sample composition during devulcanisation process.

From Figure 3 to 8, it can be said that wavelength range which are 1300 and 3500 cm^{-1}, there is no appearance of a peak other than broad peak which is apparent at above 3000 cm^{-1} wavelength range. Therefore, this shows there is still presence of water inside the rubber mixture sample. Thus, it can deduced that there is low amount of degradation rubber which contains the O-H group.

All in all, various conclusion can be deducted that through FTIR analysis. It was determined through FTIR analysis that –S-S or sulphur-sulphur bond is the only bond which is leaved during devulcanisation process which proves a successful devulcanisation process at an optimum heating temperature of 130℃. Other bonds are not broken or cleaved as there was insufficient energy to cleave them. Hence, the main carbon chain is still maintained even after devulcanisation process was carried out which further proves that devuclanised rubber has excellent physical properties.

3.2.2 Thermogravimetric Analysis

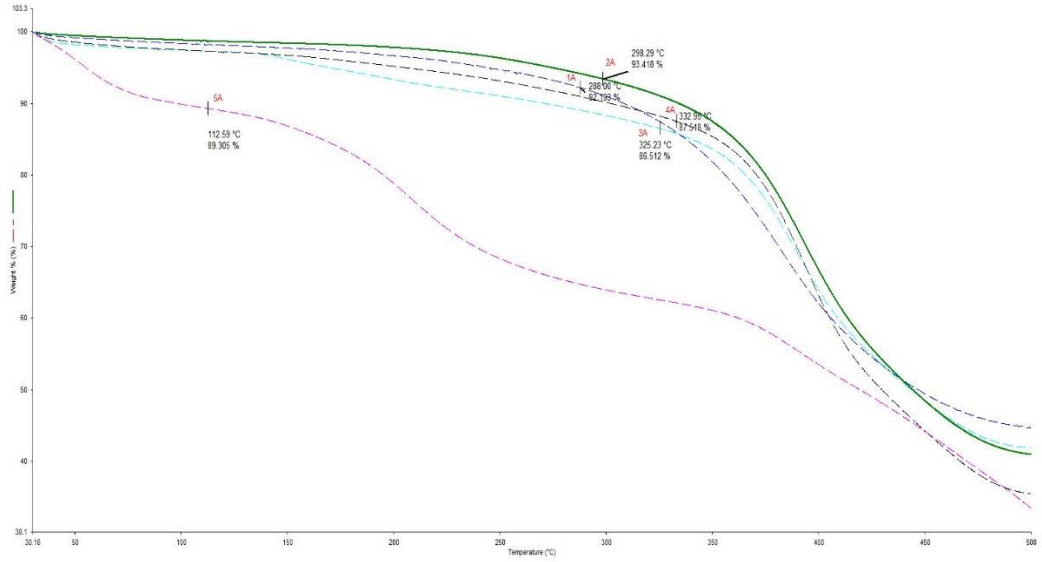


Figure 9: TGA analysis for Samples 1A, 2A, 3A, 4A, 5A at 1:20 mass ratio

` Based on the TGA curve obtained from [15], a decreasing slope produced indicates there is a sudden drop in mass. This point at which it has a sudden drop is the degradation temperature of the rubber samples mixture. Referring to Figure 9, it can be seen that the degradation temperature for sample 1A, 2A, 3A, 4A, 5A was found to be at 288.0℃, 298.29℃, 325.23℃, 332.95℃ and 112.59℃ respectively. Degradation temperature for sample 4A is highest among the rest of the samples. However degradation for sample 1A is comparably much smaller than the rest. The values determined indicates that devulcanisation temperature must not be allowed to reach to the degradation temperature to avoid rubber degradation.

Table 6: Degradation Temperature for 1:20 mass ratio

Sample	*Degradation Temperature (℃)*
1A	288.0
2A	298.29
3A	325.23
4A	332.95
5A	112.59

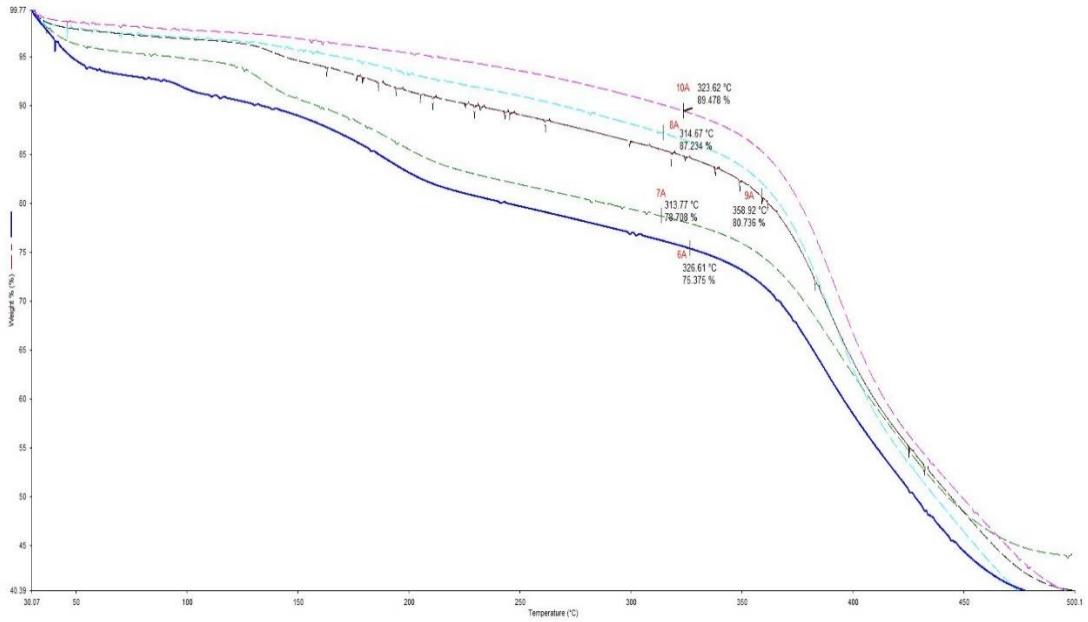


Figure 10: TGA analysis for Samples 6A, 7A, 8A, 9A, 10A at 1:30 mass ratio

Based on the TGA curve obtained from [15], a decreasing slope produced indicates there is a sudden drop in mass. This point at which it has a sudden drop is the degradation temperature of the rubber samples mixture. Referring to Figure 10, it can be seen that the degradation temperature for sample 1A, 2A, 3A, 4A, 5A was found to be at 326.61℃, 313.77℃, 314.67℃, 358.92℃ and 323.62℃ respectively. Degradation temperature for sample 9A is highest among the rest of the samples. However degradation for sample 7A is comparably much smaller than the rest due to the fact there might have been contamination of DES inside the sample. The values determined indicates that devulcanisation temperature must not be allowed to reach to the degradation temperature to avoid rubber degradation.

Table 7: Degradation Temperature for 1:30 mass ratio

Sample	*Degradation Temperature (℃)*
6A	326.61
7A	313.77
8A	314.67
9A	358.92
10A	323.62

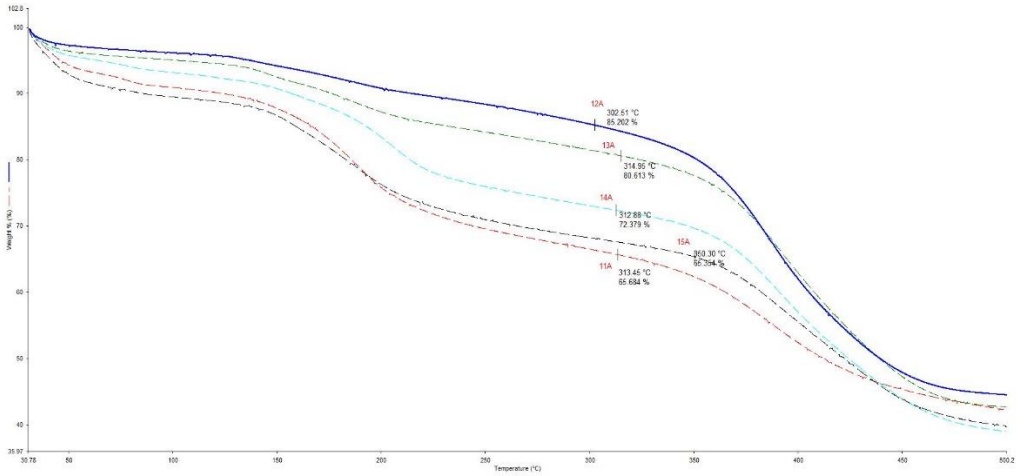


Figure 11: TGA analysis for Samples 11A, 12A, 13A, 14A, 15A at 1:40 mass ratio

Based on the TGA curve obtained from [15], a decreasing slope produced indicates there is a sudden drop in mass. This point at which it has a sudden drop is the degradation temperature of the rubber samples mixture. Referring to Figure 11, it can be seen that the degradation temperature for sample 11A, 12A, 13A, 14A, 15A was found to be at 313.45℃, 302.51℃, 314.95℃, 312.88℃ and 350.30℃ respectively. Degradation temperature for sample 15A is highest among the rest of the samples. However degradation temperature for sample 12A is much lower than the rest due to the fact there might have been contamination of DES inside the sample. The values determined indicates that devulcanisation temperature must not be allowed to reach to the degradation temperature to avoid rubber degradation.

Table 8: Degradation Temperature for 1:40 mass ratio

Sample	*Degradation Temperature (℃)*
11A	313.45
12A	302.51
13A	314.95
14A	312.88
15A	350.30

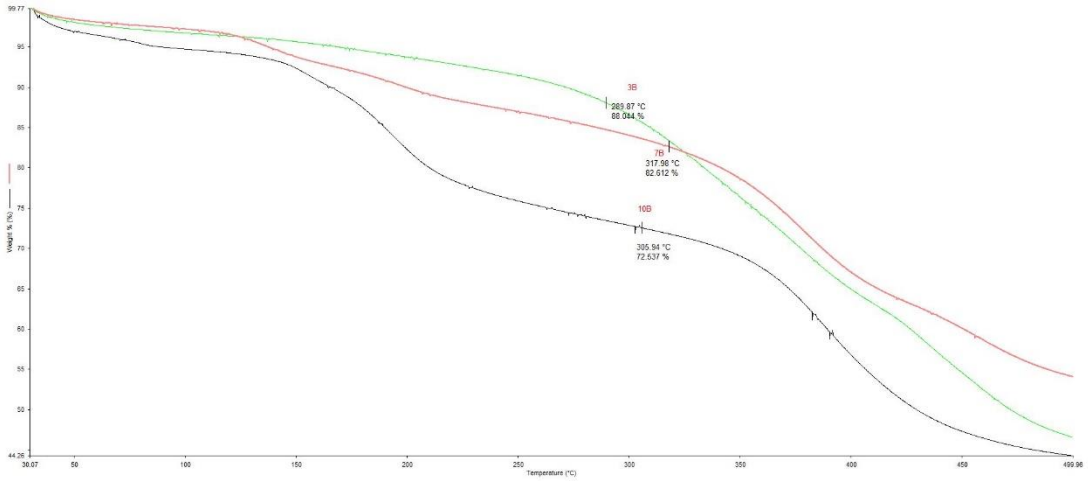


Figure 12: TGA analysis for Samples 3B, 7B, 10B

Based on the TGA curve obtained from [15], a decreasing slope produced indicates there is a sudden drop in mass. This point at which it has a sudden drop is the degradation temperature of the rubber samples mixture. Referring to Figure 12, it can be seen that the degradation temperature for sample 3B, 7B, and 10B was found to be at 289.97℃, 317.98℃, and 305.94℃ respectively. Degradation temperature for sample 7B is highest among the rest of the samples. However degradation temperature for sample 3B is much lower than the rest due to the fact there might have been contamination of DES inside the sample. The values determined indicates that devulcanisation temperature must not be allowed to reach to the degradation temperature to avoid rubber degradation.

Table 9: Degradation Temperature for sample 3B, 7B, 10B

Sample	*Degradation Temperature (℃)*
3B	289.97
7B	317.98
10B	305.94

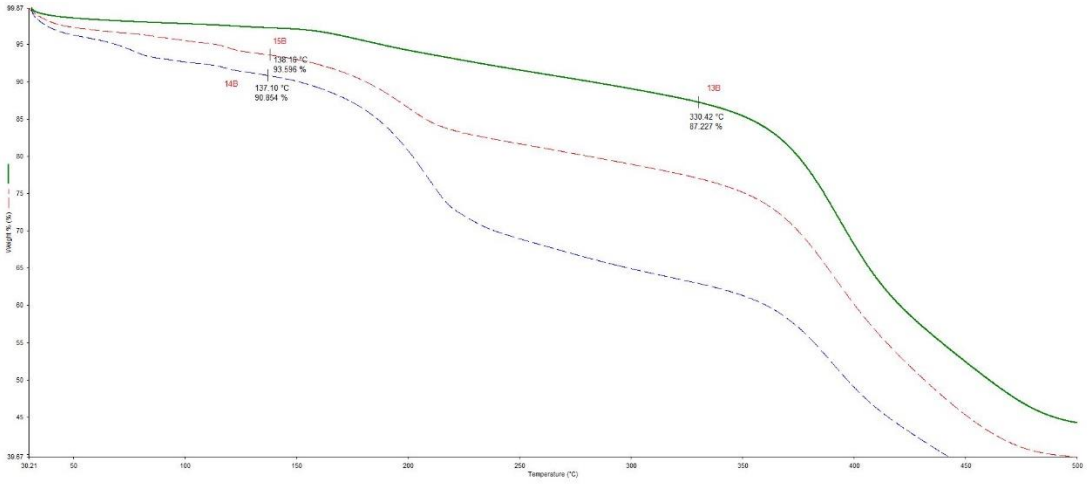


Figure 13: TGA analysis for Samples 13B, 14B, 15B

Based on the TGA curve obtained from [15], a decreasing slope produced indicates there is a sudden drop in mass. This point at which it has a sudden drop is the degradation temperature of the rubber samples mixture. Referring to Figure 13, it can be seen that the degradation temperature for sample 13B, 14B, and 15B was found to be at 330.42℃, 137.10℃, and 138.16℃ respectively. Degradation temperature for sample 13B is highest among the rest of the samples. However degradation temperature for sample 14B is slightly lower than sample 15B due to the fact there might have been contamination of DES inside the sample. The values determined indicates that devulcanisation temperature must not be allowed to reach to the degradation temperature to avoid rubber degradation.

Table 10: Degradation Temperature for sample 13B, 14B, 15B

Sample	*Degradation Temperature (℃)*
13B	330.42
14B	137.10
15B	138.16

3.2.3 EDX Analysis

Results acquired for composition of rubber sample from before and after devulcanisation process through EDX analysis is depicted in Figure 5.2.1.1 for $ZnCl_2$: urea for 2:7 molar ratio, whereby the graph is plotted in terms of sulphur removal percentage against heating temperature.

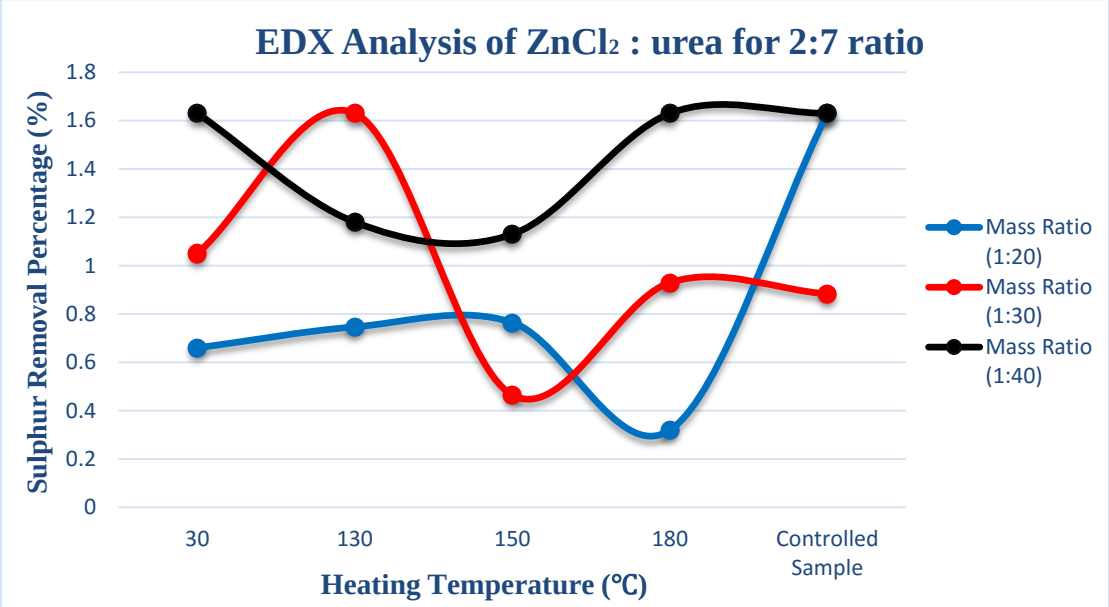


Figure 14: EDX Analysis for $ZnCl_2$: Urea for 2:7 molar ratio

Referring to Figure 14, it can be observed that, for mass ratio of 1:30 and 1:40, the sample is having an increase in devulcanisation process efficiency as the temperature increases from 150℃ to 180℃. Thus, this shows that cross-link network is being broken and soluble fraction is increasing. In fact, at temperature 130℃, it has the highest percentage removal of sulphur which indicates that devulcanisation efficiency is particularly high at that temperature. Reduction in devulcanisation efficiency can be seen for rubber sample under mass ratio of 1:20 as the temperature increases from 150℃ to 180℃. This is due to the fact that bond reformation is occurring during heating treatment as the sulphur cross-link bonds are being reformed again**.**

Based on the results acquired, it can deduced that during devuclanisation, bond reformation and bond cleaving of the sulphur-sulphur bond or carbon-sulphur bond can simultaneously occur as proven by [7] . Therefore, heating temperature is key process parameter in order to have a successful devulcanisation process. Hence, for this case, the optimum heating temperature is 130℃ for rubber samples at 1:20 and 1:30 mass ratio at maximum removal of sulphur content

With bond reformation happening, it can explained that as bonds are cleaved or broken down, sulphur still remains inside the rubber sample together with free electrons

which are detached from the C-S bond. Thus, this leads to carbon active sites formation which allows the sulphur to reform the sulphur cross-link bonds again by utilising those free electrons released. At a temperature of 130℃, rubber samples will have the highest removal of sulphur content if the heating treatment is stopped at moment. Despite that, temperature above 130℃ will result in decrease in devulcanisation efficiency and bond reformation, allowing removed sulphur to reform back again with carbon backbone by utilising those free electrons. Therefore, it is important to stop at the optimum temperature in order to avoid bond reforming from occurring and to also ensure the maximum removal of sulphur content from the rubber sample mixture.

Based on Figure 14, in terms of mass ratio, it can be shown that using higher amount of DES will result in higher devulcanisation efficiency. This means that degree of sleavage on the cross-link bonds will be greater. This is because DES capacity is higher allowing the bond to break more easily. Nonetheless, it is an inconclusive hypothesis due to the uneven trend displayed for the rubber sample at 1:30 mass ratio.

The cause of such uneven trend displayed by the rubber sample might be due to non-homogenous of rubber sample mixture. This is because the sample mixture might not been completely well mixed, thus leading to such trend as shown in Figure 5.2.1.1. Another cause to it might be due to the rubber not completely mixed with DES as DES has a very high viscosity, making it hard to mix both components. This will eventually leads in forming a two layered mixture due to density difference whereby devulcanisation process under ultrasonic treatment will be affected entirely

3.2.4 FESEM Analysis

For this analysis, study on the morphology of rubber before and after devulcanisation was carried out using FESEM analysis. The findings of the results were discussed in detailed in the following section below.

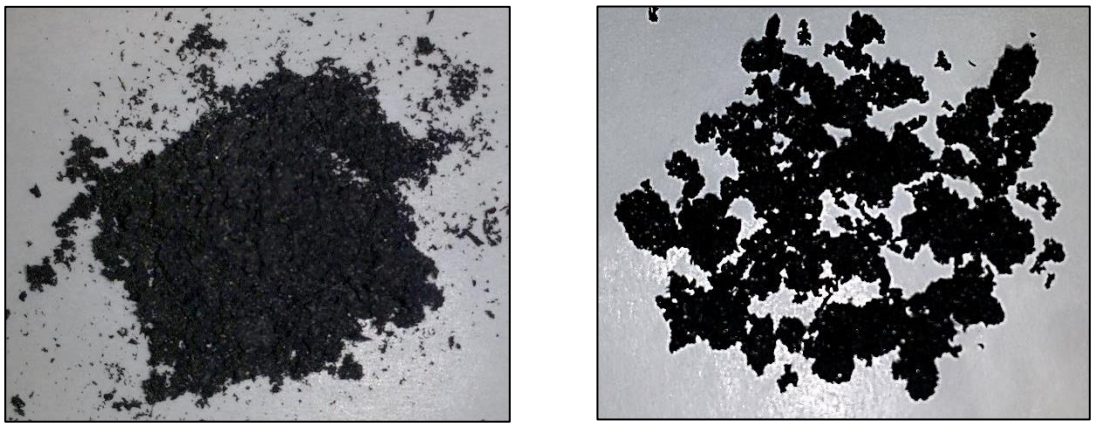
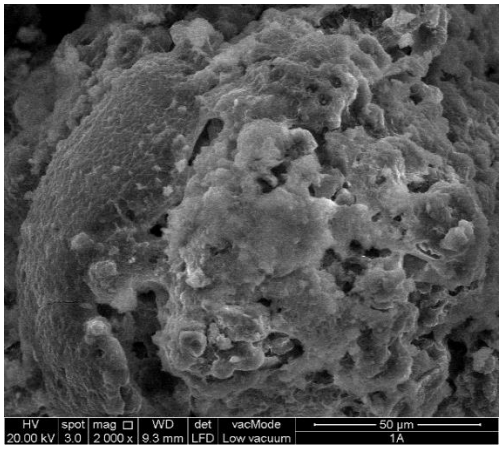
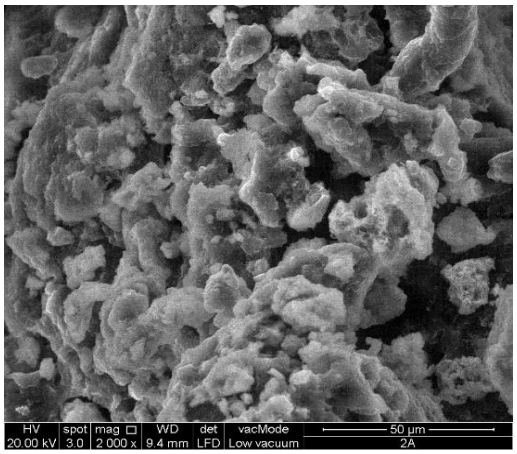


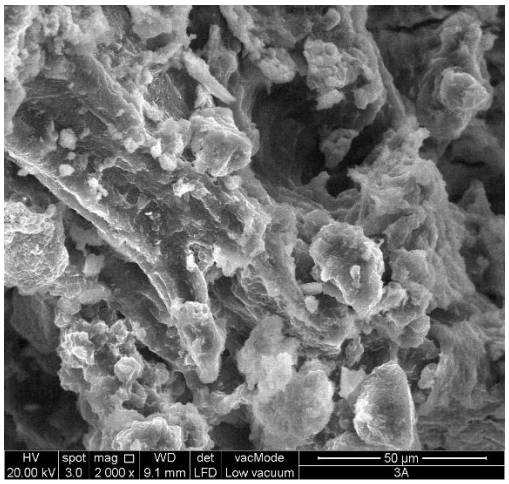
Figure 15: Vulcanised rubber sample (left) & Devulcanised rubber sample (right)

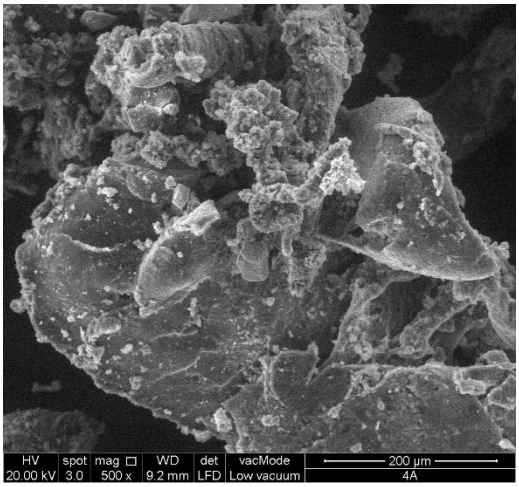
Properties of devulcanised rubber as shown in Figure 15 consist of soft, sticky in nature and feels rougher compared to unvulcanised rubber. Displaying these kind properties indicates that devulcanisation process was a success. FESEM analyses is carried out for each rubber sample through the use of different solvent agent. To make

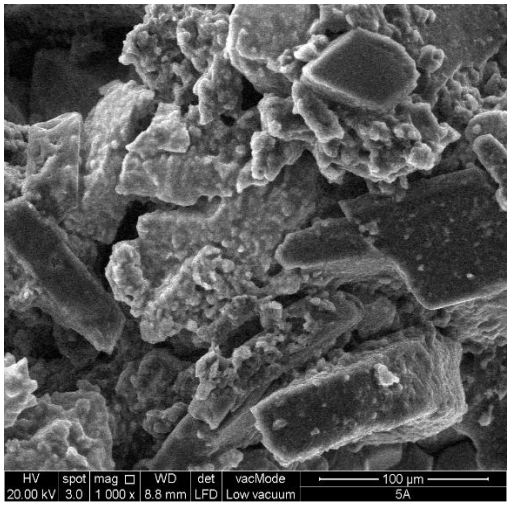
a confirmation on whether rubber has been vulcanised efficiently, it depends entirely on the gaps presence and smooth surface of the rubber morphology sample. In Figure 16, it shows the FESEM analysis on devulcanised rubber for all of the samples based on $ZnCl_2$: urea for 2:7 molar ratio.

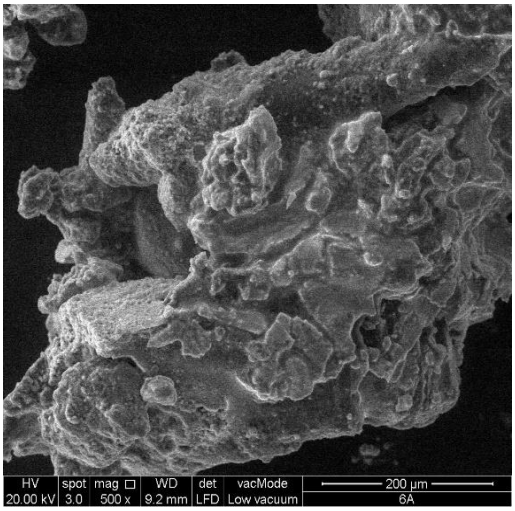


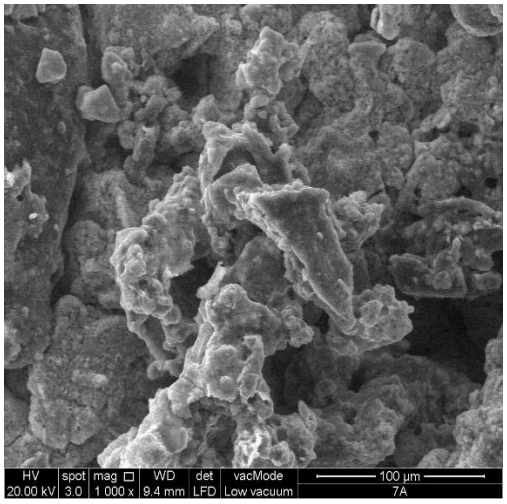


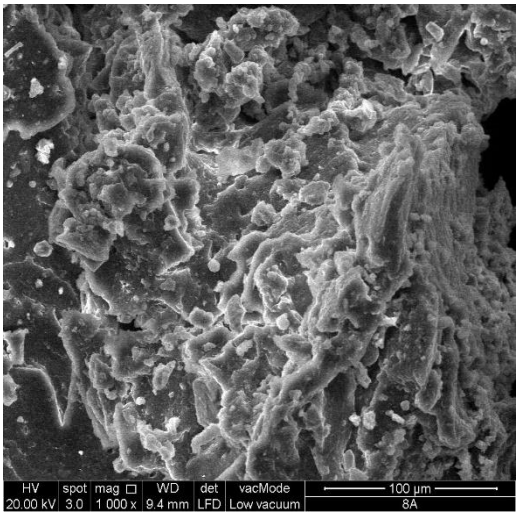


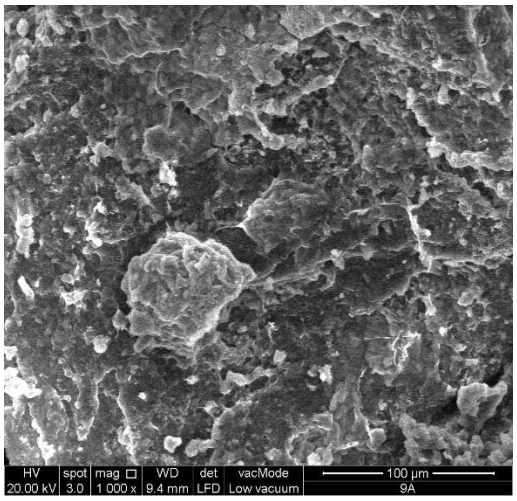


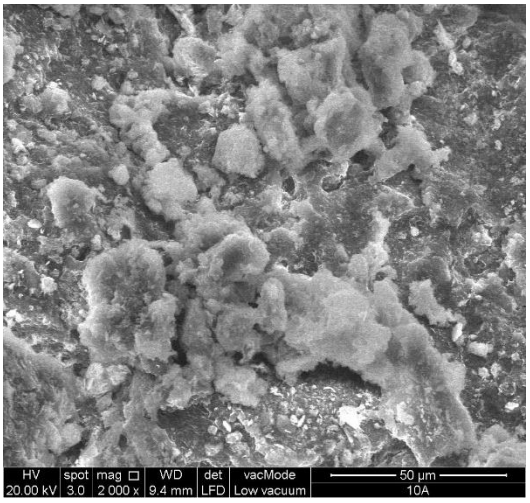

HV spot mag WD det vacMode 100 µm
20.00 kV 3.0 1 000 x 8.8 mm LFD Low vacuum
5A


HV spot mag WD det vacMode 200 µm
20.00 kV 3.0 500 x 9.2 mm LFD Low vacuum
6A


HV spot mag WD det vacMode 100 µm
20.00 kV 3.0 1 000 x 9.4 mm LFD Low vacuum
7A


HV spot mag WD det vacMode 100 µm
20.00 kV 3.0 1 000 x 9.4 mm LFD Low vacuum
8A


HV spot mag WD det vacMode 100 µm
20.00 kV 3.0 1 000 x 9.4 mm LFD Low vacuum
9A


HV spot mag WD det vacMode 50 µm
20.00 kV 3.0 2 000 x 9.4 mm LFD Low vacuum
10A

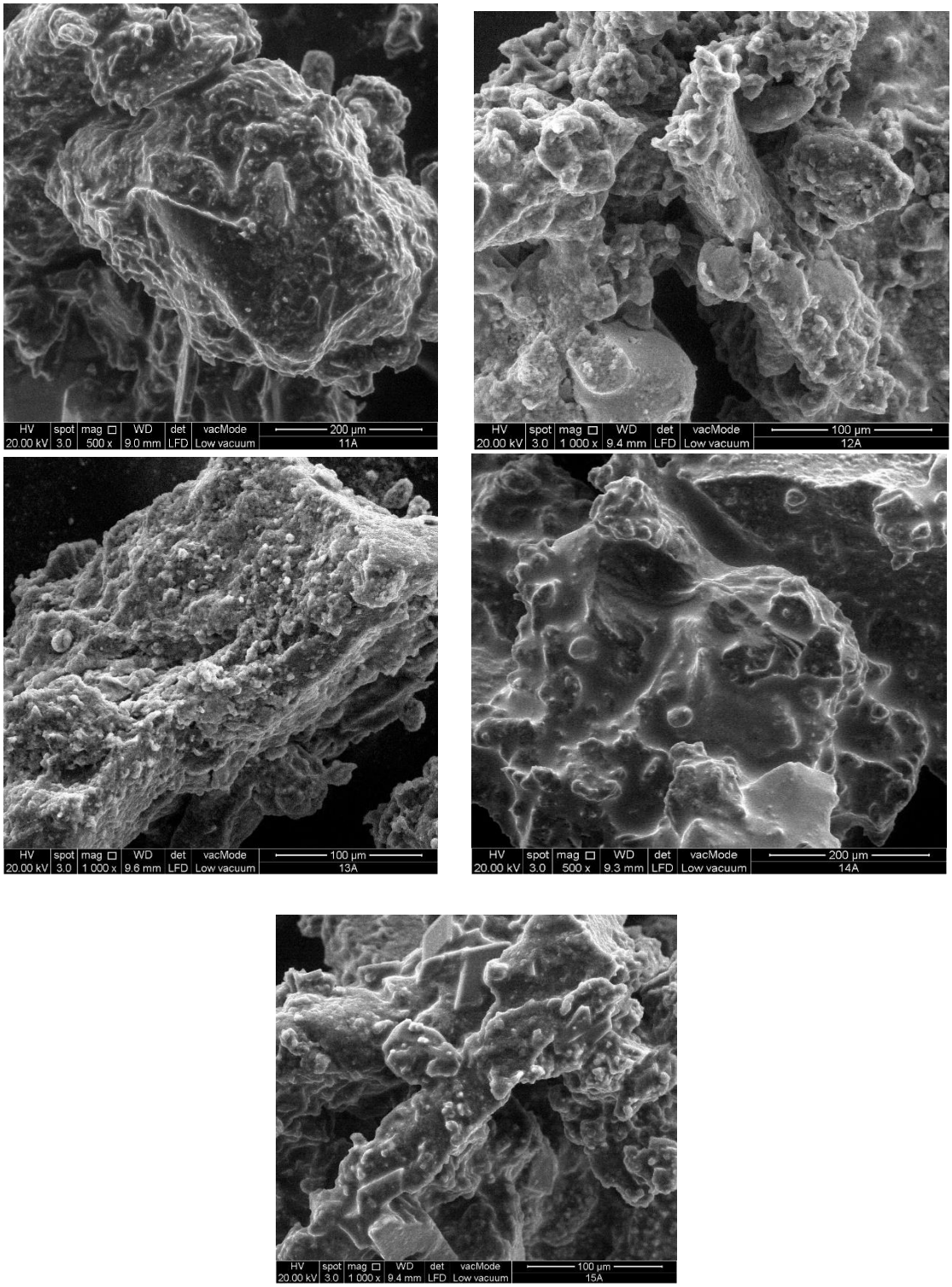


Figure 16: FESEM Analysis on Rubber Samples for $ZnCl_2$: Urea for 2:7 molar ratio

Referring and comparing all of the figures with accordance to Figure 16, the morphology of the samples were evaluated. Along with sample 1A, 2A, 3A, 4A and 5A under mass ratio of 1:20, it can be noticed that Sample 2A as the smoothest surface out of all the other samples, followed by 1A, 3A, 4A and finally 5A. From a microscopic view, it can observed that sample 1A is still rough in surface and stiff compared to sample 2A. From the micrograph, it is clearly seen that sample 1A is still very rough

and rigid in surface in comparison to sample 2A. Despite that sample 3A has a similar surface as to sample 2A, hence the result tallies with EDX analysis result where the amount of sulphur removed is nearly similar. Such findings is said to be in equilibrium reformation for which if the heating temperature is more than optimum temperature, bond reformation will occur. A perfect example is sample 3A. Furthermore, small particles can been on top of the surface of the rubber sample. This could be due to contamination or left over of DES solution.

With sample 6A, 7A, 8A, 9A and 10A under mass ratio of 1:30, it can be shown clearly that sample 7A has the smoothest surface out of all the other samples, followed by 6A, 8A, 9A and finally 10A. Sample 7A has almost similar surface area to sample 5A. Hence, it is presumed that both these samples will have similar characteristics as shown in EDX analysis whereby the percentage of sulphur removal is almost the same.

For sample 11A, 12A, 13A, 14A and 15A, under the mass ratio of 1:40, it can be observed clearly that sample 12A has the smoothest surface out of all the samples since its surface is less rigid compared to others. Similar deduction is made for which the optimum heating temperature for devulcanisation is 130℃.

All of the respective figures shown above for morphology structure, neither of the figures showed any failure, damage or quality on the rubber samples. This indirectly comes to conclusion that devulcanised rubber properties are maintained without destroying the backbone chain of the rubber. It proven through the analysis of FTIR and FESEM, hence it safe to conclude.

3.2.5 Gel Content Analysis

Gel content samples were carried out and determined in accordance to ASTM D2765 [42].The degree of devulcanisation process of the sample rubber was determined by obtaining the soluble and gel fraction through Soxhlet extraction apparatus using boiling toluene. Then, the samples were collected and immediately dried inside an oven at a temperature of 70℃ once a steady mass was obtained. Hence, the lower the content of the gel, the higher the efficiency of the devulcanisation process [21]. Soluble fraction is determined from the following equation;

$$\textit{Soluble fraction} = (W_o\text{-}W_1/W_o)*100\text{------ [1]}$$

Whereby, W_0 is dry weight of devuclanised rubber before extraction process and W_1 is dry weight of devulcanised rubber after extraction process. From there, the gel fraction is determined from the expressed equation. The following Table 11 and 12 shows the gel content analysis tabulation and the analysis was thoroughly discussed.

Table 11: Gel Content Analysis on 2:7 molar ratio of $ZnCl_2$: urea

Sample	W_o	W_i	$(W_i/W_o)*(100)$
1A	0.7276	0.7437	102.2127543
2A	0.6779	0.6788	100.1327629
3A	0.8463	0.8252	97.50679428
4A	0.8647	0.8505	98.35781196
5A	0.9188	0.8171	88.93121463
6A	0.8801	0.8182	92.96670833
7A	0.8069	0.7198	89.20560169
8A	0.8681	0.8487	97.76523442
9A	0.8875	0.8448	95.18873239
10A	0.7573	0.741	97.84761653
11A	0.8667	0.7962	91.86569747
12A	0.8865	0.8518	96.0857304
13A	0.8565	0.7715	90.07589025
14A	0.8659	0.783	90.42614621
15A	0.9059	0.8201	90.52875593

Table 12: Gel Content Analysis on 1:4 molar ratio of $ZnCl_2$: urea

Sample	W_o	W_i	$(W_i/W_o)*(100)$
1B	0.8582	0.834	97.18014449
2B	0.8802	0.8577	97.44376278
3B	0.8645	0.8562	99.03990746
4B	0.7617	0.7445	97.74189313
5B	0.8975	0.8714	97.09192201
6B	0.8654	0.7756	89.62329559
7B	0.8817	0.8499	96.39333106
8B	0.8821	0.8251	93.5381476
9B	0.8994	0.8686	96.57549477
10B	0.9056	0.8176	90.28268551
11B	0.8865	0.7762	87.55781162
12B	0.8376	0.8069	96.334766
13B	0.9141	0.9039	98.88414834

14B	0.8686	0.7829	90.13354824
15B	0.8641	0.7941	91.89908575

4. Conclusion

Waste rubber is a polymeric material containing 50 % of rubber and is generally referred to as waste tyre rubber. Less attempts were taken to recycle these waste tyre rubber to a point where it actually becomes a pollution source. There is a large amount of vulcanised residue that comes from the production of rubber materials and it considered as major problem as the material is not easily decomposed, accumulates hazardous waste and incurs high cost. Current methods used are capable for devulcanisation of rubber material, however up to a certain limit due to the fact that few of the solvents used are not suitable as it is costly and hazardous. One of the emerging alternative solvent which shows similar properties to ILs is known to be Deep Eutectic Solvent (DES). Researchers found that the removal efficiency of sulphur is as high as 99.48% which further proves that DES is the perfect replacement for ILs as DES is cheap and non-toxic solvent in removing sulphur. Furthermore, it can be used for devulcanisation process.

Through this, it then leads to the two objective of the research project. The first objective being is to synthesize and characterize $ZnCl_2$: Urea as a deep eutectic solvents (DESs) of various molar ratio in terms of freezing point, moisture content and degradation temperature. Based on research, it was found that amine- based solvents gives the highest sulphur removal and hence it is chosen as a devulcanising solvent. Based on physiochemical properties of DES analyses, it was determined that the moisture content is lower than maximum allowable limit which reduces the chance of DES crystallizing. It was also determined that the freezing point is below 60℃ and degradation temperature is averagely around 200℃.

The second objective of the research is to optimise the sonication time, heating temperature and rubber: DES mass ratio on devulcanisation of the waste rubber. Objective was achieved by varying heating temperature from 130-180 ℃ under rubber: DES mass ratio of 1:20, 1:30 and 1:40. Such findings would result in bond reformation and bond cleaving. Based from this research study, it was observed and found that the optimum heating temperature is 130℃ for devulcanisation process. At this temperature rubber samples will have the highest removal of sulphur content if the heating treatment is stopped at moment. Despite that, temperature above 130℃ will result in decrease in devulcanisation efficiency and bond reformation, allowing removed sulphur to reform back again with carbon backbone by utilising those free electrons. Therefore, it is important to stop at the optimum temperature in order to avoid bond reforming from occurring and to also ensure the maximum removal of sulphur content from the rubber sample mixture. FESEM analysis showed that most samples at 130℃ gives the smoothest surface of rubber sample thus indicating the devulcanisation process was a success.

On the other hand, it was determined through FTIR analysis that –S-S or sulphur-sulphur bond is the only bond which is cleaved during devulcanisation process

which proves a successful devulcanisation process at an optimum heating temperature of 130℃. Other bonds are not broken or cleaved as there was insufficient energy to cleave them. Hence, the main carbon chain is still maintained even after devulcanisation process was carried out which further proves that devuclanised rubber has excellent physical properties. In addition to that, degradation temperature for all the sample rubber mixtures analysed is suitable to be used as most of the samples are higher than 180℃.

With that being said, an efficient and successful devulcanisation process through ultrasonic treatment and heating treatment utilising Deep Eutectic Solvent has a great capability in improving industrial applications. With DES being cheaper and greener solvent, it is expected to be more environmental-friendly process in such way that it increases the devulcanisation efficiency of the waste rubber.

References

[1] O. E. Ikwuagwu, I. C. Ononogbu, and O. U. Njoku, "Production of biodiesel using rubber seed oil," vol. 12, pp. 57–62, 2000.

[2] S. Rooj, G. C. Basak, P. K. Maji, and A. K. Bhowmick, "New Route for Devulcanization of Natural Rubber and the Properties of Devulcanized Rubber," *J. Polym. Environ.*, vol. 19, no. 2, pp. 382–390, 2011.

[3] P. J. H. van Beukering and M. A. Janssen, "Trade and recycling of used tyres in Western and Eastern Europe," *Resour. Conserv. Recycl.*, vol. 33, no. 4, pp. 235–265, 2001.

[4] M. Sienkiewicz, J. Kucinska-Lipka, H. Janik, and A. Balas, "Progress in used tyres management in the European Union: A review," *Waste Manag.*, vol. 32, no. 10, pp. 1742–1751, 2012.

[5] S. Ramarad, M. Khalid, C. T. Ratnam, A. L. Chuah, and W. Rashmi, "Waste tire rubber in polymer blends: A review on the evolution, properties and future," *Prog. Mater. Sci.*, vol. 72, pp. 100–140, 2015.

[6] A. Joseph, B. George, M. K N, and R. Alex, "THE CURRENT STATUS OF SULPHUR VULCANIZATION AND DEVULCANIZATION CHEMISTRY: DEVULCANIZATION," *Rubber Sci.*, vol. 29, no. 1, pp. 62–100, 2016.

[7] K. Bredberg, B. Erik Andersson, E. Landfors, and O. Holst, "Microbial detoxification of waste rubber material by wood-rotting fungi," *Bioresour. Technol.*, vol. 83, no. 3, pp. 221–224, 2002.

[8] a. Zanchet, L. N. Carli, M. Giovanela, J. S. Crespo, C. H. Scuracchio, and R. C. R. Nunes, "Characterization of Microwave-Devulcanized Composites of Ground SBR Scraps," *J. Elastomers Plast.*, vol. 41, no. 6, pp. 497–507, 2009.

[9] X. Zhang, C. Lu, and M. Liang, "Properties of natural rubber vulcanizates containing mechanochemically devulcanized ground tire rubber," *J. Polym. Res.*, vol. 16, no. 4, pp. 411–419, 2009.

[10] H. Wang *et al.*, "Multifunctional TiO2 nanowires-modified nanoparticles bilayer film for 3D dye-sensitized solar cells," *Optoelectron. Adv. Mater. Rapid Commun.*, vol. 4, no. 8, pp. 1166–1169, 2010.

[11] V. V. Rajan, W. K. Dierkes, R. Joseph, and J. W. M. Noordermeer, "Science and technology of rubber reclamation with special attention to NR-based waste latex products," *Prog. Polym. Sci.*, vol. 31, no. 9, pp. 811–834, 2006.

[12] V. A. Online, "Deep eutectic solvents based on N -methylacetamide and a lithium salt as suitable electrolytes for lithium-ion batteries," no. 3, pp. 20054–20063, 2013.

[13] G. Garcia, S. Aparicio, R. Ullah, and M. Atilhan, "Deep Eutectic Solvents: Physicochemical Properties and Gas Separation Applications," *Energy & Fuels*, vol. 29, pp. 2616–2644, 2015.

[14] Q. Zhang, K. De Oliveira Vigier, S. Royer, and F. Jérôme, "Deep eutectic solvents: syntheses, properties and applications," *Chem. Soc. Rev.*, vol. 41, no. 21, p. 7108, 2012.

[15] S. Seghar *et al.*, "Devulcanization of styrene butadiene rubber by microwave energy: Effect of the presence of ionic liquid," *Express Polym. Lett.*, vol. 9, no. 12, pp. 1076–1086, 2015.

[16] C. Acids, C. Florindo, and A. M. Fernandes, "Insights into the Synthesis and Properties of Deep Eutectic Solvents Based on Cholinium Chloride," ACS Sustainable Chemistry Engineering, vol. 2, pp. 2416-2425, 2014.

[17] A. I. Isayev, S. P. Yushanov, S.-H. Kim, and V. Y. Levin, "Ultrasonic Devulcanization of Waste Rubbers: Experimentation and modeling," Rheol. Acta, vol. 35, no. 6, pp. 616–630, 1996.

[18] S. Seghar, N. A. Hocine, V. Mittal, S. Azem, B. Schmaltz, and N. Poirot, "Devulcanization of styrene butadiene rubber by microwave energy : Effect of the presence of ionic liquid," vol. 9, no. 12, pp. 1076–1086, 2015.

[19] R. U. N. D. Anwendungen, "Devulcanization of Whole Passenger Car Tire Material," pp. 20–25, 2013.

[20] P. S. Garcia, F. D. B. De Sousa, J. A. De Lima, S. A. Cruz, and C. H. Scuracchio, "Devulcanization of ground tire rubber : Physical and chemical changes after different microwave exposure times," vol. 9, no. 11, pp. 1015–1026, 2015

[21] F. Endres, D. McFariane and A. Abbot, Electrodeposition from Ionic Liquid, Germany: Wiley-VCH, 2008.

[22] K. Shahbaz, F. S. Mjalli, M. A. Hashim, and I. M. AlNashef, "Prediction of deep eutectic solvents densities at different temperatures," *Thermochimica Acta*, vol. 515, pp. 67-72, 2011.

[23] K. Aoudia, S. Azem, N. A??t Hocine, M. Gratton, V. Pettarin, and S. Seghar, "Recycling of waste tire rubber: Microwave devulcanization and incorporation in a thermoset resin," *Waste Manag.*, vol. 60, pp. 471–481, 2017.

[24] A. I. Isayev and B. Sujan, "Nonisothermal vulcanization of devulcanized GRT with reversion type behavior," *J. Elastomers Plast.*, vol. 38, no. 4, pp. 291–318, 2006.

[25] E. T. Thostenson and T.-W. Chou, "Microwave processing: fundamentals and applications," *Compos. Part A Appl. Sci. Manuf.*, vol. 30, no. 9, pp. 1055–1071, 1999.

[26] C. Guo, L. Zhou, and J. Lv, "Effects of expandable graphite and modified ammonium polyphosphate on the flame-retardant and mechanical properties of wood flour-polypropylene composites," *Polym. Polym. Compos.*, vol. 21, no. 7,

pp. 449–456, 2013.

[27] L. Landini, S. G. de Araújo, A. B. Lugão, and H. Wiebeck, “Preliminary analysis to BIIR recovery using the microwave process,” *Eur. Polym. J.*, vol. 43, no. 6, pp. 2725–2731, 2007.

[28] V.YU.Levin, S.H.Kim, and A.I.Isayev, “Ultrasound Devulcanization of Sulfur Vulcanized SBR Crosslink Density and Molecular Mobility,” *Rubber Chemistry and Technology*, vol. 69, no. 1. pp. 104–114, 1996.

[29] A.Pelofsky, “Rubber reclamation using ultrasonic energy,” US3725314 A, 1971.

[30] M. Okuda and Y. Hatano, “Devulcanization of cured rubber,” US5891926 A, 1998.

[31] N. Senapati and D. Mangaraj, “Ultrasonic vulcanization,” US4548771 A, 1984.

[32] G. Garcia, S. Aparicio, R. Ullah, and M. Atilhan, “Deep Eutectic Solvents: Physicochemical Properties and Gas Separation Applications,” *Energy & Fuels*, vol. 29, pp. 2616–2644, 2015.

[33] A. R. Ferreira, M. G. Freire, J. C. Ribeiro, F. M. Lopes, J. G. Crespo, and J. A. P. Coutinho, “Ionic liquids for thiols desulfurization: Experimental liquid-liquid equilibrium and COSMO-RS description,” *Fuel*, vol. 128, pp. 314–329, 2014.

[34] V. A. Online, “Deep eutectic solvents based on N -methylacetamide and a lithium salt as suitable electrolytes for lithium-ion batteries,” no. 3, pp. 20054–20063, 2013.

[35] S. Seghar *et al.*, “Devulcanization of styrene butadiene rubber by microwave energy: Effect of the presence of ionic liquid,” *Express Polym. Lett.*, vol. 9, no. 12, pp. 1076–1086, 2015.

[36] Q. Zhang, K. De Oliveira Vigier, S. Royer, and F. Jérôme, “Deep eutectic solvents: syntheses, properties and applications,” *Chem. Soc. Rev.*, vol. 41, no. 21, p. 7108, 2012.

[37] M. H. Chakrabarti *et al.*, “Prospects of applying ionic liquids and deep eutectic solvents for renewable energy storage by means of redox flow batteries,” *Renew. Sustain. Energy Rev.*, vol. 30, pp. 254–270, 2014.

[38] L. Bahadori, M. H. Chakrabarti, F. S. Mjalli, I. M. Alnashef, N. S. A. Manan, and M. A. Hashim, “Physicochemical properties of ammonium-based deep eutectic solvents and their electrochemical evaluation using organometallic reference redox systems,” *Electrochim. Acta*, vol. 113, pp. 205–211, 2013.

[39] R. Saputra, “Devulcanization of Waste Rubber Tyre Utilizing Deep Eutectic Solvents and Ultrasonic Energy,” Taylor’s University Lakeside Campus, 2016.

[40] S. Ghose and A. I. Isayev, “Recycling of unfilled polyurethane rubber using high-power ultrasound,” *J. Appl. Polym. Sci.*, vol. 88, no. 4, pp. 980–989, 2003.

[41] T. Liang, “Continuous Devulcanization of Ground Tire Rubber of Different Particle Sizes Using an Ultrasonic Twin-Screw Extruder,” 2013.

[42] S. Ramarad, C. T. Ratnam, M. Khalid, A. L. Chuah, and S. Hanson, “Improved crystallinity and dynamic mechanical properties of reclaimed waste tire rubber/EVA blends under the influence of electron beam irradiation,” *Radiat. Phys. Chem.*, vol. 130, pp. 362–370, 2017.

Design of Biomass Combined Heat and Power (CHP) Systems based on Economic Risk using Minimax Regret Criterion

Ling Wen Choong[1*], Wan Yoke Kin[1], Viknesh Andiappan[2]
[1]Department of Chemical Engineering,
School of Engineering, Taylor's University, Malaysia
[2]Department of Chemical Engineering, University of Bath, Claverton Down, BA2 7AY, Bath, United Kingdom.

[*]Corresponding Author Email: wenchoong.ling@taylors.edu.my

Abstract
Combined heat and power (CHP) systems are typically required to meet uncertain and varying energy demands. As such, it is a great challenge to identify optimum technologies for CHP systems that utilise biomass and convert it into heat and power. In this respect, industry decision makers are lacking in confidence to invest in biomass CHP due to economic risk from varying energy demand. This research work presents a linear programming systematic framework to design biomass CHP system based on potential loss of profit due to varying energy demand. This research work utilised LINGO programming tool to maximise the gross profit of the biomass CHP system at a certain energy demand. Then, Minimax Regret Criterion (MRC) approach was used to assess potential loss of profit of the given biomass CHP design based on energy demand. MRC approach quantified potential loss of profit based on maximum regret between selections of biomass CHP technologies. The term "maximum regret" is defined as the as maximum amount of profit loss by making a wrong decision in design. Based on this, the model determined an optimal biomass CHP design with minimum loss of economic opportunity. As Feed-in Tariff (FiT) rates affects the revenue of the CHP plant, sensitivity analysis was then performed on FiT rates on the selection of biomass CHP design. Besides, design analysis on the trend of the optimum design selected by model was conducted. To demonstrate the proposed framework in this research, a case study was considered and solved using the proposed approach. The case study focused on designing a biomass CHP system for a palm oil mill (POM) due to large energy potential of oil palm biomass in Malaysia. Based on MRC approach, the optimal design for the biomass CHP system in this case study is the direct combustion of biomass in boilers with steam turbine with revenue of RM 19, 104, 000 and capital expenditure (CAPEX) of RM9, 139, 780. Meanwhile, the sensitivity analysis indicated that boilers with steam turbine was generally favoured as the FiT rates increases. Biogas with gas engine (GE) is favoured for lower power capacity while boilers with steam turbine is favoured for high power capacity based on the design analysis of optimum biomass CHP design.

Keywords: Biomass, Combine Heat and Power, Minimax Regret Criterion approach, Palm Based Biomass, Optimisation

Introduction

Global energy demands are projected to increase 48% from 2012 by 2040 [1, 2]. To meet this projected increase in energy demand, biomass energy is expected to play an imperative role over the coming years. In fact, global biomass energy demands from 2000 to 2015 have seen a significant increase as compared to stable hydropower demands [3]. Such increase indicates that biomass is gaining attention in the renewable energy market. Biomass can be categorised into lignocellulose biomass, municipal waste and animal manure. These biomass resources can be obtained from agricultural residues, biomass plantations and organic wastes from residential areas [4]. Approximately 70% of these biomass are lignocellulosic biomass from plantations such as cereal, oil and sugar crops [5]. Intergovernmental Panel on Climate Change Special Report on Renewable energy (IPCC-SRREN) reported that solely on biomass from plantations are estimated to have potential energy up to 700 x 10^{12} MJ/year whereas other sources of biomass such as food and municipal waste had only 300 x 10^{12} MJ/year of potential energy [4]. Due to the high availability of lignocellulose biomass, recent studies on biomass utilisation focus on converting biomass into bioenergy and biofuels.

In Malaysia, one major source of lignocellulose biomass is oil palm biomass from the palm oil industry which provides approximately 82.61wt% of total biomass in Malaysia [6]. The palm oil industry generates biomass such as empty fruit bunches (EFBs), palm mesocarp fibre (PMF), palm kernel shell (PKS) and palm oil mill effluent (POME). These oil palm biomass are wastes produced during the extraction of crude palm oil (CPO) and crude palm kernel oil (CPKO) from fresh fruit bunches (FFB). Based on Malaysia Palm Oil Board [7], amount of FFB processed in Malaysia palm oil mill in 2016 is approximately 60 million tonnes. Solid oil palm biomass such as EFB, PMF and PKS are generated at about 28.42 million tonnes while POME is produced at about 40.04 million tonnes during palm oil extraction annually in 2017 [6–8]. These biomass have high calorific value that can be converted into heat and power using biomass combined heat and power (CHP) systems. This provides an opportunity for the industry to harness high amount of bioenergy from sources that were initially disposed as waste by-products.

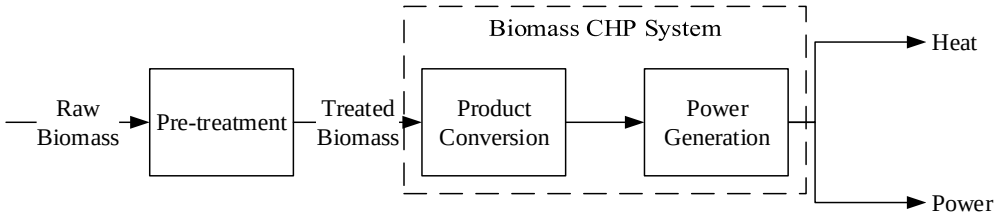


Figure 0.15: Simple Illustration of Biomass CHP system

Figure 1.1 above illustrates a biomass CHP is a system to generate power and thermal energy from biomass sources for industrial and/or residential needs [9]. A biomass CHP system commonly consists of pre-treatment unit, product conversion unit and power generation unit. Pre-treatment units such as shredder and dryer are required to reduce size and moisture content in biomass to allow efficient conversion into products through conversion units such as (but not limited to) boilers, gasifiers, digesters [6, 10, 11]. Biomass undergoes combustion in boilers to produce steam where

steam produce can be used to produce energy using a steam turbine. Gasifiers convert biomass into syngas and digesters convert biomass into biogas. Syngas consists of carbon monoxide and hydrogen that could be combusted in gas engines, gas turbines and micro-turbines. Similarly, biogas consist of mostly methane gas can be combust in similar power generation units to produce power [10, 11].

The Malaysian government had announced a program known as Small Renewable Energy Power (SREP) program back in 2001 to encourage industrial players to utilise agricultural wastes to generate power. With support from United Nation Development Programme and Global Environment Facility and SREP, the first demonstration of 13 MW CHP plant using EFB was built in Bahau, Negeri Sembilan [8]. Currently in Malaysia, most palm oil mills have CHP plants installed to meet internal energy demands. However, the power generated from these CHP plants are insufficient to supply to national power grid. This is due to some challenges met by these power plants that was outlined by several work from Umar et. al.[11–13] and it is summarised as following.

- Varying energy demand and biomass supply – Subjected to energy demand, palm oil mill will have sufficient biomass supply to meet energy demand for operation of the palm oil mill. However, feeding any power generated to national grid will have difficulties to ensure stable supply of biomass to fed into CHP systems due to seasonal nature of palm oil production to cope with varying energy demand.

- Non-favourable government program and schemes – SREP and Feed-in-Tariff (FiT) had proposed by the government in hope of palm oil mill owners to utilise their oil palm biomass to generate electricity and feed into gridlines. However, respondents from these work expressed that current FiT rates are not attractive enough to them. Hence, most of the power generated from biomass CHP plant were used for self-consumption in palm oil mill instead of feeding it into power grid.

- Location of palm oil mill from gridlines – Approximately 62.3% of palm oil mills in Malaysia are situated at least 10 km from any electricity network system. Connecting these CHP systems in palm oil mill to the gridlines requires intensive amount of capital cost. A heuristic value regarding cost required for connection of grid is given as approximately RM 1 to 1.5 million per km of gridline [14]. Hence, palm oil mill owners are reluctant to invest such capital cost when there are risk of having unstable power generation with varying biomass supply.

- Perspective of palm oil mill owner – Respondents considers biomass energy systems as a highly intensive capital invest with long payback period. Since the palm oil industry focuses on edible oil production as their main traditional business, most mill owners prefer not to risk participating in the renewable energy industry. Furthermore, mill owners have expressed that challenges in financial capability to participate in such capital-intensive projects.

Due to uncertainty of biomass supply in meeting varying energy demands, palm oil mill owner possess a lack confidence to invest in a capital-intensive biomass CHP system. Others factors such as distance of palm oil mill from gridlines and unattractive government subsidy or tariff programs contribute further to this lack of confidence. Therefore, there is a need of a framework to design CHP system that cope with varying

energy demands and subsequently provides an optimal design with low economical risk in order to gain confidence from palm oil mill owners.

In a similar area of research, several research works have been proposed to analyse economic risk of renewable energy technologies (RET) using an approach known as Monte Carlo Simulation (MCS) approach. MCS considers uncertainty in variables behaviour through probability distribution to quantify the possibility of a certain condition will occur [15]. Arnold et al. [16] assessed economical risk for renewable energy infrastructures using MCS to compare different boundary conditions such as climate, capital and operating cost. However, it is stated by the author that this MCS model requires a matching tool to select suitable RET for each case study of interest. In addition, Edinaldo et al. [15] presented a similar mathematical model to help in justifying whether the selected RET is worth investing through MCS approach. However, MCS approach used in both Arnold and Edinaldo's work only analyses a certain RET potential economic risk without providing clear suggestion on selection of optimal RET. Therefore, there is a need for a framework that is able to analyse potential economic risk and subsequently synthesise an optimal RET system.

Recent studies by Yokoyama [17, 18] used Minimax Regret Criterion (MRC) approach to evaluate economic risk and subsequently providing optimal design of energy supply system. However, Yokoyama's study only focuses on conventional energy supply system. Besides, challenges faced in utilising biomass CHP such as varying biomass supply and energy demand were not addressed in recent work. Therefore, in this work, a mathematical optimisation model was developed to synthesise an optimal design for biomass CHP systems based on potential loss of profitable opportunity using MRC approach at varying energy demand. The objective of this developed framework are as follows:

1. To determine the optimal design for the biomass CHP system based on maximum gross profit.
2. To assess potential economy risk for a given biomass CHP design based on varying energy demand using MRC approach.

Such model will enable designers to systematically design a biomass CHP with minimal economic risk using MRC approach.

Methodology

As described previously, a mathematical model framework was developed to design an optimal biomass CHP system to meet certain energy demand with minimal economic risk through Minimax Regret Criterion (MRC) approach. A case study based on palm oil mill biomass was conducted using the framework generated. To carry out the case study, a palm oil mill case study superstructure was developed to show possible biomass CHP designs to convert palm oil mill biomass into heat and power. With the superstructure developed, mathematical model equations were formulated for each biomass CHP technology unit. These equations correlates biomass mass flow rates, efficiency of CHP systems, heat and power produced and capital expenditure (CAPEX) of equipment. The mathematical model will ultimately provide biomass CHP design based on maximum gross profit at different energy demands. Following this, MRC approach was utilised to select the optimum biomass CHP design which has the lowest

maximum regret value. The term "maximum regret value" is defined as the as maximum amount of profitable opportunity loss by making a wrong decision in design [19]. A sensitivity analysis of Feed-in Tariff (FiT) rates on selection of optimum biomass CHP design was conducted to analyse the impact of the change of FiT rates on the selection for optimum design of biomass CHP. Lastly, design analysis on optimum biomass CHP design was conducted to study the trend of selection for biomass CHP design by the framework base on case study.

Generic Superstructure of Biomass CHP Design

Resources i represents biomass supply with flow rates F_i can be used to convert into product $p \in P$ through technology $j \in J$. The product p can be further converted to energy $e \in E$ via power generation technology $j' \in J'$. Figure 2.1 below shows the generic superstructure of Biomass CHP design. With the generic superstructure, equations formulated in the following sections are based on Figure 2.1.

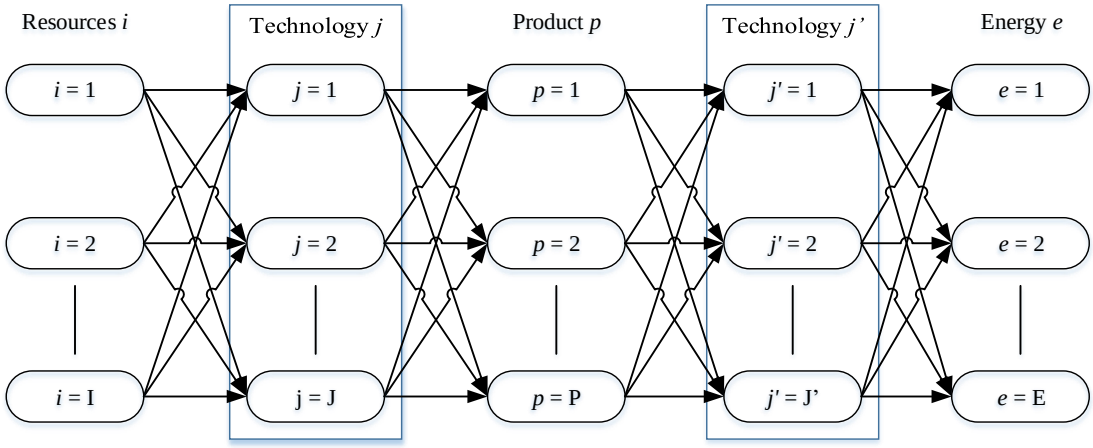


Figure 0.16: Generic Case Study Superstructure

Mathematical Model Equations

Referring to Figure 2.1, following mathematical modelling equations were formulated based on data collected for the respective process unit to convert biomass to heat and power. Mass and energy balance equation was developed first for each biomass CHP system to convert biomass to heat and power. Following this, the equation for capital expenditure (CAPEX) of each equipment was developed based on the equipment capacity parameters such as flow rates and energy produced. With CAPEX of equipment and energy production equations, the optimum biomass CHP design that provide maximum gross profit was generated using LINGO programming software. The data of gross profit and optimum biomass CHP design at different power demand will be utilised in Minimax Regret Criterion (MRC) approach to solve for optimum biomass design that provide maximum gross profit with minimal economical risk.

Mass and Energy Conversion Mathematical Equations

Eq. (1) shows the component balance for biomass i where f_i and x_i are the component mass flow rates and composition respectively based on Figure 2.1 where F_i represents the total flow rate of biomass i.

$$f_i = F_i x_i \qquad \forall i \qquad (1)$$

Biomass *i* is allocated to potential technology *j* as shown in in Eq. (2) where F_{ij} is the flow rate entering technology *j*.

$$F_i = \sum_{j=1}^{J} F_{ij} \qquad \forall i \forall j \qquad (2)$$

Technology *j* converts entering biomass F_{ij} into product p. Eq. (3) shows the conversion of F_{ij} into mass flow rate of product F_{jp} with a conversion factor of k_{jp} for each technology.

$$F_{jp} = k_{jp} F_{ij} \qquad \forall i \forall j \forall p \qquad (3)$$

Total rate of production for product *p* for all technologies *j* is shown as Eq. (4).

$$F_p = \sum_{j=1}^{J} F_{jp} \qquad \forall j \forall p \qquad (4)$$

The product *p* is then distributed to power generation technology *j'* to convert into energy *e*. The distribution of product p is as shown in Eq. (5).

$$F_p = \sum_{j'=1}^{J'} F_{pj'} \qquad \forall j' \forall p \qquad (5)$$

Eq. (6) shows distributed product *p* converts into power $E_{j'e}$ through power generation technology *j'*. $n_{j'p}$ is the conversion efficiency of each power generation technology *j'*.

$$E_{j'e} = n_{j'p} F_{pj'} \qquad \forall e \forall j' \forall p \qquad (6)$$

The total power generated by technologies *j'* is calculated as Eq. (7) below.

$$E_T = \sum_{e=1}^{E} E_{j'e} \qquad \forall e \forall j' \qquad (7)$$

Capital Expenditure (CAPEX) of Equipment Mathematical Equations

The capital expenditure (CAPEX) equations of each technologies shown in Figure 2.1 were formulated based on data collected. CAPEX of each technologies C_j and $C_{j'}$ are determined via Eq. (8) and (9). k_{cj} and $k_{cj'}$ are the cost factor of each technologies correlated to its technology size factor M_j and $M_{j'}$ respectively. Example of size factor M_j are flow rates through the equipment (F_{ij} or F_{jp}) and power capacity of the equipment $E_{j'e}$.

$$C_j = k_{Cj} M_j \qquad \forall j \qquad (8)$$
$$C_{j'} = k_{Cj'} M_{j'} \qquad \forall j' \qquad (9)$$

The total capital expenditure (CAPEX) of the technologies is as shown in Eq. (10).

$$CAPEX = \sum_{j=1}^{J} C_j + \sum_{j'=1}^{J'} C_{j'} \qquad \forall j \forall j' \qquad (10)$$

Solving Case Study by Minimax Regret Criterion (MRC) Approach

With the total *CAPEX* of equipment and energy produced from biomass CHP design calculated using Eq. (10), gross profit based on energy produced through CHP

system were calculated with power tariff data at the location of the palm oil mill. Eq. (11) below shows the gross profit P_{gross} calculation of the CHP system. AOT is the annual operation time of the plant and (A/P) is the capital recovery compound interest factor for uniform payment of the biomass CHP plant.

$$P_{gross} = E_T \times Tariff \times AOT - CAPEX \times (A/P) \quad (11)$$

By maximising gross profit from Eq. (11) at different power demand, the data of gross profit are subsequently used in Minimax Regret Criterion (MRC) approach to decide on the optimum design of biomass CHP with minimal regret. The term "regret" refers to a quantifiable value on loss of profitable opportunity due to a decision made in design. For example, if the design selected have much higher power capacity than the power demand, the biomass CHP plant will be running on low capacity which will generate lower gross profit than its potential gross profit. MRC approach is commonly used in business and finance model to make decision that minimises the possible maximum regret [13, 18]. Generic tables used for MRC approach are shown in Table 2.1 and 2.2 below.

Table 0.16: Generic gross profit table used for MRC approach

Factor 1	**Factor 2**		
	j_1	j_2	j_3
i_1	P_{11}	P_{12}	P_{13}
i_2	P_{21}	P_{22}	P_{23}
i_3	P_{31}	P_{32}	P_{33}

Where i_n is the levels of factor 1, j_n is the levels of factor 2 and P_{ij} as stated in the table are the gross profit of the system.

Table 0.17: Generic Regret Table used for MRC approach

Factor 1	**Factor 2**			**Maximum Regret Value**
	j_1	j_2	j_3	
i_1	R_{11}	R_{12}	R_{13}	$R_{max,1}$
i_2	R_{21}	R_{22}	R_{23}	$R_{max,2}$
i_3	R_{31}	R_{32}	R_{33}	$R_{max,3}$

Where R_{ij} is the regret value of each level combination of the factors and $R_{max,i}$ is the maximum regret value of each row.

The MRC approach calculations based on Table 2.1 and 2.2 with i = 1, 2, 3 …, I and j = 1, 2, 3…, J are as following:

For gross profit table,

1. $P_{i,j}$ is gross profit calculated with Eq. (11) at energy demand and capacity of the CHP designed are equal to each other. (diagonal row of the table from top left to bottom right)
2. $P_{i,i+j}$ are equal to $P_{i,j}$ since the profit is limited by the maximum capacity of the CHP designed where energy demand is more than designed CHP capacity. (columns on top of diagonal row of the table)
3. $P_{i+j,j}$ is calculated with Eq.(11) at energy demand is lesser than capacity of CHP designed. (Columns below of diagonal row of the table)

For regret value table,

1. $R_{i,j}$ (diagonal row from top left to bottom right) equal to zero since energy demand occurred is equal to capacity of CHP designed.
2. $R_{i,i+j}$ (columns on top of diagonal row of the table) are calculated by Eq. (12).

$$\boldsymbol{R}_{i,i+j} = \boldsymbol{P}_{i+j,i+j} - \boldsymbol{P}_{i,i} \quad (12)$$

3. $R_{i+j,j}$ (columns below of diagonal row of the table) are calculated by Eq. (13)

$$\boldsymbol{R}_{i+j,j} = \boldsymbol{P}_{i+j,j} - \boldsymbol{P}_{j,j} \quad (13)$$

4. Determine the maximum regret value for each row.
5. Select the design criteria with the smallest maximum regret value.

Palm Oil Mill Case Study Superstructure

Figure 2.2 below shows the palm oil mill case study superstructure developed for the mathematical model.

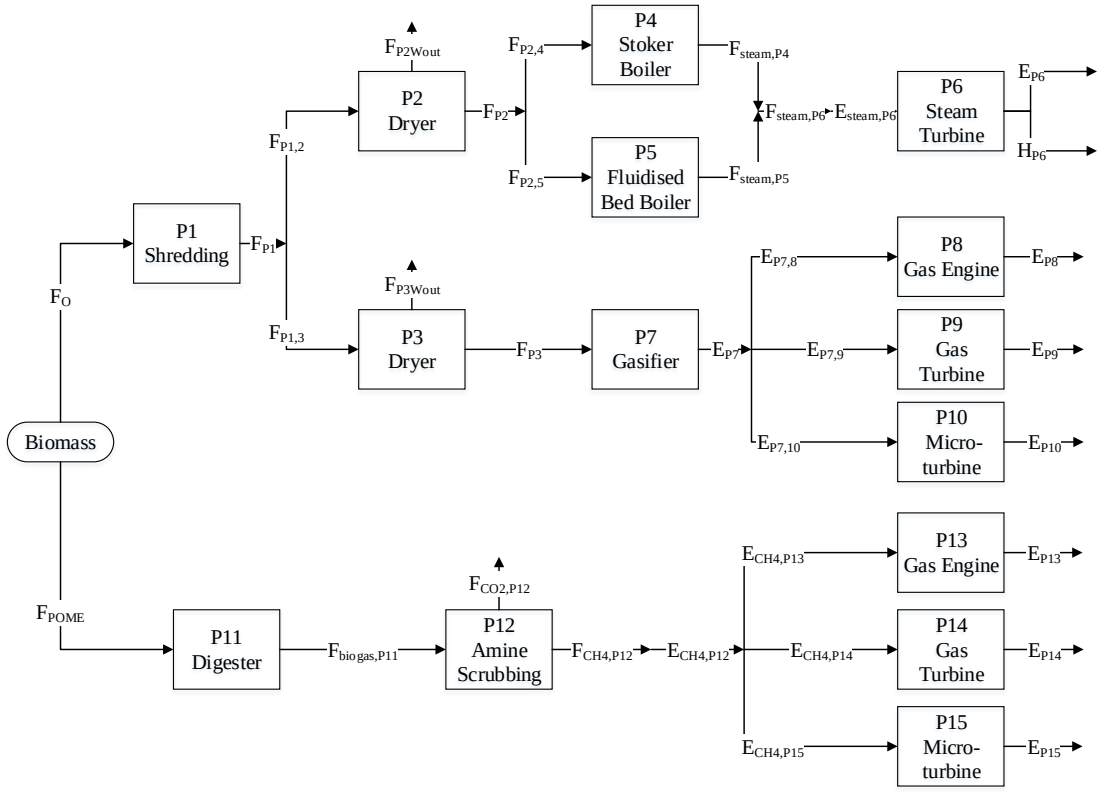


Figure 0.17: Palm Oil Mill Case Study Superstructure

The amount of biomass supply for this case study is taken as 10000 kg/hr of mix solid biomass and palm oil mill effluent (POME) of 10 m^3/day. Varying the power demand as the manipulating variable, power demand range from 250 kW to 13 MW were input into the model to identity the optimum biomass CHP technology pathway.

Sensitivity Analysis of Feed-in Tariff (FiT)

Feed-in tariff (FiT) system is a distributed premium license to individual or company to legally sell renewable energy at the FiT rate to companies that distribute electricity [20]. FiT rates for power generation using biogas and solid biomass are different rates. Basic FiT rates varies with installed capacity and bonus FiT rates applies when certain criteria of the installed CHP technology is met. To ease the calculation in sensitivity analysis, the FiT rates used to calculate the gross profit of CHP plant was taken as average of RM 0.2985 per kWh for biomass power generation and RM 0.2886 per kWh for biogas power generation [20]. For the sensitivity analysis conducted, the FiT rates are changed at ±10, ±30 and ±50% from its original tariff. The purpose of doing this is to analyse the impact of the change of FiT rates on the selection for optimum design of biomass CHP technologies.

Analysis of Optimum Biomass CHP Design

Optimum biomass CHP design that are recommended by model through maximising gross profit at varying power demand for the case study was analysed to study the trend of optimum selection for biomass CHP design. Besides, the analysis identifies which biomass CHP design is compulsory across a certain range of power demand. These "must-have" design is compulsory to have in order to achieve the required power demand. The analysis also identifies "optional" equipment that can be invested in if process designers are ambitious to meet higher power demands and equipment that are never selected throughout the power demand range appear as a "must-avoids". This analysis helps plant designers to narrow down their selection of biomass CHP design and subsequently decide on the optimum selection of biomass CHP design.

Results and Discussion

As described previously, the methodology for this work was carried out to determine an optimum biomass CHP design for palm oil mill using Minimax Regret Criterion (MRC). In this section, the results obtained from the case study are analysed and discussed. Following this, a sensitivity analysis on Feed-in Tariff (FiT) rates was performed to analyse the impact of FiT rates on the selection of biomass CHP design. Lastly, a design analysis was done on the optimum design of biomass CHP to study the trend of recommended design by the mathematical model. In the design analysis, "must-have", "optional" and "must-avoid" designs were identified to ease plant designer decision on selecting the optimum selection of biomass CHP design.

Optimum Biomass CHP Design using MRC Approach

To select the optimum design of CHP plant throughout the wide range of power demand, Minimax Regret Criterion (MRC) approach was utilised as described in methodology. Taking the power demands are 3000, 5000, 8000 and 10000 kW, Table 3.1 below shows the gross profit table of optimum biomass CHP designs at different power demand.

Table 0.18: Gross Profit Table of Case Study in unit RM/year

Designed Capacity (kW)	Power Demand (kW)			
	3000	**5000**	**8000**	**10000**
3000	4,470,740.00	4,470,740.00	4,470,740.00	4,470,740.00
5000	1,481,316.30	6,154,717.00	6,154,717.00	6,154,717.00
8000	(2,213,380.58)	2,460,019.42	9,964,220.00	9,964,220.00
10000	(3,897,126.95)	776,273.05	8,280,473.05	12,938,480.00

As shown in Table 3.1, values in parentheses represent loss of profit. The mathematical model provided the biomass CHP design at its respective designed capacity. The equipment that were selected while the gross profit of biomass CHP design is maximised will have CAPEX value shown in the mathematical model while solving gross profit for each designed capacity. Hence, the biomass CHP design for each designed capacity identified are listed below in Table 3.2.

Table 0.19: Biomass CHP Design at each Designed Capacity

Biomass CHP Design	Plant Power Capacity (kW)
Biogas with GE	3000
Syngas + Biogas GE	5000
Boiler with Steam Turbine	8000
Combined Boiler with Steam Turbine and Biogas with GE	10000

The regret table was developed to identify the maximum regret value of each biomass CHP technology. The biomass CHP technology with the smallest value between the maximum regret values was selected as the optimum biomass CHP technology. The regret table was developed as below.

Table 0.20: Regret Table of Case Study in unit RM/year

Designed Capacity (kW)	Power Demand (kW)				Max Regret Value
	3000	**5000**	**8000**	**10000**	
3000	-	1,683,977	5,493,480	8,467,740	8,467,740
5000	2,989,423	-	3,809,503	6,783,763	6,783,763
8000	6,684,120	3,694,697	-	2,974,260	6,684,120
10000	8,367,866	5,378,443	1,683,746	-	8,367,866

Selecting the smallest maximum regret value in Table 3.3, the optimum design capacity of biomass CHP plant is 8000 kW. Based on Table 3.2, the optimum biomass CHP technology at 8000 kW is steam generation using boiler with steam turbine to generate power. Therefore, boiler with steam turbine power generation is the recommended optimum biomass CHP technology that provide maximum gross profit with minimal regret/loss of opportunity.

Sensitivity Analysis of Feed-in Tariff (FiT) Rate on Selection of Optimum Biomass CHP Design

The optimum design recommended by the developed model through MRC approach at different FiT rates are shown in Table 3.4 below using similar case study assumptions in Section 2.3. Lowest maximum regret value, potential minimum and maximum gross profit values between different biomass CHP designs are included to show their changes with FiT rates.

Table 0.21: Optimum Design of Biomass CHP Plant at Different FiT Rates

FiT Rates (%)	Optimum Design	Minimax Regret Value (RM/yr)	Potential Minimum Gross Profit (RM/yr)	Potential Maximum Gross Profit (RM/yr)
-50	Biogas GE	96,457.00	1,007,540.00	1,103,997.00
-30	Syngas + Biogas GE	3,137,180.00	2,392,820.00	5,811,957.00
-10	Syngas + Biogas GE	5,567,543.00	3,778,100.00	10,562,280.00
0	Boiler Steam Turbine	6,684,120.58	4,470,740.00	12,938,480.00
10	Boiler Steam Turbine	6,684,120.58	5,163,380.00	15,314,680.00
30	Boiler Steam Turbine	6,684,120.58	6,548,660.00	20,067,090.00
50	Boiler Steam Turbine	6,684,120.58	7,933,940.00	24,819,490.00

As the FiT rates decreases, the optimum design of biomass CHP plant changed into combined syngas and biogas with gas engine (GE) as power generation technology. At 50% reduction of FiT rates, the optimum design of biomass CHP plant is small capacity biogas generation. The lowest maximum regret value reduces significantly as FiT rates decreases. Although the magnitude of regret value reduces, the potential minimum and maximum gross profit reduces significantly as well. Lower profit margin as FiT rate reduces causes smaller scale biomass CHP design such as biogas and syngas generation with GE more economical compared to boiler with steam turbine. As FiT rate increases, the selection of optimum design for biomass CHP plant remain the same as boiler with steam turbine. Increasing FiT rates will not change the selection on boiler with steam but will significantly increase potential gross profits. This is due to higher revenue on feeding in power to grid thus giving a higher potential of profit as FiT rate increases.

In summary, the impact of FiT rate on selection of biomass CHP design based on Table 3.4 is summarised as following:

1. Decrease in FiT rates will economically favour smaller scale biomass CHP design such as biogas and syngas generation with GE due to lower profit margin.
2. Decrease in FiT rates reduces lowest maximum regret significantly; however, potential profit from biomass CHP plant decreases significantly as well.
3. Higher revenue is generated on feeding in power to grid with higher plant power capacity and FiT rate which eventually provide higher gross profit. Hence, increase in FiT rates will favour larger scale biomass CHP design such as boilers with steam turbine which is able to provide higher power capacity.

Analysis of Optimum Biomass CHP Design

Table 3.5 below shows the optimum biomass CHP technology that provide maximum gross profit at different power demand with their respective usage of biomass using the developed model. The amount of biomass available was taken as the same as case study as described in Section 2.2.

Table 0.22: Optimum Biomass CHP Design at Different power Demand of Case Study

Power Demand (kW)	POME Consumption (m^3/day)	Usage of Solid Feed (kg/hr)	Optimum Biomass CHP Design
250	0.58	0.00	Biogas with GE
500	1.16	0.00	
750	1.75	0.00	
1000	2.33	0.00	
3000	6.98	0.00	
4000	9.31	0.00	
5000	10.00	1691.00	(Syngas + Biogas) with GE
6000	0.00	7472.37	Boiler with Steam Turbine
7000	0.00	8479.30	
8000	0.00	9486.24	
9000	1.14	10000.00	Combined Boiler with Steam Turbine and Biogas with GE
10000	3.47	10000.00	
13000	9.55	10000.00	

As shown in Table 3.5, biogas with GE engine is used for lower power demand from 250 to 4000 kW where only POME is utilised. This shows that biogas generation through anaerobic digestion of POME is preferred at lower power demand rather than utilising solid biomass such as empty fruit bunches (EFB), palm kernel shell (PKS) and palm mesocarp fibre (PMF). This occurs because utilisation of solid biomass requires pre-treatment equipment such as dryers and shredder, which requires more capital cost. Since the objective function in model focuses on maximising profit and minimising capital costs, the model favours a cheaper route, which is anaerobic digestion equipment. Meanwhile, when the power demand reaches 5000 kW, available POME supply of 10 m^3/day is completely consumed, leaving the remaining amount of power required to be met by syngas generation. Syngas generation was selected to top up remaining power required rather than utilising boiler technology at low usage of solid feed for power generation. This occurs as boilers are more economically viable at larger capacities and high usage of solid feed while syngas is more viable at lower capacities. However, as the power demand increases to range of 6000 to 8000 kW, only solid biomass is utilised through boiler with steam turbine technology without utilising any POME for biogas generation. This shows that boiler steam generation is a favoured

selection of CHP technology at higher power demand comparing to syngas and biogas generation. This is because solid biomass that used in boiler can generate higher amount of energy to satisfy higher range of power demand at 6000 to 8000kW. Alternatively, biogas and syngas can be generated to meet this demand. However, due to the high power demand, high amount of biogas and syngas would be required. This will cause the equipment to increase in size much more than of boilers as both biogas and syngas are in gaseous state. Hence, biogas and syngas generation is not economically viable at higher capacity. As the solid biomass are completely utilised as shown in power demand above 9000 kW, POME is utilised to make up to the power demand required which there are not much selection for the model to utilise both biomass. The data stops at power demand of 13000 kW due to insufficient amount of biomass to produce the required power demand. In addition, only GE is selected as power generation technology for biogas and syngas shows that it is a much better selection than micro-turbine and gas turbine. This is due to GE is a widely used and developed power generation technology compare to micro-turbine. Gas turbine is commonly used in natural gas CHP plants but it is only economically viable at very high power demand due to its large power capacity. Therefore, GE is a more economical option than micro-turbine and gas turbine for biomass CHP plant as shown in Table 3.5.

Results from Table 3.5 also indicate other important analysis. It is found that there are common equipment selected for a range of power demands. These equipment are considered as the “must-haves”, as without them, the design would be incapable of meeting the required power demands. On top of this, there are certain equipment in the CHP design that appear as “optional”. “Optional” equipment are equipment that can be invested in if process designers are ambitious to meet higher power demands. On the other hand, equipment that are never selected throughout the power demand range appear as a “must-avoid”. To allow designers to analyse these options, Figure 3.1 summarises the “must-have”, “optional” and “must-avoid” equipment in the case study.

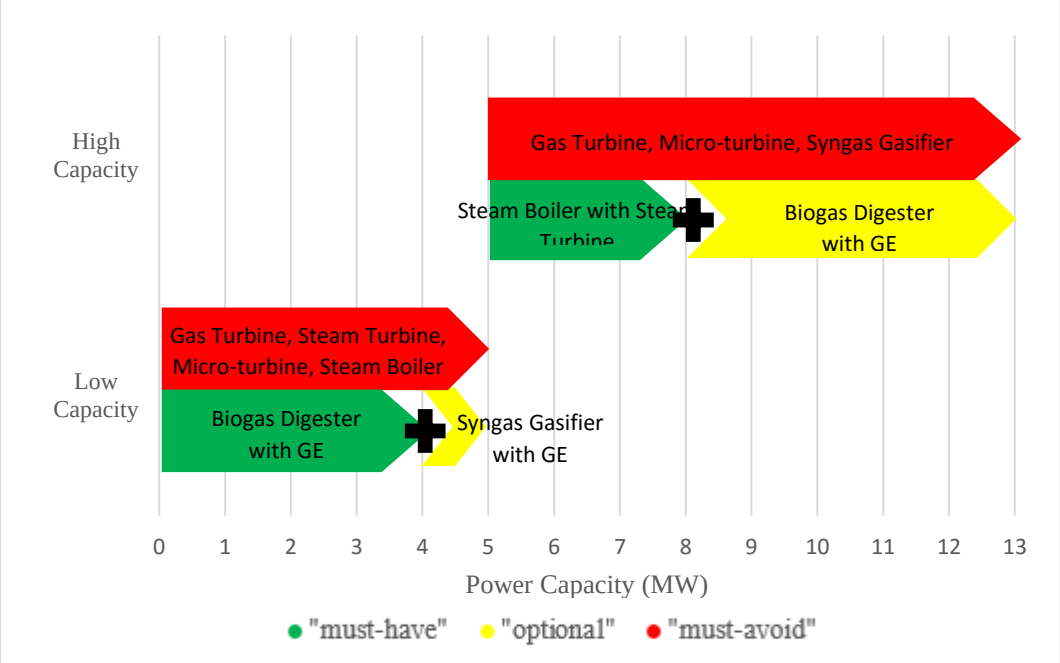


Figure 0.18: “Must-have”, “optional” and “must-avoid” Design

For low capacity biomass CHP plant ranges up to 5 MW, the "must-have" design for the CHP plant is biogas generation with GE as shown in Figure 3.1. If the designer would like to invest for a higher power demand at this range, the designer could combine "optional" syngas generation on top of biogas generation to meet higher power demand of 5 MW. For higher capacity biomass CHP plant that ranges from 5 to 13 MW, the "must-have" design for the CHP plant is boiler with steam turbine. Similarly, a higher power demand of 8 to 13 MW could be achieved by combining "optional" biogas with GE on top of boiler with steam turbine. The "must-avoid" design of biomass CHP plant are gas turbine and micro-turbine as these design are not economically viable compare to GE as described.

In a nutshell, Table 3.5 and Figure 3.1 shows a trend of biomass CHP technology selection as below:

1. Biogas generation utilising POME is selected for low power generation.
2. Combined syngas and biogas generation is selected at full usage of POME with low usage of solid biomass at mid power generation.
3. Steam generation using boiler is utilised for high power generation.
4. Internal combustion engine (GE) is used for both syngas and biogas combustion rather than micro-turbine and gas turbine.
5. The "must-have" design for low capacity biomass CHP design ranges up to 5 MW is biogas generation with GE. "Optional" syngas generation design can be invested and combined to achieve a higher power demand from 4 to 5 MW.
6. The "must-have" design for high capacity biomass CHP design ranges from 5 to 13 MW is boiler steam generation with steam turbine. "Optional" biogas generation design can be invested and combined to achieve a higher power demand from 8 to 13 MW.

Conclusion

This research work had presented a linear programming systematic framework to design biomass CHP system based on potential loss of profitable opportunity due to varying energy demand. Then, Minimax Regret Criterion (MRC) approach was used to assess potential economic risk of the given biomass CHP design based on energy demand. Based on MRC approach for the case study, the recommended optimum biomass CHP design is steam generation through boiler with steam turbine generating power. This design is selected as the optimum design due to its lowest maximum regret. This means that boiler with steam turbine biomass CHP design will provide minimum potential loss of profitable opportunity across the power demand range of 3000 to 10000 kW. Sensitivity analysis of FiT rates on the selection of biomass CHP design was conducted. Boilers with steam turbine is generally favoured as the FiT rates increases based on the sensitivity analysis of FiT rates at ±10, ±30 and ±50% from its original tariff. This is due to higher revenue is generated on feeding in power to grid with higher plant power capacity and FiT rate which eventually provide higher gross profit. On the other hand, decrease in FiT rates will economically favour smaller scale biomass CHP design such as biogas and syngas generation with GE due to lower profit margin. Besides, design analysis on the trend of the optimum design selected by model was conducted. Biogas with GE utilising POME is favoured for lower power capacity ranges from 250 to 5000 kW. Boilers with steam turbine is favoured for high power capacity ranges from 5000 to 13000 kW instead. Certain equipment will be essential for certain power demand range as described as a "must-have" design. These equipment

had been outlined to ease the decision in final selection of process designer. In overall, a systematic framework to design biomass CHP system had been established to recommend an optimum biomass CHP design which minimise the potential loss of profitable opportunity while maximising gross profit. The case study had shown that the framework was able to provide a preliminary design. The model also highlights optional design that allow process designer to invest in to achieve higher power capacity. It is worth mentioning that the mathematical model can be easily revised and reformulated to take in account of other aspects such as variation in biomass supply, variation in tariff rates, and changes in government schemes which will be considered as prospects of future work.

Acknowledgement

The author would like to acknowledge Prof. Denny K. S. Ng for generous advice and recommendation that had provide insightful analysis towards this work.

References

[1] EIA, "World energy demand and economic outlook EIA's handling of non-U.S. policies in the International Energy Outlook," *U.S. Energy Inf. Adm.*, vol. 2016, no. May 2015, pp. 7–17, 2016.
[2] T. W. John Twidell, *Renewable Energy Resources - John Twidell, Tony Weir - Google Books*, 3rd ed. New York : Routledge, 2015.
[3] EIA, "World Renewable Energy Consumption," 2016.
[4] O. Edenhofer *et al.*, *IPCC, 2011: Summary for Policymakers. In: IPCC Special Report on Renewable Energy Sources and Climate Change Mitigation*. 2011.
[5] F. Rosillo-Calle, "A review of biomass energy - shortcomings and concerns," *J. Chem. Technol. Biotechnol.*, no. March, pp. 1933–1945, 2016.
[6] S. Mekhilef, R. Saidur, A. Safari, and W. E. S. B. Mustaffa, "Biomass energy in Malaysia: Current state and prospects," *Renew. Sustain. Energy Rev.*, vol. 15, no. 7, pp. 3360–3370, 2011.
[7] Malaysia Palm Oil Board, "FFB Processed by Mill 2017." [Online]. Available: http://bepi.mpob.gov.my/index.php/my/statistics/sectoral-status/179-sectoral-status-2017/806-ffb-processed-by-mill-2017.html. [Accessed: 18-Jun-2017].
[8] Y. L. Chiew and S. Shimada, "Current state and environmental impact assessment for utilizing oil palm empty fruit bunches for fuel, fiber and fertilizer - A case study of Malaysia," *Biomass and Bioenergy*, vol. 51, pp. 109–124, 2013.
[9] K. Darrow, R. Tidball, J. Wang, and A. Hampson, "Catolog of CHP Technologies," no. March, p. 131, 2015.
[10] U. S. E. P. Agency, "Biomass Combined Heat and Power Catalog of Technologies," *Biomass*, no. September, pp. 2000–2003, 2007.
[11] M. S. Umar, P. Jennings, and T. Urmee, "Strengthening the palm oil biomass Renewable Energy industry in Malaysia," *Renew. Energy*, vol. 60, pp. 107–115, 2013.
[12] M. S. Umar, P. Jennings, and T. Urmee, "Generating renewable energy from oil palm biomass in Malaysia: The Feed-in Tariff policy framework," *Biomass and Bioenergy*, vol. 62, pp. 37–46, 2014.
[13] M. S. Umar, P. Jennings, and T. Urmee, "Sustainable electricity generation from oil palm biomass wastes in Malaysia: An industry survey," *Energy*, vol. 67, pp. 496–505, 2014.
[14] ICESN, "Biogas Asia Pacific Forum 2017," 2017, no. 15–19th May, pp. 17–18.

[15] E. J. da S. Pereira, J. T. Pinho, M. A. B. Galhardo, and W. N. Macêdo, "Methodology of risk analysis by Monte Carlo Method applied to power generation with renewable energy," *Renew. Energy*, vol. 69, pp. 347–355, 2014.
[16] U. Arnold and Ö. Yildiz, "Economic risk analysis of decentralized renewable energy infrastructures – A Monte Carlo Simulation approach," *Renew. Energy*, vol. 77, pp. 227–239, 2015.
[17] R. Yokoyama, K. Fujiwara, M. Ohkura, and T. Wakui, "A revised method for robust optimal design of energy supply systems based on minimax regret criterion," *Energy Convers. Manag.*, vol. 84, pp. 196–208, 2014.
[18] R. Yokoyama, R. Nakamura, and T. Wakui, "Performance Comparison of Energy Supply Systems Under Uncertain Energy Demands Based on a Mixed-Integer Linear Model," *Energy*, 2016.
[19] A. S. Christian and W. Winston, *Data Analysis and Decision Making*, 4th Edition. Mason, USA: South Western Cengage Learning, 2010.
[20] "SEDA PORTAL." [Online]. Available: http://seda.gov.my/. [Accessed: 23-Oct-2017].

eureca 2017 – Conference Paper
Paper Number 2CE07

Amine Based Devulcanization of Waste Tire Rubber

Mohammad Afiq Bin Zulkefly[1], Suganti Ramarad[2], Rashmi Walvekar[3]

[1]*afiq.zul007@gmail.com*
[2]*Suga4u2c@gmail.com*
[3]*rashmi.walvekar@gmail.com*

Abstract
This research project focuses on an alternative pathway of devulcanizing waste tire rubber by using amine based chemicals. Waste tire rubbers are known to be as toxic, non-degradable material due to their vulcanized crosslink carbon structure, and disposing of such waste could impose hazardous impacts on the environment. The current rubber recycling methods that are practiced today are rather uneconomical, non-environmentally friendly, and also producing recycled rubber with low quality due to the alteration in the main polymeric chains of waste rubber. This project aims to answer the question of whether the usage of amine can produce high quality rubber, where the properties of recycled rubber is almost the same as new/virgin rubber. With known potential of amine, it is a challenge for the chemical to selectively cleave the sulfur bonds without affecting the main carbon backbone chain in the rubber structure and diminishing much of the rubber properties. To study this research, amine-treated rubber must undergo devulcanisation process by applying heat and sonication energy. Then, the properties of the amine-treated rubber were determined through a set of characterization tests and analysis which are: gel content test to determine the weight of rubber before and after devulcanization, the thermogravimetric analysis (TGA) to determine the thermal degradation and stability of rubber, and Fourier Transform Infrared Spectroscopy (FTIR) to determine any structural change of the rubber. In this research so far, the first two preliminary analysis tests have been performed. The gel content test has shown that tertiary amine samples possessed a lower gel content (%) of (77 – 63 %), compared to primary amine samples (falls within the range of 80%), as well as the TGA test in which tertiary amine samples degrade faster than primary amine samples (suggesting a higher degree of rubber structure breakdown). For each type of amine, the concertation of amine did not play a major role in affecting the degree of devulcanization (as the concentration increased, the degree of devulcanization decreased for some samples). FTIR analysis showed that only sulphur-sulphur bonds were cleaved during the devulcanization process, leaving the carbon-sulphur bonds unaffected.

Keywords: Amine, Devulcanisation, High Quality Rubber, Selective cleavage, Sulphur Bonds.

1. Introduction

Rubber is an elastomer with a potential to return to its original state when deformed. External conditions (such as external force), the structure and the molar mass of the rubber are factors which can influence the deformation rate of rubber. Usually, rubbers possess regular and long macromolecule chains which can restore their initial position once the external deforming forces are removed. There are natural rubbers and synthetic rubbers used in industrial applications. Natural rubbers are usually obtained from a plant called Hevea Brasiliensis, while synthetic rubbers are mainly derived by constructional polyreactions of chain or grade nature [1]. For rubber to be used in commercial purposes, raw rubber is required to undergo treatment processes in order to increase the rubber's strength and life. Treatment processes of rubber may involve the addition and mixing of the rubber with industrial oils, additives, and carbon black filler [2].

Vulcanization is a curing process which transforms the rubber into a strong, elastic, and rubbery hard state. This process involves the crosslinking of rubber macromolecules which results in the foundation of three dimensional network of rubber matrix as shown in figure 1 [1]. This network pattern makes the rubber more durable and stronger which contributes to improved wear and durability of the rubber [2].

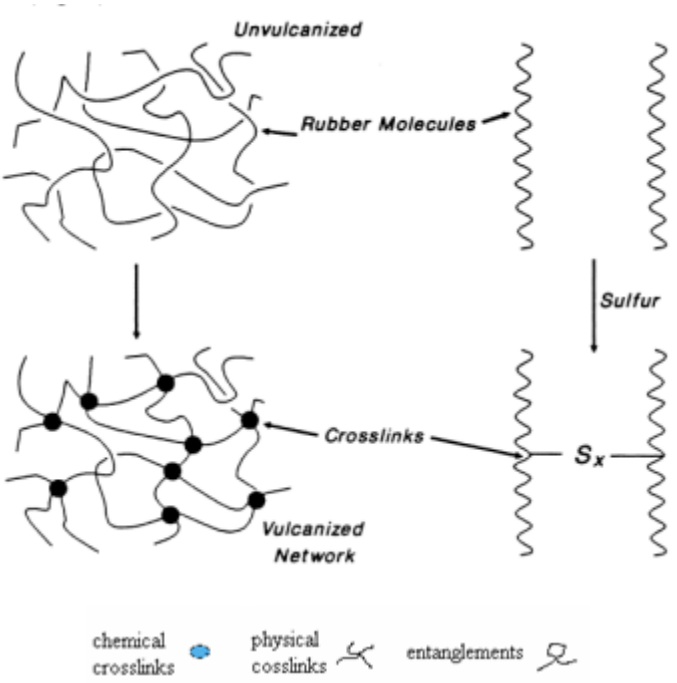


Figure 1: Three dimensional rubber matrix [1].

Different types of chemical-based crosslinking agents, such as peroxides, sulfur, metal oxides, and resins, are involved in the process of rubber macromolecules crosslinking formation. These agents are able to react with suitable functional rubber groups and to create cross-links between them. Typical composition of car and lorry tires are shown in Table 1 below. Out of all these agents, sulfur remains the most successful and economical cross linking agent even today. This is due to the fact that sulfur is low in toxicity and cost, compatible with other additives, and able to predictably provide the desired vulcanisation properties. The typical vulcanisation

system consists mainly of sulfur, metal oxide (usually zinc oxide), a fatty acid (to make the metal oxide soluble), and one or more organic accelerators, where the chemical reaction between sulfur and the rubber hydrocarbon occurs mainly at the C = C (double bonds) [3]. Vulcanization is generally considered irreversible. In other words, after it has been altered, the once long, complex, and twisted rubber molecule cannot return to its original form [3].

Table 1: Composition of a tire [4].

Ingredient	Passenger Car Tire	Lorry Tire
Rubber/Elastromers	41 – 48%	41 – 45%
Carbon black	22 – 28%	20 – 28%
Metal	13 – 16%	20 – 27%
Textile	4 – 6%	0 – 10%
Zinc Oxide	1%	2%
Sulphur	1%	1%
Additives	10 – 12%	7 – 10%

Tires produced by vulcanization are non-degradable material, which means that they could potentially stick around indefinitely. It is estimated that over 250 million tires are discarded annually. The amount of discarded waste tire rubber around the world is increasing at an alarming rate and only a small part of these wastes is recycled. The remaining are either buried, landfilled or stockpiled [4]. The disposal area of the tires contributes to the reduction of biodiversity since tires release toxic components to the environment. Tires are also very susceptible to be burned when subjected to high temperature. Once they are ignited, they will release toxic fumes and produce oil that will eventually contaminate soil and water [5]. Waste tires could also pose a threat to the humans by becoming a home ground for rodents and mosquitos that are responsible for carrying many types of disease [6]. Hence, the recycling of rubber wastes is vital in order to maintain a safe and healthy environment.

Although the rubber industry has a long time experience dealing with rubber, the perfect solution for disposal and recycling method for rubber products is yet to be found. Devulcanization is a technique where the crosslink structure, specifically the S-S and/or C-S bonds are cleaved. This can be done by various methods such as mechano-chemical, chemical, biological, and using ultrasonic energy, which are available and practiced today [7]. Common current scission processes of S-S and S-C bonds are demonstrated in Figure 2.

However, the optimum efficiency of devulcanization is yet to be discovered as the current existing processes produce uncontrolled polymer rubber chain degradation, where the breakage of main macromolecule (C-C bonds) could occur. In actuality, the breakage of C-C bonds is called a reclamation process. So in light of this, the current physical or chemical processes of converting used rubber into reusable form should be called reclamation rather than devulcanisation. Currently, when used rubber is recycled through any one of the existing processes, the main polymer chain (C-C bonds) is broken, leading to poor mechanical properties due to structural changes, where the rubber cannot be reused or re-vulcanized [8]. A proper devulcanisation process should only involve the cleavage of the S-S and/or C-S bonds, which basically means the reverse process of vulcanization, where the devulcanizates resemble the original material in quality and structure (high quality rubber).

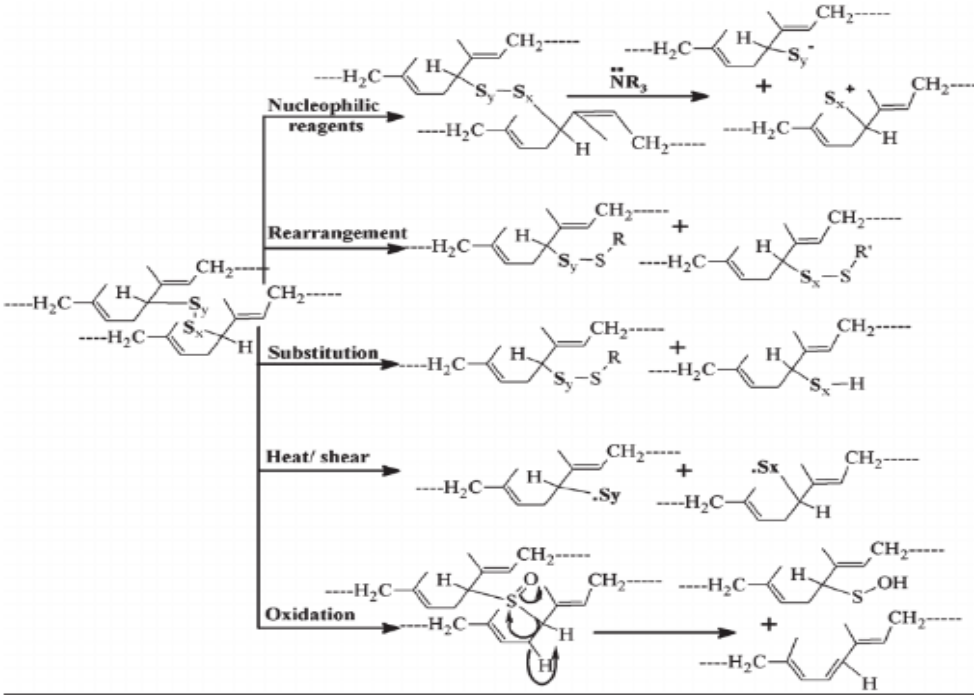


Figure 2: General principles of current devulcanization processes [9].

Today, finding and developing a more selective breakdown process in recycling used rubber is a global challenge. Some of the latest works where the introduction of amine usage as an alternative to devulcanise rubber have been initiated. Several types of amine function as degradation stabilizers for coatings and plastics. Most degradation processes such as devulcanization at high temperature, would have a free radical character, where amine could facilitate in the process reaction by serving as radical scavengers [10]. Works performed by Verbruggen et al. [10], show that amines (eg. Primary, secondary, and tertiary) could be an effective devulcanization agent. This may be due to the ability of amines to reduce the crosslink density mainly by selective reaction with sulfur bridges known as nucleophilic reaction. Figure below demonstrates the reaction of amine with rubber crosslinks.

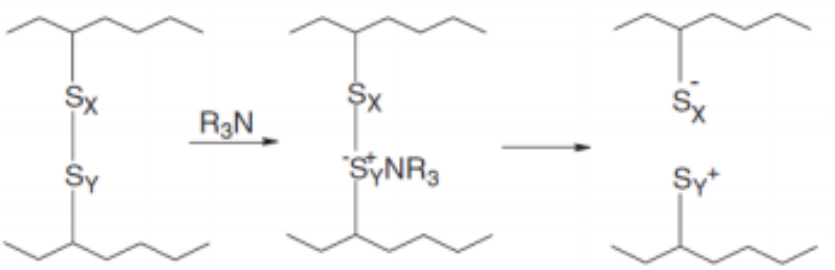


Figure 3: Amine reaction with sulphur crosslinks [11].

As such, in this research, the devulcanisation of waste tire rubber in the presence of amine to produce high quality recycled rubber is studied. Different conditions will be performed to aid the devulcanisation process, which includes varying temperature and also by sonication radiation as these two are the most effective commercial techniques. The objectives of this research are as follows:

1. To compare the effect of different types of amines on the degree of rubber devulcanization.
2. To assess the effect of amine concentration on the degree of rubber devulcanization.

2. Methodology

Quantitative research approach was applied where analysis was done based on experimental data that was collected along the way. This involved the process of analyzing the degree of devulcanization where the amount of sulfur removed was studied based on the experimental and numerical results.

2.1 Amine Preparation

Two types of amines, which are primary [(3-AminoPropylTrimethoxysilane), $C_6H_{17}NO_3Si$] and tertiary [(n-Diethyl-3-AminoPropyl) Trimethoxysilane), $C_{10}H_25NO_3Si$] amines, were bought from Nano Life Quest Sdn. Bhd. and used as the de-vulcanizing agent for ground waste tire rubber. To compare the effect of concentrations, the primary amine was prepared at three different concentrations while the tertiary amine was prepared at two different concentrations based on molarity, where at each concentration of amine, the sample was mixed with 50 ml of water as base. Every amine sample was then added to 20 g of ground waste tire rubber. In this study, the different in concentrations were referred to as different in R:A ratio. Based on preliminary study, the ratios of the amount of rubber to amine are as follows:

Table 2: Rubber (R) to Amine (A) ratio for Primary Amine.

R:A ratio	Amount of Rubber	Amine Volume
1:0.5	20 g	10 ml
1:0.25	20 g	5 ml
1:0.125	20 g	2.5 ml

Table 3: Rubber (R) to Amine (A) ratio for Tertiary Amine.

R:A ratio	Amount of Rubber	Amine Volume
1:0.25	20 g	5 ml
1:0.125	20 g	2.5 ml

On top of that, two types of control samples were also prepared as to compare the results after the devulcanization process. One solely contains rubber and the other contains a mixture of rubber and 50 ml of water, as to investigate if water would play a part in the devulcanization process.

2.2 Devulcanization Process and Rubber Sample Preparation

After the preparations of amine and rubber samples were done, the next step was to perform the devulcanization process. In this stage, every sample prepared in Schott bottle was allowed to experience and undergo the ultrasonication process. In this study, three variables were fixed; they were the sonication time and sonication frequency. In addition to that, another two variables were varied; they were the sonication temperature, and the rubber to amine ration, as shown in Table 6 and 7 for primary and tertiary amine, respectively.

One reason of why amine was chosen was because of the fact that amine is known to be an agent, suitable for desulphurization processes [12], and assumed to possess the same ability for the process of devulcanization. According to, an acceptable heating treatment for rubber, for it to not have any effects on the main polymer chain (carbon-carbon bonds), is within the range of 130 to 180°C. The heating treatment in this devulcanization process was paired together with the sonication. Since amines were involved during the process of devulcanization, the temperature chosen must be at or lower than 80°C as the boiling point of the primary amine used, is at 80°C. On top of that, since the ultrasonic water bath was used, temperatures lower than 100°C were decided on.

The temperatures chosen to be the heating environment during the sonication were 30, 50 and 80°C, while the sonication frequency of 37 Hz was also chosen as the Ultrasonic water bath equipment was only limited to this frequency. In addition to that, 37 Hz was also selected as the sonication frequency was because of the fact that it is the optimum condition with minimum degradation of rubber properties, according to Suganti R. et al. [13]. Due to safety purposes, the experiment was conducted at a pressure of 1 atm.

Varying temperatures and applying a frequency of 37 Hz were expected to agitate the rubber crosslink structure and weaken the Sulphur bonds, in order to allow the amine to penetrate through the crosslink structure. Since there were three different set temperatures, each rubber to amine ratio would then have three replications so that one rubber to amine ratio sample would experience different temperature than the other samples in the same ratio. The number of samples are summarized in Tables 8, 9 and 10.

Table 8: Rubber control samples.

Sonication Temperature (°C)	**Amount of Rubber (grams)**	**Amount of Water (mL)**	**Sample Number**
30	20	-	1
50			2
80			3
30		50	4
50			5
80			6

Table 9: Primary Amine Samples.

R:A ratio	Sonication Temperature (°C)	Amount of Rubber (grams)	Amine Volume (mL)	Sample Number
1:0.5	30	20	10	7
	50			8
	80			9
1:0.25	30		5	10
	50			11
	80			12
1:0.125	30		2.5	13
	50			14
	80			15

Table 10: Tertiary Amine Samples.

R:A ratio	Sonication Temperature (°C)	Amount of Rubber (grams)	Amine Volume (mL)	Sample Number
1:0.25	30	20	5	16
	50			17
	80			18
1:0.125	30		2.5	19
	50			20
	80			21

As shown in the tables above, there are a total of 21 samples including the control samples. Each devulcanization process (application of 37Hz sonication frequency in the respective temperature) took place for 15 minutes. Afterwards, the rubber from every sample was then filtered out by using the gravity filtration method [14]. Then, every sample was washed thoroughly by using distilled water at least three times to ensure no presence of amine in the rubber samples. Lastly, the washed rubber was then dried in the oven at 70°C for a period of 24 hours, to ensure minimum to none moisture content present in rubber samples, before characterization can take place.

2.3 Rubber Characterization

Characterization of the rubber test samples was the next stage of this research. There were three different techniques in dealing with the determination of the amount of Sulphur removed in the rubber samples, they are: gel content test, thermogravimetric analysis (TGA), and Fourier Transform Infrared Spectroscopy (FTIR)

2.3.1 Gel Content Test

The gel content test samples were determined according to ASTM D2765. 0.2±0.05g of every rubber sample was measured and placed in a stainless steel wire mesh pouch of 120 mesh size. Three pouches were ready from each sample in order to

attain an average result. In order to dissolve the soluble content, the samples placed in wire mesh were extracted in boiling toluene by using a Soxhlet apparatus for 24 hours. Then, test samples were collected and dried in an oven for 24 hourse at 70°C until a constant mass is achieved. The gel content was then calculated by using the following Eq. (1) [13].

$$\text{Gel content (\%)} = \frac{w_1}{w_0}\ x\ 100 \quad (1)$$

Where w_0 is the weight of dried sample before extraction and w_1 is the weight of dried sample after extraction. The soluble content was calculated by using the following Eq. (2):

$$\text{Soluble \%} = 100 - \text{Gel content (\%)} \quad (2)$$

2.3.2 Thermogravimetric Analysis (TGA)

TGA was responsible for the determination of the test samples' thermal degradation and stability. This was done by utilizing a computerised thermo gravimetric analyser (Perkin Elmer – TGA 8000). To assess the thermal stability, dynamic TGA experiments was carried out. Rubber sample, weighted around 5 to 10 mg was placed on a sample pan before placing it in the instrument. The experiment was conducted by heating the samples from room temperature up to a temperature of 600°C to collect the weight loss vs temperature thermogram. Every analysis was done with test samples in Nitrogen atmosphere (with flow rate of 20 ml/min) with a rate of heating of 10°C/min. Before analysis can be done, a least-squares averaging technique was used to smoothen out the curve of normalised weight loss vs temperature. T_{max} was denoted as the temperature at the maximum rate of weight loss. T_{max} will be identified from the peak of the derivative (dW/dT) curve, where W is weight loss and T is temperature. With all these temperatures, they then was referred to and used to determine the thermal degradation and stability of the test samples [15], [16].

2.3.3 Fourier Transform Infrared Spectroscopy

This method allows the evaluation of any structural change on the rubber based on which bonds are broken after the devulcanization process. Data analysis can be done based on the graphs generated by FTIR (Perkin Elmer FTIR Spectrum 100). ATR method was used for this FTIR analysis. As aforementioned, waste tire rubber with and without the help of amine as the devulanizing agent during devulcanization were examined in order to detect the degree of devulcanization.

This test analysis involved the testing of control samples and rubber samples with amine, in order to observe and detect if amine would actually impose any additional impacts in cleaving the sulphur bonds, reducing the crosslink structure of rubber during the devulcanization process. In addition to that, studies on which other bonds or compounds were removed during the devulcanization and comparisons between different samples can be made, which can be done by identifying the spectra produced.

3. Results and Discussion

As per discussed previously, the first preliminary stage of screening the rubber samples involved two tests which are: gel content test and thermogravimetric analysis (TGA).

3.1 Gel Content Test Analysis

Figure 4 shows the average gel content value for every sample at three different sonication temperatures. The results obtained portray an irregular pattern as it does not have a proper trend. At 30°C sonication temperature, all of seven samples fall within the range of 75 to 88% of gel content.

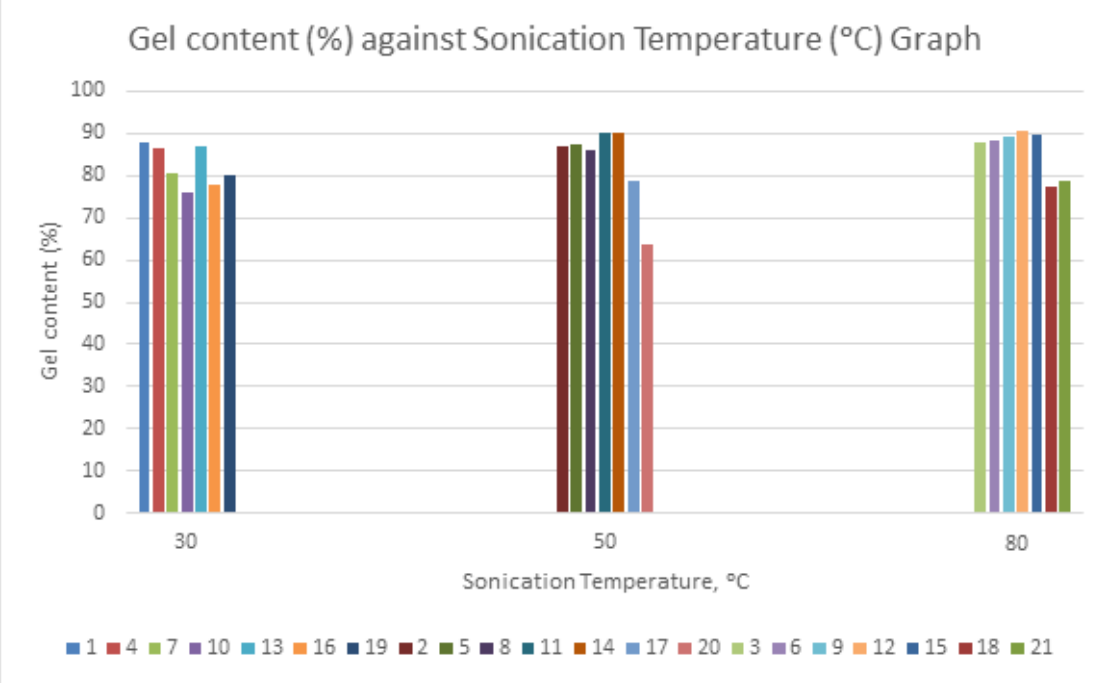


Figure 4**:** Gel content of rubber samples at different sonication temperature.

It is common for rubber to show gel content between 50% and 90% due to the presence of crosslinked structure of molecules. This can be seen from the control samples 1 – 6. The sonication temperature has a little effect on the gel content of rubber as all control samples project gel content % that is almost similar in value. However, at 30°C, as 10 ml of primary amine was added into sample 7, the gel content decreased in value from 87 to 80%, which shows that amine had an effect in aiding the breakdown of the rubber structure. As the amine volume was decreased to 5 ml in sample 10, the gel content however decreased even more up to 75%. However, when the amine concentration was further decreased to 2.5 ml in sample 13, the gel content shows a value of that near the control sample.

A feasible explanation to this results is that, as the amount of amine concentration decreases, it could become more reactive relative to the amount of rubber in one sample. When the concentration was further decreased, the sulphur bonds could have been reformed leading to the higher gel content. The results also show that as the temperature of sonication was increased, it did not have much effect of the degree of crosslinked structure cleavage. This can be seen for instance, from samples 7, 8 and 9.

The gel content tend to increase rather than decrease with an increase in temperature. One explanation to this occurrence is that, the primary amine's boiling temperature used in this experiment, is at 80°C. Increasing the sonication temperature higher near to its boiling point, may have agitated the amine too much, leading it to evaporate, and leaving no chemicals left to aid in the process of cleaving sulphur bonds through nucleophilic reaction. This may have been a factor influencing the efficiency of the devulcanization, as the temperature was increased. This can be seen from the increasing pattern of gel content in every rubber to amine ratio samples, as the temperature was increased. In addition to that, according to [4], the acceptable temperature where the crosslinked structure would be reduced effectively is within the range of 130 to 180°C. This shows that the involved heating treatment in the ultrasonicator was not sufficient to break down the rubber structure.

Similarly, tertiary amine results also portray an irregular pattern. However, the gel content analysis shows that the gel content of rubber which was treated by tertiary amine was lesser than those treated by primary amine. The gel content was managed to be reduced and has an average range of 77 to 63%. The most effective treatment was observed from sample 20, in which the rubber was treated by 2.5 ml of tertiary amine and heated at 50°C during the sonication process.

Based on Figure 4, Samples 16, 17 and 18 display an almost the same amount of gel content, even all these three samples were under different temperatures using the heating and sonication treatments. This results may have been due to the uneven distribution of amine in all samples or unequal distribution of rubber particle during the process of devulcanization. On top of that, it may have also have been because of the discrepancies in the mixture of rubber sample composition. On the other hand, the results show that the gel content decreased in value to 63% as the temperature was increased to 50°C, and increased back to around 78% as the temperature increased to 80°C. This result shows that the efficiency of tertiary amine in helping breaking down the crosslink structure of rubber increased to a certain temperature, in this case was 50°C, and would decrease when the temperature was further increased to 80°C. The increase of gel content from sample 20 to 21, must have been due to the reformation of sulphur bonds with the main backbone chain, as the amine failed to capture the free radicals during the devulcanization process.

The results from this gel content experiment show that tertiary amine was more effective and reactive towards breaking down the rubber structure than the primary amine. This is contrary to the initial expectation as primary amine is usually more reactive than tertiary amine.

3.2 Thermal Analysis

High temperature TGA (30 - 600°C) plots of samples 1, 4, 7, 10, 13 and 19 are shown in Figure 5. Based on Figure 12, all TGA plots show a one-step degradation. Different degradation temperatures calculated from Figure 5 can be seen in Table 7.

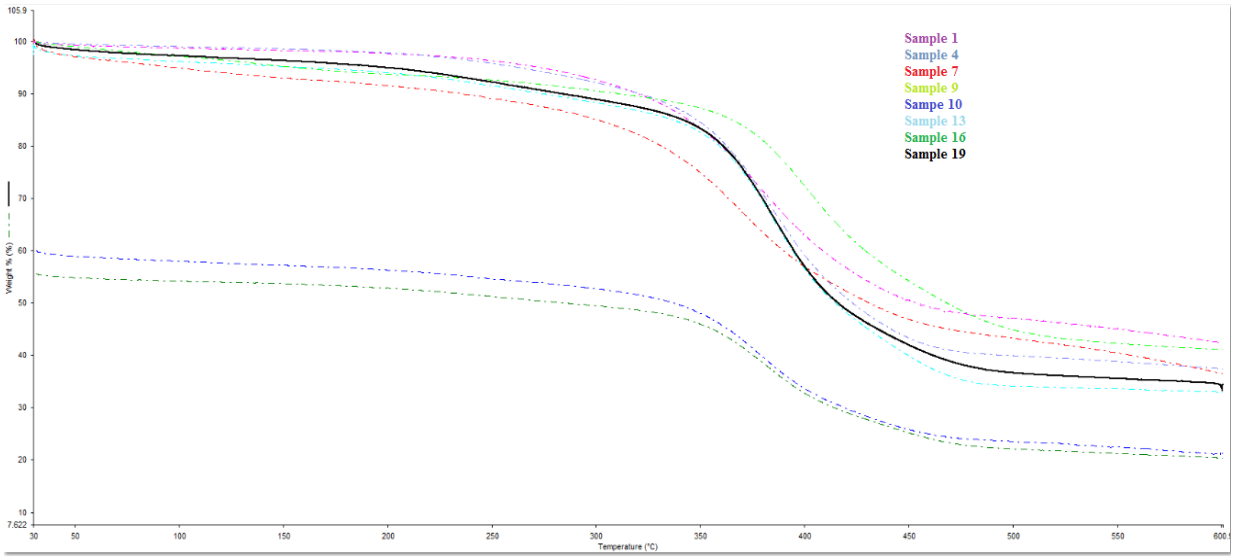


Figure 5: TGA plots of Samples 1, 4, 7, 9, 10, 13, 16, and 19.

Table 7: TGA parameters

Sample Number	T_1 (°C)	T_{40} (°C)	T_{80} (°C)
1	333.96	408.18	496.09
4	349.58	398.62	494.26
7	325.59	389.73	439.50
8	363.25	387.87	440.13
9	371.12	401.72	468.13
13	357.71	393.85	448.97
19	349.58	394.96	460.54

Based on Table 7, the onset degradation (T_1) of the control sample 4 started at 349.58°C. Forty percent degradation (T_{40}) and 80% degradation of the same control sample started at 398.62 and 494.26°C respectively. For the sample which was treated with primary amine, sample number 7, the onset degradation (T_1) occurred at lower temperature (325.59°C). The T_{40} and T_{80} of sample 7 occurred at 389.73 and 439.50°C respectively. For the sample which was treated with a lower primary amine concentration, sample number 13, the onset degradation (T_1) occurred at higher temperature (357.71°C). The T_{40} and T_{80} of sample 13 occurred at 393.85 and 448.97°C respectively. For the sample which was treated with tertiary amine, sample number 19, the onset degradation (T_1) occurred at a slightly lower temperature (349.58°C). The T_{40} and T_{80} of sample 7 occurred at 394.96 and 460.54°C respectively.

The delayed degradation of control sample 4 compared to sample 7 suggested that the treated sample 7 with the devulcanizing agent had a cross-linking structure breakdown due to the presence of amine. The control sample 4 was more stable towards thermal degradation because of the extra-cross-linking due to the absence of a devulcanizing agent during the devulcanization process. Cross-linking increased the rigidity of the system, which in turn increased the thermal stability. When the primary amine had a lower concentration as in sample 13, the rubber took longer to degrade, in comparison to sample 7. As discussed in the previous analysis section, this may due to the reformation of Sulphur bonds, which lead to a stronger crosslinked structure.

Based on Table 7, Sample 8, which was treated with primary amine at a sonication temperature of 50°C had an onset degradation (T_1) which occurred at temperature (363.25°C). The T_{40} and T_{80} of sample 8 occurred at 387.87 and 440.13°C respectively. For the sample which was also treated with primary amine, but at a higher sonication temperature of 80°C, sample number 9, the onset degradation (T_1) occurred at higher temperature (371.12°C). The T_{40} and T_{80} of sample 9 occurred at 401.72 and 468.13°C respectively. This is an indication of a more rigid structure of sample 9 compared to 8, and sample 8 compared to sample 7. As previously discussed, the gel content of sample 9 is the highest due to the amine evaporated from the rubber samples. Hence, it took sample 9 the longest for it to be degraded.

On top of that, sample 19 was treated with the same amine volume as sample 13, and it showed a lower degradation temperature than sample 13. This data also tallied with the gel content analysis, portraying that the tertiary amine had helped more in the reduction of rubber crosslinked structure than the primary amine.

3.3 Fourier Transform Infrared Spectroscopy (FTIR) Analysis

Based on Figure 6 above, it can be observed that the peaks for sulphur-sulphur bonds (in the range of 700-550 cm-1 and carbon-sulphur bonds (in the range of 720-570 cm-1) still exist based on the peaks generated from the plot. This means that during the devulcanization process, the sonication energy at a frequency of 37 Hz and at three different temperatures did not possess enough energy to cleave the sulphur bonds. It also means that water did not perform any additional effects on the rubber structure during the devulcanization process. Though there is some variation in graph patterns for devulcanization at different temperature environment, lines A and B marked on the graph still indicate that the sulphur bonds still exist in the rubber structure.

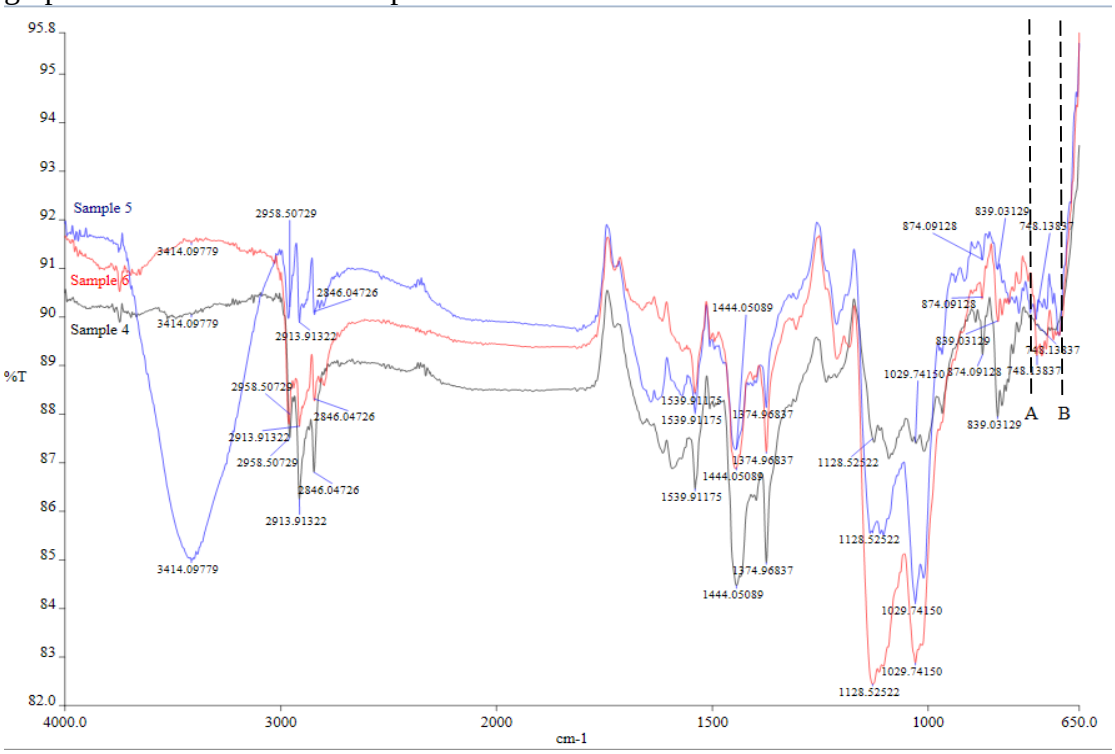


Figure 6: Plots of control samples 4, 5 and 6 (with 50 ml of water)

Based on Figure 7(a),(b),and, (d) lines A and B represent the regions for carbon-sulphur bonds and sulphur-sulphur bonds respectively. As seen from the plots, it can be seen that sulphur bonds are still present even with after going through devulcanization with the presence of primary amine. From Figure 7(a), where the amine concentration is the largest, at rubber to amine ratio of 1:0.5, there seems to be an increasing pattern in sulphur-suphur bonds. That is, the peaks seem to be appearing as the sonication temperature was increased, from Samples 7 to 9. This is an indication that the at higher the sonication temperature, the less effective the amine is to cleave the sulphur bonds. This may due to the fact that as the temperature increases to 80^{o}C the amine must have evaporated slowly out of the rubber mixture, as the boiling temperature of the primary amine used is 80^{o}C. Similarly, for the other two rubber to amine ratio, as the data presented in Figures 7(b) and (d), the sulphur-sulphur bonds tend to be more in terms of amount, as the sonication temperature increased. This pattern can be seen from Samples 10 to 12 in Figure 7(b), for rubber to amine ratio of 1:0.25, and Samples 13 to 15 in Figure 7(d), for amine ratio of 1.0.125. The explanation to this is may also be to the fact that as the temperature increases, it gets near to the primary amine's boiling temperature. Hence, the amount of amine to allow more cleavage of sulphur bonds would be less, and devulcanization becomes less effective. On top of that, there is no indication of carbon-sulphur bonds cleavage throughout the curves for the samples. This is an indication of the energy exerted on the rubber samples were not strong enough to break the carbon-sulphur bonds.

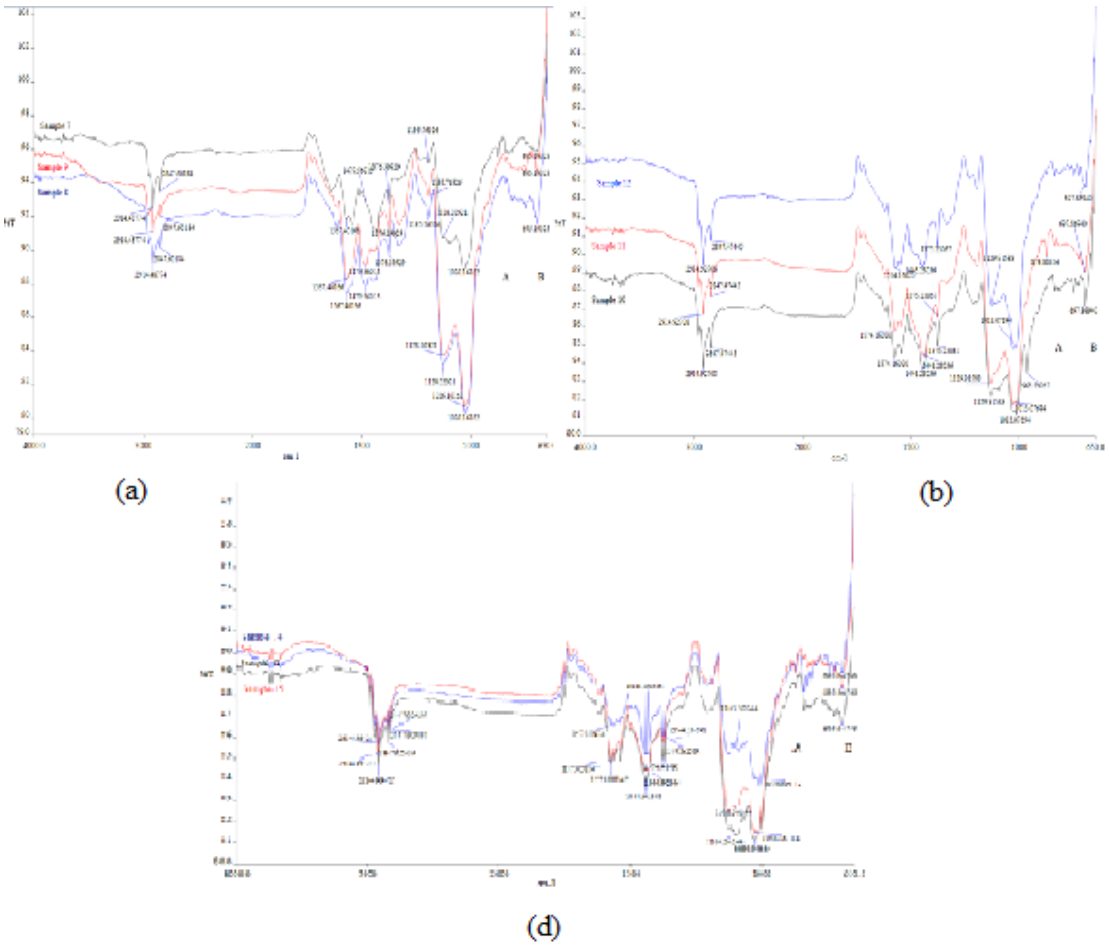
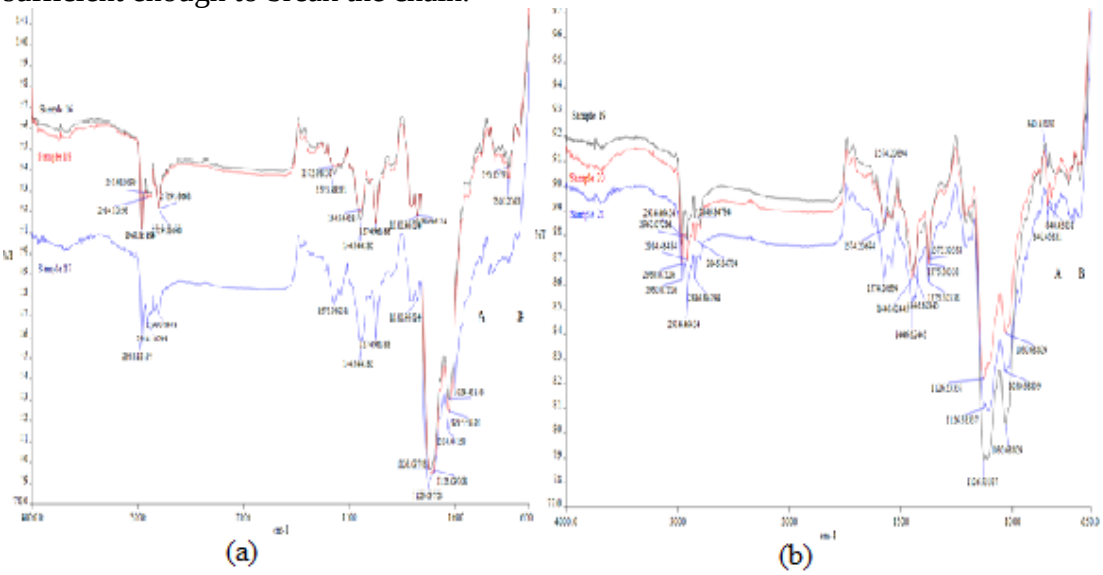


Figure 7: FTIR plots for primary amine, R:A of 1:0.5 (a), 1:0.25 (b), & 1:0.125 (d)

These results show that primary amine helps in breaking sulphur bonds to a certain degree, when compared to the results of primary amine to the control samples. The energy was sufficient enough to break sulphur-sulphur bonds, but not carbon-sulphur bonds as carbon-sulphur bonds would require higher energy to be broken. However, the findings also show that, the effectiveness of primary amine decreases as the temperature increases. This may due to the fact that, the primary amine may have escaped as the temperature gets higher, near to its boiling temperature, which leads to the lower efficiency of devulcanization

Based on Figure 8(a) and (b) the curves shown are the results generated for tertiary amine at rubber to amine ratio of 1:0.25 and 1:0.125 respectively. Samples 16, 17 and 18 curves marked at B, show an even distribution of plots, which may indicate that the amount of sulphur-sulphur bonds existing in these three samples may be almost the same. This explains as why these rubber samples possess almost the same amount of gel/soluble fraction, as previously recorded in the gel content test. Based on Sample 19 plot from the Figure 8(b), there seems to be some sulphur-sulphur bonds marked in the region B. But the peaks seem to be disappearing in Sample 20, which indicates the disappearing of sulphur-sulphur bonds in Sample 20. However, the peaks reappear in Sample 21, which indicates the reformation of sulphur bonds as the sonication temperature increases. The explanation to this phenomenon is that, as the temperature increases, the tertiary amine participated in the process of cleaving the sulphur-sulphur bonds even more as it gets more excited. However, after some time, the sulphur bonds tend to reappear which shows that to a certain degree, when the temperature increases,

the sulphur bonds tend to reform and adhere back to the rubber structure. These results may enhance the findings from the gel content test analysis where from Sample 19 to 20, the gel fraction tends to decrease. While it increases from Sample 20 to 21. Similarly, the carbon-sulphur bonds during this treatment were unaffected, which can be seen from the peaks in the graphs. Indicating that the energy applied onto the rubber was not sufficient enough to break the chain.



(a) (b)

Figure 8: FTIR plots for tertiary amine, R:A of 1:0.25 (a) and 1:0.125 (b)

Based on all the FTIR figures shown previously, the control samples are the only samples which generated some peaks beyond the range of 3000 and 1700 cm-1, which may indicate the presence of water remained in the samples. These peaks are not observed in all the other FTIR curves for any amine + rubber samples. This is an indication that there is a small degradation of bonds containing groups –OH and –C=O [17].

In conclusion, both types of amines could undergo nucleophilic reaction, due to the existence of free radicals during the process of devulcanization. Both types of amines were capable of only cleaving sulphur-sulphur bonds, where tertiary amine showed a more promising result than primary amine. The efficiency of primary amine was compromised, because of the high sonication temperature which was near to its boiling temperature. In addition to that, no other bonds were broken as there was not enough energy to break them. The main carbon backbone chain was not affected during the dvulcanization process, which is an indication of if, the devulcanized rubber were to be vulcanized, it could result in rubber with good physical property.

4. Conclusion

Based on the preliminary tests, the usage of amine as the devulcanizing agent, coupled with heating and sonication treatments has shown that there is a structural change in the rubber structure. However, the degree of structural breakdown is not substantial. One of the factors may be due to the fact that the devulcanizing environment, such as temperature, is not sufficient to encourage the scission of the Sulphur bonds in the rubber crosslinked structure. Amine is able to undergo the nucleophilic reaction, but

only to a certain extent. As oppose to the previous expected outcome, these two analysis tests have proven that tertiary amine is more efficient in breaking down rubber structure than the primary amine. This is proven by the gel content test which has shown a lower gel content (%) of (77 – 63 %), compared to primary amine samples (falls within the range of 80%), as well as the TGA test in which tertiary amine samples degrade faster than primary amine samples (suggesting a higher degree of rubber structure breakdown).

The effects of amine concentration were difficult to be studied as the results generated did not have a regular pattern, as the sonication temperature also played a role during the process of devulcanization within the 15 minutes timeframe. However, the results have portrayed that the higher the concentration of amine is, the higher the breakdown of structure takes place. However, for some types of amine such as tertiary, under a certain condition, the lower the concentration is, the higher the degree of devulcanization. This can be seen from sample 20, with rubber to amine ratio of 1:0.125, had a more structural breakdown than sample 17, whose rubber to amine ratio was 1:0.25. Hence, amine may have the capacity to cause crosslinked structure breakdown of rubber, but it still may not be efficient enough to be used on industrial levels

References

[1] J. A. Brydson et al., “Rubber Chemistry,” pp. 194–205, 1978.
[2] T. Liang et al., “Continuous Devulcanization of Ground Tire Rubber of Different Particle Sizes Using an Ultrasonic Twin-Screw Extruder,” pp 200-230, 2013.
[3] G. S. Whitby and H. E. Simmons, “Vulcanization Accelerators—I.,” *Ind. Eng. Chem.*, vol. 17, no. 9, pp. 931–935, 1925.
[4] S. Ramarad, M. Khalid, C. T. Ratnam, A. L. Chuah, and W. Rashmi, “Waste tire rubber in polymer blends: A review on the evolution, properties and future,” *Prog. Mater. Sci.*, vol. 72, no. March, pp. 100–140, 2015.
[5] F. P. Torgal, A. Shasavandi, and S. Jalali, “Tyre Rubber Wastes Based Concrete: A review,” *WASTES Solut. Treat. Oppor.*, p. 3, 2011.
[6] Rinkesh, “Tire Recycling,” *Conserv. Energy Futur.*, 2015.
[7] M. Hess, H. Geisler, and R. H. Schuster, “Devulcanization as an opportunity to recycle rubber,” *Chem. List.*, vol. 103, no. 13, 2009.
[8] S. Seghar *et al.*, “Devulcanization of styrene butadiene rubber by microwave energy: Effect of the presence of ionic liquid,” *Express Polym. Lett.*, vol. 9, no. 12, pp. 1076–1086, 2015.
[9] J. Anu Mary, G. Benny, K. N. Madhusoodanan, and A. Rosamma, “The current status of sulphur vulcanization and devulcanization chemistry: devulcanization,” *Rubber Sci.*, vol. 29, no. 1, pp. 62–100, 2016.
[10] P. Sutanto et al., “Development of a Continuous Process for EPDM Devulcanization in an Extruder,” p. 124, 2006.
[11] S. Saiwari et al., "Post-consumer tires back into new tires: de-vulcanization and re-utilization of passenger car tires". 2013.
[12] A. Bocoum, S. Hosseinnezhad, and E. Fini, “Investigating effect of amine based additives on asphalt rubber rheological properties,” *Asph. Pavements*, no. September, pp. 921–931, 2014.
[13] S. Ramarad, C. T. Ratnam, M. Khalid, A. L. Chuah, and S. Hanson, “Improved crystallinity and dynamic mechanical properties of reclaimed waste tire rubber/EVA blends under the influence of electron beam irradiation,” *Radiat. Phys. Chem.*, vol. 130, pp. 362–370, 2017.

[14] Univeristy of calgary, “Filtration Methods, Organic Laboratory Techniques,” pp. 1–5, 2012.
[15] W. J. Sichina, “Characterization of Polymers Using TGA,” pp. 1–5, 2000.
[16] ASTM International, “Standard Test Method for Compositional Analysis by Thermogravimetry,” vol. i, no. C, pp. 9–13, 2012.
[17] S. Rodsuk, S. Ritsuar, and K. Wattanakul, “Characterization the effect of disulfide compound on the devulcanization of thermoplastic vulcanizate,” *AIP Conf. Proc.*, vol. 1482, pp. 240–245, 2012.

eureca 2017 – Conference Paper
Paper Number 2CE08

Removal of Dye in Wastewater by Adsorption-Coagulation Combined System with *Hibiscus sabdariffa* as the Coagulant

Nicholas Ho Jian Hoong[1*], Nurhazwani Ismail[2]

[1,2]School of Engineering, Taylor's University, Malaysia

[*]nicholas0270@gmail.com

Abstract

The conventional process to treat dye wastewater is the physicochemical treatment such as coagulation, flocculation and adsorption process. A new approach has been demonstrated to treat Congo red dye wastewater, which is the adsorption-coagulation hybrid process. Natural coagulant extracted from *Hibiscus sabdariffa* seeds is used as the coagulant while activated carbon is used as the adsorbent in this case study. The objective of this experiment is to study the significant factors that will affect the efficiency of dye removal. Then, the optimum conditions for the hybrid process is determined using Respond Surface Methodology (RSM). The variables are pH, initial dye concentration, coagulant dosage and adsorbent dosage while the response of experiment is the dye removal percentage. A three-level and four-variable Box-Behnken design (BBD) is used for the RSM. A total of 27 sets of experimental results is required to determine the optimum conditions. Jar test is used to conduct the experiment with the addition of coagulant and adsorbent simultaneously. Based on the aggression model analysis and ANOVA, the highly significant factors that contribute to the dye removal efficiency through adsorption-coagulation hybrid process are pH of solution and initial dye concentration. The RSM results shows that the optimised process parameters for adsorption-coagulation hybrid process with *Hibiscus sabdariffa* seeds as the coagulant and activated carbon as the adsorbent are pH 2, initial dye concentration of 385 ppm, coagulant dosage of 209 mg/L and adsorbent dosage of 150 mg/L. The dye removal reaches up to 96.67% under optimum parameters

Keywords: Dye wastewater, *Hibiscus sabdariffa*, natural coagulant, Hybrid process, Optimisation.

1. Introduction

Synthetic dyes are commonly used in many industries, such as textile, paper, plastic, ink cartridge and paint manufacture factories. During the washing and finishing stage in the manufacture process, they consume and discharge a huge amount of dye contaminated water. Based on research studies, it is estimated that 280,000 tons of textile dyes are discharged annually in the textile industry as effluent worldwide, ranking the first place in the usage of dyes among various industries [1]. Direct discharge of dye wastewater into the environment can be hazardous since synthetic dyes contain carcinogenic substances and heavy metals such as chromium (Cr), lead (Pb) and copper (Cu) [2].

Most dyes are synthetic compounds with complex, highly-branched aromatic molecular structures [3]. Thus, dye wastewater is very resistant to biodegradation treatment process. The most conventional way of treating it is the physicochemical treatment. This method involves the coagulation and flocculation process which use up various coagulants such as alum, lime and ferric [4]. Chemical coagulants are capable of dissociating polyelectrolytes when in solution. The polyelectrolytes will neutralise the negatively charged dye molecules to form particle-polymer-particle complexes [4]. These contaminants will be precipitated in the form of chemical sludge when the treated water is further added with flocculants. However, the generated sludge contains a considerable amount of chemical residue such as iron and aluminium salts. These components are hazardous to human health and possess environmental impact. According to [5], aluminium-based coagulants attribute the development of Alzheimer's disease in human beings. Thus, there is an emerging trend in wastewater treatment industry using natural coagulants such as *Moringa oleifera*, *Strychnos potatorum* (Nirmali), *Cactus opuntia* etc [6]. Natural coagulants possess a few crucial advantages compared to chemical coagulants, such as environmentally friendly (sustainable and biodegradable), toxic-free and safer for application.

The usage of *Hibiscus sabdariffa* seeds as natural coagulants was first reported to clarify high turbidity water (above 300 NTU) in the Indian Journal of Environmental Health, 1974. The chemical polyelectrolyte is substituted by natural polyelectrolyte in the form of polysaccharide and proteins [7]. According to [8] and [6], these structures usually exhibit higher molecular weight compared to synthetic polymer. This greatly increase the unoccupied binding sites for the coagulation and partial adsorption process. *Hibiscus sabdariffa* seeds also contain coagulation proteins, mainly composed of cationic peptides, such as glutamic acid, aspartic acid and leucine [9]. Based on previous experiment case studies, the removal of dye using *H. Sabdariffa* as coagulant typically ranges from 81.2-93.3% [10][6].

Adsorption process is also one of the most effective and low-cost treatment process to remove dyes in wastewater. The most conventional adsorbent used in industries is activated carbon. The efficiency of adsorption using activated carbon is relatively high due to its microporous structure, large surface area and high adsorption capacity [11]. In fact, it shows a stronger affinity for dyes removal compared to zeolite [11]. In this view, activated carbon can be potentially used as the adsorbent in this case study.

Till date, the combination compromising of more than one wastewater treatment process as a single system has shown to be more effective when treating wastewater [12]. Based on previous studies, adsorption-coagulation hybrid process has been used to treat real wastewater of complex dyes manufacturing plant and wastewater containing high concentration of humic and tannic acids [12][13]. Results show that hybrid process is proved to have 90% efficient in colloidal particles removal than coagulation as an individual process [13]. In this method, the coagulant and adsorbent are added simultaneously at one single unit for reaction. The hybrid process enhances and improves the performance of dye removal because the dye molecules are eliminated from the water, and not because of the partial decomposition of dye molecules, which can potentially lead to the formation of more harmful and toxic aromatic compounds [4]. Meanwhile, the activated carbon will adsorb the colour and odour in the solution and the forming sludge.

Thus, with respect to the study that has been done extensively, the hybrid process is used to treat Congo red dye solution with *Hibiscus sabdariffa* seeds as coagulant and activated carbon as adsorbent. Congo red is targeted in this study based on a few reasons. The molecular structure is also shown in Figure 1.

(i) Congo red is a typical benzidine-based azo dye. It is widely found in the effluent of industries. After releasing it to the environment, Congo red is metabolised to benzidine, a well-known carcinogen that can cause allergic diseases in human. Thus, an effective and feasible method is needed to treat the Congo red in the effluent [3].

(ii) The potentiality of adsorption-coagulation hybrid process of Congo red removal has not yet been studied. With this in view, in this present study, an attempt has been made to identify the coagulation potential of coagulation agent extracted from *Hibiscus sabdariffa* seeds with activated carbon, for the removal of Congo red dye from aqueous solution.

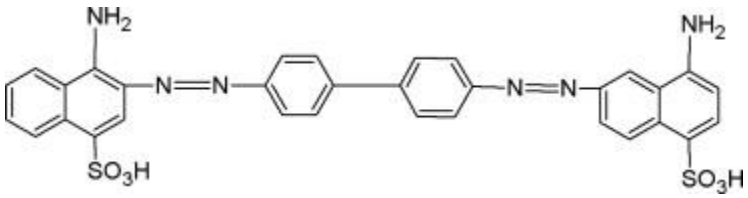


Figure 1. Molecular structure of Congo red dye [14]

The objectives of conducting this research are to study the significant factors that will affect the performance of adsorption-coagulation hybrid process with *Hibiscus sabdariffa* seeds as coagulant and activated carbon as adsorbent on Congo red dye removal. Besides that, the optimum process parameters (pH, initial dye concentration, coagulant dosage and adsorbent dosage will be determined using Respond Surface Methodology (RSM).

2.0 Methodology

In this research studies, quantitative method will be implemented extensively to collect objective measurements, then numerical, mathematical and statistical analysis of data will be conducted to verify and validate the results. Lastly, the results will be

used for RSM to determine the optimised working parameters for the adsorption-coagulation hybrid process.

2.1 Preparation of Synthetic Dye Wastewater

The stock solution is prepared by dissolving 1 gram of Congo red dye powder in 1 L of distilled water. Theoretically, the concentration of stock solution will be 1000ppm [14]. The stock solution is then diluted using distilled water to prepare the required concentration. The pH of dye solution is adjusted by adding 1.0 M NaOH solution and 1.0 M HCl solution. Noted that the color of Congo red changes from red to blue when inorganic acid is added into the solution. This is due to the resonance between charged canonical structures [15]. The pH value is monitored using a pH meter. Table 1 simply summarise the physicochemical properties of Congo red dye.

Table 1. Physicochemical properties of Congo red

Parameter	Value (unit)
Molecular Weight	696.66 g/mol
Molecular Formula	$C_3H_{22}N_6Na_2O_6S_2$
Absorption Maxima	498nm

2.2 Preparation of Natural Coagulants

2.2.1 Pre-treatment of Hibiscus sabdariffa Seeds

Hibiscus sabdariffa flowers are collected and the seeds are removed manually from their dried capsules. The seeds are quickly washed with distilled water to remove any fibrous traces and tower dried. The clean seeds are then dried in an oven at 60^{o}C for 2 hours to preserve the protein in the seed. Drying temperature higher than 60^{o}C will cause denature of the proteins [16].



Figure 2. Dried H. sabdariffa seeds

2.2.2 Extraction of Coagulating Agent

In this present work, sodium chloride solution is selected to be the extraction agent. since it can be obtained easily. During the extraction, the interaction between the peptides and the molecules of sodium chloride produces H-bonds with the adjacent molecules. The peptides will dissolve in the solution when the protein surface turns fully hydrophilic [17].

The concentration of sodium chloride solution was investigated. When the concentration of NaCl solution increases above 0.5 M, the binding sites of solvents are saturated and all protein fractions are extracted [18]. Research studies also show that there will be no significant changes of the extracted proteins when the concentration of NaCl solution increases from 0.6 M to 1.0 M, [18]. Thus, 0.5 M of NaCl solution is used as the solvent.

The seed is measured 0.5 gram and mixed with 100 mL of 0.5 M NaCl solution. The mixture is then blended in a household food blender for 2 minutes [10]. The mixture is sieved through a muslin cloth to remove any traces of seed residues. The filtrate is the extracted coagulating agent and it is milky in colour. The coagulating agent is used immediately after extraction to avoid deterioration.

2.3 Preparation of Calibration Graph

The stock solution is used to prepare various dye concentration solutions, which are 200, 400, 600, 800 and 1000 ppm. The samples are transferred into the cuvettes and placed into the UV Spectrophotometer for the measurement of absorbance value. After taking the measurements, a calibration graph of absorbance value against dye concentration (ppm) is plotted. The calibration graph is used to determine the dye removal percentage of each treated samples. The dye removal percentage can be determined using Eq (1) as shown below [10].

$$Dye\ Removal\ (\%) = \frac{Abs_o - Abs}{Abs_o} \times 100\% \quad (1)$$

Where Abs_o and Abs are the absorbance value before and after treatment process respectively.

2.4 Design of Experiment

2.4.1 Jar Test

Jar test apparatus is used to conduct the experiment in a few batches. The apparatus can accommodate a maximum of 6 beakers in a batch. Each batch will involve rapid mixing, slow mixing and sedimentation process. The dye solutions are stirred for 4 minutes at 100 rpm to allow floc formation. Then, the speed of mixer is reduced to 40 rpm and agitating process is continued for 25 minutes for flocculation process. At the final stage, the precipitate is allowed to settle at the bottom of jar for 30 minutes [10].

2.4.2 Factors

There are four factors being manipulated in this experiment, which are pH of dye solution, initial dye concentration, coagulant dosage and adsorbent dosage. The range and level of each factor is summarised in Table 2.

Table 2. Range and level of each factor

Variable	Description	Code	Range and Levels		
			Low (-1)	Central (0)	High (1)
1	pH	A	2	7	12
2	Initial Dye Concentration (ppm)	B	200	400	600
3	Coagulant Dosage (mg/L)	C	120	260	400
4	Adsorbent Dosage (mg/L)	D	50	100	150

2.4.3 Response of Experiment

The dye removal percentage is the response of the experiment. After the dye solution is being treated, the supernatant liquid is obtained without disturbing the precipitated flocs and transferred into a cuvette. It is then placed into UV spectrophotometer for the measurement of absorbance value. The dye removal percentage is then calculated using Eq (1).

2.4.4 Optimisation of Process Parameters using RSM

RSM is a mathematical statistics technique method to build models, evaluate the complex relationships between independent factors and experiment response and to determine the optimum working conditions [19]. In this experiment, a three-level and four-variable Box-Behnken design (BBD) is demonstrated. In order to further analyses the optimum combination of working parameters, a 27-runs of experiment is conducted. The experimental results for the 27 sets of experiment are the input for aggression model analysis, ANOVA and RSM for optimisation purpose. The results and justifications are discussed at the part below.

3. Results and Discussion

3.1 Model Fitting

There are four variables tested in this experiment, which are pH of dye solution, initial dye concentration, coagulant dosage and adsorbent dosage. The relative contribution of each variables to the response (dye removal) is predicted from the regression coefficient in the fitted model [19]. The regression coefficient for dye removal is obtained using a statistical software, Minitab 18.0 by least square method. Table 3 simply summarises the obtained result from the software.

Table 3. Predicted regression coefficient of the polynomial model for dye removal

Independent Variable	Regression Coefficient	t-Value	p-Value	Significant Level
Constant	1.07	0.47	0.650	
Linear				
A	-46.040	-39.986	0.000	***
B	4.526	3.931	0.002	***
C	-1.866	-1.620	0.131	
D	2.422	2.103	0.057	
Square				
A*A	51.274	29.687	0.000	***
B*B	-4.678	-2.709	0.019	**
C*C	2.202	1.275	0.226	
D*D	1.055	0.611	0.553	
2-Way Interaction				
A*B	5.375	2.695	0.019	**
A*C	-0.926	-0.464	0.651	
A*D	0.539	0.270	0.792	
B*C	-0.069	-0.034	0.973	
B*D	0.258	0.130	0.899	
C*D	-0.593	-0.297	0.771	

** $p < 0.05$; *** $p < 0.01$

Table 4. Model Summary

R^2	R^2 (adjusted)	R^2 (predicted)
99.57%	99.06%	97.56%

Based on the analysis, the pH of CR solution (A), initial dye concentration (B) and second-order effect of pH (A*A) are the highly significant variables on dye removal. Theses independent variables have p-values smaller below 0.01 ($p<0.01$). Besides that, the second-order effect of initial dye concentration (B*B) and the interaction of pH and dye concentration (A*B) are significant on dye removal. Both of the variables have p-values below 0.05 ($p<0.05$). A quadratic polynomial equation that describes the

behaviour of dye removal to optimise the process can be determined from the regression coefficients of all the significant factors. The regression equation in term of coded variables is shown below.

$$Y2 = -46.040A + 4.526B + 51.274A^2 - 4.678B^2 + 5.375AB \quad (4)$$

Coefficient of determination (R^2) is a measurement on how close the collected data are to the fitted regression line. It simply describes how well the model fits the data. Meanwhile, adjusted coefficient of determination (adjusted R^2) is an adjustment for R^2 to include the number of variables in a data set [19].

The analysis shows a R2 value of 99.57%. This indicates that 99.57% of the total variation is explained by the model and the remaining 0.43% of the variation is unexplained. The adjusted R2 is determined to be 99.06% and is in good agreement with the R2. If a new set of data is fitted to the model for dye removal analysis, it shows 99.06% similar value with the R2. Thus, the second-order regression model obtained for dye removal is satisfactory and Eq. (34) is fitted to represent the model.

3.2 Analysis of Variance (ANOVA)

Next, the fitted models obtained from section 3.1 will be further discussed by diagnostic checking. Table 5 shows the extracted results obtained from Minitab 18.0.

Table 5. ANOVA of the factors as linear, square and interaction on the effect dye removal

Source	Degree of Freedom	Sum of Square	Mean Square	F-Value	P-Value
Model	**14**	**43857.3**	**3132.7**	**196.910**	**0.000**
Linear	4	25794.5	6448.6	405.341	0.000
Square	4	17941.0	4485.2	281.929	0.000
2-Way Interaction	6	121.8	20.3	1.276	0.338
Error	**12**	**190.9**	**15.9**		
Lack-of-Fit	10	183.7	18.4	5.085	0.175
Pure Error	2	7.2	3.6		
Total	**26**	**44048.2**			

The results of ANOVA test indicate that the regression model for the data on dye removal is highly significant as the p-value is small ($p < 0.01$). The p-value of LOF for this model is large ($p>0.05$), this shows that the LOF is insignificant. According to [35], the sum of square due to pure error (SSPE) measures the inherent variability of repeated measurements which cannot be explained by any model. However, a small value of pure error is still preferred. In this model, the pure error of is very small, which is 7.2%.

In short, the ANOVA test shows that the regression model is fitted to describe the actual behaviours of dye removal based on the relationships of independent

variables and thus Eq. (4) is able to represent the model. Th interaction between variables for dye removal is essential and is discussed below.

3.3 Respond Surface/ Contour Plot and Optimisation of Parameters

The model fitting analysis and ANOVA test as shown in section 3.1 and 3.2 have clearly illustrated the relationships between the independent variables and response. Thus, RSM method can be used to evaluate the optimisation of process parameters. The regression model analysis has shown that the significant interaction between variables are A: pH and B: Initial dye concentration. The relationships can be further illustrated in the three-dimensional respond surface plot and contour plot, from Figure 3 to 5.

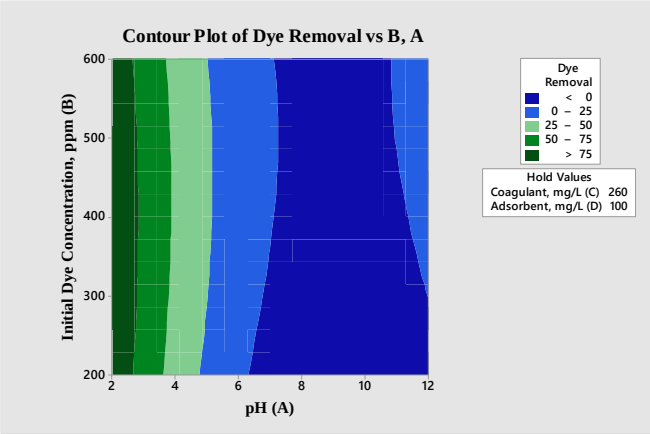


Figure 3. Contour and respond surface plot of dye removal agaisnt pH and initial dye concentration

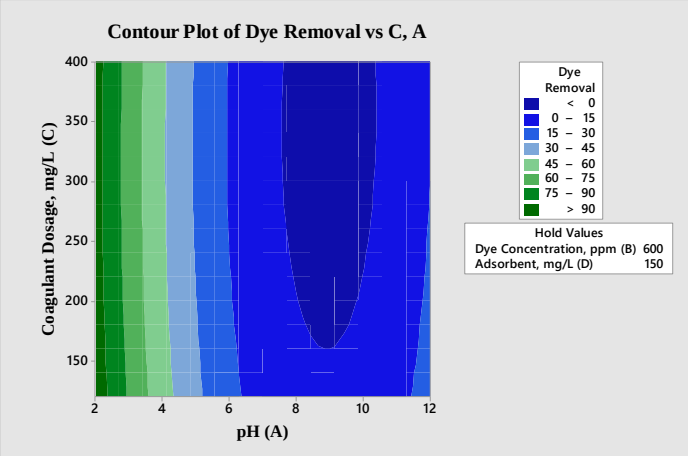


Figure 4. Contour and respond surface plot of dye removal agaisnt pH and coagulant dosage

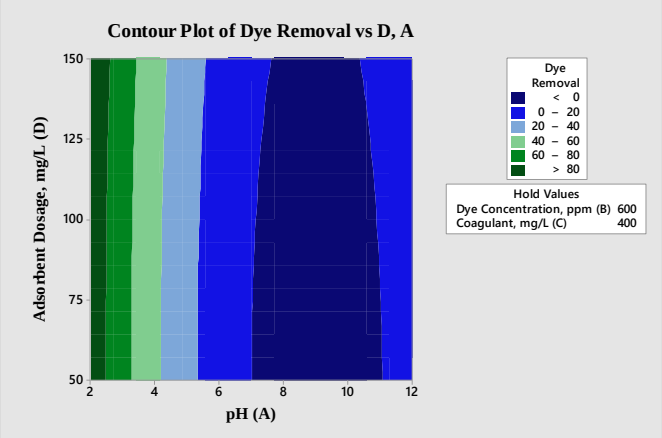


Figure 5. Contour and respond surface plot of dye removal agaisnt pH and adsorbent dosage

The optimisation of the process variables was analysed using the response optimiser function in Minitab 18.0. The optimum conditions for the adsorption-coagulation hybrid process on dye removal are pH 2, initial dye concentration of 385 ppm, coagulant dosage of 209 mg/L and adsorbent dosage of 150 mg/L. With these optimum process parameters, the predicted dye removal percentage fits up to 96.67%. Meanwhile, to further validate the predicted optimised conditions, an experiment using the stated values of variables was conducted and the experimental result shows a 98.71% of dye removal. Thus, the obtained optimised combination of process parameters are accepted.

3.3.1 Influence of pH on Dye Removal

Since natural coagulants are used in this case study, the pH is manipulated from 2 to 12 during the adsorption-coagulation hybrid process [10]. From the contour plot shown in Figure 3, the highest range of dye removal is established when the pH is between 2 and 3. This shows that acidic condition is favourable for *Hibiscus sabdariffa* seeds to perform its coagulation process. Conversely, the dye removal is reduced significantly when the pH increases from 6 to 12. Based on [9], the coagulant protein extracted from *Hibiscus sabdariffa* seeds consist of glutamic acid (27%) and aspartic acid (11%), both are the cationic amino group. When the coagulation condition is acidic, it further enhances the positively-charged environment by increasing the density of positive charges (H^+) around the coagulants hydrolysates. Charge neutralisation and complex reaction between the coagulant proteins and dissociated organic compounds of Congo red dominate the coagulation mechanism [20]. At the isoelectric point, the surface colloid particle is electroneutral and the combined effect of bridging and charge neutralisation results in higher dye removal efficiency [20]. This may explain for the coagulants to achieve optimum dye removal effect at pH 2 to 3.

According to [16], *Hibiscus sabdariffa* seeds also contain anionic peptides Under neutral and alkaline conditions, the dye removal percentage is rather low. This is because not all colloid particles will coprecipitate with the coagulant hydrolysates. In fact, most of the colloid particles and organic compounds of dyes merely absorbed on the surface of coagulants under neutral conditions when they collide with each other

[20]. The absorption occurs due to weak chemical bonding but not attraction of charges. However, there is also a slight increase in dye removal when the dye solution reaches pH 12. The possible reason is that alkaline condition (OH^-) is favourable for the dissociation of small amount of coagulant protein, arginine. This coagulating agent coagulates the dye colloid thus increases the dye removal [9].

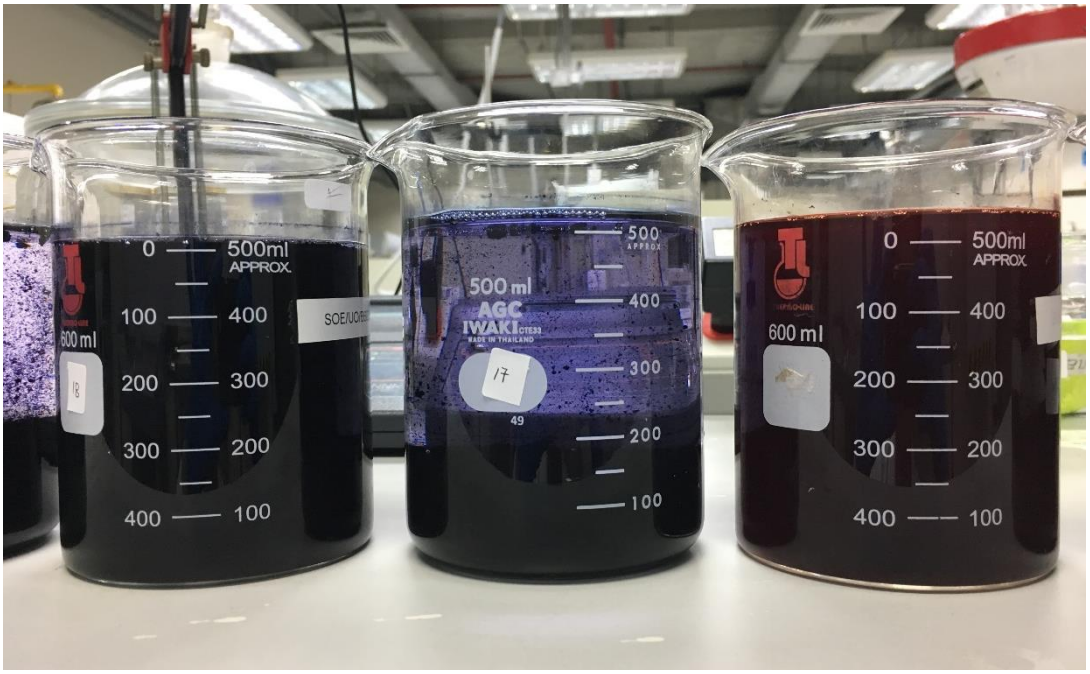


Figure 6. Sample of 400 ppm dye solutions – pH, coagulant dosage, adsorbent dosage (Left: 2, 120, 100; Centre: 2, 260, 50; Right: 7, 260, 150)

3.3.2 Influence of Initial Dye Concentration on Dye Removal

From the aggression model analysis, the initial dye concentration is also tested to be one of the highly significant factors that will attribute the dye removal percentage. In this case study, the dye concentration is manipulated from 200 ppm to 600 ppm.

From the contour plot shown in Figure 3, the dye removal increases when the dye concentration increases. As the dye concentration increases, there are more free dye colloid particles readily existed to form particle-protein-particle complexes with the coagulant and thus increases the dye removal efficiency [21]. However, according to [10], the dye removal will drop or remain unchanged when the dye concentration reaches a saturation point. At this point, the coagulating agent is said to be saturated, there is no free amino group with active site available to coagulate the colloid particles. Therefore, the dye removal percentage will drop or remain unchanged. In this case study, the dye concentration is said to be optimised at 385 ppm, which means beyond this indicated concentration, the dye removal does not increase significantly. However, Figure 2 shows that the dye removal continues to increase even the dye concentration exceeds 385 ppm. This is because dye removal is resulted from the adsorption of Congo red dyes onto the activated carbon surfaces. Thus, the dye removal increases up to 600 ppm dye concentration.

3.3.3 Influence of Coagulation Dosage on Dye Removal

In this case study, the coagulant dosage extracted from *Hibiscus sabdariffa* seeds is tested from 120 mg/L to 400 mg/L [10]. As shown in Figure 4, the dye removal increases gradually from 120 mg/L to 400 mg/L at pH 2 to 3. This is because as the cationic amino group increases, the peptides form more and stronger hydrogen bonding with the aromatic hydroxyl groups on dye particles. When abundant of coagulative components are available, it also neutralise the charges found on the surface of particles so that the particles can attract with one another more efficiently [5]. Thus, this explains for the increment of dye removal as the coagulant dosage increases.

However, it is also reported that the coagulation activity of *Hibiscus sabdariffa* seeds is decreased when the dosage reaches a certain point. This declination is caused by charge reversal which results the re-dispersion and re-stabilisation of dye colloidal particles due to overdosing of coagulant proteins [22]. However, this phenomenon will only occur when the coagulation dosage reaches up to 709 mg/L [23].

3.3.4 Influence of Adsorption Dosage on Dye Removal

The adsorbent dosage is manipulated from 50 mg/L to 150 mg/L [12]. As shown in Figure 5, It can be seen that the increase in the adsorbent dosage increases the dye removal percentage of Congo red. This is because higher adsorbent dosage provides a greater surface area with more adsorption sites and thus increase the adsorption of dye.

The adsorption of dye particles at pH 2 to 3 also shows higher removal percentage. When the density of positive charges in the solution increases, it avoids the adsorbents becoming more aggregated due to electrostatic interactions and steric repulsion force [12]. Thus, the stabilised adsorbent provides more adsorption sites. The excessive positive charges will also affect the surface charge of the adsorbent. As a result, the highly branched aromatic compounds of Congo red will gradually adsorb on the highly porous surface of the activated carbon and balances the dispersion status [24].

In short, pH and initial dye concentrations play an important role to maximise the performance of adsorption-coagulation hybrid process. The solution must be in between 2 to 3 so that the hybrid process can perform effectively (as shown in Figure 2 to 4).

3.4 Summary

The optimisation of the hybrid process and the interaction between process variables had been discussed above. The analysis shows that the dye removal can reach up to 96.67% when the pH of CR solution is 2, initial dye concentration is 385 ppm, coagulant dosage is 209 mg/L and adsorbent dosage is 150 mg/L.

Shah et al. had demonstrated the adsorption-coagulation process to remove pollutants in the textile dye wastewater from a manufacturing plant in Pakistan. In his research work, commercial coagulants such as ferric chloride ($FeCl_3$), ferrous sulphate ($FeSO_4$) and alum [$Al_2(SO_4)_3$] are used for comparison purpose and bottom based coal ash (BBCA) is used as an adsorbent in the hybrid process. According to the findings from Shah et al., the hybrid process was optimised when 1.68 g/L of $FeCl_3$ and 4 g/L

of BBCA was used to treat the dye effluent. The colour removal achieves up to 82%, turbidity removal 84% and total suspended solid (TSS) 94%.

The hybrid process performed in this current research study shows a 96.67% of dye removal. As compare with the colour removal reported from Shah et al., it shows that the properties of wastewater are important for removal efficiency. Shah et al. described the dye wastewater as effluent with high suspended organic compounds, because it consists of dyes, pigments, textile chemicals and binder emulsion. In contrast with the synthetic CR wastewater, the dye molecules are the only component presented in the solution, thus it can achieve high dye removal percentage.

In this research work, the optimum coagulant dosage is 209 mg/L, which is much lower than 1.86 g/L. This is because of the composition of wastewater and the dosage of natural coagulant is normally lower than chemical coagulant [25]. Besides that, the optimum adsorbent dosage in this research work is 150 mg/L, which is lower than 4 g/L. According to [11], the dosage of synthetic adsorbent such as activated carbon is normally lower than the dosage of natural adsorbent in water treatment process. This is because the manufacturing process of synthetic adsorbent which requires strict temperature and pressure control produces highly porous activated carbon. This greatly increase the adsorption surface area of activated carbon. Note that the dye molecules adsorbed on the surface of activated carbon is relatively small compared with the organic pollutants in real wastewater. Thus, the dosage of activated carbon is lower than the dosage BBCA.

Shah et al. had also reported that higher dosing of coagulant and adsorbent more than 1.68 g/L and 4g did not improve the removal efficiency in terms of the reduction of colour and concentration of pollutants. This is due to the occurrence of steady state condition with higher dosing of coagulant and adsorbent. This is true based on the analysis of the current experimental result. When the coagulant and adsorbent dosage reach 209 mg/L and 150 mg/L respectively in the CR solution with dye concentration of 385 ppm, the removal efficiency will drop below 96.67%.

Shah et al. also suggested that among the three coagulants used, the combination of alum-BBCA has the lowest removal efficiency, with 77% of colour removal, 79% of turbidity removal and 93% of TSS removal. This may be due to the pH of effluent that influence the coagulation activity of alum as lime is added into the water sample for pH maintenance. Based on [4], the optimum pH for alum is 5.3. Since lime is an alkaline, it will affect the performance of coagulation in the hybrid process and thus reduce the removal efficiency. In this research work, the analysis shows that the coagulation of H. sabdariffa seeds is efficient at pH 2. Thus, it can remove the dye efficiently.

From this summary, it can be concluded that the adsorption-coagulation hybrid process with *H. sabdariffa* seeds as coagulant and activated carbon as adsorbent can potentially achieve the removal efficiency obtained from RSM if it is scaled up or used to treat real dye wastewater. The process condition must be optimised so that the interaction of adsorbent and coagulant with the pollutants can be improved and thus increase removal efficiency.

4. Conclusion

In conclusion, this case study shows that *Hibiscus sabdariffa* seeds are workable natural coagulants. It also serves as an alternative to remove Cong red dye wastewater in real practice. Based on the aggression model analysis and ANOVA, the highly significant factors that contribute to the dye removal efficiency through adsorption-coagulation hybrid process are pH of solution and initial dye concentration. The RSM results shows that the optimised process parameters for adsorption-coagulation hybrid process with *Hibiscus sabdariffa* seeds as the coagulant and activated carbon as the adsorbent are pH 2, initial dye concentration of 385 ppm, coagulant dosage of 229 mg/L and adsorbent dosage of 50 mg/L. The dye removal reaches up to 98.68% under optimum parameters.

Acknowledgment

The author would like to offer a token of appreciation to Ms. Nurhazwani Ismail, Ms. Nur Farihah A. Malek and Ms. Lithnes Kalaivani for their kind support throughout the research studies until it is successfully completed.

References

[1] B. Frindt, J. Mattusch, T. Reemtsma, A. G. Griesbeck, and A. Rehorek, "Multidimensional monitoring of anaerobic/aerobic azo dye based wastewater treatments by hyphenated UPLC-ICP-MS/ESI-Q-TOF-MS techniques," *Environ. Sci. Pollut. Res.*, vol. 24, no. 12, pp. 10929–10938, 2017.

[2] A. Pirkarami and M. E. Olya, "Removal of dye from industrial wastewater with an emphasis on improving economic efficiency and degradation mechanism," *J. Saudi Chem. Soc.*, vol. 21, pp. S179–S186, 2017.

[3] C. Jiang, B. Fu, H. Cai, and T. Cai, "Efficient adsorptive removal of Congo red from aqueous solution by synthesized zeolitic imidazolate framework-8," *Chem. Speciat. Bioavailab.*, vol. 28, no. 1, pp. 199–208, 2016.

[4] A. K. Verma, R. R. Dash, and P. Bhunia, "A review on chemical coagulation/flocculation technologies for removal of colour from textile wastewaters," *J. Environ. Manage.*, vol. 93, no. 1, pp. 154–168, 2012.

[5] T. . V. K. Vijayaraghavan, G.; Sivakumar, "Application of Plant Based Coagulants for Waste Water Treatment," *Int. J. Adv. Eng. Res. Stud.*, vol. 1, no. 1, pp. 88–92, 2011.

[6] C. P. Pise and S. A. Halkude, "a New Technique for Purification of Water Using Natural Coagulant," *Int. J. Eng. Technol.*, vol. 6, no. 6, pp. 2564–2572, 2015.

[7] C. Y. Yin, "Emerging usage of plant-based coagulants for water and wastewater treatment," *Process Biochem.*, vol. 45, no. 9, pp. 1437–1444, 2010.

[8] U. A.Y and I. T.S., "The Role of Green Coagulants in Wastewater Treatment : A Review," *Wastewater Remediat. Using Plant Tech.*, no. November, 2016.

[9] A. N. Jones, "Investigating the potential of Hibiscus seed species as alternative water treatment material to the traditional chemicals," no. December, 2016.

[10] M. Y. Yong and N. Ismail, "Optimisation of hibiscus sabdariffa as a natural coagulant to treat Congo red in wastewater," *J. Eng. Sci. Technol.*, vol. 11, no. Special Issue onthefourtheureca2015, pp. 153–165, 2016.

[11] A. Bhatnagar and A. K. Minocha, "Conventional and non-conventional adsorbents for removal of pollutants from water - A review," *Indian J. Chem. Technol.*, vol. 13, no. 3, pp. 203–217, 2006.
[12] C. Jung, N. Phal, J. Oh, K. H. Chu, M. Jang, and Y. Yoon, "Removal of humic and tannic acids by adsorption-coagulation combined systems with activated biochar," *J. Hazard. Mater.*, vol. 300, pp. 808–814, 2015.
[13] A. . Shah, A.K; Memon, A.R; Metlo, G; Peerzada, "Simultaneous Coagulation-Adsorption Process Optimization for the Treatment of Real Wastewater of Complex Dyes Manufacturing Plant," vol. 45, no. 3, pp. 506–513, 2013.
[14] G. Vijayaraghavan, S. Shanthakumar, E. E. Division, and B. Sciences, "Removal of Congo Red Dye Using a Natural Bio- Polymeric Coagulant," *Int. Conf. Recent Adv. Chem. Environ. &Energy Eng.*, no. January 2014, pp. 1–5, 2014.
[15] B. Meroufel, O. Benali, M. Benyahia, Y. Benmoussa, and M. A. Zenasni, "Adsorptive removal of anionic dye from aqueous solutions by Algerian kaolin: Characteristics, isotherm, kinetic and thermodynamic studies," *J. Mater. Environ. Sci.*, vol. 4, no. 3, pp. 482–491, 2013.
[16] S. M. N. Halimatul, I. Amin, N. Mohd-Esa, A. G. Nawalyah, and M. Siti Muskinah, "Protein quality of roselle (Hibiscus sabdariffa L.) seeds," *Int. Food Res. J.*, vol. 14, no. 2, pp. 131–140, 2007.
[17] K. C. Duong-Ly and S. B. Gabelli, "Salting out of proteins using ammonium sulfate precipitation," *Methods Enzymol.*, vol. 541, no. April 2015, pp. 85–94, 2014.
[18] S. Eldein and B. Ahmed, "Some Physicochemical and Nutritional Studies on Karkade (Hibiscus sabdariffa) Seed Proteins," *Rev. Lit. Arts Am.*, no. January, 1998.
[19] T. Amir, N. Ismail, a Fm Alkarkhi, Et Al., and a Fm, "Optimization of Coagulation Process for Landfill Leachate Pre-Treatment Using Response Surface Methodology (RSM)," *J. Sustain. Dev.*, vol. 2, no. 2, p. P159, 2009.
[20] B. C. Cao, B. Y. Gao, C. H. Xu, Y. Fu, and X. Liu, "Effects of pH on coagulation behavior and floc properties in Yellow River water treatment using ferric based coagulants," *Chinese Sci. Bull.*, vol. 55, no. 14, pp. 1382–1387, 2010.
[21] S. Shamsnejati, N. Chaibakhsh, A. R. Pendashteh, and S. Hayeripour, "Mucilaginous seed of Ocimum basilicum as a natural coagulant for textile wastewater treatment," *Ind. Crops Prod.*, vol. 69, pp. 40–47, 2015.
[22] N. Fathinatul and R. Nithyanandam, "Wastewater Treatment by using Natural Coagulant," *2nd Eureca*, pp. 2–3, 2014.
[23] C. Y. Yong. (2016)"Removal of Congo red by Using Hibiscus sabdariffa for Coagulation and Flocculation Process," Malaysia: Taylor's University, School of Engineering.
[24] K. Zare *et al.*, "A comparative study on the basis of adsorption capacity between CNTs and activated carbon as adsorbents for removal of noxious synthetic dyes: a review," *J. Nanostructure Chem.*, vol. 5, no. 2, pp. 227–236, 2015.
[25] R. Sanghi, B. Bhattacharya, A. Dixit, and V. Singh, "Ipomoea dasysperma seed gum: An effective natural coagulant for the decolorization of textile dye solutions," *J. Environ. Manage.*, vol. 81, no. 1, pp. 36–41, 2006.

eureca 2017 – Conference Paper
Paper Number 2CE09

Potential of *Hibiscus Sabdariffa* and *Jatropha Curcas* as Natural Coagulants in the Treatment of Pharmaceutical Wastewater

Sheena Sibartie[1*], Nurhazwani Binti Ismail[1**]

[1]*Taylor's University*

*sheenasibartie@gmail.com

**nurhazwani.ismail@taylors.edu.my

Abstract

Pharmaceutical wastewater is one of the most difficult wastewater to treat due to the presence of pharmaceutical compounds resulting in high concentration of organic matter, high turbidity and Chemical Oxygen Demand (COD). Coagulation is a common method used to treat wastewater. It works by neutralising the negative charges of the pollutants which then accumulate at the bottom as flocs and separate from the water suspension. However, the issue that has been raised with the use of chemical coagulants is their presence in water after treatment that can cause risks to the human health such as Alzheimer and cancer. Natural coagulants can be used as a safe alternative to these chemicals in successfully treating wastewater. Therefore, the objective of this experiment was to study the effect of *H. Sabdariffa* and *J. Curcas* as natural coagulants, separately and as a combination, on the treatment of pharmaceutical wastewater. The synthetic wastewater was prepared using paracetamol, ibuprofen, naproxen and caffeine. Jar test experiment were carried out where beakers of 0.5L wastewater were mixed with the coagulants. The pH of the wastewater was varied from 2 to 12 while the coagulant dosage was varied from 40 to 200 mg/L. The turbidity was measured suing a turbiditimeter while the COD was measured using the UV spectrophotometer. This study showed that both *H. Sabdariffa* and *J. Curcas* were able to effectively treat pharmaceutical wastewater. It was found that *H. Sabdariffa* works best at pH 4 and at a coagulant dosage of 190 mg/L with a highest turbidity removal of 35.8% and a decrease of COD by 29%. *J. Curcas* was found to perform best at pH 3 and with a coagulant dosage of 200 mg/L with a highest turbidity removal of 51% and a decrease of COD by 32%. When *J. Curcas* and *H. Sabdariffa* were used in combination, the optimum composition was found to be 80% *J. Curcas* and 20% *H. Sabdariffa* by weight with a maximum turbidity removal of 46.8% and a decrease in COD by 46%. In comparison between the two natural coagulants, *J. Curcas* is found to be a better and more suited coagulative agent for the treatment of pharmaceutical wastewater. The same experiment was carried with alum at pH 6 and coagulant dosage of 750 mg/L and a turbidity removal of 48% and a decrease in COD by 38% were recorded. By comparing the results with the natural coagulants, *J. Curcas* was a better coagulant in treating the pharmaceutical wastewater. This shows that natural coagulants can be used to replace chemical coagulants in the treatment of pharmaceutical wastewater.

Keywords: Wastewater, Pharmaceutical, *H. Sabdariffa*, *J. Curcas*, Coagulant.

1. Introduction

In the last decade, traces of pharmaceuticals in the water cycle including drinking water have become a subject of discussion among the public, governments and the drinking- water regulators. Their presence in water, even at low concentrations, has raised concerns regarding its risks to human health from consuming these pharmaceuticals in drinking water [1], [2]. Therefore, it is essential to remove these pharmaceuticals from the wastewater before consumption. As a result, effective treatment methods must be applied to efficiently treat the contaminated water. Current pharmaceutical wastewater plants use methods such as activated sludge, membrane bioreactor and coagulation [3], [4].

Coagulation is a well-known technique used to reduce the pollutant contents in the water body that are present as turbidity, colour and organic matters [5], [6] . It is used as a treatment aiming to reduce the amount of pharmaceuticals such as paracetamol in the wastewater before it leaves as effluents [7]. Coagulants work by neutralising the charges caused by the colloidal particles. The suspended particles accumulate, forming flocs that then settle at the bottom and separate from the water suspension [6]. The most common coagulants used are chemicals such as the aluminium and ferric salts which are highly effective and cheap. However, recent studies have shown that traces of the aluminium based coagulants in the treated water can cause Alzheimer and other diseases such as intestinal constipation, abdominal colic and convulsions [6], [8]. Regarding the use of synthetic polymers, the presence of its residues in the water can be toxic and have strong carcinogenic properties [8]. Besides that, they are also ineffective in low- temperature water, produce large sludge volumes and significantly affect the pH of the treated water [9]. Therefore, researchers are focusing more on using natural coagulants which can be obtained from plants, animals or microorganisms as replacement to the chemical ones. They are non-toxic, biodegradable and can help to achieve the same results as the chemical coagulants [10].

Natural coagulants have been used for domestic households in the earlier days for traditional water treatment. However, due to the cheap cost and effectiveness of chemical coagulants, the use of natural coagulants was overlooked upon [10]. Furthermore, the use of natural coagulants have not been sufficiently investigated [10]. Therefore, this paper is focused on the study of *Hibiscus Sabdariffa* and *Jatropha Curcas* as natural coagulants. These plants are known as natural coagulants due to the presence of proteins in the seeds that act as an active coagulative agent [10]. These two plants are easily and readily accessible in various countries. The *H. Sabdariffa* seeds consist of 29.9% of proteins while *J. Curcas* seeds was found to contain 27.2% of proteins [11], [12]. Since the proteins inside the seeds act as a coagulative agent, both of these plants have the potential to treat wastewater.

H. Sabdariffa, most commonly known as Roselle, is used in herbal drinks, as food and as a flavouring agent in the food industry. The flower, known as calyx, is mostly used for these purposes. The seeds are most often discarded since till now, there is no use for it [11]. However, these seeds can be used to treat wastewater due to its coagulative properties. *J. Curcas* is a shrub or small tree belonging to the *Euphorbiaceous* family. Its main use is to extract oil from its fruit which is then used in the cosmetic industry, in soap making and as a substitute to kerosene or diesel. The seed and the press cake which is the waste after the oil extraction are normally discarded.

However, these contain the protein which is the active coagulating agent that is efficient in the wastewater treatment [13], [14]. These wastes and the seeds can be used for coagulation, reducing the amount of waste and promoting sustainable development [8].

This paper investigates the efficiency of *H. Sabdariffa* and *J. Curcas* as natural coagulants, individually and as a combination, in the treatment of pharmaceutical wastewater. The effect of pH and coagulant dosage on the coagulation process are also studied in this research. The performance of the natural coagulants is compared with the effectiveness of the chemical coagulant alum.

2. Materials and Methods

2.1 Materials

The materials used for this experiment include: good quality dry seeds of *H. Sabdariffa* and Jatropha Curcas, pharmaceuticals (namely paracetamol, ibuprofen, naproxen and caffeine) to simulate the wastewater, 1M hydrochloric acid and 1M sodium hydroxide (to adjust the pH of the wastewater), 0.5M sodium chloride solution (to extract the proteins from the seeds).

2.2 Preparation of synthetic wastewater

Synthetic pharmaceutical wastewater was prepared by dissolving pharmaceuticals in distilled water to simulate the pharmaceutical wastewater properties in terms of the concentration of pharmaceuticals present in the wastewater. The pharmaceuticals were crushed into a fine powder using a mortar and pestle. 62.5 mg of each pharmaceutical (paracetamol, ibuprofen, naproxen and caffeine) was added to 1L of distilled water to prepare the stock solution of the synthetic wastewater. The solution was mixed for 1 hour at 50 rpm to achieve uniform dilution of the pharmaceuticals. The synthetic wastewater was then allowed to settle for 24 hours for complete hydration before it was filtered and ready for the experiment.

The pH of the wastewater was adjusted using 1M hydrochloric acid and 1M sodium hydroxide before the jar tests.

2.3 Preparation of the *H. Sabdariffa* and *J. Curcas* seed powder

Good quality seeds were selected and washed with tap water to remove any dust or impurities on the shells. They were then dried in an oven at 60 ± 2 ℃ for 3 hours to remove all the moisture content from the seeds. The dried seeds were crushed into a fine powder using a mortar and pestle.

2.4 Preparation of the *H. Sabdariffa* and *J. Curcas* coagulant

To prepare the coagulants, sodium chloride was used as the solvent to extract the proteins from the seed powder. As studied by [13], sodium chloride was found to

be the best solvent compared to distilled water and sodium hydroxide for the extraction of the coagulative agent from the seeds.

0.5g of the seed powder was dissolved in 100 ml of 0.5M sodium chloride. The mixture was blended for 2 minutes using a food processor. The solution was filtered through a muslin cloth and the filtrate was used in the following jar tests.

2.5 Coagulation experiments

The coagulation experiments were carried out by varying the pH, coagulant dosage and wastewater concentration in terms of the concentration of pharmaceuticals in the water. The pH was varied from 2 to 12 while the coagulant dosages were varied from 40 to 200 mg/L. The initial wastewater concentration was investigated at 62.5 mg/L of each pharmaceutical. The temperature of the wastewater was kept constant at room temperature.

The jar test was used to conduct the coagulation experiments. Six 0.5L beakers were each filled with 500 mL of wastewater. The optimum pH was first tested by varying the pH while keeping the coagulant dosage constant at 200mg/L. Upon addition of the coagulant, the mixture was stirred rapidly at 100 rpm for 4 minutes followed by slow mixing at 40 rpm for 25 minutes. The rapid mixing is to promote the collision between the pharmaceuticals and the coagulant while the slow mixing is to allow the growth of the flocs. The mixture was then allowed to settle for one hour for sedimentation, after which 50 ml of the liquid was carefully collected without disturbing the flocs settled at the bottom of the beakers. The liquid was then filtered and the residual turbidity (RT) and COD of the filtrate were measured. From the results, the pH with the best turbidity and COD removal was chosen as the optimum pH.

The same procedures were repeated while experimenting with different coagulant dosages while keeping the pH constant at the optimum value. The COD and turbidity are measured and the dosage with the best turbidity and COD removal was taken as the optimum. Next, the initial wastewater concentration was varied while the pH and the dosage was kept to their optimum values. The initial wastewater concentration with the best turbidity and COD removal was selected. The same coagulation test without the addition of coagulants was carried out as a control and the residual turbidity (RT_c) and the COD (COD_c) were measured.

The jar coagulation tests were carried out for both *J. Curcas* and *H. Sabdariffa* individually and as a combination.

2.6 Analytical Method

When the pharmaceutical wastewater is put under study, different parameters are always considered to have a better indication of the characteristics of the wastewater. The parameters measured are pH, COD, Biological Oxygen Demand (BOD), turbidity, total suspended solids (TSS) and total dissolved solids (TDS) [15].

As mentioned earlier in Section 1, coagulation is used to reduce the amount of colloidal matter in the water. Turbidity measures the cloudiness of the water, and therefore measures the amount of colloidal matter present inside the water.

Coagulation is a treatment used prior to the biological treatment which involves activated sludge where microorganisms are used to treat the water [16]. During coagulation, a reduction of COD is favored so that when the treated water undergoes the biological treatment, less sludge is produced from the microbial activity. As a result, the two parameters measured in this study are turbidity and COD.

1) Turbidity

It was measured using a turbiditimeter (EUTECH Instruments TN-100). The turbidity removal was calculated as shown by Eq.1:

$$\text{Turbidity removal} = \frac{RT_c - RT}{RT_c} \text{ x } 100\ \% \quad (1)$$

Where: RT_c is the turbidity of the wastewater before undergoing coagulation
RT is the turbidity of the wastewater after undergoing coagulation.

2) Chemical Oxygen Demand (COD)

COD was measured using reaction cells of range 25-1500 mg/L which contained sulphuric acid, potassium dichromate and mercury (II) sulphate as reagents. 3 mL of the sample to be tested was carefully added to the reaction cells inside a fume hood. The cell was then vigorously shaken and heated at 150 ℃ for 2 hours using a thermoreactor. The cells were then removed and let to cool to room temperature. The COD was then measured using a photometer (Prove 300 UV/VIS Spectrophotometer). The COD removal was calculated as shown by Eq.2:

$$\text{COD removal} = \frac{COD_c - COD_i}{COD_c} \text{ x } 100\ \% \quad (2)$$

Where: COD_c is the COD of the wastewater before undergoing coagulation
COD_i is the COD of the wastewater after undergoing coagulation.

3. Results & Discussion

The synthetic wastewater was prepared to simulate the properties of the real pharmaceutical wastewater. The properties of the synthetic wastewater prepared are shown in Table 1 below:

Table 23: Characteristics of synthetic wastewater.

Characteristics of the synthetic wastewater	
Temperature (℃)	30
pH	4.5-5.4
Turbidity (NTU)	9.96
COD (mg/L)	665

The pharmaceutical compounds used to simulate the wastewater are acidic in nature and as a result, the wastewater becomes slightly acidic with an average pH of 4.95. The real wastewater is also acidic due to the acidic pharmaceutical compounds present [15].

3.1 Coagulation activity using *H. Sabdariffa*

3.1.1 Effect of pH on coagulation activity

Fig. 1 and Fig. 2 shows the effect of pH on the turbidity and COD of the treated water after jar tests. pH is an important factor to consider since the solubility of the matter depends on the pH level of the wastewater. The wastewater consists of mainly negative charges and the pH at which the particles become stable is known as the isoelectric point [6]. The pH is varied from 2 to 12 while the coagulant dosage is kept constant at 200 mg/L. From the results obtained, it can be seen that the lowest turbidity is obtained at pH 4 with a turbidity removal of 44.7% and a decrease in COD by 22.9%. This is in agreement with a previous study done by [6] in which it was found that *H. Sabdariffa* is efficient under acidic conditions, especially at pH 4.

This phenomena can be explained by studying the amino acids present in the *H. Sabdariffa* seeds and their isoelectric point. The coagulative agent present in the seeds consists mainly of glutamic acid and aspartic acid which are categorised as acidic amino acids [17]. While the isoelectric point of glutamic acid and aspartic acid are 3.2 and 2.77 respectively, the seeds also contain significant amount of the other amino acids with isoelectric point ranging from 3 to 6 as shown earlier in table 3. As a result, the coagulative agent works best in acidic conditions, especially at pH 3 and 4.

Also, from Fig. 1, pH 4 gives the lowest turbidity of 5.51 NTU with a turbidity removal of 44.7%. It can also be seen that at some pH values, the turbidity increases above its initial turbidity of 9.96 NTU. This is because the pharmaceutical wastewater can only be treated effectively at its optimum pH and at other pH far from its optimum pH, the coagulation activity fails and is unable to produce any flocs. As a result, it causes an increase in the turbidity of the water.

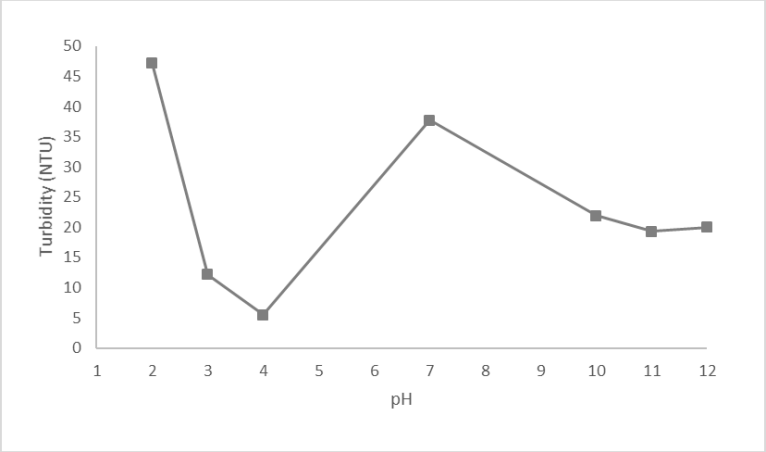


Figure 19: The effect of pH on the turbidity of the wastewater after coagulation.

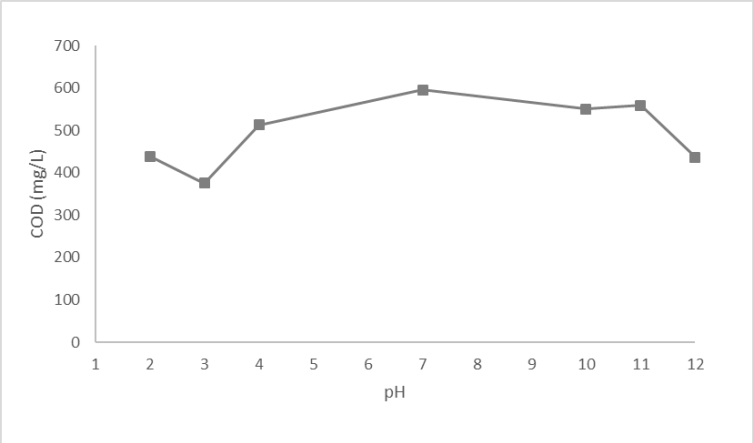


Figure 20: The trend in COD when varying the pH of the wastewater after coagulation.

Fig. 1 and 2 show the relationship between turbidity and COD. The graph for COD shows a similar trend to the graph of turbidity. This shows that pH also has an effect on the COD of the wastewater. At pH 4, the % COD removal is 22.9%.

3.1.2 Effect of coagulant dosage on coagulation activity

The formation of flocs depends on the coagulant dosage. The charges of the coagulants work by neutralising the charged ions in the synthetic wastewater. The floc strength depends on the attraction and repulsion between the particles. When the dosage is low, the particles do not have enough energy and therefore form weak and small flocs [18]. Overdosing also result in poor performance of coagulation and also directly increases the cost of dosing and sludge formation [19]. Therefore, the coagulant dosage was varied from 40 to 200 mg/L.

From Fig.3, it is found that at 190 mg/L, the coagulant gives the highest turbidity removal of 28.4% with a COD removal of 28.3%. It can be seen that at lower dosages, the turbidity removal is low due to insufficient dosages producing weak flocs that are unable to settle down. This is also in correlation with the findings of [20]. As from

90mg/L of coagulant, the COD remains stable at 476 mg/L. This shows that the dosage does not have much of an effect on the COD of the water.

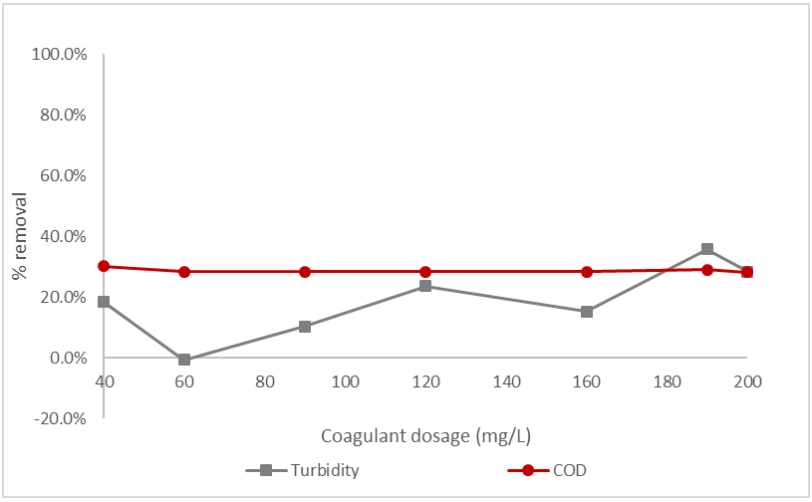


Figure 21: Percentage removal of turbidity and COD with increasing coagulant dosage.

3.2 Coagulation activity using *J. Curcas*

3.2.1 Effect of pH on coagulation activity

Fig.4 and Fig.5 show a similar trend with the effect of increasing pH. The lowest turbidity is observed at pH 3 with a turbidity removal of 41% and COD removal of 34.9%. The turbidity is reduced from 9.96 NTU to 5.88 NTU. This is in agreement with [13] where it proves that Jatropha works best in acidic conditions and works best at pH 3.

It can also be observed that only at pH 3 and 4, the coagulative agent is able to reduce the turbidity. This is because at pH 3 and 4, the positive charges on the amino acids that make up the protein molecules dominate. The composition of amino acids in the seeds of *J. Curcas* was studied by [21]. Glutamic acid and aspartic acid were abundantly found in the seeds. Since these amino acids are acidic and have an isoelectric point at 3.22 and 2.77 respectively, they favour coagulation in acidic conditions, especially at pH 3 [22]. The *J. Curcas* protein is expected to work well as a cationic coagulant agent. As an amphoteric molecule, the charge of the amino acids is dependent on the pH of the environment. As a result, this is why we can observe flocs at pH 3 and 4 [23]. However, at pH greater than 3, the positive and negative charges of the different amino acids in the protein may have reduced the cationic potential of the coagulant and as a result, no coagulation can be observed at these pH [23].

However at other pH values, *J. Curcas* is unable to neutralise the charges in the wastewater and unable to produce any flocs. This may be due to the presence of oil in the jatropha seed powder which was not extracted prior to coagulation. The oil when mixed with the sodium chloride solvent produces a milky emulsion that causes an increase in turbidity at pH 2 and at alkaline conditions [14].

Similar to the coagulation activity with *H. Sabdariffa*, the COD of the treated water shows a similar trend as the turbidity of the water. When the turbidity decreases, the COD of the water also reduces. Therefore, this shows that pH also has an effect on the COD of the water.

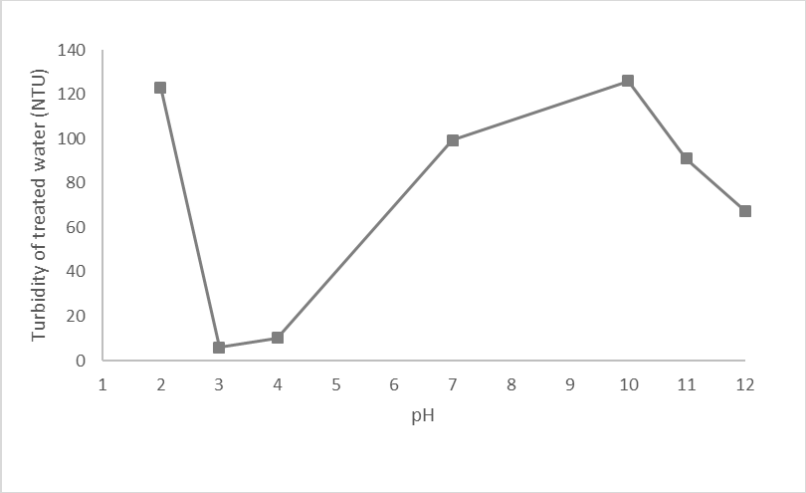


Figure 22: The effect of pH on the turbidity of the wastewater after coagulation.

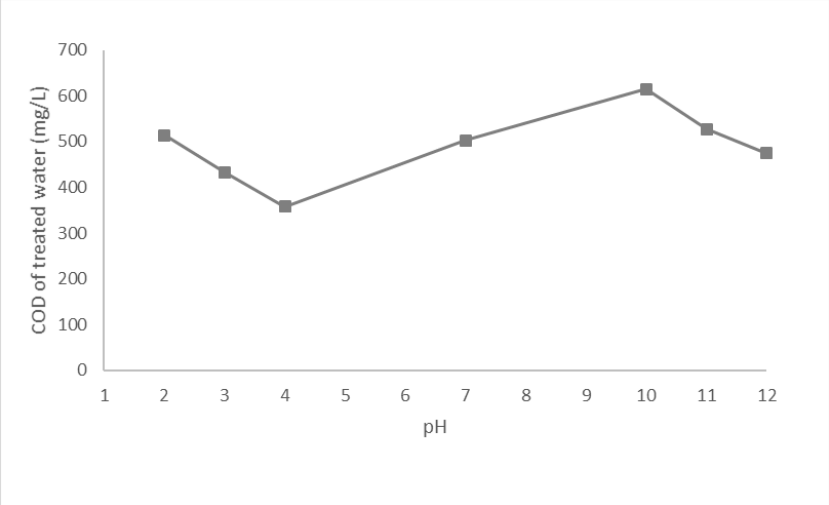


Figure 23: The effect of pH on the COD of the wastewater after coagulation.

3.2.2 Effect of coagulant dosage on coagulation activity

From Fig. 6, it can be seen that the turbidity increases when the coagulant dosage is below 80 mg/L. This is because the dosage is not enough to produce any flocs and therefore the milky emulsion of the jatropha coagulative agent causes the turbidity of the water to increase. From 90mg/L onwards, the turbidity considerably decreases and reaches its lowest turbidity of 4.81 NTU at 200mg/L. The highest turbidity reaches a 51% removal with a 32% decrease in COD.

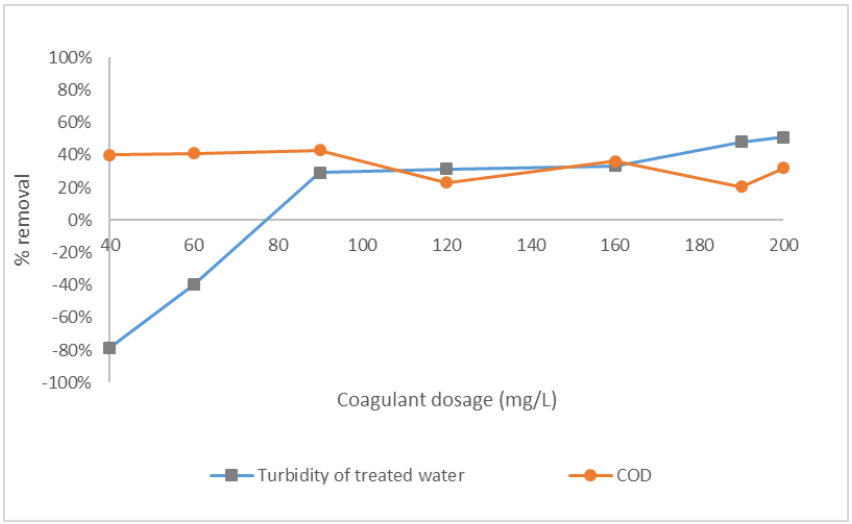


Figure 24: The effect of coagulant dosage on the turbidity and COD % removal.

3.3 Coagulation activity using a combination of *H. Sabdariffa* and *J. Curcas*

3.3.1 Effect of pH on coagulation activity

The effect of pH is studied on treatment of water by using a combination of both seeds. As mentioned in Section 3.1.1, H.Sabdariffa works best at pH 4 while in Section 3.2.1, it was found that *J. Curcas* works at an optimum pH of 3. For a combination of both, it is expected that the coagulants will work under acidic conditions as well. Therefore, the pH is varied from 2 to 7 while the combination is kept to 200 mg/L with equal amounts of *J. Curcas* and *H. Sabdariffa* (50:50%).

Fig. 7 studies the effect of pH on the turbidity of wastewater after coagulation. It can be observed that the turbidity considerably decreases at pH 3 and 4. It reaches its lowest turbidity of 7.59 NTU at pH 3 with a turbidity removal of 24% and a 32.3 % decrease in COD. Fig. 8 shows that pH also affects the COD of the wastewater. The highest decrease in COD is observed at pH 3 and pH 4.

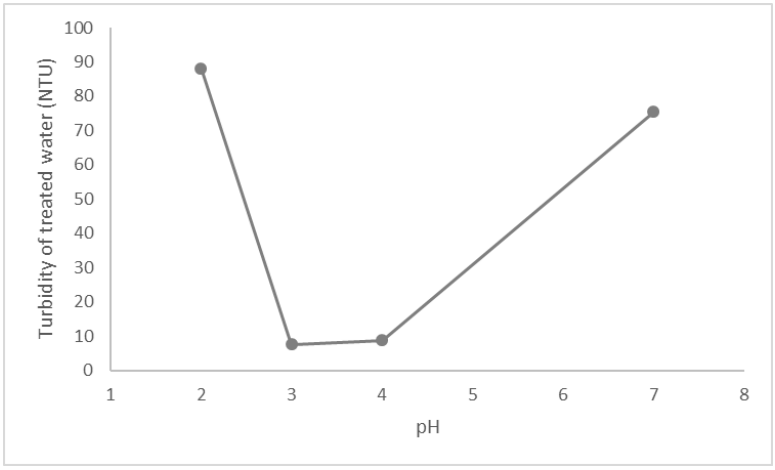


Figure 25: The effect of pH on the turbidity of treated water after coagulation.

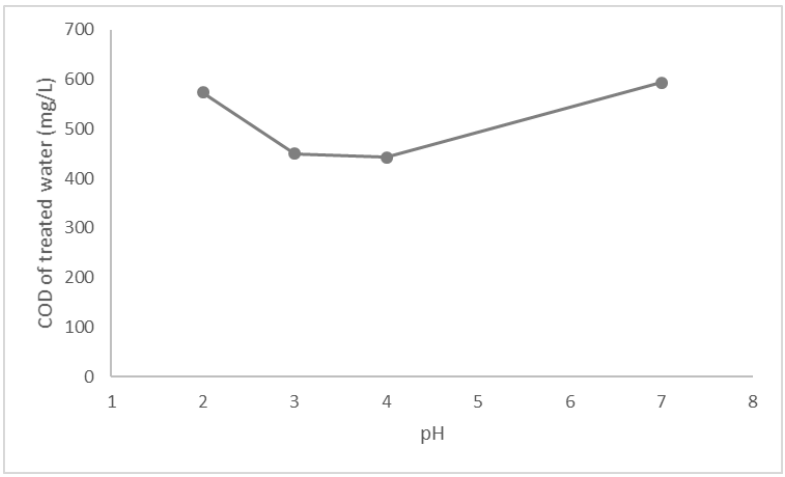


Figure 26: The effect of pH on the COD of treated water after coagulation.

3.3.2 Effect of coagulant dosage on coagulation activity

Fig. 9 shows the effect of increasing the weight of *J. Curcas* in the mixture of both coagulants on the turbidity and COD of the treated water after coagulation. It can be observed that the % turbidity removal gradually increases from 38.8% to 46.8% when the % weight of *J. Curcas* increases. However, the COD remains almost constant at a COD removal of 46%. This shows that increasing the amount of *J. Curcas* does not affect the COD of the water. The optimum composition is 80% *J. Curcas* and 20% *H. Sabdariffa* by weight with a maximum turbidity removal of 46.8% and a decrease in COD by 46%. This shows that *J. Curcas* has a higher effect than *H. Sabdariffa* in the treatment of the wastewater.

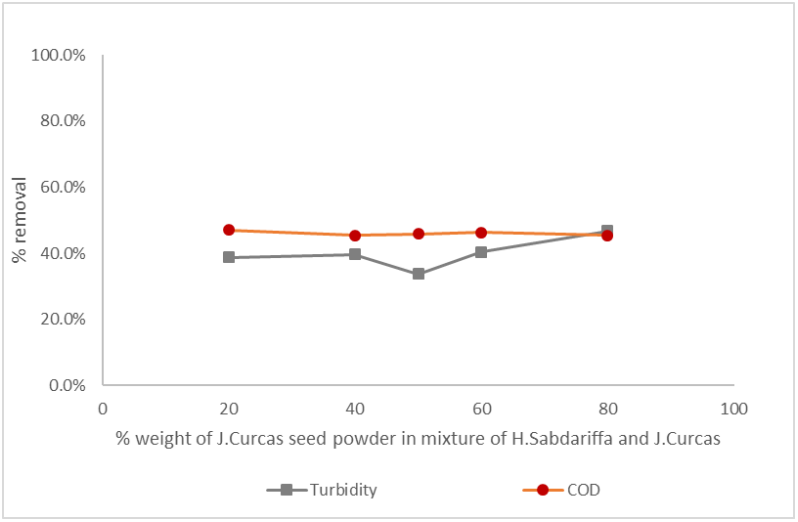


Figure 27: The effect of coagulant dosage on the turbidity and COD of the wastewater.

3.4 Coagulation with Alum

The results are compared with the conventional chemical coagulant which is alum. The effect of alum in the treatment of pharmaceutical wastewater was studied by [7]. It was found that alum worked best at pH 6 with a dosage of 750mg/L.

The synthetic wastewater was treated with alum with the optimum conditioned mentioned above. The same experiment was carried out, with only alum being used as the coagulant. The chemical coagulant was successful in treating the pharmaceutical wastewater with a turbidity removal of 48% and a COD removal of 53%.

3.5 Comparison of results for all different coagulants experimented

The results obtained for all different scenarios tested in this research are compared. The graph below shows the results obtained for all 4 scenarios.

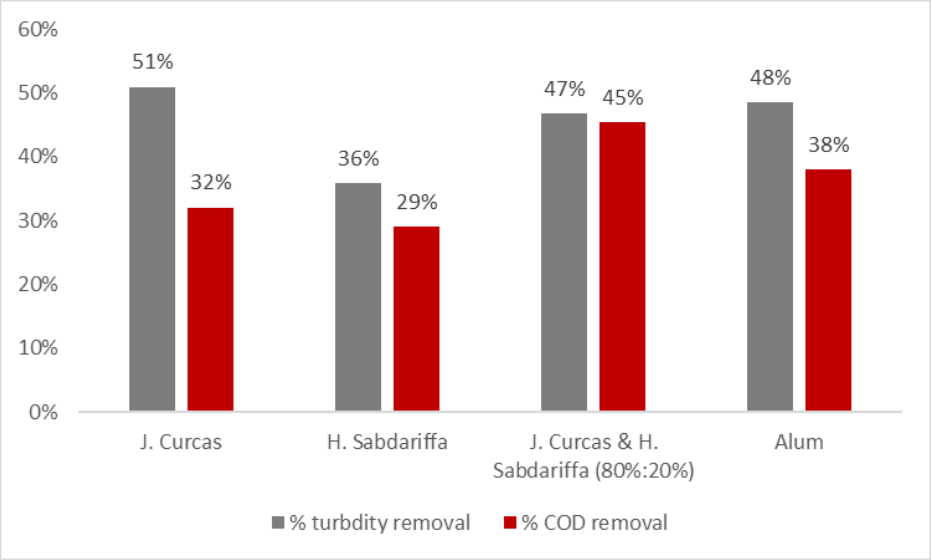


Figure 28: Result comparison of all the different scenarios tested.

From Fig. 10, it can be seen that in terms of % turbidity removal, *J. Curcas* gives the best results compared to the others. It is followed by Alum with a 48% turbidity removal. *H. Sabdariffa* gives the lowest results among the 3 coagulants. This shows that the natural coagulants can be used to replace chemical coagulants in the treatment of pharmaceutical wastewater since the results obtained are comparable and close to each other. By comparing both natural coagulants, *J. Curcas* is the most suitable one to be used as it is more effective in treating the wastewater.

7. Conclusion

In this study, it was found that both *H. Sabdariffa* and *J. Curcas* were able to effectively treat pharmaceutical wastewater. It was found that *H. Sabdariffa* works best at pH 4 and at a coagulant dosage of 190 mg/L with a highest turbidity removal of 35.8% and a decrease of COD by 29%. *J. Curcas* was found to perform best at pH 3 and with a coagulant dosage of 200 mg/L with a highest turbidity removal of 51% and a decrease of COD by 32%. In comparison, *J. Curcas* is found to be a better and more suited coagulative agent for the treatment of pharmaceutical wastewater. Even a combination of both coagulants only gave a turbidity removal of 46.8%. This study also showed that only pH has a distinctive effect on the COD of the wastewater while both pH and dosage has an effect on the turbidity of the wastewater. In comparison with alum, *J. Curcas* gave a better result in the treatment of the wastewater. This research was successful in showing that natural coagulants can be used to treatment of pharmaceutical wastewater and therefore can replace the use in alum in treatment plants.

For future work, the oil can be extracted from the *J. Curcas* seeds prior to coagulation. Also, coagulation of higher concentrations of pharmaceutical wastewater can be studied. High Performance Liquid Chromatography (HPLC) can be used to detect the pharmaceuticals still present in the wastewater after coagulation and its corresponding concentration.

Acknowledgements

I would like to extend my utmost gratitude towards my supervisor, Ms. Nurhazwani Binti Ismail, for her guidance throughout this project and for her words of encouragement. I would also like to thank the laboratory technicians for providing training for the different apparatus required and for assisting us when having difficulty with any equipment.

I would also like to thank my friends for supporting me, for providing their help whenever needed. My special thanks to Rikesh Ramsurn for always encouraging me in the tough times.

Last but not least, my sincere thanks to my parents and family for the words of encouragement and for their guidance.

References

[1] "Pharmaceuticals in Drinking-water Public Health and Environment Water, Sanitation, Hygiene and Health," Switzerland, 2011.

[2] A. Shraim, A. Diab, A. Alsuhaimi, E. Niazy, M. Metwally, M. Amad, S. Sioud, and A. Dawoud, "Analysis of some pharmaceuticals in municipal wastewater of Almadinah Almunawarah," *Arab. J. Chem.*, vol. 10, pp. S719–S729, 2012.

[3] N. Deziel, "Pharmaceuticals in Wastewater Treatment Plant Effluent Waters," *Univ. Minnesota, Morris*, vol. 1, no. 2, pp. 1–20, 2014.

[4] X. Li and G. Li, "A Review : Pharmaceutical Wastewater Treatment Technology and Research in China," *Asia-Pacific Energy Equip. Eng. Res. Conf. (AP3ER 2015)*, pp. 345–348, 2015.

[5] Hendrawati, I. R. Yuliastri, Nurhasni, E. Rohaeti, H. Effendi, and L. K. Darusman, "The use of Moringa Oleifera Seed Powder as Coagulant to Improve the Quality of Wastewater and Ground Water," *IOP Conf. Ser. Earth Environ. Sci.*, vol. 31, p. 11, 2016.
[6] N. Fathinatul and R. Nithyanandam, "Wastewater Treatment by using Natural Coagulant," 2014.
[7] M. I. Ashraf, M. Ateeb, M. H. Khan, N. Ahmed, Q. Mahmood, and Zahidullah, "Integrated treatment of pharmaceutical effluents by chemical coagulation and ozonation," *Sep. Purif. Technol.*, vol. 158, pp. 383–386, 2016.
[8] G. Vijayaraghavan, T. Sivakumar, and a Vimal Kumar, "Application of plant based coagulants for wastewater treatment.," *Int. J. Adv. Eng. Res. Stud.*, vol. 1, no. 1, pp. 88–92, 2011.
[9] H. D. Beyene, T. D. Hailegebrial, and W. B. Direrssa, "Investigation of coagulation activity of cactus powder in water treatment," *J. Appl. Chem.*, vol. 1, no. 5, p. 9, Nov. 2016.
[10] M. Schiban, M. Antov, and M. Klasnja, "Extraction and Partial Purification of Coagulation of Coagulation Active Components from Common Bean Seed," University of Novi Sad, 2006.
[11] I. Da-Costa-Rocha, B. Bonnlaender, H. Sievers, I. Pischel, and M. Heinrich, "Hibiscus sabdariffa L. - A phytochemical and pharmacological review," *Food Chem.*, vol. 165, pp. 424–443, 2014.
[12] J. M. Nzikou, L. Matos, F. Mbemba, C. B. Ndangui, N. P. G. Pambou-Tobi, A. Kimbonguila, T. Silou, M. Linder, and S. Desobry, "Characteristics and Composition of Jatropha curcas Oils, Variety Congo-Brazzaville," *Res. J. Appl. Sci. Eng. Technol.*, vol. 1, no. 3, pp. 154–159, 2009.
[13] Z. Z. Abidin, N. S. Mohd Shamsudin, N. Madehi, and S. Sobri, "Optimisation of a method to extract the active coagulant agent from Jatropha curcas seeds for use in turbidity removal," *Ind. Crops Prod.*, vol. 41, no. 1, pp. 319–323, 2013.
[14] K. Openshaw, "A review of Jatropha curcas: An oil plant of unfulfilled promise," *Biomass and Bioenergy*, vol. 19, no. 1, pp. 1–15, 2000.
[15] S. Kumar Gupta, Y.-T. Hung, and S. Kumar Gupta, *Treatment of Pharmaceutical Wastes*, no. October 2005. 2005.
[16] Hlthman, "Waste water treatment 2 2.1," *Waste Water*, vol. 20, no. 30, pp. 1–18, 2002.
[17] K. I. E. Hainida, I. Amin, H. Normah, and N. Mohd.-Esa, "Nutritional and amino acid contents of differently treated Roselle (Hibiscus sabdariffa L.) seeds," *Food Chem.*, vol. 111, no. 4, pp. 906–911, 2008.
[18] Z. Ma, J.-J. Qin, C.-X. Liou, L. Zhang, and S. Valiyaveettil, "Effects of Coagulation, pH and Mixing Conditions on Characteristics of Flocs in Surface Water Treatment," National University of Singapore, 2012.
[19] H. Patel and R. T. Vashi, "Removal of Congo Red dye from its aqueous solution using natural coagulants," *J. Saudi Chem. Soc.*, vol. 16, no. 2, pp. 131–136, 2012.
[20] M. Y. Yong and N. Ismail, "Optimisation of hibiscus sabdariffa as a natural coagulant to treat Congo red in wastewater," *J. Eng. Sci. Technol.*, vol. 11, no. Special Issue onthefourtheureca2015, pp. 153–165, 2016.
[21] J. Xiao and H. Zhang, "Comparative evaluation of Jatropha curcas L. seed meals obtained by different methods of defatting on toxic, antinutritional and nutritive factors," *J. Food Sci. Technol.*, vol. 51, no. 6, pp. 1126–1132, 2014.
[22] A. E. Ugbogu, E. I. Akubugwo, F. O. Uhegbu, C. G. Chinyere, O. C. Ugbogu, and K. A. Oduse, "Quality assessment profile of Jatropha curcas (L) seed oil

from Nigeria," *Int. Food Res. J.*, vol. 21, no. 2, pp. 735–741, 2014.

[23] Z. Z. Abidin, N. Ismail, R. Yunus, I. S. Ahamad, and A. Idris, "A preliminary study on Jatropha curcas as coagulant in wastewater treatment," *Environ. Technol.*, vol. 32, no. 9, pp. 971–977, Jul. 2011.

eureca 2017 – Conference Paper
Paper Number 2CE10

Synthesis and Optimisation of A Sustainable Wastewater Treatment Plant via Material Flow Cost Account (MFCA)-based Approach

Run Ting Siew*, Yoke Kin Wan

School of Engineering, Taylor's University, Lakeside Campus, Jalan Taylors, 47500 Subang Jaya, Selangor, Malaysia

*siewting94@yahoo.com

Abstract
In this work, the concept of material cost flow accounting (MFCA) has been used to synthesise an optimum wastewater treatment plant (WWTP). MFCA is an analysis method that able to quantify the mass flow of a process into monetary unit. The ultimate purpose of MFCA concept is to reduce waste generation and to increase environmental performance. To incorporate the concept of MFCA, several costs have been taken into consideration in this work. This included raw material cost, energy cost, labour cost, and waste management cost as well as the hidden cost and carry-forward cost. Hidden cost is the cost that associated with the process stream, while the carry-forward cost is the cost that is carried forward from one process to another process. In addition, pollutants like TSS, COD, BOD and O&G have also been considered in this work to ensure the discharged water is complied with discharged regulations. To solve this problem, MFCA-based approached has been developed by formulating a series of mathematical equations (i.e., mass balance, contaminant equations, and cost computation equations) based on a generic superstructure that presented all possible pathways of WWTP. In this work, four continuous treatment stages (pre-treatment, chemical treatment, biological treatment and tertiary treatment) with various treatment technologies have been considered in the WWTP. The optimum pathway of WWTP has been selected based on the optimisation objective. To illustrate the developed approach, an industry case study, which is a sago wastewater treatment plant, has been solved. As results, an optimum sago wastewater treatment process with minimum waste generation cost is synthesised via a commercial optimisation software, LINGO. Sago wastewater treatment technologies of grit removal, coagulation-flocculation-DAF, MBR and carbon filter are selected as optimum pathway at the end.

Keywords: Synthesis, Optimisation, Wastewater treatment, MFCA, Organic wastewater.

1. Introduction

Due to the dramatic rise of human population and the rapid growth of industries, waste production rate is getting higher. Generally, wastes can be divided into organic waste (e.g., municipal solid waste (MSW), sewage wastewater, food wastes, etc.) and inorganic waste (e.g., electronic waste, plastics, pesticide, cans, metals, chemical wastes, etc.). Organic waste refers to the waste that consist of biodegradable materials meanwhile inorganic wastewater refers to the waste that consist of relative stable substances which cannot easily degradable by organisms [1]. According to Hoornweg et al. [2], three million tonnes of wastes was produced per day in year 2000, and this amount is expected to hit 6 million tonnes by year 2025. Thus, waste management is a crucial step to reduce environmental issues and to increase economic performance of an industry. Waste management involves various types of treatment processes to ensure the treated wastes complied with discharged regulations before being discharged to the environment.

Among the wastes above-mentioned, organic wastewater is the most common waste generated from industries and households daily. This is because huge amount of water is being used daily for cleaning purpose in industrial processes and household's activity. Numerous research works have been conducted for wastewater treatment technologies. Gobel et al. [3] evaluated elimination of pollutants in secondary (e.g., activated sludge, fludized bed reactor (FBR) and membrane bioreactor (MBR)) and tertiary treatment (e.g., sand filter). Performance of upflow anaerobic sludge blanket (UASB) also being evaluated by Manjunath et al. [4]. Besides that, Mamais et al. [5] and Ekama et al. [6] had researched removal of colloidal matter by using flocculation-precipitation method. Chen et al. [7] and Edzwald et al. [8] had reviewed electrochemical technologies and DAF treatment in WWTP respectively. Other than that, Lefebure et al. [9] also had reviewed physico-chemical treatments. Sustainability of treatment technologies such as mechanical, lagoon and land treatment system in WWTP also being evaluated by Muga et al. [10]. Microbial fuel sells (MFC) hybrid process being proposed by Li et al. [11] for sustainability of wastewater treatment process. In optimisation of WWTP technology, Finger et al. [12] had evaluated grit removal performance by varying operating conditions, whereas Al-Mutairi et al. [13] conducted research on coagulant selection and sludge conditioning on slaughterhouse WWTP. These showed that there are various different treatment technologies can be used to treat organic wastewater.

Apart from the conventional technologies, some research works have been done on new technologies. Gogate et al. [14] highlighted on newer technologies of biological oxidation processes (cavitation, photocatalytic oxidation, Fenton's chemistry, ozonation and hydrogen peroxide) and the comparison among different WWTP using Life Cycle Approach (LCA) had been done by Kalbar et al. [15]. Furthermore, different modelling on WWTP also had been done. Wilas et al. [16] based on plant capacities calculation and effluents standards for selection of treatment technology, Woods et al. [17] evaluated economic viable of phosphorus recovery processes, Gernaey et al. [18] focused on modelling of WWTP using white-box model, black-box, stochastic grey-box, and hybrid modelling. Apart from that, Albino et al. [19] used enterprise input-output model. Modelling on UASB performance being conducted by Singh et al. [20]. This showed that modelling is one of the vital tool for treatment technologies selection. In economic aspect, cost modelling (operating cost and maintenance cost) for wastewater treatment process had conducted by Hernendez-Sancho et al. [21]. For optimisation of wastewater treatment plant control, Durrenmatt et al. [22] had built

software sensors based on SCADA system of plant. In environmental aspect, Corominas et al. [23] had evaluated Greenhouse Gas Emission (GHG) of entire WWTP by comparing different modelling approaches (1. simple comprehensive model from empirical assumptions and 2. sophisticated model consist of Anaerobic Digestion Model 1 and also biological reactor).

As above-mentioned, many researches had been done on wastewater treatment technologies in aspect of removal efficiency, selection based on performance and optimum operating condition. Meanwhile, development and research on new wastewater treatment technologies also getting more interested on research field. All this imply that wastewater treatment are getting more important. Research on selection of wastewater technologies by modelling also had been done by using input-output model which take consideration on material and energy flows of production process. Apart from that, modelling on economic aspect, environmental aspect and optimisation on process control had also been done. Note that although many researches had done on WWTP technologies and modelling of WWTP processes, however selection of optimum wastewater treatment pathway based on MFCA concept which considered hidden cost of waste stream and product stream haven't be applied.

MFCA is Environmental Management Accounting (EMA) for material efficiency analysis of the process [24]. It focused on material flow, energy used and cost accounting [25]. Material cost, energy cost, system cost (e.g., labour cost, depreciation cost) and waste management cost being considered in cost accounting [26]. Significant of MFCA is hidden profits from waste generated can be determined so that further improvement can be done [26]. This is due to the fact that material cost is roughly similar around the world whereas labour cost, energy cost vary significantly by different countries [25]. Thus, MFCA can be the useful tool for cost reduction, higher material and energy management [25]. By doing this, value of corporate can be enhanced. Other than that, MFCA can be the management tool for green productivity since higher energy efficiency also imply that lesser CO_2 or waste will be generated from process so environmental performance can be maximised [26]. By concluding benefits above, MFCA account for both economic and environment aspects which lead to sustainability performance [26]. In September 2011, MFCA had become international standard (ISO 14051) and its application is expected to be increased in future [25].

MFCA had been successfully applied on different fields. These fields included lens manufacturing process, printing process, ceramics tiles manufacturing, Canon firm manufacturer and many more. In most recently, Wan et al. [27] developed MFCA-based approach for prioritisation of waste recovery. Two new costs terms were introduced by Wan et al. [27], which is hidden cost and carry-forward cost using the concept of MFCA. MFCA is a concept that focuses on distribution of imputing cost to waste streams. The main purpose of MFCA is to minimise environmental impact concurrently improve economic performance with the selection of minimum total hidden cost of waste stream [27]. Since MFCA concept focused on tracking in amount, quality and cost aspects of input and output material flow in processes, there are 4 types of cost considered in MFCA which are material, system, energy and waste management costs. Waste management is also taken into consideration since waste is considered as one of the by-product in MFCA concept. Attribution of energy, material and system cost are based on the distribution percentage of material toward product and waste stream. These costs were used to determine the hidden cost and carry-forward cost. Hidden cost is the summation cost of processing cost and carry-forward cost. Material, energy and system cost attributed to processing cost. Cost associated to recycle stream or intermediate

stream was identified as carry-forward cost. In conventional cost accounting concept, hidden cost that allocated to waste which consists significant cost is overlooked which might affect the final analysed result. Thus, in MFCA, each waste stream has its associated hidden cost which represents its cumulative cost invested to generate these waste. Consideration of hidden cost make MFCA concept more suitable for waste stream prioritisation selection than other accounting prioritisation approaches.

Hence, this research aimed to develop a MFCA-based approach to synthesise an optimum wastewater treatment process with minimum waste generation cost using the concept of MFCA. The significant of this study is the developed model can be used as decision making tool for technology selection to synthesize an optimum wastewater treatment plant. Meanwhile, it is to ensure the treated water is comply with the discharged regulations. In addition, the MFCA-based approach can be used for any type of wastewater by modifying the parameters. To illustrate the developed approach, an industrial case study is solve. In this work, organic sago wastewater treatment is selected as case study. The rest of this paper is organised as follows: research methodology is first presented which is followed by mass balance equations, contaminant balance equations, and cost computation equations of the MFCA-based approach. Then, case study on sago wastewater treatment is solved to illustrate the proposed approach. Finally, conclusion and future work are given at the end of paper.

2. Methodology

A generic wastewater treatment superstructure is first developed to show all possible pathway to treat wastewater as shown in Figure 1. Based on this generic superstructure, MFCA-based approach has been developed by formulating mathematical equations for each treatment in WWTP as shown in following sections. These equations included mass balance equation, contaminant equation, and cost computation equations. To demonstrate the developed approach, an industry case study, organic wastewater treatment plant is solved.

2.1 Generic Superstructure of Wastewater Treatment

A generic superstructure of wastewater treatment plant is shown in Figure 1 below. As shown, Feedstock *WW* represents wastewater supply with volumetric flow rate F_{WW}^{in} is treated through different treatment included pre-treatment $p \in P$, chemical treatment $c \in C$, biological treatment $b \in B$ and tertiary treatment $t \in T$ before convert into product *TW* which is treated water. With the aid of generic superstructure, a series of equations are formulated in the following sections.

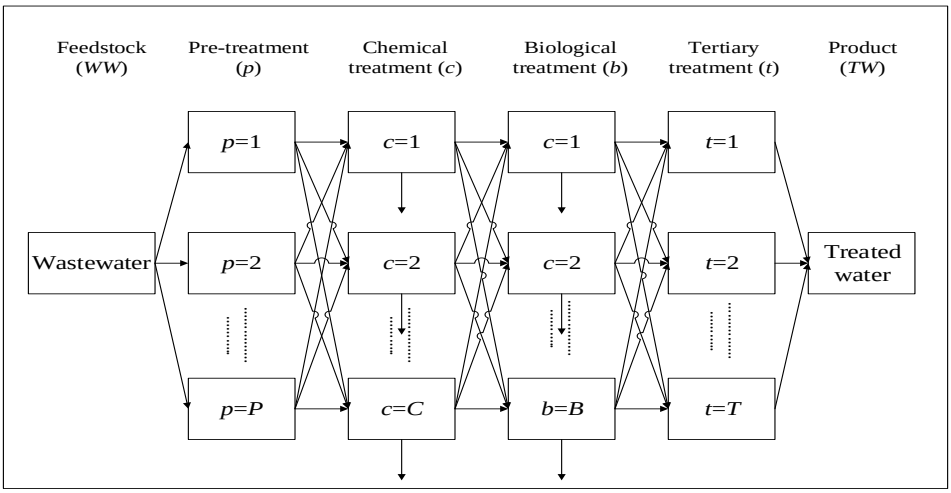


Figure 1: General superstructure for wastewater treatment.

2.2 Mathematical Equations

2.2.1 Mass Balance Equations

As shown in generic superstructure (Figure 1), the total flow rate of feedstock, $f\,F_{WW}^{in}$ will be distributed to pre-treatment, p with flowrate of $F_{WW,p}^{out}$ as shown in Eq. (1).

$$F_{WW}^{in} = \sum_{p=1}^{n} F_{WW,p}^{out} \qquad \forall WW \qquad (1)$$

In other words, the total flowrate that are received by pre-treatment, p F_p^{in} is shown as Eq. (2),

$$F_p^{in} = \sum_{WW=1}^{n} F_{WW,p}^{out} \qquad \forall p \qquad (2)$$

where $F_{WW,p}^{out}$ is the feedstock flowrate distributed to pre-treatment, p. As a generic rule of mass balance, the inlet flowrate, $F_p{}^{in}$ must be equal to outlet flowrate $F_p{}^{out}$ as shown in Eq. (3).

$$F_p^{in} = F_p^{out} \qquad \forall p \qquad (3)$$

In pre-treatment p, since it do not produce sludge. Thus, total inlet flow rate of pre-treatment, p will be distributed to chemical treatment, c with flowrate of $F_{p,c}{}^{out}$ as shown in Eq. (4) below. So, total flowrate that received by chemical treatment c, $F_c{}^{in}$ is shown on Eq. (5). Eq. (6) shown a constraint equation, inlet flowrate, $F_c{}^{in}$ must be equalled to outlet flowrate, $F_c{}^{out}$.

$$F_p^{in} = \sum_{c=1}^{n} F_{p,c}^{out} \qquad \forall p \qquad (4)$$

$$F_c^{in} = \sum_{p=1}^{n} F_{p,c}^{out} \qquad \forall c \qquad (5)$$

$$F_c^{in} = F_c^{out} \qquad \forall c \qquad (6)$$

For chemical treatment *c*, since there was additional sludge produced. So other than distribution to biological treatment, *b* with flowrate of $F_{c,b}^{out}$, another sludge produced from chemical treatment, *c* with flowrate of F_c^{sludge} is considered in Eq. (7).

$$F_c^{in} = \sum_{b=1}^{n} F_{c,b}^{out} + F_c^{sludge} \qquad \forall c \qquad (7)$$

Since there is only one stream that flow through biological treatment *b*, total flow rate received by biological treatment *b*, F_b^{in} can be defined as Eq. (8). Similarly to chemical treatment *c*, a constraint equation as shown in Eq. (9) is set,

$$F_b^{in} = \sum_{c=1}^{n} F_{c,b}^{out} \qquad \forall b \qquad (8)$$

$$F_b^{in} = F_b^{out} \qquad \forall b \qquad (9)$$

where F_b^{in} is inlet flowrate of biological treatment *b* and F_b^{out} is outlet flowrate of biological treatment. Besides, there was sludge produced on biological treatment *b*. Thus, total outlet flowrate of biological, F_b^{out} is given as Eq. (10),

$$F_b^{out} = \sum_{t=1}^{n} F_{b,t}^{out} + F_b^{sludge} \qquad \forall b \qquad (10)$$

where $F_{b,t}^{out}$ is the flowrate of biological treatment, *b* that will be distributed to tertiary treatment, *t* and F_b^{sludge} is the sludge flowrate produced in biological treatment. Similar to previous case, total flowrate which received by tertiary treatment *t*, F_t^{in} is shown in Eq. (11). Eq. (12) shown generic rule of mass balance which inlet flowrate of F_t^{in} must be equaled to outlet flowrate of F_t^{out}. In addition, Eq. (13) shown the treated water, *TW* that discharged from tertiary treatment, *t* with flowrate of F_{TW}.

$$F_t^{in} = \sum_{b=1}^{n} F_{b,t}^{out} \qquad \forall t \qquad (11)$$

$$F_t^{in} = F_t^{out} \qquad \forall t \qquad (12)$$

$$F_{TW} = \sum_{t=1}^{n} F_t^{out} \qquad (13)$$

2.2.2 Contaminant Balance Equations on COD

First, COD concentration at feed inlet is represented in $C_{WW}^{COD,in}$ in ppm unit. COD removal efficiency for pre-treatment *p*, chemical treatment *c*, biological treatment *b* and tertiary treatment *t* are given as x_p^{COD}, x_c^{COD}, x_b^{COD}, x_t^{COD} respectively. For sludge yield in chemical *c* and biological treatment *b* are represented as $Y_c^{COD,sludge}$ and $Y_b^{COD,sludge}$, both with unit of kg sludge/kg COD removed. Sludge density for chemical and biological treatment are represented by ρ_c^{sludge} and ρ_b^{sludge}.

In order to determine the mass of COD, $m_p^{COD,in}$ at inlet of pre-treatment, *p* total flow rate received by pre-treatment that determined Eq. (2) is multiplied with COD concentration at feed inlet as shown in Eq. (14).

$$m_p^{COD,in} = F_p^{in} \times C_{ww}^{COD,in} \qquad \forall p \tag{14}$$

By using removal efficiency x_p^{COD}, outlet COD mass, $m_p^{COD,out}$ and removal COD mass, $m_p^{COD,Rev}$ from pre-treatment, *p* can be determined using Eq. (15) and (16).

$$m_p^{COD,out} = m_p^{COD,in} \times (1 - x_p^{COD}) \qquad \forall p \tag{15}$$

$$m_p^{COD,Rev} = m_p^{COD,in} \times x_p^{COD} \qquad \forall p \tag{16}$$

Then, concentration of COD, $C_p^{COD,out}$ at pre-treatment outlet can be determined via:

$$C_p^{COD,out} = \frac{m_p^{COD,out}}{F_p^{out}} \qquad \forall p \tag{17}$$

Next, mass of COD $m_c^{COD,in}$ at inlet stream to chemical treatment, *c* can be calculated by using COD concentration obtained above multiplied with distribution of flowrate from pre-treatment *p* to chemical treatment *c*, $F_{p,c}^{out}$ which as shown in Eq. (18).

$$m_c^{COD,in} = C_p^{COD,out} \times F_{p,c}^{out} \qquad \forall c \tag{18}$$

By using removal efficiency x_c^{COD} for chemical treatment *c*, outlet COD mass $m_c^{COD,out}$ and removal COD mass $m_c^{COD,Rev}$ can be determined as shown on Eq. (19) and (20).

$$m_c^{COD,out} = m_c^{COD,in} \times (1 - x_c^{COD}) \qquad \forall c \tag{19}$$

$$m_c^{COD,Rev} = m_c^{COD,in} \times x_c^{COD} \qquad \forall c \tag{20}$$

Based on amount of COD removed in chemical treatment *c*, sludge volumetric flow rate F_c^{sludge} can be determine by using sludge yield $Y_c^{COD,sludge}$ and density ρ_c^{sludge} for chemical treatment *c* as shown in Eq. (21) below.

$$F_c^{sludge} = \frac{Y_c^{COD,sludge}}{\rho_c^{sludge}} \times m_c^{COD,\mathrm{Re}v} \qquad \forall c \qquad (21)$$

For biological treatment *b* and tertiary treatment *t*, same procedure can be used to determine COD outlet mass and COD removal from each treatment. Similar to chemical treatment *c*, additional sludge volumetric flow rate need to be account in biological treatment *b*. All equations involved can be represented by Eq. (22) to (30) below.

$$C_c^{COD,out} = \frac{m_c^{COD,out}}{F_c^{out}} \qquad \forall c \qquad (22)$$

$$m_b^{COD,in} = C_c^{COD,out} \times F_{c,b}^{out} \qquad \forall b \qquad (23)$$

$$m_b^{COD,out} = m_b^{COD,in} \times (1 - x_b^{COD}) \qquad \forall b \qquad (24)$$

$$m_b^{COD,\mathrm{Re}v} = m_b^{COD,in} \times x_b^{COD} \qquad \forall b \qquad (25)$$

$$F_b^{sludge} = \frac{Y_b^{COD,sludge}}{\rho_b^{sludge}} \times m_b^{COD,\mathrm{Re}v} \qquad \forall b \qquad (26)$$

$$C_b^{COD,out} = \frac{m_b^{COD,out}}{F_b^{out}} \qquad \forall b \qquad (27)$$

$$m_t^{COD,in} = C_b^{COD,out} \times F_{b,t}^{out} \qquad \forall t \qquad (28)$$

$$m_t^{COD,out} = m_t^{COD,in} \times (1 - \mathrm{x}_t^{COD}) \qquad \forall t \qquad (29)$$

$$m_t^{COD,\mathrm{Re}v} = m_t^{COD,in} \times \mathrm{x}_t^{COD} \qquad \forall t \qquad (30)$$

where $C_c^{COD,out}$ is concentration of COD at chemical treatment outlet, F_c^{out} is outlet flowrate of chemical treatment, $m_b^{COD,in}$ is mass of COD at inlet stream to biological treatment, $F_{c,b}^{out}$ is distribution of flowrate from chemical treatment to biological treatment, $m_b^{COD,out}$ is outlet COD mass, $m_b^{COD,Rev}$ is removal COD mass, x_b^{COD} is COD removal efficiency for biological treatment, F_b^{sludge} is sludge flowrate of biological treatment, $C_b^{COD,out}$ is concentration of COD at biological treatment outlet, F_b^{out} is outlet flowrate of biological treatment, $m_t^{COD,in}$ is COD mass at inlet stream of tertiary treatment, $F_{b,t}^{out}$ is distribution of flowrate from biological to tertiary treatment, $m_t^{COD,out}$ is outlet COD mass, $m_t^{COD,Rev}$ is removal COD mass and x_t^{COD} is COD removal efficiency at tertiary treatment.

In order to comply with COD discharge standard, outlet COD concentration for tertiary treatment *t*, $C_t^{COD,out}$ which is treated water need to be convert from mass that shows on

Eq. (31). Eq. (32) below shown calculated COD concentration must comply with $C^{Std,COD}$ which is standard concentration for COD.

$$C_t^{COD,out} = \frac{m_t^{COD,out}}{F_t^{out}} \qquad \forall t \qquad (31)$$

$$C_t^{COD,out} < C^{Std,COD} \qquad (32)$$

2.2.3 Contaminant Balance Equations on BOD, TSS, O&G

Formulation of contaminant balance equation for BOD, TSS and O&G is same as the formulation of COD balance equation above but just need to replace respective index value into all COD balance equations above.

2.2.4 Cost Computation Equations

Operating cost for technology in each treatment take account of raw material cost, energy cost and labour cost. Thus, operating cost of pre-treatment *p* $Cost_p^{opt}$ can be determine as Eq. (33) below.

$$Cost_p^{mat} + Cost_p^{enegy} + Cost_p^{labour} = Cost_p^{opt} \qquad \forall p \qquad (33)$$

where $Cost_p^{mat}$ is raw material cost, $Cost_p^{energy}$ is energy cost and $Cost_p^{labour}$ is labour cost. Based on calculated pre-treatment *p* operating cost, hidden unit cost for pre-treatment $UCost_p^{Hidden}$ can be determined via:

$$UCost_p^{Hidden} = \frac{Cost_p^{opt}}{F_p^{in}} \qquad \forall p \qquad (34)$$

Carry-forward cost from pre-treatment *p* to chemical treatment *c*, $CFC_{p,c}$ can be determined using Eq. (35) below.

$$CFC_{p,c} = UCost_p^{Hidden} \times F_{p,c}^{out} \qquad \forall p \forall c \qquad (35)$$

Similar to operating cost determination of pre-treatment *p*, operating cost of chemical treatment *c*, $Cost_c^{opt}$ is determined on Eq. (36) below with an additional carry-forward cost from Eq. (35). By using calculated chemical treatment *c* operating cost, hidden unit cost of chemical treatment *c* $UCost_c^{Hidden}$ is calculated using Eq. (37) below.

$$Cost_c^{mat} + Cost_c^{enegy} + Cost_c^{labour} + \sum_{p=1}^{n} CFC_{p,c} = Cost_c^{opt} \qquad \forall c \qquad (36)$$

$$UCost_c^{Hidden} = \frac{Cost_c^{opt}}{F_c^{in}} \qquad \forall c \qquad (37)$$

where $Cost_c^{mat}$ is raw material cost , $Cost_c^{energy}$ is energy cost and $Cost_c^{labour}$ is labour cost for chemical treatment *c*.

In chemical treatment *c*, instead of just carry forward cost from chemical treatment *c* to biological treatment *b* $CFC_{c,b}$, there is another hidden cost for sludge generation HC_c^{sludge} as shown in Eq. (38) and (39).

$$CFC_{c,b} = UCost_c^{Hidden} \times F_{c,b}^{out} \qquad \forall c \forall b \qquad (38)$$

$$HC_c^{sludge} = UCost_c^{Hidden} \times F_c^{sludge} \qquad \forall c \qquad (39)$$

For biological treatment *b* and tertiary treatment *t* same procedure can be used to determine operating cost, hidden unit cost and carry-forward from each treatment. Similar to chemical treatment *c*, additional sludge hidden cost need to be account in biological treatment *b*. All equations involved can be represented by Eq. (40) to (46) below.

$$Cost_b^{mat} + Cost_b^{energy} + Cost_b^{labour} + \sum_{c=1}^{n} CFC_{c,b} = Cost_b^{opt} \qquad \forall b \qquad (40)$$

$$UCost_b^{Hidden} = \frac{Cost_b^{opt}}{F_b^{in}} \qquad \forall b \qquad (41)$$

$$CFC_{b,t} = UCost_b^{Hidden} \times F_{b,t}^{out} \qquad \forall b \forall t \qquad (42)$$

$$HC_b^{sludge} = UCost_b^{Hidden} \times F_b^{sludge} \qquad \forall b \qquad (43)$$

$$Cost_t^{mat} + Cost_t^{energy} + Cost_t^{labour} + \sum_{b=1}^{n} CFC_{b,t} = Cost_t^{opt} \qquad \forall t \qquad (44)$$

$$UCost_t^{Hidden} = \frac{Cost_t^{opt}}{F_t^{in}} \qquad \forall t \qquad (45)$$

$$CFC_{t,TW} = UCost_t^{Hidden} \times F_t^{out} \qquad \forall t \forall TW \qquad (46)$$

where $Cost_b^{mat}$, $Cost_b^{energy}$, $Cost_b^{labour}$ and $Cost_b^{opt}$ are raw material cost, energy cost, labour cost and operating cost for biological treatment *b*. $UCost_b^{Hidden}$ is hidden unit cost for biological treatment *b*. Carry-forward cost from biological treatment *b* to tertiary treatment *t* and sludge hidden cost for biological treatment *b* are $CFC_{b,t}$ and HC_b^{sludge} respectively. Raw material cost, energy cost, labour cost and operating cost involved in tertiary treatment *t* are represented by $Cost_t^{mat}$, $Cost_t^{energy}$, $Cost_t^{labour}$ and $Cost_t^{opt}$ respectively. $UCost_t^{Hidden}$ is hidden unit cost for tertiary treatment *t*, $CFC_{t,TW}$ is carry-forward cost from tertiary treatment *t* to product.

Once cost accounted on all streams around each treatment by using all cost computation equations above, total hidden cost for product and total sludge produced can be determined by Eq. (47) and (48) below.

$$HC^{TW} = \sum_{t=1}^{n} CFC_{t,TW} \qquad (47)$$

$$HC^{Total,sludge} = \sum_{c=1}^{n} HC_c^{sludge} + \sum_{b=1}^{n} HC_b^{sludge} \quad (48)$$

Hence total hidden cost HC^{Total} and total operating cost of technology involved in each treatment $Cost^{Total\ opt}$ for entire wastewater treatment can be calculated via:

$$HC^{Total} = HC^{TW} + HC^{Total,sludge} \quad (49)$$

$$Cost^{Total,opt} = \sum_{p=1}^{n} Cost_p^{opt} + \sum_{c=1}^{n} Cost_c^{opt} + \sum_{b=1}^{n} Cost_b^{opt} + \sum_{t=1}^{n} Cost_t^{opt} \quad (50)$$

Finally, optimization objective of this modelling is to minimize HC^{Total} as shown in Eq. (51) below.

$$Min = HC^{Total} \quad (51)$$

In order to demonstrate approach that mentioned above, a case study is solved in the following section.

2.3 Case Study

A sago wastewater treatment is select as case study in this research. Thus, Figure 2 below shows superstructure of organic wastewater treatment with specific technologies listed on different treatment. Based on comprehensive literature review done on organic wastewater treatment technology, typical wastewater treatment technologies used in organic wastewater treatment is adopted as treatment technologies in each treatment stage which presented in Figure 2 below.

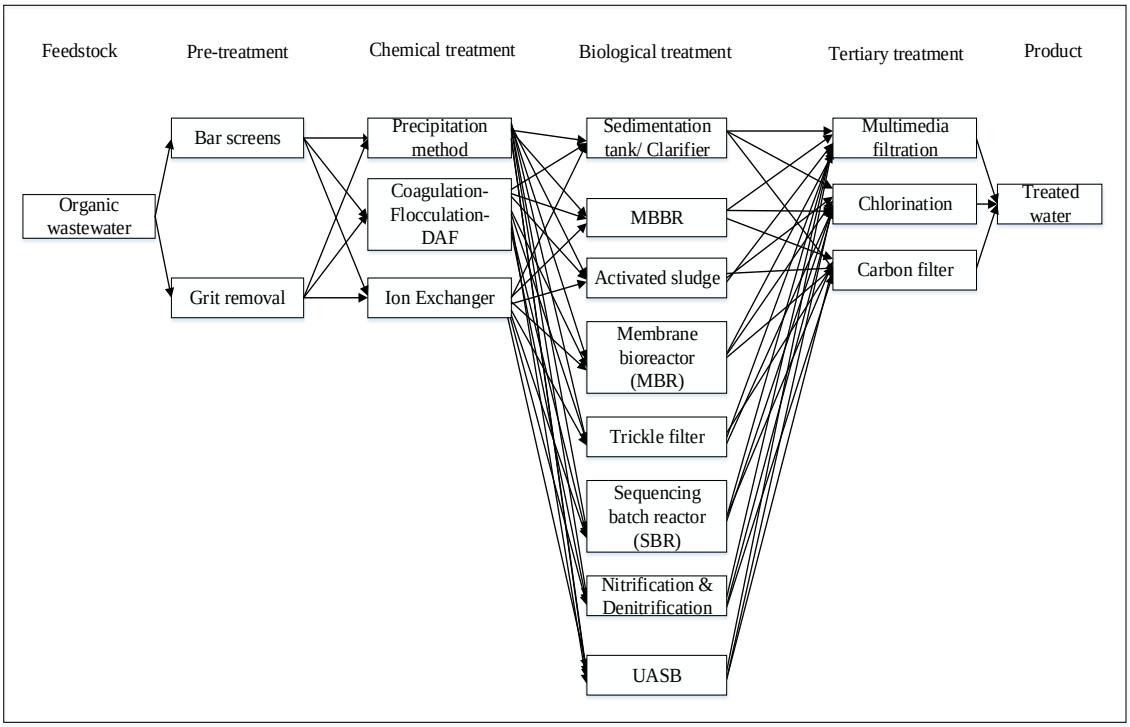


Figure 2: Superstructure of organic wastewater treatment

As shown, organic wastewater treatment begins with pre-treatment which consists of bar screen and grit removal. Next is chemical treatment with technologies of precipitation method, coagulation-flocculation-DAF and ion exchanger. Then follow by biological treatment which involved sedimentation tank/clarifier, MBBR, activated sludge and others. Tertiary treatment is the final treatment stage with multimedia filtration, chlorination and carbon filter. Through selection of technology in each treatment stage, treated water that complied with discharged regulation can be generated.

Contaminants characteristic of sago wastewater and discharged regulations are tabulated in Table 1 below. Contaminants characteristics of sago wastewater is based on sago mill industry in Sarawak [28]. Besides that, contaminant removal efficiency of each technology on different treatment stage are summarised in Table 2. Apart from that, in Table 3, operating cost such as raw material cost, energy cost and labour cost in each technology is tabulated.

For energy cost for cost computation listed in each technology on Table 3, it included electricity consumption of pumps, compressors, clarifier and other equipment which involved in that particular treatment.

Table 1: Sago wastewater contaminants characteristic and discharged regulations [28][29]

	Concentration (ppm)			
	TSS	COD	BOD	O&G
Sago wastewater	4800	11650	5750	300
Discharge regulations (Standard A)	50	50	20	10

Table 2: Contaminant removal efficiency of technologies

Pre-treatment [30][31]				
	Removal efficiency (%)			
	TSS	COD	BOD	O&G
Bar Screen	50	20	35	85
Grit Removal	50	20	30	90
Chemical treatment [32][33][34][35]				
	Removal efficiency (%)			
	TSS	COD	BOD	O&G
Precipitation Method	90	80	80	50
Coagulation-Flocculation-DAF	85	80	70	95
Ion Exchanger	0	38	38	20
Biological treatment [33][36][37][38][39]				
	Removal efficiency (%)			
	TSS	COD	BOD	O&G
Sedimentation Tank	70	20	35	20
MBBR	0	85	88	0
Activated Sludge	61	72	90	0
MBR	99	97	98	0
Trickle Filter	95	85	90	0

SBR	98	85	98	79
Nitrification/Denitrification	0	81	89	0
UASB	80	80	85	0
Tertiary treatment [40][41]				
	Removal efficiency (%)			
	TSS	COD	BOD	O&G
Multimedia Filtration	86	69	67	0
Carbon Filter	0	30	50	0
Chlorination	0	10	20	0

Table 3: Operating cost of technologies

Pre-treatment [30][31]				
	Cost (USD/day)			
	Raw material	Energy	Labour	Opt. cost
Bar Screen	0	1668.48	174	1842.48
Grit Removal	0	973.52	174	1147.52
Chemical treatment [33][34][35][38][42]				
	Cost (USD/day)			
	Raw material	Energy	Labour	Opt. cost
Precipitation Method	0.18	1264.9	632	1897.18
Coagulation-Flocculation-DAF	240.87	30.6	696	967.47
Ion Exchanger	472.22	97.22	175	1094.44
Biological treatment [33][34][42][43]				
	Cost (USD/day)			
	Raw material	Energy	Labour	Opt. cost
Sedimentation Tank	0	184.252	175	359.252
MBBR	0	695	875	1570
Activated Sludge	0	9147.3	1427	10574.3
MBR	0	8295	1095	9390
Trickle Filter	0	5840.565	1095	6935.57
SBR	0	833.33	875	1708.33
Nitrification/Denitrification	5039	702	875	6616
UASB	0	4740	875	5615
Tertiary treatment [40][41][43]				
	Cost (USD/day)			
	Raw material	Energy	Labour	Opt. cost
Multimedia Filtration	0	1043.5	875	1918.5
Carbon Filter	67	373	875	1315
Chlorination	208.33	373	875	1456.33

Based on sago wastewater treatment plant with flowrate of 79,000 m^3/day and the contaminants characteristic as shown in Table 1, mass of TSS, COD, BOD and O&G are determined as 379,200, 920,350, 454,250 and 23,700 kg/day, respectively. By input respective contaminant removal efficiency and operating cost of each

technology into previous mass and cost computation modelling equations, selection among treatment technology has been done by using LINGO software.

As results, technology that gives minimum hidden cost meanwhile comply with discharge regulations is selected in each treatment stage. Table 4 shows concentration of contaminants on selected technology in each treatment stage. Apart from that, in order to ensure the final treated water that discharged from the selected treatment technologies is complied with discharged regulation (standard A), Table 5 is presented to show the comparison between contaminants concentration of treated water with discharged regulation. It can be clear identified that all contaminants concentration of treated water was lower that discharged regulation so it is safe to be discharged to water bodies.

Next, cost computation is being considered using MFCA concept. Results of unit cost, hidden cost and carry-forward cost for each treatment technology selected by solving Eq. (33) - (46) are summarized in Table 6. Since additional sludge being produced in chemical and biological treatment, so additional hidden cost being calculated via Eq. (39) and (43). Besides that, total hidden cost of entire WWTP also shown in Table 6.

As shown, minimum total hidden cost (THC) of 12,819.98 USD/day can be achieved by selecting grit removal, coagulation-flocculation-DAF, MBR and carbon filter as treatment technology in entire WWTP. THC is calculated by summation of carry-forward cost from tertiary treatment to treated water, hidden cost for sludge generation of chemical and biological treatment. By referring to cost computation equations in section 2.2.4, calculation of unit cost, carry-forward cost and hidden cost are based on operating cost and volumetric flow rate around each treatment technology. Due to conservation of mass, inlet and outlet volumetric flow around each technology must be equal. Hence, operating cost of technology stands out to be one of the main factor in determine value of hidden cost and carry-forward cost. On other word, higher operating cost will lead to higher hidden cost and carry-forward cost.

Table 4: Contaminants concentration on selected technologies

Treatment	Technology	Stream	Contaminant concentration (ppm)			
			TSS	COD	BOD	O&G
Pre-treatment	Grit removal	Inlet	4800	11650	5750	300
		Outlet	2400	9320	4025	30
Chemical treatment	Coagulation-Flocculation-DAF	Inlet	2400	9320	4025	30
		Outlet	389	2014.177	1304.785	1.62
Biological treatment	MBR	Inlet	389	2014.177	1304.785	1.62
		Outlet	4.12	64.02	27.648	1.72
Tertiary treatment	Carbon filter	Inlet	4.12	64.02	27.648	1.72
		Outlet	4.12	44.8	13.8	1.72

Table 5: Comparison between contaminants concentration of treated water with discharged regulations

	Concentration (ppm)			
	TSS	COD	BOD	O&G
Treated water	4.12	44.8	13.8	1.72
Discharged regulations	50	50	20	10

Table 6: Results of unit cost, hidden cost and carry-forward cost of each treatment technology

Treatment	Technology	Cost (USD/day)		
		Unit cost	Carry-forward cost	Hidden cost
Pre-treatment	Grit removal	0.0145	1,147.52	-
Chemical treatment	Coagulation-Flocculation-DAF	0.02677	1,957.30	**157.69**
Biological treatment	MBR	0.1552	10,709.91	**673.38**
Tertiary treatment	Carbon Filter	0.1743	**12,024.91**	-
Total hidden cost			**5,279.65**	

In pre-treatment, grit removal is being selected instead of bar screen. This is due to both technologies have comparable contaminants removal efficiency however grit removal provide lower operating cost than bar screen which can be clearly identified on Table 3.

Among three technologies in chemical treatment, ion exchanger is eliminated due to low contaminants removal efficiency. Although contaminants removal efficiency of precipitation method is similar to coagulation-flocculation-DAF but high operating cost in precipitation method which makes it uneconomical. Thus coagulation-flocculation-DAF is selected as chemical treatment technology.

Even though operating cost for MBR ranked as second highest among technologies in biological treatment, it still selected as technology for biological treatment. The main reason is MBR provide high contaminants removal efficiency especially in COD. Although highest COD removal technology being selected in pre-treatment, chemical treatment and tertiary treatment, up to 87% of COD removal efficiency technology must be selected for biological treatment in order to meet discharged regulations This imply that technologies in biological treatment having COD removal efficiency lower than 87% would not be considered as selection. Based on Table 2, it can be clearly identified that all technologies have COD removal efficiency lesser than 87% except MBR which make MBR necessary to be selected as biological treatment technology. In biological treatment, the main factor for technology selection is technology contaminants removal performance instead of operating cost.

In tertiary treatment, since final treated water is just to discharge into water bodies. So multimedia filtration which provide high purity on treated water is not necessary to be selected. Moreover, operating cost of multimedia filtration is the highest

among tertiary treatment technologies. By comparing among chlorination and carbon filter, since chlorination operating cost is higher than carbon filter meanwhile chlorination treatment is specific on disinfection which is not necessary for sago wastewater treatment. Thus, carbon filter is selected as tertiary treatment technology.

4. Conclusion

A novel MFCA-based approach is developed in this work for optimum pathway selection of wastewater treatment plant. Hidden cost associated to treatment waste stream is considered using this approach for WWTP pathway selection. Case study of sago wastewater is solved to illustrate the proposed approach. Trends of wastewater treatment pathway selection also analysed. In case study, there are several factors such as discharged wastewater quality, technology operating cost and sludge yield that will affect selection of wastewater treatment pathway. To determine minimum THC of WWTP, these factors are traded off by using MFCA based-approach. Thus, this approach can be used as selection tools for decision maker in selection of wastewater treatment pathway so that both economic and environmental aspect can be monitored and improved. This approach could be further extended for systhesis and optimisation of wastewater treatment plant by considering sludge handling technologies and cost.

Acknowledgment

The author wish to acknowledge Dr. Wan Yoke Kin and Dr. Viknesh Andiappan for their kind support and guidance for this research work.

References

[1] N. K. S. Lawrence K. Wang, Yung-Tse Hung, *Handbook of Advanced Industrial and Hazardous Wastes Treatment - Google Books*. Taylor & Francis Group , 2010.

[2] D. Hoornweg, P. Bhada-Tata, and C. Kennedy, “Environment: Waste production must peak this century,” *Nature*, vol. 502, no. 7473, pp. 615–617, Oct. 2013.

[3] A. Göbel, C. S. McArdell, A. Joss, H. Siegrist, and W. Giger, “Fate of sulfonamides, macrolides, and trimethoprim in different wastewater treatment technologies,” *Sci. Total Environ.*, vol. 372, no. 2–3, pp. 361–371, 2007.

[4] N. T. Manjunath, I. Mehrotra, and R. P. Mathur, “Treatment of wastewater from slaughterhouse by DAF-UASB system,” *Water Res.*, vol. 34, no. 6, pp. 1930–1936, 2000.

[5] D. Mamais, D. Jenkins, and P. Prrr, “A rapid physical-chemical method for the determination of readily biodegradable soluble COD in municipal wastewater,” *Water Res.*, vol. 27, no. 1, pp. 195–197, 1993.

[6] Ekama GA; Marais GvR, “Theory, design and operation of nutrient removal activated sludge processes,” 1984.

[7] G. Chen, “Electrochemical technologies in wastewater treatment,” *Sep. Purif. Technol.*, vol. 38, no. 1, pp. 11–41, 2004.

[8] J. K. Edzwald, “Principles and applications of dissolved air flotation,” *Water Sci. Technol.*, vol. 31, no. 3–4, pp. 1–23, 1995.

[9] O. Lefebvre and R. Moletta, “Treatment of organic pollution in industrial saline wastewater: A literature review,” *Water Res.*, vol. 40, no. 20, pp. 3671–3682,

2006.
[10] H. E. Muga and J. R. Mihelcic, “Sustainability of wastewater treatment technologies,” *J. Environ. Manage.*, vol. 88, no. 3, pp. 437–447, 2008.
[11] W.-W. Li, H.-Q. Yu, and Z. He, “Towards sustainable wastewater treatment by using microbial fuel cells-centered technologies,” *Energy Environ. Sci.*, vol. 7, no. 3, pp. 911–924, 2013.
[12] R. E. Finger, J. Parrick, and R. E. Finger, “Optimization removal grit a wastewater of at treatment of,” vol. 52, no. 8, pp. 2106–2116, 2015.
[13] N. Z. Al-Mutairi, M. F. Hamoda, and I. Al-Ghusain, “Coagulant selection and sludge conditioning in a slaughterhouse wastewater treatment plant,” *Bioresour. Technol.*, vol. 95, no. 2, pp. 115–119, 2004.
[14] P. R. Gogate and A. B. Pandit, “A review of imperative technologies for wastewater treatment I: Oxidation technologies at ambient conditions,” *Adv. Environ. Res.*, vol. 8, no. 3–4, pp. 501–551, 2004.
[15] P. P. Kalbar, S. Karmakar, and S. R. Asolekar, “Assessment of wastewater treatment technologies: Life cycle approach,” *Water Environ. J.*, vol. 27, no. 2, pp. 261–268, 2013.
[16] B. M. Practices, B. Treatment, S. Treatment, and Z. D. Options, “Wastewater treatment technologies,” *Facilities*, vol. 4, pp. 33–43, 1996.
[17] N. C. Woods, S. M. Sock, and G. T. Daigger, “Phosphorus recovery technology modeling and feasibility evaluation for municipal wastewater treatment plants,” *Environ. Technol.*, vol. 20, no. March 2015, pp. 663–679, 1999.
[18] K. V. Gernaey, M. C. M. Van Loosdrecht, M. Henze, M. Lind, and S. B. Jørgensen, “Activated sludge wastewater treatment plant modelling and simulation: State of the art,” *Environ. Model. Softw.*, vol. 19, no. 9, pp. 763–783, 2004.
[19] V. Albino, E. Dietzenbacher, and S. Kühtz, “Analysing materials and energy flows in an industrial district using an enterprise input-output model,” *Econ. Syst. Res.*, vol. 15, no. 4, pp. 457–480, 2003.
[20] K. P. Singh, N. Basant, A. Malik, and G. Jain, “Modeling the performance of ‘up-flow anaerobic sludge blanket’ reactor based wastewater treatment plant using linear and nonlinear approaches-A case study,” *Anal. Chim. Acta*, vol. 658, no. 1, pp. 1–11, 2010.
[21] F. Hernandez-Sancho, M. Molinos-Senante, and R. Sala-Garrido, “Cost modelling for wastewater treatment processes,” *Desalination*, vol. 268, no. 1–3, pp. 1–5, 2011.
[22] D. J. Dürrenmatt and W. Gujer, “Data-driven modeling approaches to support wastewater treatment plant operation,” *Environ. Model. Softw.*, vol. 30, pp. 47–56, 2012.
[23] L. Corominas, X. Flores-Alsina, L. Snip, and P. A. Vanrolleghem, “Comparison of different modeling approaches to better evaluate greenhouse gas emissions from whole wastewater treatment plants,” *Biotechnol. Bioeng.*, vol. 109, no. 11, pp. 2854–2863, 2012.
[24] M. NAKAJIMA, “APO e-Learning Course on Green Productivity and Material Flow Cost Accounting (MFCA) Module,” 2012.
[25] A. W. Hiroshi Tachikawa, “(NPO)Module1_Day1_Overview_MFCA _Mr.Tachikawa_ForDistribution (1).pdf,” *Propharm Japan Co., Ltd.* [Online]. Available: https://www.dropbox.com/home/FYP/Concept of MFCA?preview=(NPO)Module1_Day1_Overview_MFCA_Mr.Tachikawa_ForDistribution+(1).pdf. [Accessed: 04-May-2017].

[26] Y. Furukawa, “APO e-Learning Course on Green Productivity and Material Flow Cost Accounting,” no. C, 2012.

[27] Y. K. Wan, R. T. L. Ng, D. K. S. Ng, and R. R. Tan, “Material flow cost accounting (MFCA)-based approach for prioritisation of waste recovery,” *J. Clean. Prod.*, vol. 107, pp. 602–614, 2015.

[28] W. Yoke Kin, “SYHTHESISE A SUSTAINABLE SAGO INDUSTRY,” 2008.

[29] E. Q. A. EQA, “Sewage Characteristics and Effluent Discharge Requirements, Volume4, Section 3.,” *Malaysian Sewerage Ind. Guidel.*, vol. 4, 1974.

[30] US EPA, “Combined Sewer Overflow Technology Fact Sheet,” *Environ. Prot.*, 1999.

[31] United States, Environmental Protection, and Agency, “Wastewater Technology Fact Sheet,” 1999.

[32] P. Molahalli, “Chemical Pre-Precipitation of Municipal Wastewater Treatment,” p. 52, 2011.

[33] A. O. Tanyi, “Comparison of Chemical and Biological Phosphorus Removal in Wastewater - a Modelling Approach,” pp. 72–78, 2013.

[34] I. Hamawand and N. Centre, “Review of wastewater treatment chemicals and organic chemistry alternatives for abattoir effluent,” pp. 1–67, 2015.

[35] F. A. Brinson *et al.*, “EVALUATING NANOFILTRATION , REVERSE OSMOSIS , AND ION EXCHANGE TO MEET CONSUMPTIVE USE CONSTRAINTS AND FINISHED WATER QUALITY GOALS FOR BROWARD COUNTY Scope of Analysis,” 2002.

[36] M. M. Socías-viciana, “Coagulation-flocculation of domestic wastewater by moroccan clays : Removal of organic matter and suspended solids MOROCCAN CLAYS : REMOVAL OF ORGANIC MATTER AND,” no. April 2016, 2014.

[37] A. G. Kapagiannidis, I. Zafiriadis, and A. Aivasidis, “Upgrading the efficiency of an external nitrification BNR system – The modified Dephanox process,” *Chem. Eng. J.*, vol. 175, pp. 124–135, 2011.

[38] K. Kim, “The characteristic of the sequencing batch reactor (SBR), anaerobic sequencing batch reactor (ASBR) and sequencing batch biofilm reactor (SBBR) Koobum Kim,” *Most*, 2011.

[39] A. Aygun, B. Nas, and A. Berktay, “Influence of High Organic Loading Rates on COD Removal and Sludge Production in Moving Bed Biofilm Reactor,” *Environ. Eng. Sci.*, vol. 25, no. 9, pp. 1311–1316, 2008.

[40] T. M. Huggins, A. Haeger, J. C. Biffinger, and Z. J. Ren, “Granular biochar compared with activated carbon for wastewater treatment and resource recovery,” *Water Res.*, vol. 94, pp. 225–232, 2016.

[41] M. L. Gulhane and A. U. Charpe, “Domestic Wastewater Treatment using Multimedia Filter Technology,” vol. 3, no. 1, pp. 1119–1121, 2015.

[42] F. Jiang, M. Beck, R. Cummings, and K. Rowles, “Estimation of costs of phosphorus removal in wastewater treatment facilities: construction de novo,” *Water Policy Work.*, no. June, pp. 1–28, 2004.

[43] A. Wendland and Y. Ozoguz, “Operation Costs of Wastewater Treatment Plants,” 2013.

eureca 2017 – Conference Paper
Paper Number 2CE11

Preliminary Study on Effect of Chemical Composition Alteration on Elastic Recovery and Stress Recovery of Nitrile Gloves

Kai Yang Tan[1*], Siew Wei Phang [1], Chee Kin Phang[2], Jing Lang Choh[2]
[1]*School of Engineering, Faculty of Built Environment, Engineering, Technology & Design, Taylor's University Lakeside Campus, Malaysia*
[2]*Top Glove R&D Centre, F25, Klang, Malaysia*

** kaiyang_9407@hotmail.com*

Abstract
Nitrile gloves are widely used in the medical and automobile field due to its superiority in mechanical strength and chemical resistance over natural latex gloves. Natural properties of synthetic latex of nitrile gloves make it stiffer and less comfortable when donned for long periods. Poor elastic recovery of nitrile glove to compressive force also creates an aesthetic issue for customers with high levels of wrinkling after removing from glove box. Aim of this project is to focus on product enhancement to improve elastic recovery and stress relaxation through chemical composition alteration of latex blend. Chemicals such as sulphur, zinc oxide and accelerator that are involved in rubber curing are selected for single factor study to test significance of chemical composition on elastic recovery (%) and stress relaxation (%). Titanium Dioxide is also considered for single factor study due it having filler properties on latex products. Three levels (High, medium, low) of concentration (phr) for all four chemicals is used for single factor study to test significance of chemicals on test results. Elastic recovery measurement using scanner for surface imaging and MATLAB analyzation resulted in data that are non-repeatable and non-significant. Elastic recovery (%) was unable to be proceeded due to limitations to MATLAB analyzation and inconsistent results. Titanium dioxide (TiO_2) showed least significant changes in SR% and mechanical strength data, hence removed from consideration for chemical composition optimization for next phase of study. Stress relaxation (SR%) showed improvement with higher sulphur and accelerator concentration while lower Zinc oxide concentration yielded better SR%. Tensile strength data results were as expected with improvement with higher concentrations of Sulphur, accelerator and Zinc Oxide. But resultant elasticity decreases, shown by lower elongation at break (%).

1. Introduction

Nitrile gloves are synthetic latex gloves also known as Nitrile Butadiene Rubber (NBR) gloves. It is a copolymer derived from 1,3 Butadiene (Petroleum derived) and Acrylonitrile instead of renewable latex source such as Natural Rubber (NR) gloves [1]. NBR gloves are preferred over NR gloves as medical examination due to its superiority in oil resistance, chemical resistance and mechanical strength over NR gloves [2]. Up to 17% of workers in the medical industry suffers from latex allergy which causes itching and drying of skin with similar traits to rashes. This makes nitrile examination glove to mainstay option for medical use.

Several terms are commonly used to describe mechanical properties of rubber, these qualities determine the type and grade of rubber found in the market. Tensile strength is defined as the amount of force (N) per square meter (m) needed to elongate a rubber sample to the point of failure (rupture). Stress Relaxation is defined as the decay of stress under constant strain for a certain period of time due to internal molecular rearrangement (Deformation) to achieve equilibrium with applied force. Rubber with higher tensile strength would require higher load (N) of stress to cause material failure. Elongation (%) is the percentage of stretch of rubber material from its initial state presented in percentage, elongation at break (%) is the measurement of stretch at breaking point of rubber sample. Rubber with high elasticity would display higher elongation (%) when stretched compared to stiffer samples. Elastic modulus also known as Young's Modulus is a measurement of stiffness of a certain material, which is defined as the amount of force exerted at a certain elongation. As such, stiffer or harder rubber samples would display a higher elastic modulus at a certain elongation compared to softer and elastic samples [3]. Rubber Creep is defined as the permanent set of plastic strain experienced by a material under constant strain. Basically rubber samples that have high stress relaxation properties have higher creep when subjected to a certain stress [4]

Issue with Nitrile Glove products

Physical properties between NBR and NR latex have contrasting difference due to their difference in molecular constituents. Natural latex (NR) rubber generally have superior elasticity, resilience and softness compared to NBR, which in nature has higher stiffness, poor elasticity, poor resilience but better tensile strength. The unique characteristics of NBR is linked to the presence of Acrylonitrile (ACN) monomer in its structure, increase in ACN content increases polarity of NBR molecule and glass transition temperature (Tg) properties. Although NBR gloves posses better mechanical properties compared to NR gloves, the stiffer and less elastic nature of NBR gloves do bring about several issues. One issue of NBR gloves is the poor elastic recovery (issue 1) from compressive stress, this results in NBR gloves easily forming surface wrinkles when subjected to compressive force when folded. The other issue regarding NBR glove is its stress retention when worn by any user, the low stress relaxation (Issue 2) property of NBR gloves makes it less comfortable when donned.

This project is a research collaboration between Top Glove Sdn Bhd and Taylor's University to address the two stated issues regarding their Nitrile glove products. The objective is to look into effect of chemical composition optimization to improve stress relaxation and elastic recovery properties. Customer feedback for Top Glove's nitrile glove products has seen customers commenting on the high degree of wrinkling when removed from glove box, which is aesthetically unpleasing as well as causing

inconvenience for customers to "open" the gloves up from wrinkled state. The poor stress relaxation of Nitrile gloves makes it less comfortable when donned for long periods as nitrile glove would not conform to the user's hand. Therefore, a glove that has higher stress relaxation properties would experience deformation (loss of stress) over time and conform to shape of user's hand giving a better comfort when worn for long durations.

Latex compounding chemicals selected for study

This study aims to look into the effect of chemical composition optimization of four chemicals to enhance nitrile glove elastic recovery from compression and stress relaxation. The four chemicals stated are as stated below:

1. Sulphur (Vulcanizing agent)
2. Zinc Oxide (Vulcanizing activator)
3. Accelerator (Vulcanizing catalyst)
4. Titanium Dioxide (Filler)

Sulphur (S) is the most common vulcanizing agent used in the rubber industry, where it provides sulphur cross-links between long chain polymer molecules which would determine the produced glove properties. Zinc Oxide (ZnO) act as a vulcanizing activator where it would enhance cross-linking between polymer chains and form ionic cross linkage between polymer molecules. Addition of ZnO enhances vulcanizing efficiency and acts as an activator for sulphur crosslinking [5]. Accelerators are also added into NBR latex as vulcanizing catalyst to greatly increase speed of vulcanization with process taking a much shorter time while reducing the use of sulphur in the system [6]. Composition of these three chemicals involved in rubber curing would hold an crosslink density of produced rubber and subsequently the mechanical properties of produced glove [7]. Titanium Dioxide (TiO_2) acts as a rubber filler which reinforces rubber structure for better mechanical properties. Preliminary study will be conducted to test significance of composition change of each chemical towards stress relaxation and elastic recovery of produced latex film. Three of the four chemicals with most significant effect will be studied for optimization to obtain resultant latex with best stress relaxation and elastic recovery properties.

Research Objectives

1. (Preliminary Study) To select three out of the four target chemicals with most significant effect on stress relaxation, tensile strength and elastic recovery properties.
2. To optimize chemical composition of target chemicals to achieve nitrile latex with best stress relaxation and elastic recovery property.
3. To achieve enhanced properties while keeping mechanical properties of nitrile latex within industry standards ASTM D6391 (Table 1.1) for nitrile examination gloves

Table 0.24 ASTM D6319 standard for Nitrile examination gloves

Mechanical Property		**ASTM D6319**
Elongation at break (%)	Before aging	Min 500
	After aging	Min 400
Tensile Strength (MPa)	Before aging	Min 14
	After aging	Min 14

Methodology

Chemical composition for significance test

Based on the four target chemicals discussed, composition of chemicals is adjusted to extreme highs and lows to test significance of each chemical towards targeted response (stress relaxation and elastic recovery). Table 2.1 shows the composition of chemicals categorized into three levels. Medium level composition represents normal phr values used in nitrile glove production. "Phr" is an industry standard of denoting chemical ratio based off 100 parts of rubber. when one chemical has its composition varied between high and low values (denoted using **bold** font), all other chemicals phr value is kept at the middle (normal) range to obtain an accurate comparison between produced latex. With this variation, a total of nine batch of latex samples is compounded for single factor study as shown in Table 2.2 below.

Table 0.25 Phr values used for each chemical for significance test

	Low level (phr)	**Medium level – Normal (phr)**	**High level (phr)**
Accelerator	0.1	0.5	3.0
Sulphur	0.2	1.5	3.0
Zinc Oxide	0.1	1.5	5.0
Titanium Dioxide	0.2	1.6	3.0

Table 0.26 Phr values for all target chemicals for each batch of variation in single factor preliminary study.

No.	**Sample name**	**Accelerator (phr)**	**Sulphur (phr)**	**ZnO (phr)**	**TiO_2 (phr)**
1	**Normal**	0.5	1.5	1.5	1.6
2	**High ZnO**	0.5	1.5	**5.0**	1.6
3	**Low ZnO**	0.5	1.5	**0.1**	1.6
4	**High Sulphur**	0.5	**3.0**	1.5	1.6
5	**Low Sulphur**	0.5	**0.2**	1.5	1.6
6	**High accelerator**	**3.0**	1.5	1.5	1.6
7	**Low accelerator**	**0.1**	1.5	1.5	1.6
8	**High TiO_2**	0.5	1.5	1.5	**3.0**
9	**Low TiO_2**	0.5	1.5	1.5	**0.2**

Chemical weight calculation

Calculation of weight of each chemicals (g) requires individual chemical's parts per hundred (phr) information and Total solid content (TSC%). The information can be subbed into (Equation 1) shown below to calculate chemical weight (g) of each

individual chemical. Latex weight is calculated based on 1000g of final solution with final solution of 19% of TSC.

Please note that TSC and Phr information for chemicals in Table 4 is not included for confidentiality reasons

$$\text{Chemical weight (g)} = \frac{\text{chemical phr} \times \text{Latex TSC (\%)} \times \text{Latex weight (g)}}{\text{Chemical TSC}} \quad (1)$$

Latex blend compounding

Latex compounding involves constant stirring of latex and added chemicals for a period of 24-48 hours to produce a homogenized solution. This step is important in order to avoid settlement of high density solid particles, which may cause uneven properties throughout surface of produced latex. For this study, several conditions are set to be constant for all compounding batches to standardize the compounding process. 24 hour period for latex compounding is chosen based on studies done by Ruslimie et.al [8] showing no increment in crosslink density (mole/g) and tensile strength (MPa) for produced latex with pre-vulcanization time over 24 hours.

1. Compounding period = 24 hours
2. Compounding temperature = Room temperature (25^{o}C)
3. Compounding conditions = Closed conditions
4. Stirrer rotation speed = 600rpm

Manual plate dipping

Lab scaled glove dipping process is done in smaller scale using 1.0 kg compounded latex solution and flat plate former instead of larger sized glove formers which require at least 10kg drum of solution for effective dipping. Former dipping conditions are help similar to nitrile glove production line conditions. Latex samples have to be cooled 24 hours before conducting any test.

1. Former temperature before coagulant dip: 55^{o}C – 60^{o}C.
2. Coagulant temperature: 55^{o}C
3. Coagulant drying conditions: 120^{o}C, 2 minutes
4. Former temperature before latex dip: 60^{o}C – 65^{o}C.
5. Latex drying conditions: 120^{o}C, 15 muntes.

Elastic recovery from compressive stress

An important note is that there is no industrial standardized method of measurement of surface wrinkles through surface imaging or elastic recovery from compressive force for thin rubber films such as glove samples. Method of surface imaging and surface wrinkle analyzation discussed below represents a new and untested method developed through collaborative efforts between Ms. Eunice Phang Siew Wei (Program director/Senior lecturer of Taylor's University) and industrial supervisors at Top Glove Sdn Bhd. This newly developed method can be categorized into 3 stages:

I. Compressive folding of latex sample (Uniform and non-uniform folding)
II. Surface image scanning using a scanner
III. Analyzation and calculation of surface wrinkles (%) through MATLAB

Produced latex samples are folded using two different methods (Figure 2.4.1) to compare which method provided substantial improvement in elastic recovery after a certain period. Surface imaging for samples are scanned for surface morphology analyzation using MATLAB to determine which method is best suited.



Figure 0.29: Standardized folding method (Left) and non-uniform crumpling method (Right)

Several conditions have to set constant for compression of latex films for both methods.

A. (Standard Folding method) each fold is 1.5cm apart measured from the top.
B. (Standard and non-uniform method) Surface imaging on surface area is only applied on area measured 13cm from top. Surface below the 13cm line is not considered.
C. All compressed film is placed under flat surface with a 2.5 kg weight placed on top
D. Compression time is set at 18 hours under the 2.5kg weight.
E. Once weight is removed, surface imaging is done on initial stage (t= 0 minute) and after 10 minutes of recovery (t=10 minute)

MATLAB surface wrinkle analysation

Surface area selection for wrinkled/folded latex samples were manually adjusted using rectangular (blue) box as shown in **Figure 2.4.2** below. Surface area selection was only done within the compounds above the indication line (13cm from top). Cautious manual adjustments were needed to ensure no surface area outside of glove sample is included to avoid error values in wrinkle analyzation results. Image processing using MATLAB results in contrasting of wrinkled surface (white region) and unwrinkled surface (black region) shown in Figure 2.4.2. Wrinkled surface area (white region) over total selected surface is calculated in MATLAB and displayed as wrinkled percentage (%). Calculation of elastic recovery for 10 minute duration is shown in Equation (2)

Elastic Recovery (%) = (percentage of wrinkles, t=0) – (percentage of wrinkles, t=10)

(2)



Figure 0.30: Selection of measurement area (Blue box) for MATLAB (left)
Contrasting of scanned image (right)

Stress Relaxation and Mechanical property test

Preparation of tensile test piece

All latex test pieces are cut based on ASTM D412 standard as shown in **Error! Reference source not found.** below. Dimensions shown are in units of millimetres (mm). **Error! Reference source not found.** (left) shows the difference in size of die cutter based on different industry standards. Produced latex samples are placed on a flat surface with die cutter placed on top of latex surface. Samples are then placed under an air-pressurized compressor to cut out samples based on die cutter size.

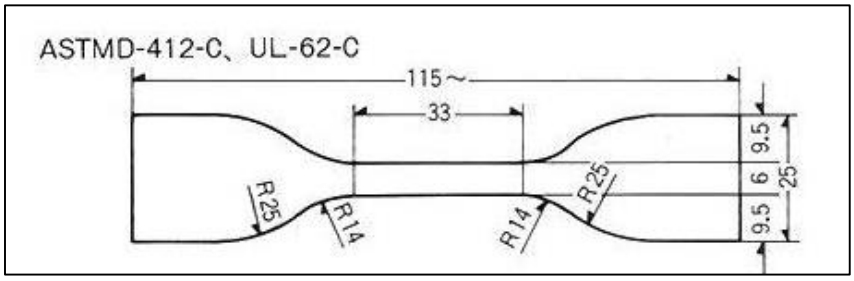


Figure 0.31 ASTM D412 Type C die cutter size [9]

Tensile strength test

Dumbbell shaped test samples were gripped on onto clips of the Universal tensile machine (Figure 2.2). **Standard ASTM tensile test before aging** standard was used, with upward tension force of 500mm/min set for all test samples. Test piece was elongated until sample gage area (middle) snaps at maximum load. Relevant results from test report for this study include:

1. Tensile strength (MPa)
2. Elongation at breaking point (%)
3. Tensile strength at 300% elongation (MPa)



Figure 0.32 Elongation of samples during tensile strength test

2.5.3 Stress Relaxation test

Universal tensile machine is used for conducting stress relaxation. Samples were gripped at both ends to clips on the test machine and elongated upwards for a length of 25.414mm. Samples was left in elongated state for a standard of 6 minutes for all samples. Stress decay of samples throughout 6 minutes with initial stress and final stress values recorded in test report with calculated Stress recovery (%). Equation (3) shows formula of calculation for stress relaxation (%).

$$Stress\ Relaxation\ (\%) = \frac{Fo-Ft}{Fo}\ x\ 100\% \qquad (2)$$

Fo **=** Initial stress value at t=0

Ft = Stres value after certain duration, t

Results and Discussion

Preliminary study for chemical significance test is a simple test to compare the significance of the four target chemicals (Sulphur, Zinc Oxide, Accelerator, Titanium Dioxide) towards the two target responses of this study (Elastic Recovery and Stress Relaxation%). Collected results are compared, to choose 3 (out of 4 target chemicals) chemicals with most significant effect on both responses when chemical composition is adjusted to very high or very low values. Chosen chemicals are selected to conduct the next stage of full factorial design and chemical composition optimization.

Elastic Recovery

Table 3.1 below shows the elastic recovery (%) of latex films measured at 0 minutes and 10 minutes for both standardized and non-standard folding method.

** elastic recovery measurement was not continued with samples from other batches (High ZnO, Low ZnO, High Accelerator…) due to results shown being unrepeatable**

Table 0.27 Elastic recovery percent of latex film for differnt folding method.

Sample Name	Wrinkle percentage %					
	Standard folding			non-standard folding		
	t=0	t=10	Recovery%	t=0	t=10	Recovery%
High Sulphur 1	34.2721	26.3442	7.9279	34.1373	40.3772	-6.2399
High Sulphur 2	53.976	54.1037	-0.1277	54.272	53.5781	0.6939
High Sulphur 3	30.5375	31.5073	-0.9698	44.2976	44.7708	-0.4732
High Sulphur 4	16.7468	22.1309	-5.3841	54.6769	50.4428	4.2341
Low Sulphur 1	51.0367	57.8281	-6.7914	45.9153	45.1422	0.7731
Low Sulphur 2	51.3293	52.9274	-1.5981	46.7022	46.8926	-0.1904
Low Sulphur 3	38.0716	32.7805	5.2911	47.1178	46.1577	0.9601
Low Sulphur 4	30.0462	25.8878	4.1584	39.0742	39.1272	-0.053

Test results as shown in Table 3.1 were clearly non-repeatable and non-sensible. Although MATLAB was not able to differentiate elastic recovery in 10 minutes, the minor differences can be seen through visual judgement based on scanned images shown in **Error! Reference source not found.** below. There is a certain amount of recovery in wrinkling depth between both samples. The scanned image after 10-minute of recovery (right) is bigger in terms of surface area compared to sample image at 0-minute due to the minor elastic recovery in wrinkle depth causing latex sample to slightly "expand" in size as it recovers. Wrinkled samples would display higher degree of elastic recovery after longer amounts of time, but that would beat the purpose of the objective, as end users were dissatisfied with the high number of wrinkles when gloves were immediately removed from glove box (Elastic recovery in short period)



Figure 0.33 Scanned images of latex surface at 0 minutes (left) and 10 minutes (right)

Hence the issue with results being non-sensible (negative values) and non-reproducible can be summarized in 2 major factors:

1. MATLAB analyzation limitations

As discussed with the industrial supervisor who wrote the coding, MATLAB was only able to contrast wrinkled (white) and unwrinkled regions (black) as shown in Figure 2.2 and calculate total surface area of wrinkled regions (white) over total selected surface area. But based on visual differences shown in Figure 3.2, regions of wrinkle lines and regions remains largely the same for samples at 0-minute and 10-minute. Only a change in depth of wrinkles were observed. Hence MATLAB was not able to distinguish the differences between both images making results insignificant. Future improvements of coding may allow or wrinkle depth to be differentiated using MATLAB.

2. Inconsistency in manual adjustment for selected surface area

As shown in Figure 2.2, selection of surface area is done by manually adjustments of the blue indication box. This adds in factor or inconsistency when surface area of 0-minute sample and 10-minute sample are selected. Since wrinkle regions show no difference in MATLAB between both images, difference in selected area may cause an increment or decrease in resultant elastic recovery (%). This explains the negative values of elastic recovery (%) shown in **Error! Reference source not found.**. Future improvements can be done in coding to automatically identify and select area of latex sample to avoid such consistency.

Significance test for stress relaxation and mechanical strenght

Target chemicals (Sulphur, Zinc Oxide, Accelerator, Titanium dioxide) have phr adjusted beyond normal production range (Refer to Table 2.1) to select three chemicals with most significant change in stress relaxation (%) response. Table 3.2 below shows stress relaxation (%) results of each chemical variation. All data shown for stress relaxation and tensile strength were averaged out between data obtained from 4 test samples of the same composition batch. Table 3.3 below shows the tensile strength, elongation at break (%) and elastic modulus at 300% elongation data for the same samples.

Table 0.28 Stress relaxation (%) after 6 minutes of constant strain

	Stress at 0 minute, *Fo* (MPa)	**Stress after 6 minutes, *Ft* (MPa)**	**Stress Relaxation (%)**	**Difference between High and Low formulation (%)**
High Sulphur	1.861	0.856	42.58	3.40
Low Sulphur	1.696	0.722	45.98	
High TiO_2	1.664	0.734	44.10	0.47
Low TiO_2	1.405	0.626	44.57	
High Accelerator	1.708	0.789	41.38	4.81
Low Accelerator	1.553	0.643	46.19	
High Zinc Oxide	0.921	0.338	36.76	13.03
Low Zinc Oxide	0.500	0.250	49.79	

Table 0.29 Tensile strength, Elongation at break(%) and Elastic modulus result for test samples

	Tensile Strength (MPa)	**Difference between High and Low formulation (MPa**	**Elongation at break (%)**	**Difference between High and Low formulation (%)**	**Modulus at 300% Elongation (MPa)**	**Difference between High and Low formulation (MPa)**
High Sulphur	46.70	23.71	460.8	73.9	12.05	6.49
Low Sulphur	22.99		534.7		5.56	
High TiO_2	21.44	1.45	481.37	26.93	6.64	1.18
Low TiO_2	22.89		508.3		5.46	
High Accelerator	23.62	2.95	473.8	94.37	7.37	2.42
Low Accelerator	20.67		568.17		4.95	
High Zinc Oxide	24.60	8.18	304.37	213.68	22.17	20.08
Low Zinc Oxide	14.19		518.05		2.09	

Titanium dioxide (TiO_2) which acts as a reinforcement filler, did not have significant effect in stress relaxation (%) when concentration is adjusted to extreme highs and lows. The other three target chemicals (Sulphur, Zinc Oxide, Accelerator) were directly involved in rubber curing process, change in concentration in these chemicals would have a significant impact in crosslink density of produced latex. Stress relaxation (%) between High concentration (3.0 phr) and low concentration (0.2 phr) only resulted in a difference of 0.47 MPa. The insignificant difference for high and low samples of TiO_2 in stress relaxation (%) can be backed up by mechanical test data shown in Table 3.3, which shows the least difference across the board for tensile strength, elongation at break (%) and elastic modulus at 300% elongation. Data shown in this table further proves that a direct influence in crosslink density can effect mechanical strength and overall stiffness of a latex sample.

An additional observation can be made in Table 3.2, stress relaxation (%) high and low concentration of Zinc Oxide (ZnO) shows an exceptionally higher difference compared to other chemicals, with difference of 13.30% in stress relaxation. This clearly shows that ZnO is the most significant factor involved in enhancing stress relaxation in produced latex. This may hint that ionic crosslinking in rubber molecules can significantly impact mechanical properties of produced rubber. By referring to results in Table 3.3, elongation at break (%) High and low Zinc Oxide samples show the highest difference of 213.68% between samples from both batch. The same trend is seen with elastic modulus at 300% elongation. High ZnO samples had exceptionally high elastic modulus at 22.17 MPa while low ZnO samples were exceptionally low at 2.09 MPa. This meant that low ZnO samples were exceptionally soft, with much lesser

load (N) needed to stretch samples to 300% elongation. Based on discussions with industrial supervisors on the relation between all these data, a summarization between the relationship of mechanical properties can be summarized below in Table 3.4 below:

Table 0.30 Relationship between mechanical properties in gloves

	Tensile strength (MPa)	**Elongation at break (%)**	**Elastic Modulus – Rubber Stiffness (MPa)**
Higher Stress Relaxation (%)	Lower	Higher	Lower Stiffness
Lower Stress Relaxation (%)	Higher	Lower	Higher Stiffness

Results from preliminary study of significance in effect of chemicals can conclude two major statements:

1. Titanium dioxide (TiO_2) was the least significant chemical towards stress relaxation (%). It will be excluded for full factorial design and composition optimization.

2. Zinc Oxide (ZnO) is the most significant factor affecting stress relaxation (%) and overall softness of produced latex.

4. Conclusion

As it stands, elastic recovery measurement through surface imaging using scanner shows that the method is not suited for this project as results obtained are inconsistent and non-repeatable. MATLAB analyzation of surface wrinkle was only able to determine the number of wrinkles / wrinkled regions of selected area but unable to distinguish the depth of surface wrinkles on nitrile latex surface. Elastic recovery of wrinkled films had recovery of wrinkled depth but little to no recovery from number of wrinkles after 10 minutes of recovery period. Hence, MATLAB was unable to distinguish difference between sample image at 0 minute and 10 minute. Manual selection of analysed surface area through manual adjustment also caused inconsistency in selected areas for 0 minute and 10 minutes samples, resulting in some samples yielding negative elastic recovery values. Titanium Dioxide (TiO_2) showed least significant changes for SR% and mechanical properties between high-low concentrations and between normal formulation samples. Increment in sulphur and accelerator concentration caused an increment in SR%, possibly due to increased sulphur crosslinking in samples. But increment of Zinc Oxide caused decrease in SR% due to ionic crosslinking between rubber molecules. Tensile strength results show an expected outcome with an increment in mechanical strength with higher concentrations of sulphur, accelerator and zinc oxide due to higher density crosslinking. But enhanced mechanical strength had a resultant effect of decreased elasticity of produced samples, with elongation at break (%) showing decreased value with higher concentrations. Sulphur, accelerator and Zinc Oxide are chosen for full factorial study for chemical composition optimization for next phase of the study.

References

[1] V. Lachat, “Dissertation: Understanding Oil Resistance of Nitrile Rubber: CN Group Interactions at Interfaces,” p. 167, 2008.

[2] C. Guo, L. Zhou, and J. Lv, “Effects of expandable graphite and modified ammonium polyphosphate on the flame-retardant and mechanical properties of wood flour-polypropylene composites,” *Polym. Polym. Compos.*, vol. 21, no. 7, pp. 449–456, 2013.

[3] N. Chaiear, S. Sadhra, M. Jones, P. Cullinan, I. S. Foulds, and P. S. Burge, “Sensitisation to natural rubber latex: an epidemiological study of workers exposed during tapping and glove manufacture in Thailand.,” *Occup. Environ. Med.*, vol. 58, no. 6, pp. 386–91, 2001.

[4] Astm, “Standard Practice for Stress Relaxation Testing of Raw Rubber , Unvulcanized Rubber Compounds , and Thermoplastic Elastomers 1,” vol. 7, no. Reapproved 2012, pp. 1–15, 2014.

[5] H. A. Rahman, S. Suhatta, and M. R. Board, “STRESS RELAXATION Haidzir Abdul Rahman and Shamheza Suhatta,” no. January 2007, 2010.

[6] C. A. Ruslimie, M. Y. Norhanifah, F. Rubaizah, and M. Asrul, “Effect of Prevulcanisation Time on the Latex Particles , Surface Morphology and Strength of Epoxidised Natural Rubber Films,” pp. 64–69, 2015.

[7] F. Zhao, W. Bi, and S. Zhao, “Influence of Crosslink Density on Mechanical Properties of Natural Rubber Vulcanizates,” *J. Macromol. Sci. Part B*, vol. 99999, no. 1, pp. 1–1, 2011.

[8] N. J ian Tao, Reno, “SOFT NITRILE MEDICAL GLOVES HAVING,” US 2002/0193488 A1, 2002.

[9] G. Heideman, “Reduced zinc oxide levels in sulphur vulcanisation of rubber compounds,” pp. 1–192, 2004.

[10] N. Fujii, “SOFT NITRILE RUBBER FORMULATION,” 6,031,042, 1981.

[11] O. Publications, “(12) United States Patent,” vol. 2, no. 12, 2014

[12] W. Salgueiro *et al.*, “Dependence of the network structure of cured styrene butadiene rubber on the sulphur content,” *Polymer (Guildf).*, vol. 45, no. 17, pp. 6037–6044, 2004

[13] F. Zhao, W. Bi, and S. Zhao, “Influence of Crosslink Density on Mechanical Properties of Natural Rubber Vulcanizates,” *J. Macromol. Sci. Part B,* vol. 99999, no. 1, pp. 1–1, 2011.

[14] A. P. Meera, S. Said, Y. Grohens, A. S. Luyt, and S. Thomas, “Tensile Stress Relaxation Studies of TiO 2 and Nanosilica Filled Natural Rubber Composites,” *Ind. Eng. Chem. Res*, vol. 48, pp. 3410–3416, 2009

Process Debottlenecking and Retrofit of Palm Oil Milling Process via Inoperability Input-Output Modelling

Chapter 1

May May Tan[1], Viknesh Andiappan[2], Yoke Kin Wan[1*]

[1]School of Engineering, Faculty of Built Environment, Engineering, Technology & Design, Taylor's university, Lakeside Campus, No. 1 Jalan Taylor's, 47500 Subang Jaya, Selangor, Malaysia.
[2]Department of Chemical Engineering, The University of Bath, Claverton Down, BA2 7AY, Bath, United Kingdom.

maymay.tan@sd.taylors.edu.my

Abstract

In recent years, there has been an increase in crude palm oil (CPO) demand due to growth in global population, resulting in palm oil mills (POMs) seizing the opportunity to increase production to make more profits. In a POM, CPO is extracted from fresh fruit bunches (FFBs) harvested from oil palm trees. This extraction process consists of a series of equipment which are designed to operate in their optimum capacities in the current existing POMs. Some equipment may be limited by their maximum design capacities when there is a need to increase CPO production. These equipment become process bottlenecks. In this research, a framework is developed to provide stepwise procedures on identifying bottlenecks and retrofitting a POM process to cater for the increase in production capacity. This framework adapts an algebraic approach known as Inoperability Input-Output Modelling (IIM), which is used to define process interactions in a POM by a set of linear equations. To illustrate the application of the framework, an existing POM was solved in this work, by maximising its production capacity. The POM model was first formulated and solved using a programming tool known as LINGO. From the model results, the Screw Press was identified as the bottleneck. The retrofitting recommendation was to purchase an additional Screw Press to cater for the new throughput. Upon re-analysing the POM, it was found to be able to achieve the targeted production capacity of 8139.65 kg/hr of CPO without any bottlenecks. This was a 7% increase in production capacity as compared to the existing POM. After the POM was free from bottlenecks, Benefit-to-Cost Ratio (BCR) analysis was performed on the implemented debottlenecking modifications to assess its economic feasibility. The BCR obtained was 54.57, proving that the income gained from the increased capacity far outweighs the cost required to purchase the Screw Press. Hence, the debottlenecking method was approved. The results have shown that there is a requirement for a framework to make informed decisions on the debottlenecking of a plant.

Keywords: Crude palm oil (CPO), process system engineering (PSE), framework, linear programming

Introduction

Crude palm oil (CPO) is a commodity with large potential and is the most versatile vegetable oil, with the ability to be processed into a range of products with different characteristics [1]. The global demand for palm oil has been increasing at a rapid speed due to the increase in consumption all over the world. The reason for the vast economic growth of palm oil is that it is cheap to produce and has a production rate 10 times that of soy oil, which is its direct competitor [2]. In a POM, CPO is extracted from fresh fruit bunches (FFBs), which are harvested from oil palm trees. The process block diagram (PBD) of a typical POM is as depicted in Figure 34.

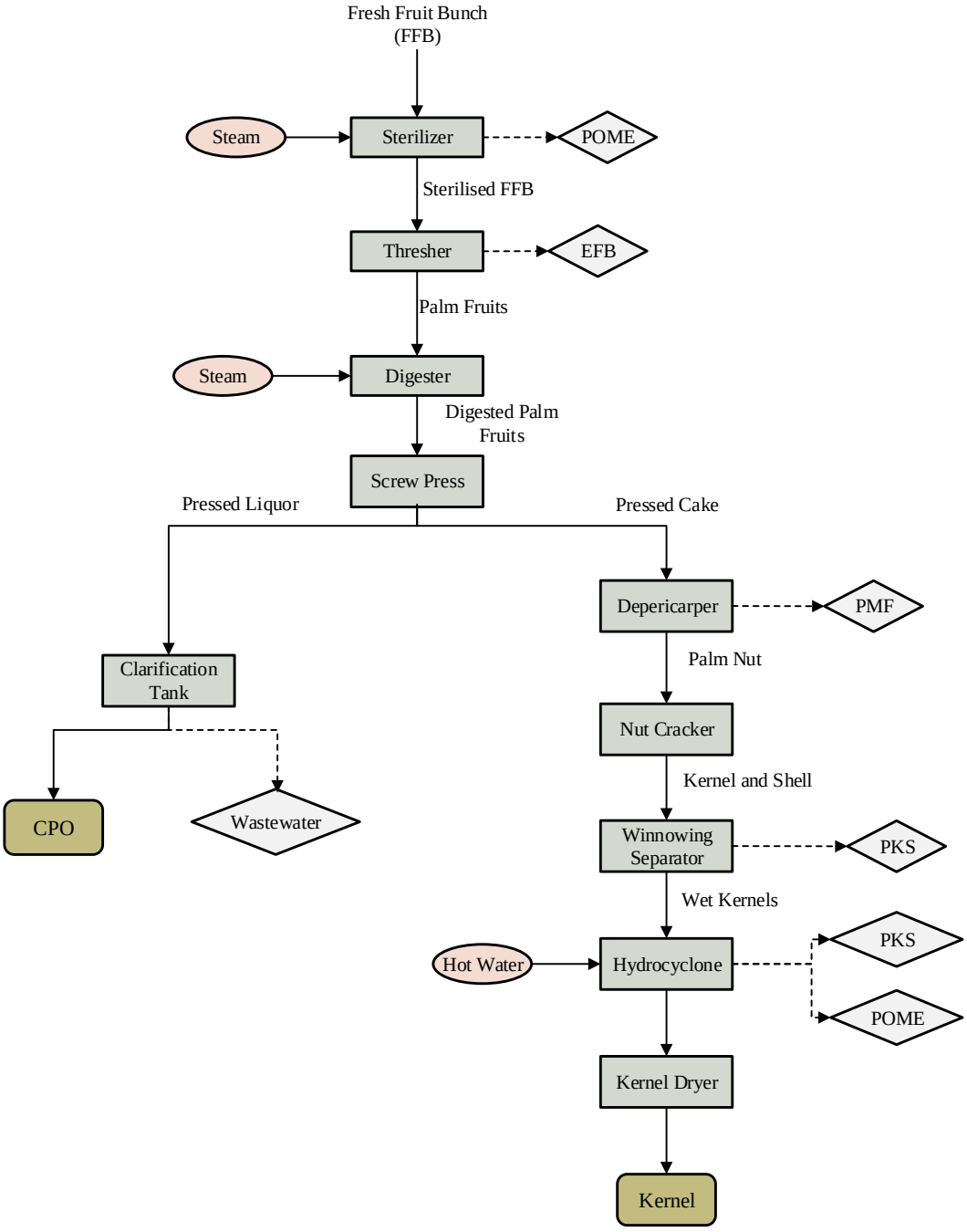


Figure 34. Block flow diagram (BFD) of a typical POM process [3].

Each equipment in the POM has very specific functions and are designed to operate at their optimum capacities. When there is a need to increase CPO production, some of its equipment may be limited by their fixed design capacities, creating a process bottleneck. A process bottleneck is a situation whereby the available capacity of a process unit is insufficient to meet the increased production rates. The challenge becomes increasingly complex when a POM experiences a drop in equipment efficiency. To solve the mentioned challenges, production capacity of a POM can be increased by retrofitting a plant (e.g. building new production facilities, debottlenecking an existing plant or by designing a plant that meets the production capacity requirement prior to building it) [4]. However, since POM plants are very well-established, it is usually more economical to retrofit an existing POM by debottlenecking it [5].

Retrofitting refers to a procedure to implement modifications to an existing process or system that may improve its energy efficiency, decrease its energy demand, increase its capacity and etc [6]. Several research works have been presented in the area of retrofitting, proving the importance of increasing the productivity of a process to fit increase in demand of a product [7, 8]. In literature, retrofitting and debottlenecking approaches have been proposed in areas including using computer-aided simulation tools, mathematical modelling and programming tools, and systematic frameworks [4, 8–12]. Previous works related to process retrofitting and debottlenecking were focused on the industries such as heat exchanger networks, pharmaceutical, biorefinery and bioenergy [4, 9, 11, 13]. However, there is limited work done on a retrofit and debottlenecking framework of a POM to cater for increased CPO production. At present, work has only been focused on palm oil-based biomass utilisation in a biorefinery and biomass tri-generation system from a palm oil mill (POM), but not the operations of the POM itself [4, 13].

Hence, this research presents a debottlenecking framework, which serves as a stepwise guideline and decision-making tool for engineers to identify bottlenecks and debottleneck the process when there is a desire to increase production capacity. To illustrate the application of the framework, an existing POM was solved in this work, by maximising its production capacity. The identification of bottlenecks was carried out by first developing the mathematical model of the process using an algebraic approach, known as Inoperability Input-output Modelling (IIM) adapted from the work of Kasivisvanathan et al. [4]. IIM assumes that each equipment is a ‘blackbox’, meaning that the operating conditions of the equipment are not considered. The model was then solved using a commercial optimisation tool, known as LINGO v17.0 [14]. The results of the model were analysed to determine the equipment which have become process bottlenecks. Upon identifying the bottlenecks in the process, the framework entails the procedures on retrofitting a POM process to cater for the increased production capacity. Following this, once the POM was free from bottlenecks, benefit-to-cost ratio (BCR) was performed on the debottlenecking methods to analyse the economic feasibility. Based on the economic performance, the decision to approve the debottlenecking solution is then made.

With this framework, process engineers are able to analyse, and make informed decisions on the debottlenecking a POM process in a systematic manner. The challenge of process bottlenecking can surface in any process. Hence, the purpose of this approach is not limited to a POM production process, it can also be applied to any process that may face potential bottlenecks.

Research Methodology

Debottlenecking Framework

The debottlenecking framework methodology in **Error! Reference source not found.** essentially acts as a step-by-step guide and a decision-making tool for engineers to debottleneck a process. Section 2.2 to 2.3 explains the framework steps in detail.

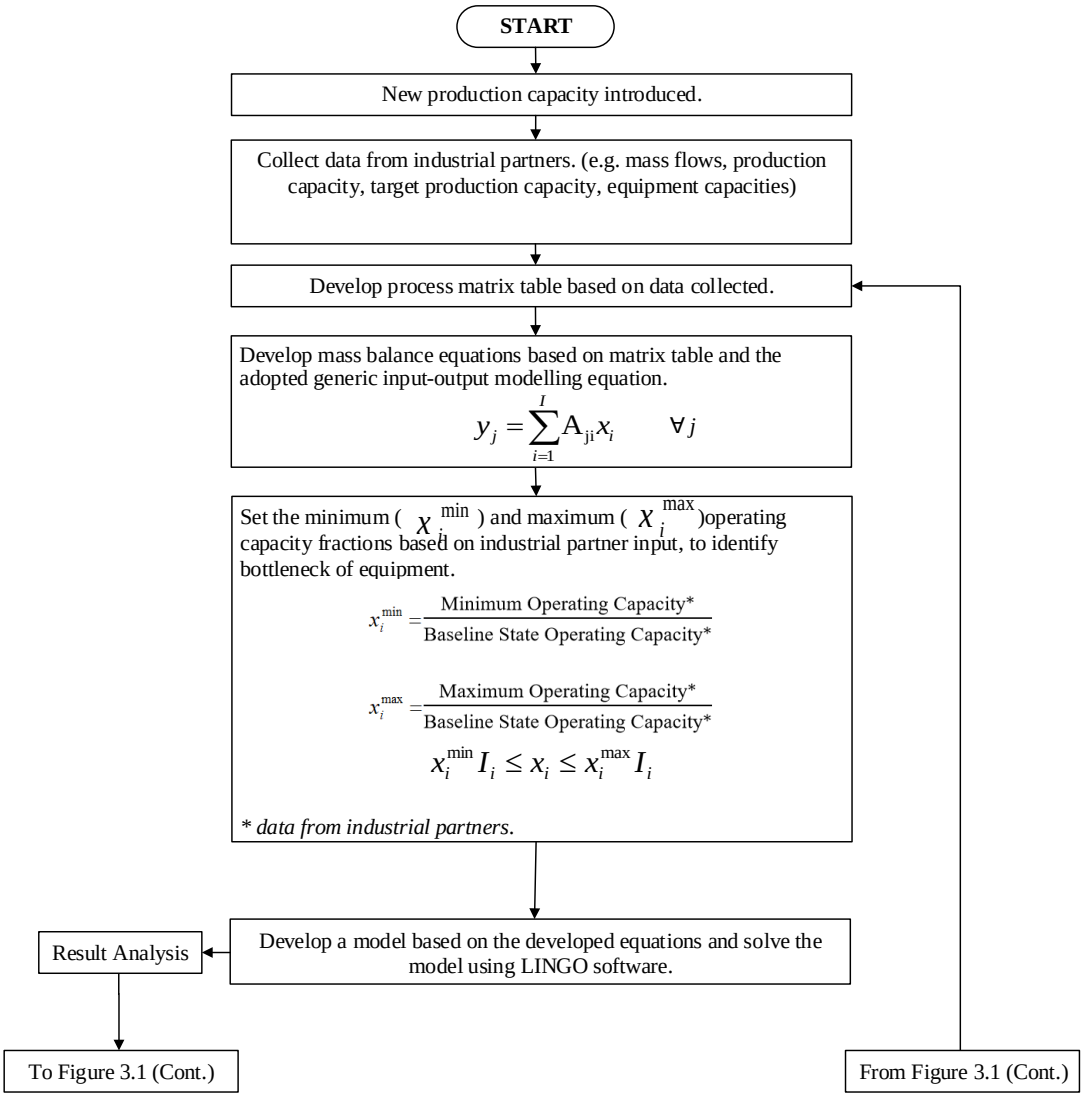


Figure 35. Debottlenecking framework methodology.

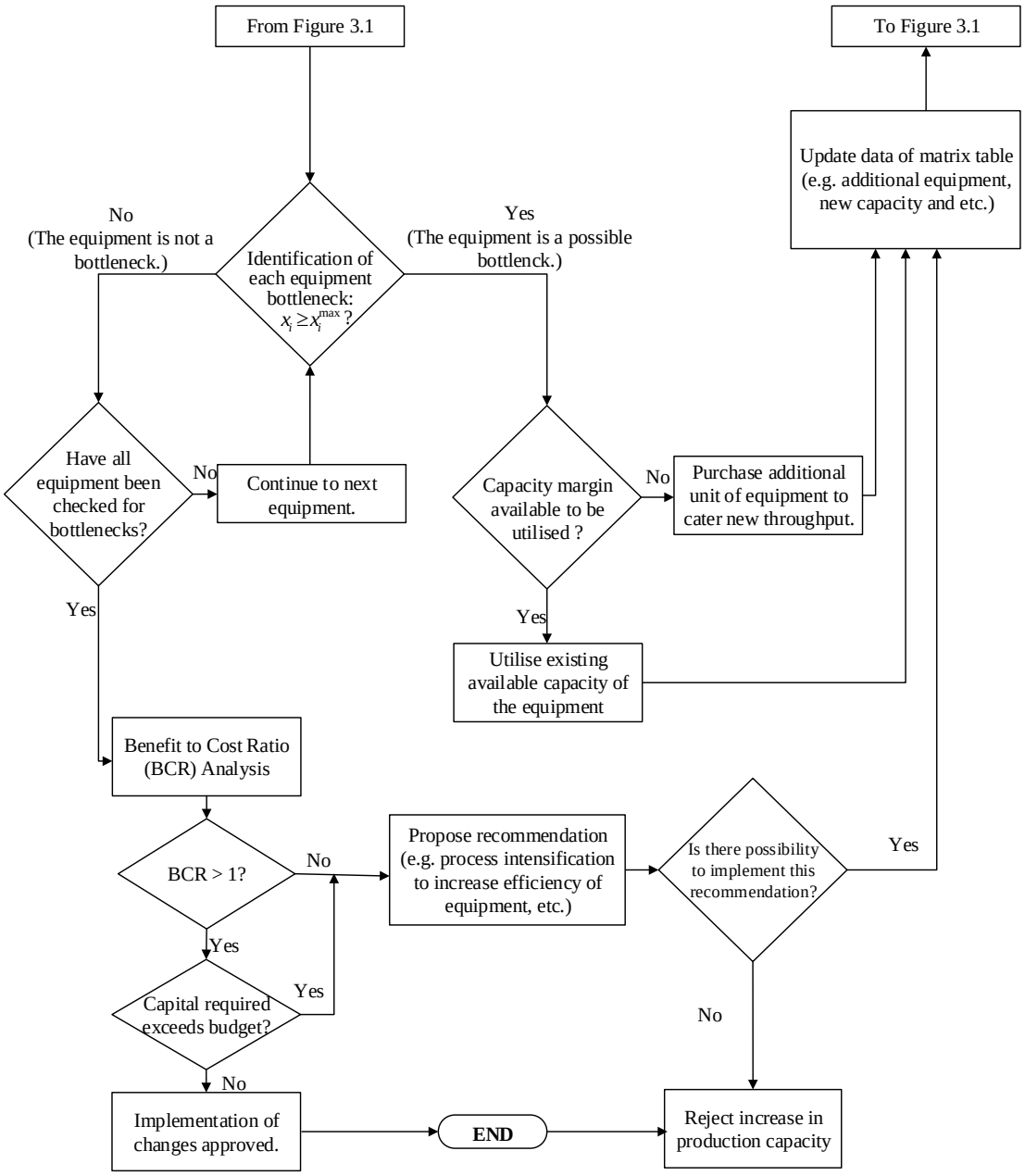


Figure 2. Debottlenecking framework methodology (Cont.).

As shown in Figure 2, when the need to increase production capacity arises, the first task in the framework is to collect information of the process and equipment from industrial partners for study and analysis as shown in Table 1. For any confidential data that was unavailable, assumptions can be made based on similar, heuristic values or theoretical calculations.

Table 31. Data required for research.

	Process	Process Unit
Data Required	• Equipment used in the process • Number of equipment of each process step • Process flow • Mass flows • Production capacity during normal operation • Target capacity for increased production	• Design capacities • Minimum operating capacity • Maximum operating capacity • Capital cost of equipment • Electricity consumption • Utility consumption (e.g. steam consumption)

Moving down the framework to the next task, a process matrix table needs to be constructed. A general example of a matrix table is shown in Table 2. It shows the mass flows of components, *j* (j=1,2,3…J), through each process unit, *i* (*i*=1,2,3…I), for baseline state operation. In this work, the baseline state operation is referred to the normal existing operating capacity of the plant, before there is an increase in production capacity. Next, mathematical model needs to be formulated based on the matrix table shown in Table 2. The detailed explanation is presented in Section 2.1.

Table 32. General example of a process matrix table.

Equipment, x_i / Component, y_j	x_1	x_2	x_3	…	x_i
y_1	$A_{1,1}$	$A_{1,2}$	$A_{1,3}$	…	$A_{1,j}$
y_2	$A_{2,1}$	$A_{2,2}$	$A_{2,3}$	…	$A_{2,j}$
y_3	$A_{3,1}$	$A_{3,2}$	$A_{3,3}$	…	$A_{3,j}$
…	…	…	…	…	…
y_j	$A_{i,1}$	$A_{i,2}$	$A_{i,3}$	…	$A_{i,j}$

Formulation of Model

Based on the matrix table in Table 2, the process is then modelled using an algebraic approach known as input-output modelling. A general expression for input-output modelling adapted from the work of Kasivisvanathan et al.[4] is shown in Eq. (1),

$$y_j = \sum_{i=1}^{I} A_{ji} x_i \qquad \forall j \qquad (3)$$

where y_j is the net flowrate of a given component, which can be an intermediate or a product. It is noted that y_j is denoted by a negative sign for inputs, a positive sign for outputs and is equal to zero for all intermediates. *i* (*i* = 1, 2, …, I) represents a process unit index, *j* (*j*= 1, 2, …, J) represents the type of component. A_{ji} showed in the matrix table represents the input and output mass flows to and from a certain process unit *i*. Meanwhile, x_i is an input-output variable of the equation, known as the operating capacity fraction for a process unit (where baseline state is denoted by 1).

Based on input-output modelling, the net output of the intermediate products in the process are fixed to zero as shown in Eq. (2) below.

$$y_j = 0 \tag{4}$$

This is to ensure that all the intermediate products will be completely converted to produce the final product at the capacity that the plant is designed for [4]. Other than the formulation of the modelling equations, the constrains required to solve the model (i.e. minimum and maximum operating capacity fractions, x_i^{min} and x_i^{max}) are formulated as well, which has been further discussed in Section 2.3.

Set the Minimum and Maximum Operating Capacity Fractions

The next task in the framework presented in Figure 2 is to set the minimum and maximum operating capacity fractions, x_i^{min} and x_i^{max}, of each process unit. As seen in Eq. (1), the input-output variable, x_i, is the operating capacity fraction of a particular process unit. Each process unit has a minimum and maximum limit of operating capacity fraction whereby it is safe to operate. This is required to limit the model, in order to properly identify bottlenecks. x_i^{min} and x_i^{max} of each process unit has to be determined using Eqs. (3) and (4) based on the information provided by industrial partners.

$$x_i^{min} = \frac{\text{Minimum Operating Capacity*}}{\text{Baseline State Operating Capacity*}} \tag{5}$$

$$x_i^{max} = \frac{\text{Maximum Operating Capacity*}}{\text{Baseline State Operating Capacity*}} \tag{6}$$

**** provided by industrial partners.***

The formulation of the range of operating capacity fraction that is to be modelled in LINGO is as shown in Eq. (5).

$$x_i^{min} I_i \le x_i \le x_i^{max} I_i \qquad \forall\, i \tag{7}$$

where x_i is the operating capacity fraction of process unit i (i = 1,2,3…, I) and I_i is a binary number (I_i = 0 or I_i = 1). For better understanding, during baseline state operation, the operating capacity fraction of an equipment, x_i, is equal to 1. When a new production capacity is introduced, x_i might move above or below 1. The model is able to compute the value of x_i of the process unit. If it is running below the normal capacity, x_i is less than 1, and is not a possible bottleneck; if it is running over the normal capacity, x_i is larger than 1, then it may be at risk of being a bottleneck. If x_i is equal or larger than x_i^{max}, then the equipment is most definitely a bottleneck.

Moving down in the framework (Figure 2), the model could be solved using a commercial optimisation software known as LINGO and data below is extracted from the results:

1. The operating capacity fraction, x_i, of all process units,
2. The production capacity of the plant (i.e. amount of product produced).

Following the solved model, Section 2.3 entails the analysis of the result obtained from the model to identify of bottlenecks in the process.

Identification of Bottlenecks

After the model is solved, the process is checked for any bottlenecks which may have occurred by analysing the results of the model. Beginning from the 'Result Analysis' box onwards in Figure 2, the analysis will be limited to only one process unit before moving to the next unit. The loop continues until all process units have been checked for bottlenecks. For example, if the equipment is a bottleneck, further analysis is carried out to determine if there is existing capacity margin available to be utilised; this will be discussed in Section 2.5. If the equipment is not a bottleneck, then the next equipment will be checked for bottlenecks. This is done until all equipment have been checked for bottlenecks, then the economic analysis is carried out to assess the feasibility of the debottlenecking method proposed as discussed in Section 2.6.

Debottlenecking

From Section 2.4, if the particular process unit is a possible bottleneck, the framework will lead to the next diamond box shown in Figure 2, to be checked for additional capacity available. Some process steps may have more than one process unit operating in parallel; meaning that if one unit is a bottleneck, there may be capacity available in another unit, allowing for the utilisation of available existing capacity in the other unit. This can be checked by first calculating the capacity required for the process step and the available capacity for the process step, using Eq. (6) and (7) which is obtained by rearranging Eq. (3) and (4).

$$\text{Capacity Required for Process} = x_i \times \text{Baseline State Capacity} \quad (8)$$

$$\text{Available Capacity} = \text{Capacity of Equipment} \times \text{Number of Equipment} \quad (9)$$

Following this, based on Figure 2, if there is margin available for adjustments, the bottleneck can be removed by utilising the available capacity in the other equipment which is operating in parallel. If there is no margin available, the debottlenecking solution is to purchase additional unit of equipment. Once the debottlenecking method for a particular process unit is decided, the data in the matrix table needs to be updated and the formulations in the model are then updated accordingly. The entire process is then reanalysed for bottlenecks again. For example, if an additional unit of equipment is purchased, the operating capacity fraction, x_i, for that particular equipment is introduced into the matrix table, then the steps described from Section 2.2 onwards are carried out again. This is done until the entire network is free from any other equipment bottlenecks. Once there are no more bottlenecks and all equipment have been checked, the economic feasibility of the debottlenecking solution is assessed in Section 2.6.

Benefit-to-Cost Ratio (BCR) Analysis

Benefit-to-cost ratio (BCR) analysis of the proposed debottlenecking solutions is performed to assess the feasibility of the modifications. BCR is to determine the ratio of profits gained by implementing the recommendation to the initial capital investment of implementing the recommendation. BCR can be calculated using Eq. (8).

$$BCR = \frac{C_j(\Delta y_j)}{C_{eq}} \quad (10)$$

where j is the valuable product of the process which brings in profits, C_j is the price of component j and Δy_j is the increased flow rates of component j after debottlenecking is performed. C_{eq} is the annualised capital cost and annual operating costs of the equipment purchased to solve the process bottleneck, calculated using Eq. (9).

$$C_{eq} = \sum_{i=1}^{I} \left(C_i x_i^{max} + C_{AOC,i} \right) \quad (11)$$

where i (i = 1,2,3 or…I) refers to the process units that have been added to the process, C_i is the annualised capital cost of the process unit at maximum operating capacity fraction, x_i^{max} and $C_{AOC,i}$ is the annual operating cost of the process unit.

Referring to the framework in Figure 2, the BCR is less than 1, this means that the cost outweighs the benefits. In this case, the process bottlenecks would have to be re-assessed and overcome using different methods (e.g. purchase smaller equipment or process intensification to increase yield of a process) if applicable. On the contrary, when BCR is more than 1, this shows that the benefits of the modification outweigh the costs. In line with BCR, a secondary evaluation is done on the allocated budget. If the investment on the debottlenecking solution falls below the budget, the decision is made to approve the solution. However, if both BCR and/or budget constraints are not satisfied (i.e. BCR < 1 and/or Capital Cost > Allocated Budget), new debottlenecking solutions will have to be proposed and the process will be reanalysed for bottlenecks. For example, a possible recommendation to reduce the initial capital investment is to reduce the maximum operating capacity of the equipment. The plant is then to be re-analysed to determine if these modifications would bring about other bottlenecks. The cycle continues until it reaches the end stage of the framework in Figure 2. In the case where all proposed recommendations have to be rejected due to not achieving the desired results for economic analysis, the entire project will have to be abandoned. This means that the plant is not suited for increase in production capacity or the budget provided is insufficient. To demonstrate the application of the developed framework (Figure 2), the bottleneck identification and debottlenecking of a palm oil mill (POM) case study is presented in Section 3.

Palm Oil Mill (POM) Case Study

Figure 3 illustrates a process block diagram (PBD) of an existing and operating palm oil mill (POM) case study that will be used to demonstrate the debottlenecking framework steps described in Section 2. The POM owner is interested in **maximising** the crude palm oil (CPO) production capacity of the existing POM with a budget allocation of US$ 500,000. This increase of CPO production may cause some of the equipment in Figure 3 to reach their maximum capacities and result in process bottlenecks. In this case, the proposed framework serves as a stepwise guideline and decision-making tool to analyse the plant for increased production and to debottleneck accordingly. Based on the framework (Figure 2), the data of the POM were first collected from industrial partners. Some information of the equipment specifications of the POM at baseline state are shown in Table 3. Table 4 is the process matrix table, which shows the capacities of the equipment in the POM at baseline state, also obtained from industrial partners. In Table 4, the negative values are the inputs into an equipment and the positive values are the outputs of an equipment.

Table 33. Current specifications of existing palm oil mill (POM) at baseline state.

Fresh fruit bunches (FFB) Consumed (kg/hr)	30,000
CPO Production Capacity (kg/hr)	7611.42
Steam Consumption (kg/hr)	15435.85
Electricity Consumption (kWh)	419.8

Table 34. Equipment specifications in Palm Oil Mill (POM).

Equipment	Unit	Maximum Capacity	Minimum Capacity	Steam Consumption (kg/kg FFB)	Electricity (kWh/unit)
Steriliser	kg FFB/unit	20000	8,000	0.25	30
Thresher	kg SFB/unit	50,000	20,000	-	28
Steam Injection	kg SFB/unit	12,500	5,000	0.13	18
Digester					
Screw Press	kg DF/unit	20,000	8,000	-	45
2 -Phase Decanter	kg PL/unit	10,000	4,000	-	40
Depericarper	kg PC/unit	5,000	2,000	-	57.3
Nut Cracker	kg PF/unit	8,000	3,200	-	26.4
4-stage Winnowing Column	kg cracked mixture/unit	15,000	3,000	-	20
Hydrocyclone	kg cracked mixture/unit	5,000	2,000	Water: 1.5 kg/kg cracked nut	30
Kernel Dryer	kg WK/unit	5,000 kg wet kernet/unit	1,000	-	37.1

The next step in the framework is to formulate the input-output model of the POM based on Eq. (1), using the mass flow values in Table 4. Based on Eq. (2), the intermediates of the process are set to zero. Next, the minimum and maximum operating capacity fractions were calculated using based Eq. (3) and (4), and the information in Table 3. The constrains were formulated using Eq. (5). After the completion of these steps, the model is ready to be solved using LINGO v17.0. The results of the model are presented and discussed Section 3.1.

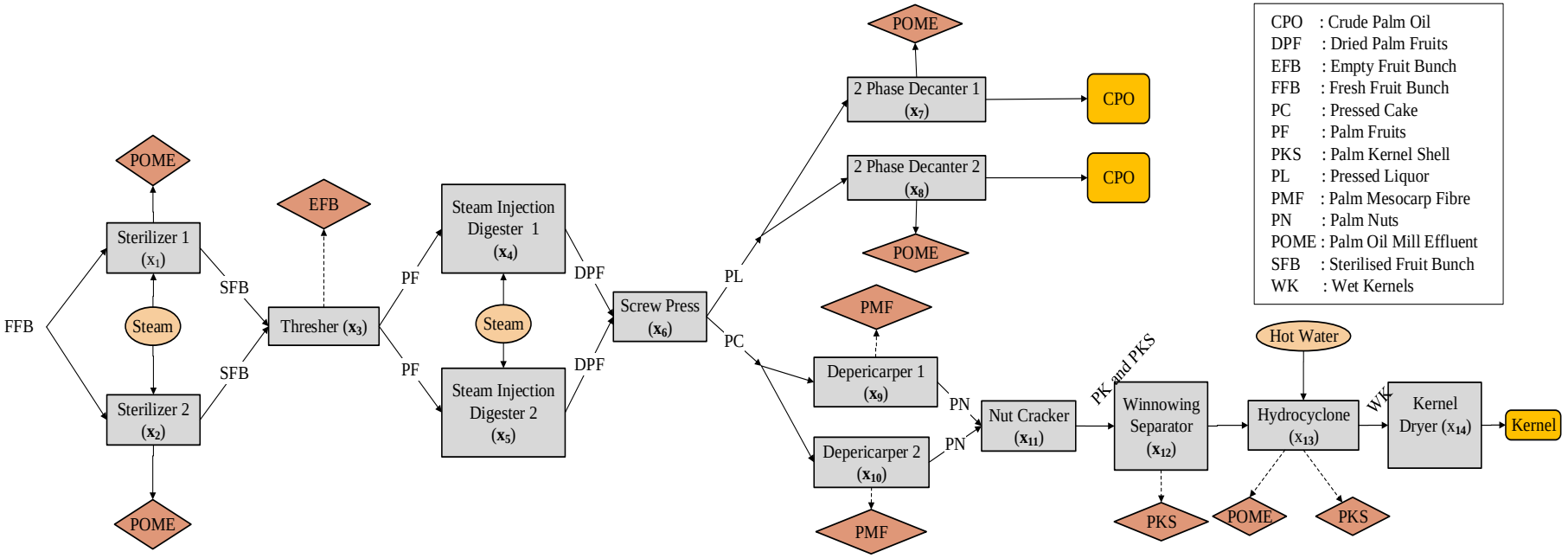


Figure 36. Process block diagram (PBD) of the palm oil mill (POM) Case Study.

Table 35. Process matrix table at baseline state.

Component, y_j (kg/h)	x_1	x_2	x_3	x_4	x_5	x_6	x_7	x_8	x_9	x_{10}	x_{11}	x_{12}	x_{13}	x_{14}
FFB	-15000	-15000												
SFB	12150	12150	-24300											
PF			17982	-8991	-8991									
EFB			6318											
DPF				9350.64	9350.64	-18701.28								
PL						10285.70	-5142.85	-5142.85						
CPO							3805.71	3805.71						
PC						8415.58			-4207.79	-4207.79				
PMF									2019.74	2019.74				
PN									2440.52	2440.52	-4881.03			
CN											4636.98	-4636.98		
UN											244.05	-244.05		
PKS												1627.82	1637.99	
PK												3253.21	-3253.21	
WK													1452.56	-1452.56
DK														1379.93
POME	4316.25	4316.25					1337.14152	1337.14					4635.82	
S	-4125	-4125		-1275	-1275								-4635.82	

Abbreviations

FFB	**Fresh Fruit Bunch**	**CN**	**Cracked Nut**
SFB	**Sterilised Fruit Bunch**	**UN**	**Uncracked Nut**
PF	**Palm Fruit**	**PKS**	**Palm Kernel Shell**
EFB	**Empty Fruit Bunch**	**PK**	**Palm Kernel**
DPF	**Digested Palm Fruit**	**WK**	**Wet Kernel**
PL	**Pressed Liquor**	**DK**	**Dry Kernel**
CPO	**Crude Palm Oil**	**POME**	**Palm Oil Mill Effluent**
PC	**Pressed Cake**	**S**	**Steam**
PMF	**Palm Mesocarp Fibre**	**E**	**Electricity**
PN	**Palm Nut**		

Legend

x_1	**Steriliser 1**	x_8	**2 Phase Decanter 2**
x_2	**Steriliser 2**	x_9	**Depericarper 1**
x_3	**Thresher**	x_{10}	**Depericarper 2**
x_4	**Digester 1**	x_{11}	**Nut Cracker**
x_5	**Digester 2**	x_{12}	**Winnowing Separator**
x_6	**Screw Press**	x_{13}	**Hydrocyclone**
x_7	**2 Phase Decanter 1**	x_{14}	**Kernel Dryer**

Results and Discussion

In this case study, the crude palm oil (CPO) production capacity was maximised and the palm oil mill (POM) was analysed for bottlenecks. The POM model is solved for the objective function to maximise the production capacity of CPO shown in Eq. (10).

$$\max CPO \tag{12}$$

Upon modelling and solving the POM case study, the results showed that the existing POM was able to achieve a maximum CPO production capacity of 8139.65 kg/hr and the results are tabulated in the fifth column of Table 6. Based on the framework, the operating capacity fractions of each equipment upon introducing the increased capacity (in the fifth column of Table 4) is to be compared with the existing maximum operating capacity fraction of the equipment (in the fourth column of Table 4). The comparisons suggested that the possible equipment bottlenecks were the Steriliser 1, Digester 2, Screw Press and Depericarper 2. These are the processes that may be at risk of becoming bottlenecks, should there be a further increase in capacity. This is probably because the Digester and any process relating to palm nut (PN) processing (i.e. Depericarper) had smaller operating capacities compared to other equipment (i.e. Capacity of the Digester is 12,500 kg palm fruit/hr for one unit and capacity of Depericarper is 5000 kg pressed cake/hr for one unit).

Table 36. Identification of possible bottlenecks.

Equipment	Input-Output Variable, x_i	Minimum Operating Capacity, x_i^{min}	Maximum Operating Capacity, x_i^{max}	Operating Capacity Fraction to Maximise CPO, x_i	Possible bottleneck?
Steriliser 1	x_1	0.5333	1.3333	1.3330	**YES**
Steriliser 2	x_2	0.5333	1.3333	0.8058	NO
Thresher	x_3	0.8230	2.0576	1.0694	NO
Digester 1	x_4	0.5561	1.3903	0.7485	NO
Digester 2	x_5	0.5561	1.3903	1.3903	**YES**
Screw Press	x_6	0.4278	1.0694	1.0694	**YES**
Decanter 1	x_7	0.7778	1.9444	0.7778	NO
Decanter 2	x_8	0.7778	1.9444	1.3610	NO
Depericarper 1	x_9	0.4753	1.1883	0.9505	NO
Depericarper 2	x_{10}	0.4753	1.1883	1.1883	**YES**
Nut Cracker	x_{11}	0.6556	1.6390	1.0269	NO
Winnowing Separator	x_{12}	0.6146	3.0731	1.0269	NO
Hydrocyclonne	x_{13}	0.6146	1.5369	1.0269	NO
Kernel Dryer	x_{14}	0.6884	3.4422	1.0269	NO

Moving down the next diamond box in the framework, the possible bottlenecks identified were then checked if there was available existing margin available to be utilised. This means that the particular process step may have more than one of the same equipment running in parallel, which has excess capacity that can be utilised (i.e. from

Figure 3, the Steriliser, Digester, Depericarper and 2-phase Decanter). The calculations were made using Eq. (6) and (7). The results tabulated in Table 7 suggested that the all the possible bottlenecks had available existing capacity to be utilised, except for the Screw Press, which was approaching its maximum available capacity. The conclusion made from this step was that the Steriliser, Digester and Depericarper had available capacity margin to be utilised, because hese processes have two process units which operate in parallel. Hence, when one is at its maximum capacity, the other still had excess capacity to be utilised. However, the Screw Pressing process had only one equipment in the existing POM, leaving no capacity available to be utilised. Therefore, the bottleneck identified and validated for the case study was the Screw Press.

Table 37. Checking for available existing capacity.

Possible Bottlenecks	Capacity Required (kg/hr)	Available Capacity (kg/hr)	Available Existing Capacity Margin to be Utilised?
Steriliser 1	32,081.99	40,000.00	YES
Digester 2	19,229.95	25,000.00	YES
Screw Press	19,999.15	20,000.00	**Approaching Max**
Depericarper 2	8,999.62	10,000.00	YES

Based on the framework (Figure 2), the subsequent step was to debottleneck the Screw Press. In this research, all equipment was assumed to be a 'blackbox', meaning that operating conditions and efficiencies are not taken into consideration and are assumed to be at optimum. However, in reality this may not be the case. Each equipment has its own range of operating conditions at which it has the best performance. For example, a Screw Press may have an optimum operating capacity fraction, x_6, between 0.8 to 0.9, where it may be able to have a higher efficiency. However, since this research is conducted with the assumption of a 'black box', this optimum range is not taken into consideration. Hence, based on the framework (Figure 2), the debottlenecking method selected was by purchasing an additional Screw Press. to cater for the new capacity. Following the decision of the debottlenecking method, the next step is to update the process matrix table, equipment constraints and mathematical model accordingly based on the modifications made. The modifications made (i.e. purchase an additional Screw Press) will allow the POM to have a new maximum CPO capacity. However, since a comparison would like to be made between existing POM and debottlenecked POM, the constraint in Eq. (11) below, has to be defined in the model.

$$CPO = 8139.65 \tag{13}$$

This was done because based on the previous LINGO results mentioned, the maximum CPO capacity of the existing plant was found to be 8139.64 kg/hr. Hence, by introducing Eq. (11) to the model, a comparison can be made to check if the bottlenecks that occurred from the said capacity have been removed. The results are tabulated in Tables 8 to 11. Table 8 shows that Screw Press 1 is at its maximum capacity and is a possible bottleneck. However, the Screw Press 2 that was just added is at zero capacity. Hence, there is existing margin available to be utilised for the Screw Press process, as shown in Table 9. With the additional Screw Press 2, the Screw Pressing

process is now able to handle a larger throughput, allowing the plant to achieve the maximised CPO capacity without any bottlenecks.

Table 38. Identification of bottlenecks after debottlenecking.

Equipment	Input-Output Variable, x_i	Minimum Operating Capacity, X_i^{min}	Maximum Operating Capacity, X_i^{max}	Operating Capacity Fraction to Maximise CPO, x_i	Possible bottleneck?
Screw Press 1	x_6	0.8556	2.1389	2.1388	**YES**
Screw Press 2	x_{6a}	0.8556	2.1389	0.0000	NO

Table 39. Check for capacity margin available for adjustment after debottlenecking.

Bottlenecks	Capacity Required (kg/hr)	Available Capacity (kg/hr)	Available margin for adjustment?
Screw Press	19999.15	40000.00	YES

According to Table 10, upon debottlenecking the existing POM for maximised CPO production capacity, it is now able to produce 8139.65 kg CPO/hr, by consuming 32,082.00 kg FFB/hr, 16,507.08 kg steam/hr and 522.1 kWh of electricity. By comparing the CPO production capacity to the baseline state shown in Table 3 (i.e. 7611.42 kg CPO/hr), the CPO capacity of the debottlenecked plant is has increased by 7%. With the increase in production, the amount of raw material (i.e. fresh fruit bunch (FFB) and steam) consumed has also increased by 7%. A trend is observed in the interactions of the mass flows, whereby an increase in production of CPO leads to the same percentage of increase in consumptions of raw material and utilities required in the process. This is because the process units in the POM are interconnected by a linear programming model. This high interdependency among individual process units results in disruption of the entire system when there are any changes made (i.e. increase production capacity of CPO). The electricity consumption was found to be the same because the additional Screw Press added into the process was not being utilised, as shown in Table 8, where the operating capacity fraction was equal to zero.

Table 40. Production capacity and process requirements after debottlenecking.

New CPO Production Capacity (kg/hr)	8139.65
New FFB Capacity (kg/hr)	32,082.00
Steam Consumption (kg/hr)	16507.08
Electricity Consumption (kWh)	419.8

Based on the framework (Figure 2), after the entire process is free from bottlenecks, the next step is to perform benefit-to-cost ratio analysis (BCR). The BCR was calculated using Eq. (8) and Eq. (9). The economic parameters used, information on the capital cost and annual operating cost of the equipment, along with the calculated values for BCR can be found in Table 9. From Table 9, by purchasing an additional Screw Press, the BCR obtained for the case study was 54.57, which is a lot more than 1. This shows that the additional income gained from increased CPO production far outweighs the cost required to purchase an additional Screw Press. This also shows that one process bottleneck could lead to a big loss in potential revenue that could be earned.

Other than that, the BCR could be very high because there was only one equipment bottleneck. After debottlenecking, the POM now has a production capacity 7% higher than the baseline. If for example, the POM owners would like to increase capacity by 50%, a lot more equipment would become bottlenecks and required to be debottlenecked. Different equipment have different costs, some have higher costs than others. These differences would reflect in the BCR results. Since in this case study, there is only one bottleneck involved, the BCR yields a value much larger than 1.

The following step in the framework was to verify if the cost to carry out the project exceeds the allocated budget of the project. In line with BCR, the initial capital investment of the Screw Press (i.e. US$ 100,000) is lesser than the budget allocated of US$500,000. Therefore, the debottlenecking solution can be justified economically and can be approved for construction.

Table 41. Benefit-to-cost ratio analysis for case study.

Total Operating Hours (hrs/yr)	6000
Additional CPO from Increased Capacity, Δy_{CPO} (kg/hr)	528.23
(kg/yr)	3,169,380.00
Selling Price of CPO, C_{CPO} (US$/kg)	0.6565
$C_{CPO}\,\Delta y_{CPO}$ (US$/yr)	**2,080,697.97**
Annualising Factor (/yr)	0.1315
Capital Cost of Screw Press (US$)	100,000.00
Annualised Capital Cost of Screw Press, C_{6a} (US$/yr)	13,150.00
Maximum Operating Capacity Fraction of Screw Press, x_{6a}^{max}	2.1389
$C_{6a}\,x_{6a}^{max}$ (US$/yr)	28,126.42
Annual Operating Cost of Screw Press (US$/yr)	10,000
Cost of Additional Equipment, C_{eq} (US$/yr)	**38,126.42**
BCR	**54.57(ACCEPTABLE)**

Conclusion

This research work presents a framework on identifying bottlenecks and debottlenecking in a palm oil milling (POM) process in the case where production capacity of crude palm oil (CPO) is required to increase. To identify the bottlenecks, an algebraic approach known as input-output modelling is adapted to first formulate the modelling equations of the process. The model was then solved in an optimisation tool, known as LINGO, to identify the bottlenecks. In addition to identifying the bottlenecks, the framework then proposes debottlenecking methods to free the process from bottlenecks. Benefit-to-cost ratio (BCR) analysis was performed on the debottlenecking methods to analyse its economic feasibility. To illustrate the developed framework, an existing POM was presented, given the objective to maximise CPO production capacity. It was found that the equipment at high risk of becoming possible bottlenecks when capacity increases were the Steriliser, Digester, Screw Press and Depericarper. The equipment which reached its maximum design capacity was identified as the Screw Press. The debottlenecking solution selected was to purchase an additional Screw Press

to cater for the increase in capacity. After debottlenecking, the plant was able to produce an additional 528.23 kg CPO/hr, which was a 7% increase from the baseline state. The BCR was found to be 54.57. This validates that the benefits of purchasing the additional Screw Press far outweighs the cost.

Acknowledgement

This research would never have been successful without the help of Dr. Viknesh Andiappan and Dr. Wan Yoke Yin. The author would like to extend the deepest gratitude for the guidance and supervision received.

References

[1] Green Palm, "Why is Palm Oil Important?," 2015. [Online]. Available: http://greenpalm.org/about-palm-oil/why-is-palm-oil-important. [Accessed: 24-Oct-2017].

[2] J. Mark, "What's Fueling the Demand for the Palm Oil Destroying the Rainforests of Indonesia?," 2013. [Online]. Available: http://www.earthisland.org/journal/index.php/elist/eListRead/whats_fueling_the_demand_for_the_palm_oil_destroying_the_rainforests_of_ind/. [Accessed: 11-Jun-2017].

[3] E. Lau, Y. Man, and A. Baharum, "A Qualitative Approach of Identifying Major Cost Influencing Factors in Palm Oil Mills and the Relations towards Production Cost of Crude Palm Oil," *Am. J. Appl. Sci.*, vol. 8, no. 5, pp. 441–446, 2011.

[4] H. Kasivisvanathan, R. R. Tan, D. K. S. Ng, M. K. Abdul Aziz, and D. C. Y. Foo, "Heuristic framework for the debottlenecking of a palm oil-based integrated biorefinery," *Chem. Eng. Res. Des.*, 2014.

[5] Malaysia Palm Oil Council, "The Oil Palm Tree." [Online]. Available: http://www.mpoc.org.my/The_Oil_Palm_Tree.aspx. [Accessed: 17-Jun-2017].

[6] T. Pinto-Varela, A. Barbosa-Póvoa, and A. Carvalho, "Sustainable batch process retrofit design under uncertainty—An integrated methodology," *Comput. Chem. Eng.*, 2016.

[7] O. Alshekhli, D. C. Y. Foo, C. L. Hii, and C. L. Law, "Process simulation and debottlenecking for an industrial cocoa manufacturing process," *Food Bioprod. Process.*, vol. 89, pp. 528–536, 2011.

[8] R. R. Tan *et al.*, "An algebraic approach to identifying bottlenecks in linear process models of multifunctional energy systems," *Theor. Found. Chem. Eng.*, vol. 46, no. 6, pp. 642–650, 2012.

[9] N. Tahouni, R. Khoshchehreh, and M. H. Panjeshahi, "Debottlenecking of condensate stabilization unit in a gas refinery," *Energy*, vol. 77, pp. 742–751, 2014.

[10] V. M. Enríquez-Gutiérrez, M. Jobson, L. M. Ochoa-Estopier, and R. Smith, "Retrofit of heat-integrated crude oil distillation columns," *Chem. Eng. Res. Des.*, vol. 99, pp. 185–198, 2015.

[11] H. Sugiyama *et al.*, "Multiobjective Retrofitting Methodology for Manufacturing Processes of Active Pharmaceutical Ingredients Considering Environment, Health and Safety Risks," in *Computer Aided Chemical Engineering*, vol. 38, 2016, pp. 79–84.

[12] L. T. Biegler and P. Saderne, "A mixed integer flowsheet optimization strategy

for process retrofits - the debottlenecking problem," vol. 13, no. 8, pp. 947–957, 1989.

[13] V. Andiappan, D. S. Ng, and R. R. Tan, "Design operability and retrofit analysis (DORA) framework for energy systems," *Energy*, 2017.

[14] Lindo Systems Inc., "LINGO," 2017. [Online]. Available: http://www.lindo.com/index.php/products/lingo-and-optimization-modeling. [Accessed: 22-Nov-2017].

eureca 2017 - Conference Paper
Paper Number 2CE13

Coagulant Dipping Time and Temperature Optimisation for Latex Glove Uneven Coating Investigation

Loong Than[1*], Siew Wei Phang[1], Kim Nam Ho[2]

[1] School of Engineering, Faculty of Built Environment, Engineering, Technology & Design, Taylor's University Lakeside Campus, Malaysia.
[2] TG Medical Sdn Bhd, F14, Klang Malaysia.

**Corresponding author email: loong.than@sd.taylors.edu.my*

Abstract
Powdered glove is produced by natural latex with the aid of coagulant. The composition of the coagulant contains wetting agent, calcium nitrate as coagulant and anti-tack agent. Generally wetting agent also known as surfactant that cause foam and resulted uneven wall thickness in glove production. As a result, the objectives of this research that needs to be achieved are selecting the suitable wetting agent sample that could be used such as sample E and sample T as well as optimising the parameter such as temperature of coagulant, weight percentage of wetting agent and coagulant dipping time to reduce of uneven glove production. In order to achieve the objective, the methodology for this research involve foam height test, cloud point test, wetting agent charactherisation using Fourier Transform Infrared Spectroscopy (FTIR), surface tension test, full factorial design of the experiment, glove thickness test, tensile strength test, glove weight test and response surface methodology analysis. Throughout the wetting agent charactherisation, sample T is chosen instead of sample E due to similar bonding of the wetting agent. With the completion of methodology, the result is recorded and plot the graph as well as contour graph with colour bar for analysis purpose. The surface tension of coagulant and tensile strength of glove sample are able to meet the requirement with the variation of wetting agent amount. With the graph being analyse, concept verification can be completed. While contour graph that being analyse, optimisation parameter can be determine to achieve the desired objective. As a result, the optimise parameter are 0.0175 wt% of wetting agent and about 5 seconds dipping time at 63 ℃. Throughout the optimum parameter that being determined, the average thickness is 0.09 ±0.004 mm with 11.33% error of thickness by comparing to 0.1mm thickness of ASTM standard. Hence, the objective of this research is achieved.

Keywords: Wetting agent, Uneven wall thickness, Coagulant, Foaming height, Surface tension

1. Introduction

In the present day, the glove has become an essential for daily activities such as housework and surgery operation. The purpose of these is basically to prevent infection and it is made up of natural latex. An example of glove that needs to be used in medical field such as surgical glove. This glove is mostly used for the doctor to treat patients. In order to produce this surgical glove, natural latex is required that can be obtained from Hevea Brasiliensis tree through bark tapping [1]. Besides, the thickness of the glove is essential in order to avoid pinhole of the glove. An uneven wall thickness or so called as 'fisheye' defect that can be refer in Figure 1. This is due to there is the presence of uneven adherence of latex on the mold. Former is basically referring to the mold that having the shape of a hand and it is used for glove production [2].



Figure 1: 'Fisheye' defect located in powdered glove.

In addition, 'fisheye' defect have a tendency to have a failure in tensile strength. For example, a glove that having variation in tensile strength would be easily torn off into pieces or difficulty when donning. With the 'fisheye' defect', the production of the powdered glove would have high rejection rate on the production. In order to reduce these issues, studies on the production of the powdered glove are necessary. However, there are various causes that could lead to 'fisheye' defect. The various causes are shown in Figure 2 below:

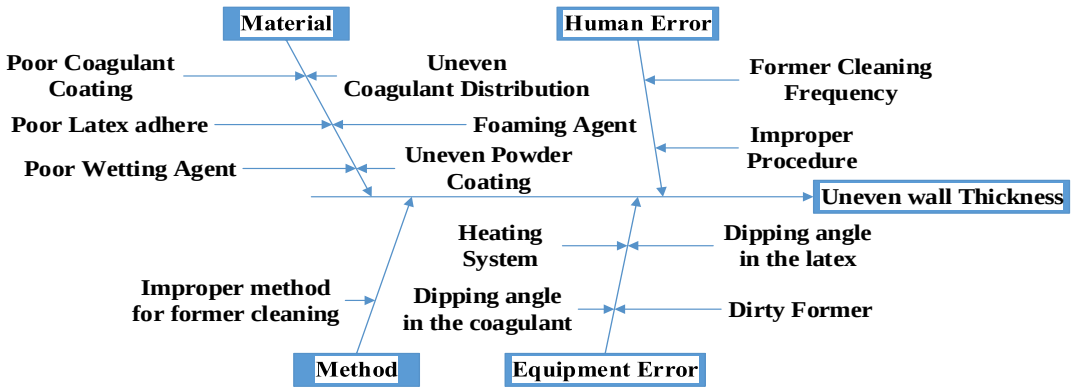


Figure 2: Ishikawa diagram for uneven thickness of glove [2-3].

By referring to Figure 2 above, 'fisheye' defect can be caused by human error, the material in the process line, equipment used and method. In term of the material in the process line, the coagulant is used for forming a coagulant layer so that latex able to adhere to the surface of the mold. An inefficient coagulant that used in the glove production would cause weak adherence of latex. For example, ammonia nitrate is one of the inefficient coagulants. Hence, calcium nitrate coagulant is mostly used in glove production where it has good adherence of latex [4]. The wetting agent is mostly used in the formulation of coagulant in the production of the powdered glove.

Wetting agent also known as foaming agent or surfactant. With the different amount of wetting agent can affect the thickness of the glove. This is because foam or bubble will be created when there is the presence of vigorous mixing of the solution with a wetting agent that adhere on the mold [5]. With this concept, repeatedly mold dipping on coagulant and stirrer that used to homogenise the coagulant can cause foam. However, the purpose of the wetting agent is to reduce the surface tension of the coagulant [5]. This is to allow coagulant is evenly coated the mold as the first layer.

In this research, foam is undesirable in the production of the powdered glove. As a result, it is necessary to understand how foam can be formed. In general, mold is required to dip into coagulant as the first layer. While coagulant consisted of a composition called as a wetting agent that functioned like a soap by which it can reduce the surface tension of the chemical solution [6]. Wetting agent will arise the issue of foam formation due to air entrapment whenever there is a presence of vigorous mixing. [5] In fact, the foam would trap about 80% of air whereby most of the production line would not desire as it would affect the productivity.[5] As a result, control on the rejection of the powdered glove is necessary as the purpose is to increase the quality of the glove and reduce the rejection rate. Meanwhile anti-tack agent is generally use to prevent the latex to adhere on the mold which result of glove to be strip off easily where it can be said as powdered agent [1].

Throughout this research paper, wetting agent named as sample E and sample would be used for experiment testing where both having general chemical functional alcohol ethoxylate. Objectives of this research that needs to be achieved are to select the suitable wetting agent sample that could be used such as sample E and sample T and optimise the parameter such as temperature of coagulant, weight percentage of wetting agent and coagulant dipping time to reduce of uneven glove production.

2. Methodology

In this research, objectives are desired to be achieved. In order to achieve the objective, quantitative research is implemented through using factorial design method to analyse glove sample. Besides, pre-screening test are needed to be done in order to screen out unnecessary experiment due to glove preparation sample consume a large amount of time. In order to optimise the different thickness in the production, analysis and optimise the parameter of the powdered glove production is determine through the tensile strength, thickness of glove. Hence, validation and verification of the result from the experiment will be performed in the section below.

2.1 Pre-screen Test – Foaming Height Test

The first screening test is initiate before the experiment is proceed. These first pre-screening test is to determine the root cause of the foaming during the agitation of the coagulant. As the coagulant need to be agitate over period of time. This is to ensure the homogeneity of the coagulant as well as avoid anti-tack agent to be sediment such as calcium carbonate [6]. Based on research, it state that wetting agent is used about 0.001 wt% to 85 wt% [7]. While based on other research, wetting agent also could be used with the range of 1 wt% to 10 wt% in production line [8]. Besides, wetting agent have been effective with a less amount where the purpose of the wetting agent is to reduce the surface tension of the coagulant [6]. Hence, small amount wetting agent from 0%, 0.005 wt%, 0.03 wt% and 0.05 wt% are require pre-screen test.

The procedure of the foaming height test is basically set the composition in weight percentage to be constant but varies the weight percentage of wetting agent. This is to verify the theory through research. After prepared the chemical sample, coagulant that added without wetting agent is placed inside the mechanical stability tester which operate at 14000 rpm. Recorded the reading of the foam height. Then repeat the same step for other weight percentage of wetting agent and test with mechanical stability tester.

2.2 Pre-screen Test – Cloud Point Test

After the first pre-screen test, it will be proceed to second pre-screen test which is cloud point test. Cloud point is basically refer to the point where wetting agent could no longer operate at its function when temperature is above particular temperature [9]. When this happen, the coagulant would turned cloudy [9]. However, sometime coagulant is added with anti-tack powder such as calcium carbonate where the coagulant would eventually turned into cloudy solution. Hence, the test would require to remove the anti-tack agent so that the coagulant is still in clear solution. The anti-tack agent is generally used for avoiding the glove to be stick on the mold when glove is being made [6]. The test would be varying 0 wt%, 0.005 wt%, 0.03 wt%, 0.05 wt% and 0.08 wt% of wetting agent with coagulant. The procedure of the test are basically coagulant without added with anti-tack agent and varies with 0 wt%, 0.005 wt%, 0.03 wt%, 0.05 wt% and 0.08 wt% of wetting agent. When the sample of coagulant without anti-tack agent and added with 0.005 wt% of wetting agent, heat the sample solution until the solution turned to be cloudy. Then repeat the experiment with 0 wt%, 0.03 wt%, 0.05 wt % and 0.08 wt% of wetting agent. With the result of the test, the coagulant temperature must be set below the cloud point where the common range is within 60℃ to 70℃ [10].

2.3 Pre-screen Test – Surfactant Characterisation

The next pre-screen test is refer to the surfactant charactherisation. In this research, there are two wetting agent sample which are sample E and sample T. Since both of this sample are alcohol ethoxylate that consist of general chemical structure of $R\text{-}(CH_2H_2O)_n\text{-}H$ [10]. Where R is refer to alkyl group and also known as hydrophobic group [11]. While $\text{-}(CH_2H_2O)_n\text{-}$ is refer to hydrophilic group and also known as ethylene oxide [11]. When more number of ethylene oxide group in one of the sample, it would have higher tendency to reduce more surface tension and creating more foam [11]. The procedure of this experiment is basically using Fourier Transform Infrared Spectroscopy (FTIR) equipment to charactherise the bonding of the chemical sample. The chemical sample are sample E and sample T. At first, wipe the diamond piece of Fourier Transform Infrared Spectroscopy with ethanol. Then of drop a liquid of water on the diamond piece on the plate and run as blank spectrum. After that, drop a of liquid of the sample E on the diamond piece that is on the top of the plate and collect the spectrum of sample E. Repeat the experiment for sample T. The sample E and sample T would be tested with Fourier Transform Infrared Spectroscopy and generate IR spectrum where bonding of the sample can be known.

2.4 Full Factorial Design

The major step of the experiment is design with full factorial design. The research are basically considering temperature of coagulant (X_1), weight percentage of wetting agent (X_2) and mold dipping time in the coagulant (X_3) that could affect the uneven thickness of the glove.

Besides, these factor consist of 3 level as well. This would provide the 3^3 full factorial design and lead to have 27 runs [12–14]. The experiment crafted with full factorial design will be conducted with triplicate.

2.5 Glove Sample Preparation

By refer to section 2.4, glove sample preparation is based on experiment design. The glove sample preparation is basically prepared manually instead of making used of production line. This is due to limitation of the equipment that could be used. The preparation of glove is called as lab dipping. Glove sample was prepared on lab scale basis, which consist of four dipping tank (volume for 7kg each). The first tank was filled with dilute acid; second tank of 0.005 wt% wetting agent; 3rd tank of pure latex, and 4^{th} tank was filled with corn-starch. Firstly, dip the mold into the acid tank for 10 seconds and rinse with water. Then place the mold inside the oven and dry it for 3 minutes at about 140℃ [1,6]. At the same time, heat the coagulant until 58℃ and took out the mold after it have dried. After that, dip the mold into the coagulant for 5 seconds and dry it again for 3 minutes in the oven. After dried, dip the mold into the latex for 3 seconds and dried it for 10 minutes [6]. Then took out the mold and dip in cornstarch for 12 seconds. Finally, dried the mold again for 6 minutes. After 6 minutes, took out the mold and let it cool down so that glove can be stripped off. Repeat the experiment based on the full factorial design in section 2.4.

2.6 Glove Sample Characterisation

After the glove sample have been prepared, various test can be performed so that analysis of the sample can be done. The test that going to be done are tensile strength, thickness and glove weight. These parameter can be measure using Tensile Strength Tester, Tensile Test Sample Cutter and Thickness Gauge equipment.

2.6.1 Tensile Strength Tester and Sample Cutter

Tensile Strength Tester was used to determine the tensile strength of the glove. Based on ASTM D-3577 standard, the glove is generally required to have 18MPa that compounded from natural rubber latex [15-16]. This shows that tensile strength for the glove sample must be above 18MPa even though there is no thickness issue. This is because this research is studying on the thickness issue while maintaining the other trait such as tensile strength. In order to use the Tensile Strength Tester, sample have to be cut into plate shape based on the ASTM standard. The glove would be puncture with the Tensile Test Sample Cutter with glove cutter to form a plate shape glove which is shown below. Glove preparation throughout the experiment is cut using the glove cutter and tested with the tensile strength tester. Table 1 below shown the ASTM standard for the plate shape cutting. Hence, the plate shape cutting from the glove sample have to be follow the standard so that can be measured with Tensile Strength Tester.

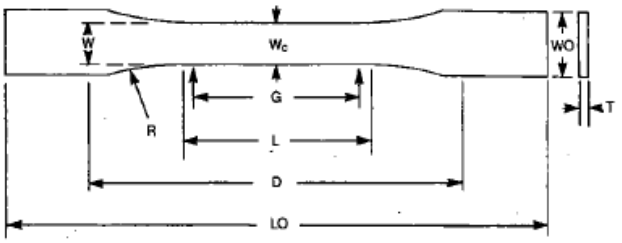


Figure 4: ASTM plate shape cutting [17].

Table 1: ASTM standard [17].

Dimension	Unit, mm
Width of narrow section (W)	6
Length of narrow section (L)	33
Width overall (WO)	19
Length overall (LO)	115
Gage length (G)	25
Distance between grips (D)	65
Radius of fillet (R)	14
Outer Radius (RO)	25

2.6.2 Thickness Gauge Test

In this research, the major scope of this studies is thickness of the glove. As a result, the sample of the glove that have been prepared would be measured with thickness gauge apparatus. Based on [15], the thickness of the glove is required to be around 0.1mm. Hence. The target of the thickness is 0.1mm.In this procedure, it is using the apparatus to measure the thickness of the glove at the location for the palm, between thumb with first finger, between first finger with second finger, between second finger with third finger and between third fingers with fourth finger.

2.7 Surface Tension Test

Based on section 2.4, the experiment is crafted through full factorial design. The coagulant of each combination with wetting agent is collected during the glove sample preparation. With this coagulant sample that being collected, it can be tested with surface tension meter DST-60 which are making use of wilhelmy plate method [18]. Based on [7], the ideal surface tension for coagulant is in the range of 1MPa to 40MPa. While any coagulant that having surface tension above 40MPa is undesirable [7].

2.8 Response Surface Methodology

After the test on section 2.6, response surface methodology can be applied to determine the optimum parameter in order to reduce uneven wall thickness issue. This methodology require full factorial design to execute. Based on section 2.4, there are 3 factor and 3 level. As a result, there would have 9 graph that would be representing the data of the glove sample. With the comparison of the graph, optimum parameter can be determine.

2.9 Verification Result

After the section 2.8 is completed, analysis for optimum parameter can be obtained. From this optimum parameter being collected, temperature of coagulant, time dipping of coagulant and amount of wetting agent would be tested for another manual dipping testing again. This is to verify the parameter on whether able to achieve the target of 0.1mm thickness of glove while maintaining the tensile strength. Then the error can be calculated based on difference of thickness comparing towards 0.1mm thickness. With this error, effectiveness of this method could be concluded.

3. Result and Discussion

Throughout the methodology that have been described, analysis on the result would be divided based three section. The four section are analysis on pre-screen test, tensile analysis, glove thickness analysis, glove weight analysis and response surface methodology analysis.

3.1 Analysis of First Pre – Screen test

As the result of the first pre-screen test is being done, the result is shown in Figure 5 below. Based on Figure 5, it shows that the increasing of the amount of wetting agent in coagulant would cause the foam height to be greater. While with no added wetting agent, there is no foam height is being formed. The purpose of this pre-screen test is to determine the root cause of the uneven thickness. This is due to uneven thickness is basically caused by various factor such as webbing foam on the between finger that appear during coagulant dipping. As a result, particular area that webbing foam occurs and rupture at the same time would lead calcium nitrate that disperse on the mold to fade. Hence, the glove thickness that produce would be affected.

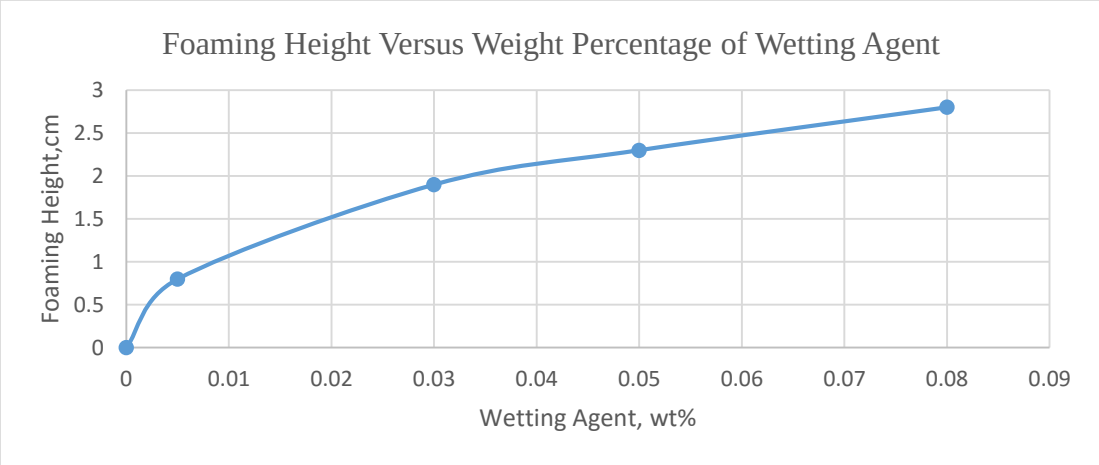


Figure 5: Foaming Height versus Weight Percentage of Wetting Agent.

With this first test of the approach, the test is basically verify the concept of the wetting agent and would cause foam. In this research, other factor that explain in section 1 would be neglected except wetting agent. This is to allow the research study to be not complex. Hence, the root cause can be finalise as foam that created through wetting agent when there is agitation [5].

3.2 Analysis of Second Pre – Screen test

After the first pre-screen test is completed, cloud point test is the most crucial point to be study. This is because the cloud point is use to determine the functionality of the wetting agent that able to be used [9]. At the particular temperature, the temperature of the coagulant would cause the cloud point to be impaired. This resulted that the coagulant would not able to be operate above the temperature during the glove sample preparation process. As a result, the design temperature have to be lowered than the cloud point temperature of the sample E and sample T. Based on Table 2, sample E and sample T is basically having cloud point that is more than 80℃.

This shows that both wetting agent able to be function below the temperature of the cloud point. Hence, the design temperature is can be set in between 58℃ to 68℃ due to common range is within 60℃ to 70℃ for coagulant temperature [10].

Table 2: Cloud Point Test result.

Chemical	Weight Percentage of wetting agent, %	Cloud Point for Sample E, ℃	Cloud Point for Sample T, ℃
Coagulant	0	No Cloud Point	No Cloud Point
Coagulant	0.005	More than 80 ℃	More than 80 ℃
Coagulant	0.03	More than 80 ℃	More than 80 ℃
Coagulant	0.05	More than 80 ℃	More than 80 ℃
Coagulant	0.08	More than 80 ℃	More than 80 ℃

3.3 Analysis of Third Pre – Screen test

The final pre-screen test can be proceed when the other pre-screen is completed. This test is to determine the bonding of the wetting agent. Since both sample E and T are alcohol ethoxylate, there is possibility of the wetting agent to be having similar bonding. The screening is necessary due to section 2.4 is undergoing full factorial design where it would consume a large amount of time for glove sample preparation.

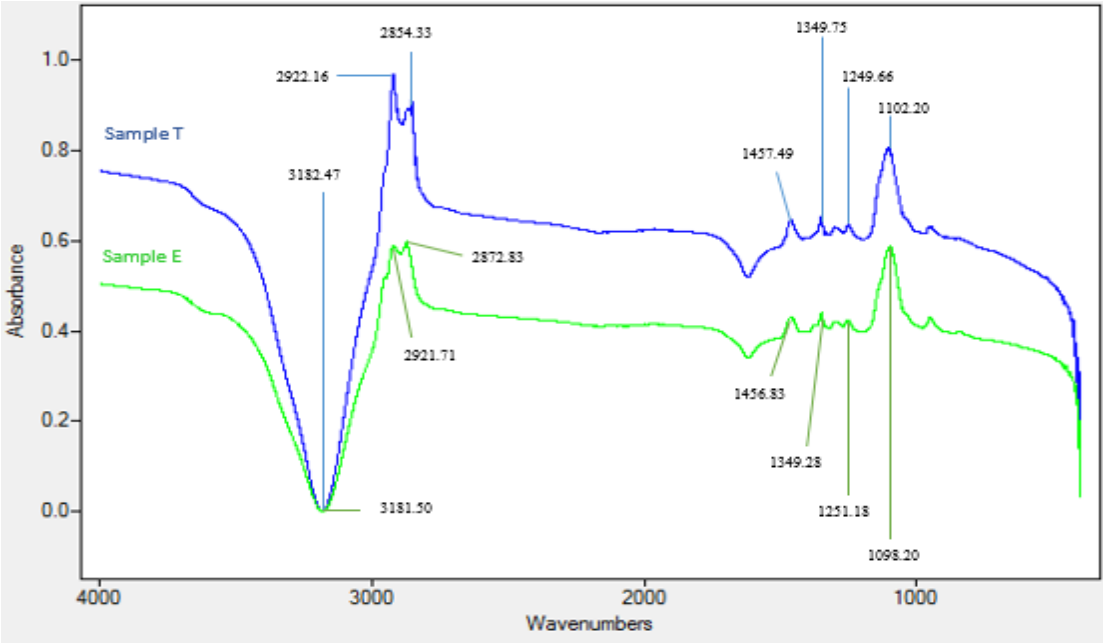


Figure 6: FTIR Spectrum of both sample

Based on Figure 6, it is refer to the spectrum of sample E and sample T. In the first zone section of sample T, there is U shape peak that located about 3182.47 cm^{-1} which in between 2650cm^{-1} to 3200cm^{-1} [19]. This U shape peak is broad and strong that would represent the OH- group [19]. On the zone 2, second peak is about 2872.79cm^{-1} and 2854.33cm^{-1} is refer to alkyl group or CH_3- which is in between 2960cm^{-1} to 2850 cm^{-1} [19]. On the fingerprint zone, peak at 1457.49cm^{-1}, 1349.75cm^{-1} and 1249.66cm^{-1} are methylene or $–CH_2$ [19].

While peak at 1102.20 cm^{-1} is refer to ether group or -C-O- [19]. While based on spectrum of sample E, in the first zone section, the U shape peak that located about 3181.50cm^{-1} that lies in between 2650cm^{-1} to 3200cm^{-1} [19]. This peak is broad and strong that represent the OH- group [19]. While on the zone 2, second peak is about 2921.71cm^{-1} and 2872.83 cm^{-1} is refer to alkyl group or CH_3- that lies in 2960cm^{-1} to 2850 cm^{-1} [19]. Lastly on the fingerprint zone, peak at 1456.83cm^{-1}, 1349.28cm^{-1} and 1251.18cm^{-1} are methylene or $–CH_2$ [19]. While peak at 1098.20 cm-1 is refer to ether group or -C-O- [19]. With both of the sample spectrum is shown in Figure 6, it shows that both of the sample of wetting agent is similar in term of bonding. This shows that sample T have more of hydrophilic and hydrophobic bonding compare to Sample E due to absorbance value is higher which mean the finger print zone of sample T have more ethylene oxide group [11]. Ethylene oxide group in alcohol ethoxylate is the role that promote foam and surface tension reduction properties [11]. As a result, sample T promote more foam and reduce more surface tension compare to sample E. Besides, sample T is easier available in market than sample E. Hence, sample E is removed.

3.4 Analysis of Surface Tension

Based on the coagulant with varies of wetting agent amount, Figure 7 below shows the decreases trends of the surface tension on coagulant with the increase of wetting agent. This test is to verifying the coagulant that need to be within the standard of the typical surface tension of the coagulant. The typical surface tension of coagulant is about 0.001 N/m to 0.040N/m [7]. Based on the Figure 7, the coagulant without the wetting agent is having greater surface tension which is 0.0486N/m. This means that the coagulant is not suitable for glove sample preparation. While with the small amount of the 0.005 wt% wetting agent added, the surface tension is about 0.04 N/m.

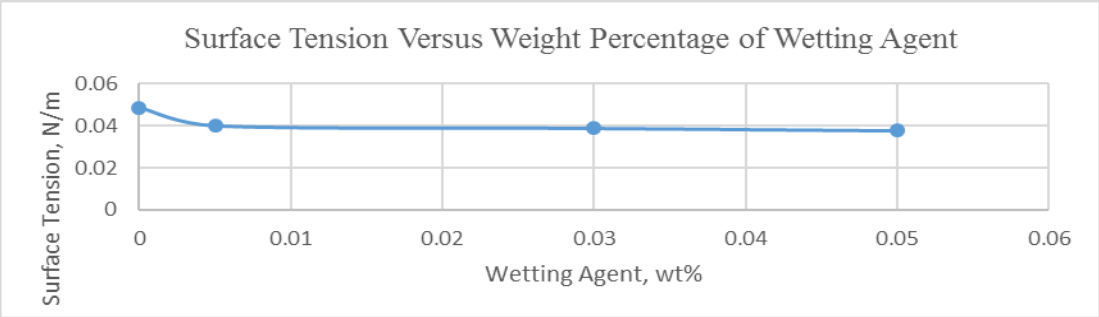


Figure 7: Surface Tension versus Weight Percentage of Wetting Agent.

3.5 Analysis of Glove Sample Characterisation

After the glove sample that have prepared, glove weight, glove thickness and its tensile strength are require to be studied so that optimisation on the parameter can be determined. With the result being collected, it can make use of Matlab software to plot the surface plot with colour bar as parameter to be studies. With the response surface methodology, optimisation of the production can be done.

3.5.1 Tensile Strength Analysis

After tested the glove with tensile strength, the glove standard need to achieve 18 MPa. The result is collected and plotted with surface plot with the factor of temperature of coagulant, dipping time of coagulant and tensile strength of the glove at different of amount of wetting agent. This plot is plotted using Matlab software.

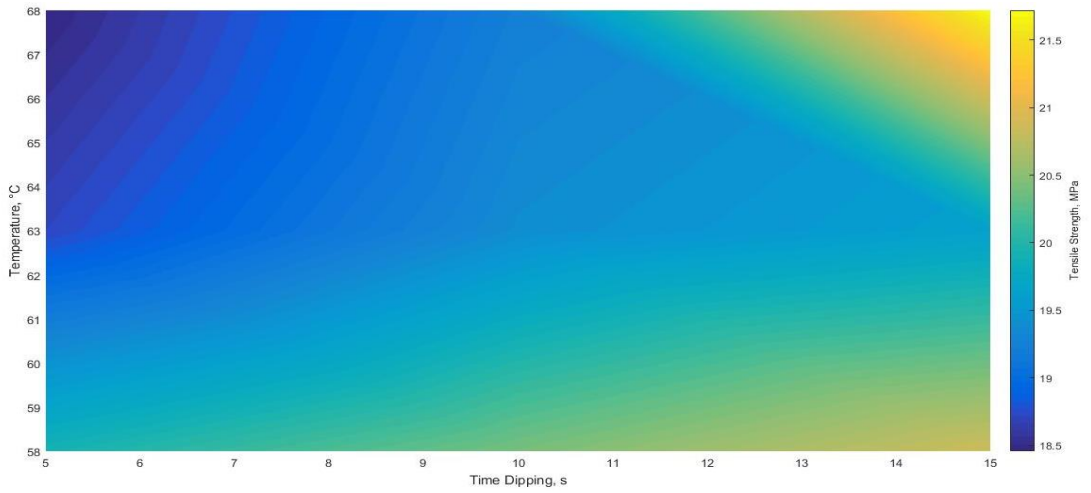


Figure 8: Contour of temperature and time against tensile strength of glove for 0.005 wt% of wetting agent

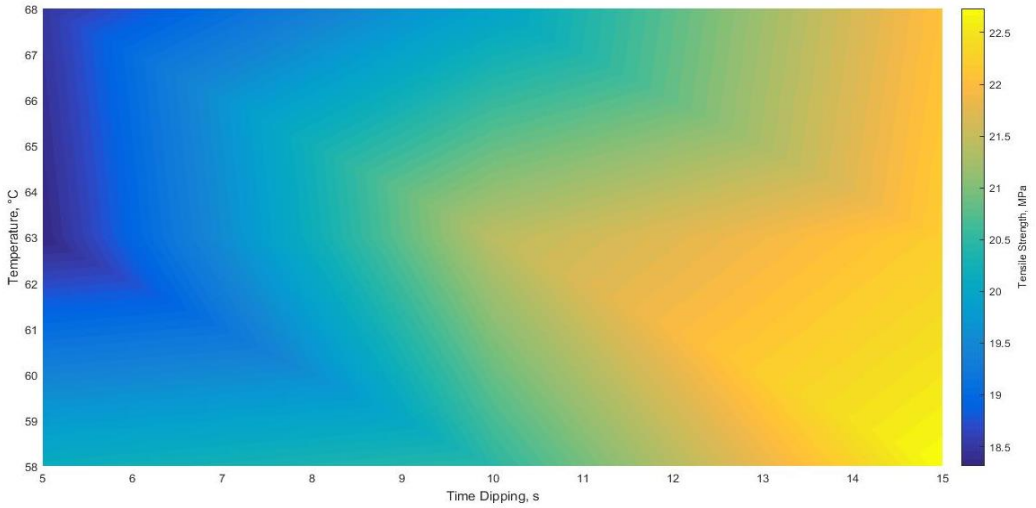


Figure 9: Contour of temperature and time against tensile strength of glove for 0.03 wt% of wetting agent

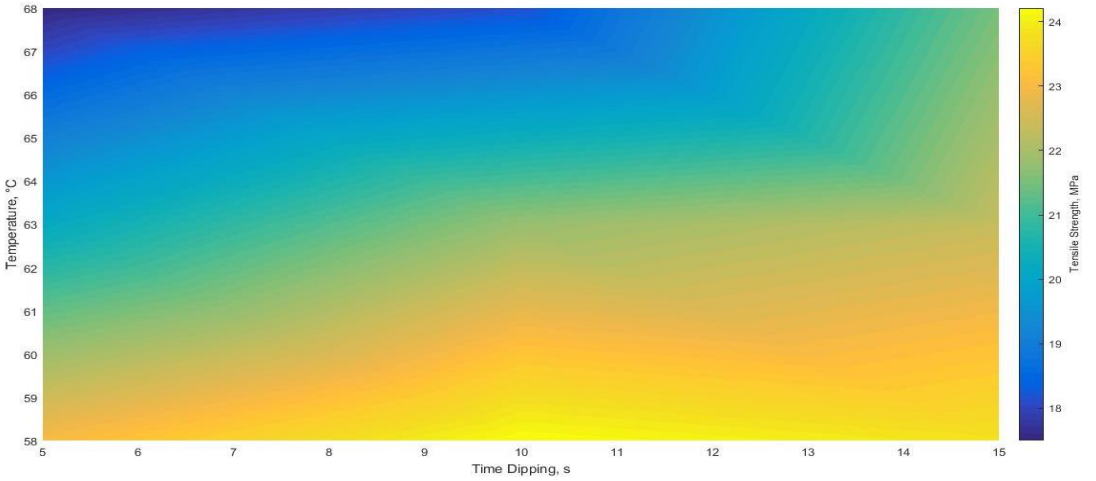


Figure 10: Contour of time and temperature against tensile strength of glove for 0.005 wt% of wetting agent

Based on Figure 8, the tensile strength against temperature and dipping time is basically meet the requirement of the standard at 18MPa which shown based on the colour bar. In this Figure 8, the glove sample prepared at 0.005 wt% of wetting agent. The glove that produce on at temperature range from 58℃ to 68℃ as well as the range of time dipping of 5 seconds to 15 seconds meet the standard requirement of the tensile strength. While at temperature of 63℃ and 15 seconds, tensile strength should have about 20MPa and above. Based on observation, whenever the temperature of the coagulant is low such as 58℃. The coagulant is hardly evaporate on the surface of the mold. This resulted the coagulant to be flowing on the mold instead of dried where the mold is having smooth surface. If the mold does not have smooth surface which allow forming of thin film without any restrain and would not dripped off [20]. This provide coagulant to adhere on the surface with a thicker film and provide higher tensile strength as well. By referring to Figure 8, coagulant is hardly evaporate at 58℃ and this allow the area on the mold that to have lesser amount of coagulant. Hence, the glove tensile strength should be lowered at lower temperature. This means that there is fluctuation in reading where it is actually require more glove sample so that the glove reading would be consistent.

While based on Figure 9, the glove sample is tested at 0.03 wt% of wetting agent. Based on the colour of the contour, it show that the tensile strength against temperature and dipping time is basically meet the requirement of the standard at 18MPa. Since the tensile strength does not varies much compare from 58℃ to 68℃, more glove sample are required to be studied so that to allow consistent reading. Based on the Figure 10, the tensile strength of the glove at 58℃ is greater than 68℃. This is basically not supposed to be happened theoretically and the result should be other way around. The reason of this difference of tensile strength is due to the dipping time for latex is not consistent that may due to allow the glove tends to be thicker. This resulted at 58℃ to have higher tensile strength. However, the reading of tensile strength against time dipping and temperature able to meet the standard of tensile strength.

3.5.2 Thickness Glove Analysis

On the other hand of glove thickness, it is the most crucial part as it determine the uneven wall thickness. Based on [14], the target standard of the powdered glove thickness is basically 0.1mm.

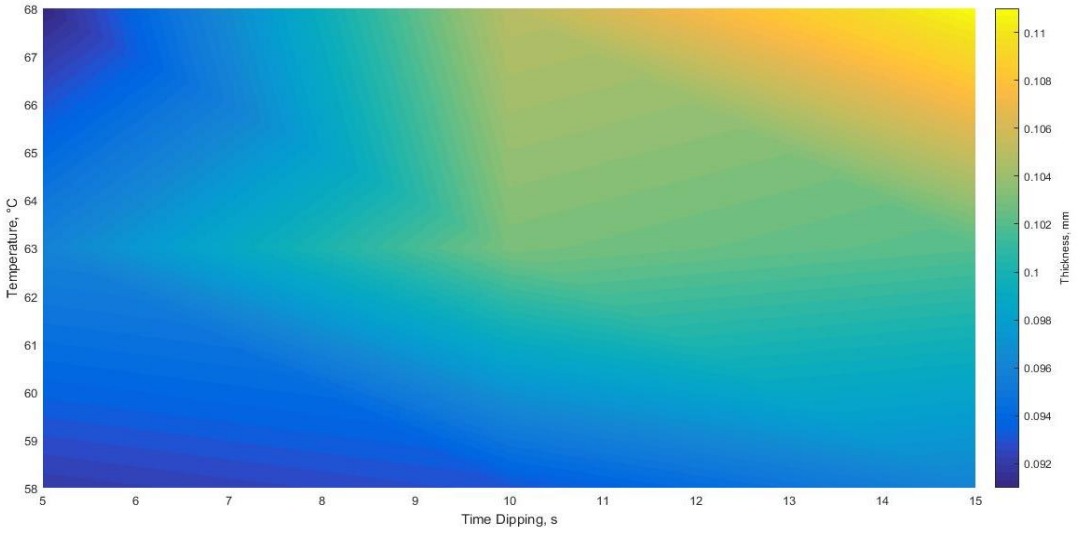


Figure 11: Contour of time and temperature against glove thickness for 0.005 wt% of wetting agent.

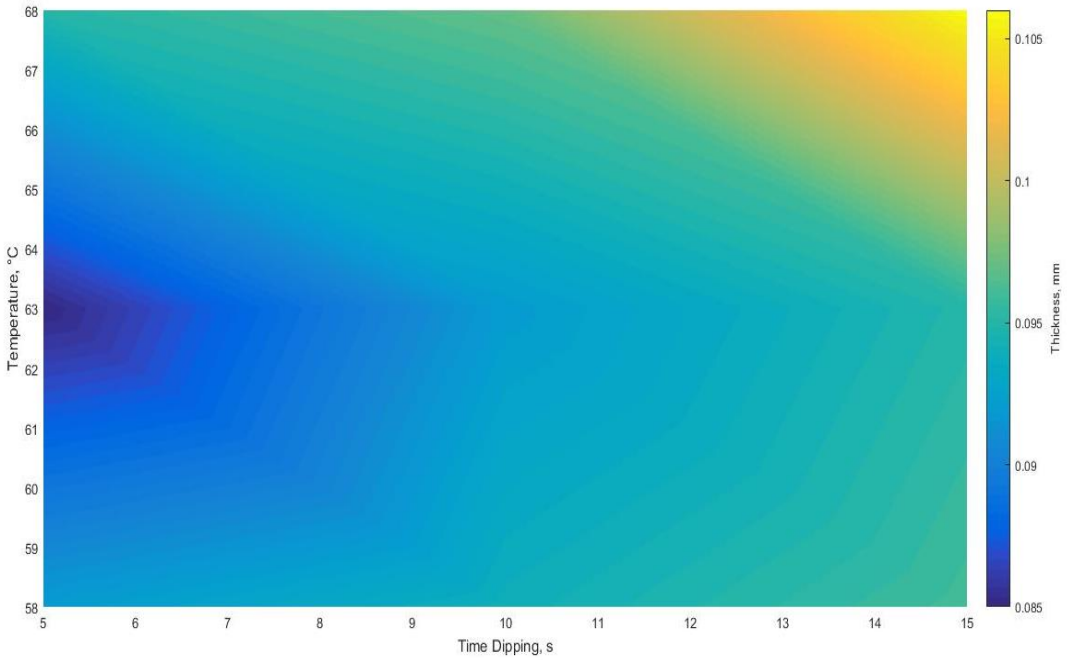


Figure 12: Contour of time and temperature against glove thickness for 0.03 wt% of wetting agent

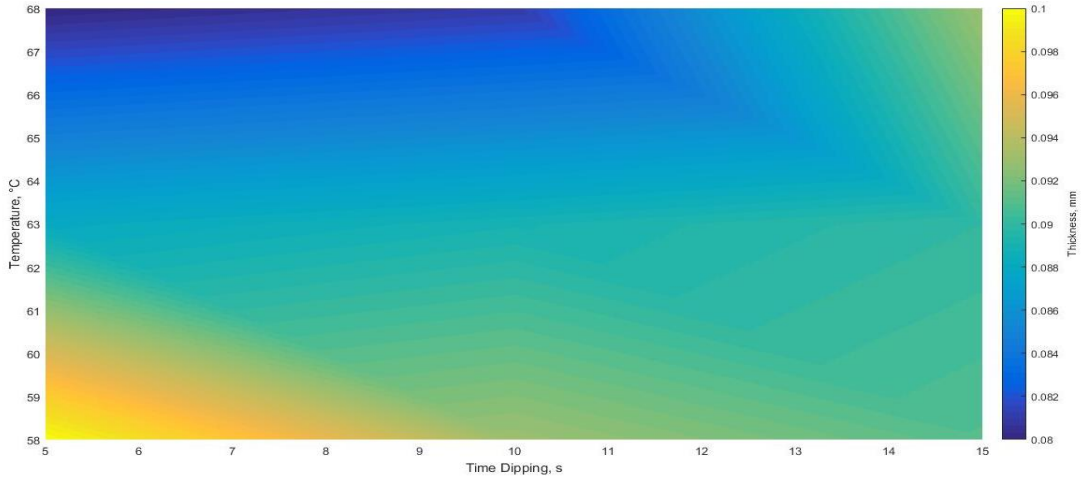


Figure 13: Contour of time and temperature against glove thickness for 0.05 wt% of wetting agent

Refer to the Figure 11, the colour bar shows the coagulant temperature at about 63℃ with 6 seconds dipping time. This enable to achieve the 0.1mm. Besides, at 68℃ with 8 seconds dipping time also able to achieved the 0.1mm. Moreover, this Figure 11 shows that the trend where thickness increases with the dipping time of the coagulant which is synchronise with the concept that mention previous section. Based on Figure 15, temperature at 66℃ until 68℃ with 12 to 15 seconds able to achieve thickness of 0.1mm. This result is not able to be applied in production line. This is because process line operate at high speed where 12 to 15 seconds is not able applicable. By comparing Figure 11 and Figure 12, Figure 12 should have better performance as 0.03 wt% wetting agent basically able to coat on the mold better than 0.005 wt%.

However, more amount of wetting agent would create more foam and bubble on the mold. Based on observation, the coagulant of wetting agent at 0.03 wt% and 0.05 wt% are having large amount of bubble compared to 0.005 wt% wetting agent. This can be shown in Figure 14. The reason that the coagulant need to be agitate constantly due to avoid the anti-tack agent to be sediment.



Figure 14: Wetting agent at 0.005 wt% (left), 0.03 wt% (middle) and 0.05 wt% on the (right)

The figure 17 below show the foam on the mold that affect the on the latex dipping. With this reason, the tensile strength of the glove is also affected by this foam that can compare Figure 9 and Figure 12. Also, higher temperature of the coagulant able to break the foam compared to the lower temperature as shown in Figure 11 and Figure 12. As a result, lower surface tension liquid would allow bubble foam of liquid would be larger [21-22]. Hence, increase in liquid drainage and lead bubble to rupture during withdrawing of mold after coagulant dipping. While at lower temperature, it would have higher viscosity that allow the bubble to retain is shape for a longer period. Besides, the bubble foam would having smaller bubble compare to higher temperature and liquid drainage tendency would be lower. As a result, the foam does not rupture. While this foam would only rupture during the drying process of coagulant in oven. This means that the rupture of foam in the certain area in oven will have less deposited of calcium nitrate. Hence, thickness of glove is affected.



Figure 15: Foam on the mold (Left) and Latex uneven coating (Middle) and Sticky Glove at the cuff area (Right).

Based on Figure 13, the foam height at 0.05 wt% is greater than 0.005 wt% and 0.03 wt% where it could be refer to Figure 5. This shows 0.05 wt% have the foam issue that similar to wetting agent at 0.03 wt% that can be based on Figure 15. But 0.05 wt% wetting agent is having more serious issue where there is presence of webbing that happen between the thumb and first finger. Even though higher temperature is said to be able to break the foam forming. However, there is too much wetting agent in this range of temperature from 58℃ to 68℃. As a result, the reading of the thickness fluctuate. This means that higher temperature is required to break more foam and more glove sample is require for consistent reading.

At 0.005 wt% wetting agent, the glove sample having issue of sticky where anti-tack agent is not disperse well enough. This is due to wetting agent is used to ensure a better coating effect on the mold. While wetting agent at 0.03 wt% and 0.05 wt%, the glove also the issue of sticky glove where located at the foam area during coagulant dipping.

3.6 Analysis of Response Surface Methodology Result

Since the result of the tensile strength on Figure 8, Figure 9 and Figure 10 show a positive result. Its narrow the optimisation of the glove thickness. Based on section 3.5.2, the best parameter of the glove sample are 63℃ with 6 seconds dipping time and 68℃ with 8 seconds dipping time. Both of this parameter able to achieve 0.1mm thickness with 0.005 wt%. But at 0.005 wt%, the glove tends to be sticky. Hence, more wetting agent is require so that anti-tack agent able to disperse evenly. Based on Figure 16 below, by choosing the parameter 63℃ with 6 seconds dipping time would be wise as lower temperature would have lower operating cost for the coagulant. While lesser dipping time that is 6 seconds would have a better profit in glove production compare to 8 seconds. This is due to lesser time require to produce the glove sample. As a result, fixing the temperature at 63 ℃ and making variation of the wetting agent amount and dipping time would the final optimisation. The optimisation parameter on Figure 19 are 0.0175 wt% of wetting agent and about 5 seconds dipping time at 63 ℃.

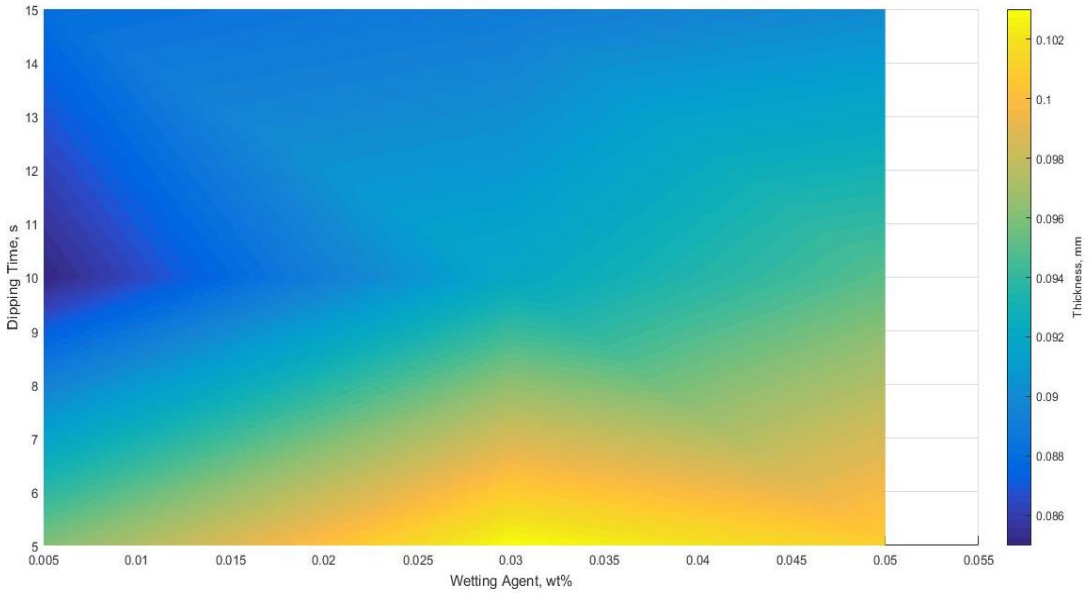


Figure 16: Predicted time and wetting agent amount against glove thickness for 63℃

3.7 Verification Result

As the optimum parameter is being collected, three sample of glove is obtained through the manual lab dipping. Table 3 below shows the average result of the thickness and tensile strength as well as error percentage of the result. By referring to Table 3, the glove that produce from the experiment is having average of $0.09 \pm 0.004\ mm$. This result is does not achieve the targeted value of 0.1mm for ASTM standard. Besides, there is having error about 11.33% lies in glove thickness result compared to targeted thickness. The reason of this error is mainly due to human error.

While the average tensile strength of glove produce at 19.480MPa is higher than ASTM standard of 18MPa. This means that the glove meet the requirement standard as the parameters suitable which synchronise with section 3.5.1 discussion. Furthermore, the glove that produce through the optimum parameter is having sticky effect on the surface of the glove. This is due to the wetting agent is not enough to disperse the anti-tack agent throughout the mold. In order to avoid this sticky issue, adding more anti-tack agent into coagulant would be able to negate this issue.

Table 3: Error percentage compared to targeted thickness.

Average Thickness, mm	Targeted Thickness, mm	Error Percentage, %	Average Tensile Strength, MPa
0.09	0.1	11.33	19.480

4. Conclusion

In conclusion, there is two potential optimum parameter that is considered before electing the wetting agent amount. The parameter are 5 seconds dipping time at 63 ℃ are compared with 8 seconds dipping time at 63 ℃. Generally, lower temperature would have lower operating cost for the coagulant and lesser dipping time that is 5 seconds would have a better profit in glove production compare to 8 seconds. With lower operating cost on time dipping and temperature, this parameter is expected to able to produce mass amount of glove with low number of unweven wall thickness issue. This would indirectly increasing the profit due to more glove can be sold instead of dispose or sold in lowered price for unweven wall thickness glove. Besides, user who using the glove would have a better confidence in doing task instead. As a result, the optimise parameter throughout the whole experiment are 0.0175 wt% of wetting agent and about 5 seconds dipping time at 63 ℃ that being selected. Throughout the optimum parameter that being determined, the average thickness is 0.09 ±0.004 mm with 11.33% error of thickness by comparing to 0.1mm thickness of ASTM standard. While sample T is being used in this experiment instead of sample E due to sample T is easier to be obtained through market. Hence, the objective of this research is achieved.

References

[1] Yip, E. & Cacioli, P. (2002). The manufacture of gloves from natural rubber latex. *Journal of Allergy and Clinical Immunology*, *110*(2), s3-s14.

[2] Ng, M. C., Ab-Samat, H. & Kamaruddin, S. (2013). Reduction of defects in latex dipping production: A case study in a malaysian company for process improvement, *The International Journal of Engineering and Science*, *2*(6), 01-11.

[3] Dafader, N. C., Jolly, Y. N., Haque, M. E., Akhtar, F. & Ahmad, M. U. (1999). The role of coagulants on the preparation of dipped film from radiation vulcanized natural rubber latex, *Polymer-Plastics Technology and Engineering*, *38*(2), 267–274.

[4] Zaharah, W. (1998). *Potential for process improvement of the rubber glovemanufacturing industrial case study process: An industry case study*. Doctoral dissertation, University of Newcastle, Newcastle.

[5] Joseph, D. (1997). Understanding foams & foaming, *Journal of Fluids*

Engineering, 1-8.
[6] Cacioli, P. (1997). Introduction to latex and the rubber industry, *Revue Francaise d'Allergologie et d'Immunologie Clinique*, *37*(8), 1173–1176.
[7] Lipinski, T. M. (2014). Powder-free coagulants with silicone surfactants, *US Patent Application Publication,1*(12), 1-38.
[8] Nile, J. G. & Gromelski, S. J. (2003). Manufacture of rubber articles, *United States Patent*, *1*(12), 0–4.
[9] Kartal, C., Akbas, H. (2006). Study of the cloud point of nonionic surfactant and nonionic-cationic surfactant mixture : Effect of electrolytes, *34*, 41–44.
[10] Dunlop Rubber Co. Ltd. (1901). Latex compounds, pp. 1–8.
[11] Arvind Mafatal Group (2010). Technical note : NR-Latex & Latex products, pp. 1–56.
[12] Bezerra, M. A., Santelli, R. E., Oliveira, E. P., Villar, L. S. & Escaleira L. A. (2008). Response surface methodology (RSM) as a tool for optimization in analytical chemistry, *Talanta*, *76*(5), 965–977.
[13] Carley, K. M., Kamneva, N. Y. & Reminga, J. (2004). Response surface methodology, *CASOS Technical Report*, October, pp. 1–26.
[14] Garcia-Cabeza, A.L., Ray, L. P., Marin-Barrios, R., Ortega, M. J., Moreno-Dorado, F. J., Guerra, F. M. & Massanet G. M (2015). Optimization by response surface methodology (RSM) of the Kharasch-Sosnovsky oxidation of valencene., *Organic Process Research & Development*, *19*(11), 1662–1666.
[15] ASTM International. (2012). Standard specification for rubber surgical gloves, *ASTM*, vol. 7, no. Reapproved, pp. 2–6.
[16] ASTM International. (2015). Standard specification for rubber examination gloves, *ASTM*, vol. 09.02, no. Reapproved 2010, pp. 1–5.
[17] ASTM International. (2003). Standard test method for tensile properties of plastics, *ASTM*, pp.46-58.
[18] Kromtek Sdn. Bhd. (2013). Digital surface tension analyzer, pp.1-2.
[19] Uddin. J. (Ed.). (2012). *Macro to nano spectroscopy*. Croatia, InTech.
[20] Sandy F. B. C., Huang W.N., and Rogers C. M. (1994), "Glove Forming Method," *US Patent Application Publication,1(19), 1-9.*
[21] L. Indrawati, Z. Wang, G. Narsimhan, and J. Gonzalez, "Effect of processing parameters on foam formation using a continuous system with a mechanical whipper," *J. Food Eng.*, vol. 88, no. 1, pp. 65–74, 2008.
[22] A. Saint-Jalmes, "Physical chemistry in foam drainage and coarsening," *Soft Matter*, vol. 2, no. 10, p. 836, 2006.

eureca 2017 – Conference Paper
Paper Number 2CE14

Assessment of Natural Deep Eutectic Solvent (NADES) Pretreatment on Sugar Production from Lignocellulosic Biomass

Jun Mun Yuen, Li Wan Yoon, Yin Hui Chia

Sh4wn95@hotmail.com

liwanyoon@gmail.com

School of Engineering, Taylor's University, Malaysia

Abstract

Due to depletion of world petroleum reserves, renewable resource such as lignocellulosic biomass has emerged as a promising source of energy due to its abundancy. Other than contribution to renewable energy, lignocellulosic biomass can be converted into value added product such as succinic acid, citric acid and pharmaceuticals. This study investigate the performance of a new class of solvent, deep eutectic solvent (DES) in pretreating sago waste which is a type of starchy biomass. The suitable type of DES in sago waste pretreatment was selected based on the sugar yield during enzymatic hydrolysis and the amount of sugar loss during pretreatment. In this study, three types of DES namely Choline Chloride-Urea, Choline-Chloride-Citric acid and Choline Chloride-Glycerol was investigated. The effect of temperature and duration on DES pretreatment was investigated. The percentage of biomass delignification and sugar yield will be calculated and tabulated in table form to study the set of parameters with the best sugar yield. The highest amount of sugar yield is expected to be obtained at the highest operating temperature, more acidic solvent and high DES ratio. To conclude this, application of DES is feasible because it made from cheap and safe raw materials. For future development of DES, improvement of DES such as its biodegradability, recyclability and more types of DES should definitely be discovered for various industrial application and processes.

Keywords: Deep Eutectic Solvent (DES), lignocellulosic biomass, pretreatment, enzymatic hydrolysis

1. Introduction

Lignocellulosic biomass has the potential to replace existing petroleum-dependant production plants among other renewable sources due to its abundancy on earth [1]. Other than contribution to renewable energy, it can be converted into value-added products such as enzymes, citric acid, succinic acid, pharmaceuticals and many more [2]. However, some of the processes to produce value-added products have not been commercialized yet due to challenges faced at commercial scale. Despite successes accomplished in laboratory, further research and experiment must be conducted to overcome challenges and provide breakthroughs to lower production costs of commodity chemicals and and biofuels from biomass [2]. It is believed that the future of lignocellulosics conversion relies on advancement and improvement of pretreatment efficiency, cellulytic enzymes, comprehensive understanding of biomass components and process integration [2].

In common practice, bioethanol is produced by following a pathway of biomass pretreatment, hydrolysis and followed by fermentation and distillation [4]. Pretreatment is the beginning process of lignocellulosic feedstock, therefore efficiency of pretreatment process is the key to effective enzymatic hydrolysis and downstream processes [4]. Pretreatment is necessary due to the presence of lignin which resists solubilization and hamper enzymatic hydrolysis process [7]. In addition to that, factors such as cellulosic compositions, crystallinity structure, rigid nature of cellulose, formation of inhibitants and particle size of biomass could contribute to hydrolysis digestibility of feedstock [7]. Therefore, a lot of approaches such as physical, chemical and biological methods have been applied. Selection of suitable pretreatment method is based solely on the application [7].Pretreated substrate would normally have a structure with increased porosity and reduced crystallinity [4]. During pretreatment, modification or removal of lignin content takes place to improve the accessibility of enzymes to the biomass substrate. By doing so, conversion of complex carbohydrates into simple sugars and subsequently fermented into biofuel is improved [6]. However, as good as conventional pretreatments may be beneficial to sugar production from biomass, the old pretreatment method comes with numerous adverse conditions to the environment. Conventional pretreatment technique has its respective drawback. As an example, acid pretreatment produce fermentation inhibitors that reduce the efficiency of fermentation.

The desire for green solvents in pretreatment has led to discovery of Deep Eutectic Solvents (DESs) and Ionic Liquids (ILs) [8]. DES is made up of a hydrogen bond donor (HBD) and a hydrogen bond acceptor (HBA). Both DESs and ILs pretreatment techniques are affected by combination of solvents used, type of biomass feedstock, size of particles and substrate loading and etc [9]. These advanced pretreatment techniques are more popular than conventional pretreatment techniques due to no requirement of extreme operating conditions such as high pressure and temperature [9].

Further advancement of DESs has been made due to its potential as green solvents to replace ILs [10]. Due to low initial costs and ease of access to raw materials, DESs are being studied extensively in various fields such as electrochemistry and pharmaceutical [8]. DESs have rised in popularity due to huge advancements and successes of ILs. Through application of DESs, similar physio-chemical properties to

ILs can be achieved with extra benefits such as easier preparation, non-complicated purification processes and usage of green and renewable components [11]. The existing pretreatment method is expected to be replaced due to association with non-environmental friendly issues, costly and poor biodegradability [11]. Majority of the DESs are Choline Chloride-based (ChCl), which is applied as food additive. With that being said, ChCl is acknowledged as safe compound for human consumption by relevant authorities [11]. Many researches have evaluated degradability of DESs and have classified DESs as " readily biodegradable " compounds [8]. Combination of Ch^+ into DESs has shown significant enhancement of biodegradability. Other than that, DESs can be utilized in a wide range of industrial practices such as purification, extraction and separation.

To date, no research has been done on the effect of DES pretreatment on starchy biomass. Starchy biomass such as sago waste which has approximately 36% starch, 40% cellulose and 13% hemicellulose serves as a promising feedstock for glucose production.

In this study, 3 types of DES namely Choline Chloride-Urea, Choline-Chloride-Citric acid and Choline Chloride-Glycerol was investigated for pretreatment of sago waste. The best DES was selected based on sugar production from enzymatic hydrolysis and sugar loss during pretreatment. The effect of temperature and duration on DES pretreatment is also investigated. Sago hampas is used as lignocellulosic biomass to study the sugar production.. The study gaps of this paper focus on utilization of sago hampas as starchy biomass for DES pretreatment and optimization of parameters for maximum sugar yield from biomass. This study aims to provide an insight on process optimization of DES pretreatment of sago hampas. The three parameter chosen to carry out process optimization are pretreatment temperature, duration and solid loading.

2. Methodology

2.1 Preparation of Natural Deep Eutectic Solvent (NADES)

DES combination of Choline chloride with urea, citric acid and glycerol were prepared at molar ratio of 1:2, 1:2 and 1:1. Each of the components were weighed at 15 g, 12.905 g, 19.788 g and 20.641 g respectively before transferred to a Schott bottle. The mixture was heated up using hot plate with magnetic stirrer using 150 rpm at 80 °C. The heating and stirring process was stopped when a homogenous/clear liquid solution is obtained. The Schott bottle was cooled down before sealed tightly and kept in a dessicator with silica gel for storage.

2.2 Preparation of Sago Hampas sample

Sago hampas is collected from Hak Mong Sago Mill, Batu Pahat, Johor, Malaysia. The sample was washed and dried at 60°C for 24 hr [12]. Sago hampas samples were grinded using blender into smaller size for pretreatment process. After that, sieving process was carried out to ensure particle size is within 500 μm.

2.3 DES pretreatment

Pretreatment was carried out with 5 % solid loading by mixing 1 g of Sago Hampas biomass and 20 g of DESs respectively in a Schott bottle. The samples were heated at 110 °C for 3 hours in an oven. The biomass/DES mixtures were then transferred to centrifuge tubes with the addition of 5 ml deionized water. The contents were centrifuged at 3500 rpm for approximately 30 minutes The supernatant (black liquor) was collected into sampling bottle and stored at 4°C. Washing and rinsing of biomass was then carried out by adding 30 mL of deionized water in every cycle of centrifugations. The pretreated biomass was obtained through filtration and was dried at 50 °C for 8 hours in an oven. The dried biomass were kept in desiccator prior to hydrolysis process.

2.4. Enzymatic hydrolysis

Enzymatic hydrolysis was conducting in 2 % solid loading by mixing 0.2 g of pretreated biomass 10 mL of citrate buffer solution (pH 4.8 and 50 mM) which was added with 0.1 g of cellulase. The hydrolysis process was carried out at 50 °C for 48 hours at 100 rpm an incubating shaker. After hydrolysis, the samples were centrifuged at 24 °C, 3500 rpm for 15 min. The supernatant was collected and glucose content was tested.

2.5 Determination of reducing sugars

2.5.1 3, 5 Dinitrosalicyclic Acid (DNS) analysis

The black liquor samples collected from pretreatment were transferred to respective test tube. DNS reagent with 1% (w/v) NaOH (Merck) was prepared and stored in dark bottle. Prior to reducing sugars analysis, 1% (w/v) of sodium metabisulfite (Merck) was added to the DNS reagent. DNS solution in 3 mL was then added into the test tube which contained 1.5 mL of sample solution. The mixture was boiled for 5 min, placed in a cold water bath and added with 1 mL of 40 % Rochelle salt (Potassium sodium tartrate tetrahydrate, Merck) solution immediately. After cooling the mixture, 0.2 mL of reaction mixture was diluted by adding 2.5 mL of ultrapure water and the absorbance of the diluted reaction mixture was measured at the wavelength of 540 nm by UV-Vis spectrophotometer. The reducing sugars concentration in the sample solution was determined from the standard curve constructed by using D(+) glucose (Merck) solution.

2.5.2 High Performance Liquid Chromatography (HPLC)

The supernatant collected from hydrolysis process to determine glucose yield. Deionized water was used as the mobile phase of HPLC with flowrate of 0.6 ml/min. The Agilent H+ column was used while column temperature is fixed at 65 °C. Before conducting HPLC analysis and 10 µL of injection volume, the sample is filtered using Nylon filter with particle size of 0.2 µm Glucose concentration was determined from a calibration curve plotted for 1 g/L to 30 g/L of glucose.

2.6 Effect of pretreatment temperature

The DES with best performance was selected to carry out this study. The pretreatment duration and solid loading was fixed at 3 hr and 5% respectively whereby temperature

varies from 90, 110 and 130 °C. All the steps mentioned in preliminary study were repeated to obtain glucose yield from enzymatic hydrolysis.

2.7 Effect of pretreatment duration

The most efficient DES combination was selected to carry out this study. The pretreatment temperature and solid loading was fixed at 110 °C and 5% respectively whereby duration varies from 1, 3 and 5 hr. All the steps in preliminary study were repeated to obtain glucose yield from enzymatic hydrolysis.

3. Results and discussion

3.1 2-way analysis of variance (ANOVA) method

3.1.1 Effect of selection of DES on sugar production

Table 3.1: Reducing sugar production under different DES pretreatment

Type of DES	Batch 1 (mg/ml)	Batch 2 (mg/ml)	Average (mg/ml)
ChCl-Urea	5.78	4.64	5.21
ChCl-CA	4.70	4.96	4.83
ChCl-Gly	0.73	0.96	0.85
Average	3.74	3.52	
Total Average	1.90		

Table 3.2: ANOVA results on the effect of pretreatment temperature and batch-to-batch difference on reducing sugar obtained

	Sum of square (SS)	Degree of freedom (DOF)	Mean square	F value	95% confidence level
SS_{DES}	23.39	2	11.69	36.56	Significant
SS_{batch}	0.07	1	0.07	0.22	Not significant
SS_{error}	0.64	2	0.32		
SS_{total}	24.10	5	4.82		

According to ANOVA table,

At 95% confidence level, $F_{0.05, 2, 2} = 19$

$F_{0.05, 1, 2} = 18.51$

Based on result above, type of DES pretreatment has significant effect on reducing sugar production. However, batch to batch difference on reducing sugar production is insignificant. Therefore, it indicates that insignificant factor in experiment is reproducible.

3.1.2 Effect of pretreatment temperature on sugar production

Table 3.3: Reducing sugar production under different pretreatment temperature

Temperature (°C)	Batch 1 (mg/ml)	Batch 2 (mg/ml)	Average (mg/ml)
90	4.32	2.02	3.17
110	4.98	5.36	5.17
130	4.75	5.21	4.98
Average	4.68	4.196667	
Total Average	4.44		

Table 3.4: ANOVA results on the effect of pretreatment temperature and batch-to-batch difference on reducing sugar obtained

	Sum of square (SS)	Degree of freedom (DOF)	Mean square	F value	95% confidence level
$\mathbf{SS_{temp}}$	4.87	2	2.44	1.98	Not significant
$\mathbf{SS_{batch}}$	0.36	1	0.36	0.29	Not significant
$\mathbf{SS_{error}}$	2.47	2	1.23		
$\mathbf{SS_{total}}$	7.70	5	1.54		

According to ANOVA table,

At 95% confidence level, $F_{0.05,\,2,\,2} = 19$

$F_{0.05,\,1,\,2} = 18.51$

Based on result above, pretreatment duration does not have significant effect on reducing sugar production. Batch to batch difference on reducing sugar production is insignificant. Therefore, it indicates that both factors in experiment are reproducible.

3.1.3 Effect of pretreatment duration on sugar production

Table 3.5: Reducing sugar production under different pretreatment duration

Duration (hr)	Batch 1 (mg/ml)	Batch 2 (mg/ml)	Average (mg/ml)
Blank	0.481	0.366	0.4235
1	2.82	3.41	3.115
3	4.39	3.58	3.985
5	3.09	3.78	3.435
Average	2.69525	2.784	

Total Average	2.74

Table 3.6: ANOVA results on the effect of pretreatment duration and batch-to-batch difference on reducing sugar obtained

	Sum of square	**Degree of freedom (DOF)**	**Mean square**	**F value**	**95% confidence level**
$SS_{duration}$	15.08	3	5.03	20.63	Significant
SS_{batch}	0.02	1	0.02	0.06	Not significant
SS_{error}	0.73	3	0.24		
SS_{total}	15.83	7	2.26		

According to ANOVA table,

At 95% confidence level, $F_{0.05,\,3,\,3} = 9.28$

$F_{0.05,\,1,\,3} = 10.13$

Based on result above, pretreatment duration has significant effect on reducing sugar production. However, batch to batch difference on reducing sugar production is insignificant. Therefore, it indicates that insignificant factor in experiment is reproducible.

3.2 Selection of DES for pretreatment

All the samples were carried out at fixed pretreatment temperature, duration and solid loading at 110 °C, 3 hr and 5% solid loading in the selection of suitable DES. The performance of these DES pretreatments was analysed and justified based on yield of reducing sugar obtained from enzymatic hydrolysis and sugar loss during pretreatment.

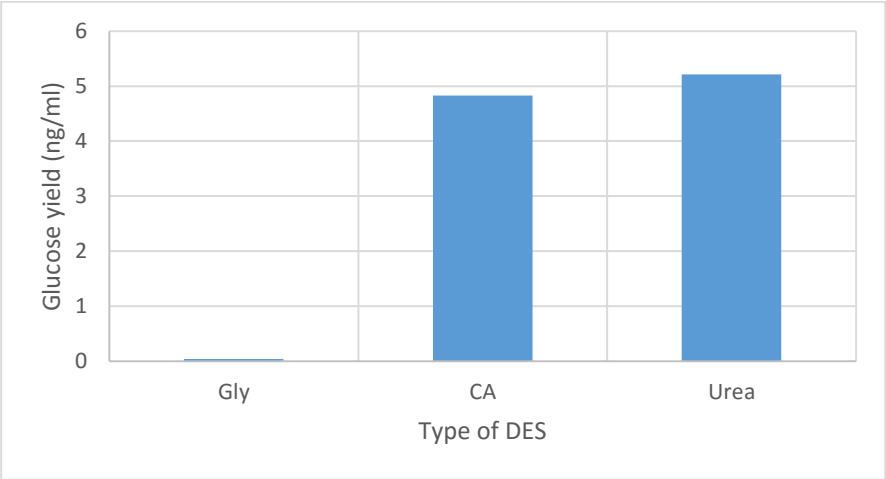


Figure 3.1: Glucose yield of different DES pretreatment

From Figure 3.1, ChCl-Urea is chosen as DES for subsequent study because it shows the highest amount of glucose yield at 5.21 mg/ml (which is 0.26 g/g of pretreated biomass) compared to ChCl-Glycerol and ChCl-CA. The average value is taken as all the samples were duplicated to give a higher precision result. Based on the nature of each DES, urea is slightly alkaline with pH ranging from 7.5 – 9 whereas both glycerol and citric acid are acidic with pH at 6.3 – 6.9 and 3.2 respectively. From the results obtained, it can be concluded that sugar yield increases in either acidic or alkaline reagent. On the other hand, ChCl-glycerol, which is having neutral pH, yielded the lowest amount of glucose with 0.85 mg/ml (which is 0.4 g/g of pretreated biomass). This finding is aligned to a research done which stated that the maximal enzymatic glucose and xylose yields from the biomass, wheat straw fraction were noticed at the most extreme pH values (pH 1 and pH 13) after pretreatment [33]. This trend can be further explained as the surface response models showed significant interactions between pretreatment temperature and pH on glucose and xylose [33]. Acidic pretreatments favor to high petreatment temperature compared to alkaline pretreatment, which is not as temperature dependent. From research, alkaline pretreatment generally proved to have better glucose yield even at lower pretreatment (110 °C considered low) temperature as compared to acidic pretreatment [33]. Therefore, the results obtained from **Figure 3.1** were found to be reliable with lower yield of reducing sugar from acid-based DES than alkali-based DES. As a result, the subsequent study was carried out using ChCl-Urea DES due to the ability in breaking down lignin that provides access of enzyme to biomass.

3.3 Analysis of reducing sugar

3.3.1 Reducing sugar loss during pretreatment

Table 3.7: Reducing sugar loss during pretreatment

Component	Absorbance value (A)	Glucose concentration (mg/mL)	Average (mg/mL)
Urea 1	0.0545	1.1	0.9
Urea 2	0.0375	0.8	
Glycerol 1	0.116	2.2	2.0
Glycerol 2	0.097	1.8	
Citric Acid 1	0.032	0.7	0.8

Citric Acid 2	0.047	0.9	

From **Table 3.7, ChCl**-Glycerol shows the highest amount of sugar loss at 0.9 mg/ml followed by ChCl-Urea and ChCl-CA. It can be deducted that ChCl-CA pretreated biomass has the most compatible structure with cellulase enzymes compared to ChCl-Glycerol and ChCl-Urea. This can be further explained due to specific substrate action of DESs in pretreatment of lignocellulosic biomass. Thus, a specific DES may be compatible for pretreating a particular substrate but not the others. In this study, ChCl-CA appeared to be the most compatible DES with cellulase enzyme as it shows the least amount of sugar loss which is 0.8 mg/ml.

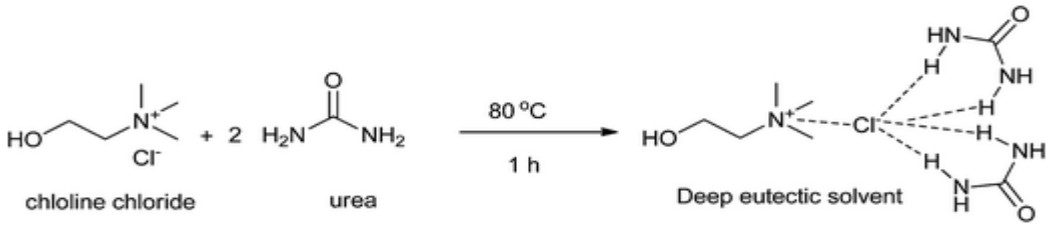


Figure 3.2: Chemical structure of Choline Chloride-Urea DES [13]

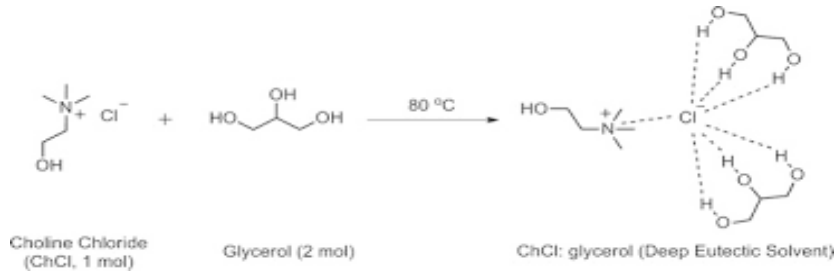


Figure 3.3: Chemical structure of Choline Chloride-Glycerol DES [8]

The chemical structure of each DES may differs its performance from one another. This is because the grouping of cations and anions in these DESs affects dissolution of cellulose [34]. According to a research, the anion in DESs plays an important role to attack and deprotonate cellulose which is made up of free hydroxyl group [34]. On the other hand, interaction happens between the electron donor - hydroxyl oxygen atoms on the cellulose and larger size cation. Cellulose dissolution takes place due to separation of hydroxyl group on cellulose when hydrogen bondings within cellulose are disturbed [34]. Therefore, in term of dissolution of biomass, glycerol ion appeared to be more efficient than citric acid and urea ion. A large amount of reducing sugar loss in pretreatment may have happened during dissolution process. Consequently, ChCl-Glycerol shows the highest amount sugar loss after pretreatment. Similar to ILs, DESs are capable for depolymerisation of polysaccharides to compounds with low molecular weight [35]. A significant loss in reducing sugar yield in pretreatment can be observed and might be due to strong depolymerisation power which could lead to low reducing sugar yield from hydrolysis. Based on **Table 3.7**, ChCl-Glycerol can be said to have the highest depolymerisation power followed by ChCl-Urea and lastly, ChCl-CA based on reducing sugar loss obtained. ChCl-urea produced the highest amount of sugar during enzymatic hydrolysis compared to ChCl-glycerol and ChCl-CA Hence, ChCl-urea was found to be the most suitable DES for pretreatment of sago hampas in this study.

3.4 Effect of temperature on DES pretreatment

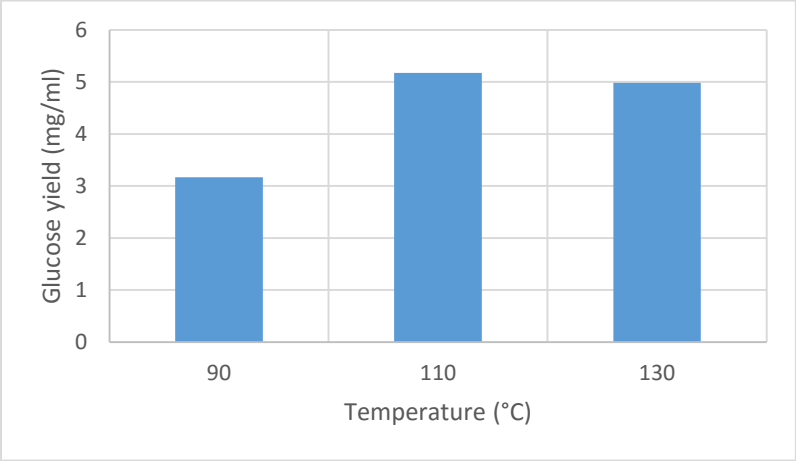


Figure 3.4: Glucose concentration under different temperature

Based on Figure 3.4, glucose concentration increases from 90 °C to 110 °C and falls at 130 °C. The result shows the optimum temperature would be at 110 °C with 5.17 mg/ml (which is 0.26 g/g of pretreated biomass) of glucose yield. The trend is aligned to a DES pretreatment study using ChCl-lactic acid to pretreat corncob with varying pretreatment temperature as efficiency of glucose extraction started to decline at certain temperature. The losses of polysaccharides could be due to the balanced effects to improve digestability of hydrolysis [28]. Also, high temperature may contribute to degradation of biomass samples, thus lead to sugar loss. This is further explained by higher pretreatment temperature increases the deconstruction of biomass components and improves amount of sugar produced [26]. Moreoever, at higher temperature, increment in pore size of biomass along with reduction of lignin is expected to happen within the biomass [26].

3.5 Effect of duration on DES pretreatment

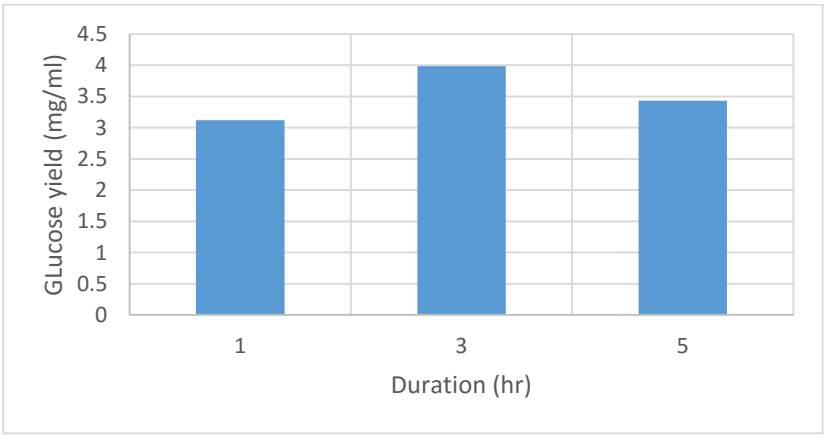
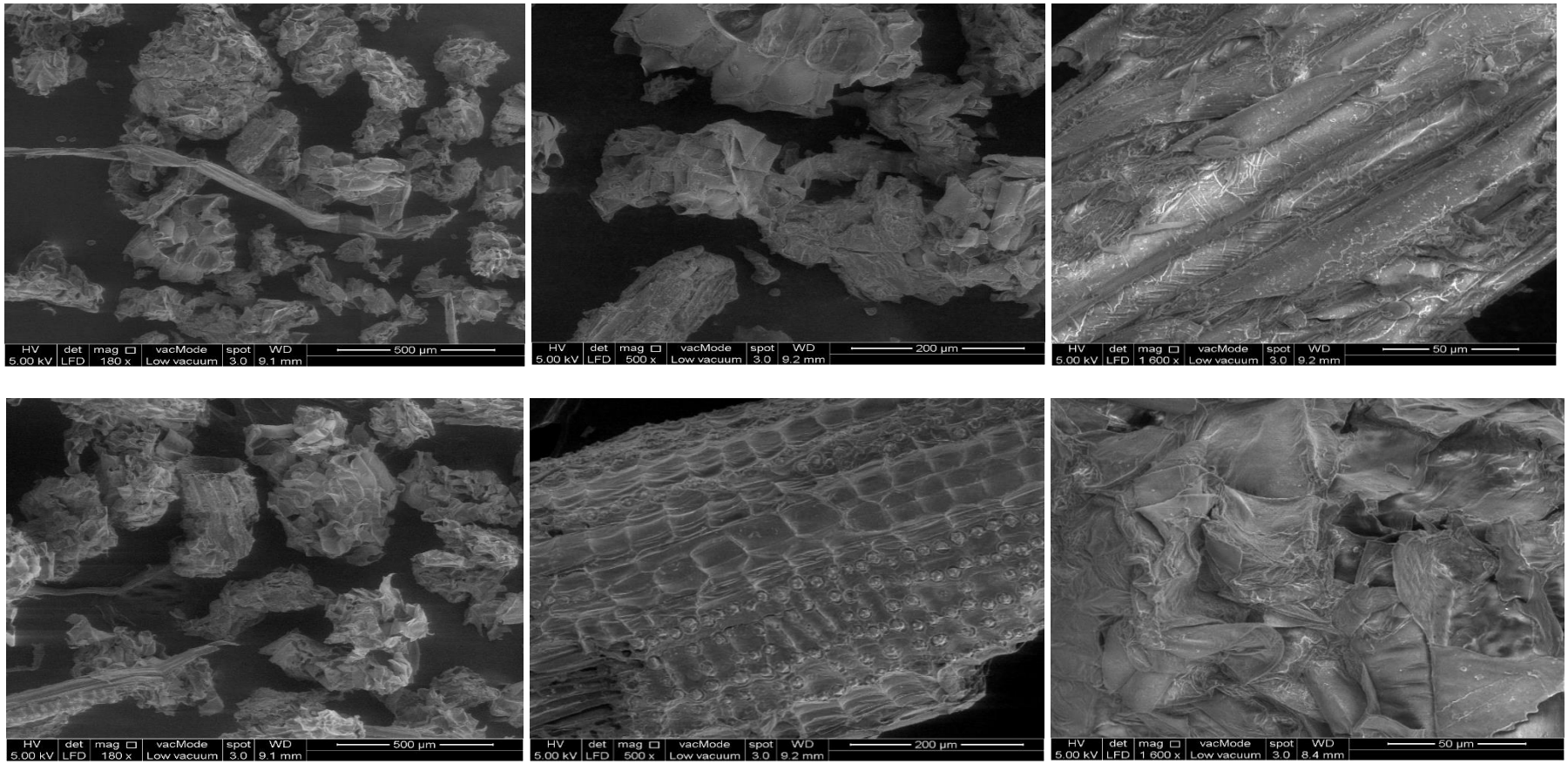


Figure 3.5: Glucose concentration at 110 °C under different duration

Based on Figure 3.5, it can be observed that glucose concentration is the highest at duration of 3 hr with 3.99 mg/ml (which is 0.2 g/g of pretreated biomass) of glucose yield followed by 5 hr and 1 hr with 3.43 mg/ml and 3.12 mg/ml. However, glucose yield declines at duration of 5 hr. This finding is agreeable to researches done recently as glucose yield increases significantly with pretreatment duration and thus better hydrolysis efficiency [36]. The experiment was done using corncob under different pretreatment duration found that better interaction between biomass and DES-based solvent was expected under prolonged duration [28]. Under extended pretreatement duration, cellulose dissolution of biomass have more time to dissolve in DES, therefore higher amount of regenerated cellulose was produced [34]. Thus, the trend of results from **Figure 3.5** is aligned with recent studies. The sugar loss happens at pretreatment duration of 5 hr may due to degradation of biomass. From **Figure 3.5**, the most suitable pretreatment duration is 3 hr because the highest amount of sugar yield, 4.0 mg/ml is obtained. Based on HPLC analysis, sugar yield for blank at 110 °C gives 0.42 mg/ml of glucose obtained. Thus, pretreatment at any temperature is proved to have higher efficiency compared to blank due to better sugar yield.

3.6 Structural Analysis

3.6.1 Scanning Electron Microscopy (SEM) Analysis



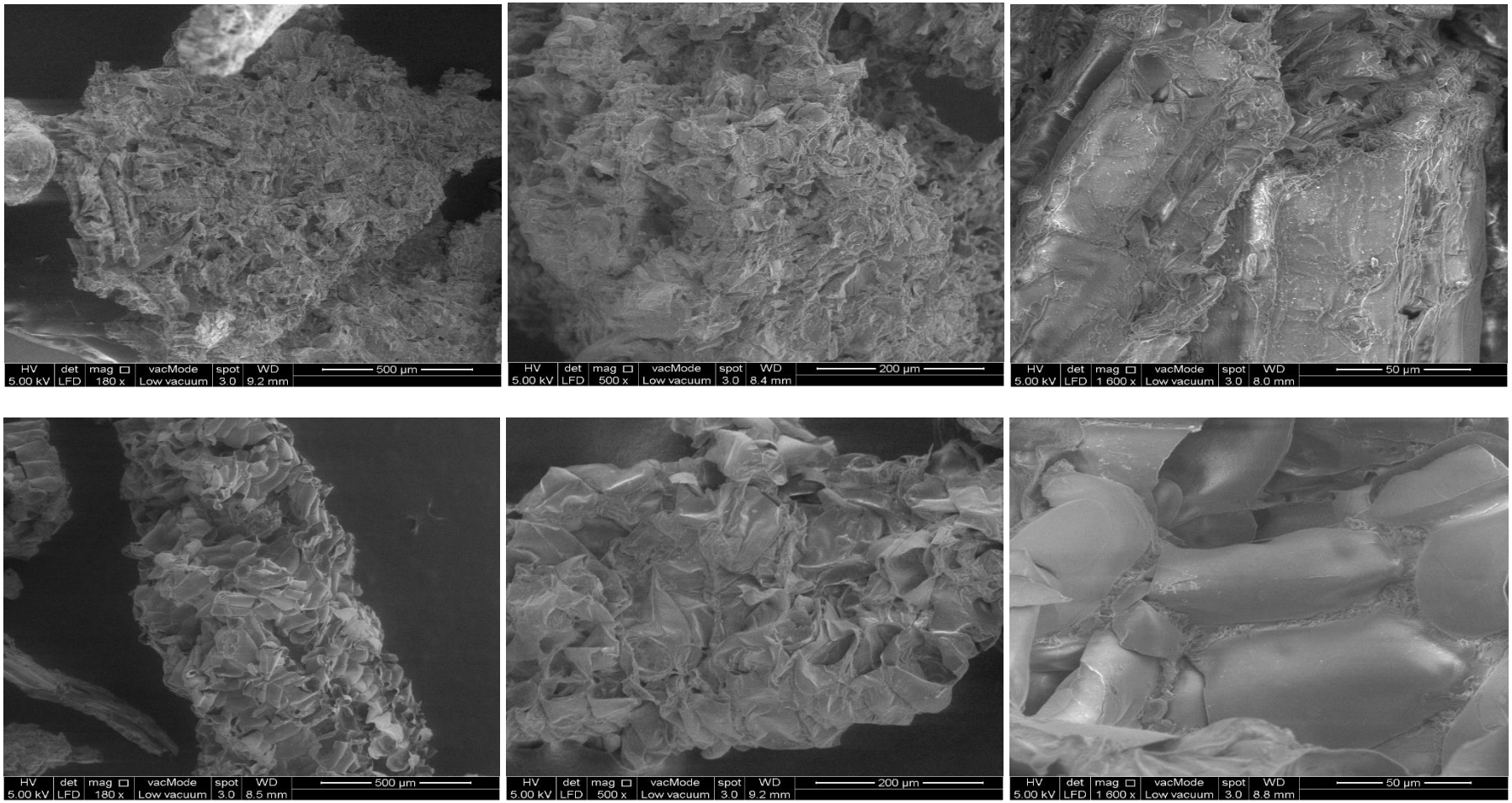

HV 5.00 kV | det LFD | mag 180 x | vacMode Low vacuum | spot 3.0 | WD 9.2 mm | 500 µm
HV 5.00 kV | det LFD | mag 500 x | vacMode Low vacuum | spot 3.0 | WD 8.4 mm | 200 µm
HV 5.00 kV | det LFD | mag 1 600 x | vacMode Low vacuum | spot 3.0 | WD 8.0 mm | 50 µm
HV 5.00 kV | det LFD | mag 180 x | vacMode Low vacuum | spot 3.0 | WD 8.5 mm | 500 µm
HV 5.00 kV | det LFD | mag 500 x | vacMode Low vacuum | spot 3.0 | WD 9.2 mm | 200 µm
HV 5.00 kV | det LFD | mag 1 600 x | vacMode Low vacuum | spot 3.0 | WD 8.8 mm | 50 µm

Figure 3.6: SEM of sago hampas, untreated sago hampas: (a) 180x magnification (b) 500x magnification (c) 1600x magnification; ChCl-Urea pretreatment: (d) 180x magnification (e) 300x magnification (f) 1600x magnification; ChCl-Citric acid pretreatment: (g) 160x magnification (h) 500x magnification (i) 1600x magnification; ChCl-Glycerol pretreatment: (j) 160x magnification (k) 500x magnification (l) 1600x magnification

Figure 3.6 shows the SEM images of untreated and pretreated samples using different DES. From SEM analysis, the result showed that all the pretreatments were successfully carried out to make the samples more susceptible for sugar extraction. Raw and untreated sago hampas is less porous and its structure is less disrupted. On the other hand, at magnification of 180x, the morphology of pretreated samples are observed to be more porous and severely disrupted due to effect of pretreatment. This is to ensure better enzymatic activity for easier penetration of hemicellulose and cellulose to be converted into sugar [29]. Without pretreatment, lower amount of sugar yield is expected from subsequent hydrolysis process.

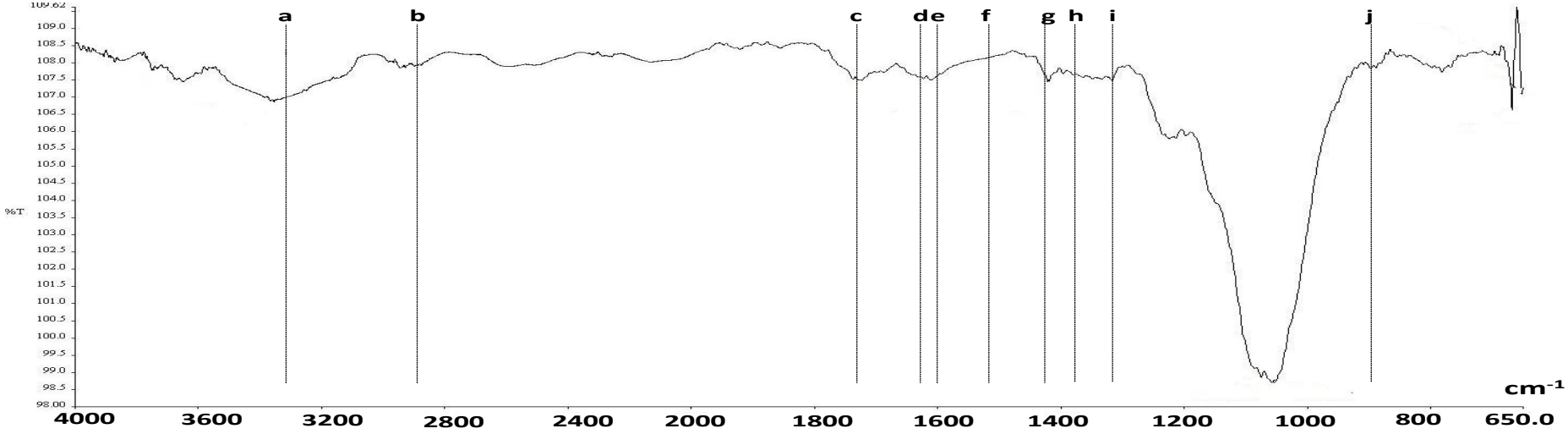
Under magnification of 500x, a rough surface is observed in ChCl-Urea pretreatment to be very destructive compared to others. The rough surface symbolizes increment in porosity of sample and breakdown of lignin, thus enzyme can attack the pores easily [29]. In Figure 3.6 (d), the fiber size was reduced due to solubility of DES which dissolved a portion of fibers in sample. As for Figure 3.6 (k), the solvent showed high destructive capability but was inconsistent at different morphology of biomass. The ability to disturb the surface structure is good for enzymatic digestion [32]. The inconsistency of is similar for application of ChCl-Citric acid in Figure 3.6 (h).

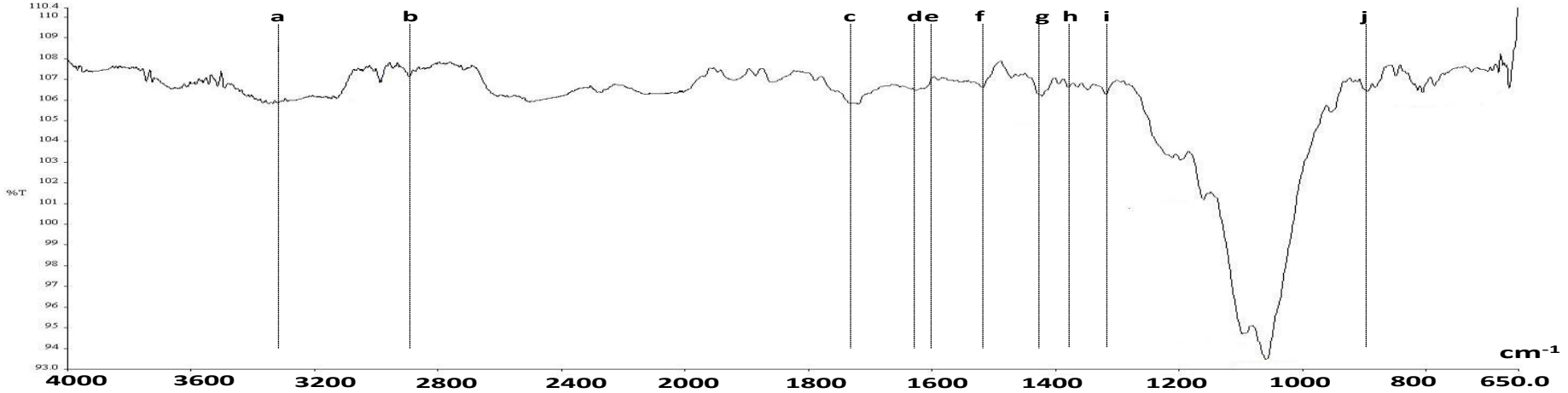
At magnification of 1600x, untreated sago hampas has a more structured and regular surface compared to the rest of the pretreated samples. On the other hand, Figure 3.6 (f) shows the most severe disruption on sample surface and higher porosity. The disruption is crucial to make biomass more susceptible to enzymatic attack in hydrolysis process, therefore higher yield of reducing sugar [34]. In Figure 3.6 (l), acidic-based DES has greater level of depolymerisation compared to ChCl-Glycerol pretreatment. Morpholgy of ChCl-Glycerol (under 1600x magnification) shows a large portion of smooth surface which indicates fiber is still intact, therefore lesser destructive power.

In general, all pretreatment methods make the surface of samples become more porous and break down of lignin structure [29]. A few studies have reported similar results regarding morphology of biomass to have higher porosity, less crystalline and vulnerable to enzymatic after using Ionic Liquid (IL) pretreatment which has similar characteristic as DES [32]. Due to similar physio-chemical properties to IL, application of DES can be compared with IL study in relevant field [13]. The result from SEM analysis is aligned to an IL study which concluded that alteration of biomass structure occurs in favor to microbial attack and enzymatic hydrolysis regardless of type of biomass [32]

3.6.2 Fourier Transform Infrared (FTIR) analysis

The changes of chemical structures in sago hampas were analysed after undergoing different DES pretreatment using ChCl-Urea, ChCl-Citric Acid and ChCl-Glycerol. The spectra of each pretreated and untreated samples are illustrated as shown below.


a
b
c
de
f
g
h
i
j
%T
cm-1
4000
3600
3200
2800
2400
2000
1800
1600
1400
1200
1000
800
650.0


a
b
c
de
f
g
h
i
j
%T
cm-1
4000
3600
3200
2800
2400
2000
1800
1600
1400
1200
1000
800
650.0

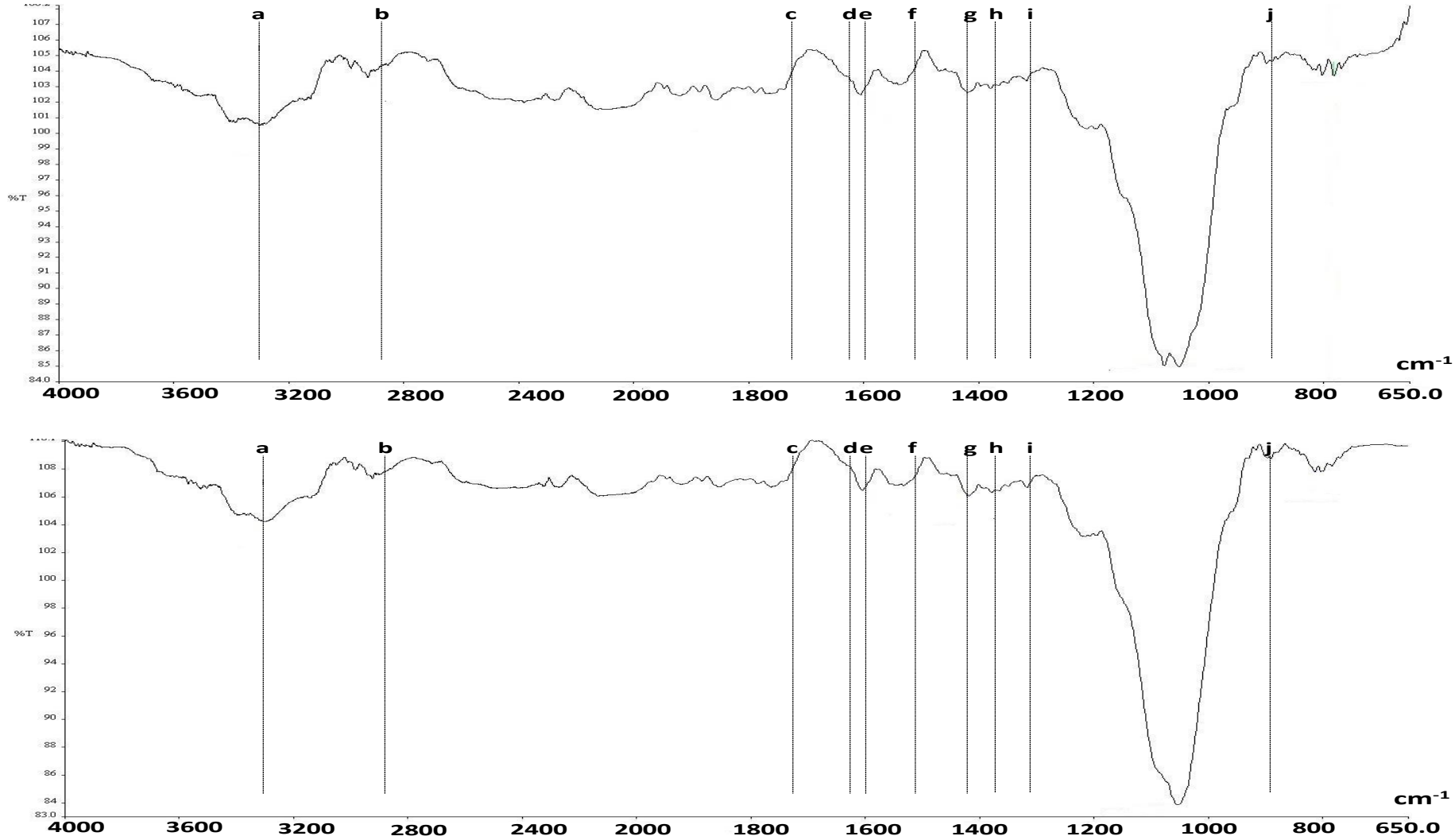

a
b
c
de
f
g
h
i
j
%T
cm-1
4000
3600
3200
2800
2400
2000
1800
1600
1400
1200
1000
800
650.0

Figure 3.7: FTIR spectra of (i) untreated (blank) SH, (ii) ChCl-Citric acid pretreated SH, (iii) ChCl-Glycerol pretreated SH, (iv) ChCl-Urea pretreated SH. (a) 3330 cm^{-1}, (b) 2905 cm^{-1}, (c) 1732 cm^{-1}, (d) 1634 cm^{-1}, (e) 1600 cm^{-1}, (f) 1515 cm^{-1}, (g) 1425 cm^{-1}, (h) 1375 cm^{-1}, (i) 1328 cm^{-1}, (j) 897 cm^{-1}

From Figure 3.7, all untreated and pretreated samples showed significant bands at 3330 cm^{-1} and 2905 cm^{-1}, which signify the hydroxyl (O-H) group, and CH stretching [37]. These peaks may contribute to compositions of lignocellulosic biomass, which is cellulose, hemicellulose and lignin in sago hampas [38]. Thus, this indicates presence of lignocellulosic compositions in this biomass.

According to research, the cellulose peak at 1425 cm^{-1} was diminished after IL pretreatment on sugarcane bagasse samples [32] Therefore, among all the lignocellulosic compositions, cellulose content is expected to undergo the most significant changes. From FTIR graphs above, the cellulose peak did not diminish and remained constant for all DES pretreatments. The spectra at 1425 cm^{-1} also represents the CH_2 scissoring motion in crystalline cellulose whereas the absorbance amorphous cellulose is at 897 cm^{-1} [38]. This peak was observed to be more intense especially in ChCl-Citric acid and ChCl-Urea pretreatment. From study, this spectrum is more vulnerable to enzymatic attack due to its porosity and asymmetrical structure in conjunction with increment of accessible surface area for sugar extraction by enzymes [38]. This outcome suggests application of ChCl-Citric acid and ChCl-Urea are better as both solvents altered the cellulose content in samples to a more amorphous matrix that is in favor to better sugar yield in enzymatic hydrolysis .

On the other hand, the peak at 1600 cm^{-1} and 1515 cm^{-1} were diminished significantly in ChCl-Citric acid pretreatment as compared to others. The reduction is lignin peaks contribute to depolymerisation of lignin [39]. The result obtained is aligned with a DES pretreatment study as acidic environment promotes depolymerisation of each components [8]. Further lignin peaks located at 1634 cm^{-1}, 1375 cm^{-1} and 1328 cm^{-1} were known as OH bending of adsorbed water, CH deformation and syringyl units in lignin [40]. From Figure 3.7, the trend of peaks showed a substantial amount of lignin was not removed from sago hampas.

The spectra at 1732 cm-1 showed the presence of hemicellulose. According to study, this band describes the stretching behavior in C=O groups in the acetyl content of hemicellulose [32]. In this study, ChCl-Urea and ChCl-Glycerol pretreatments removed higher amount of hemicellulose compared to ChCl-Citric acid pretreatment. However, hemicellulose content was not removed in bulk. The FTIR results correlates well with the SEM analysis and sugar yield analysis using HPLC. Furthermore, the pretreated SH samples have shown changes in lignin content in conjunction with increment of amorphous cellulose content.

4. Conclusion

This study highlights the use of DESs as potential green solvents for pretreatment process. At current stage, limited study is available as reference on the application of DES in pretreatment of lignocellulosic biomass. Therefore, development in this field would promote and lead to application of eco-friendly technology in the future. Moreover, this study revealed the optimization of pretreatment paramaters for optimum amount of sugar yield using starchy biomass as lignicellulosic feedstock. The predominant contribution to body of knowledge in this study would be the effect of parameters such as type of DES, pretreatment duration and temperature in conjunction with structural and compositional change can be found in this study.

In Results and Discussion section, the alkaline or acidic DES is found to be more suitable in pretreating sago hampas for the purpose of sugar production via enzymatic hydrolysis compared to neutral DES. ChCl-Urea DES, which is alkali in nature, shows the best results compared to other DES pretreatment samples. . This study is aligned with current paper, which stated that alkaline pretreatment is proved to have better glucose yield even at low temperatures [33]. Although it shows some amount of sugar loss during pretreatment, but ChCl-Urea pretreated biomass produces the highest amount of reducing sugar from enzymatic hydrolysis process. The best operating condition for sugar production from DES-pretreated biomass via enzymatic hydrolysis is 110°C and 3 hr. When pretreatment temperature increases to 130°C, sugar yield decreased slightly due to the disruption in the structure of biomass at high temperature. Similarly, prolonging the duration beyond 5 hours is hindering sugar production. In conclusion, ChCl-urea is found to be the most suitable reagent to pretreat sago hampas. Further investigation on the structural characteristics of pretreated biomass as well as the optimization of pretreatment condition should be conducted to further elucidate the process. Therefore, it can be concluded that the results shown in this study is reliable as it is aligned with most of the research found by others.

References

[1] F. Isikgor and C. R. Becer, “Lignocellulosic biomass: a sustainable platform for the production of bio-based chemicals and polymers,” Feb. 2016.

[2] S. S. da Silva, A. K. Chandel, S. R. Wickramasinghe, J. M. G. Domínguez, J. nguez, and M. G., “Fermentative production of value-added products from lignocellulosic biomass.,” *J. Biomed. Biotechnol.*, vol. 2012, p. 826162, Nov. 2012.

[3] H. Zabed, J. N. Sahu, A. N. Boyce, and G. Faruq, “Fuel ethanol production from lignocellulosic biomass: An overview on feedstocks and technological approaches,” *Renew. Sustain. Energy Rev.*, vol. 66, pp. 751–774, Dec. 2016.

[4] A. Limayem and S. C. Ricke, “Lignocellulosic biomass for bioethanol production: Current perspectives, potential issues and future prospects,” *Prog. Energy Combust. Sci.*, vol. 38, pp. 449–467, 2012.

[5] L. P. Walker and D. B. Wilson, “Enzymatic hydrolysis of cellulose: An overview,” *Bioresour. Technol.*, vol. 36, no. 1, pp. 3–14, Jan. 1991.

[6] M. Jablonský, A. Škulcová, L. Kamenská, M. Vrška, and J. Šima, “Deep

Eutectic Solvents: Fractionation of Wheat Straw," *BioResources*, vol. 10, no. 4, pp. 8039–8047, 2015.

[7] A. K. Kumar and S. Sharma, "Recent updates on different methods of pretreatment of lignocellulosic feedstocks: a review," *Bioresour. Bioprocess.*, vol. 4, no. 1, p. 7, Dec. 2017.

[8] Y. P. Mbous, M. Hayyan, A. Hayyan, W. F. Wong, M. A. Hashim, and C. Y. Looi, "Applications of deep eutectic solvents in biotechnology and bioengineering—Promises and challenges," *Biotechnol. Adv.*, vol. 35, no. 2, pp. 105–134, 2017.

[9] K. . Ellinor B. Heggset, Kristin.S, "Novel pretreatment pathways for dissolution of lignocellulosic biomass based on ionic liquid and low temperature alkaline treatment," *Biomass and Bioenergy*, pp. 194–200, 2016.

[10] D. Z. Troter, Z. B. Todorovi?, D. R. ?oki?-Stojanovi?, O. S. Stamenkovi?, and V. B. Veljkovi?, "Application of ionic liquids and deep eutectic solvents in biodiesel production: A review," *Renew. Sustain. Energy Rev.*, vol. 61, pp. 473–500, Aug. 2016.

[11] A. A. N. Gunny, D. Arbain, E. M. Nashef, and P. Jamal, "Applicability evaluation of Deep Eutectic Solvents–Cellulase system for lignocellulose hydrolysis," *Bioresour. Technol.*, vol. 181, pp. 297–302, Apr. 2015.

[12] G. H. Abdullah and M. A. Kadhom, "Studying of two choline chloride's deep eutectic solvents in their aqueous mixtures," *Int. J. Eng. Res. Dev.*, vol. 12, no. 9, pp. 2278–67, 2016.

[13] M. Pedersen, K. S. Johansen, and A. S. Meyer, "Low temperature lignocellulose pretreatment: effects and interactions of pretreatment pH are critical for maximizing enzymatic monosaccharide yields from wheat straw," *Biotechnol. Biofuels*, vol. 4, no. 1, p. 11, May 2011.

[14] L. W. Yoon, G. C. Ngoh, A. S. May Chua, and M. A. Hashim, "Comparison of ionic liquid, acid and alkali pretreatments for sugarcane bagasse enzymatic saccharification," *J. Chem. Technol. Biotechnol.*, vol. 86, no. 10, pp. 1342–1348, Oct. 2011.

[15] D. Di Marino, D. Stöckmann, S. Kriescher, S. Stiefel, and M. Wessling, "Electrochemical depolymerisation of lignin in a deep eutectic solvent," *Green Chem.*, vol. 18, no. 22, pp. 6021–6028, Nov. 2016.

[16] C.-W. Zhang, S.-Q. Xia, and P.-S. Ma, "Facile pretreatment of lignocellulosic biomass using deep eutectic solvents," *Bioresour. Technol.*, vol. 219, pp. 1–5, Nov. 2016.

eureca 2017- Conference Paper
Paper Number 2EE01

The Application of Image Processing to Solve Occlusion Issue in Object Tracking

Cheong Yun Zhe[1*], Chew Wei Jen[2]

[1,2] School of Engineering, Taylor's University, Malaysia.

*yunzhe.cheong@sd.taylors.edu.my

Abstract

Object tracking is a computer vision system that identifies, recognizes and tracks single or multiple objects in a static environment. The main objective and challenge of this research is to solve the occlusion issues in object tracking. Occlusion is a phenomenon that occurs in object tracking when two or more objects come too near and overlap each other. Occlusion also causes the object tracking system to easily lose track of the initial tracked object, and thus causing the tracking system to be inefficient. Therefore, solving occlusion in object tracking is crucial for improving the tracking system efficiency. In this research, the occlusion issues in object tracking is solved by a system. The system includes algorithms such as foreground object segmentation, colour tracking, object specification and occlusion handling. An input video is given to the system to solve the occlusion issues that occurred in the video. Every single frame of the video is analysed. The foreground objects are segmented with object segmentation algorithm and tracked with the colour tracking algorithm. ID is assigned to each tracked object. The object specification of each tracked object is identified by object specifying algorithm. Finally, occlusion issues of the input video are solved with the occlusion handling algorithm.

Keyword: Object segmentation, colour tracking, object specification, occlusion handling

1. Introduction

Multiple object tracking (MOT) is a process that requires the implementation of both computer vision system and image processing system to track objects in real life or a recorded video [1]. Development of multiple object tracking has begun since 1988 [2]. Since then, many different tracking techniques are proposed to improve and enhance the current object tracking techniques [3]. Technically, multiple object tracking recognizes and tracks each unique object with a specific ID [4]. However, there are several issues that affect the MOT process. One of the issue is the occlusion of objects [5].

Occlusion often occurs when two or more objects come too close and seemingly merge or combine to each other. Image processing system of object tracking often mistreated and wrongly tracked the occluded objects [6]. Sometime after occlusion, object tracking system wrongly identifies initially tracked objects as new objects [7].

Figure 1.1 below depicts the occlusion issues in 3 images. As observed from the 3 images in Figure 1.1, the normal colour tracking system only track the exposed region and neglected the occluded region. As observed in the second image of Figure 1.1, the blue object was wrongly tracked as 2 separate objects.

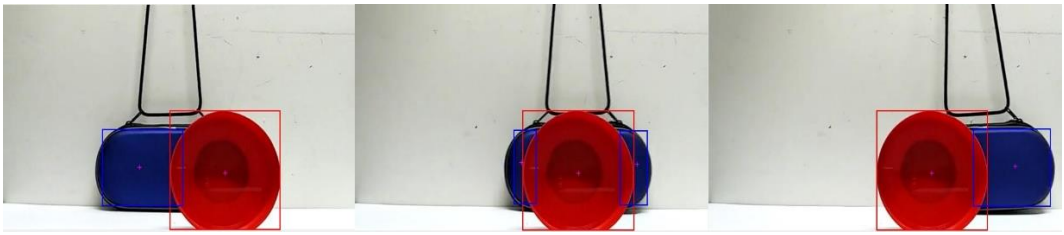


Figure 1.1: Occlusion issues in multiple object tracking

The main objective of this research is to solve the occlusions that occur in object tracking with the application of image processing.

2. Research Methodology

Generally, the research methodology is breakdown into four different phases. These phases are, modelling phase, simulation phase, measuring phase and data collection phase as shows in Figure 2 below.

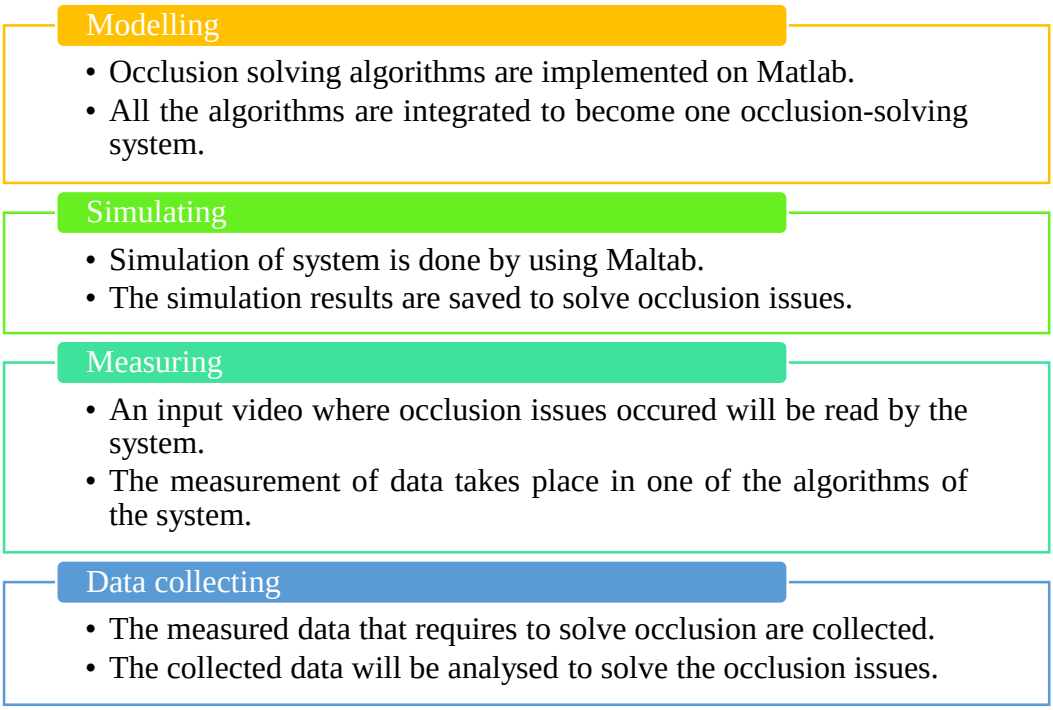


Figure 2: Project overview chart

Generally, the research methodology is broken down into four different phases. These phases are, modelling phase, simulation phase, measuring phase and data collection phase. After initializing Matlab, the system is ready to be simulated on Matlab. Firstly, an input video will be read by the system. Next, the system extract and read every frame from the input video with frame extracting function. After all the frames from the video has been read, each frame will then be processed by foreground object segmentation algorithm. Mean colour values of the foreground objects will be detected with colour detection algorithm and then the foreground objects will be tracked based on their own mean colours values with an ID. In order to identify tracked foreground objects clearly, the coordination, area, width, and height of each foreground object will be identified using the object specifying algorithm. Finally, the occlusion solving algorithm will be implemented to solve any occlusion issues the video had.

2.1 Overall Configuration of the system

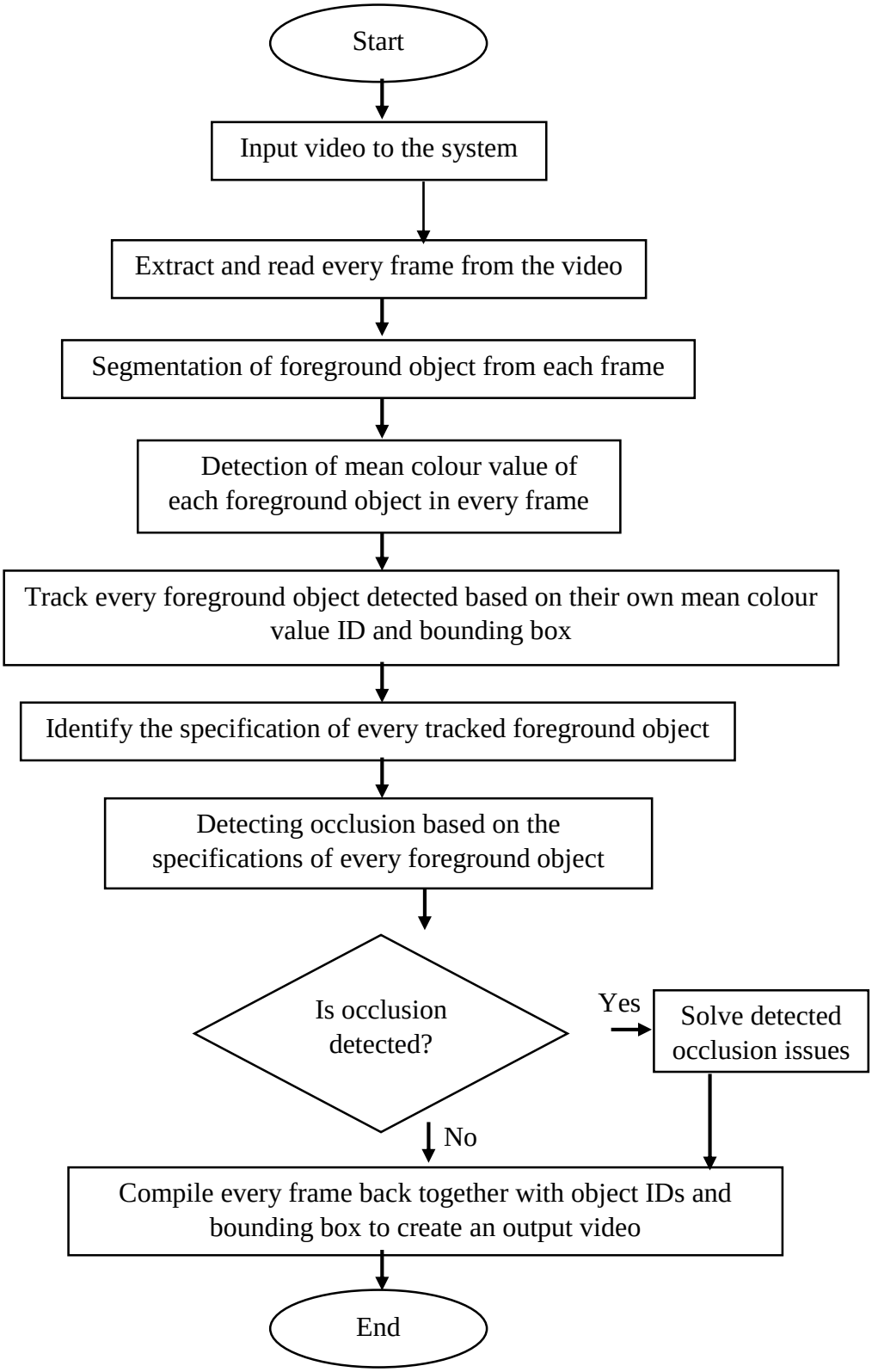


Figure 2.1: Flowchart of overall system configuration

The flowchart of overall system configuration is shown in Figure 2.1 above. Generally, the system starts off by extracting all the frames of the input video, and then read it frame by frame to segment the foreground objects. After the segmentation of

foreground objects, the system will further analyse the mean colour value of each object and track it with an ID and a bounding box. The system moves on by identifying the tracked object's specifications such as height, width and more to detect the occurrence of occlusion. The system will then proceed to handle the occlusion issues if occlusion do occur. Finally, after handling the occlusion issues, the system will compile every post-handling frame into one output video.

2.2 Object segmentation and colour tracking algorithms

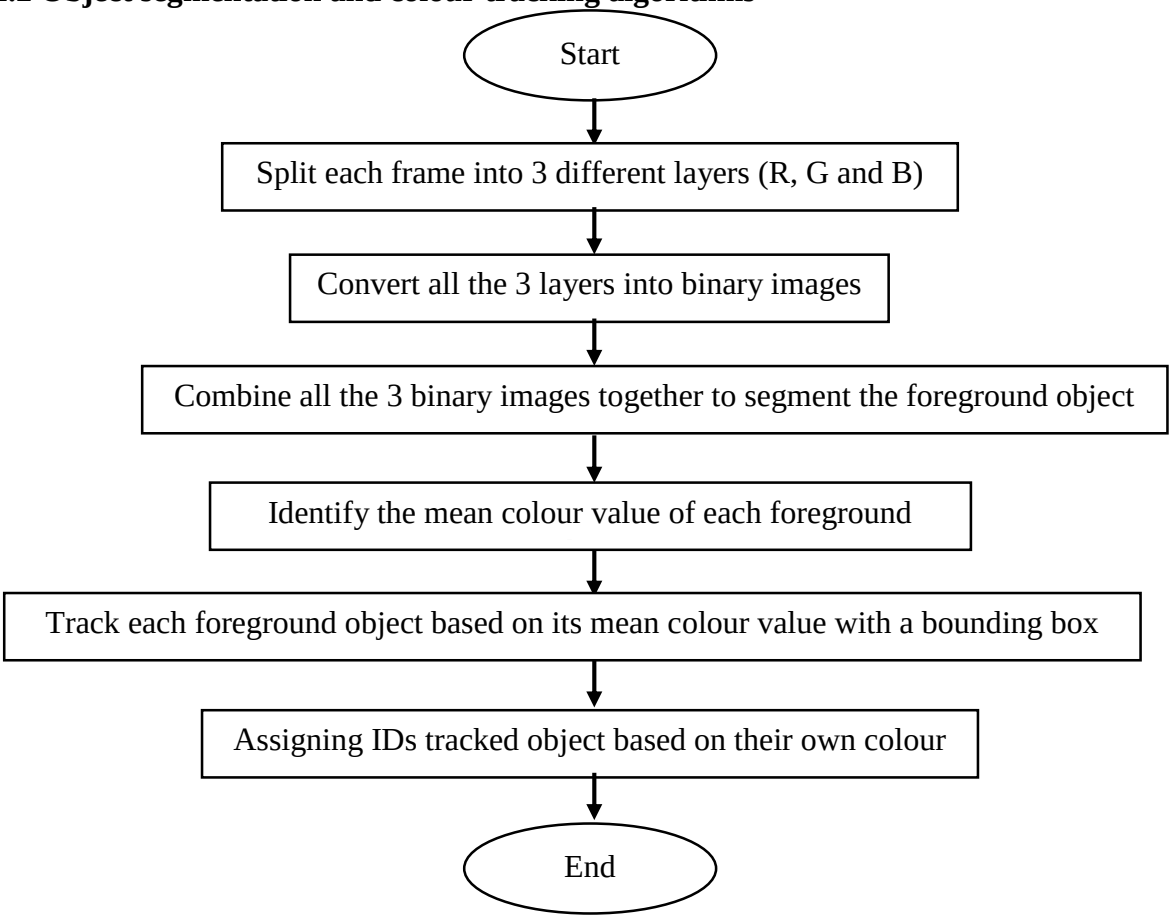


Figure 2.2: Flowchart of object segmentation and colour detection algorithms

Figure 2.2 above has shown the flowchart of object segmentation and colour detection algorithms. The segmentation of foreground objects is done by combining 3 R, G and B binary layers. After the object segmentation process, the mean colour value of each segmented object is identified. After the mean colour of each foreground object is identified, the algorithm proceeds by tracking the object with a bounding box and assigning an ID to the object in one frame.

2.3 Object specifying algorithm

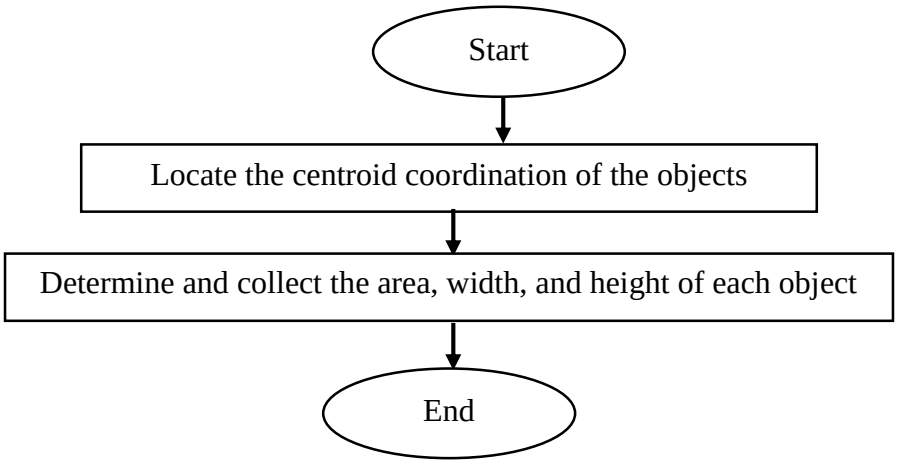


Figure 2.3: Flowchart of object specifying algorithm

Figure 2.3 above shows the flowchart of the object specifying algorithm. Technically, this algorithm detects every tracked object specification in every frame. First, the algorithm locates the centroid coordination of every tracked object. Next, it determines and saves the area, width and height of every tracked object.

2.4 Occlusion handling algorithm

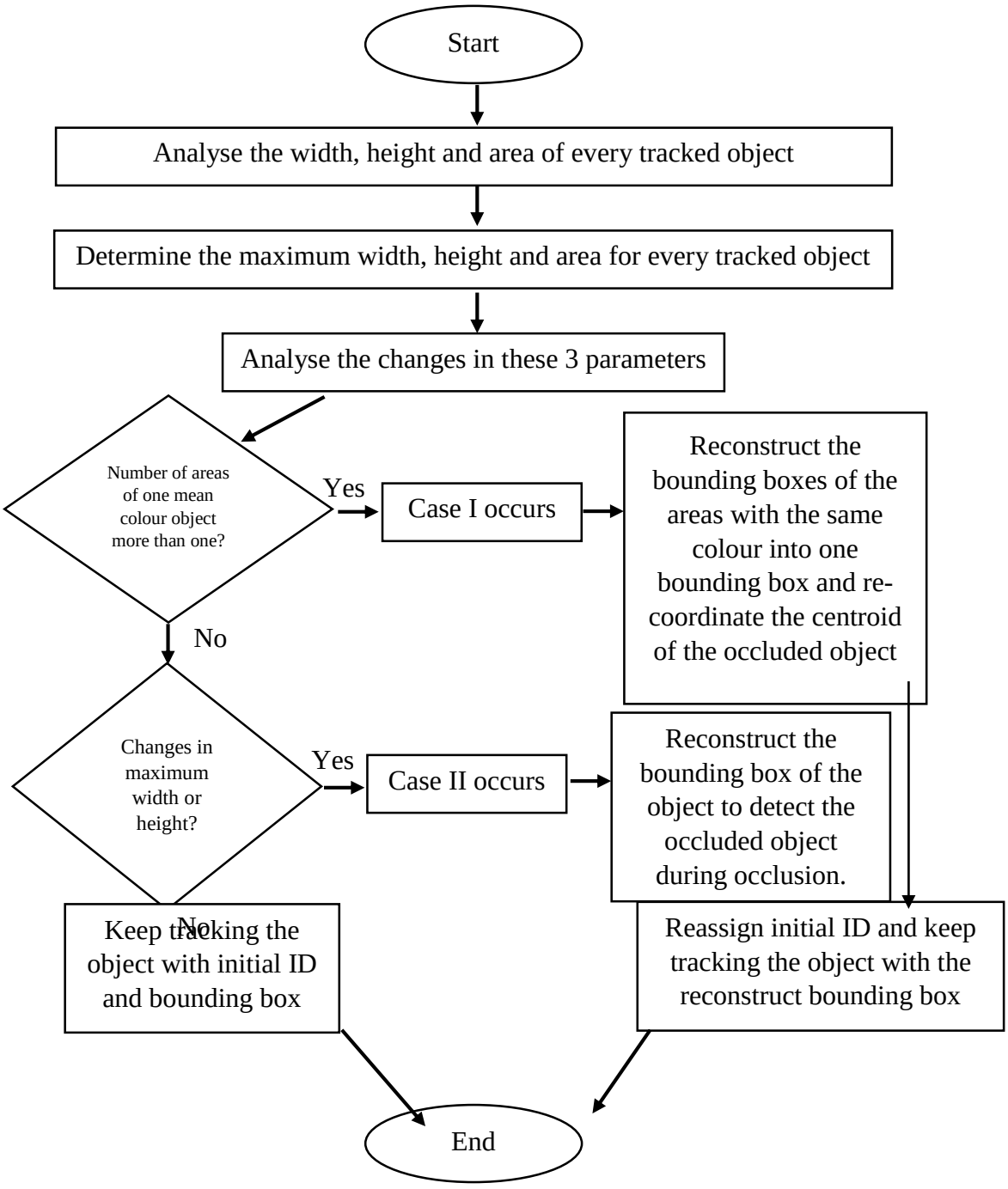


Figure 2.4: Flowchart of occlusion handling algorithm

Figure 2.4 above shows the flowchart of the occlusion handling algorithm. In this algorithm, the saved data from the previous algorithm would be analysed to detect whether occlusion issues occur in a frame. Before deciding whether occlusion do occur, the maximum width, height and area of every tracked object is obtained from the previous algorithm. Case I occurs when 2 or more areas of with the same mean colour is detected. Technically, an object with a mean colour only has one area. If the number of areas of the same colour is more than 2, then the object is being occluded in the middle while exposing its edges at left and right sides. Therefore, it is considered that the object is moving horizontally from left to right and being blocked in the middle by

another object. The Case I occlusion issue will be solved by replacing the 2 bounding boxes of two different areas with a reconstructed bounding box to track the middle-occluded object from behind. This is shown in Figure 3.3 under the simulation results section. Case II occurs when the change in width or height of an object is detected. For example, considering the same motion of moving horizontally from left to right. When the width of an object changes significantly along with the area of the object, the object might be occluded either on its left side or right side. Case II occlusion is solved by reconstructing the smaller bounding box that only tracks the exposed part of an object, with a new bounding box that tracks the whole object including its occluded part, as shown in Figure 3.4 and Figure 3.5.

2.5 Limitation of the proposed system

The proposed system's scope is limited on solving occlusion issues in recorded video with multiple single-coloured objects and a white stationary background. Also, the shapes of all the objects must remain unchanged throughout the video.

3 Simulation Results

3.1 Frame extracting and combining

Frame extracting algorithm is the first algorithm of the proposed system. Basically, this algorithm extracts all the frames in one video and temporally saved them at a temporary folder created using Matlab codes.

Frame combining algorithm is the fifth and last algorithm in the proposed system. It combines all the post-processed frames (with occlusion issues solved) into a video.

3.2 Object segmentation and colour tracking

Object segmentation and colour tracking algorithm is the second algorithm in the proposed system. In this algorithm, the foreground objects are segmented out from the background. Firstly, the RGB frames in a single frame is split into 3 different layers. These 3 different layers are R layer, G layer and B layer, each layer carries its own colour value, R layer carries red value, whereas G and B carry green value and blue value respectively. Next, every layer is converted to binary images. By combining all the 3 RGB binary layers together with certain binary thresholding value, the foreground objects can be segmented from the white background. Since white background has lower mean colour value, it does not consider as a foreground object. The combination of the 3 RGB binary layers are showed in II of Figure 3.1 on the next page.

The average mean colour of an object, V_a is determined by calculating the average value of R, G, B (R_a, G_a, B_a) in the pixels inside the box bounding box. After obtaining the average mean colour, the range of mean colour is set as $[R_a \pm 8\%, G_a \pm 8\%, B_a \pm 8\%]$, any pixel within the range of mean colour is treated as part of a foreground object's pixel. Once a foreground object with a mean colour is tracked, its pixel-area can be obtained as showed in IV and V of Figure 3.1. Finally, ID is given to

every tracked foreground object according to its mean colour For example in Figure 3.1 ID:B is given to blue object and ID:R is given to red object.

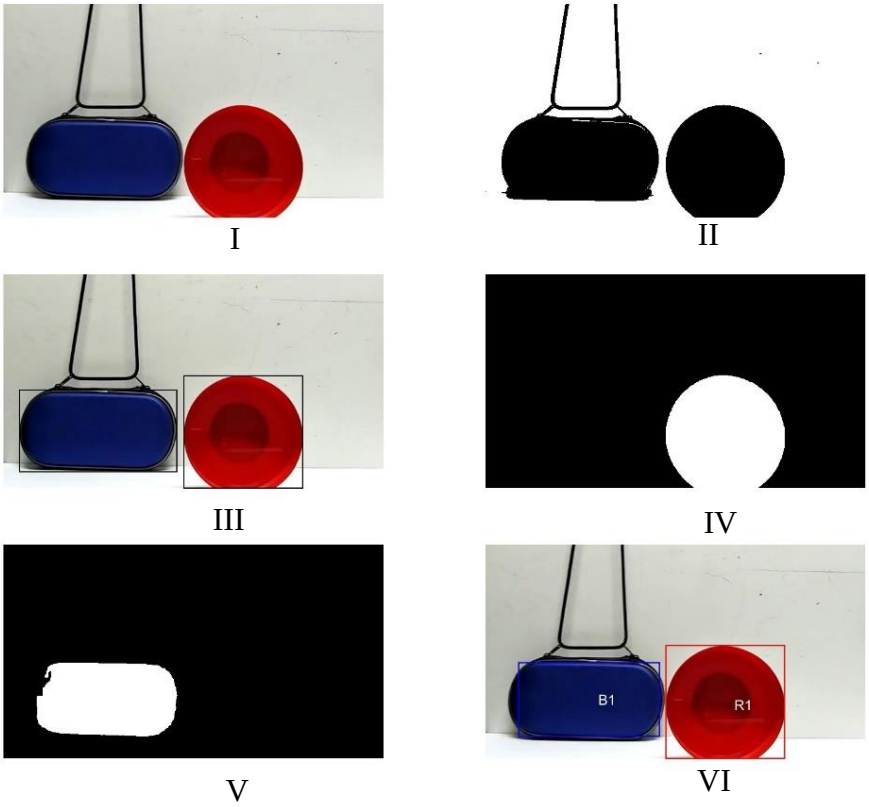


Figure 3.1: Object segmentation and colour detection results

Figure 3.1 above shows the results of object segmentation and colour tracking algorithm. The process of the algorithm is explained below:

I. The original extracted image of a frame.
II. The foreground objects are segmented by processing R, G, and B layers.
III. The mean colour value inside the box is determined. Black colour detection is removed due to shadow issues. The thread is not detected as an object because it's black.
IV. Red colour object is detected, the white region is the area of the red object.
V. Same as the previous step, the blue object is detected and the area of blue object is represented in the white region.
VI. Both blue and red objects are tracked with different bounding boxes and IDs are assigned to both objects.

The criteria for constructing bounding boxes will be explained in the next section.

3.3 Object specification

Object specification algorithm is the third algorithm of the proposed system. It is considered as a short algorithm as it only determines the specification of every tracked object. Technically, this algorithm determines the maximum areas of all foreground objects at the beginning of every input video. After the maximum area of an object is determined, the algorithm will proceed to locate the coordinates of centroid of the object. Next, the properties of the bounding box will also be determined with this algorithm.

Construction of bounding box requires four different properties, these properties are right (r_b), top (t_b), width (w_b) and height (h_b). r_b and t_b are referred to the right and top starting points of the bounding box respectively. Whereas w_b and h_b determine the width and height of the bounding box. Technically, the properties of bounding box can be expressed as:

$$b = [r_b,\ t_b,\ w_b, h_b]$$

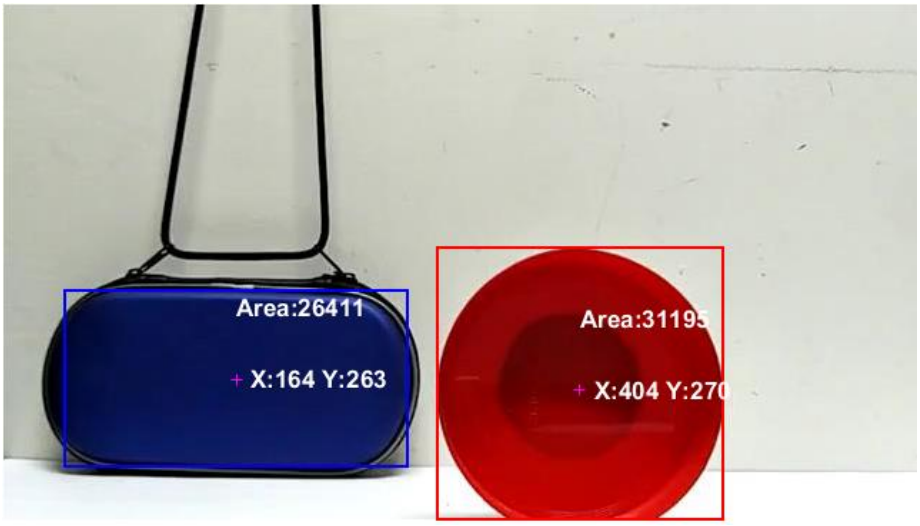


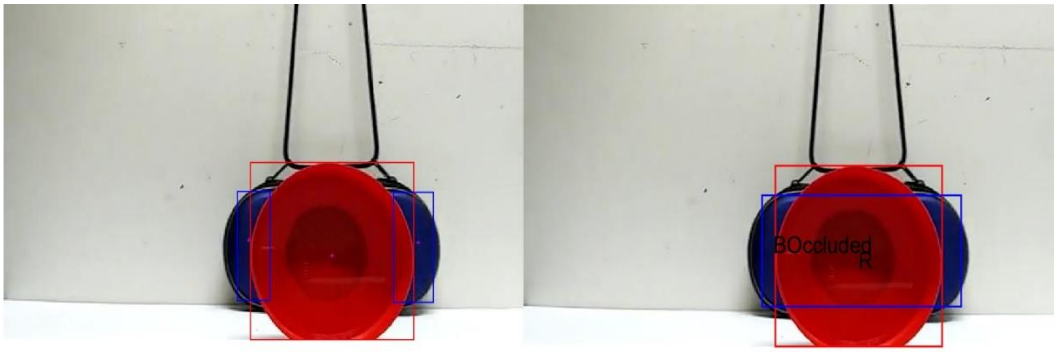
Figure 3.2: Object specification result

Figure 3.2 above shows that each segmented object is tracked with a bounding box with its centroid coordinates identified. The centroid coordinates of the objects are important to justify which case of occlusion issue occurs.

3.4 Occlusion handling

Occlusion handling algorithm is the fourth algorithm in the system that handles occlusion issues occur throughout the input video. In this algorithm, the bounding box of an occluded object is reshaped to accurately track occluded object with its true size. The bounding box is reshaped according to how the occluded is occluded. Following the project scope, there are two potential occlusion cases, Case I and Case II. Case I only occurs when an object is being occluded at the middle with its left and right sides exposed as shows in Figure 3.3 below. Case II occurs when an object is being partially occluded by another object on one side, either left or right. The different cases of occlusion issues as described previously occurred in the video are solved with occlusion handling algorithm.

Case I

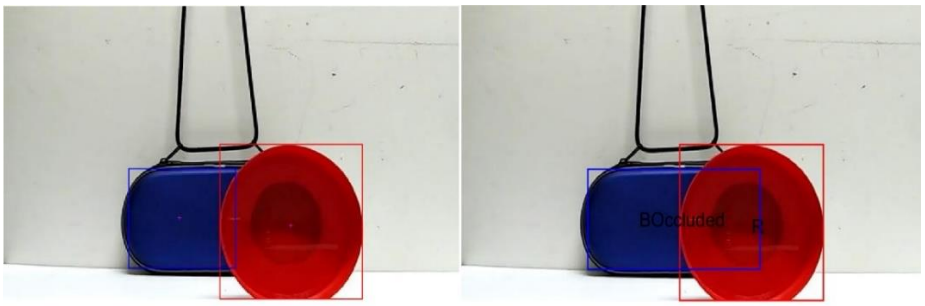


I II

Figure 3.3: Object is being occluded in the middle

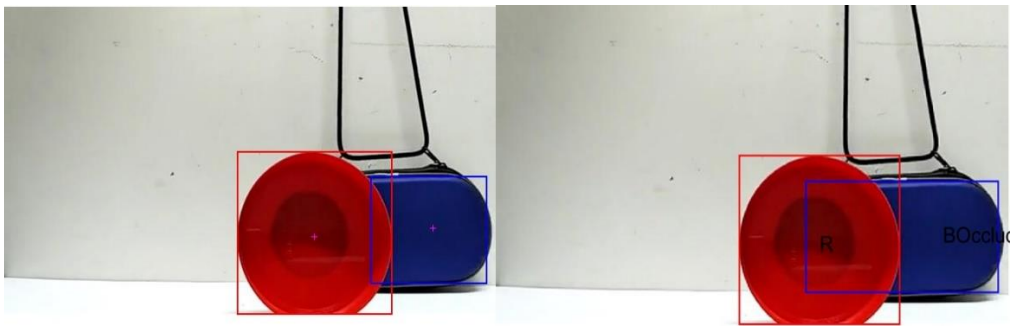
When the blue object is occluded by the red object in the middle, two different bounding boxes wrongly track a single object as two different objects with the same colour as shown in I (left) of Figure 3.3 above. To rectify this occlusion issue, a new bounding box is constructed to replace the old ones as shown in II (right) of Figure 3.3 above. In this case, the new bounding box is constructed with maximum width data obtained from the previous frame. Since the new bounding box is tracking an occluded object, the initially ID assigned for the object will be retained along with word "occluded" to indicate the occurrence of occlusion.

Case II



I II

Figure 3.4: Object is being occluded on the right side



I II

Figure 3.5: Object is being occluded on the left side.

When either side of the blue object is occluded as shown in I of both Figure 3.4 and Figure 3.5, the bounding box only tracked the exposing portion of the blue object. To rectify this occlusion issue, the bounding box is reconstructed to track the blue object even when it is occluded. In Figure 3.4, the right side of the blue object is occluded,

the system analyses the centroid coordination of both the blue and red object to select the appropriate expansion of bounding box. In this case, the x-coordinate of the centroid of the blue object is less than the red object and the exposing area of the blue object is lower than the maximum determined area of blue object. Thus, will expand the bounding box further to the right to track the occluded right portion of the blue object as shown in II of Figure 3.4. The same principle is used to solve the occlusion issue in Figure 3.5, where the x-coordinate of the centroid of blue object is greater than the red object.

4. Conclusion

In conclusion, the occlusion issue that occurs in the input video is properly handled by using the system in this research. This proposed method was able to handle 2 objects overlapping each other and was able to identify the occluded object as a single object even though it was blocked in the middle. For future work, further improvements need to be done for handling occlusion in real-life tracking system instead of inputting a video to produce an output video that handles occlusion issues.

5. References

[1] Y. Cai, H. Wang, X. Chen, and L. Chen, "Multilevel framework to handle object occlusions for real-time tracking," pp. 1–8, 2016.

[2] Pylyshyn, Z. (2007). *Multiple object tracking*. [online] Scholarpedia. Available at: http://www.scholarpedia.org/article/Multiple_object_tracking [Accessed 26 Oct. 2017].

[3] P. Ding and Y. Song, "Robust Object Tracking using Color and Depth Images with a Depth based Occlusion Handling and Recovery," pp. 930–935, 2015.

[4] I. Engineering and S. Province, "Variable Scale and Anti-occlusion Object Tracking Method with Multiple Feature Integration," pp. 426–433, 2016.

[5] W. Luo, J. Xing, X. Zhang, X. Zhao, and T.-K. Kim, "Multiple Object Tracking: A Literature Review," *arXiv, 1-39. Retrieved from http//arxiv.org/abs/1409.7618*, vol. V, no. 212, 2014.

[6] M. Intelligence, Q. Zhao, W. Tian, Q. Zhang, and J. Wei, "Robust object tracking method dealing with occlusion," 2016.

[7] Z. M. et al. Shehzad, Muhammad Imran, Yasir A. Shah, "K -means based multiple objects tracking with long-term occlusion handling," 2016.

eureca 2017 – Conference Paper
Paper Number 2EE02

Comparative Study between Planar and Bent Antenna Characterization

Lau Zheng Tung[1], Ghafour Amouzed Mahdiraji*

[1]*School of Engineering, Taylor's University Lakeside Campus, Malaysia*

*Ghafour.AmouzadMahdiraji@taylors.edu.my

Abstract
Planar antenna is usually designed in small scales which the application requires smaller bandwidth such as Wi-Fi modules or navigation system devices. There are some antenna application requires bent antenna such as wearable Ultra-Wide Band (UWB) antenna but the substrate used will have some defects after bending and crumpling from time to time. What if the planar antenna is designed that it can be bent and the bending affects the impedance matching and shift in resonant frequency? So, this research aims to achieve the limitation of the planar antenna to be bent at certain angle and given frequency range (1-8 GHz). The planar antenna is designed in the Computer Simulation Technology (CST) Software and the proposed antenna is then bend in the simulation software. The analysis of comparative evaluation for both planar and bent antenna is carried out on different characteristics such as evaluation between S-Parameters & Frequency and evaluation between Voltage Standing Wavelength Ratio (VSWR) & Frequency. The behaviour of radiation pattern for both antennas can also be obtained in the CST simulation.

Keyword: Planar & Bent Antenna, Computer Simulation Technology (CST) Microwave Software, S parameters, Radiation pattern, Voltage Standing Wavelength Ratio (VSWR)

1. Introduction

Antenna has been widely used in various forms of communications such as radio broadcasting, navigation systems, satellite communication, remote sensing, defence radar and medical scanning device. Planar antennas are commonly used in sensing devices due to its low cost and simple implementation. The frequencies of the Planar antenna can reach as high as 77 GHz which can be performed in automotive sensing devices [1]. Microstrip patch antenna is one of the popular design of planar antenna that have carried out for research in medical applications. In fact, microstrip patch antenna is smaller, lighter and electrical diversified which suits the requirement to implement on medical applications for tissue detection [2]. In recent years, many relevant researches have tried to improve planar antenna for medical application use, but there was a constraint on the planar antenna study. The planar antenna acts as a flat-solid surface that only works fine on flat surfaces. It is difficult to obtain a good measurement on non-flat surface with planar antenna due to the fact that the structure of the antenna is flat. The measurement on curvature body may not be detected by planar antenna since the antenna does not possess the bending effect in order to lean on human bodies closely. As the issue rises up, there is a high demand on non-planar bent antenna is suitable to be carried out on human body surface. Bent antennas mostly are the solutions to some application as they are suitable to be implemented onto structures or objects that are not in planar form. One of the dominant research based on bent antenna is a wearable antenna [3]. Wearable antenna requirements for all modern applications include flexibility, light weight, low cost, almost maintenance-free and simple installation. The application for wearable bent antenna mostly can be found in medical applications which applies for youngsters, the aged and athletes for monitoring purposes. Research have identified the draw backs for bent antennas which would lead to certain distortion of parameters which includes, the input impedance, directivity and phase angle when the antenna is bent [4], [5]. In some case study, modifying substrate material is applied on the antenna improves its parameters, thus allows the antenna to operate properly with better efficiency even though the antenna is bent [5].

S parameters are defined in terms of incident and reflected travelling waves which are simple to be for analysis. S parameters are easily measured using network analysers; popular in any Radio Frequency (RF)/Microwave circuit design and testing. S Parameters are complex matrix that shows Reflection/Transmission characteristics (Amplitude/Phase) in frequency domain. Figure 1 shows a two-port device which has four S-parameters. The first number following the "S" is port where the signal emerges while the second number is where the signal is applied. So, S_{21} is a measure of signal coming out from port 2 relative to RF stimulus entering port 1. If the numbers are the same (S_{11}), this indicates that the signal has a reflection measurement. Quantifying the reflection and transmission characteristics of the device is available with amplitude and phase information. There are scalar and vector characteristics that are important for the analysis. For example, return loss is a scalar measurement of reflection, while impedance results from a vector reflection measurement [1]. Meanwhile, like group delay, are referred to purely phase-related measurement. For Reflection, S_{11} /S_{22}: the relevant parameters include, Reflections (Return loss), Impedance, Admittance, VSWR. For Transmission, S21/S12: the relevant parameters include, Gain/Loss (Insertion loss), Phase, Group delay (Delay time). To identify any loss of signals that was sent, a return

signal of the transmission signal is needed which indicates the Reflection, S_{11} parameters. Return Loss is measured at the input to the coaxial cable connected to antenna and it is the difference between forward and reflected power in dB. The Return Loss calculation is given by Radiated Power (PR) which the power is reflected back, divided by Incident Power (PT) which the power transmitted by the source. The Return Loss must be as small as possible for maximum power transfer and the ratio, PR/PT should also be as small as possible and the return loss should also have the value which is as large a negative as possible.

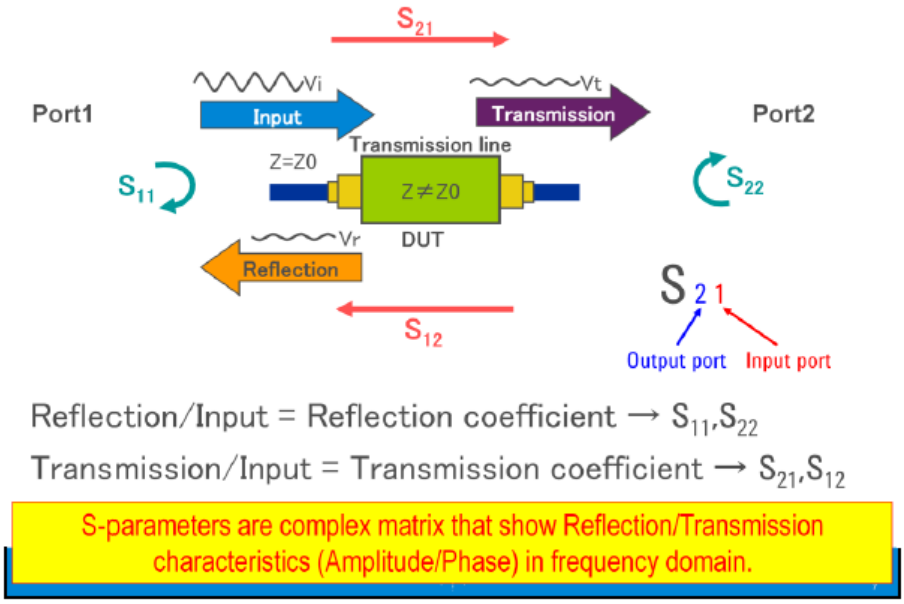


Figure 37: Reflection/Transmission Characteristics (Amplitude/Phase) in Frequency domain [1].

The main objective of this study is to design a planar antenna and bent antenna to study both comparative parameters. In order to achieve the objective of this project, the project has been divided into each individual objective as following:

i. To study the characteristics of a planar antenna, design and simulate the planar antenna characteristics.
ii. To study the characteristics of a bent antenna, perform bending on the planar antenna and simulate the bent antenna properties.
iii. To investigate and compare the simulated parameters for both planar and bent antenna.

3. Methodology

3.1 Antenna Design

Figure 2 shows the antenna design with the dimensions. The antenna is designed on Flame Retardant (FR-4) substrate with the dimension given; dielectric constant, ε_r of 4.3, loss tangent of 0.025 and thickness of 0.16mm. The copper tape with thickness of 0.035 mm is used as conductive material for patch and ground. Most research recommended transmission line model to design the width, *W* and length, *L* of the antenna [2], [3]. The implementation of transmission line model is fairly easy and antenna designs will acquire with reasonably good performance in terms of return loss and efficiency during the simulation of antenna. According to transmission line model, the length, *L* and width, *W* of the patch are calculated as [3]:

I. Calculation for patch width:
The dimension of the antenna depends on the operating/resonant frequency and value of dielectric constant.

$$W = \frac{c_o}{2f_o}\sqrt{\frac{2}{\varepsilon_r + 1}} \quad (1)$$

Where

W antenna width in mm
c_o speed of light in free space, $3x10^8$
f_o operating frequency/resonant frequency
ε_r dielectric constant of substrate

II. Calculation for effective permittivity
The effective permittivity is important in the designing process of the antenna. There is radiation travelling through from patch towards the ground, followed by passing through air then passing through the substrate and this occurrence is referred as 'Fringing'. As we know that the air and substrate have different dielectric constant, so we need to find the effective of the dielectric constant[4].

$$\boldsymbol{\varepsilon_{reff}} = \frac{(\boldsymbol{\varepsilon_r + 1})}{\boldsymbol{2}} + \frac{(\boldsymbol{\varepsilon_r - 1})}{\boldsymbol{2}}\left(\boldsymbol{1} + \boldsymbol{12}\frac{\boldsymbol{h}}{\boldsymbol{W}}\right)^{\boldsymbol{-0.5}} \quad (2)$$

Where

ε_{eff} effective permittivity
h height of the substrate in mm
ε_r dielectric constant of substrate
W antenna width in mm

III. Calculation for effective length:

$$L_{eff} = \frac{c_o}{2f_o\sqrt{\varepsilon_{reff}}} \quad (3)$$

Where

L_{eff} effective length of patch
ε_{eff} effective permittivity
c_o speed of light in free space, $3x10^8$
f_o operating frequency

IV. Calculation for length extension:
The size of the antenna is increased by an amount of length extension, ΔL due to fringing[4].

$$\Delta L = 0.412h\left[\frac{(\varepsilon_{reff}+0.3)\left(\frac{W}{h}+0.264\right)}{(\varepsilon_{reff}-0.258)\left(\frac{W}{h}+0.8\right)}\right] \quad (4)$$

Where

ΔL length extension
ε_{eff} effective permittivity
h height of the substrate in mm
W antenna width in mm

V. Calculation for patch length:

$$L = L_{eff} - 2\Delta L \quad (5)$$

Where

L length of patch in mm
L_{eff} effective length of patch
ΔL length extension

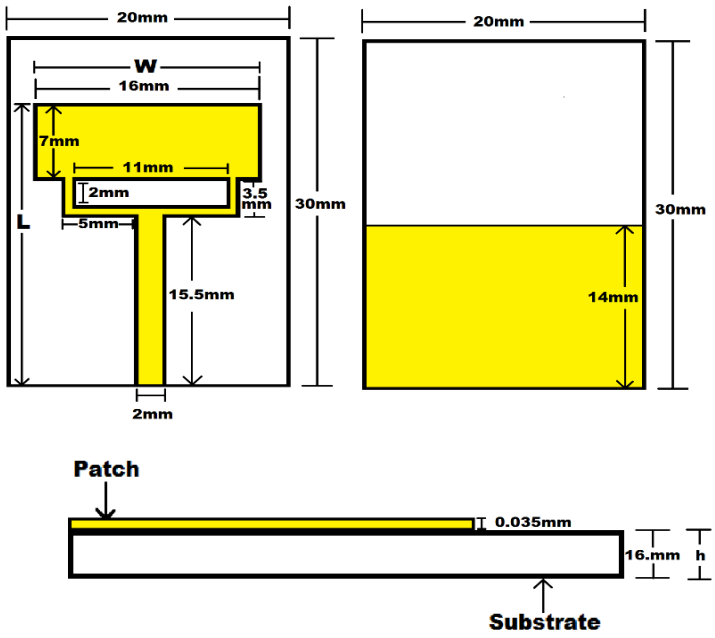


Figure 38: Parameter Design of Proposed Antenna

3.2 Antenna Bending

To demonstrate the bending of the antenna, Figure 3 shows a cylinder with radii of 5-10mm. The bending function is visualized to bend on a cylindrical surface in CST software. Figure 4 shows the bending direction towards the cylindrical surface. The antenna is bend on XZ plane which bends from both sides of the antenna. The antenna is tested on different type of radii bending of the cylinder. While the bending of antenna is increased, the radii of the cylinder is decreased. The results of S parameters, VSWR and Radiation Pattern is simulated.

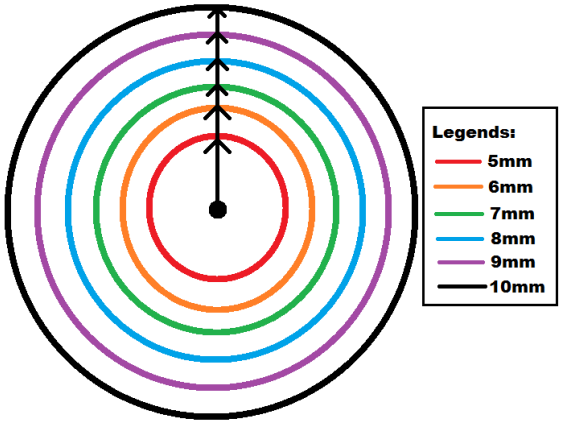


Figure 3: Different radii of the cylinder

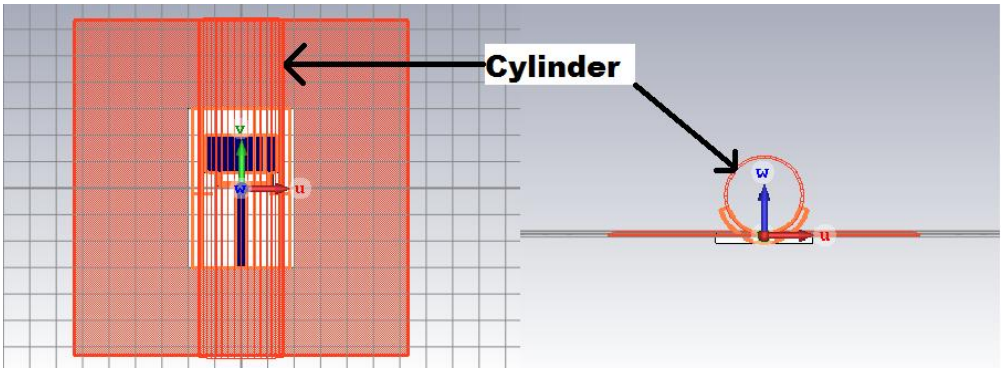


Figure 4: Cylinder object for the antenna to bent towards in CST

4. Result and Discussion

4.1 Planar Antenna Performance

Simulations are carried out using Computer Simulation Software (CST) Microwave Software to simulate the behaviour of the antenna. Figure 5 and 6 shows the simulated results in terms of return loss and VSWR of the antenna. The simulated return loss shows an impedance bandwidth of 2.67 GHz (3.08 GHz – 5.75 GHz) which is in a good operate operation. The VSWR shows a huge drop for 1 GHz to 3 GHz. One of the reason is that the frequency range is not suitable to simulate a better VSWR result since the VSWR is more than 2. The results starting from 3GHz to 8GHz has a better measurement in the VSWR which satisfies the VSWR ratio requirement of less than 2. In order to test the determine the performance of the planar antenna, the planar antenna is then bent in the XZ plane with different cylinder radii (r= 5, 6, 7, 8, 9 and 10mm). The results of the bent design are compare with the results of planar design.

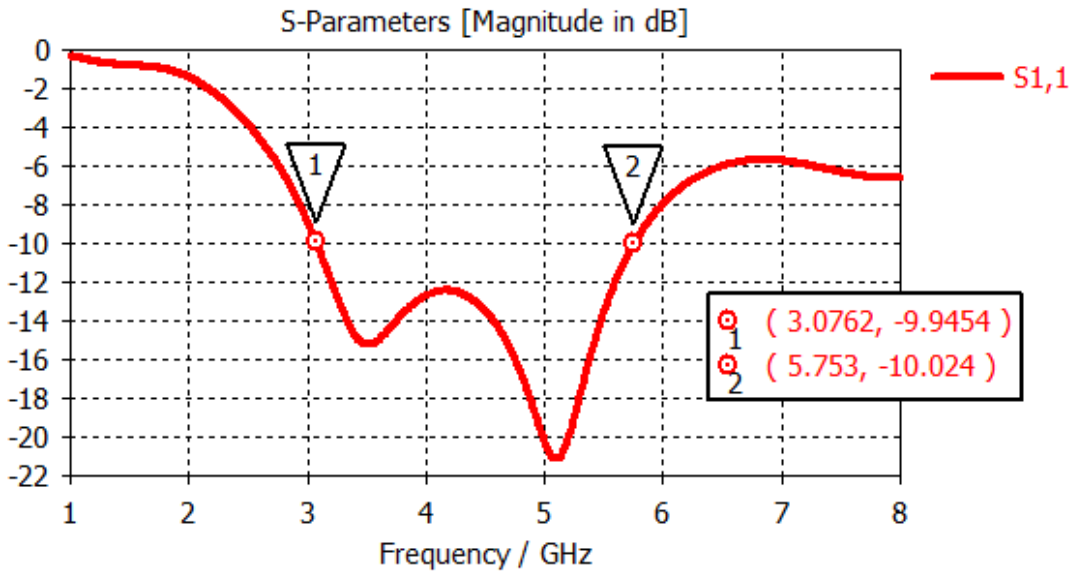


Figure 5: Simulated S Parameter for Planar Antenna

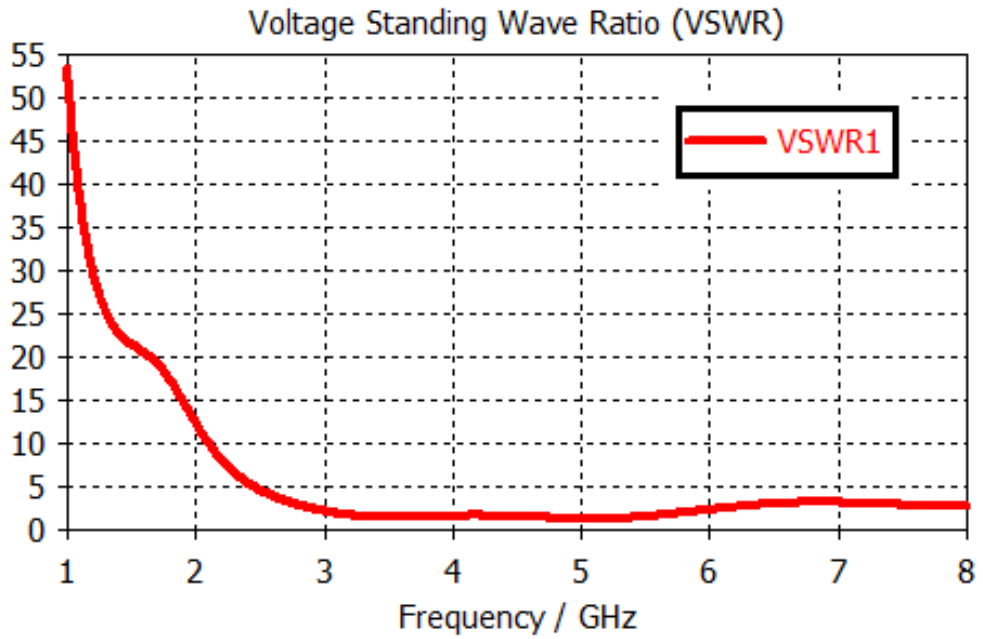


Figure 6: Simulated VSWR for Planar Antenna

4.2 Effects on Return Loss and Bandwidth

Figure 7 compares planar antenna and bent antenna that is cylindrical bent with different radii of 5-10 mm. Theoretically, the antenna changes its effective length when the antenna is bent. The bending on the antenna increases, the effective length is decreases along and the resonant frequency will shift to a higher band[5]. Table 1 show that the bandwidth is large (in GHz) due to the low permittivity of the dielectric substrate[6]. This explains that lower permittivity dielectric substrate with thicker in thickness is able to produce an antenna design with high efficiency and large bandwidth. Meanwhile, dielectric substrate with high permittivity will result in a lower efficiency in the antenna design results. The return loss shows increment along as the bending increases which means the antenna is operating normally. Generally, a larger return loss results in more energy is delivered into the antenna. The antenna is to be design in wide frequency range and the wider of the bandwidth, the better in the antenna performance. The antenna operates normally within the desire range even though there is a shift in frequency. The performance of the proposed antenna is slightly decreased while the antenna bending is increased but the antenna still operates efficiently at resonant frequency of 4.591GHz. Based on the obtained result, the return loss of bending at 6mm shows a greater return loss which indicates a good performance on the antenna. A high return loss is needed in a good antenna since it may prevent reflected signals to damage the antenna and interference is occurred if the returned signal is reflected back from previous device. The good performance is also proved in the

VSWR that the reflected power at bending of 6mm is closed to 0 which indicates that all the power is reflected.

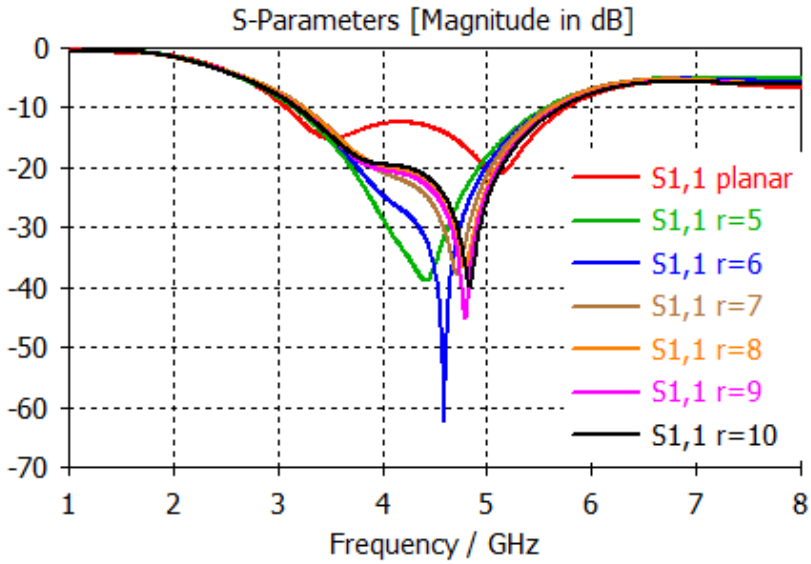


Figure 7: Variation of return loss with bending.

Table 42: Change in radiation characteristics of antenna with bending

Cylindrical Bend [mm]	Return Loss at 4.591 GHz [db]	Bandwidth [GHz]	Resonant Frequency [GHz)
r=0 (planar)	-14.17	2.68 (5.76 - 3.08)	5.095
r=5	-31.56	2.40 (5.56 - 3.16)	4.419
r=6	-62.32	2.40 (5.59 - 3.19)	4.591
r=7	-30.14	2.35 (5.59 - 3.24)	4.717
r=8	-26.12	2.40 (5.63 - 3.23)	4.787
r=9	-26.78	2.50 (5.68 - 2.50)	4..794
r=10	-24.63	2.52 (5.70 - 3.18)	4.836

4.3 Effect on Voltage Standing Wave Ratio (VSWR)

Figure 8 shows the graph of VSWR comparison between both planar antenna and bent antennas. The graph shows that the bent antennas has a similar trend as the planar antenna in terms of VSWR. From the generated Voltage Standing Wave Ratio (VSWR), the results are taken from the resonant frequency at 4.591 GHz. Table 2 shows the percentage of power delivered by the receiver reflected from the antenna. The maximum power reflected is 3.8% which 96.2% of the power is delivered to the antenna. The minimum power reflected is 5.86E-05% which 99.99% of the power is delivered to the antenna. The antennas performance is considered good and little would be gained by the impedance matching since the simulated VSWR results are less than 2. The VSWR from 1 GHz to 3GHz shows a high VSWR which means that the range of frequency is reflecting a higher power back to the antenna which may affect the antenna performance. After that, the VSWR is within the acceptable range which most of the antenna VSWR are below 2.

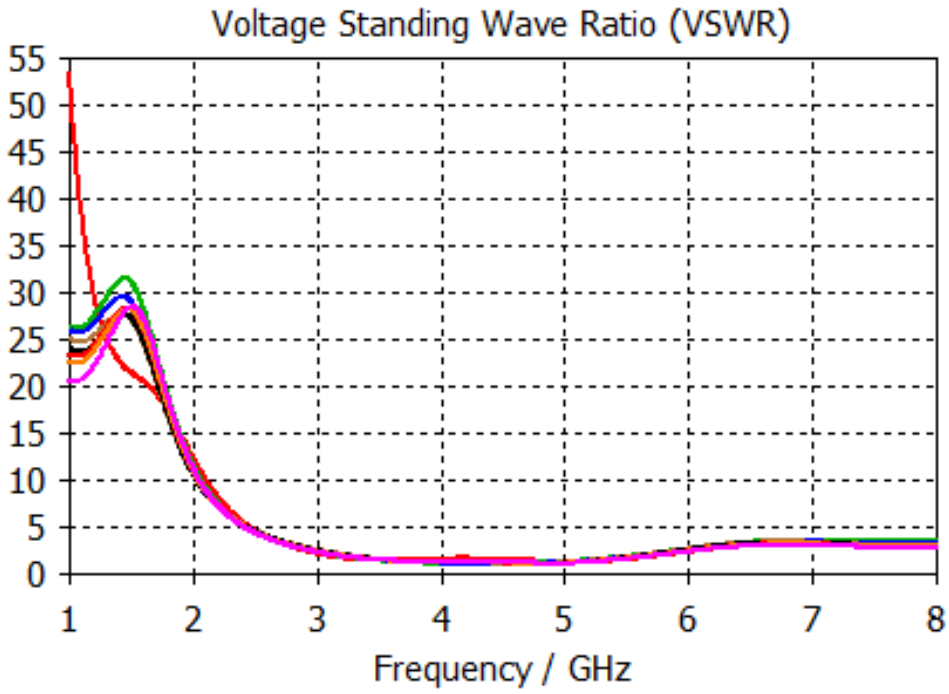


Figure 8: Comparison of planar antenna and bent antenna in terms of Voltage Standing Wave Ratio

Table 43: Change in VSWR of antenna with bending

Cylindrical Bend, r [mm]	VSWR	Return Loss at 4.591 GHz [dB]	Reflection Coefficient, Γ	Reflected Power (%)
0	1.49	-14.17	0.196	3.82
5	1.05	-31.56	0.026	0.0698
6	1.00	-62.32	0.00076	5.86E-05
7	1.06	-30.14	0.03	0.097
8	1.10	-26.12	0.049	0.24
9	1.10	-26.78	0.046	0.21
10	1.12	-24.63	0.059	0.34

4.4 Effect on Radiation Pattern

Figure 9 shows the 2D radiation patterns for planar and bent antenna on *XZ* plane. Table 3 shows the angular width (3db) tends to decrease along with the increase in bending of the antenna. This leads to shrink in the radiation pattern in bending plane which the gain and efficiency of the antenna increases with the bending. The antenna gain, *G* is related to directivity, *D* and antenna efficiency of the antenna which the efficiency of the antenna increases along with the bending of antenna.

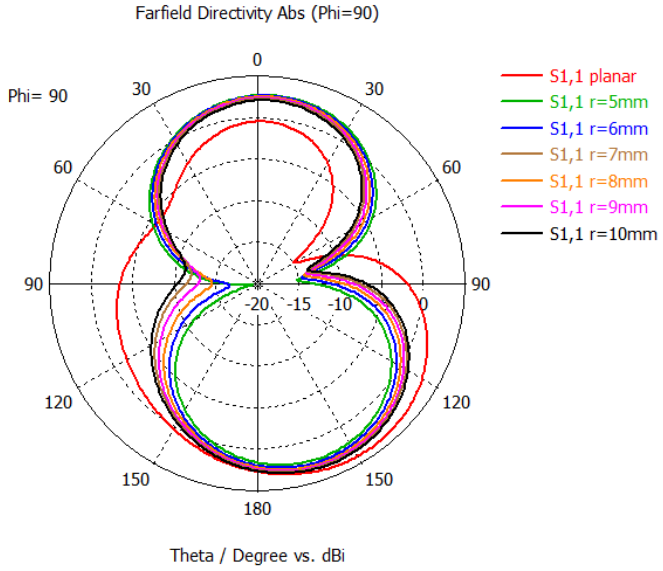


Figure 39: Radiation pattern of planar antenna and bent antenna

Table 44: Change in radiation pattern characteristics of antenna with bending.

Antenna Radii, r [mm]	Main Lobe Magnitude [dBi]	Main Lobe Direction [deg.]	Angular width (3db) [deg.]	Gain (dB)	Directivity (dBi)	Efficiency (%)
0 (Planar)	3.93	147.0	96.0	1.00	3.93	25.5
5	2.70	6.0	78.0	1.33	2.70	49.5
6	2.61	5.0	75.7	1.06	2.61	40.6
7	2.86	159.0	80.9	0.89	2.86	31.2
8	3.07	158.0	82.7	0.75	3.06	24.5
9	3.22	158.0	84.1	0.79	3.21	24.7
10	3.33	157.0	85.3	0.83	3.33	24.9

5. Conclusion and Future Work

This study is focused on the performance of a planar antenna when it is bent at given frequency range (1-8 GHz for medical applications). The results show that the performance of the planar antenna is slightly decreased when the antenna is bent. Although the performance of bent antenna is slightly reduce compared to the planar, the antenna still operates efficiently from 25.5% to 49.5% bending on the resonant frequency of 4.591GHz. The results of VSWR between both designs are within the acceptable range after 3GHz onwards. The angular width decreases in the plane of bending which results in increase in the antenna gain. Based on the obtained results, the antenna design can be implemented as a Wearable Antenna application with slightly lower performance compared to planar antenna but with the wearable properties. In future work, the performance analysis of the antenna in different angle will be done as well as different substrate material.

References

[1] "S-parameter measurement Basics for High-Speed Digital Engineers." [Online]. Available: http://literature.cdn.keysight.com/litweb/pdf/5991-3736EN.pdf. [Accessed: 20-Oct-2017].

[2] Y. Ahmed, Y. Hao, and C. Parini, "A 31.5 GHz Patch Antenna Design for Medical Implants," *Int. J. Antennas Propag.*, vol. 2008, pp. 1–6, 2008.

[3] V. Bernard, J. Paul, and I. Iloh, "Microstrip Antenna Design Using Transmission Line Model," *Microstrip Antenna Des. Using Transm. Line Model*, vol. 3, no. 11, 2013.

[4] M. A. Afridi, "Microstrip Patch Antenna − Designing at 2.4 GHz Frequency," *Biol. Chem. Res.*, vol. 2015, pp. 128–132, 2015.

[5] M. Rizwan, L. Sydänheimo, and L. Ukkonen, "Impact of bending on the performance of circularly polarized wearable antenna," *Prog. Electromagn. Res. Symp.*, vol. 2015–Janua, no. 2015, 2015.

[6] S. Dey, N. Saha, and A. Alomainy, "Design and performance analysis of narrow band textile antenna for three different substrate permittivity materials and bending consequence," *LAPC 2011 - 2011 Loughbrgh. Antennas Propag. Conf.*, no. November, pp. 1–5, 2011.

eureca 2017 – Conference Paper
Paper Number 2EE03

Inertial Sensing of Cyclists to Predict the Next Move

Mahesh A/L V.Nagarrettinam, Dr. Mohsen Nabi Poor*

[1]*School of Engineering, Taylor's University, Malaysia*

*mohsennabi.poor@taylors.edu.my

Abstract

In Malaysia, most of the accidents involving a bicycle and another vehicle is due to either the driver or rider 'failing to look properly'. This is more significant with the government initiatives to support the use of bicycle making carbon free environment, a vision of TN50. This research addresses the safety aspect of the cyclists in terms of the driver's point of view which improves cyclist visibility during driving. The proposed helmet system implements a rule-based algorithm which predicts the turning and braking movement of the cyclists. With this system, additional illumination and signalling will be provided for the cyclists. The major challenge faced is the implementation of algorithm for various situations of cycling. To ensure the system could be used on the road, the accuracy and speed of the automatic signalling system needs to be adhered. Situations that affects the output of the indicators includes bicycle speed, angle of turning, body tilt, duration of turn and random body movements. Limitations such as limited cycling movements and maximum speed are introduced to ensure the findings limited to the project scope are as accurate as possible. This project implements a 3-axis accelerometer and a microcontroller in a datalogger to acquire the required data which will then be analysed in MATLAB. Using Low Pass Filter filtering technique, the acquired data will then be cleaned to remove noise due to vibration during cycling. The characteristics of braking and turning were then analysed in time domain as well as frequency domain to ensure the optimum algorithm used for gesture recognition and movement prediction. The algorithm is based on sliding window, FFT and threshold based rule algorithm. The output based on the rule-based algorithm will then illuminate the corresponding signals which provides the safety feature of the system.

Keywords: 3-axis accelerometer, Low Pass Filter, sliding window, Fast-Fourier Transform, movement prediction

1. Introduction

70-80% of accidents between bicycle and another vehicle was found to be mainly due to human error. From initiatives raised from various governing bodies, the improved usage of bicycle was supported to reduce carbon emissions from motorized vehicle. [1] Therefore the safety aspect of a cyclist must be improved to encourage usage of bicycle while reducing the statistic of accidents.

Automated helmet signals were proposed to improve the safety aspect of. This was due to an observation that road users tend to neglect the usage of safety signals which could lead to serious repercussions. At the initial stages, as the technology for automation is still improving, the addition of automated safety signals on the helmet would not be affected in terms of speed and accuracy due to low speeds of cycling as compared to a motorized vehicle. Therefore, this research intends to provide automatic signaling and illumination such as brake signal and turning signal acquired from inertial sensors mounted on the helmet. The research objective was then proposed from the previous research as stated below:

1. To investigate and analyse suitable signal processing techniques for automated signalling and braking indication during real-time.
2. To assess suitable techniques to improve the accuracy of the algorithm proposed for automated signalling indication.

The main challenge of the project is to implement movement prediction algorithm. This was implemented by using an accelerometer. The accelerometer has an advantage over other Inertial Measurement Unit whereby it is cheap, physically small which will enable it to be easily attached anywhere, and more accurate as compared to gyroscope and magnetometer with a wide frequency range. The accelerometer could directly measure the movement of the cyclists, but this recorded raw data has limitations in which if there are excessive noise in the signal, the analysis of the raw data in time domain could not be used. Therefore, a reliable prediction technique is required if the system is to be implemented on the road.

An accelerometer-only system is designed due to its low power consumption, low cost and ease of usage. This is further backed by its capability to measure acceleration, orientation, rotation and motion. By combining the stated characteristics, an accurate and robust prediction system could be achieved with a specifically designed algorithm for prediction. Figure 1.1 shows a typical 3-axis accelerometer.

The efficiency of an accelerometer-only solution was explored from its ability to measure movement, orientation and rotation changes by O. Incel. The efficiency was then compared with a combination of accelerometer, gyroscope and magnetic field sensor. It was found that the performance of an accelerometer-only solution can achieve up to an 80% recognition which doesn't differ much from a combination of accelerometer, gyroscope and magnetic field sensor. When the gyroscope and magnetic field sensor are used alone, they do not reach the capabilities of the accelerometer. It was also found that when the motion, orientation and rotation information from the accelerometer are combined in a specifically designed algorithm, it provides a much higher accuracy as compared to using the motion information alone. Therefore, the accelerometer only system is preferred due to its low power consumption and accuracy. [2]



Figure 1.1. 3-axis accelerometer

To ensure minimal noise affecting the output of the accelerometer due to vibration during cycling, low pass filter was introduced to be incorporated to the measurement system. The low-pass filter functions by smoothing the measured signals to clean and remove noise while performing data averaging. Furthermore, important patterns and trend within a signal could be made more vivid as the frequencies due to noise are removed. The filter functions by attenuating signals above a predetermined cut-off frequency which is manually set after obtaining necessary data from tests done. Figure 1.2 shows an example of the low pass filter applied to a noisy signal. The noisy signal is denoted by the green line whereas the low pass filtered signal is shown by the blue line. [3]

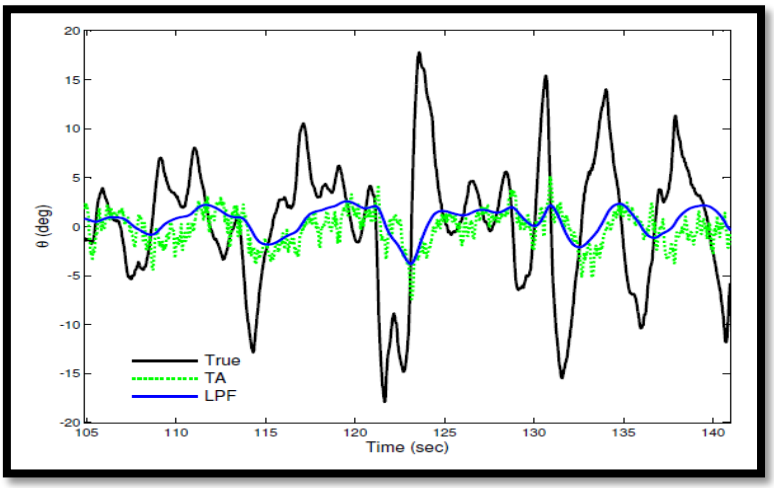


Figure 1.2. Comparison of traditional attitude and low-pass filtered signal

Implementation of sliding window function applied for easier extraction of the acceleration data in time series. The sliding window is a continuous function whereby the window length will be determined after analyzing the data sets recorded by the data logger. An example of a sliding window is shown in figure 1.3. [4]

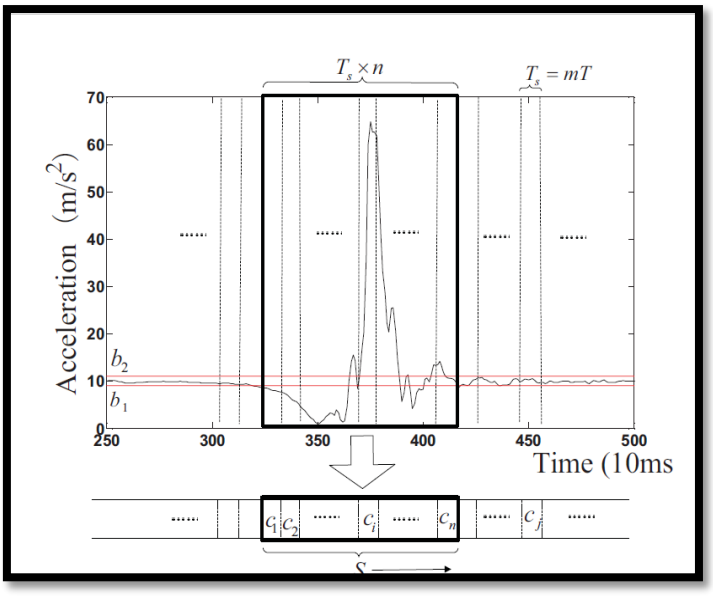


Figure 1.3. Sliding window example with window length of 10 secs

An implementation of FFT analysis was used next to determine the frequency domain of the data. From the frequency domain features, the frequency and frequencies amplitude of data of the accelerometer could be then calculated. The analysis of repetitive signals obtained from vibrations along with any harmonics within the signal could then be obtained. An example of FFT implementation with a time-series signal is seen in figure 1.4 [5]

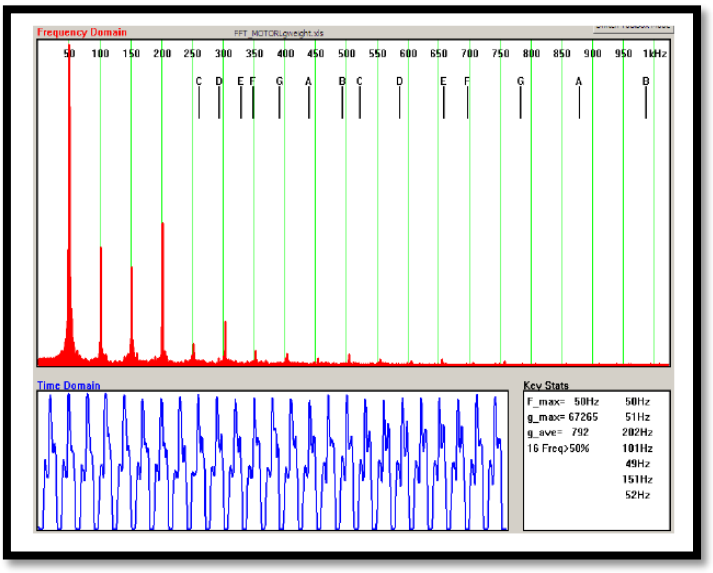


Figure 1.4. Comparison of accelerometer data in time domain and frequency domain

A rule-based system consists of if-then statements whereby the rules are implemented to act upon specific proclamations. Rule-based system often provides answers determined by validation and verification of each manually constructed rules. Such systems provide the output for any given problems automatically in place of human experts. The data was analysed in MATLAB to determine peak accelerations.

From the peak accelerations, rules were introduced using thresholding techniques. As seen in figure 1.5, the amplitude of acceleration for the movement analysed is large for a typical fall. The threshold for the fall is determined by the green dotted line whereby the rule is set to be above a predetermined threshold. [6] [7]

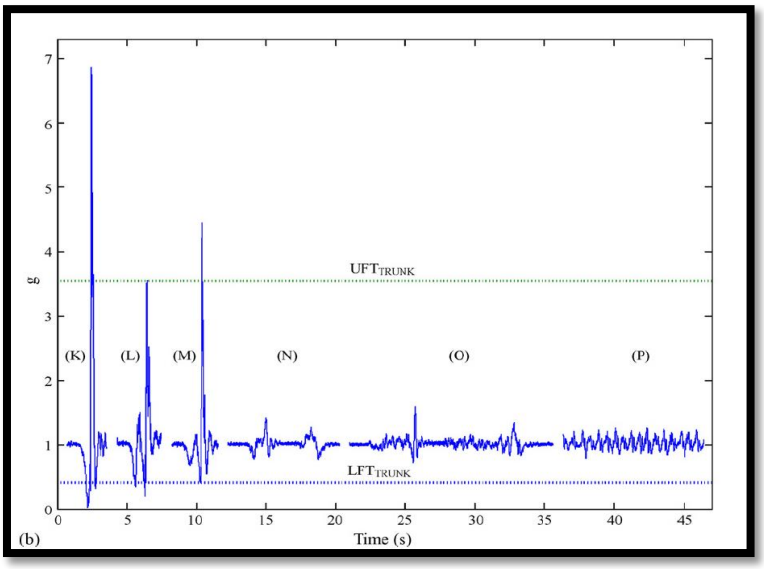


Figure 1.5. Threshold example applied to accelerometer data

The research gap analysed from the journals above shows that movement predictions through the usage of a single accelerometer hasn't been implemented in the field of bicycle helmet for automated signalling. There are variations of helmet implemented with inertial sensors, but it was proven to be bulky due to multiple inertial sensors and suitable for usage in the field. Therefore, this project will address the gap by implementing an accelerometer on the helmet. From the data measure real-time, sliding window function will be applied on the data whereby FFT will be implemented in the window length. From the frequency domain, a threshold based rule algorithm will implement the output related to the rule.

The development of the movement prediction system incorporates a single 3-axis accelerometer in the helmet to estimate the orientation or position of a body. Because of the advantages in using an accelerometer has over other Inertial Measurement Unit (IMU) which are its low power consumption, low cost and small size, the accelerometer is used. For problems related to measurement biasing and noise, it was determined from above reviews that low-pass filter is easy to implement and accurate. Various limitations such as memory constraint, sensor constraint, cost constraint and microcontroller constraint were determined before starting the project.

2. Methodology

To achieve the objectives stated, a quantitative approach will be implemented. Figure 2.1 shows the methodology chart which determines the overall steps throughout the research. Based on the outcome of each stage, the performance of the next stage will be adjusted accordingly. As the research and experiment could not be assured to be perfect, changes will be made accordingly based on the requirements and results throughout the project.



Figure 2.1. Methodology chart

2.1 Data Logging

Data logger was built to record the head movement in conjunction with the bicycle movement of the rider. The system includes an accelerometer, SD module, microcontroller and power supply mounted to a helmet. For bicycle movement logging, a switch and potentiometer were connected to the bicycle handle and is wired to the microcontroller on the helmet.

The system connection is represented and connected based on Figure 2.2 which shows the outline of system. The data recorded includes the 3 outputs of the accelerometer an output of the switch and the potentiometer output which will then be stored in the SD card and further analysed in MATLAB. The schematic design of the data logger could be seen in Figure 2.3. It was designed using FRITZING software whereby the software was available to download for free. The microcontroller used for

data logging was Arduino Nano due to its size and simplicity of usage. The microcontroller is powered by a 9V battery whereby it will provide 5V to the SD card module and 3.3V to the accelerometer.

For turning prediction, two types data were recorded which are the head movement acquired from the accelerometer and handle angle movement which were obtained from the potentiometer connected to the pivot of the handle bar. The handle movement data obtained is from the variation of voltages based on the turning of potentiometer which is due to the turn of the bicycle handles. The working operation is by setting the middle of the potentiometer in position with the centre of the handle angle. During straight cycling movement, the voltage will be half of the supply voltage. As the bicycle turns left or right, the voltage will decrease or increase corresponding to the turn. This value will then be recorded in conjunction with the recorded head movement of the accelerometer.

For braking prediction, two types of data were recorded as well, which are the head movement obtained throughout the cycle and position of brake handles which is obtained from connected switches. During braking, the output of the switch will be high and vice versa. The accelerometer data, handle movement and braking movement will be recorded simultaneously to ensure the analysis in MATLAB will be much easier and smoother.

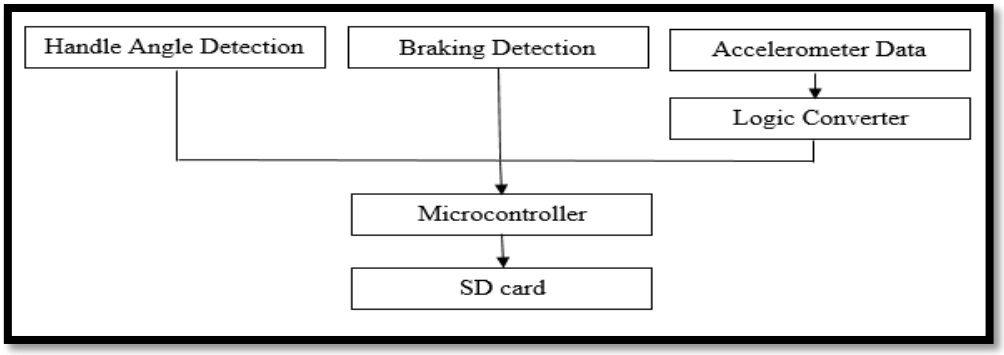


Figure 2.2. System connection of the data logger

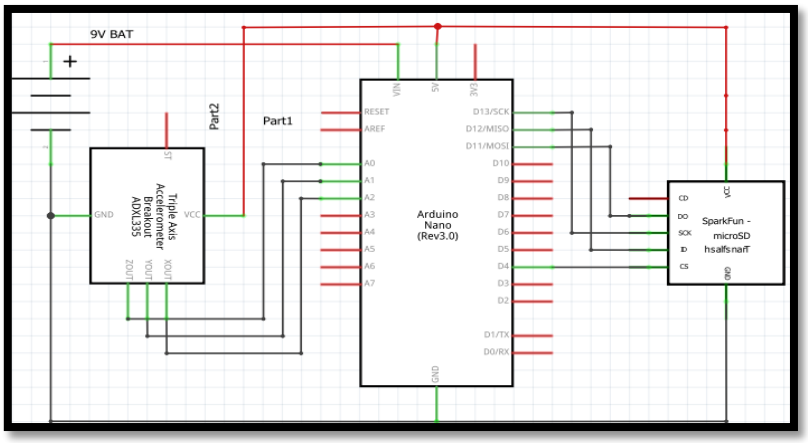


Figure 2.3. Schematic design of the Data Logger

In Figure 2.4 the connected data logger could be seen installed on a helmet. The reason of applying the data logger on the helmet is due to the need of analysing head

movement during cycling. As there is a right turn, left turn or brake, the head will move accordingly, therefore the data recorded will then be analysed to determine the characteristics of the data.

For the logging of movement of bicycle, the system was designed and is shown in Figure 2.5. The pulley system which determines the direction of turn includes a potentiometer and gear connected to the pivot of the bicycle handle which is connected by a rubber band. The brake system is designed based on a switch mechanism.

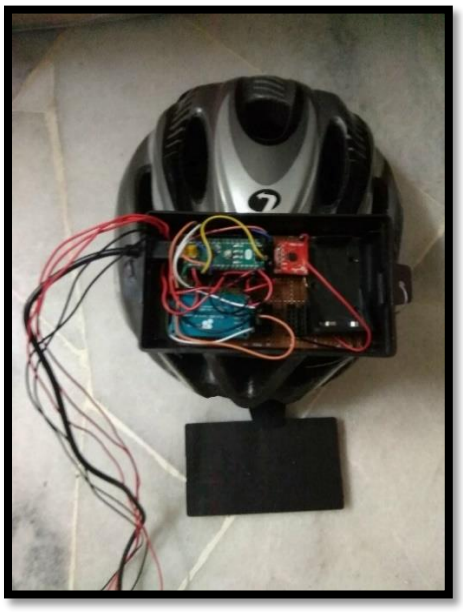


Figure 2.4. Helmet Data Logger

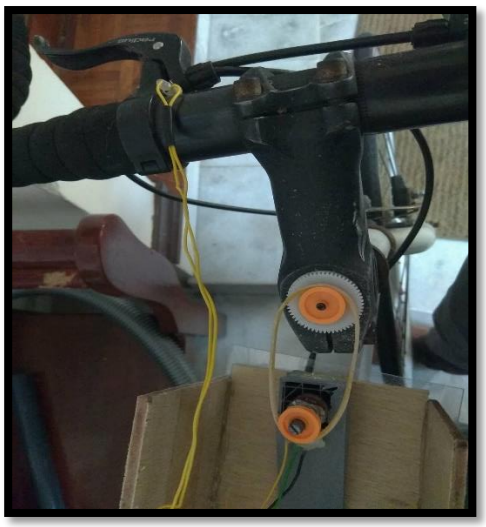


Figure 2.5. Bicycle connection of data logger

2.2 Analysis of accelerometer data

The analysis of the raw data obtained from the data logger was done in MATLAB which provides all the required functions and algorithm along with an extensive online support. The initial stage is to plot the raw data and analyse the characteristics of the braking and turning raw data. For the braking data, it can be seen in figure 2.6. A vivid indication of the braking is seen along the X-axis whereby there is sharp drop in the data. Not much changes occur in the Y and Z axis during braking. The braking signal is provided by the connected switch and indicates a high when braking and low in non-braking conditions. visible change is caused by the vibration during stopping.

The turning raw data could be seen in figure 2.7 and figure 2.8 whereby they represent left turn and right turn respectively. During turning, the most affected axis is the Y-axis. When turning to the left, the voltage of potentiometer will increase while the Y-axis signal will increase towards the negative Y-axis. When turning to the right, the voltage of the potentiometer will decrease while the Y-axis signal will increase towards the positive Y-axis.

In figure 2.9, the sliding window function could be seen by 2 parallel red lines. The window length of the sliding window is 150 which equates to 5 seconds. With this function, the data points could be analysed easily with the implementation of FFT within the window. As seen, the frequency domain is extracted from the two-different window time. By analysing the time domain graph, it could be seen that from 261 - 265 secs, a change in amplitude occurs which could be generated due to turning or braking. For this set of data, from 261 – 265 secs braking occurs and from 252 -257.03 secs the cyclist is in a constant straight motion.

In figure 2.10, FFT is applied for two different sets of data which are from 261 – 265 secs and 252 – 257.03 sec. Furthermore, for braking the FFT will be mainly applied at the X-axis as the change in braking is more prominent. Therefore, by analysing the frequency domain, there is a peak in the braking signal at around 2 Hz. During constant straight cycling which is from 252- 257.03 sec, it could be seen that there is no peak in the frequency domain.

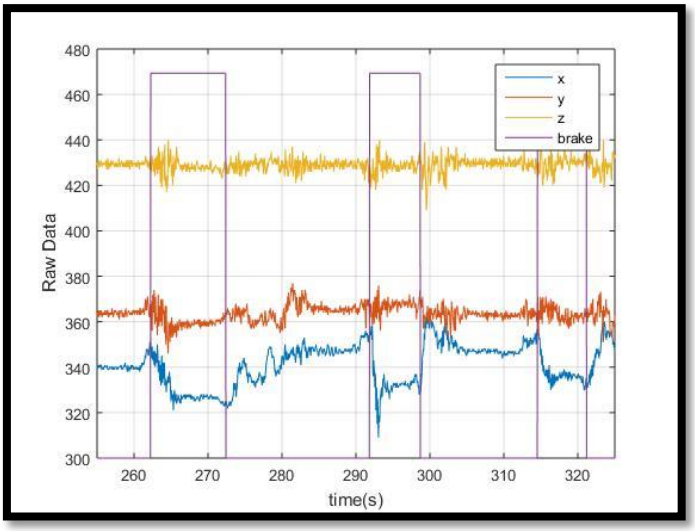


Figure 2.6. X, Y, Z axis and brake raw data

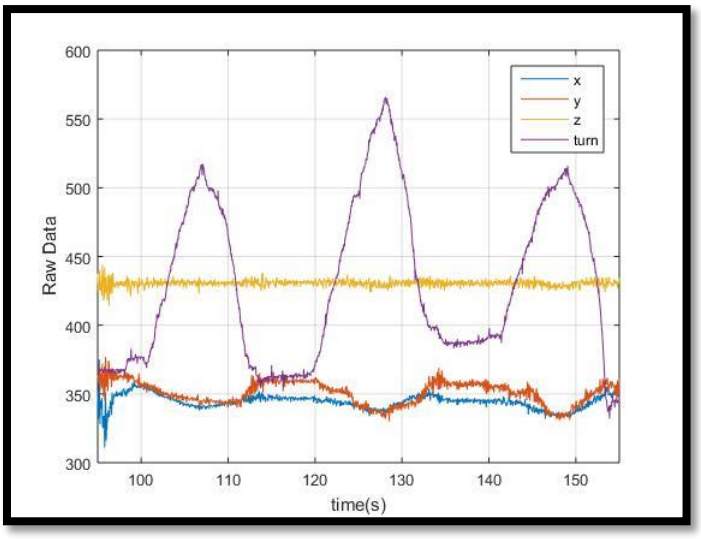


Figure 2.7. X, Y, Z axis and left turn raw data

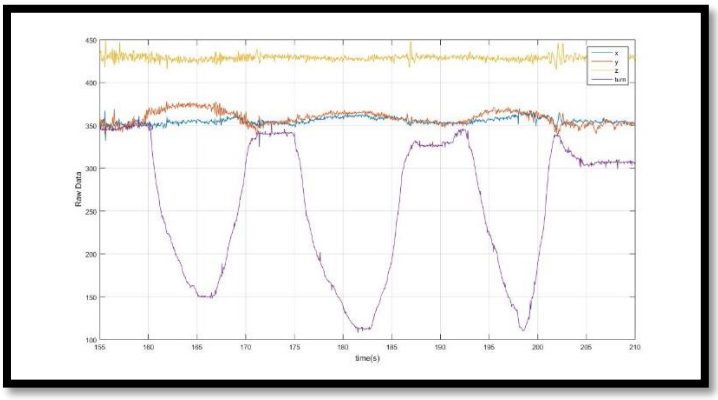


Figure 2.8. X, Y, Z axis and right turn raw data

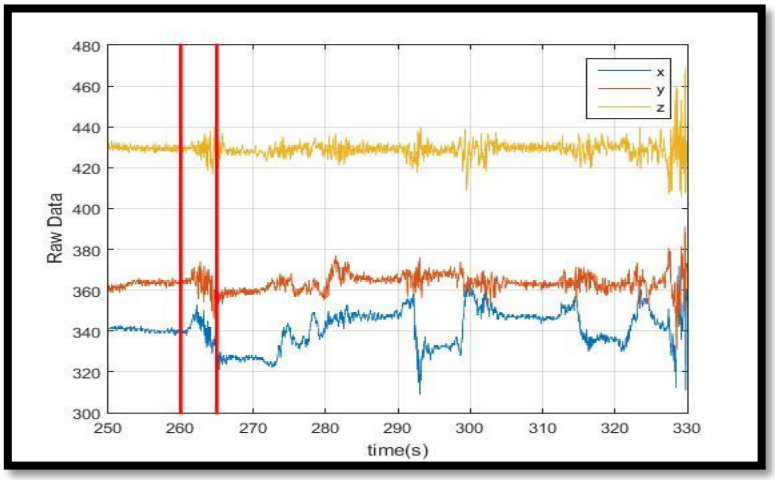


Figure 2.9. Sliding window applied to raw data

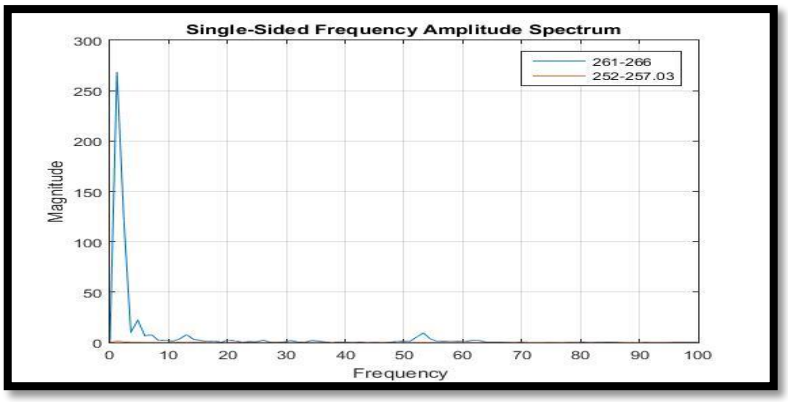


Figure 2.10. Frequency Spectrum of raw data within the sliding window

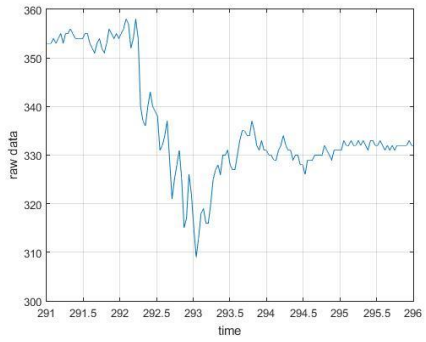
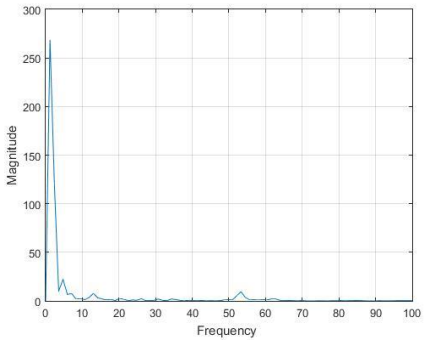
3. Results and Discussion

From the methods stated, the results were processed up to the implementation of threshold-based rule algorithm for braking analysis and turning analysis.

3.1 Braking analysis

In table 3.1, a braking was signal recorded which is from the X-axis. The data were then converted to time domain and frequency domain. In time domain, the analysis of impulse and transient accelerometer signals is possible. With the addition of external noise such as vibrations, it will be more difficult. Therefore, FFT algorithm is applied to the time domain signal to convert it into frequency domain for spectrum analysis. In the frequency domain, each individual frequency and its amplitude is displayed which will enable the analysis of repetitive signals. As seen, the peak n frequency is at 2hz. This shows that the changes in frequency during braking is very small but at a high rate.

Table 3.1. Comparison of brake data in time domain and frequency domain

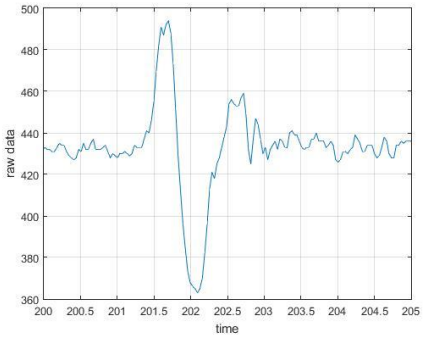
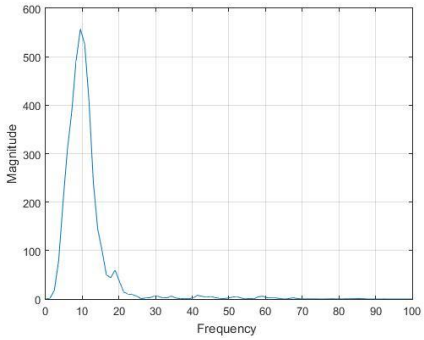
Brake data in time domain	Brake data in frequency domain
	

3.2 Cycling on a bump

In table 3.2, a data for cycling on a road bump were recorded. It was found that by plotting the data, the main axis which displays a vivid road bump cycling is mainly at the Z-axis. The data were then converted to time domain and frequency domain. In time

domain, it could be seen that the signal will peak followed by an instantaneous drop and then return to its previous position. This shows that the accelerometer will move up and down along the z-axis while in this cycling movement. When FFT algorithm is applied to the time domain and the signal is converted to frequency domain, the frequency will cluster at an average of 10 Hz.

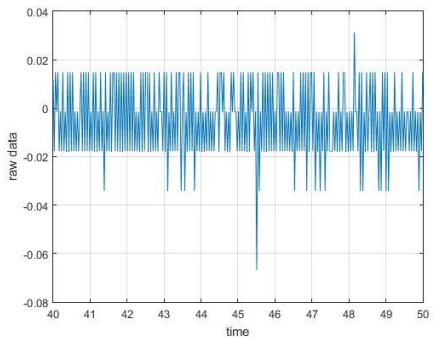
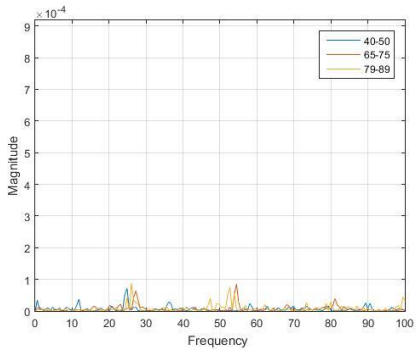
Table 3.2. Comparison of road bump data in time domain and frequency domain

Cycling on a road bump data in time domain	Cycling on a road bump data in frequency domain
	

3.3 Constant cycling

In table 3.3, a data for constant cycling were recorded. During constant cycling, not much changes occurs on all 3 axes. The data sets were then converted to time domain and frequency domain. In time domain, it could be seen that the signal maintains a constant level throughout the duration When FFT algorithm is applied to the time domain and the signal is converted to frequency domain, the frequency was found to be at a very low amplitude. As seen in the y-axis of the frequency domain, the magnitude doesn't exceed $1x10^{-4}$.

Table 3.3. Comparison of constant cycling data in time domain and frequency domain

Constant cycling data in time domain	Constant cycling data in frequency domain
	

3.4 Turning analysis

Compared to the braking implementation of prediction and gesture recognition, the turning implementation is significantly harder. This is due to various situations such as duration of turn, speed during turn and head movement during turn. In table 3.4, a

data set for left turn cycling were recorded. It was found that when the time domain of the left cycling data is converted to frequency domain, there were not much difference with the braking frequency domain. This was due to the change in frequency during turning was too small, therefore the data sets are clustered around the 1Hz frequency. The only difference this frequency domain has over braking frequency domain is that braking frequency is derived from the X-axis while turning frequency is derived from Y-axis. By analysing the time domain data which is in Y-axis, an initial rule for turning could be derived. The rule could be derived when sliding window is applied on all 3-axis separately. When there is a large change in the frequency domain for Y-axis as compared to the X and Z-axis, the algorithm can output an initial turning condition.

In table 3.5, a data for right turn is shown. Similarly, for left turn, right turn will output the same frequency in frequency domain. By following the rule stated earlier which is to apply sliding window on all 3-axis and then analyse the changes in the axis. If the change in frequency domain for Y-axis is much larger than the other axis, a turn is occurring. The next step to finalise the algorithm is to differentiate the left turn and right turn. A method suggested is that after implementing the first rule stated previously, the next step is to compare the peak amplitudes of the y-axis data in time domain. If the peak is above or below a certain threshold, the second rule will be implemented.

Table 3.4. Comparison of left turn cycling data in time domain and frequency domain

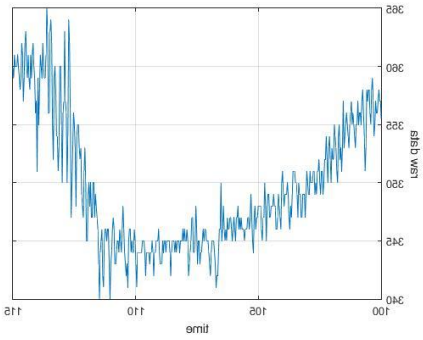
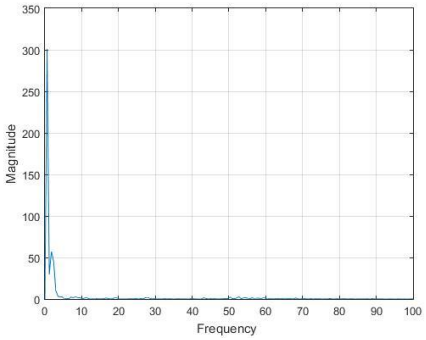
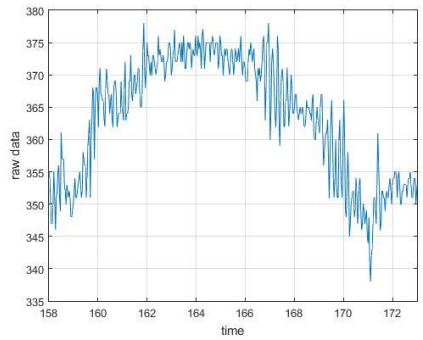
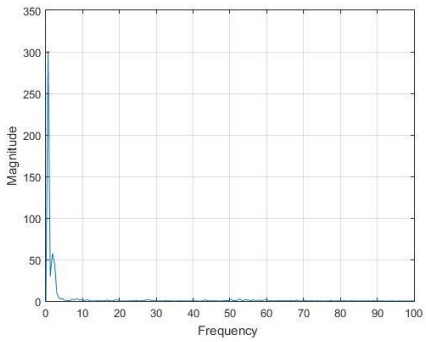
Left turn cycling data in time domain	Left turn cycling data in frequency domain
	

Table 3.5. Comparison of constant cycling data in time domain and frequency domain

Right turn cycling data in time domain	Right cycling data in frequency domain
	

3.5 Findings

In figure 3.1, the proposed algorithm flow chart is displayed. The basis of this algorithm is from the threshold based rule algorithm. The proposed system works by first recording real time cycling data, next it applies a continuous sliding wind to the data. FFT algorithm will then be applied in the data to analyse the frequency spectrum. Based on the characteristics of the frequency spectrum, the threshold rule is applied. The corresponding output will be based on the rules. The relevant output will then be displayed. The system will check if the cyclist is still in motion. If the cyclist is still cycling, the sliding window will move to the next data point and repeats the process. If the system is stopped, the algorithm will end.

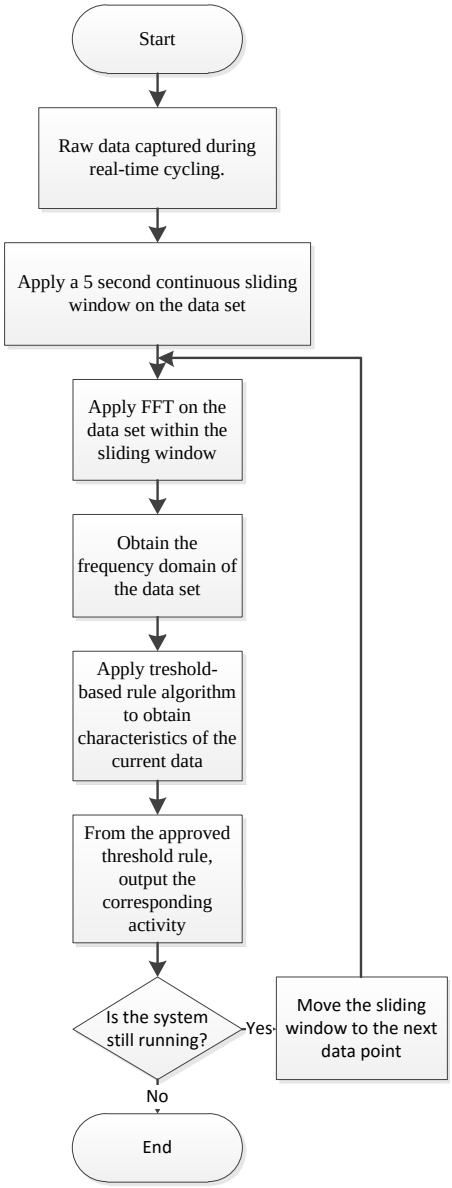


Figure 3.1. Algorithm flow chart

4. Conclusion

A concept for movement prediction was presented using an accelerometer. The algorithm is based on the sliding window function, FFT and threshold based rule algorithm. The objective of the research was to investigate and analyse suitable signal processing techniques for automated signalling and braking indication during real-time. Besides that, this project also aims to assess suitable technique to improve the accuracy and processing speed of the algorithm proposed for automated signalling indication. It could be concluded that the objectives at the current stage is partially achieved. For the first objective, it could be concluded that it was attained based on the algorithm flow chart. For the second objective, it was partially achieved. In terms of the accuracy for the turning indication it is not up to the safety standards yet. The processing speed could not be tested as the suitable microcontroller for the final product is not implemented. With the completion of this research, a significant improvement in the safety standards related to cycling could be achieved. For future work, the improvement in algorithm is a must to keep up with the safety and automated standards in the society. To further increase the efficiency of the system, a GPS and mapping software could be implemented alongside this system. Another method to improve this system is to implement the algorithm within a smart phone due to it containing all the necessary IMU such as accelerometer, gyroscope, GPS, magnetometer etc. With the constant improvement and advancement in technology, the efficiency of this IMU within the smart phone keeps improving as well. This could reduce the cost of the overall system and implementation will be easier due to decrease in components.

References

[1] R.O.S.P.A., "Cycling Accidents", *Road Safety Factsheet,* June 2017

[2] O. D. Incel, "Analysis of movement, orientation and rotation-based sensing for phone placement recognition," *Sensors (Switzerland)*, vol. 15, no. 10, pp. 25474–25506, 2015.

[3] R. C. Leishman, J. C. MacDonald, R. W. Beard, and T. W. McLain, "Quadrotors and accelerometers: State estimation with an improved dynamic model," *IEEE Control Syst.*, vol. 34, no. 1, pp. 28–41, 2014

[4] L. Tong, Q. Song, Y. Ge, and M. Liu, "HMM-based human fall detection and prediction method using tri-axial accelerometer," *IEEE Sens. J.*, vol. 13, no. 5, pp. 1849–1856, 2013.

[5] K. Tuck, "Frequency Analysis in the Industrial Market Using Accelerometer Sensors," *Sensors (Peterborough, NH)*, pp. 1–13, 2008.

[6] L. Lengyel, "Validating rule-based algorithms," *Acta Polytech. Hungarica*, vol. 12, no. 4, pp. 59–75, 2015.

[7] A. K. Bourke, J. V. O'Brien, and G. M. Lyons, "Evaluation of a threshold-based tri-axial accelerometer fall detection algorithm," *Gait Posture*, vol. 26, no. 2, pp. 194–199, 2007.

Eureca 2017 – Conference paper
Paper Number 2EE04

A New Type Of Electrical Bike Using Dual Rotor Permanent Magnet Machine

Mohd Izzat Bin Zainuddin[1], Aravind C.V[1,*], R.N. Firdaus[2]

[1]*School of Engineering, Taylor University, Malaysia*

[2]*Faculty of Engineering, Univeristy Teknikal Malaysia Melaka,malaysia*

[*]aravindcv@ieee.org

Abstract

Electric bike in urban country such as Europe and China commonly used brushless direct current machine (BLDC) as it able to produce high torque to transport the user from one place to another. However, BLDC torque density can't be improve due to limitation magnetic flux generated by the permanent magnet. Therefore, the performance of electric bike can't be improved. Outer rotor BLDC machine design able to improve the torque density of the motor due to increase radius of the motor which can be explain with simple physics equation (Torque = Force x radius). However, an outer rotor machine only generate constant speed which is not suitable for operating of tractive load condition especially electric bike. The proposed model for this project is new novel of double layer outer rotor BLDCPM machine which able to amplify the magnetic flux density and improve the torque density of the machine. The mutual magnetic coupling between inner and outer rotor of the proposed model increase the magnetic flux intensity as both of them acts as individual parts. Thus, the magnetic flux generated by both rotor are double which resulted to improving the performance of the E bike. Designing parameters and analyzing the performance of the proposed 2D model will be done using FEA tools. Evaluation of the conventional and proposed model by comparing torque performance, magnetic flux density and motor constant square density produced in order to justify objective of this project. Other than that, speed torque graph also will be evaluated to justify either it can operate similar with ICE engine with gears. Two model are design which are Single Outer Rotor Brushless Direct Current (SORBLDC) and Double Outer Rotor Brushless Direct Current (DORBLDC) operated with the same cases of 27 Amp current supplied to it and operate under various speed from 500 rpm to 2000 rpm. The average torque produce by conventional and proposed model are 2.045439 Nm and 3.102648 Nm. Furthermore, improvement of proposed model to conventional model in terms of motor constant square density by 24.92%. Therefore, the proposed model able to improve the magnetic flux by amplifying which resulted to increase the torque density of the machine. Furthermore, the speed torque graph of the proposed machine shows similarity with speed torque graph of ICE engine. Thus, the proposed machine is suitable to operate for bike application

Keywords: torque density, magnetic flux intensity, permanent magnet, electric bike

1. Introduction

BLDC motor consist rotor embedded with permanent magnet and stator coils to produce high torque density. Furthermore, the rotor of the BLDC motor is supplied with direct current (DC) supply and it will generate AC voltage waveform with trapezoidal shape which reduces the total harmonic distortion (THD) in the machine[1]. The reason BLDC machine used for electric vehicle due to the power supplied to the machine will have lesser noise and provide better performance of the motor. However, room for improvement in terms of torque density of the machine need to be done due to magnetic flux generated by the machine is fixed. In order to increase the magnetic flux the ratio of the permanent magnet needed to be doubled. However, the limitations of the project stated that the volume of this machine should be keep constant even able to increasing torque density of the motor. Plus, magnetic flux generated is not fully utilized at stator core and the torque density can't be increased which resulted to less efficient in the performance of the motor.

To achieve more powerful motor, the design of the motor and position along with the angle of the permanent magnet is research in order to obtain better torque density. Having a good design which included the position and angle of the interior permanent magnet in rotor section contribute to increase the power density of the motor[2]. However, big spaces needed to insert the slanted PM eventhough an outer rotor machine. Other than that, the torque density of a motor can be improved by increasing the radius of the rotor section. The performance of the motor can also be increased by designing new motor structure with double layer outer rotor PM. Mutual magnetic coupling between inner rotor with outer rotor improve magnetic flux intensity by making both of them as individual part of the machine[3]. The magnetic loading of the machine increased as the flux generated by the permanent magnet was amplified. Thus, the torque density of the motor can be increased. Therefore, the objective of this research is to experiment double outer rotor layer machine that amplifies the magnetic flux which configuration on the magnetic flux density to determine the torque density of the motor.

2. Design Concept

The load of machine for this project is tractive load which to be specify is the electric bike. Tractive study is was applied in order to analyze and predict the actual speed of the machine for many types of road conditions. In order to reach full capacity in working principle of an electric or hybrid vehicle, electric motor and generator machine were optimized fully in several road conditions. There are 6 conditions faced by the electric vehicle especially electric bike which are early start, normal speed, acceleration, high speed, deceleration and stop position. Figure 1 shows the diagram of operating conditions faced by the machine[4].

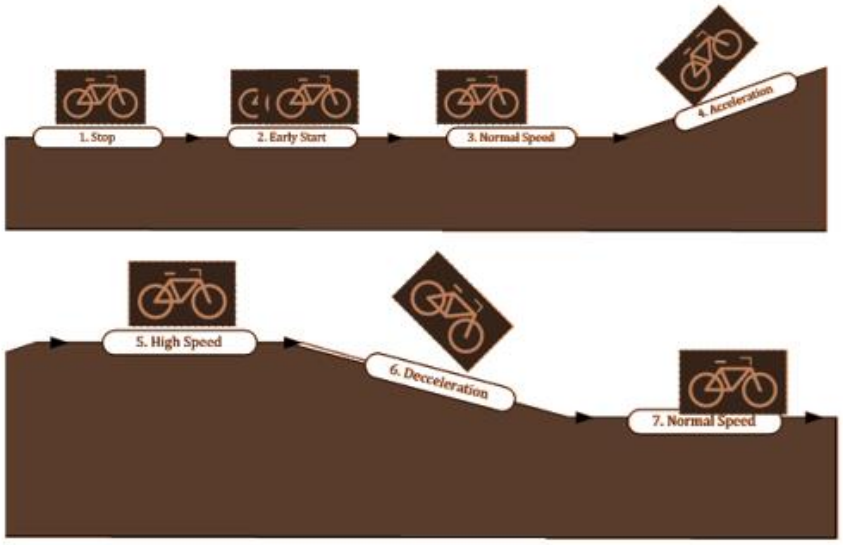


Figure 1: Operating characteristic of E-bike for all conditions

E bike is small transportation vehicle where the load on the propulsion unit is traction load. The loading characteristics of proposed machine must show similarities with ICE engine. The speed torque graph of ICE engine contains 4 parts which each of the section has its own torque and speed characteristics. Figure 2 shows the speed torque graph and speed power graph of ICE engine.

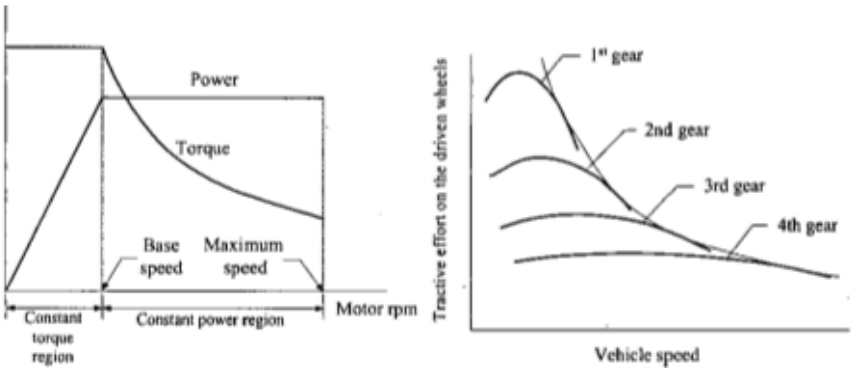


Figure 2: Speed torque graph and speed power graph of ICE engine

In order to identify the research gap, few motor design had been research and each of them has it's own benefit and drawback. Induction motor widely use for electric vehicle application high effciency and low cost. The desired torque of certain speed can be controlled with an inverter can be achieved. However, control schemes of the torque are relatively difficult to control and the constant power range is also limited[5]. Permanent Magnet Synchronous Motor (PMSM) machine has similar structure with

BLDC and induction machine. Advantages PMSM machine are eddy current loss is reduced due to segmented magnet at the rotor section thus torque density is improve. However, in order for improvement torque density of the machine, the volume of the machine needed to increased especially ratio of the segmented magnet in the rotor section[6]. Another design machine, using in wheel motor to SORBLDC machine to improve the magnetic flux by applying the concept of non-contact magnetic planetary gear with the permanent magnet outer rotor BLDC machine. With this method, the transmission torque was maximized resulted to increase the performance of the machine[7].

Coil Testing Study was also done on the SORBLDC in order to study electromagnetic flux generated by the coil windings which effect torque density of the machine. There are two types of armature coil winding implemented on the outer rotor synchronous machine which are concentrated winding and distributed winding. Finite element Analysis using JMAG application was done to simulate both coil winding technique on the conventional model for EV application. The output of the machine for each type of windings are analyzed using FEA tool in order to observer the magnetic field flow and flux density. The winding method that increase the performance of the machine in terms of magnetic field density is chosen. Concentrated windings generate higher peak and saturated flux across the model. Thus, the torque density can be increase due to magnetic flux generated by the permanent magnet and coil winding in the stator slot. Therefore, magnetic loading was more focus for the proposed model on increasing the performance of the machine without changing the output rating of the motor for electric bike application

The proposed design was conducted by applying extra rotor layer to SORBLDC in order to create mutual magnetic coupling between outer rotor with inner rotor to improve magnetic flux intensity by making both of them as individual part of the machine. Therefore, the magnetic flux generated by both of individual part will amplified and the performance of the machine improved. Other than that, the proposed model of this research study able to achieve various speed with constant power and torque region[3].

The design proposed model was obtained through calculating parameters design formulas in order to know the size of each part. The magnetic circuit was redesign in order to increase the magnetic flux in order to improve the torque density of the machine. By using FEA tools, design structure of conventional and proposed model were done. Other than that, evaluation of conventional and proposed model were done in terms of magnetic flux density, torque performance, motor constant square density and power efficiency were done in FEA tools. Speed torque graph and speed power graph of both model will be compared to ICE engine application in order to check either they are suitable for bike application. CAD tools were used to design the proposed model so that fabrication of the model can be done.

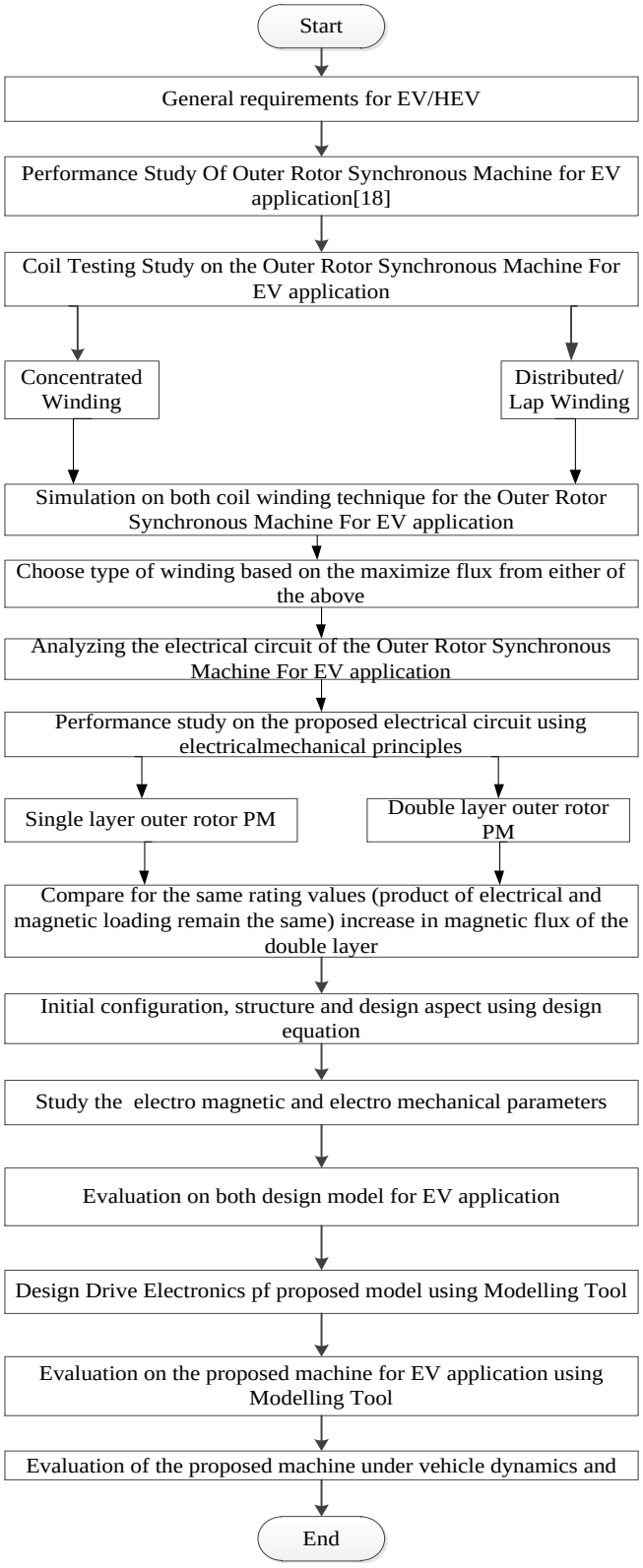


Figure 4: Flowchart of the project

3. Proposed Design

Figure 5(a) shows the 2D proposed DORBLDC model design using JMAG software and Figure 6 shows the exploded view of the proposed DORBLDC model for electric bike application using Solidworks software. The proposed machine contains double layer rotor with surgace permanent magnet that supplied with 3 phase armature coil concentrated windings, 20 permanent magnet mounted on inner surface rotor and 40 permanent magnet mounted on the outer surface rotor. The proposed model has more benefits than conventonal model as the flux is amplify which resulted to improve flux density across the machine. Table 1 shows the parameter dimensions of the proposed DORBLDC model where the outer dimension of both model are kept the same in order to compare the motor constant square density, magnetic flux density and torque density

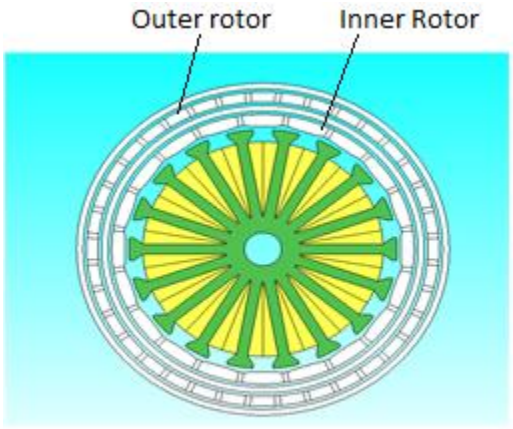


Figure 5: The Proposed 2D model

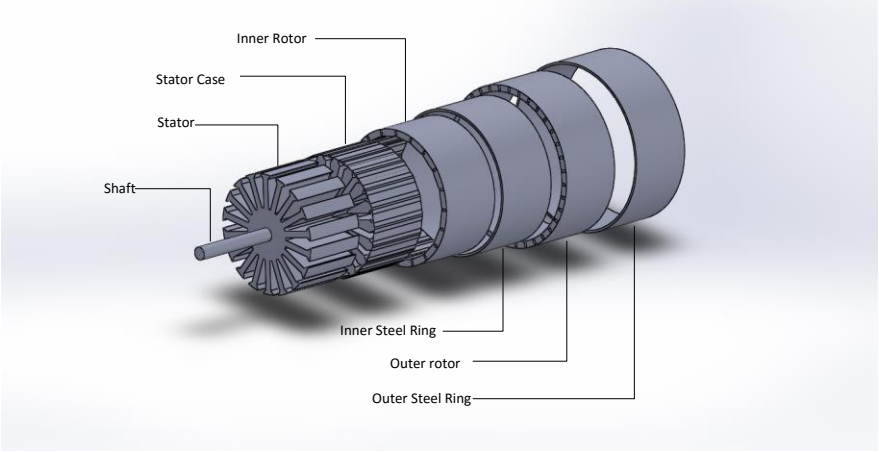
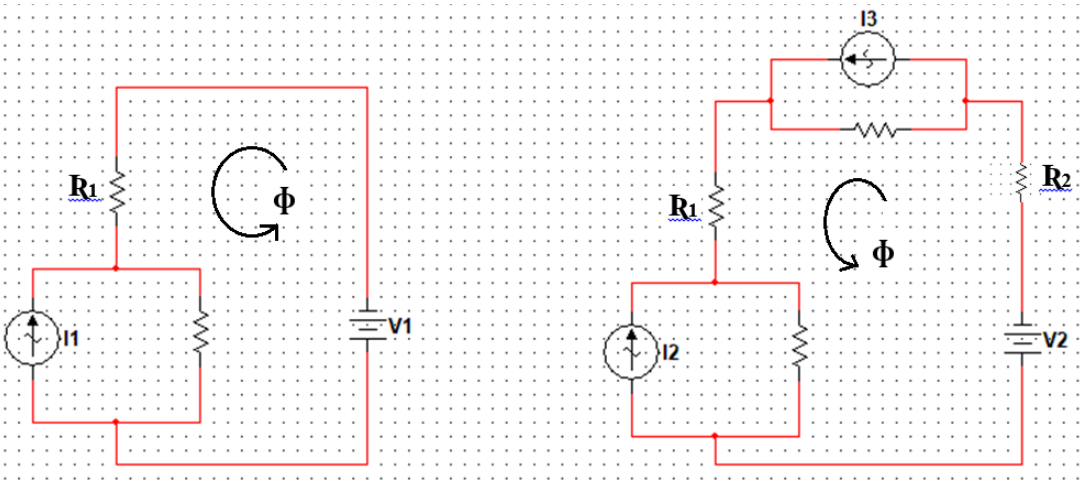


Figure 6: The Proposed model in Exploded view

Table 1: Specification of the proposed model

Parameter	Value (mm)
Diameter of the machine	50
Stack length	50
Number of stator poles	18
Stator Diameter	36
Physical Radial Air gap	1
Outer ring Diameter	1.7
Inner ring diameter	1.7
Inner rotor diameter	3.523
Outer rotor diameter	3
Inner PM diameter	3
Outer PM diameter	3
Number of poles Inner magnet	18
Number of poles Outer magnet	36



A)Conventional Model B)Proposed Model

Figure 7: Magnetic Circuit of Conventional and Proposed Model

$\phi = (mmf+Fm) / \mathcal{R}$ $\phi = (mmf+Fm1+Fm2) / (\mathcal{R}_1+\mathcal{R}_2)$

Fm = Flux generated in inner magnet of SORBLDC

Fm1 = Flux generated in inner magnet of DORBLDC

Fm2 = Flux generated in outer magnet of DORBLDC

$\mathcal{R}$ = Rotor Reluctance of SORBLDC

$\mathcal{R}_1$ = Inner Rotor Reluctance of DORBLDC

$\mathcal{R}_2$ = Outer Rotor Reluctance of DORBLDC

The magnetic equivalent circuit shows components inside conventional and proposed model by changing them into voltage source, current source and resistor. Figure 7 shows the equivalent magnetic circuit of conventional model and proposed model. Based on figure 7, we can see that proposed model has higher generated flux due to mutual magnetic coupling created between outer rotor with inner rotor to improve magnetic flux intensity by making both of them as individual part of the machine. Therefore, the magnetic flux generated by both of individual part will amplified.

4. Finite Element Analysis (FEA) Method

Designing of the proposed model in JMAG Geometry Editor is the first step applied in the simulation of FEA analysis. Each part of the model was designing based on its on parameters set for the machine. Model of the proposed machine updated in the JMAG software and configuration material for each part was done such as type of material and its properties. Several condition applied to each components such as rotational motion, torque nodal force and FEM coil. Then, FEM coil circuit was constructed by setting the parameters such as resistance and voltage or current source. Setting of the windings and resistance of each coil followed with size and type of mesh to the model. Finally simulation of the model was initialized as the steps were completed. Figure 8 shows the steps taken in FEA simulation

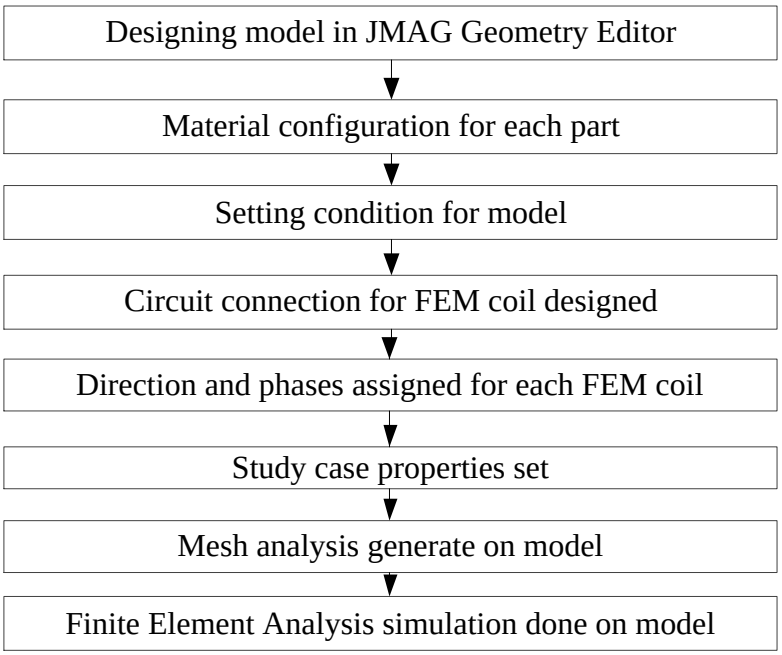


Figure 8: Finite Element Analysis Flowchart

5. Design Parameters Consideration and Evaluation of Electric Machine

Several formulae are being used to design the proposed model and analyzed the result constructed in JMAG software. Formulas below will able to determine the characteristics of the magnetic flux and torque.

i. Torque of the machine

The output of this machine is generation of torque which causes an object to rotate about an axis with applied of measured force[8]. Magnitude of torque can be obtain through Equation 1.1 below where r is radius of the object, T represent torque and F represent measured force applied to the object

$$T = F * r \quad (1.1)$$

ii. Designing the coil winding

Area of slot was measured and area of winding the coil per slot need to be focused for this section. Winding or number turn of the coil per slot effect the flux generated by the machine especially for electrical loading. The possible number of coil can be calculated through Equation 1.2 below

$$Acoil = (\pi * Rcoil\text{^}2) \quad (1.2)$$

The area of the coil (Acoil) need to be determine first by measuring the radius of the coil (Rcoil)

Then, number turn of the coil (NT) can be calculated as the area of coil and the slot are measured using Equation 1.3

$$NT = Aslot / Acoil \quad (1.3)$$

iii. Resistance of coil

The stator pole are winded with coil will produce resistance itself. Therefore, length of the coil need to measured first before finding the resistance of the wire. The Equation (1.4) below show the calculation of the length of wire (L) by combining the net winding of the stator (Nnett) with the length and width of the pole (Lp and Wp)

$$L = Nnett * 2(Lp * Wp) \quad (1.4)$$

The resistance of the coil can be calculated using Equation 1.5 below where ρ represent the resistivity of the coil follow by A represent the cross section area of the coil

$$R = (\rho * L)/A \quad (1.5)$$

iv. Power Loss

Ploss represent as power loss in machine caused by heat loss in conductor and Equation 1.6 below show the calculation where Iin represent as input current and R represent the resistance of the conductor[8]

$$Ploss = (Iin\text{^}2) * R \quad (1.6)$$

v. Torque Constant

Identified as output torque of a machine under certain condition or value. Torque constant determine the motor performance and motor square density of the machine. Tv represent as average torque of the machine and I is the maximum current set in the coil of the machine. Equation 1.7 of torque constant shown below

$$Kt = Tv/I \quad (1.7)$$

vi. Motor Constant

A method in measuring the performance of the machine by comparing output torque (K_t) of two different machine with different sizes. Furthermore, this equation convert electrical input into mechanical output of the machine. Torque constant (K_t) and Power loss (P_{loss}) is used in this equation. Motor constant is represent as K_m in the equation 1.8 below.

$$Km = (Kt\text{^}2)/(I\text{^}2)R \quad \text{or} \quad Km = Torque\ constant\text{^}2\ /power\ loss \tag{1.8}$$

vii. Motor Constant Square Density

Motor Constant Square Density is represent as G and the final equation in analyzing performance of machine design. The equation contain parameters of a machine such as power of motor, torque and volume of the machine. Motor constant (K_m) and volume of the machine is used in the equation 1.9 below.

$$G = Km/volume \tag{1.9}$$

6. Result And Discussion

6.1 Magnetic Flux Analysis between SORBLDC and DORBLDC

In this section, analyzing the amplitude and pattern flux of the machine will able to determine whether generate magnetic flux will effect the output of the machine. Based on figure 9, the magnetic flux of amplitude for proposed model is higher than conventional model. This shows that the proposed model has the highest magnetic flux density in the machine structure even the volume was kept the same with the conventional model. Furthermore, both of the model generate its magnetic flux pattern closing to the sinusoidal waveform which shows similarity to three phase power supply wave. Other than that, generating magnetic flux waveform closer to sinusoidal pattern shows that harmonic occur in the machine is minimum.

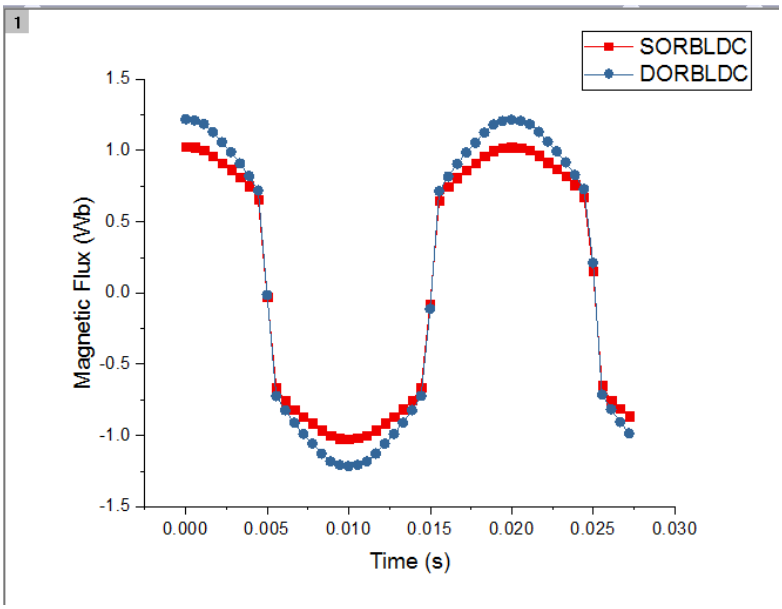


Figure 9: Magnetic flux output of both model

6.2 Torque Performance Analysis Between SORBLDC and DORBLDC

Torque performance analysis was done check whether the new proposed model improved the machine performance in terms of peak amplitude value. Having high generated torque of a machine enables the bike to operate under harsh road conditions such as high slope road that requires big amount of energy to support the weight of the user and bike to accelerate uphill. In this research project, torque evaluation was conducted to both model. Figure 10 shows the generated torque by both model. As shown in the graph, the proposed model generate the highest peak torque and conventional show the lower. This shows that by increasing the magnetic flux in the machine, the torque performance of the motor which will increase the performance of the bike

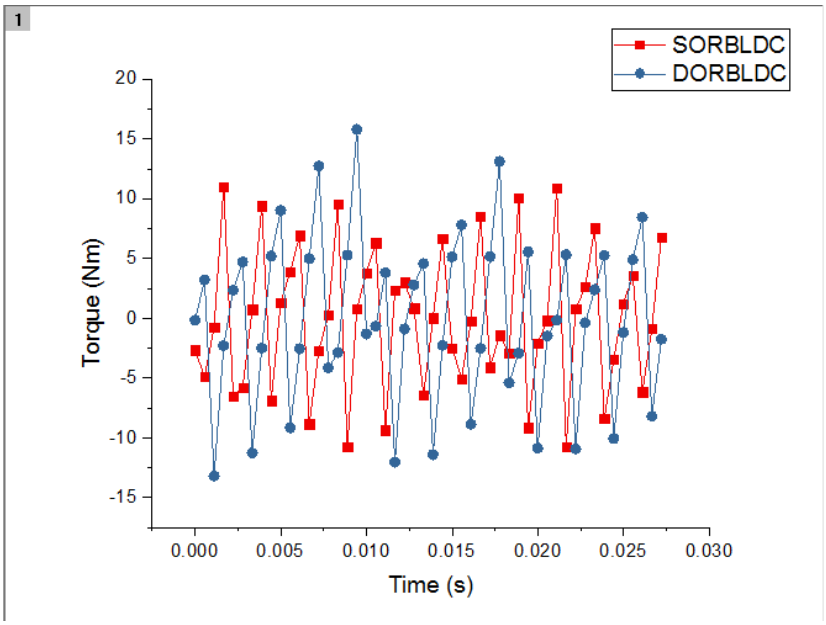


Figure 10: Torque output of SORBLDC and DORBLDC

6.3 Speed Torque Analysis Between SORBLDC and DORBLDC

E bike application require a motor that able to operate constant torque and power which show same operation like an ICE engine with gears. The speed torque graph of ICE engine has high starting torque and decrease as speed increases. Therefore, speed torque evaluation was done to both model in order to check whether the machine can operate same as ICE engine. Figure 11 shows the speed torque graph of conventional and proposed model. The speed torque graph of both model shows similarities to ICE engine speed torque. Therefore, the machine can operate for e bike application. Based on Figure 11, torque produced by proposed model is stable torque speed characteristics than conventional model. Eventhough SORBLDC produces high starting torque than DORBLDC, the proposed model generate higher and more stable torque speed characteristics as the motor operate at higher speed. Therefore, high torque produced for tougher road conditions such as uphill can be done by the proposed motor and improve the performance of the bike.

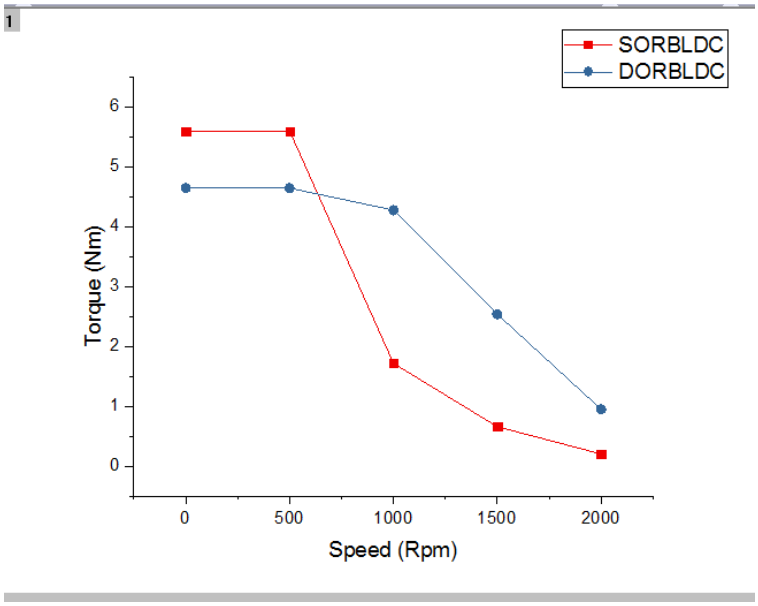


Figure 10: Speed Torque Analysis of SORBLDC and DORBLDC

6.4 Speed Power Efficiency Analysis Between SORBLDC and DORBLDC

In order to evaluate constant torque and power region of a machine, speed power analysis were conducted. The maximum speed of a machine can be identified through constant power region. Figure 11 shows speed power efficiency of SORBLDC and DORBLDC. Based on Figure 11, the speed power graph of both model shows similarities to ICE engine speed power. Therefore, the machine can operate for e bike application. SORBLDC model shows higher power efficiency during starting speed of the machine that DORBLDC model. However, DORBLDC model shows longest constant power region which means that the machine able to operate effectively at higher speed range before losing it's power at the machine speed limit which is 2000 rpm.

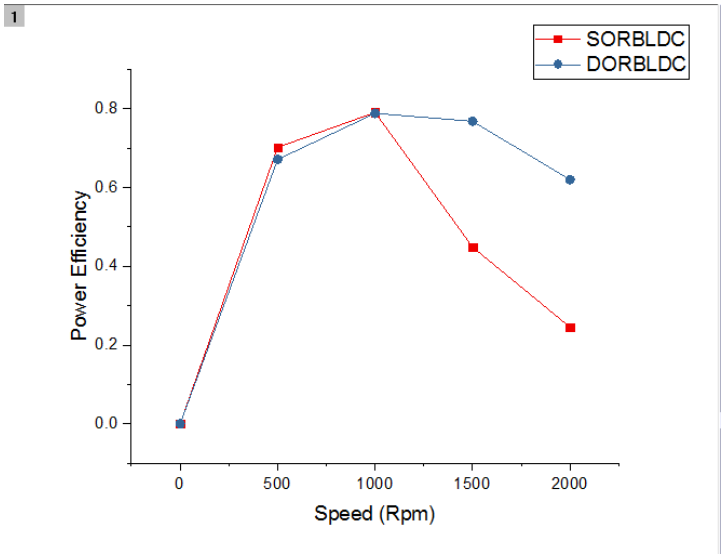


Figure 11: Speed Power Efficiency of SORBLDC and DORBLDC

6.5 Comparative Motor Constant Square Density Evaluation

In this section, both model are being compare by evaluating each G value. The volume of both model was calculated by multiplying cross sectional area of the machine with the stack length set. In the Motor Constant Square Density equation contain parameters of a machine such as power of motor, torque constant, motor constant and volume of the machine. All of the parameters are calculated and tabulated in the Table 2. All of the variable that needed to use to calculate the G value is formed in Table 3.

Table 2: Parameters of both model

Parameter	Conventional Model	Proposed model
Stack length (mm)	50	50
Volume(mm^3)	356,415.35	311,794.70
Max. Current (A)	27	27

Table 3: G value of both model

Speed (rpm)	Conventional Model				Proposed Model			
	T_{avg}	K_t	K_m	G	T_{avg}	K_t	K_m	G
0	5.595685	0.155436	4.90842E-05	1.37716E-10	4.64406	0.129002	3.38089E-05	1.08433E-10
500	5.595685	0.155436	4.90842E-05	1.37716E-10	4.64406	0.129002	3.38089E-05	1.08433E-10
1000	1.718549	0.047737	4.62976E-06	1.29898E-11	4.276233	0.118784	2.86654E-05	9.19367E-11
1500	0.66153	0.018376	6.86016E-07	1.92477E-12	2.53823	0.070506	1.00994E-05	3.23913E-11
2000	0.20599	0.005722	6.65162E-08	1.86625E-13	0.95207	0.026446	1.42093E-06	4.55726E-12

From the calculated and analyzed result in Table 3, it shows that double outer rotor BLDC motor (DORBLDC) produces higher motor constant square density than single rotor BLDC motor (SORBLDC). To avoid any error in evaluate G value of both model, the volume and outer radius of the machine are kept the same value. This is to ensure that the performance of both machine can be compare within the same size. From the table 15, we can see that motor constant square density of the proposed model is higher than conventional model. The proposed model has higher G value than conventional because of having more magnet reluctance in parallel in the magnetic circuit that cause improvement flux density across the machine. It shows that the proposed model design improve the torque density of the machine whereby the performance of the motor increase as the speed of the motor increased. The difference G between DORBLDC and SORBLDC at 2000 rpm is:

G value improvement between SORBLDC and DORBLDC = 4.55726E-12/ 1.86625E-13

= 24.41929702 %

7. Conclusions

In the conventional model, the generated magnetic flux across the machine can't improve as the structure of the model are kept the same. Furthermore, the limitations of the research project such as the volume of the machine must be kept the same especially the ratio of the segmented magnet in the rotor section. Other than that, magnetic flux generated is not fully utilized at the stator yoke and causes increases heat

loss over period of time. Although, V shape PM improved reluctance torque of the machine, the required space needed to mount the PM is high. Therefore, new proposed design by applying extra outer rotor layer to the conventional model able to reduce space for the magnet and produced high magnetic flux density due to amplify generate flux produced by the inner rotor.

In this research project, the proposed DORBLDC with mounted PM operate more effectively than conventional model such as improvement the motor constant square density by 24.42%. Although the proposed design has few weakness in terms of peak torque in speed torque graph, starting power amplitude in speed power graph. However, the benefit of the proposed model such as higher magnetic flux density and longest constant torque speed characteristics than the conventional model. This shows that the proposed model is suitable for E bike application.

References

[1] J. Zhao and Y. Yangwei, "Brushless DC Motor Fundamentals Application Note," *MPS, Futur. Analog IC Technol.*, no. July 2011, pp. 7–8, 2011.

[2] C. C. Hwang, S. M. Chang, C. T. Pan, and T. Y. Chang, "Estimation of parameters of interior permanent magnet synchronous motors," *J. Magn. Magn. Mater.*, vol. 239, no. 1–3, pp. 600–603, 2002.

[3] R. Zhang, X. Zhu, and L. Chen, "Design of a new magnetic-planetary-geared outer-rotor permanent-magnet brushless motor for electric vehicles," *2014 17th Int. Conf. Electr. Mach. Syst. ICEMS 2014*, pp. 658–663, 2015.

[4] C. M. Chang and K. S. Yang, "System integration and power flow management for the engine-generator operation of a range-extended electric vehicle," *2013 World Electr. Veh. Symp. Exhib. EVS 2014*, pp. 1–10, 2014.

[5] M. Cheng and C. C. Chan, "General Requirement of Traction Motor Drives," *Encycl. Automot. Eng.*, pp. 1–18, 2014.

[6] John Wiley & Sons, *"Part I : Theory , Construction , Principles of Operation."* 2004.

[7] B. Marthandam, K. Latha, and U. M. B, "Analysis of V – Shaped Interior Permanent Magnet Synchronous Motor for Low Torque Ripple," vol. 3, no. 3, pp. 498–501, 2014.

[8] T. W. Vickers, "Electrical Machine." 1947.

eureca 2017 – Conference Paper
Paper Number 2EE05

Electromagnetic Braking with DC Field Excited Configuration for Train Traction Systems

Preshant A/L Krishna[1], Aravind C.V[1,*], Aminath Saadha[1], F. Azhar[2]

[1]School of Engineering, Taylor's University, Malaysia
[2]Faculty of Engineering, Universiti Teknikal Malaysia Melaka, Malaysia
[*]aravindcv@ieee.org

Abstract

In urban regions and particularly in developing countires such as Malaysia with its ever growing transport sector, there is the need for energy efficient systems. In urban railway systems there is a requirement of frequent braking and start/stop motion, and energy is lost during these processes. To improve the issues of the conventional braking systems, particularly in Japan, they have introduced linear induction motor techniques. The drawbacks of this method however, is the use of permanent magents, which not only increase the weight of the entire system, but also increases magnetic cogging. Hence an alternative is required which uses the same princples as Magnetic-Levitation, but using a magnet-less system. Therefore, the objective of this research is to propose an electromagnetic rail brake system and to analyze the effect of replacing permanent magnets with a magnet less braking systems to produce a significant amount of brake thrust as compared with the permanent magnet system. The modeling and performance analysis of the model was done using Finite Element Analysis (FEA). The mechanical aspects of the model was designed on Solidworks and then imported to JMAG Software to proceed with the electro-magnetic analysis of the model. There were 3 models developed: Base Model (steel), Permanent Magnet (PM) Model and DC Coil Model. The performance of the proposed 2D models developed was evaluated in terms of average force produced and motor constant square density. By comparing the values for the 3 models for the same case of 9A current supplied for a 0.1mm/s moving velocity, the base model, permanent magnet model and DC coil model produced an average force of 7.78 N, 7.55 N, and 8.34 N respectively, however, with increase in DC current supplied to the DC coil model, the average force produced was increased to 13.32 N. Thus, the advantage of the DC coil (magnet-less) model, is, that the force produced can be controlled by varying the number of turns in the coil (N) or the current supply to the coil (I) given by the which is the simple principles of a solenoid: Force(mmf)=NI.

Keywords: Linear Motor, Magnet-less, Railway Braking, Magnetic-Levitation

1. Introduction

Conventionally brake systems use friction or mechanical traction to slow down or stop a moving object, but friction produces heat and thus heat losses. Friction generates heat, thus losing energy, and the frequent use of these type of friction based braking leads to wear and tear of brake pads, wheels and tracks leading to the requirement of frequent maintenance of the system[1]. Disc brakes require extra materials such as oil or compressed air to force the brake lining on the wheels, reduce the kinectic force of the system. Apart from the mechanical stress on the system, installing disc brakes increases the weight of the entire system, but the application is useful only during braking conditions.[2] The Figure 1.1 below shows the example of Wheel-Thread Brake System and Axle-Mounted Disc Brake System mechanisms which are of adhesion types:

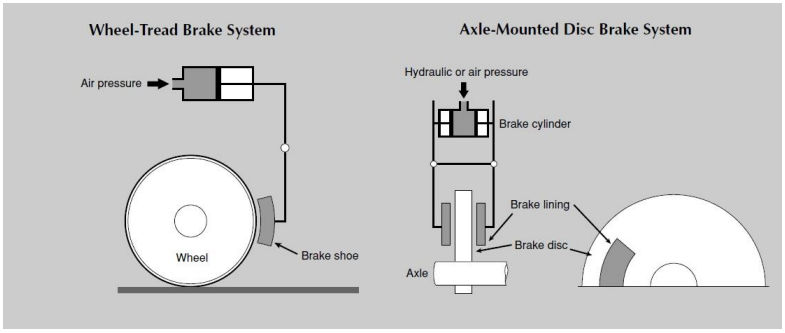


Figure 1.1. Wheel-Thread Brake System and Axle-Mounted Disc Brake System [2]

To overcome this, electromagnetic brake systems that do not rely of wheel adhesion such as eddy current braking systems were introduced using electromagnetic induction principles, with the help of permanent magents. However, the drawback of this method is that, at lower speeds, the brake force is reduced without the ability to magnetically lock the load at a standstill, which poses a safety issue, and thus the conventional friction braking system has to be incorporated as well. Furthermore, the heat generated from the braking of these types of systems would result in the overheating of the rail tracks causing the tracks to bend or deform. Another drawback with the use of permanent magents is the increase in weight of the system as well as the cogging force induced. [1, 4]. Even hybrid linear motors have been researched and the effect of the core losses have been analysed to be much more when there are permanent magnets introduced to the system. Although research has been on the losses of permanent magnet systems, there is not a suffcient amount of literature and research data available for the application of magnet-less systems for railway braking aspects. [5]. Therefore, the objectives of this research is to propose an electromagnetic rail brake system through fixed DC excitation for rail brake systems which produces a significant amount of brake thrust and to analyze the effect of replacing permanent magnets with a magnet less braking. Moreover, to compare the machine characteristics such as motor constant square density of the proposed model to the permanent magnet model, with respect to the conventional base model.

2. Research Methodology

The research encompasses the design, optimization and prototype fabrication of linear electromagnetic braking using levitating principles for railway braking systems. Then the design was simulated and analyzed in software such as JMAG for electromechanical analysis and Finite Element Analysis and Solidworks for the mechanical modeling and analysis. The limitations and scope of the research are due to the restriction to the lab environment and the specific fixed loading capacities of the prototype model. The flowchart of the flow of research methodology is given below as Figure 2.1:

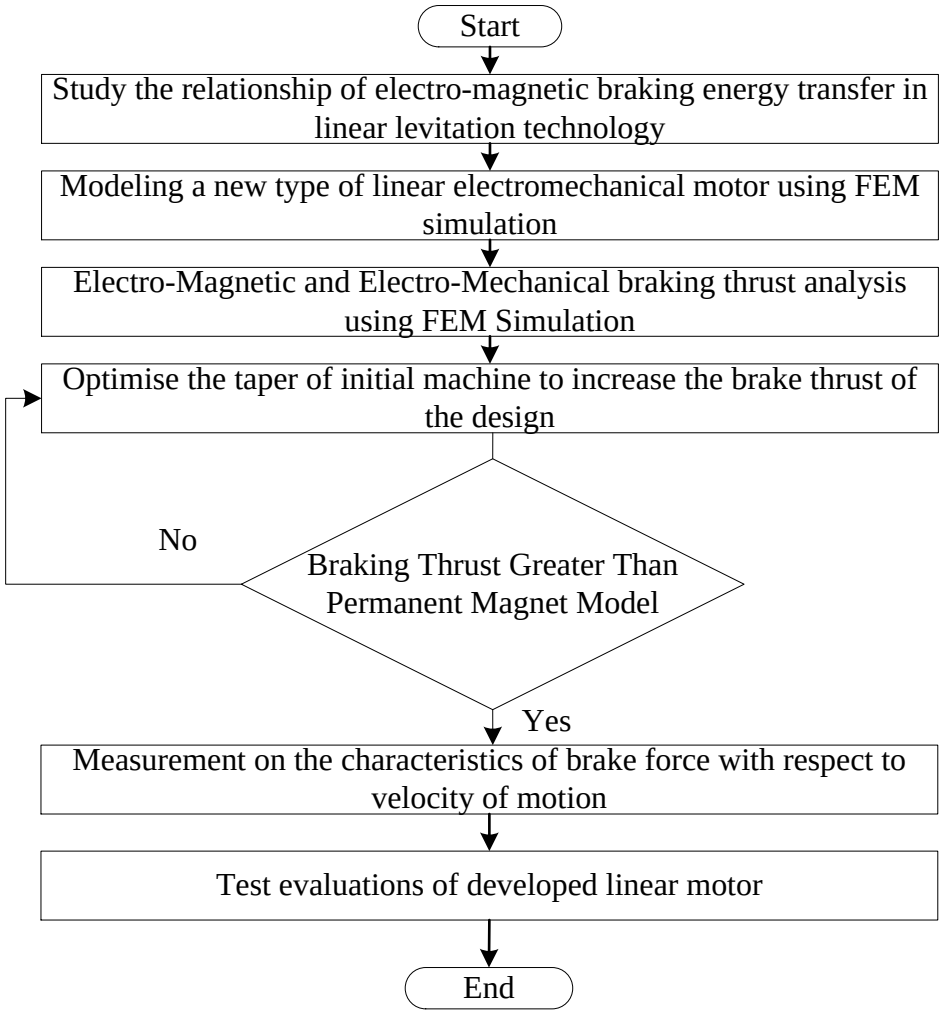


Figure 2.1. Flowchart of Methodology

The relationship between the electrical and mechanical energy to the braking performance of the motor technology was mathematically developed. The purpose the study was to investigate the performance of the overall linear electromechanical technology for braking applications in railways. A set of coils energized will attract steel and the flux flow in the air gap will hold the rail and the track to be magnetically locked, which is the principle of the motor as seen in the Figure 2.2 below:

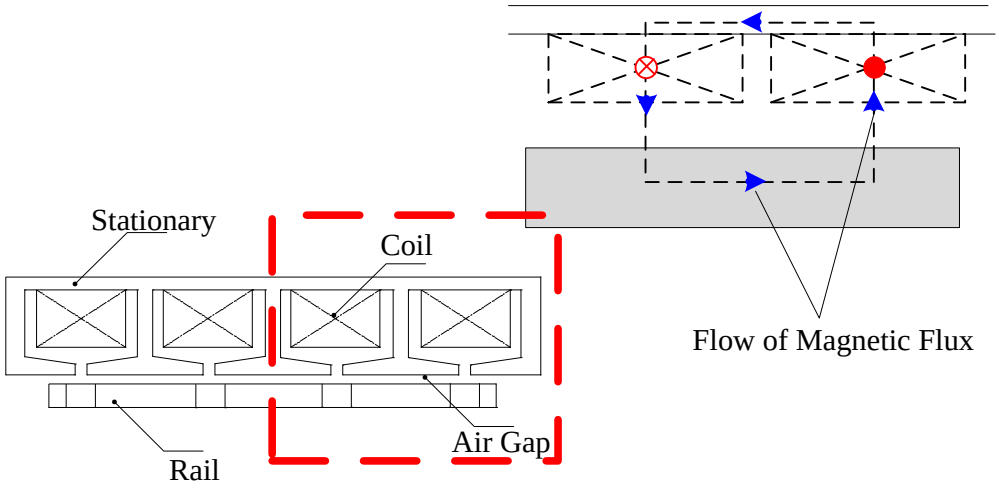


Figure 2.2 Concept of Linear Switched Motor

The flowchart for the overview of the design and development stages is shown below as Figure 2.3:

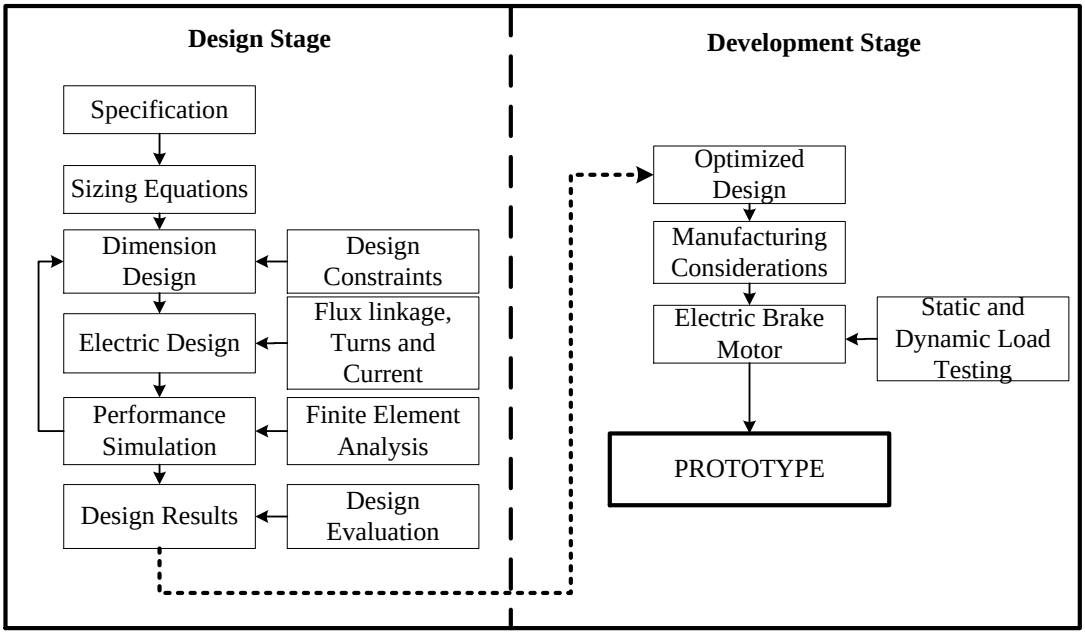


Figure 2.3. Overview of Design and Development Stages

After the relationship was established, the next step was to model the new type of linear machine using numerical analysis tool. Design details were done analytically using calculations, before the modeling process. For the modeled prototype, the motor should produce maximum braking torque. The limits were set based on the sizing (height and width) calculations of the motor. Based on the analysis of the study and optimization done, the linear electromechanical motor prototype was fabricated to validate the proof of concept. Experimental analysis for the final prototype of the linear motor and the characteristic of the motor torque with change in velocity was tested.

Experimental analysis for the final prototype for the characteristics of the motor torque and speed will be tested and compared to that of a linear permanent magnet motor.

2.1 Magnetic Circuit Analysis

The magnetic flux density is given by the Eq. (1) below: [8,9]

$$B = \mu_o H = \mu_o(\frac{NI}{x}) \quad (1)$$

Whereby, B is flux density, μo is Permeability of free space (air), H is Magnetic flux intensity, N is Number of turns of the coil and I is the current carried by the coil.

The linkage flux is given by Eq. (2) below:[8,9]

$$\psi = \phi N = (\frac{\mu_o A N^2 I}{x}) \quad (2)$$

The self inductance L, is given by Eq. (3) below:[9]

$$L = (\frac{\mu_o A N^2}{x}) \quad (3)$$

Energy stored in a current carrying coil with the self inductance of the coil L, and if there are no other current carrying coils in the system then magnetic flux ϕ, is given by the Eq.(4) below:[8]

$$\phi = IL \quad (4)$$

Therefore the energy stored W, can be written as Eq. (5) below:[8]

$$W = \frac{1}{2} LI^2 \quad (5)$$

If a system consists or more than one current carrying coils that are magnetically linked to each other, the total force of the system is the sum of all the forces acting on the coils. In a multiple loop system, the force F, associated with linear motion is defined by a variable x, and is given as Eq. (6): [8,9]

$$F = \frac{\partial W}{\partial x} \quad (6)$$

This can be substituted with Eqs.(1), (3), and(5) and rewritten to form the Eq.(7): [8,9]

$$F = \frac{d}{dx}\left(\frac{1}{2} I^2 L\right)$$

$$F = \frac{dL}{dx}\left(\frac{1}{2} I^2\right)$$

$$F = -\frac{1}{2} I^2 \left(\frac{\mu_o A N^2}{x^2}\right)$$

$$F = -\frac{1}{2\mu_o}\left(\frac{\mu_o N I}{x}\right)^2 A$$

$$F = -\frac{B^2 A}{2\mu_o} \quad (7)$$

Whereby, A is the cross section in the air gap, B is the magnetic flux density and μ_o is the permeability. The negative sign indicates the fore deceases to x, thus it is an attractive force. This force is also knows as normal force which is the force of attraction between the armature core and the reaction rail of a linear motor through air gap. [8-10]

Eq. (7) can also be written as Eq. (8) below: [8-10]

$$F = \frac{B.B.A}{2\mu_o} \quad (8)$$

Since $\phi = BA$, for a region where the magnetic field is uniform and assuming the flux density has only one directional component B with a uniform cross section A, by taking the perpendicular direction of B we get the Eq.(9) below: [8,9]

$$F = \frac{B\,\phi}{2\mu_o} \tag{9}$$

Thus the relationship can be established as Eq.(10) below:[8,9]

$$\varphi = \frac{F_{mmf}}{\mathcal{R}} = \frac{NI}{\mathcal{R}} \tag{10}$$

Thus is can be seen that keeping the area of cross section A constant, the force can be increased by increasing magnetic flux ϕ. This can be achieved by increasing the number of turns of the coil N, increasing the current I, or by decreasing the reluctance $\mathcal{R}$. Reluctance is essentially, the amount resistance to the flow of the magnetic flux through the air gap.

The effects of decreasing the reluctance can be more vividly visualized by rearranging the Eq. (9) to Eq. (10), to analyze the methods of manipulating the reluctance of the system: [9]

$$\mathcal{R} = \frac{mmf}{\varphi} = \frac{NI}{B\,A} \tag{11}$$

3. Design Aspects

The components of the linear motor that was designed are the mover, stator, and armature coil. The armature coils are supplied by AC current supply and produce magnetic flux which produces a force when acting on the mover. The armature coil is made up of copper windings, while the mover and stator are steel. The mover and the stator are separated by an air gap. For the Permanent Magnet model, part of the steel was modeled to be cut out to fit permanent magnets on the stator. The same dimensions were used for the DC coil model, but instead of permanent magnets, copper coils were selected as the material. The Figure 3.1 below shows the front view of the Base model and Figure 3.2 shows the PM/DC Coil model designed on Solidworks:

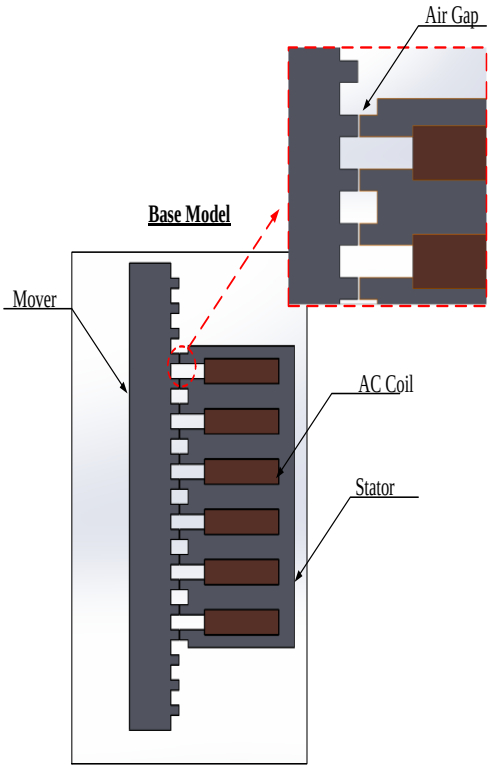


Figure 3.1. Base Model Design

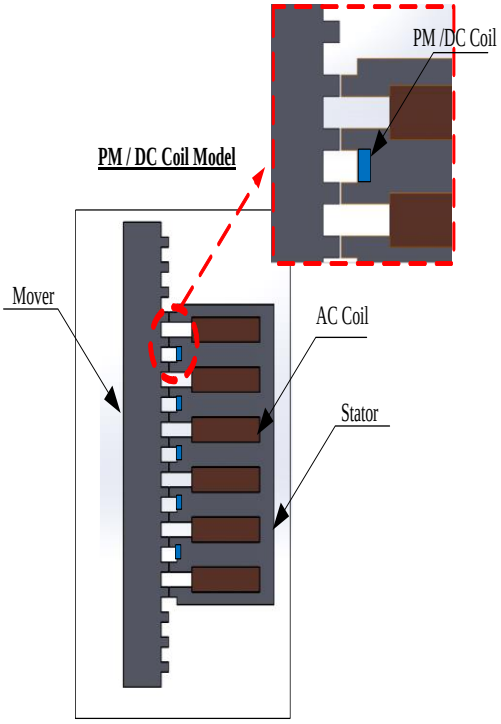


Figure 3.2. PM / DC Coil Design

The dimensions of the designed model for the permanent magnet/DC coil are given in the Figure 3.3 and Figure 3.4 respectively for the front view and the auxiliary view:

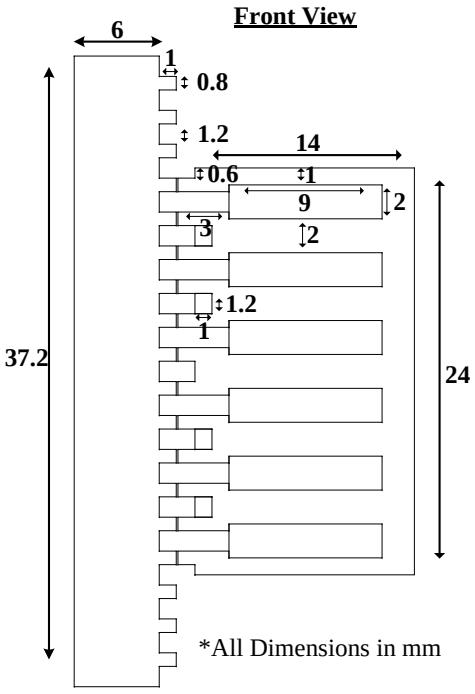


Figure 3.3. Front View of Dimensions

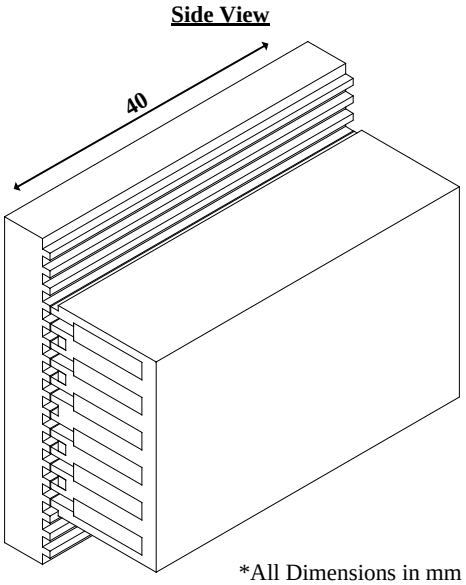


Figure 3.4. Auxiliary View of Dimensions

To compare the analysis between the comparison of the system with the permanent magnet and a magnet-less system using only coils, the dimensions for the permanent magnet slots were kept the same, and replaced by coils, for the DC coil model. The 3D models of the linear motor were designed on Solidworks and then imported to JMAG for the FEM analysis. In the FEM analysis, the magnetic field lines the magnetic flux density can also be visualized and analyzed with JMAG.

JMAG using FEM analysis, is an electromagnetic analysis software, can analyze the dynamic motion of the linear motor, and the magnetic forces induces during the motion, for different electrical and magnetic parameters. Finite Element software is capable of accurately calculating magnetic fields and the related parameters for motor design. The analysis done are shown in the Figure 3.5 and Figure 3.6 for the magnetic flux density and the magnetic field lines respectively:

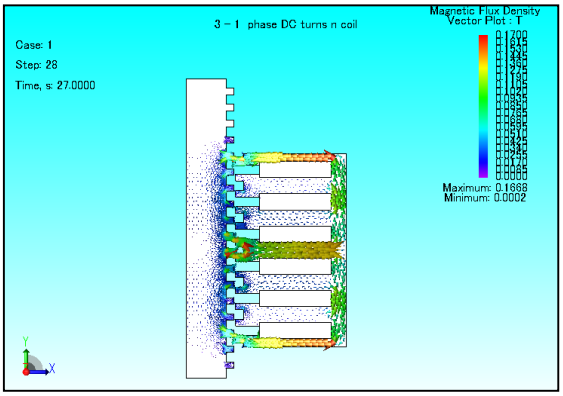


Figure 3.5. Magnetic Flux Density

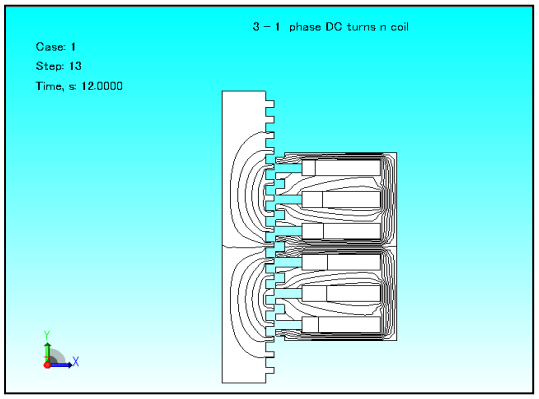


Figure 3.6. Magnetic Flux Lines

Thus, with these tools, the performance of the model could be analyzed by analyzing the flow of the magnetic field lines and flux density. It is noted that the flux originates around the armature coil and flow through the mover, back into the stator, thus producing a force on the mover. With the step feature, the movement of the mover with each step with respect to time could also be visualized and the change in magnetic flux could be seen.

The comparison FEM analysis was done for three models of linear motors: Base Model (steel), Permanent Magnet, Model and DC Coil Model (electromagnet). For the model with the DC coil, different values of current supply were also used, which were 1A, 3A and 5A current for the DC coil, while the main AC supply to the stator was kept constant for all 3 models with 5A, 7A and 9A current. For the 3 models, the average force values were tabulated for the different current values at various speeds with respect to time. The displacement values selected were 0.1mm/s, 0.3mm/s, 0.5mm/s. The force graph was obtained using JMAG and the values were tabulated and analyzed on the Origin software.

3.1 Performance Index Calculation

Thrust force produced by a machine is proportional to input power ‘P’, current ‘I’ and volume ‘V’. If the volume of a motor is larger, it has a larger area to accommodate more number of coil turns and/or coils of larger size, therefore more current and power can be injected into the machine to produce higher thrust force. [11]

Thus motor constant square density G, is used as one of the performance index in order to make valid comparisons between different models. This normalizes the factors such as volume, current and input power, to make a proper unbiased comparison between models. Thrust constant k_f, and motor constant k_m, are used as performance indices to normalize the current and input power of a motor respectively. The performance indexes are calculated using the equations Eq. (12) to Eq.(15) given below:[11]

$$k_f = \frac{F}{I} \quad \text{Eq.(12)}$$

Where k_f is the thrust constant in (N/A), F is the average thrust in (N), and I is the current injected to each coil (A). [11]

$$P = I^2 R \quad \text{Eq.(13)}$$

Where P is the input power in (W) and R is the resistance of the coil.[11]

$$k_m = \frac{F}{\sqrt{P}} \quad \text{Eq.(14)}$$

Where k_m is the motor constant in (N/$\sqrt{W}$).[11]

$$G = \frac{F^2}{P\,V} \quad \text{Eq.(15)}$$

Where G is the motor constant square density in ($N^2/(Wm^3)$), and V is the volume of the motor in (m^3).[11]

4. Results and Discussion

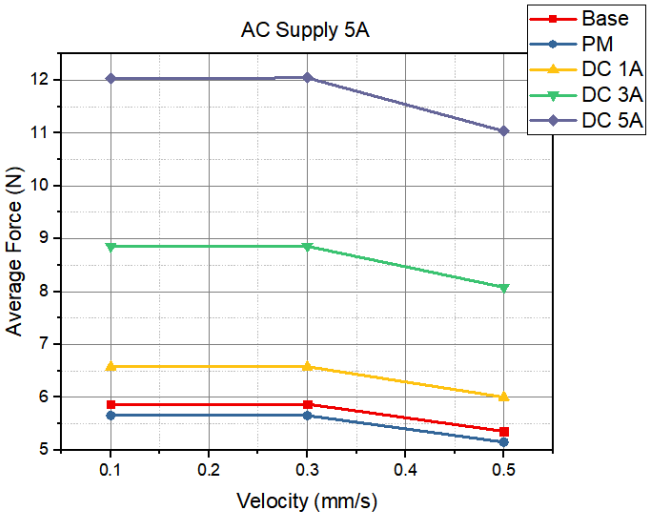
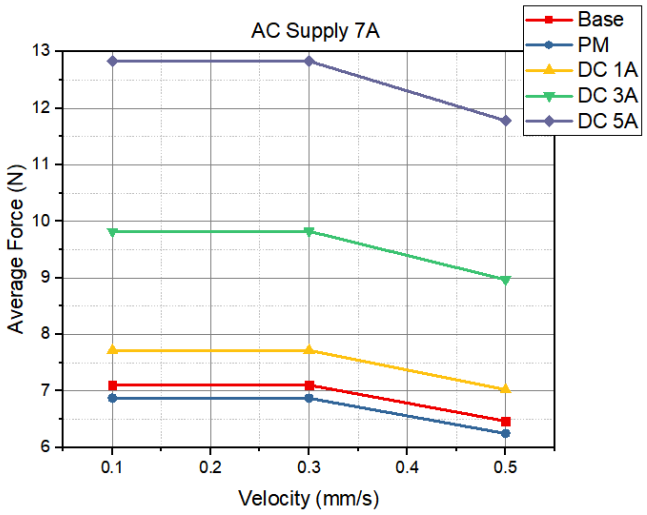
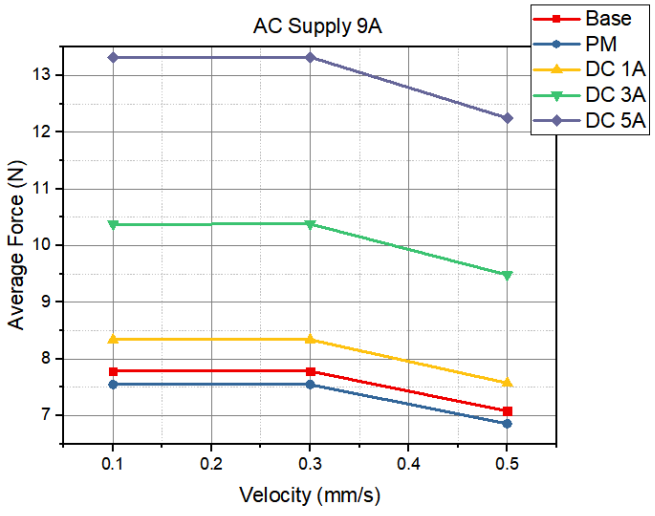
To find the average force value for each case, from the data obtained in JMAG, the force graph for each case was integrated to find the area under the graph. The integrated values for each case in the 3 models were then tabulated and plotted on the same graph, thus the average force values for each model and each case was comparatively analyzed. The Table 1 below shows the data collected from the simulation done on the average force produced for each model for various cases:

Table 1. Average force produced for various cases of different models

AC Supply		**5A**			**7A**			**9A**		
Velocity (mm/s)		**0.1**	**0.3**	**0.5**	**0.1**	**0.3**	**0.5**	**0.1**	**0.3**	**0.5**
Average Force (N)	**Base**	5.87	5.87	5.36	7.10	7.10	6.46	7.78	7.75	7.08
	PM	5.65	5.65	5.15	6.87	6.87	6.24	7.54	7.54	6.85
	Coil 1A	6.57	6.57	6.00	7.71	7.72	7.02	8.34	8.34	7.57
	Coil 3A	8.85	8.85	8.08	9.82	9.82	8.96	10.3	10.38	9.48
	Coil 5A	12.03	12.04	11.03	12.82	12.83	11.78	13.32	13.32	12.24

The Table 2 below shows the graphical comparison of Velocity Vs Average Force produced by the 3 models for the supply AC current of 5A, 7A and 9A:

Table 2. Comparison of Velocity Vs Force for Different Models

Supply Current (AC)	Comparison of Velocity Vs Force graph for 3 models: Base, PM, and DC Coil (1A, 3A, 5A)
5A	
7A	
9A	

It was realized that, with varying the current in the DC coil, the brake force produced can be altered, without disrupting the main AC supply. Thus this gives a better range of force application that can be used for various brake force requirements. DC coils are used instead of permanent magnets for the proposed model, to curb the issues with magnetic cogging and to reduce the weight of the system. It also provides a wider range of operability compared to the permanent magnet as the magnetic field intensity of the coil can be increased or decreased depending on brake force requirement, but for permanent magnets, the force produced is constant, and deteriorating over time. However, AC coil main supply to the system is still needed, to operate the railway system, as any unforeseen disruptions in the supply can be recovered by the AC supply, instead of affecting the entire system.

The forces produced however, are for the motoring condition, but if the polarity is reversed, the values obtained are for the braking condition. Since, the positive values indicate accelerating velocity and the negative values indicate decelerating velocity, hence braking condition. By combining the two conditions for the motoring and braking applications, the speed–force characteristics of the models can be obtained. The speed-force characteristics for the different models are shown in the Figure 4.1 below:

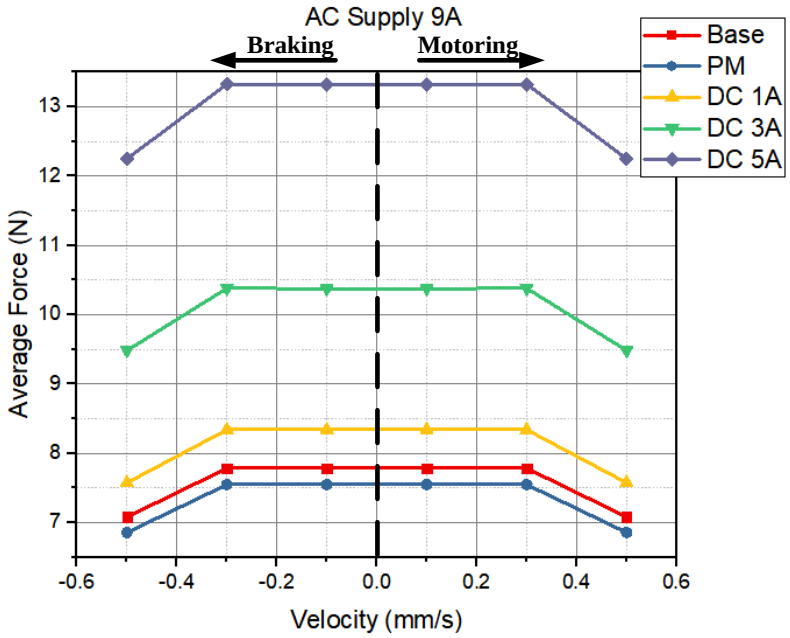


Figure 4.1. Speed-Force Characteristic of the Different Models

The x-axis of the graph is the average force and the y-axis is the various velocities. From the graph, it was visualized that the DC coil model produced an over higher average force, when compared with the other models. The added advantage of the DC coil model is the use of magnet-less systems whereby the force values can be more specifically controlled by varying the amount of current supplied to the coil given by the relationship of Force (Thrust) = mmf = NI, which is not present with the use of permanent magnets. Therefore, with an increase in number of turns of the coil or by increasing the current supplied to the coil, the thrust can be increased. As seen on the graph, by increasing the current value of the coil, there is an increase in the average force.

The Table 3 below provides the area, material and volume specifications for the proposed models. The models were kept at the same area and volume, by replacing the materials rather than adding more materials to the motor. The volume was found by multiplying the area of the model with the stack length of the model.

Table 3. Materials, Area and Volume of Models

Component	Material	Quantity	Area (mm^2)	Volume (mm^3) (Stack Length 40mm)
Mover	S45C	1	200	8000
Stator	SS400	1	192	7680
Coils	Copper windings	6	18 x 6	4320
PM / DC Coil	Neomax 35AH / Copper	4	1.2 x 4	192
	Total		504.8	20192

Thus the volumes of all 3 models were the same value of 20192mm^3.

The Table 4 below shows the parameters of the motor such as the current injected, volume of the motor, average force produced and the calculated values for the thrust constant, motor constant and motor constant square density, for a comparison of the 3 models: Base Model (steel), Permanent Magnet Model and DC Coil model for 1A, 3A and 5A.

Table 4. Parameters of Models

Parameter	Unit	Base Model	PM Model	DC Coil Model		
				1A	3A	5A
I	A	9	9	9	9	9
V	mm^3	20192	20192	20192	20192	20192
F	N	7.78	7.54	8.34	10.37	13.32
k_f	N/A	0.86	0.83	0.92	1.15	1.48
k_m	$N/A/\sqrt{W}$	0.96	0.93	1.03	1.28	1.65
G	$(N/A/\sqrt{W})^2$/ mm3	4.63E-05	4.36E-05	5.32E-05	8.23E-05	1.36E-04

From the calculated results, it was found that the DC coil model achieved a higher motor constant square density, with an increased variation in force produced without disrupting the main current supplied into the system. Comparing the motor constant square density between the permanent magnet model and the dc coil model with respect to the base model, the values are given in the Table 5 below:

Table 5. Motor Constant Square Density Comparison of Models

Formula	Permanent Magnet	DC coil 1A	DC coil 3A	DC coil 5A
$\frac{G_{model}}{G_{base}}$	0.940	1.148	1.776	2.927
$\frac{G_{model} - G_{base}}{G_{base}} x\ 100\%$	-5.98	14.76	77.64	192.72

7. Conclusion

In conclusion, the objectives to design a magnet-less linear motor for rail braking systems and to compare and evaluate the performance of the system to conventional and permanent magnet models, in terms of average force produced and motor constant square density have been achieved. The proposed model was developed on Solidworks and FEM analysis was done using JMAG. There were 3 models developed: Base model, Permanent Magnet model and the DC Coil model, whereby the average force produced and motor constant square density for each model for various moving velocities were compared and analysed. The models produced an average force of 7.78 N, 7.55 N, and 8.34 N for the base model, permanent magnet model and DC coil model respectively. The added advantage of the magnet-less dc coil model is that, the average force produce could be controlled by controlling the excitation current supplied to the coil, giving a wider range of operation, without disrupting the main AC supply to the system. From this, the average force for the DC coil model was increased to 13.32 N, by increasing the fixed DC excitation supply from 1A to 5A.With the motor constant square density parameter calculated, it gives a baseline parameter of motor performance index for the proposed model that can be compared with other linear motors with different volumes and specification. Comparing the characteristics of the models with respect to the base model, the permanent magnet model produced 5.98% decrease, while there was an increase of the DC coil model ranging from 14% to 192% with the increase of DC current supplied, for the motor constant square density.

Acknowledgments

The authors wish to express financial support of the project through the Taylor's Research Grant Scheme TRGS/MFS/1/2016/SOE/005.

References

[1] R. C. Sharma and M. Dhingra, "Braking Systems in Railway Vehicles," *Int. J. Eng. Res. Technol.*, vol. 4, no. 1, January 2015, pp. 206–211, 2015.

[2] I. Hasegawa and S. Uchida, "Braking Systems," *Japan Ralw. Transp. Rev. 20*, vol. 7, no. June, pp. 52–59, 1999.

[3] Y. Sakamoto, T. Kashiwagi, T. Sasakawa, and N. Fujii, "Linear eddy current brake for railway vehicles using dynamic braking," *Proc. 2008 Int. Conf. Electr. Mach. ICEM'08*, pp. 1–6, 2008.

[4] A. Aravind, V. R. Akilesh, S. Gunaseelan, and S. Ganesh, "Eddy Current Embedded Conventional," *Natl. Conf. Trends Automot. Parts Syst. Appl.*, vol. 5, no. 7, pp. 7–12, 2016.

[5] N. Chueng and E. K. Cheng, "Loss Analysis for the hybrid linear switched reluctance motor with no cogging force.," in *2015 IEEE International Magnetics Conference (INTERMAG)*, p. 1, 2015.

[6] W. Shangguan, J. Wang, H. Wang, J. Wang, and S. Li, "The Braking Mode Simulation and Analysis for High-speed Railway," *2011 4th IEEE Int. Symp. Microwave, Antenna, Propag. EMC Technol. Wirel. Commun.*, pp. 683–686,

2011.

[7] Y. Wang, J. Miao, and Y. Wei, “The research of traction motor energy-saving regenerative braking control technology,” *2010 Int. Conf. Intell. Comput. Technol. Autom. ICICTA 2010*, vol. 3, pp. 930–933, 2010.

[8] I. Boldea and S. Nasar, *Linear Electric Actuators and Generators*. Cambridge, GBR: Cambridge University Press, 2009.

[9] H. Toliyat and G. Kliman, *Handbook of Electrical Motors. Electrical and Computer Engineering*. CRC Press, 2004, pp. 1-24.

[10] H. Toliyat and G. Kliman, *Handbook of Electrical Motors. Electrical and Computer Engineering*. CRC Press, 2004, pp. 299-326.

[11] F. Azhar bin Abdul Shukor, H. Wakiwaka, K. Tashiro and M. Nirei, "Design and Performance Index comparison of the Permanent Magnet Linear Motor", *Progress In Electromagnetics Research M*, vol. 43, pp. 101-108, 2015.

eureca 2017 – Conference Paper
Paper Number 2EE06

Energy Recovery through Phase Layered Heat Removal using Sustainable Materials

Rikesh Ramsurn[1], Aravind CV[1*], Mohammad Taghi Hajibeigy[1]

[1]*School of Engineering, Taylor's University, Malaysia.*

[*]aravindcv@ieee.org

Abstract

Making a PVT system hybrid is to support the use of thermal and electrical energy simultaneously or independently, to control the thermal effect to improve electrical efficiency or vice-versa. This project makes use of the Parabolic Trough design with emphasis on making the system to be sustainable and also increasing the thermal efficiency of the system. Polystyrene and acrylic foam are is utilised to maximise the heat retention capability of the system. To power the pump that moves the heat transfer fluid (tested with salt water proportions) within the copper tube, a set of solar PV panel is to support its power demand making it sustainable. The closed loop setup designed achieved an improved thermal efficiency level of 66.2%, which contributes to having a reliable heat energy source for applications such as hot showers. The novel setup design also make use of PV cells to support other energy demands through power electronic control designs. Using a similar heat dissipation technique, a novel setup has been designed to improve the voltage supply by making use of liquid cooling and translucent glass PV panels. Cooling the PV panel restored up to 11.7% of its rated voltage supply. This was achieved by keeping the PV panels within its best thermal operating conditions using an energy efficient electronically controlled cooling system. The aim of this project is to contribute to the development of a sustainable solar energy source.

Keywords: Parabolic Trough, Efficiency, Sustainable, Energy, Cooling.

1. Introduction

Solar energy can be considered as the cleanest and most abundant source of renewable energy harvested from sunlight [1]–[3]. Its net input to Earth can be considered as 8000 times the rate of fossil and nuclear fuels currently being used by humanity on a worldwide scale. Methods of harvesting solar energy can vary a lot in design but are essentially made up of photovoltaic cells when it comes to generating electricity. Discovered in 1839 by the French physicist Edmond Becquerel, the photovoltaic effect majorly contributed to the foundation of the commonly known Photovoltaic (PV) cell. Due to its solid state nature, silicon based PV cells have an expectancy of operating for an indefinite amount of time without wearing out [4]. However, the efficiency of PV cells is still subjected to research and development with the aim of achieving sustainability in terms of electricity generation and consumption.

The efficiency of PV cells is known to be affected by heat during its exposure to solar radiation while in operation. Hence methods are being devised to improve the efficiency of PV cells through heat dissipation [5]. With energy sustainability in mind, the heat dissipated can be reused for applications with heat demand such as a hot water supply. A popular design currently being researched and developed for solar energy harvesting is the Parabolic Trough PVT design. Using light concentration concept, such as concentrating sunlight on an object using a magnifying glass causing it to melt or burn, the Parabolic Trough PVT design consists of a reflective sheet of metal (e.g. stainless steel) bent into a circular shape in order to reflect light rays from the sun onto a line of incidence [6]. The main application of this line of incidence is to convert the concentrated light rays into heat energy, thus contributing to the thermal aspect of the PVT design. Heat energy is collected by a copper pipe placed at the line of incidence of the reflected light rays. The heat energy collected can then be used for applications such as a hot water shower by transferring the heat to a water tank using a closed loop fluid flow circuit and a heat exchanger. The closed loop may contain water or other fluids which can facilitate faster and more efficient heat removal from the copper pipe and heat transfer to the water tank through the heat exchanger.

Following the heat dissipation concept, there is a possibility of improving electrical efficiency of PVT systems by removing the heat build-up on PV panels/cells while reusing the heat for thermal applications. This improvement is brought through restoration of the voltage supply which normally drops as the temperature of the panels rises. A cooling technique which may be used to cool PV cells is the use of heatsinks. The heat build-up on the PV cells is transferred to the heatsinks through conduction while the latter may be air-cooled or liquid-cooled. The cooling method used may vary depending on the type of PV panel used and how the heat shall be reused. Hence, it is important to further investigate and develop PVT systems such as the Parabolic Trough to achieve reliability and sustainability. In this work a parabolic concentrating trough is experimentally studied and performance evaluated with phase layered heat removal strategy.

2. Methodology

2.1 Experimental System Setup

Heat Transfer Fluids (HTF) used in this research includes water, water with 10g/L of salt and water with 20g/L of salt. Figure 1 shows the flowchart of the system's thermal optimisation implemented and experimented. The most important feature of the thermal optimisation implemented is the use of a closed loop HTF circuit which involves the use of a copper coil heat exchanger for effective heat dissipation and a pump for liquid movement around the circuit. The size of the copper heat exchanger is selected according to the container size it will be in. The maximum volume the heat exchanger can occupy in the container would favour more effective heat dissipation. As for the pump, its specification depend on the amount of liquid to be moved around the circuit as well as the flow rate at which it shall be moved. Effective heat dissipation in a closed loop circuit requires in-depth flow rate calibration. For the experiments conducted during this research, flow rate calibration was performed experimentally by controlling the DC pump's voltage. The lower the voltage, the slower the flow rate and vice versa. Thermocouples were used to measure the various temperatures involved in this research.

Experiments were conducted for each HTF for around 30 minutes under a specific weather or until the system reached a thermal settling point for the meteorological conditions it is being experimented under. The closed loop was flushed with clean water before testing with each HTF. The recorded data were then analysed graphically.

The principle of operation of the Phase Layered Heat Removal for thermal efficiency improvement is as demonstrated in Fig. 1.

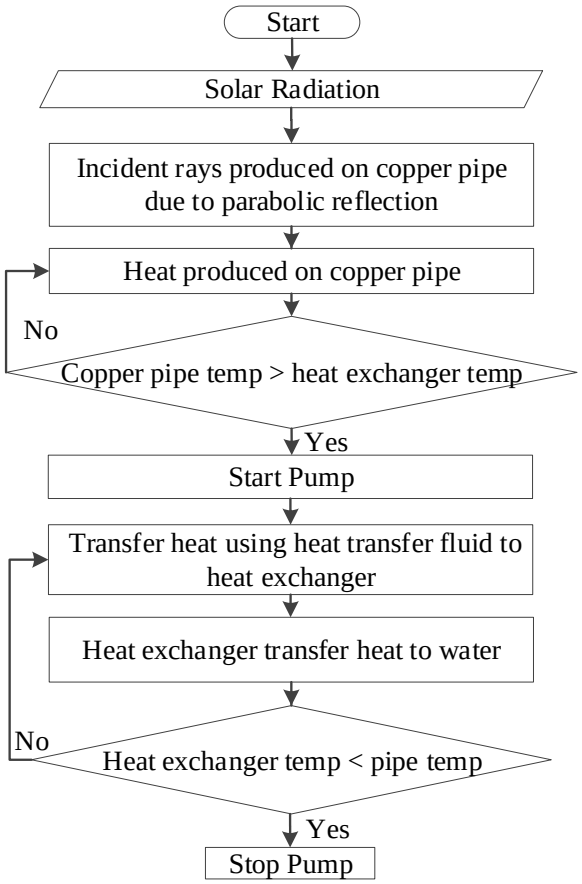


Figure 1. Closed loop heat transfer topology.

2.2 Electrical Characteristics Study

When it comes to the electrical aspect, the cooling methods can either be active or passive. The advantage with active cooling is that it can be rather faster than passive cooling. However, active cooling also affects the electrical efficiency with its power requirement [7]. Hence, the setup designed for this research is a combination of the two, whereby electricity is used by the cooling system only under specific conditions. The type of solar panel used for this research is a Silicon Thin Film of 20% Transparency. The cooling design concept involves placing the panel in between two layers of liquid for top and bottom surface heat removal. The cooling setup designed can be connected as a closed loop, making use of a pump and a heat exchanger, or as an open loop connected to the main water supply pipe of the house of building where the system is placed. As an open loop setup, electronically controlled valves are used to control the liquid flow in case the flow from the mains is not enough to cool the panel, which in case a backup water tanks is used to make up for the flow through gravitational difference.

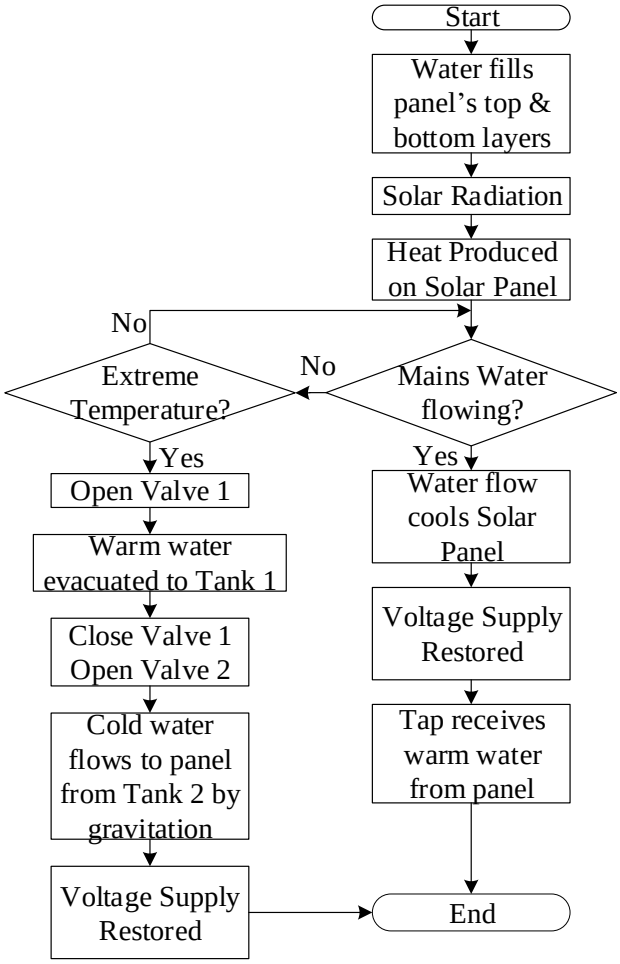


Figure 2. Open loop heat removal topology.

The heat transfer topology for closed loop is similar to the one shown in Fig. 1 where the heat is produced on the panel instead of a copper pipe. For the open loop setup, the heat removal topology is as shown in Fig. 2. The PV panel cooling technique demonstrated by Fig. 2 was implemented at Taylor's University by connecting the water tap from the Engineering Workshop to the panel's inlet. The panel's outlet replaced the role of the water tap. The PV panel was placed under the sun and started heating up. Whenever a student was to use the water tap, the water from the tap would flow into the panel's cooling layers to cool the panel. The heat from the panel would be transferred to the water and would leave the panel's cooling layers as warm water which the student using the tap could use. A warm water supply was appreciated at the Engineering Workshop for washing hands better than with cold water. If ever the panel's temperature would get too high, an electronically controlled valve would open to evacuate the hot water into a backup tank for later usage. The same principle can be applied to a home or any other building with a water supply. While the panels are cooled, warm water is also being produced for instant use or to be stored for later usage. Fig. 3 shows the cooling setup design concept.

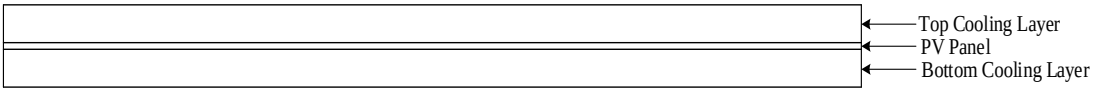


Figure 3. Top and bottom liquid containers made of Perspex for layered cooling.

3. Results and Discussion

3.1 Thermal Efficiency

The general equation for instantaneous thermal efficiency η_T is as shown in Eq. 1 [3].

$$\eta_T = F_R(n_o - \frac{U_L}{C}(\frac{T_{out} - T_{air}}{G_b}) \quad (1)$$

Using Eq. 1 and experimental or simulation results obtained for optical efficiency [8] and heat loss coefficient [9] of the parabolic trough design, the instantaneous thermal efficiency for this research's PVT system has been derived and simplified into Eq. 2.

$$\eta_T = 0.667074 - 4.124820(\frac{T_{out} - T_{air}}{G_b}) \quad (2)$$

Where η_T = instantaneous thermal efficiency; F_R = heat removal factor; n_o = optical efficiency; U_L = overall heat loss coefficient, W/m^2.K; C = concentration ratio; T_{out} = temperature of HTF leaving heat exchanger, K; T_{air} = ambient temperature, K; G_b = direct solar radiation, W/m^2.

Figure 4 to Figure 8 show the graphical results of the experiments conducted using the different HTFs and insulation.

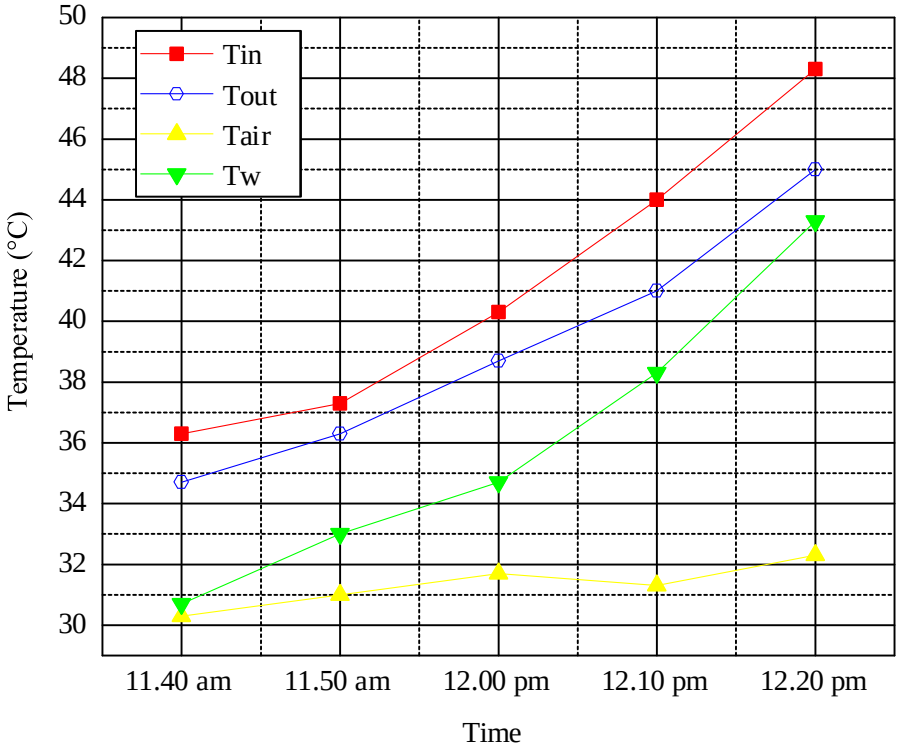


Figure 4. Water as HTF.

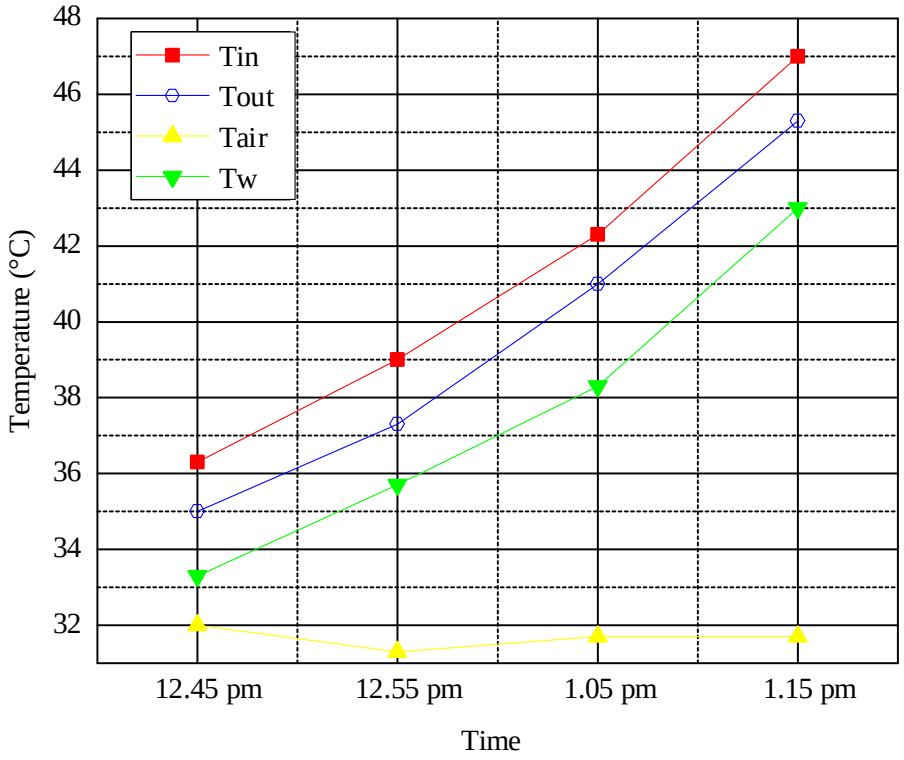


Figure 5. Salt water at 10g/L as HTF.

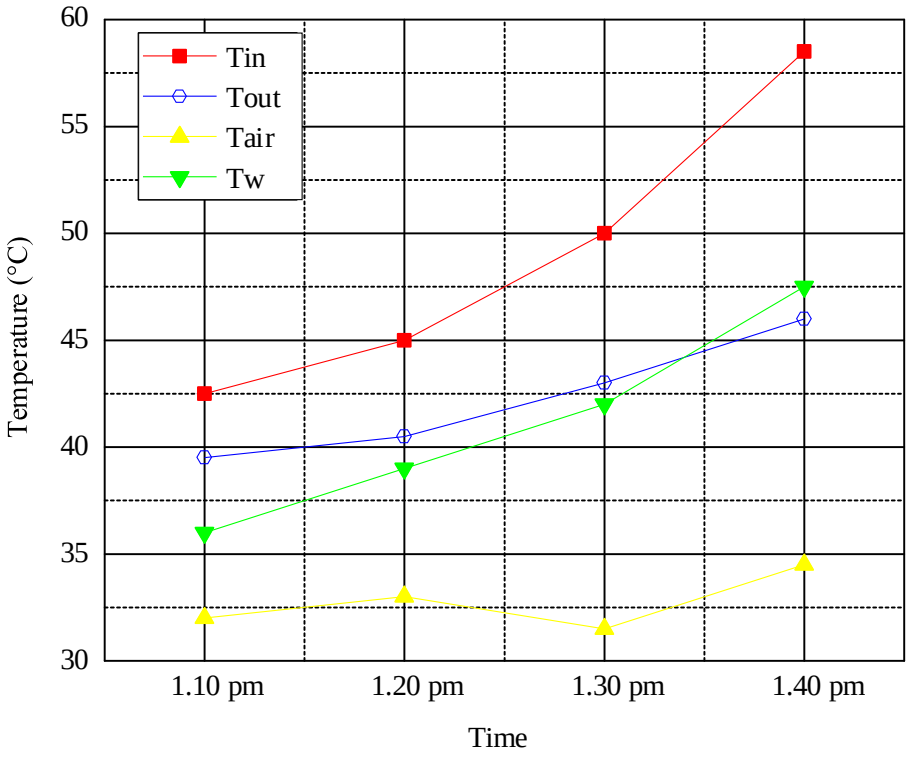


Figure 6. Salt water at 20g/L as HTF.

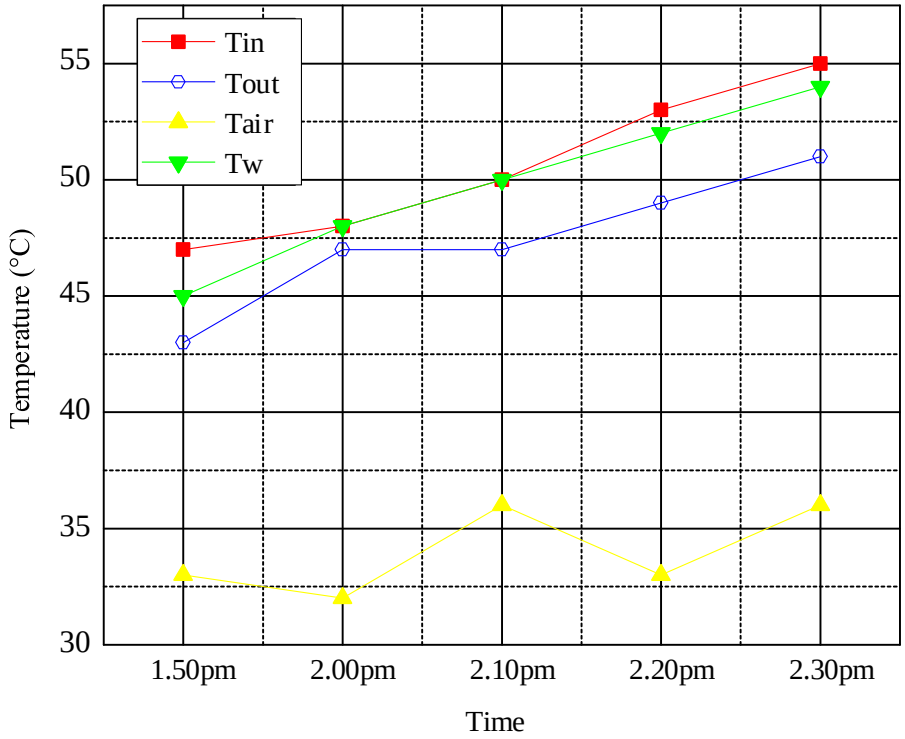


Figure 7. Salt water at 20g/L as HTF with polystyrene as pipe insulation.

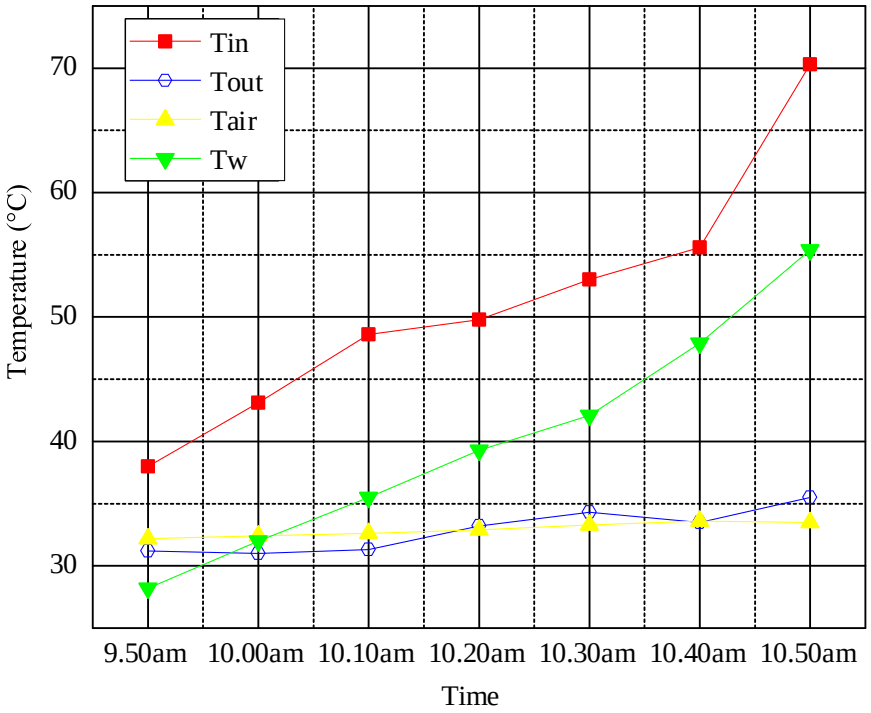


Figure 8. Salt water at 20g/L as HTF with acrylic foam as pipe insulation.

As seen from Fig. 4, water produces some appreciable results as a HTF but still is not good enough since we can observe from the graph that Tin and Tout are quite close. This indicates that the rate of heat transfer to the water in the tank is not that favourable. The results as shown in Fig. 5 demonstrate that Salt Water at 10g/L perform almost similarly as water thermally when compared to the results of water as HTF as seen in Fig. 4. It is observed that Salt Water at 20g/L is able to achieve much higher input temperatures as compared to water and the 10g/L salt solution.

The temperature of the HTF leaving the heat exchanger is much lower, indicating good heat transfer properties of the liquid. From Fig. 7 and Fig. 8, the temperature of water inside the tank quickly rises to the temperature of the HTF entering the heat exchanger. This indicates that the polystyrene and acrylic insulations helped reduce some heat loss from the copper pipe and hence the HTF flows with more heat capacity to be released into the water having a lower temperature. It is also observed that the temperature of the HTF leaving the heat exchanger is lower than the temperature of water, indicating that the salt water is able to transfer the heat to the water effectively. Almost all the graphs for the different configurations show a similar trend where Tair remains relatively constant throughout the experiment while Tin, Tout and Tw continue to increase as the time goes by in the presence of the sun. Tout is always lower than Tin and Tw.

This is because as the water enters the heat exchanger, the heat is absorbed by the water inside the tank causing T_w to increase while temperature leaving the heat exchanger decreases. Therefore, Tout is always lower than Tin. Also, Tw follows the same trend as Tin since the temperature of the water in the water tanks depends on the temperature of the HTF entering the heat exchanger. However, from the results obtained, Tin is always higher than Tw due to the closed loop not operating in an ideal scenario as there is heat loss to the environment. Therefore, the heat transfer between the HTF and the water inside the tank is not 100% efficient. Table 1 shows the efficiency based on Eq. 2 mentioned above and solar radiation, G_b averaging at 982W/m^2 for the first three results and 710.3W/m^2 for the last (for solar radiation data measured using a pyranometer).

Table 1. Efficiency of each experiment

HTF	**T_{out} (℃)**	**T_{air} (℃)**	**η_T *(%)***
Water	43	31.3	61.8%
Salt Water at 10g/L	43.2	31.7	61.9%
Salt Water at 20g/L	44.5	33.8	62.2%
Salt water at 20g/L with polystyrene as pipe insulation	46.3	36	62.4%
Salt water at 20g/L with acrylic foam as pipe insulation	34.1	33.3	66.2%

The efficiency calculation has been optimised to reflect more accurate results compared to the results previously presented in paper [1]. The main difference between the results of the previous paper and this one is that only stabilised experimental data have been considered in the efficiency calculation. By considering only the experimental results of a system which has been thermally stabilised eliminates cold start results of the system which affects the accuracy of efficiency calculation results. The thermal efficiency equation used previously was not optimised for a closed loop system with heat exchanger, while the efficiency calculation of this paper uses Eq. 2 which has been optimised for PVT systems with cylindrical heat exchangers. Comparing the results obtained, salt water at 20g/L with acrylic foam as pipe insulation is found to have the best thermal efficiency with a 4.4% improvement from using only water as HTF, a 4% improvement from using salt water at 20g/L without insulation and a 3.8% improvement from using polystyrene as insulation.

Adding 10g of salt per litre of water slightly improves the thermal efficiency by 0.1% and can be observed to absorb heat faster when compared to water, taking only 30 minutes to reach the maximum temperature for Tin while water takes 40 minutes, as observed in Fig. 5. Hence, adding salt helps dissipate heat faster from the system but 10g/L is not enough for an effective heat transfer to the water tank. This is improved by increasing the salt concentration to 20g/L which yields an efficiency improvement of 0.3% and is able to achieve much higher Tin temperatures while efficiently transferring the heat to the water tank, thus keeping low Tout temperatures. Compared to the 10g/L concentration, the 20g/L concentration improves Tin by 25.5%.

3.2 Voltage Characteristics

Fig.10 shows an insight of how temperature affected the panel and the cooling period during which voltage was restored. From Fig. 10 we can observe that as the temperature of the PV panel increases, the voltage decreases. The voltage was restored by cooling the panel as highlighted by the dashed lines showing the PV panel's cooling phase. Table 2 below also shows that the voltage preserves its restored state even under lower sunlight radiation when under a low operating temperature after being cooled. The cooling phase was from around 11.50am until 12.20pm.

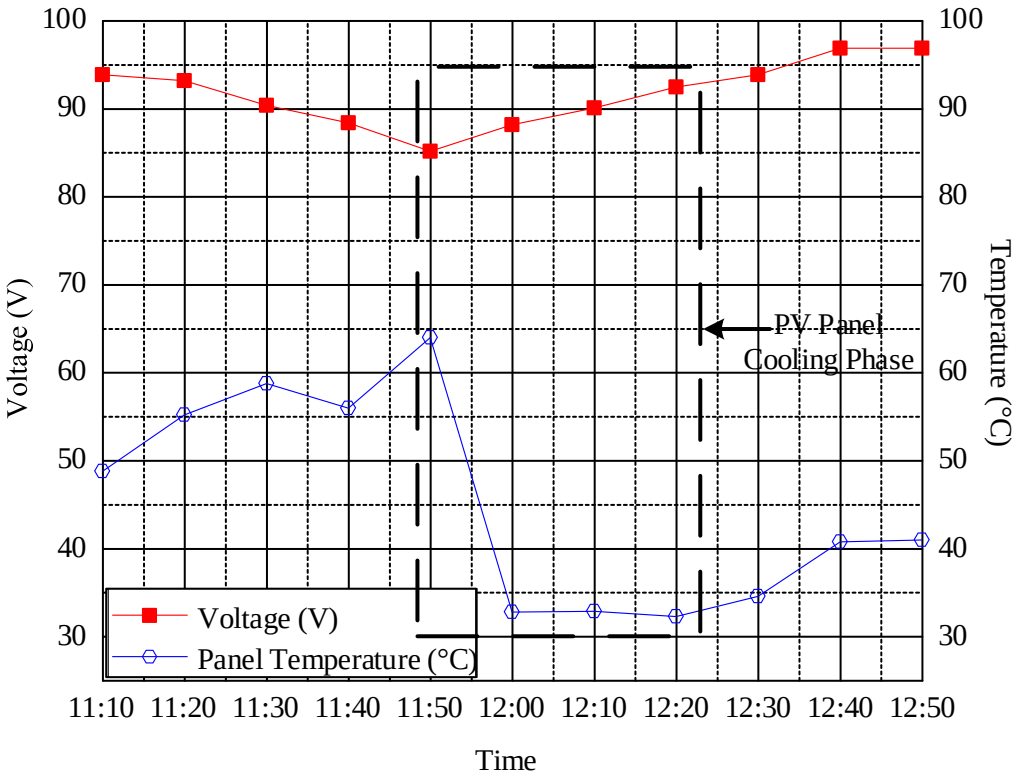


Figure 10. PV voltage compared with PV temperature with cooling enabled.

Table 2. Voltage Supply compared with Solar Radiation and Temperature.

Time	Voltage (V)	Solar Radiation (W/m^2)	Panel Temperature ($^{\circ}C$)
11:09:57	93.9	936	48.8
11:19:57	93.2	1005	55.2
11:29:57	90.4	1040	58.8
11:39:57	88.4	1037.1	56
11:49:57	85.2	1118.9	64
11:59:57	88.2	132.2	32.8
12:09:57	90.1	107.5	32.9
12:19:57	92.5	205.9	32.3
12:29:57	93.9	889.3	34.6
12:39:57	96.9	648.8	40.8
12:49:57	96.9	983.8	41

Considering the maximum and minimum voltage difference before and after cooling, a maximum improvement of 11.7% was noted when the panel's temperature was reduced by 24.1°C. This enabled the PV panel to achieve 96.9% of its rated maximum peak voltage even under lower solar radiation conditions (measured using a pyranometer) which would not have been possible without cooling the panel. However, when the PV panel is reintegrated onto the Parabolic Trough as per the experimental setup of [10] for a general comparison, the thermal efficiency of the Parabolic Trough drops by almost 40%. Hence, it would be recommended to avoid placing the panel on top of the Parabolic Trough so as not to reduce solar radiation transmittance. It would be preferable to use panels of higher transparency if their placement are essentially required to be on top of the Parabolic Trough.

4. Conclusion

Through the experiments conducted involving the thermal analysis of three HTFs with the Parabolic Trough PVT setup, it was concluded that the best out of the three HTFs was the solution with higher salt concentration. Applying insulation to the concentrator pipe yielded higher thermal efficiencies. The acrylic foam performed better than the polystyrene insulation due its advantageous thermal properties. Salt water at 20g/L with acrylic foam as pipe insulation was found to have the best thermal efficiency with a 4.4% improvement from using only water as HTF, a 4% improvement from using salt water at 20g/L without insulation and a 3.8% improvement from using polystyrene as insulation. The thermal performance may improve using higher salt concentrations but factors as corrosion caused by salt must be considered and evaluated in terms of performance over system durability and maintenance costs. The cooling technique used for restoring the voltage drop of the PV panel due to heat in this research showed its potential as a hybrid PVT system where the heat build-up can be reused or stored. The experiments were performed under no load as a study of the maximum voltage the panel can reach compared to its rated voltage. The results obtained during this research are an improvement from previous researches in terms of energy-exergy balance and efficiency. Hence, the outcomes of this study are in line with the project's

research questions and objectives. The next step of continuing this research would be to analyse the panel's electrical efficiency when connected to a load as per its rated capacity. The electrical efficiency would be an indication of where this type of solar panel stands in terms of meeting the power demand and amount of power generated as compared to the power produced per unit area by the sun (Solar Radiation).

Acknowledgements

The authors wish to express the financial support from the School of Engineering, Taylor's University, Malaysia under the SOE research grant.

References

[1] R. Ramsurn, "Investigation of Energy and Exergy Configurations for Parabolic Trough Photovoltaic/Thermal designs," in *IEEE Student Conference on Research and Development (SCOReD)*, 2017, p. 6.

[2] W. Hoffmann, "PV solar electricity industry: Market growth and perspective," *Sol. Energy Mater. Sol. Cells*, vol. 90, pp. 3285–3311, 2006.

[3] S. Kalogirou, "Photovoltaic Systems," in *Solar Energy Engineering : Processes and Systems*, Elsevier/Academic Press, 2009, p. 760.

[4] Boyle Godfrey, "Solar photovoltaics," in *Renewable Energy: Power for a Sustainable Future*, Third Edit., OUP Oxford, 2012, pp. 75–115.

[5] H. Machrafi, "Enhancement of a photovoltaic cell performance by a coupled cooled nanocomposite thermoelectric hybrid system, using extended thermodynamics," *Curr. Appl. Phys.*, vol. 17, no. 6, pp. 890–911, 2017.

[6] A. H. Jaaz, H. A. Hasan, K. Sopian, M. H. Bin Haji Ruslan, and S. H. Zaidi, "Design and development of compound parabolic concentrating for photovoltaic solar collector: Review," *Renew. Sustain. Energy Rev.*, vol. 76, pp. 1108–1121, 2017.

[7] A. Shukla, K. Kant, A. Sharma, and P. H. Biwole, "Cooling methodologies of photovoltaic module for enhancing electrical efficiency: A review," *Sol. Energy Mater. Sol. Cells*, vol. 160, no. November 2016, pp. 275–286, 2017.

[8] R. Wang, W. Qu, J. Sun, and H. Hong, "An On-site Test Method for Optical Efficiency of Large-size Parabolic trough Collectors," *Energy Procedia*, vol. 105, pp. 486–491, 2017.

[9] D. Kumar and S. Kumar, "Simulation Analysis of Overall Heat Loss Coefficient of Parabolic trough Solar Collector at Computed Optimal Air Gap," *Energy Procedia*, vol. 109, no. November 2016, pp. 86–93, 2017.

[10] L. C. Sun, "Thermal Performance Evaluation of Parabolic Trough-based Transparent PVT System," Taylor's University Malaysia, 2016.

eureca 2017 – Conference Paper
Paper Number 2EE07

Vertical Wind Energy Configuration for Low Velocity Regime

Teow Wei Wei[1*], Aravind CV[1], Charles R. Sarimuthu[1]

[1]*School of Engineering, Taylor's University, Malaysia.*

[*]twwei95@gmail.com

Abstract

In the 21st century, every country is seeking an alternative source of energy especially the renewable sources. There are considerable developments in the wind energy technology in recent years and in more particular on the vertical axis wind turbine (VAWT) as they are modular, less installation cost and portable in comparison with that of the horizontal axis wind turbine (HAWT) systems. The cut-in speed of a conventional wind turbine is 3.5 m/s to 5 m/s. Mechanical geared generators are commonly found in wind technology to step up power conversion to accommodate the needs of the generator. Wind turbine gearboxes suffer from overload problem and frequent maintenance in spite of the high torque density produced. However, an emerging alternative to gearing system is Magnetic Gear (MG) as it offers significant advantages such as free from maintenance, and inherent overload protection. In this project, numerical analysis is done on designed magnetic gear greatly affects the performance of the generator in terms of voltage generation. Magnetic flux density is distributed evenly across the generator as seen from the uniform sinusoidal output waveform. Consequently, the interaction of the magnetic flux of the permanent magnets have shown no disturbance to the output of the generator as the voltage generated shows uniform waveform despite the rotational speed of the gears. The simulation is run under low wind speed and the results show that the generator starts generating voltage of 240 V at wind speed of 1.04 m/s. This shows great improvement in the operating capability of the wind turbine.

Keywords: vertical axis wind turbine, mechanical gear, magnetic gear, finite element analysis

1. Introduction

As oil reservoirs are running low and the increase in human population with demand, every country is seeking for an alternative source of energy especially the renewable energy sources. Due to the concerns on environmental issues, the development and application of renewable and clean energy are gaining more attention among the society. The wind technology and photovoltaic (PV) systems are found to be part of the two fast growing technologies in the effort of generation of cleaner energy.

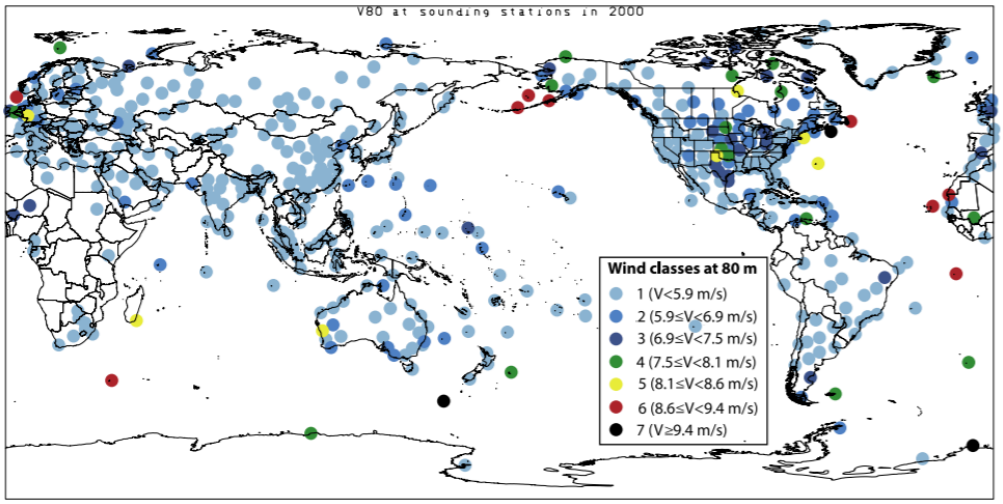


Figure 1.1: World map of wind speed extrapolated to 80 m and averaged over all days of the year 2000 [2]

The only few countries with substantial wind speed are Japan, a few islands in China Sea, Guam and Mariana Islands. The majority of these areas are not suitable for wind power generation. Generally, Southeast Asia has poor wind potential on over 80% of the territory [2]. As seen in Figure 1.1, countries situated near or on the equator experience low wind speed due to the different direction of the wind that cancel on each other at the equator.

Based on the wind speed characteristic of Malaysia recorded by the Malaysian Meteorological department, typical wind speed ranges from as low as 0 m/s to 13 m/s with the highest mean daily wind speed of 3.8 m/s recorded in Mersing, Johor [3]. Wind turbines in Mersing with a cut-in speed of 2.5 m/s would operate for 5084 hours a year [4]. Technically, the wind energy potential in Malaysia is very limited due to the low wind speed condition.

Industrial wind turbines fall into two general category based on the axis of rotation of the wind turbine with respect to the ground surface and they are: (a) horizontal axis wind turbine (HAWT), and (b) vertical axis wind turbine (VAWT). A conventional wind turbine has a cut-in speed of 3.5 m/s to 5 m/s and this is the minimal speed required to move the wind turbine blades into motion due to its inertia. At rated speed of 12 m/s, the generator is operating at its ideal condition with highest efficiency of power generation. When the wind speed is very high (above cut-out speed of 25 m/s), the wind turbine must be shut down due to mechanical constraints, while when the speed is very low (below cut-in speed), the operation is also in need of cutting off due to the variable low wind speed which is unable to move the generator at a constant speed.

Many wind turbine system works on the principle of the wind energy conversion system (WECS) which can be divided under the aspects of aerodynamic, mechanical and electrical [5]. Critically optimizing each aspect helps in producing the most

efficient output possible. WECS is projected and simplified in the form of block diagram as shown in Figure 1.2.

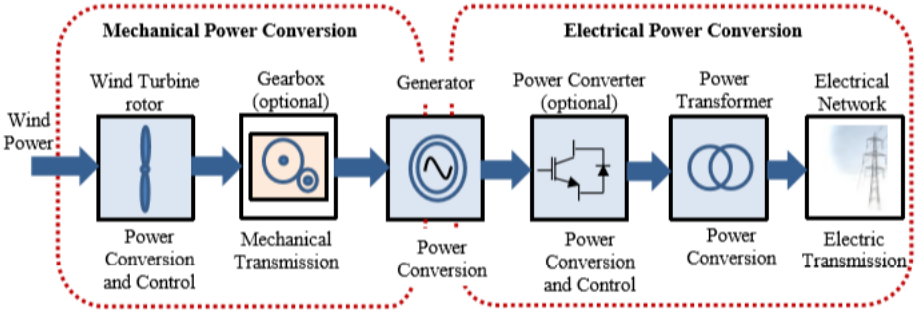


Figure 1.2: Block diagram of WECS components viewed in aspects of mechanical and electrical [5]

High-speed electric generators are commonly found in many conventional wind turbines typically to step up the relatively low rotational speed of the rotor blades to accommodate the needs of the generator [8]. As a result, a gearbox is often used in the system to perform this function and since the speed increase needed is important, planetary mechanical gear type of configuration is oftentimes used to design the gearboxes of wind turbine [8]. Mechanical gears and gearboxes are commonly employed for speed change and torque transmission in various industrial applications [9], [10]. Many wind turbine gearboxes suffer from overload problem and frequent maintenance in spite of the high torque density produced by mechanical gears [9].

In contrast, an emerging alternative to gearing system is Magnetic Gear (MG) as it offers significant pros such as reduced noise and vibration, free from maintenance, and inherent overload protection [11]. In recent years, MGs have been widely used in the field of aerospace, marine-propulsion, and renewable energy [12]. Inspired by MGs, many Permanent Magnet (PM) machines with integration of MGs are proposed to produce a higher power density than the conventional PM machines integrated with mechanical gears [12]–[14]. Nevertheless, MGs have yet to be seen to replace mechanical gears in the wind energy technology despite it being a promising technology for various torque-demanding applications due to the cost of permanent magnets.

2. Theoretical Framework

2.1 Design Concept

The conventional cut-in speed of a wind turbine is about 3.5m/s - 5m/s. A typical wind generator operates on the principle of motoring and generating. At speed lower than the cut-in, the generator operates as a motor with the help of pitch control in order to put the stationary wind turbine into motion due to the naturally occurring inertia of turbine blades. Once it reaches the cut-in speed, the generator switches into two modes, generating and motoring. In this region, the motor continues to operate until the wind turbine acquires enough momentum to match the force provided by the wind speed. The machine then switches to full generation mode as the wind turbine is capable of rotating under the wind speed (also known as rated wind speed). The operational modes discussed above is portrayed below as shown in Figure 2.1.

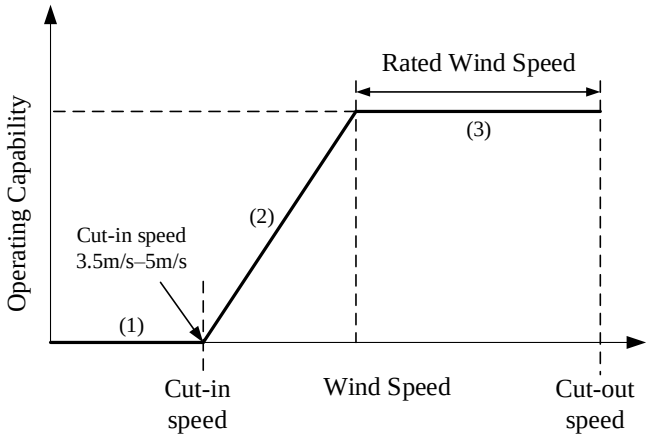


Figure 2.1 Operational modes of a typical wind turbine

Optimisation of the wind turbine system in the sense to increase the power generation capability on low wind speed condition is explained in Table 2.1 below.

Table 2.1 Optimised modes of wind turbine system

Mode	Description
Motoring & Generating	Power generation capability will be increased with the proposed magnetic gear even under a low wind operating conditions with constant output.
Generating	In this mode, the operating mode is ideal and with the permanent magnet used to integrate in magnetic gear configuration, constant speed of the generator is able to be maintained.

The conventional mechanical structure of wind turbine system involves the use of mechanical gears and this is causing one of the major issues in the free revolution of turbine structure as the coupling between the gears induces some inertia to the system. Also, this results in the mechanical losses, friction, wear and tear due to which the gears are in contact. A magnetic gear, separated between the static structure and the revolving turbine, is proposed to address this concern. Figure 2.2 below shows the magnetic circuit of the ORIPMS generator and geared ORIPMS generator.

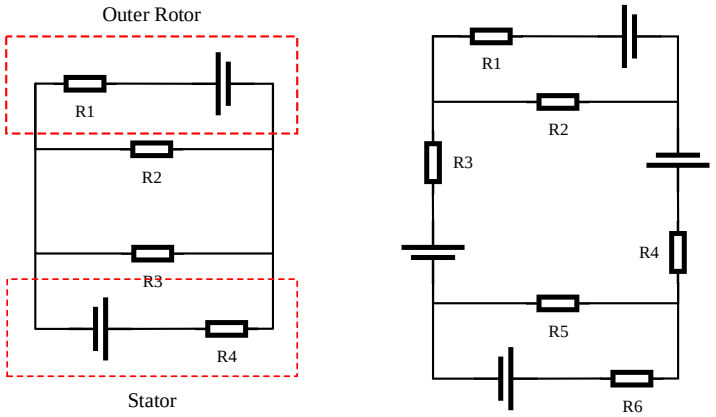


Figure 2.2 (a): Equivalent magnetic circuit of ORIPMS and (b): Geared ORIPMS

2.2 Magnetic Gear Ratio Design Concept

In a geared wind turbine mechanism, mechanical gear ratio or transmission ratio is the ratio of number of driver gear (attached to wind turbine) over the number of driven gear (attached to generator). The magnetic gear transmission ratio is analogous to mechanical gear principle and is discussed in the following. The magnetic gear ratio is expressed in Equation (1):

$$\text{Gear ratio, } G_r = \frac{V_{high}}{V_{low}} = \frac{T_{driving\ gear}}{T_{driven\ gear}} = -\frac{N_{low}}{N_{high}} \quad (1)$$

where V_{high} and V_{low} are rotational speed of high speed gear and low speed gear, respectively. $T_{driver\ gear}$ and $T_{driven\ gear}$ represent number of mechanical teeth of driver gear and driven gear, respectively. N_{high} and N_{low} are number of pole-pairs of high speed gear and low speed gear, respectively.

In order to attain the highest torque density, the number of pole pairs on each of the rotors should satisfy the following relation:

$$N_{low} = N_{ferro} - N_{high} \quad (2)$$

where N_{ferro} is the number of ferromagnetic pole-pieces.

The selection of appropriate combination of pole-pairs for the two rotating gears to produce a required gear ratio should take into consideration the torque ripples that may affect the performance of the magnetic gear. Torque ripple or cogging torque is caused by the interaction of the permanent magnets with the ferromagnetic pole-pieces. Therefore, cogging torque factor is defined to estimate the level of torque ripple on the performance (as shown in Equation (3)). The higher the factor, the higher the cogging torque is. The minimum value of this factor is unity ($C_T = 1$), which initiates a possible for good design selection.

$$C_T = \frac{N_{high} N_{ferro}}{LCM(N_{high},\ N_{ferro})} \quad (3)$$

3.5 Relationship between the mechanical and electrical power in machine

The mechanical power generated, $P_{gen,low}$ by the low speed gear is proportional to torque and speed of the gear, as shown in Equation (4):

$$P_{gen,low} = T_{low} \cdot \omega_{low} \quad (4)$$

where T_{low} is torque generated by low speed gear and ω_{low} is the angular velocity of the low speed gear. As the speed the lower speed gear is proportional to the speed of higher speed gear with respect to the gear ratio, the relationship of the speeds affected by the gear ratio, N is as shown in Equations (5) and (6).

$$v_{low} \propto v_{high} \quad (5)$$

$$v_{low} = G_r \cdot v_{high} \quad (6)$$

As the speed is proportional to angular velocity, the mechanical power generated by the ring magnetic gear, $P_{gen,high}$ is correlated to the gear ratio as shown in Equations (7) and (8):

$$P_{gen,high} = T_{high} \cdot \omega_{high} \quad (7)$$

$$P_{gen,high} = T_{high} \cdot G_r \cdot \omega_{low} \quad (8)$$

where T_{high} is torque generated by high speed gear and ω_{high} is the angular velocity of the high speed gear.

Electrical power generated by the generator is expressed as in Equation (9):

$$P = V \cdot I \cos\theta \quad (9)$$

Mechanical power from the high speed gear is converted directly to electrical power generated by generator. With this, we can say that mechanical power is equal to the electrical power output and the relationship is expressed as in Equation (10):

$$P_{gen,high} = P_{elec} \quad (10)$$

By equating Equation (7) and (8), we get:

$$T_{high} \cdot G_r \cdot \omega_{low} = V \cdot I \cos\theta \quad (11)$$

Therefore, by increasing the gear ratio of the magnetic gears, the electrical power output will increase relatively based on Equation (11).

3. Methodology

To propose a novel magnetic-geared ORIPMS generator using JMAG in a 2D model mode, a methodology based on Figure 3.1 is designed and followed as shown below.

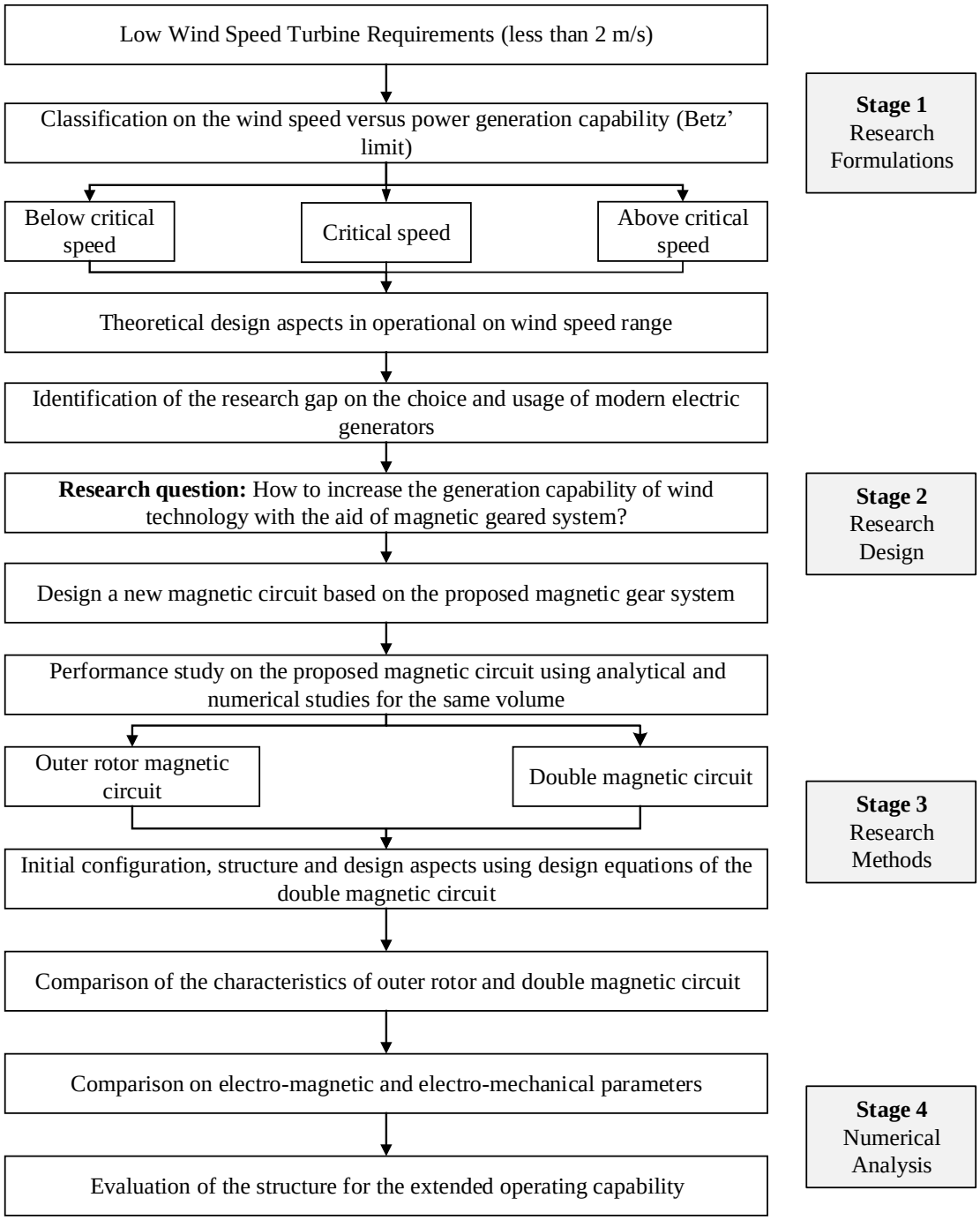


Figure 3.1 Flowchart of research methodology

Outer Rotor Internal Permanent Magnet Synchronous (ORIPMS) generator (as shown in Figure 3.2) is used employed in this project due to its minimal ripple harmonics and satisfactory amount of power produced. To further increase the efficiency of power produced of this generator, magnetic gear is introduced by increasing the flux density of the machine (Figure 3.3). FEM analysis is shown and analysed in this section below.

Comparison between the two models is done to observe the deviation of the results of the machines.

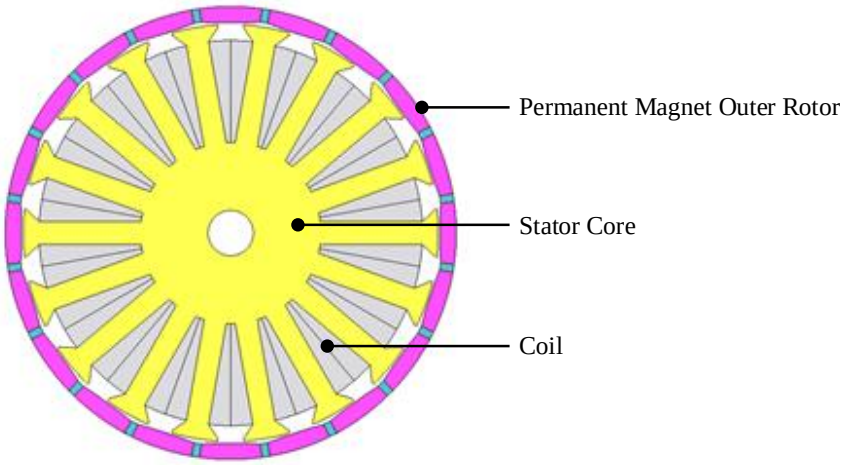


Figure 3.2 Outer Rotor Internal Permanent Magnet Synchronous (ORIPMS) Generator

Table 3.1 Parameters of ORIPMS Generator

Parameter	Value
Number of poles on high speed gear	100
Number of ferromagnetic pole-pieces	24
Number of poles on low speed outer rotor	20
Outer diameter of rotor	50.0 mm
Inner diameter of rotor	46.5 mm
Outer diameter of PM	50.0 mm
Inner diameter of PM	47.0 mm
Width of stator pole	5.0 mm
Width of stator teeth	6.968 mm
Length of stator pole	22.5 mm
Diameter of shaft	5.0 mm
Length of air gap	0.5 mm
Stack length	50.0 mm
Outer diameter of stator	46.0 mm
Inner diameter of stator	5.0 mm
Outer diameter of coils	42.5 mm
Inner diameter of coils	20.0 mm
PM pole-arc	2 degrees
Rotor pole-arc	16 degrees
Stator Teeth pole-arc	13 degrees

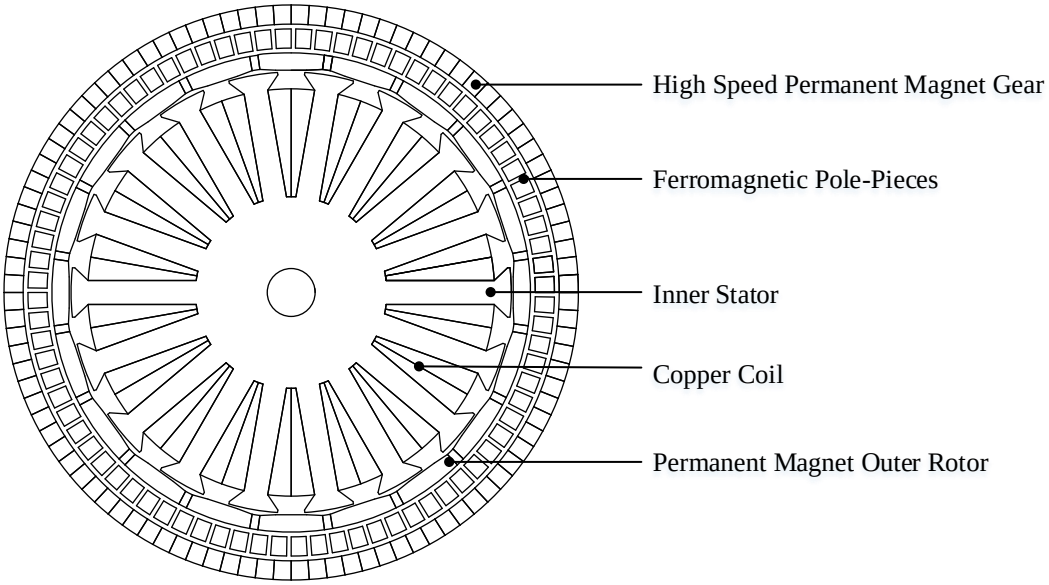


Figure 3.3 ORIPMS generator with magnetic gear

4. Results and Discussion

4.1 Magnetic Flux Density Characteristics

Magnetic flux density behaviour of any generator is the primary evaluation that should be considered in designing a machine as this analysis fundamentally determines the output of the machine. In this project, the proposed magnetic gear has a direct interaction with the outer rotor permanent magnets and this might affect the output quality of the machine negatively. Through JMAG simulation, the magnetic flux density of the generator rotating at 500rpm and magnetic gear rotating at 100rpm with a gear ratio of 1:5 is shown in Figure 4.1 below.

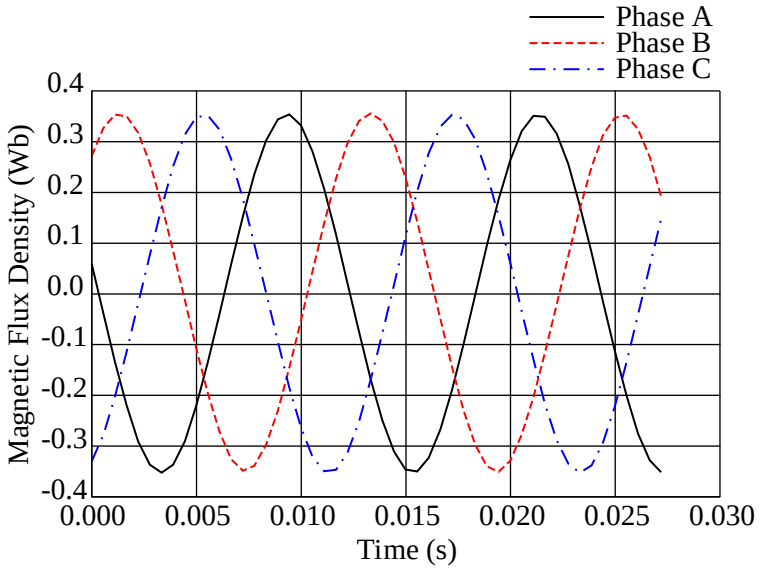


Figure 4.1: Magnetic flux density of magnetic gear rotating at 100 rpm

Fundamentally, operation principle of a generator is defined by Faraday's Law, which states that electromotive force induced in a coil is proportional to the rate of

change of the number of magnetic flux lines passing through the surface enclosed by the coil. Therefore, with this attribute, a sinusoidal induced output voltage is expected consequently and it is proven in the following section.

4.2 Generating Operation: Voltage generation at various wind speeds

Output voltage generated is presented with respect to different speed from 100 rpm to 700 rpm. Voltage produced increases with the wind speed as graphed in Figure 4.2. Also, the generator starts generating voltage even at speed lower than the conventional cut-in speed of 3.5 m/s to 5 m/s. The generator achieves a voltage of 240 V at speed of 200 rpm or equivalent wind speed of 1.04 m/s in which this is the standard voltage supply of household in Malaysia. This means that generating voltage at low wind speed condition is achievable.

Table 4.1: Various speed versus voltage generated (rms)

Speed (rpm)		Equivalent wind speed (m/s)	Voltage Generated (V_{rms})			Average RMS Voltage (V_{rms})
Magnetic Gear	Generator Outer Rotor		Phase A	Phase B	Phase C	
100	500	0.52	129.801	123.860	130.585	128.082
200	1000	1.04	253.614	253.385	253.883	253.627
300	1500	1.57	375.507	370.097	375.525	373.710
500	2500	2.62	588.734	585.307	589.443	587.828
700	3500	3.67	752.875	751.108	753.968	752.650

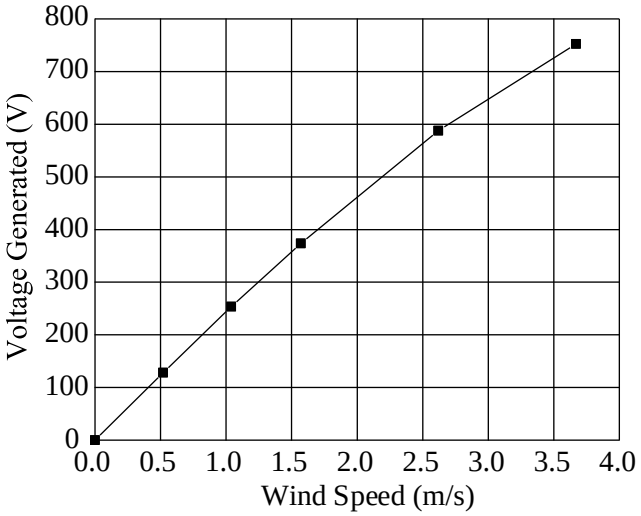


Figure 4.2: Voltage generated at various wind speeds

As expected based on theoretical knowledge, voltage generated increases with wind speed. The graph is increasing linearly from 0 m/s to 2 m/s but the graph deviates a little as the wind speed continues to increase. This is possible because the generator is starting to fall into the saturation region as the rated power of this machine is only 500W. Therefore, for this chosen generator, the size of it is only capable for low rotational speed. However, to increase its capacity, a small increment in diameter of the machine results in squared of the rated power.

4.3 Capability of Designed Magnetic-Geared Generator Topology

Based on the evaluation made above, it can be viewed that the operating range of wind turbine is improved on the low wind speed range. With this, the magnetic-geared generator enables the wind turbine to operate before the typical cut-in speed of 3.5 m/s to 5 m/s. The conventional and optimised operating capability are illustrated in the following.

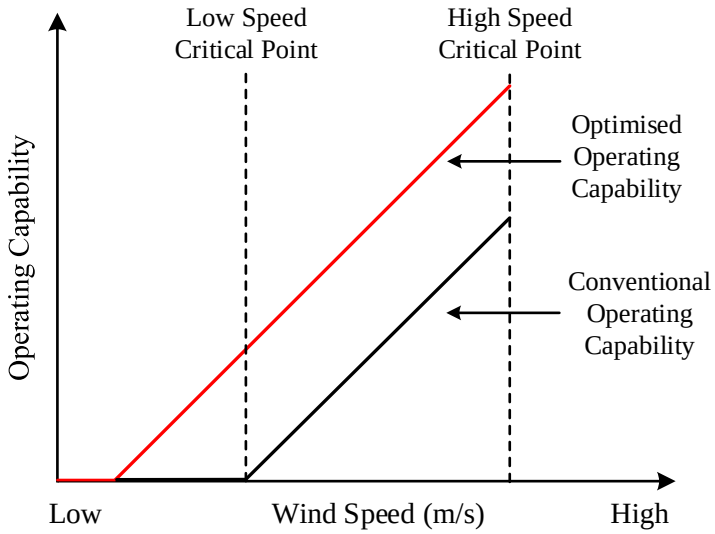


Figure 4.3: Illustration of optimised operating capability

5. Conclusion

In conclusion, designed magnetic gear greatly affects the performance of the generator in terms of voltage generation. Magnetic flux density is distributed evenly across the generator as seen from the uniform sinusoidal output waveform. Consequently, the interaction of the magnetic flux of the permanent magnets have shown no disturbance to the output of the generator as the voltage generated shows uniform waveform despite the rotational speed of the gears. The simulation is run under low wind speed and the results show that the generator starts generating voltage of 240 V at wind speed of 1.04 m/s. This shows great improvement in the operating capability of the wind turbine and the objective of this project has been achieved. For future work, the magnetisation pattern of permanent magnets should be manipulated to observe the change in the output and this opens more possibilities for optimization of this model. The numerical analysis result should be proven using analytical method by studying on the expressions formulated by other researchers for a more promising outcome.

References

[1] J. Damota, I. Lamas, A. Couce, and J. Rodríguez, "Vertical Axis Wind Turbines : Current Technologies and Future Trends," *Int. Conf. Renew. Energies Power Qual. - La Coruña (Spain), 25th to 27th March, 2015*, vol. 1, no. 13, p. 6, 2015.

[2] C. L. Archer, "Evaluation of global wind power," *J. Geophys. Res.*, vol. 110, no. D12, p. D12110, 2005.

[3] "General Climate Information - Malaysian Meteorological Department," *met.gov.my*, 2016. [Online]. Available: http://www.met.gov.my/in/web/metmalaysia/climate/climatechange/climateinformation. [Accessed: 14-Nov-2017].

[4] A. Belhamadia, M. Mansor, and M. A. Younis, "A study on wind and solar energy potentials in Malaysia," *Int. J. Renew. energy Res.*, vol. 4, no. 4, pp. 1042–1048, 2014.

[5] M. R. M. Altimania, "Modeling of Doubly-Fed Induction Generators Connected to Distribution System based on eMEGASim® Real-Time Digital Simulator," *J. Chem. Inf. Model.*, vol. 53, no. 9, pp. 1689–1699, 2013.

[6] G. Semrau, S. Rimkus, and T. Das, "Nonlinear Systems Analysis and Control of Variable Speed Wind Turbines for Multiregime Operation," *J. Dyn. Syst. Meas. Control*, vol. 137, no. 4, 2015.

[7] M. H. Chiang, "A novel pitch control system for a wind turbine driven by a variable-speed pump-controlled hydraulic servo system," *Mechatronics*, vol. 21, no. 4, pp. 753–761, 2011.

[8] C. Nutakor, A. Klodowski, J. Sopanen, A. Mikkola, and J. I. Pedrero, "Planetary gear sets power loss modeling: Application to wind turbines," *Tribol. Int.*, vol. 105, no. September 2016, pp. 42–54, 2017.

[9] K. Atallah and D. Howe, "A novel high-performance magnetic gear," *IEEE Trans. Magn.*, vol. 37, no. 4, pp. 2844–2846, 2001.

[10] K. Atallah, J. Wang, and D. Howe, "A high-performance linear magnetic gear," *J. Appl. Phys.*, vol. 97, no. 10, pp. 26–29, 2005.

[11] W. H. X. Li, K.-T. Chau, M. Cheng, "Comparison of magnetic-geared permanent magnet machines," *Prog. Electromagn. Res.*, vol. 133, no. 2013, pp. 177–198, 2013.

[12] S. Niu and Y. Mao, "A Comparative Study of Novel Topologies of Magnetic Gears," *Energies*, vol. 9, no. 10, p. 773, 2016.

[13] W. Li, K. T. Chau, and J. Z. Jiang, "Application of linear magnetic gears for pseudo-direct-drive oceanic wave energy harvesting," *IEEE Trans. Magn.*, vol. 47, no. 10, pp. 2624–2627, 2011.

[14] S. Niu, S. L. Ho, and W. N. Fu, "Performance analysis of a novel magnetic-geared tubular linear permanent magnet machine," *IEEE Trans. Magn.*, vol. 47, no. 10, pp. 3598–3601, 2011.

[15] M. M. Moh Saad and N. Asmuin, "Comparison of Horizontal Axis Wind Turbines and Vertical Axis Wind Turbines," *IOSR J. Eng. www.iosrjen.org ISSN*, vol. 4, no. 8, pp. 2250–3021, 2014.

Traffic Monitoring Using Bluetooth

Neow Way Shyun[1*], Edwin Chung Chin Yau[2]

[1]*School of Engineering, Taylor's University, Malaysia*

[2]*School of Engineering, Taylor's University, Malaysia*

[*]ws.neow@gmail.com

Abstract:
Various research have been made on method for traffic monitoring and Bluetooth is one of the potential method for research. Nowadays, Bluetooth devices have widely being implement such as car Bluetooth radio, Bluetooth on smart phone, Bluetooth on laptop and others. Each Bluetooth device is assigned with a unique MAC ID which can be interrogated with a Bluetooth detector by inquiring at various time. By placing two Bluetooth detectors on a section of a road, the Bluetooth detector will record the passing vehicle Bluetooth device's MAC ID at each time. Average speed of travelling vehicle can be estimate by calculating the duration of vehicle passing through the two nodes. However, the study on the range of a single Bluetooth detector as a means to estimate the average speed of vehicle at that location has not been the focus of previous research. Furthermore, there is a potential of that using multiple Bluetooth detector at a single node can have the ability to improve the accuracy of the system. This research will be focusing on understanding the protocol of Bluetooth, implementation of Bluetooth detectors, analyse data to determine whether the average speed of traveling Bluetooth devices can be estimated with multiple Bluetooth detectors at a point and determine if the accuracy of the system will be improved with the use of multiple readers. A total of two tests shall be conducted which are static test and dynamic test. Static test is to identify the scanning range of the Bluetooth detector. Dynamic test is to study the performance of Bluetooth detector and whether multiple Bluetooth detectors at a node will improve the performance.

Keywords: Bluetooth, traffic monitoring

1. Introduction

Traffic monitoring is a widely researched topics. Various methods have been proposed to use for traffic monitoring such as image processing, RFID, Bluetooth and others. One of the importance feature of traffic monitoring device is able to estimate the traffic condition and provide accurate data to road users.

Image processing is one of the method being research to use for traffic monitoring. The method would mainly focus on capturing the traveling vehicles at two points to estimate the average traveling speed of vehicle between two points. Static background objects will be filter away. However, image processing will involve with complex coding and higher cost for advance monitoring camera[1].

RFID sensor is another method being researched for use in traffic monitoring. The method of RFID sensor capturing traveling vehicles will record its RFID tags. By recording the vehicle passing through two RFID readers along a section of the road, traffic condition can be estimated[2]. However, according to Ahmad et al.[3], RFID tags have personal information such as attach to cash, possessions, clothing, or even entrenched within people. This had raise concerns about privacy being violate through RFID.

Aside from the method mention above, Bluetooth is also one of the method being research for traffic monitoring. Bluetooth is increasingly being implement in various devices nowadays, such as car Bluetooth radio, Bluetooth in smart phones, Bluetooth in laptop, Bluetooth gadgets and others. One of the few advantages that Bluetooth possess is that it is low cost and low power consumption. From the research by Lee et al. [4] and Saad et al. [5], comparing Bluetooth to other wireless devices such as Wi-Fi, Zig Bee and ultra-wideband (UWB), it consumes much less energy. Figure 1 shows the comparison of power consumption of Bluetooth with other wireless protocol.

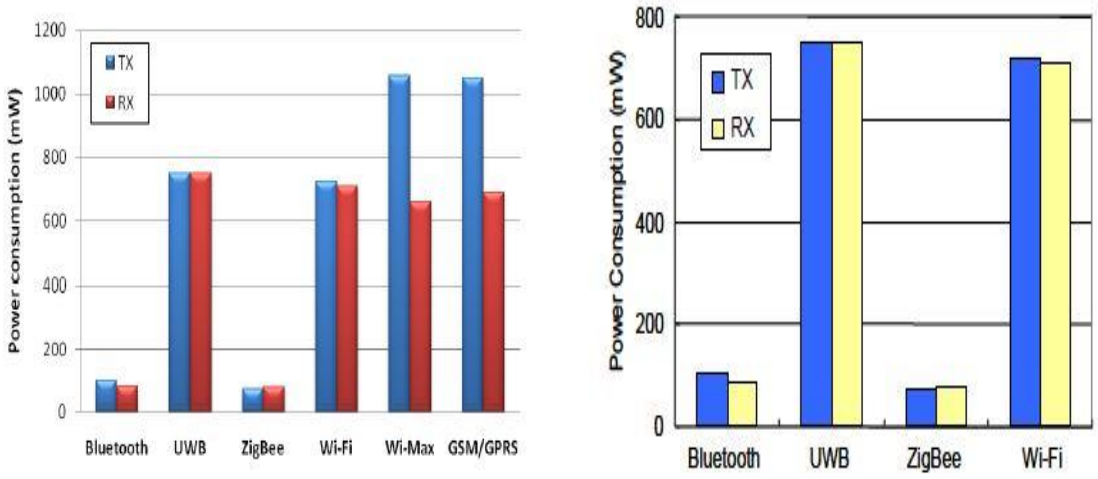


Figure 40: Comparison of power consumption of various wireless communication protocol (Left - [5], Right - [4])

The main method of using Bluetooth for traffic monitoring is to design a Bluetooth detector that is able to track down the Media Access Control ID (MAC ID) of Bluetooth device in the travelling vehicle through inquiry process. By placing two Bluetooth detectors along a section of the road as in Figure 2, the MAC ID of Bluetooth device in vehicle parry each Bluetooth detector will be recorded along with the current time. The average speed of the traveling vehicle can be estimated and from these estimated to determine the traffic condition for that segment of road.

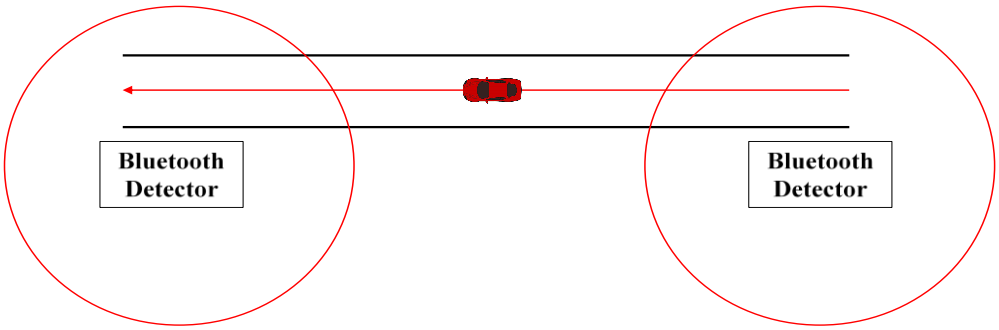


Figure 41: Two Bluetooth detectors place on a section of the road

However, there is no study being made on how well a single Bluetooth detector can predict the speed of the traveling vehicle. Able to predict the traveling speed of the vehicle at a single node can give information about the traffic condition of the node. Furthermore, it can estimate a much more accurate traffic condition.

Furthermore, there is possibilities of that vehicle speed can be estimate with a node by placing multiple Bluetooth detector on a node. From the research [6], having more Bluetooth inquirer can identify surrounding Bluetooth device faster. With more Bluetooth detector on a node, it is expected that the average speed of the traveling vehicle can be estimate with a single Bluetooth detector.

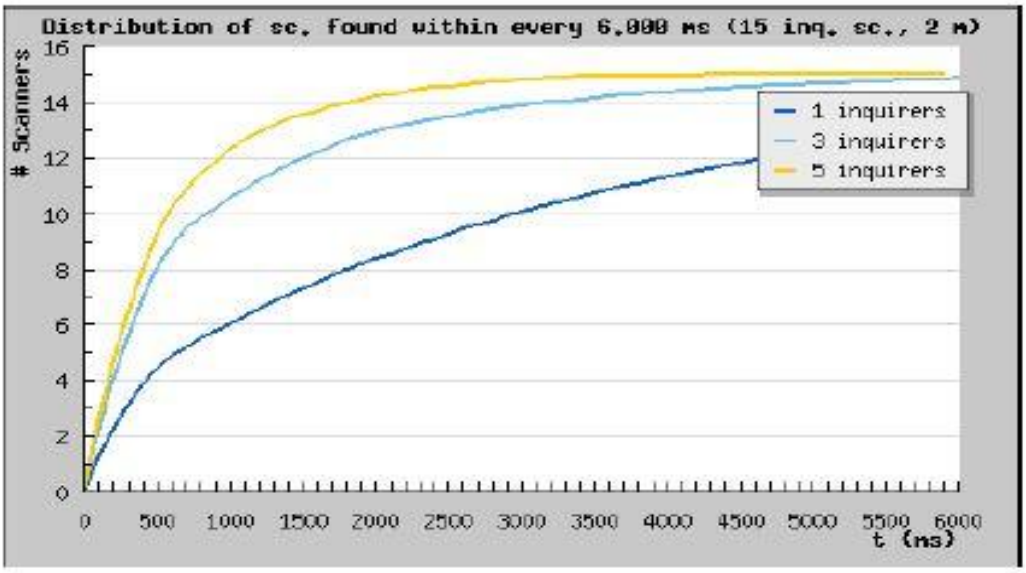


Figure 42: Comparison of time taken for 1, 3 and 5 inquirers scan to 15 inquiry scanning device[6]

2. Bluetooth inquiry process

Bluetooth utilize inquiry process to collect the MAC ID of other Bluetooth devices. During the process, inquirer (Master) will be sending inquiry packet (ID packet) to any inquiry scanner (Slave). Once the inquiry scanner receive the inquiry packet, it will send back Frequency Hop Synchronization (FHS) packet to the inquirer which consist of the inquiry scanner MAC ID. In addition, inquiry scanner may return extended packet but the current Bluetooth module being used does not request for it to send any extended packet. Figure 4 shows the MAC ID of Bluetooth devices which consist of Lower Address Part (LAP), Upper Address Part (UAP) and Non-significant Address Part (NAP).

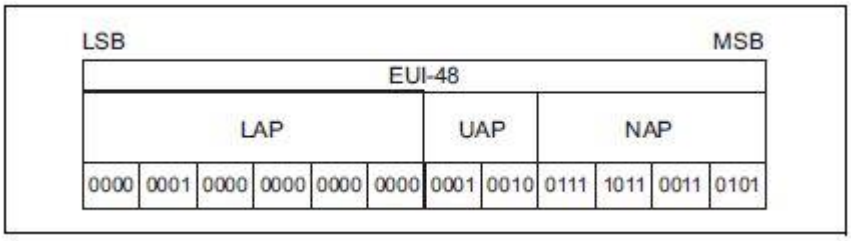


Figure 43: MAC ID of Bluetooth devices[7]

Bluetooth having 79 frequency channels for communication where 32 frequency channel are available for inquiry process. During the inquiry process, the 32 frequency channels will be separated into two train which are Train A and Train B. Each of the train contains 16 frequency channels. As Bluetooth clock ticks at 312.5us, master will send ID packet to two frequency channels at two consecutive 312.5us slot. It will listen for response at 625us after the ID packet has been sent. Figure 5 shows the timing of inquiring devices[8].

Each inquiry and response took about 625us ideally which will repeated 256 times for 16 frequency channel in a train which took a total of 2.56s to finish scanning

a bus. Every 2.56s, the inquiry device swap between the two buses. In addition, every 1.28s, one frequency is changed between train A and Train B.

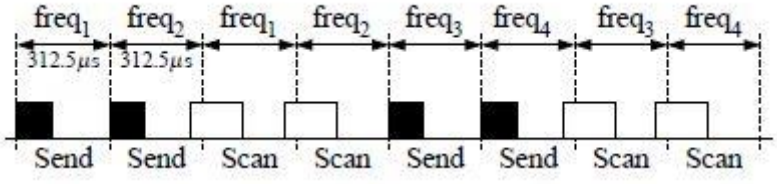


Figure 44: Timing of inquiring device's behavior[8]

3. Planning of the project

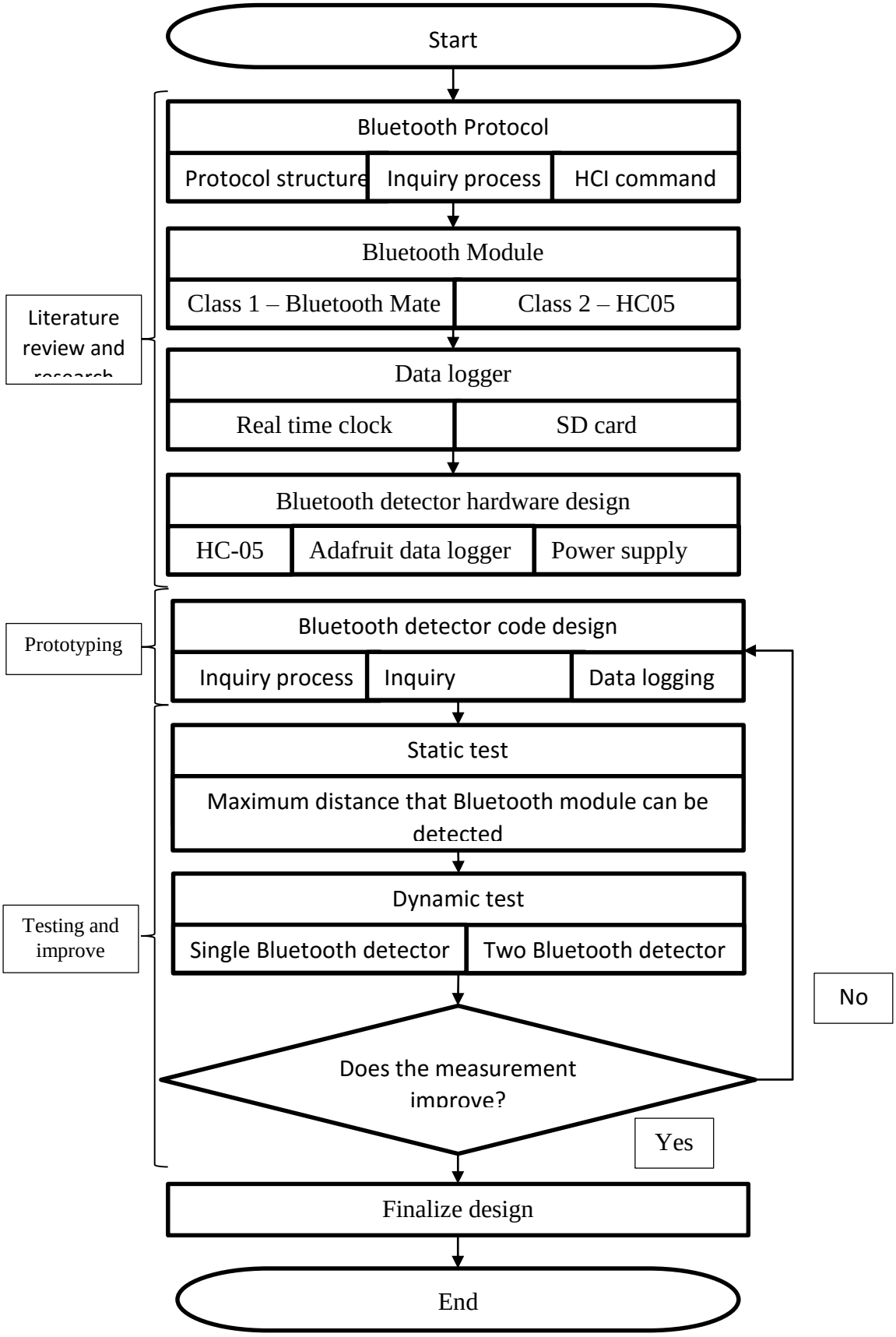


Figure 45: Flow chart of the whole project

4. Design of the Bluetooth detector

4.1 Hardware design

HC-05 Bluetooth module is chosen for the project. It is a class 2 Bluetooth module with a communication range of approximate 15 meters. The specification of the Bluetooth module is shown in Table 1. The function of pin is shown in Table 2.

Table 45: HC-05 specification [9]

Parameter	Value	Unit
Sensitivity	-80	dBm
Transmit power	4	dBm
Operating voltage	1.8 – 3.6	V

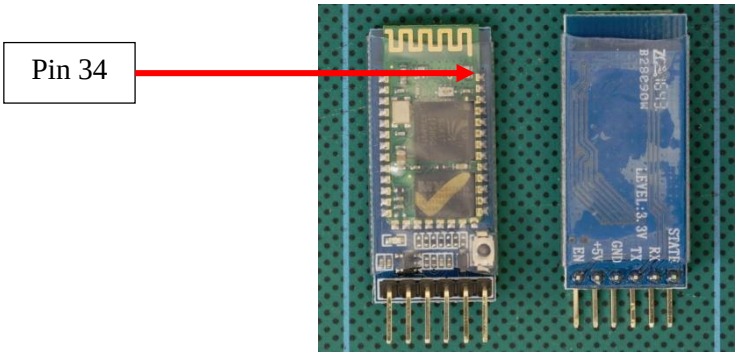


Figure 46: HC-05 module

Table 46: HC-05 pin description and function

Pin	Description	Function
EN	Disable module	Disable module with LOW input
+5V	Power supply	Supply voltage to the module
GND	Ground	Ground of power source
TX	Transmitter pin	Connect to receive of micro-controller
RX	Receiver pin	Connect to transmitter of micro-controller
STATE	Indication	To determine if the Bluetoth module is connected. HIGH when it is connected. LOW when it is not connected
Pin 34	Command mode	Provide HIGH (3.3V) input to enter command mode/AT mode

Adafruit data logging shield with RTC module and SD card module. Real Time Clock (RTC) module can be used to timestamp all the data with current time. It is power with external battery and continuously keep track of time as long as the battery still contain power. Furthermore, the data logger shield can be used with various Arduino microcontroller especially ATmega328 microcontroller.

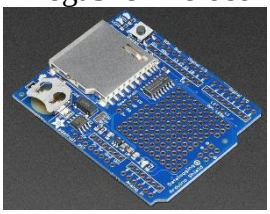


Figure 47: Adafruit data logging shield

4.2 Schematic design (Single Bluetooth detector)

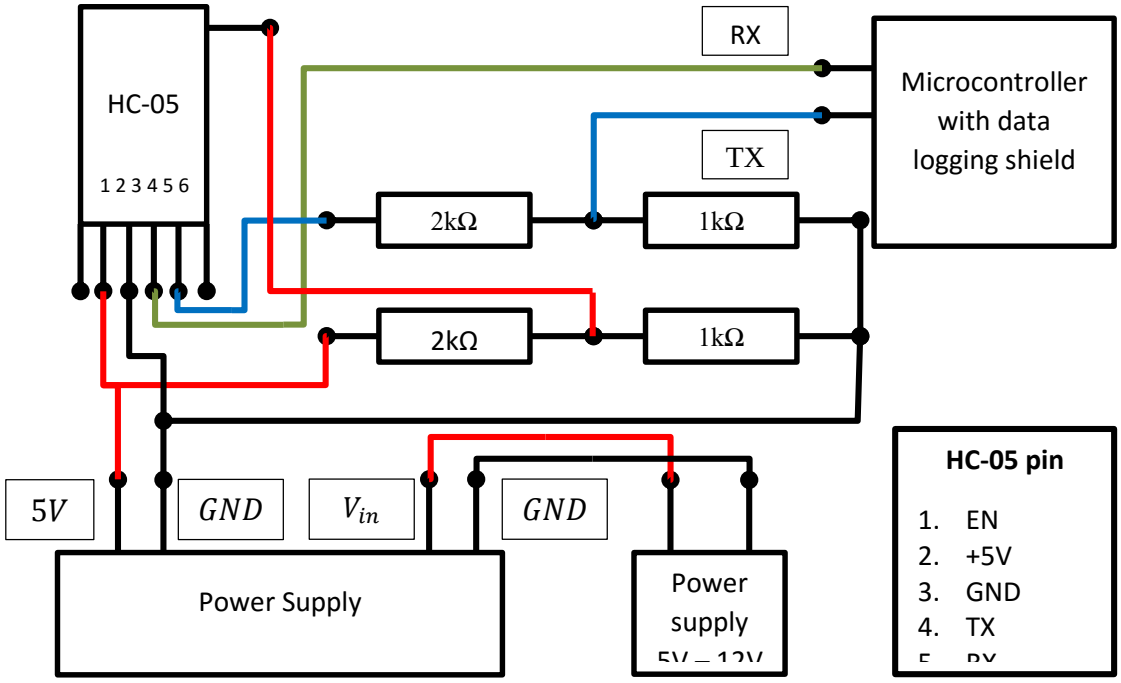


Figure 48: Schematic diagram of single Bluetooth detector

4.3 Schematic design (Two Bluetooth detector)

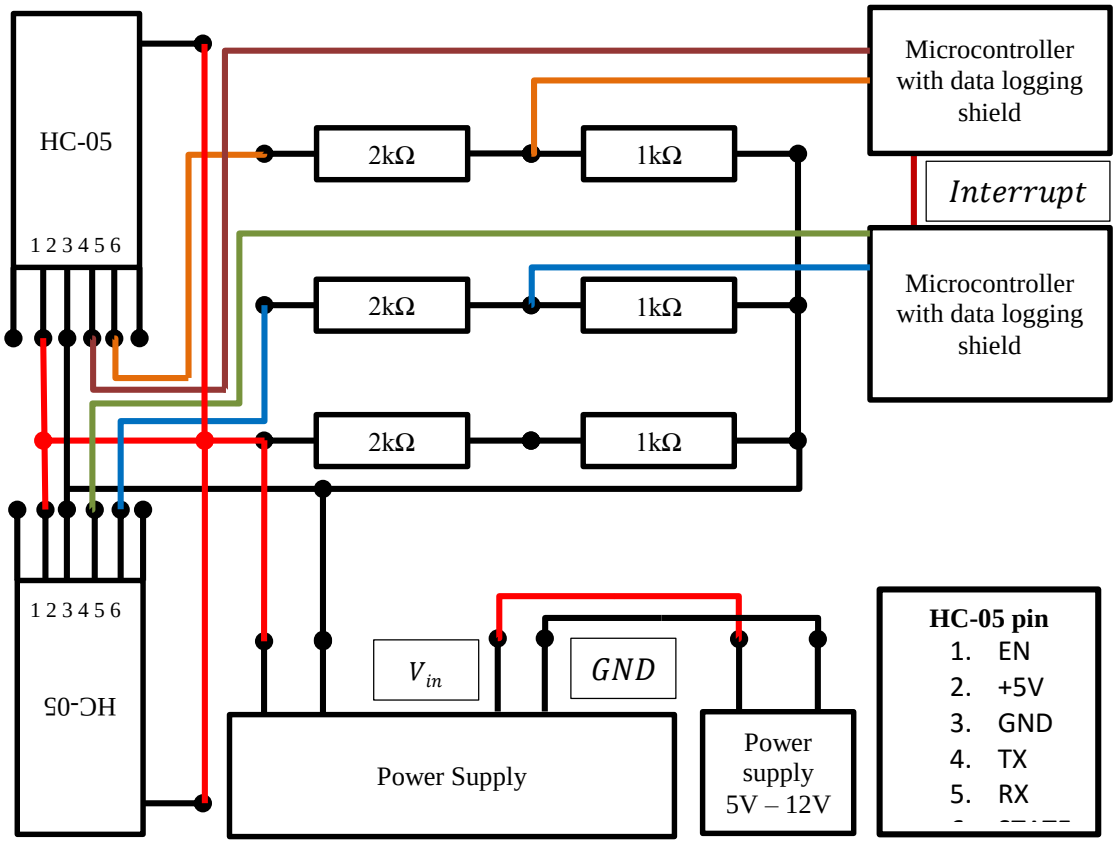


Figure 49: Schematic diagram of two Bluetooth detector

From the schematic diagram in Figure 9 and Figure 10. The serial communication conducted between HC-05 and the micro-controller it through the transmitter and receiver pin. Microcontroller will assign its receiver pin and transmitter pin through the when activate, Table 3 shows the connection. The transmitter of Bluetooth module can directly connected to the receive part of micro-controller as the micro-controller input pin can treat 3.3V signal as HIGH input. In contrast, transmit signal from the micro-controller has to step down from 5 V to 3.3V or it will damage the Bluetooth module. The 5V signal is step down with using voltage division rule with resistor (1kΩ and 2kΩ). Figure 10 shows the setting for two Bluetooth module. One micro-controller (initiator) will interrupt the other micro-controller (interrupt) to initiate inquiry process after a certain delay (depends on the setting). The interrupt shall detach interrupt from the assign pin and continue with normal inquiry process. The two Bluetooth module will initiate its own inquiry at different time.

Table 47: Bluetooth module and micro-controller communication

Bluetooth module		**Microcontroller**	
Pin 4	Transmitter	Pin 8	Receiver (Assigned)
Pin 5	Receiver	Pin 9	Transmitter (Assigned)

4.4 Initial prototype

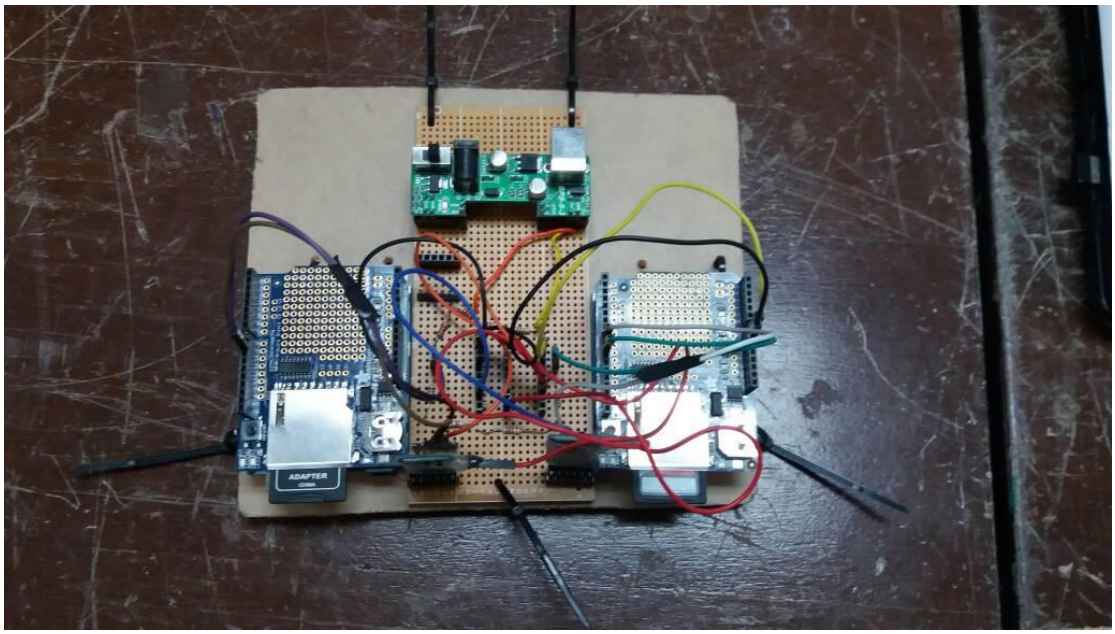


Figure 50: Initial prototype

5. Coding design

5.1 Flow chart

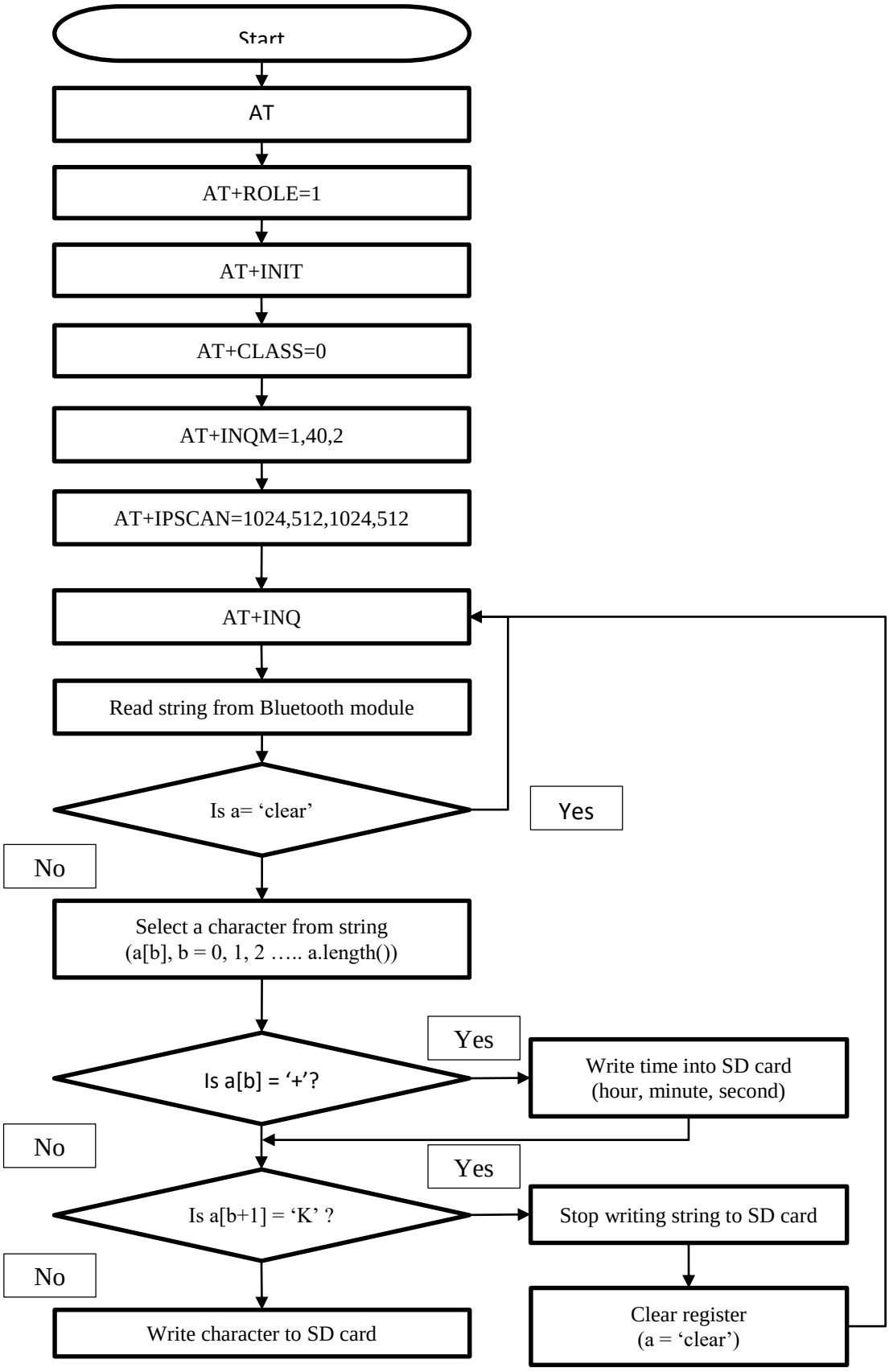


Figure 51: Flow chart

5.2 Bluetooth detector code design[10]

1. AT
   To check if the Bluetooth module setting is correct and performing without error.

2. AT+ROLE
   Designate the Bluetooth module to work as master.

3. AT+INIT
   Initialize the SPP profile library to perform inquiry process.

4. AT+CLASS
   Set Bluetooth to inquire for certain class of Bluetooth devices or default which search for all type of Bluetooth device.

5. AT+INQM
   Setting the inquiry mode, number of response and inquiry time. For inquiry mode, the inquirer can perform standard inquire or inquire with measuring the RSSI signal. For number of response, set the maximum limit of response receive by the Bluetooth inquirer. Inquiry may stop when the limit is reach. For inquiry time, to set the time for inquirer to perform inquiry. The time of inquiry is N*1.28s.

Table 1 shows six different settings of the inquirer. Each setting is tested with in an environment of at least 2 Bluetooth devices present. A total of 5 trials will be performed to identify if the number of sample gathers and Bluetooth device identify is consistent. From the result, the setting of inquiry mode does not affect much on the inquiry process. The number of response may affect the performance of the inquiry as during RSSI mode, it receive certain error. Longer inquiry time does not affect the inquiry process much if the limit of number of response is low.

The inquiry parameter is set with AT+INQM=1, 1, 1 as default. By setting number of response is 1, the Bluetooth detector shall stop inquiry process upon intercepting a MAC ID and continue timestamp and record the data. This setting allow the Bluetooth detector to record MAC ID accurately with time.

6. AT+IPSCAN
   Setting the inquiry interval, inquiry duration, paging interval and paging duration. By default can be set as 1024, 512, 1024, 512.

Associate Bluetooth HCI command[7]:

<table>
<tr><td>HCI command</td><td></td><td></td></tr>
<tr><td>INQUIRY SCAN INTERVAL</td><td>
<table>
<tr><th>Value</th><th>Parameter Description</th></tr>
<tr><td>N = 0xXXXX</td><td>Size: 2 Octets
Range: 0x0012 to 0x1000; only even values are valid
Default: 0x1000
Mandatory Range: 0x0012 to 0x1000
Time = N * 0.625 ms
Time Range: 11.25 to 2560 ms
Time Default: 2.56 s</td></tr>
</table>
</td><td>Define amount of time between consecutive scan</td></tr>
</table>

<table>
<tr>
<td>INQUIRY SCAN WINDOW</td>
<td>
<table>
<tr><th>Value</th><th>Parameter Description</th></tr>
<tr><td>N = 0xXXXX</td><td>Size: 2 Octets
Range: 0x0011 to 0x1000
Default: 0x0012
Mandatory Range: 0x0011 to Inquiry Scan Interval
Time = N * 0.625 ms
Time Range: 10.625 ms to 2560 ms
Time Default: 11.25 ms</td></tr>
</table>
</td>
<td>Define the amount of time for inquiry scan</td>
</tr>
</table>

7. AT+INQ

Perform inquiry process to get MAC ID of nearby Bluetooth devices. After receiving any response, the incoming data from Bluetooth module will be read as string.

As the reading procedure is finish, it will be written into the SD card. While writing, before the character '+' being write, it will write the time (hour, minute, second) into SD card first.

As the next character being written is 'K', the writing procedure will stop as the last data 'OK\r\n' is not needed to record.

After writing procedure is finish, the register will be clear by assigning 'clear' into it. During the next inquiry procedure, if any error occurs, the register will remain with data 'clear' ad will not write any data into the SD card.

Associate HCI command[7]:

<table>
<tr><th>HCI command</th><th></th><th></th></tr>
<tr>
<td>HCI_INQUIRY</td>
<td>
<table>
<tr><th>Command</th><th>OCF</th><th>Command Parameters</th><th>Return Parameters</th></tr>
<tr><td>HCI_Inquiry</td><td>0x0001</td><td>LAP,
Inquiry_Length,
Num_Responses</td><td></td></tr>
</table>
</td>
<td>Define amount of time between consecutive scan</td>
</tr>
</table>

The command parameter Inquiry_Length and Num_Responses is previously define in AT+INQM.

5.3 Two Bluetooth device setting

By having two Bluetooth detector working at one node, two possible scenario can be set. The first scenario will be having both Bluetooth detector working at the same time. The second scenario will be delaying one of the Bluetooth detector by a period of time. For this case, the delay will be 1.28 seconds. The reason is that during the 2.56 seconds of inquiry, the whole system still be able to detect for any response at every 1.28 seconds. Figure 13 shows each the timing of two Bluetooth detector with delay in between.

In addition, another test is conducted with inquiry parameter of AT+INQM=1, 40, 4 with the two Bluetooth device delay by 2.56 second. The scenario will be similar to Figure 13. The purpose is to allow the two Bluetooth devices to initiate inquiry process with each at different frequency train. The Frequency train as mention previously is 32 inquiry channel being separate into two train of 16 frequency channel.

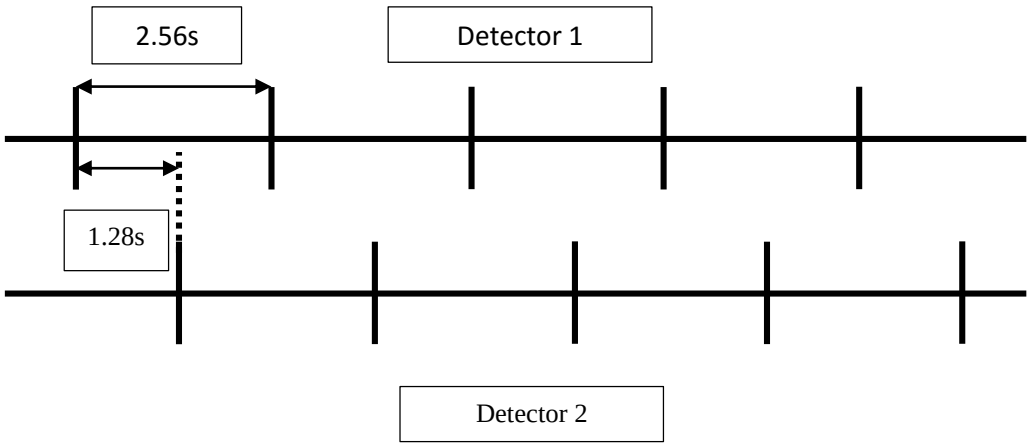


Figure 52: Timing of two Bluetooth detector with delay

5.4 Static test

The objective is to identify the maximum detecting range of the Bluetooth detector. Furthermore, to justify that class 2 Bluetooth module have a detection range of 15 meters radius. Static is conducted by having a mobile phone being place a distance away from the Bluetooth detector. The initial test is position 10 meters away from the Bluetooth detector, the continuing test will have the distance increase 10 meters further from the previous distance. The distance will be increase until the Bluetooth detector is unable to detect any signals. Each test will last for 1 minute as the Bluetooth detector is activated. A total of 5 test is conducted for each distance. The setting of the Bluetooth detector inquiry parameters is AT+INQM = 1,1,1. The target devices for inquiry are car Bluetooth radio and smart phone Bluetooth.

5.5 Dynamic test

The objective is to utilize the Bluetooth detector to predict the speed of the object for evaluating its performance and data quality. The experimented distance is the maximum detection range of the Bluetooth detector. It is determined with the result from static test. From the different scenario, the data will be compared to observe Bluetooth detector perform best at which setting which is shown in Table 4.

Table 48: Dynamic test setting

Scenario	Bluetooth detector setting (inquiry parameter)
The effect of inquiry time increase	• AT+INQM=1, 1, 1 • AT+INQM=1, 1, 2
The effect of having multiple Bluetooth module inquiry initiate inquiry process at different setting	• AT+INQM=1, 1, 1 (no delay) • AT+INQM=1, 10, 1 (delay by 5000 micro-second) • AT+INQM=1, 1, 1 (delay by 0.64 second) • AT+INQM=1, 1, 2 (delay by 2.56 second) • AT+INQM=1, 40, 4 (delay by 2.56 second)
The Bluetooth performance with multiple inquiry scanner passing by	• AT+INQM=1, 1, 1 (Single) • AT+INQM=1, 40, 4 (Delay 2.56 second)

6 Result

6.1 Static test

6.1.1 First test (14th October 2017)

The initial test was conducted with car Bluetooth. The maximum distance that Bluetooth detector is able to detect for the car Bluetooth radio is about 2 meters. From Table 5, the Bluetooth detector inquiry process start about 4 seconds after powering up. However, the first detection mostly not does not occur within initial 10 seconds. Furthermore, the final detection ends at least 30 seconds earlier.

The possibilities of Bluetooth detector able to pick up the MAC ID of car Bluetooth radio is that HC-05 antenna weak sensitivity is unable to pick up the signal correctly. However, HC-05 is able to pick up the smart phone Bluetooth signal with better result compare to the car Bluetooth radio.

Table 49: Static test with car Bluetooth radio

Distance (m)	Trial 1			Trial 2		
	Time		Sample	Time		Sample
	Start time	End time		Start time	End time	
2	15:01:40	15:02:40	7	15:09:40	15:10:40	7
	15:01:58	15:02:05		15:09:49	15:10:00	
1	15:24:50	15:25:50	11	-		
	15:25:04	15:25:12				

6.1.2 Second test (20th October 2017)

For the test will be conducted with smart phone Bluetooth device it will be used for dynamic test to prove the research question and concept. From the Table 6, the Bluetooth detector is able to pick up the smart phone Bluetooth signal in a distance of at least 35 meters. During the 20 meter and 25 meter testing shows lesser response being detect as it may be cause by nearby moving objects accidently disturb the experiment. In the future experiment, it will be conducted in a less disturb area. Furthermore, a total of 5 trials should be conducted to observe if the response receive is reduce as distance increase.

Table 50: Static test with smart phone Bluetooth

Distance (m)	Sample		
	Trial 1	Trial 2	Trial 3
10	20	28	44
15	46	44	30
20	20	26	5
25	25	26	20
30	28	-	-
35	42	-	-

6.1.3 Third test (28th October 2017)

The final static test is conducted at 10 meters, 20 meters, 30 meters and 40 meters. Upon reaching 40 meters, the detection of the phone become significantly low with 1 to 2 MAC ID being recorded for 1 minute. The result is shown at Table 7. From the table, dynamic test will be conducted with 80 meters experiment distance. From the result, it can be observe that as the distance increase the time taken to detect one MAC ID increase. The number of samples collected is decrease in the process.

Table 51: Third static test result

Distance	Sample	Duration	Average time per MAC ID
10	25	46	1.840
	17	46	2.706
	37	46	1.243
	35	46	1.314
	34	46	1.353
20	19	46	2.421
	17	46	2.706
	26	46	1.769
	20	46	2.300
	13	46	3.538
30	21	46	2.190
	17	46	2.706
	16	46	2.875
	18	46	2.556
	19	46	2.421
40	2	46	23.000
	0	46	0.000
	1	46	46.000
	1	46	46.000
	1	46	46.000

6.2 Dynamic test

6.2.1 First test (14th October 2017)

The initial test was conducted with car Bluetooth radio with smart phone Bluetooth pairing with it. The car travels at the speed of 10km/h. The Bluetooth detector is unable to detect any passing vehicle.

The possibility of unable to detect:

1. Car Bluetooth radio signal is too weak for the Bluetooth detector to pick up. During the static test, it already shows that the Bluetooth detector perform poorly with the car Bluetooth radio.
2. The Bluetooth detector is unable to pick the smart phone Bluetooth signal as certain brand of smart phone does not allow the smart phone Bluetooth be discoverable unless entering the option menu.

6.2.2 Second test (22nd October 2017)

The second test is conducted with using a single smart phone Bluetooth traveling at a fix distance with different speed. Due to the availability of the location, distance of 20 meters was used for experiment. It will be conducted by enabling the smart phone Bluetooth as the traveling starts. Figure 14 shows the example of testing location.

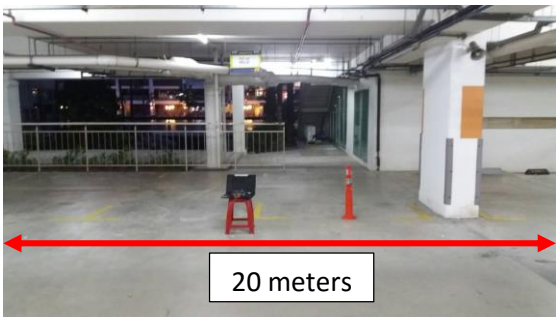


Figure 53: Second dynamic test

The smart phone with Bluetooth enable for discover will travel through the fix distance at different speed with a stop watch recording the time. Average speed will be calculated with the following Eq.(1).

$$v_{average} = \frac{distance}{travel\ time} - - - Eq.(1)$$

Table 52: Dynamic test result at 20 meter distance with smart phone Bluetooth enable

Average speed with stopwatch					Average speed with Bluetooth					
	Time (s)					First time (s)	Final time (s)			
Distance (m)	Second		value	Speed (m/s)	Distance (m)	Second	Second	Duration	Speed (m/s)	Samples
20	10	69	10.69	1.87	20	32	39	7	2.86	10
20	12	4	12.04	1.66	20	38	49	11	1.82	6
20	14	56	14.56	1.37	20	50	61	11	1.82	14
20	20	22	20.22	0.99	20	41	63	22	0.91	16
20	23	28	23.28	0.86	20	24	42	18	1.11	15

Average speed with stopwatch					Average speed with Bluetooth							
	Time (s)					First time (s)	Final time (s)			Samples		
Distance (m)	Second		value	Speed (m/s)	Distance (m)	Second	Second	Duration	Speed (m/s)	Detector 1	Detector 2	total
20	11	16	11.16	1.792	20	25	36	11	1.818	9	1	10
20	13	5	13.05	1.533	20	2	6	4	5.000	6	1	7
20	18	12	18.12	1.104	20	24	37	13	1.538	9	3	12
20	20	78	20.78	0.962	20	34	50	16	1.250	6	4	10
20	23	0	23.00	0.870	20	30	43	13	1.538	15	4	19
20	23	72	23.72	0.843	20	43	62	19	1.053	14	1	15
20	24	88	24.88	0.804	20	3	13	10	2.000	6	0	6

Average speed with stopwatch					Average speed with Bluetooth							
	Time (s)					First time (s)	Final time (s)			Samples		
Distance (m)	Second		value	Speed (m/s)	Distance (m)	Second	Second	Duration	Speed (m/s)	Initiator	Interrupt	total
20	10	44	10.44	1.92	20	44	50	6	3.33	5	3	8
20	12	32	12.32	1.62	20	54	62	8	2.50	5	3	8
20	14	59	14.59	1.37	20	2	10	8	2.50	4	4	8
20	22	0	22	0.91	20	31	47	16	1.25	7	2	9
20	23	3	23.03	0.87	20	58	78	20	1.00	11	2	13
20	25	94	25.94	0.77	20	15	35	20	1.00	7	10	17

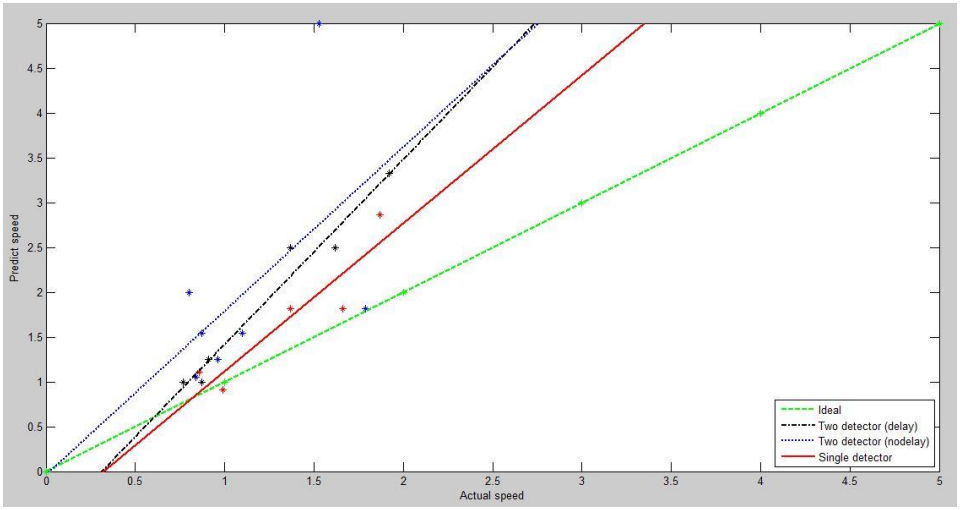


Figure 54: Predicted speed vs Actual speed graph

Straight, Red line	Single Bluetooth detector
Dot, Blue line	Two Bluetooth detector without delay
Dash dot, Black line	Two Bluetooth detector with delay
Dash, Green line	Ideal line

From Figure 15, it can be observe that at higher speed, the predicted speed is much faster compare to the actual average speed. From observation, having multiple Bluetooth detectors does not improve the efficiency of the system from observation. However, the final conclusion is unable to be made at the moment as more statistical data require for analysis. Additional factors that will be consider for next dynamic test are:

1. More samples are require to gather more accurate result (at least 10 samples)
2. Two Bluetooth detectors having possibility of outperforming single Bluetooth detector when multiple traveling Bluetooth device is present.
3. The testing distance should be more than 20 meters to gather a much accurate result.

6.2.3 Third test (4th, 18th, and 22nd October 2017)

The effect of inquiry time increase

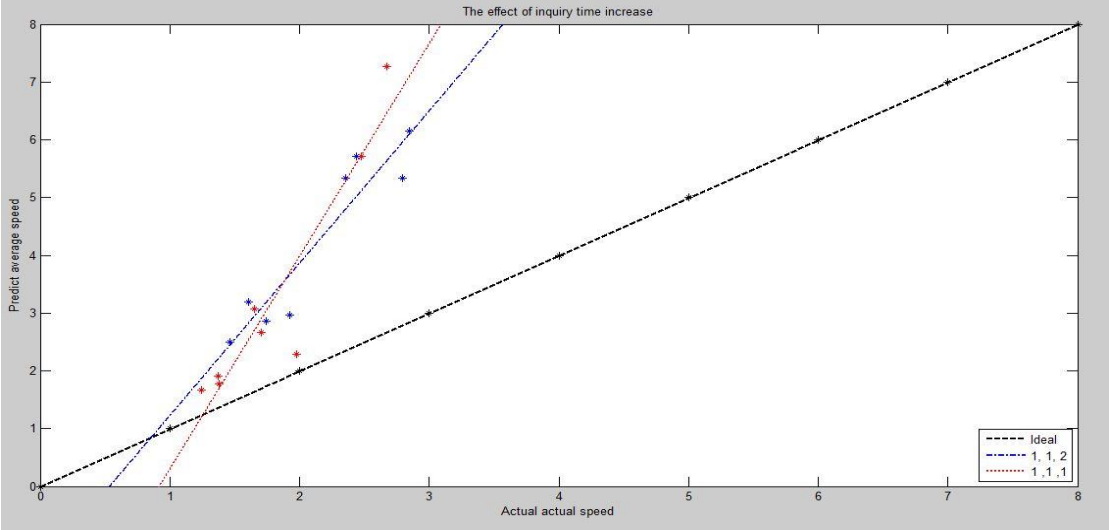


Figure 55: The effect of inquiry time increase

From Figure 16 it can be observed that the longer inquiry time allows the Bluetooth detector to search for devices for a longer period of time which allow the Bluetooth detector to detect devices as it approaching the maximum detection area (less sensitive area around 40 meters). From Figure 23, it can be observed that the gradient AT+INQM=1, 1, 2 (blue line, '-.') is much closer to the ideal line compare to the AT+INQM=1, 1, 1 (red line, ':').

The impact of having multiple Bluetooth module initiate inquiry process at different setting

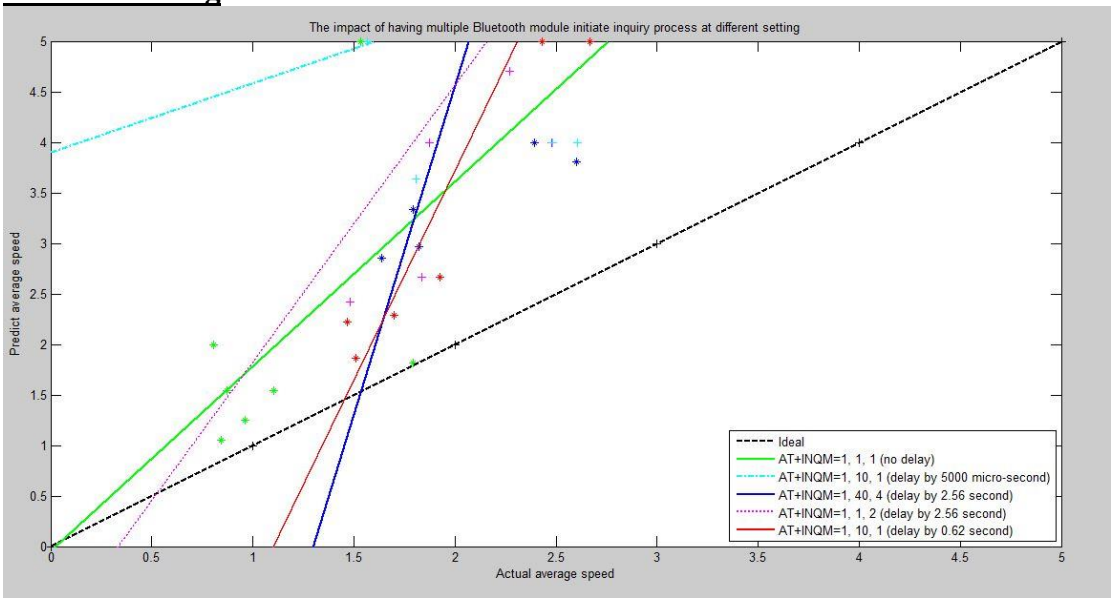


Figure 56: The impact of having multiple Bluetooth module initiate inquiry process at different setting

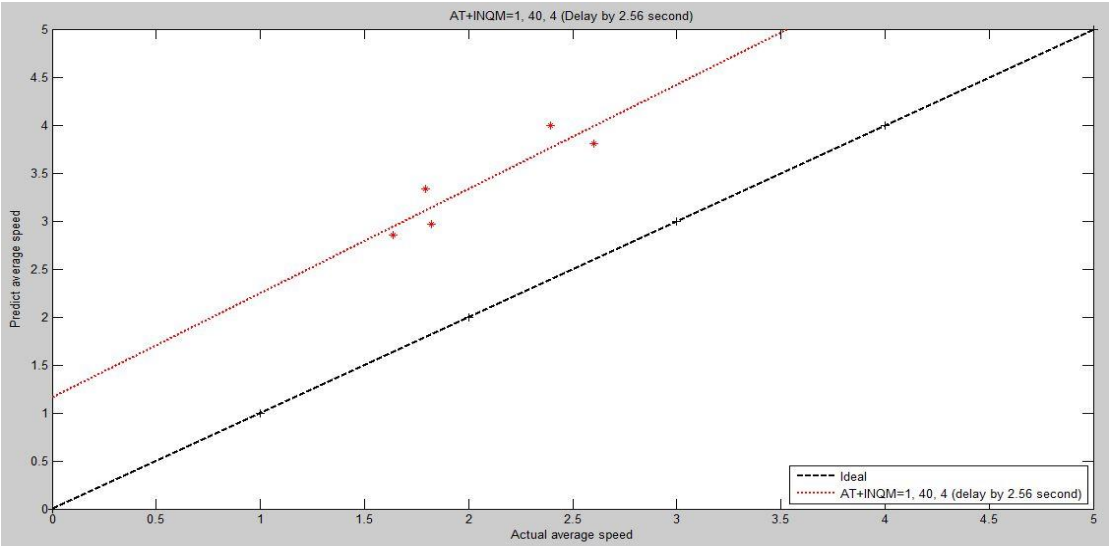


Figure 57: AT+INQM=1, 40, 4 remove extreme data

From Figure 17 it can be observed that AT+INQM=1, 10, 1 (delay by 5000 micro-second) setting has the worst detection. Delaying 5000 micro-second is not sufficient to allow the two Bluetooth modules avoiding frequency clash.

From Figure 17, AT+INQM=1, 1, 1 (no delay) has the best performance. The data is collected from earlier experiment with the experiment distance of 20 meters. However, table also shown that the data is one sided as initiator collected most of the data. From the observation of the raw data, the initial and final detection is mostly done by one of the Bluetooth module which is nothing different from the default setting (single Bluetooth module with AT+INQM=1, 1, 1). In addition, AT+INQM=1, 1, 2 (delay by 2.56 second) produce the similar result as the AT+INQM=1, 1, 1 (no delay).

From Figure 18, AT+INQM=1,40,4 (delay by 2.56 second) have three extreme data which shown in Table 9. after removing the extreme data, it is found that the setting can produce a perfect result. The initial detection and final detection is detected by different Bluetooth module each time.

Table 53: Extreme data from AT+INQM=1, 40, 4 (delay by 2.56 second)

Actual average traveling speed	**Predict average traveling speed**
1.834	6.154
2.880	10.000
2.963	16.000

The impact of having multiple Bluetooth inquiry scanners

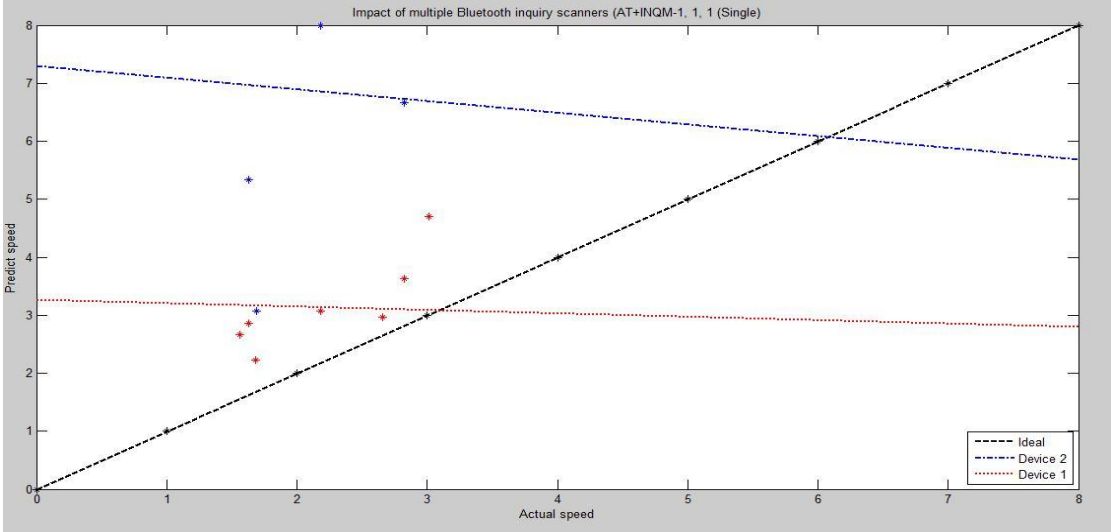


Figure 58: Impact of multiple Bluetooth inquiry scanners (AT+INQM=1, 1, 1 (Single))

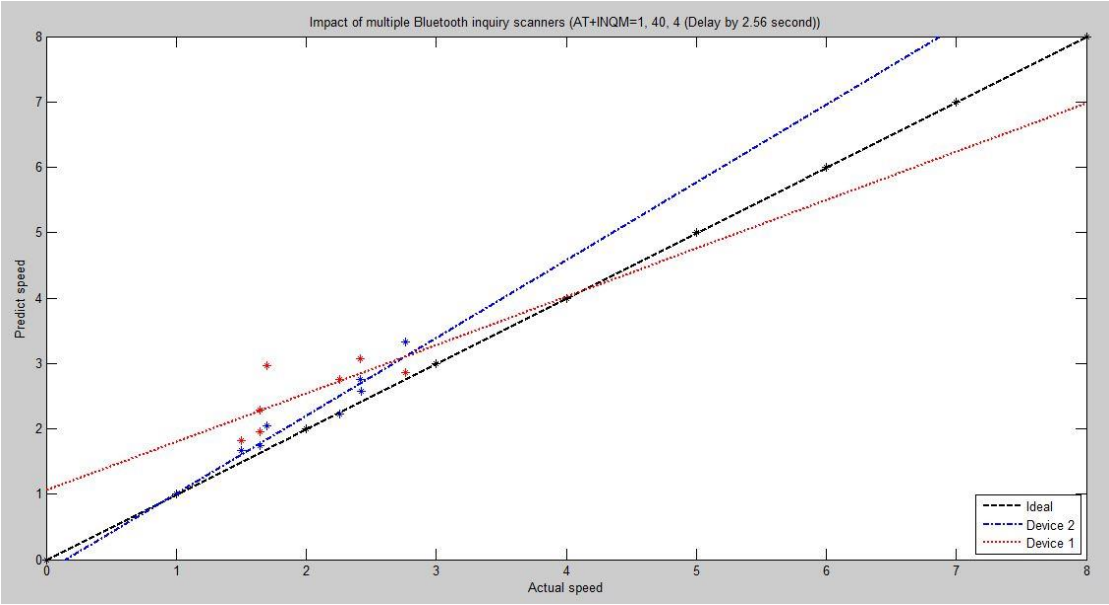


Figure 59: Impact of multiple Bluetooth inquiry scanners (AT+INQM=1, 40, 4 (Delay by 2.56 second))

From the Figure 19 and Figure 20 is can observe that the setting AT+INQM=1,40,4 (double Bluetooth module) perform significantly well compare to AT+IQM=1,1,1 (Single Bluetooth). The delay sufficiently allow two Bluetooth modules to scan at different frequency train which avoid clash in frequency as both of the modules initiate inquiry process as the same time.

7 Conclusion

Using Bluetooth for traffic monitoring has certain advantages but the challenges can be great. The first challenges is the Bluetooth detector scanning range. From the experiment, the distance not only affected by the Bluetooth class of the detector but

also the antenna it using. Furthermore, slave Bluetooth class and design can also affect the detection. Car Bluetooth radio requires a highly sensitive Bluetooth detector to detect at further distance. From the result, it shows that having multiple Bluetooth detectors in a node can increase the efficiency of the detection provided that there is no frequency clash between the two modules. Without proper delay, both Bluetooth module may sending ID packet at the same frequency channel which is the cause for frequency clash. In addition, multiple Bluetooth detectors in a node can perform well when multiple Bluetooth inquiry scanner device is present.

References

[1] P. Khanke and P. P. S. Kulkarni, "A Technique on Road Traffic Analysis using Image Processing," *Int. J. Eng. Res. Technol.*, vol. 3, no. 2, pp. 2769–2772, 2014.

[2] F. Aloul, A. Sagahyroon, A. Nahle, M. A. Dehn, and R. Al Anani, "GuideME : An Effective RFID-Based Traffic Monitoring System," in *IASTED International Conference*, 2012, pp. 353–359.

[3] S. Ahmad, R. Lu, and M. Ziaullah, "Bluetooth an Optimal Solution for Personal Asset Tracking : A Comparison of Bluetooth, RFID and Miscellaneous Anti-lost Traking Technologies," *Int. J. u- e- Serv. Sci. Technol.*, vol. 8, no. 3, pp. 179–188, 2015.

[4] J. Lee, Y. Su, and C. Shen, "A Comparative Study of Wireless Protocols: Bluetooth, UWB, ZigBee, and Wi-Fi," in *The 33rd Annual Conference of the IEEE Industrial Electronics Society (IECON)*, 2007, pp. 46–51.

[5] C. Saad, B. Mostafa, E. A. Cheikh, and H. Abderrahmane, "Comparative Performance Analysis of Wireless Communication Protocols for Intelligent Sensors and Their Applications," *Int. J. Adv. Comput. Sci. Appl.*, vol. 5, no. 4, pp. 76–85, 2014.

[6] A. Franssens, "Impact of multiple inquires on the bluetooth discovery process : and its application to localization," UNIVERSITY OF TWENTE, 2010.

[7] Bluetooth SIG Proprietary, "Bluetooth Core Specification Master Table of Contents & Compliance Requirements," *Bluetooth SIG*, 2016. [Online]. Available: https://www.bluetooth.com/specifications/bluetooth-core-specification.

[8] M. Duflot, M. Kwiatkowska, G. Norman, and D. Parker, "A Formal Analysis of Bluetooth Device Discovery," *Int. J. Softw. Tools Technol. Transf.*, vol. 8, no. 6, pp. 621–632, 2006.

[9] A. Cotta, N. T. Devidas, and V. K. N. Ekoskar, "HC-05 BLUETOOTH MODULE INTERFACED WITH ARDUINO," *Int. J. Sci. Eng. Technol. Res.*, vol. 5, no. 4, pp. 869–872, 2016.

[10] Itead Studio, "HC-05 User's Manual," 2010. [Online]. Available: http://www.electronicaestudio.com/docs/istd016A.pdf.

Suppression of Ground Borne Vibration Induced by High-Speed Lines

Ali Mohamed Rathiu[1*], Mohammad Hosseini Fouladi[2], Satesh Narayana Namasivayam[3]

[1,2,3]*School of Engineering, Faculty of Built Environment, Engineering, Technology and Design, Taylor's University, Subang Jaya, Selangor, Malaysia*

[*]rathiu.ali@gmail.com

Abstract

Vibration of high-speed lines leads to annoyance of public and lowering real estate values near the railway lines. This hinders the development of railway infrastructures in urbanised areas. This paper investigates the vibration response of an isolated rail embankment system and modifies the component to better attenuate ground vibration. Mainly velocity response is used to compare the responses and the applied force is of 20 kN at excitation frequencies of 5.6 Hz and 8.3 Hz. Focus was made on ground-borne vibration and between the frequency range of 0 and 250 Hz. 3D Numerical model was made using SolidWork software and frequency response was produced using Harmonic Analysis module from ANSYS Workbench software. For analytical modelling MATLAB was used along with Simulink to verify the mathematical model. This paper also compares the vibration velocity decibels (VdB) of analytical two-degree of freedom model mathematical model with literature data. Harmonic excitation is used on the track to simulate the moving load of train. The results showed that modified analytical model gives the velocity response of 75 VdB at the maximum peak. Changes brought to the mass and spacing of the sleeper and to the thickness and the corresponding stiffness for the ballast does not result in significant vibration response. Limitations of two-degree analytical model is suspected to be the cause of this inactivity. But resonance vibration can be reduced with the aid of damping coefficient of rail pad. Statistical analysis methods t-test and ANOVA single factor test was used verify the values with 95% confidence.

Keywords: Vibration, Rail, Embankments, Analytical model, Numerical model.

1. Introduction

Rail transportation was a novel mode of transportation created during the enlightened era of industrial revolution in 18th century [1]. Back then, the trains were driven by coal powered steam engines which were loud, dirty and puffed out nauseating thick black smoke. Nevertheless, this mode of transportation was popular among people because, compared to available alternative modes of transportation, trains had many appealing benefits. These include regular intervals of travelling to a predetermined location safely and cheaply. The benefits have increased over the years with technological advancement in engines which has allowed it to travel much faster and efficiently with cleaner and more powerful diesel engines

This popularity has been retained, despite remarkable advances in automobile technology in recent years. Moreover, train usage is raising in urbanised areas across the world for both developed and developing countries. Abe *et al.* [2] investigated rail travel demand in Tokyo from 1950 to 2010 and found that the usage was still increasing, with more travellers using underground trains nowadays. Also, a study made on the market competition of the European rail freight trains, which are large cargo trains, by Laroche *et al.* [3] similarly found that the market was growing despite high initial start-up cost in European Union countries. Furthermore, Chen *et al.* [4] stated that since the beginning of 2000, Chinese government has started to build a massive rail system infrastructure and the effects of this decision has been beneficial to the economy and livelihood.

Therefore, rail travel is still a booming and essential industry for developed countries and even greater for developing countries. But despite the advances in technology, the current railways still have many issues. The most recognisable problems with the railway are vibration and noise. This paper will focus on the ground-borne vibrations which are caused by the movement of the wheel on the track, which propagates vibration from the track to the surrounding areas. These vibrations can be an annoyance to humans who live in nearby buildings. This becomes more problematic in urbanised cities, as Connolly *et al.* [5] states that, the economical repercussion due to high vibrations in city areas are more serious as these vibrations can reduce real estate values and can entirely disrupt the work in sensitive workplaces such as record studios, tv studios and theatres. The paper states that even though these sensitive buildings are fewer compared to residential buildings, the high number of reported complaints from these places shows that there is a direct detriment to the working condition of these places due to railway lines. It also cites that ground vibration is also a growing concern in most European countries due to increasing railway lines and soaring frequency of trips per day.

This research investigates and proposes a modified track embankment to suppress the vibrations. To achieve that the components of the embankment needs to be investigated and the influence of the parameters on the vibration needs to be identified through literature review. Referring to the parameters influence on vibration, the components will be modified to form a mathematical model. Analytical calculations using this model will be conducted using MATLAB and numerical calculations using Finite Element analysis will be made using ANSYS software. The analytical and numerical calculations are compared with each other and also verified using literature data.

1.1 Objectives

Vibration induced by high speed train is a growing urban issue and mitigating methods needs to be put in place to attenuate the vibrations. Generally, the methods to lower the effects of vibration can be classified into two, which is active mitigation, where modification is applied to the railway support and passive mitigation, where nearby buildings are modified with better vibration damping properties. This paper focuses on active mitigation as this is the most sought out method in real life [4].

To modify the railway support or embankment, the properties of the components which makes up the railway embankment is investigated. Next the properties are altered and the result of that quantified using the research methods of analytical and numerical modelling.

1. Investigate the parameters which influence ground vibration induced by high speed lines.
2. To modify the embankment components parameters to achieve greater vibration suppression.
3. To verify the accuracy of the analytical and numerical modelling with each other and literature data.

1.2 Literature review

1.2.1 Railway components

A typical rail embankment has basic four components, track, sleeper, rail pad and ballast (Fig. 1). In addition to these four, external dampers are used in some railways as well. The track is the steel bar on which the train travels and the sleepers are orderly arranged blocks of concrete blocks on which the track is placed. Ballast is the floor which is made from small stones on which the sleeper is placed and half buried in. The rail pad is the placed on the sleeper and acts as the contact to the track. Dampers are external damping structures placed on the track and sleeper to absorb vibrations. The three components to which the parameter changes are made are sleepers, ballast and dampers.

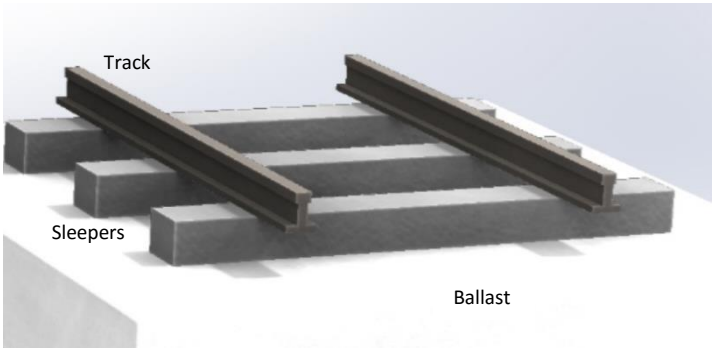


Figure 1. Rail, sleeper and ballast of a railway embankment.

1.2.2 Types of Vibration

Vibration is a periodically repeating motion. When a train moves on a rail embankment, different types of vibrations occurs. Abe *et al.* [6] states that the main causes for vibration is due to the roughness between the track and the wheel and due to differing stiffness due to periodically placed sleepers. A vibration caused by this sleeper placement is called the pinned-pinned resonance and it occurs when the vibration wavelength is same as the sleeper spacing [7]. Static loading on the track also causes vibration and in Auresh et al [8] it is modelled as a quasi-static load as the load is moved along the track. But it is the wheel/track irregularities which causes most significant vibrations. Nielsen et al [9], investigates the effect on the track as the wheel becomes more flattened due to skidding and grinding. The results showed that the level of ground vibration was much higher for trains with flattened wheels.

1.2.3 Selected parameters

For sleeper, the parameters selected are spacing between sleepers and its mass. Abe *et al.* [6] states that by reducing the spacing the pinned-pinned vibration can be reduced. It also a study by Dwight *et al.* [10] found that mass of the sleeper effects the wave frequencies of the track. The dimension of the sleeper is also investigated because changing the height decreases the bending movement as stated by Kollo *et al.* [11] and this could influence the vibration as well.

Thickness and stiffness is selected for the ballast as these two parameters can be easily altered by increasing the height by adding more stones and by changing the stiffness by altering the size of the stone. Benedetto *et al.* [12] investigated the response of a rubber mixed ballast which would have low stiffness and the results should increase in vibration in low frequency bands of 10 - 30 Hz. Zhang *et al.* [13] found that the increase in thickness, decreases particle velocity. This would decrease the vibration levels as well.

The influence of rail pad on the vibration and flexural modes of the sleeper was investigated by Kaewunruen *et al.* [14] with results showing a relation between the rail pad stiffness and the bending mode with generally high stiffness of rail pad, reducing translation and rotational modes. Results also showed that most damage occurs to the sleepers in the resonant frequencies due to the modes of vibration. It is also cited in Abe *et al.* [6] that the stiffness reduction of the rail pads can influence a lower vibration on the rail system. This component is a focus of this paper due to the ease of adjustability. Changing the rail pad is economically viable compared to changing larger components such as track, sleeper and ballast. Furthermore stiffness and damping are the only variable parameter available for this component since changes to the dimension and mass are limited by the track and sleeper dimensions.

2. Modelling Methodology

2.1 One-dimensional Analytical model and Harmonic excitation

The literature review showed that the type of model used for study reflected the objectives of that study. For example, Zhang *et al.* [15] used two-dimensional analytical model as the effect of one unsupported sleeper on the other sleeper is required to be known. For investigation into wheel and track interactions as in the case of Ferrara *et al.* [16] where a new numerical model to simulate the wheel/track irregularity vibrations is presented and in the case of Nielsen *et al.* [9] where the vibration and the force impacts caused by damaged wheels are investigates, a non-linear Hertzian theory is used would also mean a two-dimensional calculation. As for Dwight *et al.* [10] which compares the Timoshenko continuous beam theory with semi-analytical finite element (SAFE) calculations uses three-dimensional modelling as the lateral in addition to vertical movement of the beam in investigated.

To comply with the objectives of this study, the model uses a one-dimensional model as the effects of direct harmonic load is investigated. Harmonic forces are useful for the investigation as they are continuously applied forces which stimulates the effects of a moving wheel and the consequent stiffness variation in addition to allowing easier understanding of resonances or parametric excitations which provides the maximum values [8]. These extremes are useful to gauge the effectiveness of parameter changes.

Therefore, for this study series of increasing degrees of freedom models up to three degrees of freedom are formed using spring, mass and damping blocks. Only one side of the rail track is used, hence the mass of the ballast and sleeper and excitation force are halved. Further changes to the model are made based on the properties of the components

2.1 Properties of Embankment Components

The important three components are the mass, damping and stiffness of the components. While mass is an easy property to determine, stiffness and damping are more challenging. Damping of materials is very difficult to discern unless by experimentation [18] and while the stiffness of a component might be simpler in comparison, stiffness changes with the dimension of the component. This is challenging for the ballast where a small volume is required to be isolated to study the effects of vibration. The effort was simplified with the analytical data from Ferrara *et al.* [16] and Zhai *et al.* [19]. Table 1. shows the properties of different components. The data is taken from sources which has similarity to parameters which is studied in this research. This includes high-speed trains at least 100 km/s of speed, concrete sleeper and at-grade railways (not underground subways or LRTs).

To calculate the stiffness the ground directly below the sleeper is taken in to account in a diverging geometry similar to a trapezoid [19]. This geometry takes in account of the load distribution. Stiffness is calculated by the formula provided by Ferrara et al [16].

$$k = \frac{2(l-b)\tan\emptyset}{\ln\left[\frac{l(2h\times tan\emptyset+b)}{b(2h\times tan\emptyset+l)}\right]} \times E \quad (1)$$

Table 1. Data for the components

Component	Property	Value	Units
Rail track	Mass	51	kg/m
	Length	850	mm
	Young Modulus	207 [16]	GPa
Rail pad	Stiffness	20 – 3500 [14]	MN/n
	Damping coefficient	15 [9], 20 [14] 75 [19]	Ns/m
	Size	$148 \times 180 \times 10$ [20]	mm
Sleeper	Mass (half)	150 [21, 19]	kg
	Spacing	600 [6, 10]	mm
	Dimension	$1250 \times 250 \times 200$ [8]	mm
	Poisson Ratio	0.15 [8]	
	Density	2500 [8], 2750 [15]	kg/m^3
Ballast	Stiffness	280.4	MN/m
	Damping coefficient	132 [9], 165 [15] 58.8 [19],	kNs/m
	Modulus of Elasticity	0.11 [19]	GPa
	Thickness	300* (200 mm subballast) [21]	mm
	Angle	35 [19]	degree

3.1 Properties of Embankment Components

The excitation force is the axle load placed on the track from the wheels of the train. This force is not the weight or the static load of the train itself, but the downward force on the track due to the movement of train. In fact, axle load of a train changes with the speed of the train [8]. Similarly to the embankment properties, the axial force should also match with the experimental excitation. The type of train from which the measurements were taken by Connolly *et al.* [21] is a high-speed TGV *Reseau* (TGV), train which operates at an average speed of 294.7 km/h or 81.89 m/s. The axle load on the track only increases up to a certain speed and from then onwards the axial load decreases [8]. Therefore, fast trains such as Sweden's X2000 train which operates at 200 km/h [22] had a lower axial load of 18.25 kN than Spain's Talgo train which operates at 160 km/h [23] had a maximum axle load of 75 kN. As the axial load of TGV was not provide, an axle load of 20 kN is selected as this value is closer to the axle load of X2000.
The excitation frequency is selected to be 5.6 Hz and 8.3 Hz for speed of 200 km/h and 300 km/h respectively. This is for an axle distance of 10 m.

3.4 Analytical model using One, Two and Three Degrees of Freedom

The equation of motion for a single degree mass with damping and stiffness is given by Eq. 2 and the harmonic excitation by Eq. 3. [24]

$$m_T\ddot{x} + c_{eq}\dot{x} + k_{eq}x = 0 \quad (2)$$

$$F\cos(\omega t) \quad (3)$$

Where, m_T is the mass. $\ddot{x}$ is the acceleration. c_{eq} is the equivalent damping of the system. $\dot{x}$ is the velocity. k_{eq} is the equivalent stiffness of the system and x is the displacement. For the Eq. 2 the force is represented by F and ω is the driving frequency and t is time.

The amplitude of the steady force response is given by the Eq. 4 and the phase, φ is given by the Eq. (3.6).

$$X = \frac{F}{\sqrt{\left[\left(k_{eq} - m_T\omega^2\right)^2 + (c_{eq}\omega)^2\right]}} \quad (4)$$

$$\varphi = \tan^{-1}\left(\frac{2\tau\omega_n\omega}{\omega_n^2 - \omega}\right) \quad (5)$$

Where, τ is the damping ratio.

The Eqs. 4 and 5 are used to find the harmonic response of the system. Eq. 6 shows the final form of the equation. The homogenous or transient response is not included as the motion begins from zero initial velocity and displacement, therefore these responses will be zero.

$$x(t) = X\sin(\omega t - \varphi) \quad (6)$$

The analytical model is also verified using MATLAB Simulink model shown in (Fig 3). The results from Eq. 6 is verified by the Simulink model which is a second order model calculated using ordinary differential equation of Dormand-Prince method.

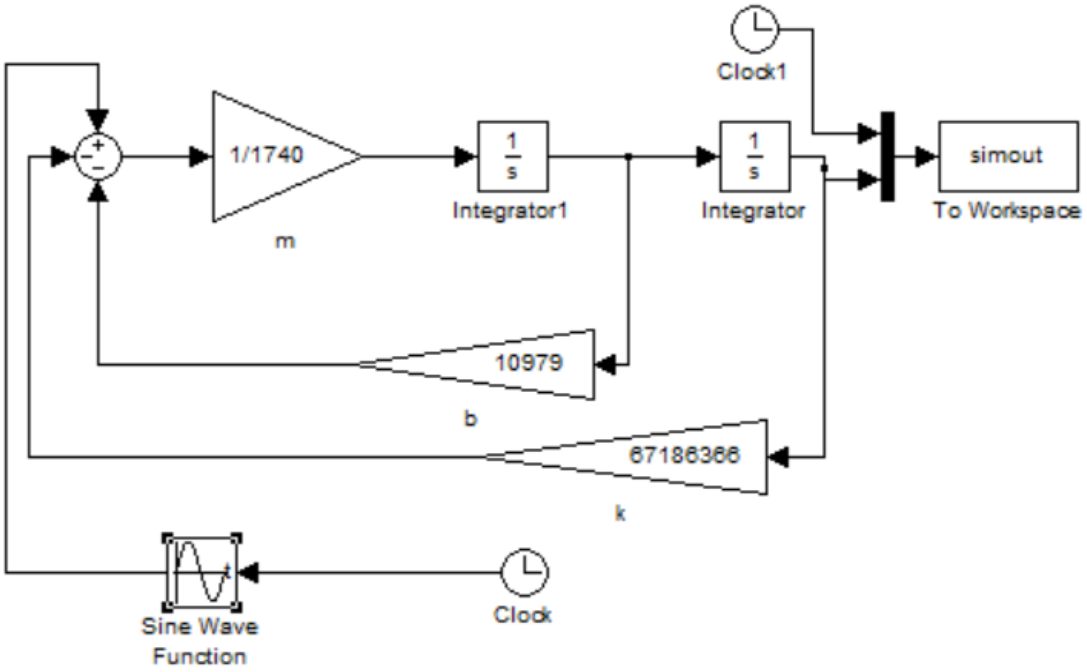


Figure 3 Simulink model for harmonic excitation for a spring damper system

Multi-degree of freedom models is more complicated than one degree of freedom as each mass are coupled with the subsequent masses. Therefore, decoupling is required to measure the individual response of the mass. Eq. 7 and Eq. 8 shows that general two-degree and three-degree of freedom system under harmonic force.

$$\begin{bmatrix} m_1 & 0 \\ 0 & m_2 \end{bmatrix}\begin{Bmatrix} \ddot{x}_1 \\ \ddot{x}_2 \end{Bmatrix} + \begin{bmatrix} c_1 + c_2 & -c_2 \\ -c_2 & c_2 \end{bmatrix}\begin{Bmatrix} \dot{x}_1 \\ \dot{x}_2 \end{Bmatrix} + \begin{bmatrix} k_1 + k_2 & -k_2 \\ -k_2 & k_2 \end{bmatrix}\begin{Bmatrix} x_1 \\ x_2 \end{Bmatrix} = \begin{Bmatrix} 1 \\ 0 \end{Bmatrix} F e^{i\omega t} \quad (7)$$

$$\begin{bmatrix} m_1 & 0 & 0 \\ 0 & m_2 & 0 \\ 0 & 0 & m_3 \end{bmatrix}\begin{Bmatrix} \ddot{x}_1 \\ \ddot{x}_2 \\ \ddot{x}_3 \end{Bmatrix} + \begin{bmatrix} c_1 + c_2 & -c_2 & 0 \\ -c_2 & c_2 + c_3 & -c_3 \\ 0 & -c_3 & c_3 \end{bmatrix}\begin{Bmatrix} \dot{x}_1 \\ \dot{x}_2 \\ \dot{x}_3 \end{Bmatrix} + \begin{bmatrix} k_1 + k_2 & -k_2 & 0 \\ -k_2 & k_2 + k_3 & -k_3 \\ 0 & -k_3 & k_3 \end{bmatrix}\begin{Bmatrix} x_1 \\ x_2 \\ x_3 \end{Bmatrix} = \begin{Bmatrix} 1 \\ 0 \\ 0 \end{Bmatrix} F \cos \omega t \quad (8)$$

Beginning from three-degree of freedom, Eq. 8 shows the general system of (Fig. 4). The masses from top to bottom with the subscript 1,2 and 3 are of track, sleeper and ballast. The stiffness and damping coefficient of subscript 1 are of the rail pad, then for the ballast for subscript 2 and 3. As the force is applied on the track, only the first matrix for force is placed by a harmonic excitation while the rest are zero.

For the two-degree of freedom, in Eq. 7 the mass (m_1) combines the mass of track and the sleeper. Also stiffness and the damping are for the rail pad and for ballast. The property of ballast is not duplicated as in the three-degree of freedom equation.

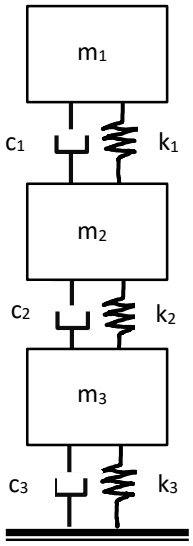


Figure 4. Three degree of freedom system

Two separate methods have been used for the solving Eq. 7 and Eq. 8. For two-degree of freedom system, mechanical impedance *Z(iω)* is used to find the response for the two-degree of freedom displacement, velocity and acceleration as shown in Eq. 9 – 3. 14. For

$$x_1(t) = X_1 e^{i\omega t} \quad (9)$$
$$x_2(t) = X_2 e^{i\omega t} \quad (10)$$

Eqs. 9 and 10 are steady state displacement solution for the amplitudes X_1 and X_2 with the forcing frequency of ω. The values for the amplitudes are obtained from the mechanical impedance Eqs. 12 and 12.

$$Z_{rs}(i\omega) = -\omega^2 m_{rs} + i\omega_{rs} + k_{rs} \quad (12)$$

The subscript rs corresponds to the location of the property in the matrices in Eq. 7.

$$X_1 = \frac{Z_{22}(i\omega)F_{10}}{Z_{11}(i\omega)Z_{22}(i\omega) - Z_{12}^2(i\omega)} \quad (13)$$
$$X_2 = \frac{-Z_{12}(i\omega)F_{10}}{Z_{11}(i\omega)Z_{22}(i\omega) - Z_{12}^2(i\omega)} \quad (14)$$

But substituting the values of X_1 and X_2 to Eqs. 9 and 10, the displacement due to force can be calculated. To find the velocity and the acceleration the Eqs. 9 and 10 are differentiated once for velocity and twice for acceleration.
An easier route has been taken for three-degree of freedom equation by using MATHLAB ordinary differential equation 23 for calculation. Appendix A shows the differential equations used where the three equations from the matric in Eq. 8 is set as six first order differential equations.
Another important formula for quantifying the level of vibration is decibels formula Eq. 15. Decibels helps to standardise results so that it can be compared with data from other sources [25].

$$L_v = 20\ log_{10}\left(\frac{v}{v_{ref}}\right) \quad (15)$$

L_v is the velocity level represented in decibels and v_{ref} is the reference velocity. This velocity is an accepted value for reference agencies such as International Organisation for Standardisation (ISO) and Federal Transit Administration (FTA). The value used in this paper is $2.54 \times 10^{-8} m/s$ which is the value used by the FTA [25].

3.5 Numerical modelling

Similarly, to the analytical model, the numerical model uses a single track, sleeper and ballast (Fig. 5). But in addition to the analytical modelling a rail pad is modelled and placed as well. Furthermore, the ballast was modelled in a trapezoid geometry for model A and model B uses two sleepers to test the response due to varying the sleeper distance. The components where modelled from SOLIDWORK and was imported to ANSYS Workbench. The bodies were given the material properties and then Harmonic Response module was selected to apply a force of 10000N on the track

surface. The boundary condition is set as frictionless support and the frequency range is selected from 0 to 250 Hz with 10 Hz increment. Same properties from Table. 1 is used for the material data.

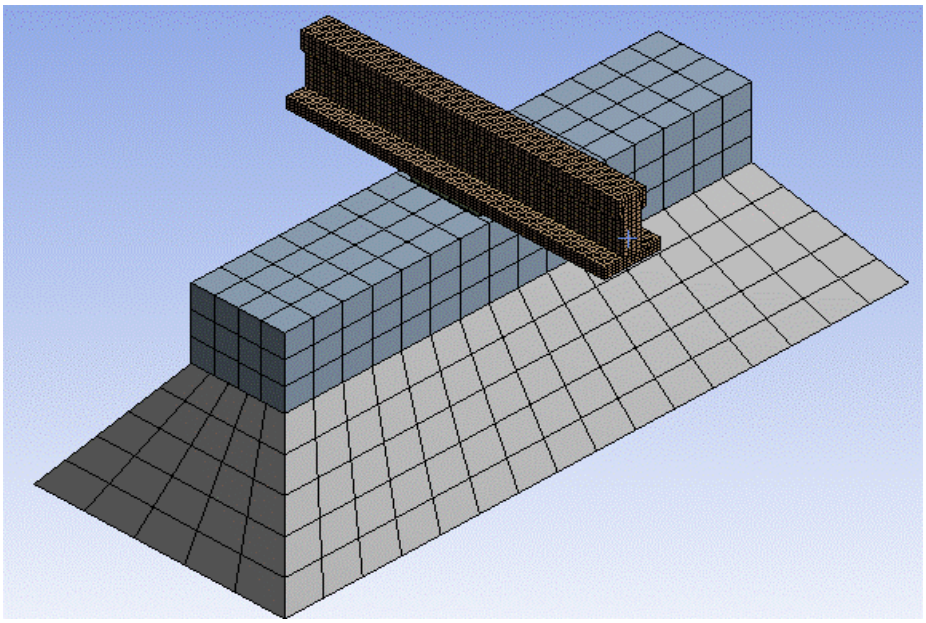


Figure 5: One sleeper model A

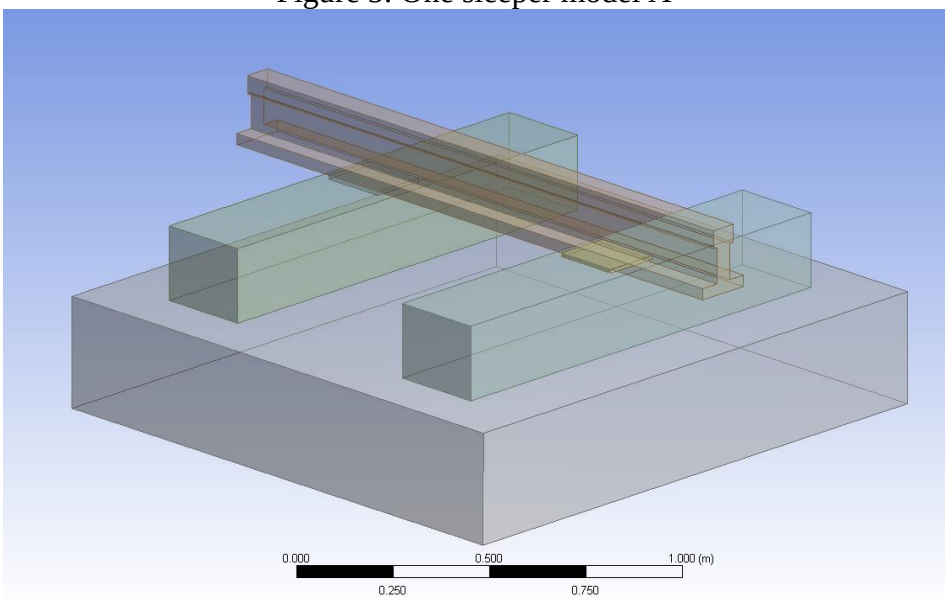


Figure 6. Numerical model of the track, sleeper and ballast with the force being applied to the track in negative y-direction.

Table 2. Mesh Property of Model A and B

Mesh Property	Model A, one sleeper	Model B, two sleepers
Element size	For track 0.01 m Rest of the body Automatic	For track 0.01 m Rest of the body Automatic
Meshing Method	Hexagonal	Hexagonal
Number of Elements	61714	1339267
Element Quality	0.955	0.962

Skewness	0.0574	0.0486

3. Results and Discussion of Analytical and Numerical Modelling

The analytical model is done using formulas and calculations. Therefore, an error might occur in the calculations which might offset the results. To verify that there is no such error, Simulink model is made to calculate the harmonic motion of a second order differential equation. The results showed that there is observable correlation and this is statistically proven with the Table .3 Pearson correlation, which indicates strong relation between the two means as the value is close to value one, and the value of the statistical test, 0.9733 is very close to one. Furthermore the t-critical is much higher than the t-statistical value, hence there is 95% confidence that the mean is similar.

There are many disadvantages of using the one-degree of freedom as the effects of individual components properties cannot be discussed as the total and equivalent values are used. Therefore, the second-degree of freedom model from Eqs. 9 and 10 are used to provide the results. The results are formed with velocity response for two masses. The first mass is the total mass of track and sleeper and the second mass is that of the ballast. These results are also given in frequency domain as well to compare with the numerical results for harmonic excitation. The three-degree of freedom is not used because second-degree od freedom model is easier to convert to velocity response and the mass of track and sleeper is not large compared to ballast, so they can be combined.

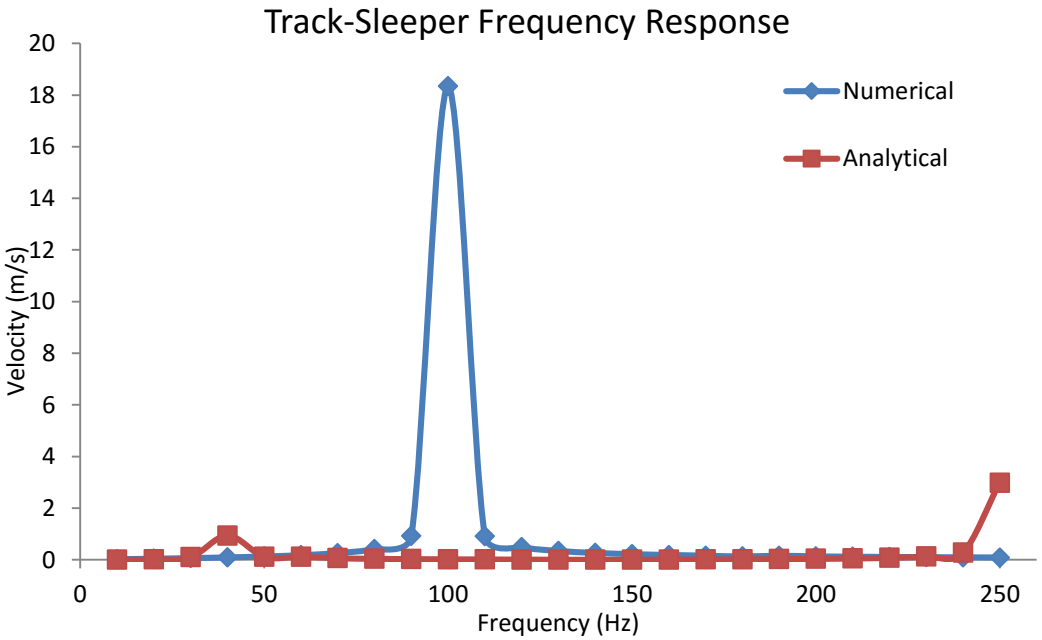


Figure 8. velocity frequency of numerical and analytical second-degree freedom model for track- sleeper

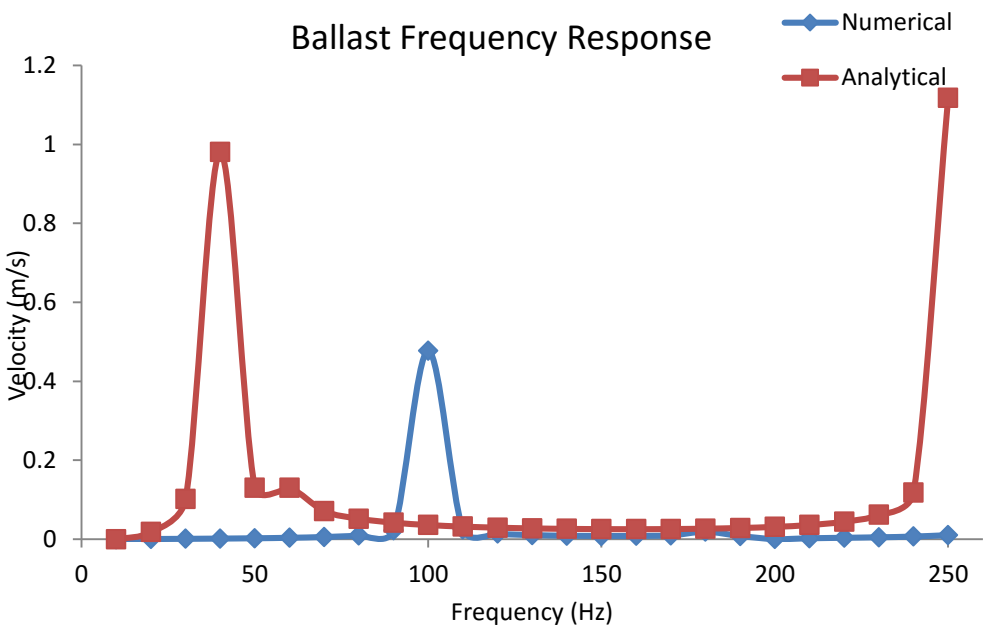


Figure 9. velocity frequency of numerical and analytical second-degree freedom model for ballast

While the visual comparison between the numerical and the analytical model (Fig. 8 and 10) might seem apparent because of the peaks, the lower values remain close to each other for both figures. Provides 95% confidence that the means are the same for both of the models. The t-statistical is lower than the t-critical for both the tests but the Pearson Correlation is low. This means that while correlation is not very high the means are nevertheless same. The peaks for numerical model is at 100 Hz and for analytical at 40 and 250 Hz The modal simulation using ANSYS Workbench modal analysis module shows that at 100 Hz the natural frequency of the rail pad is reached (Fig 10). This causes the high vibration response. Therefore, the excitation frequency must not reach this 100 Hz while using the rail pad with this particular stiffness form Table .1 of 20 MN/m.

Table 3. Paired Two Sample for Means t-test for Analytical and Simulink results

	Simulink	*Analytical*
Mean	1.48E-05	7.56E-06
Variance	1.44E-07	1.82E-07
Observations	21	21
Pearson Correlation	0.973328	
Hypothesized Mean Difference	0	
Degree of Freedom	20	
t Stat	0.317091	
P(T<=t) two-tail	0.754461	
t Critical two-tail	0.686954	

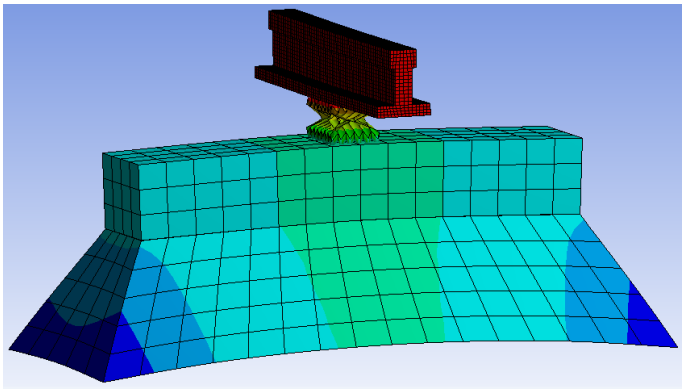


Figure 10. modal analysis for numerical Model A using modal analysis.

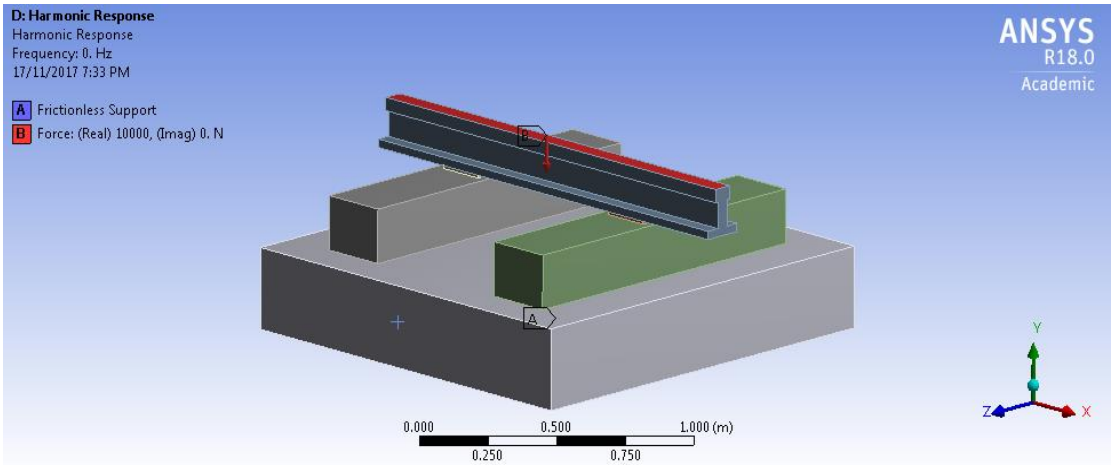


Figure 11. Model used to study the vibration response to different sleeper spacing

Numerical model to investigate the relation between acceleration response due to sleeper distances of 50, 60 and 70 cm was simulated using the (Fig. 11) model. The results provided in Appendix B gave insufficient difference to the response. This is validated using ANOVA test in Table 4.5 where the F-critical 3.12 is greater than F-statistics of 1.88. The reason for using ANOVA is that means of three sets needed to be compared.

Table 5. Show the summary of variance of the sleeper spacing and the F-test

SUMMARY

Groups	*Count*	*Sum*	*Average*	*Variance*
50cm	25	14.24983	0.569993	0.805951
60cm	25	208.6954	8.347815	578.3901
70cm	25	77.36599	3.094639	48.01165

ANOVA

Source of Variation	*SS*	*df*	*MS*	*F*	*P-value*	*F crit*
Between Groups	787.2018	2	393.6009	1.882634	0.159604	3.123907
Within Groups	15052.99	72	209.0692			
Total	15840.19	74				

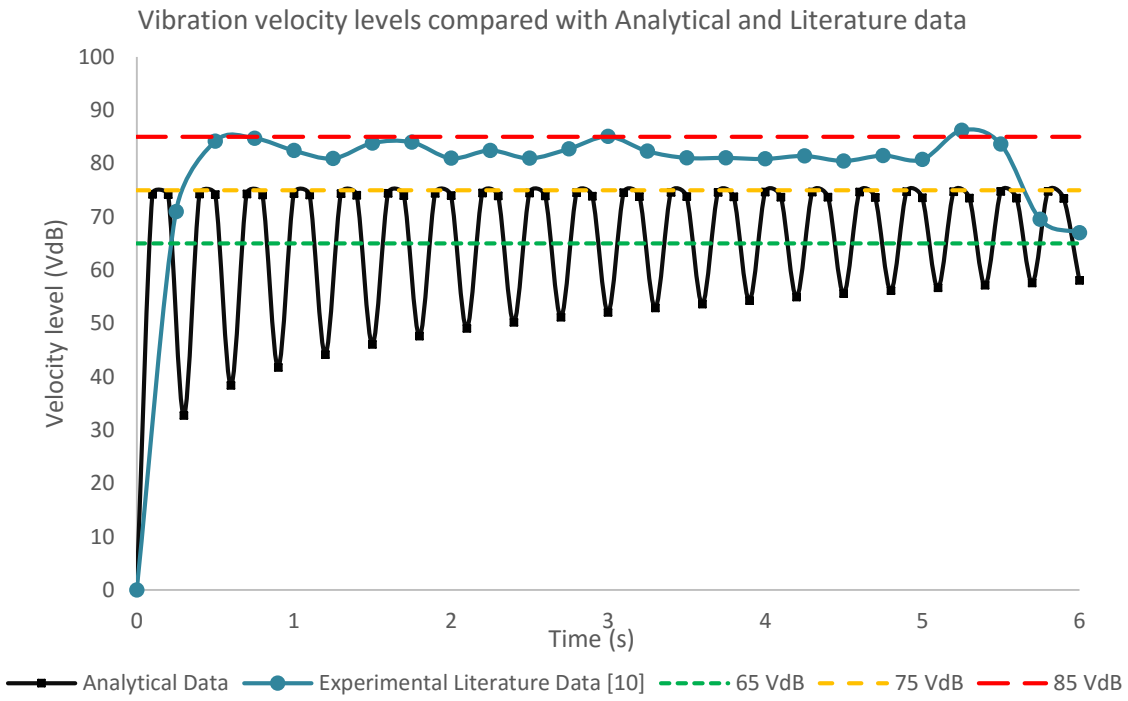


Figure 12. Actual literature data compared with analytical data with benchmarking of 65 VdB, 75 VdB and 85 VdB

It was found out by analytical calculations that rail pad stiffness produces high response on the vibration of the system. Therefore, using Matlab, the lowest possible value of vibration was produced with the provided pad stiffness from Table 3.2. The as the stiffness increases the vibration of the system decreased. Therefore, the highest stiffness value of 3500 MN/m value was used. This material corresponds to high density Ethylene vinyl acetate polymer (EVA) [14]. The maximum value from the analytical data was compared for the frequency using alternatively 5.6 and 8.3 Hz. As 8.3 Hz had higher magnitudes it was selected.

The lowest analytical vibration response was then converted to velocity decibels which has the reference value of $2.54 \times 10^{-8}\mathrm{m/s}$ [25] to make it easier to compare with the benchmark values. The three dashed lines of values 65, 75 and 85 VdB (Fig. 12) is the three bands of vibration levels which will be felt by humans with the intensity increasing with the values. This is stated in the "Transit Noise and Vibration Impact Assessment", released by American Federal Transit Administration (FTA) [25], that while 65 VdB is barely precipitable for humans and 75 VdB can be annoying for some, at 85 VdB people will find this level disruptive and is acceptable if only infrequent amount of trips.

Changes to the rail pad stiffness is effective for suppressing vibrations (Fig. 12). This statistically proven with ANOVA single factor test of 95% confidence in Table 4.4 as the F-statistical values of 8.47 larger than 3.95 F-critical. ANOVA single factor was used due to the difference in count for the results.

Table 6. Show the summary of variance of the analytical and literature data and the F-test

SUMMARY

Groups	*Count*	*Sum*	*Average*	*Variance*

Analytical Data	61	3976.862	65.19446	211.7338
Literature Data	29	2181.412	75.22116	278.9576

ANOVA

Source of Variation	*SS*	*df*	*MS*	*F*	*P-value*	*F crit*
Between Groups	1976.05	1	1976.05	8.476418	0.004558	3.949321
Within Groups	20514.84	88	233.1232			
Total	22490.89	89				

5. Conclusions

In this study, a simplified analytical model and a numerical model is made to understand the vibration response due to a train load which is simulated by harmonic excitation. The numerical modelling showed that a resonance does occur 100 Hz range which belongs to the rail pad. List of components of the rail embankment has been reviewed using journal articles and their vibration influencing parameters in addition to their other properties have been complied and refined to make sure they meet the scope of the project. Then analytical and numerical models where created using ANSYS and Matlab for numerical and analytical respectively. A model very closed to the actual literature data was made and the vibration was supressed by increasing the rail pad stiffness. Comparison between the modified analytical model gives the velocity response of 75 VdB as the maximum peak.

Two-dimensional modelling is required to investigate more complex vibrations and also take in the influence of geometry of the components such as sleeper spacing. Also scope of the project needs to be more focused on particular train or trains from certain region, as different regions uses different types of trains and embankment. Most importantly an acoustic assessment is required to understand the noise generated under the new rail pad stiffness. If the stiffness had worsened the noise, other methods needs to be explored such as using external dampers.

References

[1] H. Williams, Road and rail transportation, 1st ed. New York: Facts on File, 2004, pp. 50-52.

[2] R. Abe and H. Kato, "What led to the establishment of a rail-oriented city? Determinants of urban rail supply in Tokyo, Japan, 1950–2010", Transport Policy, vol. 58, pp. 72-79, 2017.

[3] F. Laroche, C. Sys, T. Vanelslander and E. Van de Voorde, "Imperfect competition in a network industry: The case of the European rail freight market", Transport Policy, vol. 58, pp. 53-61, 2017.

[4] Z. Chen, J. Xue, A. Rose and K. Haynes, "The impact of high-speed rail investment on economic and environmental change in China: A dynamic CGE analysis", Transportation Research Part A: Policy and Practice, vol. 92, pp. 232-245, 2016.

[5] D. Connolly, G. Marecki, G. Kouroussis, I. Thalassinakis and P. Woodward, "The growth of railway ground vibration problems — A review", Science of The Total Environment, vol. 568, pp. 1276-1282, 2016.

[6] K. Abe, Y. Chida, P. E. Balde Quinay, and K. Koro, “Dynamic instability of a wheel moving on a discretely supported infinite rail,” J. Sound Vib., vol. 333, no. 15, pp. 3413–3427, 2014.

[7] N. Persson, "Predicting Railway-Induced Ground Vibrations", Post Graduate, Lung University, 2016.

[8] L. Auersch, “The excitation of ground vibration by rail traffic: Theory of vehicle-track-soil interaction and measurements on high-speed lines,” J. Sound Vib., vol. 284, no. 1–2, pp. 103–132, 2005.

[9] J. C. O. Nielsen, G. Lombaert, and S. François, “A hybrid model for prediction of ground-borne vibration due to discrete wheel/rail irregularities,” J. Sound Vib., vol. 345, pp. 103–120, 2015.

[10] W. Li, R. A. Dwight, and T. Zhang, “On the study of vibration of a supported railway rail using the semi-analytical finite element method,” J. Sound Vib., vol. 345, pp. 121–145, 2015.

[11] S. A. Köllő, G. Köllő, and A. Puskás, “Nexus of the Load Bearing Capacity of Rails and the Stiffness of the Optimized Sleepers,” Procedia Technol., vol. 22, pp. 312–318, 2016.

[12] A. Benedetto, F. Tosti, L. Bianchini Ciampoli, A. Calvi, M. G. Brancadoro, and A. M. Alani, “Railway ballast condition assessment using ground-penetrating radar – An experimental, numerical simulation and modelling development,” Constr. Build. Mater., vol. 140, pp. 508–520, 2017.

[13] Z. Zhang, X. Zhang, H. Qiu, and M. Daddow, “Dynamic characteristics of track-ballast-silty clay with irregular vibration levels generated by high-speed train based on DEM,” Constr. Build. Mater., vol. 125, pp. 564–573, 2016.

[14] S. Kaewunruen and A. M. Remennikov, “Sensitivity analysis of free vibration characteristics of an in situ railway concrete sleeper to variations of rail pad parameters,” J. Sound Vib., vol. 298, no. 1–2, pp. 453–461, 2006.

[15] S. Zhang, X. Xiao, Z. Wen, and X. Jin, “Effect of unsupported sleepers on wheel/rail normal load,” Soil Dyn. Earthq. Eng., vol. 28, no. 8, pp. 662–673, 2008.

[16] R. Ferrara, G. Leonardi, and F. Jourdan, “SIIV - 5th International Congress - Sustainability of Road Infrastructures Numerical Modelling of Train Induced Vibrations,” Procedia - Soc. Behav. Sci., vol. 53, no. 0, pp. 155–165, 2012.

[18] D. Inman, Engineering vibration, 4th ed. Boston: Pearson, 2014, pp. 16 - 58.

[19] W. Zhai, K. Wang and J. Lin, "Modelling and experiment of railway ballast vibrations", Journal of Sound and Vibration, vol. 270, no. 4-5, pp. 673-683, 2004.

[20] J. Stead and M. Kerr, “Spc 232 concrete sleepers,” 2012.

[21] D. P. Connolly, G. Kouroussis, P. K. Woodward, P. Alves Costa, O. Verlinden, and M. C. Forde, “Field testing and analysis of high speed rail vibrations,” Soil Dyn. Earthq. Eng., vol. 67, pp. 102–118, 2014.

[22] S. A. Suhairy, “Prediction Of Ground Vibration From Railways”, Undergraduate Graduate Thesis, Swedish National Testing and Research Institute, 2000.

[23] I. Crespo-Chacón, J. García-de-la-Oliva and E. Santiago-Recuerda, "On the Use of Geophones in the Low-Frequency Regime to Study Rail Vibrations", Procedia Engineering, vol. 143, pp. 782-794, 2016.

[24] S. Rao, Mechanical vibration, 5th ed. Reading, Massachussetts: Addison Wesley, 2011, pp. 257 - 374.

[25] Federal Transit Administration, "Transit Noise and Vibration Impact Assesment", 2006.

eureca 2017 – Conference Paper
Paper Number 2ME02

Numerical Analysis and Geometry Optimisation of Vertical Vane of Room Air-conditioner

Chan Wei Yin[1*], Abdulkareem Sh. Mahdi Al-Obaidi[1], Felicia Wong Yen Myan[1], Yan Yao Chen[1]

[1]*School of Engineering, Taylor's University, Malaysia*

[*]chanweiyin@sd.taylors.edu.com

Abstract

Vertical vanes of room air-conditioners are used to control and direct cold air. This research aims to study vertical vane as part of parameters that affect the efficiency of dissipating cold air to a given space. Next, the research study will continue to analyse and optimise the vertical vane geometry for lower production cost using CFD. The optimised geometry of the vertical vane should have the same or increased efficiency of dissipating cold air and have lesser mass compared to the existing original design. In this research, the existing original design of vertical vane is simplified and analysed by using ANSYS Fluent ver. 18. 15º and 30º rotation of vertical vane inside room air-conditioner are simulated in order to calculate the efficiency of wind direction. Efficiency of wind direction is define as how accurate the direction of airflow coming out from vertical vane. The efficiency of wind direction for 15º rotation of vertical vane is 57.81 % while efficiency of wind direction for 30º rotation of vertical vane is 47.54 %. The result of the efficiency of wind direction are used as base reference for parameter. The parameter studies for optimisation of vertical vane are focused at length of long span, tip chord and short span. The best configuration of design of vertical vane is determined in analysis of parameter studies.

Keywords: Air-conditioners, CFD, Geometry Optimisation, Vertical Vane, Efficiency, Dissipating cold air

1. Introduction

Vertical vane is part of air-conditioners that can set horizontal air flow direction to left or right. Currently, vertical vane is rarely been studied as part of parameters that affect the efficiency of dissipating cold air to a given space. Most studies and researches have been done on horizontal louver's parameters that will affect the performance of air-conditioners. However, the studies that investigate the horizontal louvers can be used as reference for vertical vanes since the boundary conditions for both are the same in CFD simulation. With the assist of CFD software, geometries changes of vertical vane can be analysed without wasting money to manufacture it [1]. Moreover, CFD software can save time by simulating the case study instead of conducting physical testing with equipment such as wind tunnel. Panasonic is one of the companies that concern about any improvement can be made from design of vertical vane.

Nakanishi et al. [8] investigate the air flow passing through louver. The change of louver angle that cause pressure is studied. Three different louver model respectively with louver angle of 45º, 35º and 25º were tested. Laser Doppler Velocimetry (LDV) and smoke wire methods have been conducted to visualise the pattern and velocity of airflow. After that, CFD++ software is used to simulate the result. The result of experiment and CFD were compared where the compressible Navier-Stokes equation and k-ε turbulence model are used in CFD simulation. The CFD could have good agreement with the experimental result from LDV and smoke wire methods. It is concluded that the larger the louver angle, the larger the vortexes. The velocity of airflow is increased due to the narrowed flow path by large vortexes. As a result, the pressure loss is increased with larger louver angle.

A similar study from Noh et al. [3] was conducted which was based on the research of Nakanishi et al [2]. This research investigates how the shape of airfoil and flat louver affect the pressure drop across weather hood. Moreover, different angles of attack which were 25º, 35º and 45º were studied at both shape and flat louvers. The numerical method was conducted by using SolidWorks Flow Simulation software. Since the inlet velocity of airflow did not reach 0.3 Ma (Mach number), incompressible flow was applied [4]. Incompressible flow was applied and standard k-ε turbulence model were used in CFD simulation. It is concluded that higher louver angle will induce greater pressure drop due to the increase in velocity of airflow. Other than that, airfoil louvers show less pressure drop compared to the flat louvers. In result, airfoil louvers with louver angle of 25º contributed the lowest pressure drop compared to flat louvers and other louver angles.

CFD used as reliable tool to predict the indoor airflow in recent years [5-8]. For instance, Karimipanah et al. [6] conducted several times of researches about the indoor air quality and comfort conditions in classroom. The initiative of investigating indoor air quality is due to the reason of caring the pupil's health and those children who have allergy or asthma. In this research, Karimipanah has compared result calculated by RNG (Re-Normalisation Group) turbulence model and standard k-ε turbulence model respectively with measured result. It is concluded that RNG turbulence model can simulate velocity of airflow with higher agreement with measured result. In contrast, standard k-ε turbulence model shows better capability of predicting the temperature distribution over the classroom compared to RNG turbulence model. This research

gives a good idea of choosing suitable turbulence model to get desired simulation result which is approximated to measured result closely.

S. Sadrizadeh [9] has done a very detail study about different type of turbulence models applied for indoor airflow prediction. There is nine type of turbulence models are analysed and validated with the experimental result. The experiment is carried out in a box-shaped wind tunnel. A mannequin was built to model a people sitting inside a room (wind tunnel). The locations of measured temperature and velocity were at both front of and behind the mannequin. Most of the Reynolds averaged Navier-Strokes approach (RANS) were selected to apply in the CFD simulation in this study. RNG k-ε (Re-normalisation Group) is the best prediction of velocity of airflow out of RANS turbulence models.

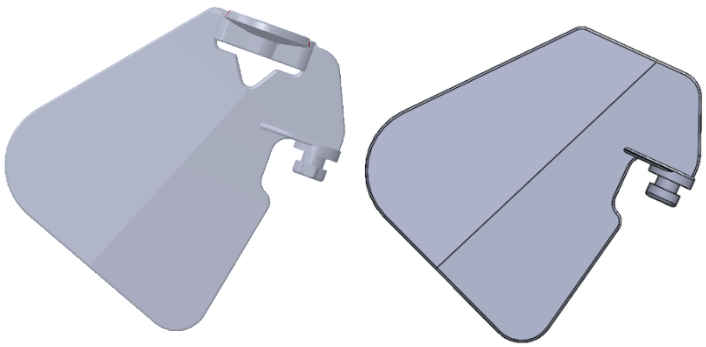
This research aims to analyse and optimise the geometry of the vertical vane in order to minimise its mass for lower production cost. Besides that, optimising geometry of vertical vane shall not bring negative impact to the performance and efficiency. Firstly, the method of defining the efficiency for simplified vertical vane is studied and analysed. Next, different geometries and dimensions of vertical vane will be analysed using ANSYS Fluent ver. 18 (CFD software) for a given set of flow conditions. The research process will be follow by optimisation to select the vertical vane shape which should have same efficiency of dissipating cold air compared to the existing original vertical vane.

2. Research Methodology

The method of doing numerical analysis of vertical vane is written and explained in this section. Besides that, the calculation of efficiency for vertical vane is defined. The study part of vertical vane has been provided [10].

2.1 3D CAD Modelling

The geometry of existing original design of vertical vane is studied and the assumptions of 3D CAD modelling is made for geometry clean-up. The simplified vertical vane is drawn by using SolidWorks ver. 2016. The existing original design and simplified vertical vane is shown in Fig 1. The simplified vertical vane is redrawn based on a few assumptions made.



(a) **(b)**

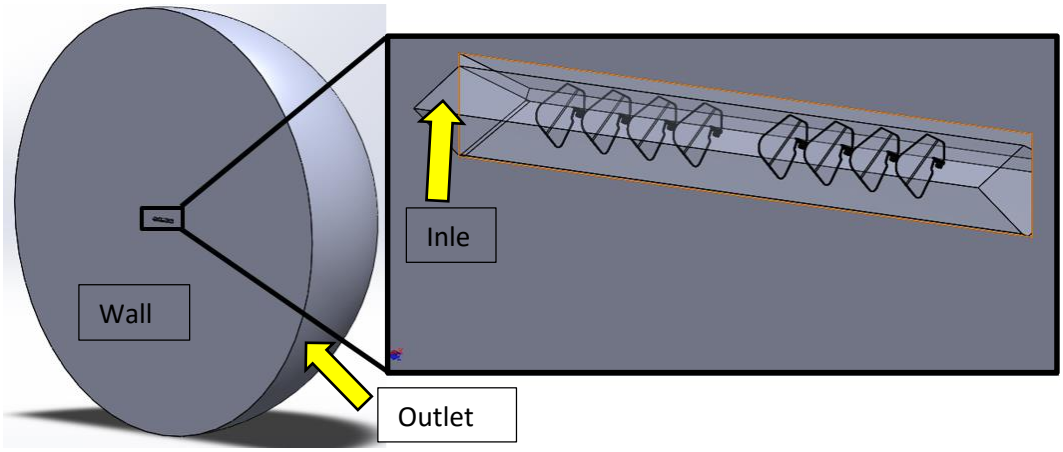
Figure 1. Vertical vane (a) existing original design (b) simplified

Firstly, the tip of vertical vane where it attached to air-conditioner is assumed no air flow into the hole. The reason is the tip part will later be locked with a nut and the volume will be filled after assembly. Thus, the tip of vertical vane is simplified to have filled volume. Besides that, the hook of vertical vane where the connecting bar attached to is simplified to become fillet instead of having irregular shape of hook. Changing the geometry of hook will not affect the air flow that much but it helps to reduce complexity of geometry in CFD simulation afterward. The circumference length of simplified vertical vane follows exactly the dimension of existing original design. For the upper surface of vertical vane, it is simplified to have same thickness as lower surface. The reason is the thickness of vertical vane contributes very small effect to velocity of air flow.

2.2 Numerical Modelling

2.2.1 Geometry modelling

Geometry model for CFD is based on a condition that air-conditioner is installed in a 6 m × 5 m × 3.5 m of room. Usually, the fluid domain should build with 5 meter square base with height of 3.5 m for this model. However, back flow of air is not the outcome that wanted to focus in simulation. Thus, the fluid domain drawn for this model is much bigger than size of the room. It can increase the accuracy of simulated result. Shell of room air-conditioner is drawn and vertical vanes are placed inside the shell. Following by that, a half sphere shape of fluid domain is drawn and shown in Fig 2. The half sphere is drawn with 10 m diameter.



(a) **(b)**

Figure 2. (a) The half sphere of fluid domain and (b) location of vertical vane in transparent view

Two different rotations of simplified vertical vane are studied. First case is to simulate the 0º of vertical vane in Fig 3 (a) and the second case is to simulate the 30º angle of vertical vane in Fig 3 (b). The case of 0º angle of vertical vane is used as base reference for meshing size. The 30º is the maximum rotation that allow to rotate for the product of room air-conditioner.

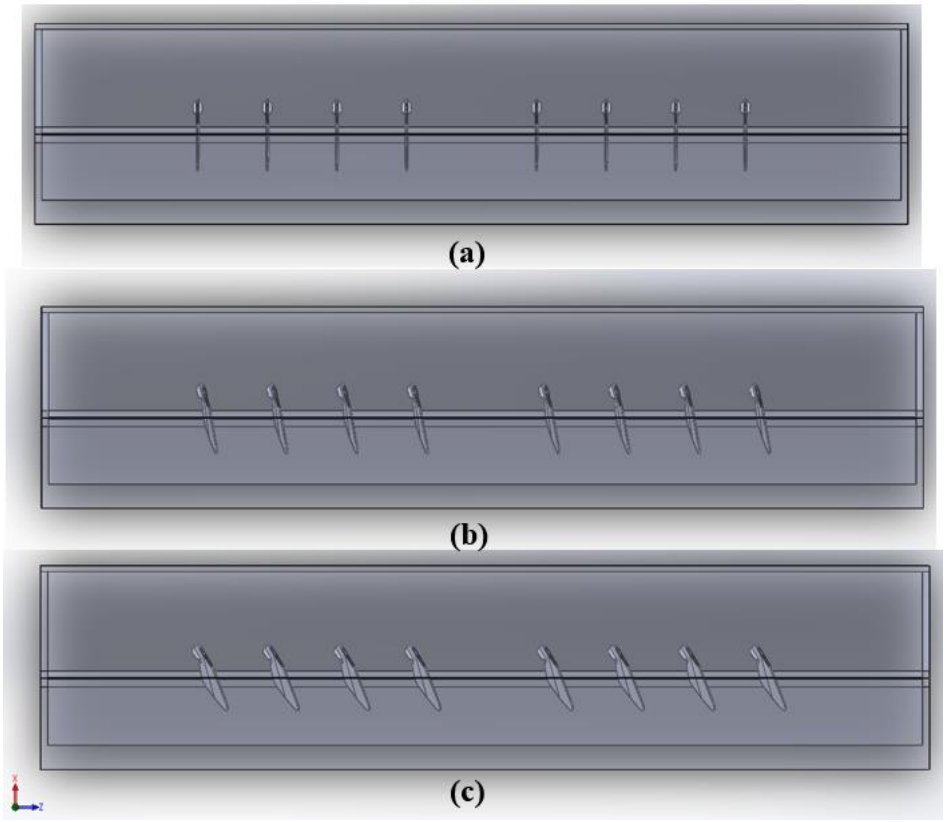


Figure 3. Rotation of simplified vertical vane (a) 0º (b) 15º (c) 30º

2.2.2 Meshing generation

The mesh quality of model is very important as it will affect the accuracy of solution generated in post-processing. First of all, unstructured type of mesh is applied for this model as the fluid domain has complicated geometry of vertical vane. By choosing the unstructured mesh, the meshing quality is improved and the computing time is also increased to solve for simulation [7].

Tetrahedral type of meshing element is selected due to the fillets and curvatures of vertical vanes and enclosed domain. After that, the edge sizing is added to shell of room air-conditioner. It is to increase the number of mesh element, so the velocity of air flow is captured with more accurate result. Moreover, inflation is added to the surfaces that bounded to the air flow inlet. The first layer thickness of 0.000643 m with 1.1 growth rate is set for the inflation. It is to ensure that the boundary layer effect is captured. The first layer of thickness is calculated based on the wall Y+ value of 30. The air flow that inside the boundary layer is named as viscous flow as it will form no slip condition where velocity of air flow equal to zero. Lastly, face meshing is added to the shell of room air-conditioner. It helps to organise the element equally over the surfaces.

However, meshing setup for 15º is slightly different from that that. In order to reach the better convergence during post-processing, another inflation is added to the surfaces of vertical vanes. When the vertical vane is rotated to 15º angle, it will cause more turbulent energy. Thus, mesh refinement is required to do for the surface of vertical vane. The meshing of model is shown in Fig 4.

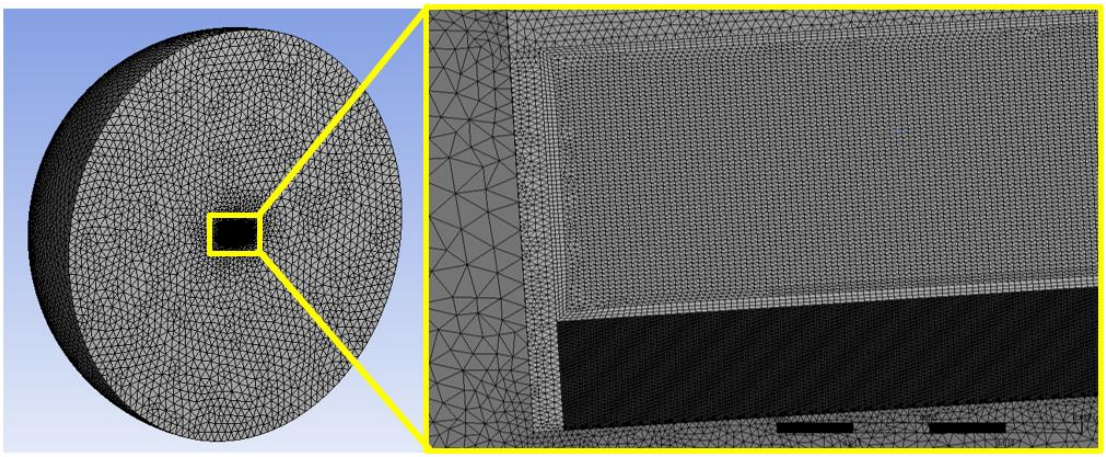


Figure 4. The meshing of CFD model

Although the meshing method applied to 15º angle of simplified vertical vane is not same as 0º angle of simplified vertical vane, it does not affect the selection of using same mesh size because meshing size is independent of grid refinement [7]. Hence, the meshing size will use the same after the grid independence.

2.2.3 Grid Independence analysis

Three level of meshing size is classified into coarse, medium and fine with respectively 0.008 m, 0.004 m and 0.002 m sizing. The purpose of doing grid independence analysis is to determine the maximum mesh size that can produce the same result as the smallest mesh size. The smallest mesh size for this model is 0.002 m as the element quality doesn't increase more after this value. The minimum growth rate for this mesh size is 1.7. Any value below 1.7 growth rate costs high increase in computing time of solving result. The advantage of doing grid independence analysis will save time on solving solution during post-processing.

As mentioned previously, 0º angle of vertical vane is used as base reference. The following result presented in table is the result of base reference. From the result of Table 1, it is not enough data to judge which mesh size to use. As the outlet velocity is the main focus in this study, the velocity of air flow should be measured and do comparison between these three different mesh size.

Table 1. Result of different mesh size

Level	Sizing (m)	Growth rate	Meshing Quality	Node	Elements	Iteration	Time (hours)
Coarse	0.008	1.15	0.80003	733666	3140164	1408	1.7
		1.17	0.79756	717586	3044681	597	0.6
Medium	0.004	1.15	0.80015	733224	3137247	2154	2.6
		1.17	0.79718	717363	3043687	831	1.0
Fine	0.002	1.15	0.79992	733761	3140411	> 4000	>10
		1.17	0.79729	717637	3043217	770	0.9

2.2.4 Numerical Setup

RNG k-ε turbulent model is derived from instantaneous Navier-Stokes equations or renormalization group which is using statistical technique. RNG k-ε turbulent is applied to the CFD model because it has been proved to have good prediction for velocity of airflow at indoor environment. [6, 8]. Next, standard wall function is used for this conditions. For the outlet surface, it is defined as pressure outlet.

Lastly, the boundary conditions that have been set in ANSYS Fluent ver. 18 are shown in Table 2. Since the inlet velocity is 5.8 m/s which is less than the 0.3 Ma (Mach number), incompressible flow is applied. On the other hands, the volume of simplified vertical vane is 2.4 X 10^{-6} m^3. This information is important to check whether the new design of vertical vane is minimised or not as compared to the simplified vertical vane.

Table 2. Boundary setting for CFD setup

Inlet velocity (m/s)	**Temperature (ºC)**	**Density of air (kg/m^3)**	**Kinematic viscosity**	**Viscosity of air (kg/ms)**
5.8	20	1.205	1.511E-05	1.82076

2.2.5 Assumptions

The assumptions of this research's study have been made as following statements:

1. The velocity inlet for the room air-conditioner is uniform and constant at the inlet surface.
2. The temperature of room which is the enclose domain is constant.
3. No backflow is occurred at the end of wall surface (outlet).

2.2.6 Calculation

The method of analysing simplified vertical vane will be defined by calculating the distance of how far the airflow can be achieved. First of all, any velocity of airflow that is below 0.25 m/s in velocity contours is considered no wind according to the standard requirement from Panasonic. From this point, the distance where the velocity of airflow is higher than and equal to 0.25 m/s will be taken into calculation.

Furthermore, simulation result of different angle of vertical vane is analysed for efficiency of how accurate the direction of airflow coming out from vertical vane. The distance where velocity of airflow is equal to and higher than 0.25 m/s in Z axis is taken into calculation by applying Trigonometry method. For distance X, it is measured 2 m away from the room air-conditioner. For the measured line of starting point will be located at 1.13 m (Y axis) below the room air-conditioner. The calculation of angle of wind is illustrated in Fig 5.

$$\tan\theta_{wind} = \frac{distance\ in\ Z\ axis\left(velocity\ equal\ to\ and\ higher\ than\ 0.25\frac{m}{s}\right)}{distance\ in\ X\ axis\left(velocity\ equal\ to\ and\ higher\ than\ 0.25\frac{m}{s}\right)} \quad (1)$$

The efficient of wind direction is defined as equation below.

$$Efficiency\ of\ wind\ direction = \frac{\theta_{wind}}{\theta_{vertical\ vane}} \times 100\% \quad (2)$$

Where θ_{wind} is the angle of wind in simulation and $\theta_{vertical\ vane}$ is the angle of rotation of vertical vane inside room air-conditioner.

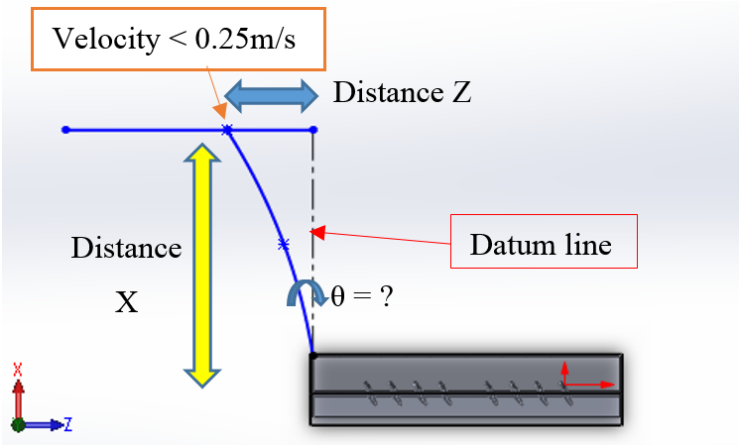


Figure 5. Calculation of angle of wind

The equation of efficiency of wind direction is used to define the efficiency of dissipating cold air. It can be applied as long as the location line is within the pathway of airflow in simulation result. In order to make the efficiency of wind direction is comparable with different angles and new designs of vertical vane, the location of measured line is fixed for all case. The location of measured line that determine the velocity of airflow from starting point to ending point is shown in Table 3.

Table 3. Distance from datum line

Location	X-axis (m)	Y- axis (m)	Z-axis (m)
Starting point	2	-1.13	0
Ending point	2	-1.13	-1.5

3. Result and Discussion

3.1 Grid Independence Analysis

The result of 0º angle of vertical vane simulated from 0.002 m, 0.004 m and 0.008 m mesh size is analysed. The velocity of airflow along the boundary edge and line 1 are measured. The measured location is shown in Fig 6 and the graph of velocity against the location is plotted in Fig 7. Observing the graph from Fig 7, the fine mesh size has higher velocity along the boundary edge as compared to medium and coarse mesh size. However, the velocity result generated by medium mesh size is more reasonable. The reason is the velocity at the middle of boundary edge reached uniform velocity of airflow where this location has big spacing between each vertical vane. Thus, the velocity of airflow is expected to have higher velocity compared to other location. Besides that, the velocity of airflow is almost symmetrical. The medium mesh size can be chosen as constant variable for meshing setting.

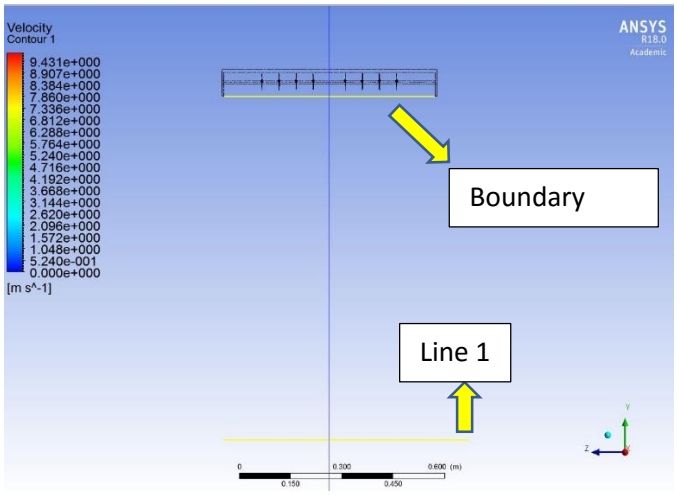


Figure 6. Location of boundary edge and line 1

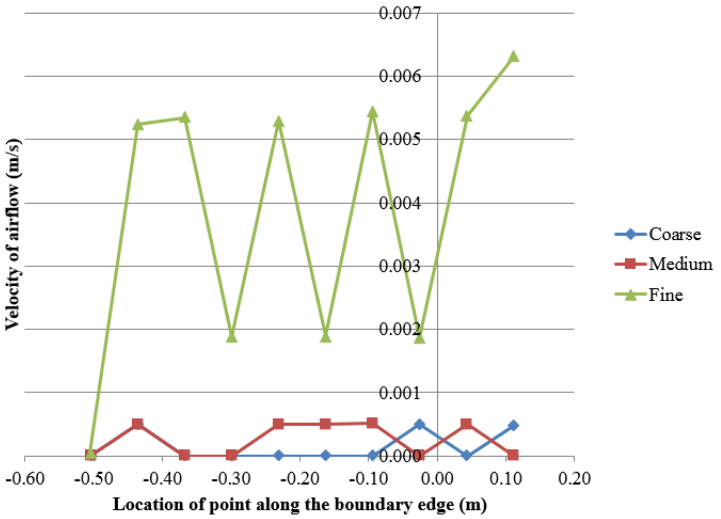


Figure 7. Graph of velocity against location of point for different mesh size

In additions, the trend line of medium mesh has the same behaviour as the fine mesh in Fig 8. For the coase mesh, it only has same pattern of trend line at left side of line 1. Hence, the grid independence analysis is done and the medium mesh which is 0.004 m is used as constant mesh size to all case studies. Lastly, the growth rate of 1.7 is selected as constant variable since its result is almost same as result generated with 1.5 growth rate.

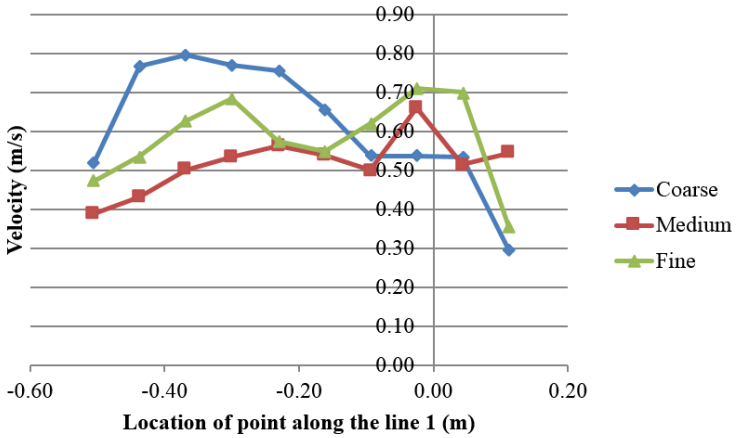
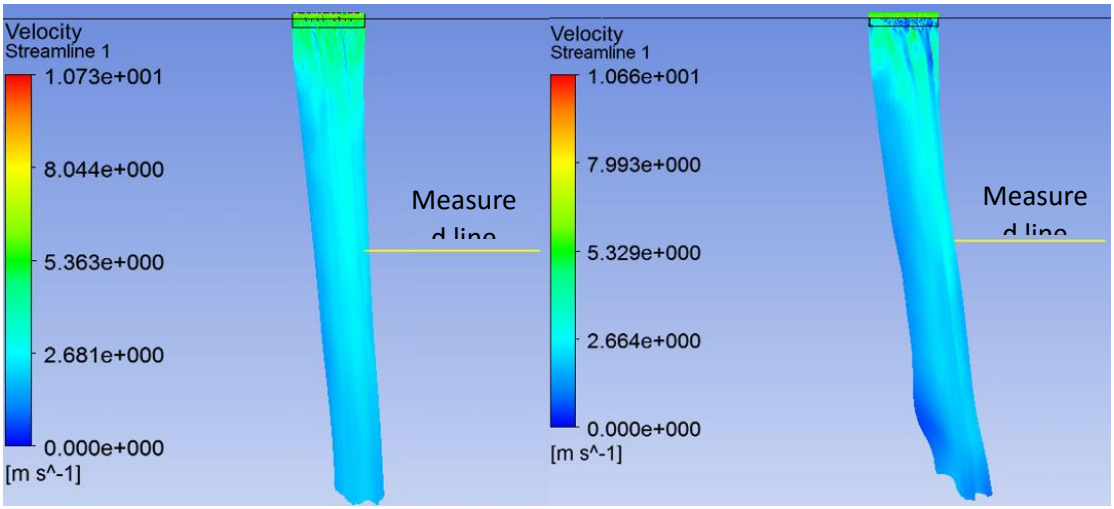


Figure 8. Graph of velocity against location of point for different mesh size

3.2 Efficiency of Wind Direction

The velocity streamline of 15º and 30º of vertical vane is plotted in Fig 9. Besides that, the result of efficiency of wind direction is calculated and shown in Table 4. Comparing efficiency of wind direction of 15º and 30º of vertical vane, it can be concluded that the efficiency of wind direction is decreased as the angle of vertical vane increased. This result explained the reason why the angle of vertical vane of this room air-conditioner has been set a limit to rotate. The higher the angle of vertical vane to rotate, the lesser the efficiency of wind direction and dissipating cold air. These result will used as based reference in order to check whether new designs of vertical vane has made improvement on it.



(a) **(b)**

Figure 9. Velocity streamline of vertical vane (a) 15º and (b) 30º

Table 4. Efficiency of wind direction

Angle of rotation of vertical vane (º)	Distance Z (m)	Distance X (m)	Angle of wind (º)	Efficiency of wind direction (%)
15	0.30503	2.00000	8.67	57.81
30	0.50839	2.00000	14.26	47.54

The velocity contours at mid-plane of vertical vane are shown in Fig 10 and Fig 11. Based on these figures, it proved that the higher the angle of rotation of vertical

vane will lead to shorter distance of the airflow can be achieved at that angle. It also explained 100 % efficiency of wind direction can't be obtained since the minimum velocity of airflow, 0.25 m/s is indicated before reaching the measured line.

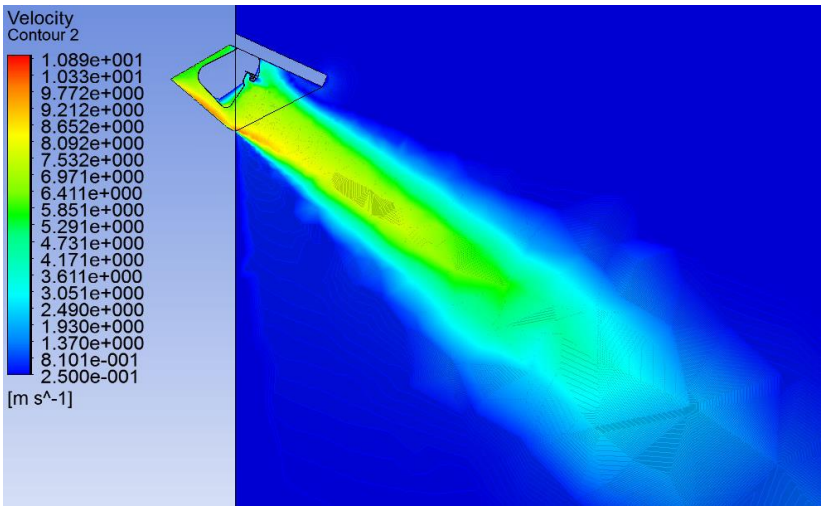


Figure 10. Velocity contour at mid-plane of 15º of vertical vane

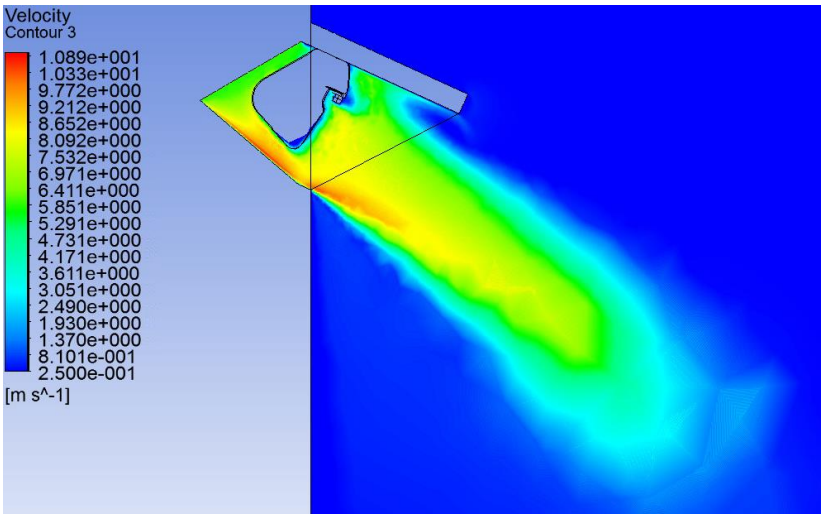


Figure 11. Velocity contour at mid-plane of 30º of vertical vane

3.3 Different Contour Analysed at 30º of Vertical vane

The pressure contour at mid-plane of 30º of vertical vane is plotted and shown in Fig 12. It is used to investigate which parts of vertical vane are main parameters of affecting the efficiency of wind direction. According to the Fig 12, high increase in gauge pressure are cleary determined at leading edge of vertical vane compared to Fig 11. Based on Bernoulli's principle, increase in velocity will cause decrease in pressure [4]. In this studies, the low velocity of airflow at leading edge induces the high increase in pressure of airflow.

Another velocity contour in Fig 13 is plotted perpendicular to the inlet and is aligned to leading edge of vertical vane. It is plotted to observe how the velocity of airflow varies when airflow is passing the vertical vane. Referring to the top view of velocity contour that perpendicular to inlet in Fig 14, the velocity of airflow passing by the left surface of vertical vane is lower than the velocity of airflow at righ surface of

vertical vane. In additions, the rear part of vertical vane induce vortex. Vortex induced at rear part of vertical vane caused decreased in velocity of airflow.

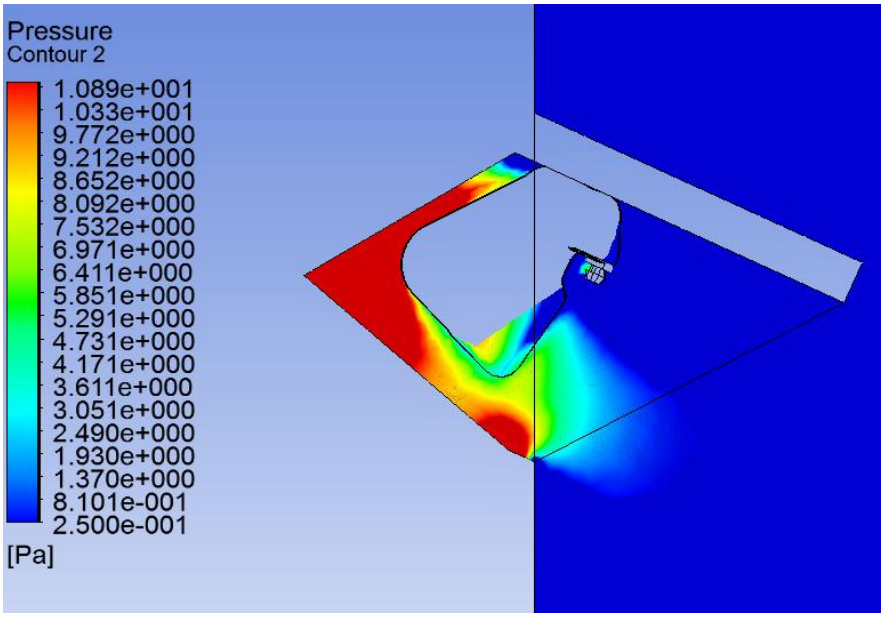


Figure 12. Pressure contour at mid-plane of 30º of vertical vane

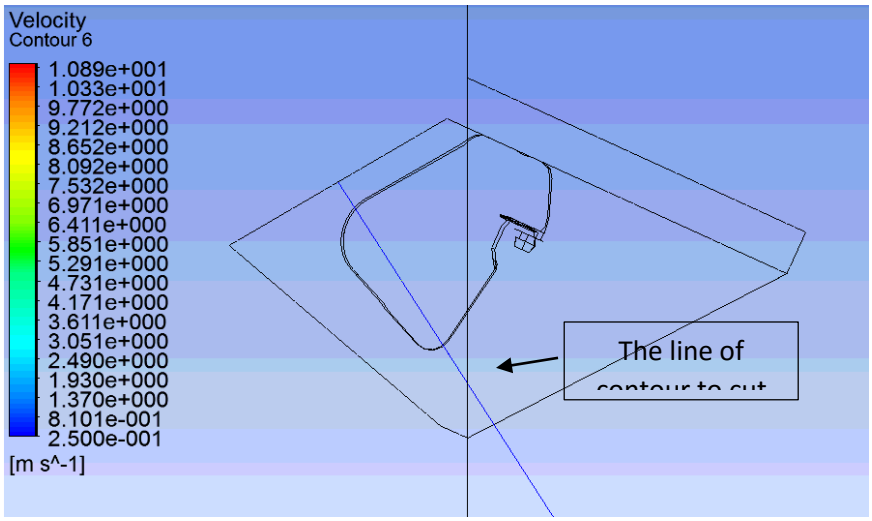


Figure 13. Position of velocity contour cut from inlet

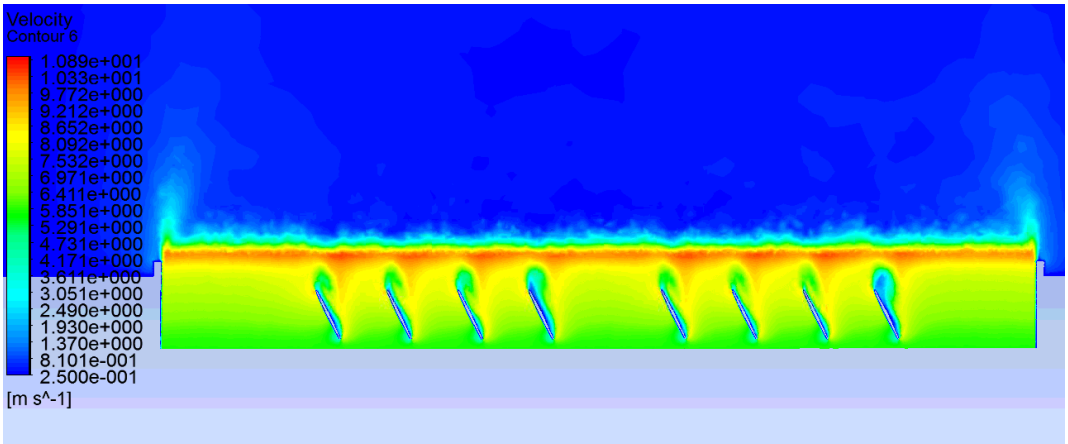


Figure 14. Top view of the velocity contour cut perpendicular to inlet

Thus, two parameters are selected to study for geometry optimisation of vertical vane. The parameters studies will be the length of span and length of tip chord. The name of length is shown in Fig 15. The span length and tip chord length of simplified vertical vane are 0.04436 m and 0.04478 m respectively.

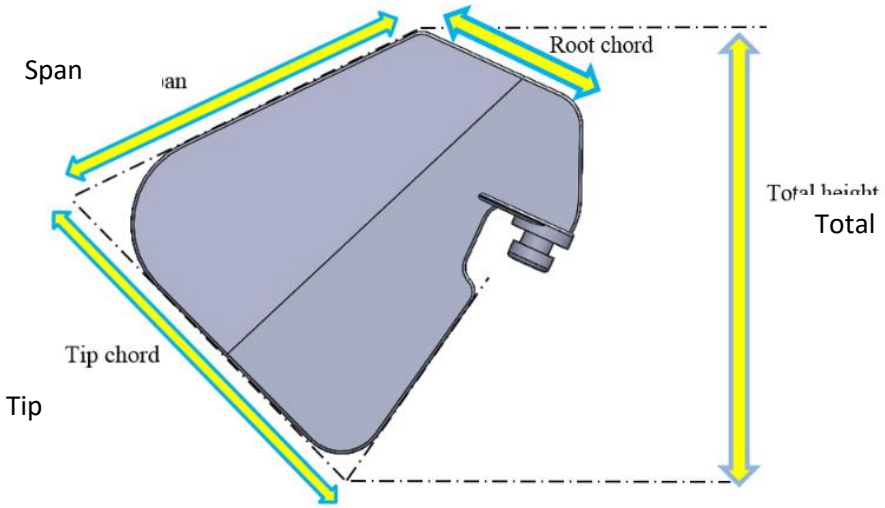


Figure 15. Name of different length of vertical vane

The restriction set for parameter studies are as following:

1. The surface of root chord that is attached to room air-conditioner is constant.
2. The total height of vertical vane is maximum length. (due to size of product)
3. The total area of vertical vane is constant.
4. The material of vertical vane is constant.

3.4. Parameter Studies for Geometry Optimisation of Vertical Vanes

Since long span, tip chord and short span are chosen as main parameter studies, new designs of vertical vane are drawn based on 5 %, 10 % and 15 % decreased in vane surface area. A basic sketching is illustrated in Fig 16 shown position of each parameter study with different percentage decreased in vane surface area.

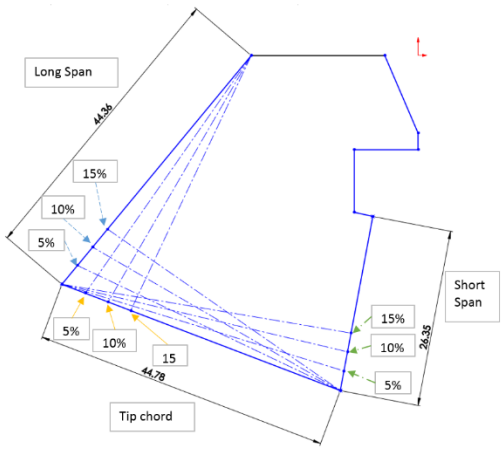


Figure 16. The position of each parameter study with different percentage decreased in vane surface area

In this research studies, the simulation is only run for one side (turning left side) of direction because the design of CFD model is symmetrical with respect to centre of

shell of room air-conditioner. Moreover, only 15 degree angle of vertical vane is studied as it is sufficient to identify which parameter is important to analyse. Furthermore, the result of new vertical vane can be compared with base reference (efficiency of 15º and 30º of simplified vertical vanes). In previous discussion, it is found that the higher the angle of vertical vane, the lower the efficiency of wind direction. As long as the result of new vertical vane has same trend as base reference, the reliability of simulation result is justified. The CAD drawing of new vertical vane based on each parameter study at different percentage decreased in vane surface area is shown in Fig 16. The simulation result of new vertical vane is tabulated in Table 5.

Table 5. Result of each parameter study at different percentage decreased in vane surface area

Parameter study	**Percentage decreased in vane surface area (%)**	**Distance from fix point (mm)**	**Distance Z (m)**	**Distance X (m)**	**Angle of wind (º)**	**Efficiency of wind direction (%)**	**Efficiency, base- Efficiency, parameter study**
Long Span	5	3.6480	0.27601	2	7.86	52.38	-5.43
	10	7.2020	0.27146	2	7.73	51.53	-6.68
	15	10.6955	0.26691	2	7.60	50.68	-7.13
Tip chord	5	3.7599	0.26236	2	7.47	49.82	-7.99
	10	7.4350	0.28966	2	8.24	54.94	-2.87
	15	11.0610	0.31847	2	9.05	60.32	2.51
Short Span	5	2.9729	0.20776	2	5.93	39.54	-18.28
	10	5.8646	0.22293	2	6.36	42.40	-15.41
	15	8.6985	0.21231	2	6.06	40.40	-17.41

According to the Table 5, the changes in efficiency of wind direction for long span are significantly small. Besides that, the trend of decreasing the vane surface area of long span gives result of dropping in efficiency of wind direction. Hence, it can be assumed that long span can't be decreased but it could be increased for improving efficiency of wind direction.

Next, all the result of short span shows negative impact to efficiency of wind direction. So, it is better to keep length of short span as constant as it can't be exceed the length of total height.

Lastly, the result of 5 % and 10 % decreased in vane surface area at tip chord show negative impact to efficiency of wind direction. However, the 15 % decreased in vane surface area at tip chord is actually higher than the efficiency of base reference which is 57.81 %. The design of this new vertical vane is selected best configuration of design since its efficiency of wind direction is 60.32 % which is increased by 2.51 % as compared to efficiency of base reference.

7. Conclusion

The efficiency of wind direction for different angles for vertical vane are studied. The efficiency of wind direction for 15º of vertical vane is 57.81 % while the efficiency of wind direction for 30º of vertical vane is 47.54 %. The result of the efficiency of wind direction are used as base reference. The parameter studies for optimisation of vertical vane is focused at length of long span, tip chord and short span. The design of 15 decreased in vane surface area at tip chord is the best optimised design of vertical vane because the efficiency of wind direction is highest as 60.32 %. Besides that, the mass of vertical vane of this design is lower than base reference and thus it is optimised without bringing any negative effect to the efficiency of dissipating cold.

References

[1] B. Xia and D.-W. Sun, (2002). "Applications of computational fluid dynamics (cfd) in the food industry: a review," *Comput. Electron. Agric*. 34 (1-3) 5–24.

[2] T. Nakanishi, T. Nakamura, W. Youichirou, H. Katsumasa, and K. Takahiro. (2007). Technical Paper Investigation of Air Flow passing through Louvers, 53(160), 1–9,

[3] M. H. M. Noh, H. Rashid, A. H. A. Hamid, and M. F. Iskandar. (2012). Comparison of numerical investigation on airfoil and flat louvers on the air duct intake, *Procedia Eng*, *Vol.* 41, (pp. 1761–1768).

[4] Y. A.Cengel and J. M.Cimbala. (2014).Fluid Mechanics: Fundamentals and Applications, 3rd (Ed). New York: McGraw-Hill

[5] B. S. Hurak. (2011). "Computational Fluid Dynamics Analysis of Air Flow and Temperature Distribution in Buildings Undergraduate Honors Thesis Presented in Partial Fulfillment of the Requirements for Graduation with Distinction in Mechanical Engineering By Bradley S . Hurak Def," The Ohio State University,

[6] T.Karimipanah, H. B. Awbi, M. Sandberg, and C. Blomqvist. (2007). "Investigation of air quality, comfort parameters and effectiveness for two flow level air supply system in classrooms," Build. Environ, 42(2) 647–655

[7] N. Mao, M. Song, and S. Deng. (2016). "Application of TOPSIS method in evaluating the effects of supply vane angle of a task/ambient air conditioning system on energy utilization and thermal comfort," *Appl. Energy*, *Vol 180*, 536–545.

[8] S. Lin, B. T. Tee, and C. F. Tan. (2015). *Indoor Airflow Simulation inside Lecture Room: A CFD Approach*. Paper presented in 7th Int. Conf. on Cooling & Heating Technologies, Bristol, United Kingdom,

[9] S. Sadrizadeh and S. Holmberg, (2016) *Evaluation of various turbulence models for indoor airflow prediction: a comparison study with experimental data* in Proceedings of 9th International Conference on Indoor Air Quality Ventilation & Energy Conservation In Buildings, 1–7.
[10] Private Communication.

eureca 2017 – Conference Paper
Paper Number 2ME03

The Fabrication of Non-Implant 3D Printed Nose

Elliot Andrews*, Yong Leng Chuan

Department of Mechanical Engineering,
School of Engineering, Taylors University, Malaysia.

*elliot.cr7@gmail.com

Abstract
Non-surgical rhinoplasty procedures which involves the use of injectable derma fillers are highly risky as patients are susceptible to side effects and complications that may cause unwanted changes in their appearance. This research explores an alternative method of non-surgical rhinoplasty for patients seeking augmentation of the nose with the use of three-dimensional (3D) printing. Most rhinoplasty procedures are conducted with the intention of enhancing the aesthetical features of the nose, a 3D model nose was designed based on the combination of the average and the ideal aesthetic parameters of the Northern European Caucasians and South Asia Chinese nose. The modelling of nose is done using the SolidWorks CAD software. An initial design was sketched in a polygon mesh form and further improved on. Different printing materials and infill densities were compared to determine the suitable printing technique. The final nose model is then printed using the Ultimaker 3D printer using Polylactic acid (PLA) with an infill density of 100% at a thickness of 1.4 mm. An inner layer to the 3D printed nose was developed for comfortable attachment of the nose model to human skin. The inner layer was fabricated using agar gelatine. Experiments were carried out to increase the strength and adhesiveness of the gelatine so that it could adhere to the human skin and the PLA surface. Tensile and adhesive strength tests were carried out to determine the suitable gel composition for the attachment of the nose to the user's face. The key outcome from the experiments using natural gelatine was capability of gel to act as an inner layer for the temporary attachment of the 3D nose model to the human skin.

Keywords: Non-surgical rhinoplasty, agar gelatine, 3D printing, egg shell.

1. Introduction

Rhinoplasty can be defined as the surgical procedure of the reconstructing or reshaping of the human nose. This procedure is usually performed on individuals who have suffered nasal trauma and are in need of reconstruction of the nose. However, recent statistics suggest that rhinoplasty has been the procedure of choice for individuals seeking to aesthetically enhance their facial features by obtaining the ideal proportions of the facial structure. With the advancement of medical sciences, patients are given the option of a nonsurgical rhinoplasty procedure using injectable fillers for the augmentation of the nose. With a variety of types of fillers to choose from, cosmetic surgeons select the required material based on their properties and desired outcome of the patient.

Some of the more common fillers used by cosmetic surgeons include hyaluronic acid, polyacrylamide gel and calcium hydroxyapatite which is a temporary filler capable of lasting for 10 to 14 month [1], [2]. These fillers are selected based its elasticity, hydrophilicity, viscosity, durability and its ability to mould according to the desired shape after injection. The selection process of the filler by a cosmetic surgeon is highly risky as patients are susceptible to side effects and complications such as bleeding, bruising, asymmetry of the nose shape, and also serious complications that lead to blindness [2]. It is important that surgeons make the selection of the fillers and injection techniques based on the individual patient and that the procedure is performed slowly and carefully to minimise the risks of the occurrence of these complications. With such complications arising from this nonsurgical procedure, people that want to aesthetically enhance their facial features are left with a single choice of surgically reshaping of the nose. This indicates that a need for an alternative method of nonsurgical rhinoplasty is to be presented.

The use of three-dimensional (3D) printing, a form of rapid prototyping technology, has been growing in many industries over the past decade. With capabilities of rapidly producing objects with complex geometrical designs, the use of this rapid prototyping technique has overtaken many conventional manufacturing processes [3]. 3D printing has also been making advances in the medical field with medical practitioners using bio-models to provide feedback and simulate complex anatomical movements that are otherwise difficult to replicate using 3D modelling software [4]. The ability of rapid prototyping technology to produce customised organ and implants to suit the needs of individuals opens a pathway for advancement in nonsurgical cosmetic procedures.

Ciocca et al. [5] have successfully fabricated an eyeglasses-supported nasal prosthesis and expected to provide a temporary prosthesis to a gunshot victim who lost his entire nose to the injury. One of the methods used to achieve this outcome was to obtain a 3D model of the patient's facial structure using a laser scanner. A CAD model of the prosthetic nose was generated based the digital model of the patient's face that was scanned. The 3D model nose was digitally placed over the digital model of the patient's facial structure. Adjustments were then made so that the prosthesis would fit comfortably over the defected area. A two-part mould was then fabricated using a 3D printer. The material used for the 3D printing of the mould was acrylonitrile butadiene styrene (ABS). The mould was then used to fabricate the silicone prosthesis using the silicone process procedures with 12 different silicone colours used to obtain a colour

similar to the patient's skin colour [5]. The final step of the fabrication of the prosthesis was to connect the nose model to the eyeglasses using a bolt.

Similarly, Y. He et al. [6] studied the use of rapid prototyping in the manufacturing of soft tissue prostheses. The use of a 3D scanner was used to obtain data for the generation of a digital 3D model for design of a negative mould of the required body part. The prostheses that was fabricated by the author was a prostheses of a human ear. The mould was then printed using a 3D printer using ABS as the material of choice. Silicone is then poured into the mould to form the desire soft tissue prosthesis. The silicone prostheses were then removed from the mould to complete the fabrication process.

Unlike the research, this research aims to use 3D printing as the primary fabrication process for an alternative nonsurgical rhinoplasty procedure. Study of the relationship between the average nose and the perspective of the ideal nose for various ethnic groups was conducted. The result of this research can eventually contribute to the designing of the nose model using a Computer-Aided Design (CAD) software. Due to budget constraints the nose designs were limited to average dimensions taken from sample groups instead of individual patients. The designing of the nose model was based on a combination of the average nasal diameters of an ethnic group and the aesthetical ideal of the given ethnic group. The ethnic groups that were chosen in this research paper was the South Asian Chinese and the Northern European Caucasians. These specific groups were chosen to proof that this research is applicable to not only the local population but also the international population. The CAD design was then fabricated into a physical model using a 3D printer using the suitable printing techniques. The model is attached to the user through an adhesive inner layer that was made of synthesised natural gelatine instead of using a mechanical support. The inner layer was made using suitable ratios of agar, glycerol as plasticisers and crushed egg shell for an increase in adhesiveness and strength. The gel compositions underwent tensile and adhesive strength testing to determine its practicality.

2. Research Methodology

The research of the fabrication of a non-implant three-dimensional (3D) printed nose can be separated into two main parts which are the fabrication of the 3D model nose and the synthesis of natural gelatine as an inner layer for a comfortable attachment of the nose. The fabrication of the 3D model nose can be further broken down in to three subcategories which are the identification and selection of nasal dimensions, 3D modelling using computer-aided design (CAD) software and the printing techniques used to fabricate the nose model.

2.1 Identification and Selection of Nasal Dimensions

The shape and parameters of the human nose varies according to an individual's ethnicity, age and gender. The differences in nose shape, facial features and proportions causes the perspective of the ideal nasal proportions required to achieve an aesthetically enhanced look to differ according to the individual. Therefore, in order to conduct this research within the proposed budget without the use of a 3D scanner, the fabrication of the 3D printed nose was to be modelled based on ethnicity and gender of a sample age

group. The sample age group chosen ranges from 21 - 29 years of age, set as a boundary for this research. Studies on the average nasal parameters of different ethnicity groups were conducted to identify the key points and dimensions that affect the shape of the nose based on each ethnic group. Some of the key parameters of a nose that was used in the CAD modelling can be found in figure 1. These key parameters include the nasal height, nasal width and nasal tip protrusion. A literature review was then conducted on the international perspective of the ideal proportions for the nose. The ideal nose was then compared to the average nose of two ethnic groups, the Caucasian nose and the Asian nose. Findings from the literature review showed that the average nose from neither ethnic groups conformed to the international perspective to the ideal nose. It was also found that the Asian perspective of the ideal nose differed from the international perspective which was based on the neoclassical canon of facial aesthetics. The review concluded that the success in achieving an enhancement of facial aesthetic value through rhinoplasty depended on the more on the ethnicity of the person than the ideal proportions. Upon obtaining the stated information, it was appropriate to model the 3D printed nose based on the European Caucasian nose and the Chinese Asian nose from each gender for this research.

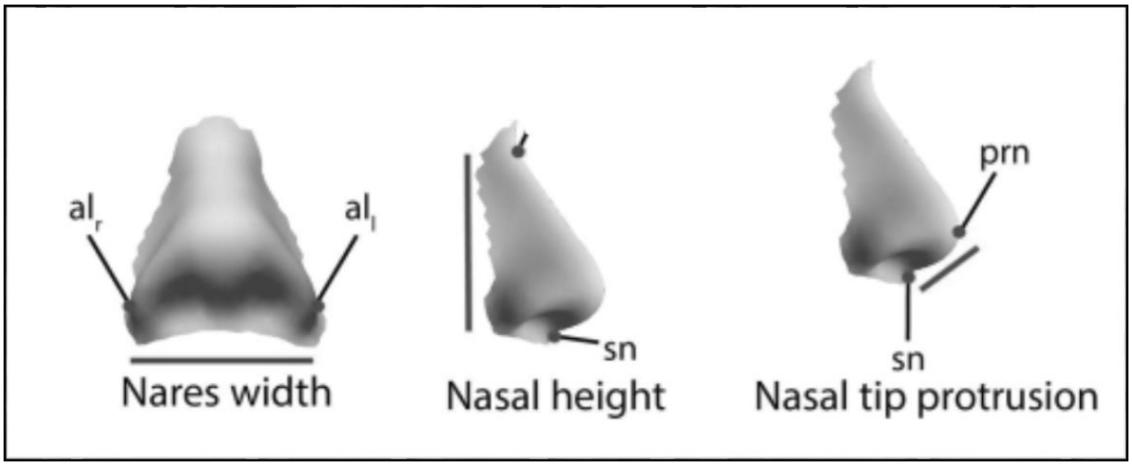


Figure 1: Key parameters of the nose used in CAD modelling [7].

2.2 Geometrical Modelling

The 3D models of the human nose were modelled utilising the CAD software Solidworks 2016 Student Edition. Solidworks was selected as the preferred CAD software as it is available to students as a university resource. An initial design was modelled by sketching a low poly or polygon mesh version of the nose to achieve the desired shape of the nose. Fillets are then applied to the edges of the polygons to obtain the roundness of the nose. This initial prototype was designed as a base model that was to be further refined throughout the research duration. It was also modelled to determine the suitable printing material and techniques. This initial design was modelled based on the average Caucasian male nose.

A more refined version of the nose was then designed according to the appropriate dimensions of the average European Caucasian male nose obtained from the journal paper by Zaidi et al. [7]. These dimensions were combined with facial angles from the international perspective of the ideal nasal proportions. Once the desired model was sketch using the CAD software. A shell feature was used to obtain an outer

shell of desired shape with the appropriate shell thickness. A tolerance value of 2 mm was set to allow space for the inner layer required for a comfortable attachment. Similarly, 3D nose models were fabricated for the Caucasian female nose and the Chinese Asian nose.

2.3 3D Printing Techniques

The completed 3D model was printed using the Ultimaker 3 printer that was available in the laboratory. There were two types of material available for the printing of the 3D model, which were Polylactic Acid (PLA) and Acrylonitrile Butadiene Styrene (ABS). PLA is considered to be the stronger of the two materials as it has a larger tensile strength compared to the ABS [8]. PLA is also has a higher elastic modulus compare to ABS [8]. On the other hand, ABS is more heat resistant of the two materials. The samples of each type of material was obtained so that a comparison could be made. The comparison made shows that due to the surrounding environment of the 3D printer, the print quality of the ABS material was not as good as the PLA material. The finishing around the edges of the ABS material was rough and cracks could be seen forming on the surface. The PLA material showed a significantly better print quality as no cracks on the surface could be found. The initial design of the nose model was printed using PLA material at a thickness of 2 mm with a 75% density. The print quality of the initial model was compared to the refined model of a Caucasian male nose which was printed using a thickness of 1.4 mm with a 100% density. The results of the comparison can be found in the results and discussion section. Once the desired 3D nose model was printed, a coat of skin colour paint was applied to give the 3D printed nose a more natural look.

2.4 Inner Layer using Synthesis of Natural Gelatine

The objective of synthesising natural gelatine as an inner layer was to provide a comfortable attachment of the 3D nose model to the user's face. This meant the gel was required to be adhesive towards the human skin. A type of natural gelatine that can be commonly found was agar which is a type of algae based natural gelatine widely used as a culinary ingredient. The gelation of agar exhibits good physical and mechanical properties such as flexibility, transparency, homogenous and is a hydrocolloid [9,10]. These characteristics make agar a suitable type of gelatine to be used as a coating material for food and edible products [9]. The combination of glycerol plasticisers improves the tensile strength and gives it a film like texture. However, increasing the concentration of the glycerol plasticiser decreases it tensile strength [9].

An experiment was conducted to test the physical characteristics of the agar gel when combined with glycerol plasticisers. The materials used in this experiment consist of commercial agar powder and food grade glycerol. Different concentrations of glycerol solution was added to the agar solution and compared. The gel samples were prepared with a thickness at 2 mm with a surface area of 2 cm x 2 cm. A qualitative analysis of these various compositions of agar and glycerol gel was carried out. The texture of the gel and an initial test for the adhesive properties of the gel was conducted on both the PLA surface and the human skin. This initial qualitative analysis provided a benchmark for the future experiments using the agar gel. One of the limitations of testing using human skin is that the adhesion properties of the gel could not be tested

over time. Therefore, the following experiments were conducted using only the PLA material that was used to print the 3D nose model.

2.5 Strength and Adhesion Testing of Gel

The results from the initial test showed that the pure agar glycerol composition lacked in rigidity. One of the solutions that was provided was the addition of eggshells in the form of impurities to increase the strength of the agar gel, a theory similar to the addition of impurities to improve the mechanical strength of metals. A tensile test was conducted to determine the relationship between the tensile strength of the agar gel and the amount of egg shell added to the composition. Due to the limitations of using a tensile testing machine, the test was conducted by fixing one end of test sample agar gel strip and applying force to the other end of the gel strips using weights. The amount of weights that was required for the failure of the gel strips were used to calculate the tensile strength of the gel. The test samples of the agar gels that was prepared for the tensile testing can be seen in the figure 2.

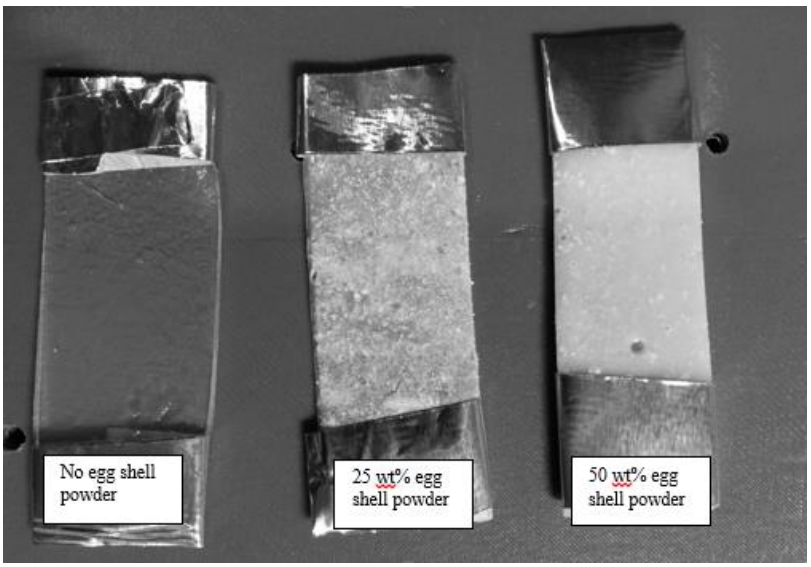


Figure 2: Test samples for tensile testing.

The adhesion strength of the agar gel was tested using two flat PLA printed surfaces to simulate the surface of the 3D nose model. The agar glycerol gel of a 1 mm thickness was placed in between the PLA printed surfaces. One of the surfaces was fixed while force was applied using weights that were tied to the other surface. Weights were added until failure in the adhesion of the agar gel to the free PLA surface was detected. The adhesion test was conducted for three different samples of the agar gel and at three separate timings at intervals of 3 hours to determine the change in adhesion properties of the gel over time. The test samples of the agar gel had a surface area of 5 cm x 5 cm. The experimental set up for the adhesive testing of the agar gel can be seen in figure 3. The maximum adhesive strength of the agar gel was compared to the total weight of the 3D printed nose model which was approximately 4.2 g, to determine its feasibility.

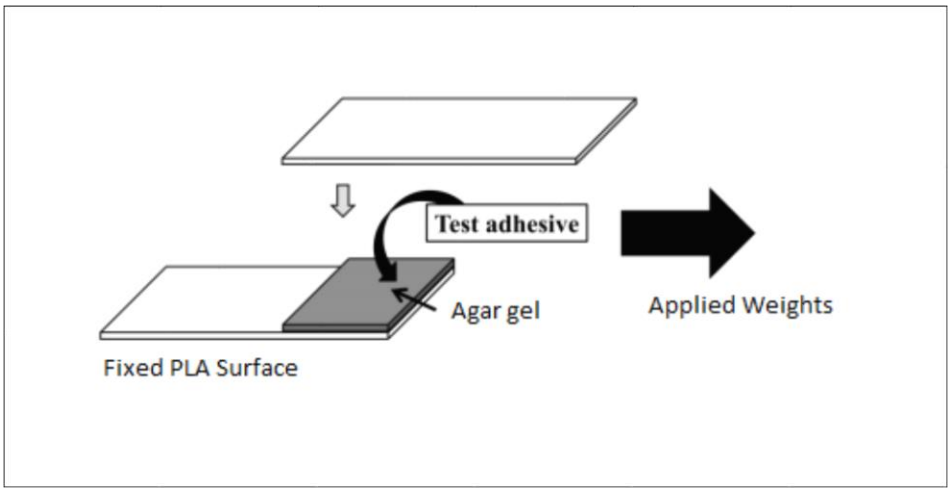


Figure 3: Adhesive strength measurement.

3.0 Results and Discussion

3.1 3D Nose Model

The 3D model of the nose was designed using Solidworks with dimensions of the average Caucasian male nose. The average nose dimension were combined with the ideal aesthetic angles according to the neoclassical canons. Parameters of the ideal naso-facial angle by S. C. L. Leong et al. was used in the modelling of the nose [11]. The key dimensions that were used in the in modelling of the 3D nose can be found in table 1 in which a tolerance of 2 mm was added to the dimensions. The shell feature that can be found in the CAD software was used to create the outer shell of the nose shape with a thickness of 1 mm. The completed CAD model of the 3D Caucasian male nose can be found in figure 4. The Caucasian female nose and a Malaysian male nose was also designed using similar techniques using the measurements data of A. A. Zaidi et al. [7] for the Northern European Caucasian nose and Y. Dong et al. [12] Chinese Asian nose respective.

Table 1. Dimensions used for the modelling of the 3D nose [7,11,12].

Population	N. European		Chinese	
Gender	Male	Female	Male	Female
Nasal Height (mm)	51.59	48.62	54.31	52.44
Nasal Width (mm)	34.29	30.91	42.88	47.48
Nasal Tip Protrusion (mm)	17.62	16.43	20.48	19.38
Alar Base Width (mm)	35.66	33.00	34.46	31.56
Naso-facial Angle(°)	36	36	36	36

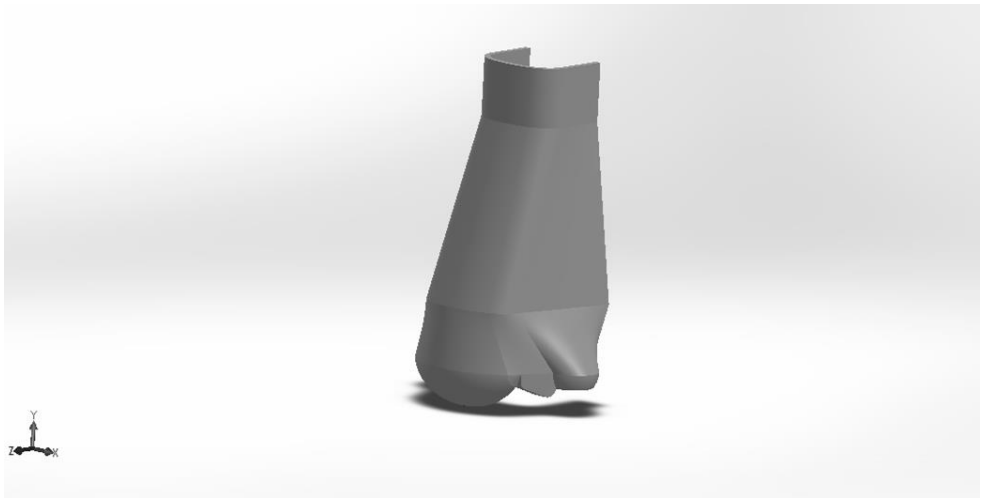


Figure 4: The completed 3D model of the Northern European male nose using Solidworks.

3.2 Printing Techniques

The 3D nose models were designed in Solidworks and exported as a .stl format to the 3D printing slicing software for the Ultimaker 3D printer. The material of choice was Polylactic acid (PLA), in which the infill density of 50% and 100% were compared. Figure 5 shows the nose model printed with an infill density of 50% did not have a same print quality around the edges when compared to the 100% infill density model. The 3D model with the lower infill density showed a rougher finish around the edges of the nose model. Furthermore, gaps can be seen in between the print material at the edges. The 100% infill density model showed better quality finishing overall. The 100% infill density model was also printed with a thickness of 1.4 mm set using the 3D printing software as compared to the model with lower density which was printed at 2 mm thickness. The model printed at a lower thickness was more flexible compared to the other model.

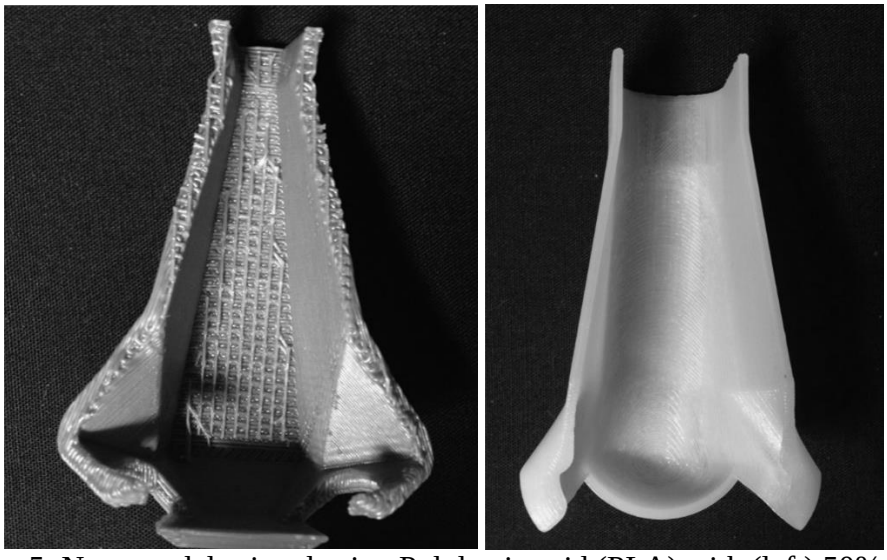


Figure 5: Nose model printed using Polylactic acid (PLA) with (left) 50% infill density and (right) 100% infill density.

The final 3D printed nose Caucasian male nose model can be seen in figure 6 which was painted using Flesh Tint acrylic paint. The printed nose model underwent smoothing using course sandpaper (80 grit) to remove the rough edges and the rough surface that was created by the support structures that were used during 3D printing. The accuracy of the desire nose shape can be further improved on by using a 3D scanner to obtain and improve the nose shape of an individual. However, due to budget constraints, the average dimensions of a sample group is taken for reference.



Figure 6: Completed Northern European Caucasian male nose model.

3.3 Inner Layer using Synthesis of Natural Gelatine

Some of the benefits of using agar as the natural gelatine of choice was that it has no toxic effect on the human skin, it is also easily available to consumers and it displays good mechanical and hydrocolloid properties. Some of these characteristics include its high shear stability, high gel formation effect and high gel strength and stability [13]. The addition of high concentration sugar solutions such as glycerol increases the strength of the gel [13]. Therefore, the following experiment was conducted to determine the use of agar as a natural gelatine as the inner layer for the attachment of the 3D nose model.

A qualitative analysis was carried out to determine the physical properties of different compositions of agar gel and glycerol solution. In the initial experiment, glycerol solutions with different concentrations were prepared. Three qualitative tests were conducted on the gel properties which are the gel rigidity, adhesiveness to PLA printed surface and adhesiveness to human skin. The results from this initial tests can be seen in table 2.

Table 2. Qualitative results of agar gel and glycerol compositions.

Glycerol Concentration (%)	Gel Texture	Adhesiveness	
		PLA Surface	Human Skin
0	Rigid	Not adhesive at 90°	Not adhesive at 90°
1	Rigid	Adhesive at 90°	Adhesive at 90°
2	Rigid	Adhesive at 90° and 180°	Adhesive at 90° and 180°
3	Easily crumbled	-	-

The analysis showed that compared to pure agar gel, the agar gel with 1% glycerol showed adhesive characteristics as it was capable of being placed on a PLA printed surface at 90° upright position. However, when rotated at 180° or at an upside down position, the 1% glycerol gel failed to stick to the PLA surface. With 2% glycerol added to the gel, the adhesiveness of the gel increased as it was able to stick to the PLA surface at 180° or upside down position. The gel was then tested against the human skin at both 90° and 180°. The gel with 3 wt% glycerol was found to be sticky but was easily crumbled when lifted from the drying pan. Observations from this experiment showed that the adhesiveness of the agar gel increased with the concentration of glycerol added to the gel. However, at a 2 mm thickness, the agar gel did not have the required strength and easily crumbled.

3.4 Strength and Adhesion Testing of Gel

The tensile strength of agar gel with different compositions of egg shell powder was determined. The results of tensile testing of the gels with compositions of 0 wt%, 25 wt% and 50 wt% egg shell powder was tabulated in table 3. Observation of the gels compositions showed that the gel with 75 wt% egg shell powder was not sticky and could not adhere to the PLA surface of human skin. Results from this experiment showed that the tensile strength of the agar gel increases with the amount of egg shell powder added into the composition. The agar gel with 50 wt% of egg shell powder could withstand the force applied of 64 g of weights.

Table 3. Tensile testing of different gel compositions.

Weight Percentage of Egg Shell Powder (wt%)	Surface Area (cm^2)	Weights (g)	Tensile Strength (kg/cm^2)
0	12	20	0.001666667
25	12	32	0.002666667
50	12	64	0.005333333

The adhesion strength of the different agar to egg shell powder composition was then compared. The adhesiveness of the agar gel test samples were using two PLA printed surfaces. Due to the limitations of conducting the adhesive tests with human skin, the tests were carried out using only the PLA surfaces. The adhesiveness of the each test sample was tested at every interval of 3 hours. For a total of 12 hours. The

adhesive strengths of the test samples can be seen in table 4. The relationship between the adhesiveness of the gel and the adhesion period could then be determined.

Table 4. Adhesion testing of different gel compositions.

Adhesion Duration (Hours)	Weight Percentage of Egg Shell Powder (wt%)	Surface Area (cm^2)	Maximum Weight (g)	Adhesion Strength (kg/cm^3)
0	0	25	10	0.00040
	25	25	6	0.00024
	50	25	2	0.00008
3	0	25	10	0.00040
	25	25	5	0.00020
	50	25	0	0
6	0	25	10	0.00040
	25	25	3	0.00012
	50	25	0	0
9	0	25	6	0.00016
	25	25	0	0
	50	25	0	0
12	0	25	4	0.00016
	25	25	0	0
	50	25	0	0

Observation from table 4 shows that the overall adhesive strengths of the agar gel decreases over time. The composition of 50 wt% egg shell powder to agar show close to not adhesion strength after the first test. The agar with 25 wt% egg shell ratio showed was only capable of adhesion of 3 g when tested after 6 hours. This significant drop in adhesive strength of the gel meant that it would not be able to withstand the weight of the 3D printed nose which was approximately 4.2 g for 6 hours. The agar gel which displayed the most adhesive strength over the 12 hour test duration was the agar without egg shell powder. The gel showed a constant decrease in adhesive strength over the testing period but is capable of withstanding the weight of the 3D nose model for at least 9 hours.

Therefore, the testing of the tensile strength and adhesiveness of the agar gel proved that the tensile strength of the agar gel can be improved with the addition of egg shell powder. However, this addition of egg shell powder would result in a decrease in the adhesive strength of the gel. It is recommended that agar gel with 2% glycerol solution without the addition of egg shell powder to be used as the most suitable inner layer for a temporary attachment of the 3D nose model. It is recommended that future work to be done in the development of an adhesive inner layer using natural gelatine to be carried out in order to achieve the desired outcomes.

4. Conclusion

The key findings from this research topic can be summarised as follows:

- A 3D nose model can be fabricated through rapid prototyping techniques such as 3D printing.
- The temporary attachment of the 3D nose model to the user's face can be used for purposes including but not limit to aesthetic purposes.
- Natural gelatine can be used as an inner layer to the 3D nose model for a temporary attachment.
- The tensile strength of the agar gel can be increased with the addition of egg shell powder.
- The adhesiveness of the agar gel and glycerol composition decreases over time.

The use of rapid prototyping techniques for the fabrication of a 3D model nose presents an alternative method of nonsurgical rhinoplasty for patients seeking an aesthetic enhancement of the nose. This alternative method of nonsurgical rhinoplasty eliminates the risk of complications involving the injection of derma fillers that are commonly used in current nonsurgical rhinoplasty procedures.

The 3D noses that were fabricated using CAD and 3D printing was designed based on the average dimensions of an ethnic group instead of individuals due to budget limitations. The concept of using 3D printing as the primary fabrication method of the noses was proven. Accuracy on the desired nose shapes may be improved in future work.

A composition of agar gel and glycerol can be used as an inner layer to the 3D printed prototype. The addition of egg shell powder increases the tensile strength of the gel but decrease the adhesive strength over time. The agar gel composition that is recommended for a temporary attachment of the 3D nose mode is at 2% glycerol and 25wt% crushed egg shell which is capable of at least 9 hours of adhesion to the PLA surface. The development of a non-toxic adhesive layer using natural gel can be further studied in future works.

References

[1] M. E. Jasin, "Nonsurgical Rhinoplasty Using Dermal Fillers," *Facial Plast. Surg. Clin. North Am.*, vol. 21, no. 2, pp. 241–252, 2013.

[2] O. N. Johnson and T. C. Kontis, "Nonsurgical Rhinoplasty," *Facial plast Surg*, vol. 32, no. 5, pp. 500–506, 2016.

[3] G. N. Levy, R. Schindel, and J. P. Kruth, "Rapid manufacturing and rapid tooling with layer manufacturing (LM) technologies, state of the art and future perspectives," *CIRP Ann. - Manuf. Technol.*, vol. 52, no. 2, pp. 589–609, 2003.

[4] Y. Chen, F. Niu, B. Yu, J. Liu, M. Wang, and L. Gui, "Three-dimensional preoperative design of distraction osteogenesis for hemifacial microsomia.," *J. Craniofac. Surg.*, vol. 25, no. 1, pp. 184–188, Jan. 2014.

[5] L. Ciocca, M. Fantini, F. De Crescenzio, F. Persiani, and R. Scotti, "New protocol for construction of eyeglasses-supported provisional nasal prosthesis using CAD/CAM techniques.," *J. Rehabil. Res. Dev.*, vol. 47, no. 7, pp. 595–604, 2010.

[6] Y. He, G. Xue, and J. Fu, “Fabrication of low cost soft tissue prostheses with the desktop 3D printer,” *Sci. Rep.*, vol. 4, no. 1, p. 6973, 2015.
[7] A. A. Zaidi, B. C. Mattern, P. Claes, B. Mcecoy, C. Hughes, and D. Shriver, *Investigating the case of human nose shape and climate adaptation*. 2017.
[8] B. M. Tymrak, M. Kreiger, and J. M. Pearce, “Mechanical properties of components fabricated with open-source 3-D printers under realistic environmental conditions,” *Mater. Des.*, vol. 58, pp. 242–246, 2014.
[9] S. Agricultural and P. Pangkep, “Physical and mechanical properties of agar based edible film with glycerol plasticizer,” vol. 23, no. 4, pp. 1669–1675, 2016.
[10] D. Phan The, F. Debeaufort, A. Voilley, and D. Luu, “Influence of hydrocolloid nature on the structure and functional properties of emulsified edible films,” *Food Hydrocoll.*, vol. 23, no. 3, pp. 691–699, 2009.
[11] S. C. L. Leong and P. S. White, “A comparison of aesthetic proportions between the healthy Caucasian nose and the aesthetic ideal,” pp. 248–252, 2006.
[12] Y. Dong, Y. Zhao, S. Bai, G. Wu, and B. Wang, “Three-dimensional anthropometric analysis of the Chinese nose,” *Br. J. Plast. Surg.*, vol. 63, no. 11, pp. 1832–1839, 2010.
[13] T. Wüstenberg, “General Overview of Food Hydrocolloids,” in *Cellulose and Cellulose Derivatives in the Food Industry*, Wiley-VCH Verlag GmbH & Co. KGaA, 2014, pp. 1–68.

eureca 2017 – Conference Paper
Paper Number 2ME04

Assessing Bioinspired Topographies for Their Antifouling Potential Control Using Computational Fluid Dynamics (CFD)

Jacky Ling*, Felicia Wong Yen Myan

Department of Mechanical Engineering, School of Engineering, Taylor's University, Malaysia.

jacky.ling@sd.taylors.edu.my

Abstract

Biofouling is the accumulation of unwanted microorganisms that settled on submerged surface with long term fluid flow in the surroundings. This study investigates the antifouling performance of bioinspired topography. A shark riblets inspired topography was designed and undergo fluid flow simulation to study the antifouling performance. The study focuses on the fluid flow velocity around the topography and the wall shear stress, vortices are to be noted to determine the possible locations biofouling would most probably occur. The simulation is carried out by using ANSYS 16.0 Fluent. The meshing of topographies was done with edge and face sizing at 1mm and 0.01mm respectively. Inflation around the wall at 0.01mm and 2 layers ensure the finer mesh elements. The inlet mass flow rate is 0.01 kgs^{-1} and wall was set to no slip condition. Mesh convergence analysis were conducted and the optimum number of elements in meshing is at 5.3 million. The model and fluid flow abide Hagen-Poiseuille's Theory. Velocity around the topography averaging at 7.213×10^{-3} ms^{-1}. However, vortices were observed between the gaps. High wall shear stress is observed at the peak of each topography, but significantly low wall shear stress is observed at the bed of topographies, suggesting the potential location for biofouling. The topography can be further modified by closing the gaps, thus preventing vortices to formed, or with the addition of features that allow fluid to escape a gap. Linear surfaces on the topography should be eliminated, this gives several possible flow directions for the fluid, could potentially increase the wall shear stress, thus better antifouling performance.

Keywords: Biofouling, Antifouling, Topographies, Biomimicry, Computational Fluid Dynamics.

1. Introduction

The accumulation of unwelcomed biological organisms on a surface due to prolonged fluid flow creates layers of biofilms, this process is called biofouling. Medical, marine and industrial are the common fields that are being challenged by biofouling.[1] There are limited methods of preventing biofouling and none of them show satisfactory effects. The nature and effects of biofouling come in different forms: biofouling in medical devices presents in layers of biofilms only; biofouling in marine and industrial applications contains layers of biofilm together with macrofouling and inorganic fouling. Macrofouling is similar as biofilm, however it is caused by the accumulation of macro sized organisms. Inorganic fouling on the other hand is caused by the accumulation of non-biological substances, such as deposits from corrosion particles, crystallization, suspended particles, fuel, oil or ice. [2]

While biofouling in marine and industrial field often lead to ineffective production and excessive cost of maintenance, it delivers fatal impact to human health in medical field. Biofouling greatly affect medical field from many common operations such as implants (prosthetic & dental), blood transfusion, body organ sensors and any other medical operation involving interaction between patient's body with the equipment. Minor problems such as equipment malfunctioning could occur due to biofouling, however on a serious situation, it may cause various organ failure due to the accumulation of unwanted fluids or substances inside the equipment being transferred into the patient's body. Statistically, approximate of 5000 annual deaths was caused by biofouling in medical equipment. [3][4]

There are many engineering approaches to prevent biofouling, but none provides sustainable and harmless solutions. Tributylin (TBT) used to be the common approach used in antifouling effort but was later banned due the harmful side effect towards marine life. [5] This indicates the non-exist possibilities in integrating tributylin into medical field for antifouling purposes. The current research field has shift the focus towards the surface topographies in hope to reduce the chances of biofouling from happening. Field tests with distinct types of surface topographies in relation antifouling effects together with numerical studies are needed to provide solid evidences that the surface topographies could potential be the sustainable antifouling approach.

Existing research on surface topographies focusing on applying biomimicry to generate potential antifouling mechanisms. Environmental friendly is one of the biggest benefits due to the absence use of chemical as such in tributylin. Self-cleaning abilities on some organisms allowing them to be free of the micro-organisms accumulation, lotus leaf and shark skin are both the common example of self-cleaning ability. Although the incorporation of biomimicry in antifouling purpose has only limited studies, but it has shown tremendous result in other relevant engineering applications. The most direct inspiration of nature towards antifouling would be from marine living organisms, although other source of inspiration should be viable too. Million years of evolution allowed some organisms to grow the ability to defend against harmful colonization on the hosts. [6]

In numerical studies, computational fluid dynamics (CFD) is the sole approach to simulate the behavior of topographies regarding their abilities in antifouling.

Through CFD, the fluid flow pattern and magnitude, together with other parameters such as vorticity and wall shear strain at specific location. These parameters are essential to determine the optimum design for better antifouling properties. This paper discusses studies on 3 different surface topographies inspired from the nature. The said parameters in each bio-inspired topography will be determined. Wall shear stress would be the main concern in deciding the antifouling performance because higher stress deny the movement of microbials, directly pushed them along the direction and prevent their localized settlements. [7] Input parameter such as fluid flow rate, viscosity, local environment condition plays the key role in the accuracy of results too and each of them will be discussed further.

2. Research Methodology

This research is conducted using CAD and CFD software due time and cost constraint, and thus field test will not be carried out.

2.1 Selection of Bioinspired Topographies

Inspiration can be obtained anywhere from all living organisms in the nature. For anti-fouling surface inspiration, shark skin's riblets, together with lotus leaf and pilot whale's nano-ridged pores poses the desired self-cleaning abilities that prevent any other particles from sticking on their skin surfaces.

2.2 CAD 3D Model and CFD Setup

After determining how the surface topographies should be like, a CAD 3D model for each topography is drawn on SolidWorks. The detailed dimension for each of the geometry in a model is justified to suit the size of simulation that is going to be carried out. CFD meshing is another crucial part in determining accurate result, a good mesh usually is complicated and time consuming, however it is much needed for a research like this, thus a mesh convergence analysis would be required after each simulation. This is to determine the best meshing quality and the accuracy of results generated.

2.2.1 CAD Modelling

Three dimensional models of the topographies were generated with the use of SolidWorks. The geometry dimension of topography is as shown in Fig. 1.

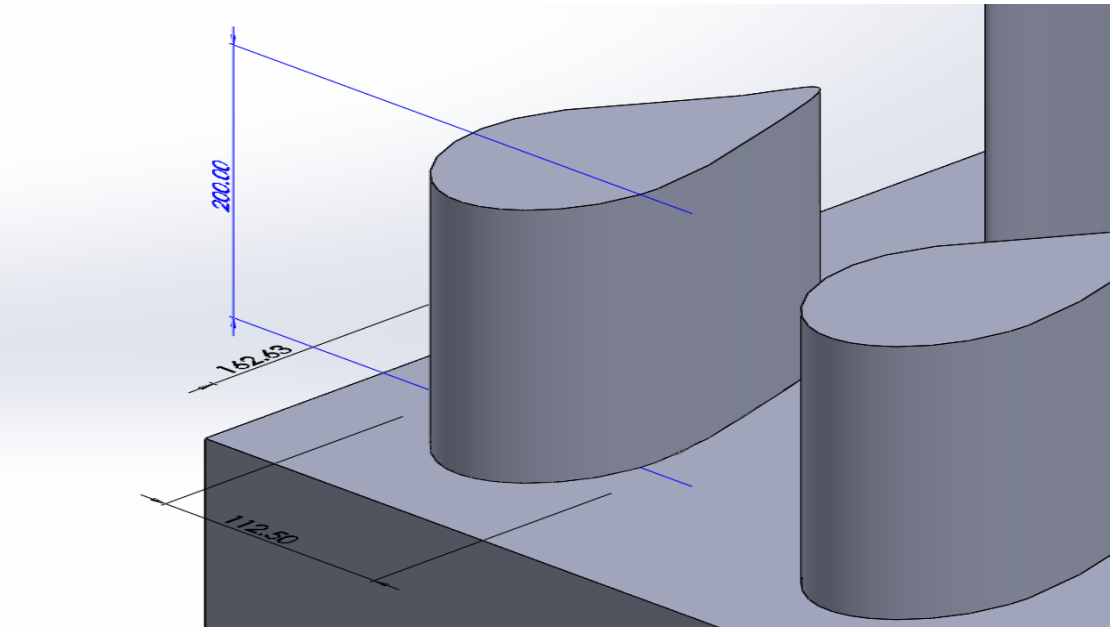


Figure 60 Dimension of the geometry features of topography.

The geometry feature has width of 112.5 μm, 162.63 μm in length and 200 μm in height. The gaps between each feature is 150 μm. The topography has 10 rows and column each on a 2mm x 3mm plate that will be used later to create the fluid domain model for use in CFD. The fluid domain was represented by a solid block of 8mmx8mmx80mm as shown in Fig. 2.

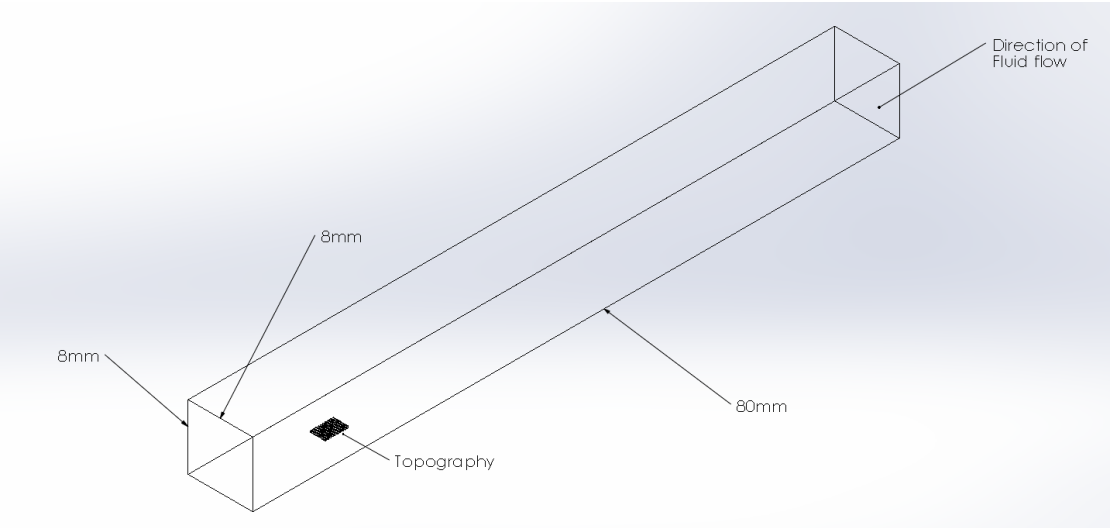


Figure 61 Dimension of block representing fluid domain.

The entire solid part will be detected as fluid domain automatically in CFD. The topography solid created earlier on will used to create cavity on the fluid domain block. The topography is placed at the bottom middle plane and 65 mm away from the inlet plane.

2.2.2 Meshing Method

Mesh quality determined the accuracy of result generated by CFD. The higher the quality, the more accurate the result is, but also takes longer time for the result to be converged due to the higher number of elements exists. ANSYS Workbench is used to create the meshing for the model. Firstly, the entire model was meshed with tetrahedral shape elements. This shape provides finer mesh around curvature and edges, which is important especially the model consist of multi-curvature topography features. Edge and face sizing was used at the edges and bottom plane respectively. The element size at edge was selected at 1 mm to give finer mesh all around. While the bottom plane, including the topography has finer mesh with smaller elements size, 0.01 mm. Fig. 3 shows the edge sizing method while Fig. 4 shows the face sizing around the topography.

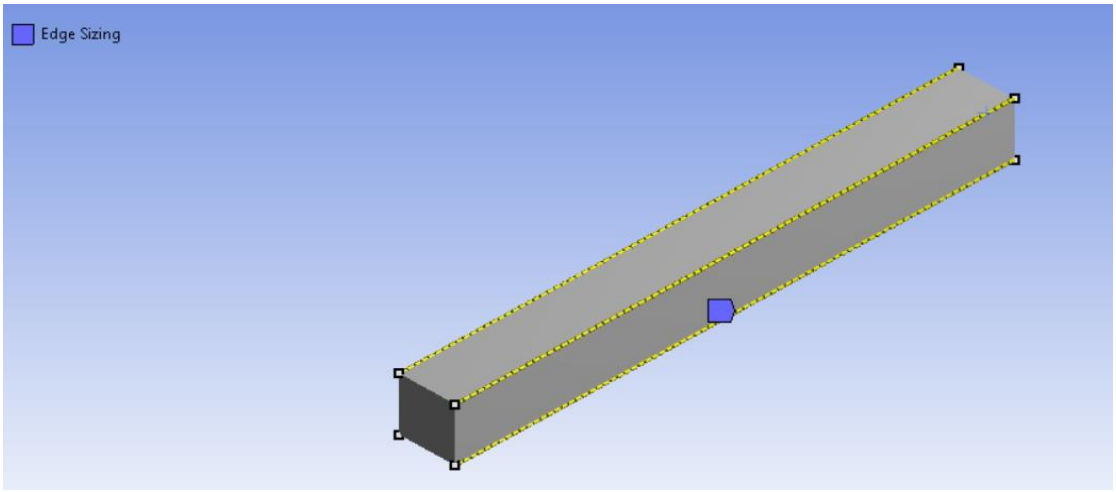


Figure 62 Edge sizing for the model

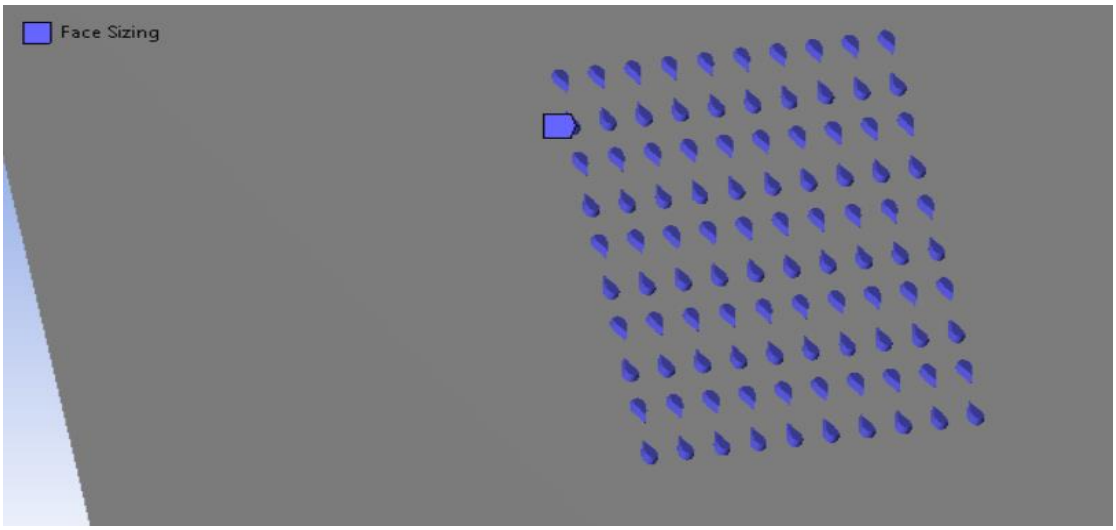


Figure 63 Face sizing around the topography surface.

Wall shear stress is important in this simulation, thus inflation around the walls are created with 2 layers inflation of elements size 0.1 mm. The resulting mesh are as shown in Fig. 5. Fig. 6 shows the close ups look at the meshing around the topography. To ease the setup of boundary conditions in CFD, the inlet, outlet and bottom wall

topography was named respectively. This reduce the confusion when setting up boundary conditions, and makes previewing results easier.

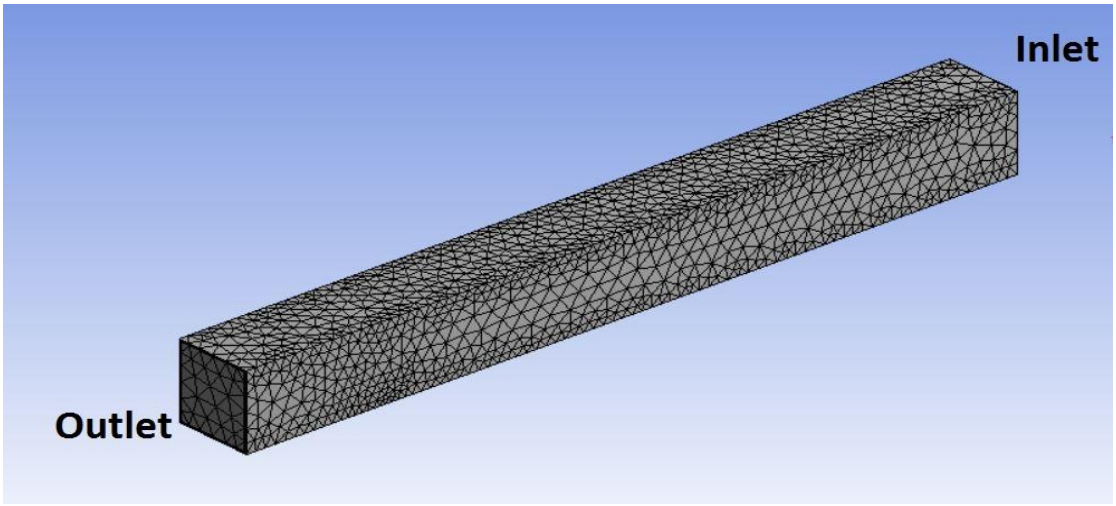


Figure 64 Resulting mesh and indication of inlet and outlet.

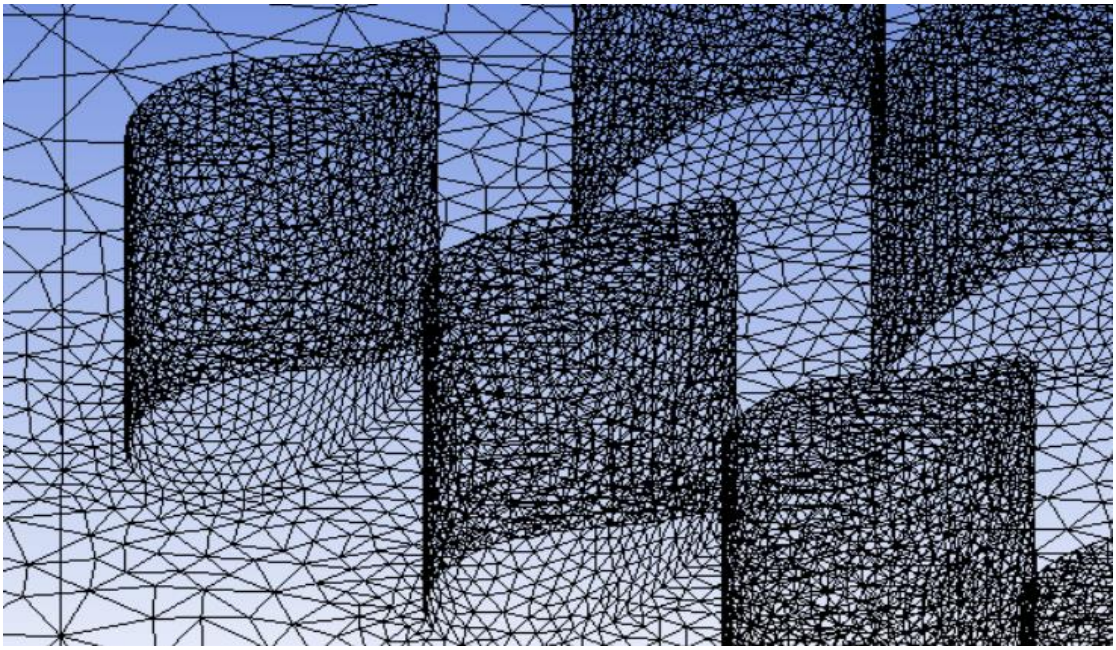


Figure 65 Close-up look at the mesh around topography.

2.2.3 Numerical Setup

The use of Navier-Stokes equations with the governing continuity equation the mass and momentum to be conserved. The flow simulation required low Reynolds number formulation, transferred from a normal wall function, thus k-omega turbulence model was selected to ensure the accuracy of results.

The flow is considered incompressible and Newtonian fluid – liquid-water was selected as the flow material. The density and dynamic viscosity of the fluid follows the default, which is 1000 $kgms^{-3}$ and 0.001 $kgm^{-1}s^{-1}$ respectively. Fig. 7 shows the

boundary condition applied on the model. No-slip boundary conditions were applied on the wall of fluid domain except inlet and outlet. Inlet mass flow rate was set at 0.001 kgs^{-1} while the outlet was set as outflow.

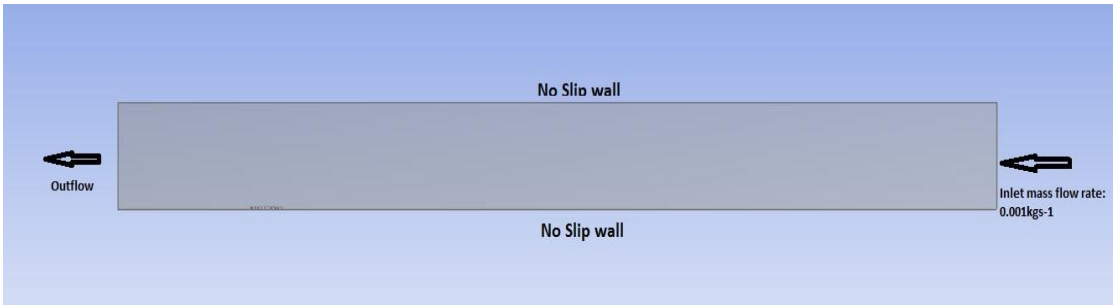


Figure 66 Boundary conditions on the model.

3. Results and Discussion

3.1 Mesh Convergence Analysis

In meshing of each model, higher number of elements does not reflect in higher quality. The quality of meshing is capped at certain number of elements and further increment of it will not change the quality. Mesh convergence analysis is carried out to determine the optimum number of mesh elements and results quality. A few mesh refinements with different number of elements will be simulated and the difference in maximum wall shear stress will be compared to each other as shown in Table 1. The optimum number of elements is met when the difference in wall shear stress is less than 5%.

Table 54 Mesh convergence at the model, mass flow rate at inlet 0.01kgs-1.

			Optimum number of elements
Mesh refinements	1.4 million to 5.3 million	5.3 million to 6.1 million	5.3 million
Difference in wall shear stress	7.82%	2.34%	

For this model, when the number of mesh element increased from 1.4 million to 5.3 million, the difference in wall shear stress exceeds 5%, indicating the result are not stable and accurate enough. When the mesh refinement increased from 5.3 million to 6.1 million, the difference is only 2.34%, this suggest that the results are nearly converged and further increase in number of elements would not give any big differences in the accuracy of results.

3.2. Velocity Contour Plot – Hagen-Poiseuille's Theory

Fig. 8 shows the fluid velocity contour plot before the topography, on XZ plane (z=65mm). On the outer layer of fluid domain, there is no fluid flow due to the no slip boundary condition applied to the wall. The concentration of velocity increased along

towards the center of flow, which has the maximum velocity. This finding shows that the fluid flow in this model abide the Hagen-Poiseuille's Theory.

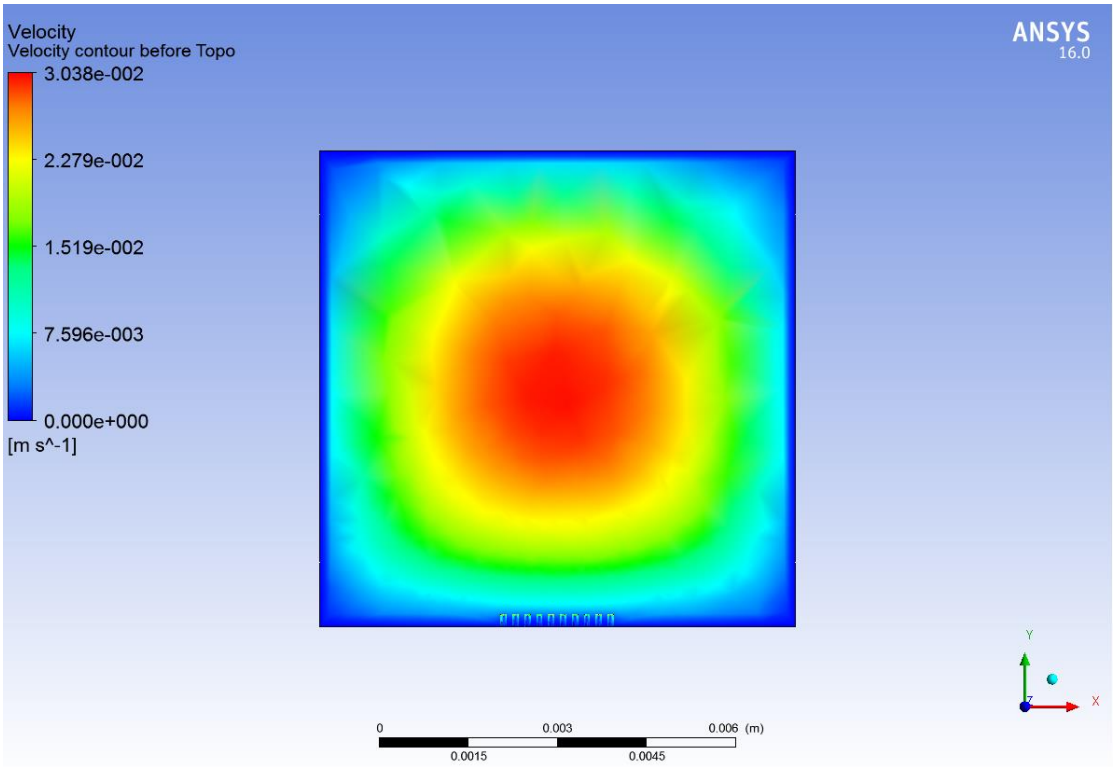


Figure 67 Velocity contour plot before the topography at full depth. The profile follows Hagen-Poiseuille's Theory, where the velocity graph present in parabolic profile with maximum fluid velocity at the center of fluid flow domain.

3.2. Velocity Streamlines and Vector Plot

Velocity streamline and vector plot shows the fluid flow pattern around the topographies. Fig. 9 presents the velocity streamline moving in between of topographies in forward direction. Fig. 10 presents the velocity vector profile between the gap of topographies.

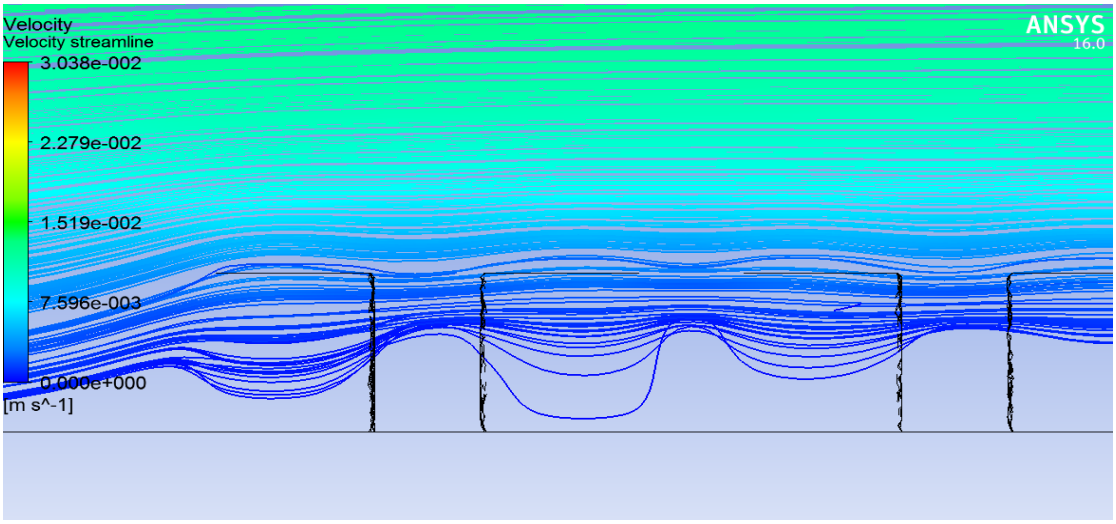


Figure 68 Velocity streamline over topography.

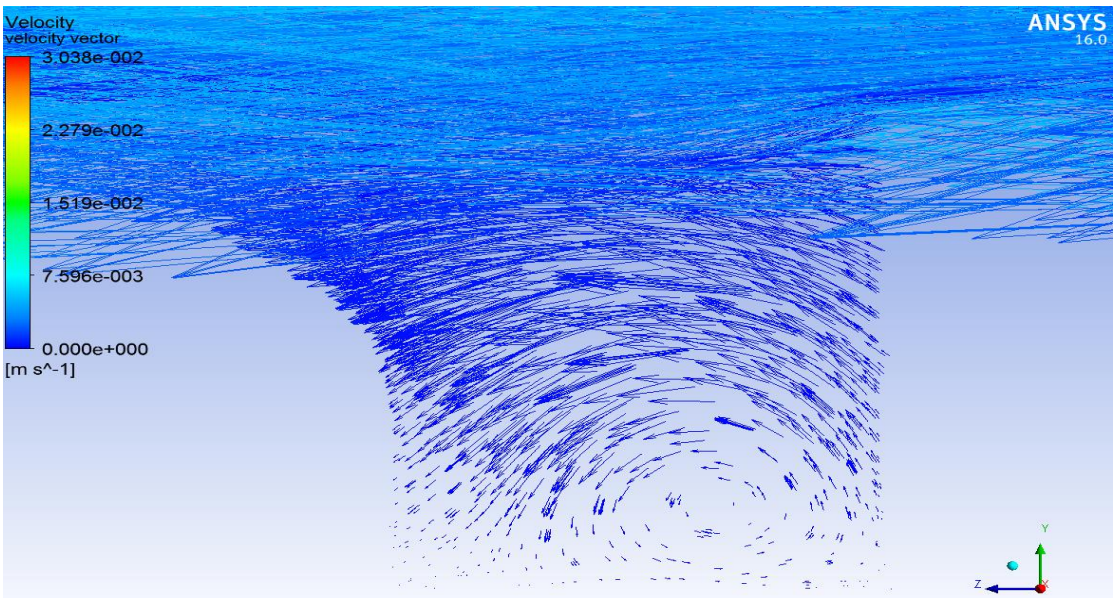


Figure 69 Velocity vector plot showing the vortices formed between the gap of feature in forward flow direction (right to left).

Velocity streamline as shown in Fig. 9 shows that the velocity is increasing towards the center of flow (Y=4mm), low velocity flow is observed around the topographies. The velocity above the topography (Y=0.2mm) averaged at 7.213 x 10^{-3} ms^{-1}. Vortices were found in the flow direction, in between of subsequent topographies gap, as shown in Fig.10. The vortices formed and move in anti-clockwise direction (Fluid flow from right to left, in Z direction), preventing fluid from escaping the gap. This could also potentially trap the microorganisms in the gaps, allowing biofouling to occur.

3.3. Wall Shear Stress

Several studies on biofouling have suggested that microorganisms have the ability to choose a suitable location for their settlements by adhesion. Thus, higher wall

shear would require better adhesive force, but not many microorganisms can achieve that. [8] This indicates that high wall shear stress directly prevent biofouling. Fig. 11 presents the wall shear stress contour on one of the topography, viewing from side wall. Fig. 12 presents the wall shear stress contour plot around the topographies at height of 100um.

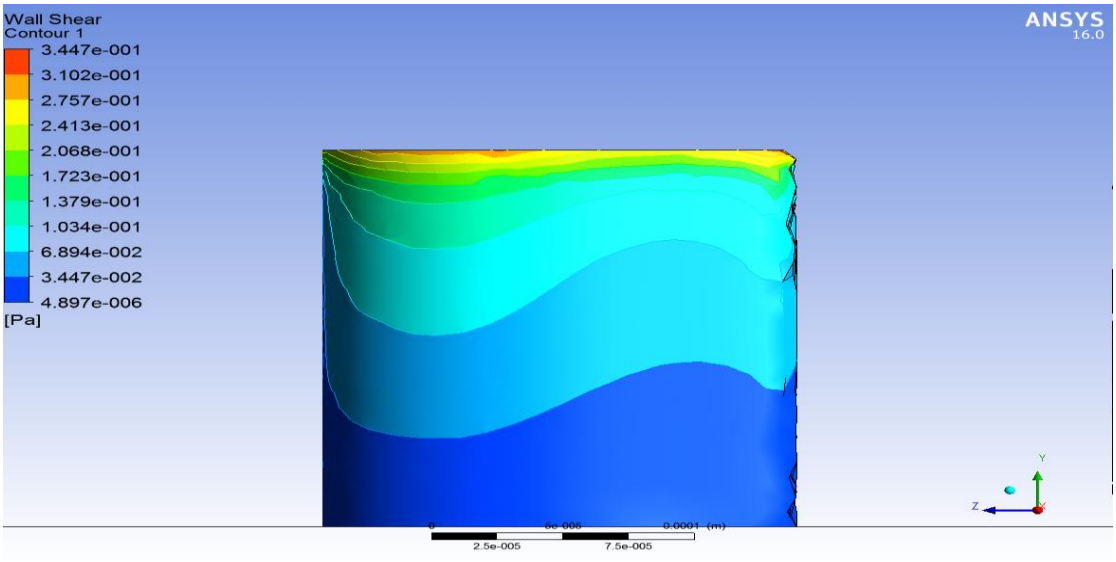


Figure 70 Wall shear stress contour on the topography feature.

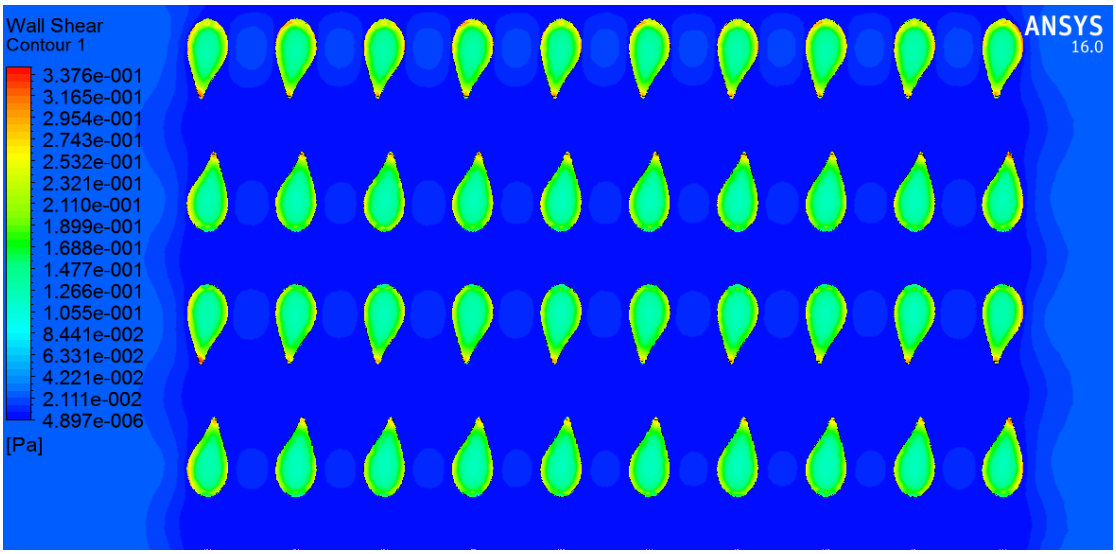


Figure 71 Wall shear stress contour around the topography (100um above the bottom plane).

Generally, the topographies have higher wall shear stress concentrated at the top, but significant low wall shear at the bed of topography. Highest wall shear stress appears at the tip of each topography, averaging at 0.231Pa. While the bed of topographies recorded an average 4.812 x 10^{-6} Pa. These values suggest that biofouling has the best chance to occur at the bed of topographies since the wall shear stress at the location are very weak.

4. Conclusion

The numerical studies carried out determined the performance of bioinspired topographies against biofouling. The shark riblets inspired topography in this study exhibits average performance in antifouling based on the results collected in the form of velocity pattern and wall shear stress. The key problems to be noted from this study are as:

- The vortices formed in the gap of topographies
- Low wall shear stress at the bed of topographies

Further modifications on the topographies design aiming to eliminate the problem stated above should generate better results in term of antifouling performance.

References

[1] G. D. Bixler and B. Bhushan, "Biofouling: lessons from nature," *Philos. Trans. R. Soc. A Math. Phys. Eng. Sci.*, vol. 370, no. 1967, pp. 2381–2417, 2012.

[2] A. I. Railkin, T. A. Ganf, and O. G. Manylov, "Marine biofouling colonization processes and defenses," *Biofouling*, vol. 20, no. 2, pp. 129–131, 2004.

[3] J. Chan and S. Wong, "Biofouling types, impact and anti-fouling," *Biofouling types, impact and anti-fouling*, pp. 1–70, 2010.

[4] M. E. Shirtliff and J. G. Leid, "The Role of Biofilms in Device-Related Infections," XII., vol. 3, M. Shirtliff and J. G. Leid, Eds. Berlin, Heidelberg: Springer Berlin Heidelberg, 2009, pp. 272.

[5] F. W. Y. Myan, J. Walker, and O. Paramor, "The interaction of marine fouling organisms with topography of varied scale and geometry: a review.," *Biointerphases*, vol. 8, no. 1, pp. 27, 2013.

[6] M. L. Carman *et al.*, "Engineered antifouling microtopographies correlating wettability with cell attachment," *Biofouling*, vol. 22, no. 1, pp. 11–21, Jan. 2006.

[7] P. Halder *et al.*, "A novel approach to determine the efficacy of patterned surfaces for biofouling control in relation to its microfluidic environment," *Biofouling*, vol. 29, no. April 2016, pp. 697–713, 2013.

[8] Y. K. Lee, Y. J. Won, J. H. Yoo, K. H. Ahn, and C. H. Lee, "Flow analysis and fouling on the patterned membrane surface," *J. Memb. Sci.*, vol. 427, pp. 320–325, 2013.

eureca 2017 – Conference Paper
Paper Number 2ME05

Design and Optimisation of Home Scale Greywater Recycling Package

Kalaichelvan a/l Arugam[1*], Dr. Azadeh Ghadimi[1], LH Chang [2]

[1]*Department of Mechanical Engineering, Taylor's University*
[2]*DD Techniche Sdn. Bhd.*

[*]kalaichelvan.arugam@sd.taylors.edu.my

Abstract
The objectives of this project are to design a home scale greywater recycling package and optimise the design by having low cost compare to existing designs in the market. This water recycling package will contribute to reduce water crisis. Water crisis is becoming one of the biggest challenge in some countries due to over population and drought. Therefore, government and non-government organisations in well-developed countries are encouraging industries to install water recycling package to reduce water usage. DD Techniche Sdn Bhd has seen the potential to market home scale greywater recycling package globally due to the attention gained by greywater recycling system in industries and the absence of greywater recycling product for household. Therefore, the company gave the project to design a home scale greywater treatment system for toilet flushing within 3,000 USD to 5,000 USD. Greywater is the waste water produced from laundry, kitchen and bathroom except the toilet waste. Greywater contains suspended solids, microorganisms, oil, nitrates and phosphorus. Greywater needed to be treated using suitable type of treatment for safe reuse. The treatments are physical, chemical and biological water treatment. The greywater treatment system designed in this project is a combination of all three treatment. The greywater treatment contains a pre-treatment stage with wire mesh and followed by the slow sand filtration. The design is evaluated using experimental methods. The treated greywater must meet the requirement of toilet flushing. Therefore, experiments to measure the turbidity, chemical oxygen demand and total suspended solid are carried out. The experimental results are compared with the standard toilet flushing quality. The greywater system consists the mechanical parts to control the flow of greywater and store the treated water. The mechanical parts are pumps, sand filtration tank, wire mesh chassis and collection tank. The final design has dimension of 6 m^3 and optimise the budget within 3,000 USD to 5,000 USD.

Keywords: Greywater, Physical treatment, Chemical treatment, Biological treatment, Home scale.

1. Introduction

Water crisis is becoming one of the biggest threat in some countries. Especially, countries in Middle East are facing severe water crisis due to drought. Countries with high population also face water crisis due to high water usage [1]. Water crisis can be reduced by controlling the water usage. One of the successful method to control water usage is by recycling rain water and greywater. Government and non-government organisations are encouraging industries to have water recycling system to reduce water crisis. DD Techniche Sdn Bhd is a water recycling package installer company has seen the potential to market a home scale greywater treatment for toilet flushing within the budget ranging between 3,000 USD to 5,000 USD. The company has come out with this initiative due the attention gained by the industrial scale greywater treatment package and the absence of home scale greywater treatment system.

Greywater is the water produced from the laundry, kitchen and toilet except the toilet wastes [2]. Greywater contains phosphorus and nitrates due to the usage of detergent, shampoo and dishwasher liquid [3]. Greywater also contains bacteria, total suspended solids, oil and grease. The total suspended solids (TSS) are hair from the bathroom, dirt from laundry and food particles from kitchen. These contents in the greywater causes infection to the user if not treated. Therefore, the greywater must be treated before reusing it for toilet flushing.

There are three types of treatment, which are the physical treatment, chemical treatment and biological treatment. Physical treatment involves filtering out particles from water based on the size using wire mesh or membrane [4]. This treatment is applicable to filter the suspended solid and reduce the turbidity. Chemical treatment is process of adding chemicals into the water to neutralise the bacteria through salt addition [5]. Chemical treatment also involves coagulation process. Coagulation is the process of accumulating the bacteria together to increase the size and filter out using the physical treatment [2]. Biological treatment is microbial reaction using microorganism to convert bacteria into gas, water and biomass [6].

Greywater treatment must consist at least two types of treatment because chemical or biological treatment can treat bacteria but need to be supported by the physical treatment to filter the solid particles. The design of greywater treatment package for this project requires to have dimension of 2 m x 2 m x 2 m and budget within 3,000 USD and 5,000 USD. The design for this project is be inspired from the existing industrial scale water recycling system. The existing industrial designs for greywater recycling system are slow sand filtration, membrane bioreactor and water treatment with clarifiers.

The final design of greywater treatment package for this project is made up of pre-treatment stage with wire mesh and followed by slow sand filtration. This design consists all three types of water treatment stated above. The pre-treatment with wire mesh involves physical treatment to filter out food particles, hair and other suspended solids. The slow sand filtration involves physical treatment, biological treatment and chemical treatment. The water is accumulated at the top of sand to form platform for biological treatment. Then, the water passes through the sand and the waste from the biological treatment is filtered out by the sand layer. The nitrates in the water are be treated through denitrification by the sand layer.

The greywater treatment package consists of mechanical parts to control the flow and store the greywater for toilet flushing. The mechanical parts are pumps, sand filtration tank, wire mesh chassis and collection tank. The mechanical parts are designed based on the flow rate of the greywater. The pumps are used to pump the water from the collection tank to storage tank at the roof top for distribution. The sand filtration tank is designed based on the flow rate entering the sand filtration and requirement of sand height by the environmental organisations. Wire mesh are designed based on the size of particles to be filtered out and budget.

The design is evaluated by comparing the treated water with standard water quality for toilet flushing. The system must be able to meet the water quality for toilet flushing. The water quality is compared by measuring the total suspended solid (TSS), chemical oxygen demand (COD) and turbidity. These three parameters must meet the standard water quality for toilet flushing. The final design is represented in 3D model with all the mechanical parts.

The objectives of this project are to design a home scale greywater recycling package and optimise the design by having low cost compare to existing designs in the market. The final design is able to treat the greywater for toilet flushing. The design is optimised by having lower cost than existing home scale greywater package.

This project creates the chance for the public to use the greywater treatment system for household. These reduces the water usage for the public, which will reduce the cost if the system is used for long term. Reducing water usage results in reduction of water crisis. This system able to gradually bring advantage to the economy and environment. Since, public are not using any water recycling system currently because water recycling systems are only manufactured in industrial scale, this project able to fulfil the gap of designing a home scale water recycling system.

2. Methodology

This project involves designing, 3D modelling, prototyping and experimental evaluation. The designing involves the designing of pre-treatment stage with wire mesh, slow sand filtration and pump. The design is modelled into 3D prototype using SolidWorks Ver. 2016. The performance of the design is evaluated using the prototype.

2.1 Designing Stage

The greywater treatment system consists of pre-treatment filter, slow sand filtration, pump, and collection tank. The greywater enters to the pre-treatment filter and follow by the slow sand filtration. The treated water is collected in the collection tank. Then, the treated water is pumped to the storage tank using the auto water pump. The treated water is distributed to the toilets from storage tank.

The pre-treatment filter consists coarse and fine wire mesh. The pore size of coarse wire mesh is 1 mm and the pore size for the fine wire mesh is 0.5 mm. The coarse mesh is used to filter out hairs and particles that are larger than 1 mm. The fine mesh is used to filter out dirt and particles larger than 0.5 mm. The pre-treatment stage is designed vertically to use the gravitational force during the filtration. The gravitational

force provides extra support to push the water through the pores of the wire mesh. The wire mesh is designed to have hemispherical surface to provide larger filtration area. The hemispherical shape also provides the slippery slope for the movement of filtered particles through the drainage pipe.

The slow sand filtration consists sand layer and gravel. The slow water flows on the sand causes the water to accumulate at the top to form water bed for the biological treatment [7]. The biological treatment transforms bacteria into gas, water and biomass. The biomass is filtered by the pores between the sand. The sand also involves chemical treatment. The sand neutralises the nitrates through denitrifications [8].

The slow sand filtration is designed based on the volumetric flow rate equations and requirement by the environmental organisation [8]. Volumetric flow rate equation is applied to calculate the filtration area of the sand. Volumetric flow rate means the volume of water passes through medium per unit time. The volumetric flow rate equation is shown below.

$$A = \frac{Q}{v} \quad (1)$$

Where, A = surface area of the sand filter (m^2)
Q = flow rate onto the filter surface (L/h)
v = loading rate of sand (L/hm^2)

The flow rate of greywater in household are obtained from the journal published by the Texas A&M University from United States [9]. The data are shown in Table 2. The loading rate is set at 400 L/hm^2 because it is the optimum loading rate for sand filtration based on the environmental organisations from United States and United Kingdom. Therefore, the surface area of the sand filter can be calculated by substituting the parameters.

The height of sand filtration and gravel are designed based on the standard dimension set by the environmental organisation from well-developed country. This dimensions are set by the organisations based on the feedbacks gathered from the existing slow sand filtration. The dimensions are listed in Table 3.

Table 1. Parameters for sand filtrations system [7][10]

Organisations	**Parameters**	**Dimensions**
Cisco Foundations	Sand depth	≥50 cm
	Loading rate	400 L/hm^2
	Gravel Depth	≥5 cm
American Water Works Association	Sand Depth	≥50 cm
	Loading rate	100 L/hm^2-400 L/hm^2

Based on requirement in Table 1, the height of sand is set to 50 cm and the height is validated by applying Darcy's law. Darcy's law is used to calculate the flow rate of liquid that passes through a porous medium. Darcy's law states that the water flows from high potential area to low potential area. Therefore, the water in the sand filter obeys this law where, the water on top flows to the bottom due to the potential

difference. Darcy's equation (2) is given as shown below. The sand depth recommended by environmental body is validated using the Darcy's law.

$$Q_{max}=k.A.\frac{h+d}{d} \quad (2)$$

Where, Q_{max}= Maximum flow rate (m^3/s)
k= Hydraulic conductivity of sand (m/s)
h= Depth of clearance above the sand (m)
d=Depth of sand (m)

The designing of pump includes the process of transferring the water from collection tank at the slow sand filtration to the storage tank. Auto water pump is used in this project because the slow sand filtration required longer time to fill in the collection tank. The pump should operate once the collection tank is full. Auto water pump activates based on the water level. Therefore, auto water pump is the ideal choice for this project.

The suitable pump can be chosen based on the water horsepower. The parameters that are related in the horsepower pump designing is the head loss and water flow rate. The equation relating these parameters are shown below. Head loss is the distance to pump the water from one point to another point. The pump for this project must be able to transfer the water from the collection tank to storage tank at the rooftop. Therefore, the head loss is the height of the house, which is generally 5.7 m.

$$WHP=\frac{Q\times H}{3960} \quad (3)$$

Where, WHP= Water horsepower (hp)
Q= flow rate of water from the pump (gallon/minute)
H= head loss or distance to pump the water (foot)

2.2 3D Modelling

The design of the pre-treatment stage and slow sand filtration are modelled as software prototype using SolidWorks Ver. 2017. The pre-treatment stage consists of three parts, which are the mesh holder, filtration chassis and chassis connector. The mesh holder is placed in the filtration chassis and the coarse filtration chassis is connected to the fine filtration chassis using the chassis connector. Since, 4 inches PVC pipe commonly used as greywater outlet, the pre-treatment stage is designed to have same dimension as 4 inches PVC pipe for ease of installation. The drawing of mesh holder is shown in Figure 1.

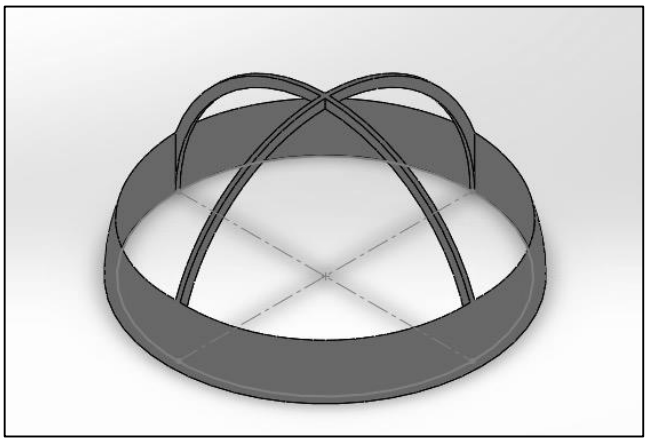


Figure 1. Mesh holder

The slow sand filtration chassis was designed based on the calculations carried out using the equations and requirements as discussed in Section 2.1. The slow sand filtration consists two parts which are the chassis and connector. The chassis is used to fill the sand and gravel. The connecter is used to connect the sand filtration to the pre-treatment stage. The complete 3D model is shown in Figure 2.

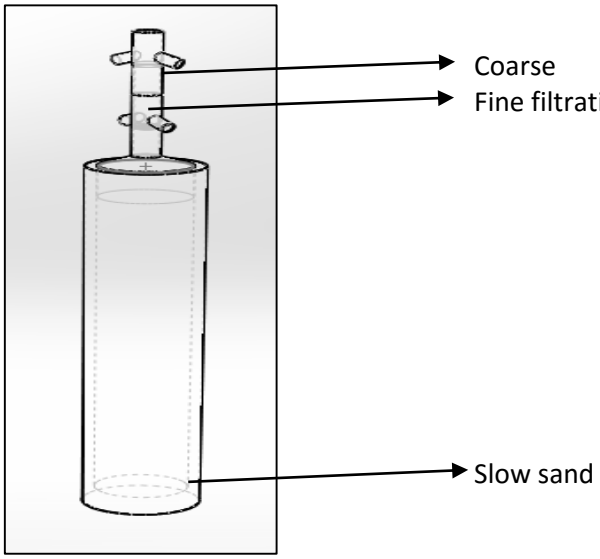


Figure 2. Drawing of the whole filtration system

2.3 Prototyping

The prototyping stage involves the manufacturing of the pre-treatment filter and the sand filtration to evaluate the design. The pre-treatment filter is built using the 110 mm PVC pipe with PVC pipe connector. The wire mesh for fine screening and coarse screening are glued in the pipe using adhesive bonding. The complete prototype model for pre-treatment filter is shown Figure 3.

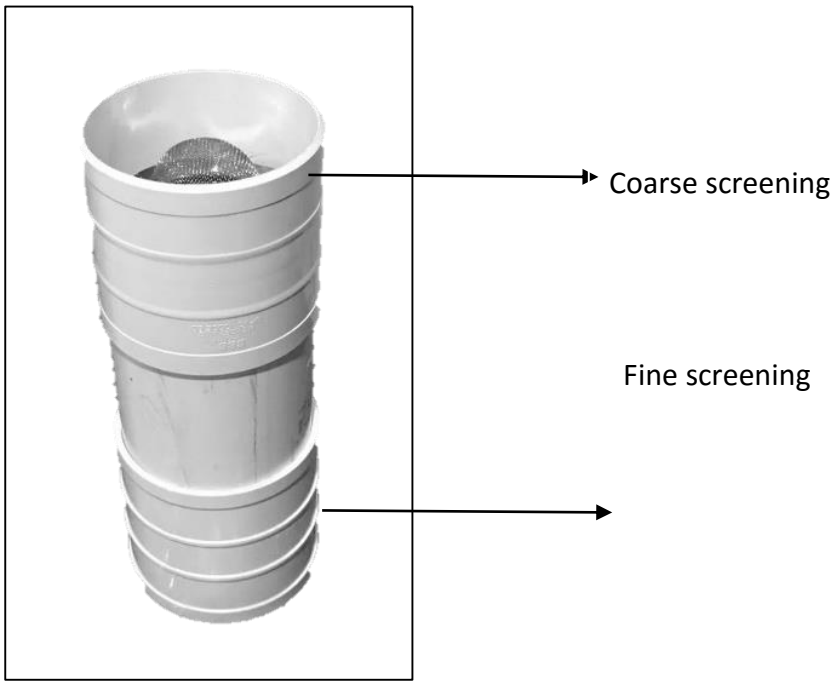


Figure 3. Pre-treatment filter

The slow sand filtration is manufactured using plastic tanks. The slow sand filtration is manufactured in scaled down dimension because the prototype is only needed to evaluate whether the system can treat the greywater to meet standard quality of water for toilet flushing. The prototypes are manufactured for use of experiments to evaluate the design.

2.4 Experiments

The project involves the experiments to measure the flow rate entering the sand filter from the pre-treatment stage, total suspended solid (TSS), chemical oxygen demand (COD) and turbidity. The TSS, COD and turbidity is measured to evaluate whether the treated water meets the standard water quality for toilet flushing. The standard water quality for toilet flushing is gathered from various water quality department as shown in Table 2. The performance of the design is evaluated by comparing the treated water with parameters in Table 2.

Table 2. Water quality for toilet flushing based on American standards

Organisation	Parameter	Value
United States Environmental Protection Agency (US EPA) [11]	BOD	≤10 mg/L
	COD	-
	Turbidity	≤ 2 NTU
	TSS	-
World Health Organization [12]	BOD	≤10 mg/L
	COD	-
	Turbidity	-
	TSS	≤10 mg/L
Canada Health Department [13]	BOD	≤10 mg/L
	COD	-
	Turbidity	≤ 2 NTU
	TSS	≤10 mg/L
The International Water Quality published book titled Milestone in Water Reuse [14]	BOD	-
	COD	≤30 mg/L
	Turbidity	-
	TSS	-

2.4.1 Flow Rate Test

The objective of this experiment is to determine the flow out rate of the greywater from the pre-treatment stage. Flow out rate is needed to calculate the surface area for the slow sand filtration. The experiment is conducted to obtain the relationship between the flow in and flow out of the pre-treatment system. The relationship can be used to approximately measure the flow out rate at any particular flow in rate for the pre-treatment stage.

The experiment is conducted by measuring the flow in rate from tap water by adjusting the tap at different angle. The time taken to fill 2 L of water at each angle is recorded. The procedures are repeated by passing the tap water through the pre-treatment filter. The time taken to fill 2 L of water with the presence of pre-treatment filter represents the flow out rate and the time taken to fill 2 L of water with the absence of pre-treatment filter represents the flow in rate. The graph of flow out rate against flow in rate is plotted and the relationship is obtained. Based on the relationship, the flow out rate is substituted into equation 1 to calculate the surface area for sand filtration.

2.4.2 Turbidity Experiment

The turbidity of the treated water is measured using the turbidity tube. Turbidity tube is measuring cylinder with a reference disk at the bottom of the tube as an indicator. The treated water is filled up until the maximum level, where the reference plane is still visible as shown in Figure 4. Then, the height of the water level in the cylinder is

measured. The height is converted into turbidity scale using the table obtained from lab manual prepared by Chicago River Schools Network [15].

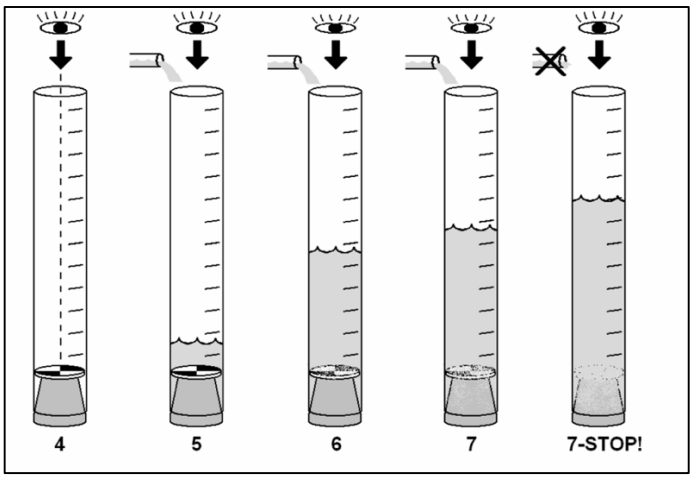


Figure 4. Filling the treated water until the maximum level, where the disk is visible

2.4.3 Chemical Oxygen Demand Experiment

Chemical oxygen demand, COD is the total oxygen consumption by all the organic substances in the water [16]. High values of COD indicate the water has high level of microorganisms and pollution [17]. The COD experiments is carried out by adding nitric acid into the treated water. Then, the mixture is heated until the oxidation process completed and the remaining unreacted nitric acid is weighed. The mass of reacted nitric acid is calculated by subtracting the remaining unreacted nitric acid added to the treated water. The mass of dissolved nitric acid represents the COD of the treated water in g/L.

2.4.4 Total Suspended Solid Experiment

Total suspended solid (TSS) is the quantity of solid particles in the water. The TSS experiment involves the evaporation of the treated water. 1 L of treated water is evaporated under the sun and leftover residue after evaporation is weighed. The mass of leftover residue represents the TSS value in g/L.

2.5 Limitation

Limitation in this project is the usage of instruments for the measurement of COD, TSS and turbidity of the water. The COD, TSS and turbidity of the water are measured using manual experimental method. The instruments are not used because budgets or facility to borrow the instruments are not allocated by the industry supervisor. Therefore, the manual methods of determining this parameter involve limitation such as the scale and sensitivity. The turbidity test only able to give minimum value of 5 NTU.

3. Results and Discussion

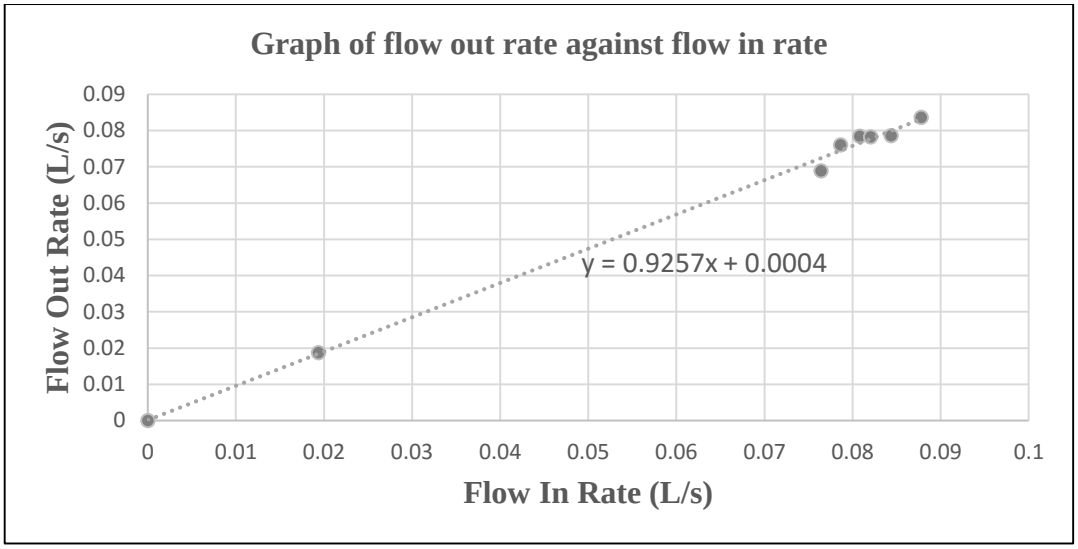
The data of time taken to fill 2 L of water with the absence of pre-treatment filter is tabulated as shown in Table 3. Table 3 shows the flow in rate when the tap is at different angle. Table 4 represents the time taken to fill 2 L of water with the presence of pre-treatment filter. The graph of flow out rate against flow in rate is plotted as shown in Figure 7.

Table 3. Results of flow in rate

Tap angle (°)	**Time Taken to fill 2 L (s)**			**Flow in rate (L/s)**
	1st	**2nd**	**Average**	
45	0	0	0	0
90	101.42	105.2	103.31	0.0194
135	26.13	26.22	26.18	0.0764
270	25.35	25.53	25.44	0.0786
360	25.12	24.37	24.75	0.0808
405	25.24	23.51	24.375	0.0821
450	23.16	24.25	23.71	0.0844
495	21.68	23.88	22.78	0.0878

Table 4. Results of flow out rate

Tap angle (°)	**Time Taken to fill 2 L with Filter (s)**			**Flow out rate (L/s)**
	1st	**2nd**	**Average**	
45	0	0	0	0
90	107.37	105.92	106.645	0.019
135	29.18	28.87	29.03	0.0689
270	27.08	25.54	26.31	0.0760
360	27.68	23.33	25.51	0.0784
405	25.63	25.48	25.555	0.078
450	27.33	23.55	25.44	0.0786
495	24.7	23.16	23.93	0.0836



1) Figure 5. Graph of flow out rate against flow in rate

Graph in Figure 5 represents the relationship between the flow in rate and flow out rate. The relationship equation is obtained to calculate the flow entering the slow sand filtration. The flow out rate is represented as y and the flow in rate is represented as x. The flow out rate represents the flow rate entering the slow sand filtration. Then, the surface area required for the slow sand filtration is calculated using equation 1 and tabulated in Table 5. Therefore, the slow sand filtration is designed based on the calculated surface area as shown in Table 5. The sand filtration surface has 21 cm of radius. Therefore, the design can be used up to maximum of 4-bedroom house.

Table 5. Flow rate entering the slow sand filtration and surface area of sand

No of bedrooms	Daily water use (gal)	Greywater flow rate (L/h)	Flow rate entering the sand filtration (L/h)	Surface Area of Sand (m^2)	Radius sand surface (cm)
1 or 2	225	35.49	32.85	0.08	16.17
3	300	47.32	43.80	0.11	18.67
4	375	59.15	54.76	0.14	20.87

Based on Table 7, the maximum flow rate entering the slow sand filtration is 54.76 L/h. Therefore, the maximum flow rate can be handled by the slow sand filtration can be calculated using the Darcy's equation as shown below. The sand depth, d is recommended to be at least 50 cm by the environmental bodies from United States. The hydraulic conductivity of the fine sand is given 2×10^{-4} m/s. The depth of clearance above the sand layer is 10 cm.

$$Q_{max} = k.A.\frac{h+d}{d}$$
$$= (2\times10^{-4})\ (\pi 0.21^2)\ (\frac{0.1+0.5}{0.5})$$
$$= 3.325\times10^{-5}\ m^3/s$$
$$= 119.70\ L/h$$

Based on the calculated $Q_{max,}$ the sand depth is designed to be 50 cm. This is because the flow of water entering the sand filtration is lower than the maximum flow rate can be handled by the slow sand filtration system with 50 cm sand depth. Based on the experiments and calculation the final design of the system with collection tank is shown in Figure 6 and Figure 7. The collection tank is design to collect 1000 L of capacity.

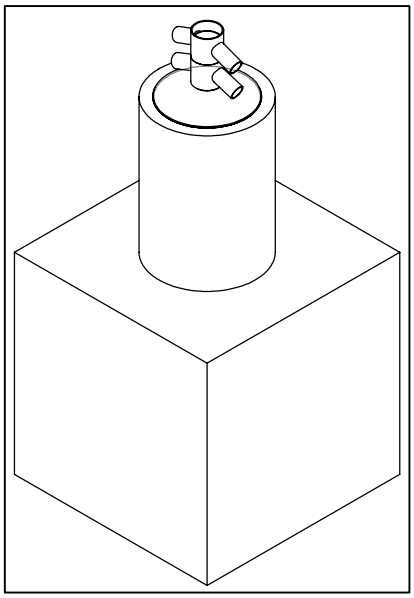


Figure 6. 3D design of the system with the collection tank

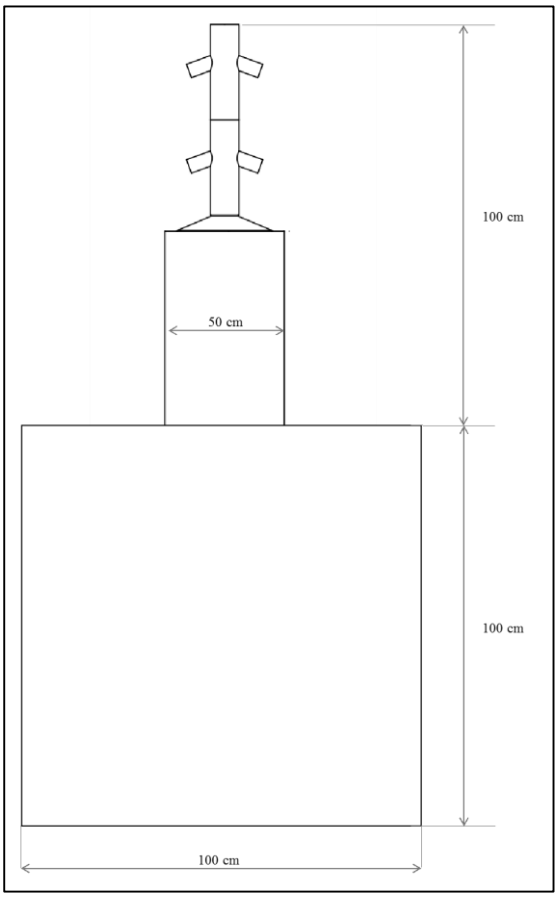


Figure 7. Detailed design of the system with the collection tank

The design is evaluated by carrying out experiments to determine the COD, TSS and turbidity value of the treated water using the small-scaled prototype. The data collected are shown in Figure 8.

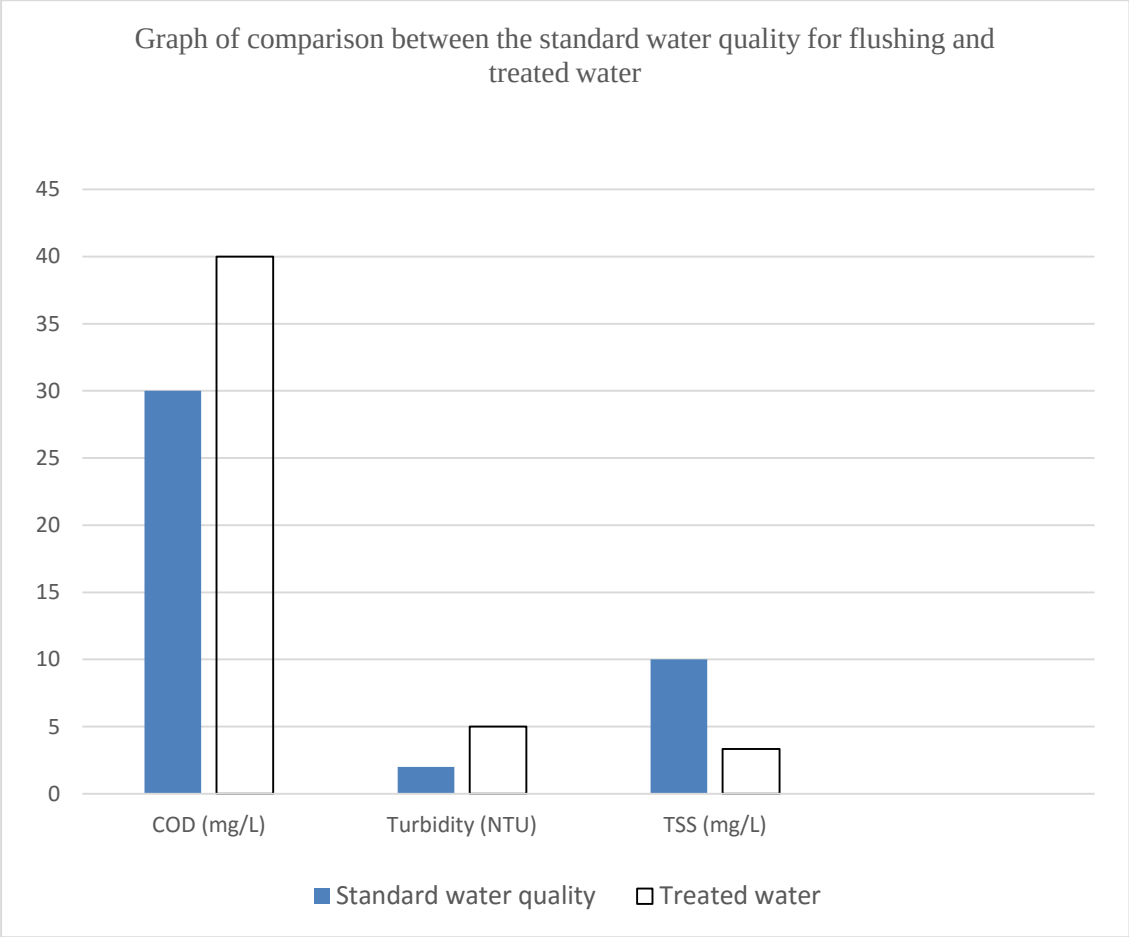


Figure 8. Bar chart comparison for standard flushing water quality and treated water

The turbidity of the treated water in this experiments is less than 5 NTU. The total suspended solid in the treated water is 3.33 mg/L. The TSS value required for the toilet flushing water is less than 10 mg/L. Therefore, the design fulfils the requirement for the TSS value. The COD of the treated water is 40 mg/L. The required COD for the toilet flushing water is less than 30 mg/L. The COD requirement was not able to fulfilled because of the small-scale prototype.

Based on the finalised design, the price to manufactured one complete filter system is estimated. The complete system includes the plastic filter chassis for the pre-treatment filter and slow sand filtration, filter sand, wire mesh, auto water pump and collection tank. The price for each product is obtained and the total cost is calculated as shown in Table 6. The experiments to evaluate the performance of system by measuring the TSS, COD, and turbidity of the treated water are conducted using the prototype.

Table 6. List of price for the filtration system

Product	Price	Quantity	Total (USD)
Filter chassis	25.80 USD/kg	10.073	259.8834
Auto water pump	133.43 USD	1	133.43
Filter fine sand	2.41 USD/kg	117	281.97
Gravel	2.31 USD/kg	80	184.8
1000 L water tank	425.55 USD	1	425.55
1 mm wire mesh	60 USD/sheet	1	60
0.5 mm wire mesh	80 USD/sheet	1	80
Total Cost (USD)			**1425.63**

Based on Table 6, the budget to manufacture one complete system using the design in this project is lower than cost of the existing greywater recycling package. The existing home scale greywater system in the market is a down-scaled of industry greywater recycling design. Therefore, the cost of this existing home scale greywater recycling package design is 8,100 USD. This design has high cost due to the technology that are used in this system. This system consists physical treatment using different size of mesh and membrane. Then, the biological treatment is carried out using the UV ray. The UV ray neutralises the microorganism in the water. The parts that cause the system to be expensive are the membrane, UV ray and pump.

This design is relatively cheaper because this designs does not uses any membrane as the physical filtration and high performance pump for the water movement through the membrane. The membrane is replaced by the sand filtration which able to meet the same turbidity and pump is replaced by the gravitational force in the sand filtration. The UV ray is replaced by the sand filtration because the water and residue accumulated at the top of the sand layer forms biological reaction bed layer. The microorganisms are neutralised at top of the sand through biological treatment.

Therefore, the optimisation of the design involves the cost of the system. The recycling package is designed at relatively lower cost with same function and requirement. This low cost provides more chances for the customer to buy this product. This can increase the attention and business value of greywater recycling package.

4. Conclusion

The greywater treatment package is successfully designed within proposed budget by DD Techniche Sdn Bhd. The design of the system is within 6 m^3 including the collection tank. The greywater treatment package contains the pre-treatment filter, slow sand filtration and collection tank. The effect of the pre-treatment stage on the flow entering the slow sand filtration is studied to design the slow sand filtration. Based on the experiments, the slow sand filtration is designed based on the volumetric flow rate and Darcy's law. The material budget of a complete system is lower than the existing home scale greywater recycling system. This design is able to treat greywater to meet the standard water quality of toilet flushing.

References

[1] K. Bani-melhem and E. Smith, “Grey water treatment by a continuous process of an electrocoagulation unit and a submerged membrane bioreactor system,” *Chem. Eng. Journal.*, vol. 198–199, pp. 201–210, 2012.
[2] M. S. Fountoulakis, N. Markakis, I. Petousi, and T. Manios, “Single house on-site grey water treatment using a submerged membrane bioreactor for toilet flushing,” *Sci. Total Environ. Journal*, vol. 551–552, pp. 706–711, 2016.
[3] J. A. Peeples, “Overview of greywater management Health considerations,” *Wastewater Use Agric.*, vol. II, pp. 119–131, 2006.
[4] B. Je, A. Laine, S. Parsons, T. Stephenson, and S. Judd, “Technologies for domestic wastewater recycling,” *Journal of Elsevier*, vol. 1, no. 1999, 2000.
[5] F. Li, K. Wichmann, and R. Otterpohl, “Science of the Total Environment Review of the technological approaches for grey water treatment and reuses,” *Sci. Total Environ. Journal*, vol. 407, no. 11, pp. 3439–3449, 2009.
[6] B. A. Mittal, “Biological Wastewater Treatment,” *FullTide Corporation*, pp. 2–9, 2011.
[7] Y. Dunets, Siobhan; Zheng, “Slow sand filtration,” *Greenh. Nurs. Watery*, 2011.
[8] W. T. Course, “Filtration involves the removal of suspended and colloidal particles from the water by passing it through a layer or bed of a porous granular material, such as sand.,” *Sci. Total Environ. Journal*, , pp. 1–2, 2012.
[9] B. Lesikar, R. Melton, D. Smith, and C. O. Neill, “Graywater-Onsite Wastewater Treatment System,” *AgriLIfe Communications and mArketing*, pp. 3–08, 2003.
[10] Centre for Affordable Water TEchnilogy, “What is the minimum depth of filtration sand, underdrain gravel and separating gravel? (particularly.” Cisco Foundation, p. 1, 2017.
[11] Members of WQA, “Residential Water Reuse Fact Sheet,” *Water Quality Association*, pp. 1–5, 2013.
[12] T. Bruursema, “These American National Standards help in evaluating and approving water reuse treatment technologies.,” *Plumbing Systems & Design Magazine*, pp. 15–22, Oct-2011.
[13] American Water Standard, “NSF/ANSI Standard 350 For Water Reuse Treatment Systems,” 2011.
[14] V. Lazarova, *Milestones in Water Reuse*. The International Water Association, 2013.
[15] Chicago School Network, “Turbidity,” *Turbid. Test Procedure.*, pp. 1–2, 2013.
[16] Y.-C. Kim, S. Sasaki, K. Yano, K. Ikebukuro, K. Hashimoto, and I. Karube, “Photocatalytic sensor for the determination of chemical oxygen demand using flow injection analysis,” *Anal. Chim. Acta*, vol. 432, no. 1, pp. 59–66, 2001.
[17] J. Chen, J. Zhang, Y. Xian, X. Ying, M. Liu, and L. Jin, “Preparation and application of TiO2 photocatalytic sensor for chemical oxygen demand determination in water research,” *Water Res.Journal*, vol. 39, no. 7, pp. 1340–1346, 2005.

Mechanical Characterization of Zirconia Ceramic Composite

2) K. Dickson[1*], W. J. Kelvin Chew[1*], S. Ramesh[2]
3) [1]*Department of Mechanical Engineering, School of Engineering, Faculty of Built Environment, Engineering, Technology and Design, Taylor's University, 47500 Subang Jaya, Selangor, Malaysia.*
4) [2]*Centre of Advanced Manufacturing & Material Processing (AMMP), Department of Mechanical Engineering, Faculty of Engineering, University of Malaya, 50603 Ku ala Lumpur, Malaysia.*
5) **KelvinWaiJin.Chew@taylors.edu.my*

Abstract
In this day and age, zirconia ceramics are used widely in the medical field as biomaterials for the replacement of damaged body parts. This is because zirconia is one of the closest replacements for bone tissue. However, there were a few cases regarding the failure of zirconia ceramic hip transplants. To overcome this issue, composite materials are being studied as they are able to combine different properties which are not present in a material. This study of Y-TZP/stainless steel 316 composite is carried out with the idea of providing a solution for failure of zirconia implants and also an improvement in biomaterials which will benefit the biomedical world. The study aims to determine the effects on how the increasing of stainless-steel content in the composite will affect the relative density, Vickers hardness, fracture toughness and ageing resistance of the Y-TZP/stainless steel 316 composite. To carry out the research, the composite samples were prepared by mixing the powder of each samples according to their determined content with ethanol. After the powders were mixed, the powders were then pressed, followed by undergoing a Cold Isostatic Press process (CIP) and then it underwent sintering at its determined temperature. After sintering, the samples underwent grinding and polishing before being ready for testing. The outcomes of the research showed that as the sintering temperature and the content of stainless-steel increase in the composite, the fracture toughness and ageing resistance improved while the Vickers hardness and relative density decreased.

Keywords:Y-TZP/stainless steel 316 composite, bulk density, fracture toughness, Vickers hardness, Ageing resistance

1.Introduction

Composite materials are being used more frequently in this modern era as it tends to enable the combination of different properties which is not present in a material. In the medical field, different materials have been used for biomaterials study as a replacement for damaged body parts. Ceramics in particular has been given close attention as it is the closest replacement for bone tissue [1]. However, ceramics does not have a high toughness when it is compared to metals. Therefore, ceramic filled metal and metal filled ceramic composites are being studied to increase the overall toughness of the replacement implants. In this modern era, prostheses that are made of purely ceramics are slowly being replaced by composite materials [2]. This is due to the improvement of the major factors, which is the strength and durability of the prostheses. Thus, studies regarding composite materials as biomaterials are being developed rapidly.

Zirconia is a ceramic which is readily used in many different sectors, especially the medical field. It has different properties when it exists at different phases, and is usually added with stabilising agents so that the phases and characteristics do not change at different temperatures. It has a high tolerance towards corrosion, high strength, high density and also high resistance towards impact. Y-TZP (Yttria-stabilized Tetragonal Zirconia Polycrystalline) in particular is more compatible to the human body. Thus, it has been used for many years as prosthetics and has not shown negative responses. Besides that, there are many different types of stainless steel which is graded based on its mechanical properties, grade compositions and also its production specifications. Generally, compared to ceramics, stainless steel has a high corrosion resistance, high toughness, high ductility and high strength. To produce implants which should be more durable, composite materials can be used to replace ceramics.

Based on the study done by Kurtz *et al.*[3], composite materials such as zirconia toughened alumina is better compared to materials such as zirconia and alumina as it is able to combine both the advantageous properties of alumina and zirconia. The addition of both alumina and zirconia results in having a higher fracture toughness and strength which reduces the probability of dislocation and impingement which leads to failure of implants. It also reduces the hardness which exist in ceramics. The stress-assisted degradation will also be reduced drastically while the wear characteristics improves. The study showed that the use of composite materials would allow the implants to last for a longer duration compared to ceramics without the need to be revised.

Agudelo *et al.*[4] did a study to determine the relative density of composite materials, zirconia and 316 stainless steel with varied compositions and heating rates. The relative density of the samples was tested with different heating rates during sintering and the results showed that, when the content of stainless steel in the samples are below 50%, the relative density of the samples decreased as the heating rates increased. On the other hand, when the content of stainless steel in the samples were above 50%, the relative density of the samples increased as the heating rates increased.

Esteban *et al.*[5] conducted a study to determine the Vickers hardness and the fracture toughness of zirconia/stainless steel composites. The zirconia/stainless steel composites were made into samples with stainless steel concentrations ranging from 15 to 30%. The results of Esteban *et al.*[5] study showed that the Vickers hardness decreased and the fracture toughness increased as the stainless-steel content in the

zirconia/stainless steel composites increased which follows the rule of mixture [6-8]. The results also showed that there was no plastic deformation when fractures occur in the zirconia/stainless steel composite samples. Besides that, the study also showed that the zirconia/stainless steel is not brittle compared to zirconia ceramic. These characteristics are important for the enhancement of materials used in biomedical implants, especially zirconia.

In the past, the medical field has reported a few cases regarding the failure of zirconia ceramic hip transplants. To overcome the issue, more and more studies have been carried out regarding the sintering of zirconia composites at low temperatures regarding its mechanical characteristics [9]. Regarding hip transplants, most of the studies carried out involve around the zirconia (Y-TZP) ceramic. In this study, the zirconia ceramic (Y-TZP) was mixed with stainless steel (316) to produce composite materials. The present paper aims to determine the relative density, Vickers hardness, fracture toughness and ageing resistance of the composite at different sintering temperatures. This study is carried out with the idea to enhance and aid the current medical field with an alternative solution regarding the production of transplants using different composite materials.

2. Methodology

2.1 Powder preparation

During the first stage of study, stainless steel 316 and Y-TZP powder were used based on table 2.1. The stainless steel 316 powder and the Y-TZP powder were mixed and measured according to the content of stainless-steel for the preparation of the samples. Firstly, the digital ultrasonic bath (Powersonic UB-410, Thermoline Scientific, Australia) was filled with water. Then, 100ml of ethanol was poured into a beaker and both the stainless steel 316 powder and the Y-TZP powder were added into the beaker to undergo mixing. The weight percentage of each samples were fixed with the content of stainless steel ranging from 0 wt%, 10 wt%, 20 wt% and 30 wt% before both the powders were mixed. The beaker was placed in the Digital Ultrasonic Bath for 15 minutes and then taken out after the mixing was completed. The mixture then underwent attrition milling using the Laboratory Attritor Mill (01-HD, Union Press, United States) for 45 minutes at 500 rpm. Both the stainless steel 316 and Y-TZP powder mixture were reduced to a slurry. After mixing, the mixture was placed in a universal oven (UN 55, Memmert, Germany) overnight at 60°C and was left to dry. A sieve of 212µm was then used to sieve the mixture through to ensure that the powder mixture was fine.

2.2 Green sample preparation

The composite powders were then pressed using a hydraulic bench press (HP10-150, RMS Hydro, Malaysia) to form round tabletsthat have a diameter of 20mm. Pressing was required to form a green body and ensure that the powder mixture was fine before cold isostatic pressing. Cold isostatic pressing was carried out using a cold isostatic press (KJYU150, Shanxi Golden Kaiyuan Co., Ltd, China) and was done by placing the green body round tablets into containers of the desired shape and under room temperature and a high pressure. This was done to ensure that the green body samples were not affected by heat or pressure when they were being pressed together.

If heat or pressure was applied to the green body samples as it was being pressed together, the green body samples might have cracks after they were pressed together.

Table 2.1: Characteristics of Stainless Steel 316 and Y-TZP powder

Materials	Composition (wt%)	Theoretical density (g/cm^3)	Tap density (g/cm^3)	D_{50} (µm)
Stainless steel 316	17Cr-12Ni-2.5Mo-1Si-2Mn	8.00	4.4	21.9 ± 0.1
Y-TZP	5.2 Y_2O_3 (Yttria)	6.1	6.0	0.6 ± 0.1

2.3 Sintering, grinding and polishing

The next stage of the study was where the samples underwent sintering to become specimens which were ready for testing. The samples underwent sintering by being placed into anelectric box furnace (LT01, LT, Malaysia) and was heated with different temperatures which are 1250°C, 1300°C, 1400°C and 1500 °C. The sintering rate was 10° per minute and the sintering process had a holding time of 2 hours. Grinding paper was then used to polish and grind the samples after sintering. The type of grinding paper used was Silicon carbide (SiC) paper. 5 different types of grinding papers, namely 120, 240, 600, 800 and 1200 were used to ensure that the samples were grinded properly. After grinding, the samples underwent polishing. There were 2 different sizes of diamond bits from the diamond paste which were used, namely 6µm and 1µm. The samples were polished using the diamond paste on a polishing clothe. Both the grinding and polishing process were carried out using a polishing and grinding machine (GP2V, LT, Malaysia).

2.4 Measurement and Analysis

2.4.1 Relative density

After the samples were prepared, a series of different test were conducted on the samples to determine different mechanical properties. To determine the relative density of the composite samples, the water immersion technique using an analytical balance with density kit (AY220, Shimadzu, Japan) was used while the immersion medium was distilled water. The technique was done based on Archimedes principle. The theoretical density of Y-TZP was determined as 6.1 Mgm^{-3} (grams per cm3). The formula for the calculation of relative density is based on (eq 1).

$$\rho = \frac{W_a}{W_a - W_w}\rho_w \quad (1)$$

where

ρ = Relative density of sample (g/cm^3)
W_a = Weight of sample in air (g)
W_w = Weight of sample in water (g)
ρ_w = Density of distilled water (g/cm^3)

2.4.2 Vickers hardness

The Vickers hardness of the samples was tested using a Vickers hardness tester (MV-01, Matsuzawa, Japan) which had a pyramidal diamond indenter and an applied load of 10kg. The load was applied on to the samples slowly without impact and was held down in place on the sampled for a duration of 10 seconds. The physical quality if the indenter and the accuracy of the applied load was defined based on ASTM E284-99 [10]and ISO 14705 [11]. After the indentation was done, the indentation was measured using a filar micrometer which was built in the attached microscope on the Vickers hardness machine. The microscope had an accuracy nearest to 0.1µm. The formula for the calculation of the Vickers's hardness is presented in (eqn 2).

$$H_v = \frac{1.854P}{(D)^2} \tag{2}$$

where

P = Applied load (kg)

D = Average of diagonals = $\frac{D_1 + D_2}{2}$ (m)

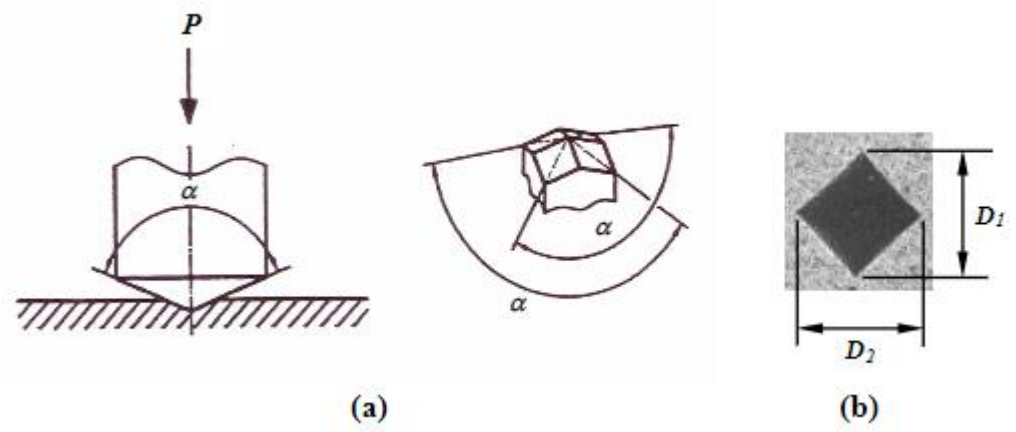


Figure 1. Schematic diagram showing the shape of the Vickers indenter (α =136º ±0.5º, angle between the opposite faces at the vertex of the pyramidal indenter) and (b) an indentation that is formed [11]

2.4.3 Fracture toughness

After the indentation was done on the sample, the fracture toughness was also measured based on the same indentations that were used to determine the Vickers hardness. The equation to calculate the fracture toughness is presented in (eqn 3) which was proposed by Niihara*et al*. [12].

$$\left(\frac{K_{IC}\Phi}{H_V a^{\frac{1}{2}}}\right)\left(\left(\frac{H_v}{E\Phi}\right)^{\frac{2}{5}}\right) = 0.035\left(\left(\frac{L}{a}\right)^{\frac{-1}{2}}\right) \tag{3}$$

Where

K_{IC} = Fracture toughness(MPa.m$^{0.5}$)

H_v = Vickers hardness (GPa)

E = Young's modulus (Pa)

a	=	Half-length of the average diagonal (m)
L	=	Average crack length (m)
Φ	=	Constraint factor which is taken as 3 [13]

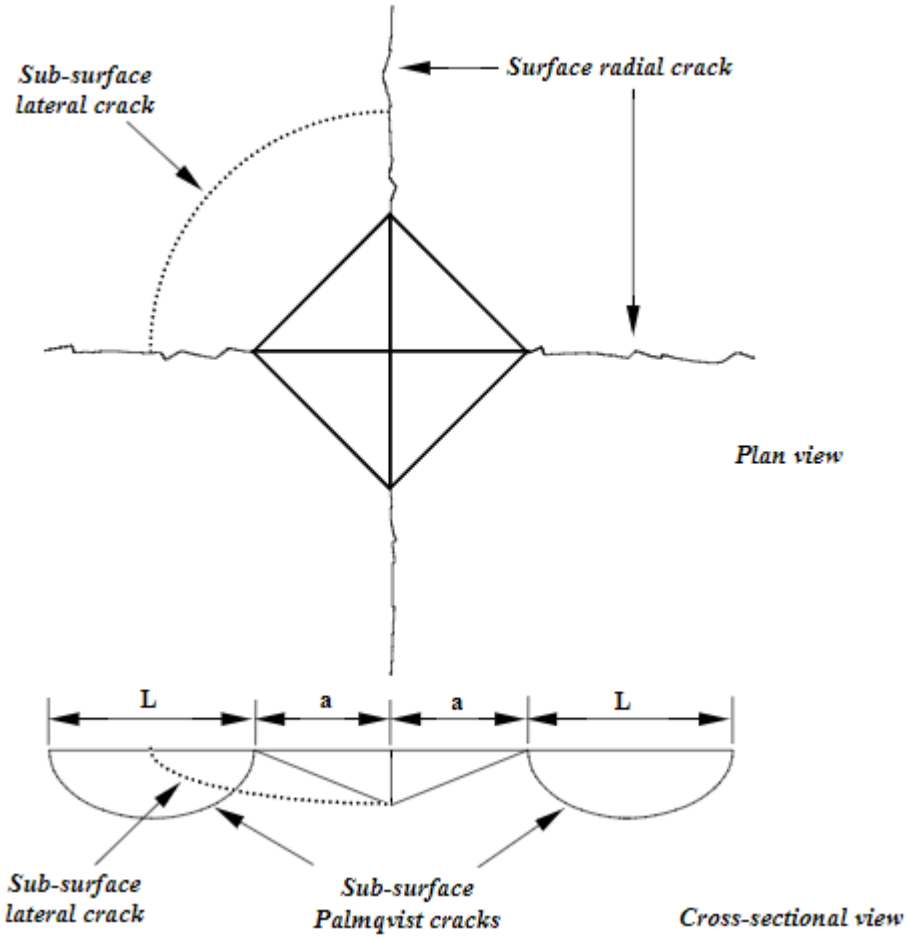


Figure 2. Schematic diagram of a typical Palmqvist crack system observed after Vickers indentation. "L" refers to the crack length which was measured to compute the fracture toughness of the sample while the length of 2a is equivalent to a diagonal of the Vickers indent (D1 or D2, based on Figure 1

2.4.4 Assumptions

A few assumptions were established at the start of the study which are:

1. The Young's modulus of Y-TZP and stainless steel 316 at room temperature is 200 GPa and 193 GPa.
2. The sintering temperature that the samples undergo are accurate based on the desired temperatures.

3. Results and Discussion

3.1 Relative Density

The relation between relative density and the sintering temperature of the composite material is shown in Fig. 3. It is shown that, for the samples which contain

10 and 20 weight percentage of stainless steel 316/Y-TZP, 1300 °C is the optimum sintering temperature as it has its highest relative density. As for the sample which contain 30 weight percentage of stainless steel 316/Y-TZP, the relative density increases as the sintering temperature increases from 1250 °C to 1500 °C. For the sample which contains pure Y-TZP, it has the highest relative density when the sintering temperature was 1400 °C. The results showed that pure Y-TZP had a higher relative density compared to composite materials of ss316/Y-TZP at higher sintering temperatures. Besides that, it also showed that as the weight percentage of stainless steel in the composite material increased, the relative density of the composite material decreased. The results obtained also showed that it was in line with the findings based on the study of Agudelo *et al.* [4] to a certain extend.

Based on Agudelo *et al.* [4] study, as the weight percentage of stainless steel in ss316/Y-TZP samples increase, the relative density of the samples increased over sintering temperatures. This is true theoretically as the heating rates and temperatures increase, the density if the samples with increasing weight percentage of stainless steel increases. However the trend of the study suggested otherwise. When the percentage of stainless steel 316 increased past 10 wt%, the relative density decreased. This can be explained due to a few factors. Firstly, the method of processing for the samples in this study and the study carried out by Agudelo *et al.* [4] was different; thus, the processing method could have an effect on the results obtained. Another possibility could be attributed to the type of powder used in the study. To have a better understanding regarding the difference in trends, further study regarding microstructure examination via scanning electron microscope (SEM) is required.

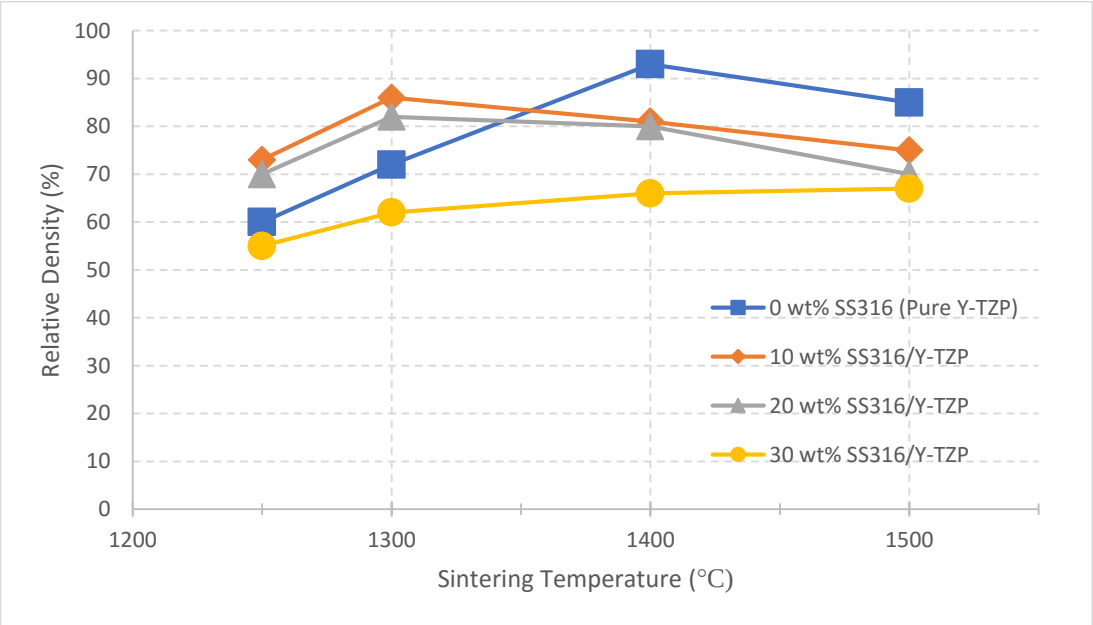


Figure 3. Relative density comparison between different weight percentage of SS316/YTZP and sintering temperature

3.2 Vickers Hardness

Figure 4 shows the relation between sintering temperature and the Vickers hardness of the composite material. Based on Fig. 4, pure Y-TZP had the highest Vickers hardness which is 13.5 GPa when its sintering temperature is 1400 °C.

However, all the composite materials with different weight percentage of stainless steel had the highest Vickers hardness at the sintering temperature of 1300 °C. This showed that the ideal sintering temperature for the stainless steel 316/Y-TZP composite was 1300 °C. It is also shown based on the results that when the weight percentage of stainless steel 316 in the stainless steel 316/Y-TZP composite increases, the Vickers hardness of the composite material will reduce. This is also true based on the study of Esteban *et al*. [5] which showed the same results compared to Fig. 3. This can be explained due to the hardness of materials as stainless steel 316 is softer than Y-TZP, which also obeys the rule of mixture [6-8].

The trend in this study is similar to the trend of Esteban *et al*. [5] study. The reduce in Vickers hardness can be explained based on the hardness of ss316 and Y-TZP. Stainless steel 316 is softer compared to Y-TZP; thus, when the content of the ss316 in the ss316/Y-TZP composite increases, the Vickers hardness will reduce as the hardness of ss316/Y-TZP composite is lower as the composition has higher amounts of stainless steel which will also cause the composite to be softer.

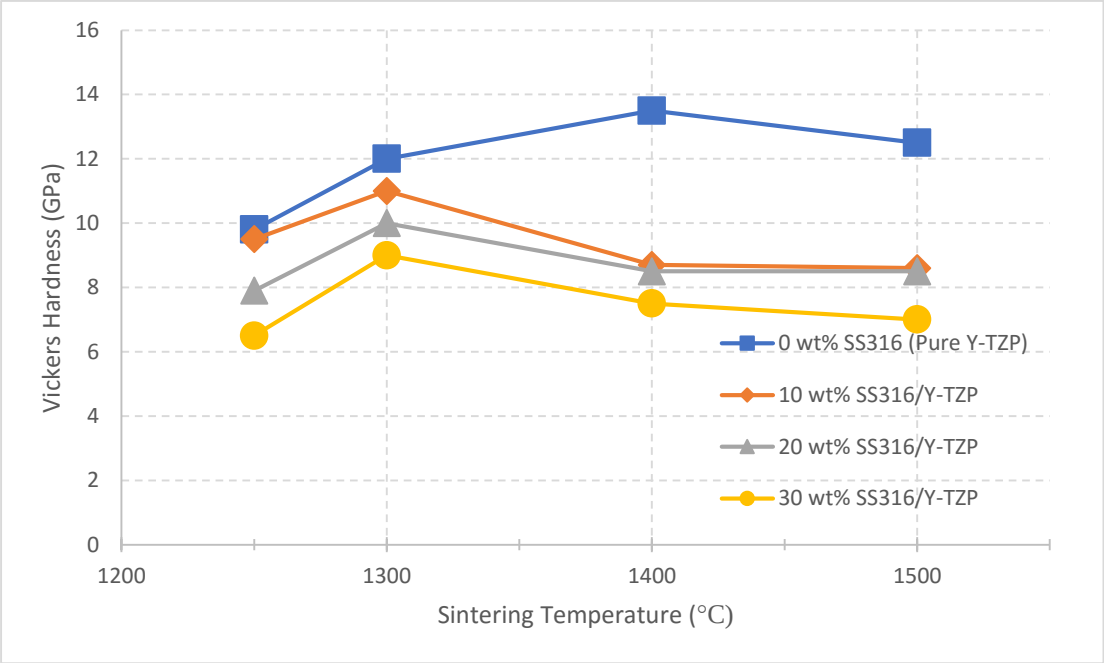


Figure 4. Vickers hardness comparison between different weight percentage of SS316/YTZP and sintering temperature

3.3 Fracture Toughness

Figure 5 exhibits the results of the fracture toughness of different weight percentage of ss316/Y-TZP at different sintering temepreatures. Based on the results of Figs. 3, 4 and 5, it showed that once again the ideal temperature for sintering of 10 and

20 weight percentage ss316/Y-TZP is 1300 °C. At 1300 °C, both the 10 and 20 weight percentage ss316/Y-TZP had the highest fracture toughness. The results also showed that the composite materials which contained stainless steel had lower fracture toughness as the sintering temperature increased after 1300 °C. The results also showed that when the weight percentage of stainless steel in the composite increased, the fracture toughness also improved. However, this is only from 0 wt% to 20 wt% ss316/Y-TZP.

The trend of the results are somewhat similar to the results obtained by studies done by Esteban *et al.* [5]. For the 10 and 20 wt% ss316/Y-TZP samples, when the number of stainless-steel 316 particles increases in the composite, mismatched thermal expansions will occur between both the zirconia and stainless-steel particles and result in radial tensile stresses to be developed internally when cooling occurs. This in turn causes debonding to happen due to the lack of interfacial bonds between the particles. When cracks happen, the cracks will propagate smoothly between the weak interface of the zirconia and stainless-steel particles which in turn produce crack deflection processes that improves that fracture toughness [5]. Figure 6 shows the crack propagation across the Y-TZP and metal. However, for the 30 wt% ss316/Y-TZP, the number of stainless steel 316 particles in the composite is too large which causes mistached thermal expansions that form thermal stresses in the composite material which is too large, causing the fracture toughness to reduce.

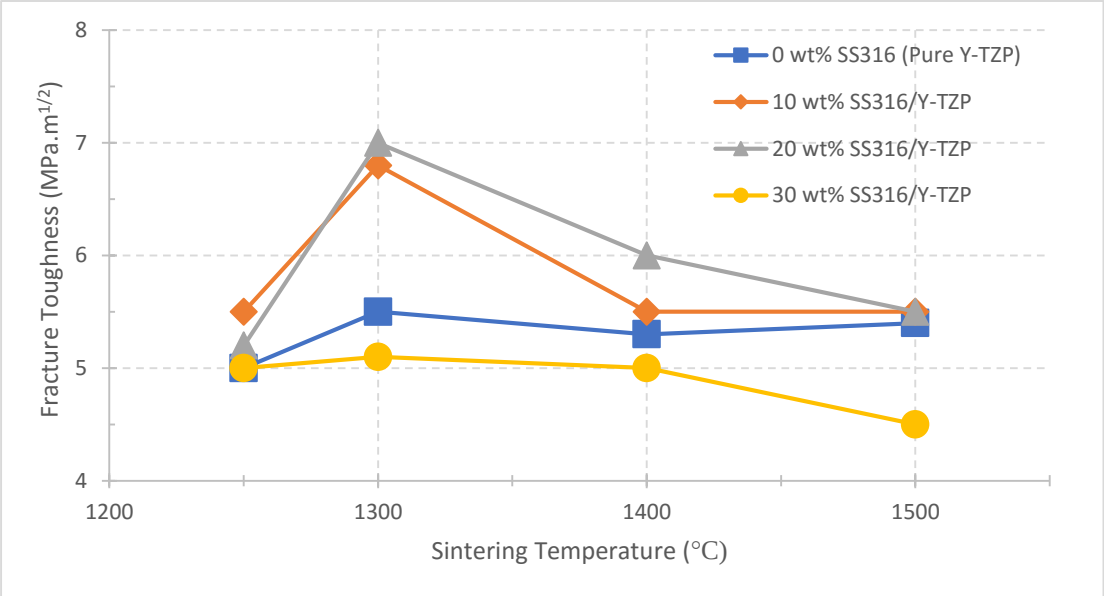


Figure 5. Relative density comparison between different weight percentage of SS316/YTZP and fracture toughness

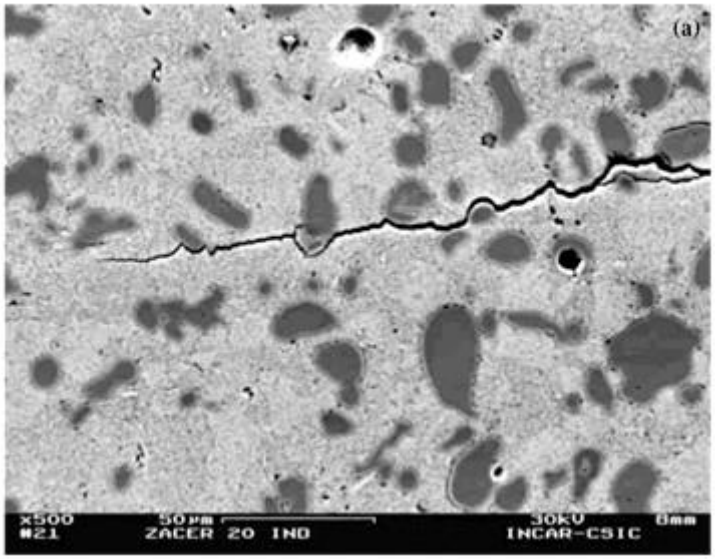


Figure 6. SEM image of crack which is initiated by Vickers indentation. Areas of lighter shade refer to zirconia while the darker phase refers to metal [5]

4. Conclusion

The mechanical characteristics of stainless steel 316/Y-TZP composite were studied through relative density, Vickers hardness and fracture toughness testing. Based on the results, it is shown that the ideal weight percentage of stainless steel 316 in the stainless steel 316/Y-TZP composite is 20 wt%. The results also showed that 30 wt% of stainless steel would result in the reduction of mechanical characteristics. Besides that, the ideal sintering temperature for the stainless steel 316/Y-TZP composite is 1300 °C as any temperature above that would result in deterioration of its mechanical characteristics. It is also found that the increase in stainless steel 316 weight percentage in the ss316/Y-TZP composite will result in areduction in relative density and Vickers hardness. However, the Vickers hardness of the composite will still be lower compared to pure Y-TZP.In addition to that, an increase in stainless steel 316 weight percentage in the ss316/Y-TZP composite will also result in an improvement in fracture toughness.

1.

References

[1] M. M. Stevens. (2008). Biomaterials for bone tissue engineering. *Materials Today*, vol. 11, no. 5. pp. 18–25.

[2] S. D. Heintze, A. Cavalleri, G. Zellweger, A. Büchler, and G. Zappini. (2008). Fracture frequency of all-ceramic crowns during dynamic loading in a chewing simulator using different loading and luting protocols. *Dent. Mater.*, vol. 24, no. 10, pp. 1352–1361.

[3] S. M. Kurtz, C. Arnholt, R. Huet, M. Ueno, and W. L. Walter. (2014). Advances in zirconia toughened alumina biomaterials for total joint replacement. *J. Mech. Behav. Biomed. Mater.*, vol. 31, pp. 107–116.

[4] L. Grajales Agudelo, V. L. Arantes, and P. L. di Lorenzo. (2014). Characterization of Composites Based on 316 Stainless Steel and Zirconia for Use as Functionally Graded Materials. *Advanced Powder Technology IX*, vol. 802, pp. 120–124.

[5] J. S. M. S.Lopez-Esteban, J.F. Bartolome, C.Pecharroman, S.R.H. Mello Castanho. (2001). Wet processing and characterization of ZrO2/stainless steel composites: electrical and mechanical perfomance. *Mater. Res.*, vol. 4, pp. 217–222.

[6] F. F. Lange. (1982). Transformation toughening. *J. Mater. Sci.*, vol. 17, no. 1, pp. 247–254.

[7] V. D. Krstic, W. H. Erickson. (1988). Effect of porosity and stress concentration associated with pores on elastic creep by crack growth in brittle solids. *J. Mater. Sci.*, vol. 23, no. 11, pp. 4097–4102.

[8] A. H. De Aza, J. Chevalier, G. Fantozzi, M. Schehl, R. Torrecillas. (2002). Crack growth resistance of alumina, zirconia and zirconia toughened alumina ceramics for joint protheses. *Biomaterials*, vol.23, no. 3, pp. 937-945.

[9] G. Schierano, F. Mussano, M. G. Faga, G. Menicucci, C. Manzella, C. Sabione, T. Genova, M. M. Von Degerfeld, B. Peirone, A. Cassenti, P. Cassoni, S. Carossa. (2015). An alumina toughened zirconia composite for dental implant application: In vivo animal results. *Biomed Res. Int.*, vol. 2015.

[10] ASTM E384-99 (1999), "Standard Test Method for Microindentation Hardness of Materials," Annual Book of ASTM Standards.

[11] ISO 14705 (2000), "Fine ceramics (advanced ceramics, advanced technical ceramics) – Test method for hardness of monolithic ceramics at room temperature".

[12] Niihara, K., Morena, R., Hasselman, D. P. H. (1982). Evaluation of K_{Ic} of Brittle Solids by the Indentation Method with Low Crack-to-Indent Ratio. *J. Mater. Sci. Letts.*, vol. 1, 13-16.

[13] Katz, R. N. (1985). Applications of High Performance Ceramics in Heat Engine Design. *Mater. Sci. Eng.*, vol. 71, 227-249.

eureca 2017 – Conference Paper
Paper Number 2ME07

Preparation and Characterization of Durian Husk Fiber Filled Polylactic Acid Biocomposites

Man Chee Lee[1*], Seong Chun Koay[1], Ming Meng Pang[1], Kim Yeow Tsai[2]

[1] *School of Engineering, Taylor's University, Malaysia.*

[2]*Faculty of Engineering, The University of Nottingham, Malaysia.*

**manchee.218@live.com*

Abstract

Polylactic acid (PLA) is biodegradable bioplastic, but its high cost and brittle properties limited its market potential. Thus, incorporates natural fiber with PLA can effectively reduce the cost of final product. In present research, the durian husk fiber (DHF) was used as natural fiber in PLA biocomposites. The DHF and PLA were compounded using Haake Internal mixer and molded using hotpress machine. This study was focus on effect of fiber and processing aid content on tensile properties of PLA/DHF biocomposite. The processing aid used was Ultra-Plast XP519. For this research, the tensile strength and modulus of PLA/DHF biocomposite increased with increasing of fiber content. This is due to reinforcing effect from fiber. However, the elongation at break of biocomposite reduced at higher fiber content owing to the reducing of ductility. At 60 per hundred resin (phr) of fiber content, the PLA/DHF biocomposite is still able to exhibit tensile strength more than 11 MPa, but it is too brittle. The PLA/DHF biocomposite showed highest tensile modulus when added with 0.5 phr of Ultra-Plast XP519, but its tensile modulus reduced at more Ultra-Plast XP519 content. The tensile strength and elongation at break of PLA/DHF biocomposite decreased with increasing of Ultra-Plast XP519 content. Thus, the suitable Ultra-Plast XP519 content used to produce this biocomposite should not more than 1 phr. Otherwise, the tensile properties of biocomposite will significantly reduce.

Keywords: Biocomposite, Polylactic acid, Durian husk fiber, Processing aid.

1. Introduction

In recent years, plastic bags and styrofoam are the most common materials used for packaging where the plastics are intended to dispose right away. Generally, not all kinds of plastic wastes can be recycled and those plastic wastes which cannot be recycled will be sent to landfill. The materials are made from petroleum and hardly degradable which is causing the environmental pollution. In 2010, 275 million metric tons of plastic wastes were produced globally [1]. Nowadays, part of the packaging materials has replaced by bioplastic which is biodegradable at the end of their service life to solve the environment pollution issue. Polylactic acid (PLA) is a type of bioplastic that synthesized raw material which fully extracted from natural resources, such as corn starch, tapioca root and sugarcane. PLA can be biodegraded during landfill, also offers other advantages, like good mechanical strength, non-toxic and sustainable with renewable resources [2-3]. Unfortunately, the production of bioplastic all over the world is about 750,000 tons per year which is still very small amount compare to 200 million tons of petroleum based plastic produced a year mainly due to the production cost [4]. The cost of producing PLA is higher (more than 2 US dollars per pound) compare to the plastics that are derived from petroleum [5]. For this reason, PLA is seldom selected by industrial as their main choice of material. In order to promote the usage of PLA material, natural filler can be added to reduce the cost of product.

Biocomposite is the composite material that is produced from bio-based polymer (as matrix) and natural filler such as sugarcane bagasse, rise husk, coconut husk and other plant fibers [6-7]. In addition, biocomposite is considered as environmental friendly material that can be fully degradable, since the polymer matrix and natural filler are made from natural products. Due to the biodegradable feature, the biocomposite materials are mainly used to produce products of short life span such as food container, water bottle, household appliance and packaging bags [8-9]. The market of biocomposites is expected to increase with an annual growth rate of 9.5% from 2017 to 2022 [10]. Thus, biocomposite will be the future trend of material because of its benefits to the environment and the exhaustion of non-renewable resources.

Filler is the substance added to plastic material to increase the commercial value of the plastic by improving the properties of end products or lower the cost. There are two types of filler which are mineral filler and natural filler. Back then, mineral fillers such as calcium carbonate, silica, and glass beads are commonly added into plastic material to reduce cost as well as improve the mouldability and stability [11]. In present, natural fillers are more on trend, since it offers many benefits over mineral filler, such as biodegradable, less abrasive, inexhaustible resources and the cost [3, 12]. The natural fillers can be obtained from agricultural crop and waste. For instance, corn husk [6], sugarcane bagasse [7] and coconut shell [8] are discarded after agricultural harvest. Usually, the disposal of agricultural waste is cost higher than utilizing the waste as natural filler are benefit to environment, technology and social of the country [12].

Durio zibethinus Murray, which also commonly known as durian is the tropical fruit that is highly produced in Southeast Asia region especially in Malaysia, Thailand, Indonesia and Philippine [13]. Durian husk is the shell of the fruit which comprises 40 percent of the whole fruit [14]. The husk is a waste that is going to be disposed after the flesh of the fruit being consumed. Seeing the production of durian in Malaysia, the amount of durian husk waste during the year of 2013 is 171,303.9 tons and the

production increases every year. The conventional disposal way of durian husk is either open burning or landfill which leads to serious environment pollution [15]. Thus, turning the huge amount of durian husk into benefit biomass is saving the environment, cost and energy [12]. The shell of the fruit contains composition which is similar with wood. The husk contained 60.45% of cellulose, 15.45% of lignin and 13.09% of hemicellulose, and the content is similar with wood fiber [16]. Therefore, this research is proposed to utilize the durian husk as natural filler in production of PLA biocomposites.

It had been reported from literatures, the processing of biocomposite materials is challenging due to high filler content, difficult to ensure a good filler dispersion and the interfacial adhesion between filler and matrix. This difficulty is because the natural filler is hydrophilic owing plenty of hydroxyl groups which holding the filler together by hydrogen bonds and difficult to establish strong adhesion with polymer matrix [17-18] Plastic additives or plasticizer such as coupling agent (e.g., malaeted polyethylene) [9], lubricant (e.g., mineral oil) [10] and processing aid (e.g., stearic acid) [11] are usually added upon the processing in order to improve the quality of mixture and filler-matrix adhesion. Processing aid is an important plastic additive for melt compounding process of biocomposite. Generally, the processing aid is a polyolefin compound which able to reduce the cost by improving the processability and improve the quality of compound [19]. The studies related to effect of coupling agent and chemical treatment on the properties of PLA biocomposite were found in numerous of literatures. However, the effect of processing aid on PLA biocomposite is rarely reported. Thus, the study on effect of processing aid on PLA biocomposite is underway.

This research is focus on the effect of filler content and processing aid on the tensile properties of PLA/DHF biocomposites.

2. Research Methodology

2.1 Raw Material

The main components to produce the biocomposites are PLA, durian husk and processing aid. The PLA resin was obtained from TT Biotechnologies Sdn. Bhd., Malaysia and processing aid used for experiment was Ultra-Plast XP519, which supplied by Performance Additives Sdn. Bhd., Malaysia. Moreover, the durian husk was collected from durian stall at SS2, Petaling Jaya.

2.2 Preparation of Corn Husk Fiber

First, the durian husk wastes were cleaned and cut into small pieces. The small pieces of durian husk were dried using oven at 70ºC. After the durian husk completely dried, it was ground into short fiber using grinder and passed through a sieve with mesh size of 600 micron to get the homogenous size of fiber. The durian husk fiber was dried again before compound with PLA resin.

2.3 Preparation of biocomposite

The biocomposite was prepared by melt compounding method using Haake internal mixer from SIRIM Malaysia, Shah Alam. The operating temperature was set at 180ºC and rotor speed fixed at 80 rpm. The compounding procedures included: i)

addition of PLA resin in to mixing chamfer for 1 minutes to fully melt the PLA resin; ii) Then, the DHF was added into melted PLA and compounded for 5 minutes; iii) Last, the compound was removed from mixing chamfer. For biocomposite with processing aid, the processing aid pellets was pre-mixed with PLA resin before compounding. All the samples were compounded according to the formulation listed in Table 1.

The biocomposite was molded into 1 mm thickness sheet using hotpress machine (model Moore) at temperature of 180^{o}C. The molding procedures included: i) preheated to soften the compound for 2 min; ii) fully compressed the softened compound under 100 MPa pressure for 1 min; and iii) Last, cooled specimen under same pressure for 20 minutes. All the biocomposite sheets were cut into tensile specimen.

Table 1. Formulation of PLA/DHF biocomposite with and without processing aid

Material	DHF (phr)	PLA (phr)	Processing aid (phr)
PLA/DHF without Processing aid	0, 15, 30, 45, 60	100	-
PLA/DHF with Processing aid	60	100	0.5, 1, 1.5, 2

2.4 Tensile Test

The tensile test was carried out according to ASTM D638 standard. The tensile properties of the biocomposite was tested by Instron Universal Testing Machine (model number 5569). The crosshead speed of 5 mm/min and a 15kN load cell was used to perform the test. The tensile strength, tensile modulus and elongation at break of the biocomposite were computed by Bluehill 3 universal software. A minimum of 7 specimens were tested for each formulation of biocomposites.

3. Results and Discussion

3.1 Tensile properties

Fig. 1 showed the tensile strength of PLA/DHF biocomposites with different DHF content. The tensile strength of PLA/DHF biocomposite exhibits an increasing trend as the DHF content increased. Usually, natural fiber displays a higher mechanical strength compared to most plastic material [20]. Thus, the addition of DHF fiber might share part of the tensile load which subjected PLA matrix and increased the tensile strength of biocomposite. Similar findings have also been reported by Yu et al. [21].

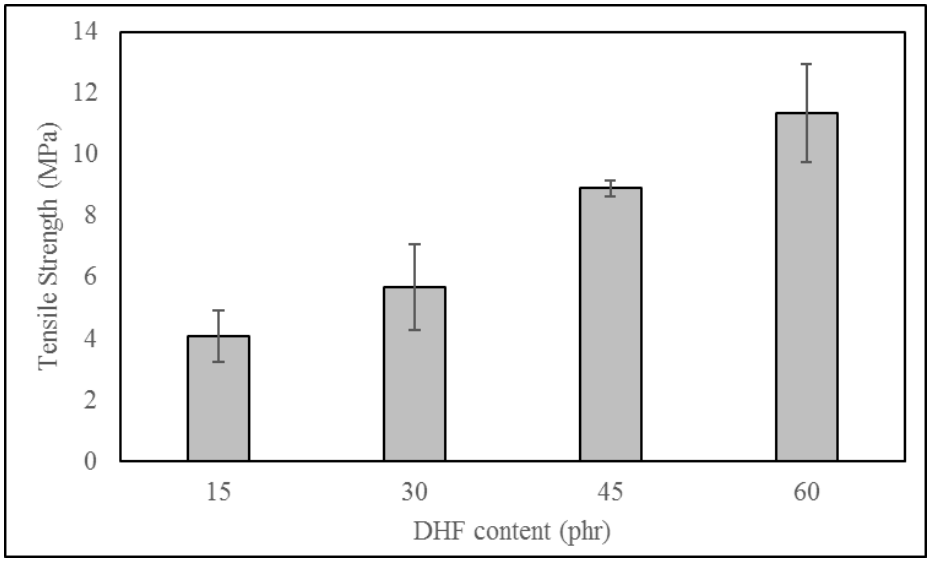


Figure 1. Tensile strength of PLA/DHF biocomposite

Fig. 2 illustrated the elongation at break of the biocomposite with different DHF content. It can be observed that as the fiber content increased, the elongation at break of PLA/DHF biocomposite decreased. The friction presents between PLA matrix and DHF fiber will significantly reduce the mobility of the polymer chains. Thus, PLA/DHF biocomposite with more fiber content became more rigid and brittle. This is in agreement with findings of Gunti et al. [22] who mentioned that the addition of natural fiber were significanly decreased the ductility of the PLA biocomposites.

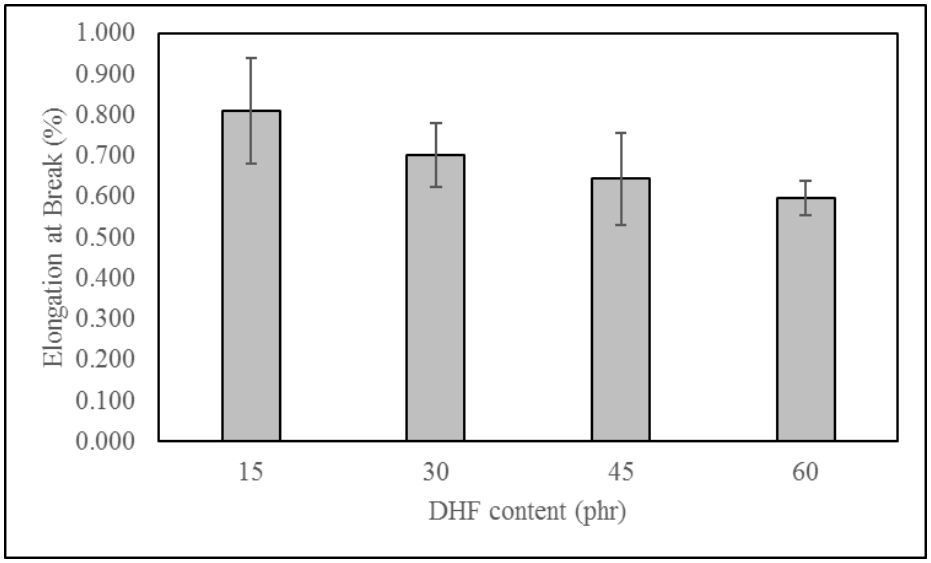


Figure 2. Elongation at break of PLA/DHF biocomposite

The tensile modulus of PLA/DHF biocomposites with different fiber contents are displayed in Fig. 3. As expected, the tensile modulus of the biocomposites gradually increases with increasing amount of DHF. It is because the modulus of DHF is usually higher than plastic. Therefore, the presence of higher amount of DHF will contribute to higher modulus of the PLA/DHF biocomposite. For this reason, the tensile modulus of PLA/DHF biocomposite increases due to addition of DHF. Moreover, Gunti et al. [23] also agreed that the modulus of biocomposite is highly depending on the amount of

filler. Hence, the biocomposite with higher fiber content showed higher tensile modulus.

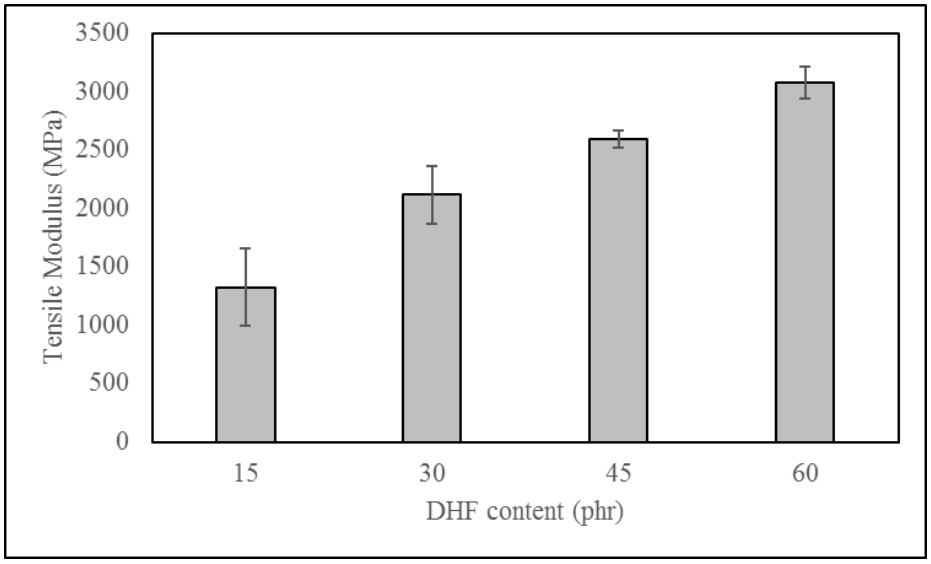


Figure 3. Tensile modulus of PLA/DHF biocomposite

Fig. 4 shows the effect of Ultra XP-519 on the tensile strength of PLA/DHF biocomposite with 60 phr of DHF. Overall, the results proposed an almost linear decrease with the increment of processing aid content. The Ultra XP-519 is a compound of fatty acid amide which behaves as internal lubricant for biocomposite. The amide groups from the Ultra XP-519 will attached on fiber surface by forming hydrogen bonding with hydroxyl groups from DHF. This finding is agreed with study reported by Chun et al. [24]. Hence, the present of Ultra XP-519 will form a fatty acid layer that covered the fiber surface (as shown in Fig. 5). The presence of this fatty acid layer will provide a lubricanting effect at the fiber-matrix interface. From Fig. 6, a mechanical interlock is usally present between fiber and matrix, and it is also known as interacial bonding. This bonding allows the stress transfer between matrix and fiber. However, the presence of fatty acid layer on fiber surface may inhibited the formation of mechanical interlock between PLA matrix and DHF surface. As a result, the stress transfer at interface region became weak and caused the tensile strength of biocomposite to decrease. Chun et al. [8] also found the strength of biocomposite was tend to decrease when the filler surface were fully covered by fatty acid compound.

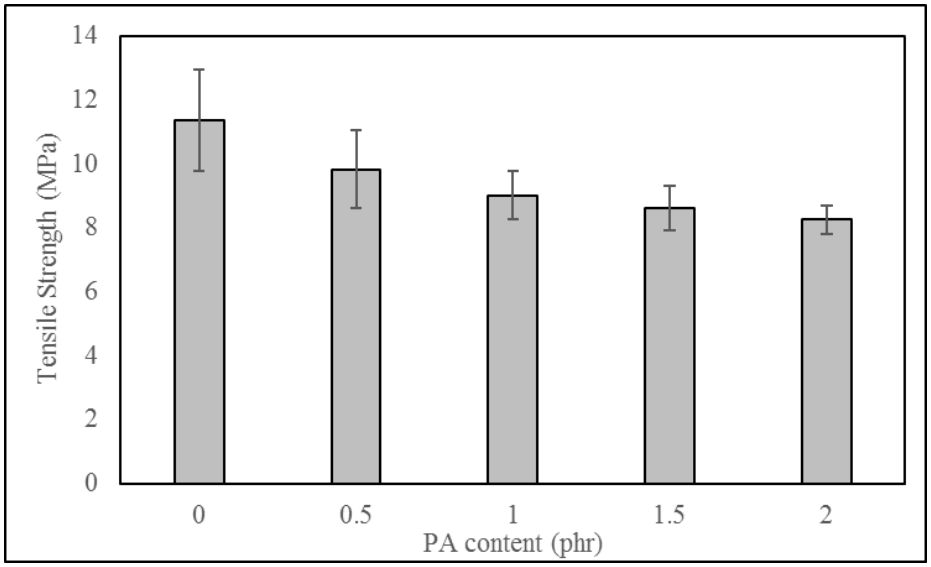


Figure 4. Effect of Ultra-Plast XP519 on tensile strength of PLA/DHF biocomposite

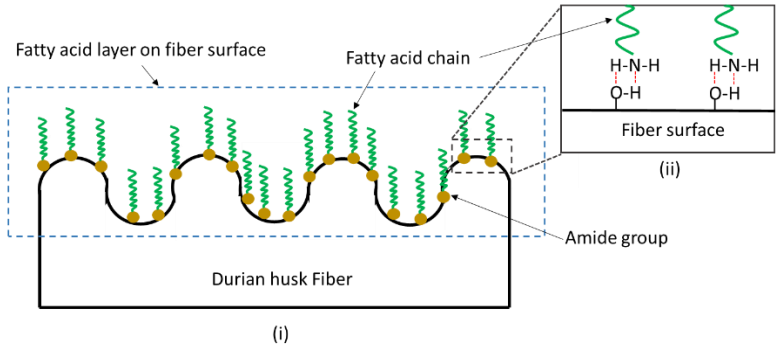


Figure 5. Proposed schematic for (i) formation of fatty acid layer when Ultra-Plast XP519 reacted with DHF and (ii) the Ultra-Plast XP519 attached on fiber surface via hydrogen bonding

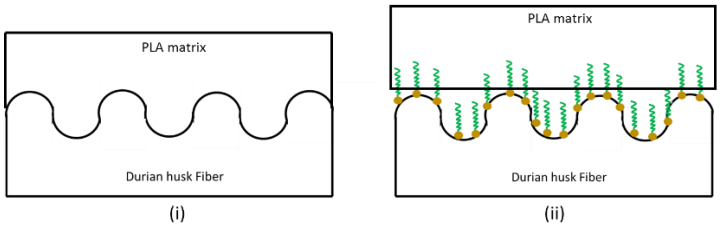


Figure 6. (i) formation of mechanical interlock at fiber-matrix interface and (ii) present of fatty acid inhibited the formation of mechanical interlock at fiber-matrix interface

As shown in Fig. 7, the elongation at break of PLA/DHF biocomposite is gradually decreased as the Ultra-Plast XP519 amount increased. Similar reason as mentioned above, the presence of Ultra-Plast 519 caused poor interlocking between matrix and fiber. For this reason, the ductility of PLA/DHF biocomposite decreased at higher content of Ultra-Plast XP519. A related finding was observed by Rasidi et al. [25] who used a different type of processing aid, Ultra Plast TP01 in PLA biocomposite. The author found that the addition of processing aid decreased elongation at break of the biocomposite.

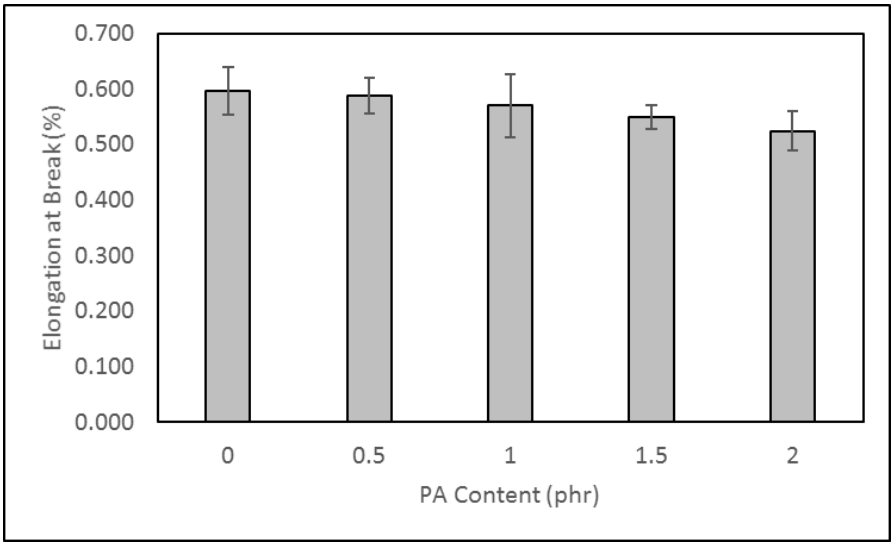


Figure 7. Effect of Ultra-Plast XP519 on elongation at break of PLA/DHF biocomposite

The result of tensile modulus against processing aid content was illustrated in Fig. 8. It can be clearly observed that the tensile modulus increased with the addition of Ultra-Plast XP519 up to 0.5 phr, but the tensile modulus decreased when the Ultra-Plast XP519 content further increased. Generally, the increase of tensile modulus in biocomposite are due to either: i) a good interfacial interlocking between fiber and matrix or ii) a premature failure occurs [26]. The average tensile modulus of PLA/DHF biocomposite with Ultra-Plast XP519 is 2.8% higher compared to PLA/DHF biocomposite without Ultra-Plast XP519. In this case, the increase of tensile modulus in PLA/DHF biocomposite might due to the presence of premature failure. Since, the biocomposite exhibits a very low elongation at break as found in Fig. 7. At higher Ultra-Plast XP519 content, the tensile modulus decreased. This is because of the lubricating effect from fatty acid layer that occurs between fiber and matrix. Panthapulakkal et al. [27] reported the processing aid reduced the adhesion between the matrix and filler and provide the lubricating effect that reduced the tensile modulus.

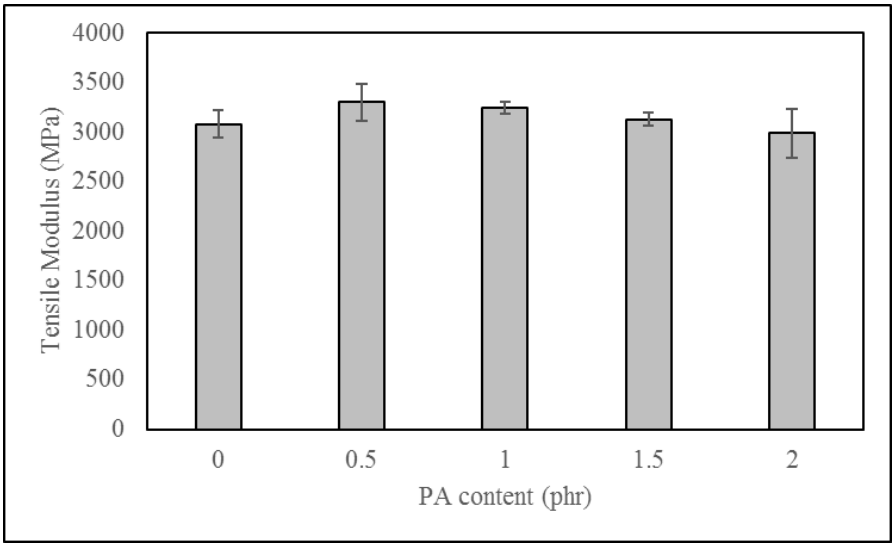


Figure 8. Effect of Ultra-Plast XP519 on tensile modulus of PLA/DHF biocomposite

4. Conclusion

The increase of DHF content increased the tensile strength and modulus of PLA/DHF biocomposite, but decrease in elongation at break. The average tensile strength of PLA/DHF biocomposite with 60 phr of DHF content is more than 11 MPa. But, the biocomposite is too brittle for any application. Generally, the addition of processing aid, Ultra-Plast XP519 able to facilitate the compounding process of biocomposite. However, it also shows a drawback in tensile properties of biocomposite. In this research, the addition of Ultra-Plast XP519 reduced the tensile strength and elongation at break of PLA/DHF biocomposite. The tensile modulus of biocomposite had slightly increased with presence of Ultra-Plast XP519, but the modulus gradually decreased with the increase of Ultra-Plast XP519 content. Even though the Ultra-Plast XP519 have positive effect on the processing of PLA/DHF biocomposite, but the content used should be less than 1 phr. Thus, the drawback from Ultra-Plast XP519 will reduce on tensile properties of biocomposite.

Acknowledgment

The authors would like to acknowledge Performance Additives Sdn. Bhd. for providing the processing aids to help in completing the research.

References

[1] J. R. Jambeck, R. Geyer, C. Wilcox, T. R. Siegler, M. Perryman, A. Andrady, R. Narayan and K. L. Law, “The ocean,” *Science Magazine*, vol. 347, pp. 768–771, 2015.

[2] M. Ajioka, K. Enomooto, K. Suzuki and A. Yamaguchi, “Properties of solutions,” *Bulletin Chemical Society Japan*, vol. 68, pp. 2125–2131, 1995.

[3] A. A. Yussuf, I. Massoumi and A. Hassan, “Comparison of polylactic acid/kenaf and polylactic acid/rice husk composites: The influence of the natural fibers on the mechanical, thermal and biodegradability properties,” *Journal of Polymer Environment*, vol. 18, pp. 422–429, 2010.

[4] F. Gironi and V. Piemonte, “Bioplastics and petroleum-based plastics: strengths and weaknesses,” *Energy Sources, Part A Recovery Utilization Environment Efficiency*, vol. 33, pp. 1949–1959, 2011.

[5] R. E. Drumright, P. R. Gruber, and D. E. Henton, “Polylactic acid technology,” *Advance Material*, vol. 12, pp. 1841–1846, 2000.

[6] P. A. Fowler, J. M. Hughes, and R. M. Elias, “Review biocomposites: technology, environmental credentials and market forces,” *Journal of Science Food Agriculture*, vol. 86, pp. 1781–1789, 2006.

[7] D. Mulinari, H. Voorwald, M. Cioffi, M. Dasilva, T. Dacruz and C. Saron, "Sugarcane bagasse cellulose/HDPE composites obtained by extrusion", *Composites Science and Technology*, vol. 69, pp. 214-219, 2009.

[8] K. S. Chun, S. Husseinsyah, and H. Osman, “Mechanical and thermal properties of coconut shell powder filled polylactic acid biocomposites: effects of the filler content and silane coupling agent,” *Journal of Polymer Research*, vol. 19, pp. 1-8, 2012.

[9] N. Peelman, P. Ragaert, B. D. Meulenaer, D. Adons, R. Peeters, L. Cardon, F. V. Impe and F. Devlieghere, "Application of bioplastics for food packaging," *Trends in Food Science Technology*, vol. 32, pp. 128–141, 2013.

[10] Lucintel LLC, *Growth Opportunities in the Global Continuous Fiber Thermoplastics Market*, Irving, Texas: Lucintel LLC, 2017, pp. 1-238.

[11] M. Tasdemir and S. Ersoy, "Mechanical, morphological and thermal properties of HDPE polymer composites filled with talc, calcium carbonate and glass spheres," *Journal of Materials*, vol. 45, pp. 147–154, 2015.

[12] R. Yevich and J. A. Logan, "An assessment of biofuel use and burning of agricultural waste in the developing world," *Global Biogeochemical Cycles*, vol. 17, pp. 1–5, 2003.

[13] L. H. Ho and R. Bhat, "Exploring the potential nutraceutical values of durian (Durio zibethinus L.) - An exotic tropical fruit," *Food Chemistry*, vol. 168, pp. 80–89, 2015.

[14] M. R. Manshor, H. Anuar, M. N. N. Aimi, M. I. A. Fitrie, W. B. W. Nazri, S. M. Sapuan, Y. A. El-Shekeil, M. U. Wahit, "Mechanical, thermal and morphological properties of durian skin fibre reinforced PLA biocomposites," *Materials and Design*, vol. 59, pp. 279–286, 2014.

[15] R. P. Singh, A. Singh and V. Srivastava, *Environmental Issues Surrounding Human Overpopulation*. Hershey: IGI Global, 2016, pp. 160-163.

[16] Y. J. Tham, S. D. Arumugam, N. H. A. Latip, A. M. Abdullah, and P. A. Latif, "Effect of activation temperature and heating duration on physical characteristics of activated carbon prepared form agriculture waste," *Environment Asia*, vol. 7, pp. 143–148, 2010.

[17] D. N. Saheb and J. P. Jog, "Natural fiber polymer composites: a review," *Advances in Polymer Technology*, vol. 18, pp. 351–363, 1999.

[18] M. M. Thwe and K. Liao, "Effects of environmental aging on the mechanical properties of bamboo-glass fiber reinforced polymer matrix hybrid composites," *Composites: Part A Applied Science and Manufacturing*, vol. 33, pp. 43–52, 2002.

[19] E. E. Rosenbaum, S. K. Randa, S. G. Hatzikiriakos, C. W. Stewart, D. L. Henry, and M. Buckmaster, "Boron nitride as a processing aid for the extrusion of polyolefins and fluoropolymers," *Polymer Engineering &Science*, vol. 40, pp. 179–190, 2000.

[20] J. Holbery and D. Houston, "Natural-fibre-reinforced polymer composites in automotive applications," *Journal of Minerals, Meals and Material Society*, vol. 58, pp. 80–86, 2006.

[21] T. Yu, J. Ren, S. Li, H. Yuan and Y. Li, "Effect of fiber surface-treatments on the properties of poly(lactic acid)/ramie composites", *Composites Part A: Applied Science and Manufacturing*, vol. 41, pp. 499-505, 2010.

[22] R. Gunti, A. Ratna Prasad and A. Gupta, "Mechanical and degradation properties of natural fiber reinforced PLA composites: Jute, sisal, and elephant grass", *Polymer Composites*, vol. 37, pp. 1-12, 2016.

[23] R. Gunti and A. Ratna Prasad, “Tensile properties of successive alkali treated short jute fiber reinforced PLA composites,” *Procedia Material Science*, vol. 5, pp. 2188–2196, 2014.

[24] K. Chun and S. Husseinsyah, "Polylactic acid/corn cob eco-composites: Effect of new organic coupling agent", *Journal of Thermoplastic Composite Materials*, vol. 27, pp. 1667-1678, 2013.

[25] M. Mohamad Rasidi, S. Husseinsyah and T. Leng, "Chemical modification of nypa fruticans filled polylactic acid/recycled low-density polyethylene biocomposites", *BioResources*, vol. 9, pp.2033-2050, 2014.

[26] C. Lei, M. Qiu, M. Zhi, and K. Friedrich, “Tensile performance improvement of low nanoparticles filled-polypropylene composites,” *Composites Science and Technology*, vol. 62, pp. 1327–1340, 2002.

[27] S. Panthapulakkal, S. Law and M. Sain, "Enhancement of processability of rice husk filled high-density polyethylene composite profiles", *Journal of Thermoplastic Composite Materials*, vol. 18, pp. 445-458, 2005.

eureca 2017 – Conference Paper
Paper Number 2ME08

Operational Research on Design and Process Optimization of Ozone Water Application in Kitchen

Lee Zhun Jing*, Chou Pui May, Hoo Choon Lih, Daniel Lu
School of Engineering, Taylor's University, Malaysia
Medklinn International Sdn Bhd, Malaysia

*isaac_zhunjing94@hotmail.com

Abstract
Food safety is a very important focus in the kitchen industry today, as bacteria such as E.Coli and Salmonella are very difficult to tackle. The objective of the present study was to optimize nozzle designs that use ozone technology to bring out the best results in cleaning and sterilizing the kitchen utensils in Taylor's University School of Hospitality kitchen area. This includes customization of the Medklinn International Sdn Bhd ozone machine and nozzle profiles that improve the effectiveness of ozone generated. Reduction or elimination of chemicals and water usage would be a part of the study. This will bring a huge impact on cost effectiveness, time saving and safety of the users. Return on investment (ROI) using ozone technology is calculated at the end of the research. To compare between the traditional way of cleaning and using ozone technology, the volume of water and dishwashing liquid used, and the Relative Light Units (RLU) before and after washing were recorded. The RLU numbers are found using the 3M Clean Trace measuring equipment. RLU was recorded to determine the cleanliness of the kitchen utensils before and after washing. It has been proved that ozone water with the accompaniment of the selected nozzle prototype is as efficient as the traditional way of cleaning.

Keywords**:** Ozone, Kitchen, Cleanliness, Cost, Nozzle

1. Introduction

The cleanliness of kitchen area, utensils and stoves is essential in the food processing industry. Diarrhea is a concerning issue for travelers as 1 out 3 people will be affected in this health issue. Hikers and people who go on adventure trips are very prone to this problem[1]. In 2015, World Health Organization (WHO) has estimated that 1 in 10 people are prone to foodborne diseases which also killed 420,000 people[2]. It was also reported that Africa and South East Asia are the two regions that are in the high risk zone[2]. There were 125,000 of children under five years old are killed due to illness from foodborne diseases every year [2]. It was found out that 16% of the foodborne diseases outbreaks from England and Wales are linked with the food preparation in the house [3, 4].

Cross contamination is one of the reason to the foodborne disease and it caused 28 out of 101 outbreaks to happen [3]. Cross contamination can happen either by hand to the plates, from the plates to the food, the utensils to the food, or even in the washing process with the usage of sponge and water [3, 5, 6, 7]. In order to reduce and eliminate this issue, different washing up systems have been created. Researchers believe that rather than tackling the cleanliness of water, the cleanliness of kitchen utensils and hand hygiene are two very important factors to prevent foodborne diseases[1, 8]. Cross contaminations on food happens very often in the process of cutting, trimming, rinsing and washing [8]. Bacteria infect almost all the kitchen area, as study shown in appendix 1 and 2, swap tests were taken in a hospital kitchen to show the amount of infected areas. These results were also picked up from pre-processing zones for food, storage area and cooking area.

Biofilm is the form of 99% of bacteria in the kitchen. Biofilm formation makes the bacteria to be able to live in either biotic or abiotic surfaces. Therefore, another study on bacteria infecting kitchen surfaces is done as well [9]. Table 1 shows the total colony forming unit count on a cafeteria kitchen. It can be seen that the bacteria count is quite alarming even in dishwashers, sink, countertop areas, food waste container and pots. These are some areas that show that even bacteria would live in cleaning environment and cooking pots which would promote cross contamination. This also shows that the existing steps of cleaning could not disinfect microorganisms efficiently, and potential biofilm formation is not effectively prevented as well [9].

Table 1. Total colony forming unit (CFU) count on a cafeteria kitchen [9]

Surface No.	Surface Area	Total Aerobic Count (log CFU/100cm^2)	Bacteria
1	Cold Room	5.90	Brachybacterium, Brevundimonas, Kocuria, Pantoea, Paracoccus, Roseomonas, Sphingobacterium
2	Pretreatment Countertops	3.83	Bacilus, Curtobacterium, Gordonia, Kocuria, Pantoea, Pseudomonas, Sphingomonas, Staphylococcus
3	Sink	4.14	Bacillus, Enterobacter, Raoultella
4	Faucet in the sink	5.35	Bacillus, Enhydrobacter, Escherichia, Kocuria
5	Roasting/frying countertop	3.63	Bacillus, Kocuria, Lysinibacillus

6	Spice rack	4.84	Bacillus, Microbacterium, Pantoea
7	Soup pot	3.59	Acinetobacter, Bacillus
8	Frying pot	2.16	Bacillus
9	Countertop for completed menu	3.16	Acidovorax, Acinetobacter, Bacillus, Chryseobacterium, Deinococcus, Enterobacter, Sphingomonas
10	Rice cooker	2.73	Acinetobacter, Bacillus, Chryseobacterium, Kocuria, Sphingomonas
11	Food waste container	3.21	Bacillus, Staphylococcus
12	Dishwasher	2.53	Bacillus
13	Sink for dishwashing	2.86	Bacillus
14	Stainless steel trays	1.60	Bacillus
15	Plastic wicker tray	4.07	Acinetobacter, Chryseobacterium, Dermacoccus, Exiguobacterium, Kocuria, Pantoea
16	Iron roasting pan	2.00	Acinetobacter, Kocuria
17	Knives	2.00	Acinetobacter, Bacillus
18	Cutting board (Completed Menu)	2.45	Arthrobacter, Bacillus, Curtobacterium, Kocuria, Microbacterium, Staphylococcus
19	Cutting board (vegetables)	2.97	Acinetobacter, Dermacoccus, Enterobacter, Kocuria, Leclercia, Methylobacterium, Roseomonas
20	Gloves	3.97	Acinetobacter, Bacillus, Kocuria
21	Apron	6.85	Bacillus, Kocura, Pseudoxanthomonas, Rhizobium
22	Fan	4.15	Bacillus
23	Floor	4.65	Achromobacter, Aeromonas, Bacillus, Cellulosimicrobium, Chryseobacterium, Cloacibacterium, Diaphorobacter, Kocuria, Pseudomonas

Hence, in order to prevent cross contamination that will lead to foodborne diseases, studies have been done to optimize the cleaning processes in the kitchen and also trying out with different disinfectants and cleaning agents. Sterilizing of kitchen surfaces using a variety of disinfectants is one of the ways to minimize microorganisms living on surfaces and also preventing cross contamination. In this case, Taylor's Hospitality and Culinary Arts School (TCHT) is used as the model of research to find out how chemical and disinfectant washing can help in the cleaning of kitchen utensils. A table (Table 2) shows the volume of water and detergent needed to clean 6 kitchen utensils and 2 kitchen stoves.

Table 2. Volume of water used to clean 6 kitchen utensils and 2 kitchen stoves

Items washed	Amount of dishwashing liquid used, ml	Amount of water used for cleaning, L
6 Kitchen utensils	30	143.7
2 Kitchen stoves	15	5.9L

TCHT has been searching for a way to reduce the cost of cleaning and also reducing the steps to do the cleaning so that cleaning of the kitchen would be faster and requires less man power. There are a few ways to optimize the current cleaning method to achieve TCHT's objective:

1. In order to reduce chemical usage, TCHT has the possibility to use higher concentration of dishwashing liquid so that less chemical will be used to dilute in water but producing the same effect. However, more concentrated dishwashing liquid will also be higher cost.

2. In order to achieve less man power, the steps of cleaning have to be reduced. An alternative which can bypass the use of degreasing and too much scrubbing can reduce man power. In this case, the alternative way has to be good in sterilizing, degreasing and cleaning off dirt in one shot. Hence, reducing cleaning steps.

Cleaning using ozone technology is one way that can reduce the use of chemicals as ozone is well known to be a good disinfectant because of its highly reactive properties[10, 11]. Ozone is also proven by many ozone technology companies to be a good degreaser. Hence, ozone is widely used in the western part of the world in industry cleaning, sterilizing and degreasing. However, ozone is not as well known in this tropical region as in the western world. Ozone technology is not unknown in kitchen area as ozone is also used in cleaning vegetables and fruits before cooking. One of the examples is in the cleaning of spinach [12].

Hence, this research is to introduce the usage of ozone technology in order to enhance and improve the ways to clean the kitchen utensils which takes up most of the cleaning time in Taylor's Hospitality and Culinary Arts School. The objective is to customize and develop designs to bring out effective applications of ozone technology in cleaning kitchen utensils. Furthermore, the research is carried out also to prove that the usage of ozone technology reduces the usage of chemicals, man powers and time consumption in cleaning process.

2. Research Methodology

This research is done by cleaning stainless steel kitchen utensils in Taylor's Hospitality and Culinary Arts (TCHT). The research done on different methods is shown in Table 3.

Table 3. Methods of testing

With Nozzle	**Without Nozzle**
Without ozone	Without ozone
With ozone	With ozone

2.1 Calculation of water and chemical usage in cleaning process

A water flow meter shown in Figure 1 is attached to the outlet of the water pipe where water flows out for kitchen utensil washing. This is to measure the amount of water used during the whole cleaning process. The amount of water used is compared between the cleaning with and without ozone, and with and without nozzles. The

volume of water was controlled during the research, not letting it to overrun before and after washing. The water was only let run when needed.

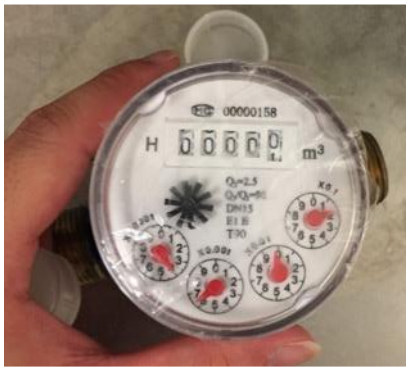


Figure 1. Water flow meter with readings in m^3

A 10 ml syringe shown in Figure 2 is used to measure the volume of dishwashing liquid used to clean the kitchen utensils. The dishwashing liquid is already diluted with the ratio of 1 L of detergent to 20 L of water. It is tested with the same methods as in Table 2. The detergent is added on by an increment of 1ml onto the dishwashing sponge until the worker feels that it is sufficient to clean the pot. This is done to ease the calculation for the efficiency of ozone water cleaning vs non-ozone water cleaning.



Figure 2. 10 ml syringe for dishwashing liquid measurement

2.2 Customization of ozone machine

The ozone machine in Figure 3 is provided by Medklinn International Sdn Bhd. The ozone capacity used was 500mg/hr. Ozone is also produced with the presence of oxygen as stated in the literature review. In this case, a consistent provided of oxygen is needed so that the ozone produced will be consistent as well. Therefore, an oxygen concentrator is used to provide the consistent amount of oxygen. A 1 LPM oxygen concentrator is used for this research. A venturi shown in Figure 4 is used for suction of ozone gas to be diluted in water is MK584 (¾ inch inlet and outlet size). This will result in a 1.8 particles per million (PPM) (without nozzle) and 1.25 PPM (with nozzle) concentration of ozone.



Figure 3. Ozone Machine



Figure 4. MK584 Venturi [13]

2.3 Nozzle profile

A nozzle is used to have a higher water impact in the cleaning process to remove oil and stubborn dirt on the kitchen utensils. The nozzle design has 16 linear 1.50 mm diameter circular holes with a 3 mm linear distance between each hole. Figure 5 shows the design of the nozzle used to clean the kitchen utensils. The design has the same number of holes compared to the nozzle used in the traditional way of cleaning in Taylors School of Hospitality and Culinary Arts (TCHT). However, the nozzle profile in TCHT is a shower pattern nozzle. A shower pattern nozzle shows a lower impact force compared to the one in linear. This is because most of the water flow is not blocked at the outlet, hence there is lesser force that pushes the water out of the orifices. However, in linear, the water is constrained to exit only at the middle of the outlet. Hence, pressure accumulates in the nozzle and more force is present to push the water out of the orifices.

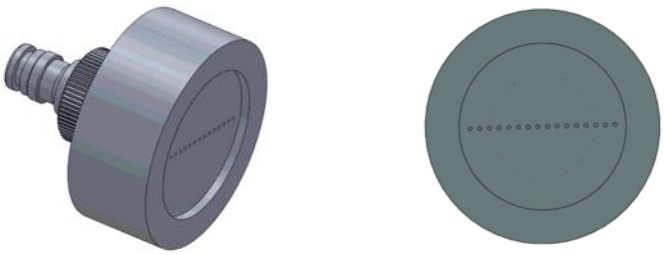


Figure 5. Linear Circular Pattern Nozzle

ANSYS Fluent CFD is ran on the nozzle profile to identify the velocity profile and also the pressure at the outlet. A multi-zone, mapped mesh type hexa/prism and free mesh type of tetra/pyramid meshing is done. Multi-zone, hex dominant is done because the outlets of the nozzles are having circular patterns and multi-zone work best for these conditions. It has a total of 108202 number of elements, average skewness 0.36274 and an average orthogonal quality of 0.79.

For the boundary conditions, Reynold's number is calculated for the flow to see whether the flow is a laminar or turbulent flow across the nozzle. The equation for Reynold's number is as follow:

$$Reynold's\ number = \frac{\rho v D}{\mu} \text{ (Eq. 1)}$$

Where,
ρ: The density of water
v: Velocity of water
μ: The viscosity of water at 28℃

According to [14], viscosity and the density of water at 28ºC is 0.8324 mPa.s and 0.9962 g/cm^3 respectively.

$$Reynold's\ number = \frac{996.2\ \frac{kg}{m^3} \times 3\frac{m}{s} \times 0.0092m}{0.8324 \times 0.001\ \frac{kg}{ms}} = 33{,}031.14$$

The flow is turbulent, Realizable k-ε is used as the viscous modelling during all the CFD analysis. The boundary conditions are set to 3 m/s inlet velocity with. This is due to the volumetric flow rate of 12 LPM measured from the pipes of the kitchen in Taylor's School of Hospitality and Culinary Arts.

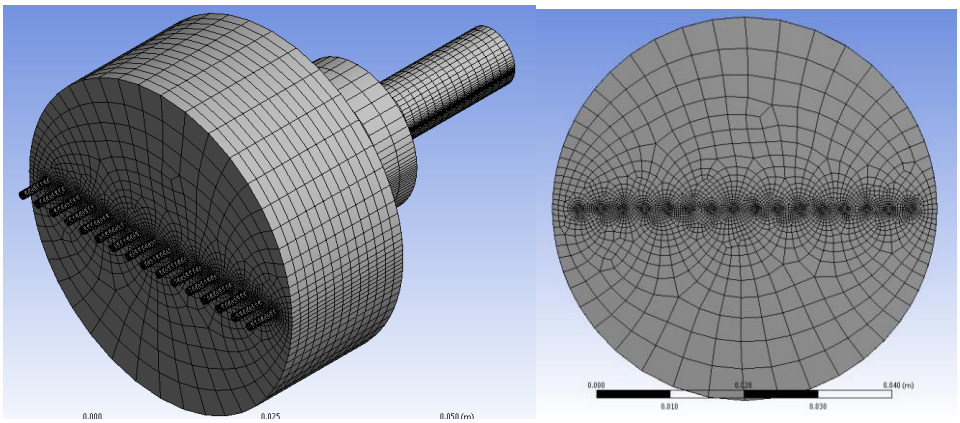


Figure 6. Multi-zone mesh type

2.4 Cleanliness of kitchen utensil

3M Clean Trace shown in Figure 7 is used as the equipment to test on the cleanliness of the kitchen utensil. Swabs are taken before and after cleaning of the kitchen utensil using the traditional way (without ozone water) and with ozone water. A cotton bud like stick shown in Figure 7 are used to swab on the surface (10cm × 10cm) of the kitchen pot before cleaning, and done it again after cleaning. Same applies to with and without nozzle. The measurement is taken as Relative Light Units (RLU). RLU is the measurement of adenosine triphosphate (ATP) present on the kitchen utensil. The higher the RLU, the dirtier the kitchen utensil is. In normal practice, RLU higher than 11 is a caution and higher than 30 is a fail. Hence, RLU lower than 10 is in the safe region [15].



Figure 7. 3M Clean Trace swab sticks

Kitchen towel and an oil control blotting paper are used to have a qualitative result on the dirt and oil left on the kitchen utensil after cleaning. Results are shown in the next section of discussion.

3. Results and Discussions

3.1 Washing of stainless steel pot

Table 4 and 5 show the amount of water and detergent is used for the different methods of washing (as discussed in Table 2). The tables also show the cleanliness (RLU) of the pots before and after washing. Comparing the results with the background reading in Table 2, averagely one utensil needed 23.95 L of water to clean. However, during the research, the volume of water was controlled well hence, there is a big reduction in the volume of water.

Table 4. Cleaning of a stainless steel kitchen pot without nozzle

Variables	Traditional way	Ozone water
Volume of water, L	10.4	11.1
Volume of detergent, ml	4	6
Ozone level, PPM	-	1.8

Pot before washing		
Cleanliness before washing, RLU	674	312
Pot after washing		
Oil and dirt detection after washing		
Cleanliness after washing, RLU (TOTAL REDUCTION OF RLU)	226 (448)	103 (209)
Temperature of water	29.6ºC	29.1ºC

Table 5. Cleaning of a stainless steel kitchen pot with nozzle

Variables	Traditional way	Ozone water
Volume of water, L	8	8
Volume of detergent, ml	5	5
Ozone level, PPM	-	1.25ppm
Pot before washing		
Cleanliness before washing, RLU	1106	679

Pot after washing		
Oil and dirt detection after washing		
Cleanliness after washing, RLU (TOTAL REDUCTION OF RLU)	156 (950)	6 (673)
Temperature of water	29.5ºC	29.1ºC

From table 4, the RLU reduction for traditional way of cleaning (using just detergent and normal 29.6ºC of water) is 66.47% while for ozone water is 67%. Traditional way uses 700ml of water and 2ml of detergent lesser compared to ozone water to achieve the RLU. The difference in water volume and detergent, and also the RLU reduction are not significant in this experiment. Table 5 shows a significant difference in RLU reduction comparing the two methods of cleaning with the same amount of water and detergent used. There was a 85.9% reduction using the traditional way with nozzle and a 99.12% RLU reduction using ozone with nozzle. This has significantly shown that with the use of nozzle in the cleaning process, it increases the RLU reduction by about 20% ~ 30% compared to without the nozzle. Ozone water with the use of nozzle also shown the cleaning process to be very efficient.

The readings are as such because it is due to the properties of nozzle. Although with nozzle, the PPM level is lower than the one without nozzle, however nozzle plays a part in cleaning and also sterilizing. Ozone needs exposure time to the surface in order to kill bacteria, hence when ozone without nozzle is applied, the reduction rate is slower. When nozzle is applied in this case, the nozzle will give impact force to the utensil surface and clearing most of the dirt and bacteria, adding on with ozone, the sterilizing effect is much higher compared to without the nozzle.

So, comparing with nozzle with ozone and without ozone, although both shows more than 80% of RLU reduction, the one without ozone has always show RLU more than 10 which is unsafe to use according to [41]. When comparing without nozzle with ozone and without ozone, both have also failed to the requirement stated in [41]. Hence, ozone and nozzle is the best combination as the RLU reduction for all the cases has shown RLU less than 10, which is safe for consumers. This has proven that even though chemicals are used to wash utensils, it might not be safe for consumption purposes.

Ozone has proven to be a strong disinfectant and the utensils that are cleansed by ozone will be definitely safe to use.

3.2 Nozzle and ozone suction in water

The inlet velocity is at 3 m/s and the outlet velocity as the result of the nozzle design is at about 12-14 m/s. Figure 9 shows the velocity path lines of the flow of water through the nozzle. It can also be seen that there is back flow occurring as it hits the head of the nozzle. The backflow also causes the high pressure of $1x10^5$ Pa to be accumulated in the nozzle itself as shown in Figure 10. As the pressure accumulates in the nozzle, the velocity decreases, the air pressure in the venturi will find it difficult to push the ozone gas to dilute in the water through the venturi. This causes the decrease in ozone suction in the venturi which was from 1.8 PPM to 1.25 PPM (from Table 4 and 5).

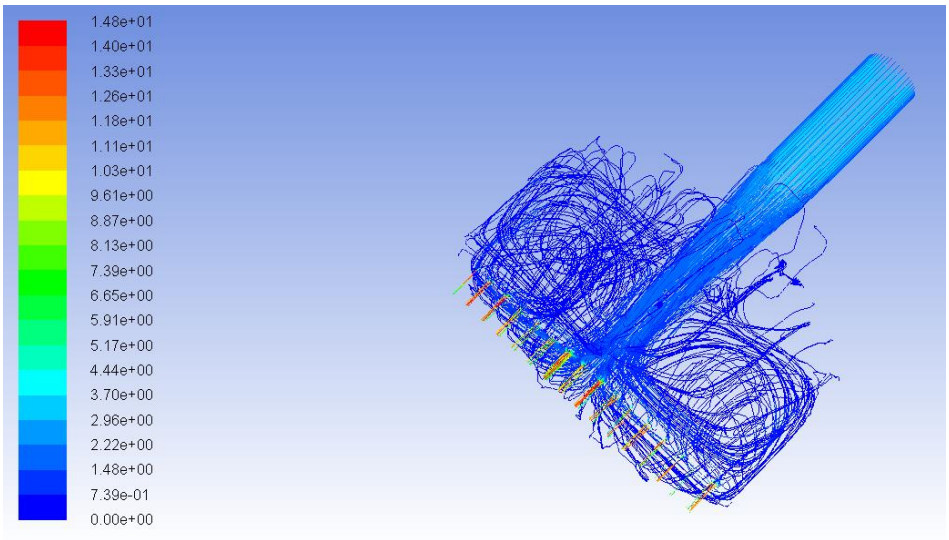


Figure 9. Velocity path lines

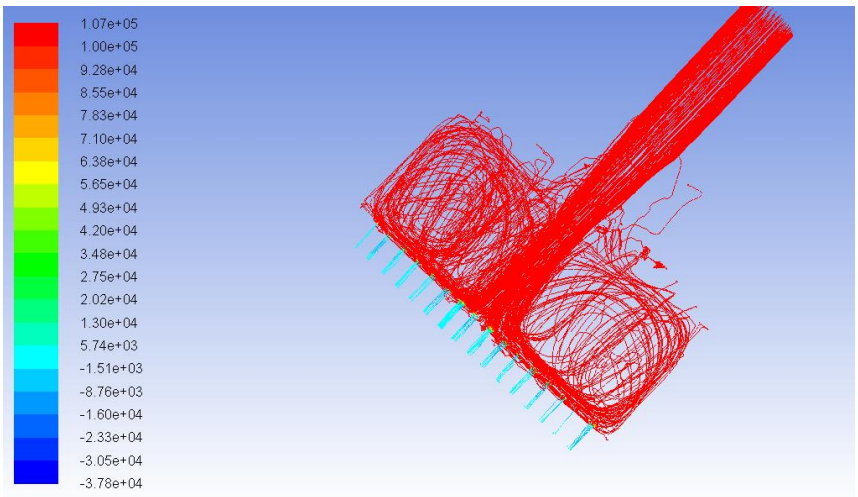


Figure 10. Pressure path lines

According to [16], the impact force is based on the angle of water distribution from the nozzle. The bigger the angle of water distribution, the lower the impact force. This is because of the kinetic energy losses when it is needed to distribute the water at the big angles. Since the impact force equation is given by,

$$Fs = \frac{1}{2}mv^2 \text{ (Eq. 2)}$$

the velocity at the outlet will play a part in determining the impact force. When the velocity is higher at the outlet, the impact force will be higher.

The design of the conventional nozzle is based on the nozzle used in TCHT kitchen shown in Appendix 3 and 4. According to literature review [16, 17], a nozzle that produces solid stream has the highest impact force compared to water distributed at an angle. Single hole will give a solid stream flow. However, a solid stream will also lose momentum quicker compared to others, even though all nozzles will lose momentum after the water exits from the orifice [17]. Hence, the distance of nozzle to the surface intended to be washed have to be nearer so that the water can hit the surface with minimal losses of momentum. A single hole is also not very user friendly to wash kitchen utensil as the focus area is small and usually a kitchen utensil is at sizes of 10 cm – 20 cm. So in order to optimize the washing, a linear pattern is done with 3 mm apart so that the water streams could wash the kitchen utensil at a bigger surface area. It can mimic a fan pattern nozzle but having solid streams as well to increase impact force.

4. Conclusion

In conclusion, the usage of ozone water in cleaning kitchen utensils has shown significant difference compared to using the traditional way of cleaning with the aid of a nozzle. The nozzle prototype has given the cleaning process a huge boost with a big increment of RLU reduction. The kitchen utensil is tested to be 99% clean after using ozone with the same amount of water and dishwashing liquid as to the traditional way of cleaning. The controlled research has definitely reduced the volume of water used and proven to be much more efficient in cleaning. In terms of manpower, there is no reduction because the time of cleaning is almost the same. The nozzle could help to ease the cleaning of stubborn dirt however, the time of cleaning is almost the same with and without nozzle. Ozone level in the water is also based on the pressure of water, as the backpressure is high, the ozone level dissolved in the water is lesser.

Acknowledgement

Throughout this research, I would like to acknowledge a few people that have guided me. Firstly, I would like to thank Medklinn International Sdn Bhd, for providing me the equipment to carry out the experiments. My extended acknowledgement to my industrial supervisor Mr. Lim Boon Han and Mr. Daniel Lu for giving me his advice based on his knowledge and experience in the ozone industry. I would also like to thank Taylor's School of Hospitality and Culinary Arts for the opportunity to allow me to carry out my research in the kitchen, alongside the supervision of Mr. Hisammudin and Mr. Kumar, the people in charge of the kitchen.

Reference

[1] J. S. Hargreaves and B. Cantab, "Laboratory Evaluation of the 3-Bowl System Used for Washing-Up Eating Utensils in the Field," *Wilderness Environ. Med.*, vol. 17, no. 2, pp. 94–102, 2006.

[2] F. Chaib and Olivia Lawe-Davies, "WHO's first ever global estimates of foodborne diseases find children under 5 account for almost one third of deaths," 2017. [Online]. Available: http://www.who.int/mediacentre/news/releases/2015/foodborne-disease-estimates/en/. [Accessed: 17-Jun-2017].

[3] K. Mattick *et al.*, "The survival of foodborne pathogens during domestic washing-up and subsequent transfer onto washing-up sponges , kitchen surfaces and food," vol. 85, pp. 213–226, 2003.

[4] H. Protection, A. Communicable, D. Surveillance, H. Protection, A. Specialist, and R. M. Division, "Foodborne general outbreaks of Salmonella Enteritidis phage type 4 infection , England and Wales , 1992 – 2002 : where are the risks ?," pp. 795–801, 2005.

[5] A. Valero, J. Carlos, G. Fongaro, M. Hern, and D. Rodríguez-l, "De fi nition of sampling procedures for collective-eating establishments based on the distribution of environmental microbiological contamination on food handlers , utensils and surfaces," vol. 77, no. 852, pp. 8–16, 2017.

[6] H. Sciences and Y. Sakyo-ku, "A study on Campylobacter jejuni cross-contamination during chilled broiler preparation," vol. 115, pp. 107–115, 2010.

[7] G. Stellato, A. La Storia, T. Cirillo, and D. Ercolini, "International Journal of Food Microbiology Bacterial biogeographical patterns in a cooking center for hospital foodservice," *Int. J. Food Microbiol.*, vol. 193, pp. 99–108, 2015.

[8] F. Timothy, "Risk of Giardiasis from Consumption of Wilderness Water in North America : A Systematic Review of Epidemiologic Data," pp. 100–103.

[9] E. Seob, J. Eun, J. Kim, and O. Kyung, "LWT - Food Science and Technology Isolation of indigenous bacteria from a cafeteria kitchen and their bio fi lm formation and disinfectant susceptibility," *LWT - Food Sci. Technol.*, vol. 77, pp. 376–382, 2017.

[10] G. H. R. Silva, L. A. Daniel, H. Bruning, and W. H. Rulkens, "Bioresource Technology Anaerobic effluent disinfection using ozone : Byproducts formation," *Bioresour. Technol.*, vol. 101, no. 18, pp. 6981–6986, 2010.

[11] S. Tripathi, V. Pathak, D. M. Tripathi, and B. D. Tripathi, "Bioresource Technology Application of ozone based treatments of secondary effluents," *Bioresour. Technol.*, vol. 102, no. 3, pp. 2481–2486, 2011.

[12] M. V Shynkaryk, T. I. Pyatkovskyy, A. E. Yousef, and S. K. Sastry, "Gaseous ozone treatment of baby spinach within the existing production chain for inactivation of Escherichia coli O157 : H7," *J. Food Eng.*, vol. 191, pp. 10–18,

2016.

[13] "Venturi Fertilizer Applications - Wassertec. Cape Town", Wassertec.co.za, 2017. [Online]. Available: https://www.wassertec.co.za/venturi-fertilizer-applications/. [Accessed: 17- Jun- 2017].

[14] "Water – viscosity table and viscosity chart", Viscopedia.com, 2017. [Online]. Available: http://www.viscopedia.com/viscosity-tables/substances/water/. [Accessed: 17- Nov- 2017].

[15] "Food & Beverage - Hygiena Monitoring Systems - Setting ATP Limits - RLU Limits | Food and Beverage Products | Hygiena | Hygiena - Rapid Solutions for Hygiene Monitoring", Hygiena.com, 2017. [Online]. Available: https://www.hygiena.com/rlulimits-food.html. [Accessed: 26- Oct- 2017].

[16] "Cleaning", Spray-nozzle.co.uk, 2017. [Online]. Available: http://www.spray-nozzle.co.uk/spray-nozzles-by-industry/food-processing-new/cleaning. [Accessed: 20- Nov- 2017].

[17] "Solid Stream Nozzles for cleaning applications", Spray-nozzle.co.uk, 2017. [Online]. Available: http://www.spray-nozzle.co.uk/resource-links/applications/cleaning/solid-stream-nozzles. [Accessed: 17- Nov- 2017].

APPENDIX

Abundance of bacterial taxa in environmental swabs from the hospital cooking center in sampling 1. Only OTUs with >0.1% abundance in more than 20% of the samples are represented.

Taxon	S_BlastChiller_Wall	S_ColdStorage_Shelf	S_ColdStorage_Wall	K_Balance	K_Sink	K_Workbench	PPF_Sink	PPF_Workbench	PPR_Cutter	PPR_Sink	PPR_Workbench	PPV_CuttingBoard
Acinetobacter	0.003	0.007	0.001	0.004	0.009	0.001	0.000	0.012	0.001	0.017	0.001	0.000
Acinetobacter johnsonii	0.004	0.071	0.007	0.005	0.096	0.001	0.001	0.009	0.001	0.079	0.001	0.000
Alicyclobacillus	0.266	0.029	0.127	0.000	0.020	0.041	0.030	0.107	0.000	0.021	0.049	0.001
Caulobacter	0.001	0.002	0.001	0.000	0.001	0.000	0.002	0.008	0.000	0.001	0.000	0.046
Chryseobacterium	0.000	0.002	0.000	0.001	0.030	0.000	0.000	0.010	0.000	0.014	0.000	0.003
Corynebacterium	0.003	0.001	0.007	0.000	0.009	0.000	0.002	0.000	0.000	0.002	0.000	0.001
Enterococcus lactis	0.000	0.006	0.002	0.001	0.017	0.000	0.000	0.000	0.022	0.040	0.000	0.000
Kocuria	0.011	0.058	0.042	0.000	0.024	0.001	0.116	0.040	0.000	0.070	0.031	0.006
Kocuria marina	0.000	0.002	0.000	0.000	0.000	0.000	0.002	0.002	0.000	0.001	0.002	0.000
Kocuria palustris	0.006	0.010	0.006	0.000	0.012	0.000	0.006	0.000	0.000	0.028	0.002	0.000
Lactobacillus	0.004	0.000	0.007	0.000	0.002	0.001	0.015	0.004	0.000	0.001	0.000	0.000
Massilia timonae	0.004	0.003	0.001	0.000	0.007	0.000	0.100	0.004	0.000	0.000	0.000	0.091
Moraxellaceae	0.000	0.002	0.000	0.000	0.005	0.000	0.006	0.003	0.000	0.002	0.000	0.000
Paracoccus	0.017	0.007	0.009	0.000	0.018	0.000	0.084	0.004	0.003	0.003	0.001	0.104
Propionibacterium	0.025	0.004	0.009	0.000	0.001	0.006	0.004	0.015	0.000	0.001	0.002	0.000
Pseudomonas	0.028	0.024	0.011	0.241	0.258	0.273	0.001	0.002	0.426	0.010	0.603	0.001
Psychrobacter	0.110	0.190	0.005	0.316	0.023	0.236	0.093	0.001	0.110	0.192	0.000	0.000
Ralstonia	0.005	0.000	0.006	0.000	0.001	0.004	0.003	0.007	0.001	0.001	0.001	0.000
Serratia	0.007	0.000	0.019	0.000	0.001	0.002	0.002	0.004	0.000	0.003	0.001	0.000
Sphingomonas	0.006	0.001	0.006	0.000	0.002	0.000	0.015	0.000	0.000	0.001	0.001	0.057
Staphylococcus	0.005	0.008	0.003	0.000	0.007	0.002	0.002	0.000	0.000	0.004	0.000	0.000
Streptococcus	0.002	0.003	0.012	0.000	0.002	0.001	0.004	0.013	0.000	0.002	0.000	0.000
Streptococcus sanguinis	0.051	0.018	0.140	0.000	0.030	0.011	0.018	0.035	0.006	0.070	0.007	0.001
Streptococcus thermophilus	0.005	0.002	0.005	0.000	0.003	0.002	0.002	0.004	0.001	0.004	0.000	0.000
Other	0.018	0.047	0.022	0.011	0.023	0.016	0.023	0.046	0.010	0.014	0.009	0.016

PPV_Grinder	PPV_Sink	PPV_Workbench	PPW_Sink	PPW_Workbench	T_Colander	T_CuttingBoard	T_Knife	T_Pan	T_SteelDish	T_SteelPincers	T_SteelShovel	T_SteelTray
0.015	0.082	0.010	0.018	0.026	0.007	0.001	0.000	0.001	0.000	0.003	0.392	0.001
0.001	0.031	0.033	0.033	0.100	0.793	0.000	0.001	0.012	0.001	0.004	0.004	0.003
0.001	0.000	0.166	0.092	0.210	0.036	0.000	0.005	0.313	0.002	0.121	0.020	0.058
0.001	0.022	0.002	0.005	0.006	0.000	0.000	0.000	0.004	0.000	0.001	0.001	0.003
0.017	0.029	0.005	0.006	0.027	0.005	0.007	0.000	0.000	0.002	0.001	0.006	0.000
0.009	0.000	0.002	0.010	0.002	0.001	0.003	0.005	0.002	0.000	0.001	0.001	0.003
0.000	0.000	0.000	0.001	0.000	0.000	0.000	0.002	0.001	0.000	0.018	0.007	0.000
0.076	0.000	0.008	0.086	0.049	0.000	0.019	0.322	0.002	0.014	0.010	0.001	0.002
0.002	0.000	0.000	0.001	0.002	0.001	0.001	0.005	0.000	0.000	0.001	0.000	0.000
0.198	0.000	0.001	0.022	0.005	0.000	0.000	0.005	0.000	0.002	0.001	0.000	0.001
0.000	0.000	0.011	0.033	0.004	0.001	0.002	0.001	0.023	0.000	0.003	0.001	0.007
0.049	0.137	0.002	0.061	0.006	0.001	0.000	0.000	0.000	0.000	0.001	0.001	0.000
0.001	0.002	0.002	0.043	0.017	0.001	0.101	0.024	0.000	0.000	0.004	0.001	0.001
0.023	0.088	0.009	0.004	0.013	0.000	0.000	0.000	0.002	0.079	0.001	0.012	0.002
0.010	0.000	0.034	0.004	0.008	0.003	0.000	0.000	0.016	0.000	0.010	0.003	0.034
0.001	0.040	0.038	0.007	0.007	0.019	0.092	0.029	0.006	0.000	0.003	0.004	0.002
0.094	0.000	0.008	0.005	0.001	0.004	0.276	0.035	0.000	0.001	0.011	0.001	0.002
0.000	0.000	0.008	0.001	0.009	0.000	0.000	0.000	0.011	0.000	0.007	0.001	0.032
0.000	0.000	0.016	0.001	0.007	0.001	0.000	0.000	0.043	0.000	0.006	0.000	0.003
0.000	0.026	0.003	0.007	0.005	0.001	0.000	0.000	0.004	0.033	0.000	0.001	0.001
0.000	0.000	0.010	0.014	0.004	0.001	0.000	0.000	0.004	0.000	0.001	0.000	0.004
0.000	0.000	0.015	0.005	0.003	0.002	0.000	0.000	0.011	0.000	0.028	0.002	0.032
0.001	0.000	0.088	0.026	0.058	0.032	0.100	0.017	0.267	0.001	0.052	0.032	0.076
0.000	0.000	0.008	0.003	0.005	0.001	0.003	0.000	0.013	0.000	0.007	0.005	0.006
0.031	0.019	0.028	0.025	0.020	0.011	0.014	0.014	0.006	0.049	0.030	0.012	0.017

Appendix 1: Bacteria count in hospital food service sample 1

Abundance of bacterial taxa in environmental swabs from the hospital cooking center in sampling 2. Only OTUs with >0.1% abundance in more than 20% of the samples are represented.

Taxon	S_BlastChiller_Wall	S_ColdStorage_Shelf	S_ColdStorage_Wall	K_Balance	K_Sink	K_Workbench	PPF_Sink	PPF_Workbench	PPR_Cutter	PPR_Sink	PPR_Workbench	PPV_CuttingBoard
Acinetobacter	0.000	0.000	0.007	0.000	0.056	0.005	0.017	0.032	0.031	0.006	0.159	0.133
Acinetobacter johnsonii	0.001	0.001	0.024	0.000	0.032	0.002	0.005	0.014	0.020	0.023	0.319	0.656
Alicyclobacillus	0.001	0.004	0.067	0.000	0.002	0.076	0.000	0.015	0.000	0.005	0.001	0.000
Brochothrix	0.002	0.285	0.013	0.024	0.000	0.005	0.000	0.003	0.004	0.030	0.000	0.000
Caulobacteraceae	0.000	0.000	0.001	0.000	0.007	0.004	0.000	0.002	0.000	0.039	0.001	0.000
Chryseobacterium	0.000	0.000	0.004	0.000	0.053	0.000	0.036	0.034	0.002	0.039	0.020	0.000
Corynebacterium	0.000	0.001	0.012	0.000	0.000	0.016	0.000	0.001	0.023	0.000	0.007	0.000
Kocuria	0.009	0.002	0.158	0.000	0.004	0.015	0.488	0.006	0.068	0.230	0.003	0.000
Kocuria palustris	0.001	0.001	0.051	0.000	0.023	0.004	0.012	0.000	0.007	0.056	0.000	0.000
Massilia timonae	0.001	0.000	0.002	0.000	0.008	0.033	0.061	0.032	0.001	0.097	0.008	0.009
Microbacterium	0.000	0.000	0.006	0.000	0.005	0.001	0.000	0.029	0.000	0.022	0.001	0.000
Moraxellaceae	0.000	0.000	0.003	0.000	0.036	0.007	0.001	0.000	0.035	0.039	0.081	0.009
Paracoccus	0.000	0.000	0.057	0.000	0.007	0.042	0.042	0.209	0.018	0.054	0.023	0.000
Propionibacterium	0.003	0.003	0.046	0.000	0.001	0.033	0.000	0.008	0.000	0.001	0.000	0.000
Pseudomonas	0.794	0.020	0.020	0.951	0.005	0.005	0.038	0.006	0.012	0.016	0.002	0.022
Psychrobacter	0.000	0.069	0.004	0.000	0.161	0.145	0.041	0.026	0.224	0.028	0.003	0.002
Rhodobacteraceae	0.000	0.000	0.006	0.000	0.002	0.000	0.000	0.015	0.000	0.016	0.023	0.001
Sphingobacterium faecium	0.000	0.000	0.000	0.000	0.008	0.000	0.058	0.037	0.002	0.000	0.000	0.000
Sphingomonas	0.003	0.000	0.002	0.000	0.001	0.000	0.001	0.056	0.000	0.004	0.001	0.000
Stenotrophomonas	0.000	0.000	0.000	0.000	0.002	0.000	0.020	0.009	0.006	0.004	0.003	0.000
Other	0.035	0.007	0.048	0.005	0.044	0.028	0.026	0.023	0.040	0.034	0.035	0.015

PPV_Grinder	PPV_Sink	PPV_Workbench	PPW_Sink	PPW_Workbench	T_Colander	T_CuttingBoard	T_Knife	T_Pan	T_SteelDish	T_SteelPincers	T_SteelShovel	T_SteelTray
0.000	0.011	0.031	0.045	0.031	0.051	0.003	0.017	0.001	0.087	0.003	0.044	0.004
0.000	0.074	0.100	0.011	0.407	0.516	0.001	0.001	0.007	0.535	0.009	0.545	0.058
0.008	0.000	0.000	0.000	0.001	0.072	0.000	0.000	0.015	0.004	0.091	0.008	0.006
0.000	0.000	0.000	0.002	0.000	0.000	0.000	0.000	0.000	0.000	0.000	0.001	0.004
0.000	0.016	0.021	0.026	0.000	0.003	0.010	0.000	0.001	0.000	0.000	0.000	0.000
0.002	0.007	0.094	0.083	0.002	0.003	0.303	0.081	0.000	0.163	0.001	0.002	0.003
0.001	0.000	0.001	0.002	0.010	0.000	0.008	0.001	0.001	0.000	0.028	0.002	0.001
0.042	0.018	0.031	0.032	0.013	0.001	0.048	0.008	0.010	0.002	0.070	0.001	0.012
0.007	0.002	0.042	0.009	0.000	0.000	0.001	0.001	0.002	0.000	0.006	0.000	0.000
0.000	0.003	0.018	0.025	0.022	0.003	0.025	0.299	0.000	0.000	0.003	0.001	0.010
0.001	0.042	0.001	0.020	0.001	0.001	0.003	0.000	0.000	0.000	0.002	0.000	0.000
0.000	0.017	0.001	0.045	0.015	0.011	0.003	0.001	0.005	0.002	0.011	0.007	0.003
0.008	0.086	0.098	0.048	0.000	0.003	0.001	0.050	0.008	0.000	0.007	0.001	0.000
0.001	0.000	0.000	0.000	0.001	0.004	0.000	0.000	0.203	0.001	0.010	0.002	0.001
0.001	0.221	0.104	0.036	0.387	0.007	0.117	0.024	0.004	0.072	0.010	0.002	0.001
0.000	0.002	0.001	0.150	0.002	0.009	0.073	0.190	0.295	0.000	0.004	0.006	0.391
0.013	0.039	0.003	0.002	0.000	0.001	0.000	0.001	0.001	0.000	0.002	0.001	0.000
0.000	0.000	0.000	0.019	0.000	0.001	0.080	0.000	0.000	0.000	0.000	0.001	0.000
0.003	0.020	0.012	0.012	0.000	0.000	0.001	0.000	0.000	0.000	0.006	0.000	0.000
0.001	0.010	0.050	0.010	0.001	0.001	0.045	0.004	0.000	0.000	0.000	0.001	0.000
0.187	0.047	0.027	0.037	0.013	0.037	0.037	0.034	0.044	0.011	0.133	0.047	0.025

Appendix 2: Bacteria count in hospital service sample 2



Appendix 3: Focus point of the water spray used in Taylor's School of Hospitality and Culinary Arts kitchen



Appendix 4: Water spray profile

eureca 2017 – Conference Paper
Paper Number 2ME09

Stabilising an Inverted Pendulum with PID Controller

Lim Yon Yaw*, Hoo Choon Lih, Felicia Wong

Department of Mechanical Engineering, School of Engineering, Taylor's University, Malaysia

* *RolandLYY@gmail.com*

Abstract

Inverted pendulum is a system in which the centre of the mass is above the pivot point, where the mass can freely rotate. The inverted pendulum has a unique trait; it is unpredictable, non-linear and consists of multiple variables. Balancing by PID controller is a continuous process where it corrects the feedback system error from the difference between the measured value and the desired value. This research mainly focusses on balancing an inverted pendulum with reaction wheel. The research objectives are to construct a self-balanced inverted pendulum and using PID controller to control the stability of the pendulum. The PID configurations is then evaluated based on the response of the system. The idea is to use the reaction torque generated by the motor to counter balance the inverted pendulum. The factor which govern the amount of torque generated is the height of the pendulum and the mass of the wheel. To balance the pendulum, tuning the PID gain is essential. Proportional gain is tuned first to get oscillation, next is to tune the integral and derivative gain to get a smoother and quicker response. Idea is to get short settling time, and minimum overshoot percentage. Hypotheses is that higher proportional gain will give a faster response rate and the acceleration of the motor is the key on generating torque. A simulation of the pendulum falling is simulated and the results are recorded in term of the response of the pendulum against time. At initial point, proportional gain, integral gain and derivative gain are set to zero to validate the simulation. The findings in this research is that torque is generated by the acceleration of the reaction wheel. Higher acceleration gives a high torque. Others findings is the PID parameter; Proportional gain increases the response rate; Integral gain is used to eliminate steady state error; Derivative gain is used to lessen the overshoot.

Key words: Inverted pendulum, PID control, Reaction Wheel, Angular acceleration, Angular Displacement

1. Introduction

Inverted pendulum is a system in which the centre of mass is above the pivot point, where the mass can freely rotate. For an example, balancing a long stick on a palm is considered as inverted pendulum. The inverted pendulum has a unique trait where it is unpredictable, non-linear and consists of multiple variables. Which is why, inverted pendulum is usually used to benchmark a control algorithm such as PID controllers, state space representation, neural networks, fuzzy control and genetic algorithms. To balance an inverted pendulum, torque must be applied on the pivot to counter balance the falling pendulum. This can done by moving the pivot point horizontally and vertically by using a cart or a reaction wheel which generate a reaction torque from spinning in opposite direction [1].

The concept of inverted pendulum is very common in the world either in man-made structure or natural things. One of the great examples of an inverted pendulum that can be seen in natural things is human being. To stand up right, human body must be constantly balance itself. Putting an unconscious person upright will lead to the person falling. A humanoid robot is also one of the example where the concept of inverted pendulum can be applied in [2]. Inverted pendulum can also be seen in advance technology such as rockets and missile where the centre of gravity is placed behind the centre of drag, results in aerodynamic instability [3]. As for the latest technology, it would be the Segway [4].

As mentioned above, there are many ways to balance an inverted pendulum. The most common way is to use a moving cart to move the pivot point to create counter moment. Another uncommon way of balancing is by rotating clockwise and anticlockwise to generate moment. Out of the many variations out there, the focus here is to balance an inverted pendulum by using reaction wheel. Unlike other type of inverted pendulum, such as rotary or cart. They require a runway or platform to balance itself, because it is balance by motion of the whole pendulum. However, reaction wheel inverted pendulum is balance by torque generated by the motor. This require no platform or runway making it compact and rigid.

Reaction wheel is mainly used in the satellite to provide precise rotation. Newton 3rd law states that for every action there is an equal and opposite reaction, thus the name of reaction wheel. To rotate the satellite in space, satellite rotated by spinning the reaction in the opposite direction. This allows the satellite to have rotational motion through its rotational axis. However, reaction does not generate translation motion, it cannot move from one point to another [5]. Because the wheel has mass, and it is moving in circular motion, the wheel itself has angular momentum. The angular momentum is conserved as long as there is no external torque applies to the system. Other than that, object with mass also subjected to moment of inertia. By relating the relation above, theoretically a reaction wheel inverted pendulum can be model out [6].

Control is one of the most essential elements nowadays, such as control in a power plant. A power plant without control is disastrous. A common control system consists of the controller, sensor and an actuator. Actuator is the component where it converts electrical signal to mechanical energy to change the physical environment. Sensor reads the change in physical environment and sends the electrical signal to the controller. Controller acts as the processor, which processes the value from the feedback sensor. It calculates the difference of the environmental value and target value,

which also known as response error. This value is then processed by the controller and the correct signal is sent to the actuator. A target value is the value which the user desire to achieve. Below in Figure 1 is a basic control diagram [7].

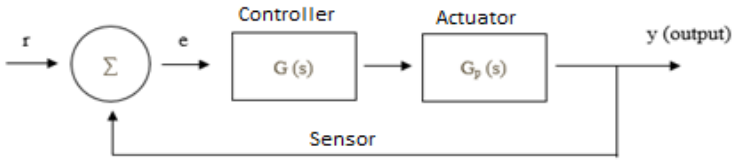


Figure 1: Control diagram.

Where,

r = input e = response error G(s) = Controller Gp(s) = actuator

Evaluating the stability of system in general

There is numerous way to test the stability of a system. One of the most common way is to test the linear system of the transfer function [8].

Consider the system has two main block-diagrams $G_P(s)\ and\ G(s)$.

The transfer function in loop:

The output can be expressed as, $y = G_P\, G$

The response error can be expressed as, $e = r - y$

The ratio of the output and response error is the closed loop function,

$$\frac{y}{r} = \frac{G_P\, G}{e+y} = G_{cl}(s) \quad (1)$$

$G_{cl}(s) = a\ closed\ loop\ function$

The transfer function above is in complex form. Once the function is converted into Laplace form, the data can be presented graphically on a complex s – plane. A closed loop function is always in the fraction form as shown in equation (1). The numerator in a function is also known as zero whereas the denominator is known as pole. The 'circle' mark on the *s*-plane shown in Figure 2 represents the zero, whereas the 'cross' mark represents the pole. Both of these factors govern the stability of the system. If a pole exists on the right plane, it means that there is an output component which gradually increases as time progress, which result in instability in the system. In other words, to achieve stability, the pole needed to be on the left half plane. Figure 3 shows a clearer response of the system depending which point the function located. In the centre of Figure 3 shows the general response of the system, with either gradually decrease, increase or remain constant. Y – axis represents the frequency of the response, where the higher the magnitude of the imaginary number indicates higher frequency.

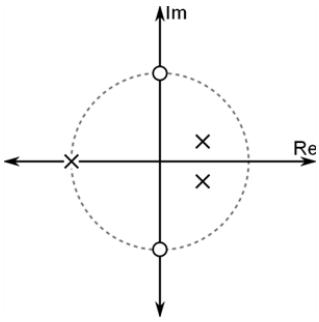


Figure 2: Data represent in a complex s – plane.

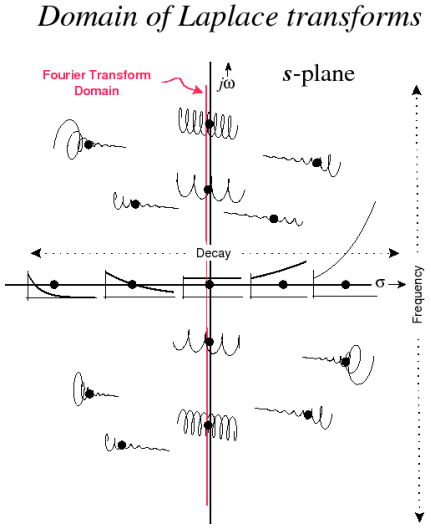


Figure 3: Complex S – plane[8].

PID Controller

PID is a very well-known feedback controller, due to its efficiency and reliability. PID consists of three parameters, proportional gain, integrated and derivative. Like most of the controller, it calculates the differences between the measured value and the desired value as shown in Figure 4. One of the example of PID in daily life is air conditioning. First air conditioning is set to a desire temperature by using the remote. Most of the air conditioning has a built-in temperature sensor to feedback the ambient temperature. The purpose of the PID is to constantly receive feedback from the ambient temperature and send the suitable voltage to the system to lower down the temperature. Once the desire temperature is achieved, the PID controller will then try to maintain the temperature within a range. This range is known as the steady state error. A good controller has a low range of steady state error, also achieve the desire value in a shorter time with low overshooting. The proportional gain acts as multiplier which multiply the error response. It is also one the factor to make the response quicker, however too much will result in oscillation and eventually unstable. The function of an integral gain is sum up all the errors produce to reduce the steady state error, whereas the derivative gain is product of rate of change of the error. The function is to increase the reaction magnitude when there is a change in error. However, it is sensitive to noises such as disturbance in the electrical signal.

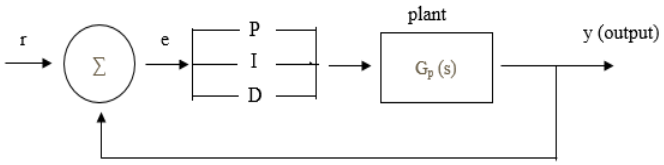


Figure 4: Flow process with PID.

The objectives of this research are to build an auto-balanced inverted pendulum and validate the performance and stability of the inverted pendulum by comparing various set of PID setup based on other research. The hypothesis is that any object that moves in circular motion produces angular momentum and it is conserved unless it is subjected to external torque. By using this theory, it is possible to balance an inverted pendulum by placing the reaction wheel at the end of the pendulum. Balancing is done by rotating and stopping the reaction wheel against the falling direction of the pendulum. Stopping the reaction wheel in a short duration, result in high deceleration, hence producing a counter force to balance the inverted pendulum. The best configuration of the PID controller in this research can be obtained by comparing the result in terms of performance and stability [8].

2. Research Methodology

2.1 Design of the inverted pendulum

The inverted pendulum on this research is very similar to reaction wheel discussed earlier. Instead of balancing on one axis, the purpose of this research is to construct a two-axis reaction wheel inverted pendulum. The main components of the design consist of a pendulum body, two reaction wheels, two motors, gyroscope and a microcontroller. The overall design is as shown in Figure 5.

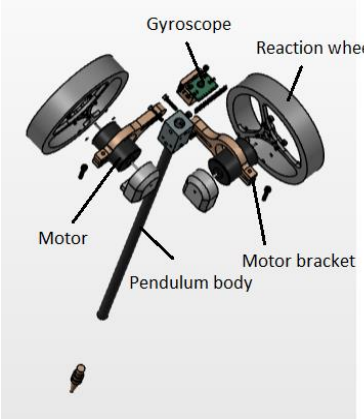


Figure 5: The overall design of the pendulum.

The pendulum body must be made from light material such as aluminium. Lighter body require lesser force to counter the falling thus, weaker motor can be used. Stronger motor is expensive and big in size. Furthermore, it adds on weight into the system.

Due to budget limitation, smaller motor is used to fit into the budget. The limitation of small motor is that, the torque generated by the motor is small. Thus, a lighter and smaller reaction wheel is used. The wheel has a dimension of 6 cm diameter and 2 cm depth. It is 3D printed with PLA (polylactic acid) filament. The density is set to 30% because of light weight requirement. The height of the pendulum is designed to

be approximately 30 cm. This height is decided based on the amount of counter torque generated by the motor.

The torque generated by the motor is 14.7×10^{-3}Nm, this value is based on the specification of the motor. This number is bigger than the torque generated by the weight which is 5.11×10^{-3} Nm. The weight is calculated by multiplying the weight of the pendulum and distance of the pivot point to centre of gravity. The whole pendulum including motor has a mass of 150 grams. The distance of the centre of gravity to the pivot point is approximately 20 cm. Assumption here is the maximum angle the pendulum can be tilted before falling is 10 degrees. Thus, after resolve the weight in vertical component the maximum torque generated by weight is 5.11×10^{-3} Nm. A bigger value is needed because overshoot better than having insufficient enough torque to counter the balance. Furthermore, the speed of the wheel can be controlled to reduce the amount of overshooting.

As mentioned above the height is designed to be 30 cm because shorter height only generates small amount of torque to counter balance the pendulum. Although greater height generates more torque, however the torque generated by the weight is also increases as the height increases. Thus, 30 cm is the optimum height for the inverted pendulum.

a. Electronic components of the inverted pendulum

Electrical components are the vital of the inverted pendulum. Table 1 shows the description of each components.

Direct current (DC) motor is used due to the ability to provide high RPM. The importance of reaction wheel is to create torque, and this is proportional to the acceleration of the wheel. High acceleration can be obtained by changing the velocity in a short time. This can be achieved by DC motor; hence DC motor is used. Since this is the dual axis system, a gyroscope is a better sensor to measure the angular position of the pendulum. Potentiometer is not a suitable selection because it can only read one axis and having two in the system, only result in complex. As for microcontroller, Arduino Uno is selected due to its reliability and low cost. Other alternative such as raspberry pi does not have the same quality as Uno. Furthermore, the software used to tune the PID is Arduino as well, thus more compatible. Mega Arduino is not chosen because of the high cost. With the number of sensors and motors, Uno is sufficient to do the job. In Figure 6, shows the connections of all the electrical components to the microcontroller.

Table 1: Electrical components in the system

Electrical components	Description
Actuator	6V DC motor
Sensor	Gyroscope IMU MPU-6050 up to 6 degrees of freedom

Microcontroller	Arduino Uno

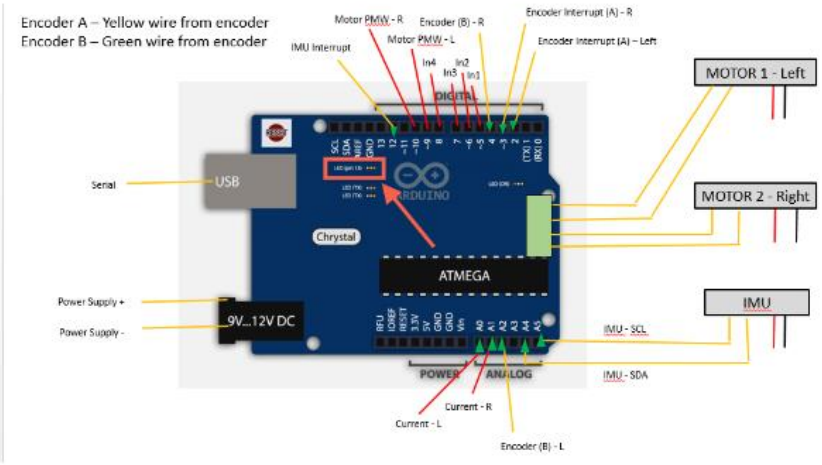


Figure 6: Electrical connection of the system.

b. Mathematical modelling

i. *Modelling using vectorial dynamic*

The structure of the system can breakdown into forces to further understand the system. Following Figure 7 is the schematic of the system. Figure 8 is the free body diagram of the system showing the point where the force is acting. Here is a list of abbreviation used below,

G_p = pendulum weight L_ω = length of pivot to wheel m_ω = wheel mass

L_p = length of pivot to centre of gravity of pendulum T_m = motor torque

m_p= pendulum mass G_ω = weight of wheel

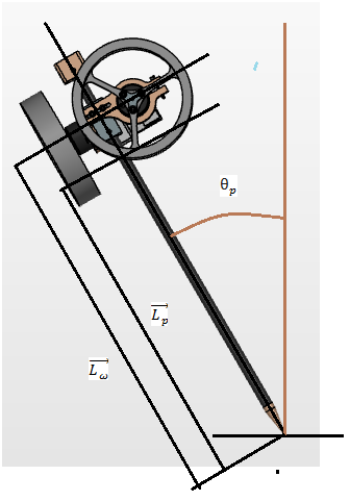


Figure 7: The schematic of reaction wheel pendulum.

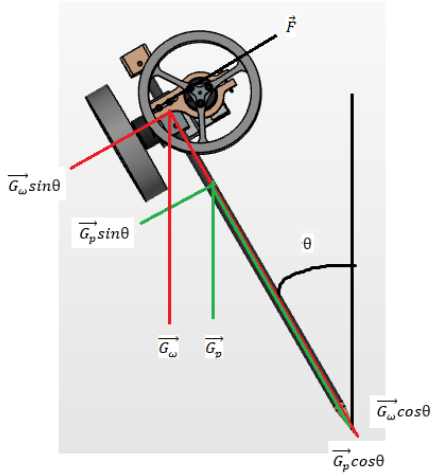


Figure 8: Forces on the system.

The moment of the system is stated as

$$\overrightarrow{M_F} + \overrightarrow{M_{G_\omega}} + \overrightarrow{M_{G_p}} = I\vec{\epsilon} \quad (2)$$

Where,

ϵ = the acceleration of whole system I = the moment of inertia

$\overrightarrow{M_F}$ = Moment caused by Force $\overrightarrow{M_{G_\omega}}$ = Moment caused by wheel

$\overrightarrow{M_{G_p}}$ = Moment caused by pendulum

$$\overrightarrow{M_F} = \vec{R} \times \vec{F} \quad (3)$$

$$\overrightarrow{M_{G_\omega}} = \overrightarrow{L_\omega} \times \overrightarrow{G_\omega} \quad (4)$$

$$\overrightarrow{M_{G_p}} = \overrightarrow{L_p} \times \overrightarrow{G_p} \quad (5)$$

Where R is the radius of the reaction wheel. In this setup, the momentum force, F can be assumed to be approximately same as the torque generated by the motor due to negligible mechanical loses from the motor to the reaction wheel [8]. Thus, Eq. (2) can be written as

$$-T_m + G_\omega L_\omega \sin\theta + G_p L_p \sin\theta = \ddot{\theta} I \quad (6)$$

ii. Modelling using analytical dynamics

To obtain the equation of the system, alternative way such as analytical dynamics is reliable.

The total energy of the system can be break down into the kinetic and potential energy. The difference in kinetic (T) and potential energy (V) is also known as Lagrangian equation.

$$L = T - V \tag{7}$$

Equation of motion expressed in Lagrangian form. This is a general formula,

$$\frac{d}{dt}\left(\frac{\partial L}{\partial \dot{\theta}}\right) - \left(\frac{\partial L}{\partial \theta}\right) = Q \tag{8}$$

Where Q is dissipative force. The force in the system is conservative, thus

$$\frac{d}{dt}\left(\frac{\partial L}{\partial \dot{\theta}}\right) - \left(\frac{\partial L}{\partial \theta}\right) = 0 \tag{9}$$

Moment of inertia is additive,

$$m_t = m_p + m_\omega \tag{10}$$

$$m_t L_t = m_p L_p + m_\omega L_\omega \tag{11}$$

$$I_{total} = I_p + I_\omega = m_p {L_p}^2 + m_\omega {L_\omega}^2 \tag{12}$$

The potential and kinetic energy are expressed as, with the assumption V = 0 at ground level

$$\mathrm{V} = m_t g h = m_t g L_t \cos\theta_p = g(m_p L_p + m_\omega L_\omega)\cos\theta_p \tag{13}$$

$$T = \frac{1}{2} I_{total} {\dot{\theta}^2}_p + \frac{1}{2} I_\omega {\dot{\theta}^2}_\omega \tag{14}$$

Substitute the previous two equations into the Eq. (7)

$$L = \frac{1}{2} I_{total} {\dot{\theta}^2}_p + \frac{1}{2} I_\omega {\dot{\theta}^2}_\omega - m_t g L_t \cos\theta_p \tag{15}$$

Partial derivative is calculated with the first generalized coordinate, θ_p

$$\frac{\partial L}{\partial \dot{\theta_p}} = I_{total} \dot{\theta}_p \tag{16}$$

$$\frac{d}{dt}\left(\frac{\partial L}{\partial \dot{\theta_p}}\right) = I_{total} \ddot{\theta}_p = \left(I_p + m_\omega {L_\omega}^2\right)\ddot{\theta}_p \tag{17}$$

On the other hand, $\left(\frac{\partial L}{\partial q_j}\right)$ is express as the moment of inertia

$$\frac{\partial L}{\partial \theta_p} = m_t g L_t \sin\theta_p \tag{18}$$

By substituting equation (17) and (18) to (8), the result is

$$\left(I_p + m_\omega {L_\omega}^2\right)\ddot{\theta}_p - m_t g L_t \sin\theta_p = Q \tag{19}$$

Replace Q with the torque generated by the motor into Eq. (19),

$$\left(I_p + m_\omega {L_\omega}^2\right)\ddot{\theta}_p - m_t g L_t \sin\theta_p = T_m \quad (20)$$

Notice in Eq. (13), the potential energy is in term of cosine. This is because when dealing with the potential energy, only the height is considered, which is the vertical axis.

3. Results and Discussions

The purpose of this research is to identify the effect of PID configuration on the response rate of inverted pendulum. The expected outcome of this research is fluctuation should be considerably low, but the settling time will be high. This is most likely due to the charge up time for the reaction wheel to deliver a counter moment. Unlike the other system where the moment is instantaneous generated by the motor, reaction wheel need to take up speed to generate counter moment.

A simulation of the inverted pendulum is designed by using Simulink. The purpose of the simulation is to theoretically simulate the outcome of the pendulum. The simulated result is then compared with the practical result to evaluate the difference between the theory and practical performance. The Simulink design is shown below in Figure 9.

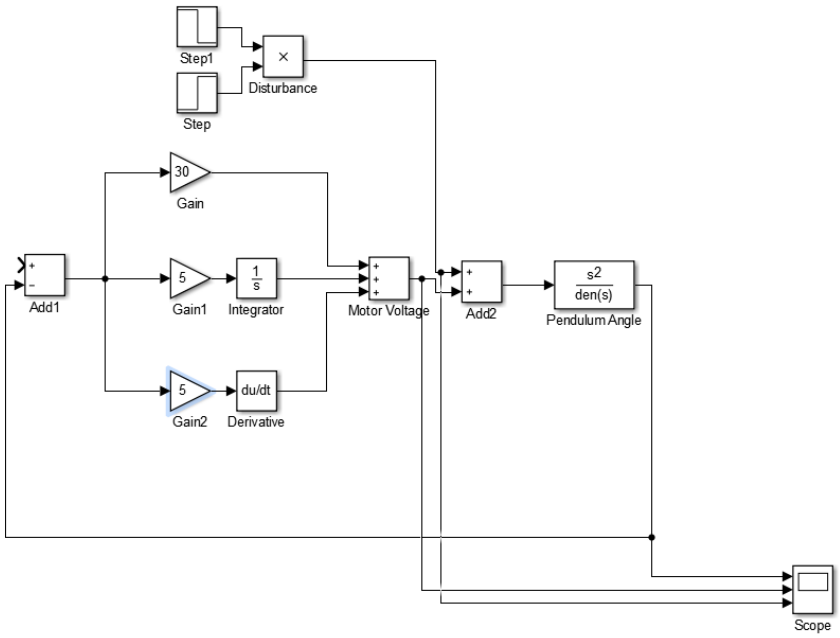


Figure 9: Design of the Simulink.

A basic PID control system consists of PID, plant, actuator and sensor to feedback the output. In Figure 10, the loop first starts by having a constant with 0 magnitude going through the PID controller. The PID controller is then produce an output as motor voltage to give specific amount of torque to balance the pendulum. After that the change in angle position is then measured by the sensor and feedback to

the PID controller. 'Step' shown in Figure 9 is the source of the disturbance which made the pendulum to be unbalance. The scope shown in the Simulink design is the result of the response rate and there are three entries to the scope which produces three variables in graph as shown in Figure 10.

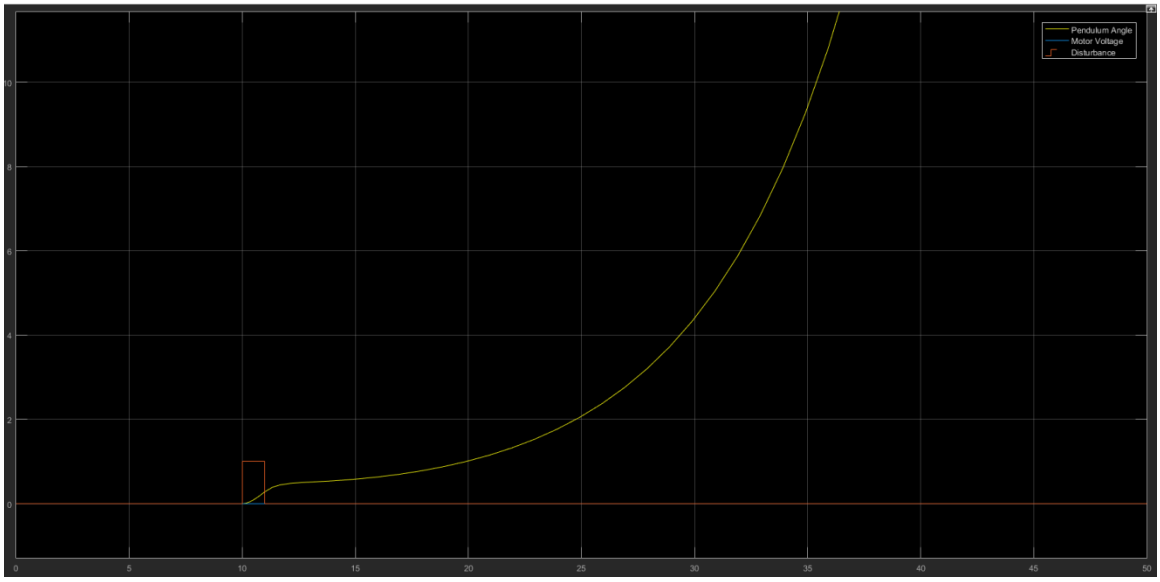


Figure 10: System response when $K_p = 0$, $K_i = 0$ and $K_d = 0$.

a. Ziegler-Nichols tuning method

One of the way to tune an unstable system using PID controller is the Ziegler-Nichols turning method. This method is very common and reliable because tuning can be done without the mathematical models of the system. This method can be used on system with known mathematical modelling as well. Ziegler-Nichols tuning method tune a system by judging the response of the system. To use this method, first, only the K_p (Proportional gain) is tuned to certain amount until the response start oscillating. Second is to tune either K_i (Integral gain) or K_d (Derivative gain) to stabilize the system. Finally, the last step is to tune the last parameter to improve the stability of the system either by reducing the fluctuation or reducing the steady state error [10].

When PID gain is zero. The response shows that the system is unstable as it grows exponentially away from stable point as the disturbance introduced into the system. Yellow line indicates the angle position of the pendulum, red line indicates the disturbance and blue line indicates the response of the motor voltage. With the zero gain, the motor is deactivated thus the voltage response is stagnant as shown in Figure 10.

Figure 11 shows when the K_p has a value of 15. The response is similar as the previous response but with a few fluctuations at the beginning.

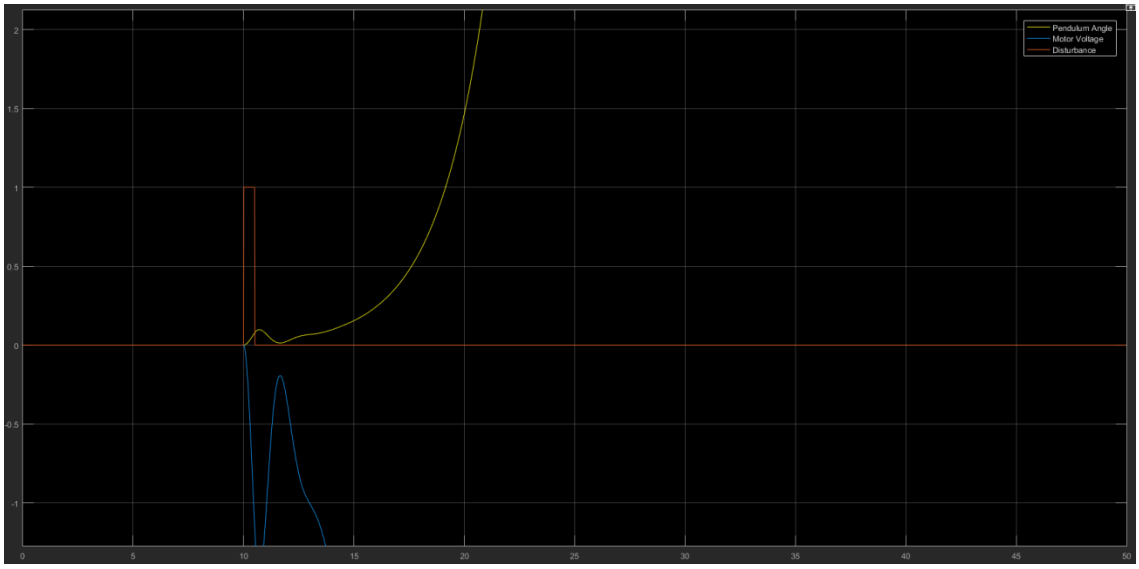


Figure 11: System response when K_p = 15, K_i = 0 and K_d = 0.

To start balancing an unbalance system, K_p is commonly the priority to tune. In this case, the proportional gain is tuned to 15 whereas the integral gain and derivative gain remain zero. With the K_p at 15, the angle of the pendulum decreases a slight amount before growing exponentially. This shows that there is a slight improvement to the stability of the system, however the voltage response of the motor has a very steep gradient towards infinity. To counter the pendulum from falling, the motor must generate torque in opposite direction, which is why the voltage response has a mirror pattern against the falling of pendulum. As the voltage response going towards infinity, which means the system require infinite amount of energy to balance the system, practically this is unachievable. Thus, higher K_p is required.

Higher K_p value is input to the simulation and the result is shown in Figure 12. More fluctuations occurred before system went unstable.

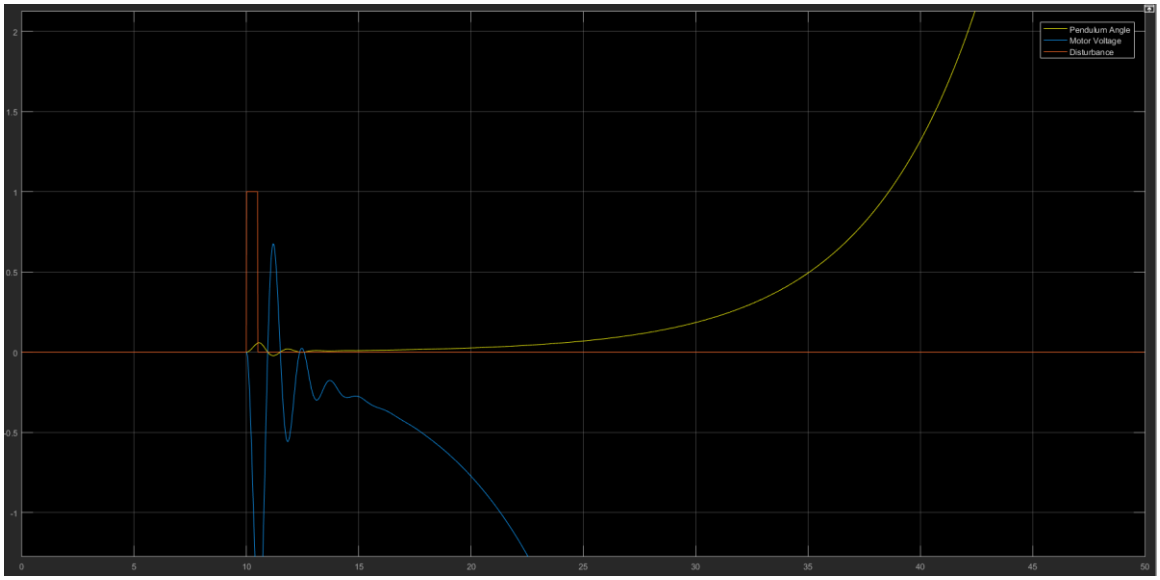


Figure 12: System response when K_p = 30, K_i = 0 and K_d = 0.

As higher K_p is added, the fluctuation occurrences increase at the beginning then gradually went unstable. The rate which the system became unstable is significantly lower with twice amount of K_p. Voltage motor also share the similar traits. This shows that the system is more stable when higher proportional gain is input into the system. One of the reason the stable time is longer is because motor voltage has more attempts to balance the pendulum. Fluctuations shows in the motor voltage is the result of motor trying to balance the pendulum. However, the lack of other parameter gains it is still unable to balance the pendulum in a longer duration. Thus, other gains are needed for the system to be balanced.

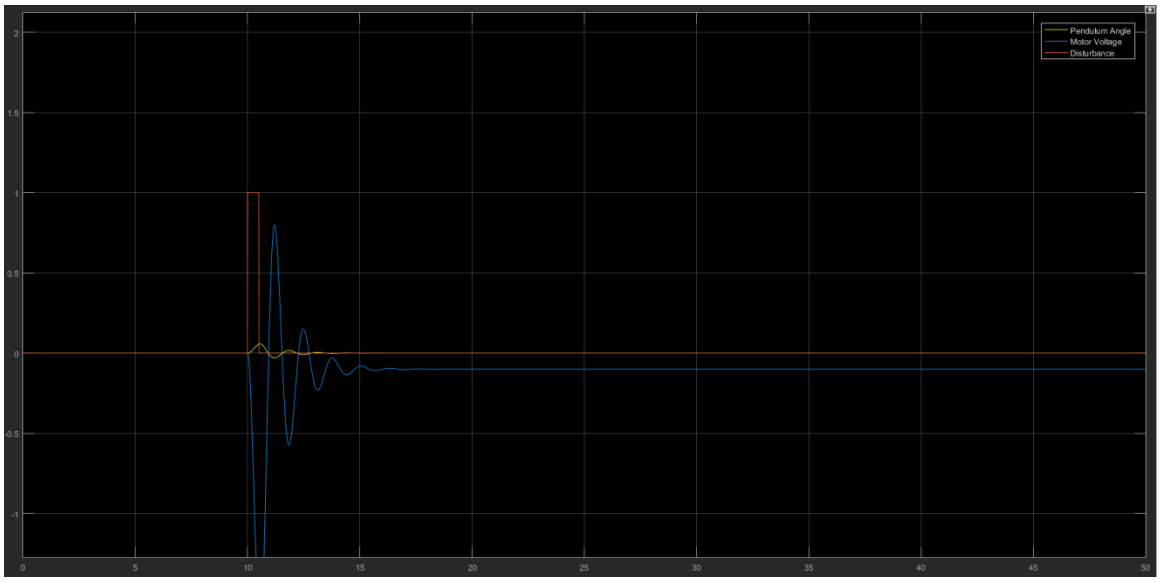


Figure 13: System response when $K_p = 30$, $K_i = 5$ and $K_d = 0$.

With $K_p = 30$ and $K_i = 5$, the system is no longer unstable. As compare to Figure 12, this response stays stable after a little fluctuation. The amplitude of the fluctuation is significantly lower as well. On the other hand, the motor voltage has more visible fluctuations and stay constant as the system is stable. The response of the pendulum has a biggest fluctuation when an external force is acted on it. The amplitude of the fluctuation is then reduced gradually until reaches zero, which is the stable point. This indicates that when the external force acted on the pendulum, it swings away from equilibrium. As it is away from equilibrium the motor generates opposite torque to bring the pendulum back to equilibrium, which is why the blue line has a peak when the response of the pendulum has a peak. After the pendulum reaches stability voltage is still supplying the motor to maintain the balance of the system, which explains the motor voltage is not in zero.

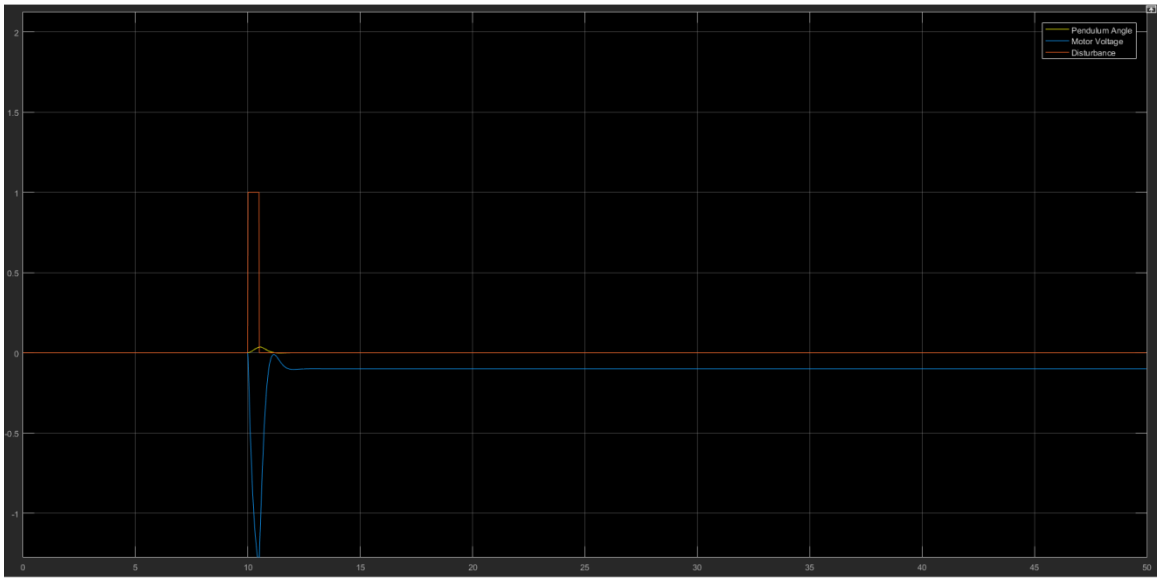


Figure 14: System response when K_p = 30, K_i = 5 and K_d = 5.

All the parameters are input into the PID controller, the system became more stable as shown in Figure 14. Only one visible fluctuation and the system is balanced without overshooting that may cause another oscillation. With addition derivative component of the PID control, the controller is now more sensitive in change in error. The moment change in error is read by the controller, it reacted quickly to neutral the change. Integral is important to make this happen as well. Only with the help of K_i, the system managed to stabilise with low stead state error else the pendulum will still swing left and right at equilibrium.

After the simulation, theoretically it is proven it is possible to balance the inverted pendulum by using PID controller. Next step will be testing on an actual inverted pendulum. The actual inverted pendulum has finish manufactured as shown in Figure 15. Same procedure will be applied on the actual inverted pendulum in future test.

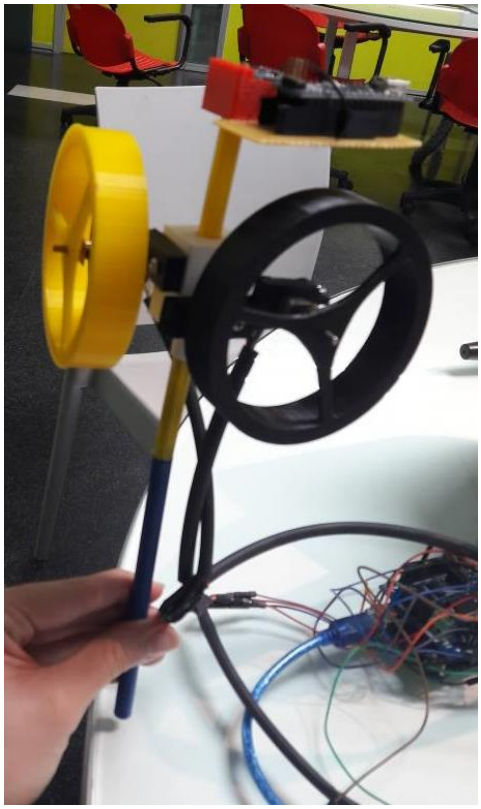


Figure 15: The actual inverted pendulum.

4. Conclusion

The simulation done by Simulink shows concrete proof that an inverted pendulum can be balanced PID controller. With Ziegler-Nichols tuning method, even if the mathematical modelling unknown it is possible to balance it by evaluating the response of the system and tune each gain until a positive result is achieve. In PID, proportional gain is responsible for amplifying the error; integral gain is to reduce the steady state error; derivative is sensitive in change in error. Based on the simulation done in Simulink, high K_p is require to balance the pendulum and the value K_i and K_d can be as low as 5 and it is sufficient for the system to be balanced.

Acknowledgements

Throughout this whole research, the author would like to show his gratitude to both of his supervisor, Dr. Hoo Choon Lih and Dr. Felicia Wong. They had guided and assisted the author in doing this research. The author also would like to thank the university for providing funds and equipment to complete his project.

References

[1] M. V Subbotin, “Balancing an inverted pendulum on a seesaw,” *Proj. Report, Univ. California, St. Barbar. …*, pp. 3–8, 2004.

[2] C. Walck, “Stabilization of an inverted pendulum using control moment gyros,” 2013.

[3] M. Olivares and P. Albertos, “Linear control of the flywheel inverted pendulum,” *ISA*

Trans., vol. 53, no. 5, pp. 1396–1403, 2014.

[4] A. Özbey, E. Uzal, and H. Yildiz, "Nonlinear control of an inverted pendulum on a cart by a single control law," *Appl. Mech. Mater.*, vol. 464, pp. 279–284, 2014.

[5] A. Rahimi, K. D. Kumar, and H. Alighanbari, "Fault estimation of satellite reaction wheels using covariance based adaptive unscented Kalman filter," *Acta Astronaut.*, vol. 134, no. February, pp. 159–169, 2017.

[6] C. N. Me-, "Stabilizing and Balancing of Linear and Rotary Inverted Pendulum System," 2016.

[7] S. Kumar, D. Sain, S. Kumar, and S. Ghosh, "International Journal of Electronics and Communications (AEÜ) Real time implementation of fractional order PID controllers for a magnetic levitation plant," *AEUE - Int. J. Electron. Commun.*, vol. 78, pp. 141–156, 2017.

[8]A. Tepljakov, E. A. Gonzalez, E. Petlenkov, J. Belikov, C. A. Monje, and I. Petr, "Incorporation of fractional-order dynamics into an existing PI/PID DC motor control loop," *ISA Trans.*, vol. 60, pp. 262–273, 2016.

[9] C. Liu, "Bachelor ' s Thesis," *Significance*, no. 6704071, pp. 1–2, 2011.

[10] T. Yucelen, O. Kayma, and S. Kur, *Self - Tuning PID Controller Using Ziegler - Nichols Method for Pr ogr ammable Logic Controller s*, vol. 39, no. 14. IFAC.

eureca 2017 – Conference Paper
Paper Number 2ME10

Evaluation of SIPIC01 and SIPIC02 on Motor Speed Control

Wei Sheng Loh[1], Mohd Hardie Hidayat Mohyi[1], Choon Lih Hoo[2*]

[1]*School of Engineering, Taylor's University, Malaysia*

[2]*School of Engineering and Physical Sciences, Heriot-Watt University, Malaysia*

[*]*c.hoo@hw.ac.uk*

Abstract

Due to its ease of use and simplicity, Proportional-Integral (PI) controller still remains as the widely used controller for motor speed control system. However, PI controller exhibits windup when the motor operates in a saturated state, which may cause degradation to the control system. In order to overcome the windup phenomenon, many researches have introduced various types of anti-windup methods such as the conditioning technique (CI), tracking back calculation (TBC), integral state prediction (ISP), steady-state integral proportional integral controller 01 (SIPIC01) and steady-state integral proportional integral controller 02 (SIPIC02). CI, TBC and ISP are anti-windup techniques with integral control switching mechanism and coupling of proportional gain, k_p and integral gain, k_i. Due to the coupled k_p and k_i, it is hard to tune for a motor performance with short settling time without experiencing overshoot. In the meanwhile, SIPIC01 and SIPIC02 are robust anti-windup methods without a switching mechanism and exhibit decoupling feature. SIPIC01 and SIPIC02 have shown better dynamic performance compared with CI, TBC and ISP. However, SIPIC01 has not been compared with SIPIC02 in terms of their decoupling effect flexibility and dynamic performance. Hence, the comparison and evaluation of the dynamic performance between SIPIC01 and SIPIC02 were done in this research in order to expand the knowledge of the field of anti-windup PI control. The mathematical model for the plant system was derived. The decoupling effect was verified through simulation with the aid of MATLAB while the performance was verified through hardware simulation and hardware testing by using Scilab. The results obtained from the simulation showed that both SIPIC01 and SIPIC02 consist of decoupling features that allow a performance with coexistence of zero or minimum overshoot and short settling time. However, SIPIC02 consists of longer rise and settling time as compared to SIPIC01. Therefore, it can be concluded SIPIC01 is better than SIPIC02 in term of dynamic performance.

Keywords: Proportional-Integral (PI) Controller, Anti-windup, Steady-state Integral Proportional Integral Controller, Decoupling Effect, Motor Speed Control

1. Introduction

A control system is one of the important components in a system which is responsible in producing desired output. Control system comprises of open-loop and closed-loop control system. Open-loop control system is a simple control system without feedback loop in which the input is totally independent from the output of a system [1]. Other than its simplicity, open-loop control system is generally stable and economical. However, the output of the open-loop control system is inaccurate and unreliable. This is due to the system which is unable to auto-correct the system error signal as there is no feedback loop in the system. In contrast, a closed-loop control system is a control system with feedback loop [1]. This type of control system contains the error auto-correction operation that gives a more accurate and reliable output. However, the design of a closed-loop control system is complicated.

In modern control, Artificial Intelligent (AI) control is a type of closed-loop control system that utilises the complex computation mechanism to imitate the human thinking. Fuzzy logic controller (FLC) [2], artificial neural network (ANN) [3], and genetic algorithm (GA) [4] are some of the commonly discussed AI controls which are robust and show good dynamic performance in motor speed control. However, due to its ease of use and simplicity, the classical proportional integral (PI) controller still remains as the controller that is widely used for motor speed control system nowadays. Yet, PI controller experiences windup which normally happens when the output of the controller exceed the limit of the input of the plant which caused the system to operates in a saturated state [5]. This phenomenon will lead to poor control response such as increased overshoot, long settling time and even system instability.

In order to improve the performance of the PI controller, the windup phenomenon should be eliminated. There are many anti-windup techniques developed to avoid windup phenomenon such as the conditional integration (CI), tracking back calculation (TBC), integral state prediction (ISP), steady-state integral PI controller-01 (SIPIC01) and steady-state integral PI controller-02 (SIPIC02) [5], [6]. Up-to-date, both SIPIC01 and SIPIC02 have been compared with the existing anti-windup PI controllers and the result shows that both of them perform better in term of dynamic performance on motor speed control. However, the evaluation between the two has yet to be studied. Hence, the dynamic performance between SIPIC01 and SIPIC02 was investigated in the present study. This work serves to expand the knowledge of the field of anti-windup PI controller.

2. Types of Anti-Windup PI Controller

In order to overcome the windup phenomenon, many researches introduced different types of anti-windup schemes. Out of the anti-windup schemes available, CI, TBC and ISP appear to be the favourite among researches. The similarity between these schemes is that they operate differently by altering their integral control component in the saturated state, and resume to the conventional PI controller under unsaturated state. Consequently, they also experience tuning difficulty when operating as PI controller due to their coupled tuning gains [5]. CI, TBC and ISP have the similar integral control under unsaturated state but consist of different integral control under saturated state. Table 1 shows the integral control of the respective anti-windup method under different states, and Table 2 shows the advantages and disadvantages of these anti-windup methods [5]. The e, k_a, u, v, ω_i, q_{ss} and q shown in Table 1 denote the input error, anti-

windup gain, controller output, plant input, positive parameter of the low-pass filter, steady state integral component and integral state respectively.

Table 1. Comparison of integral control of anti-windup schemes under different states

Controllers	Integral Control Under Unsaturated State, u = v	Integral Control Under Saturated State, u ≠ v	Switching Mechanism
Conditional Integration (CI)	e	0	Yes
Tracking Back Calculation (TBC)	e	$e - k_a(u - v)$	Yes
Integral State Prediction (ISP)	e	$\omega_i (q_{ss} - q)$	Yes

Table 2. The advantages and disadvantages of anti-windup schemes

Controllers	Advantages	Disadvantages
Conditional Integration (CI)	• No overshoot	• Integral value is large when the controller output differ from the plant input. • Difficult to choose value of gain • Consists of coupling effect
Tracking Back Calculation (TBC)	• Large value of anti-windup gain, k_a is allowed to be chosen • Improve overshoot	• Error will occur if the gain is too big. • Consists of coupling effect
Integral State Prediction (ISP)	• Steady state value is predicted to prevent state change.	• Integrator value is limited. • Consists of coupling effect

3. Generalisation of PI Controllers

The main purpose of generalisation of PI controllers is to develop a generic expression which can be used to represent all the PI-related control methods. According to [7], the function $k_i k_t (q_{ss} - q)$ can generalise any PI-related controller and the general equation is shown in Equation (1) where *l, u, v* and *w* are natural numbers while A_l, B_u and *C* are integers.

$$k_i k_t (q_{ss} - q) = \sum_{l=0}^{l=v} A_l q^{(l)} + \sum_{u=0}^{u=w} B_u e^{(u)} + C \quad (1)$$

The k_i, k_t, q_{ss}, q and e represent the integral gain, external load constant, steady state integral component, integral state and input error respectively while the *l* and *u* denote the number of coefficient of *A* and *B* for *q* and *e* respectively. Both *l* and *u* also denote the number of order for q and e respectively while *C* represent any constant. Each term in the function of $k_i k_t (q_{ss} - q)$ carries certain characteristic of the control system. For example, the existence of the constant *C* will give a pole at the origin which will result in steady state error [7]. In order to obtain a zero steady state error control performance, Equation (2) must be met.

$$\lim_{s \to 0} k_i k_t s \left(\frac{q_{ss}}{s} - Q(s) \right) = 0 \quad (2)$$

Following this condition (2), the expression of $\frac{q_{ss}}{s} - Q(s)$ needs to be reduced into a function of *s* which consists of no pole at the origin [7]. However, with the presence of constant *C* in the function of $k_i k_t(q_{ss} - q)$, Equation (2) will never be satisfied and the steady state error cannot be eliminated.

Besides, the existence of error term, *e* will lead to the coupling of k_p and k_i tuning parameters which increase the difficulty to obtain a performance of zero overshoot and short settling time. According to [7], the absence of the error term will decouple the k_p and k_i which allows a performance with coexistence of zero overshoot and short settling time.

4. Steady-state Integral Proportional Integral Controller 01 (SIPIC01)

According to the characteristic of the term in the general Equation (1) stated in section 3, Hoo et al. proposed a structure of the controller as shown in Equation (3) where A_1 can be any constant [8], [9].

$$k_i k_t(q_{ss} - q) = A_1 \dot{q} \tag{3}$$

In order to develop a controller with no steady state error and decoupling effect, A_1 can be equal to k_t as A_1 can be any constant. By substituting $A_1 = k_t$ into Equation (3), Equation (4) which describes the integral control of SIPIC01 will be formed. The Laplace transformation of Equation (4), with *Q(s)* the subject is shown in Equation (5).

$$k_i(q_{ss} - q) = \dot{q} \tag{4}$$

$$Q(s) = \frac{q(0) + k_i \frac{q_{ss}}{s}}{s + k_i} \tag{5}$$

Equation (6) is a second order error dynamic equation (EDE) formed from a common first order system plant, *P*(s) controlled by a PI controller as shown in Figure 1, where *V*(s) and T_L(s) are the control output and external load respectively. The error equation of SIPIC01 (7) can be derived through the substitution of Equation (5) into Equation (6). Equation (8) corresponds to the damping ratio of SIPIC01, which is formed from the denominator of Equation (7) by comparing with the general characteristic equation, $s^2 + 2\zeta\omega s + \omega^2$, where ζ and ω are the damping ratio and natural frequency respectively.

$$E(s) = \frac{e(0)\left(\frac{b}{f} + k_d k_t\right) + k_i k_t \left(\frac{q_{ss}}{s} - Q(s)\right)}{\left(\frac{b}{f} + k_d k_t\right)s + \frac{a}{f} + k_p k_t} \tag{6}$$

$$E(s) = \frac{e(0)\frac{b}{f}}{\left(\frac{b}{f}s + \frac{a}{f} + k_p k_t\right)} + \frac{k_i k_t(q_{ss} - q(0))}{(s + k_i)\left(\frac{b}{f}s + \frac{a}{f} + k_p k_t\right)} \tag{7}$$

$$\zeta = \frac{a + f k_p k_t + b k_i}{2\sqrt{b}\sqrt{a k_i + f k_p k_t k_i}} \tag{8}$$

As shown in Equation (7), there is no pole at the origin and this indicates that there is no steady state error. Besides, only k_p controls the *e*(0) while k_p and k_i control the $k_i k_t\left(q_{ss} - q(0)\right)$ in two separate terms. Hence, it can be concluded that SIPIC01

consists of decoupling effect which allows the controller to obtain short settling and rise time without experiencing overshoot.

5. Steady-state Integral Proportional Integral Controller 02 (SIPIC02)

Chiah at al. [6] proposed another anti wind-up PI controller based on general Equation (1) with the structure of the controller shown in Equation (9) where A_1 and A_2 can be any constant.

$$k_i k_t (q_{ss} - q) = A_1 \dot{q} + A_2 e \tag{9}$$

One of the possible option for A_1 and A_2 is k_t. By substituting $A_1 = A_2 = k_t$ into Equation (9), the integral control of the SIPIC02 can be obtained (10). The Laplace transformation of Equation (10), with *Q(s)* the subject is shown in Equation (11).

$$k_i (q_{ss} - q) = \dot{q} + e \tag{10}$$

$$Q(s) = \frac{q(0) + k_i \frac{q_{ss}}{s} - E(s)}{s + k_i} \tag{11}$$

From Equation (11) and Equation (6) with zero derivative gain, the error equation of SIPIC02 is shown in Equation (12). Equation (13) is the damping ratio of SIPIC02 obtained from the denominator of Equation (12) by comparing with the characteristic equation.

$$E(s) = \frac{e(0)\frac{b}{f}(s + k_i) + k_i k_t (q_{ss} - q(0))}{\left(\frac{b}{f}s + \frac{a}{f} + k_p k_t\right)(s + k_i) - k_i k_t} \tag{12}$$

$$\zeta = \frac{a + f k_p k_t + b k_i}{2\sqrt{b}\sqrt{a k_i + f k_p k_t k_i - f k_i k_t}} \tag{13}$$

As shown in Equation (12), there is no pole at the origin and this indicates that there is no steady state error. Theoretically, SIPIC02 consists of coupling effect which will prevent the controller from achieving a performance of zero overshoot and short settling and rise time. This is because the $k_i k_t$ in Equation (12) does not allow distinctive separable factors in the denominator. The coexistence of k_p and k_i in the pole hinder the decoupling. However, according to Chiah et al. [6], SIPIC02 shows a promising performance with short settling and rise time while maintaining low or zero overshoot.

6. Simulation and Experimental Testing

The theoretical analysis of SIPIC01 and SIPIC02 done so far will be verified in this section by conducting simulation and hardware testing. The simulation for decoupling effect will be described in section 6.1 while the hardware simulation and experiment testing for speed control performance will be described in section 6.2.

6.1 Simulation for Decoupling Effect

MATLAB/Simulink software was used in to verify the decoupling effect of SIPIC01 and SIPIC02 through simulation for a second order EDE system. The block diagram of the simulation for decoupling mode is illustrated in Figure 2. For simplicity,

the other parameters are set to unity, the input is set as 1000 rpm and the system plant is set as $P(s) = \frac{1}{s+1}$. The simulation is conducted under two conditions which are with and without load. For simulation with load, the load, L is set as 200. The simulation for both conditions are repeated for input equal to 2000 rpm.

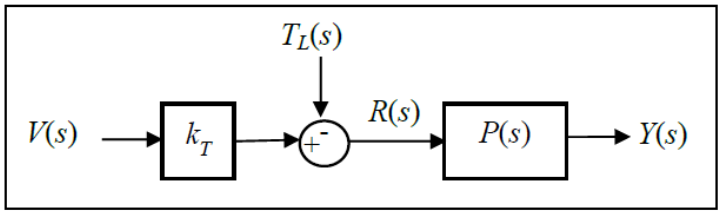


Figure 1. The block diagram for general control system

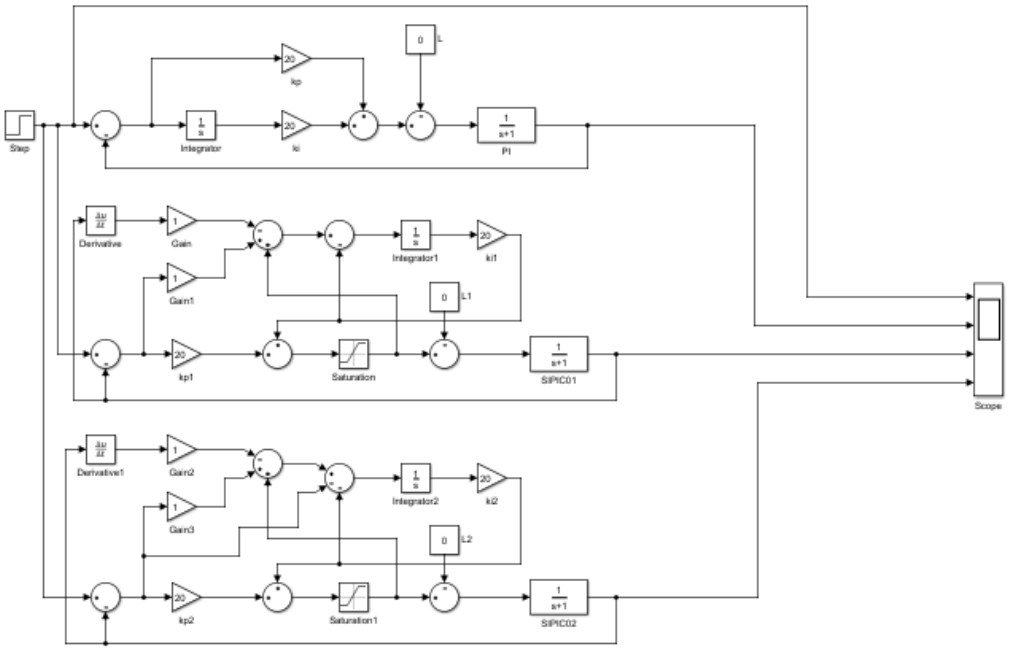


Figure 2. The block diagram of the simulation for decoupling mode

6.2 Simulation and Experiment Testing for Control Performance

The simulation testing of SIPIC01 and SIPIC02 for control performance is done through Scilab/Scicoslab. They are tested under three cases which are no load, load 1 and load 2. Load 1 is a mild steel black plating with moment of inertia of 8.63×10^{-5} kgm^2 whereas the material for load 2 is an aluminium plating with moment of inertia of 2.83×10^{-5} kgm^2. Figure 3 shows the block diagram used for the simulation testing of SIPIC01 and SIPIC02. In order to ensure that the model is reliable, system identification is performed by using Scilab/Scicoslab. The simulation result is later compared with the real hardware testing result.

For the experimental testing, the setup for the DC servo motor speed control is shown in Figure 4. The setup includes Scilab/Scicoslab, DC servo motor, host controller computer, load tuner, motor encoder, power amplifier, terminal system unit and real time interfacing platform data acquisition. Similar to the simulation, the experimental testing for SIPIC01 and SIPIC02 are also tested under the three cases. For each case, the testing was done for two speeds input, which are 50 rad/s and 100 rad/s. The specification of the DC motor is shown in Table 3.

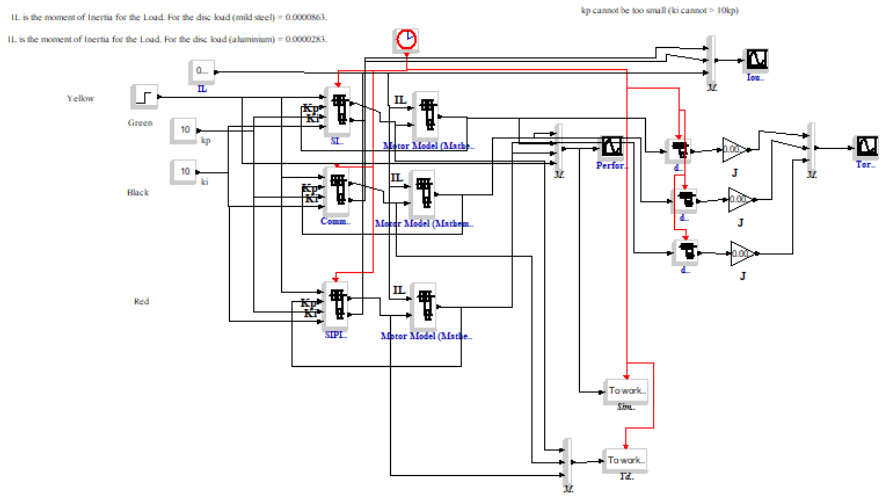


Figure 3. The block diagram for the simulation testing



Figure 4. Setup for the experimental testing

Table 3. Specification of the DC motor

Characteristics	Values
Maximum supply voltage	40 Vdc
Maximum continuous torque	14 Ncm
Maximum peak torque	36 Ncm
Motor voltage constant	10.3 V at 1000rpm
Motor torque constant	9.0 Ncm/A
Mechanical time constant	20ms
Rotor inertia	0.214 kgcm
Terminal resistance	7.8 Ohms
Rated speed	1600 rpm
No load speed	2600 rpm @ 24 Vdc
Rated torque	12 Ncm
Peak torque	27 Ncm

7. Simulation Result

7.1 Decoupling Effect

Figures 5 and 6 show the result of simulation for decoupling effect for k_p = 1, k_i = 20 at 1000 rpm under no load and loading condition respectively. PI has the shortest rise time and greatest overshoot, while both SIPIC01 and SIPIC02 have no overshoot.

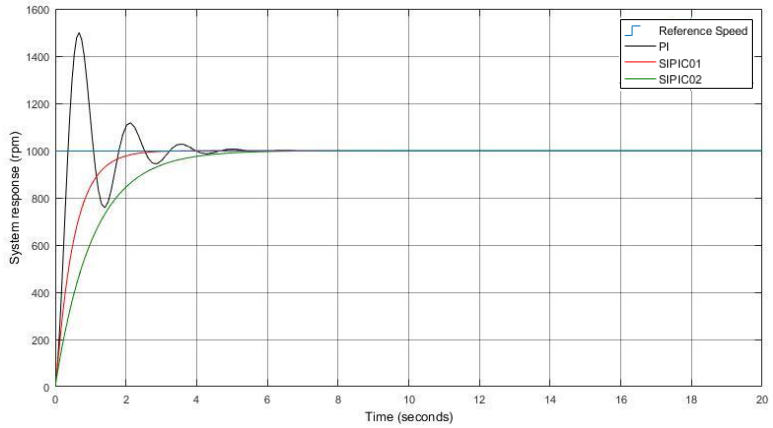


Figure 5. Simulation for decoupling effect for k_p = 1, k_i = 20 at 1000 rpm under no load condition.

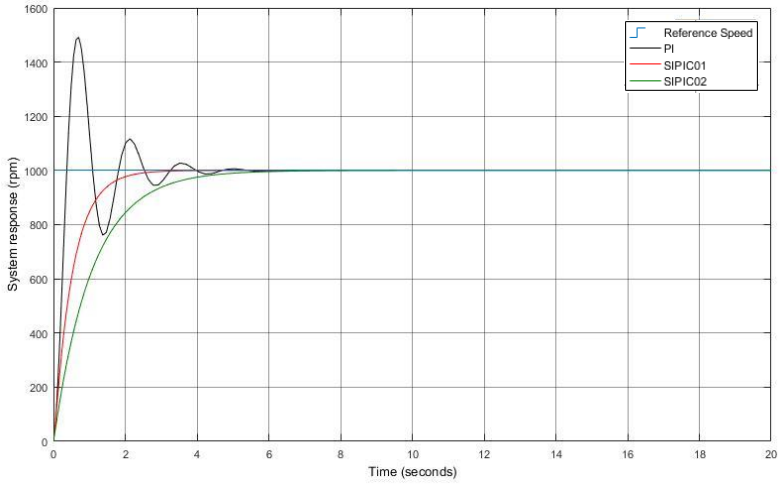


Figure 6. Simulation for decoupling effect for k_p = 1, k_i = 20 at 1000 rpm under loaded condition.

The response of simulation for decoupling effect for PI, SIPIC01 and SIPIC02 at 1000 rpm and 2000 rpm under no load condition is shown in Table 4. The response of simulation for decoupling effect under loaded condition is not shown but will be discussed in this section. As shown in Table 4, the rise time and settling time for PI reduced with increasing k_p or k_i gains. However, the overshoot percentage for PI increased when k_i is increased. This observation can be explained based on the damping ratio equation (14). By referring to Equation (14), the damping ratio of PI is directly proportional to k_p but inversely proportional to k_i. The damping ratio of PI increases with increasing k_p but conversely with increasing k_i. The system is said to experience

overshoot when the damping ratio is < 1. The lower the damping ratio, the higher the percentage of overshoot.

$$\zeta = \frac{a+fk_pk_t}{2b\sqrt{\frac{f}{b}k_ik_t}} \tag{14}$$

As for SIPIC01 and SIPIC02, their rise time and settling time also reduced with increasing k_p or k_i gains. However, both of them do not experience overshoot. This phenomenon can be explained based on Equations (8) and (13). Since the tuning parameters, k_p and k_i exist in the numerator and denominator, both of them increase or decrease together with the damping ratio. As mentioned above, increasing k_p or k_i gains will reduce the rise and settling time of SIPIC01 and SIPIC02. However, increasing k_p or k_i gains will only have slight effect on the damping ratio due to the existence of k_p and k_i gains in the numerator and denominator of Equations (8) and (13). Hence, it can be said that both SIPIC01 and SIPIC02 consist of decoupling features that allows a performance with coexistence of zero overshoot and short settling time. By comparing SIPIC01 and SIPIC02, SIPIC02 consists of longer rise and settling time. This is due to the $-fk_ik_t$ term in the denominator of Equation (13). With the $-fk_ik_t$ term, the denominator of Equation (13) will always be smaller as compared to the denominator of Equation (8). This will cause the SIPIC02 to have a greater damping ratio as compared to SIPIC01. The overdamped response with greater damping ratio will lead to longer rise and settling time. By increasing k_p or k_i gains, the rise and settling time of SIPIC02 have a greater amount of reduction as compared to SIPIC01. The performance under loaded condition is similar to the result under no load condition.

7.2 Control Performance

The simulation for speed control at 100 rad/s for k_p = 5, k_i =10 under no load condition is shown in Figure 7 while the experimental testing for speed control at 100 rad/s for k_p = 5, k_i =10 under no load condition is shown in Figure 8. Based on Figure 7, PI consists of the shortest rise and settling time, whereas SIPIC02 has the longest rise and settling time. PI experienced overshoot while both SIPIC01 and SIPIC02 did not experience overshoot. Tables 5 and 6 summarise the rise time, settling time and percentage overshoot of PI, SIPIC01 and SIPIC02 under no load condition. According to Table 5, increasing k_p or k_i gains will reduce the rise and settling time for PI, SIPIC01 and SIPIC02. When the k_p is 1, PI has the shortest rise and settling time while SIPIC02 has the longest rise and settling time. The controllers are said to have reached their lowest boundary of rise and settling time when the k_p is ≥ 5. Therefore, all controllers consist of similar rise and settling time. According to Table 6, there is no overshoot for all controllers at 50 rad/s under no load condition. The same performance can be observed when the controllers are tested at 100 rad/s under the same condition. However, PI experienced overshoot when k_i is equal to 10. When k_p increases, the percentage overshoot decreases. This can be explained by Equation (14) where the k_p is directly proportional to the damping ratio. When the damping ratio increases, the percentage overshoot decreases. The rise time and settling time for both SIPIC01 and SIPIC02 reduced by increasing k_p or k_i gains without experiencing overshoot. This is due to the decoupling effect of k_p or k_i gains in SIPIC01 and SIPIC02. By comparing SIPIC01 and SIPIC02, SIPIC01 has a much shorter rise and settling time while both of them do not experience overshoot. Hence, it can be said that SIPIC01 is better in dynamic performance as compared to SIPIC02.

Table 4. The response of simulation for decoupling effect for PI, SIPIC01 and SIPIC02 under no load condition

k_p	k_i	1000 rpm									2000 rpm								
		Rise Time (s)			Settling Time (s)			Overshoot (%)			Rise Time (s)			Settling Time (s)			Overshoot (%)		
		PI	SIPIC01	SIPIC02	PI	SIPIC01	SIPIC02	PI	SIPIC01	SIPIC02	PI	SIPIC01	SIPIC02	PI	SIPIC01	SIPIC02	PI	SIPIC01	SIPIC02
1	1	2.196	2.196	5.069	2.996	2.997	6.997	0	0	0	2.196	2.196	5.069	2.996	2.997	6.997	0	0	0
1	5	0.595	1.202	2.696	2.138	1.642	3.667	23.444	0	0	0.595	1.202	2.696	2.138	1.642	3.667	23.444	0	0
1	10	0.392	1.128	2.435	2.42	1.558	3.316	37.060	0	0	0.392	1.128	2.435	2.420	1.558	3.316	37.060	0	0
1	15	0.309	1.111	2.352	2.712	1.536	3.205	44.739	0	0	0.309	1.111	2.352	2.712	1.536	3.205	49.926	0	0
1	20	0.263	1.105	2.312	2.952	1.526	3.152	49.925	0	0	0.263	1.105	2.312	2.952	1.526	3.152	49.926	0	0
5	1	2.201	0.752	0.983	6.264	1.392	1.846	0	0	0	2.201	0.752	0.983	6.264	1.392	1.846	0	0	0
5	5	0.438	0.439	0.555	0.600	0.601	0.786	0	0	0	0.438	0.439	0.555	0.600	0.601	0.786	0	0	0
5	10	0.318	0.394	0.496	1.088	0.534	0.681	6.702	0	0	0.318	0.394	0.495	1.088	0.534	0.681	6.702	0	0
5	15	0.265	0.380	0.475	1.079	0.518	0.650	11.925	0	0	0.265	0.380	0.475	1.079	0.518	0.650	11.925	0	0
5	20	0.233	0.374	0.465	0.977	0.512	0.636	16.048	0	0	0.233	0.374	0.465	0.977	0.512	0.636	16.049	0	0
10	1	0.345	0.307	0.329	5.656	0.704	0.857	0	0	0	0.345	0.324	0.350	5.656	0.707	0.883	0	0	0
10	5	0.261	0.240	0.268	0.455	0.342	0.400	0	0	0	0.261	0.259	0.289	0.455	0.366	0.430	0	0	0
10	10	0.219	0.219	0.248	0.300	0.301	0.348	0	0	0	0.219	0.242	0.270	0.300	0.331	0.379	0	0	0
10	15	0.195	0.211	0.239	0.252	0.288	0.330	2.564	0	0	0.195	0.236	0.261	0.252	0.323	0.363	2.564	0	0
10	20	0.178	0.207	0.234	0.225	0.283	0.321	4.884	0	0	0.178	0.234	0.257	0.225	0.32	0.355	4.884	0	0
15	1	0.187	0.184	0.189	2.650	0.360	0.409	0	0	0	0.187	0.231	0.237	2.65	0.395	0.456	0	0	0
15	5	0.170	0.164	0.017	0.294	0.240	0.266	0	0	0	0.170	0.210	0.222	0.294	0.289	0.320	0	0	0
15	10	0.156	0.153	0.166	0.228	0.216	0.239	0	0	0	0.156	0.202	0.214	0.228	0.271	0.294	0	0	0
15	15	0.145	0.149	0.161	0.200	0.207	0.228	0	0	0	0.145	0.200	0.210	0.200	0.267	0.286	0	0	0
15	20	0.137	0.146	0.158	0.183	0.203	0.222	1.353	0	0	0.137	0.199	0.208	0.183	0.265	0.282	1.353	0	0
20	1	0.130	0.139	0.140	0.251	0.232	0.244	0	0	0	0.130	0.200	0.203	0.251	0.296	0.312	0	0	0
20	5	0.124	0.129	0.135	0.202	0.189	0.203	0	0	0	0.124	0.191	0.197	0.202	0.255	0.272	0	0	0
20	10	0.118	0.124	0.131	0.176	0.175	0.189	0	0	0	0.118	0.188	0.193	0.176	0.245	0.259	0	0	0
20	15	0.113	0.121	0.128	0.161	0.169	0.182	0	0	0	0.113	0.187	0.191	0.161	0.243	0.254	0	0	0
20	20	0.109	0.120	0.127	0.150	0.166	0.178	0	0	0	0.109	0.186	0.190	0.150	0.242	0.251	0	0	0

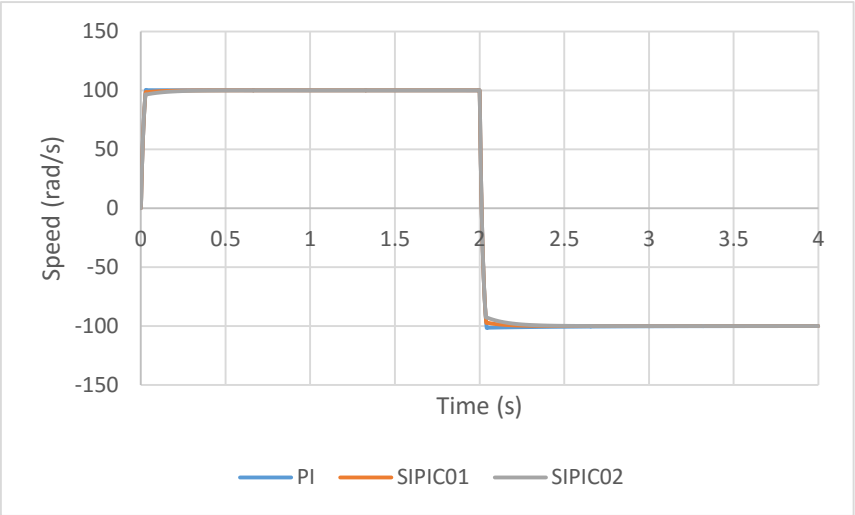


Figure 7. Simulation for speed control at 100 rad/s for k_p = 5, k_i =10 under no load condition.

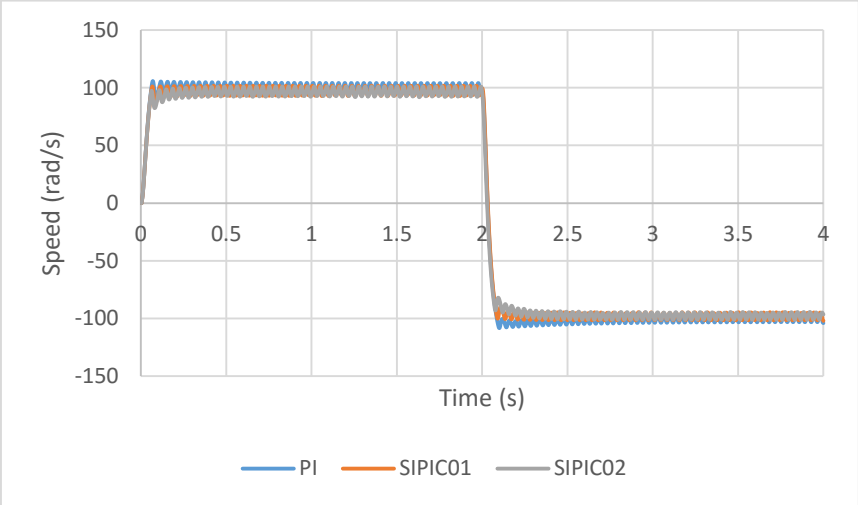


Figure 8. Experimental testing for speed control at 100 rad/s for k_p = 5, k_i =10 under no load condition.

Tables 7 and 8 summarise the rise time, settling time and percentage overshoot of PI, SIPIC01 and SIPIC02 under load 1 (mild steel) condition. According Table 7, the average rise and settling time of PI, SIPIC01 and SIPIC02 are longer compared to no load condition which is due to the higher moment of inertia. The PI experienced inconsistent settling time with increasing k_p or k_i. This is due to the coupling effect of k_p or k_i as both of them affect each other in the response. According to Table 8, SIPIC01 experience insignificant amount of overshoot which is less than 1.2 % when k_i is equal to 10. Tables 9 and 10 summarise the rise time, settling time and percentage overshoot of PI, SIPIC01 and SIPIC02 under load 2 (aluminium) condition. As shown in Table 9 and 10, the controllers have the similar performance to the load 1 condition. The only difference is that all controllers have shorter average rise and settling time which is due to the lower moment of inertia. Besides, SIPIC02 experienced overshoot under load 2 condition. However, the amount is insignificant.

Table 5. The rise time and settling time of PI, SIPIC01 and SIPIC02 under no load condition

Speed (rad/s)	k_p	k_i	Rise Time (s)			Settling Time (s)		
			PI	SIPIC01	SIPIC02	PI	SIPIC01	SIPIC02
50	1	1	0.009	0.011	0.518	0.742	0.708	2.427
	1	5	0.008	0.009	0.377	0.106	0.143	1.758
	1	10	0.007	0.008	0.334	0.016	0.072	1.032
	5	1	0.006	0.006	0.006	0.010	0.010	0.010
	5	5	0.006	0.006	0.006	0.010	0.010	0.010
	5	10	0.006	0.006	0.006	0.010	0.010	0.010
	10	1	0.006	0.006	0.006	0.010	0.010	0.010
	10	5	0.006	0.006	0.006	0.010	0.010	0.010
	10	10	0.006	0.006	0.006	0.010	0.010	0.010
100	1	1	0.021	0.023	0.885	0.690	0.709	2.341
	1	5	0.020	0.021	0.678	0.029	0.143	2.021
	1	10	0.020	0.020	0.564	0.027	0.073	1.263
	5	1	0.020	0.020	0.020	0.027	0.027	0.027
	5	5	0.020	0.020	0.020	0.027	0.027	0.027
	5	10	0.020	0.020	0.020	0.027	0.027	0.027
	10	1	0.020	0.020	0.020	0.027	0.027	0.027
	10	5	0.020	0.020	0.020	0.027	0.027	0.027
	10	10	0.020	0.020	0.020	0.027	0.027	0.027

Table 6. The overshoot percentage of PI, SIPIC01 and SIPIC02 under no load condition

Speed (rad/s)	k_p	k_i	Overshoot (%)		
			PI	SIPIC01	SIPIC02
50	1	1	0	0	0
	1	5	0	0	0
	1	10	0	0	0
	5	1	0	0	0
	5	5	0	0	0
	5	10	0	0	0
	10	1	0	0	0
	10	5	0	0	0
	10	10	0	0	0
100	1	1	0	0	0
	1	5	0	0	0
	1	10	0.693	0	0
	5	1	0	0	0
	5	5	0	0	0
	5	10	0.462	0	0
	10	1	0	0	0
	10	5	0	0	0
	10	10	0.221	0	0

Table 7. The rise time and settling time of PI, SIPIC01 and SIPIC02 under load 1 condition

Speed (rad/s)	k_p	k_i	Rise Time (s)			Settling Time (s)		
			PI	SIPIC01	SIPIC02	PI	SIPIC01	SIPIC02
50	1	1	0.048	0.054	1.084	0.565	0.632	2.226
	1	5	0.038	0.042	0.792	0.051	0.067	2.001
	1	10	0.037	0.038	0.640	0.155	0.052	1.336
	5	1	0.037	0.037	0.037	0.047	0.047	0.047
	5	5	0.037	0.037	0.037	0.047	0.047	0.047
	5	10	0.037	0.037	0.037	0.047	0.047	0.047
	10	1	0.037	0.037	0.037	0.047	0.047	0.047
	10	5	0.037	0.037	0.037	0.047	0.047	0.047
	10	10	0.037	0.037	0.037	0.047	0.047	0.047
100	1	1	0.107	0.109	2.001	0.160	0.630	1.830
	1	5	0.107	0.107	1.619	0.424	0.131	2.142
	1	10	0.107	0.107	1.130	0.445	0.130	1.830
	5	1	0.107	0.107	0.107	0.130	0.130	0.130
	5	5	0.107	0.107	0.107	0.130	0.130	0.130
	5	10	0.107	0.107	0.107	0.460	0.130	0.130
	10	1	0.107	0.107	0.107	0.130	0.130	0.130
	10	5	0.107	0.107	0.107	0.130	0.130	0.130
	10	10	0.107	0.107	0.107	0.130	0.130	0.130

Table 8. The overshoot percentage of PI, SIPIC01 and SIPIC02 under load 1 condition

Speed (rad/s)	k_p	k_i	Overshoot (%)		
			PI	SIPIC01	SIPIC02
50	1	1	0	0	0
	1	5	0.822	0	0
	1	10	9.934	0.339	0
	5	1	0	0	0
	5	5	0.362	0	0
	5	10	2.694	0.296	0
	10	1	0	0	0
	10	5	0.829	0	0
	10	10	1.974	0.804	0
100	1	1	0	0	0
	1	5	13.417	0	0
	1	10	23.940	1.173	0
	5	1	0	0	0
	5	5	3.406	0	0
	5	10	8.743	0.353	0
	10	1	0	0	0
	10	5	1.834	0	0
	10	10	4.608	0.302	0

Table 9. The rise time and settling time of PI, SIPIC01 and SIPIC02 under load 2 condition

Speed (rad/s)	k_p	k_i	Rise Time (s)			Settling Time (s)		
			PI	SIPIC01	SIPIC02	PI	SIPIC01	SIPIC02
50	1	1	0.022	0.025	0.728	0.685	0.684	2.398
	1	5	0.017	0.020	0.544	0.031	0.116	1.925
	1	10	0.016	0.018	0.465	0.024	0.041	1.164
	5	1	0.016	0.016	0.016	0.022	0.022	0.022
	5	5	0.016	0.016	0.016	0.022	0.022	0.022
	5	10	0.016	0.016	0.016	0.022	0.022	0.022
	10	1	0.016	0.016	0.016	0.022	0.022	0.022
	10	5	0.016	0.016	0.016	0.022	0.022	0.022
	10	10	0.016	0.016	0.016	0.022	0.022	0.022
100	1	1	0.049	0.052	1.572	0.547	0.685	2.174
	1	5	0.049	0.049	1.088	0.060	0.115	2.103
	1	10	0.049	0.049	0.834	0.194	0.061	1.533
	5	1	0.049	0.049	0.049	0.060	0.060	0.060
	5	5	0.049	0.049	0.049	0.060	0.060	0.060
	5	10	0.049	0.049	0.049	0.060	0.060	0.060
	10	1	0.049	0.049	0.049	0.060	0.060	0.060
	10	5	0.049	0.049	0.049	0.060	0.060	0.060
	10	10	0.049	0.049	0.049	0.060	0.060	0.060

Table 10. The overshoot percentage of PI, SIPIC01 and SIPIC02 under load 2 condition

Speed (rad/s)	k_p	k_i	Overshoot (%)		
			PI	SIPIC01	SIPIC02
50	1	1	0	0	0
	1	5	0	0	0
	1	10	0.697	0	0
	5	1	0	0	0
	5	5	0.635	0.081	0
	5	10	1.723	0.485	0
	10	1	1.325	1.263	1.132
	10	5	1.772	1.496	0.888
	10	10	2.144	1.697	0.588
100	1	1	0	0	0
	1	5	1.924	0	0
	1	10	12.639	0	0
	5	1	0	0	0
	5	5	0.746	0	0
	5	10	3.351	0	0
	10	1	0	0	0
	10	5	0.650	0	0
	10	10	1.959	0.095	0

Based on the rise time, settling time and overshoot percentage under three load cases, it can be said that SIPIC01 and SIPIC02 are better in dynamic performance as compared to PI. By comparing SIPIC01 and SIPIC02, SIPIC01 has a much faster rise and settling time. Although the percentage overshoot of SIPIC01 is slightly greater as compared to SIPIC02, the amount of overshoot experienced by SIPIC01 and SIPIC02 are insignificant. Therefore, it can be said that SIPIC01 is better in dynamic performance as compared to SIPIC02.

8. Conclusion

In conclusion, both SIPIC01 and SIPIC02 consist of decoupling feature which allow them to produce a performance with coexistence of zero or minimum overshoot and short settling time. However, by comparing SIPIC01 and SIPIC02, SIPIC02 consists of longer rise and settling time. Hence, it can be concluded that SIPIC01 is better than SIPIC02 in term of dynamic performance. As shown in Tables 6, 8 and 10, SIPIC02 does not experience overshoot except under loading 2 condition at 50 rad/s. The zero overshoot performance of SIPIC02 may be due to its longer rise and settling time and cannot reach its maximum speed with the simulated period. In future, work will be conducted to verify the stability of SIPIC02. From this research, increasing k_p or k_i gains gives a reduction trend for the rise and settling time of SIPIC02. A more in-depth study of the dynamic performance and mathematical model of SIPIC02 by determining the integral output and torque will be performed to investigate this observation.

References

[1] R. C. Dorf and R. H. Bishop, “Introduction to Control Systems,” *Mod. Control Syst.*, pp. 2–23, 2000.

[2] W. Yan, D. Wang, P. Jia, and W. Li, “The PWM speed regulation of DC motor based on intelligent control,” *Syst. Eng. Procedia*, vol. 3, pp. 259–267, 2012.

[3] P. M. Menghal and A. J. Laxmi, “Dynamic analysis & artificial intelligent control of induction motor drives,” *Annu. IEEE India Conf.*, no. December, pp. 1–6, 2014.

[4] S. K. Suman and V. K. Giri, “Performance Analysis of optimization techniques and Intelligence Techniques for speed control of DC motor,” *African J. Basic Appl. Sci.*, vol. 9, no. 2, pp. 97–104, 2017.

[5] X. L. Li, J. G. Park, and H. B. Shin, “Comparison and evaluation of anti-windup PI controllers,” *J. Power Electron.*, vol. 11, no. 1, pp. 45–50, 2011.

[6] T. L. Chiah, C. L. I. H. Hoo, E. Chin, and Y. A. U. Chung, “Hardware Simulation of a New Anti-Windup PI Control For Motor Speed Application,” *J. Eng. Sci. Technol.*, pp. 43–57, 2017.

[7] C. L. Hoo, S. M. Haris, E. C. Y. Chung, and N. A. N. Mohamed, “The generalisation and decoupling mode of PI-based control: theoretical approach,” *ICIC Express Lett.*, vol. 4, no. 5, pp. 1–6, 2010.

[8] C. L. Hoo, E. C. Y. Chung, S. M. Haris, and N. A. N. Mohamed, “Steady-state integral proportional integral controller for PI motor speed controllers,” *J. Power Electron.*, vol. 9, no. 6, pp. 1777–1782, 2015.

[9] C. L. Hoo, S. M. Haris, C. Y. E. Chung, and N. A. N. Mohamed, “Steady-state integral proportional integral controller for PI motor speed controllers: a theoretical approach,” *ICIC Express Lett.*, vol. 4, no. 5, pp. 1–6, 2010.

eureca 2017 – Conference Paper
Paper Number 2ME12

Design and Analysis of a Mechanical Regenerative Braking System

Matthew Toh Xiang Wen, Douglas Tong Kum Tien*

School of Engineering, Faculty of Built Environment, Engineering, Technology and Design, Taylor's University, Malaysia.

**douglaskumtien.tong@taylors.edu.my*

Abstract

Regenerative braking systems are on the rise in conjunction as fossil fuels are being depleted. The major forms of regenerative braking systems include electrical and mechanical systems, with the former at present the more widely adopted. Mechanical systems are still feasible, including the possible hybrid systems of two mechanical energy recovery systems. This research project was conducted through an initial literature review of related studies to determine a gap in the body of knowledge, followed by the generation of various conceptual theoretical designs. These systems were analysed based on their advantages and disadvantages to energy storage, usage, and maintenance. Based on the analysis, the most promising concept was determined to be the one that combines the flywheel and the pneumatic energy recovery systems into one system. Comparisons between existing systems and this conceptual hybrid system were performed. A theoretical design of the systems were produced through the use of SolidWorks version 2015 to visualise the design. These designs were simulated through the use of Microsoft Excel version 2016 using a validated analytical model. Data obtained from the simulations were analysed. Revisions of the simulation were conducted by varying parameters. The results showed that angular velocity heavily affects the power losses and thus energy efficiency of the hybrid system. The results validated the hypothesis that the hybrid system will provide an increase in efficiency given the most preferred parameters are chosen. However, lower total energy available may not lead to reduced fuel consumption of everyday vehicles. Future work may be done to further improve the hybrid system to improve the final energy available for the reduction of fuel usage.

Keywords: Conventional regenerative braking systems, Hybrid regenerative braking systems, Flywheel energy recovery system, Pneumatic energy recovery system, Energy efficiency.

1. Introduction

The slowing down or stopping of a moving automotive vehicle or machine is known as braking. Braking is commonly performed through mechanical means such as the use of physical brakes that apply the concept of friction by forcing the stationary brake pads against the brake discs that are fixed and rotate with the driveshaft. Consequently, the angular velocity of the wheels will be reduced and the vehicle is slowed down and eventually stopped. Heat will be generated as kinetic energy from the driveshaft is transformed into heat energy as friction occurs between the brake pads and discs when they come into contact. The dissipation of this heat to the surroundings could cause energy losses of up to 30 percent [1]. This increases fuel consumption of the vehicle as the energy lost has to be recovered. A regenerative braking system (RBS) is a system designed to capture, store, and use a large amount of this energy that is usually lost.

Most existing road vehicles run on fuel to power an internal combustion engine (ICE) which in turn powers the driveshaft and the wheels of the vehicle. Efforts are being made to research RBS to reduce the dependence on fossil fuels by ICEs, with these RBS typically being mechanical, electrical, or chemical systems that allow the stored energy to be used to accelerate the vehicle. High-tech hybrid systems have been produced which combine the conventional brakes with a RBS, more recently being energy storage systems in the form of batteries. A RBS usually combines one method of energy storage with one method of energy conversion [2]. The electrical storage hybrid vehicles appeal to the consumer market with the environment-friendly concept and reduction in fuel costs for the end user [3].

A large amount of energy is usually lost during transformations of energy. The conservation of energy states that energy cannot be created or destroyed but only transformed. Since energy is lost due to various factors such as friction, air resistance, and electrical resistance, the increase in the number of energy transformations will only cause a decrease in energy efficiency. A battery storage system shows this effect as it contains energy conversions of mechanical to electrical and to chemical to store the energy from braking. Besides the losses of energy, batteries are made up of rare-earth elements, increasing maintenance costs due to replacement of batteries after several years of use [4]. Furthermore, the batteries are only operated in 55% to 65% of the total state of charge due to discharging efficiencies and to prolong battery life [5].

Currently, the public is becoming more aware about the kinetic energy recovery systems (KERS) that use batteries to store energy as they are being integrated into the latest models of everyday road vehicles. The electrical KERS however do have direct limitations to braking, as they are less effective at lower speeds and require conventional brakes to provide sufficient braking. This is important when driving conditions vary, such as low-friction road surfaces or when driving in the rain.

Another form of energy recovery systems (ERS) also takes advantage of the inertia of the vehicle, converting kinetic energy of the moving wheels and driveshaft to stored mechanical energy and then releasing the energy back to the driveshaft for acceleration. Examples of these ERS include flywheel systems, pressurised accumulator systems, elastomeric systems, and regenerative shock absorber systems [4].

As the wheels of a vehicle are rotating during motion, storage of energy in a rotational form would be able to reduce energy losses due to the reduced changes in forms of energy. The flywheel will store the energy in the form of rotational kinetic energy. Flywheels are popular mechanical energy recovery systems, as they have high power densities and are able to compete with batteries in power storage. Flywheel KERS have been used before and have shown up to 30% fuel reduction [4]. The flywheel KERS is simple in design with a clutch that connects the driveshaft to the flywheel during braking and thus helps with the braking of the vehicle while storing energy in the flywheel. A 65 kg flywheel KERS can store up to 60 kW of power and 580 kJ of energy for a 1800 kg vehicle [4].

Pressurised accumulators such as pneumatic or hydraulic systems use fluids that are pressurised to store energy. Gear pumps connect to the driveshaft that are driven to push air into the accumulators to be stored. A pneumatic accumulator can store high amounts of energy. Storage of up to 400 kJ or energy, with hydraulic accumulators storing about 90 kJ of energy have been shown [4]. Energy storage is however limited to the size of the accumulator and efficiencies of accumulators at variable speeds. At low speeds, fixed mechanical losses cause drops in efficiency [6]. Elastomeric systems are able to store energy in the form of torsional energy if connected to the driveshaft and a fixed end, but store low energy. Storage of energy of about only 30 kJ is available, albeit for a long time [4]. The elastomer will however require frequent replacements due to decomposition caused by hysteresis. Regenerative shock absorbers recover energy from vertical oscillations of the vehicle, but only show at most a 10% improvement in efficiency [4]. Furthermore, smooth surfaces may not provide the maximum efficiency increase and may not be worth implementing due to the additional mass of the system.

Based on the review of literature conducted, this research focused on the simulation of a theoretical design of a mechanically-exclusive system that combines two mechanical KERS which would allow for the energy conversions to be reduced. This would thus provide a possible increase in the amount of power delivered to the wheels and reduce the amount of fuel used. Eventually, fuel costs could be reduced.

2. Research Methodology

2.1 Conceptualised Theoretical Designs

Various theoretical designs of hybrid mechanical RBS were conceptualised based on a critical literature review of mechanical systems. The designs were then compared and analysed amongst each other to determine the most suitable design to be further analysed and simulated through the use of energy equations and theories. A theoretical design of a non-hybrid mechanical RBS was produced. This mechanical system was used to compare the changes in energy efficiency through the implementation of the hybrid mechanical RBS.

2.1.1 Advantages and Disadvantages of Energy Recovery Systems

The previously mentioned ERS were further analysed through their various advantages and disadvantages to energy storage, energy losses, longevity of life and more. Table 2.1 summarises these advantages and disadvantages for each ERS.

Table 2.1: Advantages and disadvantages of various energy recovery systems

Energy Recovery System	Advantages	Disadvantages
Electric	Proven technology Readily available in the market •	Costly due to replacements Losses of energy due to energy transformations Long recharging times
Flywheel	Reduced losses during energy capture High energy storage capabilities Technology well proven	Loss of rotational energy over time due to friction and air resistance •
Hydraulic/Pneumatic	Very low losses during energy storage Not as costly as other ERS	Limited energy storage
Elastomeric	Ejection characteristic for high acceleration	Low life span Limited energy storage

A large amount of research is put into hybrid electrical-mechanical RBS and are now one of the most attractive fields of research for energy regeneration. However, based on the literature reviewed on the ERS available, a hybrid mechanical RBS is a possible avenue for theoretical designs. Mechanical systems such as flywheels have the ability to capture and store high amounts of energy, while hydraulic or pneumatic systems are not costly and have low energy storage losses. The accumulator system is also able to charge and discharge more periodically than batteries that require lengthy recharging durations. By combining two of these mechanical ERS based on their advantages in energy storage, losses, or lifespan, more energy efficient systems could be produced.

2.1.2 Selection of Design for Analysis

These hybrid system designs include various combinations of the flywheel, hydraulic, and elastomeric ERS. As hybrid RBS consist of two main steps of energy harvesting and energy storage, the hybrid mechanical system will implement the same concept with two mechanical systems to collect and store energy from braking respectively.

As energy harvesting or capture systems require the ability to store a high initial amount of energy from the high angular velocity of the wheels of a vehicle, high storage capable systems are preferred. Flywheel systems fit this category as they are able to store high amounts of energy while keeping the energy in the form of rotational energy, minimising the number of energy transformations and thus reducing the energy losses incurred by the system. A hollow cylinder flywheel is also able to minimise the chance of disintegration at to high speeds [7].

Hydraulic, pneumatic and elastomeric systems are not as suitable for the initial energy capture and storage as the flywheel due to their limited energy storage. Hydraulic and pneumatic accumulators are limited to the amount of energy stored based on the size of the accumulators, while elastomerics under high usage undergo hysteresis, requiring frequent replacements.

With flywheels as the most suitable selection for initial energy capture and storage, a secondary energy storage system in the form of either the pressurised accumulator or elastomer is considered to store a portion of the initial energy. The accumulator has low energy losses which allows efficient energy storage, while the elastomer has an ejection characteristic that allows for acceleration during energy transfer back to the flywheel. As the flywheel will be storing energy as rotational energy, the transfer to the secondary energy storage in the form of rotation is preferred, once again to reduce losses. Both the accumulator and elastomer are able to utilise rotational motion, with accumulators running on gear pumps and elastomers storing energy through torsion. However, the decomposition of the elastomers in elastomeric systems are not avoidable. Thus, the pneumatic or hydraulic accumulators would be more effective in terms of lifespan and maintenance. As pneumatic accumulators use air or gas as opposed to liquids such as oil that is used by hydraulics, they are preferred for high speed applications due to the lower viscosity of gases. With potentially high speeds of the wheels and thus the flywheel, the pneumatic accumulator is the more viable option.

A direct comparison was between a non-hybrid mechanical system and the hybrid mechanical RBS was done through simulations. As the hybrid mechanical RBS selected to be theoretically designed was the flywheel-pneumatic system, the conventional mechanical RBS that was simulated for comparison was be the flywheel RBS that only uses a flywheel to store energy during braking and returns it to the driveshaft for acceleration. This comparison would show any change in efficiency due to the addition of the pneumatic accumulator to the flywheel that forms the hybrid mechanical RBS.

2.2 Design of Regenerative Braking Systems

The combination of the two mechanical ERS to form a hybrid mechanical RBS is shown in Figure 2.1, with the initial energy capture and storage system directly collecting energy during braking from the driveshaft connected to the wheel, and then transferring the energy captured to the secondary energy storage system. The energy is stored over time and transferred back to the initial energy storage system and thus to the driveshaft to accelerate the wheels and the vehicle.

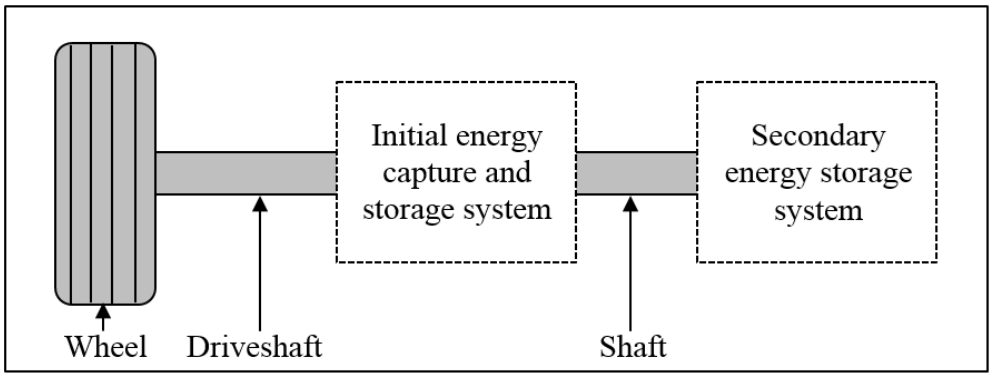


Figure 2.1: General combination of systems for conceptualised hybrid mechanical RBS

2.2.1 Flywheel Regenerative Braking System

Flywheels by themselves are able to store large amounts of energy but lose energy over time due to air resistance to the rotation of the flywheel itself and friction losses of the bearing. Figure 2.2 below shows the flywheel that connects to the driveshaft through a conventional clutch system, such as those found in manual transmission vehicles. As the system is not a hybrid system, only one ERS is used to both capture and store energy. This system was designed using SolidWorks version 2015 and is not dimensionally accurate.

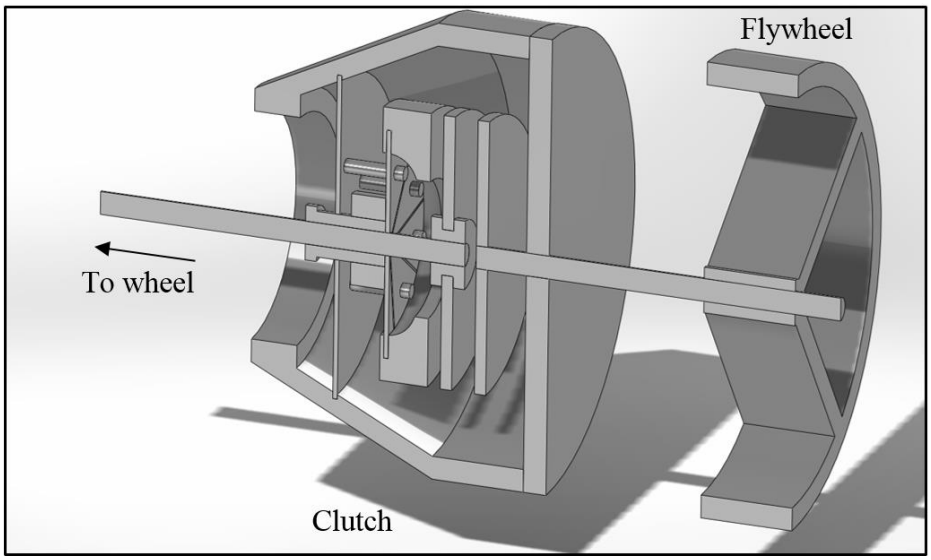


Figure 2.2: Design of the flywheel RBS

2.2.2 Flywheel-Pneumatic Regenerative Braking System

As flywheels lose energy over time due to drag and friction between bearings, the addition of an accumulator to store a portion of the energy would reduce the energy losses of the flywheel, as accumulators lose much less energy over time. Releasing this energy back to the flywheel provides higher energy that can be transferred back to the driveshaft for acceleration.

Figures 2.3 and 2.4 show the theoretical design of the flywheel-pneumatic hybrid RBS using SolidWorks version 2015. The rotation of the wheel that is fixed to the driveshaft will transfer the rotational energy during braking to the flywheel through the activation of a conventional clutch system. A similar clutch is used in between the flywheel and pneumatic accumulator to transfer energy between the two systems. The accumulator is connected to the clutch by a shaft to the gear pump that draws air into the accumulator. A secondary gear is used to transfer the energy back to the flywheel in the same rotational direction. The design is not dimensionally accurate

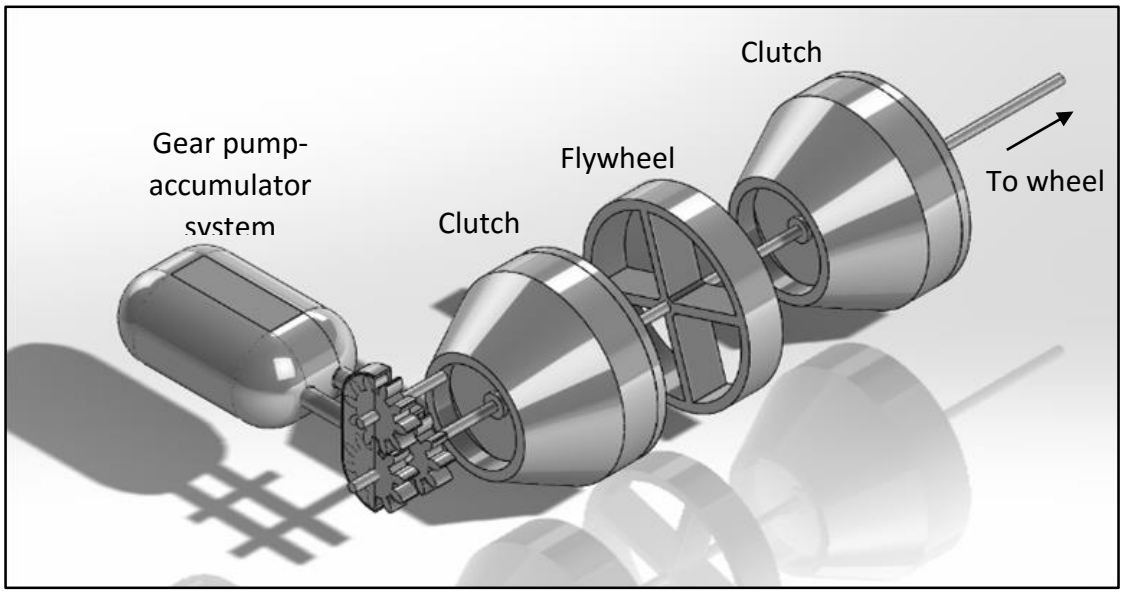


Figure 2.3: Theoretical Design of the flywheel-pneumatic hybrid RBS

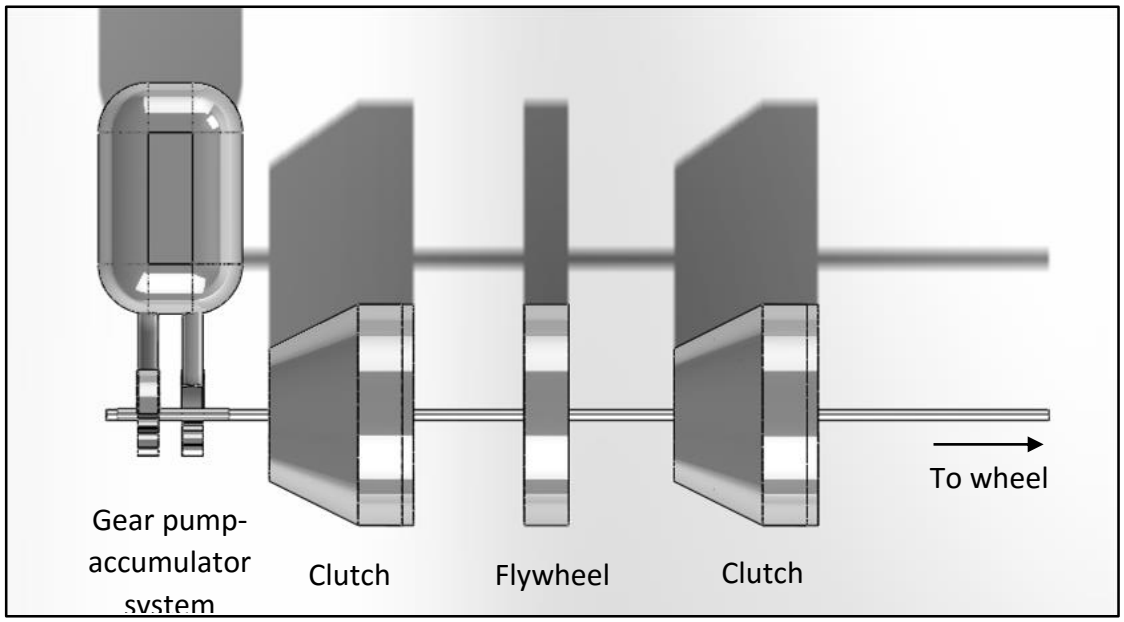


Figure 2.4: Top view of the flywheel-pneumatic hybrid RBS

2.3 Simulation and Analysis

The simulations of the theoretical designs produced were performed using Microsoft Excel version 2016. This computer software was input with various parameters and energy equations for the flywheel RBS and the flywheel-pneumatic hybrid RBS.

2.3.1 Parameters

The flywheel was simulated with a set of variable parameters shown in Table 2.2. These variables determined the energy storage and losses of the ERS of the systems. The values of the variables shown in the table were applied to the simulation of the system and then varied to determine the effect of these parameters on the energy efficiency of the system. The flywheel was chosen to be a rim type with spokes to reduce chance of disintegration of material [7]. The angular velocity of the flywheel was chosen based on low speed applications below 3000 rpm and high-speed applications between 3000 rpm and 60000 rpm. The flywheel was chosen to be of S-glass epoxy material as it has more than double the energy density value of common cast iron flywheels [8]. The mass was varied around the average flywheel mass of around 65 kg [4]. This volume change was done by reducing thickness of the flywheel while the diameter values were kept constant. This was done by determining the volume of the cylinder based on the varying mass to thus alter the thickness value as shown in Eq. (1):

Volume of Flywheel, V_f (m^3):

$$V_f = \pi\, t \left[\left(\frac{d_o}{2}\right)^2 - \left(\frac{d_i}{2}\right)^2\right] \quad (1)$$

Where

t = Flywheel thickness (m)
d_o = Outer diameter of the flywheel (m)
d_i = Inner diameter of the flywheel (m)

Table 2.2: Initial variable flywheel parameters for simulations

Flywheel parameter	**Value**
Mass, m (kg)	70.00
Outer diameter, d_o (m)	0.50
Inner diameter, d_i (m)	0.25
Thickness, T_f (m)	0.05

Table 2.3 shows constant parameters such as the density of air, dynamic viscousity of air, and gravitational acceleration.

Table 2.3: Parameters for simulations

Constant	Value
Density of air, ρ_α (kg/m^3)	1.225
Dynamic viscousity of air, β_α (Ns/m^2)	1.983×10^{-5}
Gravitational acceleration, g (m/s^2)	9.810

Parameters for the flywheel ball bearing are shown in Table 2.4. The ball bearing is used to connect the flywheel to the shaft and is a deep groove ball bearing. They include the constant friction coefficient of ball bearings, radius of the shaft that connects to the ball bearings, and the corrective force factor for unbalanced and gyroscopic forces [9].

Table 2.4: Ball bearing parameters for simulations

Ball bearing parameter	Value
Friction coefficient, μ	1.50×10^{-3}
Radius of shaft, r_s (m)	0.05
Corrective force factor, γ	1.00

The clutch discs were simulated with parameters based on technical specifications of clutch disc manufacturers [10]. These values are shown in Table 2.5.

Table 2.5: Clutch discs parameters for simulations

Clutch discs parameter	Value
Clutch mass, M_C (kg)	5.44311
Clutch diameter, D_C (m)	0.18415
Clutch radius, r_C (m)	0.09208

2.3.2 Energy equations

The equations applied to simulate the two RBS include mass moment of inertia, energy storage, power losses, energy losses, and final energy efficiency equations. These equations are shown in Eq. (1) previously mentioned and Eqs. (2) to (13) as follows:

Mass moment of inertia of a flywheel, *I* (kg.m^2) [12]:

$$I = \frac{1}{2}.m.(r_o^2 + r_i^2) \quad (2)$$

Where

m = Mass of flywheel (kg)
r_o = Outer radius of flywheel (m)
r_i = Inner radius of flywheel (m)

Initial kinetic energy of a flywheel, KE_i (J) [7]:

$$KE_i = \frac{1}{2}.I.\omega^2 \quad (3)$$

Where

ω = Angular velocity of the flywheel (rad/s)

Power loss due to air resistance of a flywheel, $P_{a,l}$ (W) [9]:

$$P_{a,l} = 0.04.\rho_a^{0.8}.\beta_a^{0.2}.(\omega.r)^{2.8}.(2.r)^{1.8}.(\alpha + 0.33) \quad (4)$$

Where

ρ_α = Density of air (kg/m^3)
ρ_α = Dynamic viscosity of air (Ns/m^2)
ω = Angular velocity of the cylinder (rad/s)
r = Outer radius of the cylinder (m)
Geometric ratio, $\alpha = \frac{h}{2.r}$

Where
h = Thickness of the cylinder (m)
Power loss due to friction of bearings of a flywheel, $P_{b,l}$ (W) [9]:

$$P_{b,l} = \mu.\gamma.r_s.m.g.\omega_b \quad (5)$$

Where

μ = Friction coefficient
γ = Corrective force factor considering unbalanced and gyroscopic forces
r_s = Radius of the shaft (m)
m = Mass of the flywheel (kg)
g = Gravitational acceleration (m/s^2)
ω_b = Angular velocity of the bearing (rad/s)

Total power loss of a flywheel, P_T (W) [9]:

$$P_T = P_{\alpha,l} + P_{b,l} \quad (6)$$

Total energy lost due to power losses, E_l (J):

$$E_l = P_T \times t \quad (7)$$

Where

t = Time of flywheel rotation (s)
Final energy of the flywheel system, E_f (J):

$$KE_f = KE_i - E_l \quad (8)$$

Final angular velocity of the flywheel, ω_f (rad/s):

$$\omega_f = \sqrt{\frac{2 \times KE_f}{I}} \quad (9)$$

Final energy efficiency of the system, η_E (%):

$$\eta_E = \frac{KE_f}{KE_i} \times 100\% \quad (10)$$

Moment of inertia of clutch discs 1 and 2, I_1 and I_2 (kg.m^2) [13]:

$$I_1 = I_2 = \frac{1}{2} \times m_C \times r_C^2 \quad (11)$$

Where

m_C = Mass of clutch disc (kg)
r_C = Radius of clutch disc (m)

Energy loss due to clutch system, P_C (W) [14]:

$$E_C = \frac{I_1 I_2 \times (\omega_1 - \omega_2)^2}{2 I_1 I_2} \quad (12)$$

Where

ω_1 = Angular velocity of clutch disc 1 (rad/s)
ω_1 = Angular velocity of clutch disc 2 (rad/s)

Energy efficiency of gear pump-accumulator system, η_A (%) [15]:

$$\eta_S = \eta_{GP} \times \eta_A \times \eta_{GP} \quad (13)$$

Where

η_S = Efficiency of gear pump-accumulator system (%)
η_{GP} = Efficiency of gear pump (%)
η_A = Efficiency of pneumatic accumulator (%)

2.3.3 Assumptions

The simulations were run with various assumptions to the system and the environment surrounding it such as the following:

- Mass of the spokes of the flywheel were considered to be negligible
- The operation of the clutch system happens instantaneously
- Corrective force factor was assumed to be 1 based on assumption that gyroscopic forces do not highly affect the power losses due to bearing friction

- Dynamic viscousity of air based on assumption that air is at room temperature

3. Results and Discussion

3.1 Validation of the Analytical Model

The analytical model for simulations produced through the use of the equations previously found was validated with existing literature. The parameters that were set are as shown in Table 3.1, while the results are shown in Figure 3.1:

Table 3.1: Parameters provided by literature source used in simulation [16].

Parameter	Value
Outer diameter of flywheel, d_o (m)	0.330
Inner diameter of flywheel, d_i (m)	0
Average radius of ball bearing, r_b (m)	0.0385
Density of air, ρ_α (kg/m^3)	1.225
Dynamic viscousity of air, β_α (Ns/m^2)	1.983×10^{-5}

The flywheel from literature was that of a solid flywheel without an inner diameter usually due to the ring flywheel design. The radius of the ball bearing was averaged and assumed as the radius of shaft, r_s from Table 2.4.

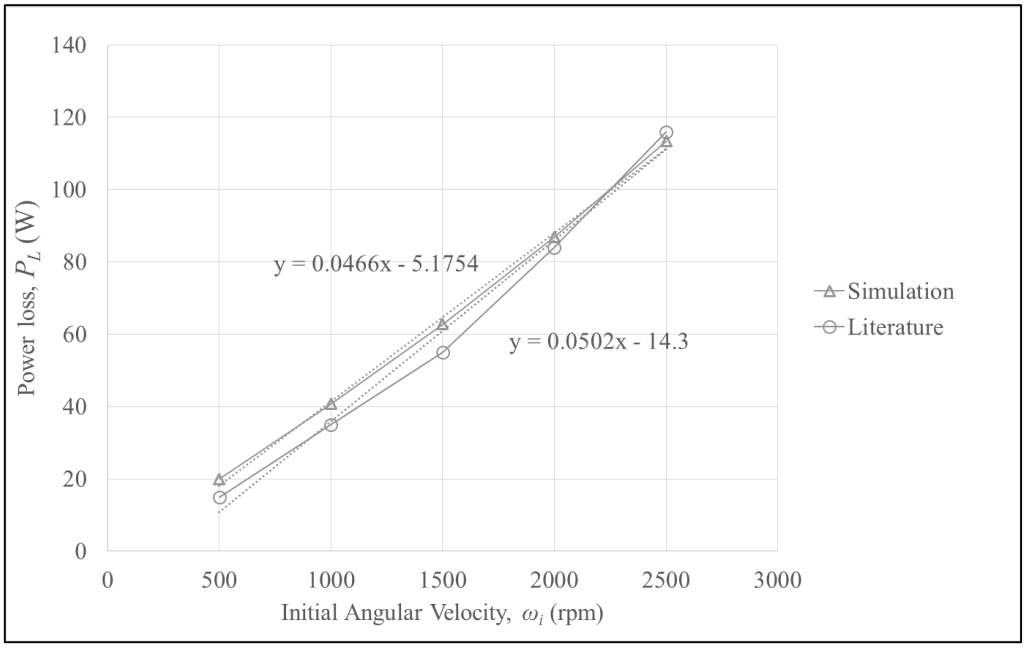


Figure 3.1: Comparison of power loss between simulation and literature source.

Figure 3.1 shows that the power loss differences between the simulation and literature are small, with the gradient difference of about only 7%. Power losses itself differ by about 5 to 7 W between the simulation and literature source.

Further comparisons with other literature sources that have mentioned that flywheels have about 70% to 90% efficiency for a short amount of time after the flywheel is left to rotate freely [17,18]. From the calculated efficiency of the simulated flywheel system using Eqs. (1) to (10), the results showed that at many varying parameters tested a 90% to 100% energy efficiency was available for the first few

seconds of the simulation. The values then drop quickly to below 90%, as in line with the information gained from the literature.

3.1 Comparison of Energy Efficiencies of Simulated Systems

3.1.1 Effect of Mass of Flywheel on Energy Efficiency

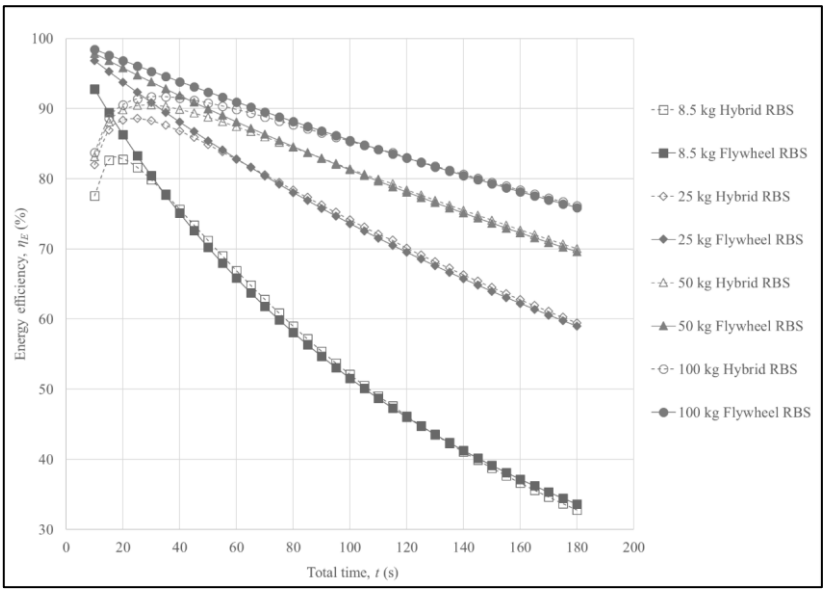


Figure 3.2: Effect of various flywheel masses on energy efficiency

Figure 3.2 shows that an overall heavier flywheel of 100 kg showed the best performance in terms of energy efficiency values, while lower weight flywheels of 8.5 kg and 25 kg showed higher improvements in the hybrid RBS over the Flywheel RBS counterparts. However, these improvements begin to decrease at a faster rate than the heavier flywheels, causing a limitation to the required total time for positive energy efficiency gains. Heavier flywheels will also cause more power to be required by the driveshaft from the engine to accelerate a heavier vehicle. This trade-off between weight and power may not be beneficial for the overall vehicle fuel efficiency.

3.1.2 Effect of Initial Angular Velocity on Energy Efficiency

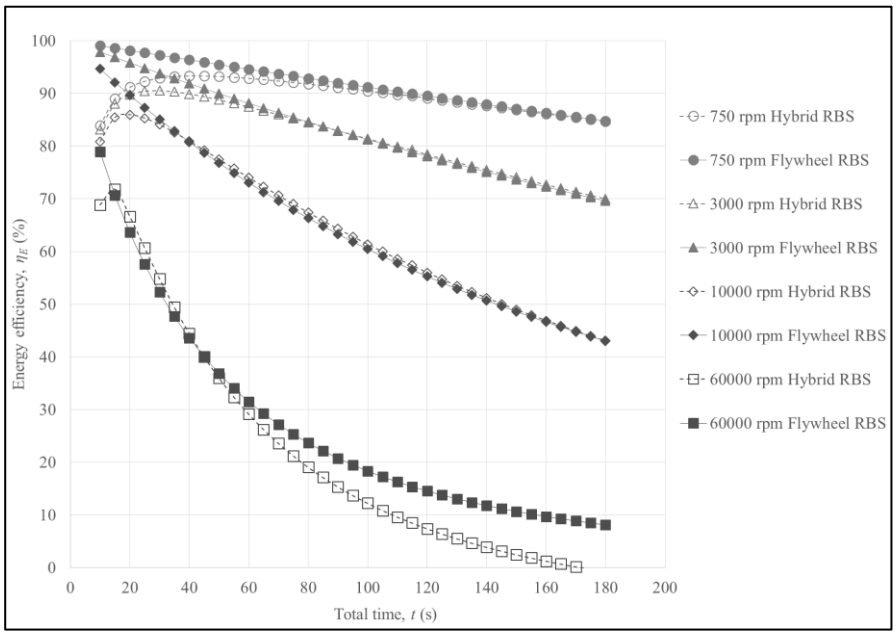


Figure 3.3: Effect of various initial angular velocities on energy efficiency

Figure 3.3 shows that the low angular velocity system of 750 rpm is the most energy efficient but also has the lowest maximum energy storage available. Thus, a low angular velocity may not be able to power a vehicle for acceleration as compared with a faster flywheel system that is less energy efficient but has more energy available to be used by the driver of the vehicle.

3.1.3 Effect of Energy Transfer and Storage Time on Energy Efficiency

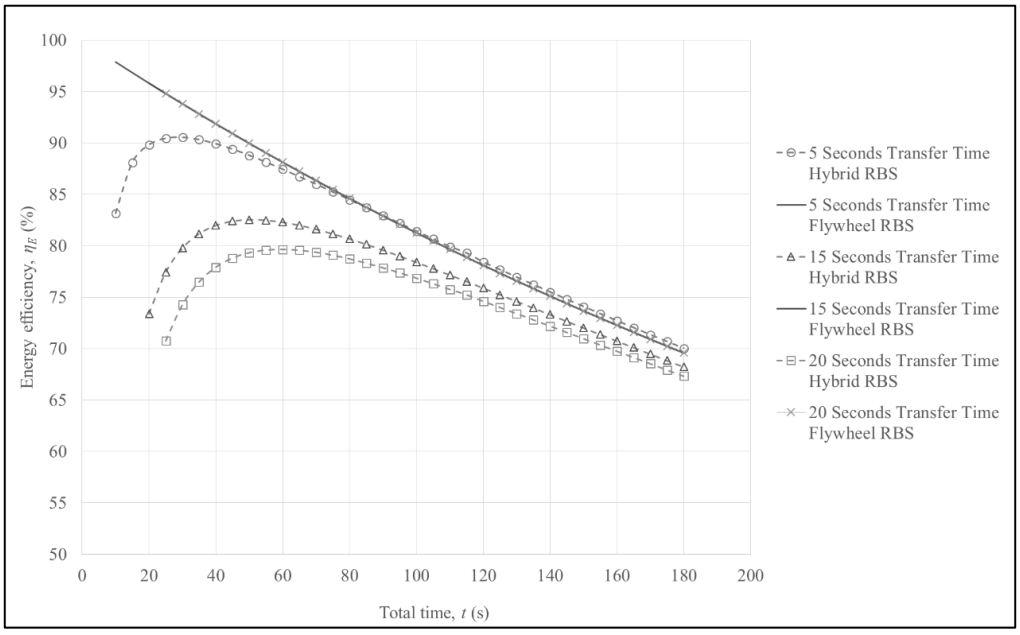


Figure 3.4: Effect of various transfer and storage times on energy efficiency

Figure 3.5 shows that the low transfer times show the highest energy efficiency values. However, the inconsistency of vehicle idle time during daily driving may not always call for total energy storage times of 180 seconds or less. As the energy efficiency of shorter transfer times close up on the energy efficiency provided by larger transfer times, an expected breakeven point and negative difference may cause the longer transfer times to be more efficient.

3.2 Comparison with Existing *Flybrid* Flywheel System

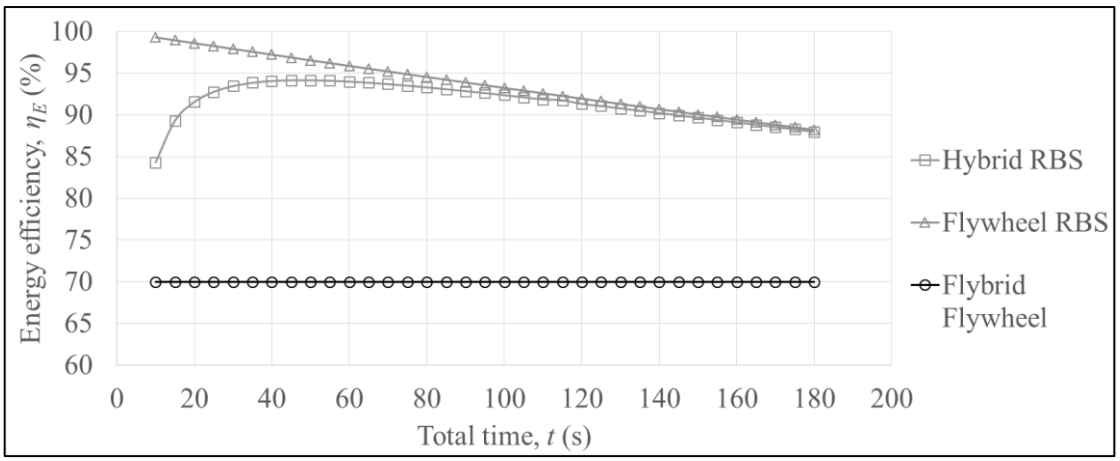


Figure 3.5: Comparison of simulated systems with existing *Flybrid* Flywheel system

Figure 3.5 shows the highest energy efficiency values for the flywheel and HRBS compared with the current *Flybrid* Flywheel system. The hybrid system was able to improve on the *Flybrid* Flywheel system, but was not able to surpass the flywheel system in terms of energy efficiency. This comparison between simulated and current systems is however not a direct comparison due to the very different parameters and the provided *Flybrid* Flywheel efficiency not dependent on the parameter or time. Specifically, the increase in mass of the flywheel will cause an increase in power needed by the vehicle to accelerate, while the lower mass *Flybrid* Flywheel system does not add as much to the total vehicle mass.

4.0 Conclusions and Future Work

The energy losses can be seen as factors that greatly affect the energy efficiencies of the systems. This is due to the high angular velocities that cause very high power losses to air resistance and bearing friction of the simulated. The simulation results have shown that the hybrid system that was theoretically designed and simulated is at times able to provide an improvement to energy efficiency to current systems based on the most suitable parameters and thus proves the research hypothesis to be true. However, overall energy values that are available for usage are not enough to take advantage of the energy efficiency due to the low angular velocity, which the *Flybrid* Flywheel system avoids by mitigating the losses.

The final findings are able contribute to the field of knowledge on a hybrid mechanical RBS regarding energy storage efficiency. Future projects could aim to produce working prototypes of these systems with or without losses to improve energy storage efficiency of the hybrid mechanical RBS simulated in this research project.

References

[1] P. Gupta, A. Kumar, and S. Deb, "Regenerative Braking Systems (Rbs) (Future of Braking Systems)," *International Journal of Mechanical And Production* Engineering, vol. 2, pp. 75–78, 2014.

[2] R. Ramakrishnan, S. S. Hiremath, and M. Singaperumal, "Theoretical investigations on the effect of system parameters in series hydraulic hybrid system with hydrostatic regenerative braking," *J. Mech. Sci. Technol.*, vol. 26, no. 5, pp. 1321–1331, 2012.

[3] U. Diego-Ayala, et al., "The mechanical hybrid vehicle: an investigation of a flywheel-based vehicular regenerative energy capture system," *Proc. Inst. Mech. Eng. Part D J. Automob. Eng.*, vol. 222, no. 11, pp. 2087–2101, 2008.

[4] Gabriel-Buenaventura, Alejandro, and B. Azzopardi, "Energy Recovery Systems for Retrofitting in Internal Combustion Engine Vehicles: A Review of Techniques," *Renew. Sustain. Energy Rev.*, vol. 41, pp. 955–964, 2015.

[5] J. B. M. William, C. David, "Comparison of regenerative braking technologies for heavy goods vehicles in urban environments," *J Automobile Engineering*, vol. 0, no. 0, pp. 1-14, 2012.

[6] S. J. Clegg, "A Review of Regenerative Braking Systems," Institute of Transport Studies, University of Leeds, Working Paper 471, 1996.

[7] H. Liu and J. Jiang, "Flywheel energy storage-An upswing technology for energy sustainability," *Energy Build.*, vol. 39, no. 5, pp. 599–604, 2007.

[8] A. Shinde, et al., "Design and Analysis of Flywheel for Different Geometries and Material," *Global Journal of Enterprise Information System*, vol. 9, no. 1, pp. 95-99, 2017.

[9] X. Zhang, C. Mi, "Vehicle Power Management", New York: Springer, 2011, pp. 86-89.

[10] Tilton Engineering. "Ford Clutch-Flywheel Assemblies". Internet: http://tiltonracing.com/product/ford-clutch-flywheel-assemblies/, 2017 [Oct. 15, 2017].

[12] B. Bolund, et al., "Flywheel energy and power storage systems", *Renewable and Sustainable Energy Reviews*, vol. 11, pp. 235-258.

[13] C. R. Nave. "Thick hoop and hollow cylinders". Internet: http://hyperphysics.phy-astr.gsu.edu/hbase/ihoop.html, 2016 [Oct. 15 2017].

[14] B. I. Silviu, et al., 'The energetic balance of the friction clutches used in automotive". *Recent Researches in Automatic Control*, no. May, pp. 252-256, 2011.

[15] R. J. V. Mark, J. W. Steven, J. R. Donald, J. M. Timothy, "Method and Apparatus for Transferring Power between a Flywheel and a Vehicle," US Patent 8,622,860, 2014.

[16] J. Abrahamsson, et al., "On the efficiency of a Two-Power-Level Flywheel-Based All-Electric Driveline", *energies*, no. 5, pp. 2794-2817, 2012.

[17] I. Hadjipaschalis, et al., "Overview of current and future energy storage technologies for electric power applications", *Renewable and Sustainable Energy Reviews*, no. 13, pp. 1513-1522, 2009.

[18] A. Boretti, "Comparison of fuel economies of high efficiency diesel and hydrogen engines powering a compact car with a flywheel based kinetic energy recovery systems", *International Journal of Hydrogen Energy*, no. 35, pp. 8417-8424, 2010

eureca 2017 – Conference Paper
Paper Number 2ME12

Sintered Properties of Stainless Steel-doped Y-TZP Ceramics

M. M. Mervyn Marlon[1*], W. J. Kelvin Chew[1*], S. Ramesh[2]

[1]*Department of Mechanical Engineering,*

School of Engineering, Faculty of Built Environment, Engineering, Technology and Design, Taylor's University, 47500 Subang Jaya, Selangor, Malaysia.

[2]*Centre of Advanced Manufacturing & Material Processing (AMMP), Department of Mechanical Engineering, Faculty of Engineering, University of Malaya, 50603 Kuala Lumpur, Malaysia.*

[*]mervynmarlon@sd.taylors.edu.my,
KelvinWaiJin.Chew@taylors.edu.my

Abstract
Yttria stabalised Tetragonal Zirconia Polycrystalline (Y-TZP) has been extensively renowned for its vast outstanding contribution in medical field such as primary function for implant biomaterial which acts as restoration of damaged body parts. Nonetheless in the past decades, there have been various reported cases that point the failure of hip transplants involving material of zirconia ceramic. This eventually leads to the birth of this research project where it studied the properties effects of Y-TZP as it was added or doped with stainless steel 316 (SS316). In this research project, the parameter of weight percentage for stainless steel 316 (SS316) to be doped with Y-TZP were as follows; 0 wt%, 0.1 wt%, 0.5 wt% and 1 wt%. The outcome of this experiment then were measured and analysed as according to properties of relative density, Vickers hardness and fracture toughness. The experiment was conducted by firstly mixed the Y-TZP and SS316 powders together as according to the weight percentage of SS316 as well as addition of ethanol solution that act for medium of enhancement. The mixture then underwent compacting pressure bench press as well as Cold Isostatic Pressure (CIP) in order to produce the green sample. After that, the green sample underwent sintering process via pressureless sintering method at mentioned ranges temperature of 1250°C, 1300°C, 1400°C and up to 1500°C. Subsequently, the sample then underwent grinding and polishing process before proceeding to the measurement and analysis process. The outcome of the measurement and analysis process revealed that as the content of SS316 doped with Y-TZP increases as well as the increased in sintering temperature, the relative density and fracture toughness profound to be increased while Vickers hardness indicated as decreased.

Keywords: Y-TZP, stainless steel 316, pressureless sintering method, mechanical properties.

1. Introduction

In this robust technological era, experimentation involving combination of two distinct materials which consist of different properties respectively often been performed via doping method in order to attained successful outcome of material with superior properties. In the past for medical field, there were numerous of different materials have been studied for the objective to produce a durable implant biomaterial which function as alternative substitution to repair damaged body parts. Zirconia ceramic in particular has gain enormous popularity and attention from surgeon and scientist across the world due to its advantage as the closest restoration for bone tissue [1]. Nevertheless, zirconia ceramic alone has been identified in which it does not exhibit a high toughness as comparison made with metals. Therefore, metals do gain consideration in which it can be added to zirconia ceramic through doping and creating metal doped ceramic or ceramic doped metal. This method and process aim to enhance the overall replacement implants toughness. Moreover, this doped material progressively replaced the prostheses that comprised of purely ceramic as taking concerned to improve the prostheses major aspects of strength and durability [2]-[3]. Hence, the studies regarding doped material to produce advance biomaterial has developed rapidly.

In addition, zirconia ceramic has been described to exhibit different properties when taking into account that it exists at distinct phases. In this case, zirconia ceramic often added with dopant or sintering additive in order for the characteristics and phases do not alter or transformed at different temperatures. Nonetheless, the advantages of zirconia ceramic were such that include high density and strength, high tolerance towards corrosion as well as high resistance towards impact. A specific zirconia ceramic type known as Yttria stabalised Tetragonal Zirconia Polycrystalline (Y-TZP) often been used as implant material in human body due to its high compatibility. Therefore, it has been applied as prosthetics for numerous years and yet displayed negative feedback. Moreover, stainless steel usually comes with different types and graded as according to its production specifications, grade composition as well as mechanical properties. Customarily when comparing zirconia ceramic with stainless steel, stainless steel in this case has displayed to have high strength, ductility, toughness as well as high corrosion resistance. Thus, the doped material can be utilised as a substitution for pure ceramic in order to create a more durable implant material.

A study was conducted to examine the doped material relative density such that considering the factors of varied zirconia and stainless steel compositions as well as heating rates [4]. In this case, the samples relative density was determined based on different sintering heating rates. The results then revealed that the samples relative density decreased when the stainless steel weight percentage (wt%) falls below 50% as well as during the increased in sintering heating rates. Vice versa, samples relative density increased when the stainless steel weight percentage (wt%) exceeding 50% as well as during the increased in sintering heating rates. A study was performed to find out the fracture toughness and Vickers hardness of zirconia stainless steel composite [5]. In this investigation, the samples were made as according to stainless steel concentration with ranges from 15% to 30%.

The results displayed to obey the mixture law such that when stainless steel content inside the zirconia/stainless steel composite increased, the fracture toughness

indicated as increased while Vickers hardness described as decreased [6]-[7]. In addition when subjected to fractures, there was no observation of plastic deformation. As comparison to zirconia ceramic, zirconia/stainless steel composite do not exhibit brittle condition [8]. In terms of biomedical implants, these types of characteristics often denoted as vital for material enhancement. In the previous years, there were various cases had been reported that address the serious issue of zirconia ceramic hip transplant failure. In order to provide solution to this dilemma, various thorough studies have been conducted that primarily emphasize on sintering of zirconia doped material at low temperature as well as mechanical properties [9]. In this research project, it fundamental objective was to study the effects of properties when adding dopant stainless steel 316 to Y-TZP. This report presented the experimental flow process as well as results for the tested physical and mechanical properties.

2. Research Methodology

2.1 Powder Preparation

The starting materials for this research project methodology begins with acquired and gathered the two essential material substances that may include Y-TZP and stainless steel 316 powders. The table 1 below displayed the Y-TZP and stainless steel 316 summaries of typical characteristics accordingly. The powder preparation process was initiated with powder synthesis process in which both Y-TZP and stainless steel 316 powders were been mixed together as well as measured based on the stainless steel 316 content. Before both of the powders to be mixed together, each of the samples weight percentage were fixed as according to the stainless steel 316 content which ranges from 0 wt%, 0.1 wt%, 0.5 wt% and 1 wt%. Ethanol with measurement of 100 ml was firstly poured into the beaker and only then followed by poured both of the stainless steel 316 and Y-TZP together into the beaker in order to undergo the mixing process.

Table 1: Typical characteristics of Y-TZP and stainless steel 316

Material	Grade / Type	Composition (wt%)	Powder Particle Size	Particle Shape
Zirconia	Partially-Stabilized Zirconia, Y-TZP	Cr 16-18, Ni 10-14, Mo 2-3, C 0.08, Fe (remaining)	0.04 µm (40 nm)	Spherical
Stainless Steel	316	5.2 Y_2O_3,HfO_2 <5, Al_2O_3 0.1-0.4, ZrO_2 (remaining)	5 – 20 µm	Spherical

The equipment of Digital Ultrasonic Bath (Powersonic UB-410, Thermoline Scientific, Australia) was utilised by filled up the equipment with distilled water. Next, the beaker then placed inside the Digital Ultrasonic Bath equipment for 15 minutes of thorough mixing process with continuous stirring and beaker later was removed from equipment itself once achieved completion of mixing. After that, the machine of Laboratory Attritor Mill (01-HD, Union Press, United States) was utilised by pouring the mixture inside it with the purpose for the mixture to undergo the attrition milling process where further break down of powder mixture for duration of 45 minutes with running at 500 rpm. Furthermore, 5 mm size of zirconia milling ball which account quarter of the mixture amount were added to the Laboratory Attritor Mill machine also with aim to enhance the entire milling process completion. A sieve utility of measurement mesh size 212 µm was used for the first time to sieve the mixture where zirconia ball were trapped and minimised the mixture to slurry conditions. The remaining mixture then created into a cake form and undergoes baking process where the mixture was stored inside the Universal Oven (UN 55, Memmert, Germany) which heated for 60°C for overnight duration and subsequently left dry. The cake mixture after the heating process was crushed into smaller form using hand tools. After that, a sieve utility of measurement mesh size 212 µm was utilised for second time with objective to produce the final powder composition of definite fine. Table 2 below shows the Y-TZP and stainless steel 316 summaries of typical properties respectively provided with condition at room temperature.

Table 2: Summary typical properties of Y-TZP and stainless steel 316 at room temperature

Material	Density (g/cm^3)	Young's Modulus (GPa)	Vickers Hardness (GPa)	Fracture Toughness ($MPa.m^{1/2}$)	Thermal Conductivity (W/m.K)	Mean Coefficient of Thermal Expansion (µm/m.K)	Electrical resistivity (Ω.cm)
Zirconia	6.02	200	12.5	13	2	10.3 (25°C – 1000°C)	$> 10^{13}$
Stainless Steel 316	8.00	193	1.47	112 – 278	13 – 17	19.9 (0°C – 871°C)	10^{-11}

2.2 Green Sample Preparation

The machine of Hydraulic Bench Press (HP10-150, RMS Hydro, Malaysia) was utilised for the compacting process of the powder mixture in which the powder mixture was poured into a round shaped die with diameter measurement of 20 mm. The subjected high pressure bench press was 1000 bar for 10 seconds. After that, the Cold Isostatic Press (KJYU150, Shanxi Golden Kaiyuan Co., Ltd, China) machine was used for the CIP process where the green body round tablets were been placed inside a glove as well as placed it again inside desired square shaped container. On the other hand, the container in this case then to be stored under room temperature which in this case aim for neither heat nor pressure to penetrate and ultimately affect the green body round tablets during the pressing process. In overall for this current process stage, the green body round tablets indeed can likewise be referred as green samples.

2.3 Sintering Process

The type of applied sintering process method was indeed pressureless sintering method and to be performed after the formation of green samples. In this process, it begins by placing the green samples inside the crucible which to be stored inside the Electric Box Furnace (LT10, LT, Malaysia). The applied heating for sintering temperatures were distinct such that ranging from 1250°C, 1300°C, 1400°C and up to 1500°C where only one sintering temperature was performed in one day. The process heating rate was also conserved at 10°C per minute. In addition, the furnace holding time was kept for 2 hours and after the process, the heating was stopped. The samples then let to be cooled down at rate of at 10°C per minute where it explained that the samples cooled through natural cooling method until approaching ambient.

2.4 Grinding and Polishing Process

2.4.1 Grinding Process

After the completion of sintering process, the samples were vitally required to be grinded and followed by polished. The equipment of Polishing & Grinding Machine (GP2V, LT, Malaysia) was utilised for both of grinding and polishing processes. For grinding process, the Polishing & Grinding Machine was installed with grinding papers and operates at 50 rpm in which two minutes for each sample. The applied grinding papers range with five grit sizes in total such that namely 120, 240, 600, 800 and 1200 that consists with surface material of silicon carbide (SiC). The samples were grinded only on one side and the other side used as samples labelling for clear identification purposes. Furthermore, the grinding results for each grade were displayed as visible one direction line and vitally covering the entire grinded side of samples surface. Each visible direction lines also represent each grade of grinding papers respectively.

2.4.2 Polishing Process

Polishing process was performed subsequently after the grinding process in which polishing clothes were utilised and injected with diamond paste as well as lubricant via syringe device. The polishing clothes were installed to the equipment of Polishing & Grinding Machine (GP2V, LT, Malaysia) and operated at 20 rpm. In addition, the diamond paste in this case consists of diamond bit with grades measurement of 1 µm and 6 µm. Moreover, the lubricant likewise been injected to the polishing clothes as well as was to function by ease the spreading of diamond paste evenly across the entire surface of the samples. The polishing process was performed for duration of two minute only for each sample.

2.5 Measurement and Analysis

2.5.1 Relative Density

The samples relative density were determined in which the testing was conducted by adhere strictly according to Archimedes principle and water immersion technique. ASTM C-29 was used as reference of standard to relate with the determined relative density. In this process, the Analytical Balance equipment with density kit (AY220, Shimadzu, Japan) was employed by filled up the equipment with distilled water that function as immersion medium. The value for density of water was declared as 0.99654 kgm^{-3}.The stated Y-TZP theoretical density was 6.1 Mgm^{-3} and below (eqn 1) shows the equation used to calculate the samples relative density.

$$\rho = \frac{W_a}{W_a - W_w} \tag{1}$$

Where

ρ	=	Relative density of the sample
W_a	=	Weight of the sample in air
W_w	=	Weight of the sample in water
ρ_w	=	Density of distilled water

2.5.2 Vickers Hardness

The samples Vickers hardness were experimented by utilising the equipment of Vickers hardness tester (MV-01, Matsuzawa, Japan) that consist of pyramidal diamond indenter as well as subjected load application of 10 kg. Only minimum duration of 10 seconds for held down implementation. ASTM E284-99 and ISO 14705 can likewise be used as a standard reference for all experiment parameter. In broad, the impression

was indicated as square such that presence with two diagonals that has identical length. The indentation in this process was measured by using the Vickers hardness tester machine microscope that has been installed together with filar micrometer which consist advantage accuracy of 0.1 µm. The equation to calculate the samples Vickers hardness was presented below as (eqn 2). Figure 1 below displayed (a) Vickers harness schematic diagram shape indenter with (α =136º±0.5º) which described as angle between the opposite faces at the pyramidal indenter vertex and (b) formed of indentation.

$$H_v = \frac{1.854P}{(D)^2} \tag{2}$$

Where

P	=	Applied load	
D	=	Average diagonals	$\frac{D_1 + D_2}{2}$

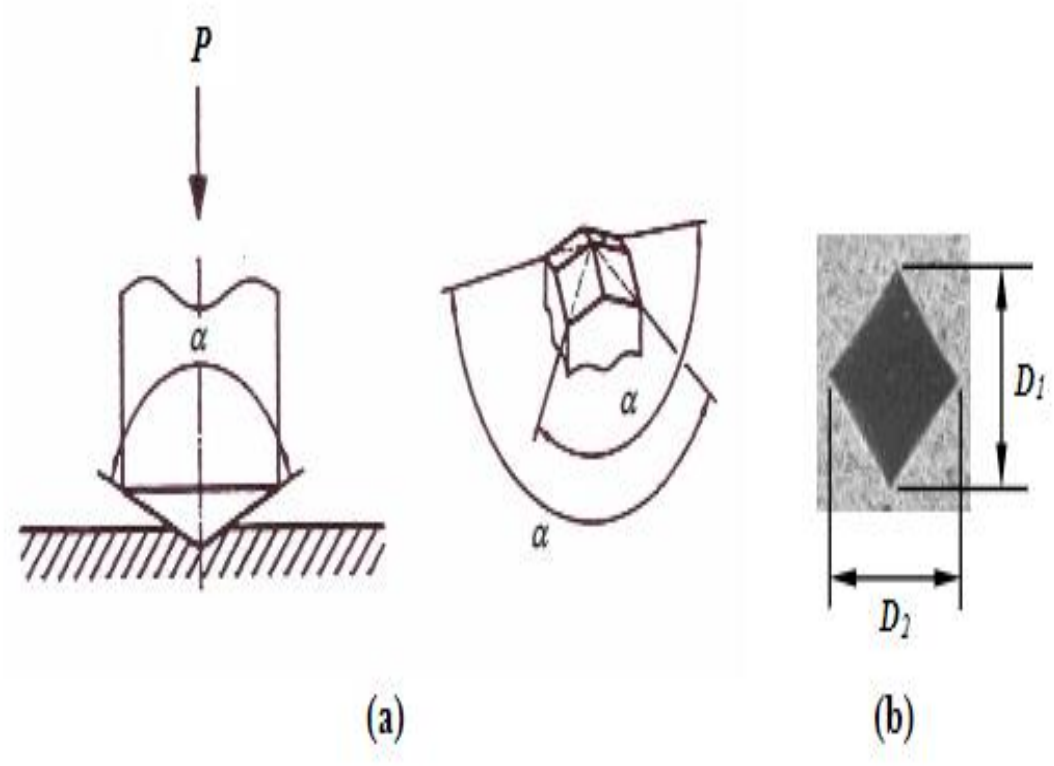


Figure 1: (a) Vickers harness schematic diagram shape indenter with (α =136º ±0.5º) which described as angle between the opposite faces at the pyramidal indenter vertex and (b) formed of indentation

2.5.3 Fracture Toughness

The samples fracture toughness were determined with an identical method of testing as the one of Vickers hardness due to it used similar indentation. The microscope filar micrometer was used to determine the crack length (L_1, L_2, L_3, and L4) and indentation length (D) after the formation of indentation. The equation for fracture toughness was indicated below as (eqn 3). Figure 2 below displayed the schematic diagram regarding typical Palmqvist crack system that emerged after Vickers indentation. In this case also, "*L*" was described as the crack measured length which used to calculate the samples fracture toughness. The Vickers indent diagonals (D1 and D2) were suggested to be identical with the length of 2a by referring to figure 1.

$$\left[\frac{K_{IC}\emptyset}{H_v a^{\frac{1}{2}}}\right]\left[\frac{H_v}{E\emptyset}\right]^{\frac{2}{5}} = 0.035\left[\frac{L}{a}\right]^{-\frac{1}{2}} \quad (3)$$

Where

K_{IC}	=	Fracture toughness	
H_v	=	Vickers hardness	
E	=	Young's modulus	
a	=	Half-length of average diagonal	
L	=	Average crack length	$\frac{L_1 + L_2 + L_3 + L_4}{4}$
ϕ	=	Constraint factor which taken as 3	

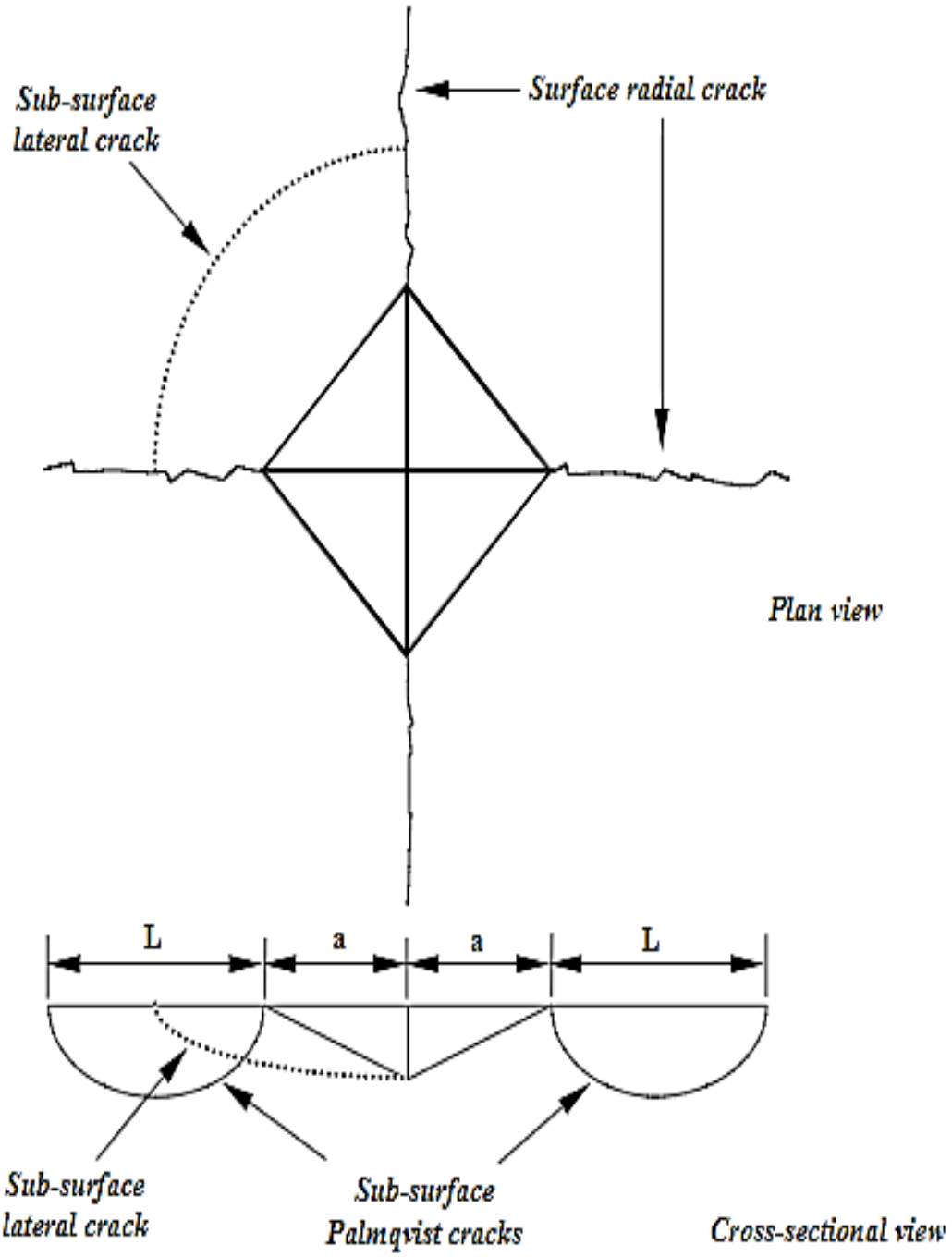


Figure 2: Schematic diagram regarding the typical Palmqvist crack system that emerged after Vickers indentation. In this case also, "*L*" was described as the crack measured length which used to calculate the samples fracture toughness. The Vickers indent diagonals (D1 and D2) were suggested to be identical with the length of 2*a* by referring to figure 1.

2.5.4 Ageing Testing

The first step for ageing test was obligatory required the samples to be store inside the acidic digestion device which has been illustrated in figure below. Consecutively, the samples were then be immersed inside distilled water with 20 ml in

measurement. After the immersion process, it later required the samples to be transferred to an oven for heating and baking process as well as provided with temperature below 180°C for duration of five hours. Segregations of samples were later to be done as according to the corresponding ageing rate intervals and examined all of it using X-Ray diffraction (XRD).

2.5.4 Assumptions

This research project had taken consideration for the following assumptions:

1. Young's modulus for Y-TZP was 200 GPa at room temperature.
2. Young's modulus for stainless steel 316 was 193 GPa at room temperature.

3. Results and Discussions

3.1 Relative Density

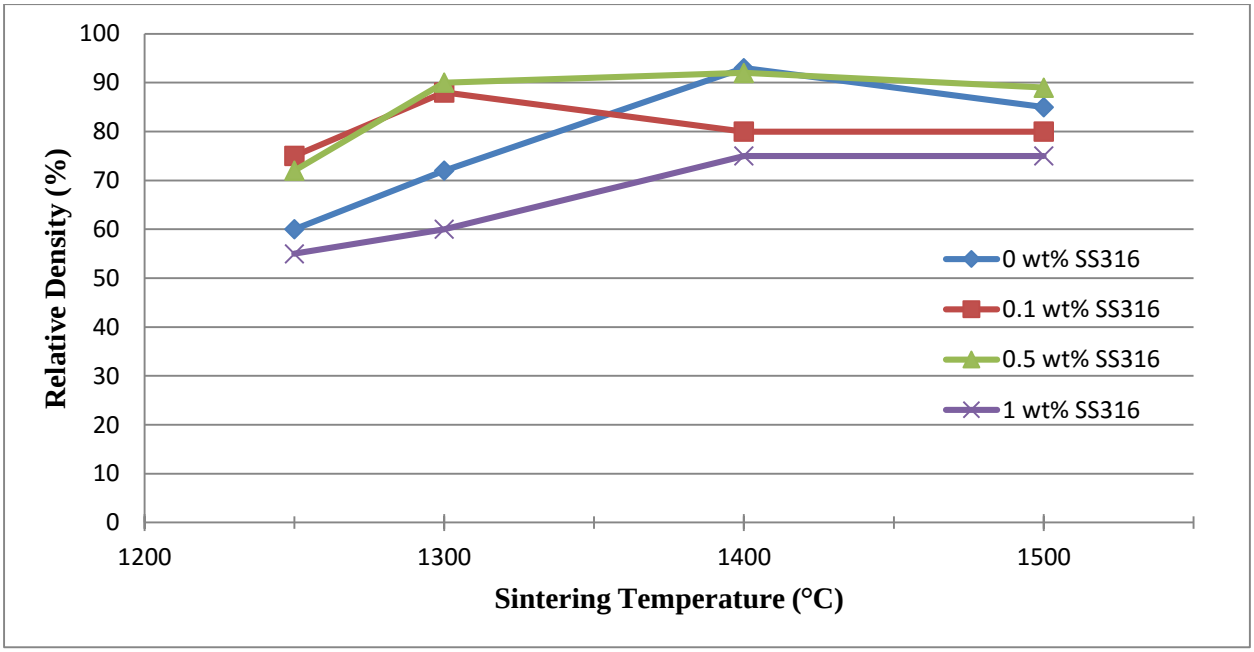


Figure 3: Graph of samples relative density against sintering temperature

By referring to the plotted graph in figure 3 above, the lowest identified relative density was 55% which consist of 1 wt% of SS316 as well as sintered at 1250°C. The relative density for 1 wt% of SS316 then continue to increased when sintering temperature increased from 1250°C to 1400°C and remained static for sintering temperature between 1400°C to 1500°C. For 0 wt% SS316 and 0.5 wt% SS316, the results showed that the maximum sintering temperature was 1400°C due to obtained the highest relative densities which were 93% and 92% respectively. In overall, considering sintering temperature between 1250°C and 1300°C, the relative densities increased when weight percentage of stainless steel increased. It can be observed that

adding dopant SS316 by 0.5 wt% to Y-TZP was beneficial to enhance the densification but provided that it must be sintered at low temperature of 1300°C.

Nonetheless taking into account of sintering temperature between 1400 and 1500, all of the samples exhibit no improvement or decreased in relative densities. This can be supported that grain coarsening could possible cause the decreased in densities as higher sintering temperature was applied. In addition, when a higher sintering temperature was applied such that exceeding 1500°C, zirconia underwent partial transformation such that transform into monoclinic or cubic phases [28]. The samples doped with 0.5 wt% SS316 indicated to exhibit the optimum benefit in terms of densification where it attained the highest relative density of 90% and 89% when sintered at temperature 1300°C and 1500°C. For the case 0 wt% SS316 which denoted as undoped or pure Y-TZP, the achieved density was 72% when sintered at 1300°C. Considering that sintering temperature was identical such that at 1300°C but different weight percentage of SS316 such that 0 wt% SS316 and 0.5 wt% SS316, the samples of doped 0.5 wt% SS316 displayed a higher relative density as compared to 0 wt% SS316. This in turn proved that adding SS316 into Y-TZP indeed contributed an enhancement for consolidation process but must in line with condition of lower sintering temperature such that below 1500°C.

Taking into account of sintering temperature between 1250°C and 1300°C which indicated nearly all samples showed an increased, as weight percentage of the dopant increased, the samples relative density indicated as increased. This was considered as truthful as compared to theory such that it mentioned stainless steel density increased when heating rate increased and therefore, promote the increased in samples densities [10]. This also means that samples with more weight percentage of stainless steel exhibits a higher density due to the total accumulated of an increased in densities based on the amount. However, considering the opposite case such that for 0.5 wt% SS316 which showed a decreased in relative density when sintered from 1250°C to 1300°C, the trend line was the opposite way. The reason for this may be due to method of processing for the samples such as shorter sintering holding time. A shorter holding time may cause the reverse of the material density value such that it became decreased [11]. Another possible reason for the decreased in relative density was due to uneven powder composition. It considered as extremely difficult to obtain the most ideal powder composition.

3.2 Vickers Hardness

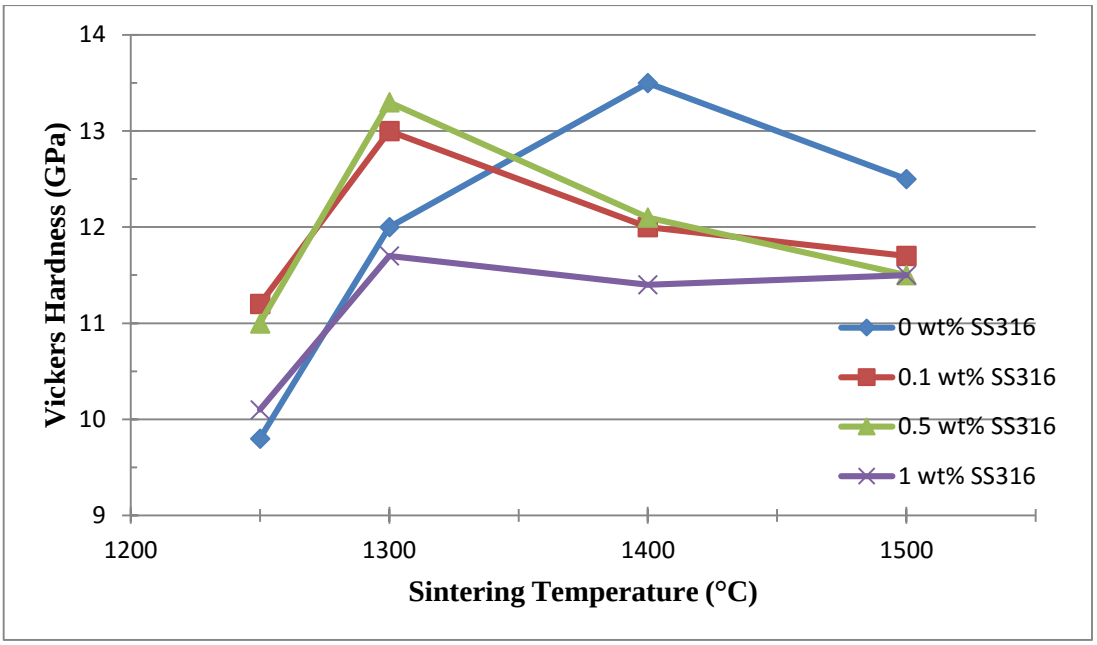


Figure 4: Graph of samples Vickers hardness against sintering temperature

As according to the plotted graph in figure 4 above, all samples exposed to have an increased in Vickers hardness when considering sintering temperature was increased from 1250°C to 1300°C. As sintering temperature continued to increase from 1300°C to 1400°C, all doped samples showed a rapid declined in Vickers hardness but for undoped sample on the other hand indicated as increased. When sintering temperature increased higher from 1400°C to 1500°C, all samples for both doped and undoped presented as decreased. Considering sintering temperature at 1300°C, sample of 0.5 wt% SS316 revealed to achieved the highest among all samples such that 13.3 GPa. In comparison with 0 wt% SS316 which denoted as pure Y-TZP or undoped sample, 0.5 wt% SS316 showed a higher Vickers hardness than 0 wt% SS316 with values 13.3 GPa and 12 GPa respectively. For all doped samples, the optimum sintering temperature to obtain the highest sintering temperature was 1300°C.

At sintering temperature of 1300°C, the Vickers hardness values for samples of 0.1 wt% SS316, 0.5 wt% SS316 and 1 wt% SS316 were 13 GPa, 13.3 GPa and 11.7 GPa. For undoped sample of 0 wt% SS316, the optimum sintering temperature was 1400°C in which it attained it highest Vickers hardness value of 13.5 GPa. Considering an increased sintering temperature between 1250°C to 1300°C, all samples exhibit improvement of Vickers hardness due to sintered body strengthens densification. Nonetheless, for the case of decreased in Vickers hardness as sintering temperature continued to increase from 1300°C to 1500°C, this issue occurred due to grain coarsening that related to cubic structure [12]. By referring at sintering temperature of 1500°C, Vickers hardness decreased as weight percentage of SS316 increased. This likewise follows the trend line as well as obeys the mixture law such that explained Y-TZP was harder than SS316.

3.3 Fracture Toughness

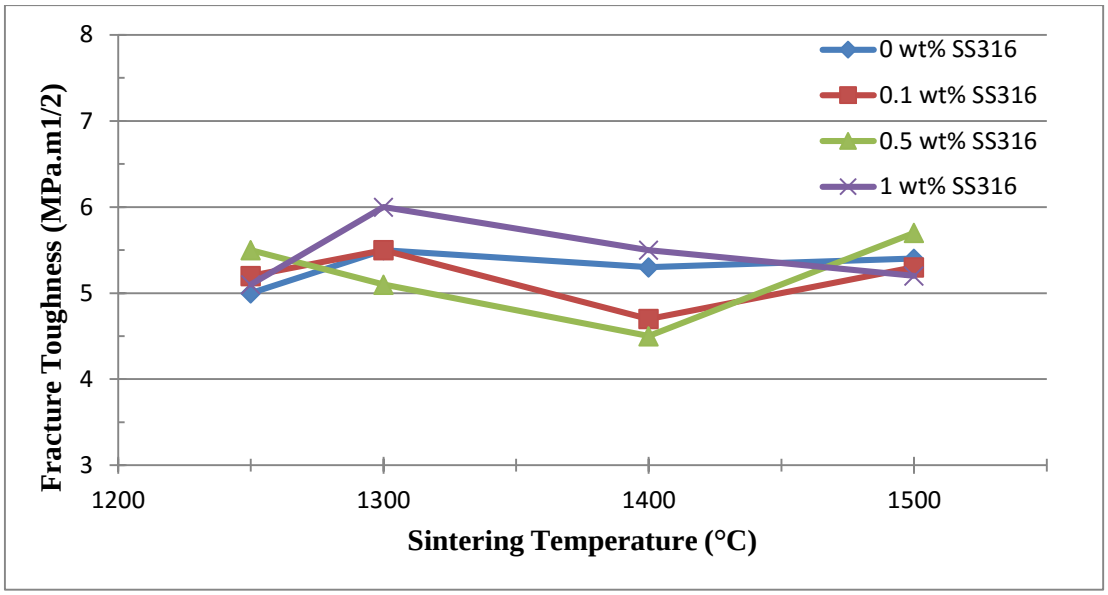


Figure 5: Graph of samples fracture toughness against sintering temperature

Based on the plotted graph in figure 5 above, samples of 0 wt% SS316, 0.1 wt% SS316 and 1 wt% SS316 profound to exhibit an increased in fracture toughness when sintering temperature increased from 1250°C to 1300°C. On the contrast side, sample of 0.5 wt% SS316 displayed a decreased in fracture toughness when sintering temperature increased from 1250°C to 1400°C. At sintering temperature of 1300°C, it indicated as the optimum sintering temperature for samples of 0 wt% SS316, 0.1 wt% SS316 and 1 wt% SS316 as all samples showed their highest fracture toughness with values 5.5 MPa.m$^{1/2}$, 5.5 MPa.m$^{1/2}$ and 6 MPa.m$^{1/2}$ respectively. As sintering temperature increased from 1400°C to 1500°C, samples of 0 wt% SS316, 0.1 wt% SS316 and 0.5 wt% SS316 identified as increased in fracture toughness whereas sample of 1 wt% SS316 showed a decreased in fracture toughness. At sintering temperature of 1500°C, sample of 0.5 wt% SS316 has the highest fracture toughness with value of 5.7 MPa.m$^{1/2}$ and 1500°C was declared as its optimum sintering temperature.

Mismatched of thermal expansions occurred at the section between stainless steel and zirconia particles provided when there was an increased in stainless steel particles [13]. Hence, radial tensile stress was developed internally during cooling process and consequently contributed towards particles with inadequate interfacial bonds which cause debonding. In addition, crack also then formed in a method that it smoothly inseminates between the unsteady interface of zirconia and stainless steel particles [33]. This in turn leads to the enhancement of fracture toughness via the process of crack deflection. Sintering temperature on the other hand suggested that it marginally affected the fracture toughness and this also considering that the all wt% SS316 exhibit fracture toughness with values varied from 5.2 MPa.m$^{1/2}$ to 5.7 MPa.m$^{1/2}$ when sintered at sintering temperature of 1500°C. In this case, homogenization developed over stabilizer which also existed within the samples ZrO2 grains and thus, produce an improved stability of tetragonal grains [14].

3.4 Ageing Resistance

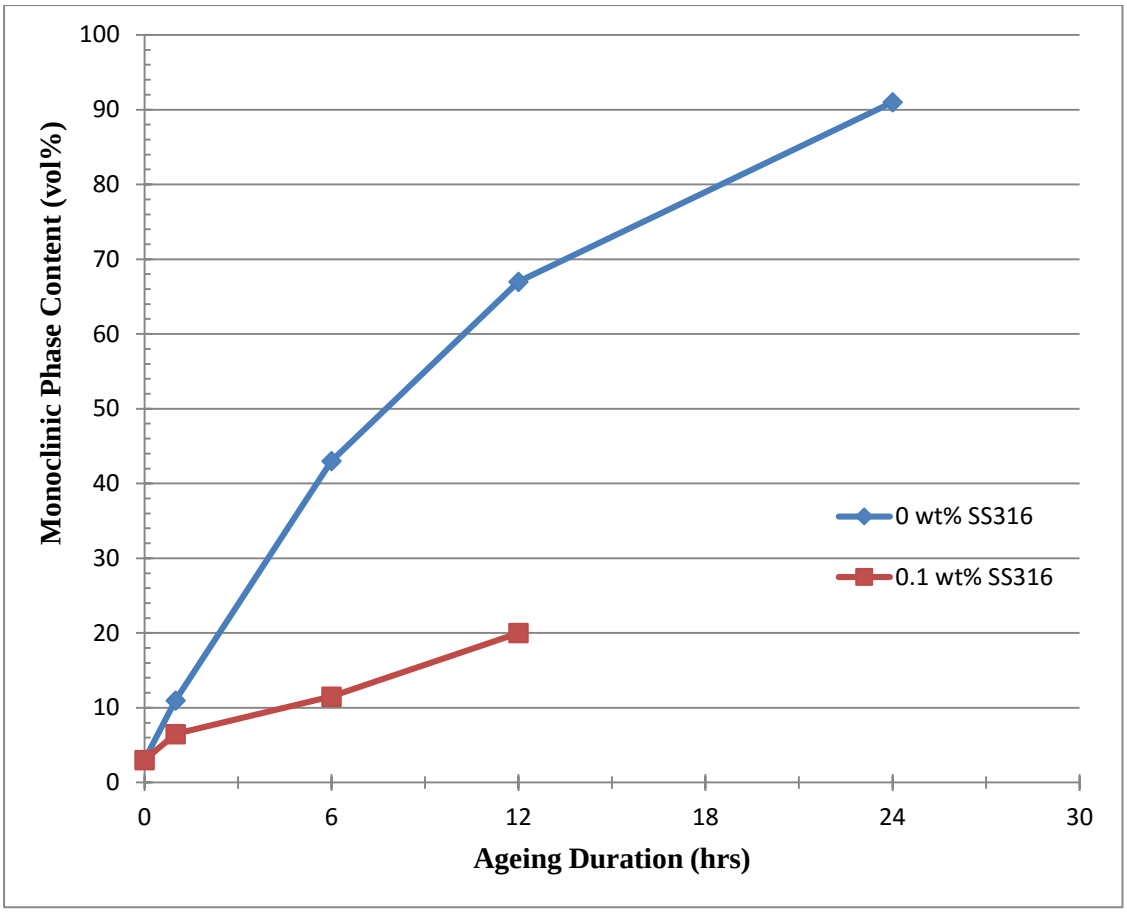


Figure 6: Graph of monoclinic phase content against ageing duration

The accelerated ageing test was subjected to selected samples with aim to determine the samples ageing resistance due to low temperature degradation (LTD) when exposed towards humid environments. Generally, samples were subjected to superheated steam at temperature of 180°C as well as 10 bar of pressure with increasing duration time. In this case, XRD analysis was utilised with the objective to monitor the samples phase content as well as identified the monoclinic zirconia (m-ZrO_2) phase content. The table above shows the monoclinic phase content for samples of 0 wt% SS316 and 0.1 wt% SS316 accordingly with increasing ageing duration up to 24 hours. The monoclinic phase content was monitored for ageing duration of 0, 1, 6, 12 and 24 hours respectively. Sample of 0.1 wt% SS316 with sintering temperature of 1300°C was chosen as reference due to optimum composition and consist of the highest mechanical properties. By observing the trend line on the plotted graph of monoclinic phase content against ageing duration in figure 6 above, it has been identified that pure Y-TZP or known as 0 wt% SS316 exhibit a rapidly continuous increasing trend line. The sample for 0 wt% SS316 then breaks during the ageing treatment for the next 12 hours which tells that data was absence for analysis.

After 1 hours of exposure, 0 wt% SS316 displayed 11 vol% of monoclinic phase content which was higher and drastic in comparison to 0.1 wt% SS316 that presented as 6.5 vol%. As approaching 24 hours of exposure, 0 wt% SS316 closed the monoclinic phase content at 91 vol%. This essentially means that the longer the ageing duration,

the higher the development of monoclinic phase content [35]. In addition, this was considered as not ideal due to monoclinic promote failure of material. The more the monoclinic phase, the worst the material properties become. Moreover, development of crack and surface spalling were observed at the sample via visual inspection as results of progressive ageing [15]. On the other hand, sample of 0.1 wt% SS316 had presented a better ageing resistance but sample then disintegrated at 12 hours which closed the monoclinic phase content with 20 vol%. This can be proved based on the trend line for 0.1 wt% SS316 stopped at 12 hours.

The disintegrated of samples will become future works consideration. By comparing both samples of 0 wt% SS316 and 0.1 wt% SS316 at similar 12 hours of exposure, 0.1 wt% SS316 was considered ideal as compared to 0 wt% SS316 due to it showed significant low of monoclinic phase content. This proved that 0.1 wt% SS316 exhibit better ageing resistance and phenomena possibly due to finer grain size obtained through sintering process. Hence, sample of 0 wt% SS316 can be further upgrade to prevent the disintegration in the future works. Pure Y-TZP (0 wt% SS316) was considered as instable which leads to lower ageing resistance. Hence, it changes phases easily from tetragonal to monoclinic supposed that polar water molecules penetrate the sample particles. Phase transformation occurs in such a way that if one of the grain experienced stress, this will interfere the neighbouring grain and hence, phase changes take placed and promote low temperature degradation. This project also aims to achieve an ideal stable matrix in order to prevent phase transformation. By doing so, ageing rate likewise can be minimised via the reduction of deterioration rate, microcracking and surface roughening.

4. Conclusion

The experiment has successfully been conducted to investigate the advantageous and effects of adding sintering additive stainless steel 316 to be doped with Y-TZP ceramics. It has been identified that the highest density would be 93% for the case of 0 wt% SS316 with sintered at sintering temperature of 1400°C. For Vickers hardness, the lowest value profound to be 9.8 GPa when taking into account of 0 wt% SS316. In addition, the optimum value for fracture toughness would be 6 $MPa.m^{1/2}$ which considering for the 1 wt% SS316. By referencing to the all the plotted graph for all wt% of SS316 for sintering temperature between 1400°C to 1500°C, the effects of adding stainless steel 316 to be doped with Y-TZP were such that the relative density nearly static, Vickers hardness decrease and fracture toughness increase. A low monoclinic phase content for samples was also the targeted outcome.

Acknowledgement

Greatest gratitude and appreciation to the lab technicians at University of Malaya for providing the permission and guidance in order to utilise the facilities such as Vickers hardness and fracture toughness equipment.

References

[1] K. J. . Burg, S. Porter, and J. F. Kellam, “Biomaterial developments for bone tissue engineering,” *Biomaterials*, vol. 21, no. 23, pp. 2347–2359, 2000.

[2] E. M. Maynard, “Visual prostheses.,” *Annu. Rev. Biomed. Eng.*, vol. 3, pp. 145–68, 2001.

[3] S. M. Kurtz, S. Kocagöz, C. Arnholt, R. Huet, M. Ueno, and W. L. Walter, “Advances in zirconia toughened alumina biomaterials for total joint replacement,” *J. Mech. Behav. Biomed. Mater.*, vol. 31, pp. 107–116, 2014.

[4] S. López-Esteban, J. F. Bartolomé, C. Pecharromán, and J. S. Moya, “Zirconia/stainless-steel continuous functionally graded material,” *J. Eur. Ceram. Soc.*, vol. 22, no. 16, pp. 2799–2804, 2002.

[5] K. L. Lin, M. Singh, and R. Asthana, “Characterization of yttria-stabilized-zirconia/stainless steel joint interfaces with gold-based interlayers for solid oxide fuel cell applications,” *J. Eur. Ceram. Soc.*, vol. 34, no. 2, pp. 355–372, 2014.

[6] I. Espitia-Cabrera, H. Orozco-Hernández, R. Torres-Sánchez, M. E. Contreras-García, P. Bartolo-Pérez, and L. Martínez, “Synthesis of nanostructured zirconia electrodeposited films on AISI 316L stainless steel and its behaviour in corrosion resistance assessment,” *Mater. Lett.*, vol. 58, no. 1–2, pp. 191–195, 2004.

[7] A. Balamurugan, S. Kannan, and S. Rajeswari, “Structural and electrochemical behaviour of sol-gel zirconia films on 316L stainless-steel in simulated body fluid environment,” *Mater. Lett.*, vol. 57, no. 26–27, pp. 4202–4205, 2003.

[8] V. K. Balla, P. P. Bandyopadhyay, S. Bose, and A. Bandyopadhyay, “Compositionally graded yttria-stabilized zirconia coating on stainless steel using laser engineered net shaping (LENS???),” *Scr. Mater.*, vol. 57, no. 9, pp. 861–864, 2007.

[9] Lenntech Com, “Stainless steel mechanical properties,” *Stainl. steel Mech. Prop.*, 2012.

[10] C. Lorenzo-Martín *et al.*, “Mechanical behaviour of yttria tetragonal zirconia polycrystalline nanoceramics: Dependence on the glassy phase content,” *J. Eur. Ceram. Soc.*, vol. 22, no. 14–15, pp. 2603–2607, 2002.

[11] S. Butković, M. Oruč, E. Šarić, and M. Mehmedović, “Effect of sintering parameters on the density, microstructure and mechanical properties of the niobium-modified heat-resistant stainless steel GX40CrNiSi25-20 produced by MIM technology,” *Mater. Tehnol.*, vol. 46, no. 2, pp. 185–190, 2012.

[12] S. Du, L. Xu, X. Zhang, P. Hu, and W. Han, “Effect of sintering temperature and holding time on the microstructure and mechanical properties of ZrB2-SiCw composites,” *Mater. Chem. Phys.*, vol. 116, no. 1, pp. 76–80, 2009.

[13] R. M. German, “Coarsening in sintering: Grain shape distribution, grain size distribution, and grain growth kinetics in solid-pore systems,” *Crit. Rev. Solid State Mater. Sci.*, vol. 35, no. 4, pp. 263–305, 2010.

[14] G. Wang, S. Zhang, C. Bian, and H. Kong, “Interface toughness of a zirconia-veneer system and the effect of a liner application,” *J. Prosthet. Dent.*, vol. 112, no. 3, pp. 576–583, 2014.

[15] E. Zapata-Solvas, D. Gómez-García, C. García-Gañán, and A. Domínguez-Rodríguez, “High temperature creep behaviour of 4 mol% yttria tetragonal zirconia polycrystals (4-YTZP) with grain sizes between 0.38 and 1.15 μm,” *J. Eur. Ceram. Soc.*, vol. 27, no. 11, pp. 3325–3329, 2007.

eureka 2017 – Conference Paper
Paper Number 2ME13

Design and Fabrication of Collapsible Scissor Bridge

Mohamad Nabil Aklif bin Bero[*1], Noor Zafirah binti Abu Bakar[1]

[1]Department of Mechanical Engineering, School of Engineering, Taylor's University, Malaysia.

* nabil.aklif@yahoo.com

Abstract

Collapsible scissor bridge is a portable bridge that can be deployed during emergency state to access remote areas that are affected by disaster such as floods. Temporary transportation via boats are the only preferred transportation for evacuation. Alternative routes are required to access remote areas that has been disconnected from safe areas in order to save victims, supply foods and medical needs. A portable scissor bridge is one of the solution to eliminate the limitation in such desperate situation. The objective of this research is to design a collapsible scissor bridge which is able to be transported by a 4x4 vehicle and to be deployed to connect remote areas that has been affected by flood. The research is done based on the Conceive, Design, Implement and Operate (CDIO). The design is done by using Solidworks and numerical analysis was made to analyze the bridge's structural strength. The research starts with setting the parameters of the bridge and modelling. It is continued by element analysis to analyze strength of each components of the bridge. The structure analysis provides the input and feedback for the improvement cycle to modify the design to ensure the structure is stronger and lighter. There are five major components of the scissor structure to be analysed; pin, deck, cross shaft and deck shaft. These components mostly serve as a support structure. The structure is controlled by hydraulic pump driven by a motor for expansion and retraction motions. Material used in simulation throughout this project is A36 Structural Steel due to limited library in ANSYS software. However, the proposed material to be used as the main material is Fiber Reinforced Polymer (FRP) composites as they have a high strength to weight ratio. FRP also tends to be corrosion resistance and this characteristic is useful in flooded area. The bridge is fabricated in proportionate scale. The purpose of this prototype is to demonstrate the mechanism of the bridge; to expand and retract with simple electronic parts.

Keyword: Collapsible Scissor Bridge, Flood, Nuremberg Scissor

1.0 Introduction

Flood is one of the common disaster in tropical countries. Malaysia East Coasts Environmental Research Institute of University Sultan Zainal Abiden (USZA) claimed that 29,800 km^2 of vulnerable area to this disaster sourcing from a few numbers of river basins in peninsular Malaysia and almost 4.82 million residents are at risk especially during monsoon seasons [1]. As a result, certain areas that are heavily affected are disconnected from the outside world. This causes the victims to have no interaction or even to call for help from the unaffected areas due to shortage of electricity and broken communication facilities.

According to the annual report of 2014 by Malaysia Rescue Team or BOMBA, it was suggested that they revise their existing disaster Standard Operating Procedure [2]. It was also mentioned in the report that they would have to increase logistics capabilities such as adding more equipment and have more boats and trucks to standby for this disastrous phenomenon. However, this suggestion might not be the best solution to this problem in accessing remote areas. In conjunction to that, a research team at Hiroshima University has successfully developed and test a folding bridge which is inspired by Japanese traditional origami. This bridge, according to the researchers is intended to serve as the same purpose which is to be deployed during chaotic situations. Nevertheless, the structure made is heavy and complex and it would cost about one hour to assemble the components [3]. The bridge that the researchers from Japan made is shown in Fig.1.



Figure 72: Mobile Bridge 4.0 [3]

Adapting from the Nuremberg scissor concept, a collapsible bridge will be the solution for the problem of poor evacuation during times of flooding. Nuremberg scissors is a planar mechanism consisting several links and pins forming a scissor like structure which have the ability to collapse and expand with a given ratio. The purpose of having this bridge is that it will have the advantage in terms of mobility and can be easily deployed. The motion of the structure is dependent on the Kutzbach equation or criterion by determining the degree of freedom of the mechanism. This is done by obtaining the number of links and number and types of joints that is included in the

system as a whole [4]. Fig. 2 shows a Nuremberg scissor concept that could be used in the development of this bridge.

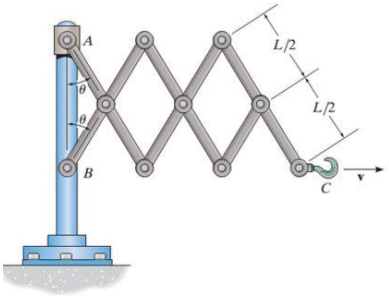


Figure 73. Nuremberg Scissor concept [5].

This type of mechanism is now commonly adopted in scissor lift or Mobile Elevated Working Platform (MEWP) and also folding gates. This simple mechanism only requires to move one link to move all other links. For example, referring to Fig. 2, when point *C* is pulled to the direction of ***v***, the angle of *A* and *B* increases and causes the whole arm to extend. Another example can be seen from Fig. 3.

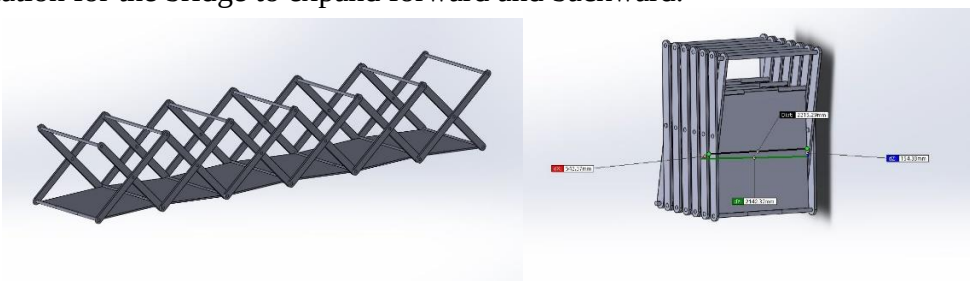


Figure 74: Folding gate and MEWP [6][7].

This mechanism is adapted to design a mobile deployable bridge could accommodate to aid the situation by providing a reliable transferring mode for victims and supplies. This bridge will be able to operate with a minimum amount of force to expand and retract. With a force in the horizontal direction of the link, it will provide a collateral force to the other link and expand the bridge.

Fig. 4 (a) shows the expanded scissor bridge structure (in operation mode) and Fig. 4 (b) shows the condition for storage or mobile mode. The design of the bridge is made to be 14.3 meters in length for operation mode and approximately 2-3 meters in mobile mode. This project aims to design a collapsible light weight scissor type bridge using computer aided drafting (CAD) software. Following from that, numerical analysis has been conducted and scaled model of the bridge is built and fabricated. Apart from that, the design of the bridge should be able to satisfy the Kutzbach

Equation [8] to obtain a degree of freedom of 2 as to provide a horizontal and vertical translation for the bridge to expand forward and backward.



(a) (b)

Figure 75. Scissor structure (a) Expanded mode and (b) Retracted mode

1.1 Research Questions

This project requires several inquisitive items to ensure that the interest of developing the project is constant throughout the dedicated period.

1. How a Nuremberg scissor concept can be applied to build a collapsible lightweight bridge?
2. How to proof that the bridge is able to withstand maximum allowable load?
3. How to demonstrate the motion mechanism of Nuremberg scissor concept?

1.2 Research Objectives

To fulfill the research question, targets are listed down as research objectives so that the achievement by the end of this project is clear.

1. To design a collapsible light weight scissor type bridge using computer aided drafting (CAD) software.
2. To conduct numeral analysis on the collapsible bridge.
3. To build and fabricate scaled model of the bridge.

1.3 Research Hypotheses

1. The bridge will be able to withstand the maximum allowable load which is the force caused by the bridge itself and a typical 4x4 vehicle average weight with its cargo supplies.
2. The design of the bridge should be able to satisfy the Kutzbach Equation to obtain a degree of freedom of two as to provide a horizontal and vertical translation for the bridge to expand forward and backward.

1.4 Project Scope

This bridge will be designed to fit a typical 4x4 pick-up truck which has the dimension of (W: 1860 mm x H: 1815 mm x L: 5362 mm). The outer dimension of the collapsed bridge will be design for a dimension of (W: 2200 mm x H: 2000 mm x L: 2800 mm). The expansion ratio is adapted from an industrial scissor lift which has a common ratio of 1:5 and this will provide a minimum length of 14000 mm for the expanded state of the bridge. The expected weight for this bridge can withstand is the maximum allowable load; the total weight of all bridge components and external load which is 1950 kg (4x4 pick-up truck with cargo) which is approximately about 19110 N.

The design and fabrication of this collapsible bridge does not consider the ground elevation or ground damping during flooding. Soil damping will naturally occur to areas where rivers are near and also during heavy rainfall that causes flood. Upon operation of the bridge at the area, ground condition might cause the bridge to operate at a certain angle which is not specifically analyzed in this project. Regarding the material, the proposed material for future development is FRP but however due to limited library function in ANSYS, which is unable to mix the properties of FRP and A36 Structural Steel for one component, A36 Structural Steel is chosen in the simulations made.

Wind speed is another factor to be considered in this project. The design of the bridge will be according to the setting of the average wind speed of 3 m/s [9]. This wind speed is selected because it is the only value applicable in the area studied, which is in Malaysia. However, the actual wind speed might be slightly higher due to theory of friction because above the river water will cause less friction to the air particle and hence have a higher wind speed as compared to land wind speed. Research supports that objects provide more friction compared to water [10].

2.0 Research Methodology

2.1 Project Framework

This project undergoes a few stages of method in which Conceive, Design, Implement and Operate served as the framework. The first part of conceiving consists of brainstorming which research will kick off with collecting ideas from challenges and problems to narrow down the scope to obtain the solution. Design stage will be adapted in the modelling phase where computer software such as Solidworks, ANSYS Workbench and Computational Fluid Dynamics (CFD) will be used. With the finalized model, further analysis will be made using ANSYS Workbench to perform stress analysis at joints and also the overall deck. Implementation is whereby the design of each component are assembled together forming a complete scissor bridge. Lastly, operate will be a looping process to ensure failure is identified and corrected. In addition, as supported by B. Glisic and A. Sigrid scissor type structure are increasingly used in a wide range of mechanical and space engineering fields due to its advantages over disadvantages [14].

2.1.1 Modelling

In order to develop a design of a bridge, it is essential to be able to recognize and identify the basic components of the bridge and its materials. Each of the component experiences different combination of tension, compression and shear. As a basic understanding, bending load causes tension and compression and transverse forces causes shear stresses to the components. Solidworks is used to model each of the component throughout the duration of the project. After modelling has completed, the completed bridge model is ready for the next stage. The dimension of the collapsed bridge will be (W: 2200 mm x H: 2000 mm x L: 2800 mm)

2.1.2 Element Analysis

From the model acquired, finite element analysis is done to further study the characteristic of the bridge. There are variety of analysis that can be done with this method such as real-world forces, vibration, heat and fluid flow. Even though it is defined by the name of an analysis, but it is actually a development process of a product to simulate what will happen to the product if some of the factors are altered and applied [15]. In this case, the factors studied is the deformation and the shear stresses of the structure when load is applied. This method has the advantage to readily handle very complex geometry. However, it must be noted that data acquired from this method are only approximate solutions and might differ to experimental values [16]. By doing this, detailed inspection of failure of component can be done. Once the components are identified, it will be noted and taken into consideration for resizing or change its material to improve strength.

2.1.3 Data Acquisition and Analysis

Once element analysis has been done, computed data are to be analyzed further to forecast its weight and provide costing for a few types of material selection. Data on stresses point can be obtained from element analysis and from this information alteration of design can be made, if necessary to ensure the design is strong enough. Other than that, by examining the fluid flow characteristic on the bridge, it will tell when will the bridge be safe to use according to certain wind conditions. Upon finishing the design and analysis, the net weight of the bridge will be obtained and from that piece of information transportation method of the bridge can be further explored such as power needed to tether it to a certain vehicle and it's on road speed limit.

2.1.4 Fabrication

Fabrication of the prototype is initiated during the second phase of the project. The dimension of each component is as designed and shown in the next section. The expanded length of the bridge will be scaled down sized of less than 1 meter as the prototype is only intended to demonstrate its mechanism and component functionality. The fabrication of the prototype is done during the second half of the project which is during Final Year Project 2.

2.1.5 Results and Reports

After data collection and analysis, documenting results with reports are done to ensure that a proper documentation of the work done is recorded. First report would be the

interim report which is completed at the end of semester for Final Year Project 1. Results and reports are important as they will provide instance reference to other researches if they decide to study the same area as this scissor bridge. Other than that, mathematical analysis is included in reports to support the project research theoretically.

2.2 Design Parameter

2.2.1 Structure

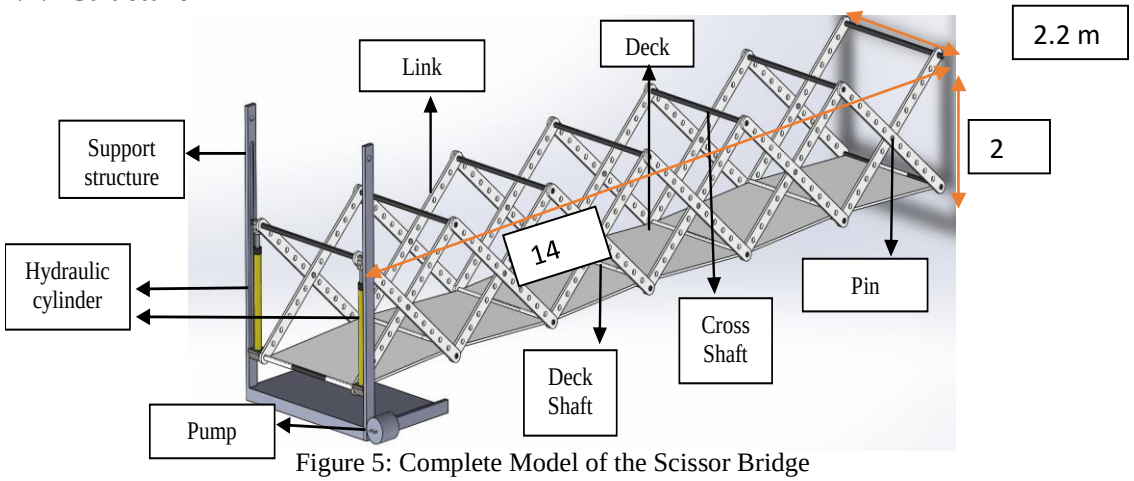


Figure 5: Complete Model of the Scissor Bridge

The design of the structure is mostly based on the retracted or the final length of the bridge needed which is approximately 14 m. From the aforementioned scope, the dimension set is (W: 2200 mm x H: 2000 mm x L: 2800 mm), whereby the length will be multiplied by the common ratio of scissor lift; 1:5. Fig. 5 depicts the complete model of the Scissor Bridge which inclusive of six sets of scissor link crosses (white), support structure (grey) and hydraulic cylinders (yellow). This structure operates on the mechanism of scissor concept, which when one set of links increases or decreases distance between two links, the similar motion will be applied to the other sets of links. In this design, the source of motion will be dedicated to the hydraulic cylinders to provide motion in horizontal direction to the first set of links to expand or retract the structure.

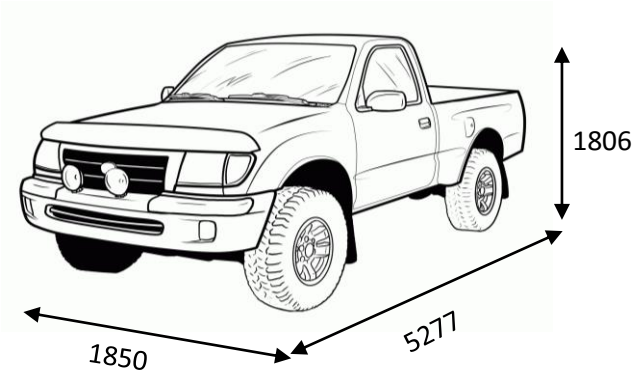


Figure 6: 4x4 vehicle with dimension [23]

2.2.2 Auxiliary Component

To complete the mechanism of the bridge, auxiliary component which are hydraulic cylinders as in Fig. 7 and pump is required to be specified. The purpose of hydraulic cylinder is to provide or act as the source of motion by moving the piston in the cylinder. In addition, the movement of the cylinder is powered by the pump which acts to pump in or pump out fluid in the cylinder.

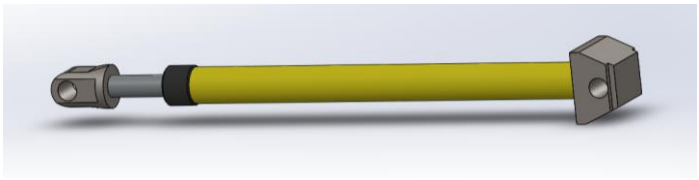


Figure7: Hydraulic piston embedded in design

The operation of the structure is mainly dependent on the piston's movement. This hydraulic concept is chosen because of its common technology and simple mechanism. It follows the same concept adapted by scissor lift which as the piston gain distance by the pressure from the fluid used, the structure will expand to increase the distance between links. *P* is the pressure of the working fluid in the cylinder, *F* is the force to operate or needed and *A* is the area in contact with working fluid. The pressure calculated from the equation:

$$P = \frac{F}{A} \quad (1)$$

Pressure obtain is the minimum pressure needed in the cylinder which is called as line pressure. Single-acting cylinder should suffice as the mechanism is very simple and straight forward. Single-acting cylinder is a type of cylinder that is pressurize at only one end and the other end is vented or exposed to the atmosphere [17].

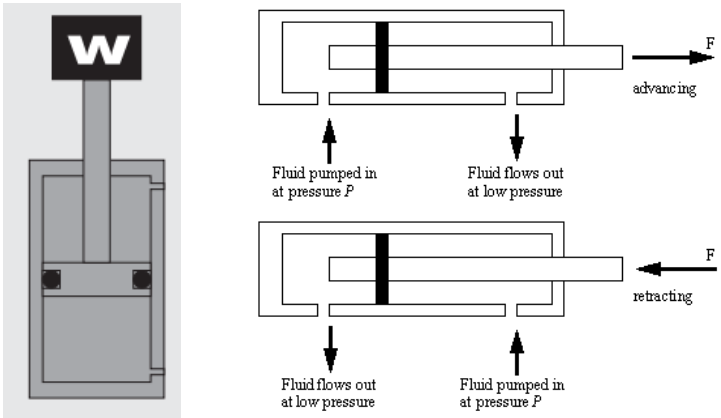


Figure 8: Single-acting cylinder

Pressure obtain will be the minimum pressure needed in the cylinder which is called as line pressure. Single-acting cylinder should suffice as the mechanism is very simple and straight forward. Single-acting cylinder is a type of cylinder that is pressurize at only one end and the other end is vented or exposed to the atmosphere [17]. The motion of the scissor bridge is governed by the principle of work and energy whereby the governing equation is:

$$T1 + \sum U_{1-2} = T2 \quad (2)$$

Based on equation (2), *T1* is the initial state of the structure, $\sum U_{1-2}$ is represented by $F\Delta d + mgh$ where $F\Delta d$ is the work done by the external for which in this case is the force from the pump and mgh is the potential energy from the structure's mass and height.

T1 = 0 as the initial state of the structure is static. The summation of work done by forces is inclusive of work done by the piston and the potential energy of the structure from its weight. *T2* = final kinetic energy of the structure. During expanding the structure, the motion of piston which is downwards is in the same direction to the gravitational potential energy of the structure and this is the reason they are in the same side in the equation. From the principle of work and energy, *T1* and *T2* represents the initial and the final kinetic energies respectively and $\sum U_{1-2}$ is the total of work done by all forces included in the system.

In the retraction of the structure, gravitational potential energy is on the right-hand side along with the final kinetic energy because of the direction of piston is now the opposite of the gravitational potential energy.

Recapping the motion of the structure, the hydraulic piston will be the key component to move the structure to either expand or retract/collapse. The direction of the piston's motion will be in vertical; upwards and downwards. To justify this motion significance, when the piston moves downward, it will provide a horizontal translation to increase distance between links and vice versa for the upward motion of the piston. Velocity is fixed in this case as to determine the power needed with the pressure and force value obtained from (1) and (2).

2.3 Design Modelling

The design of the bridge was proceeded to detailed design whereby the dimensions and shapes were taken into consideration. With the specifications set, Solidworks is used to create the 3D sketch of the design. The purpose of using this software is to ensure that all the parts design is able to fit to each other to assemble as a whole model of a Scissor Bridge. Also with the aid of this software, motion analysis can be done by using Motion Study function to visualize the motion of the structure. In developing the model, basic functions were used such as Sketching, Extruded Boss/Base, Extruded Cut and Mating component in assembly. There are 56 parts in total for the scissor structure only; pins, links, decks and shafts.

2.3.1 Link

In designing the link, the dimension was selected according to the optimum strength and weight of the link. These links hold up 40% of the total weight of the bridge and considered as a major component to the structure. Fig. 9 demonstrate the real part of link used in the modelling software.

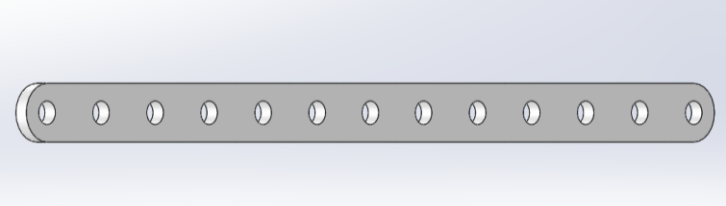


Figure 9: Link

2.3.2 Cross Shaft

As aforementioned, the cross shaft shown in Fig. 18 is a component to hold the links together and provide angular movement to the links. This cross shaft is designed in the shape of a normal cylindrical rod with the length of 2440 mm and diameter of 78 mm to fix in the link.

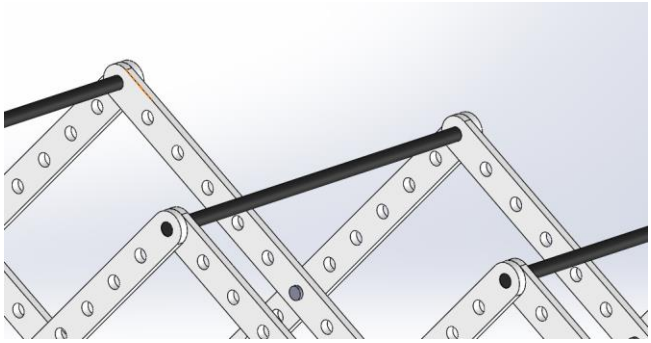


Figure 10: Cross Shaft (in black)

2.3.3 Deck

Fig. 11 depicts the deck which serves as the main unit to allow traffic on the scissor bridge to pass through. The design of the deck was made with the interlocking method. With multiple arrangement of the deck, it can be combined to expand the length. Another feature of using this interlocking design, it allows the folding mechanism for the bridge to retract to the folded state as shown in Fig. 12.

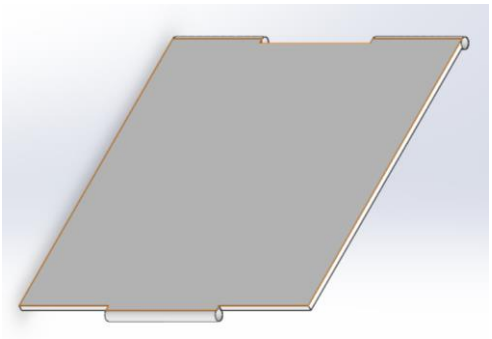


Figure 11: Deck of Scissor Bridge

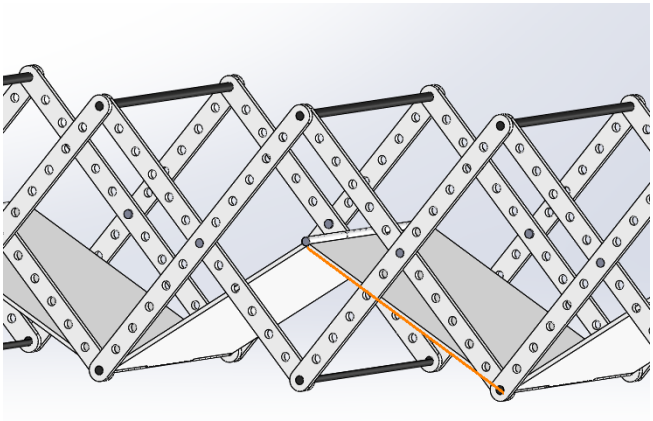


Figure 12: Half-folded structure

2.3.4 Pin

The pin serves a simple purpose to the structure which is to hold the links in position and to provide angular movement or rotation to the links. In other meaning, the pin acts similar enough to a bearing. However, in the real scale scissor bridge this pin will be accompanied with sets of bearing as it will be a welded component to the links.

2.3.5 Deck Shaft

Deck shaft serves a similar purpose to the cross shaft except that in the middle part it has a flat surface a shown in Fig. 13 below. The flat surface is designed to allow the deck to rest on it when the structure is opened and the deck is in a horizontal state.

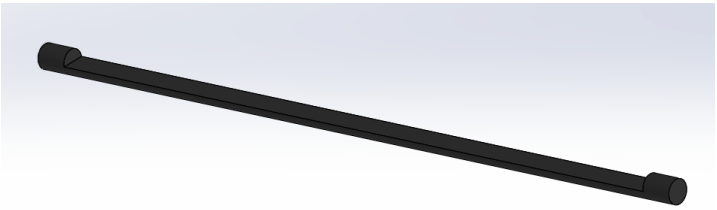


Figure 13: Deck Shaft

2.4 Structural Analysis

2.4.1 Stress analysis by ANSYS Workbench (Static Structural)

Stress analysis was simulated by utilizing ANSYS Workbench with the feature of Static Structural. In this analysis, the main objective is to validate whether the structure assembly is able to withstand the targeted load or break by showing a major deformation. In ANSYS Workbench, the simulation is done with a few fixed parameters. Meshing is done by using coarse span angle center for a faster simulation and meshing processes. Element size is set to default which will give the software to decide the best element size for the model. The nodes obtained from this meshing is 302927 and generated 131688 elements, which shows sufficient numbers of element to proceed the analysis.

2.4.2 Computational Fluid Dynamics (CFD) by ANSYS Fluent

CFD analysis will be done as a future work as it is only a minor priority from the scope of the project. However, as a note the wind condition as mentioned earlier, the wind speed will be 3 m/s according to the average wind speed in Malaysia [18].

2.5 Motion Analysis

2.5.1 Solidworks Motion Study

Motion Study is done by Solidworks. In this function, force is applied to the piston to provide movement to the structure and the animation of the structure is successfully developed. The motion is vice versa as the force to the piston is directed to the opposite side.

2.5.2 Kutzbach Equation (Degree of Freedom)

It is important to determine the degree of freedom of a design or mechanism to ensure the movability [4]. This is done by determining the number of links and joints included in the system. In this case, taking one set of the scissor structure should suffice to prove that the degree of freedom would be two; in horizontal and vertical motion of the structure. Kutzbach Equation or Criterion is as follows:

$$n = 3(l - 1) - 2j - h \quad (3)$$

Where, n = number of degree of freedom, l = total number of links, j = total number of primary joints and h = total number of higher-order joints.

2.6 Material Selection

As suggested by studies, Fibre Reinforced Polymer composites has some advantages when compared to conventional construction materials [19]. FRP is very strong as it dominates the high specific strength and stiffness. It also has a high strength to weight ratio which means the future scissor bridge could be lighter than expected if FRP is chosen to be its main material [20]. Other than that, it is a corrosion resistance material and this could reduce the maintenance cost of the bridge [21]. As claimed by studies, deck with FRP are usually multilayer which is also known popularly as sandwiches. The weight of this FRP is approximately lower by 20% compared to the conventional concrete slab [19]. However, this section is not covered in detail as it is not in the scope

of the project and this preliminary study should suffice for the project up to this stage. Throughout this project, A36 Structural Steel is selected for simulation due to the limitations experienced as ANSYS library is not able to support mixture of material properties.

2.7 Moment Analysis

In order to fully define the characteristic and the properties of the scissor structure, s simple analysis on structural deflection and moment is done. For the sake of simplicity, the scissor structure is considered to be a beam shape and this structure requires two type of beam which is cantilever beam as in Fig. 14 and simply supported beam as Fig. 15. This is because when the structure is expanding from the closed position, only one end is fixed, therefore this fulfills the cantilever properties. When the structure is full opened or expanded, it is considered to be a simply supported beam as both end is on the ground. Any of the cases presented is considering a uniformly distributed load.

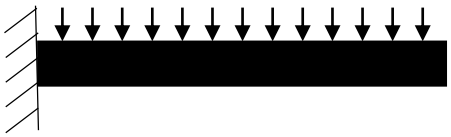


Figure 14: Cantilever Beam Free Body Diagram

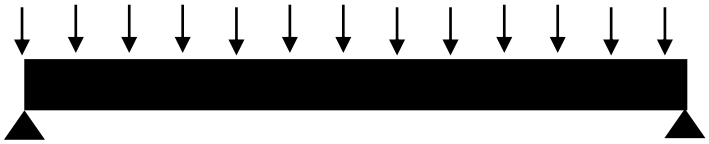


Figure 15: Simply supported beam

3. Results and Discussion

3.1 Dimension Table

After running a few processes in designing the Scissor Bridge, the dimensions of each component are finally obtained. Several design iterations were needed to ensure that the structure is at its optimum strength and meet the scope of the project. Table 1 below shows the summary of the dimensions of the components for the scissor structure.

Table 55: Components list and design specifications

Component	Function	Dimension	Material
Link	• Structural support	• Length: 3312 mm • Hole diameter: 80 mm	Steel (A36)
Cross Shaft	• Structural support • Provide angular movement	• Length: 2440 mm • Diameter: 78 mm	Steel (A36)

Deck	• Main feature as platform for usage	• Length: 2340 mm • Width: 2200 mm • Hole diameter: 78 mm	Steel (A36)
Pin	• Minor structural support • Provide angular movement	• Length: 120 mm • Diameter: 78 mm	Steel (A36)
Deck Shaft	• Structural support • Provide angular movement • Support deck placement	• Length: 2440 mm • Diameter: 78 mm	Steel (A36)

3.2 Stress analysis

This section discusses regarding the stress analysis conducted to the whole structure of the scissor bridge using ANSYS Static Structural. Fig. 16 shows the forces applied to the structure which in total of 210070 N. These forces are assumed to be the forces that will be exerted by the 2.6 unit of 4x4 pick-up truck during its operation. In this simulation, both of the end of the structure is set to be the fixed support.

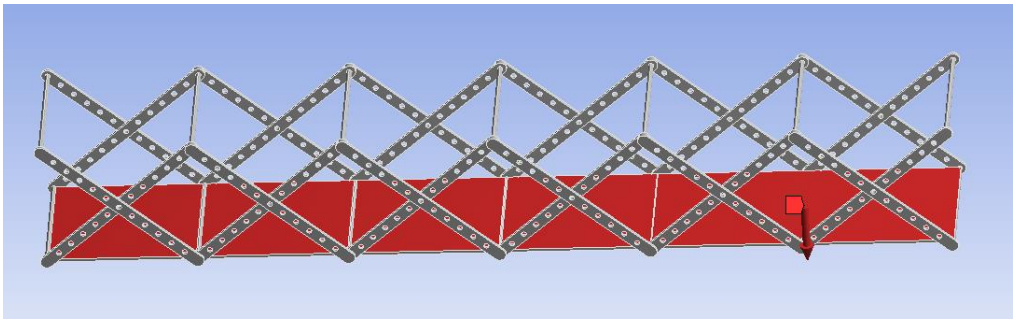


Figure 16: Uniform load applied to the structure

Fig. 17 shows the total deformation of the scissor structure after load of 210070 N is applied to the middle section (red contour). As can be seen from Fig. 35, the maximum deformation is 15.741 mm. This shows that when the targeted load which is the typical 4x4 pick-up truck passes by, the structure will be able to withstand the force exerted. Take note that the load applied is the kerb load of the truck which means it is inclusive of the weight of the vehicle with its cargo on the back side. With remarks from a study made by a group of researchers, the similar design of structure passed the experimental test to carry two set of loads; 13.6 kN and 10 kN and also it is claimed that the analytical value had less than 10% of error [22].

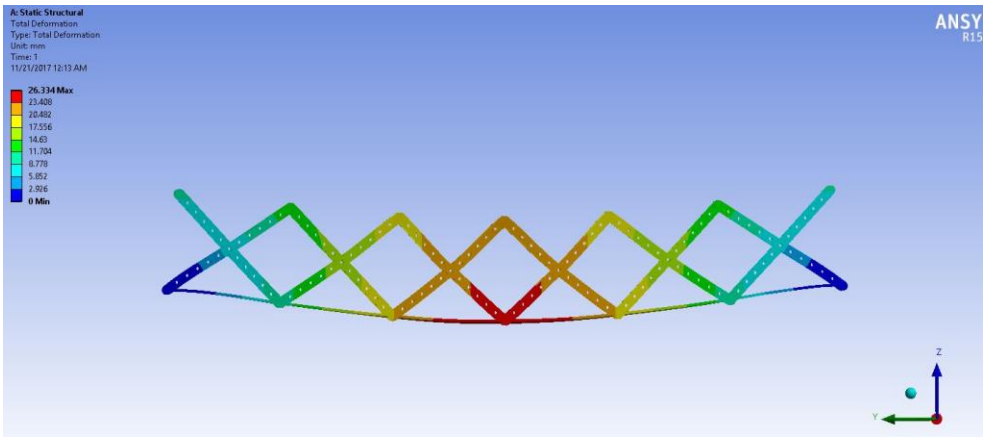


Figure 17: Total Deformation contour of scissor structure

There are two type of stresses that can be obtained from ANSYS Static Structural analysis, von-mises stress (equivalent stress) and also maximum principle stress. Based on Fig. 18, the highest value of maximum principle stress is 138.64 MPa and from Fig. 19 the equivalent stress has the value of 149.48 MPa at maximum.

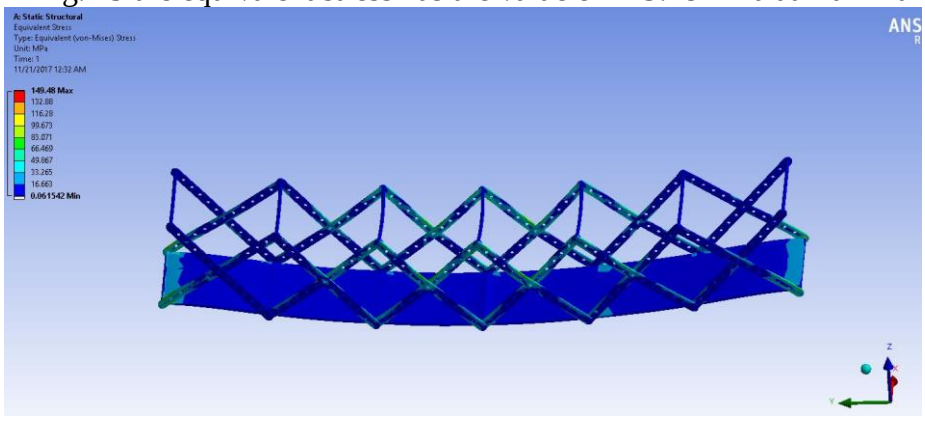


Figure 18: Maximum Principle Stress on structure

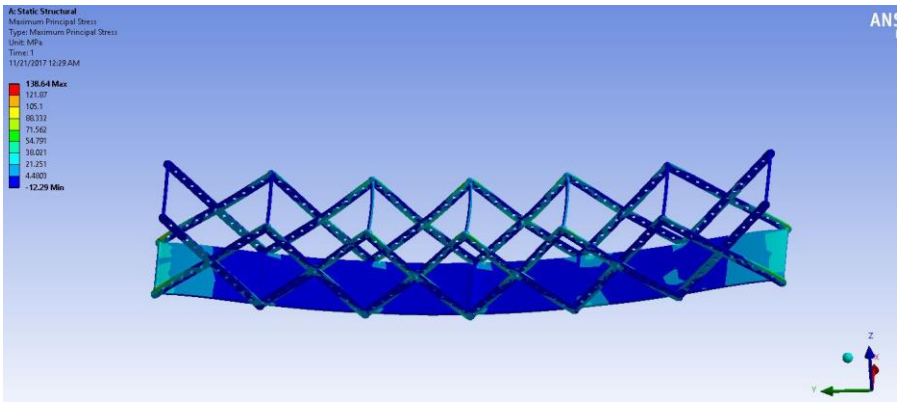


Figure 19: Von-mises stress

These values are used to obtain the safety factor of the scissor bridge by using the equation;

$$Factor\ of\ Safety = \frac{Yield\ Stress}{Allowable\ Stress} \quad (4)$$

In this case, yield stress is provided by the properties of A36 Structural Steel which is 250 MPa. By using the value from maximum principle stress and equivalent stress (von-mises) which is 138.64 MPa and 149.48 MPa respectively, the factor of safety is obtained.
From maximum principle stress:

$$Factor\ of\ Safety = \frac{250\ MPa}{138.64\ Mpa}$$
$$Factor\ of\ Safety = 1.803$$

From equivalent stress:

$$Factor\ of\ Safety = \frac{250\ MPa}{149.48\ MPa}$$
$$Factor\ of\ Safety = 1.672$$

These values support that the structure is able to withstand the load of 210070 N and to clarify this value, the load value used is a summation of the total weight of the structure and the maximum load of 2.6 units of the trucks on the bridge by taking one length of the truck, 5277 mm and fitting as many truck as possible onto the 14000mm scissor bridge.

However, this value changes when only one 4x4 truck is allowed to pass at one time. When this condition is used, the load applied will be only 19100 N and the maximum deflection is 13.451 mm with 118.47 MPa of maximum principle stress and 127.73 MPa of equivalent stress (von-mises). These values can be found in Fig. 20, Fig. 21 and Fig. 22.

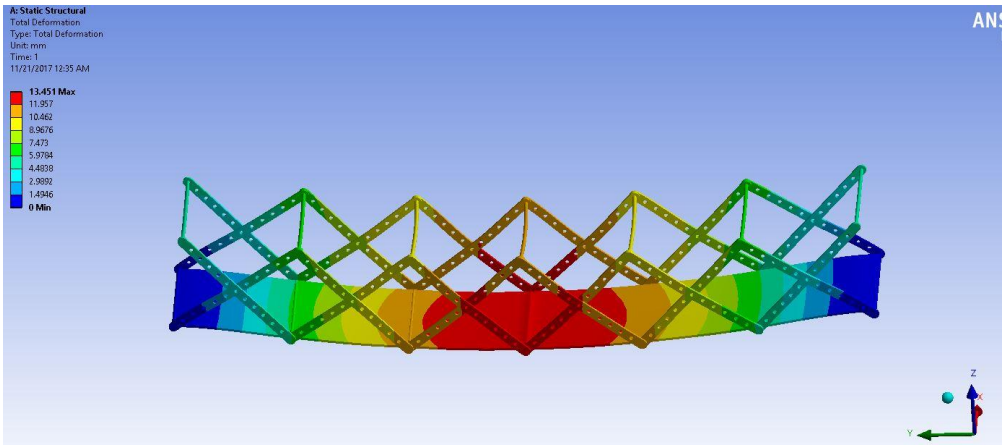


Figure 20: Total Deflection for 1 Truck Loading

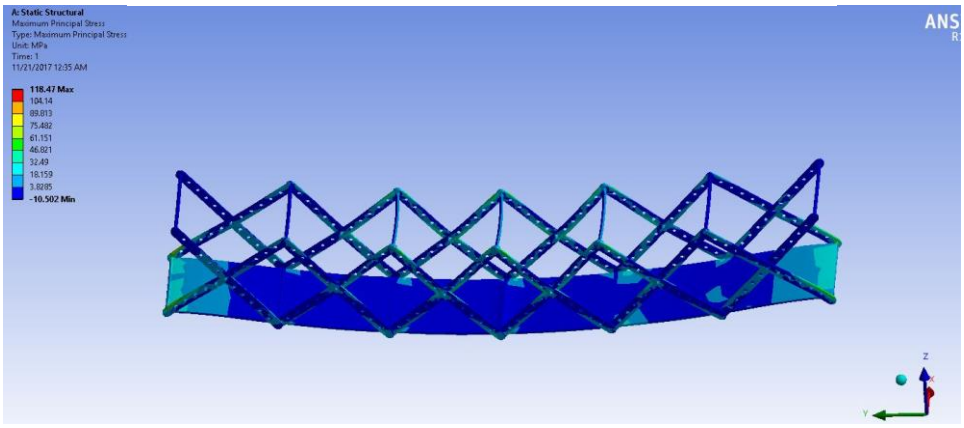


Figure 21: Maximum Principle Stress for 1 Truck Loading

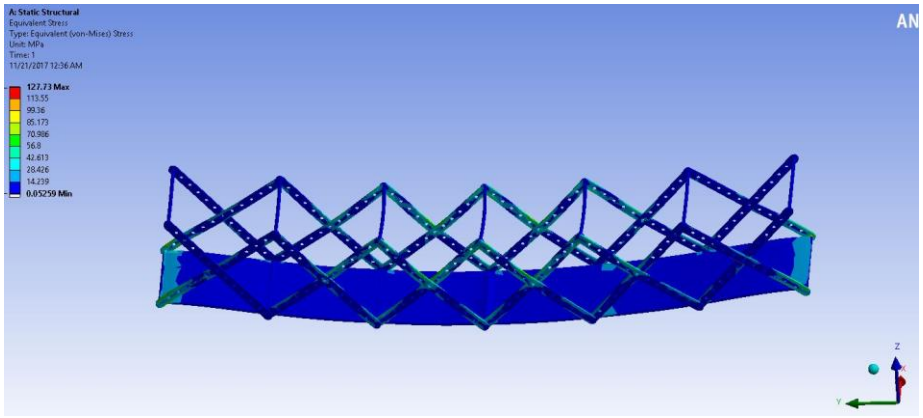


Figure 22: Von-mises stress for 1 Truck Loading

3.3 Moment Analysis

For the case of cantilever beam, there will be two lengths analyzed which is when only 2 sets of the scissor structure are opened and 4 sets of the scissor structure are opened. The weight of used in this case is 160410 N which is only the weight of the scissor structure without any loading. A maximum deflection of $6.994\ x\ 10^{-6}$ m and $5.577\ x\ 10^{-7}$ are obtained when assuming the moment of inertia, I equal to $1.46\ m^4$ and the modulus of elasticity, $E = 200\ GPa$ for A36 Structural Steel. The length, L for 2 sets is 4.67 m and for 4 sets is 9.33 m. This can be obtained by using factor of 2/6 and 4/6 of the (6 sets) 14 m total bridge length. The moment at the free end is calculated to be 374.56 kNm for 2 sets and 748.27 kNm for 4 sets.

$$\delta_{\max @\ 4.67m} = \frac{qL^4}{8EI} \quad (5)$$

$$M = \frac{qL^2}{2} \quad (6)$$

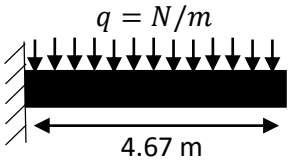


Figure 23: FBD for Cantilever beam case 1

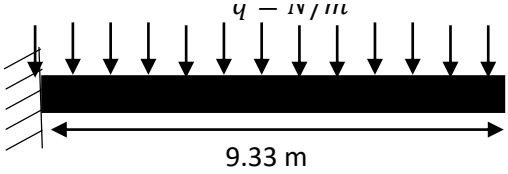


Figure 24: FBD for Cantilever beam case 2

Similar method is used to analyzed the structure when it is expanded fully and the assumption made is that the structure to be a simply supported beam. There are two cases analyzed which is one 4x4 truck loading and 2.6 of 4x4 truck loading. From this analysis, the maximum deflection is obtained by using the same input as equation (5) and (6) except for the length, *L*. The FBD are as depicted in Fig. 45.

$$q = N/m$$

$$q_{case\ 1\ truck\ loading} = 11457\ N/m$$

$$q_{case\ 2.6\ truck\ loading} = 15005\ N/m$$

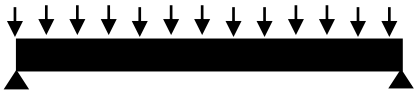


Figure 25: Simply supported beam with two q values

Table 2: Summary of moment and deflection for both cases

Cantilever Beam Case		**Simply Supported Beam Case**	
Length = 4.67 m		**Length = 14 m**	
Moment at Free End (Nm)	**Maximum Deflection (m)**	**Unit of 4x4 truck**	**Maximum Deflection (m)**
374557	$6.994\ x\ 10^{-6}$	1	$1.962x10^{-5}$
Length = 9.33 m		2.6	$2.570x10^{-5}$
Moment at Free End (Nm)	**Maximum Deflection (m)**		
1495021	$1.114\ x\ 10^{-4}$		

3.4 Calculation

3.4.1 Force Needed to Operate Scissor Bridge by Work-Energy Principle

Force needed for structure to expand will be governed by eq. (2) with an input of velocity in kinetic energy equation. Table 2 below shows the variation of velocity input and force required. Force needed for structure to expand will be governed by eq. 2 with an input of velocity in kinetic energy equation. Table 2 shows the variation of velocity input and force required. From Table 3, the optimum velocity of the structure is 4.43 m/s as it would require minimum amount of force to expand (40.06184 N) and force to retract (324393.8 N). Higher force needed to retract is caused by the extra work needed to counter the gravitational force downwards as the piston will need to move upwards.

Using equation (1),
Substituting force to expand and force to retract from velocity of 4.43 m/s,

a) F = 40.06184 N – force to expand
b) F = 324393.8 N – force to retract

Fixing area, *A* with design of the piston radius of 0.125 m,

$$\boldsymbol{P = 6608479\ Pa // 6608.48\ kPa}$$

In the selection of motor in the future, this value of pressure is important as this value will determine the specification of the motor. The working motor should be able to provide force of 324393.8 N to ensure that the bridge is able to expand.

Table 3: Calculation summary for Varied Velocity

Velocity of Structure (m/s)	Force to expand (N)	Force to retract (kN)
4	-29.5967	294.4308
4.3	-9.23875	315.0129
4.43	**0.040062**	**324.3938**
5	43.98626	368.8238
6	133.921	459.7485
7	240.2075	567.205

3.4.2 Kutzbach Equation to Prove Movability

By extracting one set of the scissor structure;

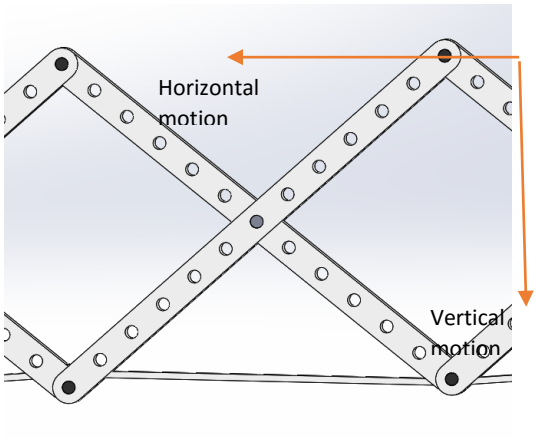


Figure 26: One set of scissor structure

Substituting into equation (4), where n = number of degree of freedom, l = 5 - total number of links, j = 5 - total number of primary joints, h = 0 - total number of higher-order joints. Therefore, $n = 2$. By obtaining number of degree of freedom = 2, it is proven that the structure will be able to provide horizontal and vertical motion.

3.5 Computational Fluid Dynamic Analysis

External force by the wind was taken into consideration in this project as stated in the scope. However, the weightage of wind factor is not as high as the other factor such as design and material of the structure. In this section, pressure exerted by 3 m/s average wind in Malaysia was found to be 146 Pa at maximum and lowest recorded is 18.4 Pa. Pressure of 146 Pa can be found at the major component which is the link whereby the highest wind resistance exists. Fig. 27 shows the surface of the inlet of the structure accompanied by the contour of the static pressure generated from the wind.

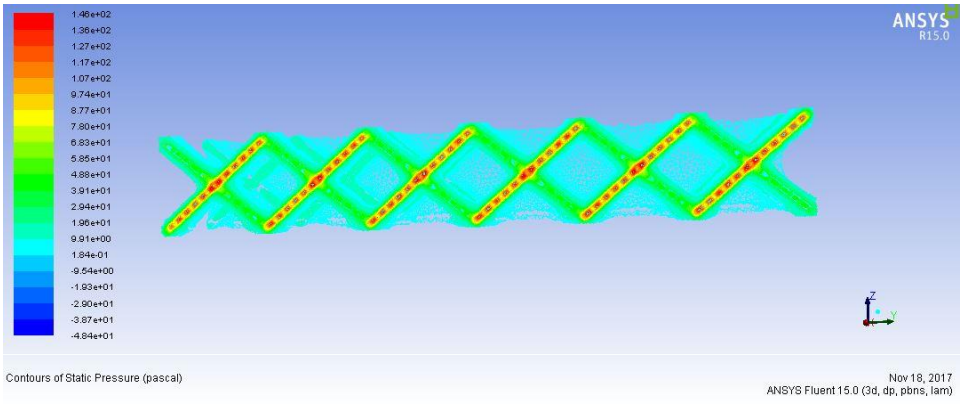


Figure 27: Pressure on Structure on wind effects

4.Conclusion

This paper presented a thorough theoretical and mathematical analysis of the scissor structure accompanied with the auxiliary components. Design of the structure are based

on the literature review and cited studies from other research papers supported with structure analysis in results and discussion section. Kutzbach equation used aided to obtain number of degree of two which satisfies the hypotheses. Hence, the objectives of the project are also met which is to design to design a collapsible light weight scissor type bridge using computer aided drafting (CAD) software. Following from that, this project has numerical analysis on the collapsible bridge and also built and fabricate scaled model of the bridge. Lastly, the results support that this structure is able to withstand the load that is intended to be carried. This paper also reveals the basic design of the collapsible scissor bridge by parts and each function of the parts are justified. With the aid of Computer-Aided Design (CAD) software, it has enable the possibility to discover more improvement for the current existing design. Apart from that, a simple analysis using ANSYS software has assisted this project to understand the characteristic and the ability of the components when load is applied.

References

[1] S. G. D/iya, M. B. Gasim, M. E. Toriman, and M. G. Abdullahi, "Floods in Malaysia: Historical Reviews, Causes, Effects and Mtigations Approach," *Int. J. Interdiscip. Res. Innov.*, vol. 2, no. 4, pp. 59–65, 2014.

[2] J. B. dan Penyelamat, "Laporan Tahunan 2014."

[3] N. Bronner, "MB 4.0: THE FUTURE OF BRIDGE TECHNOLOGY." [Online]. Available: http://www.pitt.edu/~nbb8/eti.html. [Accessed: 18-Nov-2017].

[4] J. . G. R.S Khurmi, *Theory of Motion and Mechanism*. 2005.

[5] R. C. Hibbeler, *DYNAMICS*. .

[6] "Folding Gate." [Online]. Available: https://www.goodwincole.com/wp-content/uploads/2011/12/foldinggate-1024x768.jpg. [Accessed: 17-Nov-2017].

[7] "MEWP." [Online]. Available: http://www.nationwidehire.co.uk/wp-content/uploads/2015/11/Genie-2046.jpg. [Accessed: 17-Nov-2017].

[8] "Degree of Freedom (Kutzbach Criterion)," *Physics Forums*, 2013. .

[9] CHRISTOPHER TEH BOON SUNG, "Possibility of electricity from wind energy in Malaysia: Some rough calculations," 2010. [Online]. Available: http://www.christopherteh.com/blog/2010/11/wind-energy/. [Accessed: 13-Nov-2017].

[10] NDBC, "Are wind speeds the same over land as they are over the ocean?"

[11] K. A. I. Ario, Y. Chikahiro, I. Tanikura, S. Onno, M. Nakazawa, S. Nakatani, K. Yamada, S. Nakamura, Y. Tanaka, R. Tsubaki, S. Matsumoto, "No Title," in *Consider recovering method by mobile bridge how to install a disaster*, 2016.

[12] I. Ario, "Structure with Expanding and Folding Equipment," 2006–037668, 2012.

[13] I. Ario, "Scissor Type Retractable Structure," WO2015/193930A1.

[14] B. Glisic, S. Adriaenssens, and P. Szerzo, "Structural analysis and validation of a smart pantograph mast concept," *Comput. Civ. Infrastruct. Eng.*, vol. 28, no. 9, pp. 651–665, 2013.

[15] Autodesk, "Finite Element Analysis Software," 2017. .

[16] O. de Weck and I. Y. Kim, "Finite Element Method," *Eng. Des. Rapid Prototyp.*, vol. 810, p. 26, 2004.

[17] T. R. Mount and R. B. Data, "Design Engineering Guide," pp. 177–195.

[18] CHRISTOPHER TEH BOON SUNG, "Possibility of electricity from wind energy in Malaysia: Some rough calculations," 2010. [Online]. Available: http://www.christopherteh.com/blog/2010/11/wind-energy/. [Accessed: 17-Nov-2017].

[19] P. B. Potyrała, "Use of Fibre Reinforced Polymer Composites in Bridge Construction. State of the Art in Hybrid and All-Composite Structures," *Thesis*, 2011.

[20] T. a Hoffard and L. J. Malvar, "Fiber-Reinforced Polymer Composites in Bridges : a State-of-the-Art Report," *Navfac*, no. May, 2005.

[21] IABSE, "Use of Fibre Reinforced Polymers in Bridge Construction," vol. 7, 2003.

[22] Y. Chikahiro *et al.*, "Structural Analysis and Experimental Study for realsized MB Travelable Vehicles," vol. 2, pp. 2–3, 2014.

[23] M. Jenning, "No Title." [Online]. Available: https://www.google.com/url?sa=t&rct=j&q=&esrc=s&source=web&cd=3&cad=rja&uact=8&ved=0ahUKEwj0gP6yrs3XAhXGOo8KHchfBsoQFgg9MAI&url=https%3A%2F%2Fwww.jenningsmotorgroup.co.uk%2Fnewvans%2Fford%2Franger%2Franger-dimensions%2F&usg=AOvVaw3SRnVzr8nTqa_pGSbZzJxP. [Accessed: 20-Nov-2017].

eureca 2017 – Conference Paper
Paper Number 2ME14

Comparisons of Flow Patterns over a Hierarchical and a Non-hierarchical Surface in Relation to Biofouling Control

Mohammed Ridha Bin Ahmad Fawzan[1*], Felicia Wong Yen Myan[2]

[1]*School of Engineering, Taylor's University, Malaysia*

[*]*mohdridha88@gmail.com*

Abstract

Biofouling can be defined as unwanted deposition and development of organisms on submerged surfaces. It is a major problem as it causes water contamination, infrastructures damage and increase in maintenance and operational cost especially in the shipping industry. There are a few methods that can prevent this problem. One of the most effective methods which is using chemicals particularly Tributyltin has been banned due to adverse effects on the environment. One of the non-toxic methods found to be effective is surface modification which involves altering the surface topography so that it becomes a low-fouling or a non-stick surface to biofouling organisms. Current literature suggested that non-hierarchical topographies has lower antifouling performance compared to hierarchical topographies. It is still unclear if the effects of the flow on these topographies could have aided in their antifouling properties. This research will use Computational Fluid Dynamics (CFD) simulations to study the flow on these two topographies which also involves comparison study of the topographies used. According to the results obtained, it is shown that hierarchical topography has higher antifouling performance compared to non-hierarchical topography. This is because the fluid characteristics at the hierarchical topography is more favorable in controlling biofouling. In addition, hierarchical topography has higher wall shear stress distribution compared to non-hierarchical topography.

Keywords: Biofouling, surface modification, hierarchical topography, non-hierarchical topography, CFD

1. Introduction

Biofouling is any unwanted deposition and development of organisms on submerged surfaces [1]. It is a major problem as it contaminates water and medical instruments inflicting health risk. Biofouling also causes unnecessary drag leading to low fuel efficiency of marine industry and reduces operational range. Other than that, biofouling promotes physical damage to infrastructures resulting in increased maintenance cost [2]. US$2.3 million were spent annually on a vessel due to biofouling of the vessel hull which causes increase in fuel consumption by 20.4% due to drag [3]. In oil and gas sector, the cost to repair equipment damaged by biofouling is approximately US$ 960 to US$ 1280 million [4]. These examples show that it is important for researchers to develop antifouling measures to control this problem.

T. Vladkova (2009) explained in her study that there are three principles to control biofouling [5]. The first is to use the mechanical approach to detach the biofoulers from the surface. The second approach is the application of chemical agents to exterminate or inactivate the biofouling organisms. The last approach is surface modification which involves altering either surface chemical composition or surface topography so that it becomes a low-fouling or non-stick surface to biofouling organisms. Rosenhahn (2012) also recommended similar approach which include toxic antifouling coatings, fouling release coating and foul release via surface modification as shown in Figure 1 [6].

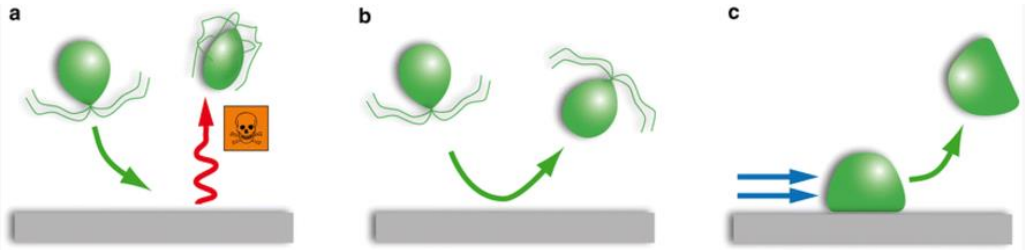


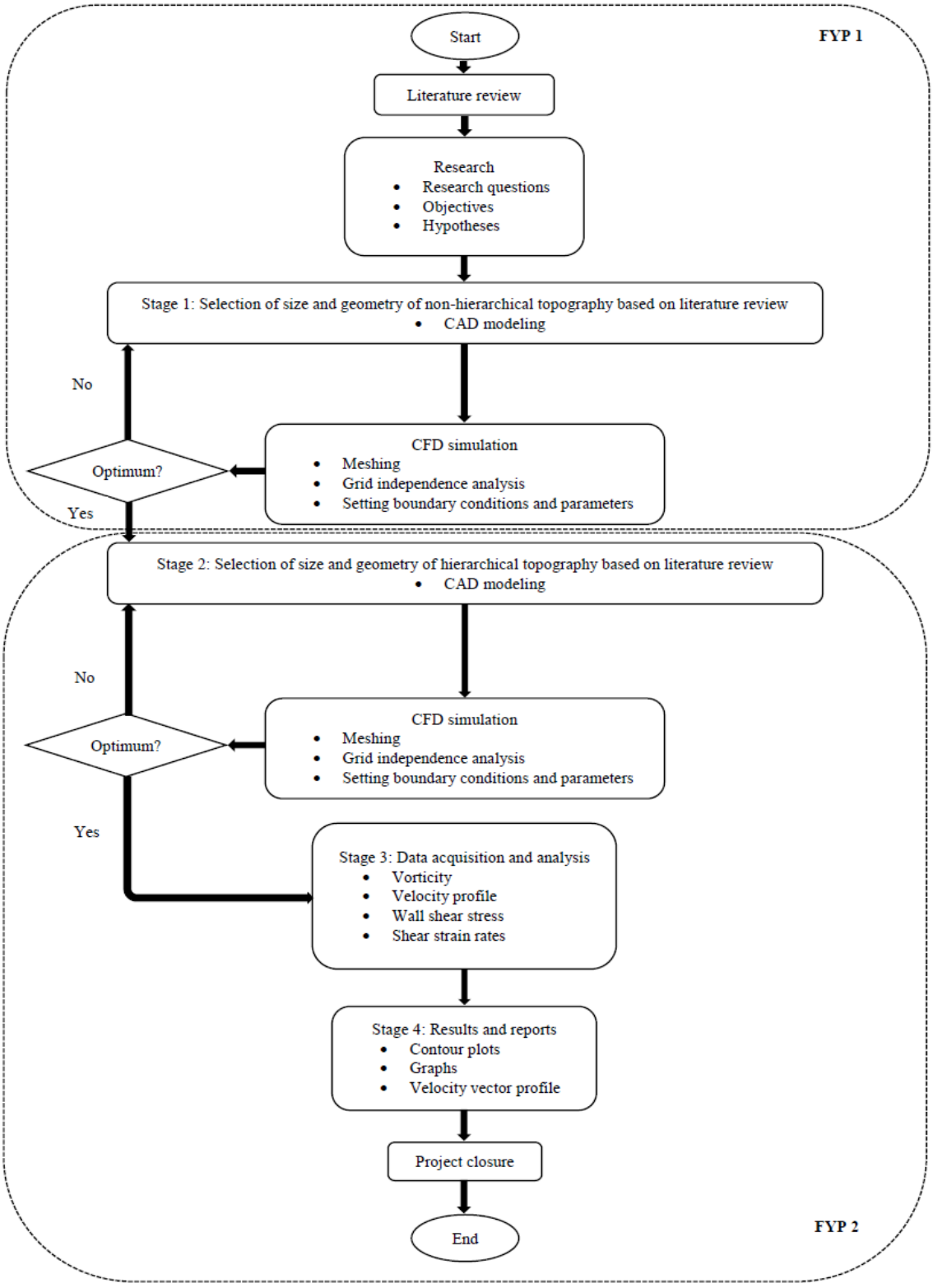
Figure 76. Various approach in preventing biofouling: (a) toxic antifouling, (b) foul release, (c) foul inhibition [6]

A variety of chemical approaches were used in order to prevent biofouling of surfaces and some of it has been banned because of its adverse effects on the environment. Decades ago, a type of biocide named Tributyltin (TBT) was used as a coating on vessel hulls to prevent biofouling and by far this is the most effective method to mitigate biofouling in the history of antifouling technology to date [7]. However, this method was banned by the International Maritime Organisation (IMO) in November 2001. This is because IMO discovered that TBT causes detrimental effects on the environment like abnormal growth of the oysters, imposex (female gastropods developing male characteristics) and others [8]–[10]. K. A. Dafforn (2011) also mentioned about the usage of copper as a co-biocide to increase the efficacy of TBT in paints for vessel hulls [11]. Copper is essential for metabolic functioning but it becomes toxic when the bioavailability level of copper exceeds the tolerance level of an organism [12]. The adverse effects of copper on the environment also eventually lead to restrictions of copper usage in paints for vessel hulls in countries like Canada,

Denmark and the United States [13]. These were two popular chemical approaches that were used to control biofouling.

As mentioned above, surface modification is another method that can be used for antifouling applications. This method is preferable over other chemical approaches because it is environmental friendly. Previous studies have investigated the effects of surface topographies modification and the results are promising. The surface topographies' modification includes modifying the size and geometry. In recent years, these studies uses Computational Fluid Dynamics (CFD) assessment to study the flow of the fluid on top of these modified surfaces [14]. By studying the flow, researchers can come out with an optimum size and geometry of surface topographies that can control biofouling effectively. More study on this method is needed due to the fact that it is relatively new compared to other methods and also to measure its efficacy for antifouling applications.

2. Research Methodology



2.1. Geometry Modeling

Solidworks 2013 software was used in creating the fluid domain. The fluid domain was created as a rectangular block as shown in Figure 3 with a length of 80 mm and a square cross section of width and height of 8 mm. The distance between the inlet of the fluid domain and the topography array is 65 mm. The creation and placement of the array nearby outlet follows the Hagen-Poiseuille's flow theory [15]. This theory explains that in a fluid will develop a laminar flow in any fluid domain with a very significant difference in length compared to the size of its cross section. The development of the laminar flow is induced by the pressure drop along the flow. Two models were created for this research. Figure 4 shows close up view of non-hierarchical topography while Figure 5 shows close up view of hierarchical topography with circular pillar.

The selection of the geometry and size for these topographies are based on the literature review. In a study conducted by Halder et al. (2013), the author found that well circumscribed geometries like circle, rectangle, hexagon and others develops higher shear bounded isolated areas compared to continuous geometries like ridges. Hence, cube was chosen as the first layer for non-hierarchical topography. Circular pillar was chosen as another well circumscribed geometry for the second layer of the topography to develop hierarchical topography. According to Nick Aldred et al. (2010), the optimum size of topography to control biofouling is between 64-256 μm. Most of the biofouling organisms failed to attach to the surface at this range of size [16]. Therefore, all dimensions used in this research are within this range as shown in Figure 4 and 5.

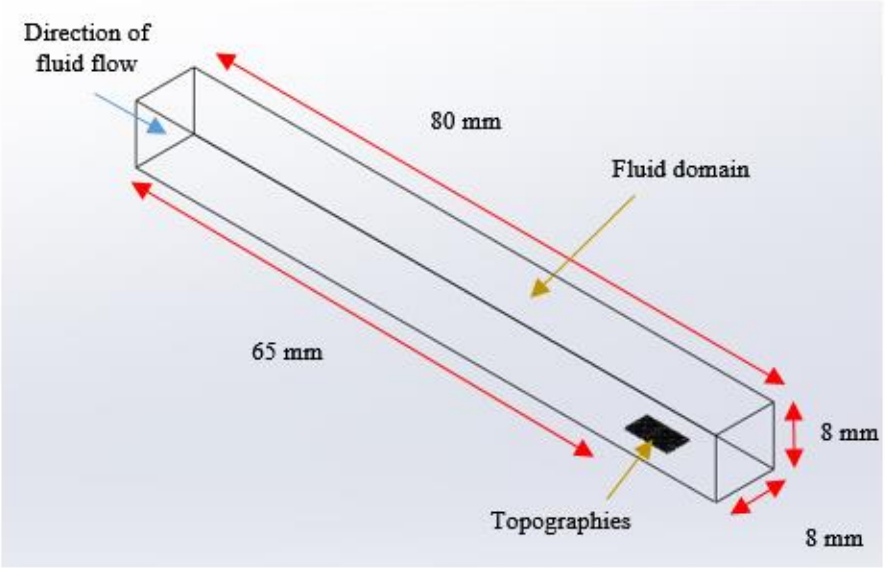


Figure 77. Dimensions of the fluid domain and the location of the topography array in the fluid domain

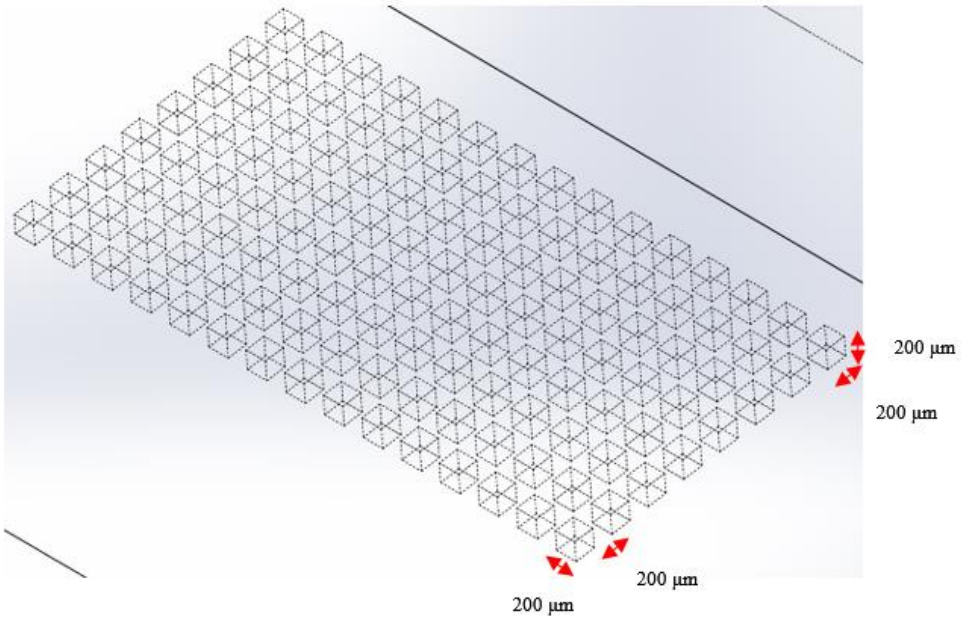


Figure 78. Dimensions of the non-hierarchical topography

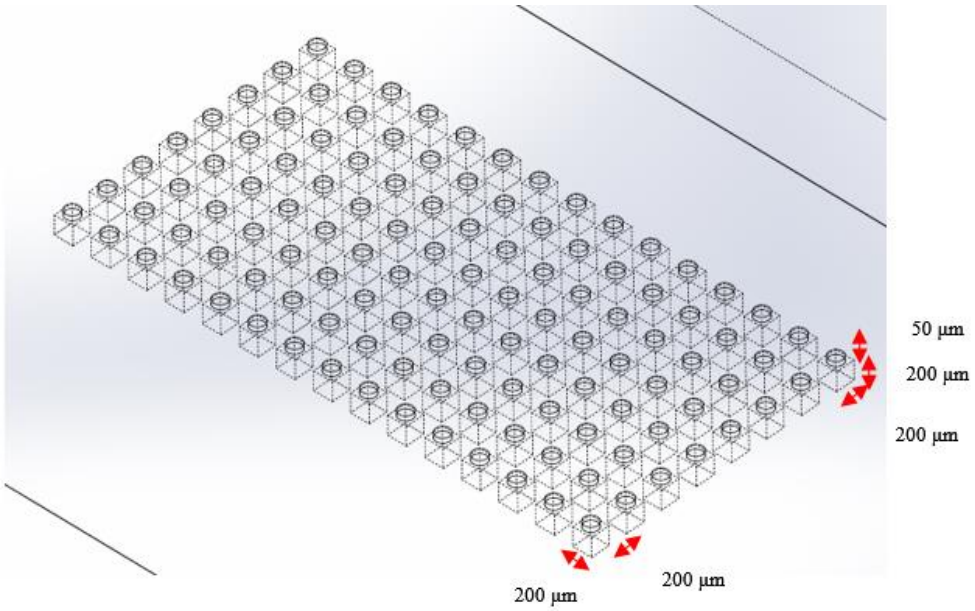


Figure 79. Dimensions of hierarchical topography

2.2. Meshing Method

The meshing of the models must be done properly in order to get accurate results. The models created using Solidworks were imported as STEP file into ANSYS. Then, the meshing module was opened to start the meshing process. A fine mesh was created when tetrahedron method was used (Figure 6 and 7).

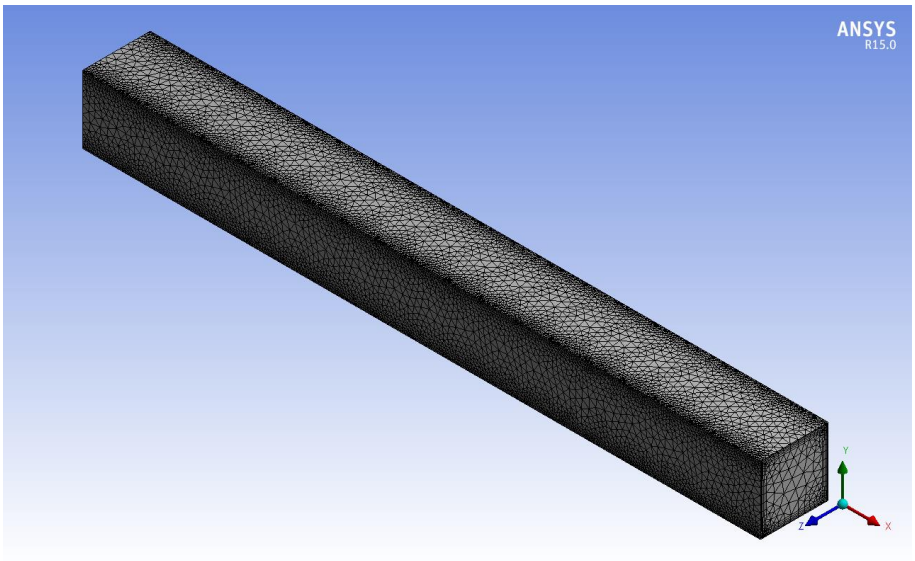


Figure 80. Meshing using tetrahedron method

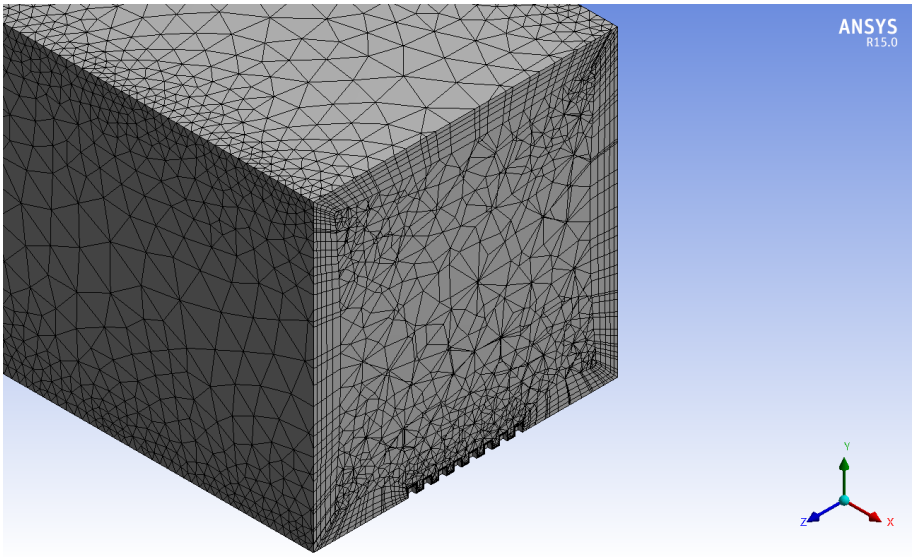


Figure 81. Close up view of the meshing around topography

To get a higher quality meshing, face and edge sizing function around the topographies were used (Figure 8 and 9). All faces and edges of the wall present in each model was selected. Using this function, a smaller size of elements can be produced around the topographies and the surface of the fluid domain. Other than that, 5 layers of inflation was used as shown in Figure 7 to produce finer mesh elements around the wall. Mesh produced from these functions are more refined and highly concentrated to increase the sensitivity and accuracy of the flow around the topography. In return, more accurate results can be acquired. For each model, different number of elements was used for grid independence analysis which will be explained later. Element quality and skewness parameter was also used to check the meshing quality of each model.

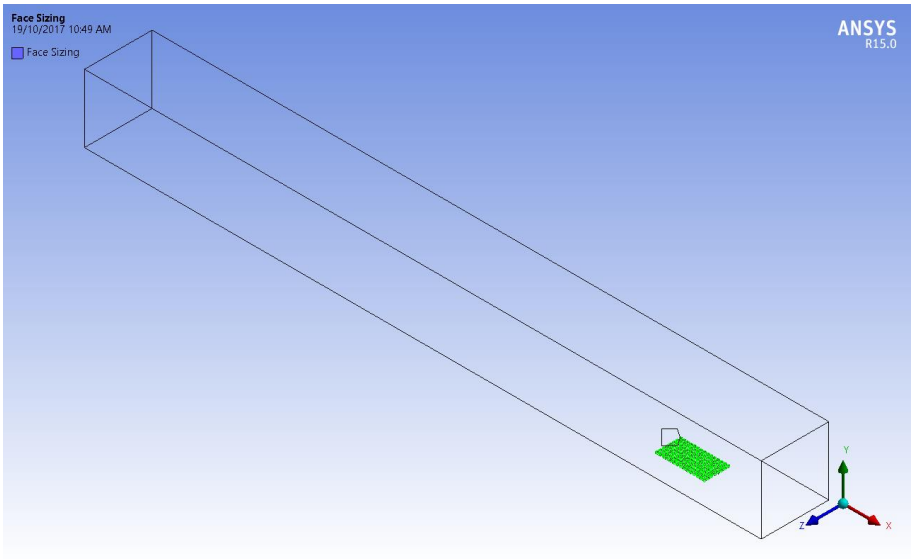


Figure 82. Face sizing at the topography

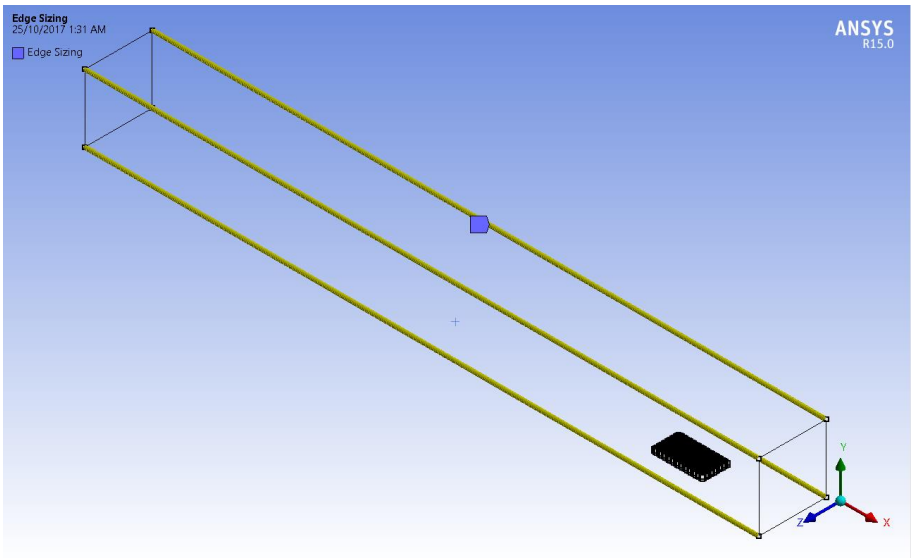


Figure 83. Edge sizing at the edges of the wall

2.3. Boundary and Numerical Setup

The boundary and numerical setup for the research was done using CFD software package ANSYS FLUENT, version 15. The inlet, outlet and topography of the model are named as 'Inlet', 'Outlet' and 'Wall' as shown in Figure 10. The fluid used for this simulation is water with density ρ, of 1000 kgm^{-3} and dynamic viscosity μ, of 0.00001 $kgm^{-1}s^{-1}$. The k-ω turbulence model was used to simulate the flow as this model is able to provide higher accuracy of wall shear results [14]. The wall of the fluid domain was set with no-slip boundary condition. According to the study done by Halder et al. (2013), the mass flow rate was set at 0.001 kgs^{-1} at the inlet and outlet. It is important to note that the mass flow rate was set faster than Halder's study as the model used in this research is longer and has larger cross section [14].

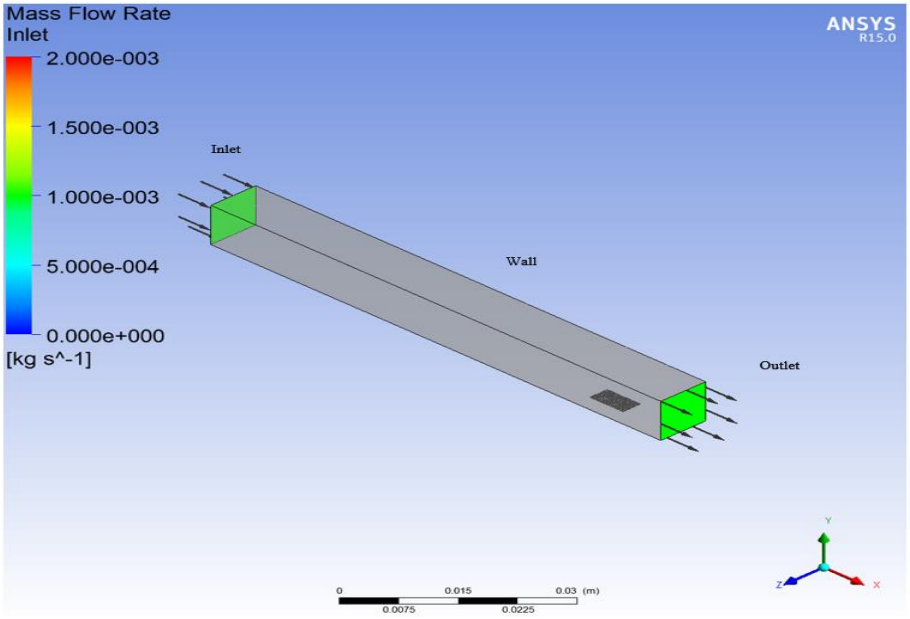


Figure 84. Boundary setup

The Navier-Stokes equations (Equation 1 to 3) and the continuity equation (Equation 4) was used in this flow study. The continuity equation was used to ensure the conservation of mass and momentum [17].

$$\frac{\partial \rho u}{\partial t} + \nabla \cdot \rho u V = -\frac{\partial \rho}{\partial x} + \nabla \cdot (\mu \nabla u) + S_{m,x} \quad (1)$$

$$\frac{\partial \rho v}{\partial t} + \nabla \cdot \rho v V = -\frac{\partial \rho}{\partial y} + \nabla \cdot (\mu \nabla v) + S_{m,y} \quad (2)$$

$$\frac{\partial \rho w}{\partial t} + \nabla \cdot \rho w V = -\frac{\partial \rho}{\partial z} + \nabla \cdot (\mu \nabla w) + S_{m,z} \quad (3)$$

$$\frac{\partial \rho u}{\partial t} + \nabla \cdot (\rho V) = 0 \quad (4)$$

Where *u*, *v* and *w* represents the velocity in *x*, *y* and *z* direction, ρ and μ are the fluid density and dynamic viscosity, *V* is the velocity and $S_{m,x}$, $S_{m,y}$, and $S_{m,z}$ are the source terms for *x*, *y* and *z* component.

3. Results and Discussion

3.1. Grid Independence Analysis

A grid independence analysis is an important part of this research in order to find an optimum number of mesh elements. This is required to ensure that the computational time taken are minimized while getting accurate results.

These analyses followed the grid independence analysis used by Halder et al. (2013) and Myan et al. (2016) to study flow over a few topographies. In Halder's study, the number of mesh elements was increased in successive models and simulation was carried out for each successive models at inlet velocities of 0.1 ms^{-1}. Wall shear stress was taken as the key parameter to determine the optimum number of mesh elements. The percentage difference the key parameter for each mesh refinement is then calculated to get the relative error. Relative error of less than 5% is acceptable for each successive models used in mesh refinements. Table 1 shows the grid independence analysis done in this research.

Table 56. Grid independence analysis of the models

3D model				Optimum number of mesh elements
Non-hierarchical	Mesh refinements	522171 → 2233727	2233727 → 6481004	2233727
	Relative error (%)	45.83	3.33	
Hierarchical	Mesh refinements	817734 → 1941795	1941795 → 2169321	1941795
	Relative error (%)	13.04	4.17	

3.2. CFD Results

3.2.1. Hagen-Poiseuille's Theory

The development of the flow follows the Hagen-Poiseuille's Theory. Figure 11 shows the development of the flow from the inlet to become a parabolic flow before it reaches the topography at YZ plane (z = 0). Figure 12 shows the velocity contour plot at 64.5 mm from the inlet which is 0.5 mm before reaching the topography. It shows that the flow has developed parabolic flow before it reaches the topography. The velocity profile shows that it has the highest velocity at the center of the flow with zero velocity at the area around the wall of the fluid domain which is typical of parabolic flow. Both models used in this research exhibits similar results.

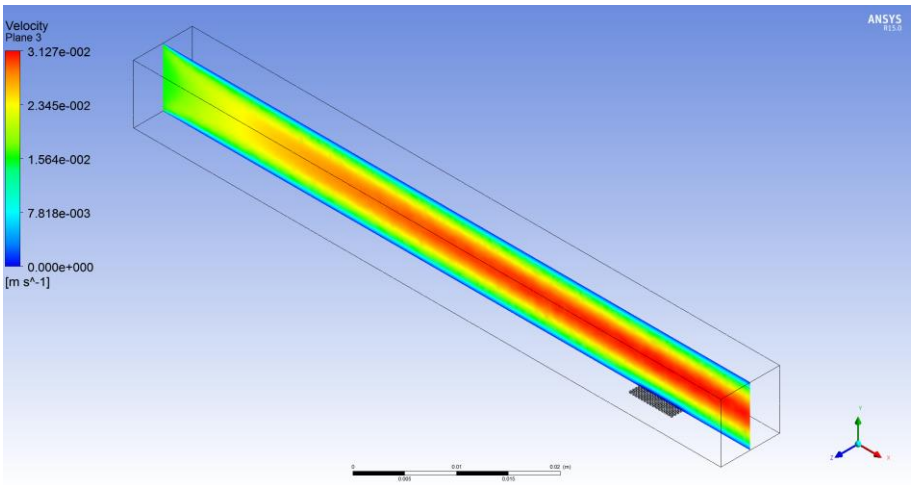


Figure 85. The velocity contour plot at XY plane (z = 0)

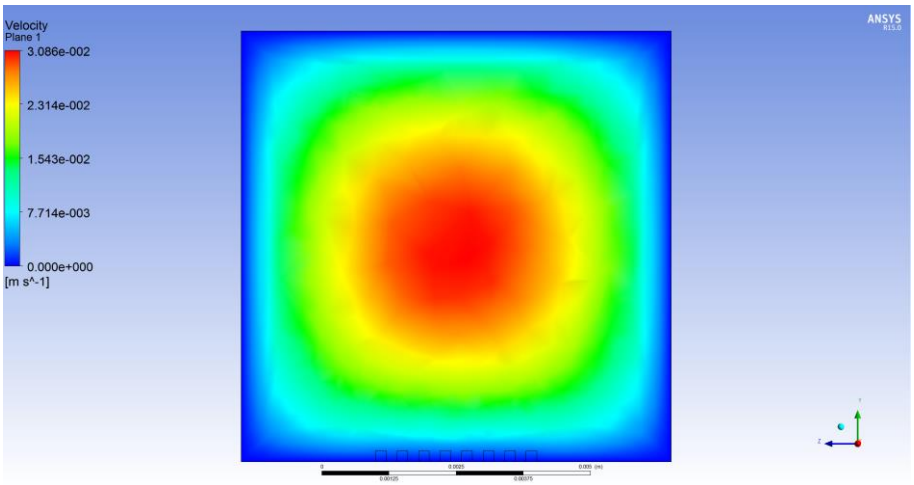


Figure 86. The velocity contour at YZ plane (x = 64.5 mm)

The velocity profile as shown in Figure 5.3 shows the fully developed parabolic flow before it reaches the topography and it proves that it follows the Hagen-Poiseuille's theory where the maximum velocity is located at the central height with zero velocity at the wall.

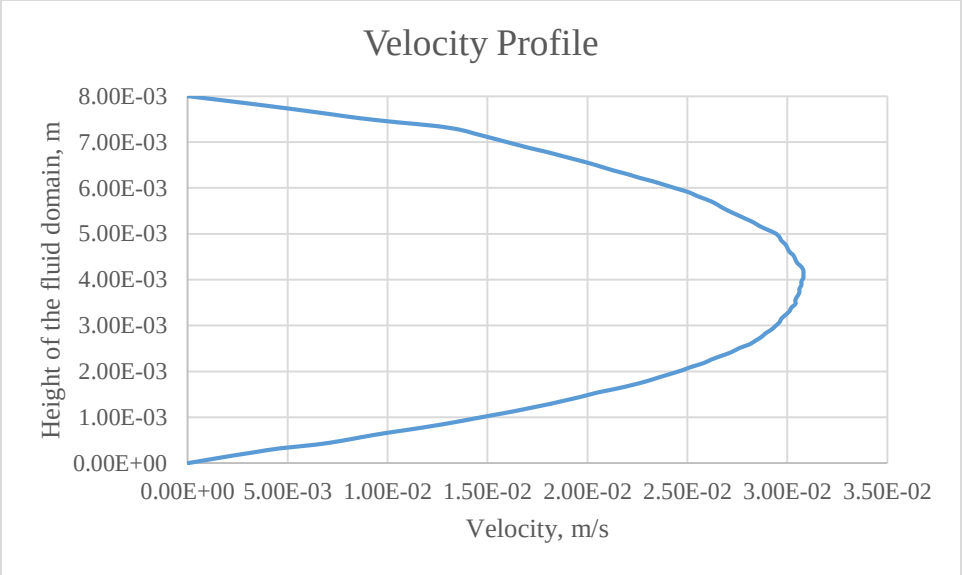


Figure 87. Velocity profile before it reaches the topography

3.2.2. Velocity Streamlines and Vector Plot

Figure 13 and 14 shows streamlines and vector plots for non-hierarchical topography where fluid flows over the 200 μm cubic topography with distance of 200 μm. The streamlines (Figure 13) show that the fluid flowing above the surface of the cube has higher speed. Then, the fluid flows into the gaps in between the cubes and brought out of it with low velocity. The average velocity above the gap is 4.41×10^{-4} ms^{-1}. From the vector profile (Figure 14), the fluid flow into the gaps at its lowest velocity and there is formation of vortices and slips. These vortices were rotating in clockwise direction in the gaps.

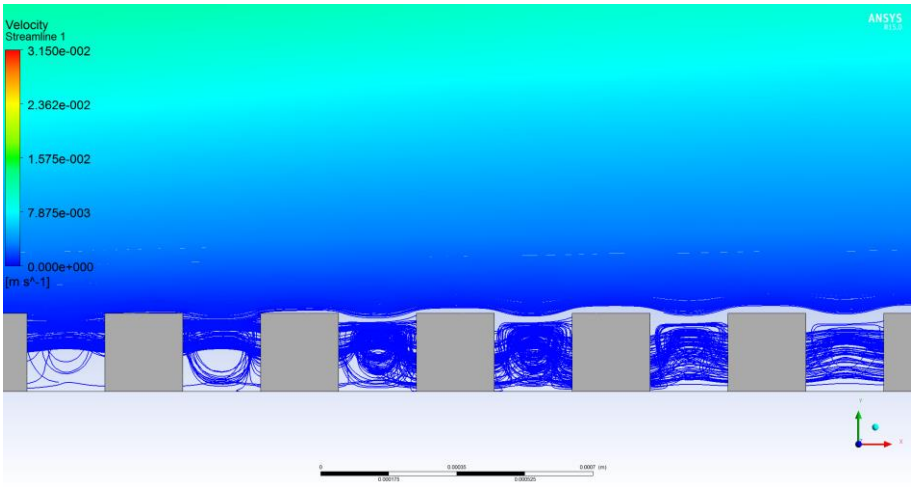


Figure 88. Streamlines over non-hierarchical topographies

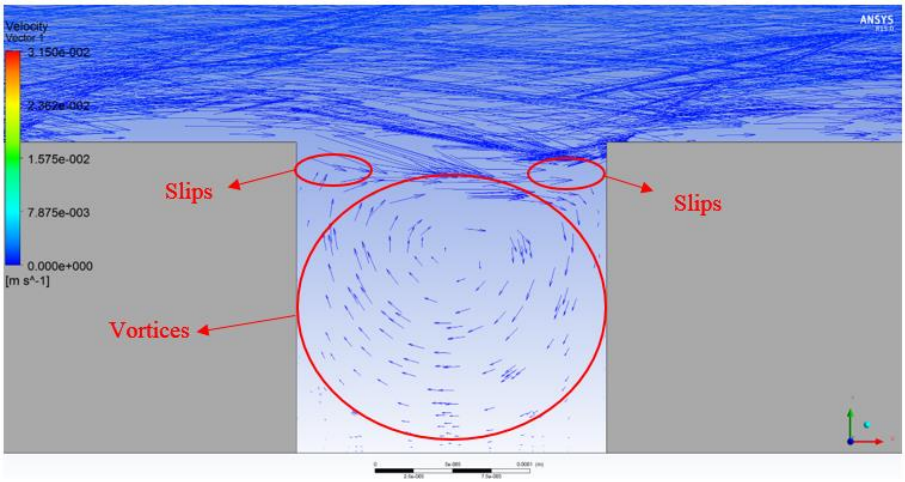


Figure 89. Vector plot for non-hierarchical showing formation of vortices and slips

Figure 15 and 16 shows streamlines and vector plots for non-hierarchical topography where fluid flows over the 250 µm hierarchical topography consists of cube and circular pillar with distance of 200 µm. The streamlines (Figure 15) show that the fluid flowing above the surface of the cube has higher speed. Then, the fluid flows into the gaps in between the cubes and brought out of it with low velocity. The characteristics of the flow is similar to non-hierarchical. However, it is important to note that the average velocity above the gap is 8.474×10^{-4} ms^{-1} which is higher than the average velocity in non-hierarchical topography. A higher velocity is preferred in controlling biofouling as microorganisms have less surface exploration time [18]. From the vector profile (Figure 16), the fluid flow into the gaps at its lowest velocity and there is also formation of vortices and slips. The vortices were rotating in clockwise direction in the gaps.

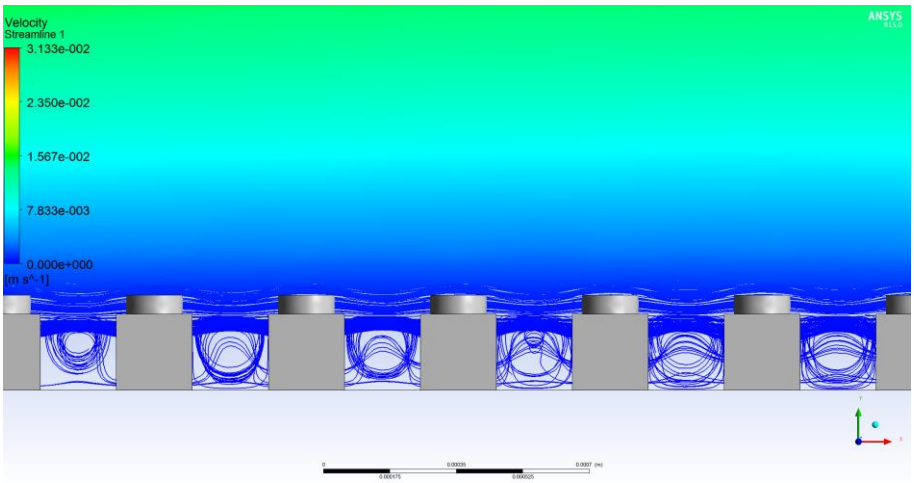


Figure 90. Streamlines over hierarchical topographies

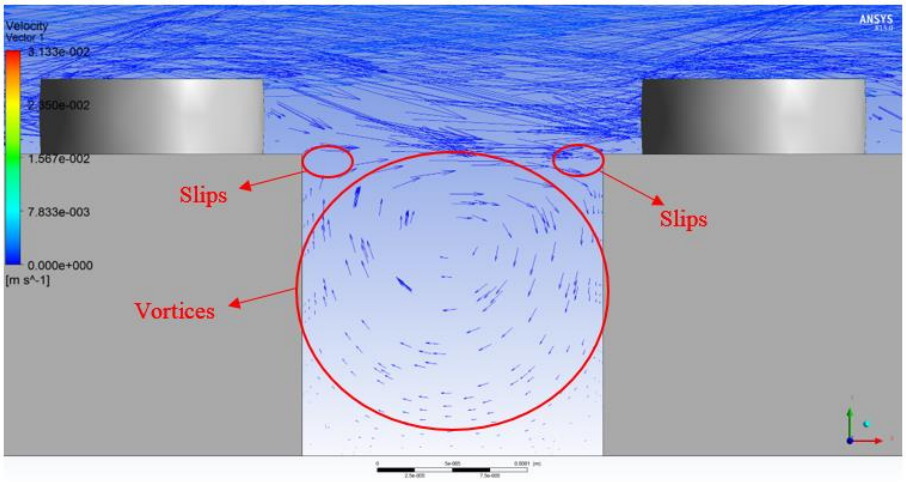


Figure 91**.** Vector plot for non-hierarchical showing formation of vortices and slips

In a study conducted by Friedmann et. al (2010), similar findings were found where there is formation of vortices in between the riblets. The redirection of the flow of the fluid into and out of the gaps between riblets had significantly decreases the fluid flow velocity. The author also explained that the velocity of the fluid at the peaks of the riblets is high and causes it to slip over the fluid in between the riblets.

In this study, the findings are slightly similar to Friedmann's study. When the fluid flows through the topography, the fluid is redirected into the gaps in between these topographies. As a result, it causes interruption of the flow direction and there will be significant reduction of velocity in this area. Hence, there will be slip in between different layer of fluid flow with different velocities. Then, the vortices were formed as the slips force the fluid in the gaps to rotate [19].

Slips and vortices could possibly help microorganisms to settle in the gaps. This is because at this region, the velocity of the fluid is low which makes it favorable for the microorganisms or other biofouling material to settle and accumulate in this region. Since these gaps are not enclosed and there is fluid flowing around these spaces, there is a possibility for the biofouling materials to be brought out along with the flow that exists in the area.

3.2.3. Wall Shear Stress

Studies have shown substrates that are favorable for settlement and attachment are tend to be explored by microorganisms. For instance, in a study conducted by Rosenhahn et al. (2012), spinning action by algae spores at a place determines the strength of adhesion for permanent attachment. Therefore, biofouling can be prevented by reducing the contact between the microorganisms with the surface.

The possibility of the microorganisms to be detached from the surface can be measure by the wall shear stress. This is one of the crucial parameters in determining the antifouling potential of a surface [14], [20]. The shear stress of the adjacent fluid

layer to the wall can be calculated by wall shear stress and it is induced by the velocity of the fluid flow over the topographies.

Figure 17 shows the wall shear stress distribution in non-hierarchical topography. The highest wall shear stress can only be seen slightly at the edges on the first column from the right which is the first column of the topography being hit by the flow of fluid. There is less or minimal wall shear stress at the spaces in between the topographies. The middle and left most region shows similar wall shear stress which is low.

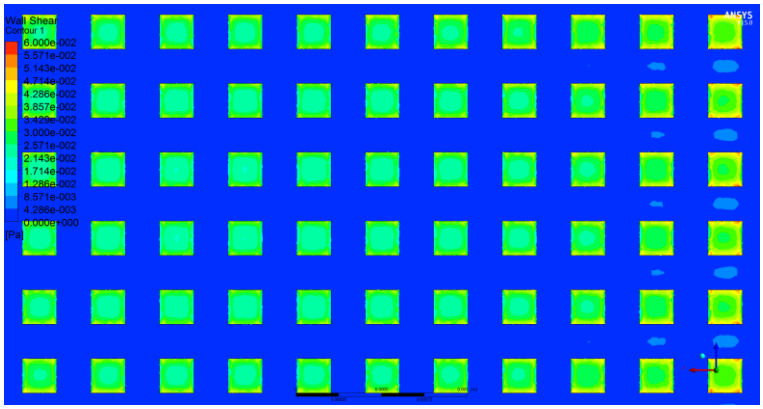


Figure 92. Wall shear contour plot for non-hierarchical topography

Figure 18 shows the wall shear stress distribution in hierarchical topography. The pattern of wall shear distribution is different from non-hierarchical topography. It is observed that almost all edges of the circular pillars have high wall shear stress. There is also less or minimal wall shear stress at the spaces in between the topographies. It is important to notice that only the first column from the right shows the most edges with high wall shear stress as it is the first column to be hit by the flow of the fluid. Nevertheless, the wall shear stress distribution in Figure 5.10 and 5.11 shows that hierarchical topography has higher wall shear stress distribution compared to non-hierarchical topography.

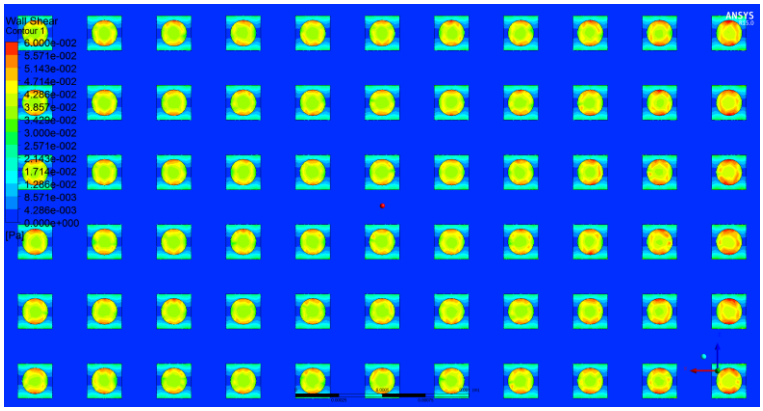


Figure 93. Wall shear contour for hierarchical topography

Since hierarchical topography have higher shear stress, it is likely that this topography would have better antifouling performance compared to non-hierarchical topography. A high shear stress is an important parameter in shearing off any microorganisms that is trying to attach to the substrates. Similar results were obtained in a study conducted by Lee et al. (2013) where the antifouling performance of micro-sized prisms was investigated. In this study, the peaks of the prisms were less fouled in lab experiments as it exerts higher shear stress in CFD simulations [21].

Figure 19 shows a comparison of wall shear over the topographies at the measurement line shown in Figure 3.10, 3.11, 3.12 and 3.13. The graph shows that hierarchical topography's fluctuation of wall shear stress is higher compared to non-hierarchical topography. This fluctuation of wall shear helps in preventing settlement of biofouling material. The range for wall shear of hierarchical topography is between 0.00281 Pa and 0.00452 Pa while non-hierarchical topography is between 0.00165 Pa and 0.00301 Pa. The data clearly shows that hierarchical topography is superior in controlling biofouling because it has higher wall shear stress.

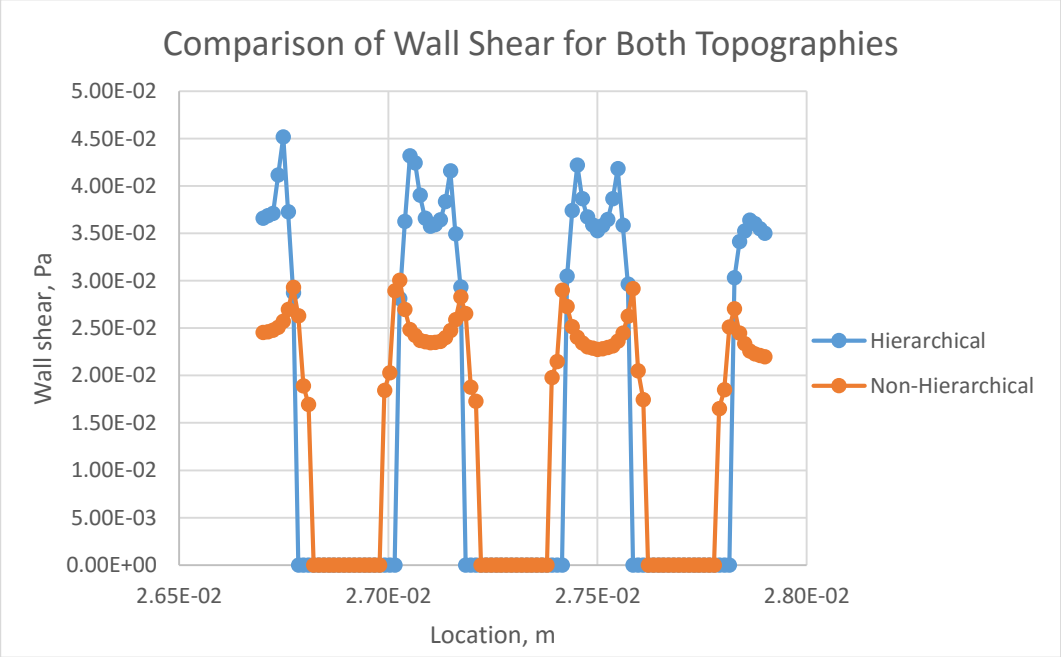


Figure 94. Graph of wall shear for both topographies

4. Conclusion

The methodology of analyzing the effect of hierarchical and non-hierarchical topography in controlling biofouling using CFD (ANSYS-CFX version 15, Solidworks 2013) has been demonstrated. The numerical method and boundary settings used in this study is sufficient to analyze the flow charateristics. This proved that numerical analysis is one of the best methods in studying the flow patterns over these topographies. It is shown that hierarchical topography has higher antifouling performance compared to non-hierarchical topography. This is because hierarchical topography has higher wall shear stress distribution compared to non-hierarchical topography. In addition, the

flow characteristics of hierarchical topography indicates that it is superior in controlling biofouling compared to non-hierarchical topography.

References

[1] H.-C. Flemming, "Biofouling in water systems--cases, causes and countermeasures.," *Appl. Microbiol. Biotechnol.*, vol. 59, no. 6, pp. 629–40, 2002.

[2] T. Vladkova, "Surface modification approach to control biofouling," in *Marine and Industrial Biofouling*, 2009, pp. 135–163.

[3] M. P. Schultz, J. a Bendick, E. R. Holm, and W. M. Hertel, "Economic impact of biofouling on a naval surface ship.," *Biofouling*, vol. 27, no. 1, pp. 87–98, 2011.

[4] R. Steinhagen, H. Müller-Steinhagen, and K. Maani, "Problems and Costs due to Heat Exchanger Fouling in New Zealand Industries," *Heat Transf. Eng.*, vol. 14, no. 1, pp. 19–30, 1993.

[5] T. Vladkova, "Surface Engineering for non-toxic Biofouling Control," *J. Univ. Chem. Technol. Metall.*, vol. 42, no. 3, pp. 239–256, 2007.

[6] A. Rosenhahn and G. H. Sendra, "Surface sensing and settlement strategies of marine biofouling organisms," *Biointerphases*, vol. 7, no. 1–4, pp. 1–13, 2012.

[7] K. A. Dafforn, J. A. Lewis, and E. L. Johnston, "Antifouling strategies: History and regulation, ecological impacts and mitigation," *Mar. Pollut. Bull.*, vol. 62, no. 3, pp. 453–465, 2011.

[8] Imo, "International Convention on the Control of Harmful Anti-Fouling Systems on Ships," *Afs/Conf/26*, no. 1, pp. 1–28, 2001.

[9] P. E. Gibbs and G. W. Bryan, "Reproductive Failure in Populations of the Dog-Whelk, Nucella Lapillus, Caused by Imposex Induced by Tributyltin from Antifouling Paints," *J. Mar. Biol. Assoc. United Kingdom*, vol. 66, no. 4, pp. 767–777, 1986.

[10] C. Alzieu, J. Sanjuan, P. Michel, M. Borel, and J. P. Dreno, "Monitoring and assessment of Butyltins in Atlantic coastal waters," *Mar. Pollut. Bull.*, vol. 20, pp. 22–26, 1989.

[11] J. A. Nichols, "Antifouling paints: Use on boats in San Diego Bay and a way to minimize adverse impacts," *Environ. Manage.*, vol. 12, no. 2, pp. 243–247, 1988.

[12] Z. C. Xie, C. W. Nga, P. Y. Qian, and J. W. Qiu, "Responses of polychaete Hydroides elegans life stages to copper stress," *Mar. Ecol. Prog. Ser.*, vol. 285, pp. 89–96, 2005.

[13] K. Schiff, D. Diehl, and A. Valkirs, "Copper emissions from antifouling paint on recreational vessels," *Mar. Pollut. Bull.*, vol. 48, no. 3–4, pp. 371–377, 2004.

[14] P. Halder *et al.*, "A novel approach to determine the efficacy of patterned surfaces for biofouling control in relation to its microfluidic environment," *Biofouling*, vol. 29, no. April 2016, pp. 697–713, 2013.

[15] N. A. Mortensen, F. Okkels, and H. Bruus, "Reexamination of Hagen-Poiseuille flow: Shape dependence of the hydraulic resistance in microchannels," *Phys. Rev. E - Stat. Nonlinear, Soft Matter Phys.*, vol. 71, no. 5, 2005.

[16] N. Aldred, A. Scardino, A. Cavaco, R. de Nys, and A. S. Clare, "Attachment strength is a key factor in the selection of surfaces by barnacle cyprids (Balanus amphitrite) during settlement.," *Biofouling*, vol. 26, no. 3, pp. 287–299, 2010.

[17] P. M. Palaskar, "Effect of Side Taper on Aerodynamics Drag of a Simple Body Shape with Diffuser and without Diffuser MIRA Reference Car and Geometry," *SAE Tech. Pap.*, 2016.

[18] J. F. Schumacher *et al.*, "Engineered antifouling microtopographies - effect of feature size, geometry, and roughness on settlement of zoospores of the green alga Ulva.," *Biofouling*, vol. 23, no. 1–2, pp. 55–62, 2007.

[19] E. Friedmann, J. Portl, and T. Richter, "A study of shark skin and its drag reducing mechanism," in *Advances in Mathematical Fluid Mechanics - Dedicated to Giovanni Paolo Galdi on the Occasion of His 60th Birthday*, 2010, pp. 271–285.

[20] P. Halder *et al.*, "An assessment of the dynamic stability of microorganisms on patterned surfaces in relation to biofouling control.," *Biofouling*, vol. 30, no. 6, pp. 695–707, 2014.

[21] Y. K. Lee, Y. J. Won, J. H. Yoo, K. H. Ahn, and C. H. Lee, "Flow analysis and fouling on the patterned membrane surface," *J. Memb. Sci.*, vol. 427, pp. 320–325, 2013.

eureca 2017 – Conference Paper
Paper Number 2ME15

Modelling and Simulation of Rail Vehicle Ride Quality

Nigel Lopez Michael[1*], Mohd Farid Bin Aladdin[2]

[1]*Taylor's University, Malaysia*
[2]*Taylor's University, Malaysia*

[*]lopez.nigelmichael@sd.taylors.edu.my

Abstract

Knowledge regarding vibration levels and comfort is imperative for any nation rapidly expanding its public transport systems. This is especially true for Malaysia. This study's objective is to analyse vibration levels in an LRT train, specifically on the floor and seat. This study was done using mathematical modelling via Matlab and field data obtained from the LRT seat and floor using a vibration sensor on the seat and an accelerometer. Mathematical modelling was done up to 3 degrees of freedom, using values and parameters obtained from literature. The results were then compared to actual vibrational acceleration values obtained from the LRT train. In the 3 degree of freedom model, transmissibility was used in the mathematical model to relate the floor vibration to the seat. The transmissibility value from literature used in the mathematical model was less than 1. However, data analysed from the LRT showed a transmissibility greater than one. Magnitude of vibration differed as well, with the highest value of acceleration (floor) from the mathematical model being 0.0065 m/s^2, while the highest value from field data (floor) is 0.088 m/s^2. This difference becomes more pronounced for vibration from the seat, with model acceleration being 0.00942 m/s^2 while field data is 0.128 m/s^2. Results from both the field and the mathematical model fared similarly when evaluated using ISO 2631-1 and 2631-4, where the results were below thresholds that cause discomfort in passengers.

1. Introduction

Public transport is largely becoming close to a necessity in the rapidly urbanising country of Malaysia, especially in states such as Selangor, Kuala Lumpur, Penang, and others. The expanding cities and development within them are providing much needed jobs and financial support for the economy of both the country and its citizens. However, transport is a vital component of any rapidly growing development, and the traffic conditions in urban areas continue to worsen. With the rising population moving from the outskirts to the towns, the concentration of people within cities continues to rise. The need for affordable and efficient transportation is nearly absolute when it comes to the requirement of a well-managed city.

Malaysia has seen an increase in development of public transport in recent years, with the extension of the Putra and Ampang LRT lines as well as the introduction of the new MRT line. These are essential to providing a good support system for the towns' inhabitants and workers.

However, one of the biggest reasons why people are not switching as rapidly as they should to using public transport such as trains is the perception of comfort. While other factors are involved in their choice, such as convenience and versatility, people also largely choose to drive their own car as they feel more comfortable inside their car as opposed to travelling on a train.

In their perception of comfort on the train, vibration experienced by passengers are a large source of comfort or discomfort. A high percentage of people use public transport for routine use such as going to work or to secure household items. During their routine travels, a high level of vibration can be a significant factor in determining whether the travel is comfortable enough to be performed nearly every day of the week.

While studies on rail vibration are relatively well-developed, there has been little development and exploration of the field here in Malaysia. As such, this study is part of a relatively new effort to advance the betterment of travelling by train in the rapidly developing parts of Malaysia.

2. Literature Review

Vibration may be caused by several factors. The roughness of the track and wheel are among the main causes of vibration. For train speeds between 40 and 250 km/h, which includes the peak speed of the LRT trains analysed in this study, the vibration generated from rolling is a major source of vibration and noise. The roughness of the wheels and the rail leads to significant vibration. [10] Vibrational discomfort is also caused by many other factors such as vehicle condition, characteristics of the track as well as the operating conditions while travelling. [8] These complementary sources of vibration are not analysed in this study. The focus is instead on the role suspension and its

characteristics can play in reducing vibration, as it is one of the main vehicle systems. Its main purpose is significant in the realization of parameters determining comfort, stability and safety. [9]

Modelling

Using Simulink, it is possible to move beyond ideal, linear models to explore non-linear models that factor in many other factors such as friction, air resistance, gear slippage and others. These are helpful in describing real-world phenomena. The block diagrams allow for the building of models in a similar fashion to using pen and paper, simplifying the process through visualization of complex systems. In addition to an extensive array and library of blocks that are suited to a large number of processes, it is also possible to create new blocks. Due to the visualized nature of complex processes, changing and experimentation with ranges of parameters is vastly simplified. [1]

At this stage of the research, a full analysis of the literature involved is unavailable. However, from the research currently done, the area of vibration assessment in rail systems is extensively explored. There are many systems and techniques that have been used successfully used to assess vibration, be it vertical or other forms of vibration.

However, this project derives its contribution to the body of knowledge by being part of the relatively new research that is currently developing in relation to Malaysia's railway systems. While there are extensive methods to assess vibration available in literature, there remains much room for testing and implementation to be done for systems in Malaysia.

Therefore, this study contributes mainly in terms of application of methods in railway systems of Malaysia. The methods used are developed well in literature, and this study seeks to apply them in a unique location, and on systems that have not been assessed in this manner before.

Also part of the review of current literature contained in this research is insight into roughness levels and how they interact with frequency, velocity and wavelength. Roughness levels itself, from difference locations are also analysed. Stages of modelling, with increasing complexity of Simulink models are also explored. Basic models are sourced and augmented to suit the needs of this research.

In particular, parameters for the suspension system modelled in this research are also available. Due to the inability to acquire the specifications of the LRT system used in the Kelana Jaya line, values from literature are sourced. Though there is little knowledge of how close the parameters are to the LRT system studied in this research, it is of a similar train system. Since the capability and parameters of the suspension system are of paramount importance in modelling the system, there will be further attempts to acquire these values from the relevant sources. It is advisable for the institution that this research is being submitted to help in pursuing these specifications as it contributes greatly to the accuracy of these findings.

Thus, as mentioned above, there is significant literature contained in the results portion of this research that although is not found in this section, reveals an analysis of critical literature nonetheless.

3. Modelling

Mathematical and Simulink modelling:

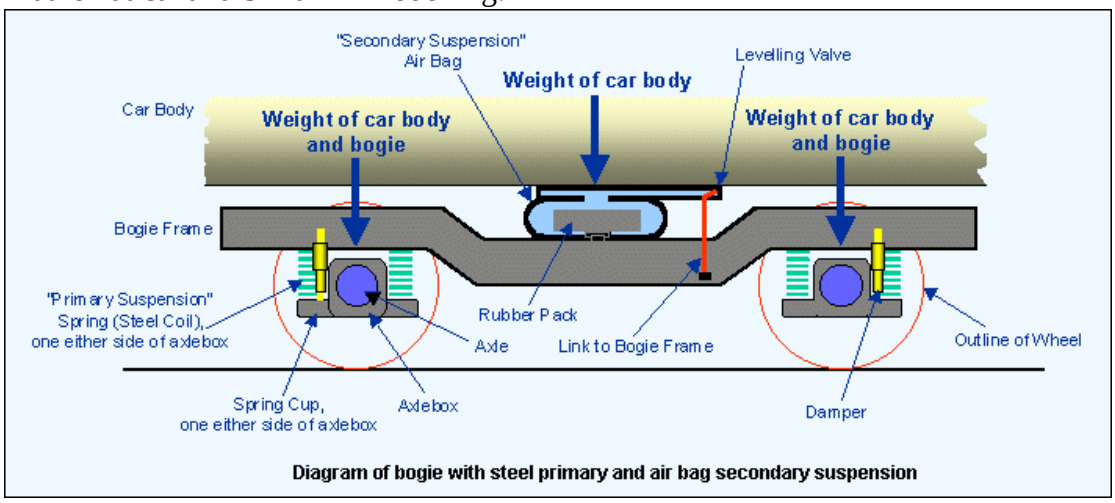


Figure 1: Diagram of train suspension

The above is an image (sourced from google) that give a typical diagram of the primary and secondary suspensions used in a train. In the creation of the mathematical model below, the air bag, denoted as the secondary suspension above, was modelled as a secondary system of a spring and damper. The above image is then translated into mathematical models below.

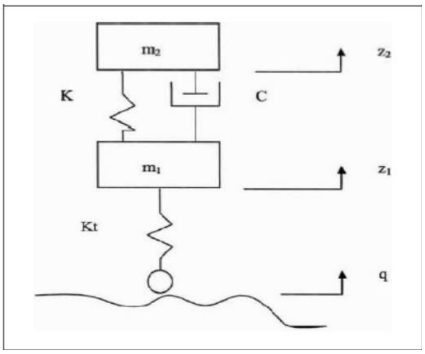


Figure 2: Free-body Diagram of 2 degree of freedom suspension system with 2 springs and 1 damper. [1]

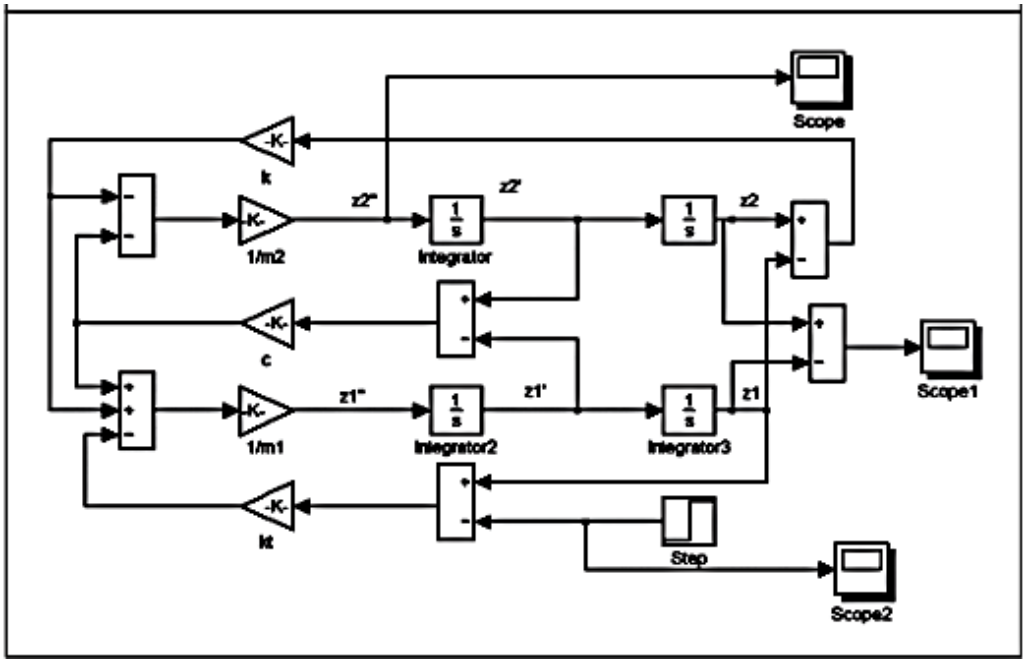
$$m_2\ddot{z}_2 + C(\dot{z}_2 - \dot{z}_1) + K(z_2 - z_1) = 0$$

$$m_1\ddot{z}_1 + C(\dot{z}_1 - \dot{z}_2) + K(z_1 - z_2) + K_t(z_1 - q) = 0$$

Figure 3: Equations of motion from free-body diagram

Above are shown the basic equations of motion from the free-body diagram. Using MATLAB Simulink, the equations can be modelled as a system with the excitation force being the roughness of the surface on which the system is moving on. [1]

Figure 4: Simulink Block Diagram of a Suspension System. [1]



The above system relates the input from the Step block, which contains the height of the obstacle the system is encountering on the surface, or roughness, with the values of the two springs, of stiffness K and K_t, the two masses, m_1 and m_2, and damper, C. The Scope blocks enable analysis of various values returned from the simulation to assess the effect of the various parameters. The two upper Scope blocks function to retrieve the values of acceleration and displacement experienced at block m_2.

The above system, while reasonably functional, lacks a damper. In reality, the primary suspension of a railway track, the train bogie, includes damping as well as springs. Therefore, the system should include two dampers.

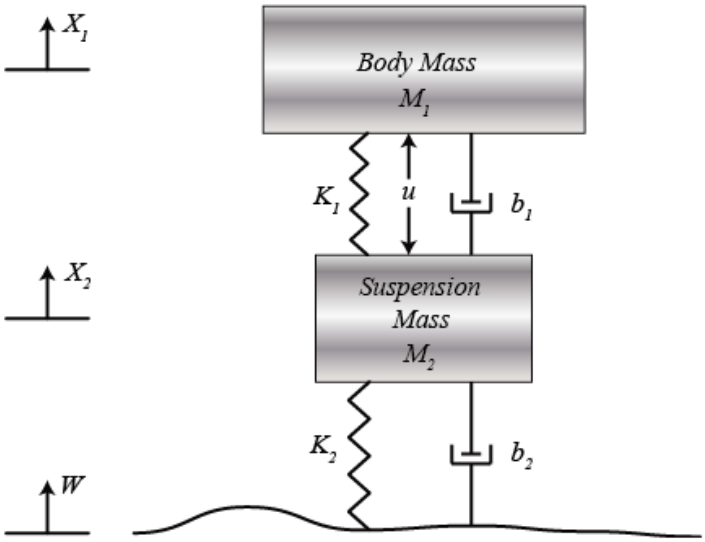


Figure 5: Free-body Diagram of a 2-degree of freedom system with 2 masses, 2 springs and 2 dampers. [2]

The above diagram features a system closer to a realistic model of a modern suspension system, with two springs and dampers. Value W refers to the height of the obstruction on the surface, or roughness.

$$M_1\ddot{X}_1 = -b_1(\dot{X}_1 - \dot{X}_2) - K_1(X_1 - X_2) + U$$

$$M_2\ddot{X}_2 = b_1(\dot{X}_1 - \dot{X}_2) + K_1(X_1 - X_2) + b_2(\dot{W} - \dot{X}_2) + K_2(W - X_2) - U$$

Figure 6: Equations of motion from free-body diagram. [2]

The free-body diagram and the equations of motion derived from it shown above feature the force U. In the source of these equations, force U refers to a force that would be added to the system as part of a design to reduce the vibration transmitted to the passenger. Since this analysis only considers the present vibration levels without any augmentation or improvement, the force shall not be considered in the simulation.

The system contains two masses, two springs, two dampers and the excitation in the form of the Step block labelled W. Also, the force U will be configured to be of no effect to the system, leaving the only input to be the roughness, W. Another scope is added to analyse a1, which is the acceleration experienced by the car body and therefore transmitted to the seat of the train. Based on a model present in the source, the model below shows the Simulink model created for 2 degree of freedom analysis.

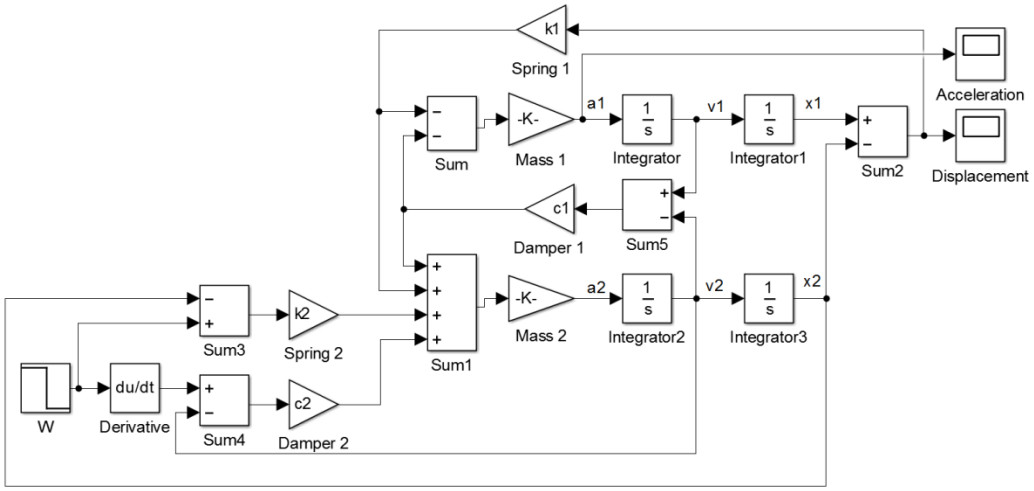


Figure 7: Final Simulink Model.

3.1 Parameters of mathematical analysis:

Table 1: Parameters of analysis (source taken from technical specification of ALRT). [3]

Car body mass	34320 kg
Vertical rigidity of secondary suspension	2.4 MN/m
Vertical damping of secondary suspension	68.88 kNs/m
Bogie mass	3200 kg
Vertical rigidity of primary suspension	4.4 MN/m
Vertical damping of primary suspension	52.21 kNs/m

The above values that were sourced from literature were of a train design similar to the LRT train analysed in this study.

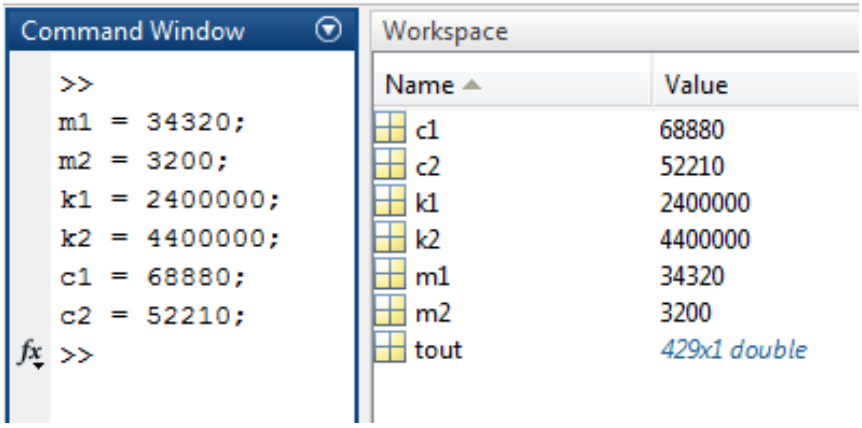


Figure 8: Commands input into MATLAB prompt.

As seen above, based on Table 1 and Figure 3, car body mass is m1, bogie mass is m2, stiffness/rigidity of secondary suspension is k1, stiffness/rigidity of primary suspension is k2, damping constant of secondary suspension is c1, and damping constant of primary suspension is c2.

Analysis of roughness:

Due to the unavailability of data pertaining to roughness levels of Malaysian LRT tracks and trains, values from literature were obtained.

The roughness that translates to vibration is dependent upon the velocity of the train, the frequency and the wavelength of the vibration. Roughness is usually measured as noise, with the unit dB re 1 μm at different wavelengths or speed of train.

Passengers have sensitivity to vibration/noise in frequencies ranging from 20 Hz to 20 kHz, with the highest sensitivity towards a frequency range of approximately 2 to 5 kHz. [4] Thus, with the employment of the formula $v=f\lambda$, where v is velocity, f is frequency and λ is wavelength, a range of wavelengths can be determined for analysis with speed and frequency ranges.

Wavelength ranges (in millimetres) corresponding to frequency ranges of interest.

		20 m/s (72 km/h)	50 m/s (180 km/h)
Audible ground-borne noise[16]	25–250 Hz	80–800	200–2000
Structure-borne noise[19]	100–2000 Hz	10–200	25–500
Wheel–rail rolling noise[18]	100–5000 Hz	4–200	10–500
Range of greatest human sensitivity[15]	2–5 kHz	2–10	5–25
Range of human sensitivity[15]	20 Hz–20 kHz	1–1000	5–5000

Figure 9: Range of wavelengths corresponding to 2 velocities and frequency ranges. [4]

From Figure 9, we can see the application of the formula for certain parameters to gauge the ranges of wavelengths that can be analysed from roughness graphs.

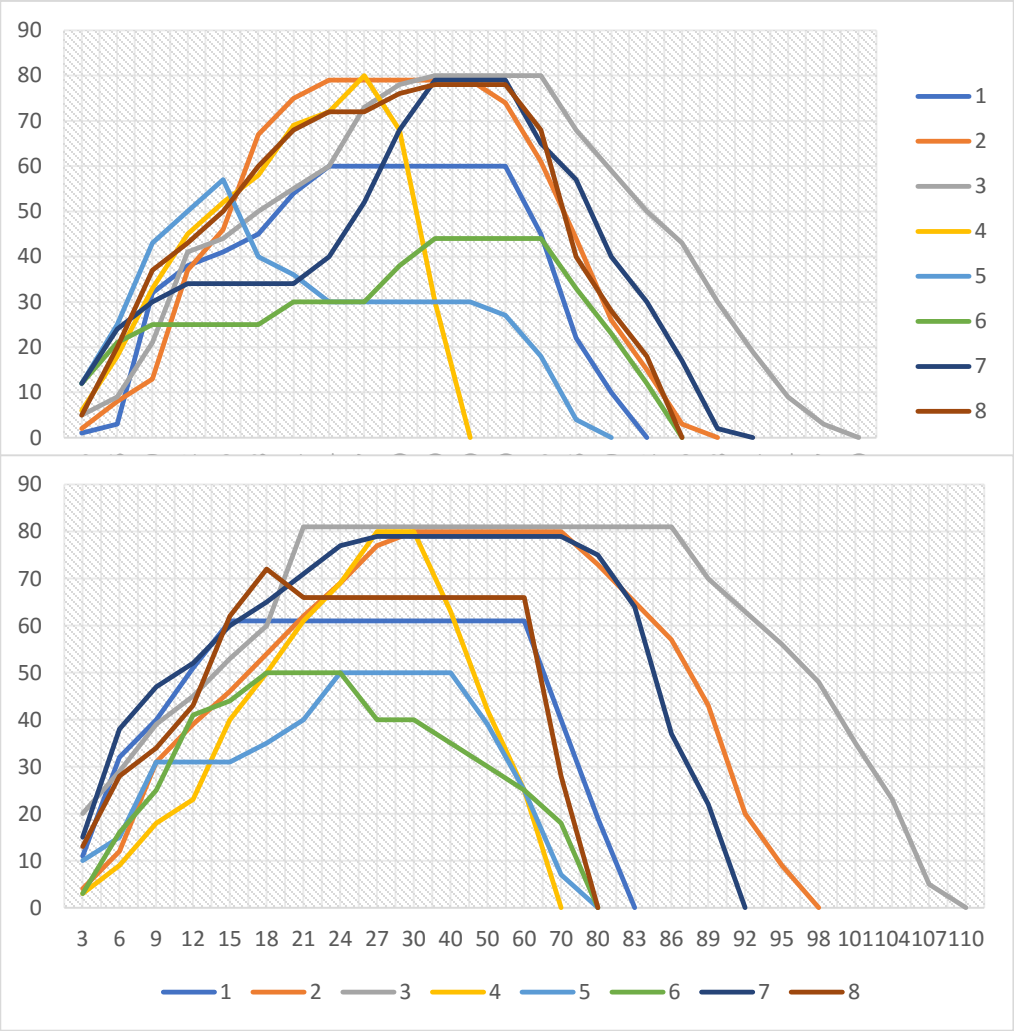
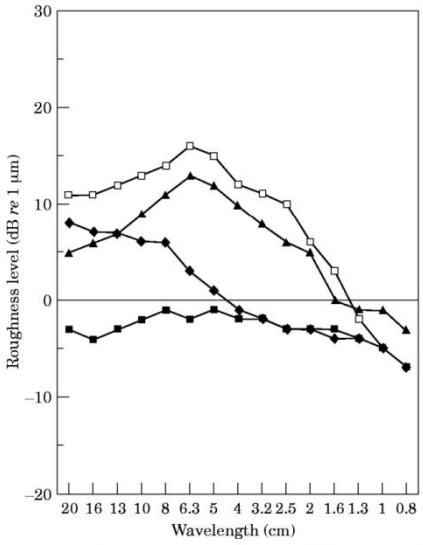


Figure 10: Two graphs, (y-axis: speed in km/h, x-axis: time in seconds) showing the speed profile of LRT for each station.

The graphs in Figure 10 were constructed using data from use of GPS Speedometer and Odometer by COOL NIKS with an Android smartphone. The data was analysed by travelling through nine stations on the LRT Kelana Jaya line, from Kelana Jaya station to KL Sentral and back. Each line on a graph shows the speed profile while travelling from one station to the other. From the data collected, the highest speed recorded was approximately 82 km/h (22.78 m/s), while the average speed was approximately 33 km/h (9.17 m/s).

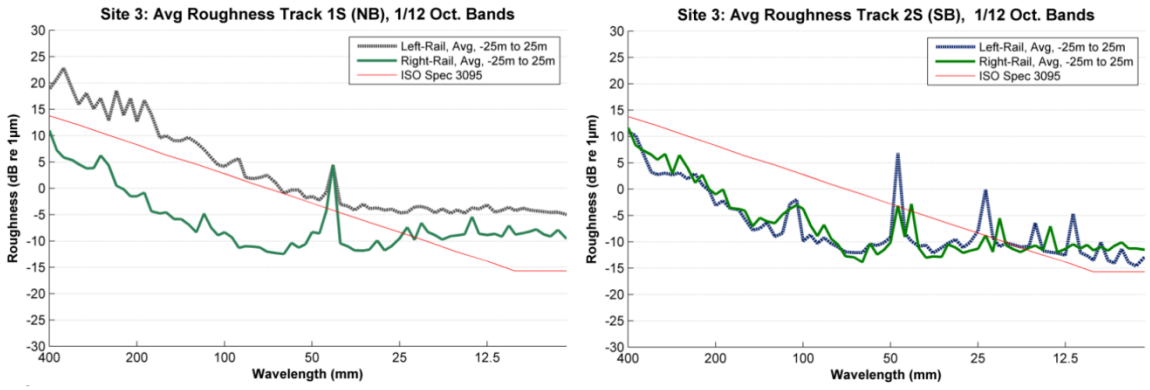
Table 2: Ranges of wavelength for analysis.

	Speed = 22.78 m/s	Speed = 9.17 m/s
Frequency range: 20 Hz – 20 kHz	Wavelength range = 1139 – 1.139 mm	Wavelength range = 458.5 – 0.4585 mm
Frequency range: 2 kHz – 5kHz	Wavelength range = 11.39 – 4.56 mm	Wavelength range = 4.585 - 1.834 mm



Wheel roughness after 200 000 km. ■, Sinter block; ◆, disc braked; ▲, block braked; □, cast-iron braked.

Figure 11-1: Wheel roughness [10]



21 **Figure 8: 1/12 Octave Band Roughness, Site 3**

Figure 11-2: Roughness [5]

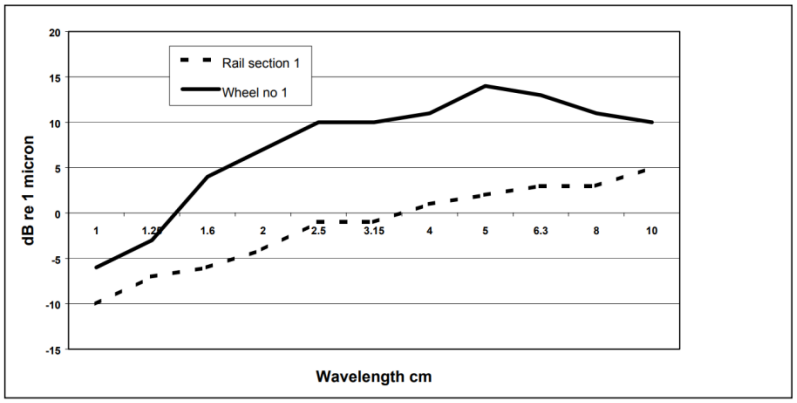


Figure 1-2 Typical representation of rail and wheel roughness.

Figure 11-3: Roughness [6]

The above graphs show roughness levels of track and wheel from three different sources together with wavelength. The roughness is given in dB re 1 µm unit. The formula is given by:

Roughness in dB, $L_r = 20 \log r_{eff} / r_0$

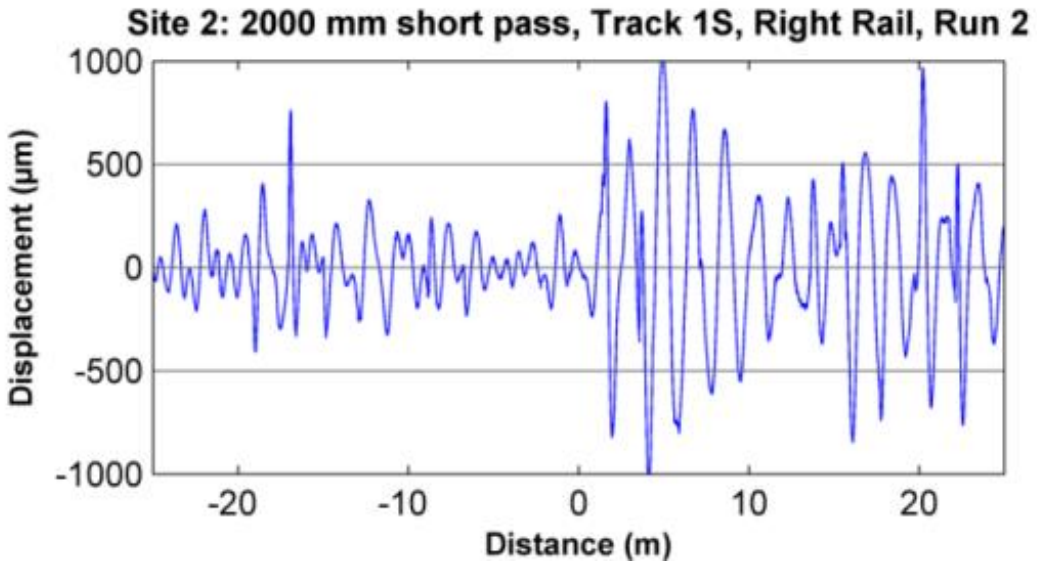
The amplitude of roughness r is commonly expressed in µm. Using the formula above, with r_0 = 1 µm, r_{eff} can be found by reversing it with chosen values from the graphs. The effective roughness amplitude is the root-mean-square value that is expressed with a given distance. With the above formula, an effective roughness of 10 µm gives a roughness level of 20 dB, and 1 µm is equal to 0 dB.

For each wavelength range, the highest value of roughness will be used as the input in the model.

Table 3: Highest roughness values for each wavelength range.

Wavelength range (mm)	Figure 11-1 Roughness(m)	Figure 11-2 Roughness(m)	Figure 11-3 Roughness(m)
1139 – 1.139	6.68×10^{-6}	14.9×10^{-6}	5×10^{-6}
11.39 – 4.56	6.68×10^{-6}	1.78×10^{-6}	5×10^{-6}
458.5 – 0.4585	6.68×10^{-6}	14.9×10^{-6}	5×10^{-6}
4.585 - 1.834	3.55×10^{-6}	1.78×10^{-6}	4.46×10^{-6}

Figure 12: Raw roughness data in terms of displacement. [5]



The above Figure shows raw roughness data. The highest displacement recorded is approximately 1000 µm, or 0.001 m. This is another roughness value that can be simulated.

The analysis in MATLAB will be done with varied roughness values as seen in Table 3 and figure 5. These values will be input into the Step Block labelled W. The results from the two scopes, acceleration and displacement will be shown.

3.2 Model Analysis Results

Table 4: Highest acceleration and displacement values for each level of roughness.

Roughness (m)	Highest Acceleration (m/s^2)	Highest Displacement (m)
6.68×10^{-6}	4.2×10^{-4}	4.7×10^{-6}
3.55×10^{-6}	2.25×10^{-4}	2.6×10^{-6}
14.9×10^{-6}	9.4×10^{-4}	10.5×10^{-6}
1.78×10^{-6}	10.9×10^{-5}	1.26×10^{-6}
5×10^{-6}	3×10^{-4}	3.4×10^{-6}
4.46×10^{-6}	2.76×10^{-4}	3.15×10^{-6}
0.001	6.5×10^{-3}	7×10^{-5}

Table 5: Reactions of comfort to vibration in the environment, ISO 2631-1 [7]

Less than 0.315 m/s^2	Not uncomfortable
0.315 m/s^2 to 0.63 m/s^2	A little uncomfortable
0.5 m/s^2 to 1 m/s^2	Fairly uncomfortable
0.8 m/s^2 to 1.6 m/s^2	Uncomfortable
1.25 m/s^2 to 2.5 m/s^2	Very uncomfortable
Greater than 2 m/s^2	Extremely uncomfortable

From the table above, it is clear that according to this design of model and values for roughness obtained, the values of acceleration transmitted to the passenger is well below the values that create discomfort.

3.3 Three Degrees-of-freedom and Transmissibility

The next stage of modelling and analysis was initially determined to be a mathematical model featuring three degrees of freedom:

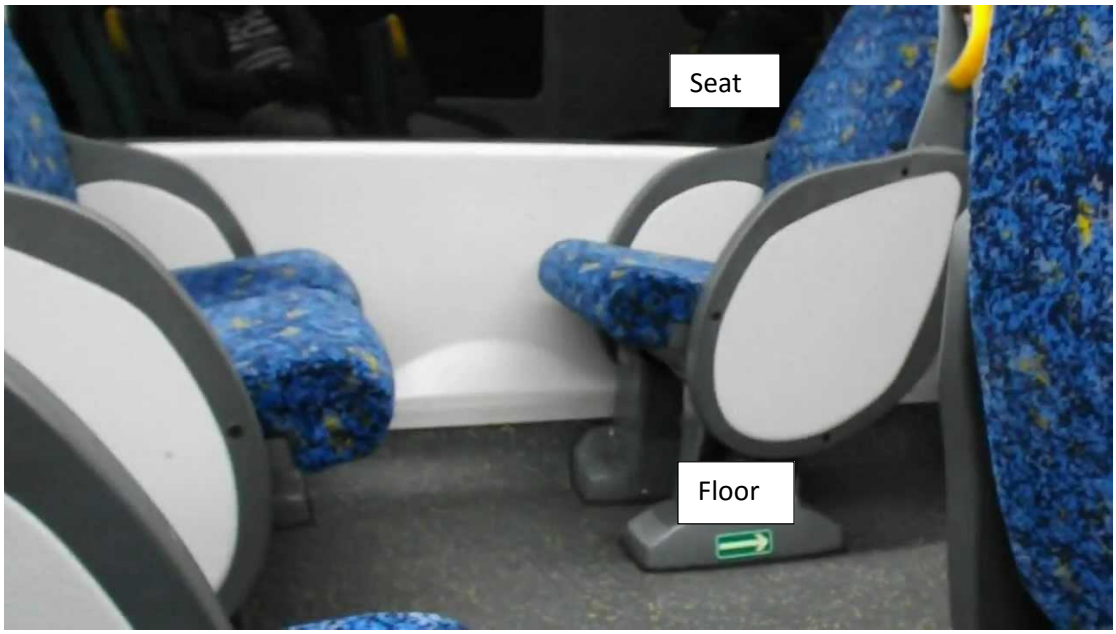


Figure 13: Picture of the seat and floor in a train car

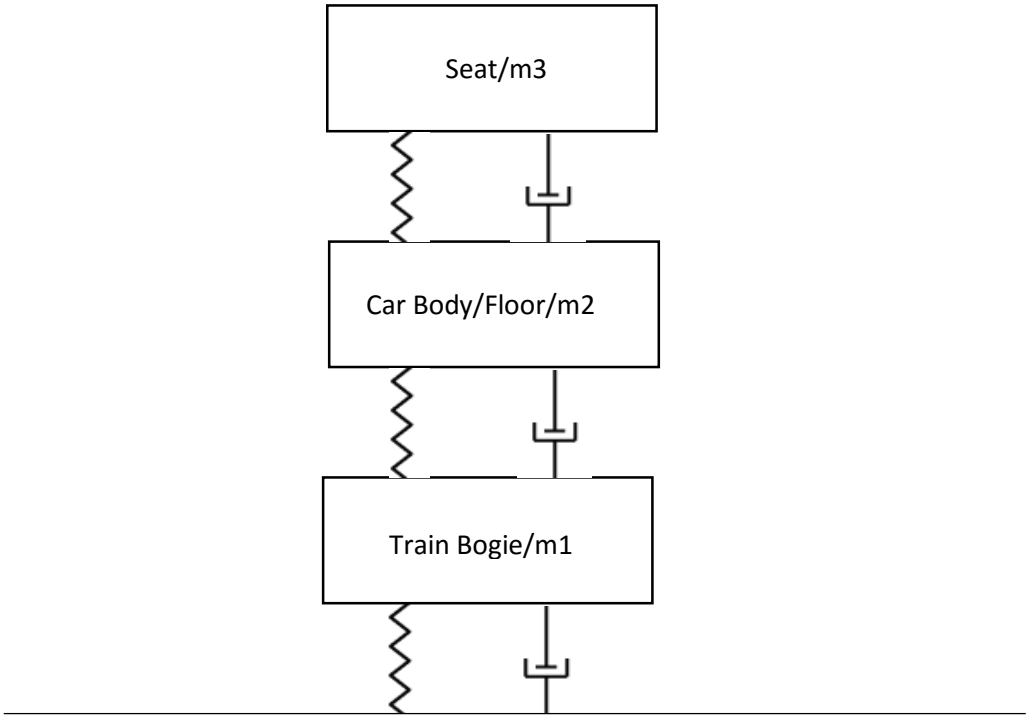


Figure 14: 3 Degree-of-freedom Free-Body Diagram

The above system is an approximation of when m_1 is the primary suspension, m_2 is the secondary suspension, and m_3 was designated as the train car seat.

Modelling the vibration after the secondary suspension as coming from the floor of the train car, as well as initially modelling the seat as a spring-damper-mass system, we obtain the below model.

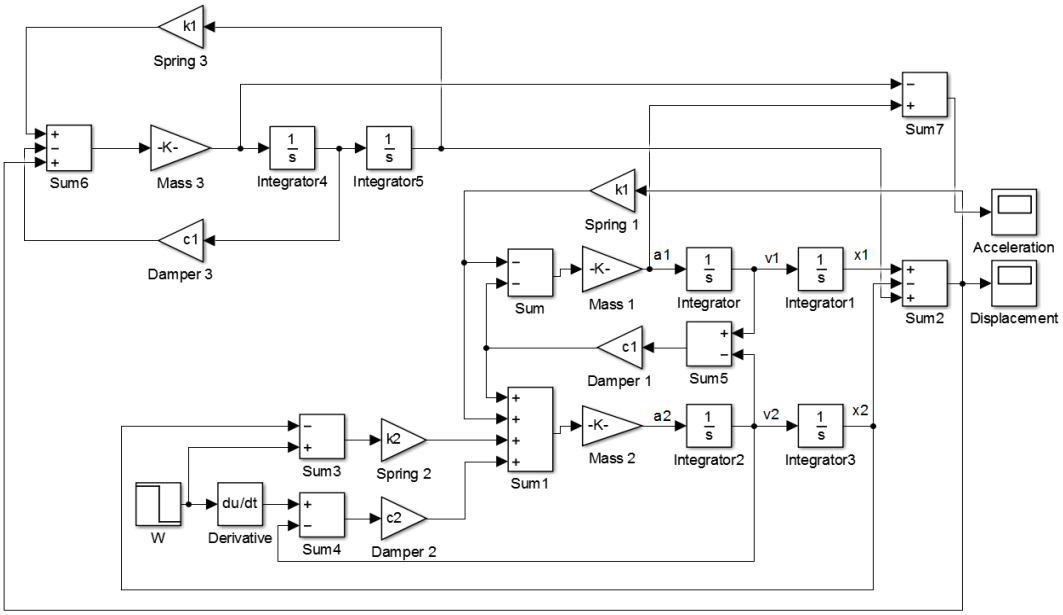
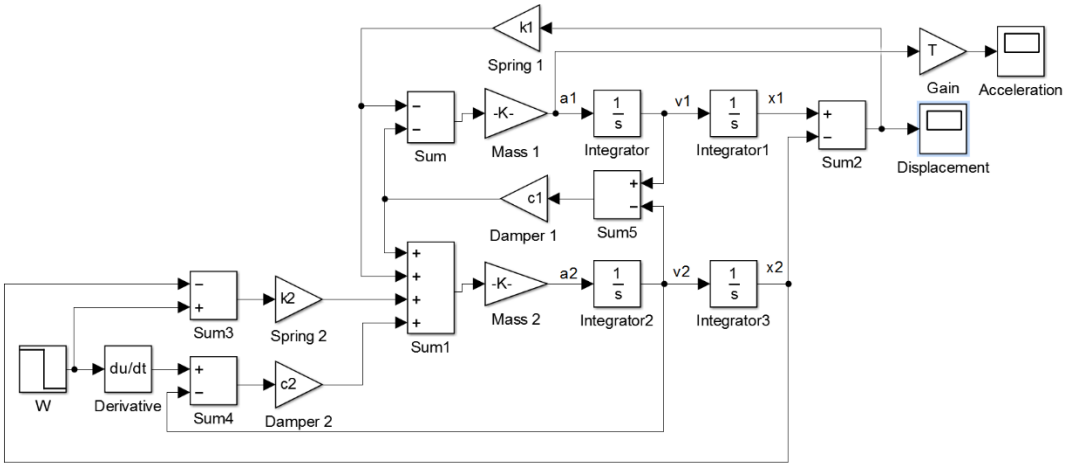


Figure 15: 3 Degree-of-freedom Simulink mathematical model

Following literature review, however it was subsequently determined that another approach can be used. Using some assumptions, the vibration transferred to the seat can be approximated using an analysis of transmissibility. The vibration transferred to the passenger is due to the complex dynamic interaction between vehicle seat and body [13]. This transmissibility can be approximated via the seat-human body model [12]. The transmissibility can be simplified from the transfer function seen in [11] into a simple ratio of seat vibration/floor vibration given some assumptions. One assumption



used in this part of the analysis is that comparison of accelerations can be done through a simple ratio as stated above. Another assumption is that transmissibility can be approximated from r.m.s. values from field data. Another assumption is that the resulting values of acceleration can be modelled using an extra Gain block with the value of transmissibility obtained from literature or field data.

Figure 16: Simulink model with added gain block for transmissibility.

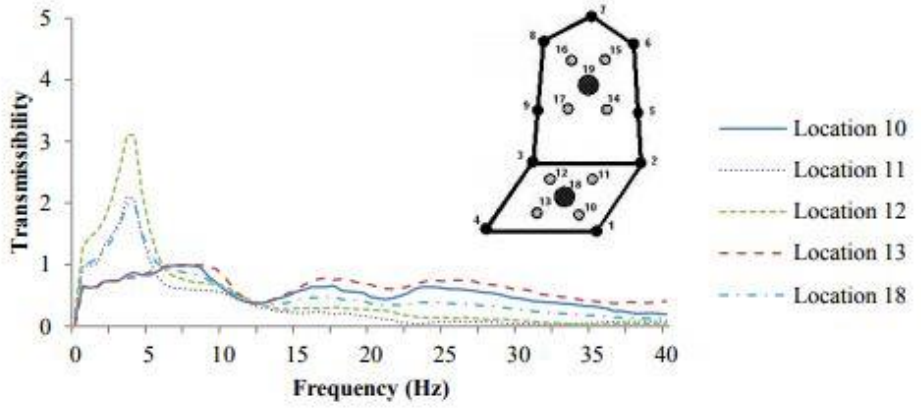


Figure 17: Vertical transmissibilities at measurement locations on seat cushion surface.

The above figure shows the analysed transmissibilities of acceleration in the vertical direction. This study was chosen simply because it is the most recent of the studies cited in this study. From the graph above, it is observed that the highest transmissibility that can be observed at frequencies 20 Hz or higher, which is the lowest frequency analysed in this study, is approximately 0.8 from a visual estimation. While not large, this does indicate that the seat studied does reduce the vibration transmitted to the passenger. Using this transmissibility, and the assumed formula stated above (seat vibration/floor vibration), the acceleration levels at m_3 can be approximated using this constant, 0.8, as the value of the gain block in the Simulink model.

Table 6: Acceleration on seat

Roughness (m)	Highest Acceleration (m/s^2)	Acceleration on seat (m/s^2)
6.68×10^{-6}	4.2×10^{-4}	3.36×10^{-4}
3.55×10^{-6}	2.25×10^{-4}	1.8×10^{-4}
14.9×10^{-6}	9.4×10^{-4}	7.52×10^{-4}
1.78×10^{-6}	10.9×10^{-5}	8.72×10^{-5}
5×10^{-6}	3×10^{-4}	2.4×10^{-4}
4.46×10^{-6}	2.76×10^{-4}	2.21×10^{-4}
0.001	6.5×10^{-3}	5.2×10^{-3}

4. Methodology



Accelerometer with metal block on ground



Sensor placed on seat and orientation



Interface of signal processing unit

The above images show the method of placement and orientation of the apparatus in the LRT train. The sensor is placed on the chair and an individual was seated on top of it. This sensor then picked up vibrations originating from the LRT seat in the vertical direction, which were then stored in the signal processing unit. The accelerometer was placed upon the floor of the LRT. A weighted metal block was attached to the magnetic accelerometer in order to enable it to remain pressed against the floor to properly receive vibration readings. Thus, the sensor sensed the vertical acceleration originating from the LRT train seat while the vertical vibration from the LRT train floor was picked up by the accelerometer. All readings and raw data were stored in the signal processing unit. Readings were taken for a total of 4 seconds. The data, which are vertical acceleration levels, are shown below. Specifications and further information about the apparatus are included in the appendix.

5. Data and Further Analysis

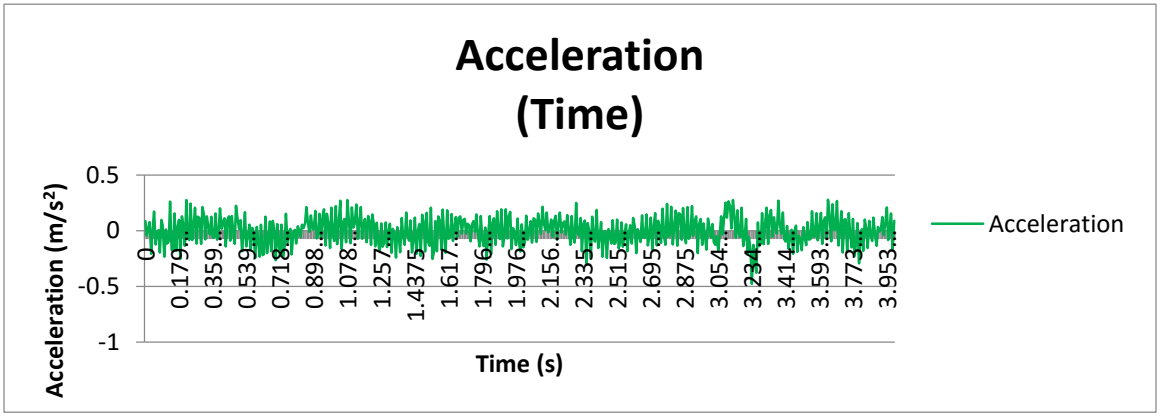


Figure 18: Acceleration values on seat with respect to time

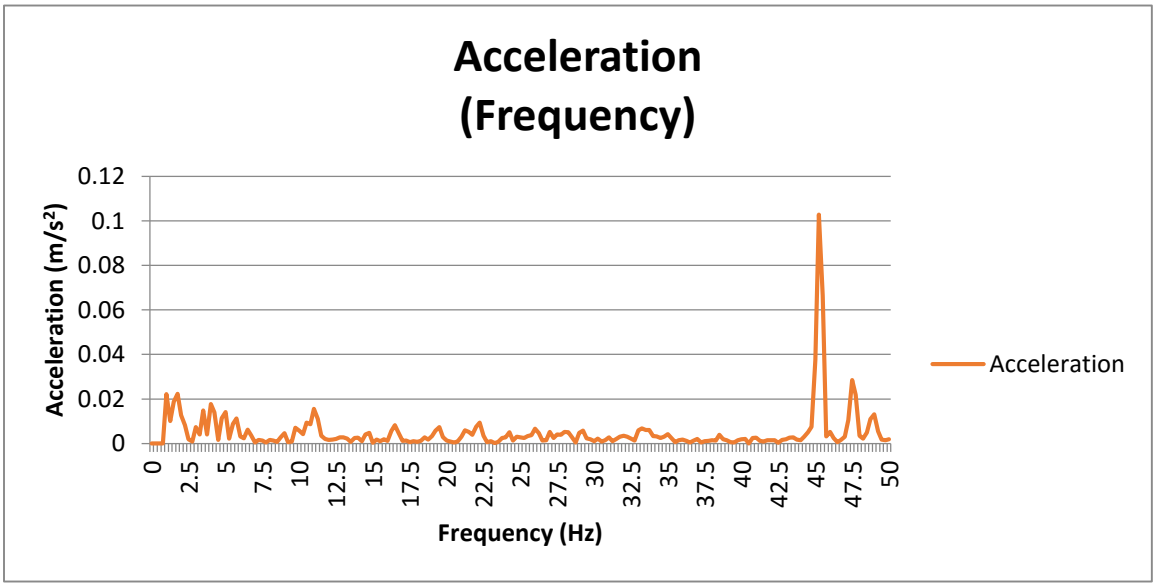


Figure 19: Acceleration values on seat with respect to frequency.

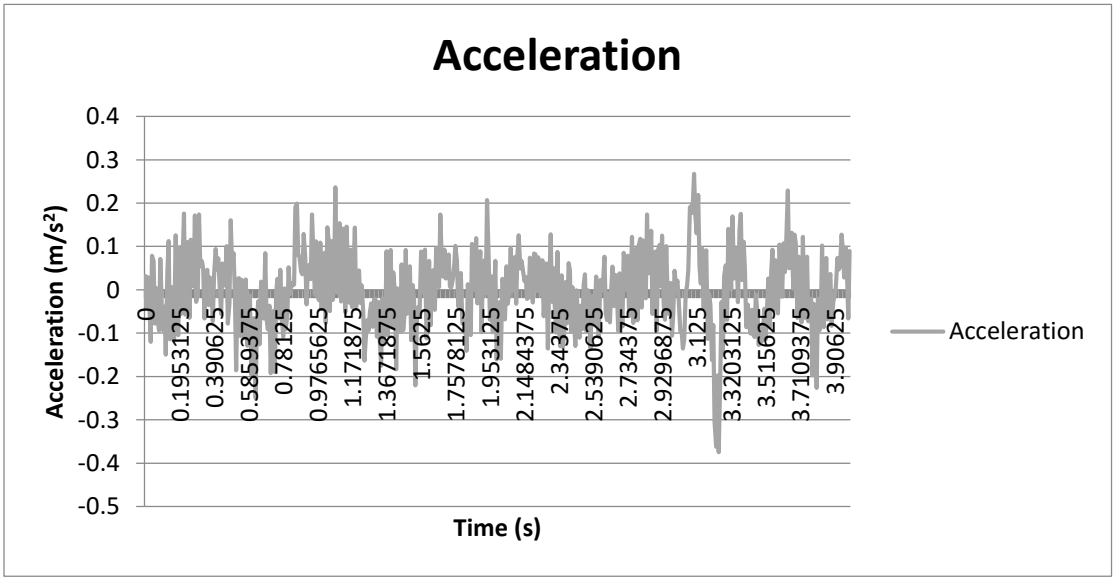


Figure 20: Acceleration levels on floor with respect to time.

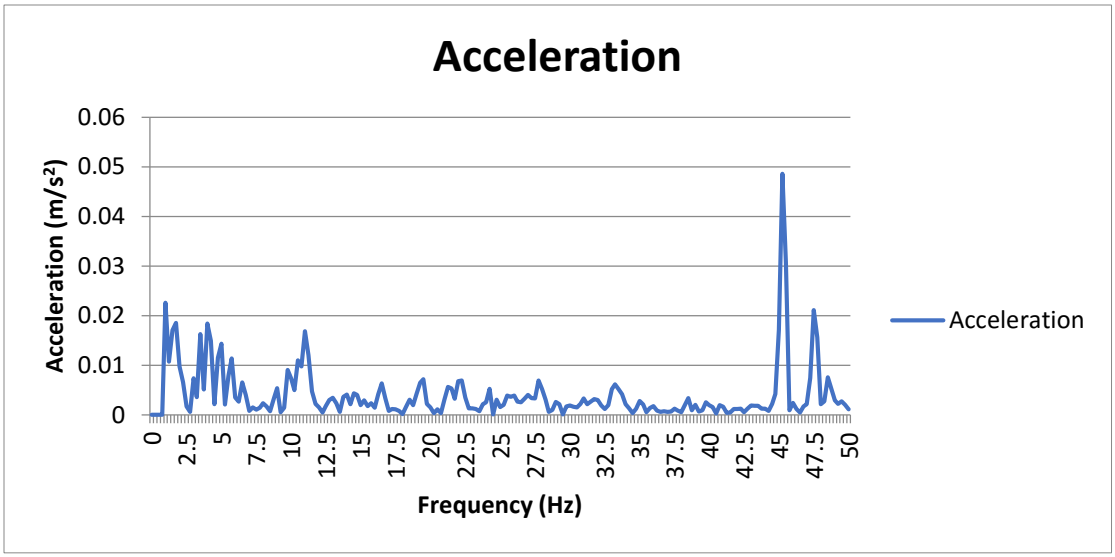


Figure 21: Acceleration levels on floor with respect to frequency.

Table 7: Overall r.m.s. values for vibration on seat and floor

	Overall R.m.s. values (m/s^2)
Seat	0.128
Floor	0.088

The above shows the acceleration levels with respect to frequency and time, as well as the overall r.m.s. values for vibration on the seat and the floor. Observation of these results shows that the vibration sensed on the seat is significantly higher than the floor. Using the simple formula from above: seat vibration/floor vibration, the transmissibility ratio can be determined using this data to be used in the Simulink model. This transmissibility was determined to be 1.45.

Table 8: Acceleration on seat using transmissibility from field data

Roughness (m)	Highest Acceleration (m/s^2)	Acceleration on seat (m/s^2)
6.68×10^{-6}	4.2×10^{-4}	6.09×10^{-4}
3.55×10^{-6}	2.25×10^{-4}	3.26×10^{-4}
14.9×10^{-6}	9.4×10^{-4}	1.36×10^{-3}
1.78×10^{-6}	10.9×10^{-5}	1.58×10^{-4}
5×10^{-6}	3×10^{-4}	4.35×10^{-4}
4.46×10^{-6}	2.76×10^{-4}	4.00×10^{-4}
0.001	6.5×10^{-3}	9.42×10^{-3}

As seen above, the acceleration experienced from the seat is higher using the transmissibility from field data as opposed to transmissibility from literature.

However, all values from assessments using the mathematical model are all similarly small and well below the thresholds for perception of comfort seen in Table 5. This is in contrast to the r.m.s. values obtained from field data, which show acceleration levels

much higher than those obtained from the mathematical model. Nevertheless, the higher r.m.s. value is still significantly below the lowest threshold of perception of comfort in Table 5. Thus, although the levels of vibration levels obtained from the mathematical model differ greatly from the field data, they share the characteristic of being well within comfort levels.

6. Conclusion

In conclusion, it was shown that the mathematical model, within the current parameters and inputs, produces acceleration levels due to vibration that differ greatly from field data. The reasons for this may be numerous, such as the fact that the mathematical model only considered vibration due to the roughness of the rail track, and that the data used is not from the same rail track used by the LRT train studied. Also, vibration within the train car and from the seat may come from many other sources such as the rocking motion of the train, vibration from engines, mechanical appliances such as air-conditioning systems and others. Also, the specifications of the suspension systems used in the mathematical model were not the actual specifications but rather a close approximation.

Due to the challenges outlined above, the Simulink model above can be greatly enhanced by obtaining more data regarding the separate sources of vibration within the train car, and then these data could be combined in a more complex model of greater degrees of freedom so as to obtain a more accurate result. Additionally, actual specifications of the LRT train car should be obtained from the relevant parties. Also, more analysis of the roughness of the LRT track would increase the relevance of roughness levels used in the model.

Acquiring actual specifications for the train car was attempted for this study, however, the relevant parties were only interested in a study of Master's level and above. This shows promise for a future expansion of this study that could be done together with the manufacturers and operators of the LRT trains.

Acceleration levels from both the mathematical modelling and field data show that the vibration experienced by seated passengers on the train are well below thresholds that cause discomfort. This result, coupled with the response of 40 respondents in a qualitative study attached in the appendix, show a rough agreement, with the vast majority of respondents ranking the comfort level of the LRT with a median score of 3 from a scale of 1 to 5.

References

[1] SIMULINK MODEL OF SUSPENSION SYSTEM AND IT'S VALIDATION ON SUSPENSION TEST RIG, J B Ashtekar and A G Thakur. http://www.ijmerr.com/v3n3/ijmerr_v3n3_92.pdf

[2]http://ctms.engin.umich.edu/CTMS/index.php?example=Suspension&section=SimulinkModeling

[3] SUSPENSION DAMPING INFLUENCE ON RIDE COMFORT OF PASSENGER RAIL VEHICLE, Mohamedamin Gemeda. http://etd.aau.edu.et/bitstream/123456789/7860/1/Mohamedamin%20Gemeda.pdf

[4] Rail irregularities, corrugation and acoustic roughness: characteristics, significance and effects of reprofiling, Stuart L Grassie. http://railmeasurement.com/wp-content/uploads/2015/05/120827-corrugationroughness.pdf

[5] LIGHT RAIL VEHICLE NOISE: EVALUATION OF RAIL ROUGHNESS 2 AND NOISE FROM WHEEL RAIL INTERFACE, Shankar Rajaram, Hugh Saurenman, Andrew Wong. http://docs.trb.org/prp/16-4464.pdf

[6] Rail and wheel roughness - implications for noise mapping based on the Calculation of Railway Noise procedure, AEJ Hardy and RRK Jones. http://www.laermorama.ch/m5_krachmacher/pdf/railway-noise.pdf

[7]International Standard ISO 2631-1, Second Edition 1997-05-01

[8] WHOLE BODY VIBRATION ANALYSIS FOR RIDE QUALITY OF LRT PASSENGER, AHMAD ABQARI BIN ABU SAMAH. http://eprints.uthm.edu.my/9116/1/Ahmad_Abqari_Abu_Samah.pdf

[9] THE EFFECT OF STIFFNESS AND DAMPING OF THE SUSPENSION SYSTEM ELEMENTS ON THE OPTIMISATION OF THE VIBRATIONAL BEHAVIOUR OF A BUS, Dragan Sekulić & Vlastimir Dedović. http://ijtte.com/uploads/2011-12-19/d4c8811d-2f84-d9fa231-244.pdf

[10] ROUGHNESS ON DUTCH RAILWAY WHEELS AND RAILS, P. C. Dings & M. G. Dittrich. http://ac.els-cdn.com/S0022460X96902503/1-s2.0-S0022460X96902503-main.pdf?_tid=62917626-5fc2-11e7-bde7-00000aab0f27&acdnat=1499067594_812fa054157fdc530e561479baeec9d6

[11]http://citeseerx.ist.psu.edu/viewdoc/download?doi=10.1.1.953.9354&rep=rep1&typ=pdf

[12] http://e-i-s.org.uk/wp-content/uploads/2013/04/2013_04_06-modelling_of_seating_dynamics-final-YQ.pdf

[13]https://www.acoustics.asn.au/conference_proceedings/INTERNOISE2014/papers/p293.pdf

eureca 2017 – Conference Paper
Paper Number 2ME16

The Enhancement of Pre-Storage Filtration Efficiency for The Rainwater Harvesting System in Malaysia

Yoong Sion Ong[1*], Ken Sim Ong[2], Y.K. Tan[3], Azadeh Ghadimi[1]

[1]School of Engineering, Taylor's University, Malaysia

[2]Bina Plastic Industries SDN. BHD., Malaysia

[3]Besstem Plastic (M) SDN. BHD., Malaysia

[*] yoongsion.ong@sd.taylors.edu.my

Abstract

A conventional design of rainwater harvesting system collects and directs the rainwater through water piping from roof of building to the water storage. The Filration system which locates before the water tank storage and first flush bypass system is the main focus of the research. A filtration system consists of a control volume of filter compartment, filter screen (stainless steel mesh) and water piping that direct the water flow. The filtration efficiency of an existing filter "3P Volume Filter VF1" by industrial company is to be enhances. Suitable filtration method and modifications are proposed based on the researches through existing filters available in the market gloabally. A full scale new filter design prototype with filter screen of 1000 μm stainless steel metal mesh is tested to compare with the original filter system design. Three type of water inlet setups are tested on the prototype to determine the filtration efficiency and all of them have achieve better filtration rate than the original design. Among the proposed water inlet setups for the new filter system design, the 90^o inlet setup with extension provides the best filtration rate per unit time, following by the 45^o inlet setup and the 90^o inlet setup. The 45^o and 90^o inlet setup has similar filtration efficiency at low to medium flow rate while 45^o inlet setup has slightly better efficiency at high flow rate. The filtration efficiency with the 90^o inlet setup with extension is observed to maintained at highest value at medium to high flow rate.

In comparison with the original filter system design, the overall improved filtration performance achieved by the 90^o inlet setup with extension at low to high flow rate is between 34.1% to 35.7%.

Keywords: Rainwater Filtration, Pre-storage Filtration, Enhancement of Rainwater Filtration Efficiency, Rainwater Harvesting System

1. Introduction

Rainwater harvesting practice can be traced since thousands of years using different types of techniques to collect and store the rainwater from rooftops and land surfaces. A conventional design of rainwater harvesting system will collect and direct the rainwater through water piping to the water storage [1]. The dimensions of the rainwater harvesting system are highly dependent on the size of rainwater catchment area. For industrial scale usage, a simple rainwater filtration process is carried out before it is stored in storage. Particles like leaves, rocks, debris and dusts are removed at the filtration process to avoid the risk of clogging up in the water storage.

A conventional rainwater harvesting system consists of four major components which are shown as Fig. 1. The rainwater will first be collected by the catchment area at the rooftop. Filration system which locates before the water tank storage and first flush bypass system is the main focus of the research. A filtration system consists of a control volume of filter compartment, filter screen (stainless steel mesh) and water piping that direct the water flow.

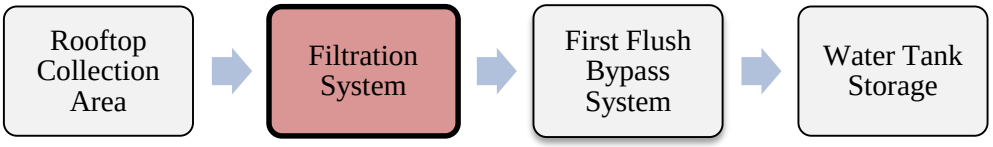


Figure 1. Components of rainwater harvesting system

Large industrial scale filtration system which commonly used in the market is based on a parallel setup concept with a few of horizontal positioned filter compartments as shown in Fig. 2. More filter compartments can be added by increasing the number of the inlet.

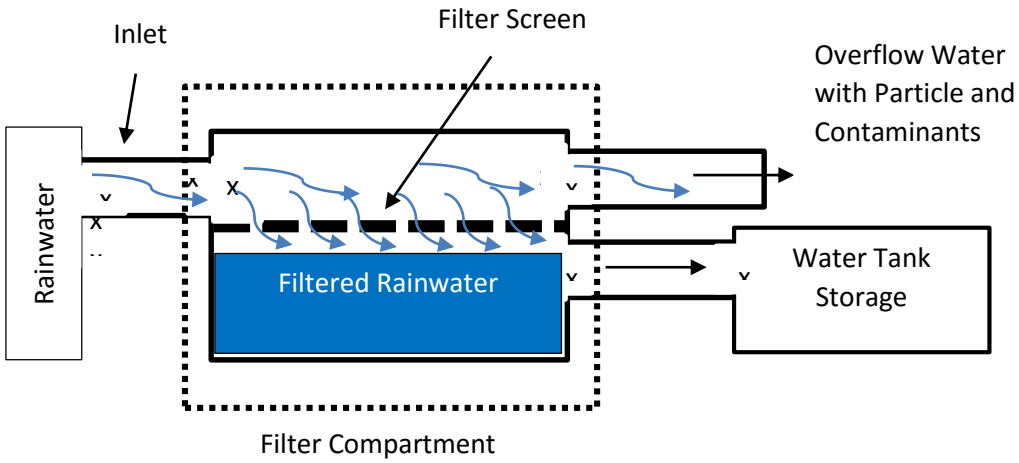


Figure 2. Schematic diagram of single filtration compartment in filtration system

The inlet will direct the rainwater into the filter compartment which consists of a metal mesh filter screen for filtration process. The large particles and contaminants will be pushed out of the filter compartment by rainwater flow. Filtered rainwater that has passed through the horizontal positioned filter screen due to gravitational force will be stored into water tank storage. However, the performance of the design will decrease significantly during high rainwater flow rate operation. The small mesh size of the filter screen not only resist the particles from passing through, it also decreased the permeability of rainwater. The high rainwater flow rate which has filled up the whole water piping will only stay a short period in the filter compartment. There is just a small portion of water near the filter screen that can be directed to the water tank storage while large portion of water have overflowed and left the filter compartment [2].

1.1 Existing Filter "3P Volume Filter VF1"

This research is an industrial project in collaboration with the industrial partners, Bina Plastic Industries Sdn. Bhd. and Besstem Plastic Sdn. Bhd, which is a class leading plastic pipe and rainwater filtration system supplier in Malaysia respectively. Both companies have provided technical support to build the prototype and product testing. Fig. 3 shows the filter system 3P volume filter VF1 and its filter design, which is a product from Germany currently used by DD Techniche Sdn. Bhd. company specialises in installation of rainwater harvesting system for both residential and commercial buildings in Malaysia. The rainfalls in Malaysia are commonly heavy but in a short period of time. The high filtration rate from the filtration system is desired to take advantage in harvesting more filtered rainwater in a limited duration. The projects that the company had done previously were to be capable of sustain a high rainwater flow rate range from 50 L/s to 200 L/s.



(a) (b)

Figure 3. (a) 3P volume filter VF1 by 3P Technik from Germany [3]; (b) Original filter design

The design and functionality of the filter VF1 is similar to the parallel setup concept as discussed in Fig. 2. The filter VF1 is installed by the company whenever the installation location is limited, which will be discussed in this paper. The most

significant difference is that the filter screen is placed at an incline instead of horizontal position. Refer to Fig 3(a), the rainwater flow into the filter compartment and accumulate at top section of the filter compartment at stage 1. At stage 2, the rainwater will be filtered while flowing along the slanted metal mesh filter screen (Fig. 3(b)). Next, the clean water that has passed through the filter screen is collected at the bottom section of the filter compartment at stage 3. While the clean water is directed to the water tank storage at stage 4, the suspended particle will be removed togetehr with the overflow water through a drain outlet at stage 5. The filter design does provide a self-cleaning process to increase the maintenance interval. However, the filter has the filter process characteristic same as the horizontal filtration method as large portion of rainwater flows towards the drain outlet directly during high flow rate.

Fig. 4 shows the official data by the company regarding on the graph of hydraulic efficiency against inflow of rainwater for filter VF1. Based on Fig. 4, the filter achieve 100% efficiency at flow rate of 0.01 L/s to 0.2 L/s but started to drop after that. It can be seen that the filter compartment has started to fail to capture all the inflow rainwater even before reaching flow rate of 1 L/s. Furthermore, the efficiency is just around 50% at flow rate of 3.5 L/s, which means only 1.75 L of rainwater is being filtered and collected into water tank storage every second. At this point, the filter has reached its peak filter performance as shown in the sudden drop of efficiency in the graph. Further increment of inflow of rainwater will only result in more overflow rainwater due to failure to capture. Hydraulic efficiency is the filtration rate efficiency, η is equal to the fraction of total filtered water, $Q_{out,filtered}$ devided by total inflow water, Q_{in} which is shown as Eq. (1).

$$\eta = \frac{Q_{out,filtered}}{Q_{in}} \quad (1)$$

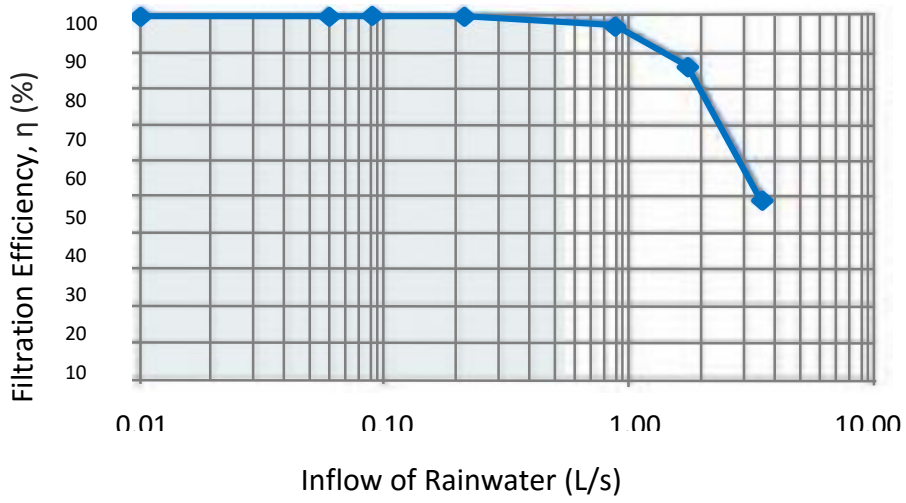


Figure 4. Graph of hydraulic efficiency vs inflow of rainwater for filter VF1 [3]

This paper aims to identify suitable filtration method to achieve higher filtration efficiency under high flow rate to coordinate with the heavy rainfall in Malaysia. The

research focuses on developing a sustainable mechanical operated rainwater filtration system for home and small industrial scale usage. The desired solution is to attain higher hydraulic efficiency at higher inflow rate for this specific filter VF1 by applying suitable modifications without modifying the shape of filter compartment. The study of existing filtration system methods and designs available in the market globally were conducted and their specifications were compared. A prototype filter screen was built by integrating features from different types of filtration system. The filter screen must be able to fit inside the original compartment of filter VF1. The rainwater filtration efficiency, in term of filtration rate difference between the original and prototype filter screen design is to be obtained throughout the testing.

2. Specifications Comparisons of Different Types of Filter System

2.1 Cyclonic Rotation Filter

A cyclone filter is a design of rotational separator which lead the water flow to be circular in the filtration compartment. Fig. 5 shows a schematic diagram of rotational separator which direct the water from inlet to rotate around the compartment. The centrifugal forces produced by the rotating water will acts on large particles and contaminants pushing them outwards leaving the centre vertical axis-z. With the assist from gravitational forces, the suspended particles and contaminants will move towards the bottom of the compartment due to no drainage outlet while leaving the cleaned water to be directed into the storage.

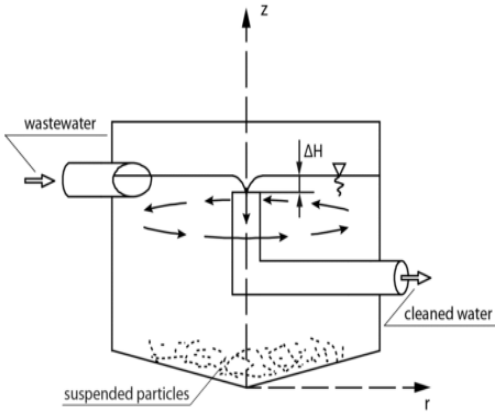


Figure 5. Schematic diagram of rotational separator [4]

The cyclone filtration method performs well under high flow rates of water. However, the suspended particles are not removed from the cyclone filter compartment throughout the operation [4]. Fig. 6 shows an improved design of cyclone filtration method product by Rainharvesting Systems company from UK. This design overcomes the challenges by having a self-cleaning process which will remove the suspended particle out of the filter compartment. The rainwater flow into the compartment from the inlet and perform cyclonic rotation. When the rainwater is approaching the cylindrical shape metal mesh filter, the centrifugal force will pull the water pass through the metal screen. The collected filtered water will be directed to the water tank storage, leaving the filtered particle falling through centre of the filter and are washed

off by the overflow water [5]. However, it only work on high flow rate, else, the rainwater will not perform rotation and flow down the drain directly.



Figure 6. Wisy vortex filter by Rainharvesting Systems company from UK [5]

2.2 Gravity Downpipe Filter

The conventional method of installing the downpipe in any building is vertically from top to bottom. The rainwater catchment area is normally placed on the roof, which the collected rainwater will flow down in the pipe vertically at high speed. By utilising the gravitational force with the speed of rainwater flow, the rainwater can pass through the filter screen right below the inlet easily due to the extra downward force. Fig. 7 shows a filter product by Rainharvesting company from Australia which utilises the gravitational force. The rainwater is directed from top of the filter and the cleaned water is directed to the water tank storage through the outlet at below. During this process, all the particles like leaves and debris are deflected by the filter screen and washed off out of the filter along the slanted filter screen. This design enhances the filtration efficiency as the particles are quickly removed without contaminate on the filter screen [6].

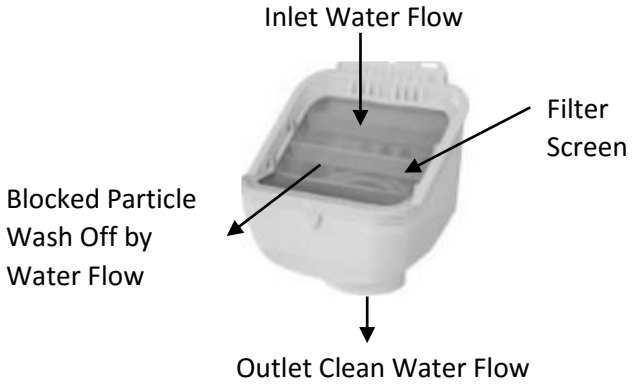


Figure 7. Leaf eater advanced filter by Rainharvesting company from Australia [6]

2.3 Justifications on Selecting the Suitable Filtration Features for the Prototype

Table 1 shows the specifications of different filter product in the market. By referring to Table 1, the general relationship between filter mesh size, filter rate and

filtration method can be determined. First of all, product (1) using the largest mesh size among the other competitors. The filter has the horizontal filtration method design which only achieve a filter rate of 90 L/min. Secondly, a medium mesh size range from 0.8 – 0.955 mm is used for filter product (2) to (4) which utilise the gravitational force to speed up the rainwater along the downpipe. Even though a small mesh size is used, the filter manages to achieve a filter flow rate range from 113 – 120 L/min. The last group of products (5) to (7) have the feature of cyclonic rotation to filter the rainwater. It is found that they have the smallest mesh size among the competitors, however their filtration performances are better than both horizontal and gravity filtration method.

Table 1. Specifications of different filter product in the market

Ref.	No.	Company (Country)	Metal Mesh Size	Roof Area	Rainwater Filter Rate	Filtration Method
[3]	**(1)**	**3P Technik (Germany)**	1.4 mm	350 m^2	90 L/min	Horizontal
[7]	**(2)**	**SuperHead (Australia)**	0.8mm	-	120 L/min	Gravity
[6]	**(3)**	**RainHarvesting (Australia)**	0.8 mm	-	113 L/min	Gravity
[8]	**(4)**	**BRAE (US)**	0.955	-	-	Gravity
[9]	**(5)**	**Rainharvestmo (US)**	0.28 mm	232 m^2	90% Recovery	Cyclonic Rotation
[5]	**(6)**	**Rainharvesting (UK)**	0.28 mm	200 m^2	66 L/min (not tested on maximum condition)	Cyclonic Rotation
[10]	**(7)**	**Allegiance India (India)**	0.25 mm	112 - 500 m^2	105-340 L/min (depends on the volume of collector)	Cyclonic Rotation

Based on real life application experiences, the space of the room that is prepared for the installation of rainwater system in the building and factory is very limited, especially the height of the room. During the installation, the height measured from ceiling to the ground is taken into consideration, conventionally 3.5 m per floor. The size of the water tank storage is normally installed with the largest size to store more filtered clean rainwater. Besides that, a stand is placed below the water tank storage for easier maintenance and cleaning purposes which result in a total of around 3 m in height.

By taking into the consideration of the atmospheric pressure acting on water, the water tank storage inlet must be positioned as high as possible. Otherwise, the cleaned rainwater will not able to be pushed into water tank storage at higher level without the support from water pump if the inlet is positioned at lower level. Fig. 8 shows the schematic diagram of the installation of rainwater filtration system in a room for industrial scale usage.

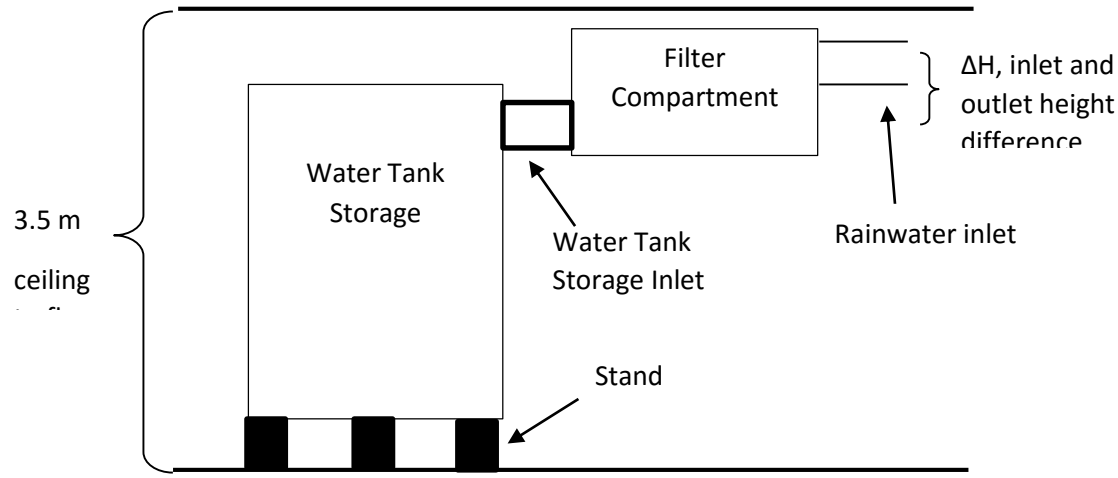


Figure 8. Rainwater filtration system in a room for industrial scale usage

Due to the space constraint of room, the overall height of the rainwater filter compartment must be maintained at smallest scale. Therefore, the height difference between rainwater inlet and water tank storage inlet, ΔH need to be taken into consideration at design stage. The compact sizing of the VF1 filter with dimension of 470 mm x 490 mm x 451 mm is very capable and has advantage during the installation in real life application. The cyclonic rotation filtration method require a big and long in vertical dimension filter compartment to make it functional. Hence, it is more suitable for the installation area without space constraint. It is observed that the horizontal filtration method shows the least efficiency in filtering rainwater at high flow rate as discussed previously. However, by integrating the features from gravity downpipe filtration method may obtain significant improvement in filtration rate. Therefore, this feature is selected.

3. Development of New Filter Screen Design and Fabrication of Prototype

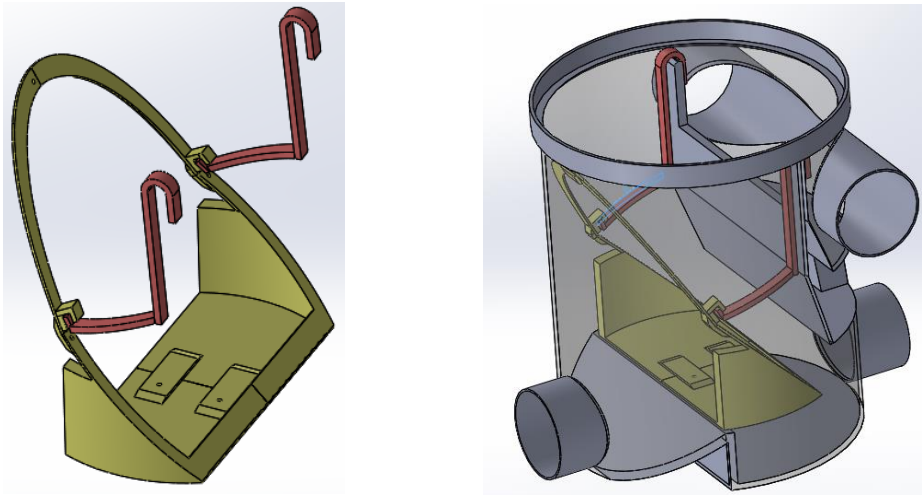
There were two preliminary designs for the filter screen before the final approved design was developed. To construct the new filter screen design to accurately fit into the filter compartment, the filter compartment VF1 was modelled into 3D geometry using Solidworks (2015) as shown in Fig. 9. It had made the task easier to sketch and modify the new filter screen design within a round shape compartment with complicated structural design within it.



(b) (b)

Figure 9. Existing filter compartment VF1: (a) Real life product; (b) 3D geometry model

The new filter screen holder was designed to cover as much filtration area as it can within the limited space within the filter compartment. The model was then inserted into the original filter compartment VF1 to check any error in dimensions to achieve high fit and finish quality as shown in Fig. 10.



(a) (b)

Figure 10. (a) 3D geometry model of new filter screen holder; (b) Filter screen holder inserted into original filter compartment VF1 model

The approved 3D geometry model was then fabricated into full scale prototype using 3D printer with plastic PLA material. The filter screen holder was then attached a layer of 1000 μm stainless steel metal mesh, the same metal mesh size used for the original filter. The completed full scale prototype was fitted to the original filter compartment VF1 as shown in Fig. 11.



(a) (b)

Figure 10. (a) Full scale new filter screen holder; (b) Filter screen holder inserted into original filter compartment VF1

4.0 Experimental Testing of Filtration Rate for Original and New Design

The experimental equipment is set up as shown in Fig. 11. The setup is based on real life installation application where the water source is collected from the downpipe that linked to the roof. The horizontal water pipe will direct the water to the rainwater harvesting system room where the water flow into the filter compartment VF1 through the water inlet.

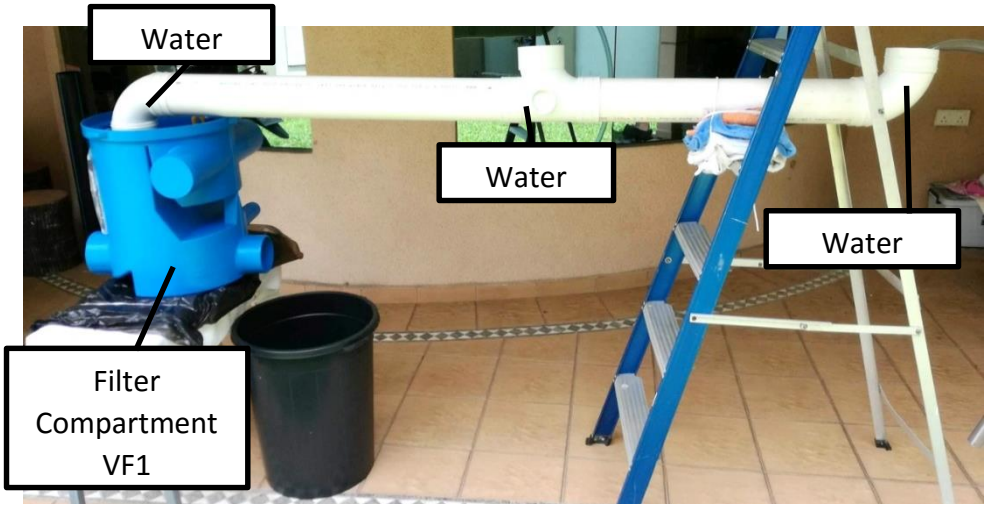


Figure 11. Set up of experimental equipment

Tap water is used for the testing of filtration rate because the lack of rainwater harvesting system in testing location. The water source is fed in through water tap and water pump to mimic the rainwater flow. Before starting the experiment, the water flow rate is measured. The filtration rate for the original filter system design is tested using

the original method. Due to the horizontal positioned water piping that direct the rainwater flow, the positioning of water inlet is manipulated to test the differences in filtration rate as shown in Fig. 12. The step is taken to integrate the features of gravity downpipe filtration system onto the new filter system design. For the original filter system design, the 90° inlet will fill up the water at top section of the filter compartment and flow down to the filter screen. For the new filter system design, the 90° and 45° inlet allow the water to flow towards the filter screen directly.



(a) (b) (c)

Figure 12. (a) Original filter system design with 90° inlet; (b) New filter system design with 90° inlet; (c) New filter system design with 45° inlet

The filtration rate testing for both the original and new filter system design are carried out and the data are tabulated. Each round of testing is run for 15 seconds to collect the filtered clean water and 3 sets of data are recorded to obtain the average value. Low, medium and high flow rate for water inlet are used in testing. The low flow rate is obtained through normal water tap while medium and high flow rate are obtained by using a water pump with a reservoir.

Before starting the experiment, the water flow rate is measured. The low flow rate water is feed into the experimental equipment through the water source inlet and allow to run for 5 second to reach steady flow within the system. Next, an empty pail is used to collect the water from the water inlet for 15 seconds and then weighted on the scale. It is measured that the mass of empty pail is 1.5 kg, the total water mass flow rate at the inlet, $Q_{Total\ inlet}$ of the equipment can be obtain using the Eq. (2). Where m_T is the total mass of the water with the pail, m_{pail} is the mass of the pail and t is the duration to collect the water, in this case t is 15 seconds. The density of water is 1000 kgm^{-3}, therefore, 1 L/s mass flow rate of water at the inlet can be converted as 1 kg/s volume flow rate.

$$Q_{Total\ inlet} = \frac{m_T - m_{pail}}{t} \quad (2)$$

5. Results and Discussions

The original filter design was attached into the filter compartment VF1 for filtration testing. Table 2 shows the data of filtration rate testing for the original filter system design with the original filtration method which consists of low flow rate (0.203 L/s and 0.301 L/s), medium flow rate (1.134 L/s and 1.598 L/s) and high flow rate (2.167 L/s).

Table 2. Data of filtration rate testing for the original filter system design

Inlet flow rate (L/s)	Total filtered water per second by original filter system design (L/s)				Filtration Efficiency
	1	2	3	Average	
0.203	0.137	0.122	0.130	0.130	0.639
0.301	0.187	0.198	0.191	0.192	0.638
1.134	0.705	0.689	0.711	0.702	0.619
1.598	0.949	0.956	0.962	0.956	0.598
2.167	1.208	1.197	1.205	1.203	0.555

Based on Table 2, it is observed that the filtration efficiency has significant difference with the official data by the company as shown in Fig. 4. At 0.2 L/s of inlet flow rate, the tested filtration efficiency is just 63.9% instead of nearly 100% from the official data. As the inlet flow rate increases, the filtration rate of the original filter system design continues to decrease and hence results in just 55.5% filtration efficiency at inlet flow rate of 2.167 L/s. Fig. 13 shows the graph of hydraulic efficiency against inlet flow rate for the original filter system design.

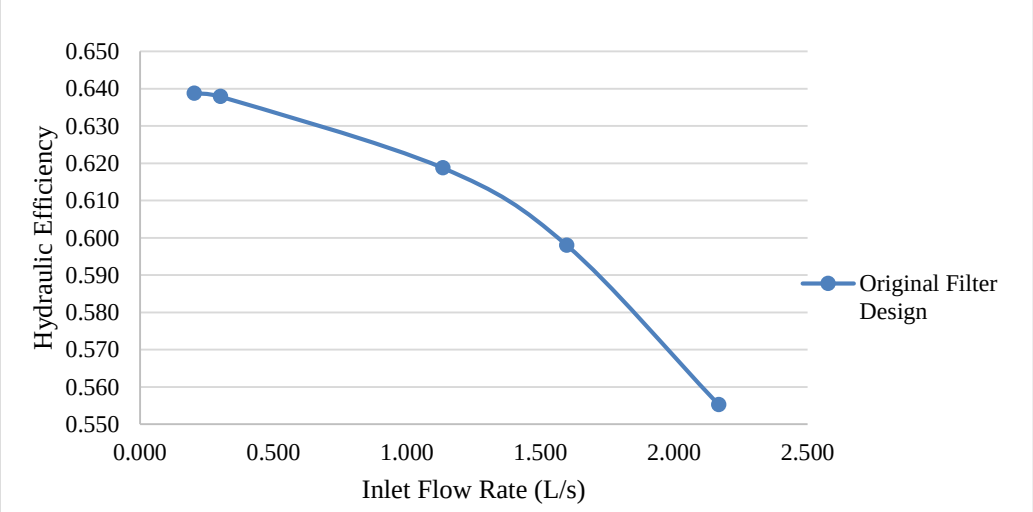


Figure 13. Graph of hydraulic efficiency vs inlet flow rate

By comparing Fig. 13 with Fig. 4, it is observed that the experimental data is nowhere near to the official data from the company. As a reference from both the graphs at inlet flow rate of 2 L/s, the tested hydraulic efficiency is just 56% while the official data shows an efficiency of 80%. Since the testing is done by the current equipment, the obtained experimental data is selected to be the reference for comparison with the new filter system design.

Throughout the filtration rate testing for the new filter system design, there is sign of water loss can be observed through overflow drain outlet of filter compartment. For the 45^{o} inlet setup, the water is directly flowing towards the filter screen rather perpendicularly as shown in Fig. 14(a). This has caused some of the water being reflected away from the filter screen without being filtered and hence the loss of collectable water. As for the 90^{o} inlet setup, due to the sudden change in direction of water flow, a portion of water do not flow downward vertically onto the filter screen as planned. Instead, the water is reflected by the wall of the 90^{o} water pipe joint and flow towards the overflow drain outlet as shown in Fig. 14(b). The results of water loss from the 45^{o} inlet setup is acceptable as it already meets the requirement of integrating the features from gravity downpipe filtration method. However, enhancement is needed to apply for the 90^{o} inlet setup to determine the full potential of filtration rate. Therefore, a simple modification by adding a transparent plastic cover as extension around the 90^{o} inlet joint to avoid the reflected water leaving the filter screen. Fig. 14 (c) shows the addition of transparent plastic cover extension around the 90^{o} joint.



(a) (b) (c)

Figure 14. (a) Water flow with 45^{o} inlet; (b) Water flow with 90^{o} inlet; (c) Addition of transparent plastic cover extension around the 90^{o} joint

Table 3 shows the data of filtration rate testing for the new filter system design with integrated features of gravity downpipe filtration method. By referring to Table 3, there are no significant differences of filtration efficiency for 45^{o} and 90^{o} inlet setup between low and medium flow rate. The 45^{o} inlet setup has slightly better filtration efficiency of 78.1% at high flow rate compare to 76% for the 90^{o} inlet setup. Although there are water loss due to reflection at both inlet setup, there is still slightly advantage for the water to flow directly towards the filter screen with the 45^{o} setup. The extra water flow speed act as external force to push more water pass through the filter screen while the 90^{o} setup reduce the flow speed and reflect the water to opposite direction as the water hit the pipe wall. Hence, the 45^{o} setup achieves better filtration rate by comparing to the 90^{o} setup.

Table 3. Data of filtration rate testing for the new filter system design

Type of Inlet	Inlet flow rate (L/s)	New Filter System Design				Filtration Efficiency
		1	2	3	Average	
45°	0.203	0.200	0.198	0.199	0.199	0.980
	0.301	0.296	0.297	0.299	0.297	0.988
	1.134	0.997	0.995	1.006	0.999	0.881
	1.598	1.359	1.367	1.364	1.363	0.853
	2.167	1.684	1.701	1.692	1.692	0.781
90°	0.203	0.199	0.201	0.199	0.200	0.984
	0.301	0.297	0.299	0.296	0.297	0.988
	1.134	0.990	1.005	0.996	0.997	0.879
	1.598	1.368	1.357	1.362	1.362	0.853
	2.167	1.641	1.652	1.647	1.647	0.760
90° with Extension	0.203	0.198	0.199	0.200	0.199	0.980
	0.301	0.299	0.296	0.297	0.297	0.988
	1.134	1.071	1.076	1.079	1.075	0.948
	1.598	1.477	1.472	1.485	1.478	0.925
	2.167	1.984	1.975	1.970	1.976	0.912

For the 90° inlet setup with the transparent plastic cover extension, it is proven to be a good addition modification onto the filtration system based on Table 3. Water is now able to flow downwards vertically onto the filter screen with no wall reflection. The filtration efficiency is observed to maintained at higher value at medium to high flow rate. An overall increasing in filtration efficiency of 6.9% to 15.2% is achieved by comparing with the 90° inlet without the extension and 6.7% to 13.1% with the 45° inlet setup. Fig. 15 shows the graph of hydraulic efficiency against inlet flow rate for the new filter system design.

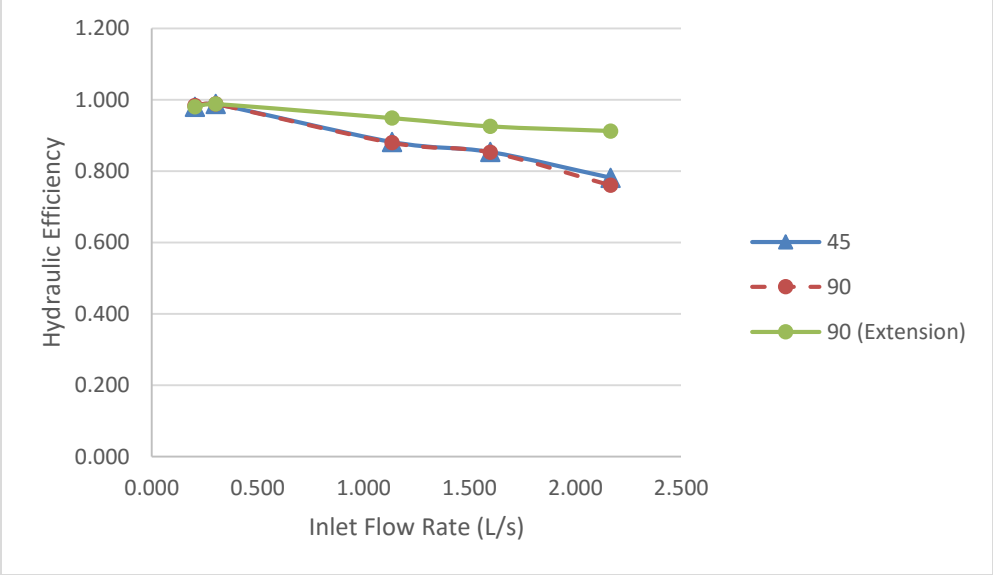


Figure 15. Graph of hydraulic efficiency vs inlet flow rate with different inlet setup

Based on Fig. 15. It is observed that the 45^o and 90^o inlet setup has similar filtration efficiency at low to medium flow rate while 45^o inlet setup has slightly better efficiency at high flow rate. The 90^o inlet setup with extension has the highest efficiency among the three setups. By comparing the filtration efficiency with the original filter system design, all the new filter design manage to achieve higher filtration rate. The overall improved filtration performance achieved by the 90^o inlet setup with extension from low to high flow rate is between 34.1% to 35.7% compared to the original filter system design.

6. Conclusion

In conclusion, the objective to improve the pre-storage filtration efficiency of a rainwater harvesting system is achieved. Suitable filtration methods and modifications for the original filter system design to sustain high rainwater flow rate are proposed. The selections are justified with the researches done on the existing filter system in the market globally. The proposed prototype meets the requirements of fitting accurately inside the filter compartment VF1 and is operated mechanically.

Besides that, the rainwater filtration efficiency, in term of filtration rate difference between the original and prototype filter screen design is obtained throughout the testing. First, there is significant differences of filtration efficiency between the experimental and official data from the company for the original filter system design. As the testing is done by the current equipment, the obtained experimental data is selected to be the reference for comparison with the new filter system design.

Among the proposed water inlet setups for the new filter system design, the 90^o inlet setup with extension provides the best filtration rate per unit time, following by the 45^o inlet setup and the 90^o inlet setup. The 45^o and 90^o inlet setup has similar filtration efficiency at low to medium flow rate while 45^o inlet setup has slightly better efficiency at high flow rate. The filtration efficiency with the 90^o inlet setup with extension is observed to maintained at highest value at medium to high flow rate. An increment in filtration efficiency of 6.9% to 15.2% is achieved by comparing with the 90^o inlet without the extension and 6.7% to 13.1% with the 45^o inlet setup. In comparison with the original filter system design, the overall improved filtration performance achieved by the 90^o inlet setup with extension at low to high flow rate is between 34.1% to 35.7%.

In this paper, the experimental results only cover one high flow rate of 2.167 L/s at the water inlet. The water pump that is used to represent the real life rainwater harvesting operation has reached it maximum output in the experiment equipment setup. Therefore, a water pump with higher water pumping rate can be used in future to further test the peak filtration rate of original and new filter system design. Moreover, more layers of filter screen with 1000 μm stainless steel metal mesh can be attached onto the new filter design to test on the filtration rate as future works. The smaller pore size of

the filter screen will provide better filtration quality. The relationship between filtration efficiency against reduced pore size of filter screen can be determined.

References

[1] A. I. Che-Ani, N. Shaari, A. Sairi, M. F. M. Zain, and M. M. Tahir, “Rainwater harvesting as an alternative water supply in the future,” *Eur. J. Sci. Res.*, vol. 34, no. 1, pp. 132–140, 2009.

[2] R. H. Kim, S. Lee, and J. O. Kim, “Application of a metal membrane for rainwater utilization: filtration characteristics and membrane fouling,” *Desalination*, vol. 177, pp. 121–132, 2005.

[3] 3P Technik, “3P Technik Filtersysteme GmbH - Volume Filter VF1,” 2017.

[4] M. A. Gronowska, “Specification of forces in rotational separator,” *Arch. Hydro-Engineering Environ. Mech.*, vol. 59, no. 1–2, pp. 49–62, 2012.

[5] Rainharvesting Systems UK, “WISY® Vortex Filters - Rainharvesting Systems,” 2016.

[6] Rainharvesting Australia, “Leaf Eater Advanced | Rain Harvesting,” 2010.

[7] Superwall Systems, “Superhead Rainwater Tanks Filter - First Flush Diverters Australia,” 2015.

[8] BRAE, “Commercial Rain Heads,” 2012.

[9] Rainharvestmo, “Rainwater Harvesting Supply Company, LLC | Products1 Vortex Filter,” 2016.

[10] Allegiance Enterprises, “Rooftop Rainwater Harvesting Filters Products - Allegiance Enterprises,” 2017.

Simulations of thermal performance on bicycle helmet

Chris Carl Rosette[1*], Ms. Noor Zafirah Abu Baker[2],

Taylor's Lakeside University

*chris.carl.rosette@gmail.com

Abstract
The purpose of this project is to re-design the current bicycle helmet's geometry to be thermally efficient by reducing the discomfort cyclists' faces when cycling in hot climate areas. The level of discomfort can tend to make cyclist cycle without helmet putting their lives at risk. To do this simulations are done on the current model helmet using the fluent method. The improvements done on the modified helmets that have been analyzed by other engineers will be taken into consideration to aid in improving the thermal performance of the current helmet design. The goal is show positive convective cooling from simulating geometries. Results from the simulations show how the frontal and central part of the helmet's front has more concentration of pressure, at higher velocities. The vents if the area can be reduced by adding tubes higher velocities can be attain increasing the cooling rate. There is already a convection cooling base due to the vents present on the base helmet, using Dyson's bladeless fan design concept to increase air flow by using venturi effect design, which causes a change in pressure, which influences positive air flow, and this also compresses the air in order to attain faster flow. These improvements are along the lines of providing solutions that could greatly improve the thermal performance by an estimate of 15%. The thermal performance of a helmet depends on using Newton's law of cooling, firstly the Reynolds's number is calculated, due the subjection of low (1,000) to high (20,000) Reynolds value, a specific equation related to the law of cooling. Given the different outlet of the new design geometries, the convection cooling coefficient is found, hence, finding the cooling power, q, watts. Using this base helmet is compared to the geometries where by the geometry modified design 1 shows more positive convection cooling.

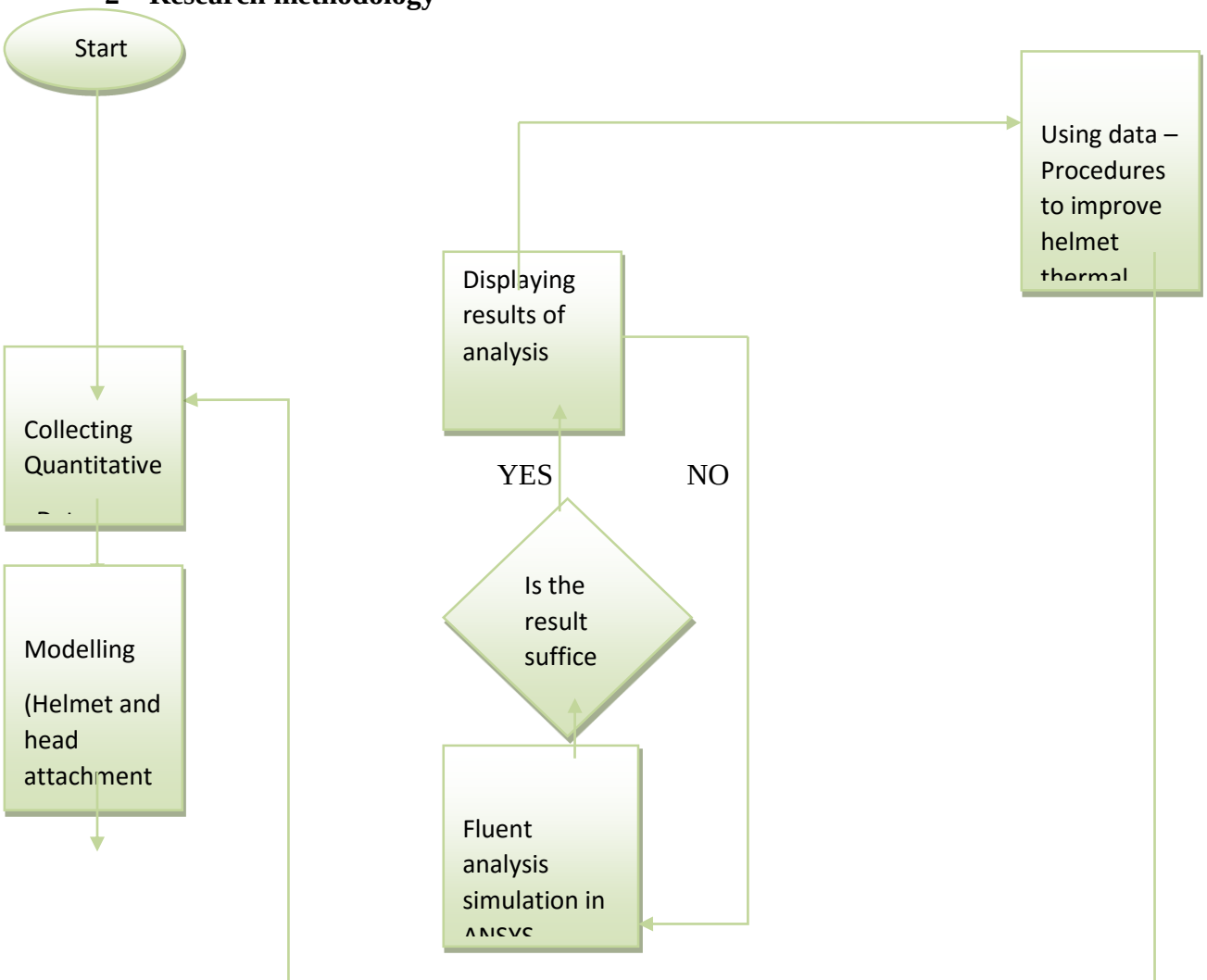
Keywords: Newton's Law of cooling coefficient, Reynolds's number, venturi effect, laminar flow

1. Introduction

When it comes to riding bicycles it is a fact that at least 3,000 people are killed or have attained serious injuries in the year 2015. Most of these accidents occurred during the seasons of spring and summer and the type of accidents that occurs involved mostly in cyclists' head- on collisions [1]
. Therefore it has become a necessity to wear helmets when cycling and it serves as a reliable protective tool for the human head to avoid injuries.

In tropical and hot/warm climate countries, the majority of the cyclists find wearing a bicycle helmet can prove to be quite uncomfortable [2]. This is due to the worn bicycle helmet which causes an increase in heat gain around the cyclist's head. The heat gain affects the sweat rate and the cyclist's skin temperatures while the cycling. The sweating is generated due to body heat rise in attempts to cool the whole body down, which would results in the cyclist to deal with a certain level of discomfort especially around the head area [2]. The discomfort is described by two conditions. The first condition is the cyclists find themselves irritated due to the sweat dripping into the eyes and the second condition is the cyclist might experience exhaustion due to the heat loss. These conditions might tempt the cyclists to ride without helmet which will exposure to high risks [3]. Therefore the main aim of this project is to enhance the thermal performance of the bicycle helmet so that discomfort can be reduced.

2 Research methodology



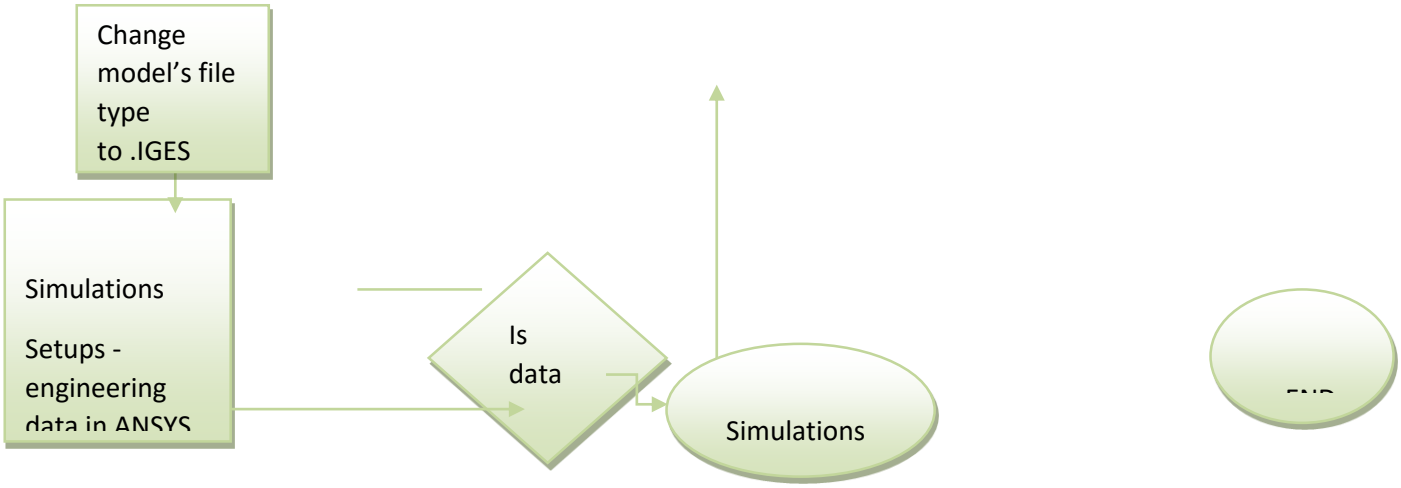


Fig. 13 Methodology work flow diagram

2.1 Collecting Quantitative Data for Fluent

A suffice amount of numerical data on the cyclist's velocity is needed, in order to justify the type of turbulence model to utilize in the fluent analysis. From the literature review, due to the nature of air under conditions of riding a bicycle, high Reynolds value is accounted for, therefore turbulence models such as RANS, k-omega is justifiable to use. Based from the literature review, standard k-omega is suitable for the analysis.

There will be two different analyses that will be done. The first one will be a fluent analysis on the base model helmet, to justify where the modifications can be focused on and applied, using parameters of pressure, velocity and finding the drag coefficient. With the drag coefficient, the areas with high drag would be the ideal areas to focus on to change and remodel. The main velocity will be 5m/s, and for extreme cases 16.7m/s. 5m/s for cyclists who are average cyclists, and 16.7m/s for professional cyclists.

The second fluent analysis will be done on the newly designed modified design geometry of the base helmet to justify its thermal improvement via convective cooling. The main velocities are, 5m/s, 10m/s, 13m/s.

2.1.1 Calculating numerical Data from Fluent – Convection Cooling

To find the convective cooling for the base and the modified to compare effective cooling with be analyzed numerically to justifies the modified helmet's thermal performance.

Using the equation on Newton's law of cooling, the parameters needs to be found based from the nature of the convection cooling, q, watts. Before finding the power of cooling, the h parameter is the most important parameter.

.

$$q = -(k/\delta)A\Delta T = -hA\Delta T \quad \text{eq.1}$$

The equation know has Reynolds's number, is very essential in order to find the correct relating equations of convection cooling coefficient h.

$$Ra = (v.L)/V \quad \text{eq2}$$

The convection coefficient, h, can be found below, by making it the subject which will result in, finding d, m, and the k, W/mK to calculate the values, after finding all the important coefficients. This equation is valid for Reynolds of 10,000 and higher. This equation is used due to the almost cylindered shape of the cyclist's forehead.

$$\frac{h\delta}{k} = 0.3 + \frac{0.62.Re^{\frac{1}{2}}.Pr^{\frac{1}{3}}}{\left[1+\left(\frac{0.4}{Pr}\right)^{\frac{2}{3}}\right]^{\frac{1}{4}}}\left[1+\left(\frac{Re}{282000}\right)^{\frac{5}{8}}\right]^{4/5} \quad \text{eq3}$$

2.2 Review of fluent CFD Analysis

From this simulation it can be seen how the blue areas demonstrate lower pressures, indicating signs of increasing velocity. This shows potential areas to modify the base helmet.

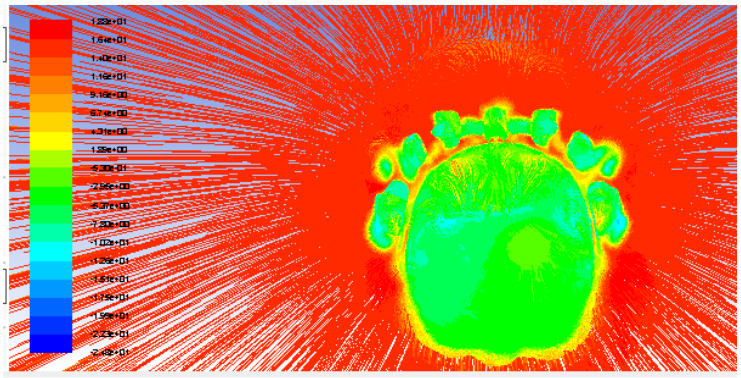


Fig 21. Path lines of total pressure (inlet velocity 5m/s)

For professional cyclists, their velocites reach 50km/hr onwards, from the analysis of the total pressure it can be seen, fig 22, how the pressure increases towards the centeral area of the base helmet. This shows how for very high velocities, a more aerodynamic designed helmet is needed, such as the time trail helmet figure 10, or the advantage helmet figure 1.

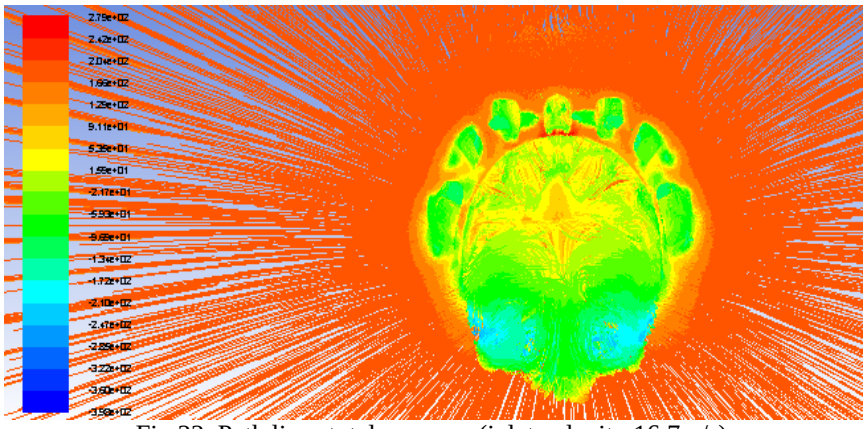


Fig 22. Path lines total pressure (inlet velocity 16.7m/s)

Areas of high drag are located at the most front and back of the base helmet. This is due to the positioning of the vents which causes the high value of drag coefficient.

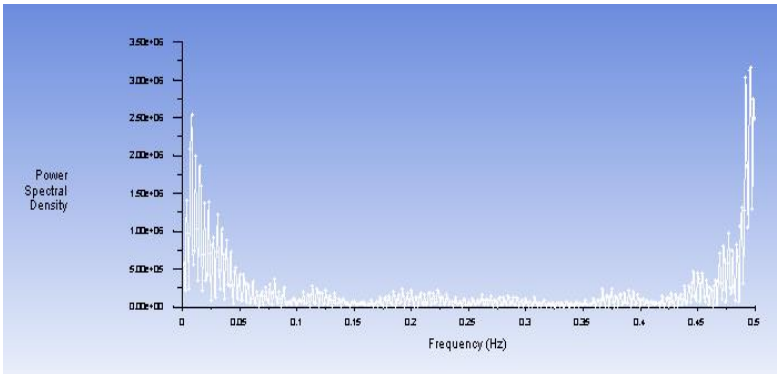


Fig 23. Spectral analysis of drag coefficient (inlet velocity 5m/s)

Positive influence of velocity is seen around the edges of the base helmet, noticed by the green colour. Partial parts marked by the black circle shows increases of velocity compared to the blue areas around the middle area. The pattern also indicates turbulent flow. For more effective convection cooling, a laminar flow is much more desirable.

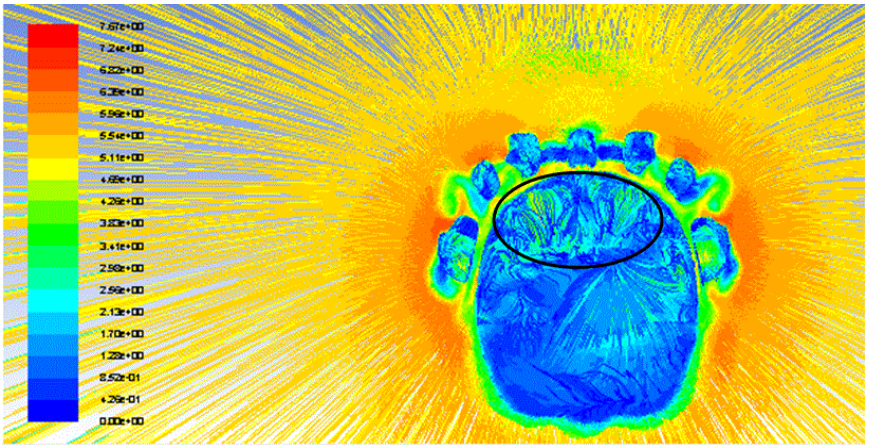


Fig 25. Path lines of velocity (inlet velocity 5m/s)

Looking at the black circled areas, there are swirls of green velocities amongst the blue areas indicating low velocities. The vents towards the edges show positive influence in increasing velocities indicated by the green colour areas.

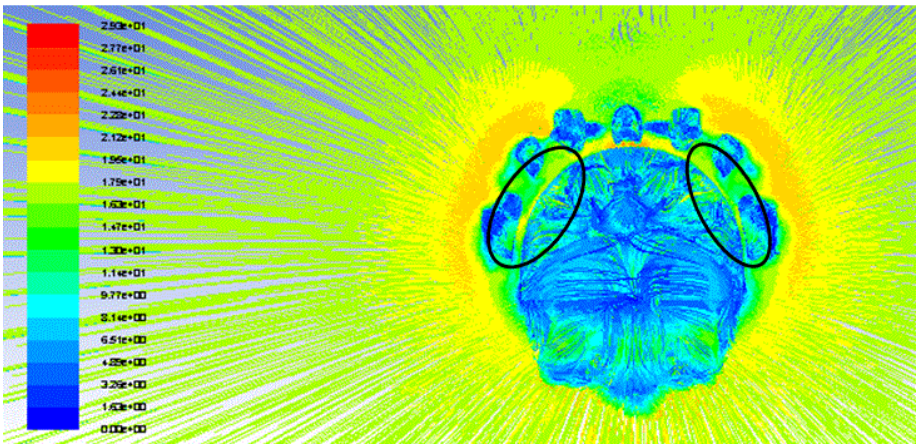


Fig 26. Path lines of velocity (inlet velocity 16.7m/s)

2.2.1 Review of fluent analysis on modified designs

From figure below it can be seen that vent 2 and vent 1 is simulated from the base helmet, to find its effective cooling to compare with the modified design geometries.

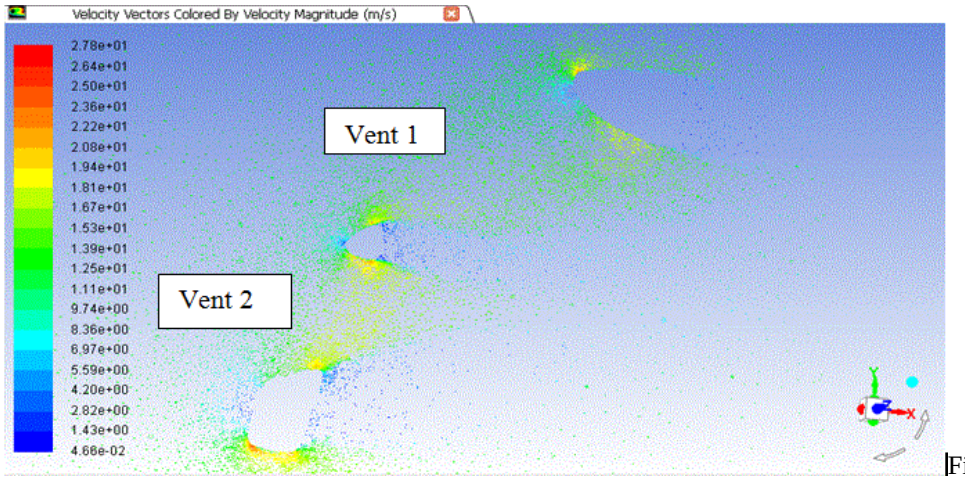


Fig 27. Vector Base helmet model for analysis

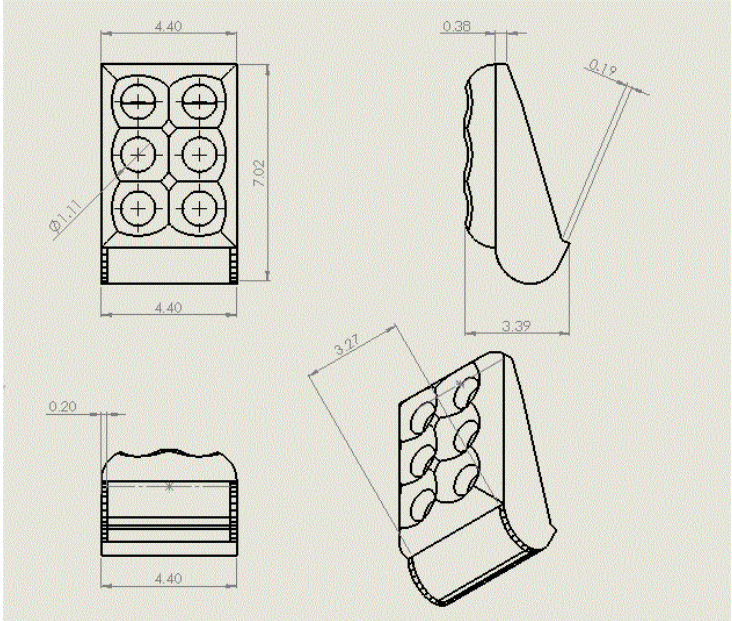


Fig 28. Modified design 1 (MD1) units in cm

Result of fluent analysis on MD1. The outlet flow potential of attaining a laminar flow.

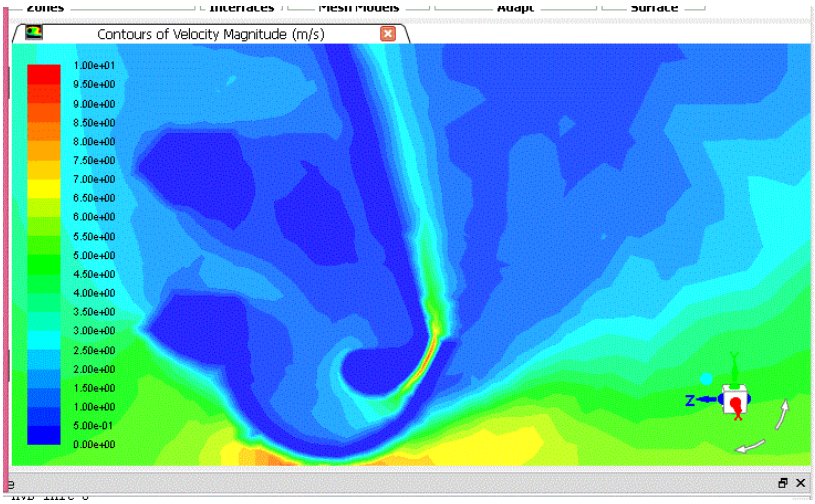


Fig 29. contours modified design 1, inlet velocity of 13m/s (min = 0m/s, max = 24.85295m/s)

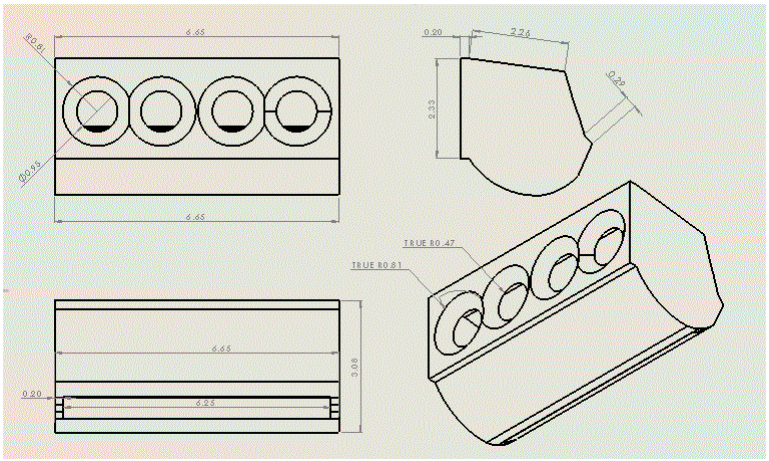


Fig 30. Modified design 2

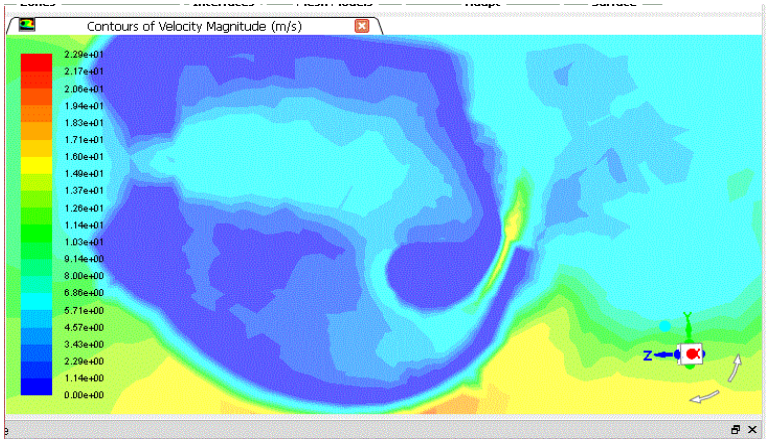


Fig 31. Contours Modified design 2 with inlet velocity of 13m/s. (min = 0m/s, max =22.85652 m/s)

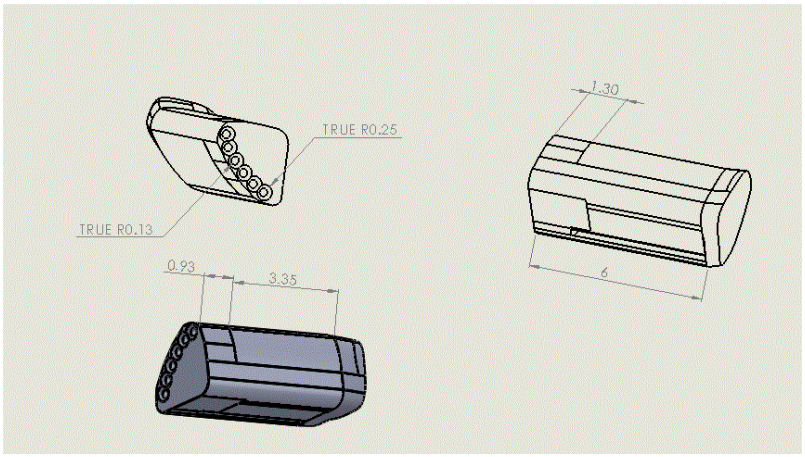


Fig 32. MD3 for side edge of the base helmet

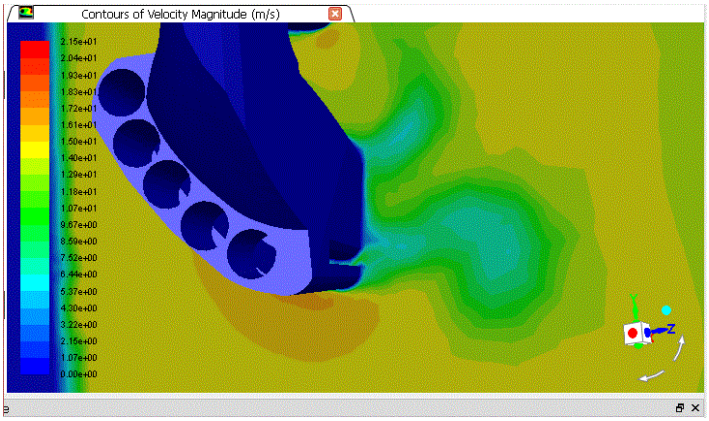


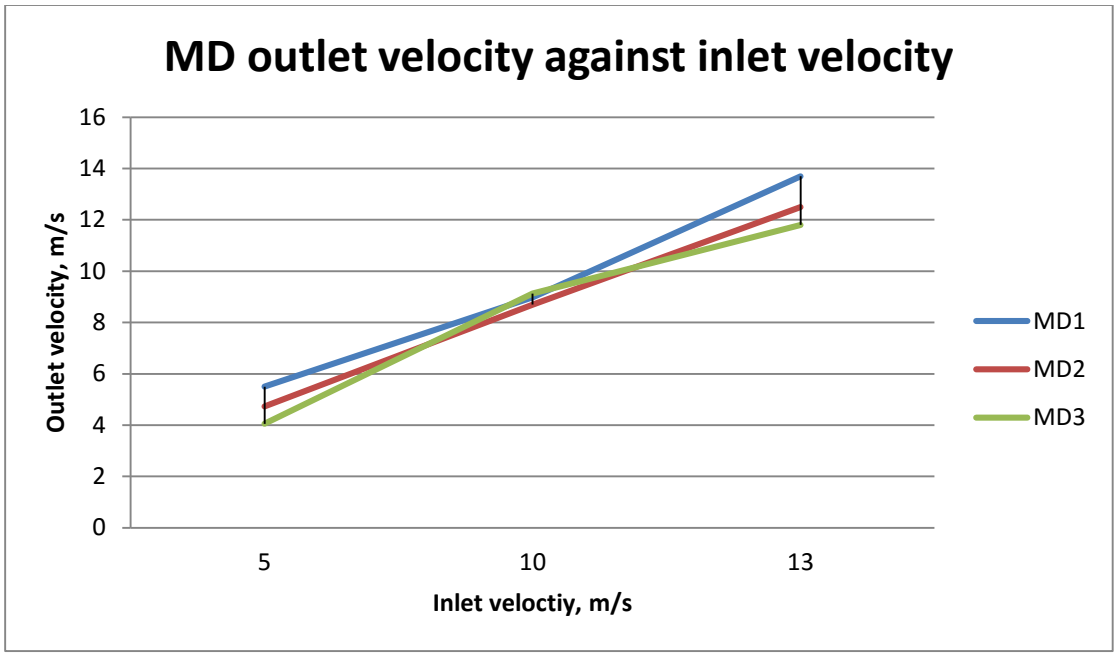
Fig. 33 Modified design 3, 13ms inlet (min = 0, max = 21.47834)

Table 2: Modified geometries and inlet, output velocities

Modified designs	5	10	13
Modified Design 1, outlet velocity	5.50	8.98	13.7
Modified Design 2, outlet velocity	4.73	8.70	12.5
Modified Design 3, Outlet velocity	4.05	9.13	11.8

Modified design 1 (MD1) shows potential of giving out more velocity compared to the other two geometries, from inlet velocities of 7.5 till 11.5m/s. Whilst MD2 and MD3 shows very poor performance compared to MD1.

Graph 1: Outlet against inlet modified geometries



2.3 Evaluation of convection cooling using Newton's Law of cooling

2.3.1 Evaluations of convection cooling on vent 1 and vent 2 of the base helmet

Analysis on the base helmet will compared to the new improve designs

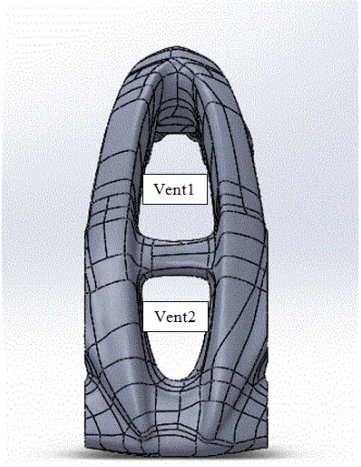


Fig 34: Front base helmet

Using equation 3, accommodating for large ranges of Reynolds's number

$$\frac{h\delta}{k} = 0.3 + \frac{0.62.Re^{\frac{1}{2}}.Pr^{\frac{1}{3}}}{\left[1+\left(\frac{0.4}{Pr}\right)^{\frac{2}{3}}\right]^{\frac{1}{4}}}\left[1+\left(\frac{Re}{282000}\right)^{\frac{5}{8}}\right]^{4/5} \qquad \text{eq3}$$

To calculate the Reynolds's number, the length found in table is needed.

Table 3. Dimensions of average vents' base helmet

	d, Diameter, m	L, Length, m
Vent 2	0.034979073	0.01436
Vent 1	0.056420427	0.02453

To compare the two vents design, its convective cooling power in watts, by finding h W/(m^2K) first, then q can be calculated.

Table 4. Analysis on base helmet vent1

outlet Velocity (m/s)	Re_1	$\frac{h\delta}{k}$	h, W/(m^2K)	q(watts)
6.14	9229.3768	51.36344	136.6781138	8.987187366
11.70	17586.92322	73.72428	196.1803091	12.89971852
16.70	24200.808	88.410449	230.7512719	15.1791143

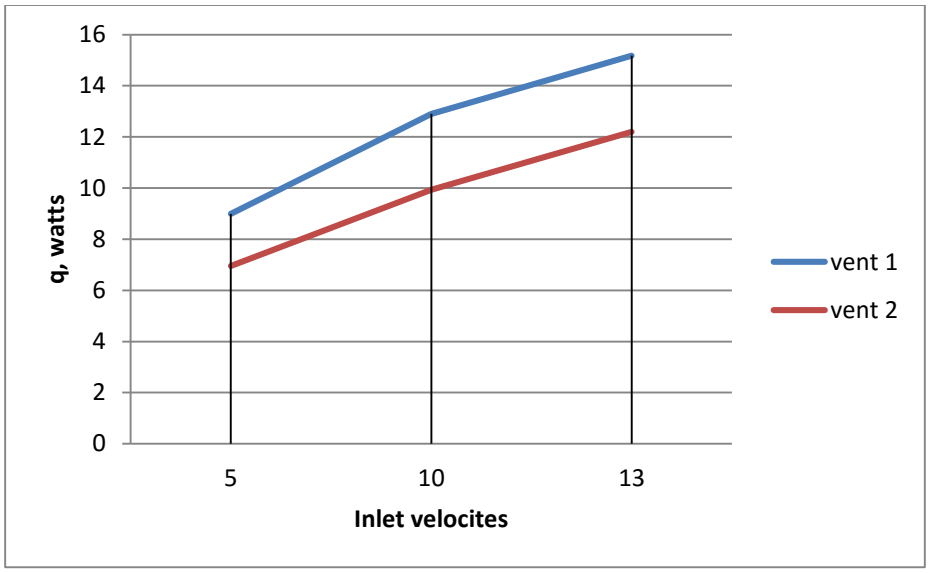
The same procedure is done for the second vent.

Table 5. Analysis on base helmet vent2

outlet Velocity (m/s)	Re_2	$\frac{h\delta}{k}$	h	q(watts)
6.65	5851.7066	39.805666	105.9228772	6.94895237
12.70	11175.43967	56.78967	151.1173119	9.936628174
18.10	15927.20142	69.66987	185.391541	12.19030954

From graph 2, vent 1, have more convective power, this is due to its larger size compared to vent 2.

Graph 2. Convective power, p, watts, of vent1 and vent 2



Evaluation of convection cooling on Modified design 1 (MD1)

Length of geometry is found using the geometry which is 0.0366m in fig 35. This is used to calculate the Reynolds's number in table 6.

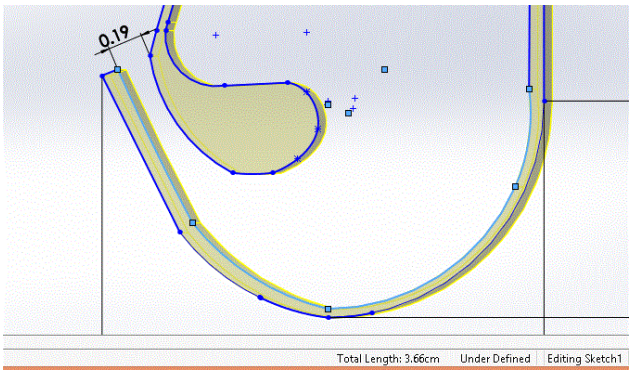


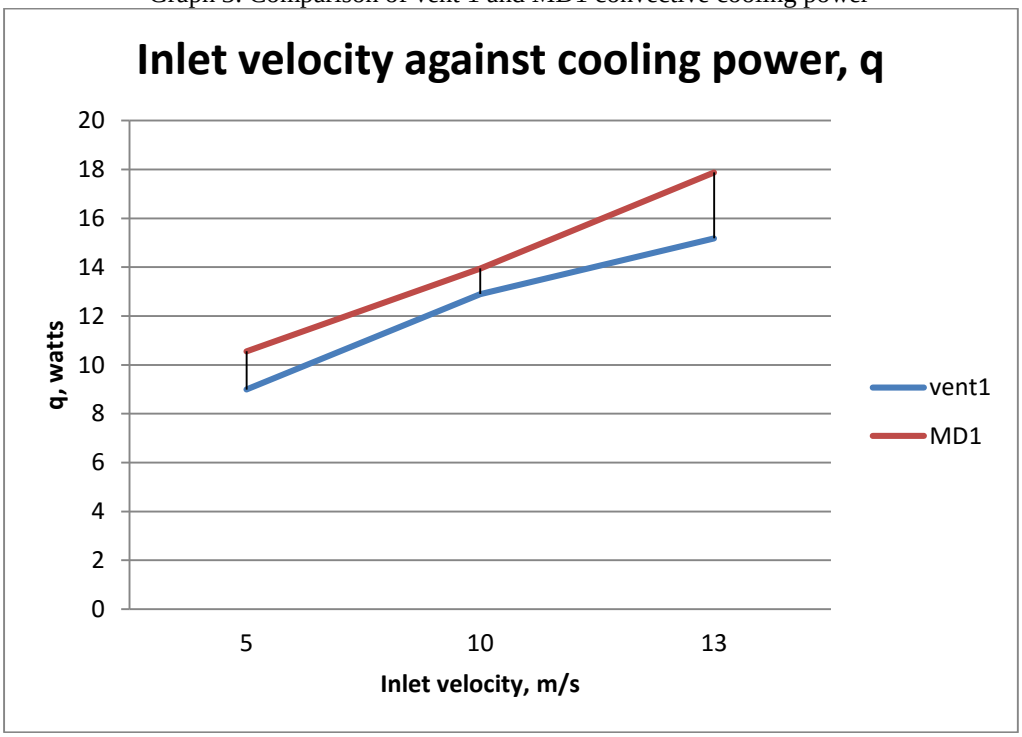
Fig 35. L, length of geometry light blue highlighted

Table 6. Results of convection cooling on modified design 1

Outlet Velocity (m/s)	Re	$\frac{h\delta}{k}$	h	q
5.50	12335.31466	60.32044975	160.5127168	10.55441739
8.98	20140.20467	79.7063344	212.098558	13.94641342
13.7	30726.14744	102.1864707	271.918985	17.87985971

MD1 shows more power, q, watts, then vent 1 base helmet, this proves that the new design geometry makes the thermal performance improve.

Graph 3. Comparison of vent 1 and MD1 convective cooling power



This will be the finalized design of the helmet. The MD1 is fitted over the vent 2 space.

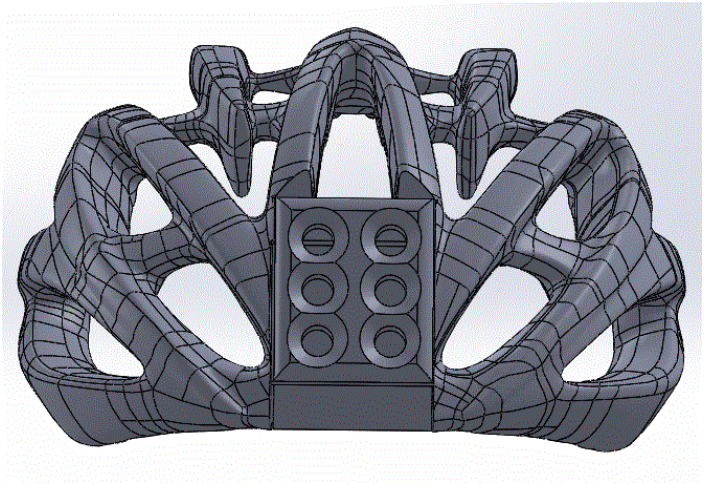


Fig 36. Finalized helmet design

3. Conclusion

Increasing in inlet air velocity would improve the thermal performance of the helmet as well as the distances it travels [14] [15]. Given that MD1 has a minor increase from it inlet velocities to its outlet, shown in graph 1. The distance, at which the air flow travels is subjected to a curved distance, giving an increase in the Reynolds's and overall increasing the convective cooling. The thermal performance is about 15% improved. Potential in simulating better geometries with longer curved lengths can be done to greatly improve the thermal performance, as well as, adding other places with venturi vents to increase convection.

It is also noted that from fig 29, as the flow is distant away from the outlet, the stream demonstrates a laminar flow with an inlet of 5 m/s. Fig. 37 shows Comparing that to fig 38, with an inlet of 13m/s, the outlet shows turbulent rather than laminar. [16].

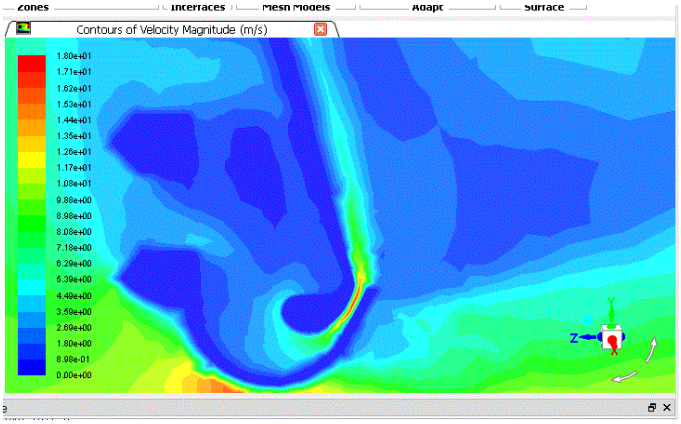


Fig 37. A mixture of turbulent and laminar flow

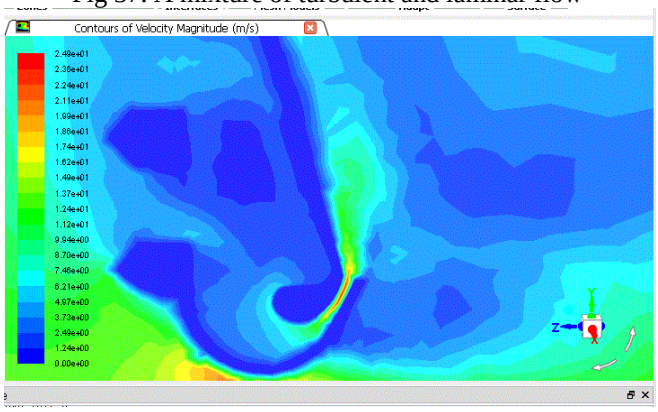


Fig 37. Turbulent flow from the outlet of MD1

4. References

[1] A. Hamzah, A. Ariffin, M. Solah, N. Paiman and M. Osman, "Exploring cycle crash characteristics in Malaysia", *MATEC Web of Conferences*, vol. 90, p. 01056, 2016.

[2] C. P. Bogerd *et al.*, "A review on ergonomics of headgear: Thermal effects,"

Int. J. Ind. Ergon., vol. 45, pp. 1–12, 2015.

[3] G. De Bruyne, J. Aerts, J. Vander, J. Gof, I. Verpoest, and D. Berckmans, "International Journal of Industrial Ergonomics Quanti fi cation of local ventilation ef fi ciency under bicycle helmets," vol. 42, pp. 278–286, 2012.

[4] Engineering Flow and Heat Exchange. Springer Verlag, 2016.

[5] S. Science, "Prolonged exercise in the heat," pp. 10–15.

[6] L. Wang, H. Yin, Y. Di, Y. Liu, and J. Liu, "Physiology & Behavior Human local and total heat losses in different temperature," *Physiol. Behav.*, vol. 157, pp. 270–276, 2016.

[7] P. N. Doval, "Aerodynamic Analysis and Drag Coefficient Evaluation of Time-Trial Bicycle Riders," no. December, 2012

[8] F. Menter and Y. Egorov, "The Scale-Adaptive Simulation Method for Unsteady Turbulent Flow Predictions. Part 1: Theory and Model Description", *Flow, Turbulence and Combustion*, vol. 85, no. 1, pp. 113-138, 2010.

[9] Z. Zhai, Z. Zhang, W. Zhang and Q. Chen, "Evaluation of Various Turbulence Models in Predicting Airflow and Turbulence in Enclosed Environments by CFD: Part 1—Summary of Prevalent Turbulence Models", *HVAC&R Research*, vol. 13, no. 6, pp. 853-870, 2007.

[10] F. Alam, H. Chowdhury, H. Wei, I. Mustary and G. Zimmer, "Aerodynamics of Ribbed Bicycle Racing Helmets", *Procedia Engineering*, vol. 72, pp. 691-696, 2014.

[11] K. Takizawa, H. Takagi, N. Kostov and T. Tezduyar, "2B16 Boundary fitted meshing for arterial flow analysis : Boundary fitted meshing for arterial flow analysis", *The Proceedings of the Bioengineering Conference Annual Meeting of BED/JSME*, vol. 201325, no. 0, p. 302, 2013.

[12] I. Djodikusumo, I. Diasta and I. Sanjaya Awaluddin, "Geometric Modeling of a Propeller Turbine Runner Using ANSYS BladeGen, Meshing Using ANSYS TurboGrid and Fluid Dynamic Simulation Using ANSYS Fluent", *Applied Mechanics and Materials*, vol. 842, pp. 164-177, 2016.

[13] N. COLLEY, J. TREMBLE, G. HENSON and T. COLE, "Head circumference/abdominal circumference ratio, ponderal index and fetal malnutrition. Should head circumference/abdominal circumference ratio be abandoned?", *BJOG: An International Journal of Obstetrics and Gynaecology*, vol. 98, no. 6, pp. 524-527, 1991.

[14] A. Van Brecht, D. Nuyttens, J. Aerts, S. Quanten, G. De Bruyne and D. Berckmans, "Quantification of ventilation characteristics of a helmet", *Applied Ergonomics*, vol. 39, no. 3, pp. 332-341, 2008.

[15] S. Passler, J. Mitternacht, M. Janta and V. Senner, "Conceptual Development and Evaluation of Heat Relief Principles for the Application in Bicycle Helmets", *Procedia Engineering*, vol. 147, pp. 501-506, 2016.

[16] H. Li, X. Jin, H. Deng and Y. Lai, "Experimental investigation on the outlet flow field structure and the influence of Reynolds number on the outlet flow field for a bladeless fan", *Applied Thermal Engineering*, vol. 100, pp. 972-978, 2016.

eureca 2017 – Conference Paper
Paper Number 2ME18

Fabrication of Non-Implant 3D Printed Skin

Shivani Amish Kumar Pandya[1*], Yong Leng Chuan[1]

[1]*School of Engineering, Taylor's University, Malaysia*

[*] *Shivani.7111@gmail.com*

Abstract

Many bandages tend to be harmful when being removed from the human skin. This is a crucial issue, especially faced by burn victims. When bandages are removed from the burn wound, they tend to be harmful by peeling off the newly formed layer of skin over the burn wound. Such nature causes the patient to endure a longer recovery time with additional pain. The objective of this project is to 3D print artificial skin for the victims of burn wounds by using natural gelation. The main aim for creating the artificial skin will be used in place of the current burn wound treatment techniques of dressing the wounds in bandages. The inner layer of this skin was lined with a natural adhesive, a thin layer of agar-agar, which has been reinforced with crushed eggshells to increase its adhesive strength and durability. The synthesized gel contained non adhesive behavior, yet aids in wound healing abilities. Applying hydrocolloids ensures that the wound is kept cool and the gel also ensures efficient heat transfer. This was done so that less sweating occurs on the patient. Based on the experiments that were conducted, the results conclude that the best ratio of artificial skin layer would be 2:1 of agar gel: crushed eggshells. This golden ratio of gel: crushed eggshells for the longest period of time for attachment on the skin without sweating, is achieved. The skin will be printed using Acrylonitrile-Butadiene-Styrene (ABS). The colour of the skin and the shape of the skin was individually designed for each specific patient. The inner gel has the capabilities of reducing the rehabilitation time, without compromising the comfort of the patient. This approach has the potential to be used as a new method to treat burn wounds.

Keywords: 3D printed, skin, burn victims, burn wounds, bandage wounds, gelation, eggshell

1. Introduction

The main purpose of creating the 3D printed skin is to aid burn victims. According to the World Health Organization (WHO), there are an estimated of 265,000 fatalities every year caused by burns alone [1]. There are countless more people with burn injuries that are admitted into hospitals every year. Treatment for burn patients depends on the severity of the burn and how many layers of skin have been damaged from the burn. That will also determine the number of days the treatment will take and how many days the patient needs to be hospitalized.

When victims have severe burn wounds, it will be a long and painful process to treat them all properly. Not all the skin layers can be treated at once, hence multiple surgeries have to be performed. The human skin has to be given some time to heal on its own before surgery can be performed again [2]. Whilst waiting for the patient to heal, the wound cannot be exposed to air and must be wrapped with gauze and bandages to prevent bacterial infections [3]. Despite this being a commonly practiced method that is used by hospitals worldwide, there are many accidents that are caused by the bandages themselves. When the bandages are removed from the area of the burn, it may cause tearing and stripping of the skin, which causes the burned skin to be further irritated, hence prolonging the recovery time. Based on a study of 155 residents in a long-term care facility who were at least 65 years of age, the incidence of new tape-related skin injuries was 15.5% over an 8-week period with skin injuries developing at 34 sites in 24 patients [4].

For burn victims, plastic surgery is a luxury and is not affordable for everyone. It is an expensive procedure that may contain plenty of risks. Especially, in the case of a deep skin injury, multiple procedures are required to fix the wound and get the skin surface looking normal again by placing multiple layers of skin grafts. Non-implant skin can be an alternative to solve this issue. This can be used by people of all financial means and has significantly less risks compared to undergoing surgery. Non implant skin means that there is no surgery required as the skin will not be embedded into your body. This is a cheaper alternative and relatively safer than surgery. The non-implant skin can be reused and the gel created with natural substances is compatible with the human skin, which will also promote recovery [5]. Fortunately, medical technology constantly advances, creating better healthcare and opportunities for patients. New discoveries have been made in the field of 3D printing, where a 3D printer is used to print tissues samples and skin layers that can be implanted into the human body using stem cells. However, this too is still an experimental procedure and costs a lot of money [6]. There are two main reasons for creating 3D printed skin for burn victims. Firstly, there is for the purpose of covering up their scars after their burn wounds have been treated. Secondly, it can be used for the healing process of the burn victims. The second reason is what will be discussed in this report based on the healing of the wounds of the burn victims. This is because the gel layer synthesized has natural organic substances, all of which promote skin growth, which aids in the recovery time of the burn victims.

A 3D printer is used so that the skin can be easily customized to the different types of structures that each person has. 3D printing is an efficient option as it can cater to each patient's specific applications. It is also a fast prototyping method with high accuracy and low fabrication cost. The filament to be used for the 3D printer is the acrylonitrile butadiene styrene (ABS). ABS is used as the filament because it is a material that can be easily sterilized and that is easy to mould. With medical applications, sterilization is a very important factor [7]. Another crucial element for the non-implant 3D skin will be the gelatinous substance that will be used to attach the 3D printed skin to the patient's burnt skin. The gel will be synthesized using hydrocolloids which have excellent healing properties for the skin and have adhesive strength that will be able to replace the current adhesives in bandages.

This research is done to have an alternative method to apply to the current care of burn victims. Instead of using the bandages and any medical adhesives, a 3D printed skin mask is to be used to promote healing. Furthermore, the gel produced will be nontoxic and hence will not be an irritant to the skin.

2.0 Research Methodology

2.1 Raw materials for gel formulation

The raw material that has been used to synthesize the inner layer of the artificial skin is agar, crushed eggshells and glycerol. The eggshells were roughly crushed using a pestle and mortar and were mixed with the agar. The reason for using roughly crushed eggshells compared to using eggshell powder is that the hand crushed eggshells contain the permeable membranes of an eggshell. The permeability of these membranes ensure that the entire solution remains "breathable". Agar has excellent rheological properties and hence have many applications in the biomedical industry. Agar is from a plant origin, along the walls of certain types of algae. The agar in the seaweed provides the flexible motion for the seaweed to be able to follow the current of the ocean [8]. The flexibility of agar can be useful in the project as the contours of the human body are not easy to adapt to and hence the flexibility will ensure the easy adhesion of the gel to the skin. The agar was then reinforced with crushed eggshells and glycerol.

The eggshell of a chicken egg contains 95% of calcium carbonate and 5% of organic materials such as collagen. Collagen is the main component in the extracellular matrix of all tissue types. It is biocompatible and is non-toxic. This collagen will be helpful in tissue regeneration [9]. It is useful for burn victims as it also would help speed up the recovery of the patient.

Another substance that was tested with was glycerol. A preliminary experiment conducted with plain agar and glycerol was also not particularly effective in showing good spreading.

During the formulation, the crushed eggshell powder was added to the boiled agar solution and blended homogeneously. This was tested in different concentrations to see which one was the optimum solution. Secondly, the eggshell powder was added to the solution along with glycerol. This was then compared with the solution of agar and eggshells. The best synthesized gel was chosen from these experiments.

2.2 Breathability

Breathability is one of the crucial factors of this project. The gel that is created should be "breathable". This is to ensure that no sweating occurs between the gel layer and the human skin. If there is sweat that pools up between the two layers, it will cause slippage of the artificial skin and hence would reduce the duration that the skin can remain attached to the human skin. Agar is a permeable substance that allows diffusion to occur. This will ensure that the sweating of the skin will not pool. Furthermore, all the additives that are tested with to create the gel, are permeable. The eggshells are used in crushed form instead of powder form because when the eggshells are crushed, the inner and the outer membrane is also included in the mixture. Both the inner and out membrane are permeable. This is added to the mixture when creating the gel. Furthermore, glycerol is also a substance that permeable. Hence, when the gel mixture is created, it is ensured that there is low risk of slippage of the artificial skin. Moreover, there ABS that is used to print the artificial skin also has the properties of being water permeable. This means that the sweat that would occur would have room to escape and would not affect the gel layer.

2.3 Determination of gel : crushed eggshells ratio

The aim of this step is to determine the best spreading and adhesion by adding crushed eggshell powder and glycerol to the agar gel. The factors that will be considered in the synthesizing of the gel is the concentration of the crushed eggshell powder that is put in the agar gel. The experiment was conducted by testing the gel and 3D printed skin on a test subject. The time taken for the gel to dry and the time that the printed skin remained stuck to the human skin were both measured.

The aim of this experiment is eventually to determine the best combination of the three raw materials – agar, crushed eggshells and glycerol, to be able to produce a gel that is quick to dry on the skin and has the ability to stick to the human skin for longer periods of time. Figure 1 below shows the raw materials used while Figure 2 shows the mixture of the substances.

(a) (b)



Figure 1. (a) Dry Agar. (b) Crushed Eggshells



Figure 2. (a) Combination of agar gel and glycerol. (b) Combination of agar gel, glycerol and eggshells.

The results for this experiment was found by applying a layer of the gel synthesized on the 3D printed skin. This 3D printed skin is held in place until the solution is dry on the human skin. The time taken for the solution to dry on the human skin is measured and then the time the skin remains on the human skin is also measured and recorded. The thin layer of the gel spread on the 3D printed skin and how the 3D printed skin was tested on the human skin is shown in the Figure 3 below. For this research, there was only a single test subject as the concept was trying to be proven where this new research could be a viable alternative in place of bandages. To be able to incorporate this into the medical field, further testing is required on more skin types.



Figure 3. (a) A layer of synthesized gel (agar, crushed eggshells and glycerol) applied on the 3D printed skin. (b) The adhesion testing of the 3D printed skin on the human skin

2.4 3D Printed Artificial Skin Outer Layer

To design the 3D printed skin, measurements were taken of an actual test subject and the skin was printed to fit the user's arm perfectly. Once the measurements of the subject's arm were taken, design was modelled using Solidworks. The material selected to print the skin was ABS. Figure 4 below shows the customized arm design of the printed skin in Solidworks.

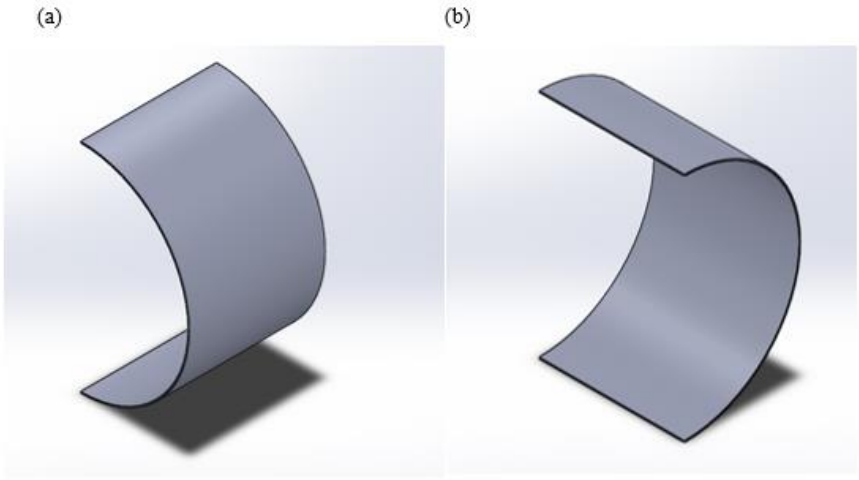


Figure 4. The arm design of the 3D printed skin

The measurements of the artificial skin had the height of 8cm and the width of 5cm, with the radius of curvature of 4cm. The thickness selected for the skin was 0.5 mm. This is selected as the thickness of the skin as the actual thickness of human skin is 3 mm and the aim was to ensure the printed skin was light enough to not be able to be felt by the user and flexible enough to fit the contours of the human body, without being too fragile to break. Figure 5 below shows the actual printed skin.

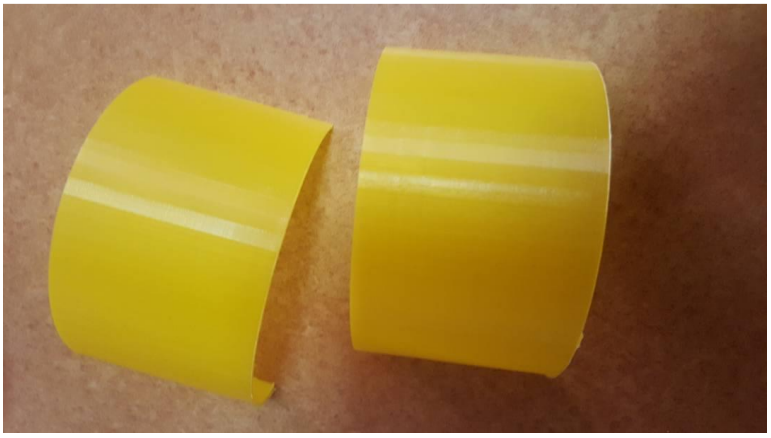


Figure 5. The 3D printed skin for the arm

The issue of safety always arises when creating something for human usage. This is why, special consideration was made when creating the skin. It was initially printed as a rectangular piece with sharp edges to ensure the dimensions taken from the test subject were correct. Once the printed piece was fitted to check if the skin fits the wound, the edges of the skin were filed to ensure that the sharp edges do not do further damage to the skin. Figure 6 shows the rounded edges of the skin.



Figure 6. The 3D printed skin for the arm with rounded edges

3.0 Results and Discussion

There are two experiments that were conducted. The first experiment tests which mixture is optimum for the gel synthesis. The second experiment tests the different concentrations of eggshells to see how the varying concentrations of eggshells affect the adhesive strength of the gel. A preliminary experiment was conducted to minimize the mixtures to be tested. The initial experiment tested the time taken for the mixture to dry on the human skin along with the duration it adhered to the human skin. The agar gel with the glycerol takes the shortest time on average to completely stick the paper on the human skin. Whilst plain agar had a lower time to dry completely, the adhesiveness of agar was weaker than that of the rest of the mixtures. This means that while doing routine work with the arm, the paper detached itself from the human skin. This means that the adhesive strength of plain agar is too weak to be able to allow the artificial skin onto the human skin if it cannot support a piece of paper to stay stuck to the human skin. Similarly, for the glycerol and the agar mixture, the mixture has very low adhesiveness. Since both the substances are water based, it has low stickiness and the paper slips very easily when some force is applied on it. Hence, for further experiments, the plain agar and the agar with glycerol mixture were not considered and only the other two mixtures were tested.

The reason for the agar and the glycerol mixture to dry faster compared to the neat agar is because both glycerol and agar are water based solutions, which has lower viscosity compared to the neat agar. The addition of glycerol to the neat agar makes it a more watery solution and hence has less adhesiveness and the ability to dry quicker.

3.1 Gel formation theory

The first experiment conducted was to compare the two different mixtures that are tested to synthesize the inner gel. The first experiment measures the time taken for the mixture to dry on the human skin and the duration for which it remains attached on the skin. The results showed when the two different mixtures are applied to the 3D printed surface and given time to allow them to continue adhering to the human skin. Figure 7 below represents the duration for which the printed skin remained adhered to the human skin.

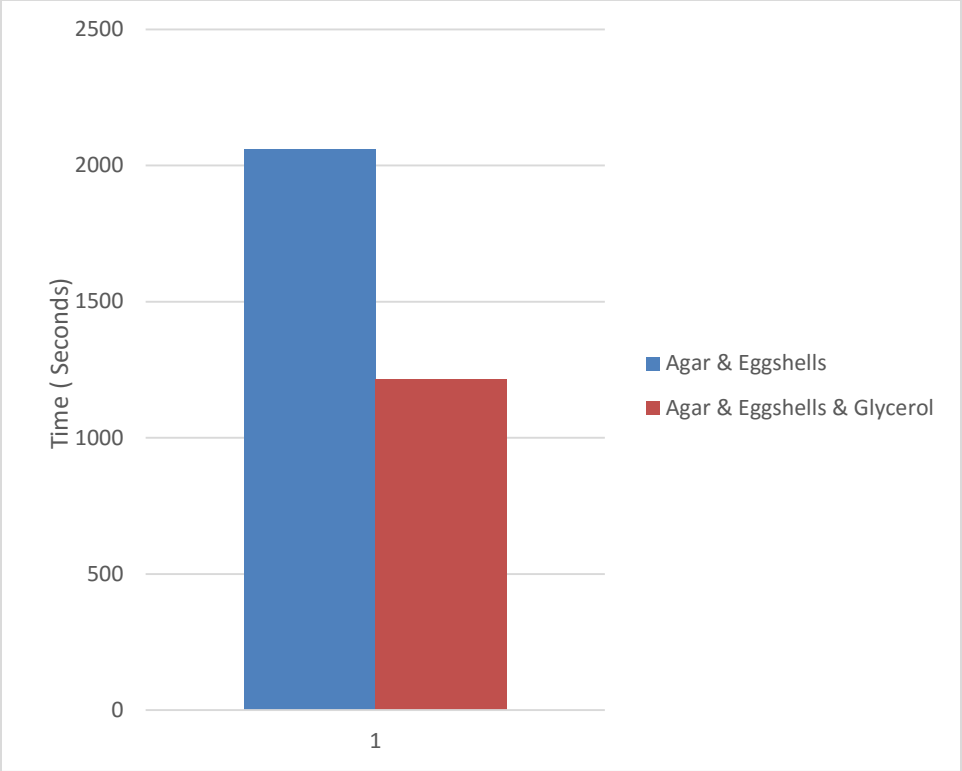


Figure 7. Graph representing Experiment 1

From the results obtained in the first experiment that the more effective solution to be used as the gel is the agar and the eggshells when compared to the agar, eggshells and the glycerol. The agar and eggshells solution takes a lesser time to dry and has the capabilities of remaining on the human skin for a significantly longer period of time. This results were obtained after conducting the experiment twice and taking the average reading for more accurate results. The experiment is also conducted at the same time period and in the same area so there are no environmental factors that affect the results of the experiment.

3.2 Gel Adhesion Testing based on different crushed eggshells composition

Another factor that can affect the duration for which the synthesized gel can remain on the human skin is the percentage of eggshells that are added into each mixture. Hence, the gels are tested again with different concentrations of eggshells to be able to see which concentration is optimum to be used for the gel synthesis. The results below shows that the experiment conducted when different concentrations of eggshells were used for both the separate mixtures. Figure 8 shows the graphical representation of the results obtained.

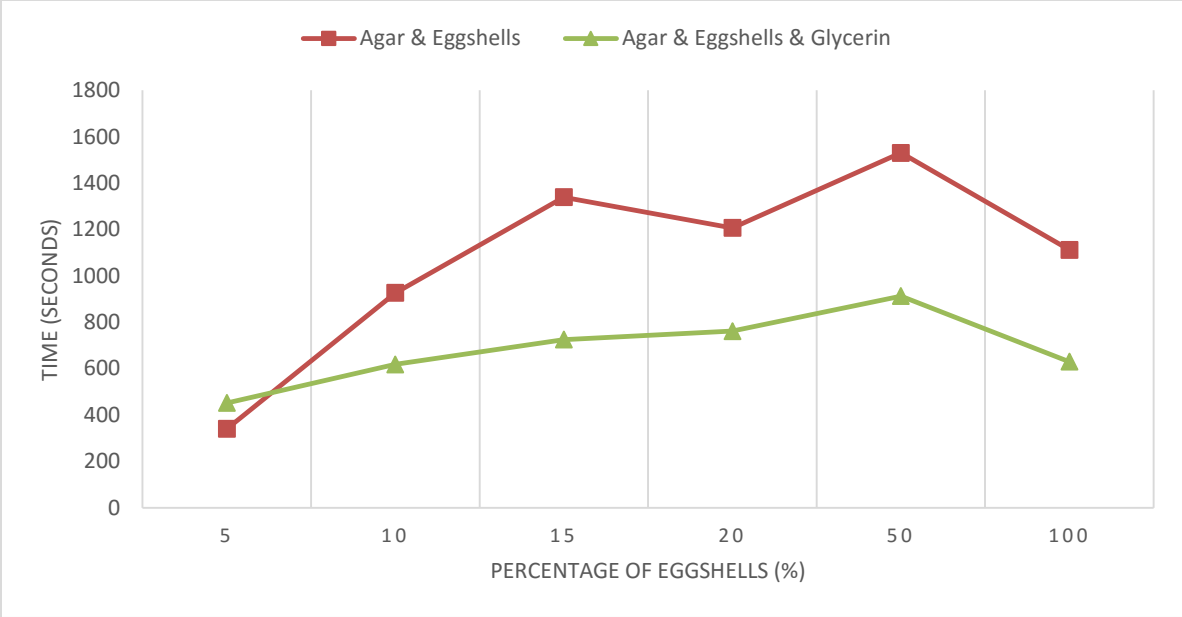


Figure 8. Graph representing Experiment 2

It can be concluded from the results obtained in the second experiment that the optimum concentration of eggshells that should be used for the gel is 50%. The agar with the 50% concentration of eggshells has the longest duration of time that the printed skin was stuck to the human skin. When compared between the two mixtures, the longest duration that the mixture with glycerol is 15 minutes, whereas the longest duration that the mixture without glycerol is about 1.6 times more than the mixture with glycerol at 25 minutes. Hence, it can be said that the mixture that should be used to synthesize the gel should be agar gel with 50% eggshells.

It can be observed that at 20% of eggshells concentration, there is an anomaly in the results. It can be seen that at the 20% concentration of crushed eggshells, the duration of it sticking to the human skin decreases. This is due to some inconsistencies in the experimental results. This is why it does not follow the trend of the overall graph.

At 100% of eggshells, the boiled agar solution is already saturated with the crushed eggshells and hence does not produce more efficient results in terms of the duration of time it is allowed to stick on the human skin. The trend of the graph is observed closely, hence it can be deduced that the optimal percentage of eggshells to be added to the boiled agar solution is 50% of eggshells, without the additional glycerol.

The results show that the better solution to use as the gel is the agar and crushed eggshell solution without the usage of glycerol. This is because the usage of glycerol causes slippage of the artificial skin. The addition of the glycerol makes the solution reduce in adhesive strength. The adhesive strength is measured on the basis of the duration the artificial skin can adhere to the human skin without any external applied force. For the purposes of this experiment, the adhesiveness is not tested based on the

amount of force each mixture can handle. This is why, the selected solution for spreading on the artificial skin is agar and 50% of crushed eggshells.

4.0 Conclusion

The optimum ratio of gel: crushed eggshells is 2:1. This ratio showed that the ability of the 3D printed outer layer to adhere to the human skin has been achieved. Using the optimum ratio, there was a short drying time along with it being able to adhere to the human skin for a long duration of time. Furthermore, the artificial skin showed no adhesive stains or marks after the skin was peeled off the human skin. This is beneficial for burn victims as there would be no additional disinfecting of the wound required once the artificial skin is removed.

The curvatures of the human body is also another consideration when designing the exact area for the 3D printed skin. It is important to consider the tolerances and the limitations of the 3D printer when the measurements are taken. Each printed skin has to be designed specifically for that user. The edges of the skin have designed to be rounded and not sharp so that it is safer for the user to use.

5.0 References

[1] M. W. Michell, H. M. Oliveira, M. P. Kinsky, S. U. Vaid, D. N. Herndon, and G. C. Kramer, "Enteral Resuscitation of Burn Shock Using World Health Organization Oral Rehydration Solution: A Potential Solution for Mass Casualty Care," *J. Burn Care Res.*, vol. 27, no. 6, pp. 819–825, 2006.

[2] M. Bezuhly and J. S. Fish, "Acute Burn Care," *Plast. Reconstr. Surg.*, vol. 130, no. 2, p. 349e–358e, 2012.

[3] D. Church, S. Elsayed, O. Reid, B. Winston, and R. Lindsay, "Burn wound infections," *Clinical Microbiology Reviews*, vol. 19, no. 2. pp. 403–434, 2006.

[4] Konya C, Sanada H, Sugama J, et al. Skin injuries caused by medical adhesive tape in older people and associated factors. J Clin Nurs 2010;19:1236-42.

[5] T. Lefrancois, "Foot and Ankle Surgery Evidence based review of literature on detriments to healing of diabetic foot ulcers," *Foot Ankle Surg.*, 2016.

[6] A. N. I. D. Gantry, K. Johnson, A. Dubey, C. Harris, and D. Sasaki, "CARO 2016 optimizing image accuracy through the development of CARO 2016," *Radiother. Oncol.*, vol. 120, pp. S33–S34, 2016.

[7] R. Ricotti *et al.*, "Physica Medica 3D-printed applicators for high dose rate brachytherapy : Dosimetric assessment at different infill percentage," *Phys. Medica*, vol. 32, no. 12, pp. 1698–1706, 2016.

[8] W.-K. Lee, Y.-Y. Lim, A. T.-C. Leow, P. Namasivayam, J. Ong Abdullah, and C.-L. Ho, "Biosynthesis of agar in red seaweeds: A review," *Carbohydr. Polym.*, vol. 164, pp. 23–30, 2017.

[9] S. Hsieh, H. H. Chou, C. W. Hsieh, D. C. Wub, C. H. Kuo, and F. H. Lin, "Hydrogen peroxide treatment of eggshell membrane to control porosity," *Food Chem.*, vol. 141, no. 3, pp. 2117–2121, 2013.

eureca 2017 – Conference Paper
Paper Number 2ME19

Lift and Drag of Non-conventional Wings at Subsonic Speeds and Zero Angle of Attack – an Experimental Investigation

Ting Chern Wei*, Abdulkareem Shafiq Mahdi Al-Obaidi

Department of Mechanical Engineering,
School of Engineering, Taylor's University, Malaysia.

* tingchernwei02@sd.taylors.edu.my

Abstract
Various non-conventional wing development shows potential in increasing the aerodynamic performance of airplanes but airline operators are not seriously considering this solution due to the high manufacturing and possibly high maintenance cost of non-conventional wing design. If the non-conventional wing only improves the aerodynamic performance by a small margin, conventional wing is still a better option for airline operators. This provide opportunity to continue research on non-conventional configurations that can greatly improves the fuel consumption. This research was conducted to examine the lift and drag of non-conventional wings at low subsonic speed and low angle of attack. Analytical method based on DATCOM was used to calculate the lift and drag coefficient of non-conventional cranked wing for comparison with experimental results obtained by using Taylor's wind tunnel (TWT). Experimental lift coefficient shows similar values with the analytical results but experimental drag coefficient had an average difference of 44%. The error was found to be caused by the test rig holding the vertical upright test wing model in the test section. The lift coefficient was not affected by the test rig due to the test rig's symmetrical shape. Further experiments was conducted to subtract the effect of drag caused by test rig and based on the comparison, it was found that TWT gave accurate drag coefficient results but less precise than lift coefficient which are both accurate and precise. The experimental setup was verify and further case studies on non-conventional wing model featuring trailing edge notches was carried out. Analysation on the results from case studies shows that generally the effect of varying the number of notches only had significant effect on drag reduction if the notch depth was higher. For flight condition that does not exceed 4° angle of attack, lower number of notches at higher notch depth had the best aerodynamic performance. On the other hand, for flight condition that requires cruise angle of attack that exceed 4°, higher number of notches at higher notch depth had the best aerodynamic performance.

Keywords: Lift coefficient, Drag coefficient, Non-conventional wings, Experimental, Wind tunnel.

1. Introduction

Airline operators are aware of the high demand for air travelling as the number of passengers increased exponentially over the past two decades. These numbers are expected to further increase in the future, providing two main challenges for airline operators. The first challenge is to lower down operating cost of airplanes in order to increase profit and secondly to uphold the company's corporate social responsibilities in putting effort to reduce air pollutions caused by combustion emission [1]. A viable solution is to improve aerodynamic performance of airplanes with the aim of reducing fuel consumptions which will decrease operating cost and also minimize negative environmental impact caused by emissions from airplanes. One key component in improving the aerodynamic performance of an airplane is to improve the design of wings because it is the main source of lift force. Referring to Fig. 1, when lift force, L is greater than the weight, W, the airplane will have more upward force and when drag force, D is lesser than thrust force, T, the airplane will have lesser resistance moving forward. This indicates that having a better lift to drag ratio can improve the aerodynamic performance because for the same amount of fuel consumption, the airplane can now travel for a longer distance. The potential of applying non-conventional wing design to improve aerodynamic performance of an airplane can be considered as an option for airline operators [1].

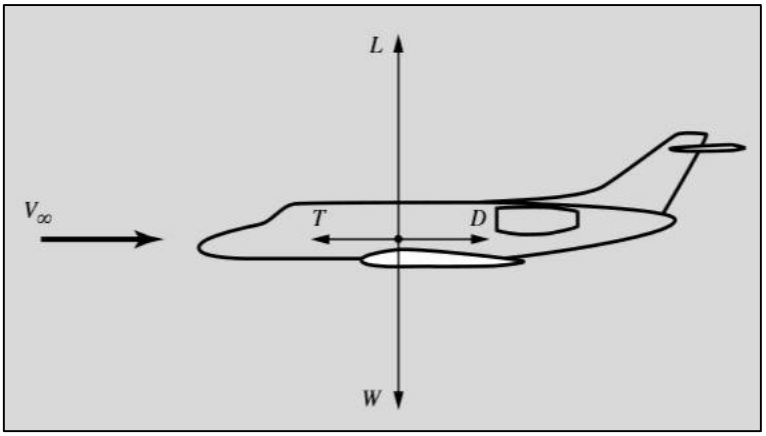


Figure 1. Forces Acting on an Airplane [2]

The development of new technologies in the field of non-conventional wings is also part of the NASA's subsonic fixed wing project that aims to improve aerodynamic performance of subsonic transport airplane in the future [3]. Currently, C-wing, blended wing body (BWB) and split wing are the more common non-conventional wing configurations under development. These non-conventional configurations have the same aim of improving aerodynamic performance by reducing fuel consumptions.

Kaushik and Anemaat [4] conducted research on the split wing which has a non-conventional configuration where the left and right wing of the airplane are not aligned. The purpose of this design is to remove the horizontal tail from the low tail which is a common feature on conventional airplanes. Conventional airplanes having horizontal tail experiences downwash from the wings onto the horizontal tail which requires high power control that will leads to additional drag force. If the flaps on the wings are deployed, even more drag force is produced. The removal of horizontal tail on the split wing decreases drag force which will lead to a better fuel consumption. However, in

terms of safety aspect, the split wing has asymmetric lift that will results in high tendency for the airplane to roll.

Reist and Zingg [5] studied the blended wing body (BWB) which has a non-conventional configuration of combining the airplane body and wings as one component. This configuration was proven to have high potential in improving aerodynamic performance on larger airplanes. The BWB was designed to have lesser wetted surface area that aims to reduce skin drag friction that contributes to total drag force. Reducing the skin drag friction improves the lift to drag ratio of the BWB. Additional advantages of the BWB is to have a lower operating noise due to the acoustic shielding provided by the aerodynamic design. However, Lyu and Martins [6] stated that the BWB configuration has a challenge in maintaining trim due to uneven pressure distribution over the body and wings. Furthermore, the BWB features thick airfoil shape that increases the difficulty in achieving good lift to drag ratio at a reasonable deck angle which is also a concern.

Skinner and Zare-Betash [7] conducted research on the non-conventional C-wing configuration that features a non-planer c-layout that provides high stability and control through the reduction of wing tip vortices. The decrease in wing tip vortices also improves lift to drag ratio through reducing vortex drag. The limitation of the C-wing is the challenge in manufacturing the uncommon wing architecture but this is more minor compared to the disadvantages of the split wing and BWB. Based on the advantages and disadvantages, C-wing is more suitable to be applied on commercial airplanes when compared to split wing and BWB.

The development of non-conventional wings have high potential in improving aerodynamic performance of airplanes but the manufacturing process of non-conventional designs are more complicated which increases the cost of manufacturing. Due to this reason, airline operators will only seriously consider applying non-conventional configuration if the aerodynamic performance can be greatly improved to cover the high manufacturing cost. This provide great opportunity to conduct research and develop new non-conventional configuration that is worth to be considered for application on commercial airplanes. One of nature's creation, the bird wing is good candidate to inspire a novel non-conventional design.

Different bird species have different wing shapes but are all considered as non-conventional configurations. Besides the compositions of the bird wing such as muscles, bones and feathers that are not considered from an aerodynamic point of view, the different wing shapes may have impacted and contributed positively to the aerodynamic performance of bird flight.

Dvorak [8] perform research on the aerodynamics of bird flight which consists of different functional studies from different parts of the wings. A bird wing can be mainly divided into two parts which are the primaries and secondaries. From the studies, lift force is mainly generated from the secondaries that resembles the airfoil shape for the bird. Primaries also contributes by forming tip slots that reduces wing tip vortex that produces induced drag. A bird varies the tail area located just behind the wing to maintain stability and balance. Overall, main studies on the lift can be perform on the secondaries section to act as a fixed wing for airplanes.

This research was conducted to compare the lift and drag of a non-conventional cranked wing by using analytical method from Data Compendium (DATCOM) and also experimental method using Taylor's wind tunnel (TWT). Further studies were performed to determine the lift and drag of non-conventional wings with the effects of notches on the trailing edge. The non-conventional configuration of having notches shape was inspired from the secondaries section of a bird wing which is the main section to generate lift. Most articles available are researching on the application of the flapping mechanism of bird wing and there are limited studies on the effect of shape, especially notches on the trailing edge of bird wing. This provide opportunity to research on the aerodynamic characteristics, lift and drag of fixed wing with different numbers and different sizes of trailing edge notches. To determine the wing design with better lift to drag ratio, the non-conventional configuration featuring notches will be compared with conventional wing configuration through experimental investigation using TWT. The scope of this experimental investigation is at conditions of low subsonic speeds and low angle of attacks close to zero angle.

2. Research Methodology

This research examines the lift and drag using analytical method and mainly experimental method which is practicing a quantitative study approach. The research methodology includes analytical method for cranked wing, three dimension (3D) modelling of test model, low subsonic speed wind tunnel and case studies on trailing edge notches.

2.1 Analytical Methods

Hoak [9] published a document that consist of four volumes with the title of DATCOM. The DATCOM discussed about analytical prediction methods for static aerodynamic coefficients and dynamic derivatives. Analytical methods in DATCOM allows calculation of individual flying component and summed up for the total result of the whole flying body. This research applies DATCOM analytical method which is in fact a semi-empirical approach, to calculate lift and drag of cranked wing at subsonic speeds. Semi-empirical approach consists of calculated values summed up with values obtained from experimental graphs.

2.1.1 Calculation of Lift Force for Cranked Wing

Based on DATCOM method, the rate of change of lift coefficient with angle of attack for non-conventional cranked wing at subsonic speed can be determined by applying Eq. (1):

$$C_{L_\alpha} = (C_{L_\alpha})_{pred} \frac{(C_{L_\alpha})_{test}}{(C_{L_\alpha})_{pred}} \quad (1)$$

where $(C_{L_\alpha})_{pred}$ is the predicted lift-curve slope of the cranked wing and $\frac{(C_{L_\alpha})_{test}}{(C_{L_\alpha})_{pred}}$ is the empirical correlation factor of subsonic lift-curve slope for cranked wing. $\frac{(C_{L_\alpha})_{test}}{(C_{L_\alpha})_{pred}}$ can be obtained from Figure 4.1.3.2-52 of DATCOM which is presented as a function of aspect ratio and Mach number. $(C_{L_\alpha})_{pred}$ can be obtained from Figure 4.1.3.2-49 of DATCOM which is presented as a function of aspect ratio, surface-roughness height,

Mach number parameter and sweepback angles of mid-chord line of exposed wing ,where all parameters can be calculated using Eq. (2-4):

$$(\cos \Lambda_{c/2})_{eff} = \frac{1}{S_w}[\left(\cos \Lambda_{\frac{c}{2}}\right)_i S_i + \left(\cos \Lambda_{\frac{c}{2}}\right)_o S_o] \quad (2)$$

$$c_{l_{\alpha_M}} = \frac{c_{l_\alpha}}{\beta} \quad (3)$$

$$k = \frac{c_{l_{\alpha_M}}}{(2\pi/\beta)} \quad (4)$$

where $\Lambda_{c/2_{eff}}$ is the effective sweepback angle of mid-chord line of exposed wing. $\Lambda_{c/2_i}$ is the sweepback angles of mid-chord line of wing inboard panels. $\Lambda_{c/2_o}$ is the sweepback angles of mid-chord line of wing outboard panels. $S_w$is the wing area , S_i is the total area of inboard panels of wing and $S_o$is the total area of outboard panels of wing. $c_{l_{\alpha_M}}$ is the lift-curve slope corrected for compressibility effects. $c_{l_\alpha}$is the section lift-curve slope with angle of attack at constant flap deflection. β is the Mach number parameter and k is the surface-roughness height.

2.1.2 Calculation of Drag Force for Cranked Wing

For the case of drag force, the total drag can be divided into C_{D_0}, zero-lift drag and C_{D_L}, drag due to lift which can be express as Eq. (5):

$$C_D = C_{D_0} + C_{D_L} \quad (5)$$

Zero-lift drag consist of friction drag and form drag which are mainly affected by surface roughness, wetted area and also airfoil shape. Zero-lift drag of non-conventional cranked wing at subsonic speed can be calculated using Eq. (6):

$$C_{D_0} = C_f[1 + L\left(\frac{t}{c}\right) + 100\left(\frac{t}{c}\right)^4]R_{L.S.}\frac{S_{wet}}{S_{ref}} \quad (6)$$

where $C_f$is the turbulent flat-plate skin friction coefficient that can be obtained from Figure 4.1.5.1-26 of DATCOM which is presented as a function of Mach number and Reynolds number based on the reference length. L is the airfoil thickness location parameter and is equal to 1.2 for $(\frac{t}{c})_{max}$ located at $x_t \geq 0.30c$. $\frac{t}{c}$ is the average streamwise thickness ratio of the wing. $R_{L.S.}$ is the lifting-surface correction factor obtained from Figure 4.1.5.1-28b of DATCOM which is presented as a function of the Mach number and the cosine of the sweep angle of the airfoil maximum thickness line, $(\Lambda_{t/2})_{max}$. $S_{wet}$is the wetted area of the wing and S_{ref} is the reference area which is equal to the S_{wet}. Since the cranked wing features inboard and outboard panels, C_{D_0} for both panels has to be calculated and summed up for total zero-lift drag.

To calculate drag due to lift of non-conventional cranked wing at subsonic speed, apply Eq. (7):

$$C_{D_L} = \frac{C_L^2}{\pi Ae} + \Delta C_{D_L} = \frac{C_{D_L}}{C_L^2} C_L^2 + \Delta C_{D_L} \quad (7)$$

where C_L is the wing lift coefficient, A is the aspect ratio, e is the span-efficiency factor over the parabolic-drag region and ΔC_{D_L} is the portion of the drag due to lift resulting from a breakdown in the leading-edge suction at lift coefficients above the parabolic-drag-polar region. An empirical correlation of ΔC_{D_L} as a function of lift coefficient and aspect ratio is avalaible in Figure 4.1.5.2-54 of DATCOM. Additional equation required is express as Eq. (8-10):

$$\frac{C_{D_L}}{C_L^2} = \frac{1}{\pi Ae} \quad (8)$$

$$e = \frac{C_{L_\alpha}/A}{R'(C_{L_\alpha}/A)+(1-R')\pi} \quad (9)$$

$$R' = R_i \left(n_B - \frac{d}{b}\right) + R_o \, (1 - n_B) \quad (10)$$

where R_i is inboard panel leading-edge-suction parameters, R_o is outboard panel leading-edge-suction parameters. R_i and R_o can be obtained from Figure 4.1.5.2-53 of DATCOM which is presented as a function of the Reynolds number based on the leading edge angle, Mach number and leading edge radius which is given as 0.00229 of mean chord length. n_B is the dimensionless distance from plane of symmetry to break span station, $\frac{d}{b}$ is the ratio of maximum body width to wing span and e is the span-efficiency factor over the parabolic-drag region.

2.2 Test Model

To compare the experimental results of lift and drag with the calculated lift and drag using DATCOM analytical method, an identical wing model has to be 3D modelled and manufactured. The wing model is having a non-conventional cranked wing configuration and using the NACA 0012 airfoil.

2.2.1 3D Modelling

The cranked wing was modelled using 3D computer aided design (CAD) software of SolidWorks 2016 version. The method used for 3D model was to import x and y coordinates of the NACA 0012, available at [10] and generate the airfoil shape using the imported coordinates. These coordinates are in ratio to chord length. Lofted boss function is used to generate solid between each airfoil to form a cranked wing. Fig. 2 shows the top view of the cranked wing with dimensions that are same with the dimensions used for the analytical calculation.

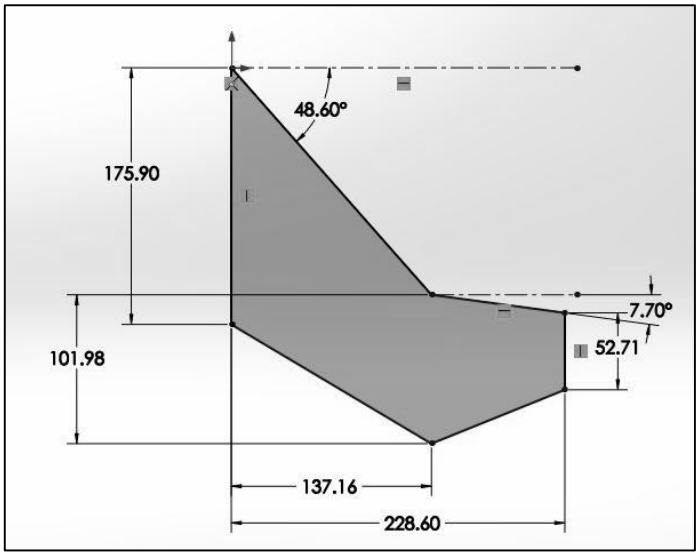


Figure 2. Dimensions of the cranked wing with units of mm shown in SolidWorks

2.2.2 Manufacturing

The cranked wing SolidWorks drawing was sent to 3D printer branded as Raise 3D for 3D printing using PolyLactic Acid (PLA) as the printing filament. The print density is set to 100%. Fig. 3 shows the 3D printed cranked wing with NACA 0012 airfoil as the test model.

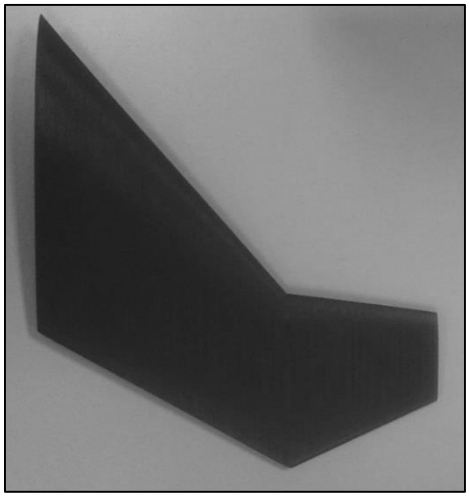


Figure 3. 3D printed cranked wing

2.3 Low Subsonic Speed Wind Tunnel

The experiments of this research was conducted using a wind tunnel located at Taylor's University, named as Taylor's Wind Tunnel (TWT). Fig. 4 shows the TWT that consists of different sections which are the settling camber, contraction section, test section, diffuser and fan. The TWT is an open circuit subsonic wind tunnel model of TDA_M630/12AA/7/28 with a contraction ratio of 3:4:1 [11]. Open circuit wind tunnel, requires air following through an essentially straight path from the entrance to the exhaust section after the fan [12]. The test section of the TWT is rectangular in shape and consists of a square cross section of 0.303 m x 0.303 m with a length of 0.885 m.

The TWT is able to collect force and moment readings through a Gamma DAQ F/T transducer. Readings obtained will be displaced using a PC1 DAQ card model of NI PCI-6220 installed in the computer. The 0.63 m diameter fan is powered by a 3 horsepower motor with an output torque of 4145 V / 50 Hz [11].

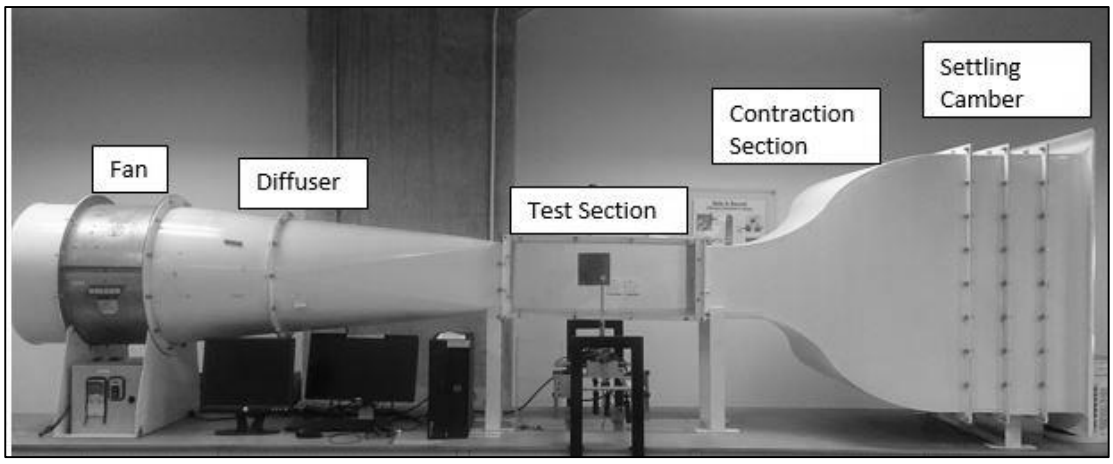


Figure 4. Taylor's Wind Tunnel

2.3.1 Experimental Setup and Conditions

The cranked wing model was mounted on a test rig and placed in the test section as shown in Fig. 5. The location of test rig was mounted 0.1266 m measured from the leading edge of root chord, which is the aerodynamic centre of the test model. Aerodynamic centre of non-conventional cranked wing can be calculated by using methods presented by Alexander [13].

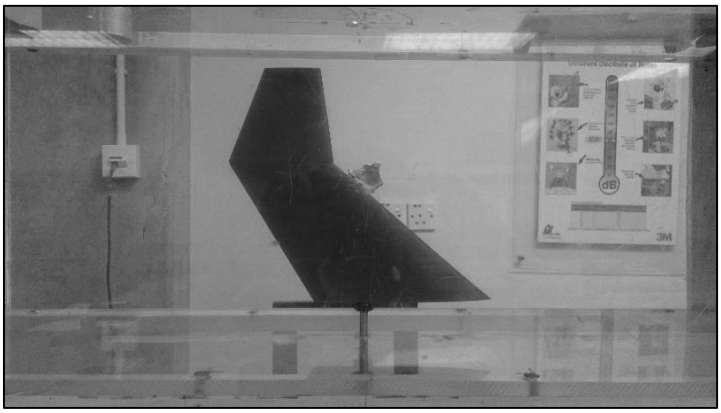


Figure 5. Test model setup in test section

The experimental was conducted at Reynolds number, Re = 1 x 10^5. To achieve this Reynolds number, the velocity of air flow was calculated to be 11.79 m/s. The variable that can be vary on the TWT was the frequency of the fan, and the linear equation between frequency and velocity is express as Eq. (11), which was derived from conducting experiment using hot wire and data logger.

$$f = 1.437\, v + 0.4359 \tag{11}$$

where f, is the frequency of the fan and v is the velocity of air.

2.3.2 Calculating Lift Coefficient and Drag Coefficient

The reading obtained from the TWT computers is lift and drag force instead of lift and drag coefficient which can be calculated using Eq. (12-13) [2]:

$$Lift\ force = \frac{C_L x\ \rho\ x\ v^2 x\ s}{2} \tag{12}$$

$$Drag\ force = \frac{C_D x\ \rho\ x\ v^2 x\ s}{2} \tag{13}$$

where C_L is the lift coefficient, C_D is the drag coefficient, ρ is the density of air, v is the velocity of air and s is the wing area. Lift and drag force was obtained by averaging 30 respective force readings from the raw data presented in TWT computer for different angle of attacks. Angle of attack of the test model is adjust based on a protractor located on top of the test section.

2.3.2 Effect of Test Rig on Drag Coefficient

One important factor that has to be taken in consideration is the effect of test rig. The test rig that was used to mount the test wing model will affect the readings taken from TWT. However the presence of the test rig only affects the drag force and will not affect the lift force due to the shape of the test rig. Since it is a cylindrical rod, it was assume to have symmetrical shape and no difference in angle of attack which will not produce lift force as the air flow passes the test rig. However, the test rig will induced drag by contributing to the friction drag and form drag. Because of that the drag force obtained from TWT is the combination of wing model and test rig while the lift force reading was not affected. To obtain the drag coefficient only for the test model, an equation as shown in Eq. (14) [14] was applied. The effect of test rig was consider in all experiments because it caused large difference in the drag coefficient.

$$C_{D_{model}} = C_{D_{total}} - C_{D_{rig}} \frac{S_{rig}}{S_{model}} \tag{14}$$

where $C_{D_{model}}$, is the drag coefficient of test wing model, $C_{D_{total}}$, is the total drag coefficient, $C_{D_{rig}}$, is drag coefficient of test rig, S_{rig}, is the area of test rig, and S_{model}, is the wing area of test model.

2.4 Case Studies on the Trailing Edge Notches

As mention in the introduction, a new non-conventional wing design can be development through inspiration from nature's creation, the bird wing. However, not all types of bird wings are suitable to be applied on airplanes because most bird species applied flapping flight which requires constant movement of wings and some bird species features wings that are unable to fly. In fact only wings from soaring bird species can have potential to be applied on airplanes. Soaring bird species have the ability to maintain flying without flapping its wing which also saves energy through the reduction of metabolic caused by flapping wing movement [15]. This situation is

similar to the fixed wing of airplanes. Besides having good aerodynamic characteristic of high aspect ratio, the shape of soaring bird wing may also contributes to the increase in lift to drag ratio.

This research aims to examine the lift and drag of wing model featuring trailing edge notches. Fig. 6 shows the notches from the secondaries of a golden eagle which consists of rounded edge. Notches on the primaries have shaper edge and have the ability to bend upwards to act as a wing tip which reduces size of vortices around the wing tip [16]. Experiment will be conducted only on the rounded edge notches because the main wing section that generates lift for the bird is the secondaries wing which have similar shape to airfoil. Experimental investigation was conducted by determining the lift and drag of a NACA 0012 wing with a chord length of 0.15 m and a span length of 0.15 m which gives an aspect ratio of 1. Keeping the aspect ratio and wing area as constant, add notches on the trailing edge for different case studies as shown in Table 1 to study the effects of trailing edge notches on the lift and drag force. Fig. 7 shows the top view and isometric view of the 3D test model for trailing edge notches.

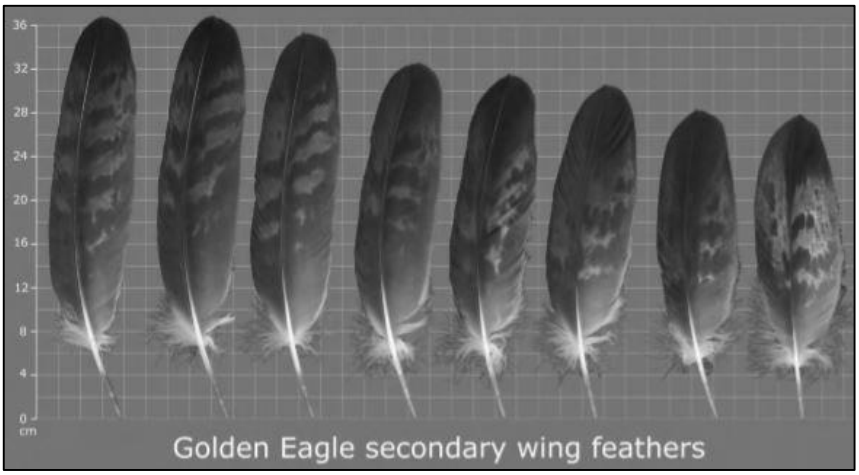


Figure 6. Rounded Edge Notches of a Golden Eagle [17]

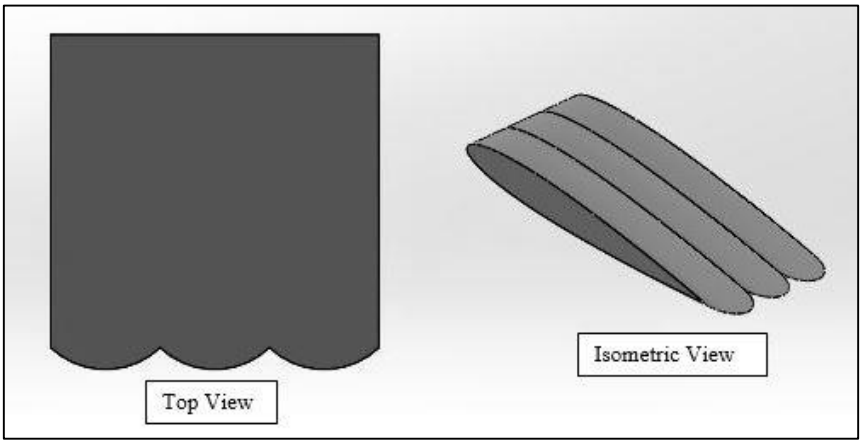


Figure 7. Top View and Isometric View of Test Model with Tailing Edge Notches in SolidWorks (Not According to Scale)

Table 1. Case Studies on Trailing Edge Notches

Experiments	Number of Notches	Depth of Notches	Wing Area	Aspect Ratio
Case 1	-	-	22500 mm	1
Case 2	3	10 mm	22500 mm	1
Case 3	5	10 mm	22500 mm	1
Case 4	3	15 mm	22500 mm	1
Case 5	5	15 mm	22500 mm	1

3.0 Results and Discussion

Results obtained according to the research methodology will be divided into analytical results and experimental results for more detail discussion. Table 2 shows the list of parameters and values used to perform calculation for both analytical and experimental methods.

Table 2. Parameters and Values Used for Calculation

Parameters	Values (Units)
Mach number, Ma	0.4
Mach number parameter, β	0.91652
Aspect ratio, A	4
Wing area, S_w	0.02612 m^2
Total area of inboard panels of wing, S_i	0.01906 m^2
Total area of outboard panels of wing, S_o	0.00707 m^2
Sweepback angles of mid-chord line of wing inboard panels, $\Lambda_{c/2_i}$	40.9°
Sweepback angles of mid-chord line of wing outboard panels, $\Lambda_{c/2_o}$	-7.7°
Section lift-curve slope with angle of attack at constant flap deflection, c_{l_α}	5.7869 per rad
Reynolds number, R_l	5.97 x 10^6 per m
Mean chord length of inboard panel, $\bar{C}_i$	0.14219 m
Mean chord length of outboard panel, $\bar{C}_o$	0.08001 m
Leading edge angles of wing inboard panels, Λ_{LE_i}	48.6°
Leading edge angles of wing outboard panels, Λ_{LE_o}	7.7°
Aspect ratio of outboard panels, A_o	2.37
Taper ratio of outboard panels, λ_o	0.517
Dimensionless distance from plane of symmetry to break span station, n_B	0.6
Ratio of maximum body width to wing span, $\frac{d}{b}$	0.139
Sweep angles of the airfoil maximum thickness line of wing inboard panels, $(\Lambda_{t/2})_{max,i}$	44.2°
Sweep angles of the airfoil maximum thickness line of wing outboard panels, $(\Lambda_{t/2})_{max,o}$	-2.01°
Wetted area of inboard panels of wing, $(S_{wet})_{max,i}$	0.03812 m^2
Wetted area of outboard panels of wing, $(S_{wet})_{max,o}$	0.01414 m^2
Average streamwise thickness ratio of the wing, t/c	0.12
Density of air, ρ	1.225 kg/m^3
Viscosity of air, μ	1.81 x 10^{-5}
Mean chord length, $\bar{C}$	0.12526 m
Airfoil	NACA 0012

3.1 Analytical Results

Analytical results of the lift coefficient, C_L and drag coefficient, C_D of non-conventional cranked wing was calculated using DATCOM method and the results were plotted into Fig. 8 – Fig. 10. Based on Fig. 8, the lift coefficient of the test model

is directly proportional to the angle of attack with a gradient of 0.0605. At zero angle of attack the lift coefficient is zero because the test model is using NACA 0012, which is a symmetrical airfoil. In the case of drag coefficient, an increase in the angle of attack regardless of positive or negative angle will still result in an increasing value which is shown in Fig. 9. However, unlike lift coefficient, drag coefficient is presence even at zero angle of attack. This is because total drag coefficient is the summation of C_{D_o}, zero-lift drag and C_{D_L}, drag due to lift. At zero angle of attack, even there is no drag due to lift, friction drag and form drag are still contributing to the zero-lift drag with the value of 0.011. For further analyzation, a polar curve as shown in Fig. 10 was plotted, to determine the maximum lift to drag ratio of the test model. The point of maximum lift to drag ratio is actually the tangent line to the C_L vs C_D curve from zero y-intercept. For the non-conventional cranked wing test model, the maximum lift to drag ratio was found to have a value of ten.

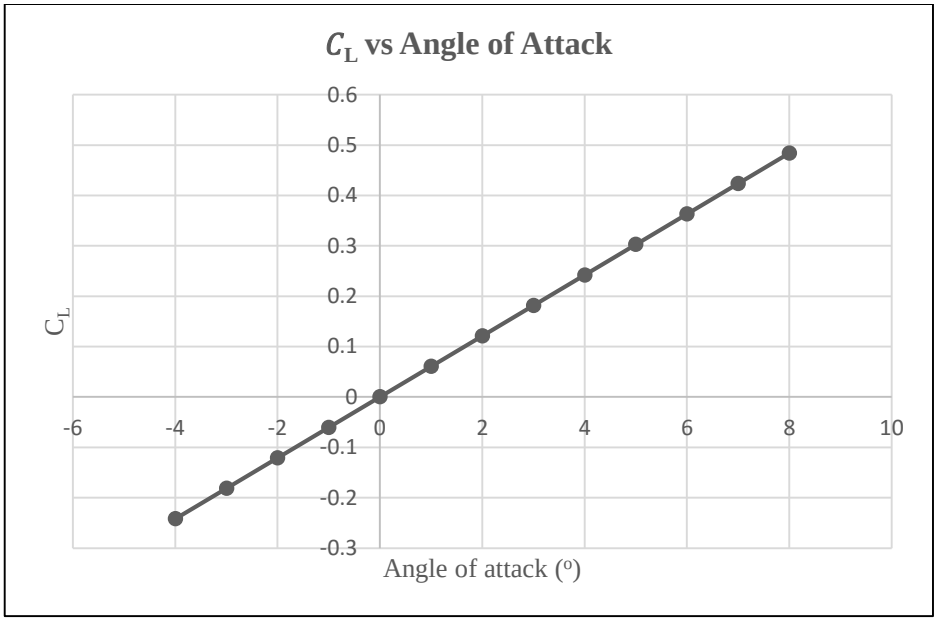


Figure 8. Graph of Lift Coefficient Against Angle of Attack

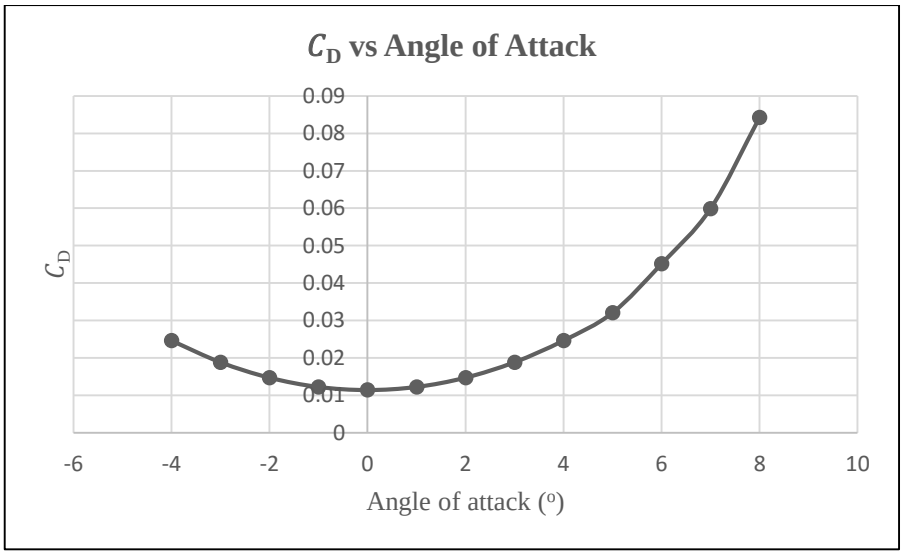


Figure 9. Graph of Drag Coefficient Against Angle of Attack

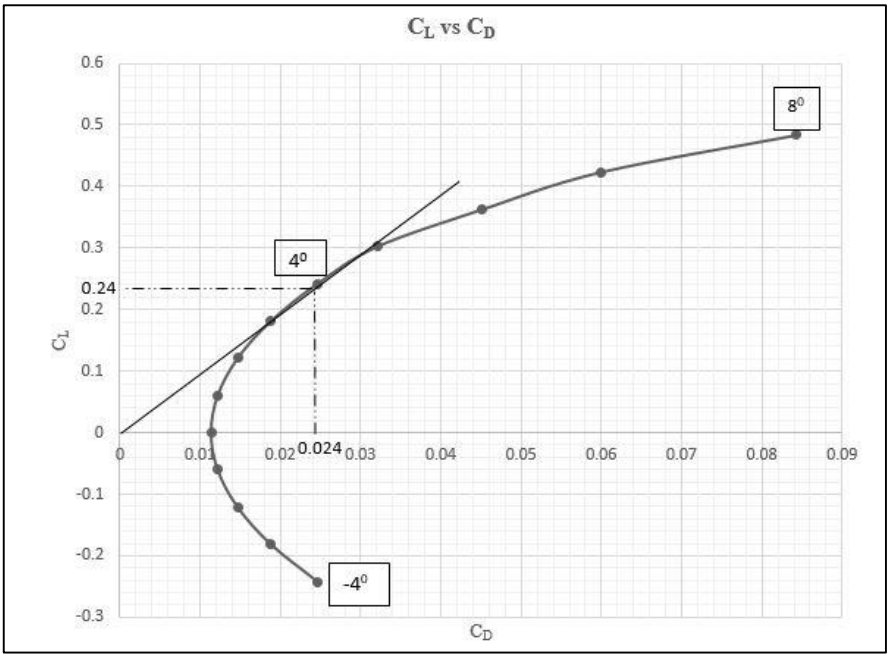


Figure 10. Polar Curve Graph of Lift Coefficient Against Drag Coefficient

3.2 Experimental Results

Experimental data was obtained by using Taylors' wind tunnel and the results were plotted into Fig. 11 and Fig. 12 for comparison with the analytical results to verify the experimental setup before conducting experimental investigation on the effect of trailing edge notches. Referring to Fig. 11, the experimental lift coefficient was approximate to be linearly increasing with angle of attack at a gradient of 0.0608 which is very near to the 0.0605 gradient value found using the analytical results. However, as shown in Fig. 12, experimental drag coefficient is not as accurate as experimental lift coefficient. Experimental drag coefficient has an average difference of 44% when compared to analytical drag coefficient. This error is caused by the drag induced by the test rig holding the test model. The presence of the test rig does not greatly affect the lift coefficient because of its symmetrical shape but it increases the friction drag and form drag that contributes to the total drag force. Because of that, the experimental drag coefficient curve is located higher than the analytical drag coefficient curve but still showing similar curve trend. An experiment was conducted to determine the drag force induced by the test rig and by applying Eq. (14), the drag coefficient for only the test model was calculated. Fig. 13 indicates that after subtracting the drag coefficient caused by test rig, the accuracy of experimental results had improved greatly. Based on the comparison, it is found that TWT gives accurate drag coefficient results but less precise than lift coefficient which are both accurate and precise.

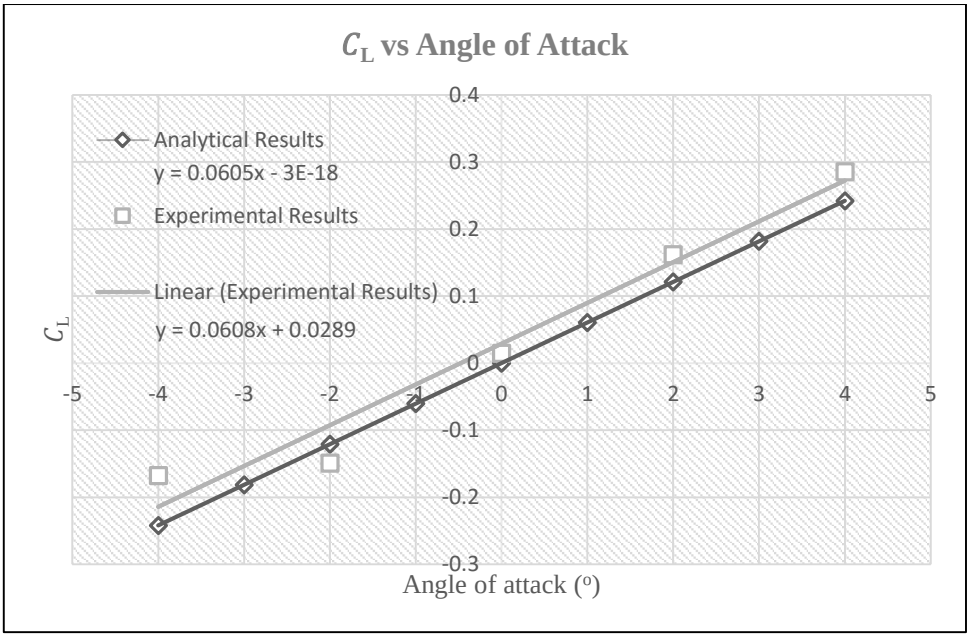


Figure 11. Graph of Lift Coefficient Against Angle of Attack

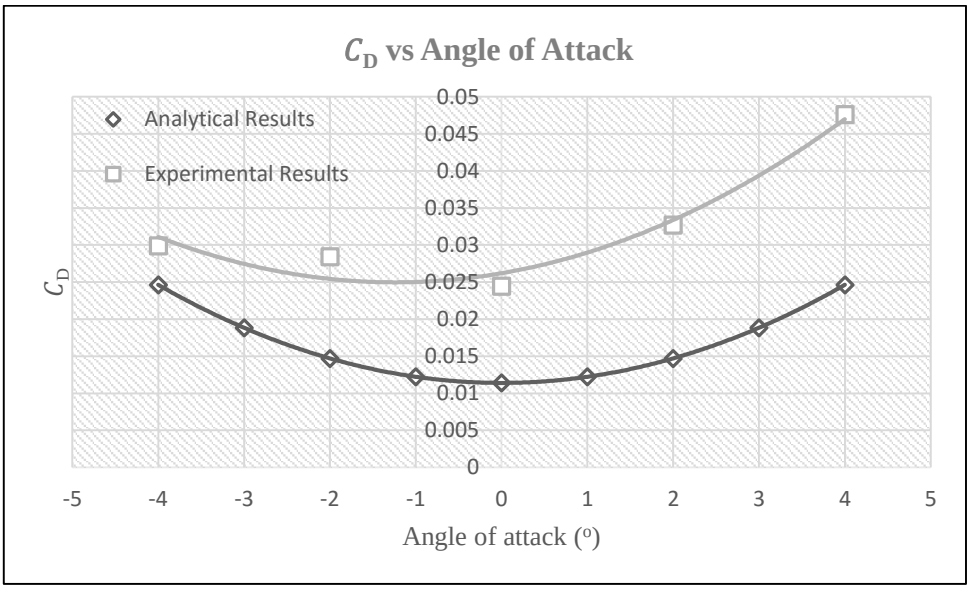


Figure 12. Graph of Drag Coefficient Against Angle of Attack

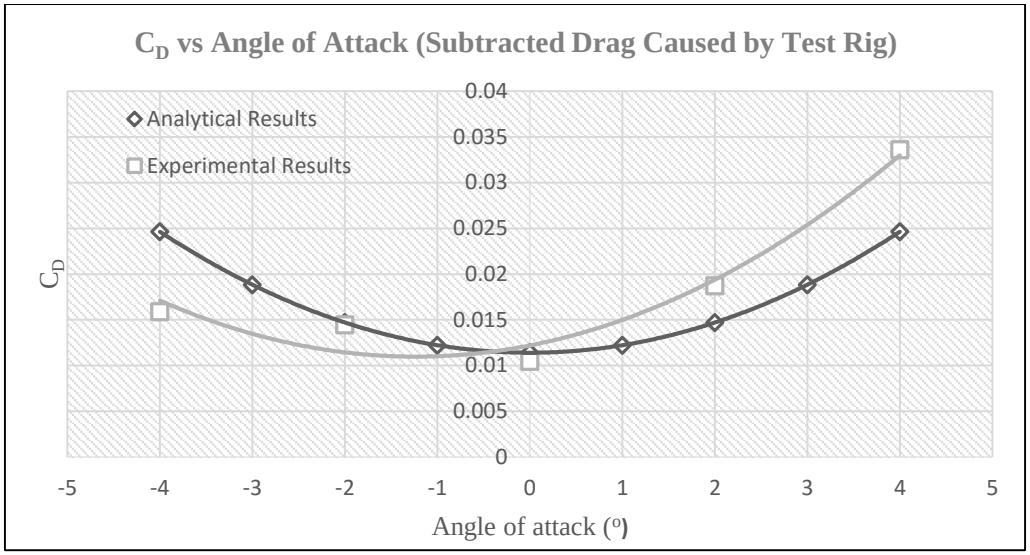


Figure. 13 Graph of Drag Coefficient (only wing model) Against Angle of Attack

The experimental setup was verified and further experiments was carried out to study the effects on lift and drag of non-conventional test wing models featuring trailing edge notches and comparing the results with conventional wing model with the same wing area and aspect ratio. Based on the experimental results, it was found that lift force was not greatly affected because all wing models are having the same wing area. However, applying notch shape on the trailing edge may have reduce the vortices at the wake area behind the trailing edge which may result in reduction of drag force. Further analysis from case studies shows that at notch depth of 10 mm, there was no significant reduction in terms of drag even by varying the number of notches from three notches to five notches. However the effect of drag reduction can be clearly seen when the notch depth was increases to 15 mm. With comparison to conventional wing model, non-conventional wing model featuring three notches with 15 mm notch depth was chosen as the best model for flight condition that does not exceed 4° angle of attack while non-conventional wing model featuring five notches with 15 mm notch depth was the better option for flight condition that will exceed 4° angle of attack.

4. Conclusions

To examine the lift and drag of non-conventional wings at low subsonic speed and low angle of attack, analytical and experimental approach was practiced. By using DATCOM analytical method, the lift and drag coefficient of a cranked wing was calculated and plotted in graphs as a function of angle of attack. When compared with experimental results, it was found that the lift and drag obtained from TWT are accurate, provided that the effect of the extra drag caused by the test rig is subtracted. The experimental setup was verify using the comparison results from cranked wing model before conducting further case studies on the non-conventional wing model featuring various trailing edge notches. By analysing the experimental results, it can be concluded that the effects of varying the number of notches only had significant effect on drag reduction if the notch depth is higher. For flight condition that does not exceed 4° angle of attack, lower number of notches at higher notch depth has the best aerodynamic performance, while higher number of notches at higher notch depth has better aerodynamic performance for flight condition that requires cruising angle of attack that exceed 4° angle.

List of Abbreviations

TWT	Taylor's Wind Tunnel
BWB	Blended Wing Body
DATCOM	Data Compendium
3D	Three Dimension
NACA	National Advisory Committee for Aeronautics

References

[1] Z. W. Teo, T. H. New, B. Nagel, and V. Gollnick, "An experimental and numerical study on a small-scale joined-wing aircraft," *AIAA SciTech Forum Expo.*, no. January, pp. 1–10, 2016.

[2] J. D. Anderson, *Fundamentals of Aerodynamics*, 5th ed. Boston: McGraw-Hill Education, 2010.

[3] B. K. Stanford, C. V. Jutte, and C. D. Wieseman, "Trim and Structural Optimization of Subsonic Transport Wings Using Nonconventional Aeroelastic Tailoring," *AIAA J.*, pp. 1–17, 2015.

[4] B. Kaushik and W. Anemaat, "Design methods for an unconventional split wing aircraft configuration," *28th Int. Congr. Aeronaut. Sci.*, pp. 1–13, 2012.

[5] T. Reist and D. W. Zingg, "Aerodynamically Optimal Regional Aircraft Concepts: Conventional and Blended-Wing-Body Designs," *52nd Aerosp. Sci. Meet.*, no. January, pp. 1–13, 2014.

[6] Z. Lyu and J. Martins, "Aerodynamic Design Optimization Studies of a Blended-Wing-Body Aircraft," *J. Aircr.*, pp. 1–14, 2014.

[7] S. Skinner and H. Zare-Betash, "Aerodynamic and Stability Optimisation of Non-Planar Wings," *Aerosp. Ecosyst.*, p. 1, 2015.

[8] R. Dvorak, "Aerodynamics of bird flight," *Exp. Fluid Mech. 15*, vol. 114, pp. 1–8, 2016.

[9] D. E. Hoak, "USAF Stability and Control DATCOM.," *Flight Control Div. Air Force Flight Dyn. Lab. Rept. 0410, Revis.* April 1972.

[10] I. H. Abbott and A. E. Von Doenhoff, *Theory of Wing Sections: Including a Summary of Airfoil data*, 2nd ed. New York: Dover Publication, 1959.

[11] S. Eftekhari, "Numerical and Experimental Investigation of a Cruising Fixed Wing MiniUnmanned Aerial Vehicles Performance Optimization," Taylor's University, 2017.

[12] A. P. Jewel B. Barlow, William H. Rae, *Low-Speed Wind Tunnel Testing*, 3rd ed. Wiley-Interscience, 1999.

[13] M. G. Alexander, "Subsonic Wind Tunnel Testing Handbook," no. May, pp. 1–291, 1991.

[14] H. Wibowo, "Improving the Accuracy of Taylor's Wind Tunnel Measurement," Taylor's University, 2017.

[15] J. M. Mallon, K. L. Bildstein, and T. E. Katzner, "In-flight turbulence benefits soaring birds," *Auk*, vol. 133, no. 1, pp. 1–8, 2016.

[16] M. A. Aldheeb, W. Asrar, E. Sulaeman, and A. A. Omar, "A review on aerodynamics of nonflapping bird wings," *J. Aerosp. Technol. Manag.*, vol. 8, no. 1, pp. 7–17, 2016.

[17] P. W. Trail, "Identification of Bald and Golden Eagle Feathers," vol. 1, no. 15, pp. 1–26, 2014.

eureca 2017 – conference paper
Paper number 2ME20

The Study of Seating Comfort in Passenger Vehicles

Umi Salmah Binti Seraj[1*], Mohd. Farid Aladdin[2], Douglas Tong Kum Tien[3]

[1,2,3] *School of Engineering, Taylor's University, Malaysia.*

[*]umi_salmah1994@yahoo.com

Abstract

In today's automotive market, comfort is huge selling point of a vehicle. Priority is given by buyers to how comfortable a seat feels during purchase decisions. The measure of comfort is harmonious mix of many aspects such as human ergonomics and physiological factors. However, a gap still exists between objective and subjective measures due to lack of emphasis by past researchers. This is particularly obvious in the lumbar support feature that has still not been able to address the health problems related to driving. This project focuses on bridging the gap by giving users the ability to define true preferred posture in realistic settings. This is done by the creation of a apparatus that allows users to individually manipulate the seat contour for optimum support in more segments than just lumbar area. The experiment is performed in 3 parts, where in each part different segments of the apparatus are manipulatable (lumbar segment, sacral & thoracic segment, and all segments). Sixty human subjects' statistics are recorded (gender, age, BMI and height) and the subjects are palpated to locate internal joints. These joints are marked and postural angles between them are measured using a goniometer. In each seat configuration, the angles are measured and a comfort rating is taken to be compared. It was found that the posture angles are different among the 3 experiments, and there is a change in comfort felt. Some human factors have also been proven to contribute heavily to angles chosen by occupants.

Keywords: Seating Comfort, Automotive Seating, Posture, Joint Angles, Subjective Comfort, Lumbar Support, Sacral Support, Thoracic Support

1. Introduction

The comfort facility of a seat is now as equally important as the functional and aesthetic aspects of automobiles for consumers to have an enjoyable ride [1]. The feeling of comfort has been collectively agreed on as [2]: a rise of a subjectively-defined personal character; exaggerated by physical, physiological, psychological characters; and a response to the environment. Normally the term comfort is more appropriately defined and studied as the absence of discomfort as it is easier to quantify discomfort than to measure comfort [2]. There is a large body of literature devoted to the study of automotive seating comfort, likely due to the economic costs associated with discomfort and injury in the motor-vehicle workplace. Studies have shown that low-back pain and serious conditions like spinal disc herniation worsen with increased driving hours [3], thus requiring ergonomic interventions in the early designing stages.

The two categories in ergonomic criteria assessment studies are the physiological and anthropometric factors [4] . Due in large part to Akerblom's work, anthropometric studies have long been considered a key aspect of comfortable seating, repeatedly verified by Parkinson and Reed [5], Ziolek et al., [6] and Seitz et al., [7]. Designers aim to ensure that a wide range of people can fit and utilize the seat, commonly adapting the constraining anthropometric values of 5th percentile female and 95th percentile male for corresponding seat dimensions. However, the identification of posture based on anthropometry is difficult because people with similar body dimensions have proven to assume completely different positions [8]. Basic demographic information (e.g. BMI, age, etc.) is usually included to understand its effects on and classify the varying assumed position.

Examples of physiological factors on the other hand are: objective measurement using pressure distribution [9,10], vibration analysis [11,12], surface electromyography [13,14] and temperature at seat (On the other hand, the subjective measurement methods often use a rating scale and a questionnaire that elicits a rating for each of the defined seat regions in the experiments. Most research involves the changing of a critical aspect of the seat to form various iterations around which the research can be conducted and subjective comfort relationships studied. Some previous experiments define the subjective regions based on the part of the body that are interfaced with the cushion (upper back, middle back, lower back, etc.) [2] while other researchers tend to identify regions on the surface area of the seat (e.g. seat back - upper/mid/lower).

However, ergonomics criteria related to physiology have also recently come under scrutiny. Reed et al. described the automobile seat designer's dilemma of prescribing a physiologically suitable seated posture while accommodating a driver's preference, reasoning that prescribed postures sometimes compromise actual comfort. An important finding by Reed et al. vitally highlighted the incompatibility between the common practice of designing seatbacks to induce a large degree of lumbar lordosis and satisfying occupant-selected spinal configurations (which are more kyphotic for some). Lordosis is associated with lower pressure in the lumbar intervertebral discs compared with more flexed (flat or kyphotic) lumbar spine postures, therefore regarded as more comfortable. Schneider verified this incompatibility in a follow-up study. Kolich et al. came to a similar conclusion.

Due to the varying preferences, comfortable accommodation in the lumbar region is thought to be best achieved through adjustability. However, evaluation of market products confirm that existing lumbar supports do not function as well as intended even with a wide range of adjustments. Yun Choi et al. found that even the recommended maximum prominence from past studies produced insignificant restoration of lordosis, while causing additional discomfort due to increased pressure concentrations and peaks at the lumbar area from firm padding. Warrow et al. described the conflict between the recommended heights of the support verses the large variability in occupant lumbar spine configuration, highlighting the placement issue of the support. More importantly, Eby discovered that the task of driving constrains postures to a great extent and prevent occupants from selecting lordotic postures that may cause them difficulty in vision and manoeuvrability, particularly those with extreme body proportions. This conclusion was reached by many other researchers.

The discrepancy in recommendations has proved to be difficult task for designers to interpret and integrate into current seats. A more recent discovery in seating is the appropriateness of sacral + thoracic support over lumbar support for seating comfort. Nairn, B.C found that sacral support will stabilize the pelvis in the proper neutral position, and lower thoracic support will apply an extension force that will result in elevation of the sternum and optimal curvature of the spine, restoring the proper axial/neutral relationship of the thorax and pelvis. This finding has been incorporated into many industrial products (e.g.: office chairs, massage equipment, wheelchairs, etc.) Latest seat configurations in luxury vehicle brands have also somewhat developed supports in these regions, although no standardization has been set due to lack of experimentation and data.

As stated by Hanson et al., it is not sustainable to rely on old recommendations when competing on a changing market. Therefore, it is necessary to study how much improvement the sacral and thoracic supports bring to the comfort of users in a passenger vehicle. With no current method to do so, an apparatus must be constructed to allow the study of different supports and the corresponding postures, and evaluate the differences in comfort rating felt by the passengers. Joint postural angles can be used to compare preferred postures as they are quantifiable and easily compared to one another, and verifiable with existing data where comfort feelings are not. It is also necessary to study the human factors that affect the chosen posture, which can be done by classification of the passengers' physical characteristics. Understanding this is important for future prediction, modelling and experimentation.

Therefore, the objectives of this study aligned to the theoretical framework and arising problems are: 1) To create an apparatus that allows drivers to define their own preferred posture in realistic settings. 2) To identify the potential differences between existing and preferred posture in terms of postural angles, as well as the resulting difference in comfort. 3) To evaluate the human factors that affect the outcoming preferred posture the most in terms of postural angles.

2. Methodology

2.1 Design of Support Apparatus

There are two important considerations for this artefact, which are:

a) adaptability to the adjustment preferences of a large variety of subjects; and
b) adherence to current seating contour constraints (lateral support).

The apparatus is only capable of forward extension (support prominence). By having separate adjustable segments at different fixed heights, the intended height of the prominence can also be somewhat varied. It has a maximum adjustment of 45 mm to accommodate any extreme postures. The anthropometric values used to ensure a wide fit was taken between the 5th and 95th percentile of Malaysian drivers. The sitting shoulder height for 95th percentile male (645.55 mm) is chosen to allow subjects in that range to make adjustments in the upper back area. The width should also be according to the 95th percentile male (480.00 mm), however due to current seats already having lateral supports, the flatback was set to be 280 mm which is the average width of the flat surface. The curvature was measured at 80 mm radius for most vehicles, which will be the minimum distance of the supports from the flatback to not be affected by them.

The apparatus has 3 main parts, which are the flatback, the jacks and the supports. To keep within the project's budget, most materials are obtained free or at a lower cost from associates. The jacks are made of aluminium links, steel left-hand/right-hand male threaded rods, steel left-hand (LH) and right-hand (RH) female nuts, steel left-hand and right-hand female hex coupling nuts and steel flat plates. The flatback is made of a wooden board, with fabric to cover the wood and avoid damage to car seats. The supports utilized armrest cushion for wheelchairs. An issue was the sizing, as the longest armrests available were 14 inches (355.6 mm) which is 125 mm shorter than the intended length. This might affect the comfort felt by larger occupants. The width of the armrest was 2.25 inches (57.15 mm), making the vertical distance between the centres of each cushion when stacked lengthwise also at least 57.15 mm. This value is close enough to the common 50mm height interval in many researches.

The tests performed to ensure the prototype met the following requirements were:

a) Constraint fitting – the product needs to fit to the seat constraints.
b) Comfort feel – the product should not cause unnecessary discomfort to the subject as it diminishes the purpose of the study.
c) Versatility – the product's adjustability should be able to conform to the preference of a variety of subjects.
d) Stability – the product need to be sturdy and stable under the weight of subjects.

The most challenging aspect during testing was stabilizing the prototype. The weight caused a resistance force on the prototype that halted its expansion capability because the links were not strong enough on their own to support the occupant. The expansion of the prototype was not uniform on both sides and a bending moment was being produced that made the jack deflect slightly downwards when expanded. Two alternatives were finalized to address these issues: scissor mechanism or support block. The support block solution was chosen as the solution as the alternative was too time-

consuming and its outcome unpredictable. The block idea involves including an expandable hollow block in the centre of the jack to direct most of the weight exerted on the cushion onto it. The strong opposing forces of the block will be able to balance out the weight of the occupant, and it's structure will ensure both sides expand/contract simultaneously. Deflection will also no longer occur as the block ensures only linear movement as according to its path. Figure 1 shows the completed prototype and apparatus



Figure 1: First successful prototype (left); completed apparatus tested in vehicle (right)

2.2 Postural Study

There are many ways to represent a vehicle occupant's posture including body landmarks, external body contours and segment linkage models. The chosen method is in terms of orientations (joint angles) of body segments. In the torso, the lumbar, thorax and cervical regions of the spine are each represented by a single segment instead of a singular torso segment to clearly represent the intra-subject posture changes corresponding to change in backrest supports as shown in Figure 2. Additional segments would provide better illustration, however since most studies have utilized these three-segment torso division, it would be easier to compare the data with verified value. Palpated surface landmarks shown in Figure 3 of the spinous process will be used to identify the joint locations that define the linkage.

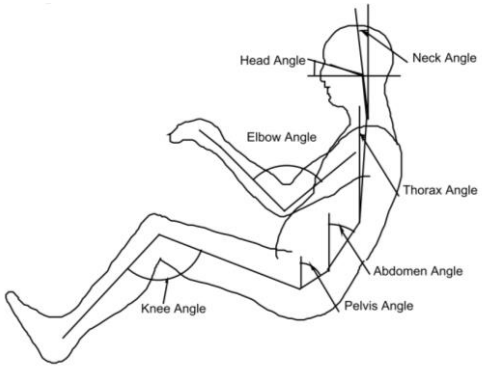


Figure 2: Segment joint angles [15]



Figure 3: Identification of palpation points

2.3 Landmark-to-Joint Transformations

The landmark-to-joint transformation methods used here are mostly based on the data analysis and summary presented by Reed, who referred his work from several sources, including a three-volume publication by Robbins. Robbins used external landmark data to estimate the internal joint locations of three categories of humans (large male, mid-sized male and small female) from experimentation and previous sources. The locations of joints relative to the surface landmarks are calculated using simple linear scaling relationships. Ultimately, the scaling approach for all subjects uses the midsize-male data as the reference geometry because the underlying data on which the landmark-to-joint transformations are based relied exclusively on male subjects, and because there are very minor differences between each category.

Table 1: Landmarks assigned to each joint estimation [15]

Joint	Landmarks
Upper Neck (atlanto-occipital)	Infraorbitale, Tragion
Lower Neck (C7/T1)	C7, Suprasternale
Upper Lumbar (T12/L1)	T8, T12, C7, Suprasternale
Lower Lumbar (L5/S1)	ASIS, PS, PSIS
Hip	ASIS, PS, PSIS
Shoulder	Acromion, C7, Suprasternale
Knee	Lateral Femoral Condyle (plus Hip Joint and Lateral Malleolus)
Elbow	Lateral Humeral Condyle (plus Shoulder Joint and Wrist land-mark)
Wrist	Wrist
Ankle	Lateral Malleolus (plus Lateral Femoral Condyle and Hip Joint)

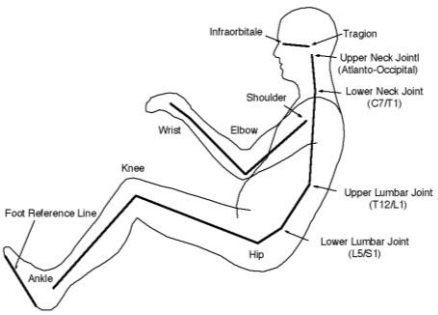


Figure 4: Internal joints [15]

Since the definition of drivers' seat positions are almost always made in relation to their hip locations, the determination of the pelvis geometry is one the main parts of this study. Due to the occurrence of laterally tilted pelvises, the hip joint locations are calculated in three dimensions, then averaged in the XZ plane to obtain a mean hip joint location. The hip joint and lower lumbar joint locations are calculated using the anterior-superior iliac spine (ASIS) landmarks (right and left), the pubic symphysis

(PS) landmark, and the posterior-superior iliac spine landmark (PSIS). Seidel [16] defined three pelvis dimensions to further increase accuracy of the location: pelvis width (PW) and pelvis height (PH) and pelvis depth (PD). Notably, Seidel also found no important differences between male and female pelvis in these scaling relationships.

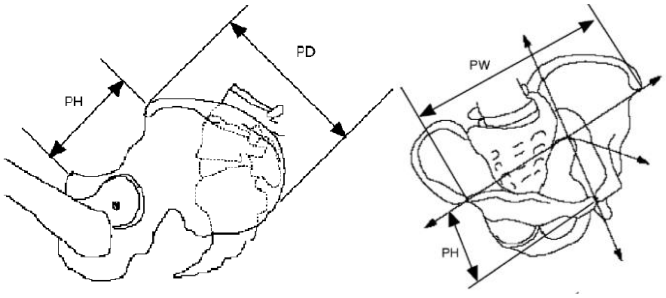


Figure 5: PW and PH dimensions (left) [15]; PW and PH dimensions (right) [15]

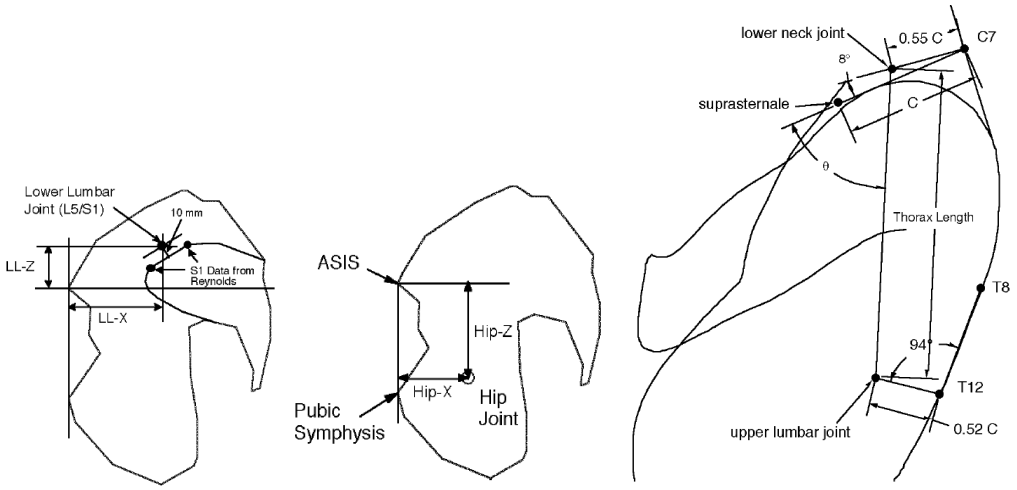


Figure 6: Lower lumbar joint scaling (left) [15]; hip joint scaling (middle) [15]; upper lumbar and lower neck joint scaling (right) [15]

2.4 Flesh Margin with BMI and Age Effects

Recent papers published corrected hip joint estimates based on adiposity of high-BMI-value subjects as well as old age [17], [18]. The adjusted calculations shown below were based on the fact that skeletal dimensions are mostly independent of body mass index (unless when referring to those with unusual muscle development, e.g: athletes and professional body builders) as well as the degeneration of bones with age.

The pelvic depth (PD) was adjusted by subtracting the effect of BMI shown in Equation 1. The adjusted depth was calculated as:

$$PDadj = PDmin + PDmeas - PDpred, \quad (1)$$

where PDmin would be the mean expected PD for the subject with the lowest BMI based on the regression given in Equation 2. PDpred is the PD predicted by Equation 2 for the subject accounting for BMI, and PDmeas is the measured PD for the subject.

$$PDpred = 65.6 + 4.38 * BMI, R2 = 0.43 \quad (2)$$

The bispinous (bi-ASIS) breadth (BB) was adjusted for BMI by subtracting the effect of BMI as shown in Equation 3. (BBpred) was subtracted from the measured bispinous breadth (BBmeas) and the result added to BBmin per Equation 4.

$$BBadj = BBmin + BBmeas - BBpred \quad (3)$$

$$BBpred = 165.3 + 2.64 * BMI, R2 = 0.23 \quad (4)$$

The PSIS flesh margin was set to a vector along the pelvic x-axis with a length of 0.0006*BMI^3 mm based on the adjustment in Reed's [17] study of the ASIS flesh margin. Due to the lack of study at the intimate region of the pubic symphysis, flesh margin at that area will be kept at the 25mm estimate.

The hip joint was also adjusted for age as shown by equation 5. LL is length leg measured in millimetres and the origin from which the equation is measured is the midpoint of the biponous (bi-ASIS or PW).

$$Hip - Z = -18 - 0.063LL - 5.403age \quad (5)$$

2.5 Experimental Set-up

The car chosen to be used as the test vehicle is a 2015 Nissan X-Trail due to long seat tracks and wide opening doors for all subjects to use the apparatus without constriction. 4 main factors used in experiments: Stature (Height), BMI, Age and Gender (Sex) as recommended from literature review. Sample size of 50 subjects were calculated with a 0.75 power and 0.12 error margin. The subjects are firstly given a survey to fill in.

The subjects are then categorized by the four factors of BMI, age, stature and gender. For stature, an online calculator is used to calculate the percentile of each occupant based on their height. Occupants below 25th percentile are considered short while those above 75th percentile are considered tall, and the remaining in between are average. For BMI, the occupants are classified according to the World Health Organization (WHO)'s descriptions of body mass index. However, the 'overweight' and 'obese' categories, the were merged due to the lack of participants falling in the obese category, with most of them being relatively close to the overweight limit. For age, occupants are divided to being above and below 50.

The study is carried out in a few stages. Firstly, the participants are palpated and marked according to the methods previously described. Then, the joint locations of the occupants are marked using the discussed transformations and apparatus like rulers, multi-angle rulers, Vernier callipers and spirit level gauges. Then the experiments are conducted. Participants are asked to assume their most comfortable posture with hands on the steering wheel and right leg on the accelerator (Figure 7). There are 3 parts of

the experiment. In the first one, occupants are only allowed to adjust the lumbar supports. Second part is adjustment of the thoracic and sacral supports. Third is adjustment of any and all supports. At the end of each adjustment, the joint angles are measured using a digitalized angle ruler for better accuracy (Figure 8), and the occupants fill in the comfort ratings. Finally, the last parts of the survey are filled in.

Ahead of conducting the experiment, the participants adjusted the seat recline, seat distance, seat height, steering wheel distance and height. The seat recline angle and seat and steering wheel height were fixed after this point. Seat distance and steering wheel distance was allowed to be varied because occupants may feel too constrained after increasing the prominence of the seat apparatus.

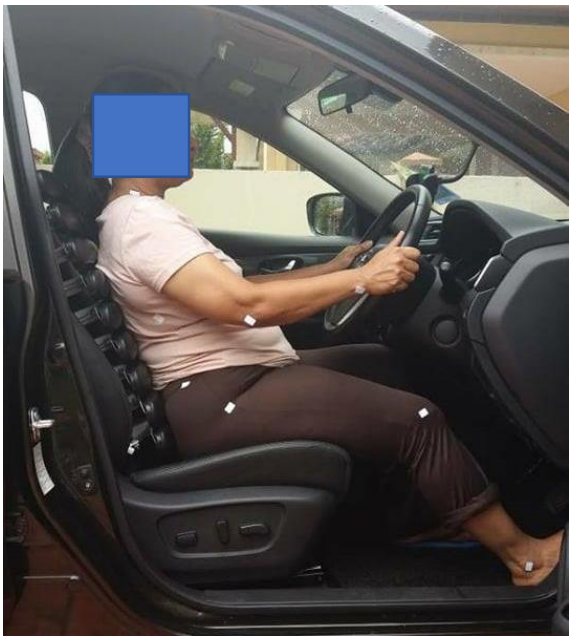


Figure 7: Subject during experiment

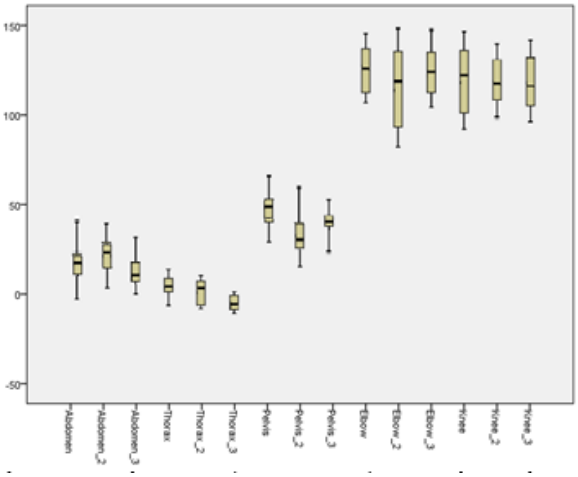


Figure 8: Meausring angle

2.6 Data analysis

Of the 50 participants, there were 28 females and 22 males. 12 were short, 22 were average and 16 were tall. 29 are below 50 and 21 are above 50. 10 were underweight, 23 were normal weight and 17 were overweight/obese. The data is analysed using IBM SPSS Statistics 22. A significance value (p-value) of 0.05 is used to test for significance, as according to the significance level used in most other literatures. Ahead of the tests, checks for normal distribution and equality of variance were performed to determine use of parametric or nonparametric test. There were no outliers and the data was normally distributed at each configuration, as assessed by boxplot in Figure 9. The Shapiro-Wilk's test in Table 2 is conducted. The null hypothesis is that there is equal variance across all measures. No significant values were found; therefore, it is concluded that all variances are equal.

Table 2: Test of Normality



Tests of Normality

	Shapiro-Wilk		
	Statistic	df	Sig.
Abdomen	.830	50	.320
Abdomen_2	.837	50	.108
Abdomen_3	.953	50	.421
Thorax	.961	50	.620
Thorax_2	.959	50	.554
Thorax_3	.955	50	.451
Pelvis	.924	50	.123
Pelvis_2	.949	50	.294
Pelvis_3	.929	50	.150
Elbow	.966	50	.660
Elbow_2	.922	50	.109
Elbow_3	.967	50	.684
Knee	.921	50	.102
Knee_2	.945	50	.302
Knee_3	.940	50	.243

*. This is a lower bound of the true significance.

Figure 9: Box plot

3. Results and Discussion

Angle values of this study are compared to 12 other studies conducted between this year and 1998 in Figures 10-14 below. Aside from previous studies, the measured values are also compared to predetermined range of motion values. The comparison is necessary to ensure the angles measured from this study are reasonable within human capability and preference, and sustainable in future researches. More importantly, comparison will ensure the method and apparatus used is somewhat accurate.

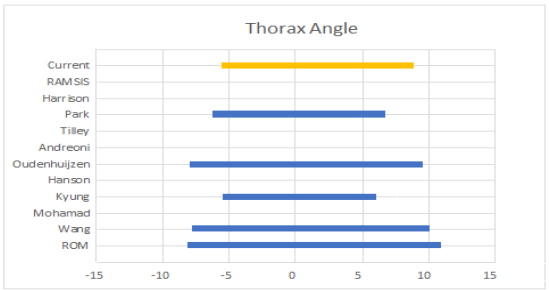


Figure 10: Thorax comparison

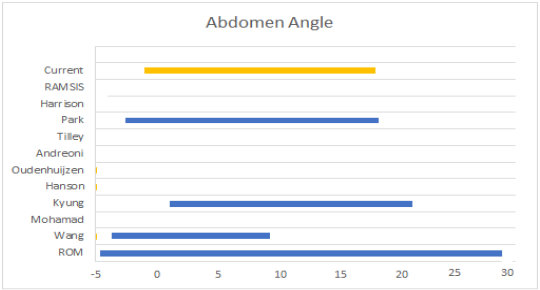


Figure 11: Abdomen comparison

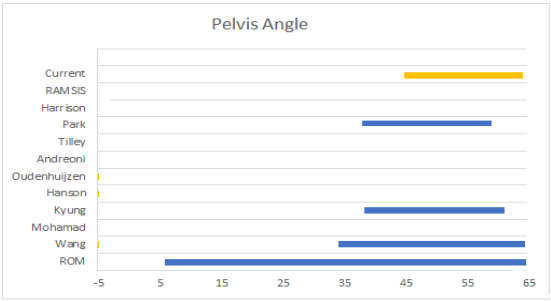


Figure 12: Pelvis comparison

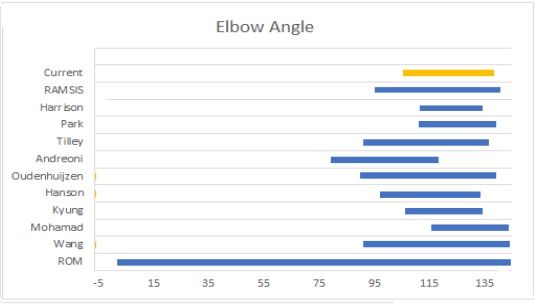


Figure 13: Elbow comparison

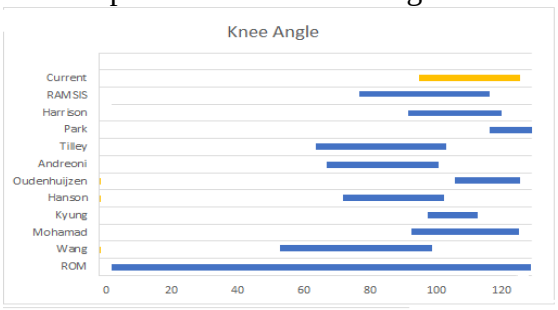


Figure 14: Knee comparison

Firstly, all angles are verified to be within acceptable ROM, so the apparatus was confirmed to be reliable. Moving on from that, the measured data was compared to previous studies, and some differences were noted. Due to the complexity of measuring posture and the interdependence of joint angles, the main problem in comparing different studies is that the results are influenced by the heterogeneity of experimental settings. Factors like data type (2D or 3D), number of participants, number of joints, recording time, symmetry, experimental method (field of laboratory), car type (sedan, SUV, etc.), study region, optimum vs. preferred, questionnaires, measurement method and reference point (H-point or Seat Reference Point).

One-Way Repeated Measures ANOVA was performed to test for difference in the 5 angles between each experiment. The null hypotheses of this ANOVA test states that there are no differences in the means of angles between the three seat configurations. The alternate hypotheses state that there are differences in the means of angles between the three seat configurations. The different seat configurations did not lead to any statistically significant changes in the elbow angle, F (2, 48) = 1.503, p = .235. or in the knee angle F (2, 48) = 1.218, p = .307. The null hypothesis is accepted for these two cases. This would mean that regardless of the seat configuration, participants did not alter their knee and elbow angles, possibly due to constricts from the task of driving. However, there were statistically significant differences in the thorax angle F (1.545, 39.353) = 5.138, p = .045, as well as in the abdomen angle F (1.505, 38.591) = 17.096, p = .000 and the pelvis angle F (1.693, 42.170) = 3.466, p = .042. For these cases, the null hypothesis is rejected and the alternate hypothesis is accepted.

To identify the human factors and its interactions' effects on each joint, Factorial ANOVA was carried out. actorial ANOVA is then carried out. It is important to understand how Factorial ANOVA works in SPSS. The analysis essentially tests for the variance between means. In this software, the analysis chooses one standard mean

and compares all the rest of the means to it. The default settings are to choose the combination of the highest numerical coded factors. Categories are coded as seen in Table 3:

Table 3: Coding for each category

Stature	3 - Average	2 - Short	1 - Tall
BMI	3 - Normal	2 - Underweight	1 - Overweight/Obese
Age		2 - Below 50	1 - Above 50
Gender		2 - Male	1 - Female

This is to set the standard as a normal BMI, male, below 50 with average stature. Every mean angle of all other categories in any combination is compared to this standard. The ANOVA analysis is then performed with the null hypothesis that the mean of all other combination of categories are equal to the mean of the standard. The parameter estimates in Table 4 tell us which specific category combinations are most influential on the angles. The intercept below is the standard mean angle of a normal BMI, male, below 50 with average stature

Table 4: Parameter estimates

Thorax

Parameter	B	Std. Error	Sig. level	Observed Power
Intercept	11.0	0.222	0.000	0.738
(BMI = 1)	+14.0	4.184	0.020	0.514
(Gender = 2) * (BMI = 1)	+16.0	3.254	0.018	0.582
(Age = 1) * (Gender = 1)	+9.0	0.360	0.031	0.640
(Age = 1) * (Stature = 2)	-10.0	0.252	0.028	0.715
(Stature = 1) * (BMI = 1)	+13.0	3.895	0.023	0.534
(Stature = 1) * (Gender = 1) * (Age =1)	-9.0	0.428	0.031	0.685

Abdomen

Parameter	B	Std. Error	Sig. level	Observed Power
Intercept	23.0	0.141	0.000	0.749
(Age = 1)	-19.0	0.190	0.038	0.725
(Gender = 2) * (BMI = 1)	-17.0	5.125	0.032	0.599
(Age = 1) * (Gender = 1)	-21.0	0.235	0.040	0.692
(Stature =1) * (BMI = 1)	-24.0	4.605	0.046	0.612
(Stature =1) * (Gender =1) * (Age = 1)	-25.0	0.360	0.008	0.677

Pelvis

Parameter	B	Std. Error	Sig. level	Observed Power

Intercept	41.0	0.192	0.000	0.741
(BMI = 1)	+12.0	6.420	0.028	0.489
(Gender = 2) * (BMI = 1)	+18.0	8.214	0.009	0.475
(Gender = 1) * (BMI = 1)	+9.0	6.104	0.031	0.501

Elbow

Parameter	B	Std. Error	Sig. level	Observed Power
Intercept	114.0	0.184	0.000	0.748
(Age = 1)	-11.0	0.345	0.022	0.692
(Stature = 1)	-9.0	0.241	0.034	0.710
(Stature = 2)	+16.0	0.219	0.018	0.721

Knee

Parameter	B	Std. Error	Sig. level	Observed Power
Intercept	129.0	0.202	0.000	0.742
(BMI = 1)	-23.0	0.451	0.013	0.652
(Gender = 1) * (BMI = 1)	+10.0	0.520	0.024	0.640

By studying the perimeter estimates, we can tell which interactions or main factors caused the biggest deviation from the standard mean. In the thorax angle, the interaction of male and high BMI caused the biggest change in angle, at an estimated mean of 26.0°. In the abdomen, the biggest effect was from a tall, older female making the angle -2.0° In the pelvis, it was the interaction of male with high BMI, causing a 59.0° angle. In the elbow, it was the from the short occupants causing a 130.0° angle. Finally, in the occupants with high BMI, causing an angle of 106.0°. There are larger errors in some of the mean angles, like the pelvis and abdomen, where the joints used are covered with a lot of fat and harder to palpation and predict.

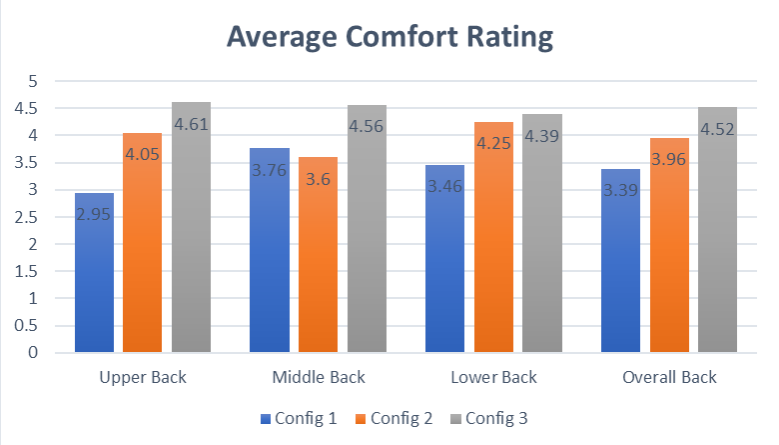


Figure 15: Graph of Comfort Ratings

The comfort rating survey divided the back into 3 segments: upper, middle and lower. Ratings were on a scale of 1 – 5, 1 being 'Uncomfortable' and 5 being 'Comfortable'. The overall back comfort is calculated as the average comfort of all three areas. From the graph in Figure 15, there was a definitely increase in all three segments and the overall back in the last experiment of the seat that had all supports utilized. In the first experiments, occupants felt very little comfort in the upper back and lower back, though the middle was relatively higher. This could be due to the lumbar support only allowing occupants to have support in that region and not in the upper and lower. It could be possible that occupants had to compromise one for the other. In the second experiments, with sacral and thoracic support, most occupants had better overall back comfort, though they were some who felt the middle part was now lacking. Finally, in the last experiments, all three segments were the highest with the highest overall back rating. It is clear that there is a definite different in the comfort felt by occupants in their true preferred posture compared to ones that they had less adjustability in.

4. Conclusion

All the objectives of the experiment were met. The apparatus was able to allow occupants to define their preferred posture in a realistic setting with accuracy. The incorporation of the apparatus was proven to cause changes in postural angles that positively affected the static comfort of occupants. It was also identified that human factors affect the joint angles in a variety of ways, and have different influences on different joints. A limitation that may have potentially influenced the accuracy of the results is the palpation and determination of joints that may not have been very accurate. For future work, a more advanced apparatus could be created using similar concept that will allow more adjustments (support tilt, height variation, etc.) and have lesser influence over the subject's comfort perception. The angles recorded in this study can be used to verify predicted posture from Digital Human Models in the future, as well as benchmark data for similar experimental set-ups. More objective measures like EMG, pressure mapping and vibration analysis can be done as extensions to further validate the efficiency of the sacral + thoracic support.

References

[1] B. Selangor, "Integration of Comfort into a Driver ' s Car Seat Design Using Image Analysis Darliana Mohamad , Baba Md Deros , Dzuraidah Abdul Wahab , Dian Darina Indah Daruis and Ahmad Rasdan Ismail Department of Mechanical and Materials Engineering , Faculty of Engin," vol. 7, no. 7, pp. 937–942, 2010.

[2] M. P. DE LOOZE, L. F. M. KUIJT-EVERS, and J. VAN DIEËN, "Sitting comfort and discomfort and the relationships with objective measures," *Ergonomics*, vol. 46, no. 10, pp. 985–997, 2003.

[3] M. P. Reed, L. W. Schneider, and L. L. Ricci, "Survey of Auto Seat Design Recommendations for Improved Comfort," no. April, pp. 1–96, 1994.

[4] B. M. Deros *et al.*, "ScienceDirect Incorporating Malaysian's Population Anthropometry Data in the Design of an Ergonomic Driver's Seat," *Procedia* -

Soc. Behav. Sci., vol. 195, no. 195, pp. 2753–2760, 2015.
[5] M. P. Reed, M. B. Parkinson, and D. B. Chaffin, "A New Approach to Modeling Driver Reach," *Sae Tech. Pap. Ser.*, no. 724, 2003.
[6] S. A. Ziolek, "Beyond Percentiles : An Examination of Occupant Anthropometry and Seat Design," *Hum. Factors*, no. 724, 2004.
[7] T. Seitz and H. Bubb, "SAE TECHNICAL Measuring of Human Anthropometry , Posture and Motion," no. 724, 1999.
[8] B. Deros *et al.*, "Advances in Natural and Applied Sciences Incorporating Anthropometrics Data in Designing Driver ' s Seat for Malaysian Made Compact Cars," vol. 8, no. June, pp. 915–919, 2014.
[9] M. D. Stinson, A. Porter-Armstrong, and P. Eakin, "Seat-interface pressure: A pilot study of the relationship to gender, body mass index, and seating position," *Arch. Phys. Med. Rehabil.*, vol. 84, no. 3 SUPPL. 1, pp. 405–409, 2003.
[10] G. Andreoni, G. C. Santambrogio, M. Rabuffetti, and A. Pedotti, "Method for the analysis of posture and interface pressure of car drivers," *Appl. Ergon.*, vol. 33, no. 6, pp. 511–522, 2002.
[11] M. J. Griffin, "Whole-Body Vibration," *Encycl. Vib.*, pp. 1570–1578, 2001.
[12] H. Nahvi, M. H. Fouladi, and M. J. Mohd Nor, "Evaluation of whole-body vibration and ride comfort in a passenger car," *Int. J. Acoust. Vib.*, vol. 14, no. 3, pp. 143–149, 2009.
[13] T. R. Bush, F. T. Mills, K. Thakurta, R. P. Hubbard, and J. Vorro, "The Use of Electromyography for Seat Assessment and Comfort Evaluation," *Soc. Automot. Eng.*, no. 412, pp. 143–1995, 1995.
[14] S. J. Park and B. Min, "Development of the Evaluating System for Ride Comfort and Fatigue in Vehicle," *SAE Tech. Pap.*, no. 724, 2013.
[15] M. P. Reed, M. A. Manary, and L. W. Schneider, "Methods for Measuring and Representing Automotive Occupant Posture," *Soc. Automot. Eng.*, no. 724, 1999.
[16] G. K. Seidel, D. M. Marchinda, M. Dijkers, and R. W. Soutas-Little, "Hip joint center location from palpable bony landmarks-A cadaver study," *J. Biomech.*, vol. 28, no. 8, pp. 995–998, 1995.
[17] M. P. Reed, S. M. Ebert-Hamilton, and J. D. Rupp, "Effects of Obesity on Seat Belt Fit," *Traffic Inj. Prev.*, vol. 13, no. 4, pp. 364–372, 2012.
[18] R. Hara, J. McGinley, C. Briggs, R. Baker, and M. Sangeux, "Predicting the location of the hip joint centres, impact of age group and sex," *Sci. Rep.*, vol. 6, no. 1, p. 37707, 2016.

eureca 2017 – Conference Paper
Paper Number 2ME21

Preparation and Characterization of Plastic Wood Composite Made Up of Durian Husk Fiber and Recycled Polystyrene Foam

Varnesh Subramaniam*[1], Koay Seong Chun[1], Pang Ming Meng[1], Albert Tsai[2]
[1]School of Engineering, Taylor's University, Malaysia
[2]Falculty of Engineering, The University of Nottingham, Malaysia

*varnesh-subramaniam@hotmail.com

Abstract
In search of a constant life of quality and luxury, the human kind has impacted the environment in a negative way with immense amount of side effects such as pollution. As well known, pollution is caused by improper and poor disposal of solid waste material. The polystyrene foam waste is one of the major waste hardly recycled. The objective of this research is to recycle the polystyrene foam as raw material to produce wood plastic composite (WPC). In present research, the WPC was made up of recycled polystyrene (rPS) and durian husk fiber (DHF) via melt blending technique using Haake Internal Mixer. Then, the WPC was formed using compression molding process. Besides, a processing aid called XP 516 was added to improve the properties of WPC. This final year project focuses on the effect of filler and processing aid content on tensile and thermal properties of rPS/DHF composite. The results obtained shows that tensile strength and modulus increase with fiber content while elongation at break decreases. With the added processing aid, all tensile strength, modulus and elongation at break decreases with increase of processing aid. This research also found that the WPC containing rPS, 60phr of DHF and 0.5phr of processing aid have strengths of about 18Mpa which is lower compared to commercial WPC. However, this WPC is still able to be made into any plastic application that does not require high strength.

Keywords: Recycled Polystyrene Foam, Durian Husk Fiber, Processing Aid, Wood Plastic Composites.

1. Introduction

With an ever increasing demand for wood around the world, researchers are constantly trying to come up with new ways to overcome this demand by providing an alternative solution. One of the solution which minimizes the negative effects of this demand on natural resources is by creating a composite made up of wood and plastic called wood-plastic composite (WPC). WPC is an alternative way to natural wood. In general, WPC is made from wood sawdust and plastic resin [1]. Now, the market demand for WPC is growing fast with an increase of 1046.1 kilo tonnes to an estimated 1728.9 kilo tones from the year 2014 to 2019 and making a compound growth rate of about 10.5% [2]. WPC is widely used in replacing natural wood in construction industry (e.g window fitting, door frame, and flooring panel) and other products (e.g furniture). Therefore in order to ensure its sustainability, WPC nowadays are made from natural fibers produced from agricultural waste and recycled plastic materials [3].

Natural fibers are fibers that are produced by plants animals and geological processes which exhibits plenty of benefits for instance, it is biodegradable, it is from a renewable source, low density and very low cost. Examples of natural fibers which can be used are empty palm oil fruits, corn husks, sugar cane bagasse and coconut shells [4-9]. Recently, there are many manufacturers focusing on producing WPC from agricultural waste besides wood fiber. For example, Seven Trust® company is a company producing WPC from various types of natural fibers, including coconut shell, rice husk, and rice straw [10].

Durian is a tropical plant found abundantly in countries like Thailand and Malaysia [11]. Every durian fruit has 30% to 40% of flesh which can be consumed while the rest of the fruit such as the husk (skin of the durian) are discarded. These parts make up for 60% to 70% content of the fruit, are discarded and usually end up in landfills or burnt which in turn, poses environmental issues. Back in 2013, 320 164 metric tonnes of durian were harvested in Malaysia alone. The major components of durian husk are lignin, cellulose and hemicellulose, and those components are similar to natural wood [12-14]. In this regards, the durian husk can be used as natural fiber to produce WPC.

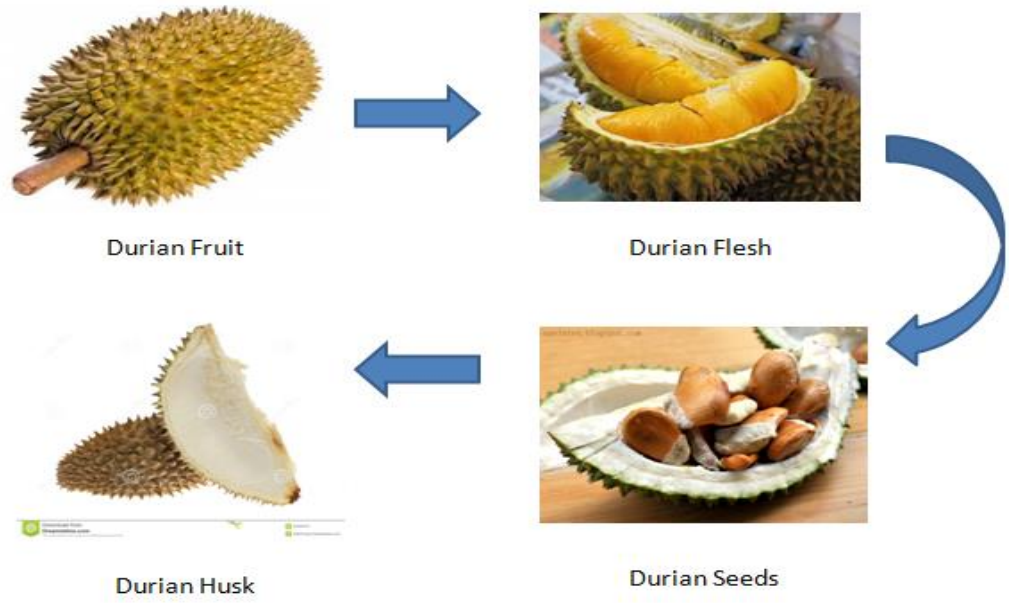


Figure 1: Parts of the durian fruit

Polystyrene foam, also known as Styrofoam®, is commonly used in many industries for packaging and storage purposes, food & beverage and electronic industries. The wide variety of application is due to the properties of polystyrene having good machinability, has good strength, transparency and stiffness [15-16]. Besides that, polystyrene foam is cheap in production cost, light weight, has high energy absorption properties and makes a good heat insulator [17-18]. Unfortunately, due to its high demand and production, it is reported that at least 1000 tons of polystyrene foam are being disposed into landfills and this causes environmental issues. Recycling rate for polystyrene is relatively low due to its size to weight ratio. Being made up of 98% of air, polystyrene takes up space with minimal weight and this causes difficulties in recycling due to high transportation costs [19-20]

This paper will focus on the effect of processing aid on tensile properties of WPC made from recycled polystyrene (rPS) and durian husk fiber (DHF).

2. Research Methodology

The aim of this research is to prepare plastic wood composite made up of recycled polystyrene and durian husk fiber. Some of the property tests which would be carried out on the DHF/rPS composites are mechanical properties test such as tensile test. Fig. 2 shows the flow chart of research methodology.

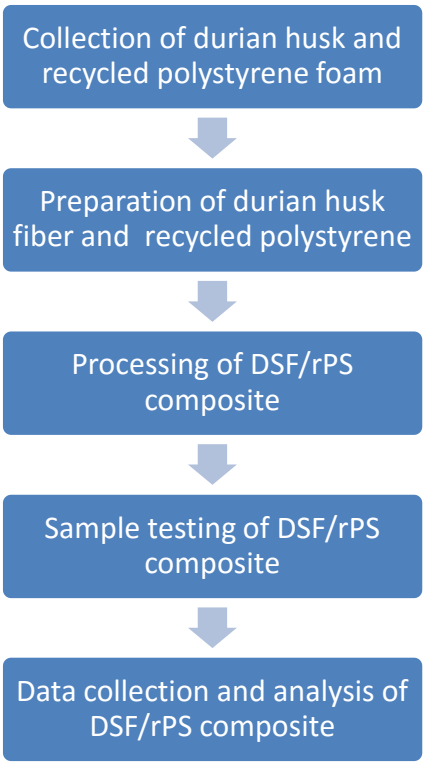


Figure 2: Flow chart of progress

2.1 Materials

The main components used in this experiment are durian husk fiber (DHF) and polystyrene (PS). Durian husk was obtained from a fruit stall and is usually a waste. The PS foam is a major waste material for electronic product shops and it was collected to be used as matrix. Processing aid ULTRA-PLAST 516 was supplied by Performance Additives Sdn Bhd.

2.1.1 Preparation of durian husk

To obtain the durian husk fiber (DHF), firstly durian husks were washed to remove any impurities or dirt and cut into small pieces. Next, the pieces of DH were further ground into short fiber using mechanical grinder. The collected DHF was dried at 60^{o}C using oven to remove moisture. Upon drying, a sieve (mesh size: 600 micron) was used to obtain homogenous size of DHF. The DHF would be dried again in an oven before melt blending process to avoid more moisture content.

2.1.2 Preparation of recycled polystyrene

The collected polystyrene foam was first dissolved in acetone solvent in order to remove air foam. Then, the dissolute polystyrene foam was filtered and dried using an oven at 60^{o}C to remove acetone. The polystyrene will be cut into smaller pieces and stored for melt blending process.

2.1.3 Preparation of composite

The rPS/DHF composite were prepared via melt blending process using a Haake internal mixer. The operation temperature was set at 190^{o}C and rotor speed of 80 rpm. The composite was blended according to the formulation listed in Table 1. The composite compound was molded into 1 mm thickness sheet using hot press. The molding temperature was similar to compounding process. The operating procedures are: i) preheat the compound for 4 minutes, ii) fully compress the compound for 1 minute, iii) cool the specimen to temperature below 50^{o}C, iv) remove the composite sheet from mold. The composite sheet was cut into tensile specimen and the dimensions of tensile specimen were following ASTM D638 standards.

Table 1: Formulation of composite.

	rPS (phr)	**DHF(phr)**	**ULTRA-PLAST 516 (phr)**
rPS/DHF composite without processing aid	100	0, 15, 30, 45, 60	-
rPS/DHF composite with processing aid	100	60	0.5, 1.0, 1.5, 2.0

2.2 Testing and Analysis

2.2.1 Tensile Test

The tensile testing for the rPS/DHF composite was carried out based on the ASTM D638 standards using an Instron universal testing machine with a model number of 5596. The crosshead speed was set at 15mm/min and a 15 kN loading cell was used to perform the test. Tensile modulus, tensile strength and elongation at break of the biocomposite were calculated on both the control and the composite with processing aid.

3. Result and Discussion

3.1 Without Processing Aid

3.1.1 Tensile Strength

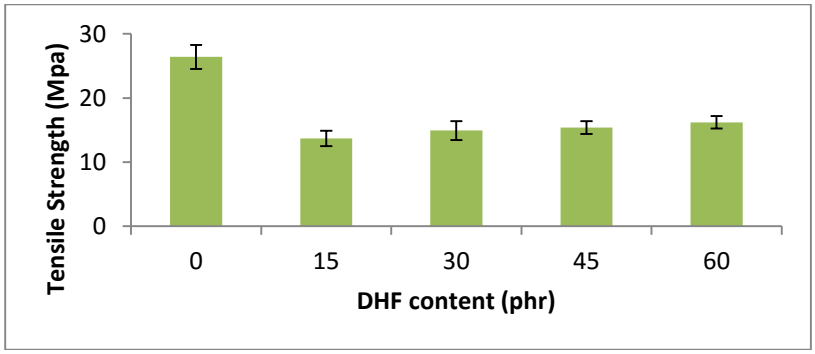


Figure 3: Graph of tensile strength with fiber content

Fig. 3 shows the chart for the tensile strength of different DHF contents. The tensile strength is highest when there is no DHF content present in the composite while an addition of 15 phr DHF yields the lowest tensile strength.

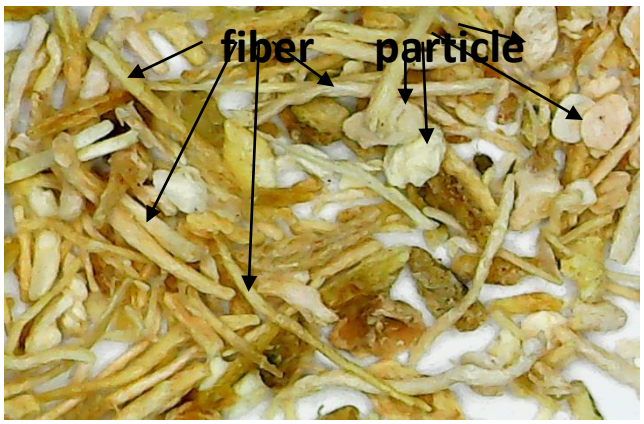


Figure 4: Micrograph of durian husk fiber

Fig. 4 displays the micrograph of durian husk fiber. The DHF mainly is in fiber form, but part of the durian husk is particulate. The presence of particulate DHF causes the decreasing of tensile strength in rPS matrix. Since, the particulate DHF will act as stress concentrator in rPS matrix, the composite will fracture at lower tensile strength compared to neat polymer. Moreover, short fiber usually does not contribute much on tensile strength of composite due to its random fiber orientation in composites, but this depends on the fiber content. In this case, the increase of DHF content possibly increased the number of fibers that parallels orientated to axial loading. Thus, the tensile strength of rPS/DHF composites increased at higher fiber content.

3.1.2 Tensile Modulus

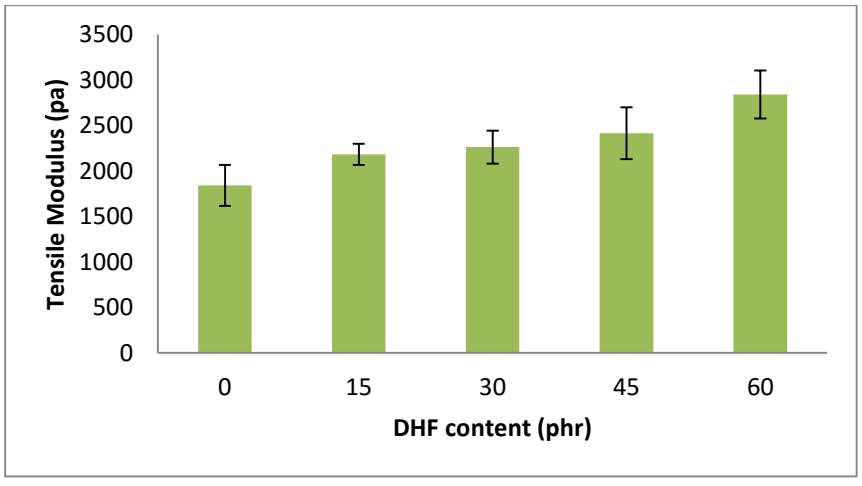


Figure 5: Graph of tensile modulus with fiber content

Fig. 5 shows the trend for the tensile modulus for different fiber content in the rPS/DHF composite. With zero dhf fiber added, it yields the lowest tensile modulus while the highest fiber content shows the highest tensile modulus. The reason why there is an increase of trend of tensile modulus with the addition of fiber is that natural fiber have

higher tensile modulus compared to plastic and with the addition of higher modulus component to plastic material it will cause an increase in tensile modulus (normal trend).

3.1.3 Elongation at Break

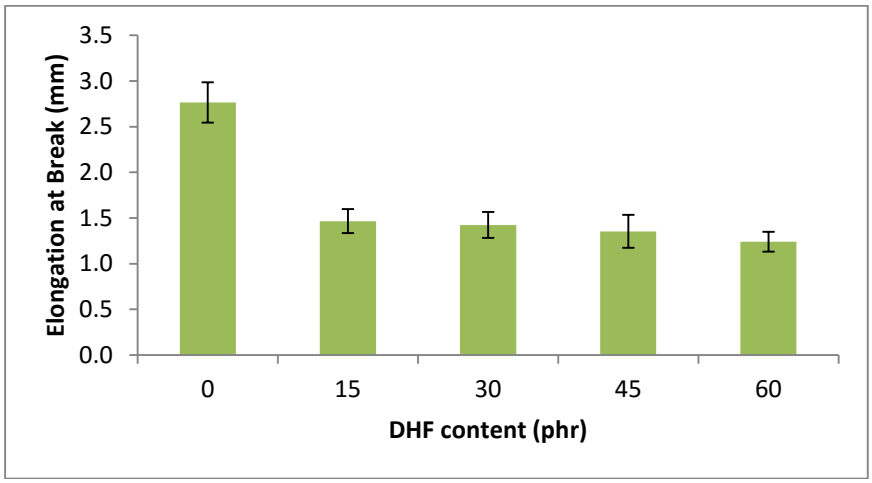


Figure 6: Graph of elongation at break with fiber content

Fig. 6 shows the graph of elongation at break with different fiber content. Elongation is highest with neat PS while lowest with 60 phr of DHF. The trend shows that with the increase of fiber content the elongation at break also reduces. The reason why there is a decrease in elongation at break is because the friction which occurs between fiber and matrix will cause the reduction of chain mobility of polymer. Usually polymer chain is flexible (since polymer chain can move while stressed) and it can elongate while subjected to stress. If chain mobility decreases, the elongation at break would also decrease.

3.2 With Processing Aid

3.2.1 Tensile Strength with Processing Aid

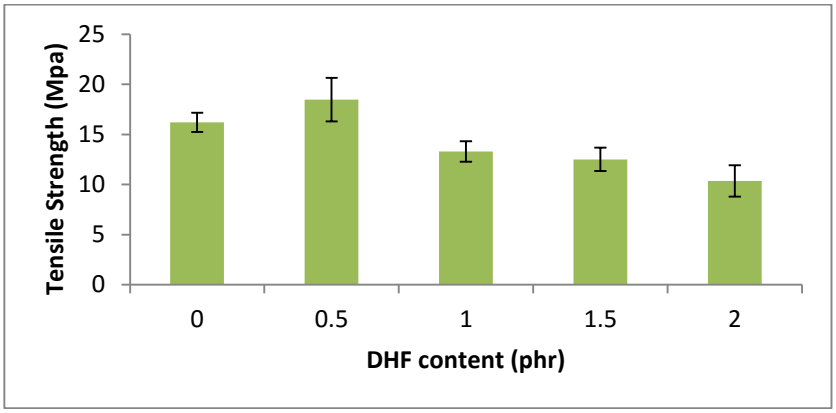


Figure 7: Graph of tensile strength with different processing aid content

As shown in Fig. 7, the trend shows a gradual reduction with the increase of processing aid. The highest tensile strength is recorded with 0.5 amount of processing aid while the lowest is at 2. Processing aid mainly consists of fatty acid amide which is used to

improve the process of the mixture. Low amount of fatty acid amide attached to fiber would improve the compatibility or enhance the interfacial adhesion thus increasing its strength. In this case, high amount of fatty acid is used and with an increase of fatty acid amide on fibers, the fatty acid amide itself would block the polymer matrix from forming a good interfacial adhesion.

3.2.2 Tensile Modulus with Processing Aid

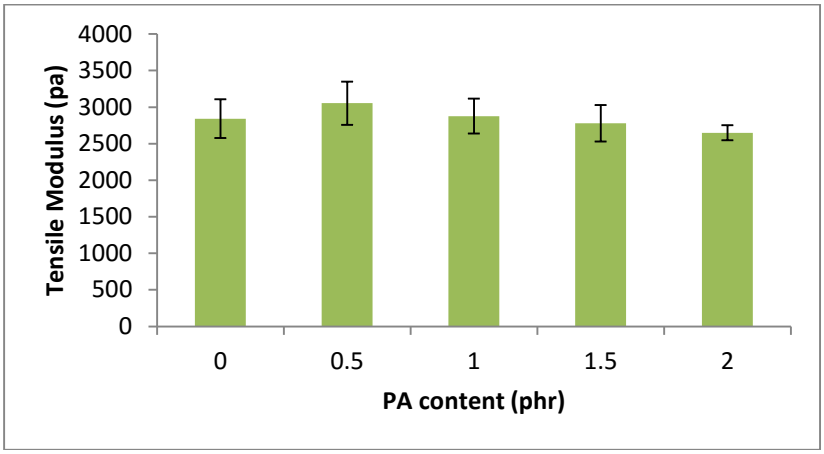


Figure 8: Graph of tensile modulus with different processing aid content

Fig. 8 shows the graph of tensile modulus with the different amount of processing aid used. It is shown that the highest tensile modulus is recorded with 0.5 processing aid while the lowest is 2 processing aid. This shows that as the amount of processing aid increase, the tensile modulus tends to decrease. The reasons are similar to the trend of tensile strength as the increase of processing aid, the fatty acid amide blocks proper adhesion between polymer and fiber.

3.2.3 Elongation at Break with Processing Aid

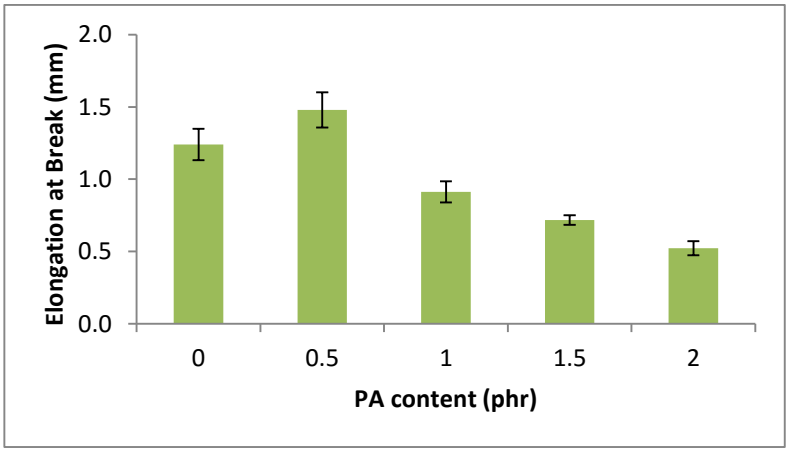


Figure 9: Graph of elongation at break with different processing aid content

Fig. 8 shows the graph of elongation at break with different processing aid content. It shows that the elongation is highest when there is 0.5 processing aid and the lowest when there is 2 amount of processing aid. This shows that the elongation at break reduces as the processing aid is increased. The reason as to why the elongation at break

is highest at 0.5 content of processing aid which is the lowest amount is that, fatty acid amide provides a lubricating effect which increases chain mobility thus providing longer elongation. Too much fatty acid would cause poor adhesion among the matrix and fiber thus providing smaller elongation.

4. Conclusion

In conclusion, the addition of DSF to the rPSF matrix will most definitely cause changes in terms of morphological properties, water absorption properties and thermal properties. The expected outcomes from this research would be similar if not better than existing literature reviews done by other researchers on rPSF filled DSF composites. The effects of the parameters for this research are as summarized as follows:

I. Tensile strength increase with fiber content
II. Tensile modulus increase with fiber content
III. Elongation at break decreases with fiber content
IV. Tensile strength decreases with processing aid
V. Tensile modulus decreases with processing aid
VI. Elongation at break decreases with processing aid

Acknowledgement

Throughout this research, various guidance and supports were received. Much gratitude to Man Chee as research partner and Performance Additive Sdn Bhd for providing the processing aid required to conduct this research.

Abbreviations

WPC	Wood Plastic Composite
DHF	Durian Husk Fiber
rPSF	Recycled Polystyrene Foam
PHR	Parts Per Hundred Rubber

References

[1] S. Butylina, O. Martikka and T. Kärki, "Physical and mechanical properties of wood-polypropylene composites made with virgin and/or recycled polypropylene", *Polymer-Plastics Technology and Engineering*, vol. 50, no. 10, pp. 1040-1046, 2011.

[2] "Wood-plastic composite market to reach 1728.9kilotons", *Reinforced Plastics*, vol. 59, no. 2, pp. 72, 2015.

[3] N. Ayrilmis and S. Jarusombuti, "Flat-pressed Wood Plastic Composite as an Alternative to Conventional Wood-based Panels", *Journal of Composite Materials*, vol. 45, no. 1, pp. 103-112, 2011.

[4] "Performance Additives unveils product range based on palm oil for WPC applications", *Additives for Polymers*, vol. 2009, no. 9, pp. 5-6, 2009.

[5] N. Chand and M. Fahim, Tribology of natural fiber polymer composites, Boca

Raton: CRC Press, 2008.

[6] H. Khademieslam, R. Khatibi and A. Pour, "Investigation on Physical and Mechanical Properties of WPC from Corn stalk (Lignocellulosic Fiber) and HDPE", *Macromolecular Symposia*, vol. 320, no. 1, pp. 70-74, 2012.

[7] J. Payá, J. Monzó, M. Borrachero, L. Díaz-Pinzón and L. Ordóñez, "Sugar-cane bagasse ash (SCBA): studies on its properties for reusing in concrete production", *Journal of Chemical Technology & Biotechnology*, vol. 77, no. 3, pp. 321-325, 2002.

[8] A. Bledzki, A. Mamun and J. Volk, "Barley husk and coconut shell reinforced polypropylene composites: the effect of fibre physical, chemical and surface properties", *Composites Science and Technology*, vol. 70, no. 5, pp. 840-846, 2010.

[9] H. Yang, H. Kim, J. Son, H. Park, B. Lee and T. Hwang, "Rice-husk flour filled polypropylene composites: mechanical and morphological study", *Composite Structures*, vol. 63, no. 3-4, pp. 305-312, 2004.

[10] "Timber Decking & Fencing Company: Melbourne, Brisbane & Sydney » ModWood", *Modwood.com.au*, 2017. [Online]. Available: http://www.modwood.com.au/. [Accessed: 08- May- 2017].

[11] B. Watson, *Durian*, Cairns: Rare Fruit Council, 1983.

[12] M. R. Manshor, H. Anuar, M. N. Nur Aimi, M. I. Ahmad Fitrie, W. B. Wan Nazri, S. M. Sapuan, Y. A. El-Shekeil, and M. U. Wahit, “Mechanical, thermal and morphological properties of durian skin fibre reinforced PLA biocomposites,” *Mater. Des.*, vol. 59, pp. 279–286, 2014.

[13] R. Manshor, H. Anuar, W. Wan Nazri and M. Fitrie, "Preparation and Characterization of Physical Properties of Durian Skin Fibers Biocomposite", *Advanced Materials Research*, vol. 576, pp. 212-215, 2012.

[14] M. A. Sawpan, K. L. Pickering, and A. Fernyhough, “Effect of fibre treatments on interfacial shear strength of hemp fibre reinforced polylactide and unsaturated polyester composites,” *Compos. Part A Appl. Sci. Manuf.*, vol. 42, no. 9, pp. 1189–1196, 2011.

[15] E. Sakai, J. H. Qiu, T. Murata, I. Kazushi, J. Kobayashi, and T. Takahashi, “Degradation Characteristics of Rice Straw/Poly(Lactic Acid) Composites,” *Adv. Mater. Res.*, vol. 391–392, pp. 1268–1272, 2011.

[16] N. Aimi, H. Anuar, M. Manshor, W. Nazri and S. Sapuan, "Optimizing the parameters in durian skin fiber reinforced polypropylene composites by response surface methodology", *Industrial Crops and Products*, vol. 54, pp. 291-295, 2014.

[17] J. Schellenberg and M. Wallis, "Dependence of Thermal Properties of Expandable Polystyrene Particle Foam on Cell Size and Density", *Journal of*

Cellular Plastics, vol. 46, no. 3, pp. 209-222, 2010.

[18] J. Schellenberg and M. Wallis, "Dependence of properties of expandable polystyrene particle foam on degree of fusion", *Journal of Applied Polymer Science*, vol. 115, no. 5, pp. 2986-2990, 2010.

[19] V. Mathur and K. Sharma, "Thermal response of polystyrene/poly methyl methacrylate (PS/PMMA) polymeric blends", *Heat and Mass Transfer*, 2016.

[20] Y. Zhang, J. Sun, X. Huang and X. Chen, "Heat transfer mechanisms in horizontal flame spread over wood and extruded polystyrene surfaces", *International Journal of Heat and Mass Transfer*, vol. 61, pp. 28-34, 2013.

EURECA 2017 – Conference Paper
Paper Number 2ME22

Development of a PID Controlled Arduino-Based Stabiliser

Wah Yee Lyn[1*], Felicia Wong Yen Myan[2], Tai Jun Jet[3], Hoo Choon Lih
[1,2,3]*School of Engineering, Taylor's University*

* [1]*yeelynwah@hotmail.com*

Abstract

Inverted pendulum remained as the most popular topic for control theory researches because of its characteristic of being non-linear, unstable and under-actuated system. It is ideal for verification, validation and enhancement of control theory by stabilizing the inverted pendulum in an upright position using various controller and stabilizer mechanism. For this project, Proportional-Integral-Derivative (PID) controller is used to stabilize the inverted pendulum by tuning the respective gains (k_P, k_I, and k_D) to control the parameters of inverted pendulum which includes the rise time, settling time, overshoot and steady-state error in cooperation with of Arduino microcontroller. The objective of this project is to design and build a stabilizer mechanism with the integration of mechanical and electrical components to stabilize two Directional (2D) inverted pendulum similar to 3D printer mechanism. Besides that, PID controller will be tuned in Arduino microcontroller and control the output of stabilizer mechanism. The stabilizer mechanism is designed in SolidWorks software and built using various manufacturing techniques, raw materials and 3D printing, while the electronics components such as gyroscope and Direct Current (DC) motors are controlled using Arduino Due in C++ language. The gyroscope determines the tilting angle of the pendulum as a feedback in the control loop, and the gains of PID are used to control the speed and direction of DC motor to provide sufficient force/torque to keep the inverted pendulum in an upright position. The stabilizer mechanism with inverted pendulum has been built and the gains of PID has been tuned using "trial and error" method as friction is now taken into consideration. The inverted pendulum is successfully stabilized in an upright position (0^o measure at *z*-axis) using control theory.

Keywords: Inverted Pendulum, PID Controller, Stabilizer

1. Introduction

Inverted pendulum remained as one of the most popular problems existing in control theory and has been studied in many researches for the control community [1]. The unstable, nonlinear and under-actuated characteristics of an inverted pendulum system raise a challenging task for testing different control algorithms due to its large uncertainties attached with the system [2]. There are many methods to stabilize the inverted pendulum and one of the methods is by using a Proportional-Integral-Derivative (PID) controller. PID controller is a control instrument that is commonly used in the industrial control applications to regulate processes as part of a control loop [1].

Each controller in a PID contains of their respective tuning gain, k_P, k_I, and k_D. Tuning any of the gain in PID controller affects the control system parameters: rise time, settling time, overshoot and steady-state error. Rise time is the time taken for the waveform to go from 0.1 to 0.9 of the final value. Settling time is the time taken for the transient's damped oscillations to reach and stay within $\pm$2% of the steady-state value. Overshoot is the amount of waveform overshoot from the final value or the steady-state value. Steady-state error is the difference between output value and desired output value [3].

A one-dimensional (1D) inverted pendulum is commonly used as study material. The inverted pendulum is placed on a cart and stabilized using linearization method. The distance travelled by the cart produces force to keep the inverted pendulum upright. The distance travelled by the cart alters based on the difference of pendulum angle relative to *y*-axis [1]. The pendulum angle is measured and the difference of the pendulum angle is calculated and fed into PID controller for stabilizing the inverted pendulum by producing an ideal system response with optimal gain value to drive the cart for a certain distance. The limitation of one axis inverted pendulum is that the stability of the pendulum can only be studied for one axis.

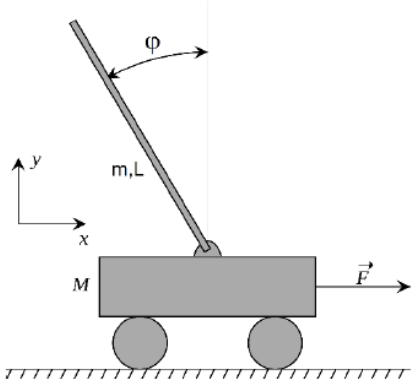


Figure 1 : Cart Pendulum System [1]

To further study on the inverted pendulum, a two-dimensional (2D) inverted pendulum will be chosen. Increasing one axis will increase the number of uncertainties and nonlinearity of the pendulum which introduces a wider range for testing control algorithms. A mechanism with the integration of mechanical components and electronics components will be built to stabilize the 2D inverted pendulum using pulley

system and sliding mechanism. The difference of the pendulum angle relative to *x*-axis and *y*-axis is measured using a gyroscope sensor.

A gyroscope sensor determines the position, orientation and angular velocity using Coriolis force applied to a vibrating object [4].When the gyroscope is rotated, the Coriolis force acts upon the drive arms and produces vertical vibration. The vertical vibration then produces a sensing motion in the sensing arms. The motion on the sensing arms creates a potential difference where the angular velocity is measured and converted into small current signals. The signals are then amplified and fed into a controller. Gyroscope sensor is placed onto the 2D inverted pendulum. The orientation and position of inverted pendulum are measured, converted into signals and compared with the desired output value in the control system and the error is calculated [5]. The error is then fed into PID controller and each parameter of the gain is tuned to produce and output angle to drive the mechanism to stabilize the 2D inverted pendulum.

2. Design of the Stabiliser

The stabiliser design consists of two parts, which are the mechanical and electrical parts. Mechanical part contains the inverted pendulum, pulley system and sliding mechanism. The PID control and communication between the microcontroller and the actuators (motors) are discussed under electrical part.

2.1 Mechanical System

Linearisation method is one of the easiest methods to stabilise an inverted pendulum. A cart moves in *x*-axis and *y*-axis linearly to a desired position where the pendulum is stabilized when the pendulum tilts but does not exceed the tilting maximum angle (30^o relative to *z*-axis), if tilting angle is exceed the pendulum falls to maximum position. Using this method, the first stage of this project is to build a 2D inverted pendulum on a moving cart and the stabiliser mechanism to stabilize or balance the inverted pendulum to an upright position.

The ideology of the stabiliser mechanism is a mock of a 3D printer mechanism shown in Figure 2 because of the accuracy and precision exhibited by a 3D printer. The extruder of 3D printer moves on along the Cartesian plane in *x*-axis and *y*-axis with four directions on the gantry. The extruder receives *xy* coordinates from the software, where each part of the object needs to be printed and the heater cartridge on extruder heats and melt the filament to be deposit onto the bed of 3D printer [6]. Therefore, 3D printer has high accuracy and precision in coordination to print the objects as they are designed to be. To balance an inverted pendulum requires the accuracy and precision exhibited by the 3D printer, hence the stabiliser mechanism is built similarly to the mechanism of a 3D printer.

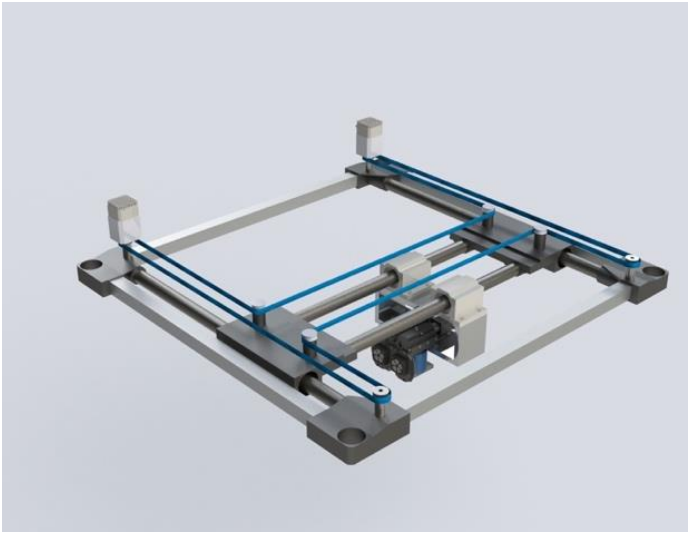


Figure 2: 3D Printer Mechanism

From the 3D printer mechanism, a pulley system and four sliding mechanism is implemented to allow the 3D printer to move at x-axis and y-axis. The similar pulley system and sliding mechanism is implemented on the cart to form a stabiliser mechanism and moves the cart of inverted pendulum along the x-axis and y-axis.

2.1.1 Pulley System

The pulley system is implemented to convert rotational motion produced by motors into translational motion for the inverted pendulum cart. The components in this system includes timing pulleys, timing belts, flanged bearings and solid rods. A 60T timing pulley is mounted on the shaft of Direct-Current (DC) motor and connected to 20T timing pulley [7], with a closed-loop timing belt [8], as shown in Figure 2.1.1.

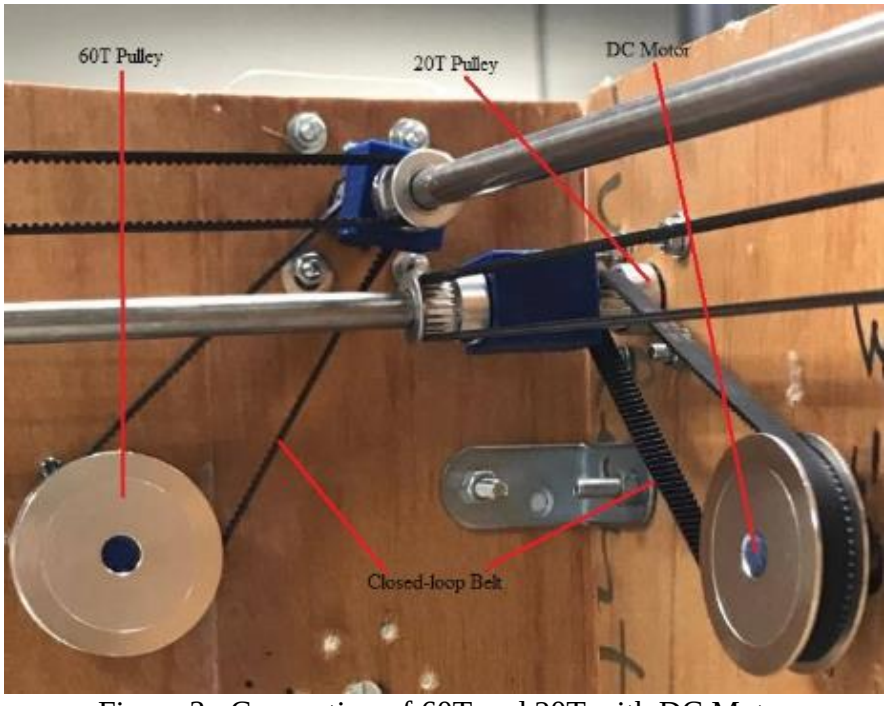


Figure 3 : Connection of 60T and 20T with DC Motor

Due to the friction and requirement of high acceleration to hold the inverted pendulum upright, the DC motor rated speed was not sufficient to provide such acceleration. Therefore, the number of teeth on pulley attached to motor is triple the number of teeth on pulley attached to solid rod to increase the translational speed by three times using pulley system.

$$\frac{N_1}{N_2} = \frac{T_2}{T_1} \qquad (2.1.)$$

Where ;
N_1 = Speed of gear on DC motor
N_2 = Speed of gear on Solid Rod
T_1 = Number of teeth of gear on DC motor
T_2 = Number of teeth of gear on Solid Rod

2.1.2 Sliding Mechanism

The sliding mechanism is integrated with the pulley system to provide guidance for inverted pendulum cart to move along *x*-axis and *y*-axis. Since there are two axes, the pulley system of x-axis overlaps with the pulley system of *y*-axis, therefore the design of inverted pendulum cart requires high accuracy of dimension where the solid rod of *y*-axis on cart is perpendicular to *x*-axis and does not collide or touches each other. Similarly, the design of sliding mechanism to hold the inverted pendulum cart by each end of stabiliser mechanism requires high accuracy for inverted pendulum cart to travel in straight line on *x*-axis and *y*-axis. The designs are shown in Figure 4 and Figure 5.

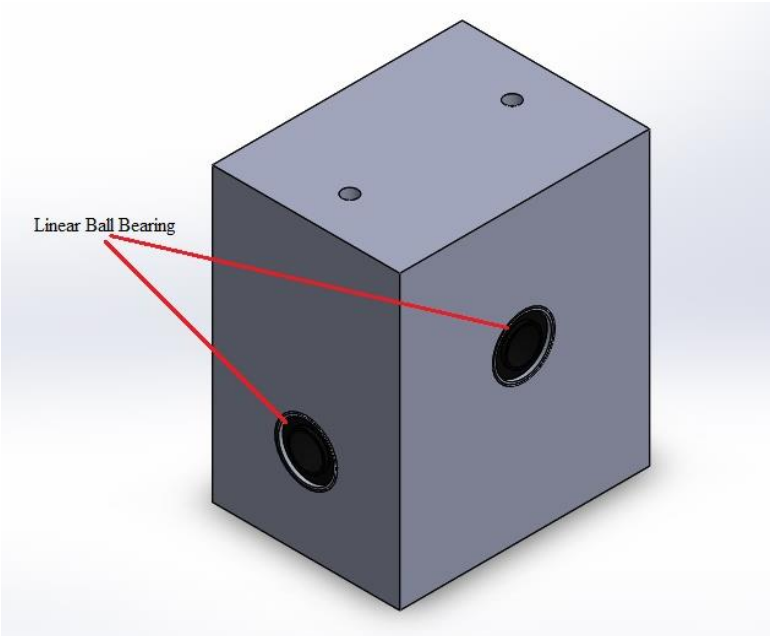


Figure 4: Inverted Pendulum Cart

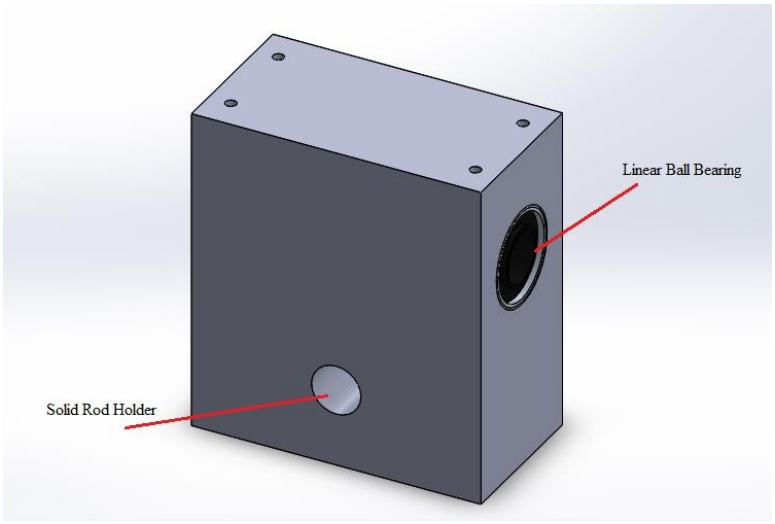


Figure 5: Sliding Mechanism

The main component for sliding mechanism is the linear ball bearing. The linear ball bearings assist in reduction of friction by allowing solid rod of *y*-axis to rotate while the sliding mechanism of *x*-axis to have precise translational motion [9]. Due to high accuracy of dimension, the sliding mechanism parts are manufactured through 3D printing and linear ball bearing are inserted into each block of sliding mechanism.

2.1.3 Inverted Pendulum and Cart

The inverted pendulum is made out of an aluminum hollow rod with the length of 750 mm and weight approximately 100g. To attach the inverted pendulum onto the cart, a component is designed to guide the inverted pendulum to tilt along *x*-axis and *y*-axis and eliminates rotation around *z*-axis. This component also increases the accuracy in determining the angle of tilt for inverted pendulum. The component is as shown in Figure 6.

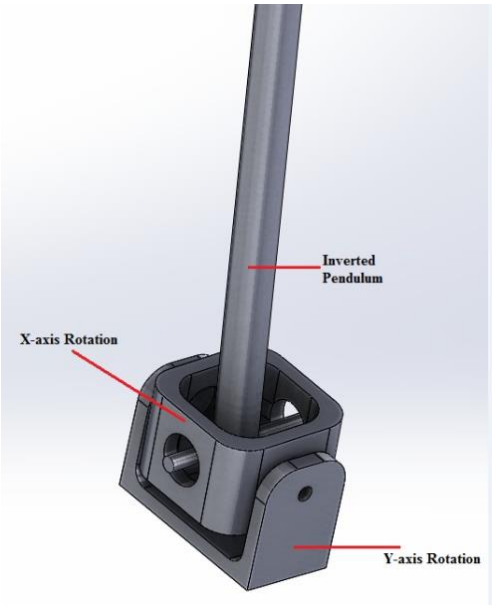


Figure 6 : Inverted Pendulum Holder

The gyroscope is attached onto the inverted pendulum to determine the position and orientation of inverted pendulum which will be converted into electrical signals and fed into a microcontroller to control the direction of rotation and speed of both DC motors.

2.2 Electrical and Electronics Methodology

The translation motion of the cart is controlled by 2 DC Geared motor as each DC geared motor is assigned to control one axis of translational motion. Both motors are coupled with the motors through the pulley system and sliding mechanism. The DC geared motor is used to rotate a vertical gear and a horizontal gear for a transmission of torque from horizontal to vertical and rotates the timing belt pulley to pull the timing belt on the cart. In order for the cart to have sufficient force in balancing the inverted pendulum, the torque and speed of DC geared motor are significant in producing the amount of force. The speed of motor is measured in revolution per minute (rpm) and torque would be newton per meter (N.m). Both DC geared motor has the same specification where each motor has the speed of 380 rpm (0.12 m/s) and torque of 637.43 mN.m (6.5 kg.cm) [10], which is able to produce the force needed to keep the inverted pendulum upright.

The tilting angle of pendulum is measured using gyroscope and the current signals from gyroscope is fed into microcontroller to convert angle analog signals to digital signals to provide a feedback. If the angle of pendulum is more than 0^o and less than 5^o, the difference between desired angle of pendulum (0^o) and measured angle of pendulum is calculated for an error signals to be converted into Pulse Width Modulation (PWM) signals. The error signals determine the amount of PMW signals to be fed into DC geared motor and rotate the motor in clockwise direction. If the angle of pendulum is less than 0^o and less than -5^o, the difference between desired angle of pendulum (0^o) and measured angle of pendulum is calculated for an error signals to be converted into PWM signals. The PMW signals is fed into DC geared motor and rotate the motor in counter-clockwise direction. However, if the angle of pendulum remains at 0^o, the PWM signals are LOW to stop the DC geared motor from rotating. Below is the flowchart of DC Geared motor shown in Figure 2.1.5.

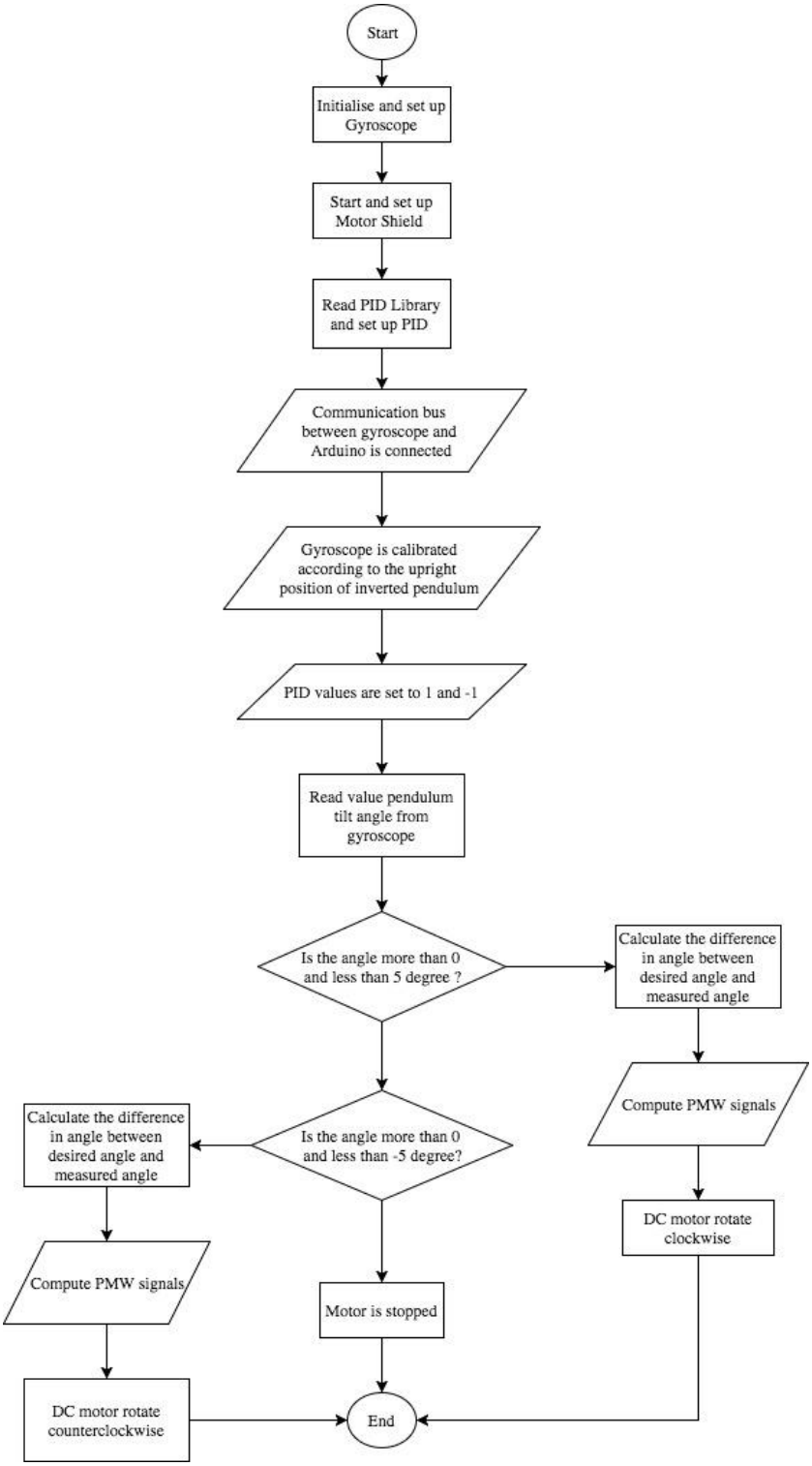


Figure 7: Flowchart of Electrical Components

Methods from Research Methodology are executed in order to achieve the objectives of this research. Experimental testing on the stabilizer mechanism and electrical and electrical components are done such ensuring the stabilizer mechanism is able to move the cart in *x*-axis and *y*-axis, inverted pendulum tilt only along *x*-axis and *y*-axis, angle of tilt for inverted pendulum is read by gyroscope, microcontroller process the angle of tilt, tuning the PID gains and vary the speed and direction of DC motors.

3. Results and Discussion

3.1 Mechanical System

The 20T timing pulley is mounted on a solid rod which is connected from one end to another end of the frame of stabiliser mechanism with flanged bearing to allow smoother rotation of solid rod [11], shown in Figure 8. When the DC motor rotates, it rotates the 60T timing pulley and with the closed-loop timing belt, the rotation is translated to the 20T timing pulley and solid rod.



Figure 8: Rotational Motion Components

The pulley system is also used to move the inverted pendulum and cart by having two sets of 20T timing pulley mounted on a solid rod that hinged on the frame of stabiliser mechanism as shown in Figure 9. This is implemented on the right end and left end of the frame of stabiliser mechanism. Both of the solid rod are connected with

timing belt to form a closed-loop and the ends of timing belt are attached onto the sliding mechanism of inverted pendulum. This allows the inverted pendulum cart to move along *x*-axis. The same configuration is implemented for the cart to move along *y*-axis.

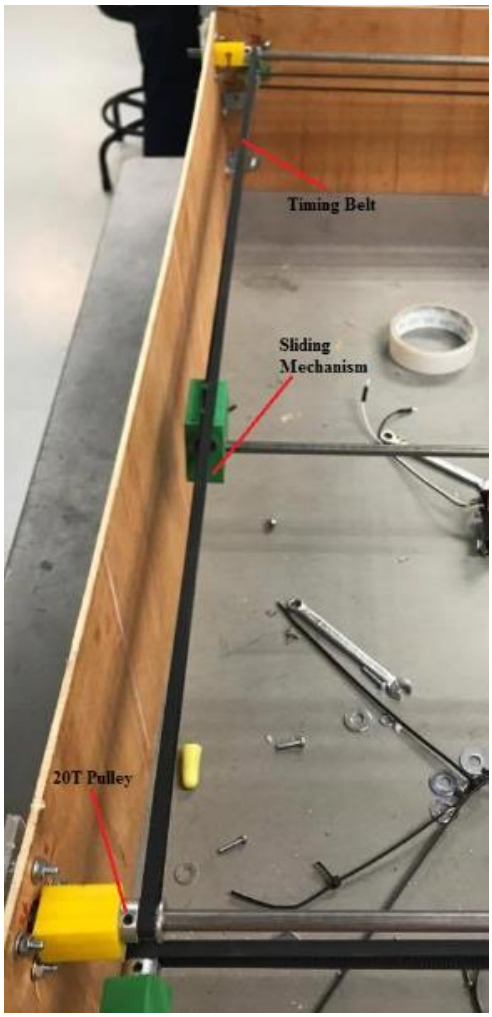


Figure 9: Left End of Stabiliser Mechanism

As the DC motor rotates clockwise, the 60T pulley translate the clockwise rotational motion to 20T pulleys and solid rod. The rotational motion is then converted to translational motion by rotating the timing belt attached on sliding mechanism allowing the cart to move at positive direction of *x*-axis. While if DC motor rotates counterclockwise, the cart moves at negative direction of *x*-axis. This applies in moving the cart for positive and negative direction of *y*-axis. This creates force through acceleration of motor to keep the inverted pendulum at an upright position, $\theta = 0°$.

3.2 Electrical and Electronic System

The overall schematic diagram of electrical and electronic system is shown in Figure 10 on how each components are related to each other and the process of the system.

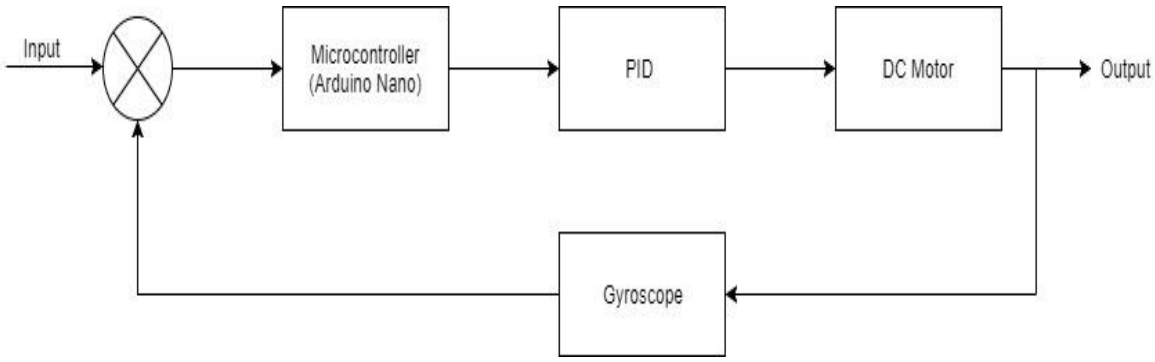


Figure 10: Schematic Diagram of Electrical and Electronic System

3.2.1 Microcontroller (Arduino Nano)

Microcontroller forms a communication between input devices and output devices through programming languages. In this research, Arduino Nano communicates with gyroscope and DC motors through C++ programming to identify the angle of tilt from inverted pendulum as input and the speed required from DC motor to keep the inverted pendulum upright as output. Acceleration of DC motors are converted into linear force by pulling the timing belt in clockwise and counter-clockwise direction subsequently moving the cart in *x*-axis and *y*-axis. However, to keep the inverted pendulum upright, the acceleration is constantly changing and increases the difficulties in providing theoretical value of force required to balance the inverted pendulum. PID controller is used to assist the response of DC motor towards the angle of tilt from inverted pendulum. The ideal response characteristic includes low rise time, small percentage of overshoot and zero steady-state error of DC motor. This is done by tuning the gains of PID controller which can be alternated in C++ programming of Arduino Nano. The angle of tilt is monitored through Serial Monitor from Arduino Nano and the gains are tuned according to measured angle of tilt until desired value of angle of tilt is obtained. The current gains of PID for *x*-axis and *y*-axis are -1 to 1 which includes the friction arise from pulley system and sliding mechanism.

3.2.2 Gyroscope (MPU6050)

The gyroscope is attached perpendicular to the inverted pendulum facing downwards because the jumper wires to be connected from gyroscope to Arduino Nano cannot exceed 5cm. This is due to the disturbance of noise and interference on the bandwidth of gyroscope when transferring signals to Arduino Nano. The longer the jumper wire, the higher the resistance, noise and interference of bandwith. Therefore, shorter jumper wires are recommended. The gyroscope is tuned in such way that it only measures the *x*-axis and *y*-axis rotational motion. *Z*-axis and acceleration motion are tuned out to reduce the processing time of signals (faster signal transfer between gyroscope and Arduino Nano) as these two parameters are not in the scope of this research. Gyroscope has an internal voltage regulator to reduce 5V supplied from Arduino Nano to 3.3V as required to eliminate excess of voltage and causes damage to the gyroscope.

3 ports of gyroscope are connected to Arduino Nano namely, Signal Data (SDA), Signal Clock (SCL) and Interrupt. SDA processes the rotational motion (x-axis and y-axis) of inverted pendulum, stores the value as angle of tilt and send it to Arduino Nano. SCL is the frequency of transmission of data between gyroscope and a microcontroller and the built in frequency range about 400kHz which allows one data to be transferred at 2.6 nano second. The Interrupt port is to identify the status of gyroscope. When the gyroscope is ready to function, Interrupt port sends a signal to Arduino Nano and the program in Ardunio will run because the gyroscope requires initialization before running the program. Due to the limitation of bandwidth from gyroscope, the maximum tilting angle of inverted cannot exceed $\pm 5^{o}$ on *x*-axis and *y*-axis.

3.2.3 Motor Shield

The current and voltage draw with load of one DC motor are 1A and 12V. Both DC motors are connected in parallel which means the total voltage needed would be 12V, however the current would be 2A. The maximum voltage can be supplied by Arduino Nano is only up to 5V, insufficient to power even one DC motor. To assist and increase the voltage and ampere supplied to DC motors, a motor shield is used. The motor shield is able to supply up to 6A of current to each motor but only 5V can be drawn out from motor shield. However, the motor shield has input ports for external voltage supply to be connected to DC motor, hence an external power supply with 5A and 12V is connected to the motor shield to increase the voltage and current for both DC motors. Each motor connects to three ports of motor shield. Two ports are to control the direction of rotation (clockwise and counterclockwise) for DC motor. One port is to power the DC motor with voltage accumulated from power supply and motor shield. The motor shield receives processed signals from Arduino Nano and controls the speed and direction of rotation of DC motors and converts rotational motion to translational motion on pulley system.

As all components are assembled, communication of electrical components are programmed by C++ programming and PID gains tuned, experimental testing is done on the stabiliser mechanism to balance the inverted pendulum. Table 3 indicates the achievable tasks by stabiliser mechanism and inverted pendulum.

Table 3 : List of Function Achievable by Stabiliser Mechanism and Inverted Pendulum

Tasks	Achievable ?
Transmission of rotational motion to linear motion by DC motors and pulley system	✓
Increases the speed of rotational motion of pulley system by 3 times of the speed of DC motors	✓
Moving the cart along *x*-axis	✓
Moving the cart along *y*-axis	✓
Moving the cart along *x*-axis and *y*-axis at the same time	✓
Tilting inverted pendulum along *x*-axis	✓
Tilting inverted pendulum along *y*-axis	✓

Tilting inverted pendulum along *x*-axis and y-axis	✓
Eliminates rotational motion of inverted pendulum and moving along *z*-axis	✓
Inverted pendulum balanced at *x*-axis	✓
Inverted pendulum balanced at y-axis	✓
Inverted pendulum balanced from negative *x*-axis	✓
Inverted pendulum balanced from positive *x*-axis	✓
Inverted pendulum balanced from negative *y*-axis	✓
Inverted pendulum balanced from positive *y*-axis	✓
Limited tilt angel can be recovered	✓

4. Conclusion

In conclusion, the stabiliser mechanism has been successfully designed and built. The inverted pendulum cart is able to travel along the *x*-axis and *y*-axis and produce force to keep the inverted pendulum in an upright position. The gyroscope is able to measure the angle of tilt of inverted pendulum and sends values to Arduino Nano to be processed. By analyzing the received signals, the PID gains are tuned through C++ programming in Arduino Nano and the response of inverted pendulum and DC motors are observed. The inverted pendulum is balanced in an upright position from negative and positive of *x*-axis only and *y*-axis only.

The future work includes balancing the inverted pendulum from various coordination on *x*-axis and *y*-axis as with increasing number of coordination, the PID gains will be tuned differently in order to receive same outcome as balancing inverted pendulum from negative and positive of *x*-axis only and *y*-axis only. The response curve of an inverted pendulum changes with number of coordination or number of uncertainties. The aim of this future work is to obtain characteristic includes low rise time, small percentage of overshoot and zero steady-state error of inverted pendulum and identifies the mathematical modelling to determine gains for PID controller that stabilizes 2D inverted pendulum.

Acknowledgment

The author would like to thank Dr. Steven Hoo Choon Lih for providing necessary guidance, knowledge and information regarding this research and ensuring each part of the process of the research is done in proper manner to achieve the objectives of this research. The author would also like to thank Tai Jun Jet and Lee Kit Hong in assisting the programming of C++ and partial SolidWorks design of stabiliser mechanism.

References

[1] K. H. Lundberg and J. K. Roberge, “Classical Dual-Inverted-Pendulum Control,”

Proc. IEEE Conf. Decis. Control, vol. 5, pp. 4399–4404, 2003.

[2] "PID Theory Explained - National Instruments." [Online]. Available: http://www.ni.com/white-paper/3782/en/. [Accessed: 27-Apr-2017].

[3] A. N. K. Nasir, R. M. T. R. Ismail, and M. A. Ahmad, "Performance Comparison between Sliding Mode Control (SMC) and PD-PID Controllers for a Nonlinear Inverted Pendulum System," pp. 122–127, 2010.

[4] L. Blitzer, "Inverted Pendulum," *Am. J. Phys.*, vol. 33, no. 12, p. 1076, 1965.

[5] "Accelerometer vs. Gyroscope: What's the Difference?" [Online]. Available: http://www.livescience.com/40103-accelerometer-vs-gyroscope.html. [Accessed: 27-Apr-2017].

[6] "How exactly does 3D printing work? - Technology & Science - CBC News." [Online]. Available: http://www.cbc.ca/news/technology/how-exactly-does-3d-printing-work-1.1371800. [Accessed: 27-Oct-2017].

[7] "GT2 Pulley 20 Teeth 8mm Bore – 6mm Belt Width - 3D Gadgets Malaysia." [Online]. Available: http://3dgadgets.my/belt-pulley/228-gt2-pulley-20-teeth-8mm-bore-6mm-belt-width.html. [Accessed: 27-Oct-2017].

[8] "Gt2 Closed-loop Belt 200mm - 3D Gadgets Malaysia." [Online]. Available: http://3dgadgets.my/belt-pulley/244-gt2-closed-loop-belt-200mm.html. [Accessed: 27-Oct-2017].

[9] "LM8LUU Linear Ball Bearing - 3D Gadgets Malaysia." [Online]. Available: http://3dgadgets.my/bearings/242-lm8luu-linear-ball-bearing.html. [Accessed: 27-Oct-2017].

[10] "DC Geared Motor 12V High Power 380RP (end 9/14/2017 1:15 PM)." [Online]. Available: https://www.lelong.com.my/dc-geared-motor-12v-high-power-380rpm-stelectronics-182767385-2017-09-Sale-P.htm. [Accessed: 27-Oct-2017].

[11] "F688ZZ Flanged Bearing - 3D Gadgets Malaysia." [Online]. Available: http://3dgadgets.my/bearings/240-f688zz-flanged-bearing.html. [Accessed: 27-Oct-2017].

eureca 2017 – Conference Paper
Paper Number 2ME23

Electrical Energy Harvesting From Cooker's Wasted Heat With Using Conduction Cooling

Wincent*, Ghafour Amouzard Mahdiraji
School of Engineering, Taylor's University, 47500, Subang Jaya, Selangor, Malaysia.

* wincent@sd.taylors.edu.my

Abstract

In order meet the demand of electricity in current era, the need for new sources of energy even in very minimal amount, could be done with proper research and technology advancement in order to convert as much waste energy as possible. Collecting and analyses cooker's waste heat as a main waste energy source become the main interest for this research. This application can be installed either in household usage or commercial usage. Based on majority stove in household datasheet it shown that the efficiency of the stove is approximately 50%. With half of the efficiency turn into waste heat, this application is suitable for thermoelectric generator (TEG) to harvest the heat. The objective of this research is to determine whether the thermoelectric generator (TEG) would able to power the 3V LED light as a small lighting system in household. Several designs with five TEGs in series circuit are tested to the application to analyses which method generated a better result. Since this research only focus in using a conduction cooling, aluminum heat sink will be utilized either for heat absorption or heat rejection. The maximum temperature differences between hot side and cold side is 209.83°C with average power approximately 0.0991W.

Keywords: Thermoelectric Generator, cooker, Energy harvesting, Waste heat, testing TEG.

1. Introduction

In this contemporary society, energy demand has become one of the crucial challenge. Based on Energy Information Administration, the demand of energy in the society is annually increase without any sight of peaking. Thus, this challenge has become one of the popular topic to discuss and to motivate the society to increase the energy supply. A lot of efforts is made by researchers to meet the demand of the energy by considering either other source of energy or renewable energy. An improvement has been done by other extensive research on renewable energy such as wind turbine, tidal energy, and solar power to supply the energy demand and, yet it still could not entirely cover the demand. Therefore, new methods to gain an extra energy is developed and one of the method is to absorb the waste heat produce in daily household appliances.

Thermoelectric energy is known to be the usable source of electricity from the conservation of waste heat and this energy is operate based on Peltier and Seebeck effecting. In year 1821, German physicist Thomas Johann Seebeck discover that a temperature differences is existed between two dissimilar metals, electricity will be generated since the electron level in each material shifted differently. Electron from the surface that is supplied with enough heat will eventually jump to the metal with colder surface. Thus, the movement of the electron is known to generate the thermoelectric energy [1].

Thermal energy is commonly being classify as a by-product from various forms of energy such as mechanical energy, chemical energy and electrical energy. It is known that, machinery such as washing machine, refrigerator, cooker is used daily by the people either in household or commercial. With the usage of the machinery, the electrical energy that supplied it will generated a lot of waste heat due to the moving part of the machine or the heat loss due to the appliances product efficiency. Therefore, this waste heat energy contain wasted efficiency percentage that can be absorb and covert to the usable electrical energy [2].

Due to the increasing of the energy demand, research is done to find the new method to discover renewable and available energy. As such, by absorb the waste heat from the machinery heat loss and convert them to usable electrical energy. To perform this research, Thermoelectric generator (TEG) is become one of the solution. This technology is initially used to convert the geothermal energy to the electrical energy.

Thermoelectric technology is a rather new, developing technology that is inexpensive to build and is space saving due to their small size as shown in Fig.1. It is also easy to use. In addition, this technology is sustainable as well as it is eco-friendly and does not produce greenhouse gases or sound pollution. A downside to this technology is its low efficiency when generating electricity, which is of approximately 5 – 10 % of the total heat energy [4][5]. In order to calculate the efficiency of the TEG, figure of merit (ZT) is known to represent the dice's performance. This parameter also known to have dimensionless numerical expression.



Figure 1: Thermoelectric Generator

The concept behind kitchen appliances, such as a cooker is studied in order to understand the heat transfer from the cooker's flame and to discover the most optimum location to install the thermoelectric generator. Efficiency and total power generated from each design will be calculated together with the total cost. This is to determine whether this application would be a success.

In year 2005, researcher form Xiamen University has done and experiment with applying same TEG material Bismuth telluride with antimony doping to the usage on the plantation machine. During its experiment it found that the temperature difference that produce by the machine heat with water cooling technique as heat rejection is approximately 77ºC. this produce the ZT value as big as 1.15 and voltage generated is less than 0.5V [6].

By reducing the thermal conductivity, it may enhance the *ZT*. Pei He Jiangqing, a Student from School of material science and engineering in Beihang University, found that Ca-doped BiCuSeO material exhibits low thermal conductivity and resulted in increasing the *ZT* by 0.9 at 923K [7]. Meanwhile, Dr.Li Dong Zhao from Northwestern University reported that SnSe single crystal that measured along with room temperature orthorhombic unit cell b axis produced the *ZT* of 2.6 at 923[8].

2. Research methodology

The method in conducting this research is discusses in this section. The research that was conducted was a quantitative study based on the simplest and most effective method. TEG has been done by so many researchers especially for energy experts.

Several types of thermoelectric modules have been utilised and fabricated. However, in this study only Bi_2Te_3 thermoelectric module was used due to its reliability and capability to produce the higher *ZT* among other type in room temperature. Moreover, the availability of Bi_2Te_3 thermoelectric module is common in the market. Although thermoelectric generator is easy to operate, multiple experiments are required to find the most effective method [9].

The initial project's progress was focus on studying literature review for both thermoelectric module and cookers from either journal or online to have a better understanding on what it will dealing with and what the device are. This includes executing initial experiment two of designs and find the best location to install the TEG, and lastly was purchasing the suitable equipment. ANSYS software was used to find the best location to install the TEG. For the first design (Design A) the TEG was attach to the acrylic and hanged near the heat source which is approximately 5cm. small heatsink was placed at the cold side in order to release the heat from the hot side. This design has a convection heat transfer thus the temperature obtained was lower compare to the other design. For second design TEG (Design B) was placed to the aluminium plate which design to have a hole at the left, this is to allow the fire to go through to heat the pot/pan. To place the TEG, ANSYS computer software was utilized to find the best location, and at the purple line as show in Fig.2 which is approximately 10cm from the heat source was selected in order to prevent the TEG overheat easily conduction heat transfer was applied in this design. In the simulation, it shown that the temperature of the aluminium was reach 180^{o}C in 10 minutes usage. Thus, this was suitable for the TEG application which needed high temperature in the hot side. Both, the simulation and the two experiments were done in implement stage where initial experiment was conducted. Results of the experiment were analysed and both methods were compared.

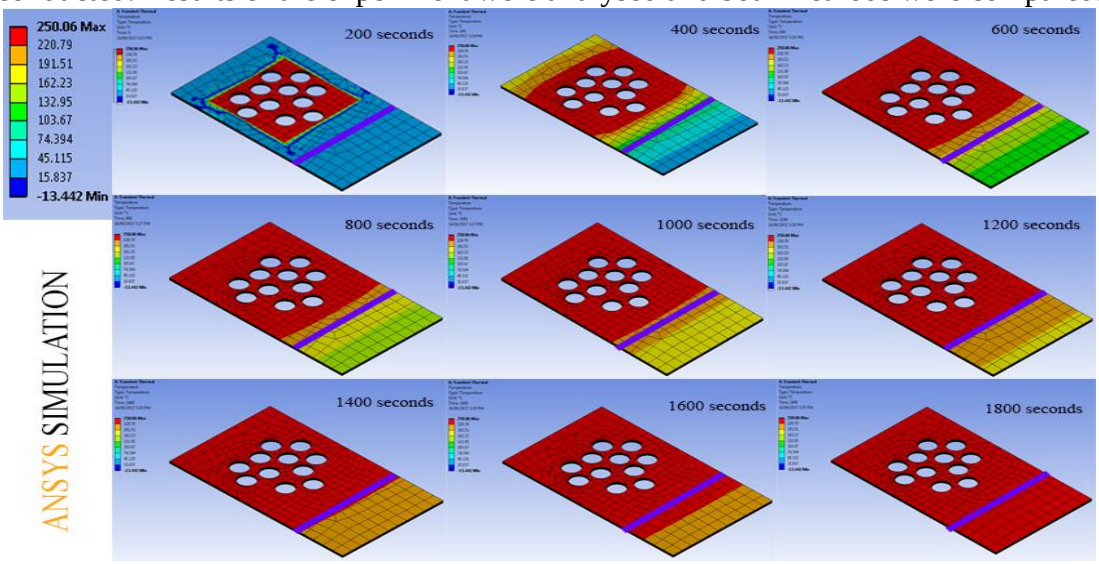


Figure 2: ANSYS simulation for aluminium plate.

Meanwhile, to observe the differences of the result, another three Designs which are convection heat transfer and two calcium silicate with TEG facing aluminium plate (Design C), convection heat transfer and single calcium silicate with TEG facing heat source (Design D) and Design E, convection and conduction with TEG attach with L aluminium plate are tested for the experiment. Not only new designs were proposed, but high performance Bi_2Te_3 TEG, calcium silicate Ca_2SiO_4 and big aluminium heat sink also introduce to the experiment since the old TEG performance was consider low

and inefficient, the calcium silicate was to prevent the heat to transfer to the cold side and heat sink was to reject more heat to generate large temperature differences. However, with using new high performance TEG, the experiment was only conducted with using single TEG instead of using multiple TEG that form into series circuit. This was done to check whether the TEG is efficient to use before purchase multiple of them. Fig.7 show that the visual experiment setup for design C, in this design the calcium silicate that place near to the heat source was aims to reduce the convection heat transfer to the heatsink so that the temperature differences was larger. While the calcium silicate in the bottom of TEG was aims to prevent the TEG to experience over heat since the maximum temperature of high performance TEG can withstand was 300^{o}C while the aluminium plate itself has temperature of 270^{o}C by using infrared thermometer gun to measure. Small heatsink was attach to the hot side which is inside the calcium silicate in order to absorb more heat and big heat sink was attached to the cold side to maximize the heat rejection. This design place near the edge of the aluminium edge which is 20cm from the heat source due to consideration of the convection heat transfer to the big heatsink. Since the hot side is cover by calcium silicate, temperature of the calcium silicate was becoming the temperature for the hot side.

While, Design D was designs to place the TEG facing the heat source with 4 differences distance which were 15cm, 10cm, 5cm and 2.5cm from the heat source. calcium silicate was used to cover and protect the TEG and to prevent the heat to transfer to the aluminium heatsink which was affecting the result. Small heatsink was attach to the hot side to absorb maximum heat from the heat source while big aluminium was attach to the cold side to reject the heat. In order to obtain a perfect connection, thermal grease was applied on both hot side and cold side. In addition, aluminium plate was placed to produce a better heat transfer by convection. 4 experiments were conducted and compare to each other to analyse the changes of generating voltage.

Lastly, Design E as shown in Fig.3 was conducted by placing one end of the aluminium and steel L bracket to attach to hot side of the TEG and the other end to fire, this was done so that conduction heat transfer was occurred and to maximize the heat absorption. Meanwhile same as the previous design, big heat sink was placed at the cold side to reject the heat and aluminium plate was placed to ensure the convection heat transfer was maximized. The results of both L bracket's material were compared. Since aluminium have a better heat conductivity with 209.5 W/m.K, three differences size of aluminium L bracket 30cm, 20cm and 15cm (Fig.4) were tested and compared. Again, the best results among three differences size of L bracket was tested with four difference resistors which were 10ohm, 7.5ohm, 2.2ohm and 1ohm. This was to find the power produce from the single high performance TEG. The reason several resistors were tested was to observe the behaviour of the TEG.

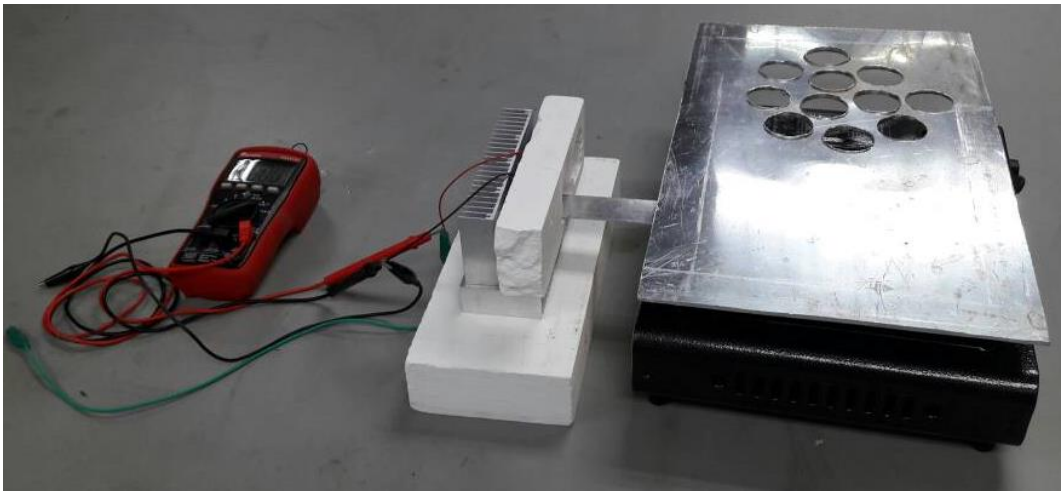


Figure 3: 20cm aluminium L bracket experiment setup.

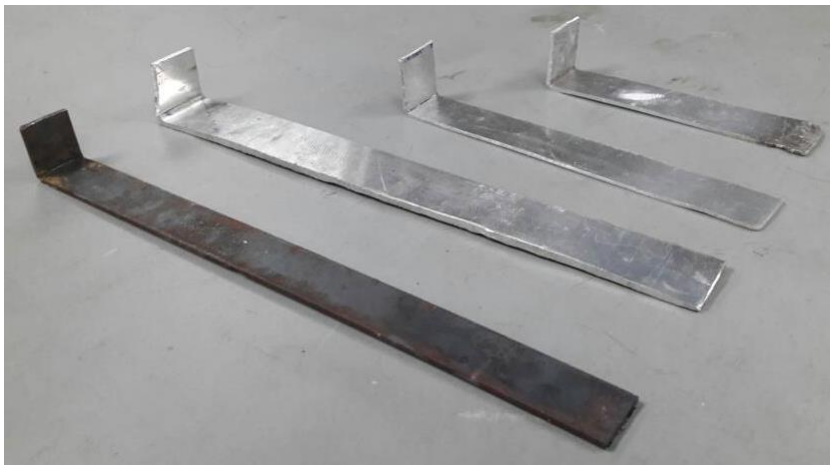


Figure 4: steel and aluminium L bracket.

3. Result and discussion

Table 1: Experiment result based on each model.

Design	mV	mA	P(Watt)	Th	Tc	ΔT	*ZT*	Efficiency
A (5 TEG)	40.65	8.55	0.0003	148.4	134.5	13.9	0.0326	0.0008
B (5 TEG)	100.54	7.69	0.0008	271.3	242	29.3	0.0688	0.0028
C	28.64	0.0000	0.0000	66.66	39.99	26.67	0.0626	0.0076
D (15cm)	7.23	0.0000	0.0000	37.39	27.49	9.9	0.0232	0.0018
D (10cm)	12.49	0.0000	0.0000	45.75	32.36	13.39	0.0314	0.0026
D (5cm)	17.02	0.0000	0.0000	59.59	34.22	25.37	0.0595	0.0078
D (2.5cm)	79.55	0.0000	0.0000	126.7	37.25	89.45	0.2099	0.0506
E1 (steel)	25.09	0.0000	0.0000	80.33	34.47	45.86	0.1076	0.0202
E2 (30cm Al)	258.63	0.0000	0.0000	100.98	35.51	65.47	0.1536	0.0337
E3 (20cm Al)	409.12	0.0000	0.0000	113.12	37.59	75.53	0.1772	0.0400
E4 (15cm Al)	822.71	0.0000	0.0000	228.52	46.59	181.93	0.4269	0.1108
E4 (10Ω)	891.81	53.091	0.0473	212.64	44.64	168	0.3942	0.1027
E4 (7.5Ω)	935.13	59.645	0.0558	196.9	39.95	156.95	0.3683	0.0986
E4 (2.2Ω)	916.71	63.954	0.0586	195.72	46.41	149.31	0.3504	0.0884
E4 (1Ω)	883.68	112.16	0.0991	254.76	44.93	209.83	0.4924	0.1306

Based on table 1 it shows the average result of each experiment. For experiments design C, D and E, the power are zero because no resistor is connected to the experiment. Resistor is only applied to experiment design E4 and not applied to the others is because based on the result, E4 experiment generate the highest voltage which is 822.71mV. four different resistors are applied to E4 to observe the changes of the current by the TEG. Based on the observation it is shows that the current generated by the TEG is indirectly perpendicular to the resistant of the resistor. Table 1 also shown that the design E4 experiment with one-ohm resistor produce the highest power with approximately 0.1Watt. In order to increase the generated power, TEG can be connect series with another 4 TEGs.

For experiment design A it shows that the setup was inefficient since the voltage generated is relatively low with small temperature difference. During the experiment, the voltage of the TEG is keep fluctuating up and down rapidly. This show the connection is unstable and it only generate a very small current which is not worth the investment. Meanwhile, for design B experiment is more suitable to utilize for the superior quality TEG since the temperature in both side of the TEG is too high. During the experiment, the soldering flux on the TEG cables were melted and spoiled the device after the first experiment.

In experiment design C the result is also not satisfy since the average voltage result is low. This is because the TEG is located too far from the heat source and the convection heat transfer was tended to spread to environment instead of absorbing by TEG. While, if the TEG placed nearer to the heat source this will result the big aluminium heat sink that supposed to reject heat from the TEG to act inversely. Meanwhile, experiment design D is done with testing 4 difference distances. In this experiment it shows that distance of 2.5cm show the best result. However, the hot temperature of the TEG is still consider low since the average temperature is only half from the heat source temperature which is 126.7 ^{o}C.

The last design is created in order to allow the TEG hot side can reach approximately >200^{o}C. initially 30cm steel and aluminium L bracket are tested to compare which material provide a better result based on the voltage. Since aluminium has higher heat conductivity, 3 difference size of it is created. The longer the aluminium bracket, the greater heat loss will be occurred due to convection heat transfer. Therefore, shorter aluminium L bracket is preferable. Not only have higher conduction heat transfer, but shorter L bracket also allow the TEG to get closer to the heat source where convection and radiation heat transfers is higher. To prevent the heat to transfer to the big aluminium heatsink, calcium silicate is place as the TEG holder as shown if Fig.3. The shortest aluminium bracket is chosen as the final design since the result is quite satisfying and able to produce both average closed and close circuit voltage 0.8V with 0.12A in closed circuit current.

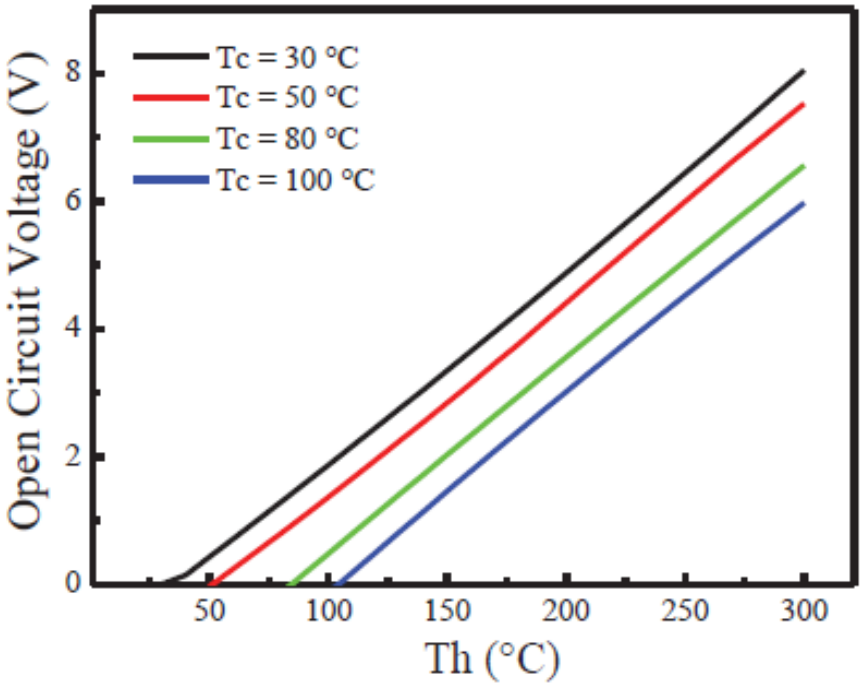


Figure 5: Chart for open circuit voltage V_s T_h under various T_c.

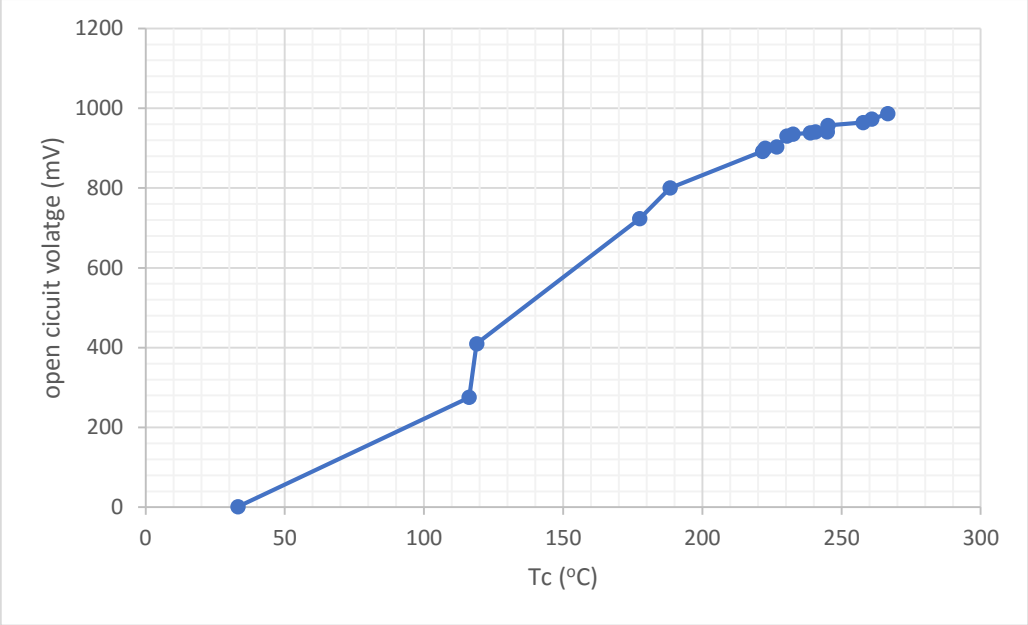


Figure 6: experiment chart for open circuit voltage V_s T_h under T_c 50°C.

Fig.5 it shows the performance of the high performance TEG based on the provided device's data sheet. Since the average of the T_c of the experiment is approximately 45°C, the result will be compare to the red colour line where the temperature of T_c is 50°C. Meanwhile in Fig.6 shows the result of the Voltage generated with average T_c 45°C. in the experiment result it shows that the voltage generated is increase rapidly when hot side start reaches temperature 100°C to 220°C this is because the temperature difference is also increase rapidly. While, the voltage only increases slightly when temperature reach 220°C and above since the temperature of the heat supply is only 270°C and with effect of external factor such as environment temperature, the temperature on the hot side is only fluctuating between 230°C to 260°C. Based on the comparison between two graphs, it shows that the voltage that generated in the experiment is relatively low even the temperature T_h is follow the temperature from the data sheet. Several factors are stated as the factor that cause the changes such as inconstant T_c during the experiment, fluctuate T_h during experiment and environment condition. In order to investigate another factor, more experiment will be conducted to the future. Table 1 shows that the maximum power that can reach by the TEG is only 0.1Watt in design E4. The voltage of open circuit E4 and closed circuit 1-ohm E4 still remain the same, this mean that this circuit still able to undergo smaller resistant. 0.5 and 0.2 ohm resistant will be test in the future to observe the changes and 5 TEGs in series closed circuit also will be tesedt to increase the power. it is expected by combining 5 TEGs into Series closed circuit with smaller resistant, the result will be better and worth the investment since less maintenance is require and it is long last technology.

4. Conclusion

In conclusion, TEG technology is consider as green technology since this technology have no moving part, long last and require less maintenance. The temperature differences between hot side and cold side of the TEG has become the main parameter in order to generate electricity. Generated energy from the TEG is directed perpendicular with the temperature difference. The higher the temperature differences so do the electric generated. To maximize the efficiency of the power generated, all type of heat transfer which are conduction, convection and radiation is apply to the latest design. While, only conduction cooling with aluminium heat sink was applied to reduce to ease the installation and usage. Design E4 produce the best result in open circuit with voltage 822.71mV. Thus, this design is continued to close circuit with using four difference resistors. Based on the result, design E4 with 1ohm resistor produce the best result with voltage ampere and power are 883.68 mV, 112.16 mA and 0.0991 Watt.

Abbreviation

TEG	Thermoelectric Generator

References

[1] P. Gokhale, B. Loganathan, J. Crowe, A. Date, and A. Date, "Development of Flexible Thermoelectric Cells and Performance Investigation of Thermoelectric Materials for Power Generation," *Energy Procedia*, vol. 110, no. December 2016, pp. 281–285, 2017.

[2] D. Li *et al.*, "Enhanced thermoelectric performance in SnSe based composites with PbTe nanoinclusions," *Energy*, vol. 116, pp. 861–866, 2016.

[3] X. Zhang and L.-D. Zhao, "Thermoelectric materials: Energy conversion between heat and electricity," *J. Mater.*, vol. 1, no. 2, pp. 92–105, 2015.

[4] D. Champier, "Thermoelectric generators: A review of applications," *Energy Convers. Manag.*, vol. 140, pp. 167–181, 2017.

[5] R. Y. Nuwayhid, A. Shihadeh, and N. Ghaddar, "Development and testing of a domestic woodstove thermoelectric generator with natural convection cooling," *Energy Convers. Manag.*, vol. 46, no. 9–10, pp. 1631–1643, 2005.

[6] M. Otake, K. Sato, O. Sugiyama, and S. Kaneko, "Pulse-current sintering and thermoelectric properties of gas-atomized silicon-germanium powders," *Solid State Ionics*, vol. 172, no. 1–4 SPEC. ISS., pp. 523–526, 2004.

[7] H. Pang, Y. Y. Piao, Y. Q. Tan, G. Y. Jiang, J. H. Wang, and Z. M. Li, "Thermoelectric behaviour of segregated conductive polymer composites with hybrid fillers of carbon nanotube and bismuth telluride," *Mater. Lett.*, vol. 107, pp. 150–153, 2013.

[8] Y. Zhu, C. Wang, H. Wang, W. Su, J. Liu, and J. Li, "Influence of Dy/Bi dual doping on thermoelectric performance of CaMnO 3 ceramics," *Mater. Chem. Phys.*, vol. 144, no. 3, pp. 385–389, 2014.

[9] Y.-L. Pei *et al.*, "High thermoelectric performance of oxyselenides: intrinsically low thermal conductivity of Ca-doped BiCuSeO," *NPG Asia Mater.*, vol. 5, no. 5, p. e47, 2013.

eureca 2017 – Conference Paper
Paper Number 2ME24

Anti-windup PI controller, SIPIC For Motor Position Control Application

Kah Kit Wong*, Choon Lih Hoo[2], Mohd Hardie Hidayat Mohyi[3]

[1]*School of Engineering, Taylor's University, Malaysia*
[2]*School of Engineering and Physical Sciences, Heriot-Watt University, Malaysia*
[3]*School of Engineering, Taylor's University, Malaysia*

*kah.kit@outlook.com

Abstract
Control system plays a major role in the industry nowadays as it simplifies workload and reduce manpower. Among all the applicable field, control system is highly in motor speed and motor position control. Although there are various types of controller available, PID controller remains as one of the main controller due to its simplicity. However, PID controller experiences windup phenomenon which affects the controller's performance. This paper proposes a new type of anti-windup PI controller, SIPIC for motor position control application and aims to validate the performance of this controller as compared to conventional PI controller. Both controller was experimented using hardware testing where no load condition and loading condition were used to test the ability of the controllers under few circumstances. Two different inputs were used: 0˚ to 90˚ and 270˚ to 90˚. The results obtained shows that under no load condition, both controller showed acceptable performance. However, SIPIC controller slightly outperforms PI controller by having lower overshoot and shorter settling time for a wider range of gains. The rise time of both controllers are similar as it is the lowest possible rise time due to hardware limitation. Moving on to loading condition, for both input, when the K_p is 1 and K_i is 15, PI controller shows unstable performance by having large amount of oscillations and overshoot. The settling time was also unable to be determined as the controller did not settle within the given step time. On the other hand, at the same gain, SIPIC controller still shows acceptable performance. This shows that SIPIC controller have more stable performance for a wider range of gains while PI controller needs to be finely tuned to a specific gain to obtain desired results.

Keywords: SIPIC, motor position control, PI controller, anti-windup, PID controller.

1. Introduction

In the 21st century where manual manpower is increasingly being replaced by automatic robotic system, control system plays a major role in ensuring the quality of product and efficiency of the automated system. The involvement of control system in the industry can mainly be found in speed control and position control.

In a position control system, the system output is usually the mechanical position of an arm or a pointer, and the performance of the controller highly affects the accuracy of this arm/pointer. Applications of position control system that can be commonly found includes the solar tracking system and robotic system Servomotor is usually used as the actuator for position control system. Servomotor is a type of direct current (DC) motor that is capable of precise control of angular and linear position, velocity as well as acceleration. Many types of controller had been used for the application of position control system and these controllers include fuzzy logic controller, fractional order controllers, controller that utilizes finite control set model predictive controller as well as a proposed controller that combines the characteristics of μ-synthesis and neural network.

[1] proposed a modified crisp fuzzy logic controller where modifications were done on both the input and the output of the controller. The input of the controller utilizes crisp rectangular adjacent non-overlapping membership function, distributed along the discourse universe whereas modification for the output was done on the computation method. The controller showed acceptable performance and shorter processing time than conventional fuzzy logic controller. [2] proposed a new controller for the application of motor position controller that combines the characteristics of μ-synthesis and neural network.

[3] proposed a controller based finite control set model predictive control for the application of permanent magnet synchronous motor (PMSM). This controller predicts the future behavior of the actuator and perform action that is chosen from a model set. Other than that, many also applied fractional order calculus in motor position control. [4] used a fractional order PI controller and compared to integer order PI controller, fractional order controller contains two extra variables which allows more flexible and precise tuning. From the result, it can be concluded that fractional order PI controller experience less overshoot and lower maximum percentage of error than conventional PI controller. [5] further expanded the application and added differential evolution algorithm into fractional order PI controller. This adds a self-tuning ability to the controller and the author used the proposed controller for the application of voice coil motor (VCM). Result shows that the proposed controller experience lower settling time, tracking error as well as lower maximum overshoot as compared to conventional PI controller and fractional order PI controller.

In this paper, Proportional-integral-derivatives (PID) controller is chosen due to its simplicity[6]. By tuning the three individual components of the controller, the overshoot, steady-state error, rise time and settling time of the system can be altered. The limitation of a conventional PID controller is often caused by the limitation of the actuator being used instead of the controller itself. When the output of the controller exceeds the limit of the actuator, the controller begins to lose the ability to control the system. Example can be shown through the flushing mechanism. The system controls

the opening of the valve to limit the flow rate of the water depending on the tank level. However, if the error continues to grow even after the valve is fully open, the flow rate of the water will not continue to increase due to the limitation of the valve. This condition is known as the integral windup phenomenon, where the integral component continues to offset the error even when the output remains the same.

Over the years, several anti-windup schemes had been proposed to eliminate the integral windup phenomenon and to increase the efficiency of PID controller. These schemes include the Conditional Integration (CI), Tracking Back Calculation (TBC), Integral State Prediction (ISP), pole placement method and gain scheduling method.

Conditional Integration is one of the most common schemes and it functions by switching off the integral component during saturation state then turns it back on when the controller enters linear state again. Tracking Back Calculation measures the difference between the output signal and the non-saturation state signal before feeding the error back to obtain higher accuracy. There is also scheme that uses different method such as Integral State Prediction (ISP). This scheme predicts the steady-state value and feed the value back to the integral state when the controller re-enters linear state[7].

Recently, pole placement method and gain scheduling method were introduced. In pole placement method, the author proposed to first transform the desired plant into a type-1 plant as type-0 plant will always have error. Pole placement method is then used for the derivation of the controller gain[8]. Lastly, gain scheduling proposed the use of various gain and constant for different state of the controller for higher accuracy[9].

This paper utilizes a new type of controller known as Steady-state Integral Proportional Integral Controller (SIPIC) scheme for the application of position control system. Steady-state Integral Proportional Integral Controller (SIPIC) scheme is also another proposed controller that can overcome integral windup. It does that by having a separate closed loop feedback with the steady state integral value as an input. This constantly leads the integral control towards the steady state integral value[7]. It was mentioned earlier that different component of PID controller will have different effect on the performance and for PI controller, it will often have a short settling time with overshoot performance. SIPIC scheme made it possible to have a controller with short settling time with no overshoot performance due to its tuning decoupling ability. This ability allows the proportional gain (K_p) and integral gain (K_i) to be tune separately.

SIPIC has shown ideal performance with little overshoot while maintaining short settling time on a DC motor speed control application[7]. However, no work had been done on applying the SIPIC scheme on a DC motor position control application. Therefore, this research aims to validate the usage of proposed SIPIC controller in the application of motor position control. The objectives of this research are as below:

- To develop a new anti-windup PI controller that is suitable for motor position control.
- To validate the stability and performance of the new PI controller by studying the overshoot, steady-state error and settling time of the controller.
- To investigate and determine the range of gain that will maximize the performance of the PI controller for motor position control.
-

2. Research Methodology

2.1 Experimental Setup

Hardware testing was done to verify the proposed SIPIC controller. Comparison was done between SIPIC controller and conventional PI controller. The performance of the controllers is evaluated based on theirs steady-state error, overshoot, rise time as well as settling time. SCILAB and SCICOSLAB software were used to carry out experiment and data analysis for both the controllers. Figure below shows the equipment used for experimental testing purpose.

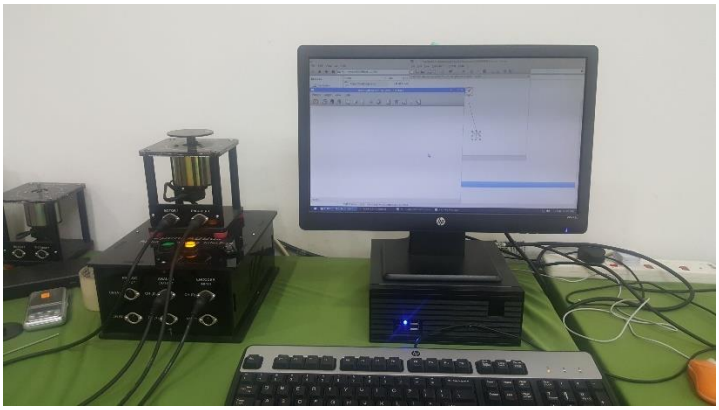


Figure 1. Experimental setup

2.2 SIPIC

This section focuses on the SIPIC controller and its characteristics. Based on previous work done by [7], Eq. 1 shows the generic template where SIPIC was developed from. $Q(S)$, q_{ss}, $f(s)$, s and n represents Laplace form of integral state, integral during steady state, function in Laplace form, Laplace domain and non-negative integer respectively. A and B are constants. Eq. 2 below shows integral component of SIPIC after various substitutions and derivations while Eq. 3 shows the error equation of SIPIC.

$$\frac{q_{ss}}{s} - Q(S) = As^n f(s) + B \tag{1}$$

$$k_i q_{ss} = v - \frac{b}{f k_T}\dot{y} + \frac{a}{f k_T} e \tag{2}$$

$$E(S) = \frac{e(0)\frac{b}{f}(s+k_i)+k_i k_T[q_{ss}-q(0)]}{\left(\frac{b}{f}s+\frac{a}{f}+k_p k_T\right)(s+k_i)-k_i k_T} \tag{3}$$

2.3 Input Reference

Based on the previous work done on SIPIC controller, the input reference was modified for the application of motor position control. Fig. 2 shows the block diagram for motor position control. From this, Eq. 4 was derived, and Eq. 5 shows the final input reference for motor position control for SIPIC controller. Fig. 3 shows the SIPIC controller block diagram for experimental setup whereas Table 1 shows the parameter used to obtain the input reference.

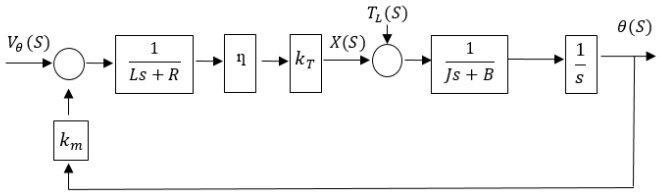


Figure 2. Motor position control block diagram

$$X(S) = \frac{v_\theta(S) - \theta(s)k_m}{Ls+R} * \eta k_T \tag{4}$$

$$k_i q_{ss} = v_{ss} = v_\theta + \frac{LJ}{\eta k_T}\dddot{e} + \frac{B+RJ}{\eta k_T}\ddot{e} + \frac{BR}{\eta k_T}\dot{e} + \frac{\eta k_T k_m}{\eta k_T}e \tag{5}$$

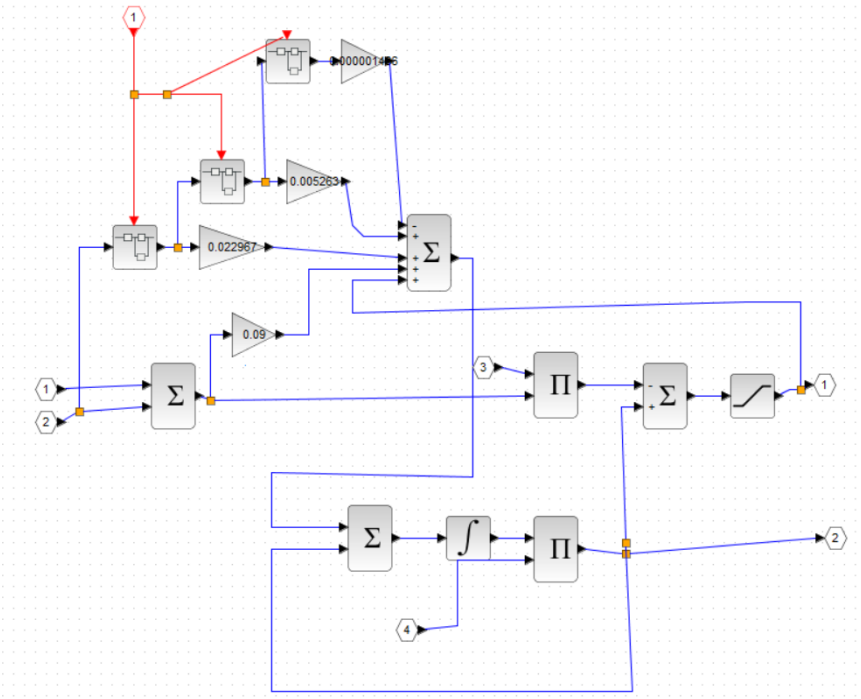


Figure 3. SIPIC experimental setup block diagram

Table 1. Parameters for experiment [7]

Characteristics	Values
Viscous damping coefficient, *B*	2.12 x 10^{-4} kg m^2/s
Inductance, *L*	0.005 H
Moment of inertia of motor, *J*	2.14 x 10^{-5} kg m^2
Torque constant, K_T	0.09 Nm/A
Back-emf constant, K_m	0.09 Nm/A
Efficiency, η	0.8
Resistance, *R*	7.8 Ω
Moment of inertia of mild steel black plating	8.63 x 10^{-5} kgm^2

3. Results and Discussions

This section shows the results obtained from hardware testing. Necessary information was obtained from the extracted data and analysis was done to verify the performance of each controller. Comparison was done between the two controllers to verify the proposed SIPIC controller for motor position control under no load condition and under load condition.

Two different step inputs were used for testing. For the first step input, the controller travels from 0˚ to 90˚ and for the second input, the pointer travel from 270˚ to 90˚. To put this into real life application, the first input is similar as to when changing steering direction of a vehicle while travelling in straight line while the second input is similar as to changing the direction of a vehicle from left directly to right. The stability in each case is different.

3.1 No Load

3.1.1 0 to 90

Table 2. Results for no load condition first input

		Overshoot		Rise Time		Settling Time	
K_p	K_i	PI	SIPIC	PI	SIPIC	PI	SIPIC
1	1	0.132	0.05	0.078	0.086	1.737	2.34
1	5	0.452	0.21	0.064	0.091	0.504	0.671
1	10	0.722	0.374	0.056	0.095	0.576	0.981
1	15	0.949	0.487	0.05	0.094	0.93	0.762
5	1	0.515	0.471	0.021	0.021	0.172	0.165
5	5	0.55	0.33	0.02	0.022	0.183	0.314
5	10	0.59	0.286	0.02	0.024	0.187	0.223
5	15	0.59	0.327	0.02	0.03	0.193	0.187
10	1	0.537	0.524	0.019	0.019	0.176	0.179
10	5	0.55	0.474	0.019	0.019	0.183	0.287
10	10	0.575	0.443	0.019	0.019	0.188	0.223
10	15	0.597	0.43	0.019	0.019	0.191	0.178
15	1	0.543	0.521	0.019	0.019	0.178	0.154
15	5	0.55	0.493	0.019	0.019	0.193	0.231
15	10	0.553	0.458	0.019	0.019	0.204	0.201
15	15	0.562	0.443	0.019	0.019	0.21	0.168

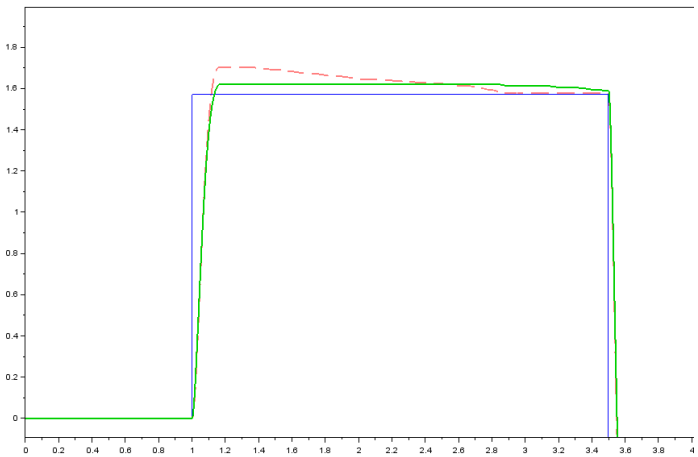


Figure 4. Performance graph when $K_p = 1$, $K_i = 1$

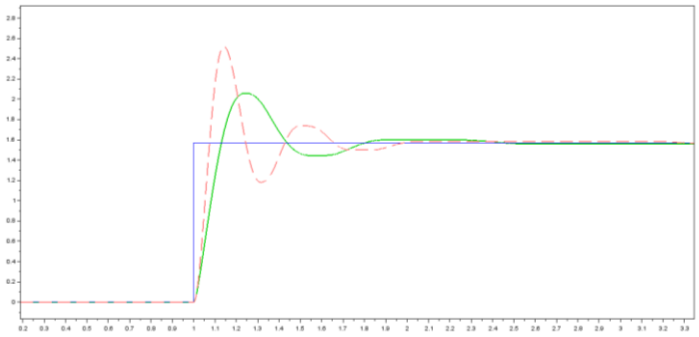


Figure 5. Performance graph when K_p = 1, K_i = 15

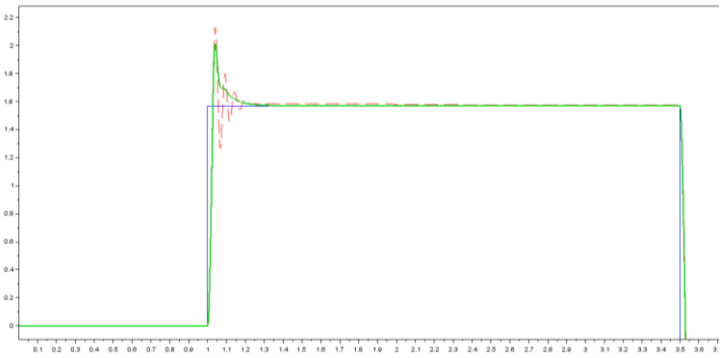


Figure 6. Performance graph when K_p = 15, K_i = 15

Table 2 above shows the performance of both controllers when K_p is 1 and K_i is 1, 5, 10 and 15 respectively. As the integral gain increases, both controllers experience an increase in overshoot but SIPIC controller have a significantly lower overshoot especially at higher K_i value. Moving on to the rise time of the controllers, different pattern is seen in each controller. For PI controller, rise time decrease as the integral gain increase but for SIPIC, rise time increase alongside the integral gain. However, SIPIC shows higher rise time compared to PI controller. Lastly, the settling time of the controllers is compared. Under comparison, when both the gain is 1, SIPIC shows a higher settling time. When the integral gain is increased to 5, both controller experience a big drop in settling time but as the integral gain continue to increase, settling time gradually increase in PI controller but experience minor up and down changes in SIPIC controller.

Next, K_i is kept at 1 and K_p is increased from 1 to 5, it is seen from results that the overshoot for both controllers increased significantly. Rise time and settling time decreases for both controller. Both controllers now experienced similar overshoot, rise time as well as settling time. As the integral value increases, PI controller experience slight increase in overshoot but SIPIC controller experience slight decrease in overshoot. The rise time of PI controller remain constant whereas SIPIC controller has slight increase in rise time when the integral gain increases. For settling time, PI controller experience slight increase. For SIPIC controller, when the K_i value is increase from 1 to 5, there is an increase in settling time but setting time experience a descent when the K_i value is further increased.

The K_p value was then increased to 10. The increased of K_p value causes the same effect to both controllers, increase in overshoot and settling time but decrease in rise time. SIPIC controller still has a lower overshoot than PI controller, similar settling

time and both controller now have the same rise time. As the integral gain increase, overshoot for PI controller has a slight increase but a slight decrease is experienced by SIPIC controller. There are no changes in rise time for both controller as this is the lowest possible rise time due to hardware limitation. PI controller continue to experience slight increase in settling time as K_i increases while settling time for SIPIC controller first increase then decreases, like where the K_p is 5.

Lastly, K_p was increased to15. The rise time for both controllers is still 0.019s, same as before. The increase in K_p causes a slight increase in overshoot and settling time of PI controller but a slight decrease in overshoot and settling time of SIPIC controller. Increasing K_i value continue to cause slight increase in overshoot of PI controller but decrease in overshoot for SIPIC controller. Same pattern is also seen in settling time of both controller. The increase in K_i value results in increase of settling time for PI controller but for SIPIC controller, the settling time first increases then start to decrease when the K_i value is further increased from 5.

Under no load condition first input, both controller shows very close performance. The proposed SIPIC controller have lower overshoot at all parameter as compared to conventional PI controller. SIPIC controller experiences higher rise time at low K_p value but both controller experience similar rise time when K_p value is further increased. Comparing the condition when both K_p and K_i is 15 as shown in Fig. 6, SIPIC controllers outperform PI controller by having a lower overshoot as well as lower settling time. This is because at higher K_i value, SIPIC controller experience decrease in both overshoot and settling time but PI controller experience increase in both components.

3.1.2 270 to 90

Table 3. Results for no load condition second input

		Overshoot		Rise Time		Settling Time	
K_p	K_i	PI	SIPIC	PI	SIPIC	PI	SIPIC
1	1	0.358	0.213	0.069	0.076	2.209	1.942
1	5	0.986	0.468	0.061	0.089	0.584	0.647
1	10	1.486	0.785	0.053	0.091	0.499	0.868
1	15	1.756	0.967	0.049	0.095	1.223	1.137
5	1	0.697	0.685	0.03	0.03	0.184	0.943
5	5	0.782	0.672	0.03	0.03	1.212	0.485
5	10	0.905	0.769	0.029	0.031	0.916	0.328
5	15	0.964	0.873	0.029	0.03	0.721	0.223
10	1	0.682	0.682	0.029	0.03	0.196	0.496
10	5	0.71	0.691	0.029	0.03	0.255	0.435
10	10	0.776	0.741	0.029	0.03	0.98	0.307
10	15	0.826	0.801	0.029	0.03	0.943	0.237
15	1	0.694	0.682	0.029	0.03	0.214	0.224
15	5	0.704	0.688	0.029	0.03	0.223	0.36
15	10	0.732	0.691	0.029	0.03	0.631	0.267
15	15	0.769	0.713	0.029	0.03	0.935	0.219

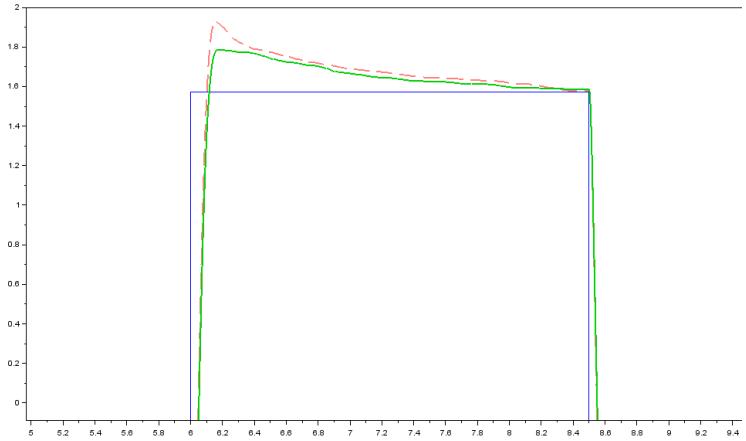


Figure 7. Performance graph when $K_p = 1$, $K_i = 1$

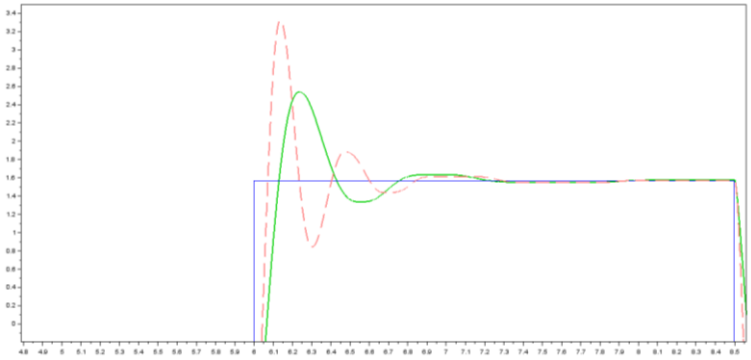


Figure 8. Performance graph when $K_p = 1$, $K_i = 15$

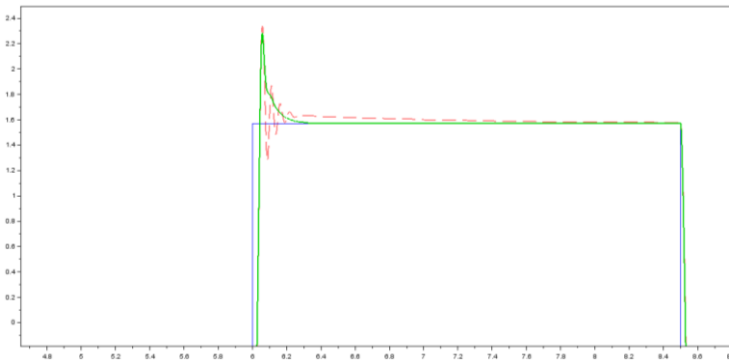


Figure 9. Performance graph when $K_p = 15$, $K_i = 15$

As shown in Fig. 6, when both value is 1, SIPIC controller has lower overshoot and settling time as compared to PI controller, but higher rise time. When the K_i value is increased, both controller experience an increase in overshoot but the increase in PI controller are far more significant. Rise time for PI controller decreases as the value of Ki increases but SIPIC controller experience higher rise time at higher K_i value. For settling time, both controller first experience a decrease before increasing again as Ki value is further increased. When K_p is 1 and K_i is 15, SIPIC controller performs slightly better by having lower overshoot and settling time but higher rise time as compared to PI controller.

Moving on, K_p value was increased from 1 to 5. Compared to when K_p value is 1, both controller now have higher overshoot, lower rise time and lower settling time.

As the value of K_i increases, both controller experience an increase in overshoot. The changes in rise time are insignificant in both controller. For settling time, SIPIC controller goes through a steady decrease in settling time but an increase then decrease in the PI controller. As the K_i value increases, the settling time of the SIPIC controller starts to be significantly lower than the PI controller.

When the K_p is further increased to 10 and 15, the rise time of both controllers remain the same as it is the lowest rise time possible. Both controller also experience minor changes in overshoot with SIPIC controller still having lower overshoot than PI controller. For settling time, SIPIC controller continue to show higher settling time than PI controller when the K_i value is small but SIPIC controller then outperform PI controller when the K_i value increases.

3.2 With Load

3.2.1 0 to 90

Table 4. Results for loading condition first input

		Overshoot		Rise Time		Settling Time	
K_p	K_i	PI	SIPIC	PI	SIPIC	PI	SIPIC
1	1	0.543	0.521	0.096	0.1	0.532	1.18
1	5	1.121	0.697	0.083	0.097	1.314	1.423
1	10	1.624	0.876	0.075	0.095	N/A	1.804
1	15	N/A	0.923	N/A	0.09	N/A	2.012
5	1	0.895	0.939	0.037	0.037	0.593	0.762
5	5	0.961	0.971	0.039	0.037	0.718	0.65
5	10	1.037	1.037	0.036	0.037	0.73	0.658
5	15	1.106	1.065	0.036	0.037	0.815	0.667
10	1	0.889	0.92	0.035	0.035	0.652	0.664
10	5	0.933	1.074	0.036	0.035	0.717	0.644
10	10	0.974	1.209	0.035	0.035	0.791	0.68
10	15	1.002	1.344	0.035	0.035	0.802	0.683
15	1	0.908	0.917	0.035	0.035	0.724	0.711
15	5	0.92	1.046	0.035	0.035	0.772	0.73
15	10	0.942	1.172	0.035	0.035	0.791	0.764
15	15	0.958	1.25	0.035	0.035	0.792	0.789

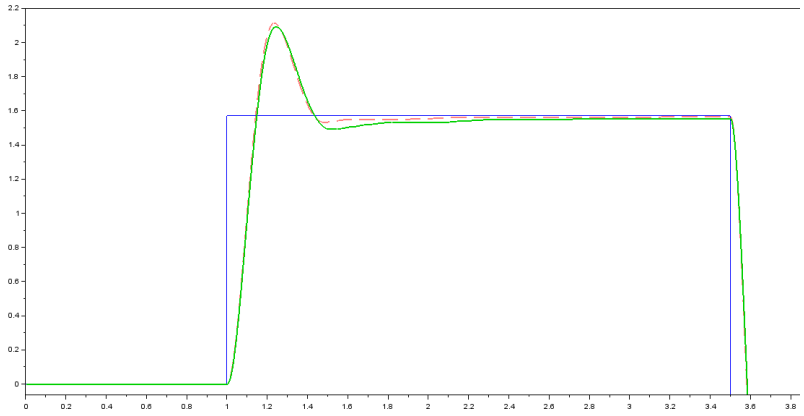


Figure 10. Performance graph when $K_p = 1$, $K_i = 1$

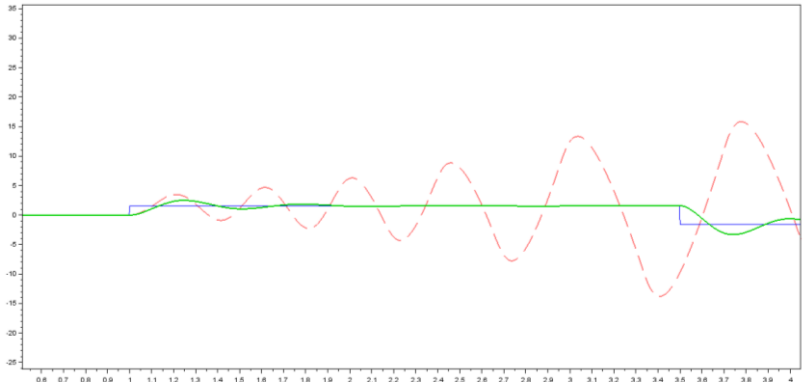


Figure 11. Performance graph when K_p = 1, K_i = 15

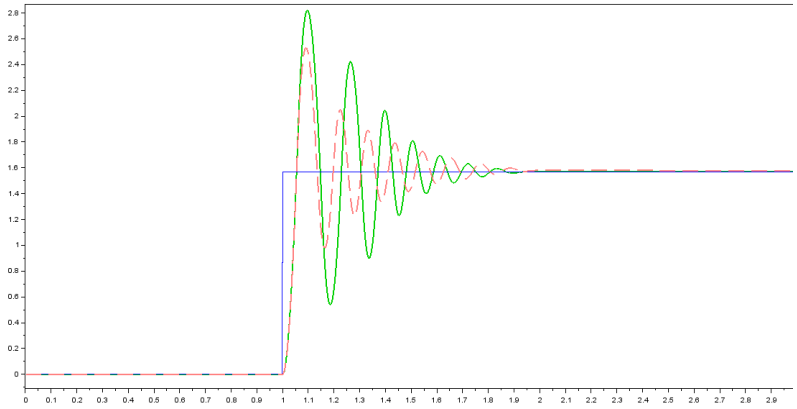


Figure 12. Performance graph when K_p = 15, K_i = 15

Table 4 shows results of controller first input under loading condition. When both K_p and K_i is 1 as shown in Fig. 10, SIPIC controller showed lower overshoot, shorter rise time and settling time as compared to PI controller. As the K_i value increases, both controller experience an increase in overshoot and decrease in rise time. Both controller also experience an increase in the settling time of the controller but for PI, the settling time were unable to be determined because the controller have not settled in the given step time. When K_p is 1 and K_i is 15 as shown in Fig. 11, PI controller shows very high oscillation and the overshoot, rise time and settling time were all not able to be determined. SIPIC controller on the other hand, still showed a very stable performance. This proves that SIPIC controller is more stable than conventional PI controller.

As the K_p value is increases from 1 to 5, both controller experience higher overshoot but lower rise time. PI controller experienced slightly longer slightly time but SIPIC controller experienced shorter settling time. As the value of K_i increases, the overshoot for both controller increases and both controller showed similar overshoot. The difference in rise time of both controllers is insignificant while SIPIC controller shows shorter settling time as K_i increases.

The K_p value is increased to 10 with K_i value being 1, 5, 10 and 15 respectively. Compared to when K_p was 5, both controller experience slight decrease in overshoot and rise time. PI controller has a longer settling time than before while SIPIC controller now has shorter settling time. As K_i increases, overshoot for both controllers increases while PI controller outperform SIPIC controller by having lower overshoot. Both

controller shows similar rise time as this is the lowest possible value. Both controllers also experience longer settling time as K_i increases but SIPIC performs slightly better by having slightly shorter settling time.

Lastly, K_p value was increased to 15. Rise time remains the same for both controllers. The increase in K_p value causes minor changes to overshoot in both controller while increasing the settling time for both controller. As K_i increases, similar pattern as before can be seen. Both overshoot and settling time increases alongside the K_i value and PI controller still have lower overshoot while settling time are similar for both controller.

3.2.2 270 to 90

Table 5. Results for loading condition second input

		Overshoot		Rise Time		Settling Time	
K_p	K_i	PI	SIPIC	PI	SIPIC	PI	SIPIC
1	1	1.209	1.033	0.09	0.098	N/A	0.647
1	5	2.18	1.429	0.101	0.092	1.507	1.137
1	10	3.251	1.586	0.052	0.094	N/A	1.679
1	15	N/A	1.778	N/A	0.091	N/A	1.756
5	1	1.414	1.527	0.052	0.052	0.73	0.824
5	5	1.599	1.9	0.051	0.052	0.788	0.791
5	10	1.803	2.281	0.052	0.051	1.081	0.907
5	15	1.985	2.516	0.052	0.052	0.968	0.94
10	1	1.388	1.495	0.052	0.051	0.769	0.72
10	5	1.508	1.74	0.052	0.051	0.858	0.774
10	10	1.624	1.951	0.052	0.051	1.171	0.834
10	15	1.712	2.108	0.052	0.051	1.034	0.93
15	1	1.42	1.442	0.052	0.051	0.837	0.83
15	5	1.467	1.655	0.052	0.051	0.952	0.855
15	10	1.527	1.803	0.052	0.051	0.978	0.895
15	15	1.58	1.916	0.052	0.051	1.112	0.999

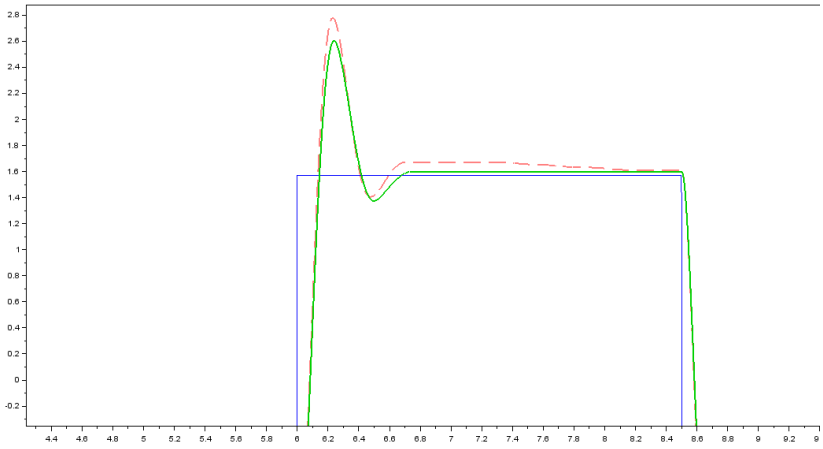


Figure 13. Performance graph when K_p = 1, K_i = 1

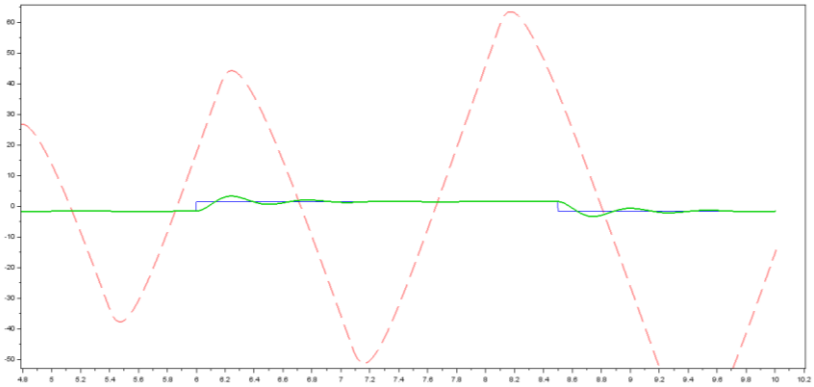


Figure 14. Performance graph when K_p = 1, K_i = 15

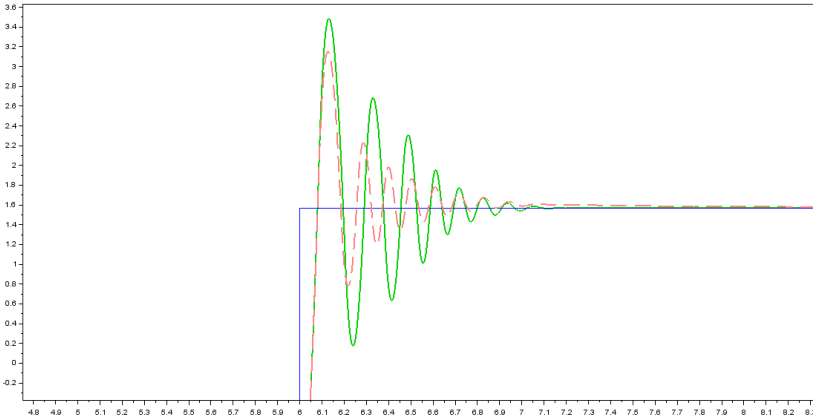


Figure 15. Performance graph when K_p = 15, K_i = 15

Table 5 show the results obtained for second input under loading condition. When both K_p and K_i is 1 as shown in Fig. 13, PI controller shows higher overshoot, longer settling time but slightly shorter rise time as compared to SIPIC controller. As K_i value increases, a major increase in overshoot can be seen in the PI controller and while SIPIC controller also experience an increase in overshoot, the increase is subtle as compared to PI controller. A very minimal spike was seen in the PI controller when Ki value was increased from 1 to 5 but the rise time then decreases when the value was further increased to 10. For settling time, a steady increase can be seen in the SIPIC controller as the K_i value increases. However, for the PI controller, it was unable to settle inside the desired range within the step time given. Fig. 14 shows the controller performance when K_p is 1 and K_i is 15, the overshoot and settling time experienced by the PI controller is far higher than the SIPIC controller.

Moving on to K_p = 5, the increase in K_p value causes the overshoot of both controller to increase and an increase in rise time can be seen in both controller. A more stable performance is seen in the PI controller as the controller can settle in the given step time while the SIPIC controller has a slightly longer settling time due to the increase in K_p value. As the K_i value increases, overshoot starts to increase in both controller and PI controller has a lower overshoot as compared to SIPIC controller. Rise time of both controllers are similar while PI controller shows slightly shorter settling time as compared to SIPIC controller.

When the K_p value is increased to 10, both controller experienced a decrease in overshoot but slight decrease in the settling time. Rise time remains the same as it is

the lowest possible rise time due to limitation of hardware. The pattern for overshoot is similar as before where overshoot increase alongside the K_i value with PI controller having lower overshoot than SIPIC controller. Similar trend can also be found in settling time of both controller. As K_i increases, both controller starts to have longer settling time and SIPIC controller perform slightly better in this aspect.

As the K_p value further increases to 15, PI controller continue to see an increase in overshoot while SIPIC controller experience decrease in overshoot. Rise time remains the same for both controller and settling time increased for both controller. The same trend is seen for both overshoot and settling time of both controllers as K_i value increases. When both K_p and K_i is 15 as seen in Fig. 15, PI controller performs better in terms of overshoot while SIPIC controller shows more ideal performance in terms of settling time.

4. Conclusion

To conclude this paper, a new type of anti-windup PI controller was used for the application of motor position control and the performance of the proposed controller was used to compare with the performance of a conventional PI controller. The controllers were tested under no load and under loading condition while two different inputs were used to test the controllers: 0˚ to 90˚ and 270˚ to 90˚. Results show that under no load condition, SIPIC controller performs better than PI controller by having lower overshoot and lower settling time across various gains. Under loading condition, PI controller showed to be unstable under some of the gains as it experience large amount of oscillations and overshoot as well as very long settling time whereas under the same gain, the proposed SIPIC controller still shows acceptable performance. As a conclusion, the proposed SIPIC controller shows a more reliable performance as compared to PI controller when experiment was conducted. A wider range of gain can be used for the SIPIC controller whereas PI controller only performs well under a small range of gain.

As this paper only compares the performance between the proposed SIPIC controller and conventional PI controller, the future work includes further validating the performance of SIPIC controller in motor position control by comparing it with other anti-windup PI controller. SIPIC controller can also be further refined to achieve lower overshoot, shorter rise time and settling time. Wider range of gain can also be used to test the performance of SIPIC controller to further test the stability of the controller.

References

[1] A. . Benmakhlouf, A. . Louchene, and D. . Djarah, “Fuzzy logic and modified crisp logic applied to a DC motor position control,” *Control Intell. Syst.*, vol. 38, no. 3, pp. 173–180, 2010.

[2] N. Bianchi and M. Dai Pre, “Active power filter control using neural network technologies,” *IEE Proceedings-Electric Power Appl.*, vol. 150, no. 2, pp. 139–145, 2003.

[3] V. Slapak, K. Kyslan, and F. Durovsky, “Position Controller for PMSM Based on Finite Control Set Model Predictive Control,” no. 1, pp. 17–22, 2016.

[4] K. Orman, A. Basci, A. Derdiyok, E. Engineering, and E. Engineering, “Speed and Direction Angle Control of Four Wheel Drive Skid-Steered Mobile Robot by Using Fractional Order PI Controller,” pp. 14–20, 2016.

[5] S.-Y. Chen and C.-S. Chia, “Precision Position Control of a Voice Coil Motor Using Self-Tuning Fractional Order Proportional-Integral-Derivative Control,” *Micromachines*, vol. 7, no. 11, p. 207, 2016.

[6] K. Kawamura and Y. Ishida, “Approach to New Model Recovery Anti-windup Scheme with PID Controller,” *2015 3rd Int. Conf. Artif. Intell. Model. Simul.*, pp. 208–212, 2015.

[7] C. T. Ling, “A New Anti-windup PI control for Motor Speed Application,” no. June, 2016.

[8] K. Sakai and Y. Ishida, “A Design of an Improved Anti-Windup Control Using a PI Controller Based on a Pole Placement Method,” no. 2, pp. 1–7.

[9] S. C. Pratama, E. Susanto, and A. S. Wibowo, “Design and implementation of water level control using gain scheduling PID back calculation integrator Anti Windup,” *ICCEREC 2016 - Int. Conf. Control. Electron. Renew. Energy, Commun. 2016, Conf. Proc.*, pp. 101–104, 2017.

eureca 2017 – Conference Paper
Paper Number 2ME25

Design and Fabrication of Small Vertical-Take-Off-Landing Unmanned Aerial Vehicle

Yasir Ashraf Bin Abd Rahman[1*], Mohammad Taghi Hajibeigy[2], Abdulkareem Shafiq Mahdi Al-Obaidi[3]

[1,2,3]*School of Engineering, Taylor's University*

[*]yasirashrafabdrahman@sd.taylors.edu.my

Abstract

Modern UAVs available in the market have well-developed to cater to countless field of application. UAVs have their own limitations in terms of flight range and manoeuvrability. The traditional fixed-wing UAVs can fly for long distance but require runways or wide-open spaces for take-off and landing. On the other hand, the more trending multirotor UAVs are extremely manoeuvrable but cannot be used for long distance flights because of their slower speeds and relatively higher consumption of energy. This study proposed the implementation of hybrid VTOL UAV which have the manoeuvring advantage of a multirotor UAV while having the ability to travel fast to reach further distance. The design methodology and fabrication method are discussed extensively which would be followed by a number of flight tests to proof the concept. The proposed UAV would be equipped with quadcopter motors and a horizontal thrust motor for vertical and horizontal flight modes respectively.

Keywords: UAV, VTOL, RC aircraft, drone

1. Introduction

Unmanned aerial vehicles (UAV) are aircrafts which are controlled remotely via direct radio frequency communication or are equipped with autonomous devices to performed autonomous mission flights. The active development in the field of UAV in recent years has led to its increase in versatility in terms of its functionality and range of application. Early UAVs development are generally divided into two separate types, Fixed Wing UAV (FWUAV), and rotorcraft UAV (RUAV). FWUAVs typically have longer endurance and thus can reach further than RUAV in a single flight, but require runways for take-offs and landings. RUAVs on the other hand, are more maneuverable and able to take-off and land vertically without any runway, but has much lesser endurance due to their low efficiency in power consumption and low speed.

Therefore, to bridge the performance gap between RUAVs and FWUAVs, the solution is to have a hybrid Vertical-Take-Off-Landing (VTOL) aircraft. This type of aircraft will have the advantages of both FWUAV and RUAV and to a substantial extent should be able to eliminate their shortcomings. In the aviation industry, major companies have already successfully mass-produced and commercialized numerous models of VTOL aircraft. A famous example of such aircraft is the Bell Boeing V-22 Osprey which combined the features of fixed wing aircraft and rotary wing aircraft via the concept of tilt rotor mechanism. The tilt rotor mechanism is only one of the concepts that was proven for successful VTOL flights. Other researchers have also explored other concepts to incorporate into similar hybrid VTOL aircrafts. In the small to medium UAV applications, particularly in the Radio-Controlled (RC) drone world, only a few small-scale projects have been successful in flying VTOL aircrafts [1]. Also, those projects that are successful experienced great difficulty in optimizing the transition flight from rotor to fixed wing flight and vice versa. In addition, manufacturers are still developing their own VTOL UAV for aerial-photography drone market, but they are still yet to be commercialized.

The hybrid VTOL UAV design, however, have its own shortcomings compared to both FWUAV and RUAV. The addition of extra propulsion system to cater for horizontal and vertical flights resulted in significant extra weight carried by the vehicle. Normally, a conventional RUAV model would only need four brushless motors for its vertical propulsion and other maneuvers. An addition of horizontal flight would require at least an extra motor for horizontal propulsion as well as a number of servo motors for different maneuvers. There is also a notable increase in the complexity of the design and control mechanism. The common VTOL UAV design can be classified into three types. This include 1) TYPE1, which is a fixed wing aircraft with tilting rotor mechanism, 2) TYPE2, which has no wings and has fixed vertical rotor(s), 3) TYPE3, which has wings and vertical rotor(s) [2].
Each of these designs have its own complexity, with the TYPE1 being most complex than others. Moreover, due to the difficulty in optimizing the transition flight from vertical to horizontal flight and vice versa, the VTOL UAV may lose its balance during the transition process and can lose a lot of altitude. Therefore, it is vital to design the VTOL UAV that is lightweight, able to perform transition flight safely and also relatively simple yet efficient propulsion system.

This study reviews previous attempts at developing a VTOL UAVs as well as current projects and combine suitable concepts into a better efficient prototype of a VTOL UAV. Particularly, this study would emphasize the control development on the transition flight mode for better stability and safety. This study proposed the implementation of a TYPE3 VTOL UAV without the tilting mechanism as the scope of this research. TYPE3 VTOL UAV is the least complex system and better stability and safety during the transition flight mode as compared to the VTOL UAV with the tilting mechanism. Another factor of the choice of VTOL type is limited time and cost factor.

The proposed aircraft motor configuration would consist of four motors for its vertical propulsion, a single motor for the horizontal propulsion and servo motors on the control surface for horizontal flight maneuvering. Basically, the vertical propulsion motors would be attached to the fixed wing platform to produce a hybrid VTOL UAV system. Unlike the tilt rotor VTOL UAV, the vertical propulsion motors would not tilt and would function to fulfill the vertical flight mode while the horizontal motor is used for horizontal flight. This would reduce the system's complexity as a result of different flight modes are controlled by separate actuators.

In this paper, theoretical concepts behind the flight dynamics of a VTOL UAV are established which would be the basis of this study. Later, detailed design process is presented where the estimations, calculations, selection of materials, conceptual designs and 3D modellings are justified by the mission requirement stated. At the end of the design process, fabrication and assembly process of a VTOL UAV prototype are done which are followed by a series of software simulations and actual flight tests to support the concept of a non-tilting rotor VTOL UAV.

The concepts of how a fixed wing aircraft and multirotor works are quite simple. However, developing a VTOL hybrid aircraft requires integrating the flight characteristics of both fixed-wing aircraft and multirotor platforms. Therefore, it is important to first have separate understanding on the general theory of how a fixed-wing aircraft and multirotor aircraft works as well as the effective control technique to stabilize the whole system.

The primary aim of this project is to determine the potential performance of a small VTOL UAV. First, the VTOL UAV is to be designed and fabricated using scientific methodologies. Then, a number of flight tests are performed under different weather conditions to assess the stability performance during hover, transition and winged flight. The secondary aim is to identify the flight duration of a VTOL UAV compared to a common RUAV of similar specifications.

2. Theoretical Backgrounds

2.1 General Theory

Basically, a VTOL aircraft has the ability to fly like a fixed-wing airplane and at the same time hover like a multirotor. A body fixed coordinate system is usually used in flight dynamics where the coordinate system is fixed relative to the aircraft.

For a multirotor aircraft in motion, it is appropriate to classify the three rotation axes that can alter the craft's attitude as 1) Roll: Rotation of x-axis, 2) Pitch: Rotation of y-axis, 3) Yaw, rotation of z-axis. These axes of rotation are shown in Figure 1 below.

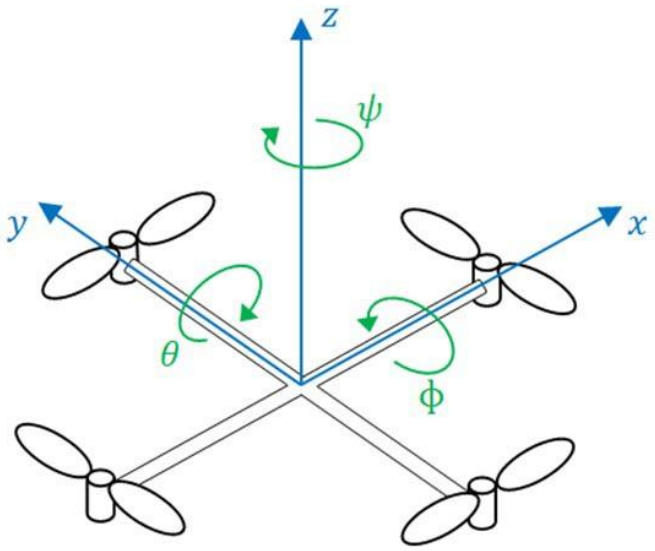
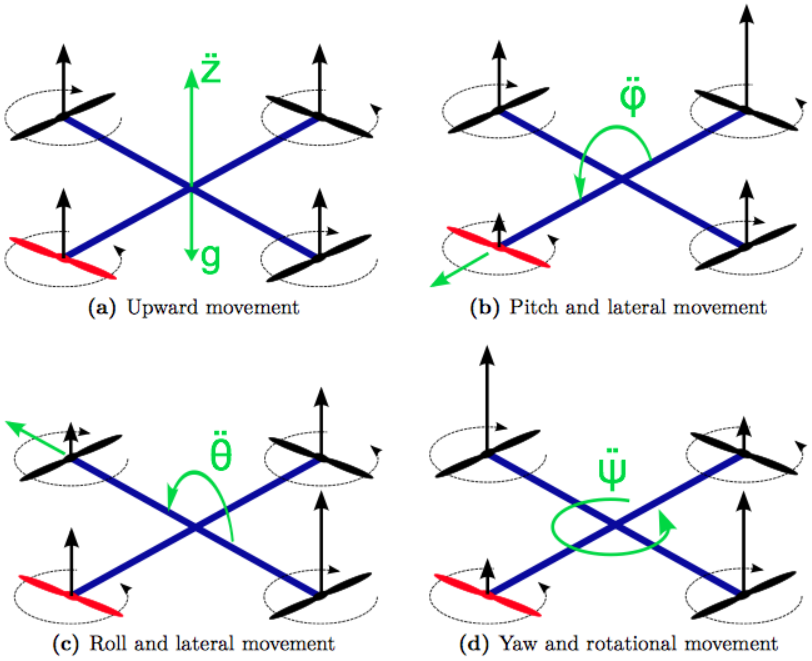


Figure 1: Coordinate system of a multirotor aircraft

A common multirotor propeller configuration usually consists of four propellers or better known as a quadcopter. Other known multirotor configurations include tricopter, hexacopter and octacopter. Different configurations are for different area of application and have performance variation in terms of flight time, agility, stability and payload capacity [3][4]. The propeller's main task is to generate enough lift force to bring the aircraft up to the sky and also deliver adequate thrust to move its current position to forward, backward, left and right. The attitude of multirotors is actuated by the difference in rotation speed of each propeller. Figure 2 shows how the aircraft's attitude change and the corresponding body movement when rotation speed of certain propellers is manipulated [5]. There are four basic movement for multirotors.



(a) Upward movement (b) Pitch and lateral movement

(c) Roll and lateral movement (d) Yaw and rotational movement

Figure 2: Attitude and Body Movement Change due to rotation speed change in individual propeller

The multirotor must be able to achieved a reasonably stable flight during hover before attempting to maneuver it in its pitch, roll and yaw axes. Stable flight requires that the pitch and roll axes must be first stabilized. The multirotor will be at risk of tipping over and crash if these axes are not controlled adequately. The pitch and roll attitudes are determined using the gyroscope and accelerometer which is built onboard the Flight Controller Unit (FCU). As for the yaw axis, it is less critical to stabilize the axis provided that the multirotor is still controllable. Unstable yaw axis would slightly drift the multirotor body in that axis but can be balanced by using the radio controller.

For a fixed-wing airplane in motion, the coordinate system is similar to that of the multirotor. A clear difference is that airplanes use propellants that is aligned to its fuselage for forward propulsion. Lift in this case is generated by the aerodynamic pressure difference between the upper and lower surface of the wing. The attitude of the aircraft is controlled using the control surfaces attached on the main wing, horizontal tail wing and vertical tail wing. The three control surfaces are called 1) Elevator: Control the pitch axis, 2) Aileron: Control the roll axis, 3) Rudder: Control the yaw axis.

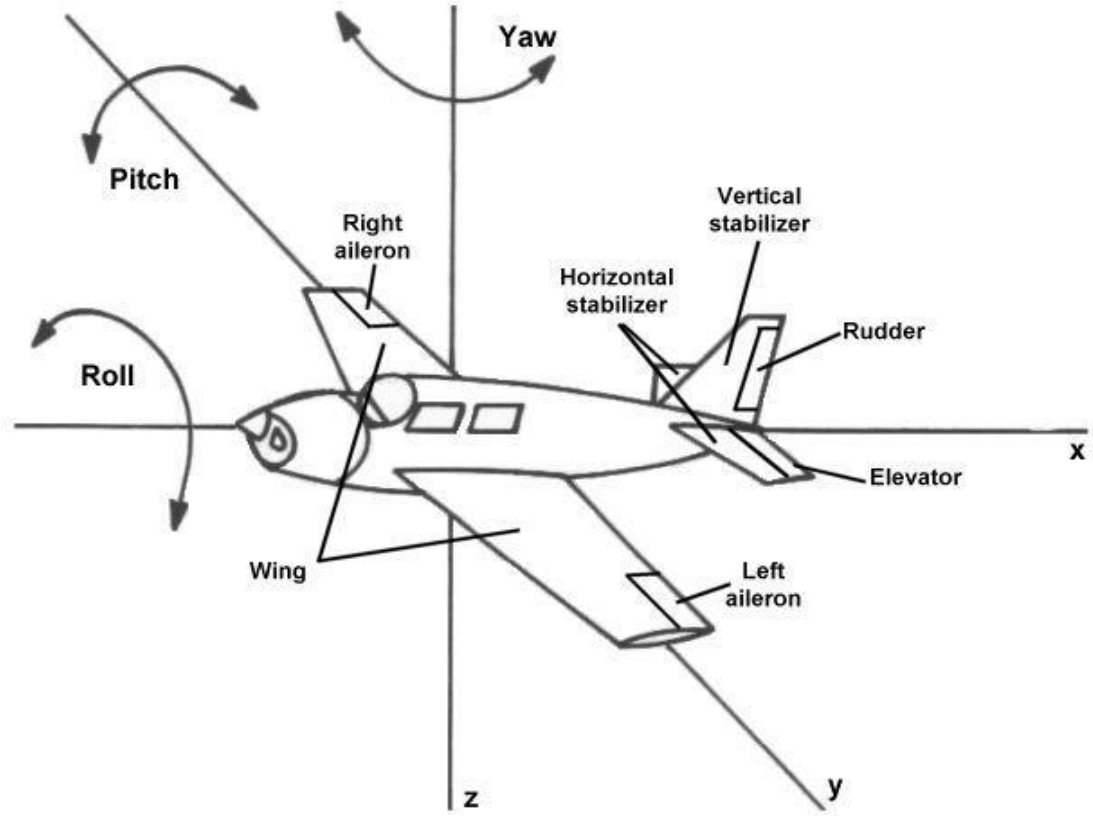


Figure 3: Coordinate System of a fixed-wing aircraft [6]

Similar to multirotors, to fly fairly stable while in straight-and-level flight, the roll and pitch axes must be stabilized properly. In full-scale manned aircraft, this can be done by directly trimming the ailerons and elevators. In the case of small-scale

unmanned fixed-wing aircraft, the roll and pitch axes can be stabilized by using the attitude sensors such as the accelerometer and gyroscope.

Designing and fabricating a hybrid VTOL UAV system involves considering the flight dynamics of both multirotor and fixed-wing systems. The dynamics would become more complex due to propulsion units for longitudinal and vertical movements. To simplify the hybrid VTOL UAV concept, during vertical flight mode, the UAV is assumed to follow the flight dynamics of a multirotor system, whereas during horizontal flight mode, it is expected that the craft's flight dynamics follow fixed-wing flight dynamics. During the transition flight mode, the aircraft will be in a varying stated and the gravity can be overcome by both vertical and longitudinal propulsion units until the craft has complete the transition process. Optimizing the altitude requires the controlling motor outputs properly. In the transition to horizontal flight mode, lack of vertical motor outputs while not achieving minimum stall speed would severely decrease the altitude. Inversely, while transiting to vertical flight mode, reducing the longitudinal motor output below minimum stall speed before the vertical motors achieve adequate thrust would lead to reduce in altitude. It should be noted that maximum airspeed is limited to the rated power of the longitudinal propulsion unit. Moreover, additional structure to support the vertical propulsion system may add to the drag during horizontal flight mode. However, these extra drags can be counteracted by having wings with high lift coefficient characteristics.

2.2 PID Control Technique

Proportional, integral and derivative (PID) control is one of the most attractive techniques used to stabilize as well as optimize the control of UAVs [7]. During flight, it is preferred to have a stable flight where the aircraft maintained its desired attitude effortlessly without external inputs from the user. In cases where wind or other external disturbance detected, the FCU as processing unit will compute the errors between current and desired attitude and perform necessary corrections. PID control try to balance out these disturbance by giving out more motor and/or servo outputs accordingly.

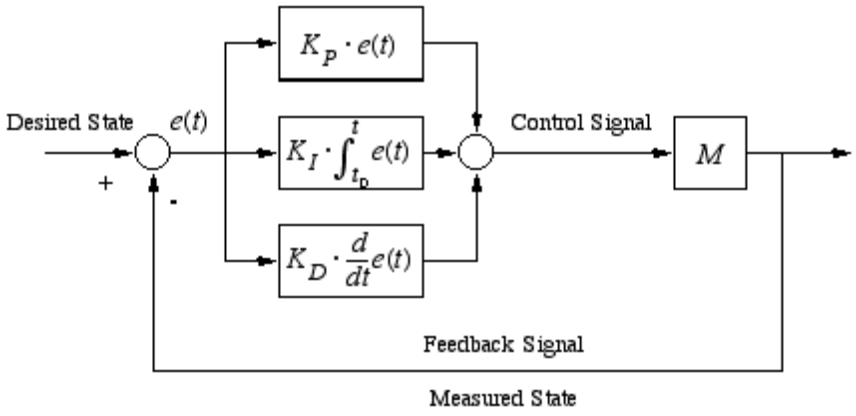


Figure 4: General PID Block Diagram

PID control can be easily understood by representing it in block diagram shown in Figure 4 above. The steps for PID control are:

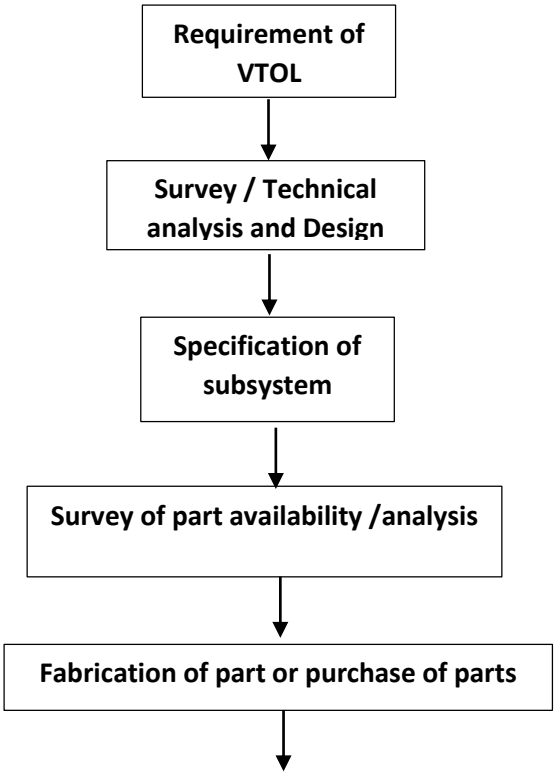
1. The desired state is first determined and the previously measured state is presented at the beginning of the loop to compute the state error *e(t) = Desired State – Measured State*
2. The proportional, integral and derivative terms are calculated as K_P*e(t), K_I*(integral of e(t))* and K_D*(derivative of e(t))* respectively.
3. . The 3 terms are totaled up to obtain the motor/servo output, *u(t) = P + I + D*

In reality, it would be difficult to obtain a stable system by concurrently tuning the control gains, (K_P, K_I and K_D) of the PID controller on all three axes. Therefore, the more critical axes, which are the pitch and roll are first stabilized separately before the yaw axis. PID Control method will yield the desired stability performance characteristics on all axes when the control gains are tuned correctly.

PID control is the most widely used method in theoretical approach and engineering applications partly because exhaustive dynamics models are not required to implement this method. Obtaining the best control gain parameters can be done by modifying the gains live during flight tests according the control effect of the UAV until the desired response is achieved [8]. Many researchers who have resorted to develop UAV based on PID control have achieved stable flights on their experimental platforms in different modes. Therefore, due to its reliability, PID control is adopted in this study.

3. Design Methodology

3.1 Flow Chart



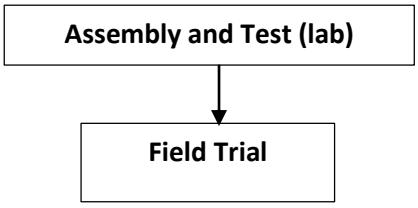


Figure 5: Design Methodology Flowchart

The flow chart for the overall research design (Figure 5) was prepared at the beginning of this project. This flow chart will serve as the general guidance to steer this project on the right direction. The flow chart is divided into two parts, in which the first part concentrate on the design and the second part focus on the fabrication and flight tests. The outcome of this research is to study the performance of the proposed hybrid VTOL UAV by analysis of flight data recorded during test flights.

3.2 Specifying Requirements

The requirements of the proposed TYPE3 VTOL UAV are established after considering the information obtained from literature survey conducted. These requirements are set in a way that the UAV is practically feasible in term of design, fabrication and flight test.

There are a few basic UAV requirements established in this study. First, TYPE3 VTOL UAV, which consist of conventional fixed wing aircraft attached with fixed vertical rotors to be incorporated into the VTOL design. The UAV should have long flight range and able to reach desired location as fast as possible at reasonable time. The UAV should be maneuverable at narrow and confined spaces like a helicopter. Maximum payload of 1 kg is to be allowed which may consist of imaging equipment, gimbals, etc. The UAV should be capable of performing VTOL operations with acceptable safety and stability characteristics. The transition flight mode from rotor flight to fixed-wing flight and vice versa is to be handled manually or autonomously. All-Up-Weight (AUW) of less than 3.5 kg. Wing span of about 1.5 – 2.0 m. Five-rotor system (vertical quadrotors and single horizontal rotor) for stability and reduction in complexity. The expected cruise velocity range of approximately 15 – 20 m/s. The stall speed is thus should be around 70% of the minimum cruise velocity. Lastly, it would be equipped with versatile flight controller unit able to handle manual controls and execute autonomous missions.

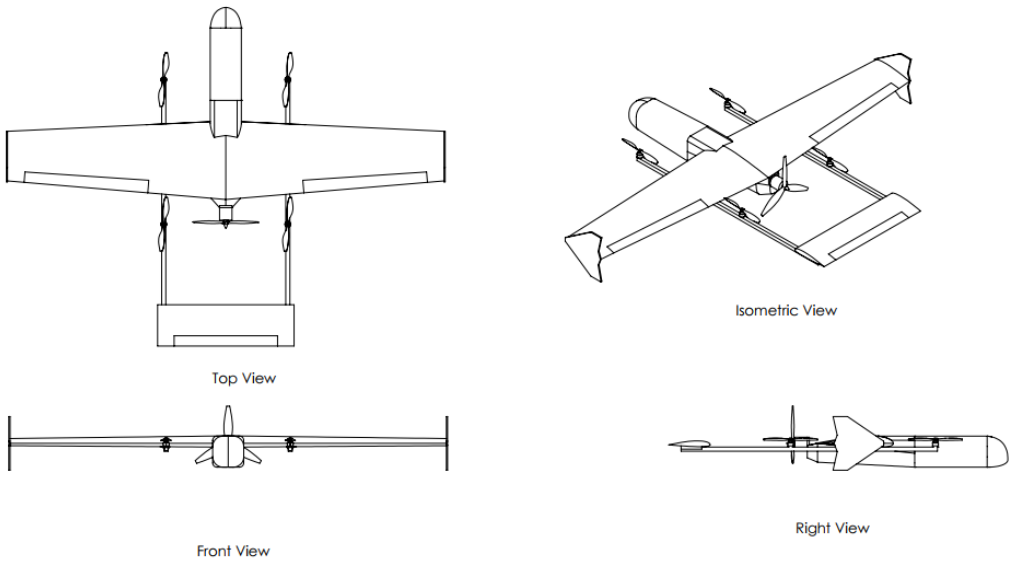


Figure 6: Overview of the proposed VTOL UAV

3.3 Test Protocol

The prototype would be conducted in both manual and autonomous flights. The UAV would take off vertically in vertical flying mode, then perform transition to horizontal flying mode, fly straight and level to a certain designated waypoint, then perform transition to vertical flying mode again and finally land the UAV safely. For manual flight, a ground user would pilot the UAV via radio control transmission.

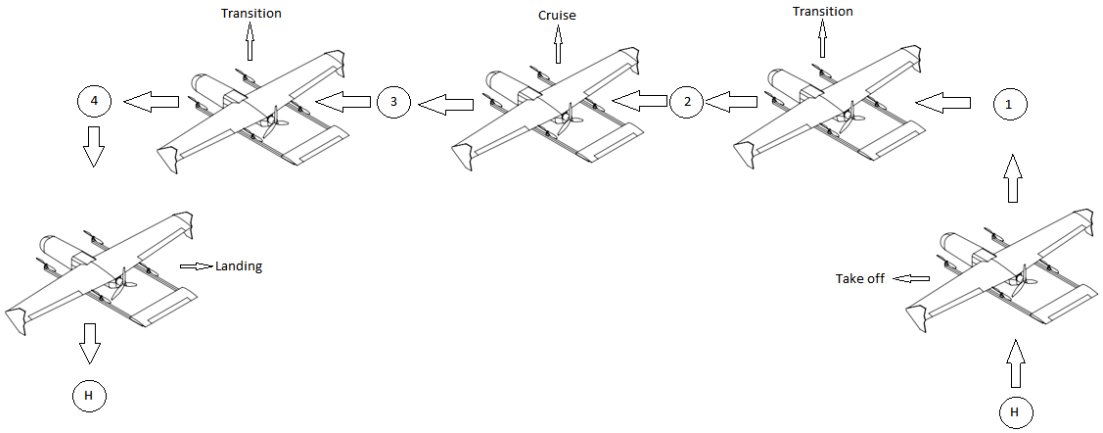


Figure 7: Prototype Mission Profile

From Figure 7, the biggest challenge is to perform the transition flight from horizontal flight to vertical flight mode and vice versa. During this portion of the flight, the UAV may lose some altitude due to the reduction in lift force vector while slowing down the vertical motors. Hence, the horizontal motors need to produce enough thrust to accelerate the UAV quickly for the wings to replace the vertical motors in generating lift. Another method to address this possible altitude lose is to develop and effective

control system where the vertical motors would continue to generate enough lift while in transition until it passed the minimum stall speed.

3.4 Structural Design Parameters

To design a small-scale VTOL UAV, it is important to limit certain parameters of sizes to a practically reasonable figure so that other parameters concerning dimensions would be feasible for fabrication. The design parameters chosen should also obey known theoretical concepts and equations to confirm that the VTOL UAV will be able to accomplish stable and safety flights across all its flight modes. The general procedures to determine basic structural design parameters are:

1. Estimate the All-Up-Weight of the aircraft
2. Wing Design: Determine the size of the wing loading, wing span, aspect ratio and chord
3. Fuselage Design: Determine the size of the fuselage
4. Tail Design: Determine the size of the tail wing and its distance from the main wing

These general procedures will be used to estimate the size of the prototype. After fabrication and flight tests, the actual dimensions will be adjusted accordingly.

3.5 Weight Estimation

Before fabricating the prototype, some components which are readily available was weighed while the weight of components that needed to be work is estimated. The total All-Up-Weight (AUW) would be designed slightly higher than the total estimated weights. This is because normally, the actual prototype weight will be higher than the initial weight calculations. Estimating the extra weight also increase the margin for the extra payload. It is important to determine the right AUW for the prototype as the subsequence design calculations are based entirely on this parameter.

Table 1: Weight Estimate for proposed prototype

Item	Mass (g)	Quantity	Total Mass (g)
Motor	85	5	425
ESC and PDB	65	5	325
Battery 3s 6000mAh	422	1	422
FCU, gps, power module, receiver	114	1	114
Propeller	12	5	60
Servo	60	4	240
Aluminium frame	700	1	700
Polystyrene Board	600	1	600
Plywood base	200	1	200
Consumables (bolts, nuts, cable ties, glues, etc)	150	1	150
Total All-Up-Weight			3236

Hence, AUW would be estimated a bit higher than the calculated value to be 3.5 kg.

3.6 Wing Design

First, Wing Loading, W_l is to be calculated (Equation 1).

$$W_l = \frac{AUW}{S_W} \tag{5}$$

The wing loading needs to be as low as possible to ensure minimum stress exerted during flight can be sustained by the wing. Wing loading value is more important than the actual weight of the aircraft because it tells how much weight is carried by each unit of wing area, S_W. From literature survey, 10 kg/m^2 is selected which would make S_W to be about 0.32 m^2. Next, the wingspan, b can be calculated from the wing's Aspect Ratio formula given in Equation (2) below.

$$AR = b^2/S \tag{6}$$

Generally, for normal aircrafts that are designed for low speed flights have typical Aspect Ratios around 5-10. Higher Aspect Ratio increase the gliding capability of the aircraft and can fly at lower speed. AR = 10 is chosen so that the proposed VTOL UAV can safely glide in case of motor failure. Therefore, b_W = 1.8 m.

To determine the wing chord, C_W, the wing is considered to have rectangular shape, this is shown in Equation 3.

$$S = b * C \tag{7}$$

Hence, C_W = 0.18 m

For the Aileron sizing, the suitable Aileron area, S_a = 20% of S_W
Therefore,
$S_a = 0.32*0.2 = 0.064$ m^2
$b_a = (0.064*10)^{0.5} = 0.8$ m
$C_a = 0.064/0.8 = 0.08$ m

For the chosen wing size, the Reynold's number, Re have to be confirmed to be in the laminar region. Reynold's number is given as in Equation 4.

$$Re = \frac{VC}{\nu} \tag{8}$$

At STP air condition, ρ = 1.225 kg/m^3, ν = 1.46e-5 m^2/s

For the estimated cruise speeds,
$Re_{@V=15m/s}$ = 1.85e-5
$Re_{@V=20m/s}$ = 2.46e-5

Therefore, the flow will be in the laminar region.

3.7 Tail Design

For the tail sizing, the calculations are similar to the wing sizing calculations. For this study, a flat horizontal tail consisting of only elevator control surface is chosen. The yaw axis of the prototype would not be controlled as it would add to the complexity and for the time being is unnecessary to proof the concept of hybrid VTOL UAV. Instead, the yaw axis can still be controlled while the UAV is in vertical flight mode.

The initial step is to determine the location of the tail wing from the main wing. This location should produce enough moment to control the pitch axis. As a general rule, the distance from leading edge of the wing to the leading edge of the tail should be around thrice of C_W, in this case it would be approximately 0.6 m.

The next step is to determine the surface area of the horizontal tail, S_{ht}, which is normally about 30% of S_W.

$S_{ht} = 0.3*0.32 = 0.096\ m^2$

The Aspect Ratio of horizontal tail is taken as 3. The subsequent calculations to find tail span and tail chord are the same as Equation (2) and (3) respectively. This gives b_{ht} = 0.53 m and C_{ht} = 0.18 m.

For the Elevator sizing, the the suitable Elevator area, S_e = 20% of S_{ht}
Therefore,
$S_e = 0.096*0.2 = 0.0192\ m^2$
$b_e = (0.0192*3)0.5 = 0.24$ m
$C_e = 0.0192/0.24 = 0.08$ m

3.8 Fuselage Design

The fuselage does not have any specific calculations as the prototype will use the F450 quadcopter frame as the base fuselage. This frame's aerodynamic shape can be improved to cater for the horizontal flight mode by covering the center hub using light materials and incorporating shape that can improve lift and reduce drag. Covering the center hub also protects the exposed main electronics part such as the flight controller unit, battery, GPS unit and power distribution board.



Figure 8: F450 frame

3.9 Material Selection

Key and critical parameters in the design of such UAV is choice of material. Every single part from the smallest item such as screw to the largest part such as wing, weight is the critical factor when come to selection. Ideally the lightest material and yet roust against mechanical (drop, shock) and environment (water proof, salt spray compliant, altitude /low pressure, oil/chemical contamination/corrosion) shall be selected. Such UAV that normally use in harsh environment shall comply with some international standard of complaint to ensure the product is robust and can be use in any kind of application/situation. High investment in design/fabrication and qualification test shall be anticipated.

However, final choice of material and choice of manufacturing/fabrication techniques is also depending on cost affordability and quantity to be produced. For this study which is consider a prototype or PoF (Proof of Concept) model the choice of material is not at all compliant to the above Mil Standard. What most important in this study is the VTOL is really working and demonstrable. Material for the wing should be light enough and easily available. In this study, wing material is made out of Depron foam which is very lightweight, easy to shape and low cost [9]. The frame support would consist of combination of the ready-made F450 frame to house the electronics components and hollow 1" by ½" aluminium bar.

3.10 Electronics Design

No specific electronic design take place in this stud. Most electronic parts such as the motor, control module, radio frequency modules and battery/charger are COTFs (commercial on the shelf) item. Main activities in the electronic is on parts/systems integration activities.
Key and critical electronic part /subsystem of the UAV are:

- Radio Remote control
- Brushless Motor
- Battery capacity /voltage

3.10.1 Brushless Motor

Most important in the selection of this motor are specification of RPM vs supply voltage and durability and also some spec of water proof and temperature. Long flight duration could cause heat issue and to some extend it could melt the insulation of the motor coils and causing short circuit. It is advisable not to use the motor up to the maximum limit of voltage supply. For real design for commercial use, water proof or splash proof is a must for this motor. IP65 standard which outlined protection against contact and infiltration of water and dirt (IP) standard recognized internationally and is available free download from internet. For this study which is proof of concept project, requirement such as IP65 is not really consider. What most important is the capability in term is RPM and weight.

3.10.2 Battery

There are many battery technologies available commercially, named NiCd, Li-Ion, Li-Polymer, Lead Acid etc. For this mobile application, capacity density (how

energy stored in a specific volume/weight) is critical. The smaller the size with the higher energy density is the preferred technology. As far as today is concern Li-Ion battery is the most common battery technology for mobile application. It is a stable technology. Li-polymer is better in term of energy capacity and with flexible shape, but is more expensive. NiCd is obsolete technology and Lead Acid is for automotive application.

Rechargeable Li-Polymer battery is the best choice, cheap and good energy capacity and current rating value. In addition, this batter has a good life cycle (charge/discharge) 1000 cycle, long lasting usage.

3.10.3 Electronics Layout and Operation

Figure 9 below is the wiring diagram on the electric part of the VTOL-UAV. The heart or the core engine of the system is the Pihawx Flight Control Unit, a control processor unit. Its control the rotation or RPM of the motor during takeoff, landing or horizontal movement of the VTOL-UAV.

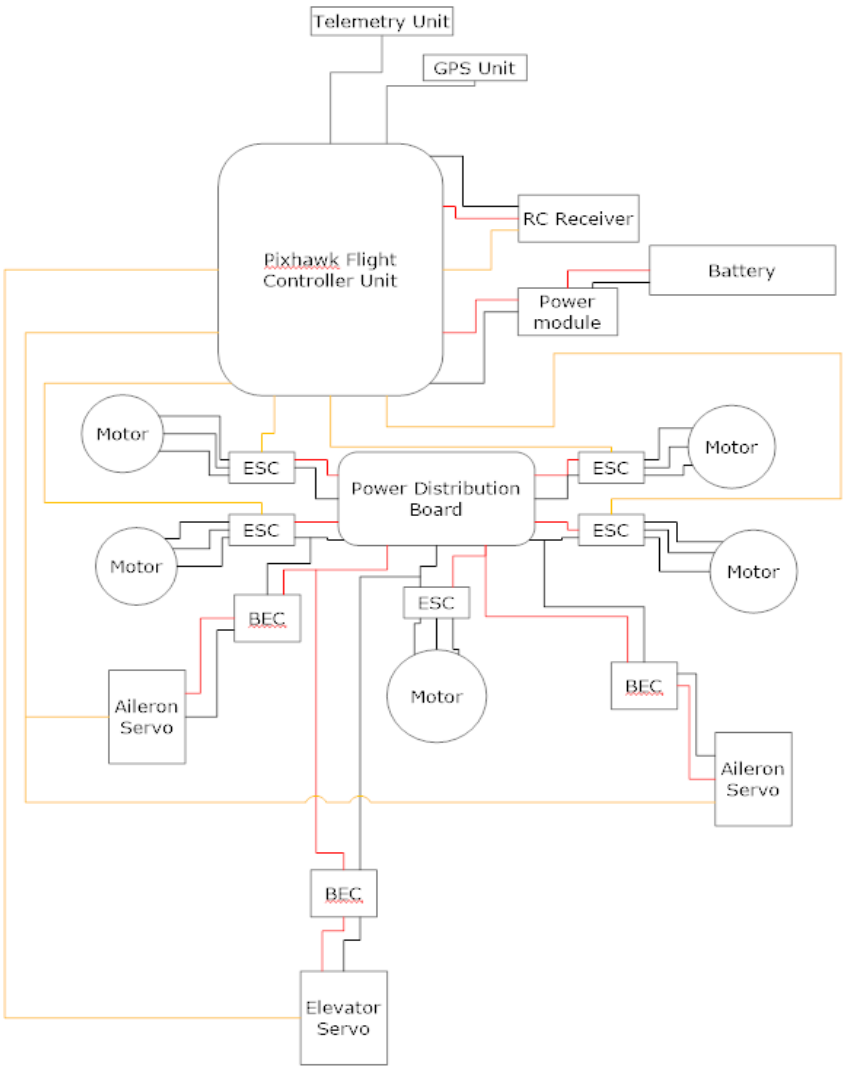


Figure 9: Wiring Diagram for Onboard

The input of speed (increase or decrease the motor RPM) are come from the operator at the ground. Data was transmitted from the transmitter RC at the ground to receive remote control on the VTOL-UAV by microwave signal operating at 2.4Ghz (ISM unlicensed band for commercial application). Other data transmitter from the ground is the controlling /navigation info for the aircraft. The range (how far the UAV can fly from the operator) is determined by transmitted power of the RC at the ground and the receiver sensitivity of the RC receiver on board the UAV. It must me line of sight link, i.e. any blockage such as rain, cloud, trees will degrade the reachable range of the remote control.

Beyond the reachable range of the RC or due to blockage it will cause the VTOL-UAV be flying with control and the risk it fall/drop to ground will be unavoidable.

On board of the VTOL-UAV there is GPS and telemetry unit. GPS device read the position, speed? and altitude of the UAV. These GPS data together with information on battery status and sensor (such as camera) could be send back to the ground center the telemetry transmitter operating at 915Mhz. In this prototype mode camera was not installed as it is not part of the scope of the project.

The supply for all the system is comes from the reachable 11.1V LI Ion battery. The battery could be later change to 14.8V (will extra cell) to increase the RPM of the motor, in case the 11.1V does nt adequate to lift the VTOL-UAV.

The duration of the flight depends on the capacity of the battery. The higher battery capacity the longer the VTOL-UAV can fly.

3.11 VTOL mechanism

Key element to ensure the VTOL capability of the four (4) motors with rotary blade stability to lift the load. All the four rotary blades will be at the same speed (Rotation per minute) and acceleration rate i.e. changing the RPM from one state to another state. Increasing the RPM mean increasing the height or takeoff stage. Decreasing the speed or RPM mean reducing the altitude or to land. Same RPM for all the vertical blade and weight balance are the key to ensure stability during takeoff landing and horizontal movement. The speed of the propeller and stability will be achieved by mean of PID stability control techniques as described in the earlier section 3.2 above.

Horizontal movement (speed of the UAV) is by mean of controlling the RPM of then horizontal motor/propeller. Attitude control and stability is achieved by adjusting the control surface accordingly and tuning the PID control gains. Manual adjustments of speed/RPM of all motor/propeller are remotely done by mean of radio remote control while during autopilot missions, the UAV would follow the designated speed as programmed in the software.

3.12 3D Modelling

The 3D modelling is done in Solidworks software. Basically, the critical parts that need to be modelled are the main wing and the horizontal tail wing which would

be made from Depron foam. Other parts such as the plastic and aluminium frames are less important to model because these parts are known for their reliability and strength during actual flight test and would not be easily be damaged by light crashes. The steps for the 3D modelling are:

1. Determine the airfoil shape of the wing
2. Project the airfoil cross-section into 3D model
3. Assemble of the wings with the frame

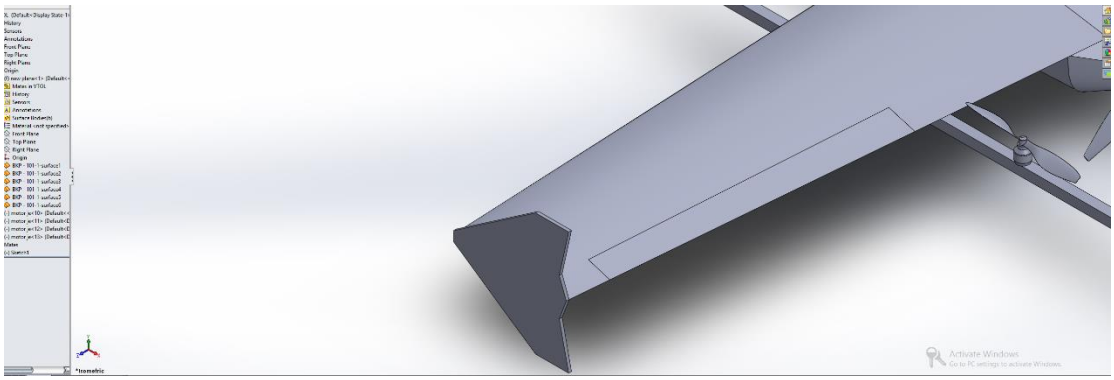


Figure 10: 3D Modelling of Wing Section

The cross-section (airfoil shape) of the wing is modelled using standard NACA coordinates which are available online. For the proposed prototype, the suitable airfoil would be the NACA 3414 airfoil family. It has low camber and the lower surface is quite flat and therefore would produce good Lift-Drag ratio for the estimated airspeeds.

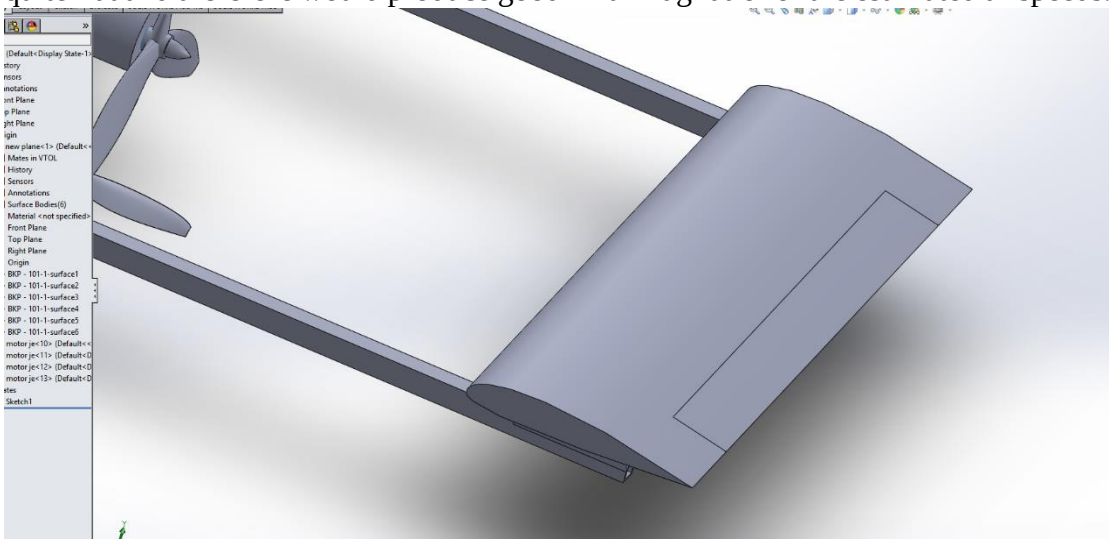


Figure 11: 3D Modelling of Tail Section

For the horizontal tail cross-section, NACA 0012 airfoil family is used which is thinner and result in lower drag. As calculated before, the area of the horizontal tail is quite small and therefore the tail is expected to be able to withstand pressure during flight. In addition, both the main and tail wing would be reinforced with aluminium angled beam if the actual flight tests fail to sustain it from crashes.

3.13 Software setups

Mission planner software is used to setup the Pixhawk flight controller unit. This software uploads the correct firmware to Pixhawk to match the prototype's vehicle type which is a hybrid VTOL UAV. This software is also used to tune the PID control gains to achieve optimum stability. This can be done during actual flight tests where the gains are adjusted accordingly by the pilot or can be set before flight tests and Trial-and-Error method is used to obtain the best result.

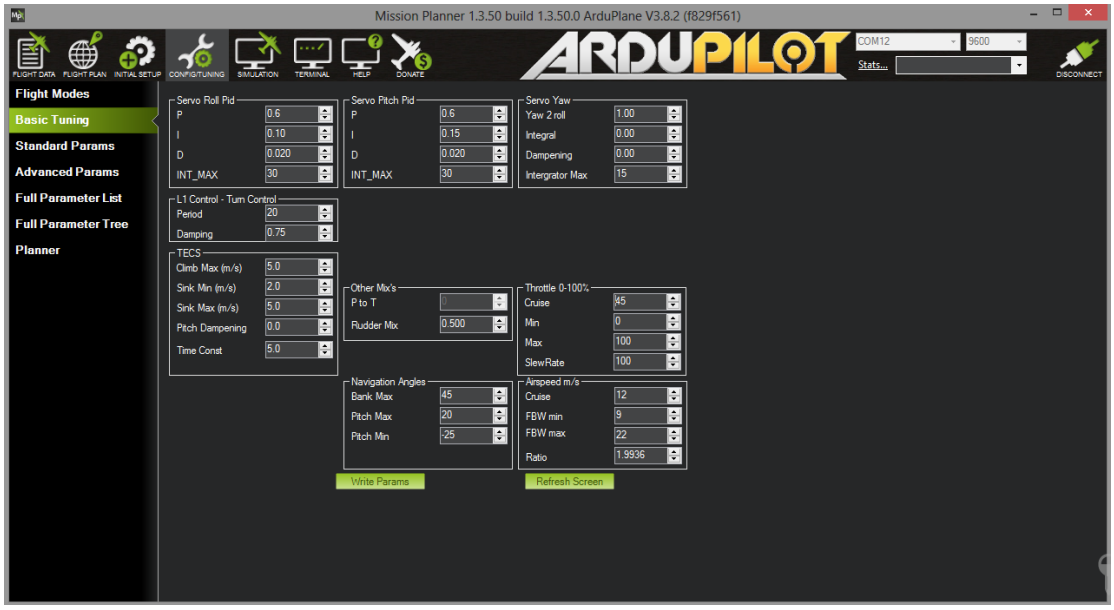


Figure 12: Mission Planner PID Tuning Tab

4. Results and Discussions

The fabrication was done successfully and the final prototype was tested to be fully functional. The built of the prototype is shown in Figure 5.1. After complete fabrication and assembly has been done, physical inspection along with subsystems and full system tests were performed.

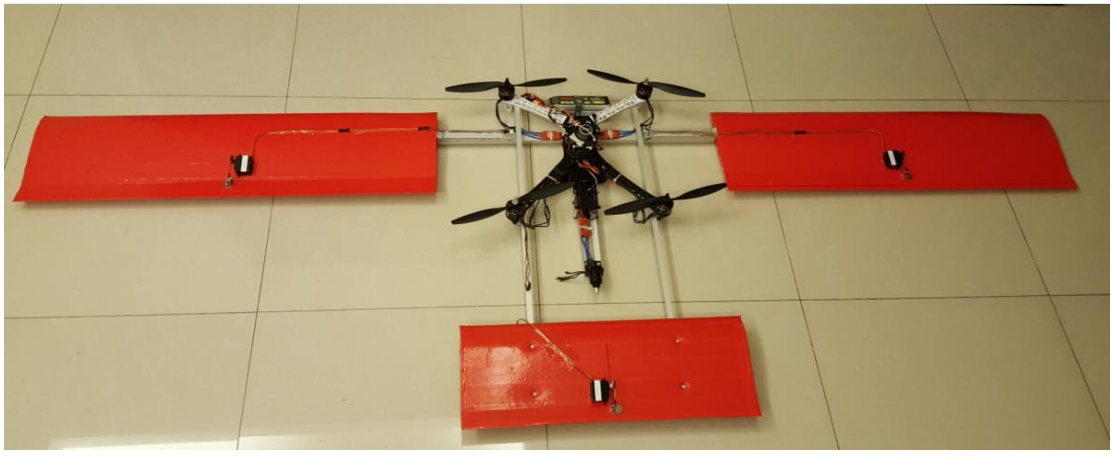


Figure 13: Final Prototype After Complete Fabrication and Assembly

Apart from this, the dataflash logs from actual flight tests were successfully recorded for further analysis. Using the advanced FCU which is equipped onboard the system, various type of data can be recorded. However, the data that are of interest for this project includes the PID response performance within the 3 axis of rotation, the vibration level about the three axes and also the flight trajectory data.

The flight modes that were used when the data was recorded are stabilize, altitude hold and loiter mode. These three modes are the flight modes in vertical flights. As for the horizontal flight modes, the flight tests could not be done yet due to limitations in available open space that are safe for flight tests. In stabilize mode, the position and altitude control is performed manually. In altitude hold mode, the altitude is controlled autonomously while the UAV position can still be drifted due to wind. In loiter mode, both altitude and position hold is controlled autonomously. In all these three modes, the accelerometer onboard the FCU is automatically stabilized where minimum user intervention is required to hold the UAV in a perfect hover.

The graph shown in Figure 14 and Figure 15 highlight the vibration level (m/s/s) as well as the roll response (m/s/s) against time. These graph is display the flight time of about 1 minute to ease the visualization of the graphs. In summary, the stability performance in roll and other axes was at acceptable levels where the response of the system, recorded in unit of m/s/s, followed closely to the desired inputs either from the user or the FCU itself as it tried to auto-stabilize the axes continuously. Further tuning of the PID gain values may be required to obtained a more desired performance. As for the vibration levels, the values recorded also fell within acceptable level of vibrations in all axes (below 60 m/s/s). This suggests that for future works, it would be suitable to install a camera onboard for in-flight monitoring and for other purposes.

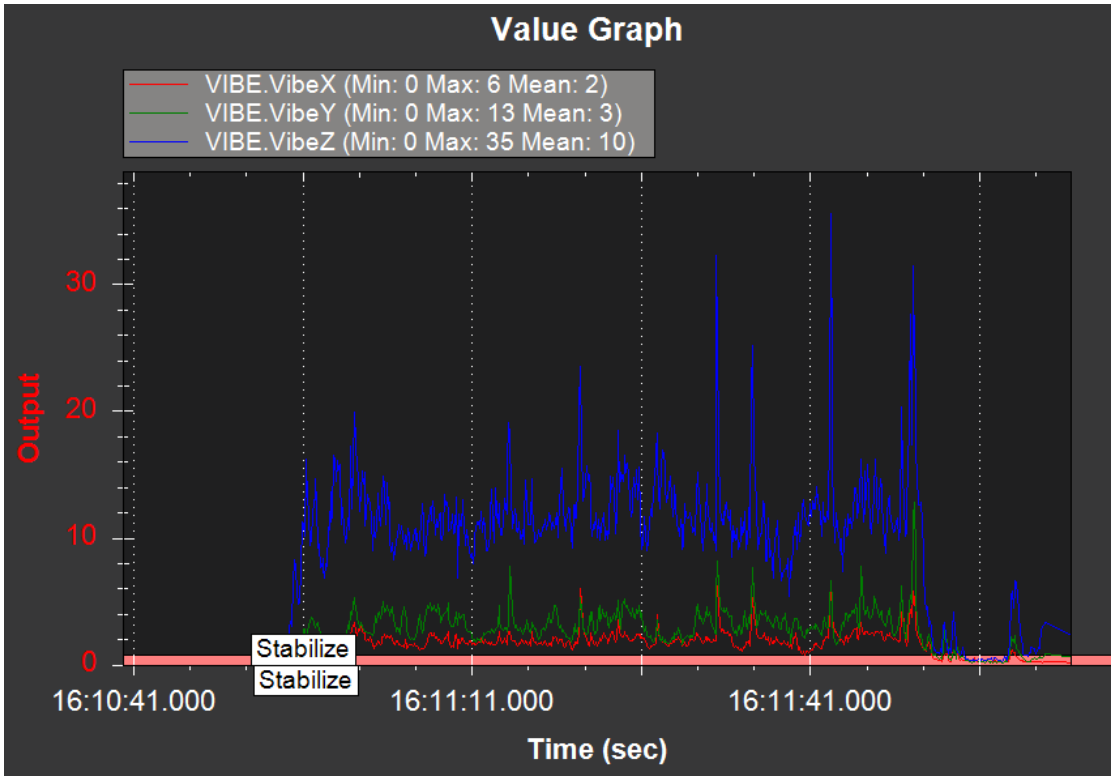


Figure 14: Graph of Vibration levels in all three axes.

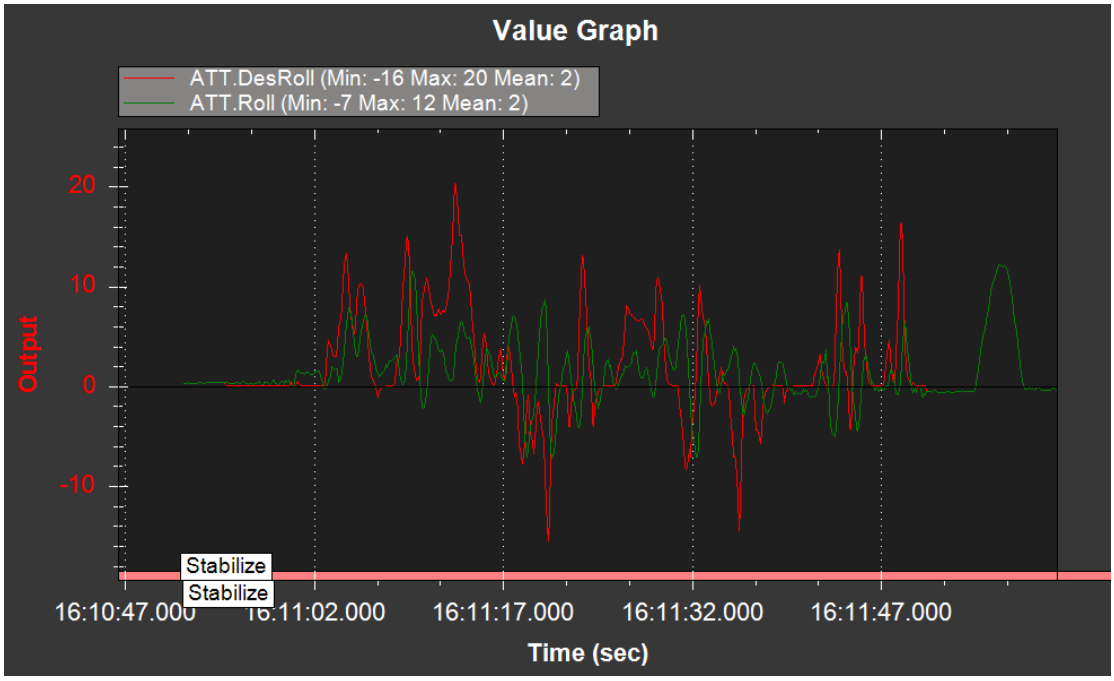


Figure 15: Graph for desired roll and roll response axis

5. Conclusion

Based on the theoretical study and flight data analysis, the proposed hybrid VTOL UAV system would achieve the predicted flight performance in terms of stability and flight range. This study encountered some challenges where the fabrication of the prototype cannot be completed within the specific time due to delay in receiving new part (motors) due to defect and also sourcing the right material for the wing.

6. Future Work

The model VTOL-UAV assembly are still in progress. Main components such as the motors/ and RCs are functional well. Below show some of the pictures of parts or and the construction of the assembly which is still in progress.

The design and development of "VTOL" vertical takeoff and landing UAV prototype is really a preliminary stage in the design, and commercialization of this platform needs much more improvement. With the limitation of facilities, budget and expertise, it is difficult to release the prototype to fully meeting the targeted objectives. The VTOL is not only mechanical product that require Only mechanical expertise, it does require competency in electronic and RF (Radio frequency) communication as well. Using COTF solution for the electronic and communication could be adequate as stating point in the study phase but customization does required in order to be able to meet the desire targets I,e. range, robustness, interference free etc.

The proposed product is not a hobby kind of UAV, it is rather to be used for professional application. Certification and validation by authorized agencies such as DCA and SIRIM is required. The following are recommendation and steps in order to proceed the project.

7. References

[1] A. K. Patra, K. Patel, G. S. Bundela, and V. P, "Design and Development of Transition Autopilot For VTOL UAV," *Int. J. Innov. Eng. Res. Technol.*, vol. 4, no. 6, pp. 57–72, 2017.

[2] D. Jo and Y. Kwon, "Analysis of VTOL UAV Propellant Technology," *J. Comput. Commun.*, vol. 5, pp. 76–82, 2017.

[3] V. Kadamatt, "Tricopter vs Quadcopter vs Hexacopter: A Comparison," *Droney Bee*, 2017. [Online]. Available: http://www.droneybee.com/tricopter-vs-quadcopter-vs-hexacopter/. [Accessed: 24-Oct-2017].

[4] F. Thomas, "What is a Tricopter, Quadcopter, Hexacopter and Octocopter," *Droners Guides*, 2017. [Online]. Available: https://www.dronersguides.com/what-is-a-quadcopter/. [Accessed: 24-Oct-2017].

[5] S. Said, "Quadcopter Mechanics," 2014. [Online]. Available: http://uav-society.blogspot.my/2014/06/quadcopter-mechanics.html. [Accessed: 24-Oct-2017].

[6] J. Yoon, "Adverse Yaw and Aircraft Turns," 2001. [Online]. Available: http://www.aerospaceweb.org/question/dynamics/q0045.shtml. [Accessed: 24-Oct-2017].

[7] J. Dryden and R. Barbaccia, "Quadcopter Design Project," 2014.

[8] L. Zhong, H. Yuqing, Y. Liying, and H. Jianda, "Control techniques of tilt rotor unmanned aerial vehicle systems : A review," *Chinese J. Aeronaut.*, vol. 30, no. 1, pp. 135–148, 2017.

[9] M. F. Saharudin, "Development of tilt-rotor unmanned aerial vehicle (UAV): material selection and structural analysis on wing design," in *IOP Conference Series: Materials Science and Engineering*, 2017.

eureca 2017 – Conference Paper
Paper Number 2ME26

Design and Analysis of an Eddy Current Braking System

Yeoh Joe Han[1*], Douglas Tong Kum Tien[2], Mohd Farid Aladdin[3]

[1]*Department of Mechanical Engineering, Taylor's University, Malaysia.*
[2]*School of Engineering, Taylor's University Malaysia*
[3]*School of Engineering, Taylor's University Malaysia*

[*]joehan.yeoh@sd.taylors.edu.my

Abstract

The biggest challenge of current high speed rail in a train is getting it to stop. The operating speed of these trains has placed a heavy load on brakes, causing it to wear out quickly thus required more frequent maintenance and replacements. This posed as a large disadvantage to its operating cost and safety rating. The idea is to utilize contactless braking as an alternative solution; circular eddy current braking system. Circular eddy current braking system works by converting the mechanical energy to heat and is wasted away by dissipating it to the surrounding. This causes massive amounts of heat generated and dissipated to the surrounding which negatively affects the lifespan of the mechanical components. This study is intended reduce the heat generated from eddy current braking and also to study the possibility of circular eddy current brakes in recycling the mechanical energy to electrical energy by implementing a generator to simultaneously function along the circular eddy current brakes which could also contributes to the braking force as well. The study is conducted through simulation using COMSOL multiphsysics to measure the current density, heat produced in watts and time taken for the disc's angular velocity to achieve zero. From the results, it is shown that by changing the type of material for the disc, the overall heat generated from braking has been reduced by approximately 19.68%. Throughout the substitution of material, despite the reduction in heat generation, the braking force did not experience reduction in strength and is still able to maintain the same braking time.

Keywords: Contactless Braking, Circular Eddy Current Braking System, Energy Recycling, Regenerative Braking, Generator

1. Introduction

The primary objective for railway transportation is to get from a departure point to designated location within the lowest travel time possible. As such requirement has brought railway transportation to the development of high speed railway. In order to be categorized as a high speed rail, the trains are required to be able to achieve a speed limit of approximate 250km/h on specific tracks and at least an approximation of 200km/h on alternative sections of the tracks [1]. With travelling time significantly improved, productivity increases and in turn, the overall transportation efficiency benefits greatly.

The conventional braking system currently implemented is known as the "dynamic and regenerative braking" system which basically is an electrical traction motor system that is electrically powered and coupled with direct current generators to slow and stop the train [2]. This form of braking is categorized under contact braking where parts are in contact generating resistance for the said desired output [2].

However, these conventional braking systems are prone to overheat with generally being exposed to high angular velocity and inertia. Inducing the electric traction motors to heat exposure for a long period of time would cause damage to the insulator through premature aging, instability characteristics of traction motor due to change in resistance when heated and reduced mechanical strength of the conductors and insulation, ultimately resulting engine failure [3].

For eddy current braking, the concept revolves around magnetism which obeys the Faraday's Law and Lenz's Law. In layman terms, braking is induced from introducing same polarity against each other which results in repelling motion to create resistance in motion. This is all achieved under electronic contactless braking (ECB) with the control of electrical current in varying the resistance or "braking strength". Under ECB technology, the brake is essentially wear-free, able to be more resistant to higher temperatures during operation, has fast, simple and effective actuations from derived from utilizing electric signals, and lesser susceptibility to wheel lock [4].

The concept of utilizing eddy current as an alternative for resistance force motion is currently widely accepted on railway transportation although implementation are still under preliminary stages. Theoretically, eddy current braking would prove to be a better replacement for current braking system used in conventional high speed rails.

2. Literature Review

High speed rails exist since the invention of railways in the 1830's [5]. With the progression of time, high speed rails improve radically, achieving greater velocities without compromising safety, ultimately aiming for the objective of getting to destination in the shortest time possible safely. As of year the 2017, the world's fastest rolling stock production train goes to the "Harmony CRH380A" trainset, capable of achieving 486.2km/h [6] which was manufactured by CRRC Qingdao Sifang Co., Ltd. in China and operates using traction motor [6]. As for traction motors, heat is generated due from the electrical losses within the components of the system primarily sourcing from the copper loss and iron loss in the conductor [7]. As such, the traction motors adapted self-circulation cooling method in which a fan is mounted on the armature of the shaft of motor. When the armature is in motion, it would drive to fan to redirect air for cooling [7]. This is essential to the traction motors as the impact of overheating the traction motor would reduce mechanical strength of the conductors and insulators, causing increased wear rate and subsequently reducing the service life of the

components which ultimately results in mechanical failure [3]. The proposed solution to this is to replace traction motors with eddy current braking system which is capable of regenerative braking as well.

In theory, eddy current braking would prove to be a better replacement for the traction motors used in conventional high speed rails. This is due to the different braking mechanics of both systems. The traction braking system implements the "dynamic and regenerative braking" system which basically utilized electrical current, DC motor and generators to slow and stop the train [8]. This form of braking in categorized under contact braking where parts are in contact generating resistance for the said desired output [8]. For eddy current braking, the concept revolves around magnetism which obeys the Faraday's Law and Lenz's Law. In layman terms, braking is induced from introducing same polarity against each other which results in repelling motion to create resistance in motion. This is all achieved under eddy current braking with the control of electrical current in varying the resistance or "braking strength".

Under ECB technology, the brake is essentially wear-free, able to be more resistant to higher temperatures during operation, has fast, simple and effective actuations from derived from utilizing electric signals, and lesser susceptibility to wheel lock [8].

The working principle of eddy current braking system obeys two laws of magnetism which are:

- Faraday's Law of Induction
- Lenz Law

Faraday's Law of Induction, states that electromotive force (EMF) is generated when a magnetic field is interacted with an electrical circuit. The EMF voltage could be calculated using Eq. (1),

$$\text{EMF}, \varepsilon = \frac{\partial \emptyset_B}{\partial t} \tag{9}$$

Where, $\emptyset_B$represents the magnetic flux under change with respect to time. The magnetic flux, $\emptyset_B$ is calculated from Eq. (2). Essentially, the EMF calculate is used to determine the amount of voltage being able to be generated from eddy current braking prior to being dissipated as heat to the surrounding.

$$\emptyset_B = \text{B.A} \tag{2}$$

In Eq. (2) B is the magnetic field and $\boldsymbol{A}$ area perpendicular to the magnetic field that was intersected. In this case, the area $\boldsymbol{A}$, would represent the conductor cutting through the magnetic field generated by the electromagnet.

The magnetic field $\boldsymbol{B}$ is calculated from using Eq. (3) & (4) which consist of a constant derivative of μ_0 representing the permeability of free space which is also known as the magnetic constant.

$$\text{Magnetic } field\ magnitude, B = \frac{(Permeability\ of\ free\ space)(Current\ magnitude)}{2\pi(distance)} \tag{3}$$

$$B = \frac{\mu_0 I}{2\pi r} \quad (4)$$

The permeability of free space constant value would be as listed in Eq. (5) below:

$$\mu_0 = 4\ \pi \text{ x } 10^{-7} \frac{T.m}{A} \quad (5)$$

Based from the motion, in the perspective of the conductor, it experiences magnetic flux which varies with respect to time, in which proves true to Lenz's Law in regards to the electric field. This governs under the Maxwell's Equation:

when: $\nabla.\vec{E}$

$$\nabla \times \vec{E} = \frac{\partial \vec{B}}{\partial t} \quad (6)$$

From the electric field resulted, current is induced circulating around the conductor. And by Ohm's Law:

$$\vec{J} = \sigma.\vec{E} \quad (7)$$

Where:

$\vec{E}$ = Electric field strength

$\vec{B}$ = Magnetic field/flux density

J = Current density

σ = Conductivity of material `

$\emptyset_B$ = Magnetic flux

The current density *J* in this case is also known to be "eddy currents". As acknowledged, all electrical currents produce their own magnetic field and in this case, the eddy current produces its own magnetic field with its respective polarity which is highlighted in the depicted Figure 1 below.

The formation of magnetic field from the eddy current generated is location near points where the magnet's magnetic field intersects with the conductor. And from the example above, it is seen that eddy current magnetic field is formed on two sections; in front and behind the magnet. Focusing on its polarity, the eddy current magnetic field 'behind' the magnet possess polarities that tends to pull the magnet away from travelling downwards while the eddy current magnetic field 'in front' of the magnet possess polarity as such that it 'pushes' the magnet, opposing its direction of travel. Under the summation of forces, the overall magnetic force is opposing the magnet's weight, thus resisting its motion to a certain degree. The summation of forces is derived as below:

$$\Sigma F = mg - F1 - F2 \quad (8)$$

(Where mg > F1+ F2. This case would always serves true.)

The current railway transportation field, eddy current braking is still considered under preliminary stages with minimal implementation, mostly revolving around experimental stages due to lack of study in regards to this braking technology even though this braking system has been discovered over a century ago. This is due from the lack of usability of eddy current braking at low speeds and inability to hold the object; prevention of motion towards the subject. Reason being is due to the basic principles operating of the eddy current braking system which obey Faraday's Law and Lenz's Law Faraday's Law of induction states that interaction a magnetic field and an

electrical circuit would generate an EMF which is measureable in volts. Taking on Faraday's Law, Lenz's Law agrees with Faraday's Law of induction on the electromotive force generated but Emil Lenz added that from the electromotive force, the induced current generated from it would behave in such that that it would create an electromagnetic field that opposes the direction that produced it. This in hand means that eddy current would always generate an electromagnetic field which opposes the direction of that produced it of which in layman terms, in order for eddy current to exist, there must be motion between the conductor and the magnet source, whether it be a permanent magnet or and electrical powered magnet. From the above said statement, it could be deduced that the eddy current magnetic field strength is proportional to the relative velocity in between conductor and magnet. Having lower relative velocity difference means lesser electromagnetic force to act as braking force.

Upon the initial study, one of the research objective is aimed to reduce the amount of heat generated by eddy current braking system during braking sequence. However, further study determines that an electromagnet actually gains strength when operating at higher temperature. This means to say that the magnetic strength is proportional to the temperature value [9]. Given an electromagnet with the strength of 1 tesla at room temperature of 24 degree Celsius, when exposed to 0 degree Celsius room temperature, its strength was halved [9]. Upon exposing the electromagnets to dry ice with approximately -60 degree Celsius, the strength dropped dramatically, measuring about 0.3 tesla which is about 3000 gauss [9].

Reverting to the other end of the temperature spectrum, having the electromagnets to rest back at 24 degree Celsius, the electromagnets were then heated up to 100 degree Celsius. The magnetic strength measured was approximately 1.3 tesla [9]. This is due to when electricity is being exposed to high temperature, the electrons would receive energy in form of heat, increasing its atomic vibration, causing electrons to collide more with the lattice. From this manner, this would cause the drift velocity to decrease [9]. Simply put, electromagnets strength is proportional to the temperature of its surrounding. Through the equation of $\boldsymbol{V=IR}$, lower temperature results in lower resistance, thus resulting in lower voltage. By increasing the surrounding temperature, it would affect the resistance in the wire to be higher which causes the voltage of the circuit to increase. A rise of voltage in an electromagnetic circuit would increase the magnet's field strength as well [9].

With the aforementioned matter, it is established that the heat generated from eddy current braking which primarily concentrates on the conductor disk and electromagnets would not have any adverse effects on negatively affecting its braking strength thus aiming to reduce the heat from the braking system would rendered unnecessary.

The objectives for the present paper aims to identify air gap factor affecting the braking strength of an eddy current braking system and simulate the method of regenerative braking through the implementation of a generator.

2.1 DC Generator EMF Voltage Value.

In order for the eddy current braking system to be capable of regenerating the back the mechanical energy to electrical energy from braking, a DC generator would be utilize. Method of calculation for the DC generated EMF value is shown in Eq. (9).

Note that $\frac{60}{N}$ represents the time taken for the generator to perform one revolution and $\frac{Z}{A}$ would represent the number of connected conductors in series.

$$\text{EMF}, e = \frac{\Phi P}{\frac{60}{N}} . \frac{Z}{A} \text{ volts} \quad (9)$$

Where:
Φ = Flux produced by each pole in weber unit (Wb)
P = Number of poles in the DC generator
N = speed of armature conductor in rpm
Z = total number of conductors
A = number of parallel paths

2.2 Eddy Current Braking Force.

According to Shieber's Model which is in Eq. (10), which translates to a more general simplified method of solution, it shows that by decreasing the air gap distance, the deceleration or the reduction of torque would subsequently improve, meaning that the braking strength would increase resulting in lesser time to stop.

$$T = \frac{1}{2}\sigma\delta\omega\pi r^2 m^2 B_Z^2 [1 - \frac{(r/a)^2}{\{1-(m/a)^2\}^2}] \quad (10)$$

Where:
σ = electrical conductivity of the rotating disk
δ = sheet thickness rotating disk
ω = angular velocity
r = radius of electromagnet
m = distance of disc axis from pole-face center
a = disk radius
B_z = z component of magnetic flux density, z axis is the direction of the center of the electromagnetic pole

3. Research Methodology

3.1 Geometry Modelling

The wheel for ECB would be modelled after an actual rolling stock rail wheel. Terminology for the wheel is shown in Figure 3-1.

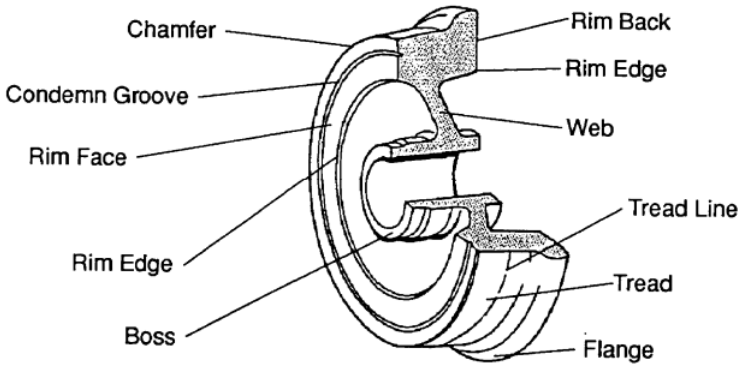


Figure 3-1. Standard terminology for rail wheel.

A 3D representation of the conceptual design for the circular ECB has been modelled using Solidworks as shown in Figure 3-2 and 3-3.

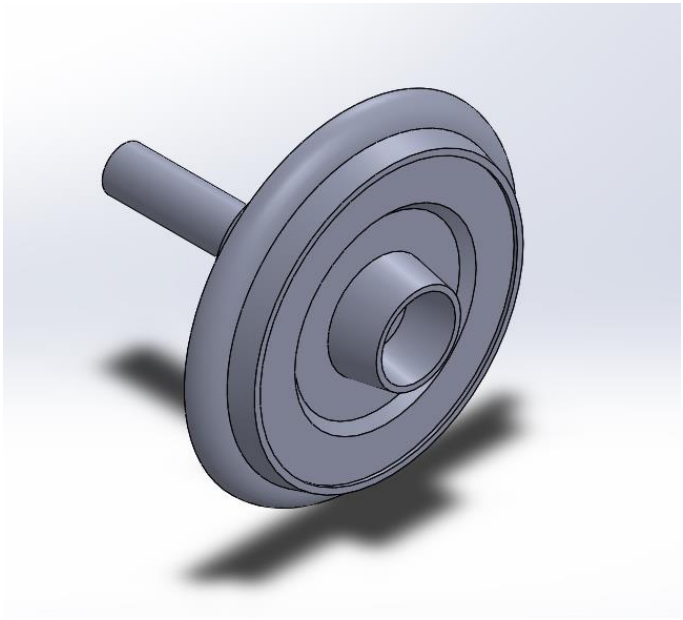


Figure 3-2. Isometric view of the modelled rail wheel.

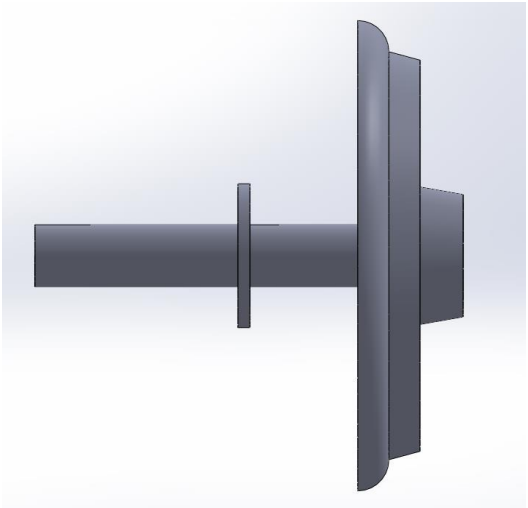


Figure 3-3. Front view of the rail wheel with the aluminum conductor visible.

The specifications for the aforementioned 3D modelled wheel are referred from the Engineering Standard Rolling Stock entitled "wheel and axles reference manual" published by the NSW Transport Railcorp [10]. This is referenced in Table 3-1. The high speed rail is designed for passenger travel and thus the "passenger car wheel data table" is used as the referenced 3D modelled dimension [10]. Note that the conductor of the eddy current brakes are not the actual wheel of the high speed rail, thus it does not come in contact with the track or ground, but it is mounted on the same axle as the wheel. The Solidworks 3D modelled image shows a representation of the aforementioned design.

Table 3-1. Passenger car wheel data specification.

Passenger car wheel data table

All dimensions in mm

	AK Cars (2CP bogies)
Wheel type	
New wheel diameter (mm)	940
Condemn wheel diameter (mm)	
Thickness of Rim at Condemn on Back Flange (mm)	
Thickness of Tread at Condemn on Back Flange (mm)	
Minimum flange width (mm)	19
Maximum flange height (mm)	35
Maximum tread hollowing (mm)	3
Wheel width (mm)	
Wheel drawing	
Clearance to structure gauge (mm)	

As for the determining the appropriate conductor size, by referring the angular to linear Velocity formula shown in Eq. (11), a smaller radius would contribute to a higher RPM.

$$v = r \times \omega \tag{11}$$

Where:
v = linear velocity
r = radius of conductor
ω = angular velocity (RPM)

In theory, a higher rpm will increase the electromagnetic which is known to be the Lorentz force. This is seen in Eq. (12).

$$F = qE + qv \times B \tag{12}$$

Where:
F = Lorentz Force
qE = electrical field
qv = Velocity
B = *Magnetic Field*

Lorentz Force is a vector quantity and the direction of force is determined in Eq. (12) where the angle, θ is <180 degrees between the magnetic field and the instantaneous conductor velocity direction. This shows that if the conductor wheel is not moving or resting at v = 0, the angle difference would be zero, which results to the magnetic force being zero as well. This means that when rpm is reducing, the angle θ would be lesser and approaching to zero, resulting in lesser braking force.

From Eq. (11) and having initial linear velocity of 97.22m/s, and radius of 0.3m, the calculated angular velocity would be approximately 4642.012 RPM. Analysis for the eddy current braking simulation was done using COMSOL which was provided by the Taylor's University School of Engineering. The model used for the simulation is constructed in COMSOL multiphysics. Rendered image is depicted in figure 3-4.

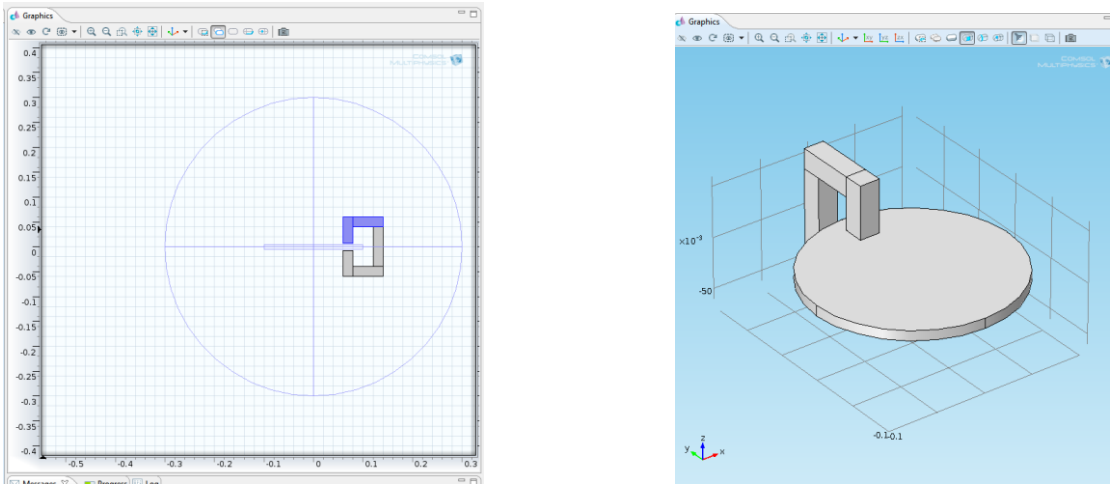


Figure 3-4. Rendering of the model using COMSOL multiphysics.

3.2 Meshing

The meshing size type for this study utilizes the free tetrahedrons meshing with different sizing. The electromagnets mounts uses a larger, coarser sizing while for the electromagnet and the disc uses extremely fine meshing for a more accurate simulation and representation of results. Reason being for the electromagnets mount being meshed under coarser mesh is because the mount serves a medium to connect the magnets together and does not participate in affecting the results of the study. By simply applying a coarser mesh to the mounts, this would simplify the study for calculation, having not to go in detail to calculate the elements of the mounts which does not affect the current density at all. Figure 3-5 depicts meshed model with coarse sizing and extremely fine sizing. This is further indicated in figure 3-6 where extremely fine meshed elements are highlighted in blue.

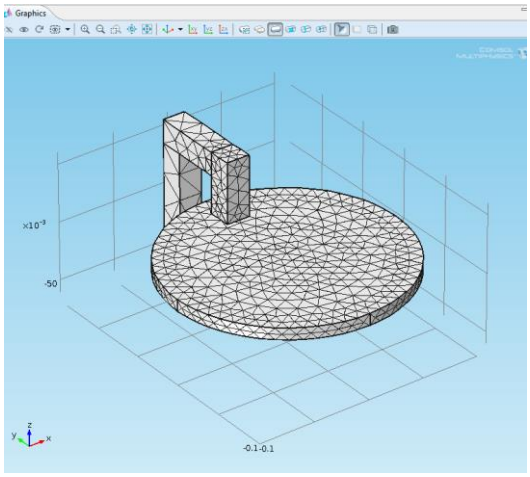


Figure 3-5. Isometric view of free tetrahedrons meshing with multiple sizing.

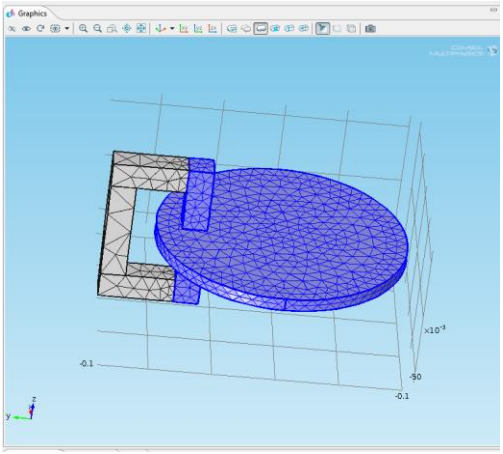


Figure 3-6. Coarser mesh and extremely fine mesh highlighted in blue.

4. Simulation of Results

4.1 Validation

An experimental analysis was conducted by Rodrigues et. al.[11] shown that under 1mm air gap with initial angular frequency of 2500 RPM, the braking time for simulated result is 13.3 seconds. As for theoretical aspect, the braking time took 14.57 seconds. Running the test in COMSOL multiphysics with same initial conditions; initial angular frequency of 2500 RPM, the results produced came to a similar outcome, with stagnation of angular velocity at the 14th second where the angular velocity dropped to a minimal velocity and experiences very minor deceleration. Figure 4-1 depicts the angular velocity deceleration which is approaching to zero but does not achieve zero.

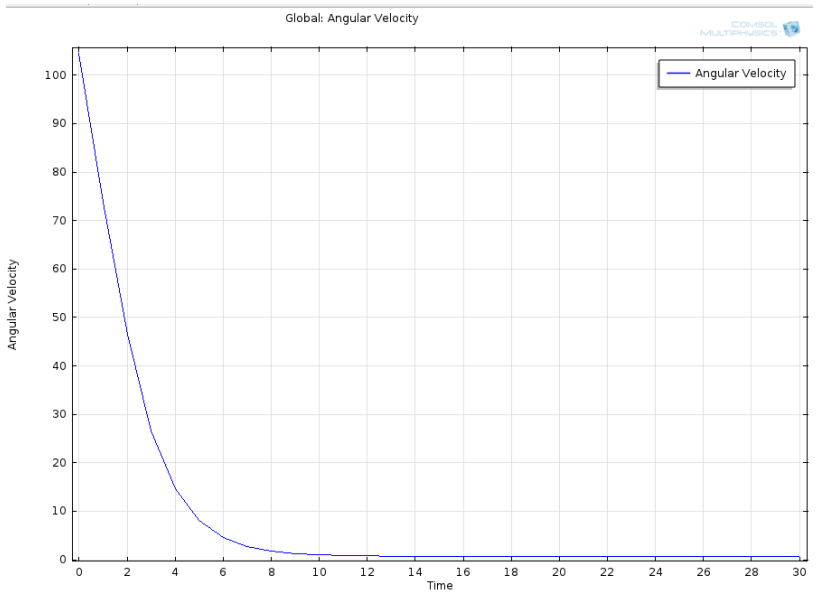


Figure 4-1. Angular velocity deceleration graph.

From the simulated results, it shows that the angular velocity labelled as "Height" in Table 4-1 is very slowly approaching zero but never reaching zero. This is due to the fact that eddy current braking force is proportional to the angular velocity as explained in the Lorentz Force. With the angular velocity dropping to close zero, Lorentz Force itself would result in the same as well, resisting with force that is close to zero. This means that it is practically impossible for ECB to fully bring the disc to a complete stop. Thus, during the 14th second where the angular velocity value is approximately 0.692ω, rounded off to 3 decimal places, it has been considered that the disc has been fully stopped by ECB. It is concluded that the simulated data in comparison are very much close, with only a deviation of 6.67%. The validation is justified.

Table 4-1. Angular Velocity labelled as "Height" experiencing deceleration approaching to zero.

% x	Height
0	104.5632354839851
1	74.00697706968468
2	47.401274080649884
3	27.752543281058532
4	15.310190198605484
5	8.383868200948037
6	4.723858587822394
7	2.8252125813509887
8	1.6975993936574112
9	1.1786365030452284
10	0.9274365460469332
11	0.7989102533707415
12	0.7402070442216507
13	0.7048975560585363
14	0.6922766740810019
15	0.6849686016951928
16	0.681950762096003
17	0.6789329224968134
18	0.6774411158727303
19	0.6762141822750543
20	0.6752535577909452
21	0.6747829669398603
22	0.6743123760887753
23	0.6741472569901907
24	0.6740351585201815
25	0.673965903291217

If taken into account where the experiment runs in a frictionless environment, the angular velocity will never approach zero due to the absence of the air property to creating friction around the disc.

4.2 Simulation Parameters.

Table 4-2 shows the initial global parameter input for the COMSOL multiphysics simulation.

Table 4-2. Global input parameter for simulation.

Parameters

Name	Expression	Value	Description
dt	1[cm]	0.010000 m	Disc thickness
dr	30[cm]	0.30000 m	Disc radius
mh	12[cm]	0.12000 m	Magnet height
mw	2[cm]	0.020000 m	Magnet width
ml	8[cm]	0.080000 m	Magnet length
mt	2[cm]	0.020000 m	Magnet thickness
mg	1[mm]	0.0010000 m	Magnet air gap
mB	1[T]	1.0000 T	Magnet flux
ymur	4000	4000.0	Yoke relative permeability
dV0	4642.012[rpm]	77.367 Hz	Disc initial angular frequency

4.2 Results

The simulation through COMSOL multiphysics model was setup with the input parameters of 1 mm air gap thickness, disc material identified as aluminum 6063-T83 and an initial angular frequency of 4642.012 RPM. The electromagnet was set to 1T and connected to the iron yoke with iron and copper losses taken into the equation. Figure 4-1 depicts the current density field for the disc. At time, t = 0 secs, this is when the disc is rotating at 4642.012 RPM.

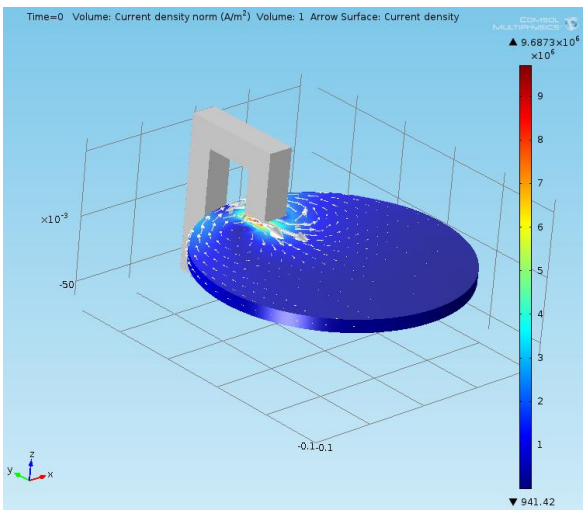


Figure 4-1. Current density field at time, t = 0 secs.

4.2.1 Aluminum 6063-T83

The total heat generated from braking was then observed under 1 Dimensional graph plot. Figure 4-2 depicts the total heat generated in Watts. For the angular velocity results, please refer to Table 4-1.

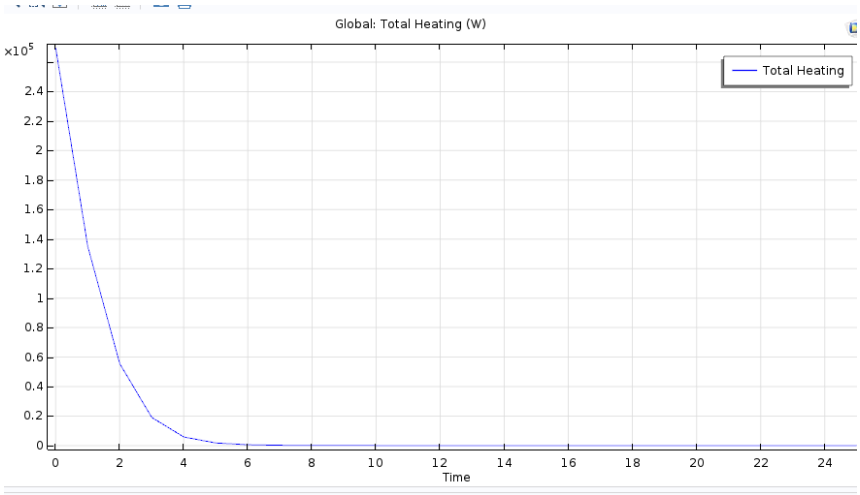


Figure 4-2 Heat generated from braking in Watts (aluminum 6063-T83).

Table 4-2. Tabulated results for the heat generated in Watts labelled as “Height”.

% x	Height
0	269785.40896117943
1	135176.06702922806
2	55491.40818100143
3	19038.34814777042
4	5798.597430348981
5	1739.9400428344788
6	552.6813642307119
7	197.78860957992453
8	71.44570551427427
9	34.457036598046834
10	21.34525811914256
11	15.846208755867547
12	13.610170034267261
13	12.349150244321956
14	11.917361208451695
15	11.673836160162514
16	11.578276824299822
17	11.483417675947504
18	11.44073784235024
19	11.407404875041575
20	11.383432805007452
21	11.376342300163019
22	11.369605293189673
23	11.373524134648955
24	11.379591611485953
25	11.387467385117194

Based on Table 4-2 above, it shows that the amount of heat generated at initial angular velocity was approximately 269.785 kW. The heat generated dissipated quickly to the surrounding air and achieved stagnation at around 14th second, which correlates accurately with the initial experiment validation where the ECB force is at minimal during the 14th second.

4.2.2 Aluminum 6061-T6

The same test is then conducted again with another aluminum of different grade, 6061-T6. Results of the heating value are shown in Figure 4-3.

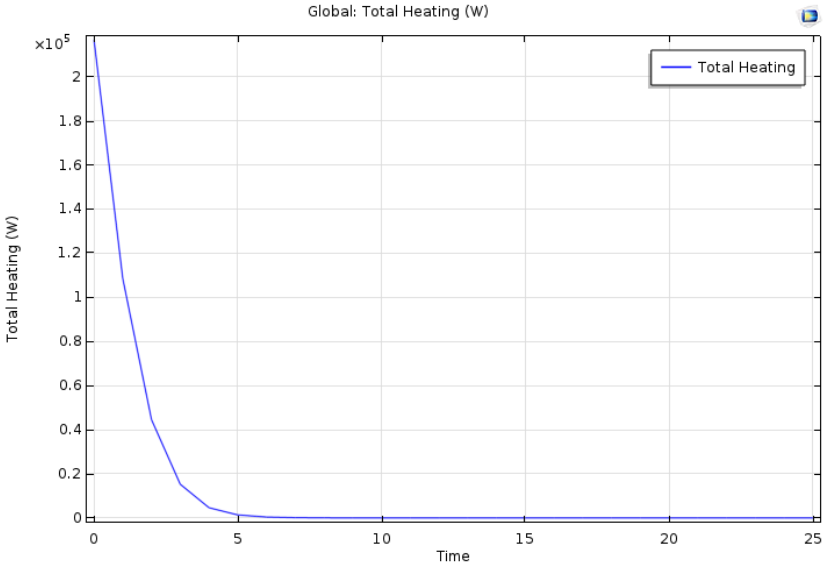


Figure 4-3. Heat generated from braking in Watts (aluminum 6061-T6).

Referring to Table 4-3 below, it is shown that the initial heat generated at time, t = 0 seconds measure up to approximately 216.685 kW. The heat dissipation achieved stagnation point at around 13th second where breaching further would result in heat fluctuation at around 9 W.

Table 4-3. Tabulated results for the heat generated in Watts labelled as "Height" (aluminum 6061-T6).

% x	Height
0	216685.4532069675
1	108570.31690390104
2	44569.42640854014
3	15291.164605960215
4	4657.300470763158
5	1397.4799385417857
6	443.9009965309501
7	158.85927512176536
8	57.38355213005546
9	27.675101556330784
10	17.144021788189697
11	12.727311455051629
12	10.931376435274345
13	9.918554260274666
14	9.57175120933274
15	9.37615747556124
16	9.299406408558431
17	9.223217716105799
18	9.188938252581718
19	9.162165977699155
20	9.142912160824247
21	9.137217229947181
22	9.131806220453017
23	9.134953744038212
24	9.139827002281919
25	9.146152643039153

Simulation was ran using COMSOL Multiphysics under the magnetic and electric field study section. The purpose of this simulation is to prove true for Shieber's Model where previously stated that the air gap between the electromagnets and conductor would affect the braking strength.

5.0 Conclusion

Comparing the results obtained from utilizing two different grades of aluminum, 6063-T83 and 6061-T6, it is seen that the aluminum 6061-T6 generates lesser heat when braking and achieve thermal equilibrium at a faster rate than aluminum 6063-T83. The results shows approximation of 19.68% reduced heat generation when tested with the same conditions. The deceleration chart for aluminum 6061-T6 ended up having the same value as aluminum 6063-T83. This means that by changing the material, not only it reduces the heat generated when braking, the braking strength remains uncompromised.

References

[1] "FAST TRACK TO SUSTAINABLE MOBILITY", *HIGH SPEED RAIL*, pp. 4-18, 2015.
[2] R. Hill, "Electric railway traction. Part 1: Electric traction and DC traction motor drives", *Power Engineering Journal*, vol. 8, no. 1, pp. 47-56, 1994.
[3] I. Uteshevs and A. Levchenkov, "Modeling of overheat process control of electric motor", *Scientific Journal of Riga Technical University. Power and Electrical Engineering*, vol. 25, no. 25, 2009.
[4] S. Anwar and B. Zheng, "An Antilock-Braking Algorithm for an Eddy-Current-Based Brake-By-Wire System", *IEEE Transactions on Vehicular Technology*, vol. 56, no. 3, pp. 1100-1107, 2007.
[5] T. Gourvish, "The High Speed Rail Revolution: History and Prospects", *High Speed 2*, pp. 3-5, 2010.
[6] "Foreign correspondents in China interviewed reporters from Shanghai-Hangzhou high-speed rail", *International Press Center*, 2010.
[7] J. Bates and A. Tustin, "Temperature rises in electrical machines as related to the properties of thermal networks", *Proceedings of the IEE Part A: Power Engineering*, vol. 103, no. 11, p. 471, 1956.
[8] S. Clegg, "A REVIEW OF REGENERATIVE BRAKING SYSTEMS", *Institute of Transport Studies, University of Leeds*, pp. 2-11, 1996.
[9] A.Yadav, "Effect of Temperature on Electric Current, Magnets and Electromagnet", *International Journal of Advancements in Technology*, vol. 07, no. 04, 2016.
[10] "WHEELS AND AXLES REFERENCE MANUAL", *Engineering Standard Rolling Stock*, no. 1, pp. 8-22, 2013.
[11] O. Rodrigues, O. Taskar, S. Sawardekar, H. Clemente and G. Dalvi, "Design & fabrication of Eddy Current Braking System", *International Research Journal of Engineering and Technology (IRJET)*, vol. 3, no. 4, pp. 809-815, 2016.
[12] R. He, X. Liu and C. Liu, "Brake Performance Analysis of ABS for Eddy Current and Electrohydraulic Hybrid Brake System", *Mathematical Problems in Engineering*, vol. 2013, pp. 1-11, 2013.
[13] M. Baharom, M. Nuawi and G. Priyandoko, "Parameter Analysis of Electromagnetic Braking Using Fully Nested and Two Way ANOVA", *Applied Mechanics and Materials*, vol. 663, pp. 193-197, 2014.
[14] J. Wu and R. Lee, "The advantages of triangular and tetrahedral edge elements for electromagnetic modeling with the finite-element method", *IEEE Transactions on Antennas and Propagation*, vol. 45, no. 9, pp. 1431-1437, 1997.
[15] M. Baharom, M. Nuawi, G. Priyandoko and S. Harris, "Eddy current braking experiment using brake disc from aluminium series of A16061 and A17075", *IOP Conference Series: Materials Science and Engineering*, vol. 36, p. 012005, 2012.
[16] M. Jou, J. Shiau and C. Sun, "Design of a magnetic braking system", *Journal of Magnetism and Magnetic Materials*, vol. 304, no. 1, pp. e234-e236, 2006.

[17] M. González, "Experiments with eddy currents: the eddy current brake", *European Journal of Physics*, vol. 25, no. 4, pp. 463-468, 2004.

[18] R. He and D. Hu, "Physical Mechanism of Eddy Current Demagnetizing Effect for Eddy Current Brake", *Journal of Computational and Theoretical Nanoscience*, vol. 13, no. 10, pp. 6810-6822, 2016.

[19] P. Wang and S. Chiueh, "Analysis of eddy-current brakes for high speed railway", *IEEE Transactions on Magnetics*, vol. 34, no. 4, pp. 1237-1239, 1998.

[20] S. Kitanov and A. Podol'skii, "Analysis of Eddy-Current and Magnetic Rail Brakes for High-Speed Trains", *The Open Transportation Journal*, vol. 2, no. 1, pp. 19-28, 2008.

[21] D. Bell, "Permanent magnets versus electromagnets", *Electronics and Power*, vol. 11, no. 9, p. 314, 1965.

eureca 2017 – Conference Paper
Paper Number 2ME27

A Gesture Detection Algorithm for a Game Console

Edmund Tan Ee Loon[1*], Mohsen Nabi Poor[2]

[1]*School of Engineering, Taylor's University, Malaysia*

[2]*School of Engineering, Taylor's Univeristy, Malaysia*

[*] Corresponding Author: edmundtan11@gmail.com

Abstract

The objective of this study is to determine if there is a gesture recognition algorithm which is light yet accurate enough to be applied onto the Arduino microprocessor. The algorithms studied to help accomplish this task are the 'Hidden Markov Model', 'Dynamic Time Warping' and 'Support Vector Machine'. The data collection was carried out using an Arduino Mega 2560, XD-204 Data Logger Shield and an ADXL335 accelerometer. The Arduino Mega 2560 is the main microprocessor for data collection. The XD-204 Data Logger Shield's function is to record the data generated by the accelerometer when the user carries out the gesture patterns. The data on the gesture patterns are then transferred to MATLAB where it is processed and analysed. The coding on the Arduino is for data collection. The code for MATLAB includes signal pre-processing and signal classification. The results of this study include the study of different machine learning algorithms, recording of training data for analysis of the gesture classification algorithms, signal processing and the design of a gesture algorithm.

Keywords: Arduino, Accelerometer, Gesture recognition, Microcontroller, MATLAB

1. Introduction

There are various companies which implement gesture based algorithms into their game consoles. Examples of such consoles include: PlayStation VR developed by Sony Computer Entertainment [1] and Nintendo Switch developed by Nintendo [2]. All these motion sensing consoles are assumed to use signal-processing algorithms to detect the gesture algorithms. These gaming consoles contain powerful processors and huge amounts of memory. The drawback of having such powerful specifications is the price. This brings the question, would a gesture algorithm on a microprocessor be good enough to function as a game controller?

Some of the signal-processing algorithms used for hand gesture recognition include the Hidden Markov Model, Dynamic Time Warping and Support Vector Machine.

The use of the Hidden Markov Model in hand gesture recognition was first discussed by Yamato *et al* [3]. The main factor that differentiates the Hidden Markov Model from the other gesture algorithms is that at the time of observation of the output or result, the state of the process is not known by the observer that is, it is hidden from the observer. This hidden process must follow Markov's property. That is, the current state is independent of all prior states and the variable of the hidden state is discrete [4].

Euclidean Distance can be defined as the distance of a straight line between two points [5]. For gesture recognition, the two points refer to two points on the same time period. However, unlike Euclidean Distance, The distance matrix of the Dynamic Time Warping does not compare the distance between points of the same time series; rather it looks for the best alignment between the two time series [6]. This implies that multiple points of one time series can be compared to a single point on the other time series.

The Support Vector Machine uses transformation of matrixes into fixed length vectors. It is a linear classification method which can have non-linear extensions in the form of kernels. Incoming sensor data is transformed and normalized before it can be read and categorised by the Support Vector Machine [7]. The support vector machine is able to classify data through support vectors and disregards other training data. A support vector is the data point of a variable which is closest to the decision boundary drawn to divide linear variables.

Z. Prekocs'ak [7] conducted the comparison of accuracy between the Support Vector Machine and The Hidden Markov Model through the use of a built-in accelerometer of a cell phone. The Hidden Markov Model provided an accuracy of 97.4% on average and the Support Vector Machine provided an accuracy of 96% on average. He also noted that the Support Vector Machine algorithm did not have any false positives or false positives whereas the Hidden Markov Model had false positives and false negatives due to the noise filter incorporated.

The main issue with these gesture recognition algorithms is that they require either a huge dataset and constraints set to be accurate or a lot of processing power. Either of which is not possible with a microprocessor such as the Arduino Mega 2560.

The present paper aims to determine if there is a gesture algorithm which is light enough to fit the Arduino microprocessor. The goal is to fabricate and analyze a machine-learning algorithm to see if it is possible to develop an accurate gesture recognition algorithm. A total of 10 gesture patterns will be designed to be tested by these algorithms. These gesture patterns will be performed and recorded through the use of an Arduino Mega 2560, XD-204 data logger shield and an ADXL335 accelerometer. The data recorded will then be studied and processed through the use of MATLAB. The data will be processed referring to the signal processing flowchart in

Figure which is in the Research Methodology section under Signal Processing. The code for data collection on the Arduino and the study of the key features of available machine learning algorithms are also objectives of the paper.

2. Research Methodology

The project's aim is to determine if there is a gesture recognition algorithm which is light enough in terms of processing and storage to be implemented onto an Arduino microprocessor. The research methodology will cover the steps and methods taken to achieve the project objectives and the justifications for each task. The research methodology will mainly cover: Data Collection and Signal Processing.

2.1 Data Collection

To perform the data collection, the system is setup as shown in Figure 1. Figure 2 shows the ADXL335 chip.

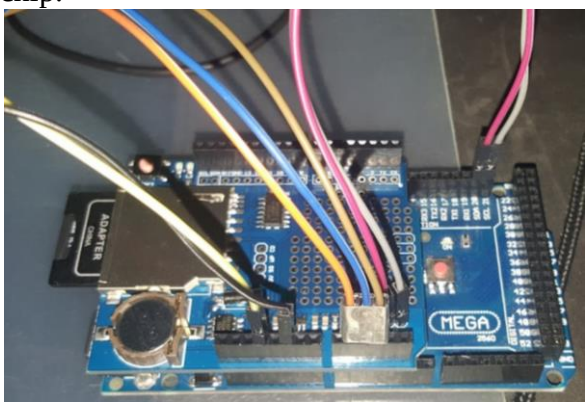


Figure 1: Setup of the system for data logging



Figure 2: The ADXL335 Accelerometer

The yellow wire connects the 3.3v pin of the Arduino to the Voltage Common Collector (VCC) of the ADXL335 chip, The black wire connects the ground of the Arduino to the ground of the ADXL335. The Z, Y and X axis are connected to the A3 , A2 and A1 analog inputs of the Arduino respectively. All these connections are made through the data logger shield and as such, any data that the sensor reads can be programmed to be recorded into the SD storage card.

The Arduino code was written to program the real time clock present in the data logger shield as well as read and record data from the sensors of the accelerometer into the onboard storage card. The data is stored in via comma separated values (.CSV) file. Figure 3 shows the process flowchart of the data collection code. The recorded data is then converted into a spreadsheet in excel and saved to be imported into MATLAB.

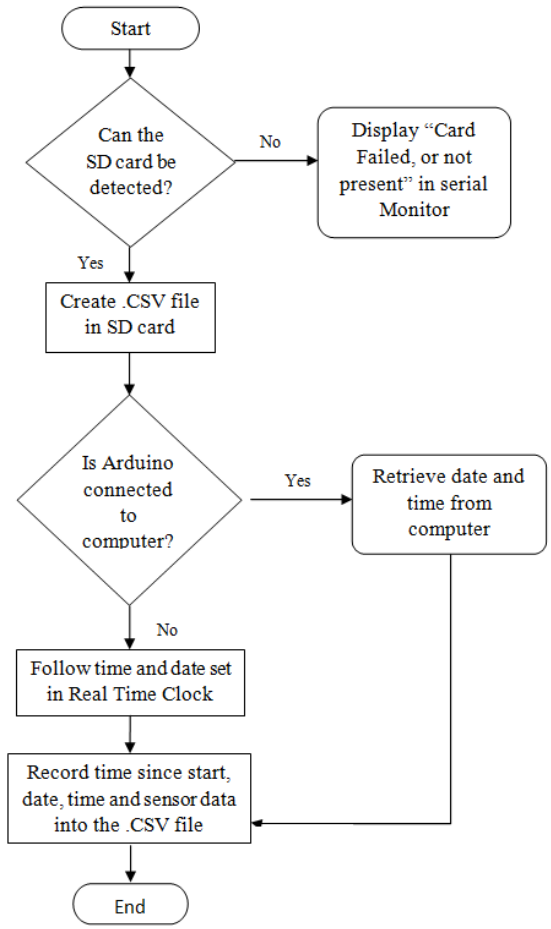


Figure 3: Process Flowchart for Data Collection

2.2.1 Training Patterns

For this paper, 10 different gestures were created to be tested with the gesture algorithms. Every pattern was designed only to be performed in the y-axis and z-axis. The patterns were designed based on common movements to ease the recording of data to reduce inconsistencies. The gesture patterns can be seen in Figure 4 with a label for each pattern. Each pattern has to be performed in the direction shown for them to function.

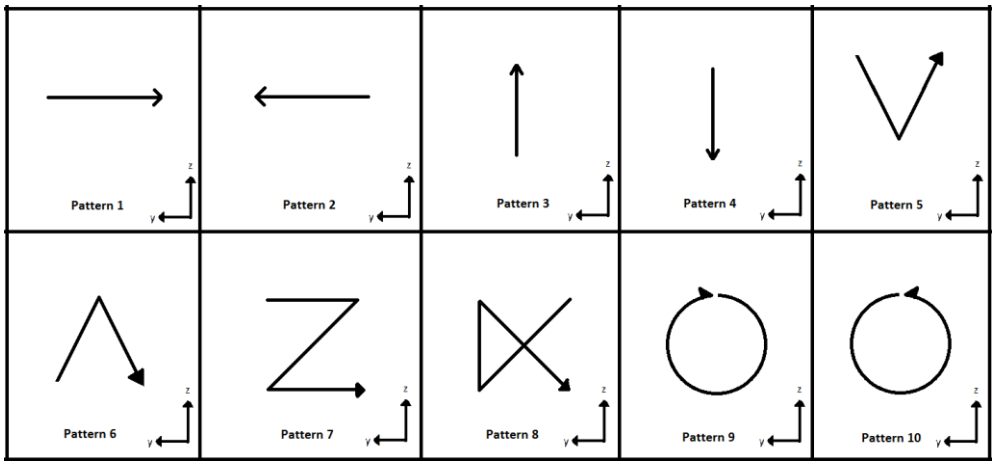


Figure 4: Gesture Patterns for the algorithm

Each gesture pattern is performed three times by an individual. The gesture pattern is recorded three times for three sets of data. One set of data would be used as the training data, the other 2 sets will be used for testing of the gesture algorithm through the analysis of the difference in between the two datasets when compared to the training algorithm. This is done in MATLAB.

2.3 Signal Processing

Signal Processing of the gesture patterns can be divided into two sections: Signal pre-processing and signal classification. As the aim of the project is to determine if there is a machine-learning algorithm which is simple enough to be implemented onto the Arduino microprocessor, the MATLAB code will be coded without the use of MATLAB toolboxes available. This is to determine if a code in its simplest form without the use of toolboxes or libraries is able to process the signal of a gesture pattern. The signal processing flowchart can be seen in Figure 5.

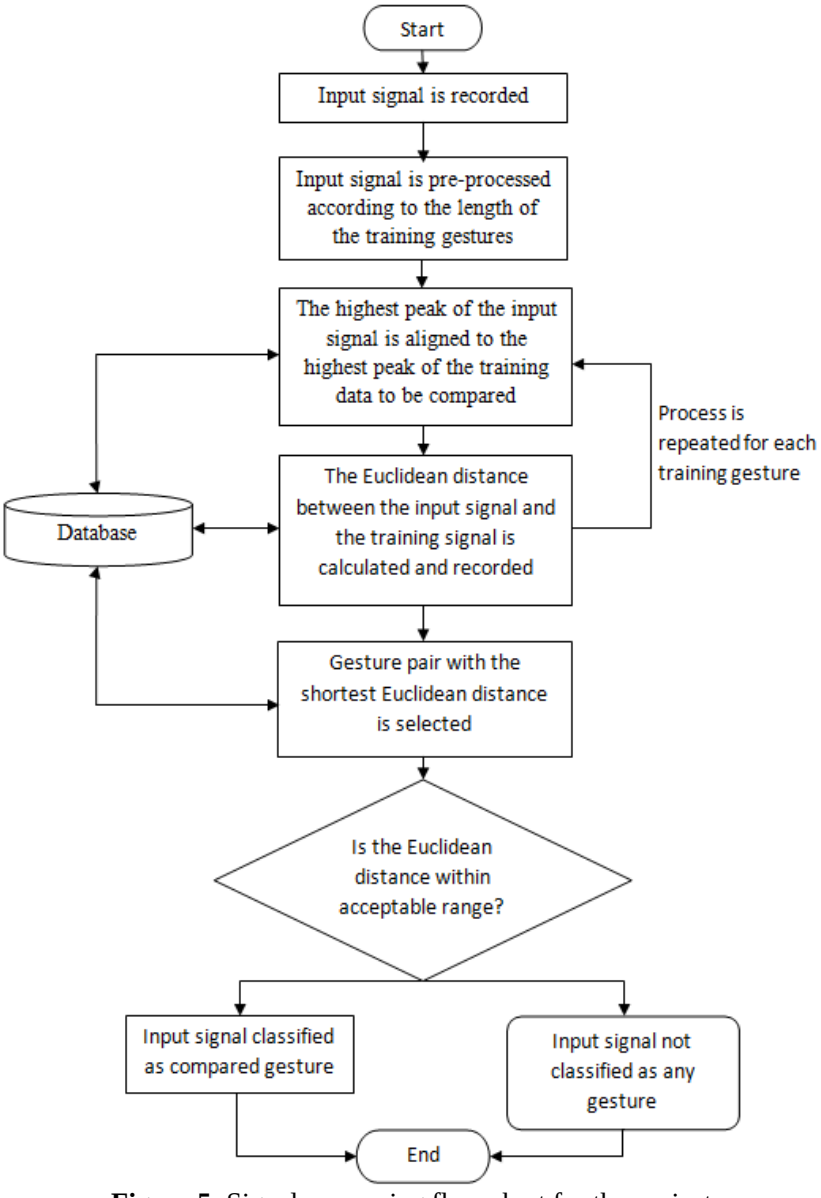


Figure 5: Signal processing flow chart for the project

2.3.1 Signal Pre-processing

Figure 6 shows an example of a graph plotted of raw sensor data of the Y-axis recorded from the performance of Gesture Pattern 2. It can be seen from the plot that there is a lot of noise in the graph. Noise is data which comes from various acts that are not part of the gesture performed. This noise can be due to the shaking or vibrating of the user's hand when performing the gesture pattern.

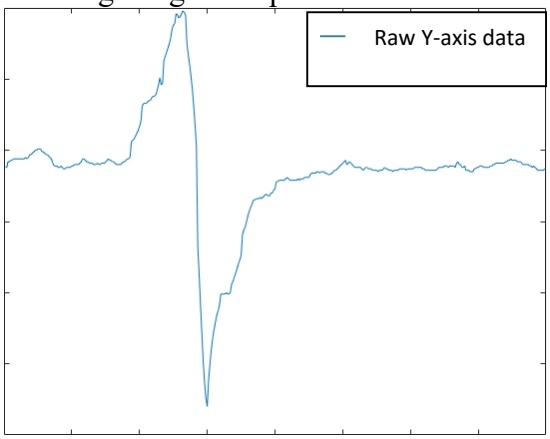


Figure 6: Graph of raw Y-axis sensor data against data points

To reduce noise, various pre-processing processes can be implemented. For this project, three processes will be implemented. They are: Averaging, resampling, dead zone filter and signal offsetting

The first process carried out would be averaging. Averaging allows the signal to be smoothened by replacing each data in each point of the graph with a mean of the data in the surrounding points, the number of points to obtain the mean from can be set, the more points, the smoother the graph [13]. The equation for determining the data at the point x can be seen in Eqn. (1).

$$a_x = \frac{sum\, y_{(x,(x+1),(x+2),(x+3),\ldots,(x+n))}}{n} \quad (1)$$

Where: a is the label for the data of the signal after being averaged
y is the y-axis sensor data
x is the index or point at which the data is being averaged
n is the filter length or number of points being used to obtain the mean.

This equation is done for every point in the graph except the points at which the sum of the index and filter exceeds the size of the last index of the signal, at this point the equation changes to Eqn. (2).

$$a_x = \frac{sum y_{((x+n-m),(x+1+n-m),(x+2+n-m),(\ldots))}}{n} \quad (2)$$

Where: a is denotation of the new signal after being averaged
y is the y-axis sensor data
x is the index or point at which the data is being averaged
m is the last index or point of the signal being averaged

Plotting a will give the new data in the same points as y function. This process is done for the Z-axis as well replacing the y with the z-axis sensor data.

The second process carried out when pre-processing is resampling of the signal. This process is carried out to match the size of the input signal to the training data signal. This process is done by first determining the number of data points contained in both the input signal and the training data signal. The ratio of the input signal to the training data signal determines if the data needs to be upsampled or downsampled. Referring to Eqn. (3), if the value of q is smaller than 1 then the data needs to be upsampled and if the value of q is greater than 1, the data needs to be downsampled.

$$q = \frac{m}{n} \quad (3)$$

Where: q is the ratio of the input to output signal sample rate
m is the size of the input signal
n is the size of the output signal

To upsample data is to add zeroes to specific points in the signal. The points between the zeroes are then interpolated to find the actual value of the zero in the signal. The zero is then replaced with said value. The position of the points can be determined by dividing the total number of points to be added with the size of the input signal. The number of points to be added into the signal can be determined using Eqn. (4).

$$k = n - m \tag{4}$$

Where: k is the number of points to be added into the signal
n is the size of the output signal
m is the size of the input signal

To downsample data is to remove data points from a signal. The position of the points can be determined by dividing the number of points that require removal to the size of the input signal. To find the number of points to be removed, Eqn. (5) is used.

$$k = m - n \tag{5}$$

Where: k is the number of points to be added into the signal
n is the size of the output signal
m is the size of the input signal

The next process is to add Dead zone filter also known as a Band pass filter to remove noise caused by vibration or shaking of the hands when the user performs a gesture pattern [8]. To do this, the raw data is analyzed and a suitable value is measured to determine the values to be filtered. Figure 7 shows an example of how the value is measured. If the value is between the threshold set, the value of the data will be set to the value of the neutral axis. This value isn't determined by evaluating one graph but all the graphs plotted for each gesture pattern. The average of the values is determined and set as the threshold for points to be filtered. Eqn. (6) shows the positive and negative threshold set.

$$if\ y \geq h\ and\ y \leq d,\ y = y_{neutral\ axis} \tag{6}$$

Where: y = data of y-axis
d = positive threshold value
h = negative threshold value

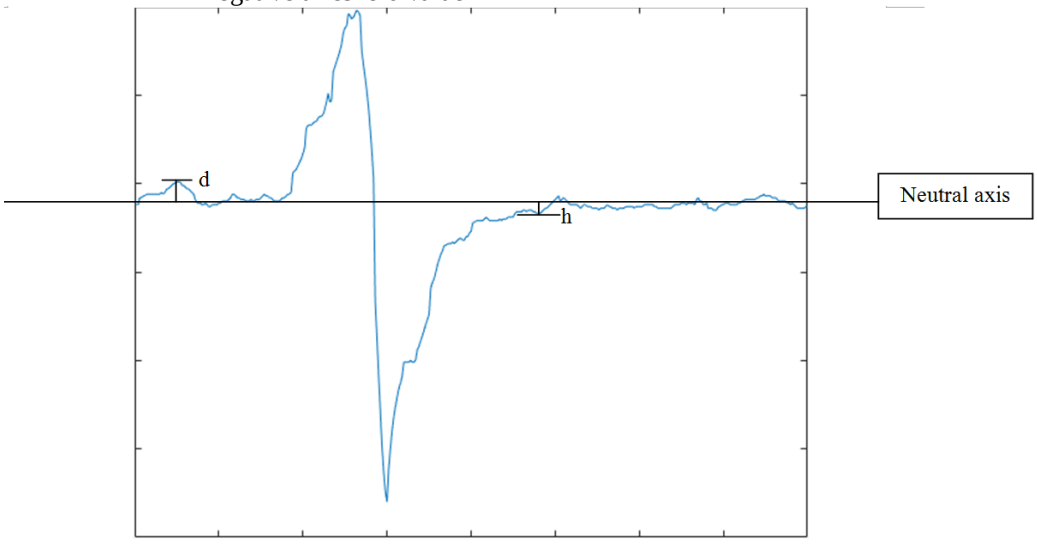


Figure 7: Values of h and d measured on the graph

Signal offsetting is the last process done on a signal before it is able to be classified. The process of offsetting requires the features of the graphs to be extracted before the signal can be offset. A signal is offset either to the left or the right depending on the requirements. A signal is offset to align the signal to the training data. To offset a signal, data is added to either the start or end of a signal. The data added is a copy of the start

or the end of the data. The number of points added can be calculated by determining the distance between the highest peaks of the input signal and the training data signal to be aligned to. MATLAB is used to find the highest peak of both the input signal and the training data signal. Figure 8 illustrates distance between peaks of the two signals.

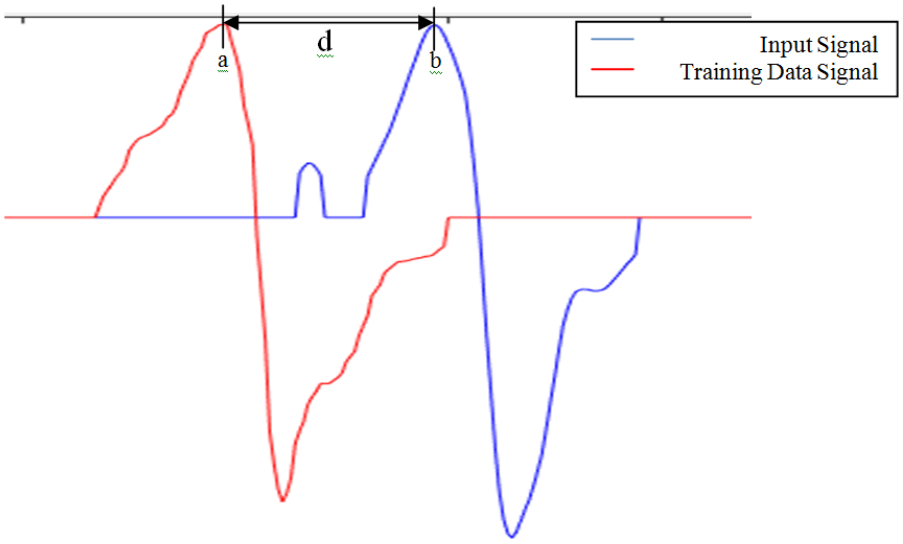


Figure 8: Illustration of d in the graph between two misaligned signals

In MATLAB, the distance is measured using Eqn (7). If d is positive, data is added to the start of the signal and if d is negative, data is added to the end of the signal. When data is added to the start of the signal, the signal is moved to the right of the graph and when data is added to the end of the signal, the signal is moved to the left of the graph.

$$d = x_{training}(a) - x_{input}(b) \quad (7)$$

Where: d is the distance between the two peaks
$x_{training}(a)$ is the value of x at point a
a is the point at which the highest peak of the training signal is located
$x_{input}(b)$ is the value of x at point b
b is the point at which the highest peak of the input signal is located

2.3.2 Signal Classification

The final step of processing a signal of a gesture is to classify it. That means to label the signal. In the case of this thesis, the signal will be assigned to the closest gesture pattern that it resembles. For this, the signal would have to be compared to all the training data and the one that it is closest to will be the signal that it is classified as. This is why signal pre-processing is required. It is to ensure that the signal is being compared with the correct parameters in mind.

To compare an input signal to each training gesture, the Euclidean distance between the two signals is compared and recorded. The pair with the shortest Euclidean distance is the gesture pattern that the signal will be assigned as. Each time before the Euclidean distance is calculated, the input signal has to be aligned to the training data signal. To do this, the highest peak of the input signal is compared to the highest peak of the training data. The distance between these peaks is calculated and the input data is offset according to this distance. To calculate Euclidean distance, Eqn. (8) is used [5].

$$d^2(a,b) = (a_1 - b_1)^2 + (a_2 - b_2)^2 + \cdots + (a_n - b_n)^2 \quad (8)$$

Where: d is the Euclidean distance

a is the input signal data
b is the training data
n is the last point in the signal data

3. Results and Discussion

3.1 The Advantages and Disadvantages of the Learning Algorithms studied

3.1.1 Hidden Markov Model

The advantages of the Hidden Markov Model are that it is a strong statistical foundation which can handle inputs of variable lengths [8].

The limitation of the Hidden Markov Model is that it requires every state of the system to be modeled, causing a severe over-sizing of the algorithm. This issue can be fixed through use of constraints when carrying out the signal processing. The training dataset required to have a good accuracy for the Hidden Markov Model is huge. The parameters set when using the Hidden Markov Model affects the speed and accuracy of the algorithm drastically. This means a lot of trial and error is required when using the Hidden Markov Model parameters.

3.1.2 Dynamic Time Warping

With the use of Dynamic Time Warping, it is possible to compare signals of differing length, meaning that there is no need for the normalization of the signals when processing with this algorithm. This does not imply that the signals to be processed need to be of differing lengths, instead, signals which are of the same length are able to be analysed with Dynamic Time Warping without any effects to the accuracy [9]. Dynamic Time Warping does not require huge datasets to function efficiently.

The main shortcoming of Dynamic Time Warping is that it creates a huge computational load when determining the best alignment between signals.

3.1.3 Support Vector Machine

The support vector machine's main strength is the ability to work on a wide range of classification problems, even if the problems lie in a high dimension and is not linearly separable [8].

The main disadvantage of Support Vector Machine is similar to the Hidden Markov Model algorithm in a sense, which is that it requires the key parameters to be set correctly to achieve the best results. As such it also requires a lot of trial and error to ensure the best results [8].

3.2 Data Collection

Ten gesture patterns were created for the purpose of data collection. Some patterns were unique while some were the same pattern but performed in the opposite direction. The reasoning for this is to see if the gesture patterns would provide similar signals when performed in similar fashions except with different directions. Figure 9 shows each gesture pattern and the plotted raw signal data for both the Y-axis and Z-axis of the sensor. The Y-axis signal is plotted in red and the Z-axis signal is plotted
in blue.

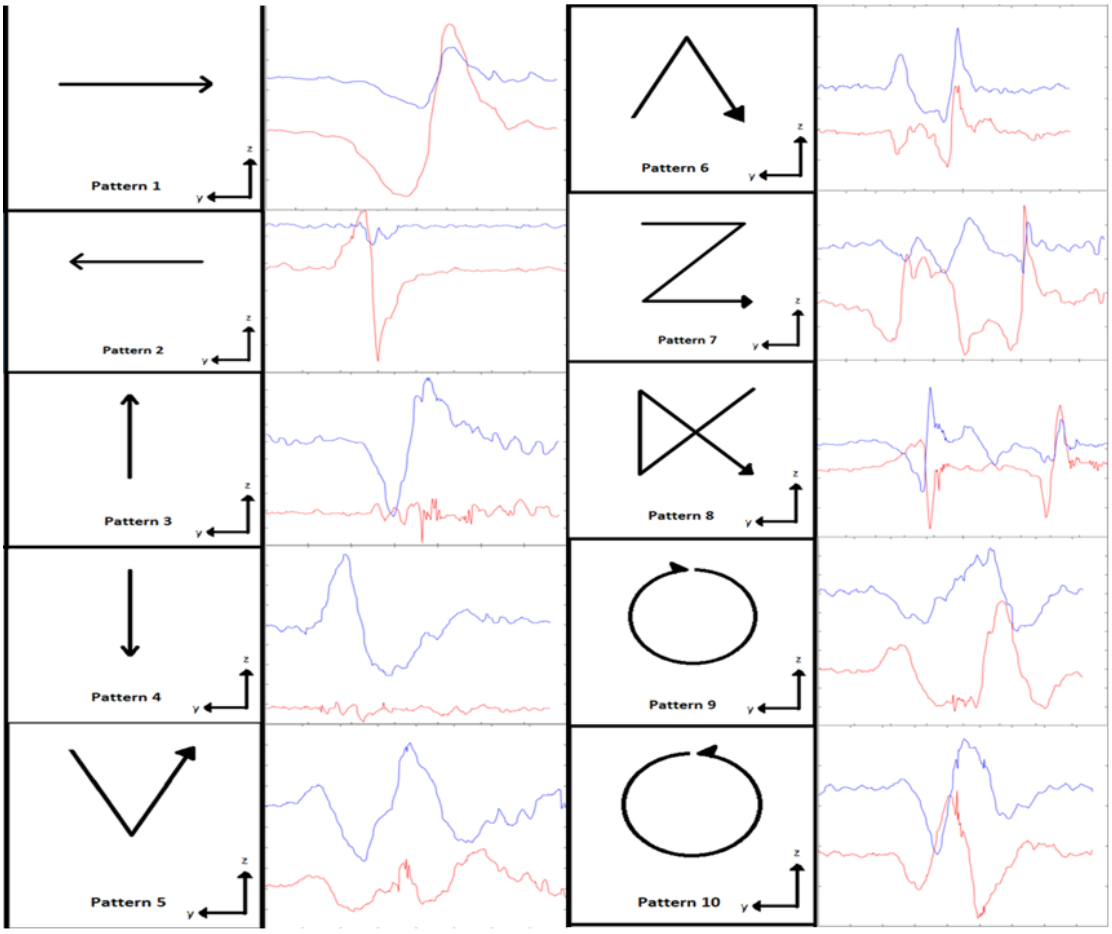


Figure 9: Gesture patterns and the plots of raw Y-axis (red) and Z-axis signal (blue)

From the Figure it can be seen that each plotted signal is unique in their signals even those that are just performed in opposite directions. It can also be seen that there is a lot of noise in each plot of the signals. The noise will be reduced after the signal is pre-processed. Generally, it is noticeable that when a pattern is performed towards the right, the Y-axis will produce a signal in the negative direction and when a pattern is performed towards the left, the Y-axis produces a signal in the positive direction. When a motion is performed upwards, there will be a signal produced towards the negative direction of the Z-axis. When a motion is performed downwards, there will be a signal produced towards the positive direction of the Z-axis. From these reading, it can be deduced that the Y-axis receives positive readings when motions to the left are produced and the Z-axis is positive towards the ground. After each motion, there will be a rebound of the signal in the opposite direction. This due to Newton's Third Law of motion which states that 'for every action, there is an equal and opposite reaction'. This reaction is recorded by the accelerometer's sensors.

3.3 Signal Processing

3.3.1 Signal Pre-processing

Every signal received raw has to be pre-processed or normalized before the features are extracted or the signal is classified. To do this, the signal undergoes four different pre-processing processes. The processes that are carried out include: Signal averaging, signal resampling, Dead zone filter and offsetting. The process flowchart of the pre-processing can be seen in Figure 10. The compilation of pre-processing on the training signals can be seen in Figure 17. The detailed processes and equations of each

pre-processing process have been discussed in the methodology section of this paper. The results, benefits and disadvantages of each pre-processing process will be discussed after the flowchart.

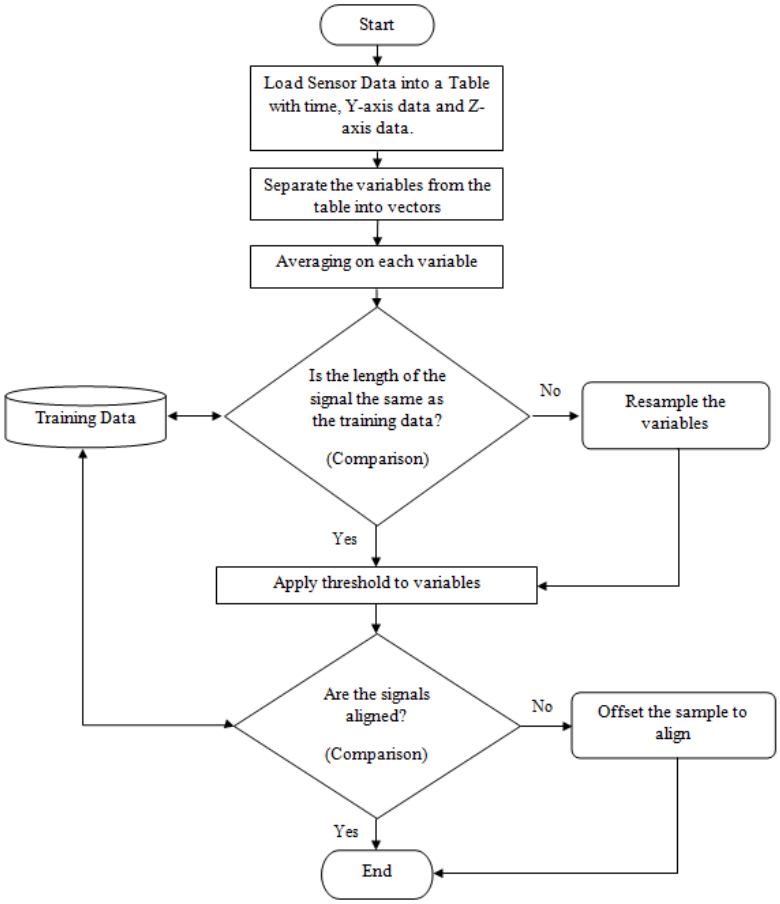


Figure 10: Signal Pre-processing flowchart

The first pre-processing process done on any signal would be averaging. The process of averaging allows the noise in a signal to be reduced. This reduction causes the signal to be smoother, but this also means that precious features of the signal can be dulled or lost due to this process. An example of containing the comparison between an averaged signal and a raw signal can be seen in Figure 11, where the blue line is the raw signal data and the red line is the averaged signal. The number of points sampled for each mean or average in this example is four. It can be seen from the figure that the noise of the averaged signal is reduced but the maximum peak of the signal and lowest point or minimum of the signal is also reduced.

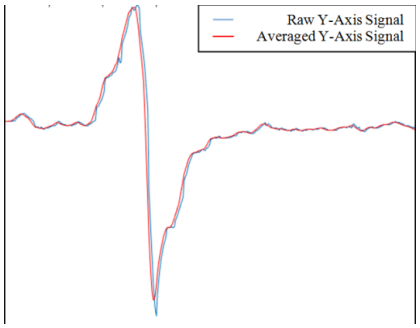


Figure 11: Raw Y-axis Signal (Blue) compared with Averaged Y-axis Signal (Red)

As the signal length or size of the signal is not always equal to the size or length of the training data signal, resampling is required. If the tested signal is longer, downsampling is required and if it is shorter, upsampling is required. Downsampling of a signal removes data points from the signal to match the length of the training data. Upsampling interpolates data to add points in between existing points. The only reason upsampling is done is to match the sampel rate of the input signal to the training data. The reason upsampling is not encouraged is because it increases the processing power and memory needed when processing a signal. Figure 12 shows a comparison of a downsampled data with its original length. The red line is the averaged signal data from Figure 11 and the green line is the same signal data but hast has been downsampled. Downsampling also helps to reduce the processing power and memory needed when processing a signal as the number of data points is reduced. An example of upsampling can be seen in Figure 13. As it can be seen, resampling does not affect the features of the signal.

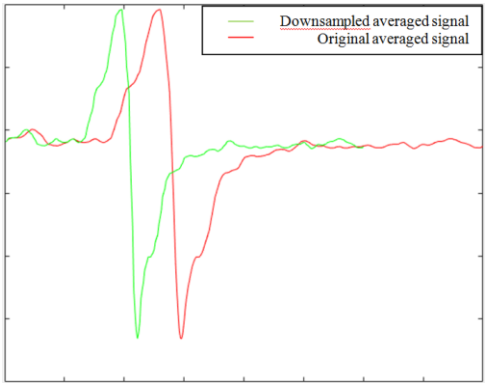


Figure 12: Downsampled averaged signal (green) compared to original averaged signal (red)

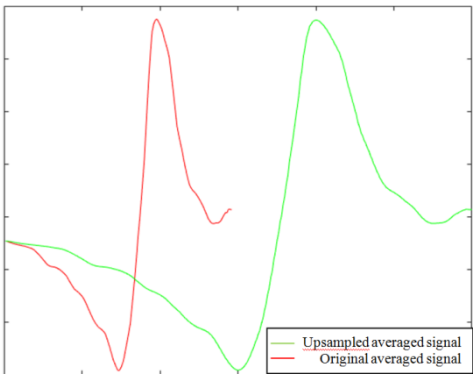


Figure 13: Upsampled Averaged signal (green) compared to original averaged signal (red)

To reduce more noise from the signal, Dead Zone filter can be applied to the signal. For this example, the threshold set is 15 points below and above the neutral axis. Figure 14 shows a comparison between the signals, the signal from Figure 12 (green) to the signal which has a threshold applied to it (blue). It can be seen that features of the signal are preserved as the two signals overlap each other but the signal in blue has noise drastically reduced. The downside of applying a threshold filter to the signal is that if the threshold set is too high, there can be features from the signal that is removed or lost in the process.

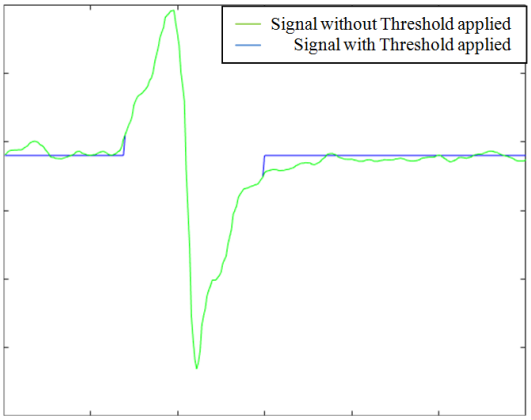


Figure 14: Comparison between signal with (blue) and without (green) dead zone filter applied

The final pre-processing step is to align the input signal with the training data. This was discovered while signal classification was being carried out. As such, valuable time was wasted when analyzing signals that were not aligned to each other. Figure 15 shows an example of two signals with similar features which are misaligned. The blue signal is the input signal and the red signal is the training data signal.

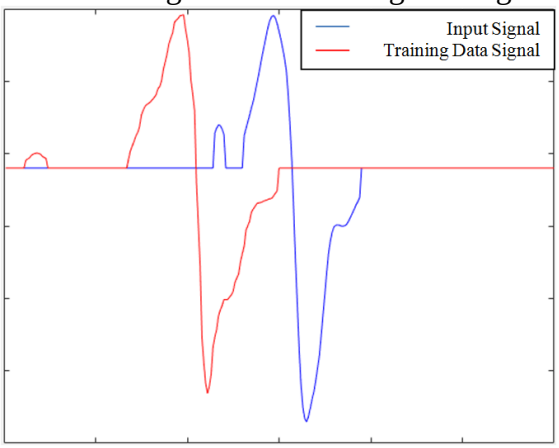


Figure 15: Two signals which have similar features which are misaligned.

To rectify this error, offsetting is required. The full steps to offsetting a signal have been discussed in the methodology. The result of aligning two signals is that the Euclidean distance calculated between the two signals is more accurate and the error percentage which is used in the classification of signals is reduced. This will drastically improve the accuracy of the system in detecting the correct signals. Figure 15 shows the input signal after it has been offset in green. It can be seen that the peak of the signal is aligned with the training data signal.

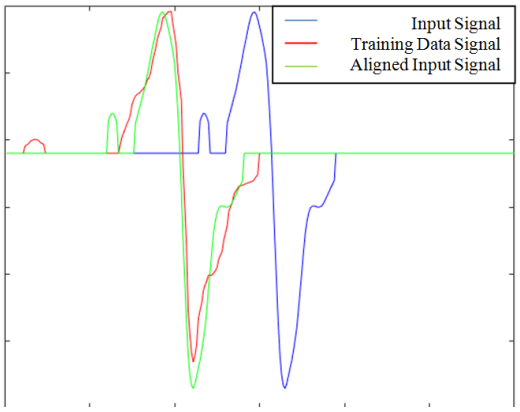


Figure 16: Aligned input signal (green) compared to misaligned signal (blue)

Figure 17 shows a compilation of all the training data signals after they have been pre-processed. These signals are the signals that any input signal will be compared to when the input signal is being classified. As it can be seen from the figure, most of the noise (except for a few outliers) has been removed compared to when the signals were first recorded in Figure 9.

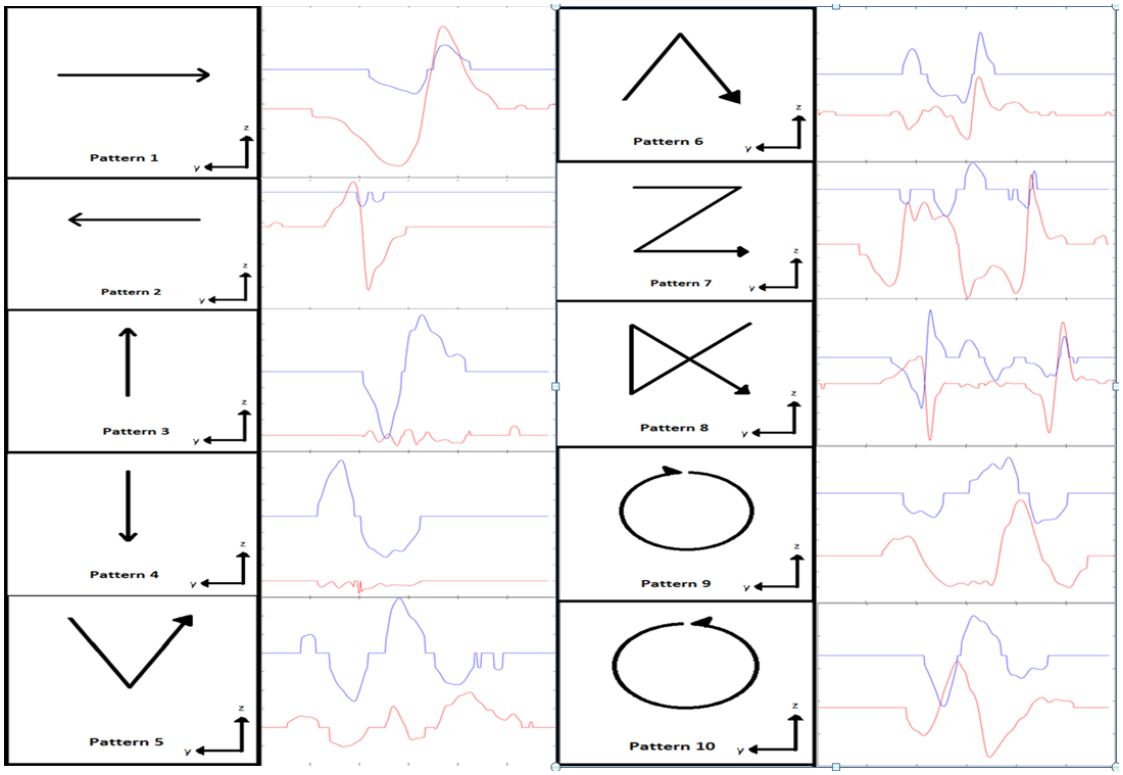


Figure 17: Compilation of pre-processed training gesture signals

3.3.2 Signal Classification

The flowchart in figure 18 covers the whole signal classification process found in the code in Appendix C. The process was tested with the samples of each gesture and it was able to classify each input signal to the correct gesture pattern.

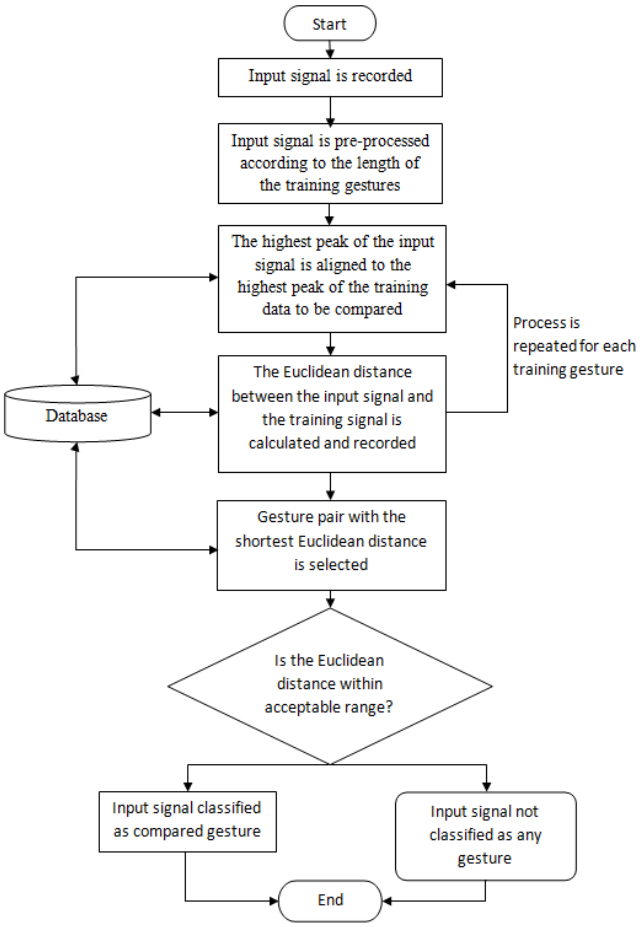


Figure 18: Flowchart of signal classification process

4. Conclusions

This paper presents a gesture recognition algorithm through the use of MATLAB that is able to record, pre-process and classify signals to gesture patterns which have been recorded in the system. The key features of machine learning algorithms have also been discussed. As such, the objectives of the project have been achieved. The main limitation of this project is that the code of the gesture algorithm has to be kept as simple as possible. This is so that the code can be implemented onto the Arduino at later stages.

From the analysis which has been done, the possibility of implementing a gesture algorithm which is light yet accurate enough to the Arduino microprocessor is high. This is the conclusion that can be deduced from the work that has been done on this project.

Some future considerations for the project include the exploration of other machine learning algorithms not discussed in this paper to improve the designed gesture recognition algorithm. A wireless module could be implemented with the sensor to reduce the restraints on movement due to the length of the wire. The signal pre-processing procedure can be further refined to further remove noise caused by sudden jerking movements. More complex gestures can be implemented to test the gesture recognition algorithm further.

References

[1] "Playstation VR | Playstation.", 2017. [Online]. Available: https://www.playstation.com/en-gb/explore/playstation-vr/ , [Accessed: 01-Apr-2017].

[2] "Nintendo Switch™ - Official site – Nintendo gaming system.", 2017. [Online]. Available : http://www.nintendo.com/switch [Accessed: 01-Apr-2017].

[3] J. Yamato, J. Ohya, and K. Ishii, "Recognizing human action in timesequential images using hidden Markov model," in Proc. IEEE Int. Conf. Comput. Vis. Pattern Recogn., Champaign, IL, pp. 379–385,1992.

[4] Z. Ghahramani, "An Introduction to Hidden Markov Models and Bayesian Networks ", in *International Journal of Pattern Recognition and Artificial Intelligence*, vol. 15, no. 01, pp. 9-42, 2001.

[5] P. Black, "Euclidean distance", in *Dictionary of Algorithms and Data Structures* , 17 December 2004. [Online]. Available: https://www.nist.gov/dads/HTML/euclidndstnc.html. [Accessed: 20- Oct- 2017].

[6] E. Keogh and C. A. Ratanamahatana, "Exact Indexing of Dynamic Time Warping" *Knowledge and Information Systems*, Hong Kong, China, pp. 406-417, August 2002.

[7] Z. Prekocs'ak, "Accelerometer Based Real-Time Gesture Recognition", 2008.

[8] N. Gillian, *Gesture Recognition Toolkit*. MIT Media Lab, 2013.

[9] C. A. Ratanamahatana and E. Keogh, "Everything you know about Dynamic Time Warping is Wrong", University of California, 2004.

[10] S. Smith, "Chapter 15: Moving Average Filters," in *Digital signal processing*. Amsterdam, Netherlands]: Newnes, 2012.

APPENDICES

APPENDIX A: Arduino Code For Data Collection

```
#include <DS1307RTC.h>
#include <SPI.h>
#include <SD.h>
#include <Wire.h>
#define LOG_INTERVAL  1000 // mills between entries (reduce to take more/faster data)
#define SYNC_INTERVAL 1000 // mills between calls to flush() - to write data to the
card
uint32_t syncTime = 0; // time of last sync()
#define ECHO_TO_SERIAL   0 // echo data to serial port
#define WAIT_TO_START    0 // Wait for serial input in setup()
// the digital pins that connect to the LEDs
#define redLEDpin 2
#define greenLEDpin 3

// The analog pins that connect to the sensors
#define x 1                // analog 1
#define y 2                // analog 2
#define z 3                // analog 3
#define DS1307RTC RTC; // define the Real Time Clock object
tmElements_t tm;
const char *monthName[12] = {
  "Jan", "Feb", "Mar", "Apr", "May", "Jun",
  "Jul", "Aug", "Sep", "Oct", "Nov", "Dec"
};
// for the data logging shield, we use digital pin 10 for the SD cs line
const int chipSelect = 10;
// the logging file
File logfile;

void error(char *str)
{
  Serial.print("error: ");
  Serial.println(str);

  // red LED indicates error
  digitalWrite(redLEDpin, HIGH);

  while (1);
}

void setup(void)
{
  Serial.begin(9600);
  Serial.println();

  // use debugging LEDs
  pinMode(redLEDpin, OUTPUT);
  pinMode(greenLEDpin, OUTPUT);

#if WAIT_TO_START
  Serial.println("Type any character to start");
  while (!Serial.available());
#endif //WAIT_TO_START

  // initialize the SD card
  Serial.print("Initializing SD card...");
  // make sure that the default chip select pin is set to
  // output, even if you don't use it:
  pinMode(52, OUTPUT);

  // see if the card is present and can be initialized:
  if (!SD.begin(10, 11, 12, 13)) {
    error("Card failed, or not present");
  }
  Serial.println("card initialized.");

  // create a new file
  char filename[] = "LOGGER00.CSV";
  for (uint8_t i = 0; i < 100; i++) {
    filename[6] = i / 10 + '0';
    filename[7] = i % 10 + '0';
    if (! SD.exists(filename)) {
      // only open a new file if it doesn't exist
```

```
      logfile = SD.open(filename, FILE_WRITE);
      break;  // leave the loop!
    }
  }

  if (! logfile) {
    error("couldnt create file");
  }

  Serial.print("Logging to: ");
  Serial.println(filename);
  bool parse = false;
  bool config = false;

  // get the date and time the compiler was run
  if (getDate(__DATE__) && getTime(__TIME__)) {
    parse = true;
    // and configure the RTC with this info
    if (RTC.write(tm)) {
      config = true;
    }

    if (parse && config) {
      Serial.print("DS1307 configured Time=");
      Serial.print(__TIME__);
      Serial.print(", Date=");
      Serial.println(__DATE__);
    } else if (parse) {
      Serial.println("DS1307 Communication Error :-{");
      Serial.println("Please check your circuitry");
    } else {
      Serial.print("Could not parse info from the compiler, Time=\"");
      Serial.print(__TIME__);
      Serial.print("\", Date=\"");
      Serial.print(__DATE__);
      Serial.println("\"");
    }
  }

  logfile.println("millis,stamp,datetime,x,y,z");
#if ECHO_TO_SERIAL
  Serial.println("millis,stamp,datetime,x,y,z");
#endif //ECHO_TO_SERIAL
}

void loop(void)
{
  tmElements_t tm;

  digitalWrite(greenLEDpin, HIGH);

  // log milliseconds since starting
  uint32_t m = millis();
  logfile.print(m);           // milliseconds since start
  logfile.print(", ");
#if ECHO_TO_SERIAL
  Serial.print(m);         // milliseconds since start
  Serial.print(", ");
#endif

  // fetch the time
  if (RTC.read(tm)) {
    logfile.print(tm.Hour);
    logfile.print(':');
    logfile.print(tm.Minute);
    logfile.print(':');
    logfile.print(tm.Second);
    logfile.print(", Date (D/M/Y) = ");
    logfile.print(tm.Day);
    logfile.print('/');
    logfile.print(tm.Month);
    logfile.print('/');
    logfile.print(tmYearToCalendar(tm.Year));
    logfile.print('"');
#if ECHO_TO_SERIAL
    print2digits(tm.Hour);
    Serial.write(':');
```

```
    print2digits(tm.Minute);
    Serial.write(':');
    print2digits(tm.Second);
    Serial.print(", Date (D/M/Y) = ");
    Serial.print(tm.Day);
    Serial.write('/');
    Serial.print(tm.Month);
    Serial.write('/');
    Serial.print(tmYearToCalendar(tm.Year));
    Serial.print('"');
#endif //ECHO_TO_SERIAL
  }
  int xReading = analogRead(x);
  int yReading = analogRead(y);
  int zReading = analogRead(z);
  logfile.print(", ");
  logfile.print(xReading);
  logfile.print(", ");
  logfile.print(yReading);
  logfile.print(", ");
  logfile.print(zReading);
#if ECHO_TO_SERIAL
  Serial.print(", ");
  Serial.print(xReading);
  Serial.print(", ");
  Serial.print(yReading);
  Serial.print(", ");
  Serial.print(zReading);
#endif ECHO_TO_SERIAL
  logfile.print(", ");
  logfile.println();
#if ECHO_TO_SERIAL
  Serial.println();
#endif // ECHO_TO_SERIAL
  digitalWrite(greenLEDpin, LOW);
  if ((millis() - syncTime) < SYNC_INTERVAL) return;
  syncTime = millis();
  // blink LED to show we are syncing data to the card & updating FAT!
  digitalWrite(redLEDpin, HIGH);
  logfile.flush();
  digitalWrite(redLEDpin, LOW);
}
void print2digits(int number) {
  if (number >= 0 && number < 10) {
    Serial.write('0');
  }
  Serial.print(number);
}
bool getTime(const char *str)
{
  int Hour, Min, Sec;

  if (sscanf(str, "%d:%d:%d", &Hour, &Min, &Sec) != 3) return false;
  tm.Hour = Hour;
  tm.Minute = Min;
  tm.Second = Sec;
  return true;
}
bool getDate(const char *str)
{
  char Month[12];
  int Day, Year;
  uint8_t monthIndex;

  if (sscanf(str, "%s %d %d", Month, &Day, &Year) != 3) return false;
  for (monthIndex = 0; monthIndex < 12; monthIndex++) {
    if (strcmp(Month, monthName[monthIndex]) == 0) break;
  }
  if (monthIndex >= 12) return false;
  tm.Day = Day;
  tm.Month = monthIndex + 1;
  tm.Year = CalendarYrToTm(Year);
  return true;
}
```

APPENDIX B: Matlab Code for Pre-processing procedure for one training signal and one reference/training signal

```
clear;
clf;
load('pattern2traintestaverageoffset.mat');
millist = (Pattern2ZTrain{:,'millis'})';
Ztraw = (Pattern2ZTrain{:,'z'})';
Ytraw = (Pattern2ZTrain{:,'y'})';
millis = (Pattern2ZTest{:,'millis'})';
Zraw = (Pattern2ZTest{:,'z'})';
Yraw = (Pattern2ZTest{:,'y'})';
m = size(millis,2);
mt = size(millist,2);
classlength = 300;
filter = 4;
filtert = 4;
for i = 1:mt
    if i+filtert < mt
    Yt (i) = mean(Ytraw (i:i+filtert));
    Zt (i) = mean(Ztraw (i:i+filtert));
    elseif i+filtert >= mt
    filtertnew = i+filtert - m;
    Yt (i) = mean(Ytraw (i-filtertnew:mt));
    Zt (i) = mean(Ztraw (i-filtertnew:mt));
    end
    end


for i = 1:m
    if i+filter <=m
    Y (i) = mean(Yraw (i:i+filter));
    Z (i) = mean(Zraw (i:i+filter));
    elseif i+filter >= m
    filternew = i+filter-m;
    Y (i) = mean(Yraw (i-filternew:m));
    Z (i) = mean(Zraw (i-filternew:m));
    end
end
     qt = (mt/classlength);
     for it = 1:classlength
          if floor(qt*it) == 0
     ct = 1;
          else
     ct = 0;
          end
         jt = floor(qt*it)+ct;
         millistnew (it) = millist (jt);
         Ztnew (it) = Zt (jt);
         Ytnew (it) = Yt (jt);
     end
     q = (m/classlength);
      for i = 1:classlength
         if floor(q*i) == 0
     c = 1;
         else
     c = 0;
         end
         j = floor(q*i)+c;
         millisnew (i) = millis (j);
         Znew (i) = Z (j);
         Ynew (i) = Y (j);
      end
at = size(Ytnew,2);
a  = size(Ynew,2);
for i = 1:at
    if i+filtert < at
    Ytsmooth (i) = mean(Ytnew (i:i+filtert));
    Ztsmooth (i) = mean(Ztnew (i:i+filtert));
    elseif i+filtert >= at
    filtertnew = i+filtert-at;
    Ytsmooth (i) = mean(Ytnew (i-filtertnew:at));
    Ztsmooth (i) = mean(Ztnew (i-filtertnew:at));
    end
end
for i = 1:a
    if i+filter <=a
    Ysmooth (i) = mean(Ynew (i:i+filter));
    Zsmooth (i) = mean(Znew (i:i+filter));
```

```
    elseif i+filter >= a
    filternew = i+filter-a;
    Ysmooth (i) = mean(Ynew (i-filternew:a));
    Zsmooth (i) = mean(Znew (i-filternew:a));
    end
end
for i = 1:size(Zsmooth,2)
    if Zsmooth(i)>=400 && Zsmooth(i)<=440
        Zsmooth(i)=420;
    if Ysmooth(i)>=320 && Ysmooth(i)<=360
        Ysmooth(i)=340;
    end
    end
end
for i = 1:size(Ztsmooth,2)
    if Ztsmooth(i)>=405 && Ztsmooth(i)<=435
        Ztsmooth(i)=420;
    if Ytsmooth(i)>=325 && Ytsmooth(i)<=345
        Ytsmooth(i)=340;
    end
    end
end

Zflag = 0;
Ztflag = 0;
Yflag = 0;
Ytflag = 0;
for i=2:at-2
    if Ztsmooth (i)> Ztsmooth(i-1) && Ztsmooth (i) > Ztsmooth(i+1) || Ztsmooth(i)==
max (Ztsmooth)&& Ztsmooth(i)>Ztsmooth(i+1)
        Ztpeak = [i,Ztsmooth(i)];
        if Ztflag == 0
        Ztpeaknew = Ztpeak;
        Ztflag = 1;
        elseif Ztflag == 1
        Ztpeaknew = [Ztpeaknew;Ztpeak];
        end
    end
    if Zsmooth (i)> Zsmooth(i-1) && Zsmooth (i) > Zsmooth(i+1) || Zsmooth(i)==
max(Zsmooth) && Zsmooth(i)>Zsmooth(i+1)
        Zpeak = [i,Zsmooth(i)];
        if Zflag == 0
        Zpeaknew = Zpeak;
        Zflag = 1;
        elseif Zflag == 1
        Zpeaknew = [Zpeaknew;Zpeak];
        end
    end
    if Ysmooth (i)> Ysmooth(i-1) && Ysmooth (i) > Ysmooth(i+1) || Ysmooth(i)==
max(Ysmooth) && Ysmooth(i)>Ysmooth(i+1)
        Ypeak = [i,Ysmooth(i)];
        if Yflag == 0
        Ypeaknew = Ypeak;
        Yflag = 1;
        elseif Yflag == 1
        Ypeaknew = [Ypeaknew;Ypeak];
        end
    end
        if Ytsmooth (i)> Ytsmooth(i-1) && Ytsmooth (i) > Ytsmooth(i+1) ||
Ytsmooth(i)== max(Ytsmooth) && Ytsmooth (i)> Ytsmooth(i+1)
        Ytpeak = [i,Ytsmooth(i)];
        if Ytflag == 0
        Ytpeaknew = Ytpeak;
        Ytflag = 1;
        elseif Ytflag == 1
        Ytpeaknew = [Ytpeaknew;Ytpeak];
        end
        end

end

Zflag = 0;
Ztflag = 0;
Yflag = 0;
Ytflag = 0;
for i=2:at-2
```

```
    if Ztsmooth (i)< Ztsmooth(i-1) && Ztsmooth (i) < Ztsmooth(i+1) || Ztsmooth(i)==
min(Ztsmooth)&& Ztsmooth(i)<Ztsmooth(i+1)
        Ztmin = [i,Ztsmooth(i)];
        if Ztflag == 0
        Ztminnew = Ztmin;
        Ztflag = 1;
        elseif Ztflag == 1
        Ztminnew = [Ztminnew;Ztmin];
        end
    end
    if Zsmooth (i)< Zsmooth(i-1) && Zsmooth (i) < Zsmooth(i+1) || Zsmooth(i)==
min(Zsmooth) && Zsmooth(i)<Zsmooth(i+1)
        Zmin = [i,Zsmooth(i)];
        if Zflag == 0
        Zminnew = Zmin;
        Zflag = 1;
        elseif Zflag == 1
        Zminnew = [Zminnew;Zmin];
        end
    end
    if Ysmooth (i)< Ysmooth(i-1) && Ysmooth (i) < Ysmooth(i+1) || Ysmooth(i)==
min(Ysmooth) && Ysmooth(i)<Ysmooth(i+1)
        Ymin = [i,Ysmooth(i)];
        if Yflag == 0
        Yminnew = Ymin;
        Yflag = 1;
        elseif Yflag == 1
        Yminnew = [Yminnew;Ymin];
        end
    end
        if Ytsmooth (i)< Ytsmooth(i-1) && Ytsmooth (i) < Ytsmooth(i+1) ||
Ytsmooth(i)== min(Ytsmooth) && Ytsmooth (i)< Ytsmooth(i+1)
        Ytmin = [i,Ytsmooth(i)];
        if Ytflag == 0
        Ytminnew = Ytmin;
        Ytflag = 1;
        elseif Ytflag == 1
        Ytminnew = [Ytminnew;Ytmin];
        end
        end

end

[maxpeakYt, maxpointYt] = max(Ytpeaknew(:,2));
[maxpeakY, maxpointY] = max(Ypeaknew(:,2));
[maxpeakZt, maxpointZt] = max(Ztpeaknew(:,2));
[maxpeakZ,maxpointZ] = max(Zpeaknew(:,2));
[minYt, minpointYt] = min(Ytminnew(:,2));
[minY, minpointY] = min(Yminnew(:,2));
[minZ, minpointZ] = min(Zminnew(:,2));
[minZt,minpointZt] = min(Ztminnew(:,2));
gapt = Ytpeaknew(maxpointYt)-Ytminnew(minpointYt);
gap = Ypeaknew(maxpointY)-Yminnew(minpointY);

S = Ytminnew(minpointYt)-Yminnew(minpointY);
if S>=0
    for i = 1:S
        Yoffset(i)= Ysmooth(1);
        Zoffset(i)= Zsmooth(1);
    end
    for i=S+1:a
        Yoffset(i)=Ysmooth(i-S);
        Zoffset(i)=Zsmooth(i-S);
    end
end

if S< 0
        for i = a+S:1:a
        Yoffset(i)= Ysmooth(a);
        Zoffset(i)= Zsmooth(a);
    end
    for i= 1:a+S
        Yoffset(i)=Ysmooth(i-S);
        Zoffset(i)=Zsmooth(i-S);
    end
end
```

APPENDIX C: Matlab Code for classification of an input signal

```
load('pattern2traintestaverageoffset.mat');
load('gesturepatternclassifcation.mat');
millis = (Pattern2ZTest{:,'millis'})';
Zraw = (Pattern2ZTest{:,'z'})';
Yraw = (Pattern2ZTest{:,'y'})';
m = size(millis,2);
classlength = 300;
filter = 4;
for i = 1:m
    if i+filter <=m
    Yavg (i) = mean(Yraw (i:i+filter));
    Zavg (i) = mean(Zraw (i:i+filter));
    elseif i+filter >= m
    filternew = i+filter-m;
    Yavg (i) = mean(Yraw (i-filternew:m));
    Zavg (i) = mean(Zraw (i-filternew:m));
    end
end
     q = (m/classlength);
      for i = 1:classlength
          if floor(q*i) == 0
     c = 1;
          else
     c = 0;
          end
          j = floor(q*i)+c;
          millisre (i) = millis (j);
          Zre (i) = Zavg (j);
          Yre (i) = Yavg (j);
      end

a  = size(Yre,2);

for i = 1:a
    if i+filter <=a
    Ysmooth (i) = mean(Yre (i:i+filter));
    Zsmooth (i) = mean(Zre (i:i+filter));
    elseif i+filter >= a
    filternew = i+filter-a;
    Ysmooth (i) = mean(Yre (i-filternew:a));
    Zsmooth (i) = mean(Zre (i-filternew:a));
        end
end
for i = 1:size(Zsmooth,2)
    if Zsmooth(i)>=400 && Zsmooth(i)<=440
        Zsmooth(i)=420;
    if Ysmooth(i)>=320 && Ysmooth(i)<=360
        Ysmooth(i)=340;
    end
    end
end

Zflag = 0;
Yflag = 0;
for i=2:a-2
    if Zsmooth (i)> Zsmooth(i-1) && Zsmooth (i) > Zsmooth(i+1) ||
Zsmooth(i)== max(Zsmooth) && Zsmooth(i)>Zsmooth(i+1)
        Zpeak = [i,Zsmooth(i)];
        if Zflag == 0
        Zpeaknew = Zpeak;
        Zflag = 1;
        elseif Zflag == 1
        Zpeaknew = [Zpeaknew;Zpeak];
        end
    end
    if Ysmooth (i)> Ysmooth(i-1) && Ysmooth (i) > Ysmooth(i+1) ||
Ysmooth(i)== max(Ysmooth) && Ysmooth(i)>Ysmooth(i+1)
```

```
        Ypeak = [i,Ysmooth(i)];
        if Yflag == 0
        Ypeaknew = Ypeak;
        Yflag = 1;
        elseif Yflag == 1
        Ypeaknew = [Ypeaknew;Ypeak];
        end
    end
end

Zflag = 0;
Yflag = 0;
for i=2:a-2
    if Zsmooth (i)< Zsmooth(i-1) && Zsmooth (i) < Zsmooth(i+1) ||
Zsmooth(i)== min(Zsmooth) && Zsmooth(i)<Zsmooth(i+1)
        Zmin = [i,Zsmooth(i)];
        if Zflag == 0
        Zminnew = Zmin;
        Zflag = 1;
        elseif Zflag == 1
        Zminnew = [Zminnew;Zmin];
        end
    end
    if Ysmooth (i)< Ysmooth(i-1) && Ysmooth (i) < Ysmooth(i+1) ||
Ysmooth(i)== min(Ysmooth) && Ysmooth(i)<Ysmooth(i+1)
        Ymin = [i,Ysmooth(i)];
        if Yflag == 0
        Yminnew = Ymin;
        Yflag = 1;
        elseif Yflag == 1
        Yminnew = [Yminnew;Ymin];
        end
    end
end

[maxpeakY, maxpointY] = max(Ypeaknew(:,2));
[maxpeakZ,maxpointZ] = max(Zpeaknew(:,2));
[minY, minpointY] = min(Yminnew(:,2));
[minZ, minpointZ] = min(Zminnew(:,2));
gapY = Ypeaknew(maxpointY)-Yminnew(minpointY);
gapZ = Zpeaknew(maxpointZ)-Zminnew(minpointZ);
gapY = abs(gapY);
gapZ = abs(gapZ);
sizepeakZ = size (Zpeaknew);
sizepeakY = size (Ypeaknew);
if gapY> gapZ
    flagpeak=0;
for j=1:10
S(j) = Ytmaxpeak(j)-Ypeaknew(maxpointY);

if S(j)>=0
    for i = 1:S(j)
        Yoffset(i)= Ysmooth(1);
        Ztest(i)= Zsmooth(1);
    end
    for i=S(j)+1:a
        Yoffset(i)=Ysmooth(i-S(j));
        Zoffset(i)=Zsmooth(i-S(j));
    end
end

if S(j)< 0
        for i = a+S(j):1:a
        Yoffset(i)= Ysmooth(a);
        Zoffset(i)= Zsmooth(a);
    end
    for i= 1:a+S(j)
        Yoffset(i)=Ysmooth(i-S(j));
```

```
        Zoffset(i)=Zsmooth(i-S(j));
    end
end
if flagpeak == 0
Ytest = Yoffset;
Ztest = Zoffset;
flagpeak =1;
elseif flagpeak == 1
Ytest = [Ytest ; Yoffset];
Ztest = [Ztest ; Yoffset];
end
end
end
if gapY < gapZ
    flagpeak = 0;
    for j=1:10
S(j) = Ztmaxpeak(i)-Zpeaknew(maxpointZ);
if S(j)>=0
    for i = 1:S(j)
        Yoffset(i)= Ysmooth(1);
        Zoffset(i)= Zsmooth(1);
    end
    for i=S(j)+1:a
        Yoffset(i)=Ysmooth(i-S(j));
        Zoffset(i)=Zsmooth(i-S(j));
    end
end

if S(j)< 0
        for i = a+S(j):1:a
        Yoffset(i)= Ysmooth(a);
        Zoffset(i)= Zsmooth(a);
        end
    for i= 1:a+S(j)
        Yoffset(i)=Ysmooth(i-S(j));
        Zoffset(i)=Zsmooth(i-S(j));
    end
end
if flagpeak == 0
Ytest = Yoffset;
Ztest = Zoffset;
flagpeak = 1;
elseif flagpeak == 1
Ytest = [Ytest ; Yoffset];
Ztest = [Ztest ; Yoffset];
end
    end
end
flagE = 0;
for j=1:10
    Ye=Ytest(j,:);
    Ze=Ztest(j,:);
    Yt=YTrain(j,:);
    Zt=ZTrain(j,:);
    E1 = sum((Ye(1:classlength)-Yt(1:classlength)).^2);
     if flagE == 0
         E = E1;
         flagE=1;
     elseif flagE == 1
         E = [E ; E1];
     end
end
    [F, GesturePattern] = min(E);
   GesturePattern
```

eureca 2017 – Conference Paper
Paper Number EUG01

Design and Implementation of a GSM-Based, Seismic Activities Monitoring and Warning System Using Fuzzy Logic Algorithm

Kenneth C. Lopez[1], Sydney Girl C. Panganiban[1], Orland Jos R. Parducho[1], Gian Miguel M. Reyes[1], Glofett T. Velasco[1],Johnrenz R. Villegas[1], Favis Joseph C. Balinado[2],Rio A. Aguilar[2]

Lyceum of the Philippines University – Laguna
Calamba City, Laguna, Philippines

[*]kenneth_lopez69@yahoo.com

Abstract

Philippines is one of the country located in Pacific Ring of Fire that makes it prone to seismic activities. These seismic activities are unpredictable and historical records are the only basis for these events. In order to reduce the risk and disaster of this events, the study; Design and Implementation of a GSM-Based, Seismic Activities Monitoring and Warning System using Fuzzy Logic Algorithm is presented.

The project aims at designing a monitoring and precaution system, which is suitable of determining seismic activities as well as sending information to warn people around the area to give necessary precautions. A system is design to respond as quickly as possible the sensor meets its settings. This project provides a hardware and software design of a GSM-Based, Seismic Activities Monitoring and Warning System using Fuzzy Logic Algorithm. The goal of this study is to send information to the people around the area using the GSM Module of the system. The project uses an algorithm in implementing and designing a warning monitoring system of seismic activities. The project showed a prototype of a GSM based Seismic Activities Monitoring and Warning System. The goal of this project is to model a seismic warning detector to lessen casualties and for risk reduction using Arduino UNO to process the input into required output needed in the project.

Keywords: Earthquake, SMS, Arduino, GSM model, vibration sensor, fuzzy logic

1. Introduction

Seismic activities have taken up the interest of many engineers and scientists since it is one of the most destructive and fatal natural event. This was made due to the movement of earth's tectonic plates. The effect of the collision of the tectonic plates produces seismic waves, which is quite slow in movement but dangerous and disastrous [1]. Earthquakes can also considered as shaking, vibrating and displacement of the earth's soil. Volcanic activity, nuclear test, landslides and mine blast can also produce earthquake. It is rarely cause any living organism but the incident its trigger such as collapse of the infrastructure; such as building, bridge, roads, etc., tsunami, fires, etc. are the most important reasons behind the destruction [2].

Philippines is one of the country that is covered in the Pacific Ring of Fire, it experiences several earthquakes of various magnitudes almost every day; some are weak while most are disastrous. Philippines has five major faults within its archipelago. The West Valley fault that is part of Marikina Valley fault covers Quezon City, Marikina, Pasig, Makati, Parañaque, Taguig and Muntinlupa, provinces of Cavite and Laguna that ends in Canlubang [3]. According to Philippine Institute of Volcanology and Seismology, "West Valley Fault is due for the Next Big One within our lifetimes and a possible 7.2 earthquake looms around the corner if the West Valley Fault along the eastern side of Metro Manila cracks" [4]. Philvolcs said that the fault was four times move in the past 1,400 years. The last seismic activity occurred along the West Valley fault was around 358 years ago [5], and it can happen within our generation or the next generation.

Since Brgy. Makiling, Calamba City is near Canlubang where the fault line ends, the earthquake may still be felt if it occurs. Due to the alarming effect of this disaster, different government agencies make their move to alert and notify people regarding this earthquake. They are preparing their selves and the people within the area to the possible outcomes that may happen before, during and after the event.

2. Objective(s) of the Study

The main objective of this study is to develop and construct a system which can monitor the seismic activities for the area of Barangay Makiling at the same time, displaying it for precautions.

The specific objectives of this study is o identify hardware and software requirements of the system; To identify the input signals for the microcontroller using vibration sensors; To design and construct the prototype; To provide the Fuzzy Logic algorithm to the Arduinos for the processing of data for the GSM modules and the display unit; To test the performance of the system based on the performance required.

3. Conceptual Framework

6)

The best way to show the method used in the system is to display figures that would represent the contents, the functions and the flow of the proposed program.

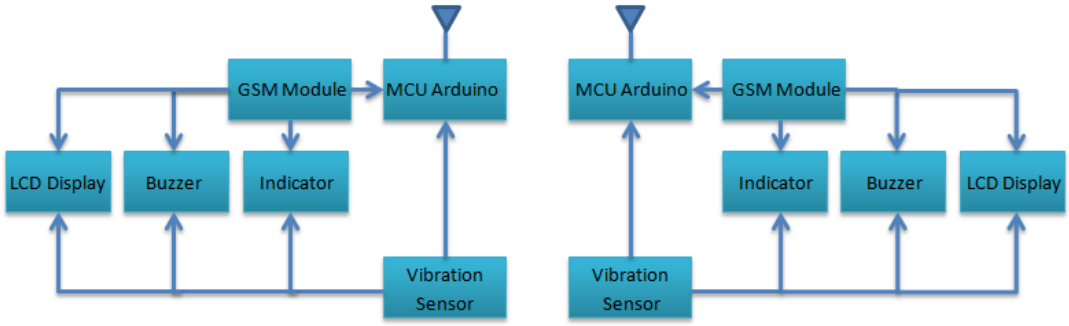


Figure 1. Conceptual Framework

7)

Figure 1 shows the Sensor, Microcontroller, GSM Module, Alarm, LCD Display, LED and Algorithm in establishing the control program using Arduino. The Vibration Sensor will be the triggering input [6] for the Arduino to collect the data from the sensor then display it on the LCD, alarm the Buzzer, ON the LED and also GSM will send a message to another GSM and the community. Arduino will collect the received message and display it on the LCD and trigger the alarm.

8)

9) 3.1 Proposed Design

10)

In order to make this system work and execute its functions, the group decided to use Arduino Software or Arduino Integrated Development Environment (IDE) to program the microcontroller unit of the system. It is a computer software application that provides comprehensive facilities, contains an area for writing a code, toolbar for common functions and menus. Matrix Laboratory or MATLAB used to simulate the processed data. A software comprises all the areas of applied mathematics [7]. It is also a programming language and commands useful for signal operation, conditional simulations, image procedure, etc.

11)

12) 4. Define and Design the System Requirements

13)

The table below is the list of inputs, process and outputs of the system. The input is the data needed to perform the system which will proceed to the process which is a task that will be carried out to complete the task. Lastly, the output, which describes the end result provided by the system.

Table 1. IPO Chart of the system

14)

INPUT	PROCESS	OUTPUT
• Vibration signals • SMS sent to the GSM module	• Arduino will process the generated PWM signals • Arduino will process the message to be displayed	• Vibration measurement and level are displayed in the LCD • Buzzer & light indicator ON • Residents receive the location of the earthquake

15)

Figures 2 and 3 show the graphic representation of the logical sequence of the steps that should be followed when the system is operated. In figure 2, when the sensor is triggered, these vibration signals are converted into PWM signals. Then these processed values will be classified to certain levels according to the measured vibrations. The LCD will display these information and alarm the system through a buzzer and light indicators. Meanwhile, in figure 3, the flowchart shows how the system responds when a message is received.

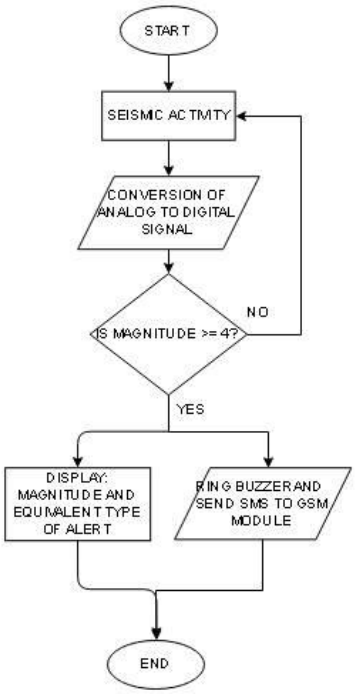


Figure 2. Flowchart for the Sensor as the System's Input

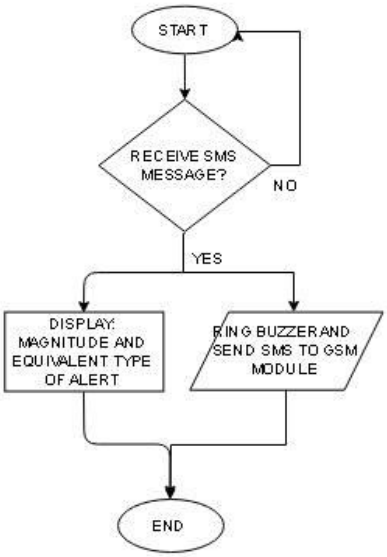


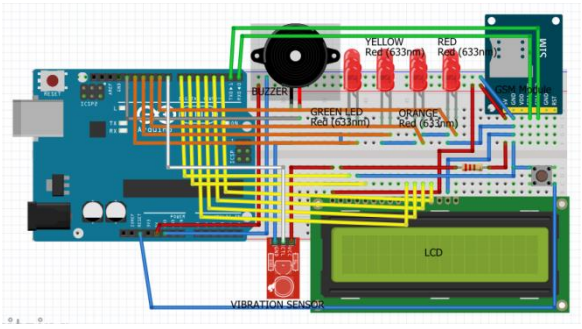
Figure 3.Flowchart of the system having SMS as Input

16) 4.1 Hardware Design

17)

Figure 4 shows the breadboard layout of the data gatherer of the project that is composed of an Arduino UNO, a vibration sensor that will detect the vibration and will trigger the buzzer, LEDs, LCD will display the measurement and GSM Module that will transmit an alert message to the nearest barangay.

18)



19) Figure 4.GUI of the system

Figure 5 shows the schematic diagram of the project that is composed of an Arduino UNO, a vibration sensor that will detect the vibration and will trigger the buzzer, LEDs, LCD will display the measurement and GSM Module that will transmit an alert message to the nearest barangay.

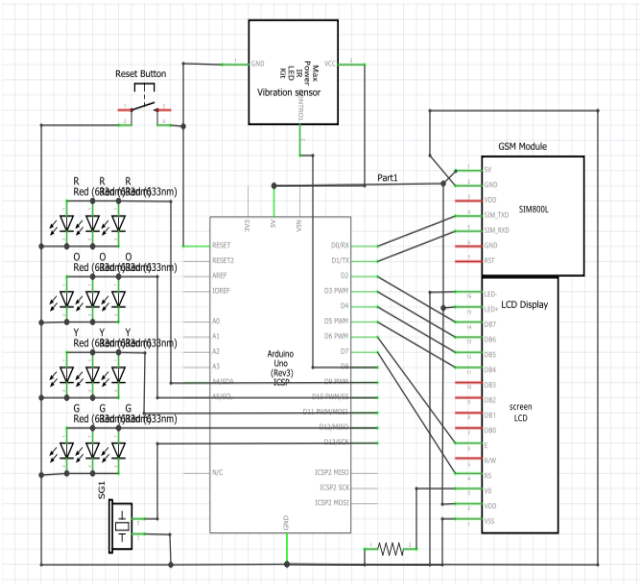
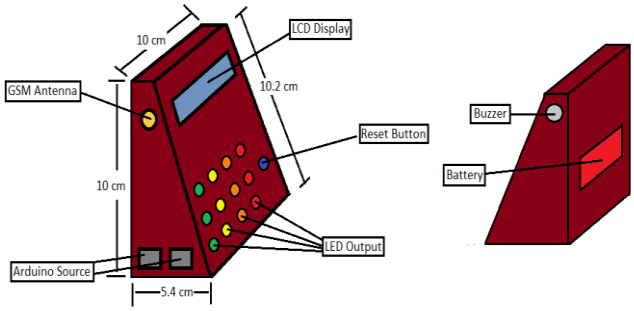


Figure 5. Schematic Diagram of the system

20)



21) Figure 6. CAD Illustration

22) 5. Experiments
23)

The complete system was designed in C language in Arduino and use Fuzzy Logic to analyse the output of the system. The first tab represents the fuzzy logic, how it processes the input. The last tab represents the Vibration Sensor. The explanation of matching solutions of the real time earthquake are in each of the sections below.

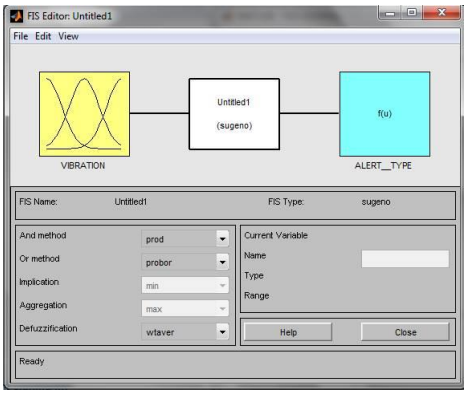


Figure 7. MATLAB Fuzzy Logic

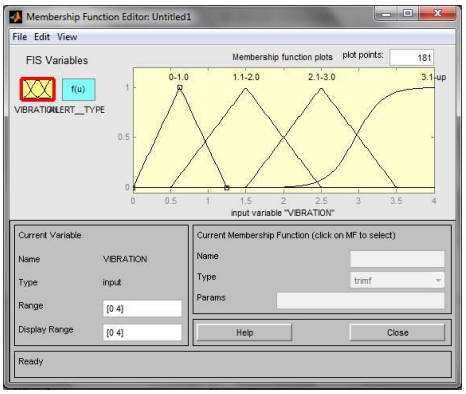


Figure 8. Assigning Input

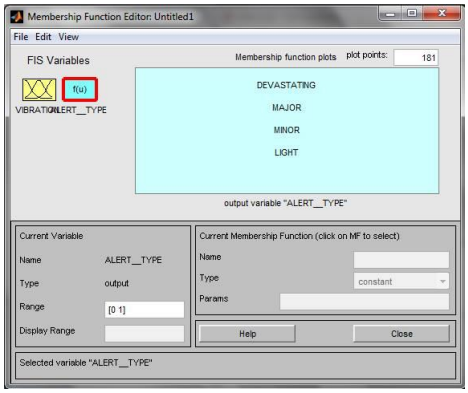


Figure 9. Assigning Output

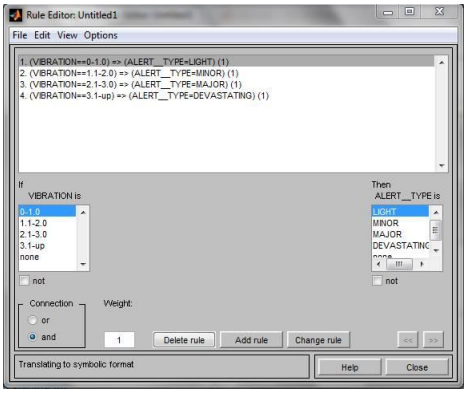


Figure 10. Fuzzy Logic Ruling

Display 1 to 3 show the software algorithm using fuzzy logic. Assigning input as "vibration" and output as the "alert type". Once the sensors measured sudden movements, these signals will then be classified as the input parameter of the system, having 4 stages- 0 to 4.99, 5 to 5.99, 6 to 6.99 and 7 to 10. Meanwhile, Figures 10 to 12 show the measurement and level of the vibration signals processed. If the measured values are between 0 and 4.99, level is classified as "Light Level", if values are between 5 and 5.99 then, "Minor Level". If 6 and 6.99, level is classified as "Major Level" and if values are between 7 and 10, "Devastating Level".



Display 1 (Minor Level)



Display 2 (Light Level)



Display 3(Devastating level)

24) 5. Conclusions

In this paper, the project showed a prototype of a GSM based Seismic Activities Monitoring and Warning System. The study uses Arduino UNO to process the input into required output needed in the project. A set of C programming language were used and studied in the process for desired results. The project also provides a proto-type hardware that allows transfer of information between two modules. The goal of this project is to modelled a seismic warning detector to lessen casualties and for risk reduction.

25)

26)

Acknowledgment

27)

28) The researchers would like to extend their deepest gratitude to all the people who help them in making this research study possible.

29) To God Almighty, for giving them the strength, the knowledge, the ability and the guidance;

30) To their parents, who helped us for always being there for the researchers and especially for their financial support.

31) To their adviser, Engr. Favis Joseph C. Balinado and Engr. Rio A. Aguilar for always being there to help the researchers and give them guidance throughout the whole study;

32) To their classmates and the members, who helped and made valuable comment and suggestions on this research.

33)

34)

References

[1] Sherki, Yogesh, Nikhil Gaikwad, Jayalaksmi Chandle, and Anil Kulkarni, “Design of Real Time Sensor System for Detection and Processing of Seismic Waves for Earthquake Early Warning System”, 2015 International Conference on Power and Advanced Control Engineering (ICPACE), 2015.

[2] Rahinul Hoque, Shoaib Hassan, MD. Akter Sadaf, Asadullahil Galib, Tahia Fahrin Karim, “Earthquake Monitoring and Warning System”, 2015 International Conference on Advances in Electrical Engineering (ICAEE), 2015.

[3] Rolly E. Rimando, Knuepfer, Peter, “Neotectonics of the Marikina Valley fault system (MVFS) and tectonic framework of structures in northern and central Luzon, Philippines”, Tectonophysics, 2004.

[4] “Are you ready for the big one”, The Manila Times, 2015.

[5] “PHIVOLCS’ Solidum discusses CL earthquake, tsunami threats in PNP forum”, Bagong Aurora Website ng Bayan, 2013.

[6] D. Mohan Kumar, “Vibration Sensor”, 2015.

[7] Kristian Sanderg, “Introduction to MATLAB”, MATLAB, 2013.

eureca 2017 – Conference Paper
Paper Number EUG02

Development of an Android – Based Home Illumination System

Derrick J. Castillo[1*], Carlo C. Medina[1], Allen B. Flores[1], Patrick Lawrence D. Sorezo[1], Kim Jairus B. Mendoza[1], Neil P. Balba[2], Rio B. Aguilar[2]

[1]*Computer Engineering Department*

[2]*Computer and Electronics Engineering Department*

Lyceum of the Philippines University, Calamba City, Laguna, Philippines

[*]*derrick.castillo02@yahoo.com*

Abstract

Nowadays, Arduino Microcontrollers are widely used for projects, experiments and even monitoring activities due to its large database of libraries together with the use of sensors and other modules compatible. Arduino Microcontrollers are also known for reliability, versatility and low power consumption as it only uses 5 volts DC input voltage and has a several output pins with 5 volts DC out. In this paper, the proponents used a HC-05 Bluetooth module programmed in Slave Module to make the project possible to communicate via Android Application. Commands were sent from an Android device and then, the Arduino Microcontroller Unit will interpret the data that has been sent after that, the Microcontroller will also send signals to the relay module that has been made by the proponents. The relay module will able to act as a switch as the relay module can handle alternating current (AC) voltages as well as direct current (DC) voltages that is suitable for the lighting devices attached to the system. In the android application, there will be eight switches that will be active, the Android device should be connected first to the Bluetooth module before the user can start interfacing. A small model of a house was shown to visualize the project created. Some figures are represented showing that the android application, the microcontroller unit and the relay module is communicating and working properly. In addition, the Bluetooth Switch is a power saving equipment because of its low power consumption and will give comfort to the user due to its wireless communications.

Keywords: Bluetooth, Relay Module, Arduino Microcontroller, Home Appliances, Switches.

1. Introduction

Currently, having lighting at home is considered normal. Lighting helps the household greatly by easing some work and increase the times a person's capability to do work especially at night. From cooking to cleaning and even relaxing, many people grew up with the presence of home lighting and have become dependent of its usage. This proves how important lighting have become to everyone's life. However due to having too many switches for lighting, controlling those lightings can sometimes be a tedious task to do. Even just turning on or off a light bulb can be a bother for the user if the person is occupied in doing some other tasks. In those times, having a way to easily turn on or off a light bulb while doing other tasks might be the answer. Ordinary android cell phones with Bluetooth features can act as a remote control designed as a helping hand to human by reducing manual work thus saving human energy [1]. In this research, the proponents will develop a prototype that can be used to control home lighting with Bluetooth technology and Arduino Microcontroller.

Considering that having a phone is now a must especially smart phones, many people have their own smart phone especially Android Users. Smart phones normally have Bluetooth technology and taking advantage of that, an application will be installed in the phone so that the phone will serve as a remote for the appliances. The application is made for android phones due to it being recognized of its extra features and having majority of the mobile developers use the system [2]. The Bluetooth technology will send the signal wirelessly to the appliance instead of the user going in front of the appliance to control the appliance manually [3]. The use of smart phones for home control and automation is applicable due to its flexibility, low cost and ease of use [4]. This application utilizes Android based UI for control of home machines. Association with the smart living system can be produced using the outlined application by means of Bluetooth or web association [5].

. Using mobile phones as a remote controller can also be of help for those who are handicapped and old aged people to control appliances without having to do it manually [6].

Arduino Microcontroller will also be used along with Bluetooth technology in developing the prototype. Arduino Microcontroller can be associated to work with other programs or machines and utilized in taking inputs from switches and sensors and send signals as outputs to several kinds of devices that produces an output [7]. A Bluetooth module, HC-05, is used so that the commands from the android application will be interpreted. A relay module is also present which will serve as the switches for the light system is managed by the Arduino Microcontroller.

Due to the continuing improvement of modern technology, a wireless connection is now becoming essential for everyone's daily life. Having a wireless switch to control the home lighting system to continue in improving everyone's life condition is becoming necessary. The problem of the study also comprises the accuracy and measurability of the system, reliability and flexibility of the machine and lastly, consistency and dependability of the mechanism.

The study intends to develop an Arduino – based Bluetooth switch that can control switches for home lighting system using an android smartphone. The design of the system must be also cost effective and a user friendly type of a system. For added innovation, the wireless home lighting system should be controlled by an android smartphone. And lastly, a safe system that will give the best comfort especially for android users, handicapped people and also for the elderly people.

2. Methodology

The first process will be based on the Android application installed in an Android Mobile. Then once the user opened the application, the application will tell the user to first turn on the Bluetooth of the mobile phone, after opening the Bluetooth, the application will prompt the user to connect to the HC-05 Bluetooth module. Once paired, the user is now enabled to send commands to the Arduino Microcontroller and based on the commands sent, the Arduino Microcontroller can also set the relay module to ON or OFF per switch or ON ALL or OFF all. The relay module acts as a switch for the lighting system that makes the lights go ON or OFF state. The overall operation of the project is shown in Figure 1.

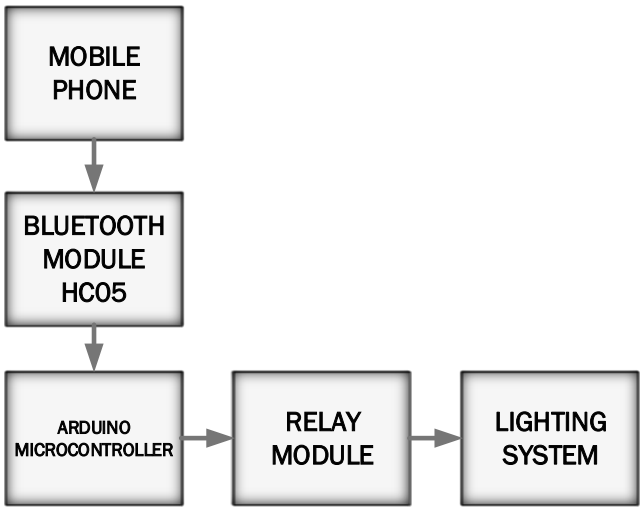


Figure 1. Over all operation of the system

The proponents used an Arduino UNO Microcontroller, a type of microcontroller board that is based on the ATmega328P IC. This type of microcontroller uses a 14 digital input/output pins, 6 of the pins can be used as Pulse Width Modulation outputs, it can be programmed also through the USB connection and the Arduino Software that uses Arduino Programming language. If the IC itself damaged, it can be replaced easily because the IC of this kind of Arduino is removable. [8] An image of an Arduino Microcontroller is shown in Figure 2.

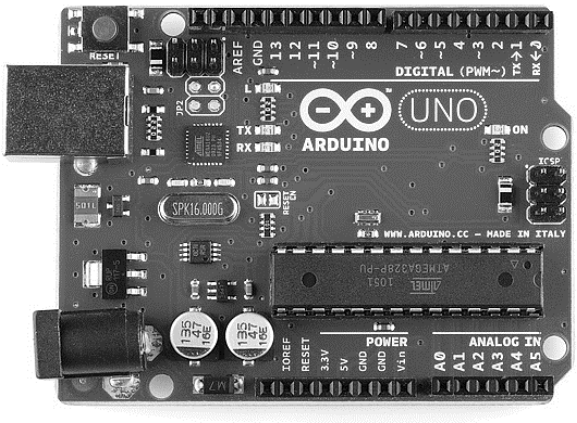


Figure 2. The Arduino Microcontroller

HC-05 is a popular Bluetooth module that was based on the EGBT-045MS Bluetooth Module. HC-05 can operate as a master or slave device. Master device is a configuration where the HC-05 can initiate a connection between a device. Slave device is a configuration where the HC-05 will only receive command from a master device. [9]. An image of HC-05 Bluetooth module is showed in Figure 3.

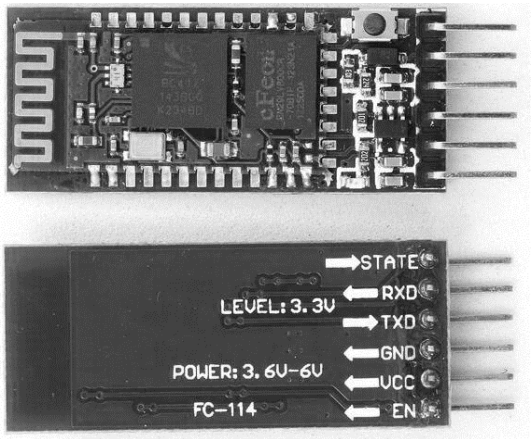


Figure 3. The HC-05 Bluetooth Module

The figure below (Figure 4) shows the Relay module that has been made by the proponents. This relay module will be attached to the Arduino microcontroller and its output will be attached to the lighting system.

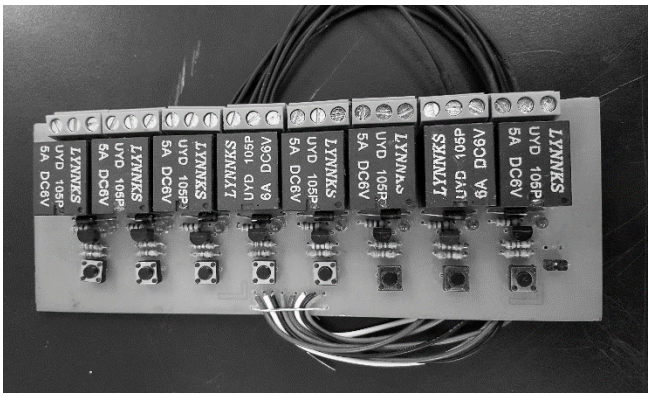


Figure 4. The DIY Relay Module

The Arduino IO Pins from 2 to 8 is connected to the relay module and pins 10 and 11 were assigned as soft TX and RX of the Bluetooth module. A common AC strip is connected with the neutral and the other individual end were connected at normally closed of the circuit. The main schematic from the Arduino UNO to the HC-05 Bluetooth Module and Relay Module is shown in Figure 5.

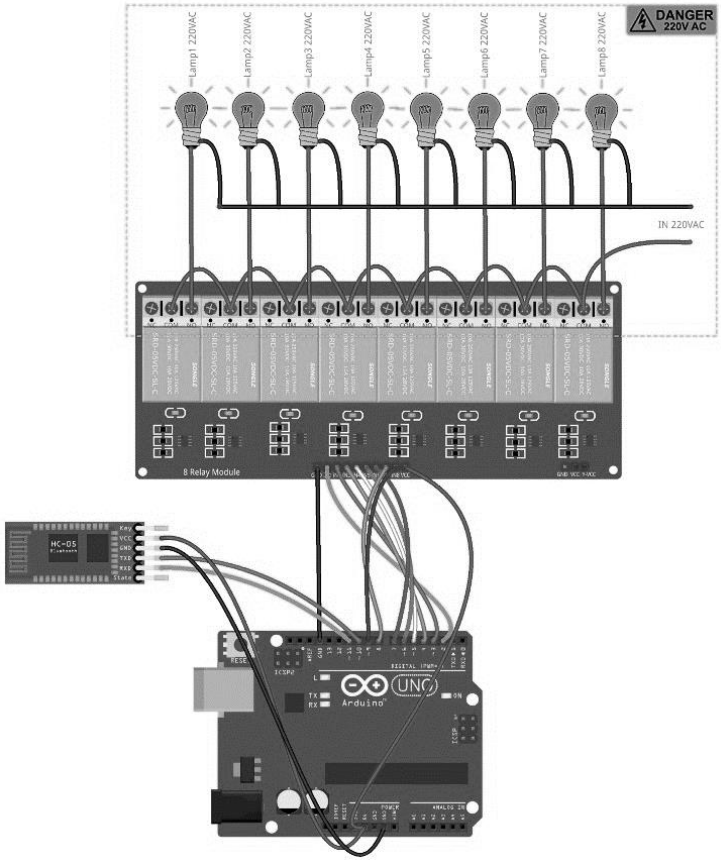


Figure 5. The Main Schematic from the Arduino UNO to the HC-05 Bluetooth Module and Relay Module

Before to start interfacing with the system, the Android Phone must be paired first with the HC-05 Bluetooth Module. A corresponding pin must be entered so that the two devices will be able to pair. A screenshot of the pairing request is shown in Figure 6.

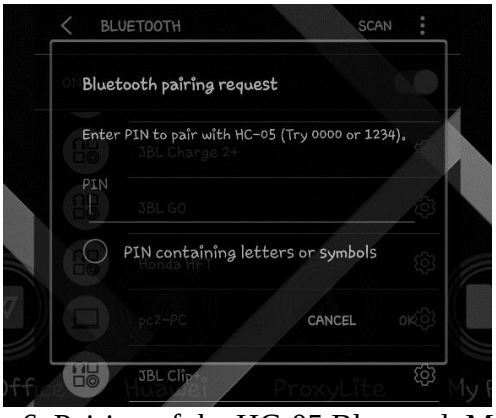


Figure 6. Pairing of the HC-05 Bluetooth Module

The connection button on the upper left area of the application will lit up if there is a successful connection with the HC-05 Bluetooth module, the button also can be a switch if the user wants to connect or disconnect to the HC-05 Module. There are eight individual buttons for eight individual lighting systems and two other buttons beside the connection button which can be touched to turn on or off all of the eight previously mentioned buttons as shown in Figure 7.



Figure 7. The GUI of the Android Application

3. Results and Discussion

Figure 8 to 10 show the representation of the system with the android phone present.



Figure 8. The Arduino – based Bluetooth wireless switch for home lighting system using an Android smartphone prototype

The figure above shows the completed prototype. Small LED were used as the light bulbs of the house. The user will be able to see whether their desired light was turned on or off in this prototype.



Figure 9. The prototype with some lights on

Figure 9 shows that the turned on switched in the Android smartphone corresponds to the specific light bulb assigned on that switch.



Figure 10. The prototype with all lights turned on

Figure 10 shows that if the button with the label “On all” in the Android phone is touched, all the lights of the house will also be turned on.

4. Conclusion

The researchers were able to develop a prototype of the Arduino – based Bluetooth wireless switch for home lighting system using an Android smartphone. As a prototype, small light emitting diodes were used as the light bulbs for the researchers to know that the lighting system is working. Aside from the Bluetooth module HC-05 and the Arduino Uno, every other materials and tools that were used were not too costly. Some materials were even recycled like the unused LED and wires while the application installed in the Android smartphone is free. The researchers therefore conclude that they were able to develop a cost effective and user-friendly home lighting system that

can be turned on or off at will by the user using an Android smartphone. Since this lighting is system is wireless and having a smartphone is now being considered a necessity, almost everyone will be able to use the system and can be considered as safe.

Recommendations

Every research has a room for improvements, so the researchers would like to recommend to the future researchers that if the user wants to have a larger scope of range, future researchers must use a Wi-Fi Module. A use of sensor also is one good idea to make the project more versatile. In addition, the future researchers can also use GSM Module so that users that forgot to switch on or off the light in long distances. These ideas may help this project to adapt with the present trends.

Acknowledgment

The authors of this report would like to acknowledge first and foremost the Almighty God in His name, for guiding the researchers to comply and complete the project with a proper attitude, knowledge and patience in all the struggles and tasks given. The researchers are very grateful and acknowledge their family and loved ones for giving the researchers their full support and motivation in accomplishing and completing this kind if requirements. Finally, the researchers would like to thank Lyceum of the Philippines – Laguna and their adviser Dr. Neil Balba for providing the researchers the opportunity and the capability to grasp this opportunity to start and finish this research.

References

[1] Sureshchandra, D. (n.d.), “Mobile Based Appliances Switching Using Bluetooth”, University of Mumbai, 2011.

[2] M. Puthanial, S. D., “Android and Bluetooth Technology Enabled Remote Control Using Smart Phone”, International Journal of Advanced Research in Electrical, Electronics and Instrumentation Engineering, 2014.

[3] R.Piyare, M., “Bluetooth Based Home Automation System Using Cell Phone”, 2011 IEEE 15th International Symposium on Consumer Electronics, 2011.

[4] D.Jaya Sree, M. L., “Android Mobile Based Home Automation”, International Journal of Advanced Research in Computer Engineering & Technology (IJARCET), 2014.

[5] Ahmed Sirajuddin Ahmed Alhaj, “Home automation system using Arduino”, University Teknologi Malaysia, 2015.

[6] Anandhavalli D, N. S., “Smart Home Automation Control”, International Journal of Informative & Futuristic Research, 2015.

[7] Kumar, S., “Android based smart home system with control via Bluetooth

and internet connectivity", Consumer Electronics (ISCE 2014), The 18th IEEE International Symposium, 2015.

[8] "Arduino - Introduction", Arduino.cc, 2017. [Online]. Available: https://www.arduino.cc/en/Guide/Introduction. [Accessed: 17- Mar- 2017].

[9] "arduino-info - BlueTooth-HC05-HC06-Modules-How-To", Arduino-info.wikispaces.com, 2017. [Online]. Available: https://arduino-info.wikispaces.com/BlueTooth-HC05-HC06-Modules-How-To. [Accessed: 18- Mar- 2017].

eureca 2017 – Conference Paper
Paper Number EUG03

Quadcopter Flight Controller with Four Degrees of Freedom and Data Acquisition Capability using Fuzzy Logic

Kaye Cristine Tolentino[1*], Josephine Suelto[1], Alvyn Ramos[1], Rina Quiatchon-[1], Ralph Laurence Visaya[1], Favis Joseph Balinado[2]

[1]*Electronics Engineering Department,*

[2]*Electronics and Electrical Engineering Department*

Lyceum of the Philippines University- Laguna (LPU-L), Laguna, Philippines

[*]kayecristine.tolentino@yahoo.com

Abstract

In this project, the researchers are to develop a Quadcopter Flight Controller with Data Acquisition Capability using Fuzzy Logic. To appreciate the aerodynamics and control systems present in Unmanned Aerial Vehicles (UAVs), this project is all about creating a hardware and software design of a Controller using Arduino's open-source prototyping platform as well as the use of the Fuzzy Logic for inaccurate result. The stability during takeoff and flight and its maneuverability in response to the directional inputs are processed and optimized by the controller. The installed speed, temperature, and humidity sensors give feedback to the microcontroller in order for the quadcopter to be capable of acquiring data of the environment's state during flight. The main controller board of the quadcopter manages its steady-state movement and stability in terms of the four degrees of freedom. For positional feedback to be used in the stabilization algorithm, the quadcopter uses 3-axis gyroscope, and accelerometer connected to the I^2C bus. Powered by a Li-Po battery, this quadcopter could be used to demonstrate aerodynamics and control systems while gathering information about the environment's temperature, air humidity, and the current time and date simultaneously while the quadcopter is in the air. The response of the fuzzified PID controller is faster and more reliable than that of the PID controller after the settling times has been compared to the four degrees of freedom.

Keywords: Quadcopter; Arduino; Fuzzy Logic; Data Acquisition

1. Introduction

Among the existing Unmanned Aerial Vehicles (UAV), the devices called quadcopters, quadrotor helicopters, quadrotors or quads are considered as the handiest type for they come in numerous advantages. These include simple constructions and small sizes which make them operational in confined places [1]. In addition, these quadrotor aircrafts are low cost, noiseless and highly maneuverable. Consequently, they have the ability to hover in air fixed point. They also perform the Vertical Take-Off and Landing Ability (VTOL) and specifically easy to maintain [2].

A quadcopter is composed of four high-speed rotors that are equally-spaced to the center of mass of the quadrotor in "X" configuration. These rotors are then used in producing its lifting force. It is also equipped with sensors which are used for gathering information. This is to comply with the controlling ability with a remote radio controller from the ground station. A quadcopter normally has two pairs of rotors with fixed pitch propellers turning clockwise whereas the other pair works in the counterclockwise direction. This structure will help the quadcopter keep a balanced torque and prevent rotation for itself [3]. The angular velocity and the speeds of the propellers are controlled so that these machines would perform the four degrees of freedom of the mechanical system. This is defined by roll, pitch, yaw and acceleration along a desired, common orientation [4] as demonstrated in Figure 1 [5].

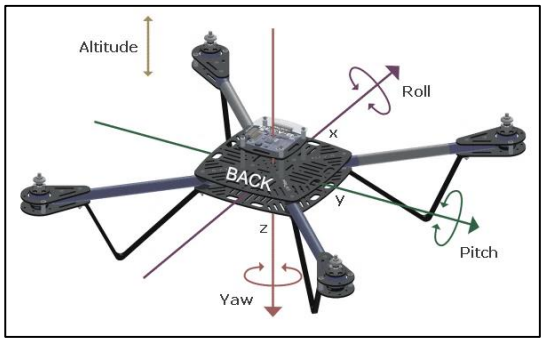


Figure 1. Basic movement of an X-quadcopter configuration

Without the necessary estimation and control algorithms, quadcopters are inherently unstable. Therefore, they need some form of automatic feedback control to help them be able to fly. This paper deals on controlling the quadcopter to basic directions of flying up, down, left, right, forward, and backward. This leads to the access of reaching a state of hovering with stability in the air and the ability to collect data through sensors attached for propellers' speed, air humidity, and ambient temperature of the environment during the flight. The output uses a controller connected to the quadcopter, and the system will be implemented on an Arduino microcontroller.

Fuzzy reasoning that is applied in this project is helpful in dealing with imprecise information such as the linguistic input variables. This method is considered to be one of the tools which allows computers handle inaccurate data. Thereafter, it enables the units to solve problems through the use of functional operators. Through the precise logic of imprecision, caged binary outputs are treated as fuzzy. This is defined as the crisp elements which are visualized to have degrees of variation as a result of a realistic situations. The creation of controllers will not require complex

mathematical skills, but at least basic human inferences between the causes and consequences of the aerodynamics present in quadcopters. Moreover, the resulting prototype of this project may be found useful in such activities wherein access to unreachable heights for humans would be highly attainable. These include photography, inspections, search and rescue missions, surveillance, construction and surveying, mapping, delivery, and further educational purposes.

The objective of this study is to develop a quadcopter device that has the ability to work with Four Degrees of Freedom of the mechanical systems namely roll, pitch, yaw and throttle through the use of Arduino microcontroller. This assembly is equipped with sensors for data acquisition, and a radio frequency module for communication.

The study covers concepts about developing a quadcopter's hardware structure and basic aerodynamic modeling. On the other hand, the study does not apply advanced algorithms to perfect the drone's capabilities in order to compete with existing drones in the market today. One of the system limitation is that the quadcopter can only operate in a sunny or dry weather and indoors, provided that there are enough space and height for the flight. Also, it is only flown within the Visual Line of Sight (VLOS). Negative heights are obviously not possible and will be equated to a value of zero. Lastly, angle restrictions are imposed for security and safety reasons. Otherwise, the quadcopter would easily lose its stability.

2. Methodology

2.1 Block Diagram

As shown in Figure 7, the quadcopter uses an Arduino-programmed Flight Control Board with wireless modules to receive directional commands and transmit data over a radio frequency connection. The data acquired by the sensors will be stored in an SD card or Secure Digital Card as the quadcopter maintains its flight. The main controller board of the quadcopter manages its maneuver and stability in terms of the throttle, roll, yaw, and pitch. The four brushless motors controlled in real-time enables steady hovering off with minimal vibrations while successfully navigating to its target location. For positional feedback to be used in the stabilization algorithm, the quadcopter uses 6-axis gyroscope, and accelerometer connected to the I^2C bus. With the power supplied by the LiPo battery, this quadcopter could be used to demonstrate aerodynamics and control systems while gathering of information about the temperature, humidity, time and date simultaneously during flight.

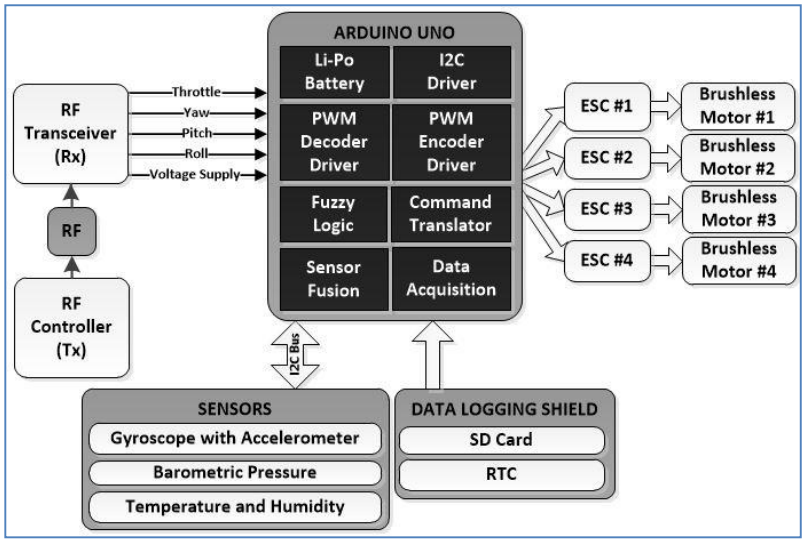


Figure 2. Block Diagram

2.2. Conceptual Framework

The researchers aim to implement a controller which maneuvers the flight of the quadcopter to a desired altitude through the use of wirelessly communicating radio transmitter and receiver with data acquisition using Fuzzy Logic as demonstrated in Figure 3. The hardware consists of the Arduino microcontroller, four Electronic Speed Controller (ESC) modules, four brushless motors with a propeller each, a gyroscope and accelerometer in one chip, a barometric pressure sensor, a temperature and humidity sensor and a light-weight frame. These are all connected on certain configurations. The brushless motors and propellers work with the ESC module. The principle of motors in aerodynamics are used with this specific aspect of the project. The calibration of the brushless motors then follows. Simultaneously, the sensors as described above are also being calibrated. After assembly and testing, the programming part focused on the implementation of the fuzzy logic algorithm linked to the installed sensors on its body. The created series of codes uploaded to the Arduino UNO microcontroller apply principles about controlling DC motors for an aerodynamic flight, and utilization of the measurements recorded from sensors for data acquisition. The system also takes external measurements of height for correcting the elevation of the quadrotor.

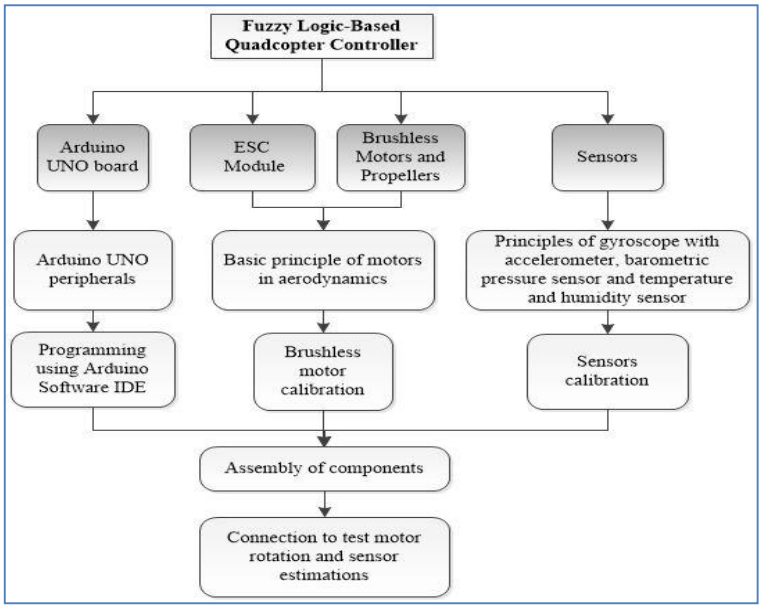


Figure 3. Conceptual framework

2.3 Four Degrees of Freedom Concept

2.3.1 Altitude Controller Concept

As illustrated in Figure 4, the altitude controller delivers the power needed by the four motors in order to correct the altitude error (z) in the quadcopter's height of flight with its only output value, μ_z.

1. $$\mu_z = f_1 + f_2 + f_3 + f_4 = 4fz$$ - Eq. 1

Where: f_1 is the force applied by the front motor, f_2 is the force applied by the left motor, f_3 is the force applied by the back motor and f_4 is the force applied by the right motor.

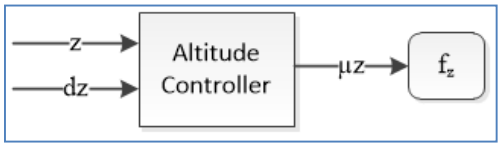


Figure 495. Altitude controller concept

The output of the altitude controller is the basis on which the outputs of the other controllers are all combined in the aggregation block or the final output aside from the power that the quadcopter always needs to hover at a specified altitude. The overlapping of motor powers from all the controllers is guided by the equation,

2. $$\mu = \mu_z + \Delta\mu_{ROLL} + \Delta\mu_{PITCH} + \Delta\mu_{YAW}$$ - Eq. 2

where μ is the control output or support force.

3.
4.
5.
6.

2.3.2 Roll Controller Concept

In Figure 5, the roll controller works on the error in roll value and its derivative. Grouping the motors on the left side, which are f_1 and f_2, separately from the motors on the right side, which are f_3 and f_4, the increase in output speed for the motors on the left side must go together with a decrease in output speed on the motors on the other side, or vice versa in order to maintain the stability of the system while rotating at the x-axis.

$$f_1 = f_2 = f_z + \Delta\mu_{ROLL}\ ;\ f_3 = f_4 = f_z - \Delta\mu_{ROLL} \quad \text{- Eq. 3}$$

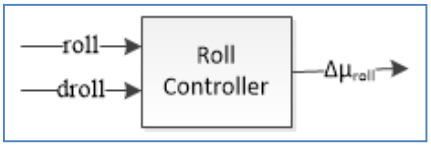


Figure 5. Roll controller concept

A negative value corresponds to a clockwise (left) rotation where forces on M1 and M2 are greater than forces on M3 and M4, and positive value corresponds to a counter-clockwise (right) rotation which goes the other way around.

Demonstration:

- To turn or roll left: if $\Delta\mu_{ROLL} > 0$ then $(f_1 = f_2) > (f_3 = f_4)$
- To turn or roll right: if $\Delta\mu_{ROLL} < 0$ then $(f_1 = f_2) < (f_3 = f_4)$

2.3.3 Pitch Controller Concept

Meanwhile, the pitch controller works on the error in pitch value and the pitch error's derivative as shown in Figure 6. This time, the motors are grouped based on whether they are at the front or back portion of the quad. The motors on the front are f_1 and f_4 while the motors on the back are f_2 and f_3. In this case, the same increment and decrement of speed apply. That is, the output $\Delta\mu_{PITCH}$ is also added to the speed of the front motors every time the same value is subtracted to the motors at the back and demonstrates rotation around the y-axis.

$$f_1 = f_4 = f_z + \Delta\mu_{PITCH}\ ;\ f_2 = f_3 = f_z - \Delta\mu_{PITCH} \quad \text{- Eq. 4}$$



Figure 6. Pitch controller concept

Demonstration:

- To pitch up or move backwards: if $\Delta\mu_{PITCH} > 0$ then $(f_1 = f_4) > (f_2 = f_3)$
- To pitch down or move forwards: if $\Delta\mu_{PITCH} < 0$ then $(f_1 = f_4) < (f_2 = f_3)$

2.3.4 Yaw Controller Concept

For rotation around the z-axis, the groupings of motors are aligned diagonally which are f_1 and f_3 turning in one direction, and f_2 and f_4 turning to the other direction. With the support force kept constant, the increase of speed in one pair comes with the decrease of speed in the other pair given by the controller output $\Delta\mu_{YAW}$. Just like the roll controller, the yaw controller returns a positive value for the quadcopter to rotate clockwise (right) and a negative value to rotate counter-clockwise (left) based on the processed yaw error and the yaw error's derivative as shown in Figure 7.

15. $$f_1 = f_3 = f_z + \Delta\mu_{YAW}; f_2 = f_4 = f_z - \Delta\mu_{YAW}$$ - Eq. 5

16.

17.



Figure 7. Yaw controller concept

Demonstration:

- To turn about to the right: if $\Delta\mu_{YAW} < 0$ then $(f_1 = f_3) > (f_2 = f_4)$
- To turn about to the left: if $\Delta\mu_{YAW} > 0$ then $(f_1 = f_3) < (f_2 = f_4)$

2.4 Properties of the Project

For this project, an X-shaped frame is used for the quadcopter which maneuver faster than the H-framed ones due to a much lower frontal aerodynamics and less throttle [7]. Furthermore, since two motors are positioned in the pitch and roll course, this configuration is naturally steadier and definitely suitable when needed [8].

The following components are used for sensing:

1. MPU6050 Gyroscope with Accelerometer - the most economical 2in1 microelectronic module for measuring the angular rates, rotational acceleration and lateral acceleration of the quadcopter [9].
2. BMP180 sensor - a piezoresistive sensor calculating air pressure against a mechanical sensor and adapts its resistance value based on that, this fused with an analog to digital converter that forwards a value to whatever instrument they are operating, and then that instrument applies some math to compute the pressure from that value [10].
3. DHT11 sensor - a basic measuring digital temperature and humidity. It exerts a capacitive humidity sensor and a thermistor to calculate the adjacent air, and declare a digital signal on the data pin [11].
4. Data logger shield - used for storing data about the surroundings that are measured by the sensors during the flight of the quadcopter.

Other components of the quadcopter are the following:

1. For the transmitter and receiver, the proponents used the Flysky FS-I6 set which has a minimum of 4 channels for regulating the quad and uses a low frequency, 2.4 GHz signals that can travel through blocks and aperture sufficiently. Its receiver output pulse has a center position of 1500 and ranges from 1000 to 2000.

2. For controlling the motors, the EMAX Simon Series 30A ESC is used because it is mainly produced for multi-rotors and it is fast-responding to control changes.
3. For the quadcopter to elevate, a set of four EMAX MT2213/935KV Brushless Motors is used. It is an ideal brushless motor because it is built to lift more weight and is run by the compatible current value as that of the ESC.
4. For the propeller, the researchers used 10”x4.5” Propellers were one pair is designed to rotate in the clockwise direction and the other air rotates in the counter-clockwise direction. This kind of propellers is light-weight with size and lift perspective such that the quadcopter can hover at less than 50% of the motor function. It is also best to have propellers that can endure soft bumps.
5. The proponents also used a LiPo Battery which has a large capacity of holding lots of energy in a small package and has a discharge rate applicable to the motor’s optimum operation.

It is installed together with a low-voltage alarm buzzer for the proponents to be warned if the battery voltage gets lower than the user-specified voltage parameter. The alarm may sound between 2.7 volts to 2.8 volts per cell. If fully charged, the LiPo battery can operate for at least 15 minutes depending on the load carried by the quadcopter.

2.5 Functions of the System

In general, the type of fuzzy inference that is used in this project is the Sugeno or Takagi-Sugeno-Kang method where the inference process composes of fuzzifying the inputs and applying fuzzy operator as well. The output membership functions of the Sugeno-type fuzzy inference are either linear or constant which makes it a good option for working with linear techniques such as PID. Moreover, it is computationally efficient and well suited for mathematical analysis [12]. This process is known as Fuzzy Inferencing System which involves three steps namely: fuzzification, rule evaluation and defuzzification. It is visually shown in Figure 8 [13].

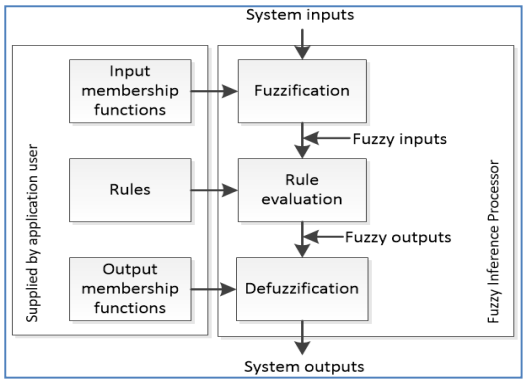


Figure 8. Fuzzy Inferencing Unit

Fuzzy Logic Inference: Fuzzy logic is infused to the flight control system of the quadcopter Matlab’s fuzzy logic toolbox and is uploaded using Arduino IDE. As adopted from [14], Figure 9 shows two input variables error (e) and change in error (Δe or deltaE), and three PID gains representing the outputs. The center box indicates the name of the file “Fuzzy Quadcopter.fis” and the type of fuzzy logic interference system used in the system which is Sugeno Fuzzy Inference Method.

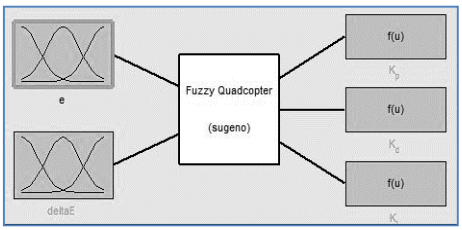


Figure 9. Fuzzy Inference System (FIS) Editor

As shown in Figure 10, the fuzzy logic control (FLC) for the input *error (e)* uses triangular membership functions with seven classifications namely: *"NB", "NM", "NS", "ZO", "PS", "PM"* and *"PB",* which stands for negatively big, negatively medium, negatively small, zero, positively small, positively medium and positively big, respectively. The same set of membership functions is also applied to the input *change in error (Δe or deltaE)*. Meanwhile, the crisp outputs of the FLC are Kp, Ki and Kd which stands for the PID gains. As shown in Figure 11, the parameters for the output membership functions for Kp are named as P, Z and N, which stands for positive, zero and negative, respectively.

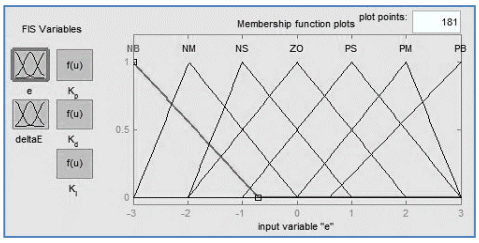


Figure 10. Input (e)

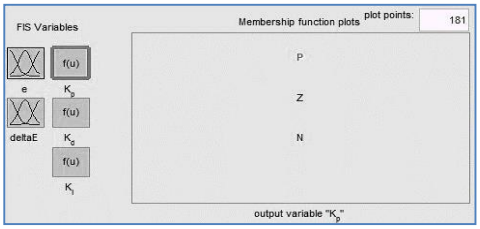


Figure 11. Output (Kp)

Particularly, fuzzy logic inferencing is applied to the quadcopter through automatically choosing the appropriate PID gains such as Kp, Ki, and Kd. The concluded values of the membership functions per output variable PID gains are applied to the Arduino code for the controlling the quad. Instead of setting fixed values for Kp, Ki and Kd, the quadcopter's software will be able to automatically choose among the values set per gain with respect to the fuzzy rules created and tested using Matlab's fuzzy toolbox.

Data Acquisition: Regarding the data acquisition capability of the quadcopter, the separate Arduino Uno with a data logger shield mounted on top is programmed to read the flight environment's condition based on percentage humidity, temperature, and

pressure. This is also where the height of flight or altitude is also measured together with the recorded date and time during the recording of information.

2.6 ESC Calibration

While the propellers are not yet assembled on the motors as well as the detachment of LiPo battery to the Arduino Uno, some additional basic checks are done by uploading the Arduino code for ESC calibration. This is to ensure that everything is working appropriately [15]. After reopening the serial monitor at 57600 baud rate, the following checks are done as with respective designated letters:

1. Receiver input check (r) - with both the transmitter sticks at the center position, all four channels should read 1500us. Moving the transmitter sticks should also read from 1000us to 2000us.
2. Gyroscope/ accelerometer angle check (a) – calibrates the roll and pitch angles at the start right after the gyroscope is done calibrating itself. It also displays the yaw value and will drop down to zero whenever the raw rotation stops. This angle check should show the following:
   a. Nose up is positive pitch and nose down is the negative pitch. (Figure 12)
   b. Left wing up is positive roll and left wing down is the negative roll.
   c. Nose right is positive yaw and nose left is the negative yaw.
3. Motor vibration check – with a cautious operation, the propellers are mounted back to the motors in order to test for excessive vibrations. The best performance of the propellers and motors is obtained by balancing each perfectly. First, the position of the clockwise and counter-clockwise propellers is checked. At the same baud rate of 57600, the numbers representing the amount of vibration measured by the accelerometer are displayed in the serial monitor for motor 1 at the right front (1), for motor 2 at the right rear (2), for motor 3 at the left rear (3), for motor 4 at the left front (4) and for all the motors (5) while slowly increasing the throttle to half. In this way, the direction of rotation is also checked is producing upward thrust. To reduce the vibration, a piece of tape is attached to one of the blades and checked if the values considerably reduce.

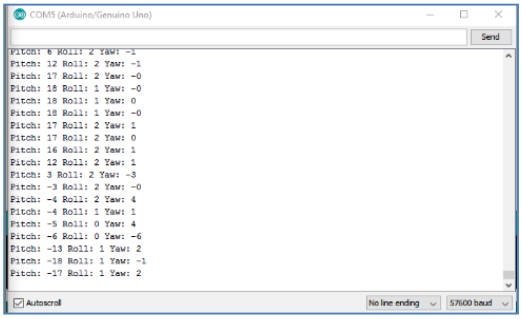


Figure 12. Nose up and nose down

3. Results and Discussion

3.1 Fuzzy Quadcopter Flight Controller Data and Analysis

Using two different algorithms, Fuzzy PID and PID, the proponents recorded the settling time of the throttle, roll, yaw and pitch using clock timer. Each algorithm is assessed ten times to further distinguish the dissimilarities in settling time among those two. The results of the experimentations are graphed below. These show that the Fuzzy PID can be more stable than PID. The data specifies proper feedback about the control system.

Table 1. Throttle Control Settling Times

TRIALS	PID	FUZZY PID
1	1.393	0.983
2	1.602	0.892
3	1.404	0.853
4	1.142	0.953
5	1.432	0.962
6	1.22	0.967
7	1.731	0.874
8	1.43	0.982
9	1.567	0.986
10	1.426	0.965

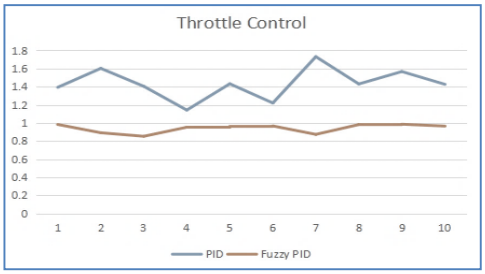


Figure 13. Graph of Throttle Control Settling Times

Table 1 shows the comparison between the settling times for PID and Fuzzy PID controls tested ten times. The settling time of the throttle is how fast the quadcopter responded to the lifting or flying upward direction signal. The test shows that the PID settling time is approximately 2 seconds while the Fuzzy PID is approximately 1 second only. Furthermore, Figure 13 shows that the fuzzified PID is more stable than the PID alone.

Table 2. Roll Control Settling Times

TRIALS	PID	FUZZY PID
1	1.46	0.897
2	1.21	0.925
3	1.12	0.856
4	1.09	0.934
5	1.23	0.878
6	1.22	0.982
7	1.22	0.821
8	1.16	0.873
9	1.37	0.913
10	1.12	0.943

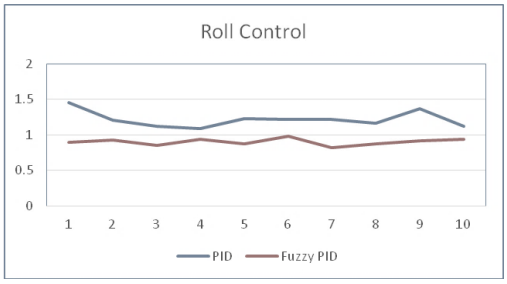


Figure 14. Graph of Roll Control Settling Times

Table 2 shows the comparison between two algorithms in terms of roll control. The roll's settling time is the time when the quadcopter responded sideward left or right. The proponents tested each algorithm ten times to further differentiate the differences in settling time of roll. The PID responded at approximately 1.5 seconds while the Fuzzy PID responded in less than 1 second. The result and the graph seen in Figure 14 show that Fuzzy PID response faster and it is more consistent and stable.

Table 3. Pitch Control Settling Times

TRIALS	PID	FUZZY PID
1	1.391	0.965
2	1.589	0.843
3	1.421	0.841
4	1.132	0.923
5	1.234	0.981
6	1.324	0.954
7	1.761	0.854
8	1.536	0.982
9	1.545	0.962
10	1.642	0.943

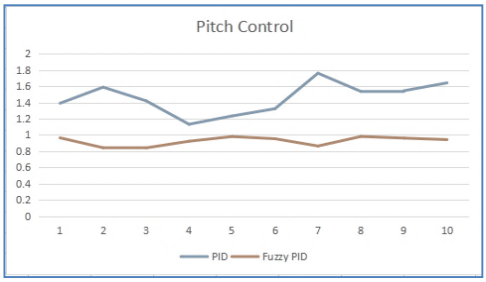


Figure 15. Graph of Pitch Control Settling Times

Table 3 shows the comparison between two algorithms in terms of pitch control. The pitch's settling time is the time when the quadcopter responded sideward forward and backward. Again, the proponents tested each algorithm ten times. The PID responded at approximately 1.5 seconds while the Fuzzy PID responded in less than 1 second. The result and the graph seen in Figure 15 show that Fuzzy PID responded faster and it is more consistent and stable.

Table 4. Yaw Control Settling Times

TRIALS	PID	FUZZY PID
1	1.401	0.963
2	1.589	0.854
3	1.403	0.834
4	1.134	0.964
5	1.454	0.943
6	1.215	0.964
7	1.741	0.871
8	1.425	0.934
9	1.435	0.976
10	1.453	0.965

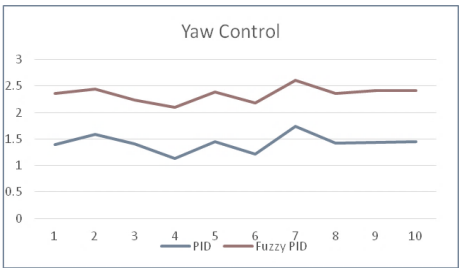


Figure 16. Graph of Yaw Control Settling Times

Table 4 shows the comparison of the settling time between those two controllers. The proponents tested the time by using clock timer and measured the time response of the quadcopter in the part of yaw controller. The yaw control is when the quadcopter is rotate either left or right. With less delay the quadcopter's stability will increase. The table and graph seen in Figure 16 show that the Fuzzy PID is faster and more stable than PID alone.

3.2 Sensor Data and Analysis

Figure 17 shows a graphical representation of the tabulated data acquired by the DHT11 and BMP180 sensors which are all mounted on a data logger shield. These data are stored on the SD card via the data logger shield and retrieved using Microsoft Excel. The stamp indicates a distinction between every set of data per row. The date and time are when the data has been recorded. Other data about the environment recorded are the percentage humidity, the temperature in degree Celsius, air pressure in millibars and the altitude in feet.

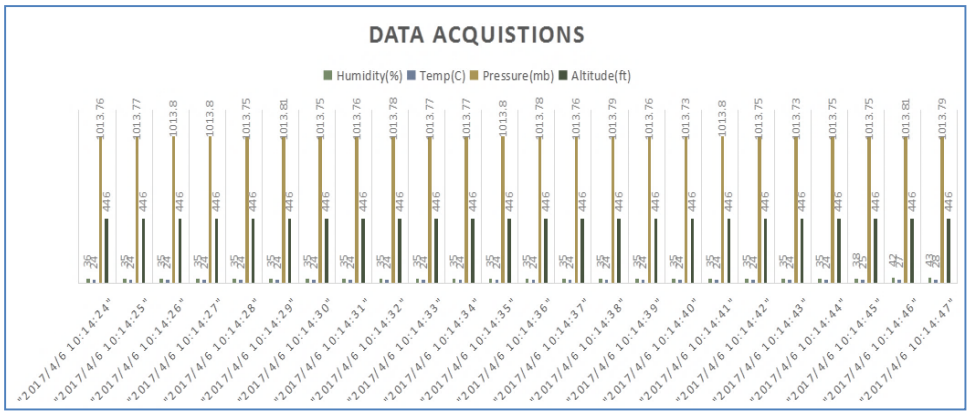


Figure 17. Graph of Data Acquired

4. Conclusion

After the whole process of developing a fuzzy logic-based quadcopter seen in Figure 20, the results were carefully studied and interpreted accordingly. Based on the data gathered and analyzed by the proponents, the flight controller was favorable and satisfactory because fuzzy logic was implemented well on the Arduino microcontroller. It is also evident that the response of the fuzzified PID controller is faster and more reliable than that of the PID controller after the settling times has been compared to the four degrees of freedom, namely throttle, roll, yaw, and pitch. The functionality tests of the individual components especially the gyroscope, barometric pressure sensor, temperature and humidity sensor, ESCs, motors and data logger shield are all initiated. Measurements of the temperature, humidity, pressure and altitude are successfully obtained and recorded via a data logger shield. Meanwhile, the battery level and connection status between the RF communication and quadcopter can be seen on the transmitter screen. Therefore, the development of the prototype with necessary data acquisition was successfully done and desirably worked which satisfied the objectives of this study.



Figure 20. The Prototype

References

Esteves, D. (2014). *Development and Experimental Validation of an Indoor Low Cost Quadrotor: Hover Stabilization with Altitude Control*.

Islam, S., Liu, P.X., EI Saddik., A. (2015). *Robust Control of Four-Rotor Unmanned Aerial Vehicle with Disturbance Uncertainty. IEEE Transactions on Industrial Electronics.*

Li, L., Sun, L., Jin, J. (2015). *Survey of Advances in Control Algorithms of Quadrotor Unmanned Aerial Vehicle, 2015*.

Lordache, A. (2013). *TED - Drones, how do they work? The basics explained.* [Online]. Retrieved from: https://www.youtube.com/watch?v=d250ix-tyew

Faial, (2013). *Basic movement of X-Quadcopter configuration*. [Online]. Retrieved from: https://fahmizaleeits.wordpress.com/2013/02/15/dasar-dasar-quadcopter-dan-setup-kkboard-2-0-pada-quadcopter-mode-x/basic-movement-quadcopter

Arduino. *Arduino Software (IDE).* [Online]. Retrieved from: https://www.arduino.cc/en/guide/environment

RCGroups. *H vs X Frame.* [Online]. Retrieved from: https://www.rcgroups.com/forums/showthread.php?2626553-H-vs-X-Frame 18.

Quora. *Why is 'x' configuration preferred over + config of quadcopter?* [Online]. Retrieved from: https://www.quora.com/Why-is-x-configuration-preferred-over-+-config-of-quadcopter

Hobden, A. (2015). *Quadcopters: Sensors.* [Online]. Retrieved from: https://hoverbear.org/2015/06/04/quadcopters-sensors/

Quadcopter Patrol. *Info Library: Altitude Hold Explained*. [Online]. Retrieved from: http://www.quadcopterpatrol.com/info-library-altitude-hold-explained/

Adafruit. *DHT11 Basic Temperature-Humidity Sensor + Extras*. [Online]. Retrieved from: https://www.adafruit.com/product/386

MathWorks. (2016). *Comparison of Sugeno and Mandani Systems.* [Online]. Retrieved from: https://www.mathworks.com/help/fuzzy/comparison-of-sugeno-and-mamdani-systems.html

Kharagpur. *Module 11: Reasoning with uncertainty-Fuzzy Reasoning. n.d*.

Visaya, R., Caldo, R. (2016). *Design, Development and Implementation of a PID Tuning With Fuzzy Logic Based Flight Controller and Smoothing Technique of an Unmanned Aerial Vehicle (Quadcopter) Using Arduino Microcontroller*

Brokking. *Project YMFC-AL – The Arduino auto-level quadcopter*.

eureca 2017 – Conference Paper
Paper Number EUG05

GSM – Based Flood Monitoring System and Data Acquisition using Smoothing Average Technique

Princess Joy V. Natividad[1*], Adrian F. Cardenas[1], Joselito P. De Castro[1], Frances Camil C. Ilagan[1], Juns Jaurigue[1], Kaye Cristine M. Tolentino[1], Favis Joseph Balinado[2], Rio B. Aguilar[2]

[1]*Undergraduate Student, Electronics Engineering Department*

[2]*Faculty Member, Electronics and Computer Engineering Department*

Lyceum of the Philippines University – Laguna (LPU – L), Laguna, Philippines

[*]princessnatividad0@gmail.com

Abstract

People has undergone extreme cases of danger which was brought by flood. Flooding occurs not only when a typhoon is existent but also during an ordinary rainy day. Early flood warning alarm system is used to detect the various water levels as indication for the approaching flood in the concerned vicinity. The system uses power generated by the solar panel. This project also utilizes the benefits of a microcontroller unit and GSM modem to send the measured data via Short Message Service (SMS) toward the disturbed population. Another form of warning comes in by means of the alarm system installed. There are several water level pointers which accommodate the need for multiple cautions that are necessary to be executed. The messages delivered contain specific data about the flood status which are being programmed and formatted previously in the unit. The ultrasonic sensor is responsible for the measurement of the water level. The water wave is varying which requires the need of a more stable and defined value of an input. The method used in the system is the smoothing average technique. We were able to measure the level of water depending on the height of it that results to different warning signals.

Keywords: Flood, Microcontroller Unit (MCU), SMS, GSM Module, Ultrasonic Sensor, Smoothing Average Technique

1. Introduction

One of the problems that we often experience is the varying and unpredictable behavior of the climate around us. One time, it's shining, yet the next minute, it's pouring. These events cause great bother to us for we cannot seem to prefigure what might come. Philippines is considered to be one of the developing countries which has suffered under quite a lot of natural phenomena including storms and typhoons. Many lives are being put at risks as the aftermath of all these disasters takes place. These events cannot be eradicated, but the hazards brought could be reduced with the availability of an early notice. The society won't only be able to prepare themselves, but the local government could make the desirable actions appropriate for the situation as well. A Fully Automated Water Level Indicator is a system that helps to indicate the level of water or any other conducting liquid. [1]

The studies about Tank Water Level Monitoring System using GSM Network shows the development of water level monitoring system with an integration of GSM module to alert the person-in-charge through Short Message Service (SMS). The water level is monitored and its data sent through SMS to the intended technician mobile's phone upon reaching the critical level. [2] Based on the previous studies, the flood warning systems that were presented usually have only a single water level and a one-time warning to be provided. Data processed by the MCU is being sent via SMS and through this, expected warning was implemented. Nevertheless, the customization of the water level boundaries has been an asset of the system for it can be set at various areas that experiences flood more often than others. There was also a research on GSM Based Water level and Temperature Monitoring System that is capable of monitoring the water level as well as the temperature of the tank which is connected to the industry. It also uses LCD to display the result. [3]

Flood is one of the most horrible disaster that world has to struggle with. Flood is uncontrolled and the consequences it leads to can be terrifying. Flood can occur suddenly and recede quickly at any place where rain fall is vulnerable, although rain is not the only impetus for flood. This can happen in a multitude of ways. The Philippines is a country that is prone in flooding. Not just because it is surrounded by bodies of water but also because of the growing population and urbanization. As the population rises, this tends to contribute a lot of waste that can cause flood. So, we should ready and aware of how to behave during floods. Using GSM Technology to Design and Implement the Water Environment Monitoring System, dam gate control system which helps in keeping an eye on the frequent usage of water resources from dam for irrigation purposes and efficient operation of dam gate according to the level of water and also helps in indicating about flood to people living in the surrounding. [4] In line with water level application, a Microcontroller Based Automated Water Level Sensing and Controlling: Design and Implementation Issue mainly focuses on investigating the microcontroller based water level sensing and controlling in a wired and wireless environment. [5]

The study aims to design and implement the GSM- Based Flood Monitoring System and Data Acquisition using Smoothing Average Technique. Specifically, it aims to identify the hardware and software requirement of the system by testing the prototype; assemble and construct the prototype; to program the microcontroller unit

that measures the parameter based on the received signal and to test the system based on the performance requirements.

This system, however, can detect diverse water heights which could reflect the different levels of threat caused by the flood. By the use of GSM modem, the clients would receive the data through SMS which were being processed by the MCU. Another form of warning is the alarm installed in the system which would siren conditional to the water levels all the same. Probability theory in the form of Smoothing Average Technique is the method used for determining the discrete level of the input parameter, which in this case is the water height.

2. Methodology

2.1 IPO Chart

Figure 1 is a summary of the system. The input makes the list of the data needed to complete the system. Obtaining the data gathered, the system will proceed to the process which lists any calculations that might have to be performed. After the process calculated the inputs, the system will provide the output.

INPUT	PROCESS	OUTPUT
Kowledge of using Arduino	Compilation of Arduino Codes	Design and Implementation of a GSM-based Flood Monitoring and Data Acquisition using Smoothing Average Technique
Averaging Technique	Charging of batteries using solar panel	
GSM Module	Implemening the use of SMS	

Figure 1. IPO Chart.

2.2 Conceptual Framework

The conceptual frame work is represented by using the system block diagram. The relationship between the blocks show how the system will work and the process of the system. In the design system block diagram, the authors exposed the blocks for system analysis.

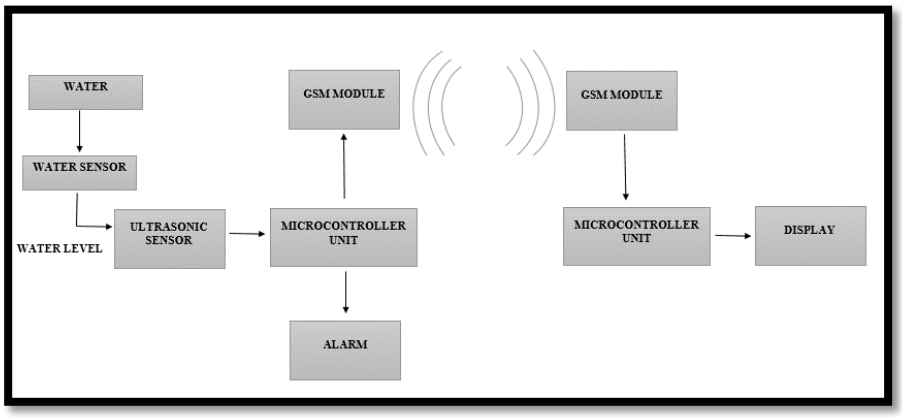


Figure 2. System Block Diagram.

2.3 Flowchart

The flowchart below shows the algorithm and commands used for the design and implementation of the project. The water sensor worked as a switch in order for the ultrasonic sensor to function. After the water level was measured, data gathered was averaged which leads to the output. This measurement hence was sent to the recipients using the GSM module.

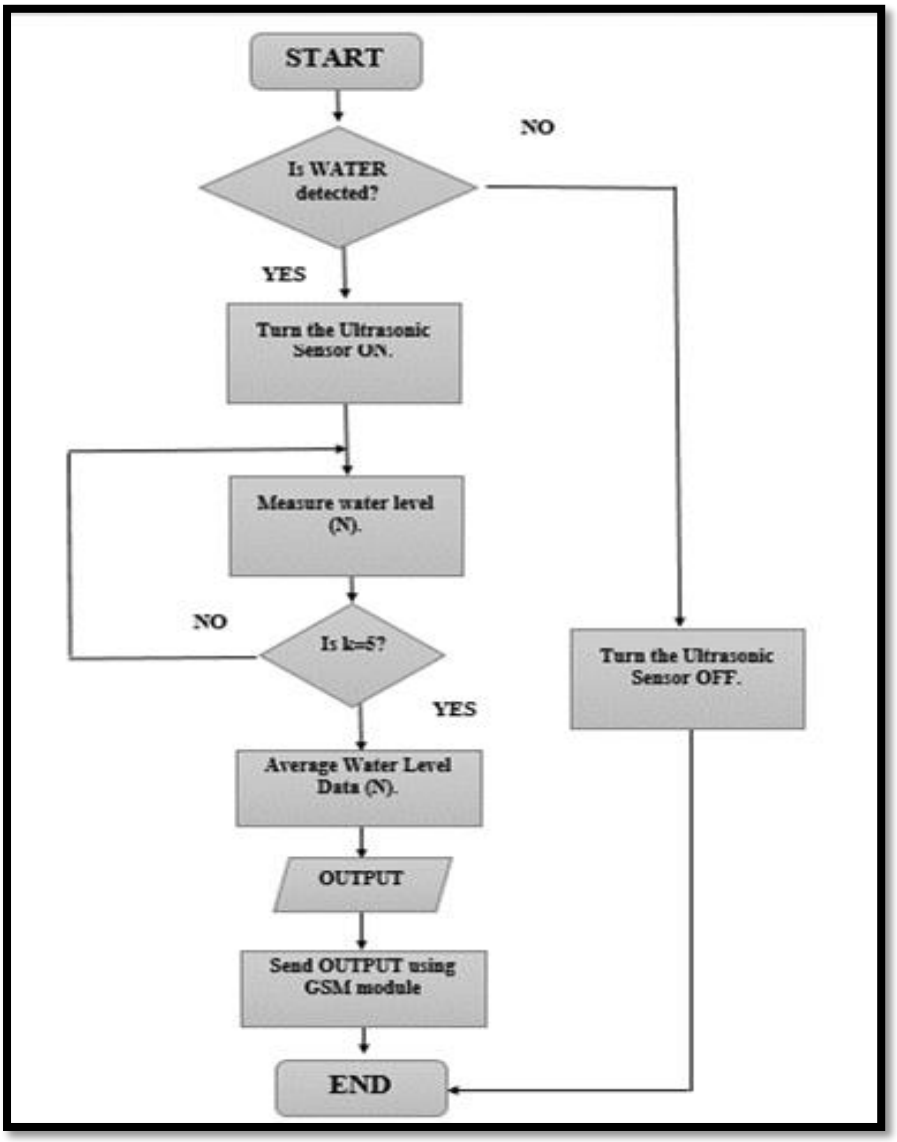


Figure 3. Flowchart.

2.4 Design Requirements

- **Hardware Specifications**

2.4.1 Arduino Uno

Arduino Uno is a microcontroller board which has 14 digital input/output pins, 6 analog inputs, a 16 MHz quartz crystal, a USB connection, a power jack, an ICSP header and a reset button.

2.4.2 Ultrasonic sensor

Ultrasonic Distance Sensor is a popular and low cost non-contact distance measurement device which can measure distances from 2cm to 400cm with an accuracy of about 3mm.

2.4.3 Grove Water Sensor

Grove water sensor is an easy-to-use, level/drop recognition sensor, which is obtained by having a series of parallel wires exposed traces measured droplets/water volume in order to determine the water level.

2.4.4 GSM Module

The GSM module is based on SIM900 module that provides a way to communicate using the GSM cell phone network. It allows to achieve SMS, MMS, GPRS and Audio by sending commands.

2.4.5 Piezo Active Buzzer

The piezo element requires a square wave (common from most microcontrollers) to produce a tone.

2.4.6 LED (Light Emitting Diode)

LEDs or light – emitting diodes, are semiconductor devices that produce visible light when an electrical current passed through them.

2.4.7 LCD (Liquid – Crystal Display)

A liquid – crystal display (LCD) is a flat-panel display that uses the light-modulating properties of liquid crystals. LCDs are available to display arbitrary or fixed images with low information content.

2.4.8 Solar Panel

Solar panels are categorized as devices that convert light into electricity. It is composed of solar cells which performs the photovoltaic effect that is necessary for converting of energy.

2.4.9 Lithium-ion Battery

The lithium-ion battery is low-maintaining which belongs to the group of rechargeable batteries. Due to its lightness and high energy density, it is very advisable for portable devices such as netbook computers.

2.4.10 Voltage Regulator (7809)

This voltage regulator is the device used for producing an output different from the input voltage.

2.4.11 Solar Charger Controller

It is a battery-operated controller unit which prevents further charging of the battery as it reaches the maximum capacity to avoid any probable damages.

- **Schematic Diagram**

These schematic diagrams represent the elements of the system using abstract, graphic symbols rather than realistic pictures.

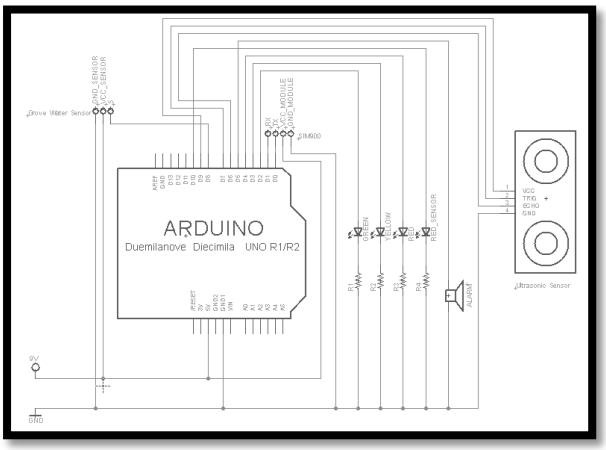


Figure 4. Water Level Sensor and GSM Sending Schematic Diagram.

The figure above shows how the ultrasonic sensor, water sensor and LEDs are interdependent by the use of the programmable microcontroller unit. Based on the commands and data gathered, message dissemination would be done by the GSM module included in the system.

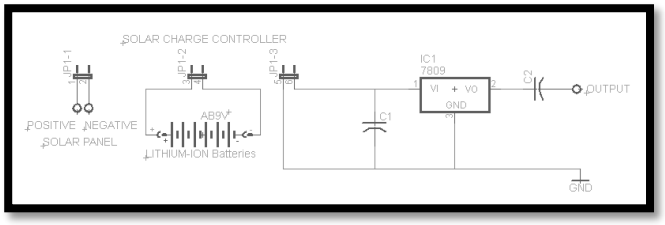


Figure 5. Battery Charging Schematic Diagram.

By the use of the solar charger controller, excessive charging of the battery from the solar panel would be reprimanded so that possible damages would then be avoided. This shows the use of a voltage regulator which is essential for the required input to support the circulation of the system by acting as a source.

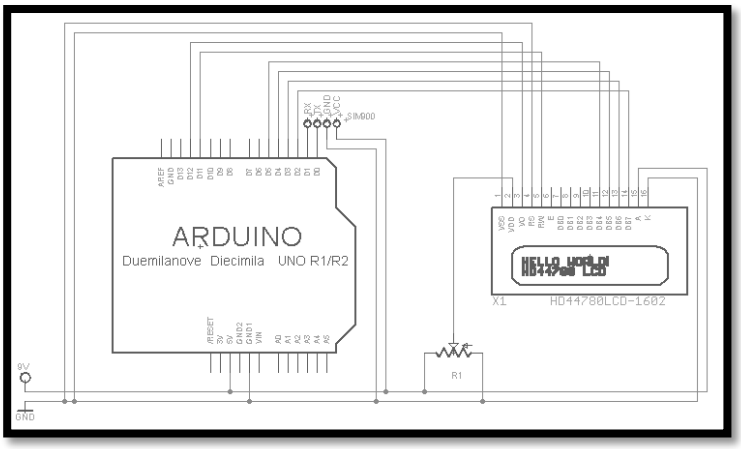


Figure 6. GSM Receive and Display Schematic Diagram.

This diagram represents the connection of the components required for the display of the message delivered from the preceding schematic involving data acquisition.

- **Software Specifications**

2.4.12 Arduino Software (IDE)

It connects to the Arduino hardware to upload programs and communicate with it.

2.4.13 AutoCAD

AutoCAD is a commercial software application for 2D and 3D computer-aided design (CAD) and drafting.

2.4.14 EagleCAD

EAGLE's easy-to-use schematic editor allows you to create an easy-to-read representation of your electronics design with zero complexity.

- **CAD Illustrations**

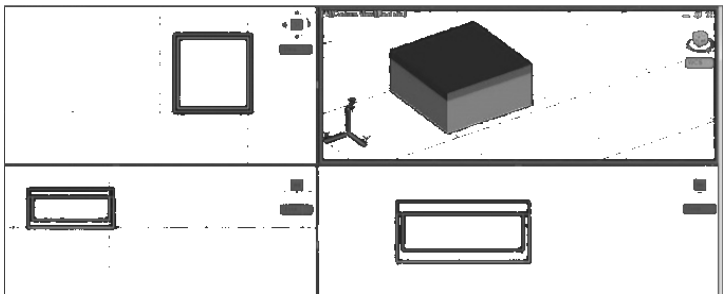


Figure 7. Proposed Actual Design (Casing).

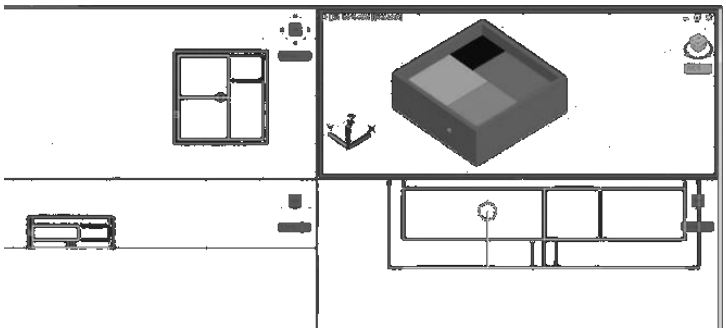


Figure 8. Proposed Actual Design (Casing).

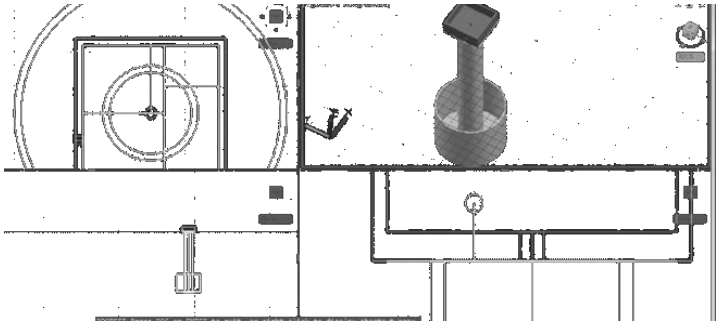


Figure 9. Proposed Actual Design.

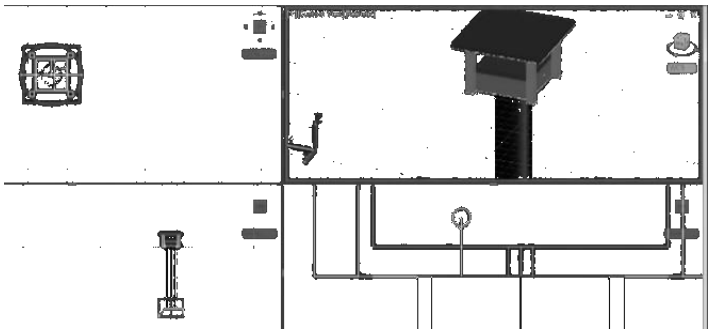


Figure 10. Proposed Actual Design.

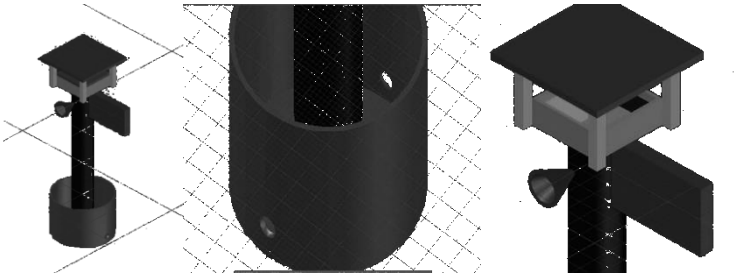


Figure 11. Proposed Actual Design.

2.5 Standards used

The proponents used IEEE standards in writing the paper for the study. For the project, the researchers used the Averaging that is widely used to calculate and to analyze data points by creating series of averages of the full data set.

- **Data Acquisition using Averaging Method**

```
void pingTime_in()
{
  pingTime_A = pulseIn(echoPin, HIGH);
  delay(1000);
  pingTime_B = pulseIn(echoPin, HIGH);
  delay(1000);
  pingTime_C = pulseIn(echoPin, HIGH);
  delay(1000);
  pingTime_D = pulseIn(echoPin, HIGH);
  delay(1000);
  pingTime_E = pulseIn(echoPin, HIGH);
  delay(1000);

  pingTime = (pingTime_A + pingTime_B + pingTime_C + pingTime_D + pingTime_E)/numReadings;
  pingTime_sec = pingTime/1000000;
  pingTime_hr = pingTime_sec/3600;
  targetDistance_miles = speedOfSound * pingTime_hr;
  targetDistance_ave = targetDistance_miles/2;
  targetDistance = targetDistance_ave*5280;
  waterLevel = height - targetDistance;
  Serial.print("\nWater Level:\n");
  Serial.print(waterLevel);
  Serial.print(" ft\n");
  delay(1000);
}
```

The specification of each warning for certain water levels is based on the average height of the Filipino people. It is believed that the male gender has a height of 5'3''. For women, the average height is considered to be 5 ft.

- **Water Levels**

Table 1. Range of the Water Levels

WATER LEVEL	WARNING COLOR	RANGE
LOW	GREEN	0.5 ft – 1.5 ft
MEDIUM	YELLOW	1.51 ft – 2 ft
HIGH	RED	2.01 ft – 6 ft

2.6 Preliminary Data and Results

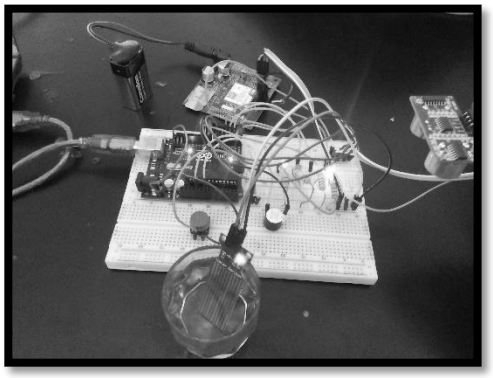


Figure 12. Board Design.

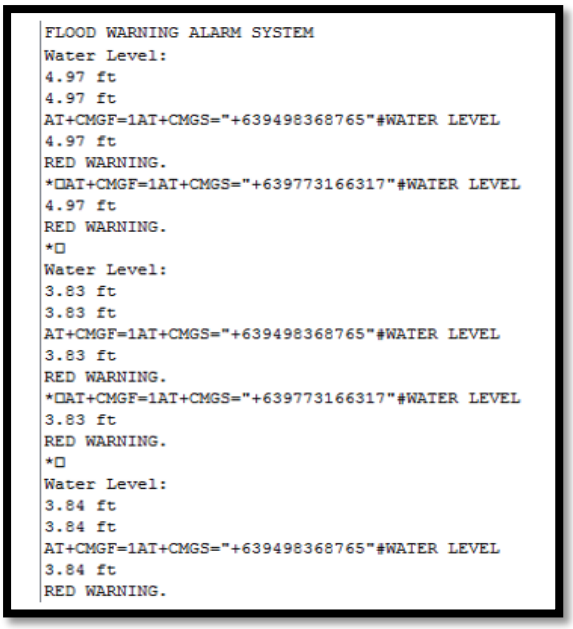


Figure 13. Serial Monitor.

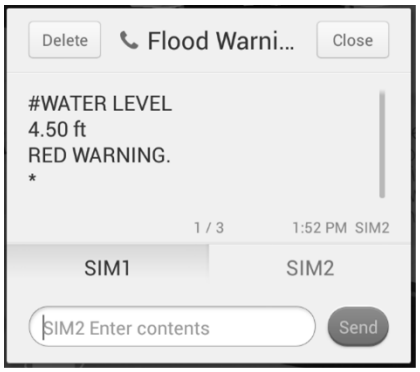


Figure 14. Message to the Recipient

Observations

- The grove water sensor sometimes functions unpredictably.
- The ultrasonic sensor is sensitive with the proximity of any nearby objects.
- The water level specification is unreliable.
- Due to the strength of the network signal, the performance of the GSM Module is affected.

3. Results and Discussion

The data gathered shows various water levels that the system was able to detect.

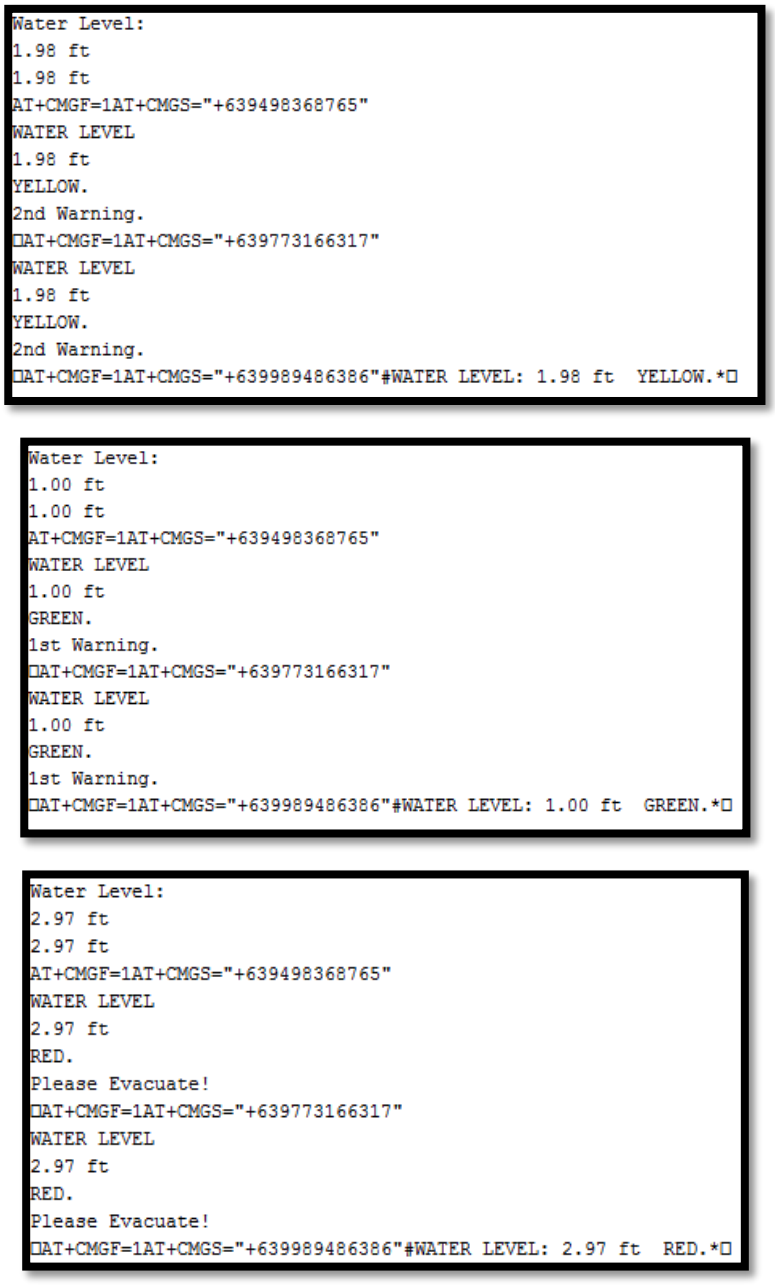


Figure 15. Serial Monitor.

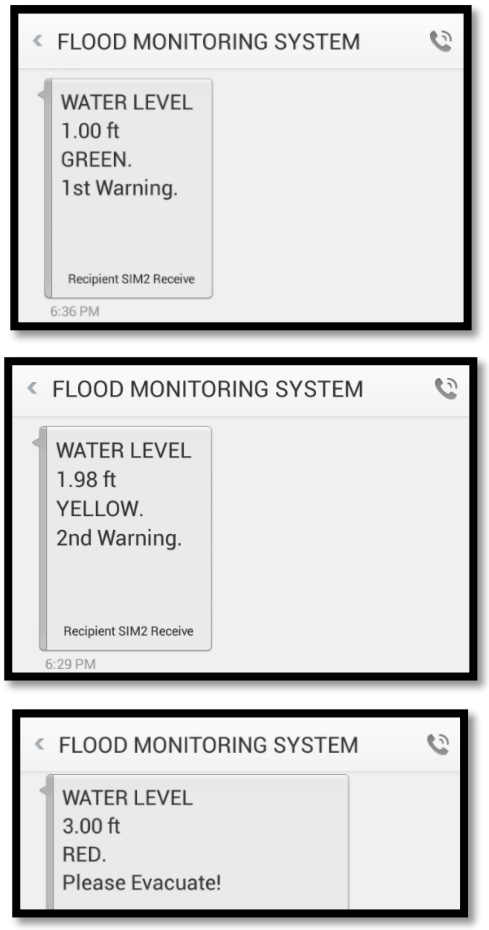


Figure 16. Message sent to the recipient.

4. Conclusion

It is a necessity for every risky situation to be warned about before the actual situation to occur. Considering flood to be one of the most common yet dangerous forms of natural events, it is such an advantage for a cautionary action of the distinguished incident. Throughout the process of developing the Design and Implementation of the GSM-Based Flood Monitoring System and Data Acquisition using smoothing Average Technique, the early warning mechanism was made possible.

By the use of the Arduino Uno, we were able to program the system as well as identify back the data needed for a much stable program using the Smoothing Average Technique. With the presence of a solar panel acting as the charger of the battery, sufficient voltage output was delivered as a supply of the microcontroller unit and the GSM necessary for message transmission. By gathering similar measurements of a constant distance, the performance of the system is considered accurate.

An appropriate application of a positive objective led to a meaningful result which lived by the goal of providing help through warnings in the most delicate of situations. We were able to measure the level of water depending on the height of it that results to different warning signals.

Acknowledgement

The authors of the study would like to acknowledge Almighty God, for giving the researchers, knowledge and wisdom to complete the study. The authors would like also to thank Lyceum of the Philippines University – Laguna for proving all the needed resources that made this study possible. Finally, the authors would like to thank their families, who supported them throughout the process of making the project.

References

[1] Jayant (2015). *Water Level Indicator Alarm.* Available Online: https://circuitdigest.com/electronic-circuits/water-level-indicator-alarm-circuit

[2] Johari, A., Wahab, M., Latif, N., Ayob, M., (2011). *Tank Water Level Monitoring System using GSM Network.* Paper presented at the International Journal of Computer Science and Information Technologies (IJCSIT), Vol. 2 (3), 1114-1120 Malaysia

[3] Abdullah, U., Ali, A., (2014, August). *GSM Based Water level and Temperature Monitoring System.* Paper presented at the International Journal of Recent Development in Engineering and Technology (IJRDET), Vol. 2 (3), 2011, 1114-1120, Pakistan

[4] Telgote, A., Narayanan, V., Dave, N., (2015, February). *Design and Implementation of Water Environment Monitoring System using GSM Technology.* Paper presented at International Conference on Technologies for Sustainable Development (ICTSD-2015), Mumbai, India

[5] Reza, K., Tariq, S., Reza, M., (2010). *Microcontroller Based Automated Water Level Sensing and Controlling: Design and Implementation Issue. Paper presented at* World Congress on Engineering and Computer Science (WCECS 2010), Volume 1, San Francisco, USA

eureca 2017 – Conference Paper
Paper Number EUG05

GSM Based Energy Consumption Monitoring with Control: A Prototype

Eufila Gerdaleen Legaspi[1*], Kenneth Agra[1], Jother Amutan[1], Kim Roylan Bundalian[1], Favis Joseph Balinado[2], Rio Aguilar[2]
[1]Electrical and Electronics Engineering Department
[2] Electrical and Electronics Engineering Department
Lyceum of the Philippines University, Calamba City, Laguna, Philippines

**eufilalegaspi@gmail.com*

Abstract
Nowadays energy meter reader from the electrical distributors goes to every house to take the reading manually then issues the bill. This method of collecting of meter readings becomes more problematic and costly, time consuming, and spends much human resource when readings have to be collected from vast, and often scattered rural areas and even the safety of the human resource assigned is in line. The proposed technique is a system that will automatically send the data of the power consumption of the consumer to the electrical distributor with the help of the Arduino microcontroller and GSM Module for the system to generate a report and send to the service provider through SMS. That data can be used to check the last reading consumed by the consumer, by the request that will be sent by the user. The system can also be used to control the load from both ends with the help of a relay circuit. Through that, the consumer can take control of the electrical load, as well as for the distributor to disconnect the supply when the customer fails to pay the bill. The system can also reconnect the electrical power when the balance is already paid. There will be an LCD display that is provided to display the readings and to update the consumer information's such as pricelist change or sudden power cut. Several tests were made and represented to address if the problem stated was resolved. Overall, the project compromises with the following requirements and performs accurately as what the results stated.

Keywords: Arduino Microcontroller, GSM Module, SMS, Relay Circuit.

1. Introduction

Over the years, measurement of electricity is depended on the traditional energy meter or electric energy meter. These meters play a key role in monitoring the power usage. Even though these meters are a master art of engineering designed a hundred of years ago, they are not capable to provide awareness to user about his consumption pattern [1].

Utility sub metering is the application of meter system that allows the admin of a commercial establishment to compute each unit for individual energy consumption through the installation of additional meters behind a main utility meter. Sub metering can be handled by a third-party entity that does not produce electricity, gas or water but resells utilities to the customers behind the main utility meter. It may install on specific appliances as part of utility-managed interruptible service rate or demand response. [2]

Due to rapid increase number of power consumers in every sector such as residential, commercial and in industrial, it is essential to ensure proper use of energy, generate correct bills and invoices and to reduce corruption [2]. The conventional method of collecting meter data in a multi-unit property is done manually by assigning an energy meter reader. This method of collecting of meter readings becomes more problematic and time consuming, and spends much human resource when readings have to be collected multiple meters. Also, human error is possible by mistakenly taking the reading of the meter. And if any tenant did not pay the bill, the operator needs to go to the electrical room or distribution panel to manually disconnect the power supply.

Automatic Meter reading (AMR) is a technology that automatically gathers data from energy, gas, and water metering devices and transfers it to the master station in order to analyze it for billing purposes. Data are read remotely, without the need to physically access the meter. The advantages include reducing peak demand for energy, enabling customers to make informed decisions, and reducing the cost of meter reading [3].

Global System for Mobile communication (GSM) is a digital mobile telephony system that is widely used in Europe and other parts of the world, GSM digitizes and compresses data, then sends it down a channel with two other streams of user data, each in its own time slot. It operates at either the 900 MHz or 1800 MHz frequency band. (Tech Target Network) [4] Philippines, known as the “texting capital of the world” and the “social media capital of the world” at various times over the last few years, has an advanced mobile market when compared to other similar countries. Half of the population subscribes to mobile services, 3G penetration is relatively high at just under 40%, smartphone adoption is rapidly growing, and internet penetration is increasing at the fastest rate of any country in Asia with the vast majority of new users coming online via mobile. [5]

A properly designed and develop GSM based metering is one way to have the tenants to reduce and control the monthly power consumption by informing the tenants about their usage on per month basis or as per their request. And also, it will help the energy meter reader to minimize his work.

The research will focus on the GSM based metering. Considerable benefits such as reduction of energy consumption by the use of the wireless disconnection of power supply by the use of GSM to control the Load. And a reference to the engineering students who are taking up subjects or courses related to automatic metering system. Lastly, this research helps the electrical facilitator and also the admin of a commercial establishment by providing an easy way of reading the multiple energy meter in a commercial establishment.

There is a need for a system that will monitor the electrical energy consumption of a commercial establishment remotely from multiple meters and for the tenants to check their own monthly usage so that they can predict their bills for the month. Also, the system must be remotely disconnected the power supply by the admin. In this regard, the proponents undertook the study to address on how the system will minimize the task of electrical facilitator to read the sub meters in a commercial establishment, the continuous monitoring of energy consumptions by the tenants, accurate measurements of energy consumption that will free from local sub meters, the storage of the history of electric consumption, accessibility through SMS and lastly, the control of the system that identifies the administrator and the user.

The study aims to design, develop and implement a GSM Based Energy Consumption Monitoring and Control through SMS that continuously monitors the electrical energy consumption. Also, to provide a device that will convert the electrical energy signal into pulse to the microcontroller. The study also aims to minimize the task of electrical facilitator to read the sub meters in a commercial establishment, an accurate meter reading is also an objective for the study. For added functionality, the system must also have a history of the energy consumption that is accessible through text messaging. The system must also be controlled through SMS and identify who is the administrator and who is the tenant for added security. And lastly, the system must be tested for its functionality, performance, accuracy and reliability.

2. Methodology

Figure 1 states about the Input-Process-Output of the system. The input variable in the system is the voltage and current that will be converted into pulse using the EVAL AD7755 that will be sent to the Arduino, and also the SMS command coming from the tenant or admin. The input variable will be processed by the microcontroller to compute for the equivalent energy consumption and the SMS that the Arduino receive from the tenant or admin will be processed by the microcontroller to give the energy consumption or the switching of the load.

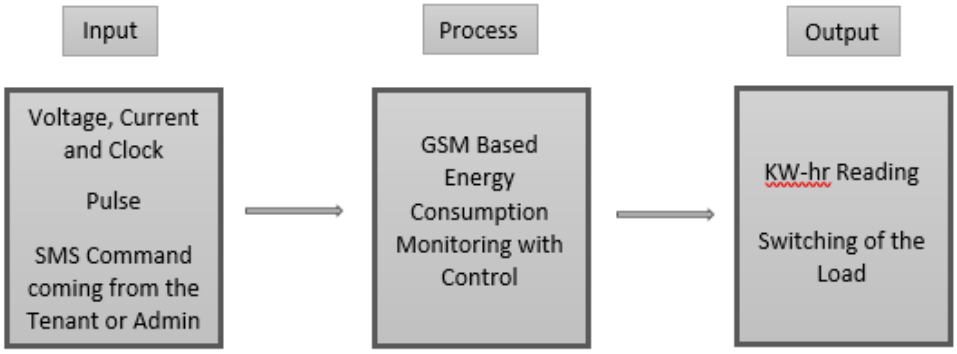


Figure 1. IPO Chart for the Research

Figure 2 shows the Arduino/ Genuino board. It is a small microcontroller board, which is a small circuit that contains a whole computer on a small chip (the microcontroller). It is a microcontroller board based on the ATmega328P. It has 14 digital input/output pins (of which 6 can be used as PWM outputs), 6 analog inputs, a 16 MHz quartz crystal, a USB connection, a power jack, an ICSP header and a reset button. It contains everything needed to support the microcontroller, simply connect it to a computer with a USB cable or power it with an AC-to-DC adapter or battery to get started. The Arduino/ Genuino Uno board can be powered via the USB connection or with an external power supply.

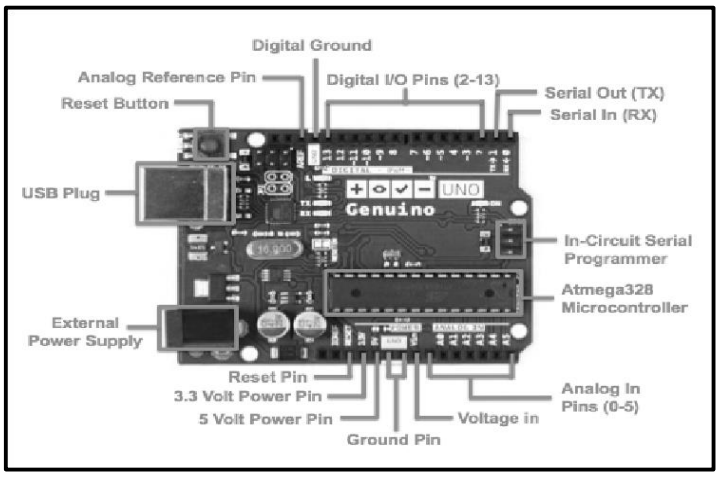


Figure 2. Genuino Uno

Figure 3 shows the Arduino GSM Shield, it allows an Arduino board to connect to the internet, make/receive voice calls and send/receive SMS messages. The GSM shield communicates with an attached Arduino through the Software Serial library. By default, communication between the modem and Arduino happens on digital pins 2 and 3.

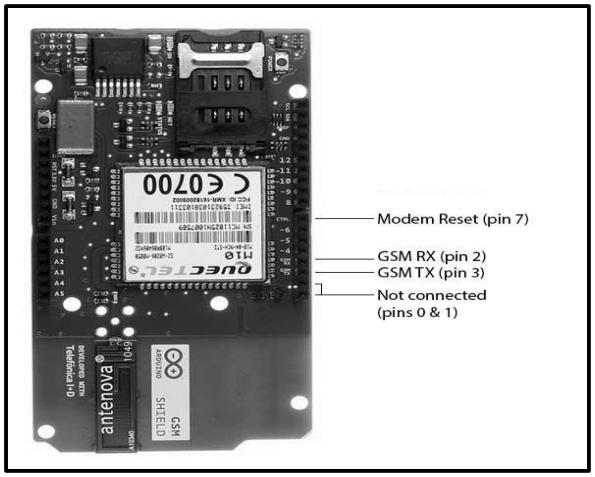


Figure 3. GSM Shield

Figure 4 shows the relay shield. A relay is an electrically operated switch. Many relays use an electromagnet to mechanically operate the switch and provide electrical isolation between two circuits. The Relay Shield is an Arduino compatible smart module with 4 mechanical relays providing an easy way to control high voltage. The max switching power is 70W DC. It can be directly controlled by Arduino through digital IOs with external 9V supply. [6]

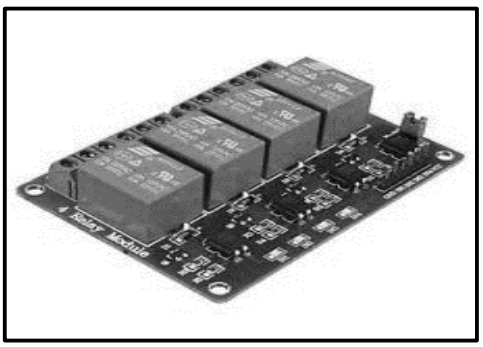


Figure 4. Relay Shield

On figure 5 is a Magnetic contactor. It is common used in automation industry for motor control application. It's function basically like a "relay". The power source into the coil of winding, it like the solenoid operation. It can deliver a large ampere to the loads and very long lasting and high durability. When the power is "on", it energized the coil and make plunger move and the switch contact is change from normally open to closed position. It allowed the current move from input terminal to output terminal. [7]



Figure 5. Magnetic Contactor

Figure 6 shows the Eval board ADE7751, it is a high accuracy, fault-tolerant electrical energy measurement IC that is intended for use with single phase distribution systems. The part specifications surpass the accuracy requirements as quoted in the IEC1036 standard. The AD7751 produce average real power information on the low frequency outputs F1 and F2. These logic outputs may be used to directly drive the electromechanical counter or interface to a Microcontroller. [8]

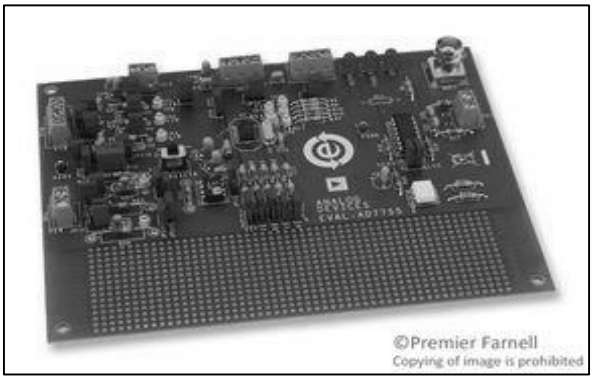


Figure 6. Eval Board AD7751

Figure 7 shows the LCD Display module with 4x20 characters and yellow/green LED backlight. LCD display uses STN technology, so it has a great contrast and a wide viewing angle. Display module is controlled by SPLC780D (same as common HD44780) parallel interface chipset that is easy to use. [9]

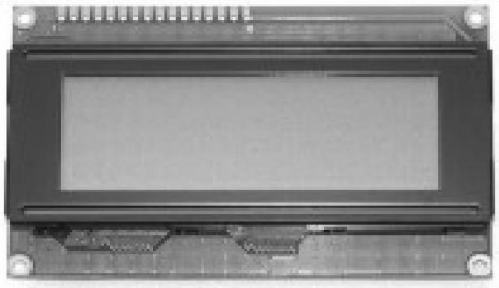


Figure 7. 4x20 LCD Display Module

Figure 8 shows the Arduino SD Card Shield. It allows you to add mass storage and data logging to your system. It is a simple solution for transferring data to and from a standard SD card.



Figure 8. SD/MMC Card Shield

The whole system is combined in one whole box. In the front view, an LCD Screen is present to show the total KW, Remaining Balance and some reminders and information that the user will need. Inside of the project box are the components of the system. An image of the proposed design of the system is present in Figure 9.



Figure 9. Proposed Design for the Research

The process of the system will be all based from the input of the energy consumed from the loads such as appliances, lights and all other electronic devices that consumes power. The LCD of the system will display the energy consumed and enable its data logging to have its own data. The user can send an SMS Message and then the system will try to check if the number that was used to message the system was registered, for added security, only authenticated or registered numbers are able to control and access the system. The system will send also a message about Load disconnections, consumption request, reconnection status, energy consumed, electric bill due dates. A flowchart of the system is shown in Figure 10.

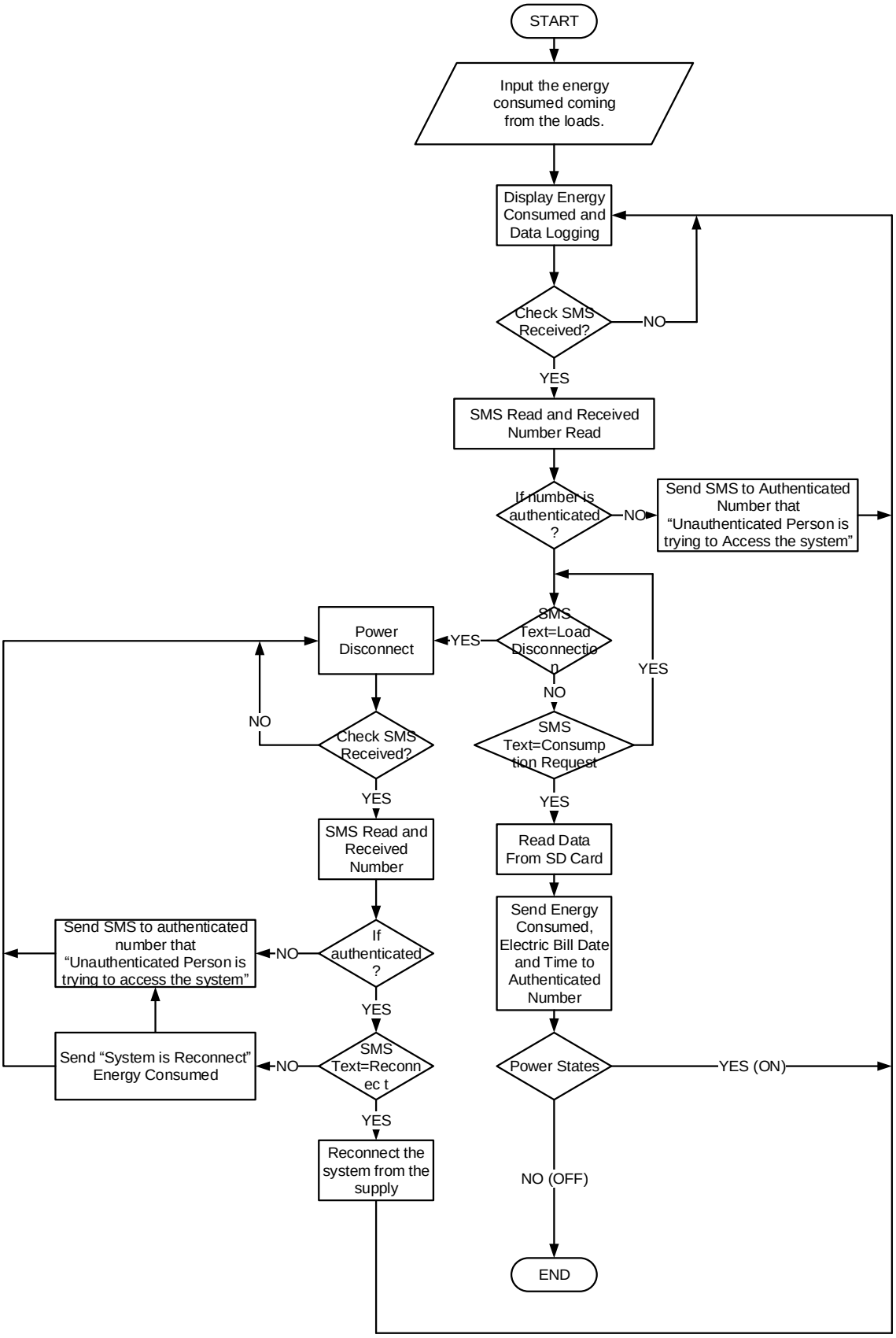


Figure 10. Flow Chart of the Research

3. Results and Discussion

Figures 11 to 12 present the simulation results of GSM Based Energy Consumption Monitoring with Control.

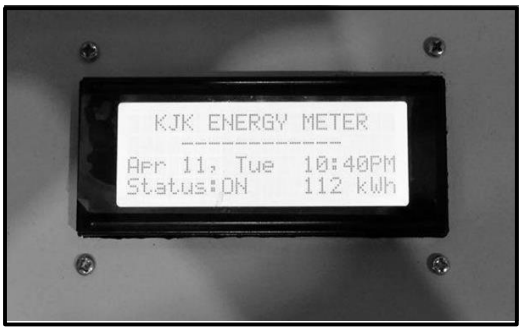


Figure 11. The Meter Unit Indicating the Supply is Connected

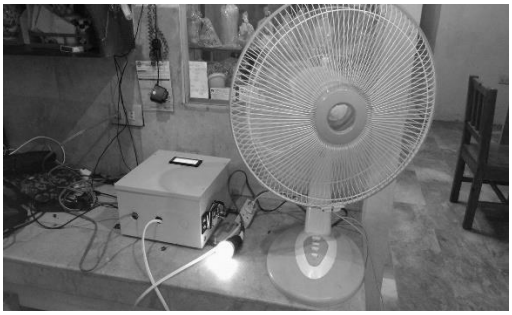


Figure 12. The Meter Unit with Load Connected

The text commands for admin and tenant doesn't have the same settings as the admin has an authority to connect and disconnect the system from the tenant. The system also knows if the text message is coming from the tenant or from the admin using algorithms in the microcontroller unit. A sample of commands are shown in Table 1.

Table 1. Admin and Tenant screenshots.

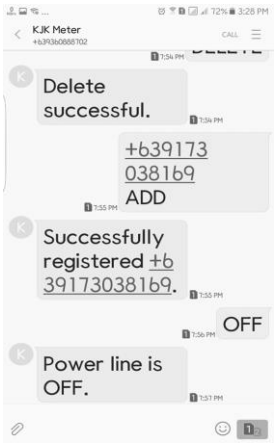
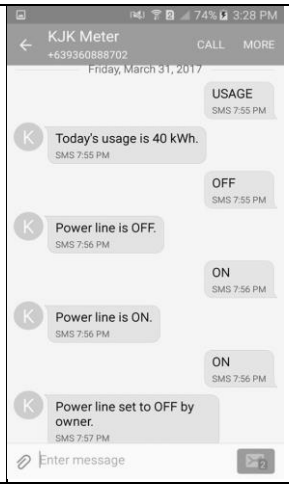
1.	Administrator	Tenant
		

Table 2 shows the SMS Command that can only be sent and GSM Module recognize by the reply that will and the message Arduino back to send by the check if the sent the sender to received or command is GSM Module. recognize by the required to load Therefore, it is the GSM the SIM card of to get an update Module in order module from the

Table 2. SMS Commands

SMS Command		Function	Reply of GSM
Administrator	**Tenant**		
USAGE	USAGE	Send the Energy Consumption of the day to the Sender	Today's Usage is __kWh
ON	ON	Connect the unit to the power grid	Power Supply is ON
OFF	OFF	Disconnect the unit from the power grid	Power Supply is OFF
ADD +639…n	-	Register the number of the tenant	Successfully registered +639…n
DELETE	-	Remove the control of the registered tenant	Delete successful

Figure 13 shows the graph of the Per Hour Energy Demand. This graph shows the consumption of energy from time to time.



Figure 13. Per Hour Energy Demand

Table 3. shows the comparison between the Actual Energy Meter and The GSM Based Energy Meter. It can be summarized that the GSM based Energy Meter is accurate based on the results with less than 1 percent error.

Table 3. Comparison: Actual Energy Meter and the GSM Based Energy Meter

Load	Actual Energy Meter	GSM Based Energy Meter	Error	Accuracy
500W Lamp	2,000 W-hr	1,998 W-hr	2 W-hr	99.91%
1100W Flat Iron	4,400 W-hr	4,396 W-hr	4 W-hr	99.90%
3,000W Water Heater	12,000 W-hr	11,988 W-hr	12 W-hr	99.90%
1,200W Microwave Oven	4,800 W-hr	4,796 W-hr	4 W-hr	99.92%
75W Electric Fan	300 W-hr	300 W-hr	0 W-hr	100%

4. Conclusion

This scheme reduces human intervention required in keeping track of the total power consumption of the users. Through GSM it will be very easy for the tenants in a commercial establishment to monitor their consumption and remotely control their supply whenever they are that can help them to reduce their energy consumption. It can also help the admin to collect data in massive amount of sub meters in a commercial establishment for the distribution of payments per month. Also for the easy disconnection and reconnection of the admin when the tenants fail to pay the bill on time. GSM Based Energy Meter can have a big role in safety because the tenants can check anytime once they forgot to turn off the supply of their unit or once there is appliances that is accidentally forgot to remove in the outlet, through GSM they can disconnect their loads in the supply and prevent causing fire and damages in the establishment.

Recommendation

For the further development and further improvement of the study and for the benefit of future researchers who will be dealing with the same study, the proponents recommends to develop a more safer system though as known no system is 100 percent safe, this kind of work can be tampered and seems to be the major setback. The future proponents can also add other control method such as wireless communication over the internet. Future researchers may tend to use also nonmagnetic enclosure. Future researchers may tend to add also algorithms that registers more than one tenant. And lastly, to lessen signal interference in the GSM module, an antenna should be added to the system.

Acknowledgement

The researchers of this study would like to express gratitude to our Almighty God for the help and guidance, to the College of Engineering and Computer Studies (COECS) for the never ending support to make this research possible, to the Lyceum of the Philippines University-Laguna (LPU-L) for it serves as the training ground of the researchers in their chosen field and to the families of the researchers who has given all the support that the researchers need to push through and finish this study.

References

[1] Azhar Fakharuddin, “A Smart Metering for Energy Management System Via SMS-SMS based Protocol”, UMP, 2011.

[2] Durkay J., "Energy Policy and Policies | State Energy Legislation and News", Ncsl.org, 2016. [Online]. Available: http://www.ncsl.org/research/energy/utility. [Accessed: 22- Oct- 2016].

[3] Prof. Dr. K. P. Satheyamoorthy, “Smart Energy Met Chunjuan Wei and Junjie Yang, “Implementation of Automatic Power Load Control” , “Meter Reading System Using PLC and GPRS”, International Journal of Advanced Research in Electrical, Electronics and Instrumentation Engineering, 8:16 (2011)4343 –4350.

[4] "What is GSM (Global System for Mobile communication)? - Definition from WhatIs.com", SearchMobileComputing, 2017. [Online]. Available: http://searchmobilecomputing.techtarget.com/definition/GSM. [Accessed: 18- Jul- 2016].

[5] Stryjak, J., Sharma, A. and Hatt, A., “Country Overview”, Philippines Growth through Innovation, pp. 3, 2014.

[6] "Relay Shield", Seeedstudio.com, 2017. [Online]. Available: http://www.seeedstudio.com/wiki/Relay_Shield_V2.0. [Accessed: 12- Oct- 2016].

[7] "Magnetic Contactor", GlobalSpec, 2017. [Online]. Available: http://www.globalspec.com/industrialdirectory/magnetic_contactor. [Accessed: 12- Oct- 2016].

[8] "EVAL-ADE7751 Evaluation Board | Analog Devices", Analog.com, 2017. [Online]. Available: http://www.analog.com/en/design-center/evaluation-hardware-and-software/evaluation-boards-kits/eval-ade7751.html. [Accessed: 13- Oct- 2016].

[9] "4x20 characters LCD Display with yellow/green backlight :: HW Kitchen", Hwkitchen.com, 2015. [Online]. Available: http://www.hwkitchen.com/products/lcd-display-4x20-characters/. [Accessed: 13- Oct- 2016].

eureca 2017 – Conference Paper
Paper Number EUG06

GSM Based Fire Notification and Data Acquisition System Using Kalman Filtering Technique

Carlene Joy A. Breganza[1*], John Carlo U. Ancheta[1], Edmar M. Atienza[1], Kevin L. Domingsil[1], Sidney Wyne R. Solas[1], Favis Joseph C. Balinado[2], Arvin Dela Roca[2]

[1]Undergraduate Student, Electronics Engineering Department
[2]Faculty Member, Electronics and Electrical Engineering Department
Lyceum of the Philippines University – Laguna (LPU-L), Philippines

[*]breganzacarlene@yahoo.com

Abstract
In this work, the proponents proposed a fire notification system that can help in the prevention of massive property loss or damage due to fire. Fires can occur anytime and anywhere. Fires are still a problem in the Philippines due to lacking fire alert systems that can alert fire departments. Because of that, many people die each year and many more are injured because of home fires. The project provides a prototype of a GSM Based Fire Notification and Data Acquisition System using Kalman Filtering Technique. The project built consists of hardware and software development. The study uses Arduino microcontroller to obtain the desired output of the project. The study uses the Arduino language, which is merely a set of C/C++ functions. The proponents also used the Kalman Filtering Technique, an ideal process for systems which measure variables that are continuously changing, is the most appropriate filtering method for real time problems and embedded systems. The goal of this study is to provide an efficient fire alarm system with a fire detector and wireless notification board with alarm system that will receive the alert message using the GSM module containing the gathered data. The results of the project show that when a fire is detected by the fire sensor, the buzzer will sound and an alert message containing the temperature in the area measured by the temperature sensor and the incident location of the fire is sent through a Short Message System (SMS) using the GSM module to the homeowner when they are away from home, and to the nearest fire station for the firefighters.

Keywords: Arduino, Fire Detector, Global System for Mobile (GSM), Kalman Filter, Wireless Notification.

1. Introduction

Fires can occur anytime and anywhere. In less than 30 seconds a small fire can turn into a devastating one. Fire is pitch black, it isn't bright. Fires at the start is bright, but it quickly emits black smoke and complete darkness. Thick black smoke can fill a house in minutes and cause the complete darkness. Most fatal fires occur in the houses at night, when people are asleep. If someone wake up to a fire, they won't have time to save their belongings because fire spreads so quick and the smoke is very thick. One may be blinded if you wake up to a fire. He or she may be disoriented and will not be able to find the way out of the burning house. There is only time to escape.

1 Hazardous smoke and toxic gases cause death to more people than fires do. Fires consume the oxygen that the people need and emits smoke and poisonous gases that may take lives of people. Breathing, even tiny amounts of hazardous smoke and toxic gases can make a person feel drowsy, bewildered and short of breath. The odorless and colorless fumes can make people fall into a deep sleep before the fires reach the door. One may not wake up in time to get out of the house and escape the deadly fire. [1]

Fires are not relatively studied in the Philippines but it can result to huge losses on properties. A study done by the Department of Health – Health Emergency Management Staff (DOH-HEMS) showed that fires contributed 39% of all events reported to the Health Emergency Alert Reporting System (HEARS) from 2005 to 2009 and caused 263 deaths and 749 injuries. The occurrence of fires and fire related casualties in the Philippines from 2010 to 2012 was assessed. All fire incidents reported in the HEARS of the DOH-HEMS during that period were incorporated in the study. Fires were a huge problem from 2010 to 2012 and affected the same geographic locations. A total of 883 fires and 824 fire-related casualties were reported, most of which occurred in Metro Manila. About 40 percent, or 271, of the 686 fires reported nationwide in February last year occurred in the National Capital Region, according to data from the Bureau of Fire Protection. [2]

2

3 Because of the rate of fire disasters here in Philippines the problem is that we have a lack of fire alerting systems that can immediately alert the Fire departments or the Barangay. Many people die each year and many more are injured because of home fires. Fires come even on the least time people expect it, like the time that people aren't at home or even when sleeping. People can be in panic when the situation comes, in which they might forget to ask for the help of fire fighters and try to quench the fire in their own.

4

Fires still occur in modern structural design, where lots of people's lives and properties are lost. In order to reduce the fire in the building, automatic fire alarm system is placed to aid everyone's safety. The study about Automatic Fire Alarm Systems Research talks about different fire sensors that can be used for the detection of fire. The paper discusses all parts of the structure of the designs for fire alarm system and fire alarm control. The researchers used the transmission algorithm for the implementation of the project. The researchers of this paper focused more on improving on the detection of fires so that it can sound an alarm as early as it can. [3]

The study on Computer Vision Based Fire Alarming System is a more comprehensive and more advanced sensing of fires because it detects the combustible instead of the by products through optical images gathered by a camera connected to a computer. It is about an alarm based on the detection of the sensors and uses the algorithm Lukas Kanade optical flow. Fire alarm system monitors the indoor surroundings and sets an alarm as part of the early warning mechanism with the ultimate goal to provide a warning at the early stage before the fire become uncontainable. Conventional fire detection systems undergo transparent delay from the fire to the sensor which is looking at a single point. The reliability of the fire detection system mainly depends on the strategic positional spreading of the sensors. [4]

The study Smart Notice Board discusses a prototype of a wireless notification board that is operated via messaging by using GSM module and Arduino microcontroller which uses transmission as the algorithm. The notice board displays message as a Short Message Service (SMS) from the user to the control unit which is placed in remote areas. [5]

The purpose of this study is to design and implement an efficient fire alarm system using a GSM based fire notification and data acquisition system. Specifically aiming to program the microcontroller to measure the parameters based on the received signal and display the data, and to send a distress message to the fire fighters containing the location of the incident, to serve as an alarm system for both fire fighters and homeowners and to measure the intensity of the fire based on the room temperature.

This study is intended to help group of people. For the homeowners, the system will serve as an alarm for fire and will send a message to the nearest fire station automatically even the owners are not at home or even if they are sleeping. For the fire fighters, the system will improve the reaction time of the firefighters because of the early detection capability of the system. For the next researchers, the study will serve as their basis for their related topics or they can use the study as their related literature.

5 But fire is a preventable disaster. A lot of fire prevention tools and materials are there, and this project can complement those that will benefit the users especially for the households that is more vulnerable to fires. Upon successful implementation of this study, the system will contribute to fire prevention and in areas that needed fire notification system. This an easy way to determine area location of the burning are and it will automatically flash on an LCD board and alert the fire department and the Concerned Barangay. Moreover, this study is addressed to the nearby community of LPU-Laguna so that they can use the system in fire prevention and risk reduction.

2. Methodology

2.1 Input-Process-Output (IPO) Chart

	INPUT	PROCESS	OUTPUT
SENSOR	Address Fire Station Hotline Home owners' Phone No. Flame Temperature	Apply Kalman Filter to reduce the noise on the data gathered by the temperature sensor. If the sensor detected a flame on a span of 5 seconds, the device will send a message to the nearest fire station and to the homeowner.	Real-time temperature readings on an LCD Display Message containing the address and the room temperature
RECEIVER	Message	Check the message received through the GSM module if it is from the sensor.	Display the message on the LCD and sound the buzzer whenever there is a new message.

Figure 1. IPO chart.

Figure 1 is the summarization of the system. The input is the data needed to perform the system which will proceed to the process which is a task that will be carried out to complete the task of the system. Lastly, the output, which describes the end result provided by the system.

2.2 Conceptual Framework

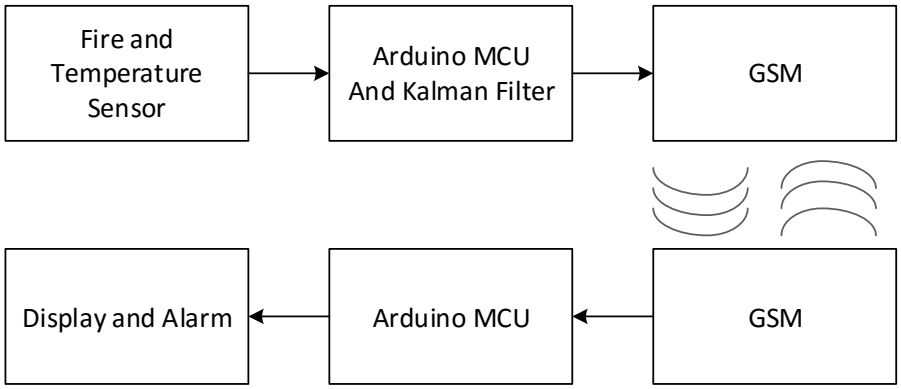


Figure 2. Conceptual framework.

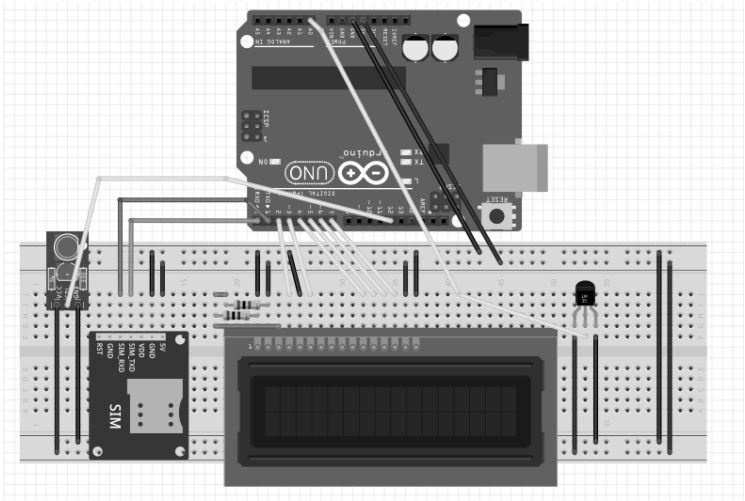
6

7 Figure 2 shows the Sensors, Microcontroller, GSM, Alarm, LCD Display and Algorithm in establishing the control programs using Arduino. The Flame and Temperature Sensor will be the triggering input for the Arduino to collect the data from the sensor and the GSM will send a message which will be received by the other GSM and the Arduino will collect the data and display the message on the LCD and trigger the alarm.

8

9 2.3 Design Requirements

10



11

12 Figure 3. Flame and temperature sensor.

13

14 Figure 3 shows the breadboard layout of the data gatherer of the project that is composed of an Arduino UNO microcontroller, a flame sensor that will detect the presence of a nearby flame, a temperature sensor (LM36) that will measure the current room temperature and will be shown on a 16x2 LCD Display, and a GSM Module that will transmit an alert message to the nearest fire station in case of fire.

15

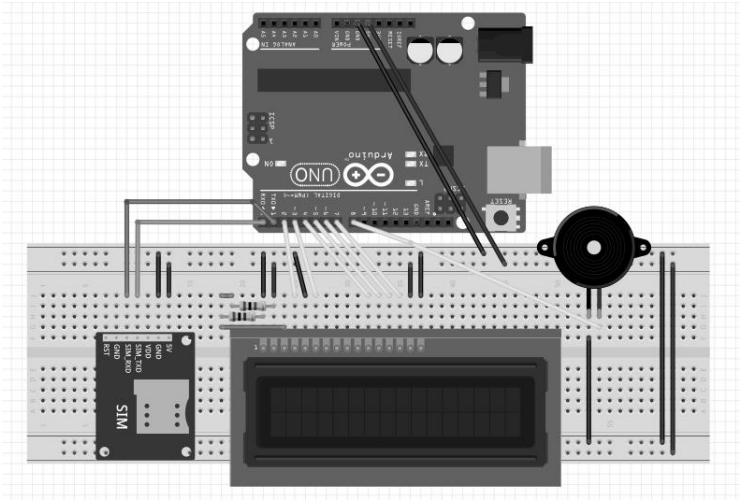


Figure 4. Message receiver.

Figure 4 shows the breadboard layout of the data receiver of the project. It is composed mainly of an Arduino UNO microcontroller, a GSM module that will receive the alert message, a piezo buzzer that will sound when a new message is received, and a 16x2 LCD Display that will show the message.

2.4 Standards Used

The proponents used IEEE standards in writing the paper for the study. For the project, the researchers used the standard Kalman Filter process that is ideal for systems that measure variables that are continuously changing such as temperature. Kalman filter have the advantage that it doesn't need to keep any record of past values, other than the previous state, and it is very fast, making it the most appropriate filtering method for real time problems and embedded systems.

2.5 Preliminary Data and Results

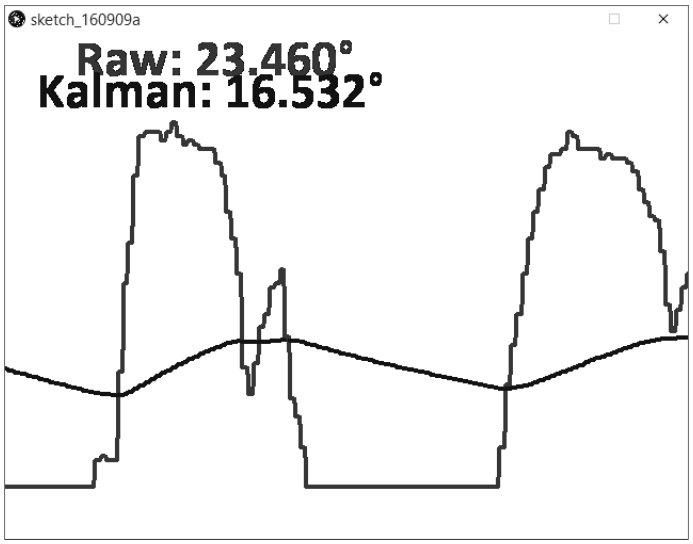


Figure 5. Kalman filtered versus raw readings.

Figure 5 shows the graph of the raw temperature readings versus the Kalman Filtered temperature readings. The graph was obtained using Processing IDE.

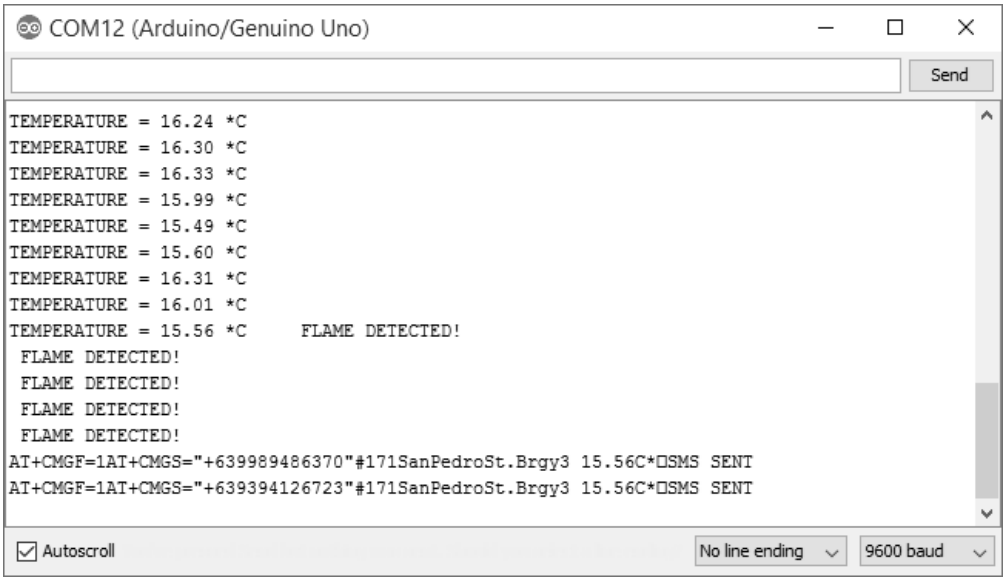


Figure 6. Kalman filtered versus raw readings.

Figure 6 shows the serial monitor window of the Flame and Temperature Sensor. It contains the Kalman Filtered temperature readings, an alert whenever the flame sensor detects a flame, and the sending of the message through the use of a GSM module.

3. Results and Discussion

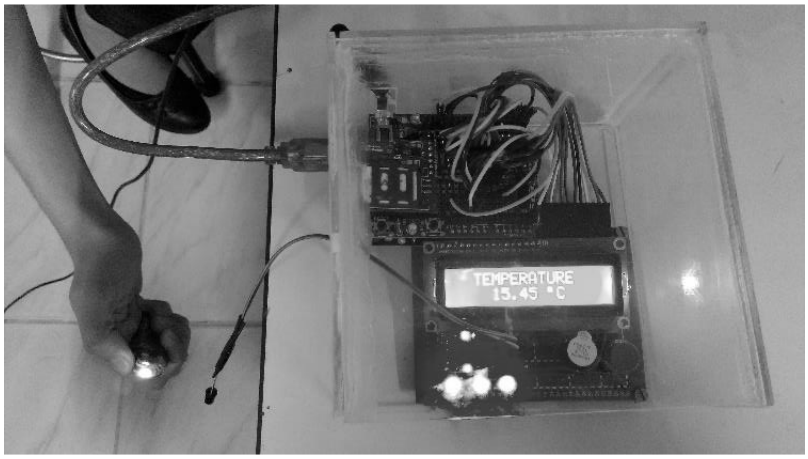


Figure 9. Flame and temperature sensor prototype.

Figure 9 shows the actual prototype of the flame and temperature sensor. The flame detected and the temperature is the input for the project. The LCD in the prototype shows the current room temperature.

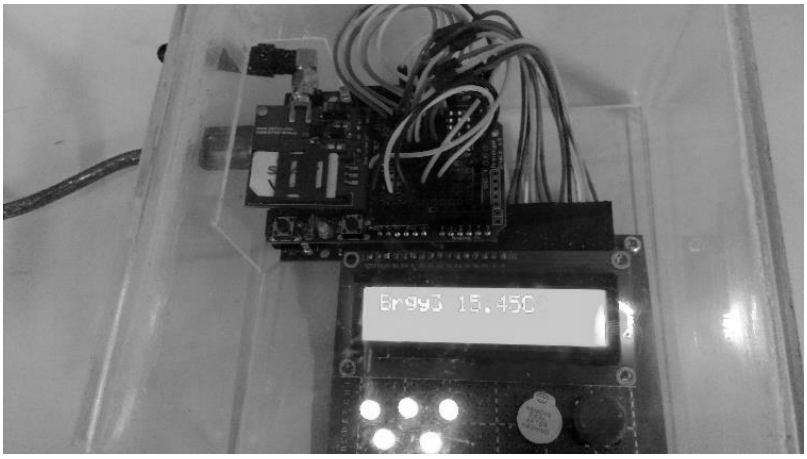


Figure 10. Message receiver prototype.

Figure 10 shows the wireless notification board of the project. The LCD is on its standby mode, waiting to receive an alert message from the sensor in time of a fire detection. When an alert message is received, the buzzer will alarm and the LCD will show the gathered data and the location of the incident where the fire happened.



Figure 11. Message received by the homeowner.

Figure 11 shows the alert message containing the temperature detected and location of the incident is sent to the homeowner notifying them about the fire.

4. Conclusions

The project provided a prototype of a GSM Based Fire Notification and Data Acquisition System using Kalman Filtering Technique. The study uses Arduino UNO to program the system and to obtain the desired output of the project. The project built consists of hardware and software development. The study uses the Arduino language, which is merely a set of C/C++ functions. The proponents conclude that they were able to develop an efficient fire alarm system with fire detector that can measure the temperature in the area and can send an alert message containing the gathered data and location of the incident to the homeowner when they are away from home, and to the

nearest fire station. The wireless notification board with alarm system receives the message from the homeowner and notify the firefighters. The use of Kalman Filter enables the proponents to measure more accurate readings as the variables like temperature is continuously changing. The receiving of message is sometimes affected because of the performance of the GSM module due to signal strength of the network. The proponents were able to obtain the data from the inputs needed for the output that will be displayed in the wireless notification board. The development of the project is successfully done and working properly.

Acknowledgement

The authors acknowledge Almighty God – the source of their knowledge, wisdom and strength in completing this study. They would like to thank Lyceum of the Philippines University – Laguna for providing the resources needed for this study. Lastly, they would like to extend their deepest gratitude to their families and loved ones for their ceaseless support and understanding throughout the span of accomplishing this study.

References

[1] The Charter Township of Waterford. *Fire Safety Fact Sheets: This is Fire.* Waterford, Michigan.

[2] Velasco, G. (2013, October). *Epidemiological Assessment of Fires in the Philippines, 2010-2012.* Paper presented at the 12th National Convention on Statistics (NCS), Mandaluyong City, Philippines.

[3] Liu, H., Li, S., Lili, G., Tao, W. (2010, April). *About Automatic Fire Alarm Systems Research.* Paper presented at The 2nd IEEE Conference on Information Management and Engineering (ICIME), Chengdu, China.

[4] Gunawaardena, A. E., Ruwanthika, R. M. M., Jayasekara, A. G. B. P. (2016, April). *Computer Vision Based Fire Alarming System.* Paper presented at the Moratuwa Engineering Research Conference (MERCon), Moratuwa, Sri Lanka.

[5] K, S., Chawla, H., Bhaduri, A. (2013, September). *Smart Notice Board.* Paper presented at the National Conference on Challenges in Research & Technology in the Coming Decades (CRT 2013), Ujire, India.

[6] Zymotico. (2015). *Simple Kalman Code*. Git Hub Gist.

[7] Zymotico. (2015*). Processing Code for Simple Kalman Demo*. Git Hub Gist.

[8] Khan, S. (2016). *Wireless Notice Board using GSM and Arduino*. Circuit Digest.

[9] Prabakar, J. (2013). *GSM Modem with Arduino UNO*. Let's Play with Arduino.

eureca 2017 – Conference Paper
Paper Number EUG09

Maximization of Machine Capacity Utilization Using Overall Equipment Effectiveness

Carmina A. Flores[1], Reniel S. Malabuyoc[1], Angela Rose R. Mijares[1*], Ryan Jeffrey P. Curbano[2]
[1]*Undergraduate Student, Industrial Engineering Department*
[2]*Faculty Member, Industrial Engineering Department*
Lyceum of the Philippines University-Laguna

[*]mijaresangelar@gmail.com

Abstract
Overall Equipment Effectiveness (OEE) is a preeminent practice for monitoring and increasing efficiency of the manufacturing processes such as machines and production lines. Efficiency of production lines is vital as it results in an improved production and utilization of available resources. However, frequent machine breakdowns, low plant availability and increased overtime are risk to a manufacturing plant since they incur high operating costs. The primary aim of this study was to maximize Overall Equipment Effectiveness (OEE) at a manufacturing company through the implementation of preventive maintenance strategies. The paper concentrates on improving the maintenance in Company-X using advanced maintenance process and strategies combined to improve overall equipment effectiveness. The results were obtained after the empirical study. The averaged value of OEE for four machines before implementation of Preventive Maintenance were found to be 71.8% and an improved OEE after implementation of Preventive Maintenance has an averaged value of 78.1% against the world class standards of 85%. The results of initial OEE emphasized the major problems of machines and losses that cause downtime and decrease in productivity. Moreover, implementation of preventive maintenance has helped the company and employees improve their production line. Thus, increasing their market share and helping them achieve high performance with minimum costs.

Keywords: Overall Equipment Effectiveness, Efficiency, Preventive Maintenance, Machine Breakdown,

.

1. Introduction

Machine efficiency is one of the factors that are frequently overlooked by the management and this can lead towards losses, which reduces the yield. Machines are meant to work efficiently, but in some circumstances machines can be less productive due to improper preventive maintenance [1]. For a manufacturing company to be successful the dependability of the equipment relies on proper preventive maintenance and it must not be taken for granted. What may come across, as a minor failure of just one machine could be integral to a production process, resulting in significant losses. This is why it is really crucial for organizations to take steps to anticipate breakdowns or inefficiencies whenever possible.

Company X is a Philippine-based manufacturing company that specializes in actuators or camera modules. The company is however experiencing frequent machine breakdowns that are causing downtime resulting in low machine availability which in turn results in low productivity of the plant. In manufacturing industries, the production process demands non-stop operation of any production line equipment. A stoppage at any stage of the production line, due to equipment failure grounds for a drop in production rate and quality of the products.

Production performance is strongly linked with utilization of inputs for maximizing outputs; in this perspective machine factor inputs are more concerned. Underutilized capacity is a capacity gap appears as non-value added inputs and eventually turns as the lower physical efficiency of the production process. Certainly, degree of capacity utilization of production resources depends on a few potential factors such as labor skills and availability of machineries. It is evident that the overall effectiveness of equipment (OEE) is deeply connected with capacity utilization. It is found that there is a strong relationship between production performance and capacity utilization [2]. Some study has resulted to an improvement in the maximization of planned productivity. This is because of proper diagnosis of the existing system and by employing proper preventive maintenance schedule. The implementation of proper preventive maintenance (PM) can greatly reduce machine failure rates and improves up time; ensuring uninterrupted production. It is found that, on production line whole line up time improvement is depends on performance of critical machines. If improvement in critical machines was implemented availability there will improve in production line up time or availability [3]. Further investigation of the causes of downtime can be done by performing root cause analysis and proposing of an affinity diagram, which will highlight several issues with implementation of preventive maintenance and will generate possible solutions [4]. For a broader tool, Total Productive Maintenance is also a suggested tool for the company to enhance its OEE. Moreover, the company can only benefit from TPM if it ensures management commitment through activities such as permitting, supporting, managing, and leading. The adoption of TPM can minimize such losses and also reduce rework to or below the acceptable levels. However, it requires well-trained employees and convinced them that TPM is sustainable. [5]

It essential is for a company to improve the productivity and quality of the products. Improving overall equipment effectiveness with less idling and minor stoppages, and less quality defects will be very beneficial to the company as well as to the employees [6]. Product quality and quantity as well as delivery targets can only be achieved through an efficient maintenance management system that will help the

company in improving plant availability, reliability and plant equipment utilization and hence productivity.

This paper focuses on improving the Overall Equipment Effectiveness through the implementation of Preventive Maintenance that will fulfill the absence of a proper maintenance management policy and strategy in the company. This will not only help the machines to run smoothly but this will also optimize their overall performance. Because the specific aims of this study are to reduce possible losses due to frequent machine breakdown; and to keep equipment in a good condition that permits them to be used at their optimal capacity without interruption.

2. Methodology

2.1 Input-Process-Output Chart

The system approach (Input-Process-Output system) was used in describing the conceptual framework of the study. As shown in Figure 1, the input consist the current output capacity and utilization rate, Overall Equipment Effectiveness, Availability, Performance and Quality. Next box shows the process, wherein, all gathered data would be analyzed and to be interpreted by the researchers, also, implementation of Preventive Maintenance will occur during the process. Lastly, the output where there will be an improved Overall Equipment Effectiveness.

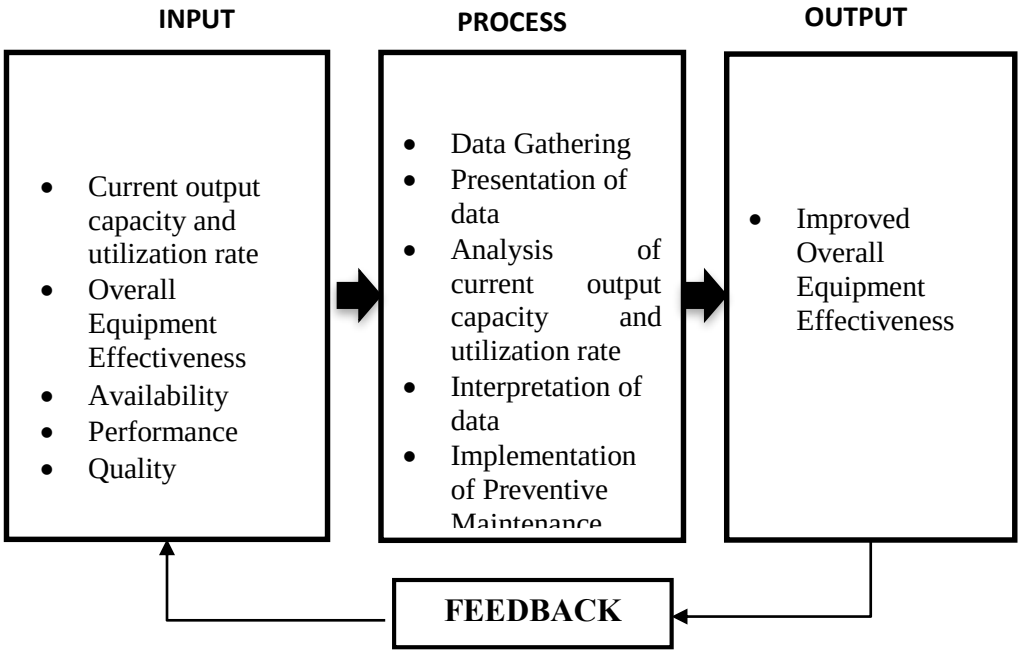


Figure 1. IPO Chart

2.2 Overall Equipment Effectiveness (OEE)

OEE (Overall Equipment Effectiveness) is a best practice metric that identifies the percentage of planned production time that is truly productive. An OEE score of 100% represents perfect production: manufacturing only good parts, as fast as possible, with no down time. [7]

OEE is useful as both a benchmark and a baseline:

1. As a benchmark it can be used to compare the performance of a given production asset to industry standards, to similar in-house assets, or to results for different shifts working on the same asset.
2. As a baseline it can be used to track progress over time in eliminating waste from a given production asset.

Overall Equipment Effectiveness is a major KPI (Key Performance Indicator) that accounts for three constituent elements:

1. Availability - the percentage of time that machines are available for scheduled production compared with the amount of time they were actually producing. Availability is calculated as:

$$\text{AVAILABILITY} = \frac{\text{Run Time}}{\text{Total Time}}$$

2. Performance - compares the theoretical machine rate with the number of items actually produced on a machine during its operating time. Performance allows a facility to compare availability downtime with efficiency. Performance is calculated as:

$$\text{PERFORMANCE} = \frac{\text{Total Count}}{\text{Target Counter}}$$

3. Quality - the percentage of items that pass the first quality inspection. This allows a plant manager to compare consistency between individual machines and, in turn, allows for comparisons between different manufacturers, as well as machine, specifications, and even individual operators. Quality is calculated as:

$$\text{QUALITY} = \frac{\text{Good Count}}{\text{Total Count}}$$

OEE takes into account all three OEE Factors and is calculated as:

$$\text{OEE} = \text{Availability} \times \text{Performance} \times \text{Quality}$$

2.3 Maintenance Management

Maintenance management is to support the equipment running at high capacity and produce quality products at lowest cost possible. Maintenance has to be taken into consideration in very early stage of work of procuring new equipment to ensure a good and cheap operation. High quality equipment will provide reliability and maintainability, which ensure improved productivity and equipment efficiency.

The basic maintenance management process design to take maintenance work from request to completion is as demonstrated in Fig 2.

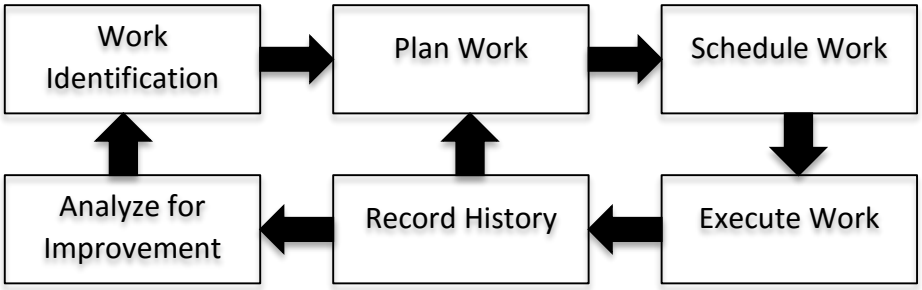


Figure 2. Maintenance Process

Maintenance activities can be divided into four general categories or strategies. The maintenance plan will be a mixture of four strategies as demonstrated in Fig 3.

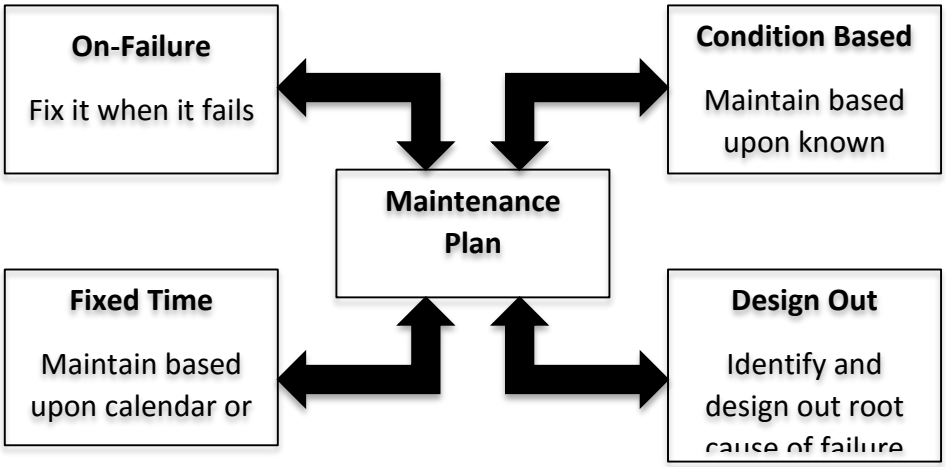


Figure 3. Maintenance Strategies

3. Results and Discussion

3.1 Initial Overall Equipment Effectiveness

The bottleneck machines that cause the entire system to have limited performance or capacity were selected as equipment for OEE calculation. There are 4 bottleneck machines in the production line in which operates 18 hours per day. The monthly production data were shown in Table 1 to 4 below.

Table 1. Data of Machine 1

Machine 1 Data	Values

Planned Operating Time	32400 minutes/month
Actual Operating Time	24975 minutes/month
Downtime	1650 minutes/month
Total Production Parts	373680
Total Rejection Parts	1410
Good Parts	372270

Table 2. Data of Machine 2

Machine 2 Data	Values
Planned Operating Time	32400 minutes/month
Actual Operating Time	25100 minutes/month
Downtime	1500 minutes/month
Total Production Parts	386820
Total Rejection Parts	1740
Good Parts	385080

Table 3. Data of Machine 3

Machine 3 Data	Values
Planned Operating Time	32400 minutes/month
Actual Operating Time	25350 minutes/month
Downtime	1800 minutes/month
Total Production Parts	371192
Total Rejection Parts	1590
Good Parts	369602

Table 4. Data of Machine 4

Machine 4 Data	Values
Planned Operating Time	32400 minutes/month
Actual Operating Time	31345 minutes/month
Downtime	1950 minutes/month
Total Production Parts	371520
Total Rejection Parts	1380
Good Parts	370140

Data distributed in Table 5 shows the performance of Machine 1, 2, 3, and 4 in terms of OEE Parameters. Data of each machine as discussed in the previous section were incorporated to the formulas mentioned beforehand.

Table 5. OEE of Machine 1 to 4

Parameters	Machine 1 (%)	Machine 2 (%)	Machine 3 (%)	Machine 4 (%)
Availability	77.08	77.45	78.24	77.85%
Performance	92.27	95.51	91.73	91.73%
Quality	99.62	99.64	99.57	99.63%
OEE	70.85	73.71	71.47	71.15%

Detailed problems occurring in the machine that causes the breakdown can be visualized in Table 6. This implied that the true performance of machines is at poor

condition and if the responsible personnel take necessary actions, an improvement can be seen.

3.2 Preventive Maintenance

Table 6. Problems Occurring in the Machine

Problems	Corrective Actions	Frequency	Duration
Misaligned needle	Check needle alignment	Every 3 hours	30 seconds
Clogging	Check clogging of chemical	Every 3 hours	30 seconds
Liquid sufficiency	Check for liquid sufficiency	Every 3 hours	30 seconds
Leaks	Check possible leaks	Every cycle	7 seconds
Availability of raw materials	Check availability of raw material	Every 3 hours	10 seconds

Preventive Maintenance actions with frequency and duration according to problems that are observed are shown in Table 7.

Preventive maintenance is a key factor that keeps the machine running efficiently through the production process. The maintenance activity on machines needs extra attention by the management along with the responsible personnel to ensure optimum usage of machineries, which will eliminate unwanted wastages due to machine stoppages. [8]

Table 7. Preventive Maintenance Actions

Problems	Occurrence	Weight
Misaligned needle	19	34%
Clogging	10	18%
Liquid sufficiency	9	16%
Leaks	7	13%
Availability of raw materials	7	13%
Availability of technician	3	6%
Total	55	100%

Table 8 displays the different breakdown of machine downtimes and their occurrences with respective percentages and percent eliminated after implementation of Preventive Maintenance.

Table 8. Percent Eliminated to Machine Downtime

Table 9. Improved OEE of Machine 1 to 4

Parameters	Machine 1 (%)	Machine 2 (%)	Machine 3 (%)	Machine 4 (%)
Availability	82.04	81.73	81.48	81.35
Performance	95.28	96.98	96.51	97.11
Quality	99.91	99.95	99.93	99.93
OEE	78.10	79.22	78.58	78.94

It is observed that considerable improvements in availability, performance, and quality rate were obtained after the implementation of preventive maintenance as shown in Table 10.

The availability improved by almost 4%, performance by 3.66% and quality rate by 0.31%. The OEE measure increased from 71.89% to 78.71%. Therefore in order to achieve parameters close to world-class performance level, continuous waste reduction is suggested.

Table 10. OEE Result Before/After Preventive Maintenance Compared to World-Class OEE

Parameters	Before %	After %	World Class %
Availability	77.66	81.65	90
Performance	92.81	96.47	95
Quality	99.62	99.93	99
OEE	71.8	78.71	85

Table 11 shows the cost-benefit analysis per machine and its corresponding production parts which were computed from the previous production data of each machines. The cost per unit is $3 while the averaged cost per month is $1,127,259 and the total cost per year is $54,108,432.

Table 11. Cost-Benefit Analysis of Machine 1-4 Before Preventive Maintenance

Machine	Total Production Parts	Cost per Unit	Cost per Month	Cost per Year
1	373,680	$3	$1,121,040	$13,452,480
2	386,620	$3	$1,159,860	$13,918,320
3	371,192	$3	$1,113,576	$13,362,912

Breakdown of Machine Downtimes	Occurrence	Percentage	Percent Eliminated
Misaligned needle	19	34%	29%
Clogging	10	18%	13%
Liquid sufficiency	9	16%	11%
Leaks	7	13%	8%
Availability of raw materials	7	13%	12%
Availability of technician	3	6%	-
Total	55	100%	73%

4	371,520	$3	$1,114,560	$13,374,720
Total	1,503,012	$3	$4,509,036	$54,108,432

Table 12 shows the cost-benefit analysis per machine after preventive maintenance and its corresponding production parts which has increased compared to the before implementation. The cost per unit is still $3 and the total cost per year has improved from $54,108,432 to $56,193,516 that is equivalent to a gain profit of $2,085,084.

Table 12. Cost-Benefit Analysis of Machine 1-4 After Preventive Maintenance

Machine	Total Production Parts	Cost per Unit	Cost per Month	Cost per Year
1	385,903	$3	$1,157,709	$13,892,508
2	390,875	$3	$1,172,625	$14,071,500
3	390,875	$3	$1,172,625	$14,071,500
4	393,278	$3	$1,179,834	$14,158,008
Total	1,560,931	$3	$4,682,793	$56,193,516

4. Conclusion

Recent studies indicate that company's performance particularly to machine breakdowns, it is Company-X's interest to formulate necessary preventive maintenance policy to reduce costly machine breakdowns and increase productivity. Overall Equipment Effectiveness (OEE) are greatly affected by these losses generally, downtime, speed, and quality losses. To reduce these losses and to attain world class OEE the formulated preventive maintenance schedule should be implemented and maintained. Through that, Company-X can improve their manufacturing process, minimize costly machine breakdown and increase productivity. Thus, leaving the company at an improved competitive state against competitors.

References

[1] B.Nordmeyer, (2017) *How to Measure Production Efficiency* [Online] Retrieved from: http://smallbusiness.chron.com/measure-production-efficiency-67787.html

[2] M. Shahidul et al., "Measuring Machinery Capacity Utilization and Its Impact on Manufacturing Performance and Environment," Manufacturing Operations Research and Sustainability, vol. 1, no. 1, pp. 7-12, July 2013.

[3] T. Kolte "Machine Operational Availability Improvement by Implementing Effective Preventive Maintenance Strategies - A Review and Case Study," International Journal of Engineering Research and Technology, vol. 10, no. 1, 2017.

[4] S.R.Vijayakumar and S.Gajendran "Improvement of Overall Equipment Effectiveness (OEE) In Injection Moulding Process Industry," Karpaga Vinayaga College of Engineering and Technology, 2014.

[5] H.A.Samat, L.N.Jeikumar, E.I.Basri, N.A.Harun and S.Kamaruddin, **"**Effective Preventive Maintenance Scheduling: A Case Study," Proceedings of the 2012 International Conference o n Industrial Engineering and Operations Management, Istanbul, Turkey, 2012.

[6] S. Fore and L. Zuze, "Improvement of Overall Equipment Effectiveness through Total Productive Maintenance," World Academy of Science, Engineering and Technology, 2010.

[7] Ellis, N. (2014). *OEE – Learn How to Use It Right.* [Online] Retrieved from: http://www.industryweek.com/quality/oee-learn-how-use-it-right

[8] Emaint, (2017), *What is Preventive Maintenance & How to Get Started*. [Online] Retrieved from: https://www.emaint.com/what-is-preventive-maintenance

eureca 2017– Conference Paper
Paper Number EUG10

Microcontroller-based 6-DOF Bolted Aluminum for Independent Gait Humanoid

Wena Rose Magpantay[1], Pamela B. Mandanas[1], Arjay Manzolim[1], John Paul S. Endaya[1*]
Favis Joseph C. Balinado[2], Arvin P. Dela Roca[3]

[1]*Undergraduate Student, Electronics Engineering Department*
[2]*Faculty Member, Electronics Engineering Department*
[3]*Faculty Member, Electrical Engineering Department*
Lyceum of the Philippines University, Calamba City, Laguna, Philippines

[*]*paul_endaya29@yahoo.com*

Abstract
Humanoid robot continues to grow and improve. The curiosity of many made humanoid robots arise from science fiction to reality. It is a humanoid robot researcher's dream to create a system that will maintain the total control system movement of the robot with a heavy-duty mechanical mounting and electrical communication to allow the brain unit to automatically modify changes in center of gravity, moment of inertia resulting from the size and weight of the robot and of course the other external behaviors. Nowadays, there are many human-like robots created. They are created to perform what humans can do and they can be used as substitute to a human being most likely when doing dangerous works. This paper presents the development of Bolted Aluminum for Independent Gait Humanoid (BAIGH) Robot to design and construct the robot framework actuated by servo motors and controllers, to embed a program using a microcontroller to control the limbs and provide the necessary kinematic motion and to test the functionality according to stability of BAIGH. The robot is designed to provide humanistic motion specifically standing and walking. Six Degrees-of-Freedom is used so that the mechanism of the robot will be more human like. The limbs are controlled using Arduino microcontroller to provide necessary kinematic motions similar to human behavior. This was achieved through a robot structure specifically constructed from aluminum and actuated by servo motors to provide accurate position. This research increased awareness that the kind of lower extremities really are not just used for carrying other parts of a humanoid robot. It will basically provide stability and mobility allowing the robot to move from one place to another in a subtle way.

Keywords: Humanoid Robot; Arduino microcontroller; Servo motor; Lower extremities; Degrees-of-Freedom.

1. Introduction

These days, robots that look like human arise because of curiosity and fantasy. Humanoid robots are still in its infancy. But with so much room for innovation and diversification, the humanoid robot continues to grow and improve. There is a continued interest in developing robots that are able to fully interact with humans and the environment.[1]

The reason why robots should walk is that the environment where we live is built for human. Robots on wheels are not capable of doing other stuff that a bipedal robot can do such as walking upstairs, kicking a ball, and obviously walking. By some estimates, 80 percent of land mass is not accessible by wheeled robots.[2] But wheel traction system is commonly use in robots nowadays in solution for mobility wherein it is a simple manner of moving in flat areas and is efficient from the energetic point of view. Those kinds of limitations can be overcome if the robot is equipped with legs that will act with degrees of freedom.[3-4]

Degrees of freedom, in a mechanics context, defined modes in which a mechanical device or system can move. The number of degrees of freedom is equal to the total number of independent displacements or aspects of motion.[5] Consider a robot leg built to work like a human leg, number of DOFs is necessary both in the waist for the fall down and legs to imitate the human walking motion.

Modern robots are designed to walk and behave like humans but until now the efficiency of the human gait is still far from being reached. Most humanoid robots walk with bended knees. This walk looks unnatural. It give the knees, the hips, and the ankle joints high torque and lead to high energy consumption.[6-7] Humans walk in a different way. A human does not need to bend their knees to walk because they bend their feet while standing on toes when taking another step. The segment between the ankle joint and the toes joint provides the extra leg length needed to shift the weight. This kind of walk is very efficient because without the bending of the knee it means that there will be less torque in the motors.

Humanoid robots are expected to sit, stand, and walk in a humanistic motion but only few created anthropomorphic robots that can mimic human behavior at all [5]. One reason for this is the difficulty of the robot to walk in bipedal motion since it requires rapid but precise control of the robot limbs. To overcome this, high-performance sensors and control systems are being used which may sacrifice funds and hinders the development of robots. A system that is efficient but resembles human movement is essential in the lower extremities of a robot. There is a need for a microcontroller that will control Bolted Aluminum for Independent Gait of a Humanoid (BAIGH) Robot.

2. Methodology

2.1 Proposed System

In this study, the goal is to develop a system demonstrated in Figure 1 using an algorithm that is implanted through Arduino IDE. The proponents chose a high torque servo motor to support a load.

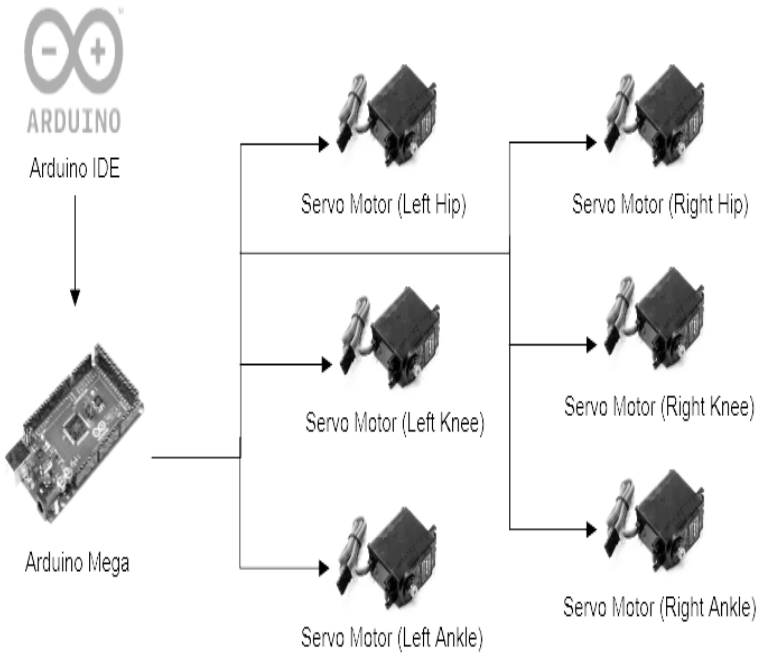


Figure 1. Proposed System

2.2 Block Diagram

As shown in Figure 2 the electronic control of Bolted Aluminum for Independent Gait of a Humanoid (BAIGH) Robot. The hips, knee and ankle, each consists of a servo motor that is programmed together by a single microcontroller. The servo motors are powered by a 5V DC supply. The microcontroller which is the center unit of the system interprets the commands given by the person. The microcontroller is driven by a 12V DC supply to give off a stable 5V output in its 5V pin. It will now generate a PWM (Pulse Width Modulation) control signals and then instruct the motor whether to accelerate, decelerate or to stop either in a clockwise or counter-clockwise direction. It will be rotated on the desired angle or position which will make the robot stand and walk. Proper tilting by limiting the angle will help maintain the stability of the robot while standing and walking.

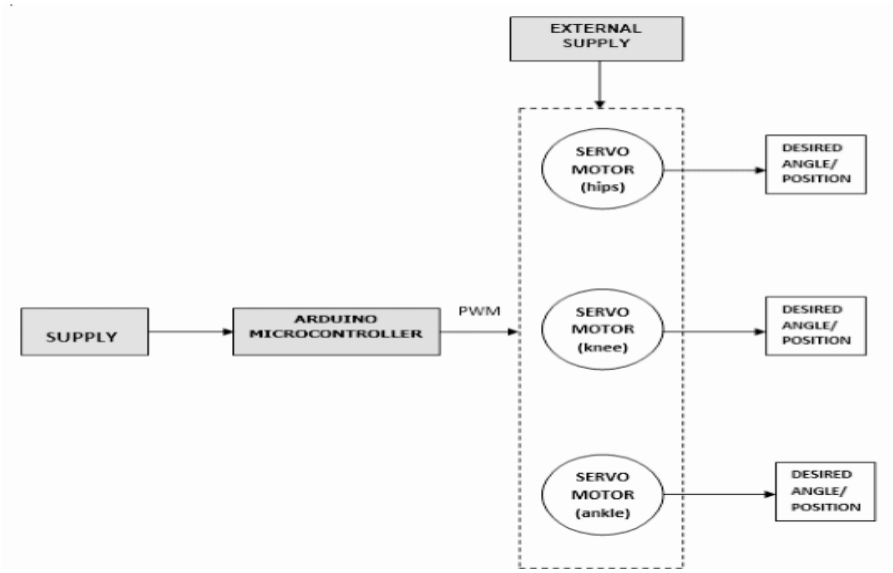


Figure 2. System Block Diagram

2.3 Input Process Output Chart (IPO)

Figure 3 shows the IPO illustration of the proposed system. In the creation of the project, the proponents need to create a program that will stabilize and provide an output desired for the system considering the robot's parameters. The robot's internal and external structure must be designed based on the materials readily available in the market. The prototype constructed must implement the programs given the necessary hardware and software. The system is required to be tested and tuned to be able to successfully create Bolted Aluminum for Independent Gait of a Humanoid (BAIGH) Robot.

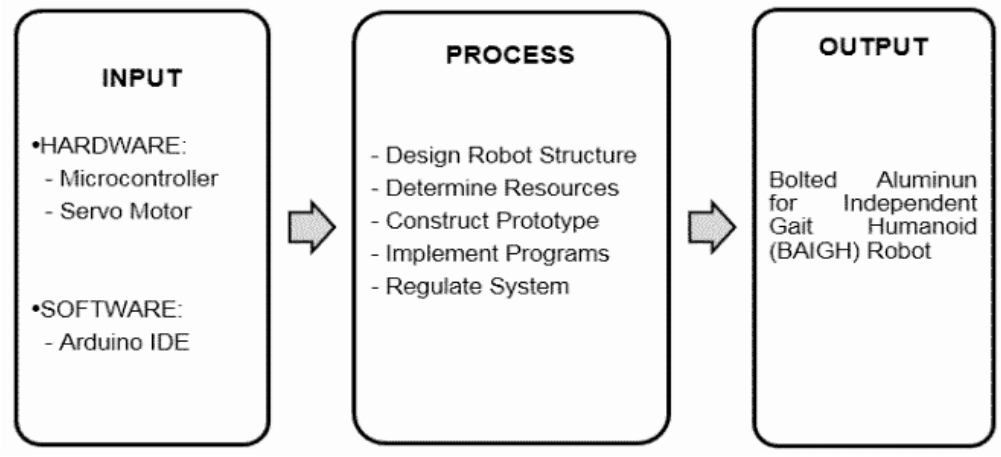


Figure 3. IPO Chart of the Proposed System

2.4 Algorithm

1. Start the system.
2. System will initialize to mid-stance position.
3. Servo motors will actuate according to the step angle.
4. End of system.

2.5 Flowchart

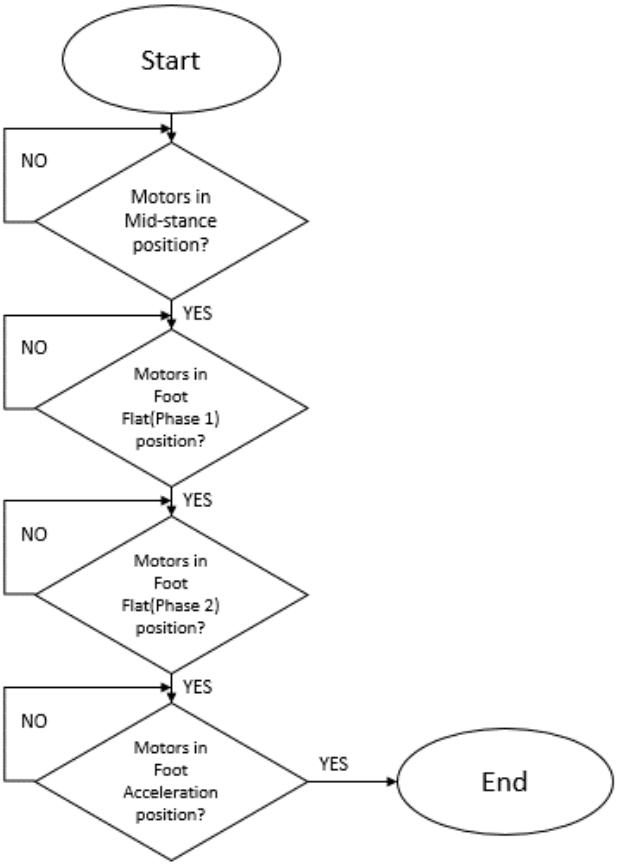


Figure 4. Flow Chart

3. Results and Discussions

3.1 Functionality Test According to Stability

Table 3.1 to Table 3.4 show the results of different angles that the proponents input during the testing period of the project. Ninety (90) degrees is the angle that should be the output for the biped robot to stand or to be in Midstance therefore ninety degrees was made as the zero degrees during the test period. To compensate for the frame's imperfections the results in the midstance position were slightly changed so that the biped robot can stand. Other tests show the results for Foot Flat (Phase 1), Foot Flat (Phase 2) and Acceleration positions where there are different values of step angles in different tests. After the series of tests the proponents conclude that the bigger the step angle the more distance the biped robot can cover

Table 3.1 Results of Midstance

Joints	Normal GAIT (degrees) Sagital Planes	BAIGH's Joints (degrees)		
		Trial 1 (10˚ Per Step)	Trial 2 (8˚ Per Step)	Trial 3 (5˚ Per Step)
Right Hip	0	5	5	5
Right Leg	5	-5	-5	-5
Right Ankle	5	2	2	2
Left Hip	0	-2	-2	-2
Left Leg	5	7	7	7
Left Ankle	5	-5	-5	-5

Table 3.2 Results of Foot Flat (Phase 1)

Joints	Normal GAIT (degrees) Sagital Planes	BAIGH's Joints (degrees)		
		Trial 1 (10˚ Per Step)	Trial 2 (8˚ Per Step)	Trial 3 (5˚ Per Step)
Right Hip	15	15	13	10
Right Leg	15	5	3	0
Right Ankle	5	12	10	7
Left Hip	15	8	6	3
Left Leg	15	17	15	12
Left Ankle	5	5	3	0

Table 3.3 Results of Foot Flat (Phase 2)

Joints	Normal GAIT (degrees) Sagital Planes	BAIGH's Joints (degrees)		
		Trial 1 (10˚ Per Step)	Trial 2 (8˚ Per Step)	Trial 3 (5˚ Per Step)
Right Hip	15	15	13	10
Right Leg	15	5	3	0
Right Ankle	5	2	2	2
Left Hip	15	8	6	3
Left Leg	15	17	15	12
Left Ankle	5	-5	-5	-5

Table 3.4 Results of Acceleration

Joints	Normal GAIT (degrees) Sagital Planes	BAIGH's Joints (degrees)		
		Trial 1 (10˚ Per Step)	Trial 2 (8˚ Per Step)	Trial 3 (5˚ Per Step)
Right Hip	20	-5	-3	0
Right Leg	60	-15	-18	-10
Right Ankle	10	-8	-6	-3
Left Hip	20	-12	-10	-7
Left Leg	60	-3	-1	-2
Left Ankle	10	-15	-13	-10

.

4. Conclusions

The motor used is a high-torque digital servo featuring a metal gear that resulted in an extra high stalling torque in a tiny package. The motors are linked together in the structural frame made of aluminum. Combining the components, given a load which required a motor with high torque rating and a material that is light and strong. By implementing a program using the Arduino microcontroller, the motors was synchronized which is required for an efficient human gait robot.

1) We were able to design and construct a robot structure that consist of servo motors and a controller.
2) We were able to synchronize the six (6) servo motors using the program installed in the system.
3) We were able to design a robot that is durable enough to withstand damages due to experimentations.

5. Recommendation

In the future, build a robot that will have the ability to respond properly to the external disturbances. Create a system that will maintain the total control system movement of the robot with a heavy – duty mechanical mounting and electrical communication to allow the brain unit to automatically modify changes in center of gravity, moment of inertia resulting from the size and weight of the robot and of course the other external behaviors. Have at least two degrees of freedom on each of the joints had it in X and Y direction especially on the ankle to allow the foot to be placed flat on a surface during walking or recovery from disturbances and Z axis for a variety of movement such as turning.

Acknowledgment

The success of this study required the help of various individuals. Without them, the researchers might not meet their objectives in doing this study. The researchers want to give gratitude to the Lyceum of the Philippines University – Laguna for providing the needed resources to accomplish this research. To our parents, for giving support and encouragement to pursue our study, for giving love and time for their children. To our panelists, Dr. Neil P. Balba, Engr. Rio B. Aguilar and Engr. Enrique B. Pioquinto for helping us improve our paper through their constructive criticisms. Without them, this study would not be possible.

References

[1] David Hanzon. *Why We Should Build Humanoid Robots.* (2011) Retrieved from https://spectrum.ieee.org/automaton/robotics/humanoids/why-we-should-build-humanlike-robots

[2] Torie Bosch. *Should Robots Walk on Two Legs?* (2011) Retrieved from http://www.slate.com/blogs/future_tense/2011/11/14/robots_should_they_walk_on_two_legs_or_move_on_wheels_.html

[3] Giuseppina Gini, Umberto Scarfogliero , Michele Folgheraiter (2007) *Human-Oriented Biped Robot Design: Insights into the Development of a truly Anthropomorphic Leg.* Retrieved from *http://home.deib.polimi.it/gini/papers/ICRA07.pdf*

[4] R. M.. Alexander. *A model of locomotion on compliant legs, Phil. Trans. roy.Soc. B.*, vol. 338, pp. 189-198, (1992)

[5] Jeakweon Han. *Bipedal walking for a full-sized humanoid robot utilizing sinusoidal feet trajectories and its energy consumption.* Retrieved April 03, 2017 from IEEE/IET Electronics Library: Mapua Institute of Technology. (2012)

[6] Margaret Rouse. *Degrees of Freedom.* (2009)
Retrieved from http://whatis.techtarget.com/definition/degrees-of-freedom

[7] Ryo Kurazume, Shuntaro Tanaka, Masahiro Yamashita Tsutomu Hasegawa *Straight Legged Walking of a Biped Robot.* (2005)
Retrieved from IEEE/RSJ International Conference on Intelligent Robots and Systems
https://pdfs.semanticscholar.org/8609/3fac59ddad53ef4f31cd041971039f71d155.pdf

eureca 2017 – Conference Paper
Paper Number EUG14

Design and Implementation of Microcontroller-based Gesture Controlled Robot Head Applying Three Degrees of Freedom

Andaya T. Leonardo [1*], Joselito P. De Castro Jr[1], Jan Vincent D. Banzuela [1], Adriel Nichol F. Malabanan [1], Arvin P. Dela Roca[2]

[1]*Students, Electronics Engineering Department*
[2]*Faculty Member, Electronics and Computer Engineering Department*
Lyceum of the Philippines University – Laguna
Calamba City, Laguna, Philippines

[*]joselitodecastro8@gmail.com

Abstract

Robotics is a dynamic field that keeps on growing. It has dominated various field from manufacturing, aeronautics, biomedical and even our homes, and more of them will be seen in the future. The researchers through this research paper aims to align their learning with regards to robotics. Understanding how robots work is a one step forward for greater innovations. The project is about designing and implementation of a microcontroller-based humanoid robot head with 3 degrees of freedom namely; yaw, pitch and roll. The system will utilize Arduino UNO as the microcontroller. Also, the system is constructed in two parts; the driver end that controls and provides the input and the robot that translate the input signal. The driver wears a cap equipped with three degrees gyro-accelerometer specifically MPU9250, it decodes the real-time position of the driver's head, it is wired to a micro-controller that tasks three servomotors to convert the input signal to angular displacement mimicking the position of the driver's head. The head of the robot is also equipped with camera for viewing purposes. The result in further experiments reveals that the robot head passed with low levels of error and falls under the acceptable margin of total error thus, the robot head can perform the mimicking in 3 degrees of freedom. The result was gained by keeping the system calibrated, adjusting of the drivers and continuous changing of the program based on tests output.

Keywords: Gyro--accelerometer, Servomotor, Microcontroller, Robot

1. Introduction

Up-to-date performance and the capability of modern robot innovate rapidly due to the demand of the present and the future time. Deeper understanding of how robots work and its complexity entails a great knowledge of different aspects and body of knowledge that constitutes it. In this modern technology, robotics has crossed traditional engineering boundaries, encompassing electrical engineering, mechanical engineering, electronics engineering, computer engineering, industrial engineering and mathematics. These body of knowledge predominantly are the elementary and foundation of robots.

This research focuses on the design and implementation of a microcontroller-based system in controlling the motion of the head of a humanoid robot with three (3) degrees of freedom utilizing a gyro-accelerometer. It can pitch tilting forward and back, it can roll tilting left and right, and yaw rotating left and right and lastly, combine these actions. A gyro-accelerometer is used to dictate the position of human head digitally sending these data to a microcontroller that interprets these data and signals actuators to imitate the position of human head in quickest time possible.

The research took advantage of a microcontroller, particularly Arduino Uno and MPU-9250 gyro-accelerometer. The researchers utilized the libraries of these devices in tuning the movement of the robot's head addressing transient time making it the least and to mention preciseness. Knowledge on other engineering disciplines was applied too in the development and modeling of the system. The proposed system focused only on three main pivotal axes of the head which are yaw, pitch and roll. Other head mechanism like facial movement would be covered through future and further research, which is highly recommended for the development of the paper.

2. Objective(s) of the Study

The general objective of this paper is to design and implement a microcontroller-based humanoid robot head allowing real actions of a human head be mimicked by the robot. Actions are within three (3) degrees of freedom; yaw, pitch and roll and combination of all. In line with these objectives

The specific objectives of this study are to design a robot head which mimics the gestures of the human head; to program the microcontroller to allow the robot head to move using sensors, motors, wires and gears; to test the overall functionality of the system.

2.1 Scope and Limitations

The researchers challenge is laid in the design and implementation of a microcontroller-based humanoid robot head specifically with three (3) degrees of freedom namely pitch, yaw and roll and combination of each. There is a need for designing and implementing the head of the humanoid robot using a microcontroller. The application of knowledge in programming in creating the algorithm of the head of

the humanoid robot, combined with knowledge on electromechanical, electronics and higher mathematics served as a challenge to which this paper is aiming for.

In line with this goal and challenges, the researchers carried out measures in attaining the goal and addressing these challenges. With this research, the researchers applied all learning and knowledge gain throughout the entire program and exhibited it thru the prototype.

3. Conceptual Framework

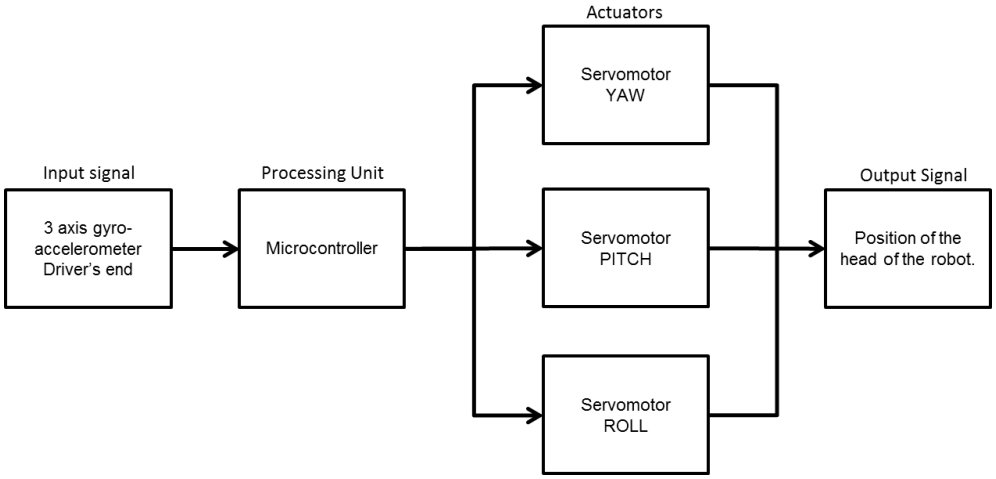


Figure 1. Conceptual Framework

Figure 1 shows the relationship of each variable of the system. The two3-axis gyro-accelerometer serves as a sensor and transducer. It evaluates the position of the head of the driver real-time and converts the information into digital format. The output of the gyro-accelerometer is transmitted via transmission line to a micro-controller that is embedded with programming codes; the signal is in turn evaluated and processed commanding the servomotors. The three servomotors that represent the three degrees of freedom will deflect the actual position of the head of the driver real-time, precise and in the quickest time possible.

3.1 Proposed Design

With enough knowledge in the field of Electronics and other field of Engineering, the researchers could conceptualize part by part the design of the whole system and how they will be integrated. Aside from technical, the researchers also considered the aesthetic part of the design for it will make an impact in the movement of the robot. Each part of the system design was carefully identified, and they play a vital role in the wholeness and functionality of the system. The design of the system is a product of the objectives and data gathered during research and foreseen challenges in this research.

4. Define and Design the System Requirements

The achievement of the desired goal comes with careful and orderly planning of the steps and procedures that are being done in the research paper. Determining the operational equipment needed for the prototype is one of the major steps in the design. Choosing the right ones will lead to the desired goals and objectives of the study.

In general, this chapter discusses the design requirement in creating the prototype. The details of the system requirements, methodologies, tools and technique used in the development of the system, the design requirements that include the hardware equipment from the technical to the aesthetic aspect, the software requirements and other tangible materials used in the creation of the prototype are discussed in this chapter as well. The system requirements focused on the input and output specifications of the system will be part of this section.

The researchers used and followed Water Fall Model to describe the process and phases that the research went through to come up with the result. This model is a sequential design process, in which progress is flowing steadily downwards through the phases of conception, initiation, analysis, design, construction, testing, production or implementation and maintenance.

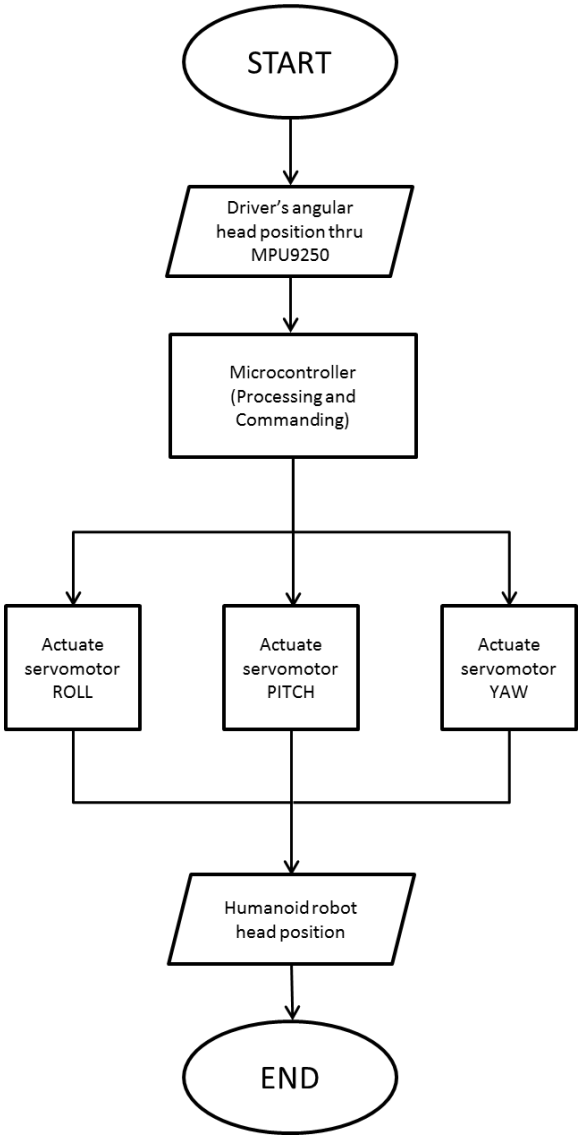


Figure 2. System requirements of Robot Head

4.1 Hardware Design

2.



Figure 3. Actual Head Design

Figure 3 shows the unpainted prototype. It is made up of fiber glass and resin molded using Styrofoam and cured for a certain period. Holes are drilled according to desired shape and polished using grinding tools and sand papers.

5. Experiments

Table 1. Test of Head Movements (Yaw)

Degree of Freedom	Trial	Base Value	Measured Value	Error	Percentage Error	Remarks
Yaw(Rotate left and right) @ 70°	1	70°	72°	2°	2.86%	Accepted
	2	70°	74°	4°	5.71%	Accepted
	3	70°	73°	3°	4.29%	Accepted
	4	70°	72°	2°	2.86%	Accepted
	5	70°	73°	3°	4.29%	Accepted
	6	70°	73°	3°	4.29%	Accepted
	7	70°	74°	4°	5.71%	Accepted
	8	70°	72°	2°	2.86%	Accepted
	9	70°	73°	3°	4.29%	Accepted
	10	70°	72°	2°	2.86%	Accepted
Average		70°	M=72.8°	2.8°	4%	Accepted

Table 1 shows the result of the movement Yaw (rotation left and right) with an error of 2.8° from base value of 70° equivalent to 4% of the total percentage error. It falls from the acceptable margin of percentage error

Table 2. Test of Head Movements (Roll)

Degree of Freedom	Trial	True Value	Experimental Value	Error	Percentage Error	Remarks
Roll (Tilt left and right) @ 45°	1	45°	48°	3°	6.66%	Accepted
	2	45°	49°	4°	8.88%	Accepted
	3	45°	49°	4°	8.88%	Accepted
	4	45°	47°	2°	4.44%	Accepted
	5	45°	49°	4°	8.88%	Accepted
	6	45°	47°	2°	4.44%	Accepted
	7	45°	48°	3°	4.44%	Accepted
	8	45°	48°	3°	6.66%	Accepted
	9	45°	47°	2°	4.44%	Accepted
	10	45°	47°	2°	4.44%	Accepted
Average		45°	M=47.9°	2.9°	6.44%	Accepted

Table 2 shows the result of the movement Roll (Tilting from left and right) with an error of 2.9° from base value of 45°equivalent to 6.44% of the total percentage error. It falls from the acceptable margin of percentage error

Table 3. Test of Head Movements (Pitch)

Degree of Freedom	Trial	True Value	Experimental Value	Error	Percentage Error	Remarks
Pitch (Tilt forward and backward) @ 50°	1	50°	52°	2°	4%	Accepted
	2	50°	52°	2°	4%	Accepted
	3	50°	54°	4°	8%	Accepted
	4	50°	52°	2°	4%	Accepted
	5	50°	53°	3°	6%	Accepted
	6	50°	53°	3°	6%	Accepted
	7	50°	53°	3°	6%	Accepted
	8	50°	54°	4°	8%	Accepted
	9	50°	52°	2°	4%	Accepted
	10	50°	52°	2°	4%	Accepted
Average		50°	52.7°	2.7°	5.4%	Accepted

3. Table 3 shows the result of the movement Pitch (Tilt Forward and Backward) with an error of 2.7° from base value of 50°equivalent to 5.4% of the total percentage error. It falls from the acceptable margin

6. Conclusions

It cannot be denied that robots have been purposeful and are continuing to innovate to meet the demands of humans, achieving their reason for creation. However,

they are getting more complex because of the development of new technologies that are being integrated to them.

To create a humanoid robot head that will mimic the movement of a human, there are three (3) major components that are essential in this project. First is the gyro-accelerometer which is attached on a cap, worn by the driver. This converts the angular displacements of the head into digital signals; second is the microcontroller this serves as the brain of the system and is connected to the gyro-accelerometer it interprets the received digital signals coming from the sensor and then gives out digital commands to the three servo motors. And the last component are the three servomotors, they are actuated by the signal they received from the microcontroller performing the three (3) degrees of freedom namely the Pitch (tilt forward and back), Roll(tilt left and right), and Yaw(Rotate left and right) and combination. As an additional feature of this project on humanoid robot head, the researchers added a camera module that will serve as surveillance in the environment. This camera is connected to a 5.8 GHz transmitter that will transmit signals to the video receiver and is connected to an LCD display to provide the output of the camera.

- The researchers could design and implement a microcontroller-based humanoid robot head that will mimic the action of a human pertaining to the three (3) degrees of freedom which are the Pitch, Roll and Yaw.
- The proponents could construct the frame of the robot consisting of the various parts that are necessary for movement.
- The idea of making the robot mimic the action or rather say the position of the head of the driver has become apparent through the test the researchers have conducted addressing the functionality of the system.
- Overall, the researchers of this project could achieve the desired outputs of the system which is to construct the head/neck framework of the humanoid robot, to program a microcontroller, and to mimic the action of a human.

Acknowledgment

Above all the researchers are grateful and thankful to the Almighty God, who unconditionally provided guidance all through the way.

The researchers also want to thank Engr. Favis Joseph Balinado and Engr. Rio Aguilar, for his great efforts of advising and leading us, to accomplish this research paper. To the Department of Engineering, for providing us with all the necessary facilities for the research. To the researchers' friends and families, they were a great source of support and encouragement.

To the researchers' parents, for the financial support they gave until the end of the project, the unceasing encouragement, love, attention and moral support. To every professor who teaches us to use the microcontrollers' software, and their provision on every step we take in making this project. To every person who help us making this project possible the researchers thank them and wish them the best of their lives.1

References

[1] Aggarwal, L., Gaur, V., Verma, P., (2013). Design and implementation of a wireless gesture controlled robotic arm with vision. International Journal of Computer Applications (0975 – 8887) VOL.79, NO. 13.

[2] Bhuyan, A., Mallick, T., (2014). Gyro- accelerometer based control of a robotic arm using AVR microcontroller. Department of Electrical and Electronic Engineering,Premier University, Chittagong, Bangladesh

[3] Bonev, I. (2014). Industrial robots, precision robotics (Paragraph 1). Retrieved fromhttp://coro.etsmtl.ca/blog/?p=374

[4] Bonini, N., Iyer, Nithya., Kim, D., Mathison, K., Wellons, L., (2014). Robotic Hand in Motion Using Arduino Controlled Servos.

[5] Carlson, G. (2002). Experimental errors and uncertainty (Paragraph 1). Retrieved from http://www.ece.rochester.edu/courses/ECE111/error_uncertainty.pdf

[6] Chattoraj, S., (2015). Gesture mimicking two-wheeler differential drive Arduino based robot and iRobot create

[7] Davy, M., Deepa, R., (2014) Hardware Implementation Based On Head Movement Using Accelerometer Sensor. Int. Journal of Applied Sciences and Engineering Research, Vol. 3, Issue 1, 2014,

[8] Goyal, D., Saini, S., (2013). Accelerometer based hand gesture controlled wheelchair. International Journal on Emerging Technologies 4(2): 15-20

[9] Gupta, M., Rohini, R., Reddy, P., Prakash, B., Kumar, K., (2015). Gesture controlled metal detecting land rover. International Journal of Engineering Trends and Technology (IJETT) – Volume 21 Number 5 (ISSN: 2231-538, www.ijettjournal.org Page 229)

[10] Joubair, A. (2014). What are accuracy and repeatability in industrial robots? (Paragraph 1). Retrieved fromhttp://blog.robotiq.com/bid/72766/What-are-Accuracy-and-Repeatability-in-Industrial-Robots

[11] Kandalkar, S., Kadam, P., (2015).Arduino based head gesture controlled robot using wireless communication, Int. Journal of Engineering Research and Applicationswww.ijera.com ISSN : 2248-9622, Vol. 5, Issue 5, (Part -3) May 2015, pp.32-34

[12] Neto, J., Pires, N., Moreira, P., (n.d.). Accelerometer-based control of an industrial robotic arm

[13]SJS.org. (2004).University of Wisconsin lab manual. Retrieved from http://www2.sjs.org/friedman/PhysAPC/Errors%20and%20Uncertainties.htm

[14] Stamatis, D. (n.d). The OEE Primer, understanding overall equipment efectiveness and reliability and maintainability (pages 205-206). Retrieved from https://books.google.com.ph/books?id=8i7NBQAAQBAJ&pg=PA206&lpg=PA2

06&dq=acceptable+percent+error+in+machines+in+the+industry&source=bl&ots=brDU9Xffc&sig=1l03KKw4i0eXF0_g5k58JUwONRc&hl=en&sa=X&ved=0ahUKwjuqNKRxqPTAhXEfrwKHUxjBEQQ6AEIPDAE#v=onepage&q=acceptable%20prcent%20error%20in%20machines%20in%20the%20industry&f=false

[15]Winokur, M. (2005).Errors and uncertainties. Retrieved from http://badger.physics.wisc.edu/lab/manual/node4.html

[16] Wolf, M., Assad, C., Vernacchia, M., Fromm, J., Jethani, Henna., (2013). Gesture-Based Robot Control with Variable Autonomy from the JPL BioSleeve

Weather Adaptive Automotive Headlights Using Arduino Microcontroller

Kevin L. Domingsil*, Frances Camil C. Ilagan, Glofett T. Velasco, Princess Joy V. Natividad, Carlene Joy A. Breganza, Arvin P. Dela Roca

Lyceum of the Philippines University – Laguna (LPU-L)
Calamba City, Laguna, Philippines

*kevindomingsil@gmail.com

Abstract
Having to drive at night, where roads become especially hazardous and the weather condition is bad, without having the right illumination from your car headlights is very dangerous. It is one of the worst conditions a driver has to go through. Extreme weather conditions dramatically reduce the vision of the driver and/or the visibility of the road ahead compared to daylight driving. Vehicular accidents that occur during night time and during extreme weather conditions are mostly fatal, and therefore must be prevented. In this work, the proponents proposed a weather adaptive automotive headlights that can help in the reduction of car accidents especially during night time and during extreme weather conditions. Automotive headlights are actually safety device used to provide better vision for the driver of the automobile. The study proposes a prototype design of a Weather Adaptive Automotive Headlights that will replace the current stock halogen-type headlights that most automobiles use. The study used an Arduino UNO microcontroller to obtain the desired function and output of the project. The project built consists of hardware and software development. The study used the Arduino language, which is merely a set of C or C++ functions. The goal of this study has been reached by retrofitting an automotive headlight, that switches between two different color temperatures (3000K and 6000K) based on what is more appropriate for the current weather condition. It also aimed and achieved to create a manual switch that overrides the sensor detection and microcontroller analysis to satisfy the need of the driver. Upon mass implementation of the project, it would contribute mainly to the reduction of vehicular accidents at night.

Keywords: Arduino, Headlight, Retrofit, High-intensity discharge (HID), Projector

1. Introduction

Driving at night has been a problem since the emersion of vehicles. When the sun goes down, extra dangers arise on the road. According to Law Offices of Michael Pines (2013), despite of having 60% less traffic on the roads, more than 40% of all fatal car accidents occur at night. From compromised vision and visibility to impaired drivers, there are plenty of hazards to watch out for.

Driving conditions are also remarkably different based on various weather conditions. Vision is reduced and it can be more difficult to see vulnerable road users such as pedestrians, cyclists, motorcyclists or even animals. Imagine having to drive at night where roads become especially hazardous and the weather is bad without having the right illumination from your car headlights. The glare of oncoming lights, amplified by the rain on your windshield, can cause temporary loss of visibility while substantially increasing driver fatigue.

Over the world's most dangerous roads by estimated death toll, the Philippines comes in as number 15 and road accidents are the fourth leading cause of death in the Philippines. In addition to that, more deaths occur in urban areas and at night. Driving in the dark often means extremely poor visibility – particularly in areas where there is insufficient lighting. Poor visibility can stem from a number of factors, including weather conditions. Driving in poor visibility increases the potential for a serious car crash to occur. [1]

Since 2013, three cities in Metro Manila have consistently topped the list in terms of number of road crashes recorded in their jurisdictions: Quezon City, Manila, and Makati. The number of road crash incidents in the three cities comprise 51% of the total 95,615 crashes recorded between January to December 2015 in the capital region. Most of the road crashes reported every year happened during day time, but the crashes that end up deadly mostly occurred at night and in the early hours of the morning. Of the 519 fatal crashes recorded, 314 happened during night time while 205 cases were recorded during the day. [2]

Driving at night during extreme weather conditions is one of the worst conditions a driver has to go through. So, in order to provide a feasible solution to the problem, the researchers proposed a weather adaptive automotive headlights that will enhance the vision of the driver.

Hence, there is a need to design and develop a Weather Adaptive Automotive Headlights using Arduino microcontroller to reduce the car accidents during nighttime and during extreme weather conditions, and prevent casualties. Nighttime and extreme weather conditions dramatically reduce the vision of the driver and/or the visibility of the road ahead compared to daylight driving.

The color assignment given to each hue in the spectrum depending on how it is seen by the human eye is called the color temperature. Color temperature is represented in Kelvin, the same as the unit for absolute temperature. Yellow light (3000K) is commonly found in the form of Halogen lamps. Yellow light is the most appropriate for bad weather because it can pass through air moisture as compared to white light. It is best for circumstances involving fog, snow, sleet, rain and storms thus it is the best

HID color for visibility during extreme weather conditions. Crystal White Light (6000K) is a white light with more blue undertones. It most closely resembles sunlight, in which the human eye sees best and therefore, the best HID color for night driving. [8]

Weather adaptive automotive headlights system is a lighting system with a bulb attached in the front of a vehicle to light the road ahead. It will adapt the color temperature of the light output of the headlamp for better vision and illumination based on the weather sensor connected to Arduino microcontroller that will detect the current weather condition and process the information for an accurate switching of the light output.

The study aims to design and develop a weather adaptive automotive headlights for vehicles. Specifically, it aims to: increase the visibility of the roads, signage's and other road users; provide an automotive headlight that can be retrofitted to the current headlight assembly of a vehicle; and provide an automotive headlight that outputs correctly the desired color temperature of the bulb.

However, the study is delimited to the production of a car headlight bulb with a module only and not the entire headlight assembly. It is also delimited to the detection of weather only and not the detection of the absence of light.

2. Methodology

2.1 System Design

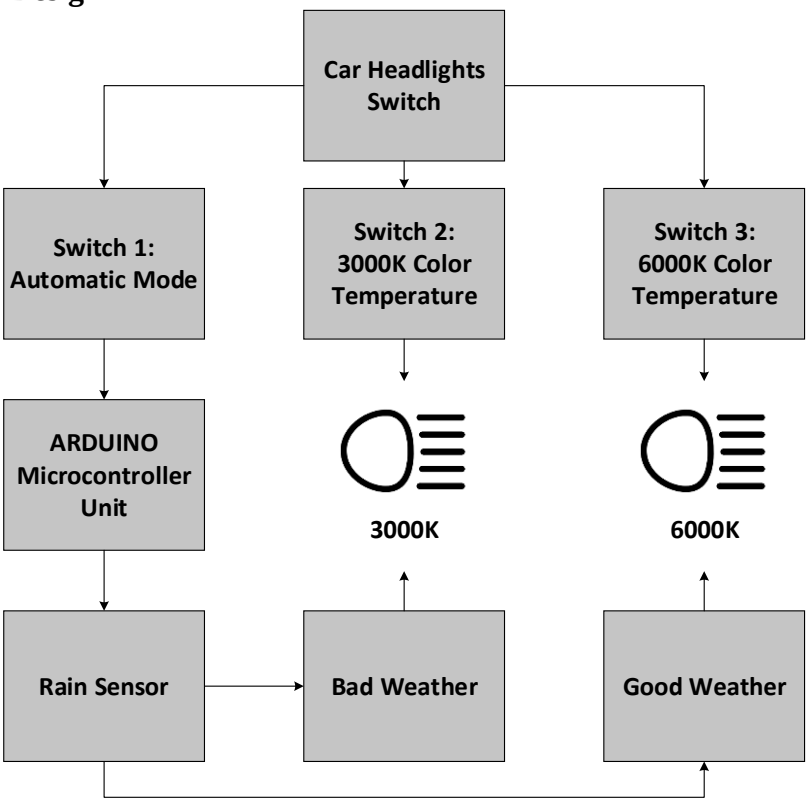


Figure 1. System Block Diagram.

Figure 1 shows the system block diagram of the project. It is mainly called the "Weather Adaptive Automotive Headlights". It has three switches, not including the main switch of the headlight on the vehicle, for three different modes namely the 3000K color temperature, 6000K color temperature and the automatic mode that uses Arduino Microcontroller Unit connected to a rain and weather sensor that automatically switches the color temperature of the headlamp to 3000K color temperature when the weather is bad and 6000K color temperature when the weather is good.

2.2 Requirements and Specifications

This part focuses on the assembly of the system hardware components. This includes the following:



Figure 2. Rain Sensor.

Rain Sensor – The rain sensor detects water that completes the circuits on its sensor boards' printed leads. The sensor board acts as a variable resistor that will change from 100k ohms when wet to 2M ohms when dry. In short, the wetter the board the more current that will be conducted. The connected microcontroller accepts the signal and performs necessary processing.

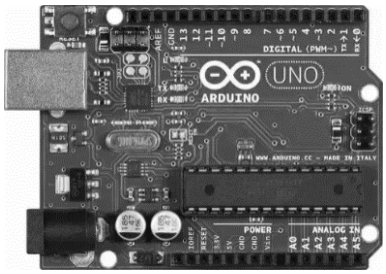


Figure 3. ATmega328P Microcontroller.

Microcontroller – Arduino Uno is a microcontroller board based on the ATmega328P. It has 14 digital input/output pins (of which 6 can be used as PWM outputs), 6 analog inputs, a 16 MHz quartz crystal, a USB connection, a power jack, an ICSP header, and a reset button. It contains everything needed to support the microcontroller.

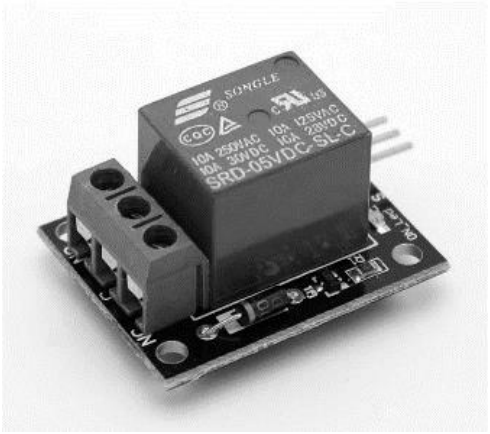


Figure 4. Relay Module.

Relays – These are switches that open and close circuits electromechanically or electronically. Relays control one electrical circuit by opening and closing contacts in another circuit. As the relay diagrams show, when a relay contact is normally open (NO), there is an open contact when the relay is not energized and when a relay contact is normally closed (NC), there is a closed contact when the relay is not energized.



Figure 5. Supply.

Supply – This is the power source of the system and the headlight bulbs. This can be found in the vehicle and is normally 12V.



Figure 6. Bi-Color HID Bulbs.

Bi-color bulbs – These are the high-intensity discharge (HID) light sources for car headlights with two different color temperature output. One is the 3000 Kelvin and the other is the 6000 Kelvin. The light has been produced by an electric arc between tungsten electrodes contained in a translucent or transparent fused quartz or fused alumina arc tube.



Figure 7. Projector Lens.

Projector Lens – This will project the output of the bulbs with proper light cutoff to prevent the glare to the oncoming traffic and enhance the illumination of the light by focusing it.

2.3 Project Design



Figure 8. Project Design.

The prototype can be retrofitted to any vehicle, meaning, the prototype can be installed inside the stock or original halogen headlights so that users can harness the power of the Weather Adaptive Automotive Headlights. Figure 8 shows an example of a retrofit in an owner type jeepney.

3. Results and Discussion

In order to assess the performance of the system, several tests and/or experiments were conducted to gather data and information about the prototype. The tables below show the data and results of the experiments.

3.1 Sensor Detection

Table 1. Sensor Detection

Test No.	Condition	Outcome	Remarks
1	Not Raining	6000K	Correct Output
2	Not Raining	6000K	Correct Output
3	Not Raining	6000K	Correct Output
4	Not Raining	6000K	Correct Output
5	Not Raining	6000K	Correct Output
6	Raining	3000K	Correct Output
7	Raining	3000K	Correct Output
8	Raining	3000K	Correct Output
9	Raining	3000K	Correct Output
10	Raining	3000K	Correct Output

Table 1 shows the performance of the sensor. The proponents put the system into a test where the vehicle was situated on two different weather conditions and the headlights were turned on and off. The test showed that the system outputs the appropriate color temperature of the bulb of the headlight.

3.2 Switching Time

Table 2. Switching on Manual Mode

Test No.	Color Temperature Switching	Switching Time
1	3000K to 6000K	Immediately
2	6000K to 6000K	Immediately
3	3000K to 6000K	Immediately
4	6000K to 6000K	Immediately
5	3000K to 6000K	Immediately
6	6000K to 6000K	Immediately
7	3000K to 6000K	Immediately
8	6000K to 6000K	Immediately
9	3000K to 6000K	Immediately
10	6000K to 6000K	Immediately

Table 2 shows the switching times on using the manual switches of the system. The headlights were switched from 3000K to 6000K color temperature and vice-versa. The result showed that the user can achieve the desired output right after the button for a specific color temperature was pressed.

Table 3. Switching on Automatic Mode

Test No.	Condition	Color Tempe-rature	Switching Time (in seconds)	Remarks
1	Not Raining to Raining	3000K	2.58	Correct Color Temperature
2	Raining to Not Raining	6000K	5.18	Correct Color Temperature
3	Not Raining to Raining	3000K	3.49	Correct Color Temperature
4	Raining to Not Raining	6000K	6.28	Correct Color Temperature
5	Not Raining to Raining	3000K	3.09	Correct Color Temperature
6	Raining to Not Raining	6000K	5.46	Correct Color Temperature
7	Not Raining to Raining	3000K	3.99	Correct Color Temperature
8	Raining to Not Raining	6000K	6.58	Correct Color Temperature
9	Not Raining to Raining	3000K	2.63	Correct Color Temperature
10	Raining to Not Raining	6000K	6.41	Correct Color Temperature

Table 3 shows the switching times on using the automatic mode of the system. The proponents simulated the weather condition by using a power spray to create an artificial rain. The headlights were switched from 3000K to 6000K by the microcontroller through the use of a sensor. The result showed that it takes an average of 3.16 seconds to switch to the right color temperature from not raining to raining and 5.98 seconds from raining to not raining.

4. Conclusion

The project provided a prototype of a Weather Adaptive Automotive Headlights Using Arduino Microcontroller. The study uses Arduino UNO to obtain the desired output of the project. The project built consists of hardware and software development. The study uses the Arduino language, which is merely a set of C/C++ functions. The proponents retrofitted the system on an owner type jeepney. The experiments conducted showed that the system outputs the appropriate color temperature of the bulb of the headlight, the manual color temperature switches immediately takes effect and the automatic mode has a delay of several seconds to output the suitable color temperature based on the current weather conditions.

Acknowledgment

The authors acknowledge Almighty God – the source of their knowledge, wisdom and strength in completing this study. They would like to thank Lyceum of the Philippines University – Laguna for providing the resources needed for this study and Engr. Favis Joseph Balinado and Engr. Rio Aguilar for being the technical adviser of the study. The researchers would also like to thank Chroma Lights Lipa for extending their help to finish the project. Lastly, they would like to extend their deepest gratitude to their families and loved ones for their ceaseless support and understanding throughout the span of accomplishing this study.

References

[1] World Health Organization. *Road traffic injuries.* (2017) [online] Available at: http://www.who.int/mediacentre/factsheets/fs358/en/ [Accessed 10 Feb. 2017]

[2] Orias, Evan (2017). *ROAD SAFETY SERIES: Multiple PH road crash databases need integration, tuning.*

[3] Yali Guo, Qinmu Wu and Honglei Wang (2012). *Design and Implementation of Intelligent Headlamps Control System Based On CAN Bus.*

[4] Victor Nutt, Shubhalaxmi Kher and Mehul Raval.Fuzzy (2013). *Headlight Intensity Controller using Wireless Sensor Network.*

[5] Priyanka Dubal and Mr. Nanaware J.D. (2015). *Design of Adaptive Headlights for Automobiles*. International Journal on Recent and Innovation Trends in Computing and Communication ISSN: 2321-8169 Volume: 3 Issue: 3

[6] Pengfei Song, Yang Zhang, Xianglong Wu and Yufan Lan (2013). *Design and Implementation of the Adaptive Control System for Automotive Headlights Based on CAN/LIN Network.*

[7] Shreyas S, Kirthanaa Raghuraman, Padmavathy AP, S Arun Prasad2 and G. Devaradjane (2014). *Adaptive Headlight System for Accident Prevention.*

[8] James, Tyler (2016). *Best HID Color: Headlight Color Guide.*

[9] Jyotiraman De (2014). *Universal Adaptive Headlight System.*

[10] Snehal G. Magar (2015). *Adaptive Front Light Systems of Vehicle for Road Safety.*

[11] Sabrine Hamdi, Hassene Faiedh, Chokri Souani and Kamel Besbes (2016) *Abnormal Moving Vehicle Detection for Driver Assistance System in Nighttime Driving*

[12] Feng Lou and Fengjian Hu (2014). *A Comprehensive Survey of Vision Based Vehicle Intelligent Front Light System.* International Journal on Smart Sensing and Intelligent Systems VOL. 7, NO. 2.

[13] Prof. R.K. Moje, Mrugesh Bannatwale, Sagar Jamdade and Preeti Halloli (2016). *Embedded Based Smart, Secured and Safe Vehicle System*. International Journal of Innovative Research on Electrical, Electronis, Instrumentation and Control Engineering Vol. 4, Issue 2.

[14] Monica Salcianu, Christian Fosalau and Anamaria Hariton (2012). *Simulation of an Intelligent-Adaptive Front Lighting System.*

[15] Robert Tamburo, Eriko Nurvitadhi, Abhishek Chugh, Mei Chen, Anthony Rowe, Takeo Kanade, and Srinivasa G. Narasimhan (2014) *Programmable Automotive Headlights.*

[16] Brendan Cavanagh, Nathaniel Keahi Goodale and Matthew Janiga (2015). *Efficient Pulse Width Modulation LED Headlight Driver.*

[17] GUAN Xiu-li and LEI Yan-min (2014). *Design of the Auto Headlamp System.*

[18] GUO Quan-min and LI Xiao-ling (2015). *Vehicles' Anti-blooming Method Based on Visible and Infrared Images Fusion.*

[19] Silea Ioan, Miclea Razvan-Catalin and Alexa Florin (2016). *System For Visibility Distance Estimation In Fog Conditions Based On Light Sources And Visual Acuity.*

eureca 2017 – Conference Paper
Paper Number EUG15

A Wired PID-Based Altitude Controlled Remotely Operated Underwater Vehicle with Data Acquisition

Frances Camil C. Ilagan [1*], Christian Jay B. Carabio [1], Marie Thalia Grace M. Amutan [1], Vanna Kaori S. Lustre [1], Kevin L. Domingsil[1], Carlene Joy. Breganza[1], Princess Joy V. Natividad[1], Arvin P. Dela Roca [2]

[1]*Undergraduate Student, Electronics Engineering Department*
[2]*Faculty Member, Electrical Engineering Department*
Lyceum of the Philippines University – Laguna
Calamba City, Laguna, Philippines

[*]francesilagan@gmail.com

Abstract
Submarines originated long time before. It is specified as watercraft that can function well underwater. Submarines are also used for aquatic and fresh water science and waterworks with depths that is too deep for human divers. Due to the functionalities of a submarine, it became popular on those applications including under water surveillance, assessment and investigations. However, problems may be encountered in operating a submarine, one good example is maintaining its position underwater. In line with that, the proponents designed and implemented a remotely operated underwater vehicle (ROV) with the use of data acquisition and altitude control. Moreover, the proponents used waterproof ultrasonic sensor for detection of depth and hovering. The JSN-SR04T ultrasonic sensor will determine the level of the water and will help the vehicle to move on a more stabilized manner. The system can be controlled using a controller box interface with input switches that will command the vehicle to move forward, reverse, left, right, upward, downward and hover. The idea of unmanned underwater vehicles has been the basis of the proponents in designing the ROV in order to develop and implement a system that will become stable and maintain its position with the help of the sensors and motors with propellers.

Keywords: Remotely Operated Vehicle (ROV), Arduino Mega2560, Arduino Uno R3, PID, Ultrasonic Sensor, Temperature Sensor

1. Introduction

There are various types of underwater vehicles which can be categorized into two categories, namely, manned and unmanned systems. [1] In manned system, we have military submarines and non-military submersibles operated for underwater investigations and assessment. Unmanned submersibles can also be further classified into different categories. The simplest and most easily described are those submersibles that are towed behind a ship. They act as platforms for various sensor suites attached to the vehicle frame. Second type is called Remotely Operated Vehicle (ROV) which is a tethered vehicle. The tether supplies power and communication to the ROV and it is controlled directly by a remote operator. Third type is an Unmanned Untethered Vehicle (UUV). These vehicles have their own onboard power but are controlled by a remote operator through a communication link. An Autonomous Underwater Vehicle (AUV) is an undersea system which has its own power and controlled by an onboard computer while doing a pre-defined task [2].

This research focuses on Underwater Vehicle using a controller box with input buttons. The study aims to design and implement a wired PID-based altitude controlled ROV with data acquisition using Arduino microcontroller. Nowadays, there is a need to implement a PID-based altitude controlled ROV in order to maintain its position and 'hover' to that specific location using a remote controller or joystick. Other remotely operated underwater vehicle were encountering problems in maintaining the position of the underwater vehicle. It uses different sensors namely ultrasonic sensor and temperature sensor for the purpose of data acquisition. The use of underwater propellers will maintain its position and altitude control with the help of sensors. An underwater camera for real time imaging is also connected that would display the image/video on an android phone.

The UUV devices utilizes commercial, off-the-shelf accelerometers and gyroscopes and novel algorithm to yield accurate navigation. The device is mainly designed for aerial vehicles, and translating the functionality of this device is one of the objectives of his study. The focus of this study is to develop a low-cost, light-weight navigation system for UUV [4]. A new electronic system for UUV implements the basic functionality of the vehicle using generic electronic components. This new electronic control system is the base for building new family of underwater vehicles [5].

The design and modeling of the ROV was done using identification in MATLAB. Two control strategies were implemented; a linear quadratic controller (LQ) and a model predictive controller (MPC). In able for the system to become stable, a weight is place so that the ROV always strive to stabilize itself [6]. A proposed UUC MCM system is cost-effective due to adapting disposable mine instruments. Relating to our present study, we can use this to survey the area wherein the mine will be disposed [8].

A board wireless camera for a local RC submarine is used in the project. The main things in the RC submarine are controller system and watertight. The fabrication phase started with making a control system for the submarine. A controller circuit consists of two important components; relays and radio control receiver. This will control pumps and motor [9].

There is a need to develop solutions on integrating and deployment of vessels on all types. The maturity of such systems varies, ranging from reasonably mature surface vessel. UUV deployment and recovery systems to less mature submarine systems [11]. UUVs are continually becoming more integral components of maritime operations, especially those associated with defense systems. This research focuses on the possible uses of flexible hull morphing, specifically the feasibility of such adaptability in terms of range, endurance, and speed. Furthermore, methods of actuating a morphing hull system are investigated as is the construction of a small scale morphing UUV model [12].

A new UUV which perform better than a survey launch. A survey launch is a boat, usually six to ten meters long. The boat is launched and recovered daily from a mother ship. Launches are usually operated only in daylight for safety and to allow time for the crew to rest [13].

Autonomous vehicle is a good tool for observing large areas of sea, since it operates for long periods of time due to the contribution of renewable energy. It correlates all sensor data for time and geodetic position. This vehicle has been used for monitoring the Mar Menor lagoon. This research is about an intelligent navigation system for an unmanned underwater vehicle [14].

An adaptive nonlinear controller for diving control of an autonomous underwater vehicle (AUV). So far, diving dynamics of an AUV has often been derived under various assumptions on the motion of the vehicle. Typically, the pitch angle of AUV has been assumed to be small in the diving plane. However, these kinds of assumptions may induce large modeling errors and further may cause severe problems in many practical applications. In this paper, through a certain simple modification, we break the above restricting condition on the vehicle's pitch angle in diving motion so that the vehicle could take free pitch motion [15].

Cost should be taken into consideration when making a project. To reduce the working load of divers and significantly accelerate inspection and/or treatment, it would be highly desirable and efficient to deploy affordable UUVs to inspect and clean these ship sea chests. Thus, this paper presents a low cost UUV prototype emphasizing the unique design issues and solutions developed for this task, as well as those attributes that are generalizable to similar systems. The prototype design consists of basic components, including main haull, two horizontal propellers, four vertical thrusters, two batteries, an external frame, and electronics inside the main haul [16].

The design of UUV that in able to control the UUV a kinematic and dynamic model is derived for the six degrees of freedom operating range. The AUV is able to operate in six degrees of freedom and the dynamics of an AUV are nonlinear and subjected to a variety of disturbances [17].

An underwater observation system and to perform utilitarian activities in order to obtain data, probes and to make measurements in marine medium, to a depth of 300 meters. In this paper, the ROV will be tested on a rectangular pool area wherein the range of the sensors that will be used is about 3ft only [18].

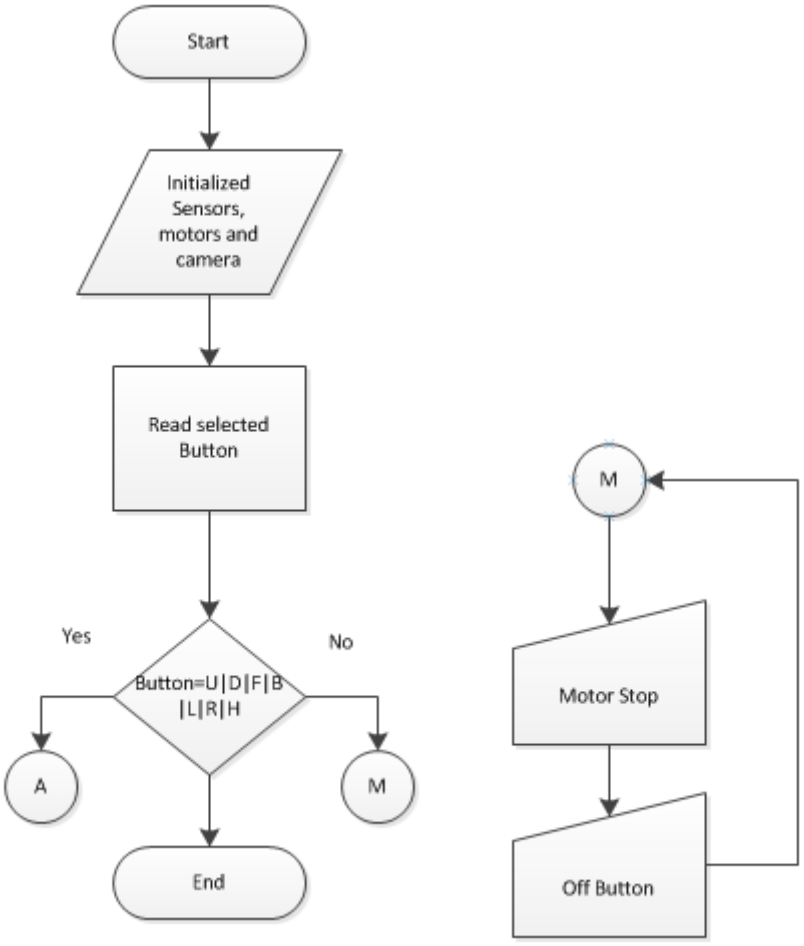
The development and deployment of unmanned underwater vehicles has contributed to the development and, in some cases, to field-tests of paradigms, vehicles and sensor systems for oceanographic and environmental data collection. One paradigm developed by researchers in the United States that has received significant attention is the Autonomous Ocean Sampling Network [19].

When designing control systems for real applications, it is important to first do testing in a simulated environment, to ensure adequate performance. This is especially important when designing control systems for applications that have high operation costs [20].

The algorithm used in the project is PSO algorithm, in order to find optimal parameters to be used on the PID controller to get feedback controls for this model. The pitch-depth double loop feedback control system has been designed to control the movement of underwater vehicle [21].

2. Methodology

2.1 Flowchart



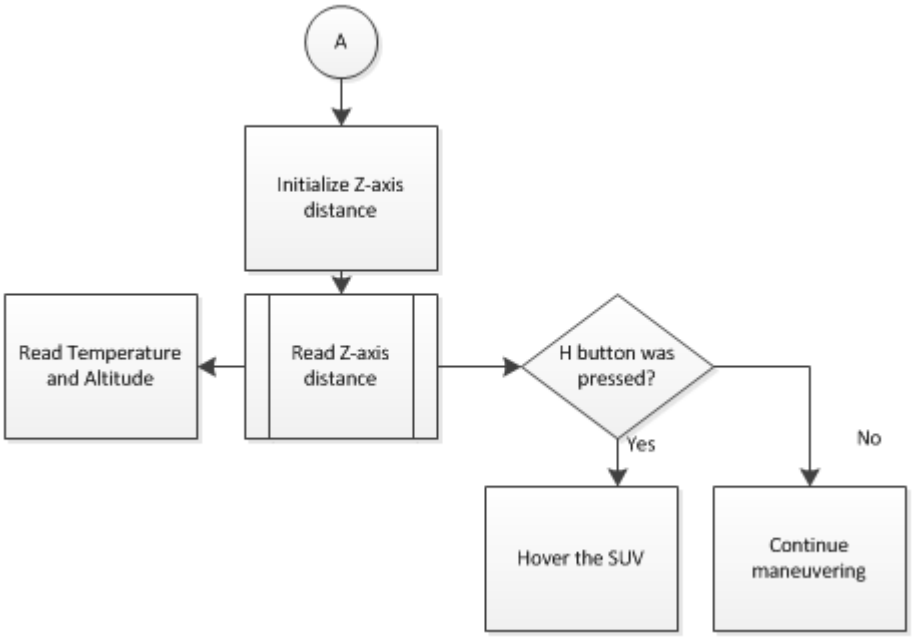


Figure 1. Flowchart

The initialization of controller commands for the SUV is shown in Figure 1. The controller or joystick is composed of 7 buttons with different direction actions. Every time the buttons are pressed, it will automatically turn on the device, sensors and motors. The microcontroller will always read the button pushed by the user.

Every time the controller sends a signal on the microcontroller, the distances will be initialized and the sensors will send data on the microcontroller to be displayed on the LCD, as well as the camera that will be displayed on the PC monitor.

2.2 Proposed Design

The proponents came to a design of ROV with data acquisition using Arduino microcontroller. The PID algorithm will be implemented to make the system stable. The used of ultrasonic sensor will aid the ROV to measure the distance from the Z coordinates. The temperature underwater will be measured using the DS18B20 waterproof sensor for the purpose of data gathering. The planned design structure should be neutrally buoyant for the vehicle to make it float and sink. The actuators (motors) that will be used are brushless motors, it has magnetic contact and has a slower speed compared to brush motors. In order to have a remote and underwater viewing, a camera will be installed for real-time viewing and can be monitored on a smart phone. The wired controller will help the microcontroller to aid the motors and propellers on which direction it will moved. The altitude of the vehicle will be measured using altitude sensor and can be observed simultaneously on a LCD display.

2.3 Hardware Design

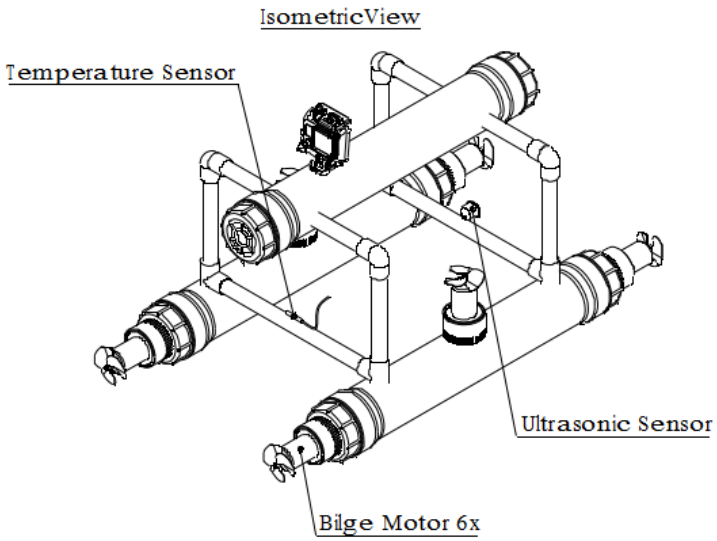


Figure 2. Hardware Design of the Prototype

The prototype is made up of PVC or Polyvinyl Chloride. The length of the ROV is 21 inches, height of 13.31 inches and a width of 15.16 inches. The proponents decided to use this kind of material in order to prevent corrosion and leakage when tested underwater. The weight of the prototype is kept neutrally buoyant in order not to sink and not to float during testing. The underwater motors used are brushless and will be placed on both end of the PVC pipe.

2.4 The prototype and the Software



Figure 3. Project Prototype

The figure above is the actual project prototype. It consist of 6 bilge motor in order to move the ROV freely. The underwater camera was placed at the front top in order to view the heading of the device. The temperature sensor and ultrasonic sensor were placed in front and at the back respectively. The placement of the motors were equally positioned in order to have a stable and balanced movement on the water.

3. Results and Discussion

Table 1. Normal Water Tank Test of the sensors

Sample Test for Temperature and Depth Test	
Depth in Feet	Temperature in Celsius
5.5	27.35
5	26. 43
4.5	25.68
4	24.76
3.5	23.45
3	23.45
2.5	23.45
2	23.45
1.5	23. 32
1	23.12
0.5	22. 15

Table 1 shows the relationship of the temperature and the depth of the water. The test was conducted on a normal tank; the sensors are not yet connected on the ROV during the test.

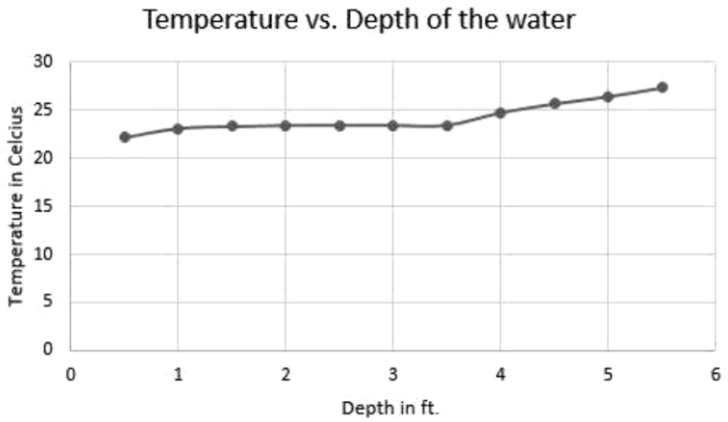


Figure 4. Graph of Temperature and Depth of the water

Figure 4 shows the relationship of the water with the depth. The proponents tested the sensors initially and found out the relationship of the depth with the temperature. As the depth sensor go deeper in water, the temperature will go down and becomes colder. As the depth is increasing the value of the temperature is also increasing, it only means that the temperature is directly proportional to the depth. This is because cold water is denser than warm water and sinks while the warm water rises. It is also due to the fact that the sun's rays can only go down so far.

The tables below show the results gathered from the ultrasonic sensor and the percentage error for each trial. The used of retractable measuring tape was the basis of the proponents for the true value.

Table 2. Data Acquired from Ultrasonic Sensor Sample 1

Trial No.	True Value (cm)	Experimental Value	Absolute Error	Percentage Error
1	82.00	81.00	1.00	1.22%
2	82.00	80.00	2.00	2.44%
3	82.00	80.00	2.00	2.44%
4	82.00	77.00	5.00	6.10%
5	82.00	78.00	4.00	4.88%

Table 2 shows the actual value of the depth which is 82 cm. The ultrasonic sensor measures 81cm (trial 1), 80 cm (trial 2 and 3), 77cm and 78 cm for trial 4 and 5 respectively. The maximum percentage error for height is 6.10% and has a minimum percentage error of 1.22%.

Table 3. Data Acquired from Ultrasonic Sensor Sample 2

Trial No.	True Value (cm)	Experimental Value	Absolute Error	Percentage Error
1	53.00	50.00	3.00	5.66%
2	53.00	51.00	2.00	3.77%
3	53.00	51.00	2.00	3.77%
4	53.00	52.00	1.00	1.89%
5	53.00	53.00	0.00	0.00%

Table 3 shows the actual value of the depth which is 53 cm. The ultrasonic sensor measures 50cm (trial 1), 51 cm (trial 2 and 3) , 52 cm and 53 cm for trial 4 and 5 respectively. The maximum percentage error for height is 5.66% and has a minimum percentage error of 0%.

Table 4. Data Acquired from Ultrasonic Sensor Sample 3

Trial No.	True Value (cm)	Experimental Value	Absolute Error	Percentage Error
1	58.00	57.00	1.00	1.72 %
2	58.00	55.00	3.00	5.17 %
3	58.00	55.00	3.00	5.17 %
4	58.00	56.00	2.00	3.45 %
5	58.00	55.00	3.00	5.17 %

Table 4 shows the actual value of the depth which is 58 cm. The ultrasonic sensor measures 57cm (trial 1), 55 cm (trial 2 and 3 and 5) and 56 cm for trial 4. The maximum percentage error for height is 5.17% and has a minimum percentage error of 1.72%.

Table 5. Data Acquired from Ultrasonic Sensor Sample 4

Trial No.	True Value (cm)	Experimental Value	Absolute Error	Percentage Error
1	55.00	52.00	3.00	5.45 %
2	55.00	53.00	2.00	3.64 %
3	55.00	54.00	1.00	1.82 %
4	55.00	54.00	1.00	1.82 %
5	55.00	54.00	1.00	1.82 %

Table 5 shows the actual value of the depth which is 55 cm. The ultrasonic sensor measures 52cm (trial 1), 53 cm (trial 2) and 54 cm for trial 3,4 and 5. The maximum percentage error for height is 5.45% and has a minimum percentage error of 1.82%.

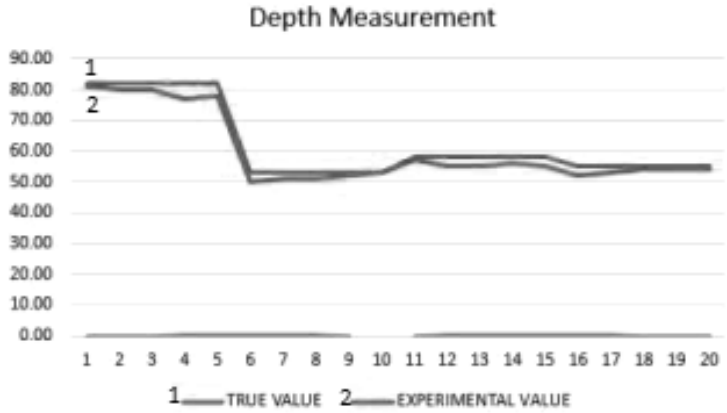


Figure 5. Actual and Experimental value for depth measurements

The figure shows the relationship between the measure depth using the ultrasonic sensor and the actual values itself. The system is not 100% accurate and as interpreted above, there are small percentage error and high percentage error.

Table 6. Statistical Acceptability of Error of Ultrasonic Sensor Using T-test

t - test: Two-Sample Assuming Unequal Variances		
	Variable 1	Variable 2
Mean	62	59.9
Variance	143.6842105	134.2
Observations	20	20
Hypothesized Mean Difference	0	
Df	38	
T stat	0.563381209	
P(T<=t) one-tail	0.288242467	
T Critical one-tail	1.68595446	

Table 6 presents that the P-value is equal to .288242467 and since the P-value serves as the evidence that null hypothesis is true, therefore, the null hypothesis is accepted. There is no significant difference between the actual value from the retractable meter and the ultrasonic sensor. If the percentage error is ⩽5% the measured value is accepted. Based on a blog at Pepper Fuchs absolute accuracies of 1% and 3% are realistic in industrial applications for ultrasonic sensors in the operating range of -25°C to +70°C. However, as the air temperature changes, the speed of sound changes by 0.17% per degree Kelvin. Since the temperature is one of the variables being tested, a 5% acceptability of error is allowed in this results [22].

Table 7. Data gathered from the temperature sensor

Sample Number	Temperature in °C	Temperature in °F
1	31.12	88.02
2	31.19	88.14
3	31.06	87.91
4	31.25.75	88.25
5	31.19.25	88.14
6	31.25.25	88.25

The data above were measured while the ROV is on hover mode. The temperature sensor displayed the measured data simultaneously on a LCD.

4. Conclusions

In conclusion, the proponents designed and constructed a functioning ROV that can be used to accumulate temperature data at a certain altitude and to display a real-time video underwater directly to a smart phone. With respect to the data accumulated by the temperature sensor on a normal water tank test, the temperature is directly proportional to the distance, which means that as the distance increases, the temperature also increases.

To comply for the objectives of the study, the proponents arrive in the following conclusions: The proponents were able to create and developed a wired altitude controlled ROV and gather data using the sensors. The ROV used a microcontroller platform namely Arduino Mega 2560 and Arduino Uno R3. The used of controller box with 7 inputs namely, UP, DOWN, FORWARD, REVERSE, LEFT, RIGHT, and HOVER were obtained to control the movement of the ROV and hover to a certain depth. The proponents were able to collect data such as temperature and depth which was displayed on the LCD and the underwater camera connected can be viewed using a smart phone. Although the temperature sensor does not work properly, the proponents tested it independently on the ROV, it was then connected to the Arduino Uno R3.

Using T-Test method, the proponents were able to determine the acceptability of error for the device. For the accuracy of ultrasonic sensor, the percentage of error range from 0% to 6.10%

These data can be used as a learning device for students of Lyceum of the Philippines-Laguna. There are some modifications to be made; however, they can be modified by the students as a way to learn more about ROVs or can be improved by the future researchers in an attempt to enhance the system.

Acknowledgment

The researchers would like to extend their deepest gratitude to all the people who help them in making this research study possible.

To God Almighty, for giving them the strength, the knowledge, the ability and the guidance;

To their adviser, Engr. Favis Joseph C. Balinado for always being there to help the researchers and give them guidance throughout the whole study;

To their classmates and the members, who helped and made valuable comment and suggestions on this research.

To the panelists, for listening to the presentation, for giving constructive criticism, and for suggesting ideas for the improvement of the proposal.

To their parents who have not stopped supporting them until the end and to their loving professors who show their support and guidance, without them this project would not be possible.

References

[1] Breivik, Morten and Fossen, Thor I. (2009). *Guidance Laws for Autonomous Underwater Vehicles*. Norwegian University of Science and Technology, Norway.

[2] S Williams, P Newman, S Majumder, J Rosenblatt, HF Durrant-Whyte. (1999). *Autonomous Transect Surveying of the Great Barrier Reef*, Australian Conference on Robotics and Automation (ACRA'99), pp. 16-20 Brisbane, QLD

[3] Tarun Agarwal. (2015). *Different Types of Sensors with their Applications*. Edgefx Technologies Pvt Ltd

[4] Steven A. Szklany. (2012).*A Feasibility Assessment of a New Navigation System for Unmanned Underwater Vehicles with Adaptive Gain Sliding Mode Differentiation.*

[5] J.C Molina et al. (2015). *A New Electronic Control System for Unmanned Underwater Vehicle.*

[6] Patrik Johansson and Jacob Bernhard. (2012). *Advanced control of a remotely operated underwater vehicle*.

[7] Agus Budiyono. (2009). *Advances In Unmanned Underwater Vehicles Technologies: Modeling, Control And Guidance Perspectives.*

[8] Song,Kwang sub, Peter C. Chu. (2014). *Future Undersea Unmanned Vehicle (UUV) System for Mine Disposal.*

[9] ZULKIPLE BIN JAMAL. (2007). *Design and Fabricate Remote Controlled Submarine With On Board Wireless Camera.*

[10] Sourangsu Banerji. (2013). *Design and Implementation of an Unmanned Vehicle using a GSM Network with Microcontrollers.*

[11] Tim Hardy, Gavin Barlow. (2008). *Unmanned Underwater Vehicle (UUV) Deployment and Retrieval Considerations for Submarines.*

[12] Russel John Rufino. (2008). *Morphing Unmanned Underwater Vehicles*

[13] Pete Alleman, Art Kleiner et al. (2009). *Development of a New Unmanned Semi Submersible (USS) Vehicle*

[14] Francisco Garcia, Antonio Geurrero-Gonzalez. (2013). *Intelligent Navigation for a Solar Powered Unmanned Underwater Vehicle*

[15] Ji-Hong Li, Pan Mook-Lee. (2005). *Design of an adaptive nonlinear controller for depth control of an autonomous underwater vehicle.*

[16] W.H. Wang, X.Q. Chen, A. Marburg et al. (nd). (2008). *Design of Low-Cost Unmanned Underwater Vehicle for Shallow Waters*

[17] J.H.A.M VERVOORT. (2008). *Modeling and Control of an Unmanned Underwater Vehicle.*

[18] O. ROBU, Elena POPESCU et al. (n.d). (2008). *Netrov Project: Underwater Remote Controlled Minivehicle*

[19] M´arcio Correia, Paulo Dias, S´ergio Fraga et al.(nd). (2005). *Operations andControl of Unmanned Underwater Vehicles*.

[20] Erik Lind and Magnus Meijer. (2014). *Simulation and Control Of Submarines.*

[21] SHI Yao , DONG Zhifeng. (nd). (2015). *Simulation of Underwater Propulsion Submersible Vehicle Based on Pitch-Depth Controlling.*

[22] Budiyono, Agus. (2009). *Advances in Unmanned Underwater Vehicles Technologies: Modelling, Control, and Guidance Perspectives*.

[23] electrical4u. (2017). *Sensor | Types of Sensor*. Electrical Engineering and Technology.

[24] Ashok Sharma. (2012). *Insight - Learn the Working of Ultrasonic Sensors*. (n.d.).

[25] Tarun Agarwal. (2013). *Types of Temperature Sensors and Their working Principles | Features*, ElProCus - Electronic Projects for Engineering Students.

[26] M. Massot-Campos and G. Oliver-Codina. (2015). *Optical Sensors and Methods for Underwater 3D Reconstruction Sensors*. vol. 15, no. 12, pp. 31525-31557.

[27] Pepperl+Fuchs Gmbh. (2014) *Ultrasonic Sensors Knowledge(Part 4): Influences on Measurement Accuracy*. Lilienthalstraße 200, 68307 Mannheim, Germany.

eureca 2017 – Conference Paper
Paper Number EUG16

SGO and Tsallis Entropy Assisted Segmentation of Abnormal Regions from Brain MRI

K. Suresh manic[1*], Nawf Al Shibli[1], Rahma Al Sulaimi[1] and Deepti Suresh

[1]Department of Electrical & Computer Engineering Caledonian College of Engineering, University College, Sultanate of Oman, Muscat.

*suresh.manic@caledonian.edu.om

Abstract

Brain abnormality is one of the aggressive diseases in human community. Early discovery may reduce the severity of disease and also lessen the death rate. In this paper, recent heuristic algorithm supported computerized technique is proposed to segment and analyze the tumor region from the brain Magnetic Resonance Images (MRI). Integration of the Social Group Optimization (SGO) and Tsallis entropy is implemented as the pre-processing stage to enhance the visibility of tumor section and the Localized Active Contour (LAC) is selected as the post-processing stage to extract the tumor from the pre-processed test image. Matlab based experimental work was executed using the benchmark brain MRI, known as the BRATS 2015 database. The superiority of the proposed approach is confirmed against the ground truths supplied by the expert members. The competence of implemented technique is established with picture likeliness measures, such as Jaccard and Dice and statistical trials, like precession, sensitivity, specificity and accuracy. The outcome of the LAC is also compared with the segmentation approaches, like the Watershed (WS) and the Level Set (LS) procedures. The results of SGO+LAC outperforms SGO+WS and SGO+LS approaches hence the proposed approach is efficient in extracting the tumor from the MRI images recorded with Flair modality.

Keywords: Brain tumor; MRI; Social group optimization algorithm, Active contour.

1.Introduction

Computer assisted disease assessment is broadly used in medical field to discover anatomical and pathological divisions using the clinical images. Medical imaging procedures will support the premature detection and examination of a collection

Abbreviations

SGO	Social group optimization
LAC	Localised active contour
WS	Watershed algorithm
LS	Level set segmentation
MRI	Magnetic resonance images
FPR	False positive rate
FNR	False negative rate

of diseases and also helps to reduce the morbidity and death rates. In literature, substantial measures are discussed and implemented by the researchers to extract important information from the conventional and medical images [1-6].

The heuristic approach assisted image processing is widely considered in recent years, due to its simplicity and easiness in implementation [7,8]. Tsallis entropy is one of the procedures, largely adopted by most of the researchers because of its dominance and elasticity [9,10]. From the image processing literature, it can be noted that, Tsallis's entropy based multi-level thresholding was largely adopted by the researchers to extract the important information from the RGB / gray scale test images [11,12] and medical images [5].

The work by Despotovic et al.[13] recommends the segmentation challenges and the available procedures in the brain image processing approaches. This work also notifies that, combination of several techniques is necessary to attain better segmentation result [9].

In the literature, a number of automated and semi-automated approaches are existing to examine brain MRI recorded with a chosen modality. All the existing methods are modality specific approaches and the method works well with a chosen modality sometimes may fail to offer better outcome with other modalities. Moreover, the soft-computing assisted approaches will enhance the outcome of the disease examination procedure. Hence, in this paper an approach based on the SGO assisted thresholding is implemented to examine the brain MRI registered with the Flair modality.

This work proposes a computer supported automated practice to segment and analyze the tumor from the BRATS 2015 database. Firstly, tri-level thresholding based on the SGO+Tsallis entropy is implemented to improve the cancerous division in brain image. Tsallis approach was initially proposed in 1988 [9]. The combination of Tsallis function and various heuristic algorithms has been presented over the past years for image thresholding applications [14]. Later, the Localized Active Contour (LAC) [16] based segmentation is implemented to extract the suspicious/enhanced region of brain MRI.

The capability of proposed segmentation task is then confirmed by means of a comparative assessment among the segmented tumor region and expert's Ground Truth (GT). The experimental results verify that, implemented technique is capable in attaining improved picture likeness index [17] and statistical trials [18].

The outcome of the proposed technique is also validated with the well known segmentation approaches, such as watershed algorithm and level set approach. This experimental work confirms that, the overall outcome of the proposed SGO+LAC is better compared with the SGO+WS and SGO+LS.

2. Methodology

This section presents the various stages involved in the proposed soft-computing assisted disease examination tool proposed in this work.

2.1 Pre-Processing

Initially, a pre-processing technique is executed by combining of the Social Group Optimization (SGO) and the Tsallis entropy value. Generally, entropy is linked with the estimation of chaos inside an image. Shannon's theory guaranteed that, when a physical structure is detached as two statistically free subsystems like '*A'* and '*B'*, then the entropy value can be expressed as [9,10]:

$$S(A+B)=S(A)+S(B) \tag{1}$$

Based on Shannon's theory, a non-extensive entropy idea was proposed by Tsallis as follows:

$$S_q=\frac{1-\sum_{i=1}^{T}(p_i)^q}{q-1} \tag{2}$$

where, *T* is the system potentials and *q* is the entropic index .

Eq. (2) will meet the Shannon's entropy when $q \to 1$.

The entropy value can be expressed with a pseudo additivity rule as:

$$S_q(A+B)=S_q(A)+S_q(B)+(1-q).S_q(A).S_q(B) \tag{3}$$

Tsallis entropy can be considered to find the optimal thresholds of an image. Consider a given image with *L* gray levels in the range {0, 1, ..., *L*-1},with probability distributions $p_i = p_0, p_1, ..., p_{L-1}$. Tsallis multi-level thresholding can then be expressed as:

$$f(T)=[T_1,T_2, \dots , T_k] = argmax \left[S_q^A(T)+S_q^B(T)+\dots+S_q^K(T)+(1-q).S_q^A(T).S_q^B(T)\dots S_q^K(T)\right] \tag{4}$$

where

$$S_q^A(T)=\frac{1-\sum_{i=0}^{t_1-1}\left(\frac{Pi}{P^A}\right)^q}{q-1},\ P^A=\sum_{i=0}^{t_1-1}Pi$$

$$S_q^B(T) = \frac{1 - \sum_{i=t_1}^{t_2-1} \left(\frac{Pi}{P^B} \right)^q}{q-1}, \; P^B = \sum_{i=t_1}^{t_2-1} Pi$$

$$S_q^K(T) = \frac{1 - \sum_{i=t_k}^{L-1} \left(\frac{Pi}{P^K} \right)^q}{q-1}, \; P^K = \sum_{i=t_k}^{L_2-1} Pi$$

During this multi-level thresholding process, the aim is to find the optimal threshold value *T* by maximizing the objective function *f(T).* The implemented work finds the arbitrary values of the *T* based on the heuristic search by the SGO algorithm. In the proposed work, the threshold value is chosen as *T* =3 thus the required probability values are P^A, P^B, and P^C. In this work, the maximization of function *f(T),* which deals with the segmentation of a given image, is carried using the SGO. The heuristic search continuously explores the gray level thresholds of the chosen MRI threshold and computes the value of f(T). This process continues till the search converges with a maximized value of the f(T) or till the maximum iteration value is reached. At the end of the search, the SGO obtains the required value of the thresholds and the maximized entropy function f(T).

SGO algorithm is a recently developed population based heuristic technique by Satapathy and Naik [15], based on the group resolve capability of the human being during complicated circumstances. It is similar to the Teaching Learning based Optimization existing in the literature [19]. In this algorithm, each person in the group is the candidate having capacity to offer the solution for the assigned task based on the fitness value. In this algorithm, the knowledge among the group members is used to find the solution for the given task.

This algorithm has two stages as follows;

i. Improving phase

Let *X* is the persons in the chosen social group with i = 1, 2,…, *N* and *D* is the dimension of the optimization problem with j = 1, 2, …, *D.*

$$Xnew_{i,j} = C * Xold_{i,j} + r * (gbest_j - Xold_{i,j}) \quad (5)$$

ii. Acquiring phase

$$Xnew_{i,j} = Xold_{i,j} + r_1 * (X_{i,j} - X_{r,j}) + r_2 * (gbest_j - X_{i,j}) \quad (6)$$

$$Xnew_{i,:} = Xold_{i,:} + r_1 * (X_{r,:} - X_{i,:}) + r_2 * (gbest_j - X_{i,j}) \quad (7)$$

where, i = 1to N; j = 1 to D, r = r_1=r_2= random number ~ U (0,1)

In this paper, the initial algorithm parameters are assigned based on the paper [15]. Other parameters are assigned as follows; the group size is assigned as thirty, the dimension of the search is chosen as three, the number of run is fixed as 1000 and the stopping criteria is considered as the maximal entropy of the Tsallis function.

2.2 Post-Processing

The post-processing stage is responsible to extract the tumor region from the pre-processed brain MRI. In order to enhance the segmentation accuracy, the post-processing stage consist two sub-operations like the morphology based enhancement and segmentation.

2.2.1 Morphology

Picture level morphology is usually approved to enhance the exterior of illustration. The essential morphological functions, such as stroke organizational constituent (*strel*) and image fill (*imfill*) are used to enhance the edges and illustration of multi-thresholded pictures.

2.2.2 Active contour segmentation

This section presents the segmentation procedure chosen to extract the cancerous region. Active Contour Segmentation (ACS) proposed in [16] is adopted to extract the image. This procedure has three essential steps such as, boundary detection, initial active contour, and final active contour which offer minimized energy. In this work, variable snake model is considered to track similar pixel groups existing in pre-processed image based on energy minimization concept.

The energy function of the snake can be denoted as;

$$\frac{min}{C}\left\{E_{GAC}(C)=\int_0^{L(C)} g(\left|\nabla I_0 C(s)\right|\, ds\right\} \tag{8}$$

where *ds* is the Euclidean component of length and *L(C)* is the length of the curve *C* which satisfies $L(C)=\int_0^{L(C)} ds$. The parameter *g* is an edge indicator, which will disappear based on the object boundary defined as;

$$g(\left|\nabla I_0\right|)=\frac{1}{1+\beta\left|\nabla I_0\right|^2} \tag{9}$$

where I_0 represents original image and β is an arbitrary constant. The energy value rapidly decreases based on the edge value, based on gradient descent criterion[12].

This procedure is mathematically represented as;

$$\partial_t C=(kg-\left\langle\nabla_g, N\right\rangle)N \tag{10}$$

where $\partial_t C=\partial C/\partial t$ represents the deformation in the snake model, *t* is the iteration time, and *k* , *N* are the curvature and normal for the snake '*C*'. In this procedure, the snake silhouette is continuously corrected till minimal value of the energy; E_{GAC} is achieved.

2.2.3 Related segmentation approaches

Along with the active contour segmentation, the well known approaches, such as the Watershed (WS) and Level Set (LS) methods are also considered in this paper to segment the tumor region. The WS is a commonly considered in image mining approaches due to its simplicity and superiority [24]. The WA consists: (i) Sobel edge detection, (ii) Marker controlled morphological operation, and (iii) Segmentation. A detailed mathematical description of WA considered in this work can be found in [25]. The main benefit of LS contrast to other approach is, it creates shapes of combined topology to hold splitting and merging action during the picture outline examination. This paper implements the LS proposed by Li et al. [26] to extract the tumor by using a single well approach. The LS is a semi-automated technique and requires a bounding box initialization with respect to the width and height of the stroke section. Other details regarding the LS can be found in [27,28].

2.2.4 Investigation

The efficiency of the proposed approach is confirmed in the pre-processing phase and segmentation phase. During first phase, well known image quality measures are computed to find the performance of SGO + Tsallis [7,8]. After the segmentation, a relative investigation among segmented tumor and GT is achieved and statistical picture trials are computed to examine the dominance of the proposed scheme [17]. Maximized values of these constraints are usually considered to validate the importance of the proposed scheme [20,21].

The mathematical expressions for the image similarity and statistical measures are presented below. During this examination, similarity constraints, like Jaccard, Dice, FPR, and FNR as well as the statistical constraints, like Sensitivity, Specificity, Accuracy and Precision are computed.

These events can be indicated as follows:

$$JI = I_G \cap I_{SE} / I_G \cup I_{PP} \tag{11}$$

$$DC = 2(I_G \cap I_{PP}) / |I_G| \cup |I_{PP}| \tag{12}$$

$$Sensitvity = T_P / (T_P + F_N) \tag{13}$$

$$Specificity = T_N / (T_N + F_P) \tag{14}$$

$$Accuracy = (T_P + T_N) / (T_P + T_N + F_P + F_N) \tag{15}$$

$$\text{Precision} = T_P / (T_P + F_P) \tag{16}$$

where, I_G is ground truth image, I_{PP} is post-processed image, T_N, T_P, F_N and F_P indicates true negative, true positive, false negative and false positive; respectively.

3. Realization

This section provides the details regarding the implementation of the proposed procedure. Initially, the SGO parameters are assigned as follows; total group size is 30, search dimension is fixed as 3 (tri-level thresholding) and number of iteration is fixed as 1000 and criteria is chosen as maximized *f(T)*. During the experimental work, each slice of the 2D MRI is separately processed with the considered pre-processing approach and post-processing approach and the corresponding performance measures are recorded to validate the superiority of the proposed image processing tool.

Fig.1 depicts pictorial representation of proposed brain MRI examination task. Initially, the skull stripped brain MRI test image is pre-processed with multi-level thresholding. This procedure will enhance the abnormal region of the test image. Later, the image morphological operation is considered to group the similar image pixels in order to get a smooth image. The post-processed image is then treated using the ACS, which extracts the tumor section from the brain MRI. Finally, the extracted tumor is analyzed to confirm the superiority of the proposed brain MRI image processing procedure.

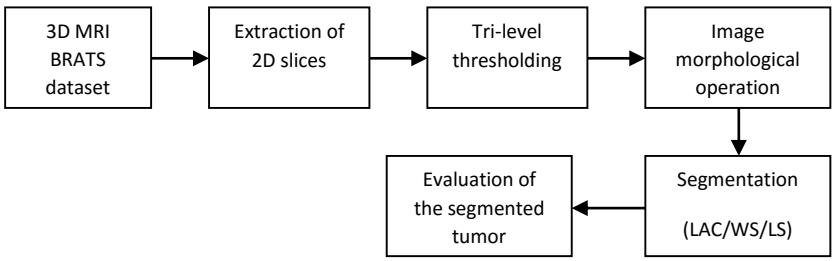


Fig. 1 Block diagram of the proposed computerised tool

4. Results and Discussions

This section presents the experimental results of the proposed work. The well known benchmark brain MRI images are obtained from the MICCAI BRAIN Tumor Segmentation (BRATS) challenge 2015 dataset [23]. This database has a three dimensional (3D) brain MRI images registered using the Flair, T2, T1 and T1c modalities. This dataset also provides the ground truth image offered by the expert member. In this study, the brain MRI image recorded with the Flair modality is considered and the 2D slices of slice numbers 95,105,115 and 125 are extracted from the 3D dataset. The main advantage of this BRATS images are, it does not have the skull section, hence, it is very easy to implement the image processing procedure.

Initially, SGO assisted Tsallis entropy based multi-level thresholding process is implemented on the test data in order to enhance the tumor region. After the thresholding, image morphology is applied to group the similar pixels values to obtain an even image. The ACS procedure is then applied to extract the tumor section from the post-processed image. Finally, the extracted tumor core is analyzed with a comparative study against the ground truth existing in the brain MRI dataset. All the simulation works are implemented by means of Matlab 2012 software.

Table 1 presents the chosen image slices and its corresponding outcomes. The quality of the pre-processed image is verified using the well known image quality measures existing in the literature [20-22] and its values are tabulated in Table 2. From this table, it is clear that, proposed approach is efficient in offering better values of RMSE, PSNR, SSIM, NCC, AD, SC and NAE. Details regarding the adopted image quality measures can be found in the literatures [7,8].

Table 1. Image processing results for the chosen image dataset

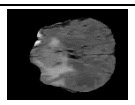
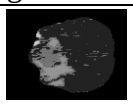
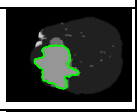
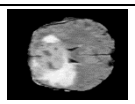
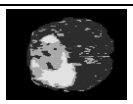
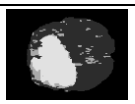
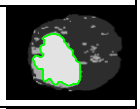
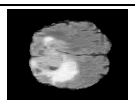
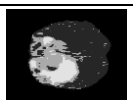
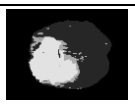
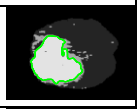
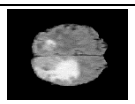
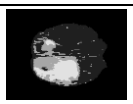
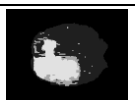
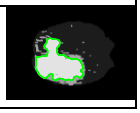
	Test image	Pre-processing	Post-processing	Segmentation
$Slice_{95}$				
$Slice_{105}$				
$Slice_{115}$				
$Slice_{125}$				

Table 2. Image quality measures between original and tri-level threshed image

Flair	**RMSE**	**PSNR**	**SSIM**	**NCC**	**AD**	**SC**	**NAE**
$Slice_{95}$	30.76	18.36	0.71	0.65	17.08	1.90	0.42
$Slice_{105}$	43.99	15.26	0.68	0.73	22.79	1.56	0.36
$Slice_{115}$	44.56	15.15	0.70	0.71	21.88	1.59	0.38
$Slice_{125}$	43.10	15.44	0.72	0.69	19.54	1.62	0.41
Mean	40.60	16.05	0.70	0.69	20.32	1.67	0.39

Table 3. Comparison of the ground truth and the extracted tumor

Test image	Ground truth	Tumor section		
		LAC	WS	LS
$Slice_{95}$				
$Slice_{105}$				
$Slice_{115}$				
$Slice_{125}$				

Table 4. Similarity measures between GT and segmented tumor (with LAC)

Flair	**Jaccard**	**Dice**	**FPR**	**FNR**
$Slice_{95}$	0.8340	0.9095	0.1526	0.0387
$Slice_{105}$	0.8291	0.9066	0.1674	0.0321
$Slice_{115}$	0.8397	0.9129	0.1368	0.0454
$Slice_{125}$	0.8221	0.9024	0.1147	0.0836
Mean	0.8311	0.9078	0.1429	0.0499

Table 6. Statistical measures between GT and segmented tumor (with LAC)

Flair	**Precision**	**Sensitivity**	**Specificity**	**Accuracy**
$Slice_{95}$	0.9963	0.9857	0.9612	0.9734
$Slice_{105}$	0.9955	0.9768	0.9679	0.9723
$Slice_{115}$	0.9937	0.9812	0.9546	0.9678
$Slice_{125}$	0.9910	0.9877	0.9554	0.9514
Mean	0.9941	0.9828	0.9598	0.9662

Table 6. Mean Values of performance measures attained with LAC, WS and LS

Approch	**Jaccard**	**DIce**	**Precision**	**Sensitivity**	**Specificity**	**Accuracy**
LAC	0.8311	0.9078	0.9941	0.9828	0.9598	0.9662
WS	0.8305	0.9032	0.9937	0.9815	0.9562	0.9659
LS	0.8309	0.9051	0.9928	0.9822	0.9571	0.9660

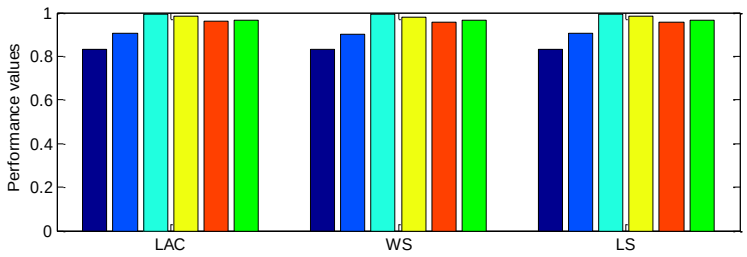


Fig 2. Comparison of the image similarity and statistical measure values obtained with the considered segmentation methods

Table 3 presents the extracted tumor section with LAC, WS and LS segmentation procedures. The comparison between the ground truth and the extracted tumor results, such as the image similarity measures and the statistical measures are presented in Table 4 and 5 respectively for LAC alone and approximately similar results are obtained with the WS and the LS techniques. From Table 4, one can observe that, the Jaccard and Dice values are greater than 0.82 (ie. 82%) and also a negligible values for the FPR and FNR. This confirms that, the extracted tumor structure is approximately similar compared to the ground truth image. The pattern of the tumor and the ground truth are identical. From Table 5, it can be noted that, the Precision, Sensitivity, Specificity and Accuracy are greater that 0.95 (ie, 95%), which confirms the superiority of the proposed approach in processing the benchmark Flair modality based brain MRI dataset.

Table 6 presents the average performance measures obtained with the considered segmentation procedures and the pictorial representation of this comparison is also presented in Fig 2. From this result, it can be noted that, the results offered by the LAC segmentation is comparatively better than the WS and AC methods. In order to confirm the superiority of the proposed approach, other test images existing in the BRATS 2015 dataset sown in Fig 3. is also considered for the examination. From this dataset, the flair and T2 modality based images are considered and satisfactory results are obtained with the proposed SGO+LAC approach. From this, it is confirmed that, proposed computerised tool works well for the flair and T2 modality based brain MRI..

5. Conclusions

This work proposes a computer assisted scheme to mine and analyze the abnormal region of the BRATS 2012 brain MRI dataset. The work implements the Social Group Optimization (SGO) and Tsallis entropy based procedure to enhance the tumor section and the Active Contour based approach to segment the tumor from the post-processed test image. To exhibit the superiority of the proposed procedure, Flair modality registered various 2D slices of the brain MRI are considered. The experimental result demonstrates that, proposed approach is very efficient in extracting the tumor section from the Flair based MRI slices. This result also confirms that, the proposed SGO assisted approach offers superior image similarity measures and the statistical measures compared to the ground truth. Hence, in future, this procedure can be used to analyse the real time clinical images recorded using various modalities, such as T1, T2 and T1c.

References

A.A. Abdullah, B.S. Chize, and Z. Zakaria, "Design of cellular neural network (CNN) simulator based on matlab for brain tumor detection," J. Med. Imaging Health Inf., vol. 2, no.3, pp. 296-306, 2012.

S. Bauer, R. Wiest, L.P. Nolte,and M. Reyes, "A survey of MRI-based medical image analysis for brain tumor studies," Phys. Med. Biol., vol. 58, no.13, pp. 97-129, 2013.

M. Sezgin, and B. Sankar, "Survey over image thresholding techniques and quantitative performance evaluation," Journal of Electronic Imaging, vol. 13, pp.146 – 165, 2004.

V. S. Lakshmi, S.G. Tebby, D. Shriranjani, and V. Rajinikanth, "Chaotic cuckoo search and kapur/tsallis approach in segmentation of t.cruzi from blood smear images," International Journal of Computer Science and Information Security (IJCSIS), vol.14, CIC 2016, pp. 51-56, 2016.

V. Rajinikanth, and M.S. Couceiro, "RGB histogram based color image segmentation using firefly algorithm," Procedia Computer Science, vol.46, pp.1449–1457, 2015.

V. Rajinikanth, N.S.M. Raja, and K. Latha, "Optimal multilevel image thresholding: an analysis with PSO and BFO algorithms. Aust. J. Basic Appl. Sci., vol. 8, pp. 443-454, 2014.

N.S.M. Raja, V. Rajinikanth and K. Latha, "Otsu based optimal multilevel image thresholding using firefly algorithm," Modelling and Simulation in Engineering, vol. 2014, Article ID 794574, 17 pages, 2014.

C. Tsallis, "Possible generalization of Boltzmann-Gibbs statistics," Journal of Statistical Physics, Vol.52, No. 1-2, pp 479-487, 1988.

C. Tsallis, "Entropic nonextensivity: a possible measure of complexity," Chaos, Solitons & Fractals, vol.13, no.3, pp. 371-391, 2002.

B. Akay, "A study on particle swarm optimization and artificial bee colony algorithms for multilevel thresholding," Applied Soft Computing, Vol.13, No.6, pp. 3066–3091, 2013.

K. Suresh Manic, R. Krishna Priya and V. Rajinikanth, "Image multithresholding based on Kapur/Tsallis entropy and firefly algorithm," Indian Journal of Science and Technology, vol.9, no.12, 89949, 2016.

Despotovic, B. Goossens, and W. Philips, "MRI Segmentation of the human brain: Challenges, Methods, and Applications," Comput. Math. Method M., vol. 2015, Article ID 450341, 23 pages, 2015.

M. Tuba, "Multilevel image thresholding by nature-inspired algorithms: A short review," Computer Science Journal of Moldova, vol. 22, pp.318-38, 2014.

S. Satapathy, A. Naik, "Social group optimization (SGO): a new population evolutionary optimization technique," Complex & Intelligent Systems, vol.2, no.3, pp. 173–203, 2016.

X. Bresson, S. Esedoglu, P. Vandergheynst, J-P. Thiran, and S. Osher, "Fast global minimization of the active contour/snake model," J. Math. Imaging Vis., Vol.28, no.2, pp.151-167, 2007.

Chaddad, and C. Tanougast, "Quantitative evaluation of robust skull stripping and tumor detection applied to axial MR images," Brain Informatics, vol.3, no.1, pp.53-61, 2016.

H. Lu, A.C. Kot, and Y.Q. Shi, "Distance-reciprocal distortion measure for binary document images," IEEE Signal Process. Letter., vol. 11, no.2, pp.228-231, 2004.

V. Rajinikanth, N.S.M. Raja, and K. Kamalanand, "Firefly algorithm assisted segmentation of tumor from brain MRI using Tsallis function and Markov random field," Journal of Control Engineering and Applied Informatics, vol.19, no.3, pp. 97-106, 2017.

S.C. Satapathy, N.S.M. Raja, V. Rajinikanth, A. S. Ashour, and N. Dey, "Multi-level image thresholding using Otsu and chaotic bat algorithm," Neural Computing and Applications, pp.1-23, 2016. DOI:10.1007/s00521-016-2645-5.

V. Rajinikanth, M.S. Couceiro," Optimal multilevel image threshold selection using a novel objective function," Advances in Intelligent Systems and Computing, vol.340, pp. 177-186, 2015.

V. Rajinikanth, N.S.M. Raja, and S. C.Satapathy, "Robust color image multi-thresholding using between-class variance and cuckoo search algorithm," Advances in Intelligent Systems and Computing, vol.433, pp.379-386, 2016.

Brain Tumor Database (BraTS-MICCAI), http://hal.inria.fr/hal-00935640.

M. Kaleem, M. Sanaullah, M.A. Hussain, M.A. Jaffar, and T.S. Choi, "Segmentation of brain tumor tissue using marker controlled watershed transform method," Communications in Computer and Information Science, vol.281, pp.222–27, 2012.

G. Deng, and Z. Li, "An improved marker-controlled watershed crown segmentation algorithm based on high spatial resolution remote sensing imagery," Lecture Notes in Electrical Engineering, vol.128, pp.567-72, 2012.

C. Li, C. Xu, and C. Gui, and M.D. Fox, "Distance regularized level set evolution and its application to image segmentation," IEEE T. Image Process, vol.19, no.12, pp. 3243-54, 2010.

V. Rajinikanth, N.S.M. Raja, S.C. Satapathy, and S.L. Fernandes, "Otsu's multi-thresholding and active contour snake model to segment dermoscopy images," Journal of Medical Imaging and Health Informatics, vol.7, no.8, pp. 1837–1840,2017.

N.S.M. Raja, V. Rajinikanth, S.L. Fernandes, and S.C. Satapathy, "Segmentation of breast thermal images using Kapur's entropy and hidden Markov random field," Journal of Medical Imaging and Health Informatics, vol.7, no.8, pp. 1825-1829, 2017.

eureca 2017 – Conference Paper
Paper Number EUG17

A Novel Image Processing Scheme to Evaluate Breast Thermal Images

N. Sri Madhava Raja*, Deepti Suresh, A. Kirthini Godweena

Department of Electronics and Instrumentation Engineering,
St. Joseph's College of Engineering,
OMR, Chennai 600119, India.

*nsrimadhavaraja@stjosephs.ac.in

Abstract
In literature, a considerable number of approaches are existing to examine the breast abnormality, such as cancer and Ductal Carcinoma In Situ (DCIS). In this paper, a novel image processing procedure is proposed to analyze the breast abnormality recorded with thermal imaging procedure. This work implements a pre-processing procedure based on the Kapur's tri-level thresholding and post-processing approach based on the watershed algorithm. In order to improve the quality of pre-processing technique, recent heuristic algorithm known as the Social Group Optimization (SGO) is adopted. The proposed approach in this paper has the following stages: i) Tri-level thresholding based on the Kapur + SGO, ii) Edge detection based dimension analysis of left and right breast region to identify the abnormality, and iii) Watershed based segmentation to extract the DCIS region. The proposed technique is tested using the benchmark breast thermal dataset available at Visual lab. The experimental work is implemented using the Matlab software and the results of this work confirm that, proposed approach is efficient in examining the breast thermal images when compared to conventional heuristic approaches. It extracts the initial changes of tissues when affected by diseases. The advantage of infrared images combined with SGO multi-thresholding method provides more vital information for early diagnosis.

Keywords: Breast cancer; Thermal image; Ductal carcinoma in situ; Kapur's entropy, Watershed algorithm, Image evaluation.

1. Introduction

Breast malignancy is one of a life intimidating diseases in women society [1,2]. Accessibility of the contemporary medical knowledge can help them to notice the irregular cell growth in breast section during screening. When the size and the orientation of the breast irregularity are documented, then it is possible for the doctors to plan for the suitable treatment procedure to manage/cure the disease [3].

The mainstream of breast cancer begins in the segment of the breast tissue that are made up of glands for milk creation, known as lobules, and ducts that unite the lobules to the nipple. Primarily, it will be initiated in the soft tissues of the breast, and will grow to its neighboring regions. Generally the breast tumor is due to the irregular swelling in the breast tissues. The work of Bejnordi *et al*. [4] reports that, almost 80% of breast cancer happens in epithelial cells of ducts. Identification of cancer in its preliminary stage will aid for early treatment procedure which will support for complete cure of the disease.

In literature, non-invasive imaging procedures, such as mammogram [5], Magnetic Resonance Imaging (MRI) [6] and Infrared Thermal Imaging (ITI) [2] are extensively used to register the breast tumor at the time of screening practice.

Mammogram and MRI are the frequent radiology methods, broadly considered to identify the grown tumors. These methods may give poor results when the cancer is in its premature stage. Further, exposure to radiation and procedure involved enhances disease prognosis and also causes discomfort. Hence, in recent years, ITI procedures are widely adopted by the medical practitioners to record and analyze the breast malignancy for early diagnosis [7-10]. During this practice, infrared radiation emitted by the skin exterior is recorded as a thermal map by using a special camera. The recorded thermal patterns are then examined to recognize the existing disorder.

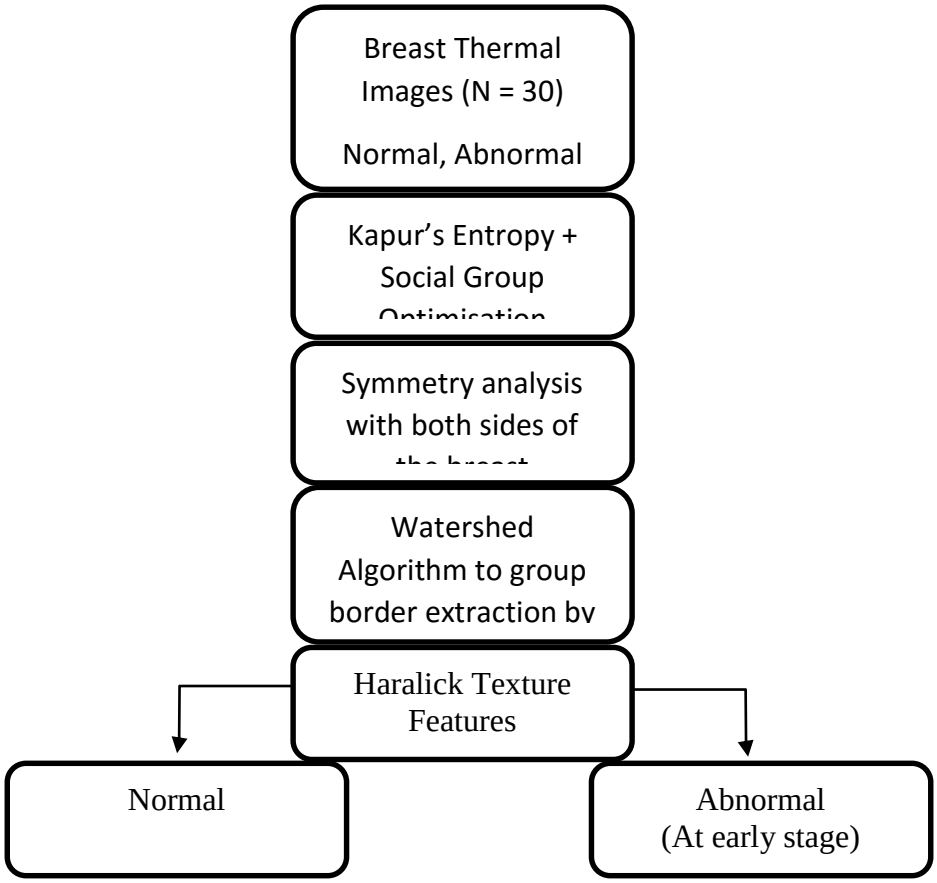
The imaging literature provides the details of a number of techniques to evaluate the abnormality in breast based on ITI [3]. In this paper, a novel image examination procedure is proposed to examine the benchmark breast thermal images existing in Visual lab database [11,12]. This work implements a pre-processing procedure based on the integration of the Social Group Optimization and Kapur's tri-level thresholding and the post-processing work implements the watershed algorithm based segmentation. In this work, the various types of images, such as normal, abnormal and abnormal images with DCIS are considered for the evaluation.

The proposed approach initially implements a tri-level thresholding procedure to group the similar pixels of the RGB scale thermal image. Later, an edge detection procedure is implemented to extract the breast region, to find the pixel similarity between the left side and right side breast. Symmetry based approach and combination of multi-threshold with SGO extracts early vital information of disease prognosis. The usage of this modality and proper processing would yield significant results for various diseases and particularly carcinoma. This procedure will help the user to confirm the abnormality in the breast section based on its size analysis. Finally, the watershed algorithm can be used to extract the abnormality, such as tumor and DCIS existing in the pre-processed image. All the experimental works are implemented using Matlab software and the results of this study confirms that, proposed approach is efficient in

identifying the breast abnormality based on the considered thermal images. In future, the proposed approach can be used to examine the real clinical images obtained from the clinics/hospitals.

2. Methodology

This section provides the overview of methodology considered in this paper is represented in Figure 1. During the simulation process, the ITI dataset images of Visual lab [11, 12] are considered. Based on the abnormality, images in the dataset are grouped in to normal, intermediate and abnormal images.



2.1 Kapur's Entropy

This section, presents a capable entropy function extensively recognized as Kapur's approach, initially proposed in 1985 [13]. Firstly, this technique was intended to separate gray level cases based on its histogram. Due to its superiority, recently, this technique is largely accepted and implemented to resolve a variety of image segmentation problems. In this paper, this approach is considered to threshold the RGB scale ITI.

This approach discovers the optimal T by maximizing the overall entropy of the image. Let, T = [T_1, T_2,..., T_{k-1}], the vector for image thresholds. Then, Kapur's function can be expressed as;

$$J_{\max} = f_{Kapur}\ (T) = \sum_{j=1}^{k} H_j^C \quad for \quad C\{1,2,3\} \tag{1}$$

Entropy for I_{RGB} is calculated for Red, Green and Blue segment based on the assigned T value. For multi- threshold case, this process can be expressed as;

$$H_1^C = \sum_{j=1}^{T_1} \frac{Ph_j^C}{\omega_0^C} \ln\left(\frac{Ph_j^C}{\omega_0^C}\right),$$
$$H_2^C = \sum_{j=T_1+1}^{T_2} \frac{Ph_j^C}{\omega_1^C} \ln\left(\frac{Ph_j^C}{\omega_1^C}\right), \quad (2)$$
$$\vdots$$
$$H_k^C \sum_{j=T_k+1}^{L} \frac{Ph_j^C}{\omega_{k-1}^C} \ln\left(\frac{Ph_j^C}{\omega_{K-1}^C}\right)$$

where, Ph_j^C is the probability allocation of intensity regions and $\omega_0^C, \omega_1^C, ...\omega_{k-1}^C$ are probability incidence for k stages. Complete description of Kapur's approach is available in [14-17].

2.2 Social Group Optimization

SGO is a recent heuristic approach by Satapathy and Naik to solve the constrained and unconstrained engineering optimization problem [18,19]. SGO consist the following stages, i) Educating stage to organize the position of citizens with respect to the cost function and ii) Knowledge accomplishing phase to allow the citizens to discover optimal results. It is approximately similar to the Teaching Learning Based Optimization (TLBO) approach [20].

The arithmetical form of SGO is shown below:

$$Let, G_{finest} = maximum \{ f(H_v) \ for \ v = 1, 2, \ldots N\} \quad (3)$$

where, H_v denotes the preliminary data the people have, $v = 1, 2, 3, \ldots, N$ specify total strength in group, and f_w is the fitness value.

The civilizing stage will alter the orientation of the agents as given below;

$$H_{updated_{v,w}} = c * H_{initial_{v,w}} + R * (G_{finest_w} - X_{initial_{v,w}}) \quad (4)$$

Here, $H_{updated}$ represents renewed location, $H_{initial}$ is the early location, G_{finest} specifies global position, R is random numeral [0,1] and c represents the self-introspection value with a choice [0,1]. The constant c assigned with 0.2 [18].

At the second stage, citizens are motivated to achieve the global position as follows;

$$H_{updated_{v,w}} = X_{initial_{v,w}} + r1 * (H_{v,w} - H_{R,w}) + r2 * (G_{finest_w} - H_{v,w}) \quad (5)$$

Where, $r1$ and $r2$ represents arbitrary values of [0,1] and $H_{R,w}$ is randomly assigned position a citizen. During the experimentation task, SGO finds the optimal threshold by maximizing the Kapur's function [18, 19]. In this work, the SGO parameters are assigned as: number of groups = 25, maximum iteration = 1000 and the stopping criterion = maximized Kapur's entropy.

2.3 Symmetry analysis

Breast evenness examination is a demonstrated practice to review the threat issue for breast malignancy [21]. Usually, the tainted breast's amount, orientation and appearance will fluctuate from the normal breast [22]. In this work, in order to analyze the abnormality and classify the images: *i).* Sobel based edge detection and binary image generation, *ii).* Dividing the image into two equal portions and execute pixel

count, *iii).* Classify the thermal images based on its pixel likeness. This procedure is simple and helps to classify the considered ITI into normal, intermediate and abnormal.

2.4 Watershed segmentation

Marker driven Watershed (WS) approach presented by Roerdink & Meijster is adopted to extract the stroke region [23]. WS is grouping of Sobel border discovery procedure, marker driven morphological procedure and mining. The clear explanation of the adopted WS can be found in [24].

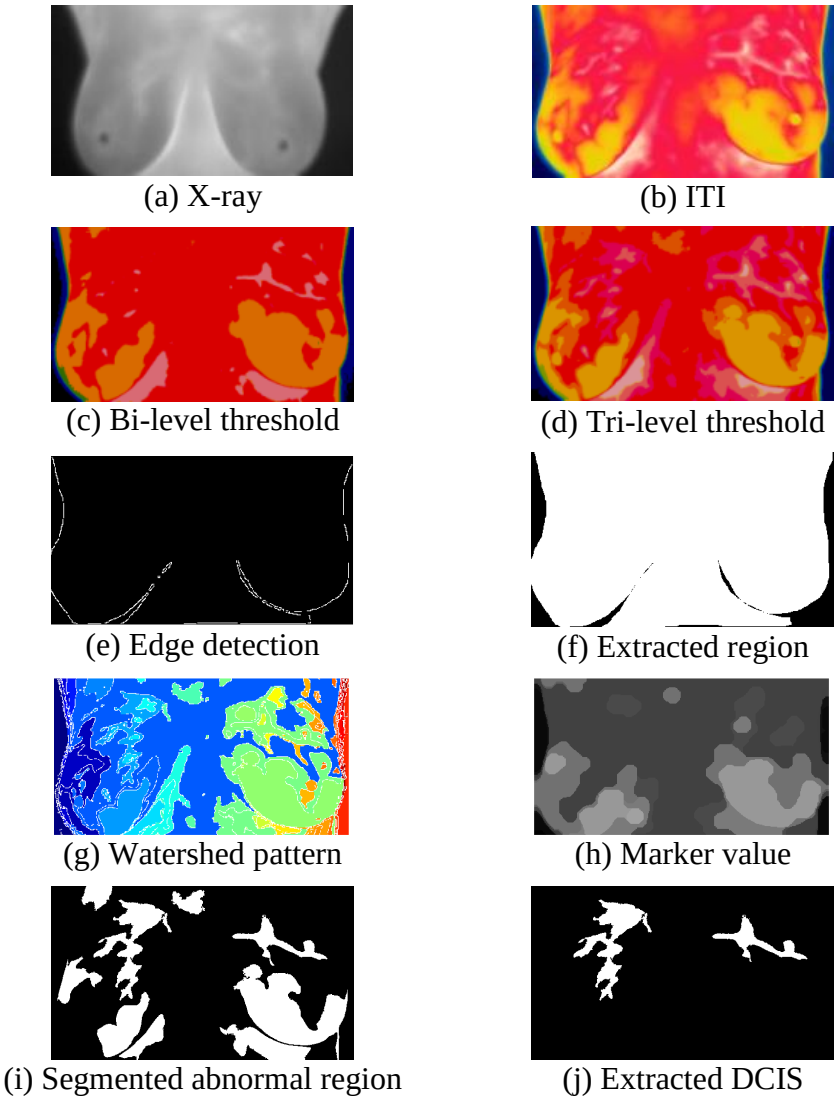
2.5 Implementation and Evaluation

In this paper, ten images of each case (Normal, Abnormal and Intermediate) are considered for the examination. In image processing domain, feature extraction plays a key role in achieving elevated information of the test image under study. Texture features are widely considered to evaluate the spatial allocation of gray pixels, by calculating neighbouring features at each point of image and surmising a set of statistical values. After extracting the abnormal section from the ITI, Haralick Texture Feature (HTF) is extracted [21]. Normally, the final image of the proposed procedure will be in the form of binary and the HTF extracts the features of the extracted pattern which has binary '1'. After extracting the HTF, it is possible to examine the severity of the ITI by simply analyzing the values. In future, the HTF can also be considered to design a classifier unit, which will help to classify the ITI as Benign or Malignant.

3. Results and Discussions

This section presents the experimental results obtained with this study. The Visual lab database consists of both the X-ray and thermal images recorded with image capturing device. The disease information available in X-ray is poor compared with the ITI.

Fig. 2 depicts the experimental results obtained for the chosen ITI. Fig 2 (a) and (b) represents the X-ray and the ITI of abnormal case. After choosing the ITI, the pre-processing is implemented using SGO + Kapur's function based multi-level thresholding. Initially, a bi-level and tri-level thresholding is implemented to preprocess the image in order to enhance the visibility of the abnormality and the corresponding outputs are depicted in Fig. 2 (c) and (d) respectively. From this, it can be noted that, tri-level thresholding offers better image visibility compared with bi-level threshold. Hence, for the remaining images, tri-level threshold is considered. Fig. 2 (e) and (f) presents the results of edge detection procedures which can be further considered for the symmetry analysis with the help of the region properties (number of pixels existing in left and right breast region). Finally, the post-processing is implemented with watershed algorithm, which can be used to extract the abnormal region from the pre-processed image. After extracting the DCIS, the seniority of the infected region is assessed by computing the HTF.



(a) X-ray (b) ITI

(c) Bi-level threshold (d) Tri-level threshold

(e) Edge detection (f) Extracted region

(g) Watershed pattern (h) Marker value

(i) Segmented abnormal region (j) Extracted DCIS

Figure 2. Experimental results for a chosen ITI

Similar procedure is repeated for the remaining images considered in this study. Fig. 3 depicts the results obtained with the normal image cases. Fig 3 (a), (c) and (e) shows the chosen ITI and Fig 3 (b), (d) and (f) shows the extracted breast region. From this figure, I can be observed that, the right breast region is approximately similar compared with the left region. Similar procedure is repeated for all the images and based on its symmetry value; it is classified as normal, abnormal and intermediate as shown in Table I.

Table 1. Evenness evaluation for chosen images

Case	Symmetry level (%)	Forecast
Normal	97.1764	Negative
Abnormal	78.9015	Positive
Intermediate	94.8156	Neutral

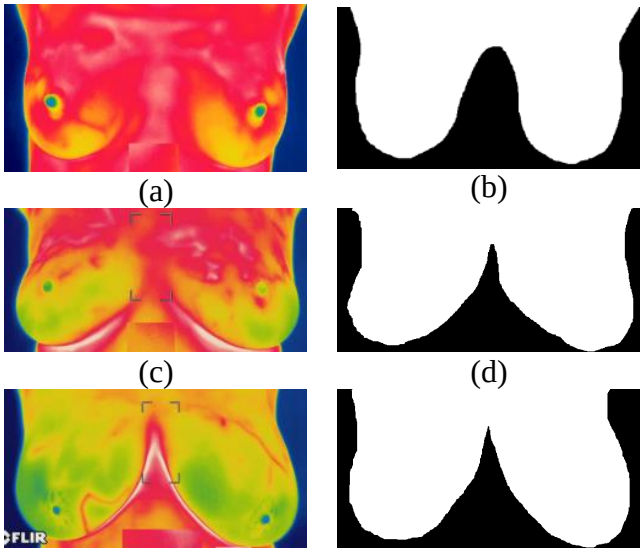


Figure 3. Normal breast images

Fig. 4 and 5 presents the outcome obtained for the abnormal breast image and the breast ITI having the DCIS.

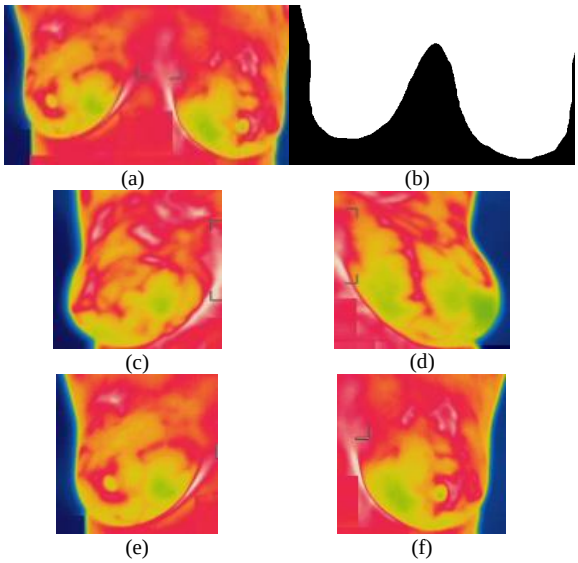


Figure 4. Abnormal breast images

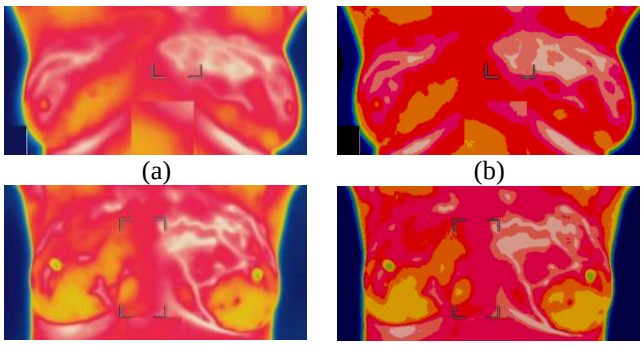


Figure 5. Breast images having DCIS

In these cases, the abnormality can be easily visualized with the ITI based on the breast un-symmetry and the abnormal blood vessel projections. Fig 4 shows the region wise analysis of the breast images in order to confirm its abnormality. Further, the mild infected regions are also extracted with the subjection of the considered algorithm. There early stage disease prognosis are detected in these images since they are evident on ITI images rather than in other modalities. Fig 4 (c) and (e) shows the right regions and Fig 4 (d) and (f) show the left regions. The pixels of these regions are then computed to categorize the image. Fig 5 shows the ITI having the DCIS and its pre-processed versions. The DCIS regions are then extracted with the proposed approach and its severity is then examined by computing the HTF as shown in Table 2.

Table 2. Texture Features for the abnormal regions

Feature name	Normal	Abnormal	Intermediate
Homogeneity	0.8426	0.7064	0.7916
Energy	0.1107	0.6177	0.3518
Entropy	0.1994	0.5693	0.3593
Correlation	0.9513	0.9482	0.9319
Variance	0.5312	0.7881	0.7007
Contrast	0.0775	0.1054	0.0815
IMC1	-0.2517	-0.6427	-0.5434
IMC2	0.1139	0.7721	0.4052
Sum Average	1.1074	2.1178	2.1843
Sum Variance	2.1162	5.2861	3.1103
Sum Entropy	0.2986	0.6361	0.4175
MCC	0.3268	0.1795	0.1891

In future, the computed HTF can be considered to design a classifier system.

4. Conclusions

This paper proposes a novel image processing procedure to examine the breast thermal images in order to discover the breast cancer. The proposed approach implements a pre-processing and a post-processing approach to extract the abnormal regions from the considered image dataset. The pre-processing is implemented with SGO + Kapur's tri-level thresholding and the post-processing is implemented with watershed segmentation. Initially, an edge detection assisted symmetry analysis is proposed to classify the considered ITI dataset as the normal, abnormal and intermediate. Finally, the extracted Ductal Carcinoma In Situ (DCIS) section is considered to extract the HTF values in order to assess its severity. Early disease diagnosis is possible in ITI since the slightest temperature variation reveals the state of the infection in the breast. The advantage of the infrared modality and the suitable image processing techniques applied in this work surfaces the disease condition even in early stage. Hence, the disease treatment can be advised to the patient well in advance when to compared to other methods of diagnosis. The results of this paper confirm that, proposed image processing approach works well on the images of Visual Lab dataset. In future, this approach can be tested on the real clinical breast thermal images obtained from the hospitals.

References

[1] Patel, B.C., Sinha, G.R., (2014). Abnormality detection and classification in Computer-Aided Diagnosis (CAD) of breast cancer images. *Journal Medical Imaging Health Informatics*, 4, 881-885.
[2] Acharya, U. R., Ng, E. Y.K., Tan, J.H. and Sree, S. V. (2012). Thermography based breast cancer detection using texture features and support vector machine. *Journal of Medical Systems*, 3(36), 1503–1510.
[3] Sree S. V., Ng E.Y-K., Acharya U.R., and Faust, O.(2011). Breast imaging: A survey, *World Journal of Clinical Oncology*, 2(4) pp. 171-178, 2011.
[4] Bejnordi, B.E. Balkenhol, M. Litjens, G. Holland, R. Bult P., Karssemeijer, N. and Laak, J.A.W.M.V.D. (2016). Automated Detection of DCIS in Whole-Slide H&E Stained Breast Histopathology Images, *IEEE Transactions on Medical Imaging*, 35(9), pp.2141-2150.
[5] Srivastava, S., Sharma1 N., Singh S.K., Rajeev Srivastava, (2014). Quantitative analysis of a general framework of a cad tool for breast cancer detection from mammograms, *Journal of Medical Imaging and Health Informatics*, 4, 654–674.
[6] Lee, J.M., Halpern, E.F., Rafferty, E.A., Gazelle, G.S. (2009). Evaluating the correlation between mammography and MRI for screening women with increased breast cancer risk, *Academic Radiology*, 16(11), pp. 1323–1328.
[7] Zadeh, H. G., Haddadnia,J., Ahmadinejad,N. and Baghdadi.M.R. (2015). Assessing the potential of thermal imaging in recognition of breast cancer, *Asian Pacific Journal of Cancer Prevention*, 16, (18), pp. 8619-8623.
[8] Sutha. M.J., Dhanaseelan, F.R. (2015). An efficient method for detection of breast cancer based on closed frequent itemsets mining, *Journal of Medical Imaging and Health Informatics*, 5, pp.987-994.
[9] Raja, N.S.M., Rajinikanth, V., Fernandes, S. L., Satapathy, S.C. (2017). Segmentation of breast thermal images using Kapur's entropy and hidden Markov random field, *Journal of Medical Imaging and Health informatics* , 7(8), pp. 1825–1829.
[10] Vishnupriya, R., Raja, N.S.M., V. Rajinikanth. (2017). An efficient clustering technique and analysis of infrared thermograms, *Third International Conference on Biosignals, Images and Instrumentation (ICBSII), IEEE,* pp.1-5,. DOI: 10.1109/ICBSII.2017.8082275.
[11] L.F. Silva et al.(2014) A new database for breast research with infrared image, *Journal of Medical Imaging and Health Informatics*, 4, (1), pp. 92-100,. DOI: https://doi.org/10.1166/jmihi.2014.1226.
[12] http://visual.ic.uff.br/dmi/prontuario/home.php
[13] Kapur, J. N., Sahoo, P. K., Wong, A. K. C. (1985). A new method for gray-level picture thresholding using the entropy of the histogram, *Computer Vision, Graphics, and Image Processing*, 29(3), pp. 273–285,.
[14] Rajinikanth, V., Raja, N.S.M., Kamalanand. K. (2017). Firefly algorithm assisted segmentation of tumor from brain MRI using Tsallis function and Markov random field, *Journal of Control Engineering and Applied Informatics*, 19(3), pp. 97-106.
[15] Manic, K.S., Priya, R.K., Rajinikanth. V(2016). Image Multithresholding based on Kapur/Tsallis Entropy and Firefly Algorithm, *Indian Journal of Science and Technology*, 9(12), 89949.
[16] Rajinikanth, V., Raja, N.S.M., Satapathy, S.C. (2016). Robust color image multi-thresholding using between-class variance and cuckoo search

algorithm, *Information Systems Design and Intelligent Applications, Advances in Intelligent Systems and Computing*, 433, pp. 379-386.

[17] Satapathy, S.C., Raja, N.S.M., Rajinikanth, V., Ashour, A.S.,Dey. N. (2016). Multi-level image thresholding using Otsu and chaotic bat algorithm, *Neural Computing and Applications*. DOI:10.1007/s00521-016-2645-5.

[18] Satapathy, S., Naik. A., (2016). Social group optimization (SGO): a new population evolutionary optimization technique, *Complex and Intelligent Systems*, 2(3), pp.173-203.

[19] Naik, A. Satapathy, S.C. Ashour, A.S., Dey. N. 2016. Social group optimization for global optimization of multimodal functions and data clustering problems, *Neural Computing and Applications*, DOI:10.1007/s00521-016-2686-9.

[20] Rajinikanth, V., Satapathy, S.C., Fernandes, S.L., S. Nachiappan. (2017). Entropy based Segmentation of Tumor from Brain MR Images–A study with Teaching Learning Based Optimization, *Pattern Recognition Letters*, Vol.94, pp. 87-95. DOI: 10.1016/j.patrec.2017.05.028.

[21] Haralick R.M., Shanmugam. K., and Dinstein. I. (1973). Textural features for Image classification, *IEEE Transactions on Systems, Man, and Cybernetics*, 3(6), pp. 610–621.

[22] Manickavasagam, K. Sutha, S. and Kamalanand, K. (2014). Development of systems for classification of different plasmodium species in thin blood smear microscopic images, *Journal of Advanced Microscopy Research*, 9(2), pp. 86-92.

[23] Roerdink, J.B.T.M., Meijster, A. (2001). The watershed transform: definitions, algorithms and parallelization strategies, *Fundamenta Informaticae*, 41, pp.187-228.

[24] Shanthakumar, P., Kumar P.G. (2015). Computer aided brain tumor detection system using watershed segmentation techniques, *Int. J. Imaging Syst. Technol*, 25 (4), pp.297–301. DOI: 10.1002/ima.22147.

eureca 2017 – Conference Paper
Paper Number EUG18

Kapur/Tsallis Entropy guided Segmentation of Plasmodium Species from Thin Blood Smear Images

Deepti Suresh, Sri Madhava Raja.N, Kirthini Godweena.A*

Department of Electronics and Instrumentation Engineering,
St.Joseph's College of Engineering,
OMR, Chennai 600119, India.

*kirthini.888@gmail.com

Abstract
A well-known mosquito-borne transmissible sickness in humans, commonly named Malaria is majorly caused due to plasmodium species. In order to minimize the disease impact, it is necessary to identify the type of the species before initiating the treatment process. Exact identification of the Plasmodium species is advisable to treat the infected person with a specific anti-malarial drug. In this work, an image segmentation scheme is proposed to extract the plasmodium species from thin blood smear images using famous entropy based procedures, such as Kapur / Tsallis function and Bat Algorithm (BA). Throughout the work, maximization of objective function is adopted to guide the BA. The proposed method is validated with a qualitative and quantitative analysis. The results shows evidence that the, proposed approach is efficient in extracting the species from blood smear images.

Keywords: Plasmodium, Entropy values, Bat Algorithm, Segmentation, Evaluation.

1. Introduction

[1] In imaging science, image processing plays a vital role in the analysis and interpretation of images in fields such as medical discipline, navigation, environment modeling, automatic event detection, surveillance, texture and pattern recognition, and damage detection [1-4]. The development of digital imaging techniques and computing technology increased the potential of imaging science. Segmentation process is one of pre-processing procedure widely employed in imaging field to extract key features from input image. Segmentation is judged as an important procedure for significant examination and interpretation of images [5-8].

[2] In recent years, biomedical image processing attracted the research community because of its significance. In this paper, an attempt is made to segment the malaria infected blood smear images. Malaria is a most common and most dangerous mosquito-borne infectious disease. Recent paper by Manickavasagam et al., presents the detailed segmentation procedure and the available anti-malarial drug based on the Plasmodium species [9]. Literature also presents the image processing methodology for Plasmodium infected blood smear images [10,11]. Even though many attempts are made on segmenting these, there is a scope of improving the efficacy of segmentation in early detection of pathology in the considered images.

[3] In most of the cases, the RGB images are segmented using the gray scale images and the outcome of this process is also in gray form. In this paper, the RGB images are converted into gray scale images and segmented using Kapur's and Tsalli's function using the BA.

In this work, thin blood smear images of plasmodium was obtained from the Parasite Image Library (DPDx) of the Centers for Disease Control and Prevention [12] and is then considered for segmentation process. In this work, BA is employed to solve the bi-level segmentation problem. The image quality measures, such as MSE, RMSE, NAE, NCC, AD, SC, MD, PSNR and SSIM are extracted [13-15]. In addition to this, statistical features, such as mean, median, standard deviation, sum and variance is extracted for the further analysis.

2. Materials and Methods

[4] In this paper, image segmentation was carried out using well known entropy based approaches, such as Kapur and Tsallis functions since these methods are proven to be successful in segmenting in the literature.

2.1 Kapur's Entropy

Kapur's function identifies the optimal threshold by maximizing the entropy of histogram [16].
The Kapur's entropy can be expressed as;

$$J_{\max} = f_{kapur}(Th) = \sum_{j=1}^{k} H_j^C \quad (1)$$

Generally, each entropy is computed independently based on the particular *th* value.
For multi-level thresholding problem, it can be expressed as;

$$H_1^C = \sum_{j=1}^{th_1} \frac{Ph_j^C}{\omega_0^C} \ln\left(\frac{Ph_j^C}{\omega_0^C}\right),$$
$$H_2^C = \sum_{j=th_1+1}^{th_2} \frac{Ph_j^C}{\omega_1^C} \ln\left(\frac{Ph_j^C}{\omega_1^C}\right),$$
$$\vdots \qquad (2)$$
$$H_k^C \sum_{j=th_k+1}^{L} \frac{Ph_j^C}{\omega_{k-1}^C} \ln\left(\frac{Ph_j^C}{\omega_{K-1}^C}\right)$$

where Ph_j^C is the probability distribution of the intensity levels, *C* is unity (1) for gray level images and $\omega_0^C, \omega_1^C, ...\omega_{k-1}^C$ probability occurrence for *k* levels. The BA based search arbitrarily adjusts the values of threshold until J_{max} is reached

2.2 Tsallis Function

Non-extensive entropy concept of Tsallis was originally derived from Shannon's theory [4] and it can be defined as [17];

$$S_q = \frac{1-\sum_{j=1}^{Th}(p_j)^q}{q-1} \qquad (3)$$

where*T* is the system potentials and *q* is the entropic index. The above equation satisfies Shannon's entropy when $q \to 1$ .The pseudo additivity rule for the entropy can be expressed as follows;

Let the gray scale image has L gray levels in the range {0,1, ..., L-1}, with probability distributions $p_i = p_0, p_1, ..., p_{L-1}$. Then, Tsallis multi thresholding can then be expressed as: $J_{max} = f(Th)=[Th_1,Th_2, ... , Th_k] = argmax$

$$\left[S_q^A(Th) + S_q^B(Th) + ... + S_q^K(Th) + (1-q).S_q^A(Th).S_q^B(T)...S_q^K(Th)\right] \qquad (4)$$

where

$$S_q^A(Th) = \frac{1-\sum_{j=0}^{t_1-1}\left(\frac{Pj}{P^A}\right)^q}{q-1},\ P^A = \sum_{j=0}^{t_1-1} Pj$$
$$S_q^B(Th) = \frac{1-\sum_{j=t_1}^{t_2-1}\left(\frac{Pj}{P^B}\right)^q}{q-1},\ P^B = \sum_{j=t_1}^{t_2-1} Pj \qquad (5)$$
$$S_q^K(Th) = \frac{1-\sum_{j=t_k}^{L-1}\left(\frac{Pj}{P^K}\right)^q}{q-1},\ P^K = \sum_{j=t_k}^{L_2-1} Pj$$

are subject to the following constraints:

$$\left|P^A + P^B\right| - 1 < S < 1 - \left|P^A - P^B\right|$$
$$\left|P^B + P^C\right| - 1 < S < 1 - \left|P^B - P^C\right| \qquad (6)$$
$$\left|P^K + P^{L-1}\right| - 1 < S < 1 - \left|P^K - P^{L-1}\right|$$

During the multi thresholding practice, the optimal threshold value *Th* which maximizes *f(Th).*

2.3. Bat Algorithm

The BA was firstly proposed by imitating the hunting actions of microbats [18]. BA consists of three mathematical equations such as velocity, position and frequency updates as described in the following equations [19]:

$$V_i^{(t+1)} = V_i^{(t)} + (X_i^{(t)} - Gbest).F_i \quad (7)$$

$$X_i^{(t+1)} = X_i^{(t)} + V_i^{(t+1)} \quad (8)$$

$$F_i = F_{\min} + (F_{\max} - F_{\min}).\beta^1 \quad (9)$$

where $V_i^{(t+1)}$ and X_i^{t+1} symbolize the velocity and position of the bat, F_{min} is the least frequency and F_{max} is highest frequency.

From Eq. (7), it is noted that, velocity renewal depends predominantly on the frequency renewal. During the heuristic investigation, a new result for every bat is produced based on the subsequent relation:

$$X_{new} = X_{old} + \varepsilon A^t \quad (10)$$

where ε= arbitrary digit of the range [-1,1] and A is the intensity of bats' discharged sound throughout the investigation of a new "area" (set of positions leading to a set of solutions).
The arithmetical illustrations for intensity alteration are shown below:

$$A_i^{(t+1)} = \alpha_1 A_i^{(t)} \quad (11)$$

$$r_i^{(t+1)} = r_i(0)[1 - \exp(-\gamma_1 t)] \quad (12)$$

In this work, Chaotic Bat Algorithm (CBA) discussed in [15] is considered with the following parameters:

Number of bats = 30; search dimension = 2; iterations = 250; stopping criteria = $J(t)_{max}$; frequency vector constant β = [0,1];ε is a random value between [-1,1]; A_0 = 10 and A_{min}= 1 (which decays in steps of 0.1); $\alpha^1 = \gamma^1$=0.65.

3. Results and Discussions

This section presents the result obtained with the proposed methodology. All the simulation works are carried using Matlab 2012a on an Intel Core i3 CPU, 4 GB RAM running in Windows 8. The multi-level thresholding problem deals with finding optimal thresholds within the threshold range [0, L−1] that maximize a fitness criterion J_{max}. In this work, search dimension of the optimization problem is chosen as two (bi-level thresholding). For each image and each threshold value, the segmentation procedure is repeated ten times and mean value of the trial is chosen as the optimal value. Fig. 1 shows the flow chart of the automated disease prediction procedure. In this paper, plasmodium species such as P. Falciparum (PF), P. Knowlesi (PK), P. Malariae (PM), P. Ovale (PO), and P. Vivax (PV) available in Centers for Disease Control and Prevention [12] is considered.

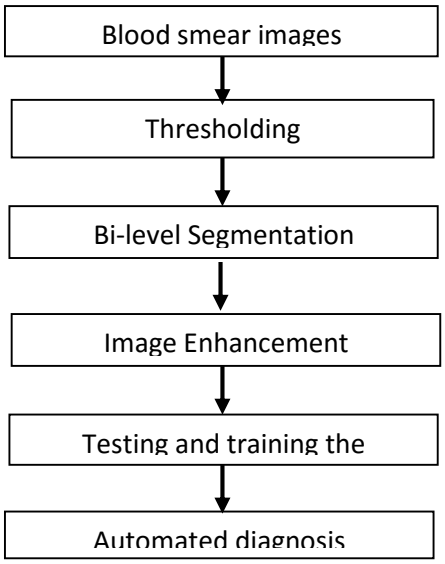
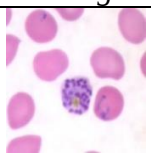
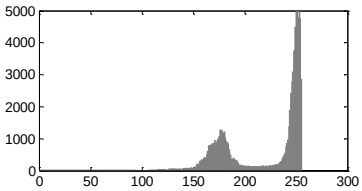
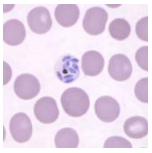
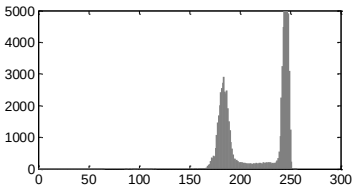
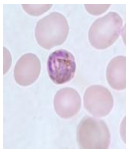
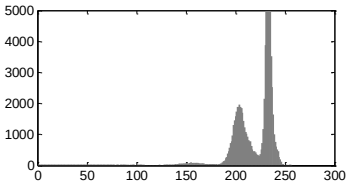
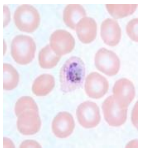
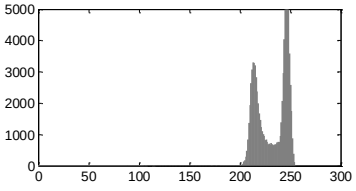
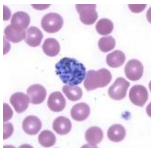
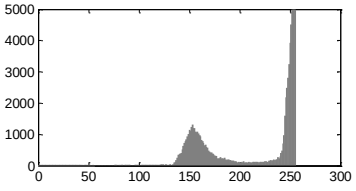


Figure 1. Flow Chart

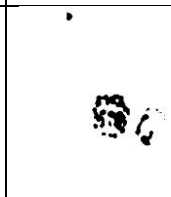
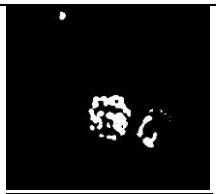
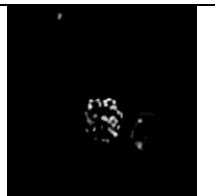
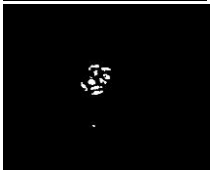
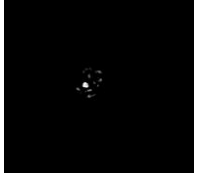
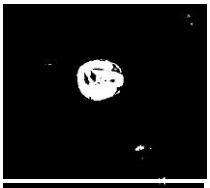
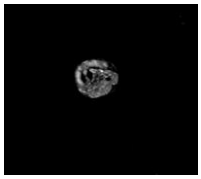
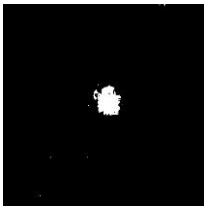
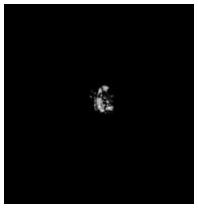
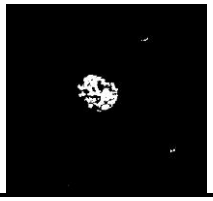
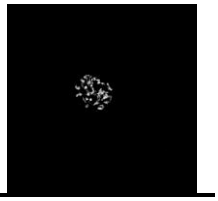
2

3 Table 1. Microscope image and its histogram

Name	*Image*	*Histogram*
P. Falciparum		
P. Knowlesi		
P. Malariae		
P. Ovale		
P. Vivax		

Before the segmentation process, because of the consistency, all the 300 x 300 blood smear images are resized as a standard 256 x 256 images. Generally, the data space in gray level histogram is simple [0, 255], whereas the RGB histogram holds a larger pixel value with a data space of $[0, 255]^3$ [20]. Hence, in this work, gray level image based segmentation is adopted. Initially Kapur based bi-level thresholding method have been tested on the dataset shown in table 1. The above discussed procedure is repeated for the same dataset using Tsallis function. The segmentation procedure is repeated 20 times on each image and the mean value is recorded for the analysis.

Table 2. Segmented and inverted image for the analysis

Image	*Kapur*		*Tsallis*	
	SI	NI	SI	IM
P.F				
P.K				
P.M				
P.O				
P.V				

The discussed bi-level thresholding process is able to separate the region of interest (plasmodium species) from the background without any loss in information. The quality of the segmentation procedure is assessed using the well-known image quality measures, such as Mean Square Error (MSE), Root Mean Square Error (RMSE), Normalized Absolute Error (NAE), Normalized Cross Correlation (NCC), Average Difference (AD), Pixel to Signal Noise Ratio (PSNR) [13] and Structural Similarity Index Matrix (SSIM) [14]. Along with these procedures, the time taken by the CPU to identify the optimal threshold is also considered to assess the performance of Kapur and Tsallis based segmentation. In order to increase the visibility of plasmodium, the

segmented image (SI) is then inverted (IM) and the geometric features of the images such as, mean, median, standard deviation, sum and variance is extracted for further analysis.

Table 3. Quantitative Measures analysis

Image	*OF*		*OT*		*CPU time (sec)*	
	Kapur	Tsallis	Kapur	Tsallis	Kapur	Tsallis
P.F	10.4472	0.7864	138,255	126,255	12.3346	12.2654
P.K	10.5183	0.8365	155,255	151,255	17.0074	16.3085
P.M	9.0036	0.8722	169,255	157,255	15.5947	17.3836
P.O	9.0173	0.8619	200,255	188,255	13.9466	15.1107
P.V	9.2884	0.8094	139,255	130,255	16.1143	16.8244

Table 4. Quantitative measures with Kapur's function

Image	*MSE*	*RMSE*	*NAE*	*NCC*	*AD*	*MD*	*PSNR*	*SSIM*
P.F	2.6709e+03	51.6809	0.1587	1.1044	-27.0488	152	13.8642	0.7922
P.K	2.3155e+03	48.1195	0.1697	1.1416	-35.0538	164	14.4844	0.7513
P.M	2.1532e+03	46.4029	0.1688	1.1184	-25.2011	187	14.7999	0.7806
P.O	1.1317e+03	33.6403	0.1081	1.0868	-20.5062	201	17.5936	0.8370
P.V	3.7262e+03	61.0425	0.1961	1.1351	-37.7511	134	12.4182	0.7413

4 Table 5. Quantitative measures with Tsalli's function

5

Image	*MSE*	*RMSE*	*NAE*	*NCC*	*AD*	*MD*	*PSNR*	*SSIM*
P.F	2.2999e+03	47.9572	0.1492	1.1195	-32.4726	139	14.5137	0.7782
P.K	2.2092e+03	47.0018	0.1674	1.1460	-36.4449	141	14.6885	0.7476
P.M	1.2333e+03	35.1178	0.1450	1.1397	-31.6187	155	17.2203	0.7665
P.O	769.1403	27.7334	0.1005	1.0948	-22.9082	182	19.2707	0.8306
P.V	3.6731e+03	60.6060	0.1941	1.1432	-41.1681	122	12.4805	0.7331

6 Table 6. Image features with Kapur's and Tsalli's function

7

Image	*Mean*		*Median*		*Standard deviation*		*Sum*		*Variance*	
	Kapur	Tsallis	Kapur	Tsallis	Kapur	Tsallis	Kapur	Tsallis	Kapur	Tsallis
P.F	247.21	252.64	255.00	255.00	43.18	16.88	1.68e+08	2.57e+07	1.86e+03	2.85e+02
P.K	253.15	254.54	255.00	255.00	21.13	7.393	4.02e+07	4.92e+06	1.63e+03	54.6608
P.M	245.17	251.58	255.00	255.00	48.60	17.95	2.13e+08	2.89e+07	2.36e+03	3.22e+02
P.O	251.57	253.97	255.00	255.00	29.03	11.11	7.58e+07	1.11e+07	8.42e+02	1.23e+02
P.V	250.08	253.49	255.00	255.00	34.53	13.64	1.07e+08	1.68e+07	1.19e+03	1.86e+02

8

Table 2 shows SI and IM obtained with Kapur and Tsallis function. Table 3 presents the quantitative mesaures obtained in this study. Table 4 and 5 presents the qualitative mesure values and Table 6 presents the statistical parameters of the image computed using the IM. From this result, one can observe that, Tsalli's function offers better results compared with the Kapur's function in all the cases. The results confirm that, the proposed segmentation procedure can be used to segment microsopic images, and in future, the extracted features can be considered for the automated classification and drug discovery process.

4. Conclusion

In this paper, an attempt is made to segment the RGB thin blood smear images using Kapur and Tsallis function using BA. Maximization of entropy function is chosen as the objective function. The performance of heuristic algorithm based segmentation is tested on 256 x 256 sized microscopic images. The qualitative measures, quantitative measures and image features are extracted using existing methods from the literature. The usage of Bat algorithm has considerably improved the segmentation efficiency in terms of detecting the vague pixels which contribute for identifying the prognosis of the disease in early stages. From this study, it is noted that, the Tsallis' function offers better result compared with the Kapur. In future, the segmented image can be used to train and test the classifier for the automated diagnosis of disease.

References

[1] Tuba, M., (2014), Multilevel image thresholding by nature-inspired algorithms: A short review, Computer Science Journal of Moldova, Vol.22, (No.3), (pp. 318-338).

[2] Raja, N.S.M., Rajinikanth, V., Latha, K., (2014), Otsu Based Optimal Multilevel Image Thresholding Using Firefly Algorithm, Modelling and Simulation in Engineering, Vol.2014, Article ID 794574, 17 pages, DOI:10.1155/2014/794574.

[3] Rajinikanth, V., Couceiro, M.S., (2015), Optimal multilevel image threshold selection using a novel objective function, Advances in Intelligent Systems and Computing, Vol.340, (pp. 177-186).

[4] Rajinikanth, V., Raja, N.S.M., Kamalanand, (2017), K., Firefly algorithm assisted segmentation of tumor from brain MRI using Tsallis function and Markov random field, Journal of Control Engineering and Applied Informatics, Vol.19, (No.3), (pp. 97-106).

[5] Manic, K.S., Priya, R.K., Rajinikanth, V., (2016) Image Multithresholding based on Kapur/Tsallis Entropy and Firefly Algorithm, Indian Journal of Science and Technology, Vol.9, (No.12), 89949.

[6] Rajinikanth, V., Raja, N.S.M., Satapathy, S.C., (2016), Robust color image multi-thresholding using between-class variance and cuckoo search algorithm, Information Systems Design and Intelligent Applications, Advances in Intelligent Systems and Computing, Vol.433, (pp. 379-386).

[7] Raja, N.S.M., Rajinikanth, V., Fernandes, S.L., Satapathy, S.C., (2017), Segmentation of breast thermal images using Kapur's entropy and hidden Markov random field, Journal of Medical Imaging and Health informatics ,Vol.7, (No.8), (pp. 1825–1829).

[8] Rajinikanth, V., Satapathy, S.C., Fernandes, S.L., Nachiappan, (2017), S., Entropy based Segmentation of Tumor from Brain MR Images–A study with Teaching Learning Based Optimization, Pattern Recognition Letters, Vol.94, (pp. 87-95), DOI: 10.1016/j.patrec.2017.05.028.
[9] Manickavasagam, K., Sutha, S., Kamalanand, K., (2014) An automated system based on 2d empirical mode decomposition and k-means clustering for classification of Plasmodium species in thin blood smear images, BMC Infectious Diseases, Vol. 14, (No. Suppl 3), (pp.13).
[10] Manickavasagam, K., Sutha, S., Kamalanand, K., (2014), Development of systems for classification of different plasmodium species in thin blood smear microscopic images, Journal of Advanced Microscopy Research, Vol.9, (No.2), (pp. 86-92).
[11] Balan, N.S., Kumar, A.S., Raja, N.S.M., Rajinikanth, V., (2016), Optimal Multilevel Image Thresholding to Improve the Visibility of Plasmodium sp. in Blood Smear Images, Advances in Intelligent Systems and Computing, Vol.397, (pp.563-571).
[12] http://www.dpd.cdc.gov/dpdx/HTML/ ImageLibrary/Malaria_il.htm
[13] Grgic, S., Grgic, M., Mrak, (2004), M., Reliability of objective picture quality measures, Journal of Electrical Engineering, Vol. 55, (No. 1-2), (pp. 3–10).
[14] Wang, Z., Bovik, A.C., Sheikh, H.R., Simoncelli, E.P., (2004), Image Quality Assessment: From Error Visibility to Structural Similarity, IEEE Transactions on Image Processing, Vol. 13, (No. 4), (pp. 600 – 612).
[15] Satapathy, S.C., Raja, N.S.M., Rajinikanth, V., Ashour, A.S., Dey, N., (2016), Multi-level image thresholding using Otsu and chaotic bat algorithm, Neural Computing and Applications, DOI:10.1007/s00521-016-2645-5.
[16] Kapur, J.N., Sahoo, P.K., Wong, A.K.C., (1985), A new method for gray-level picture thresholding using the entropy of the histogram, Computer Vision, Graphics, and Image Processing, Vol. 29, (No. 3), (pp. 273–285).
[17] Tsallis, C., (1988), Possible generalization of Boltzmann-Gibbs statistics, Journal of Statistical Physics, Vol. 52, (pp.479–487).
[18] Yang, X.S., (2013), Bat algorithm: literature review and applications, Int J Bio-Inspired Comput., Vol.5, (No.3), (pp.141–149).
[19] Yang, X.S.,(2008), Nature-inspired metaheuristic algorithms, 2nd Edn. Luniver Press, Frome..
[20] Rajinikanth, V., Couceiro, M.S., (2015), RGB histogram based color image segmentation using firefly algorithm, Procedia Computer Science, (Vol.46), (pp. 1449-1457).

eureca 2017 – Conference Paper
Paper Number EUG19

Performance Evaluation for High Transmission Rate of 40GB/S with Intensity Modulation in WDM based Long Haul SMF

MD Shahrukh Adnan Khan[1*], Sharsad Kara Kuni[2*], Md. Masum Howlader[3], Md. Moshiur Rahman[4], Aravind CV[5]

[1]*Assistant Professor, University of Asia Pacific, Bangladesh*
[2]*University of Nottingham, UK*
[3]*Assistant Professor, University of Asia Pacific, Bangladesh*
[4]*Assistant Professor, University of Asia Pacific, Bangladesh*
[5]*Senior Lecturer, School of Engineering, Taylor's University, Malaysia*

[1*]chairman.asiatech@gmail.com

Abstract
In this paper, an optical network is designed using the 'Optisystem' platform for 40 GBit/s to observe the performance of Intensity Modulation namely RZ (Return to Zero On-Off Keying) and NRZ (Non Return to Zero On-Off Keying) embedded in single channel long haul WDM (Wavelength Division Multiplexing) links. For this purpose, dispersion compensated fiber (DCF) with a combination of 4 and 16 channel WDM are selected for a set of different length of single mode fiber. BER (Bit Error Rate) is measured both for the best and worst case scenario. Standard '4 Channel wavelength division multiplexing' simulation, with "NRZ-OOK", exhibits a very persistent performance for all the 3 spans having an initial BER of ~ 10^{-20} that ended up with a final BER of ~ 10^{-13}. In the case of '16 Channel wavelength division multiplexing', "NRZ-OOK" demonstrates an optimum performance with an increase in BER from 10^{-12} to 10^{-5} for a certain length of 90km and 270km respectively. But performance of "RZ-OOK" is very ordinary with respect to the value of BER. So it is finally found that NRZ outperforms RZ with a very promising result for both the case of 4 and 16 channel WDM in investigations.

Keywords: Return to Zero (RZ), Non Return to Zero (NRZ), Wavelength Division Multiplexing (WDM), Single Mode Fibre (SMF), Next Generation High Data Rate 40GB/S.

1. Introduction

In this era, noticeable developments have been obtained in the field of optical fiber communication system because of higher data transmission rate, lower system cost and bandwidth efficiency. Consequent to researcher's opinion, increase in data rate as well as decrease in channel spacing may be the two probable solutions in order to escalate system capacity. Return-to-zero (RZ) signals and Non-return-to-zero (NRZ) are the two most commonly used modulation in the current fiber-optical communication system most of Fiber nonlinearities function e.g. dispersion management techniques, polarization division multiplexing, and optimization of the modulation format (e.g. [1-5]). Past few decades, both theoretically and experimentally between NRZ and RZ performance comparison on tolerance to optical noise fiber nonlinearities, and dispersion (e.g. [1-4]]). For long-haul transmission it is recognized that RZ has better transmission performance than NRZ. Wavelength division multiplexing (WDM) has capacity to support high bandwidth data transmission (e.g. [4-8]). The new generation light wave system has facilitated higher data rate per channel (40 Gb/s and above) (e.g. [2]). Although both RZ and NRZ have been widely used previously as traditional modulation techniques, for a next generation high data rate, they are yet to be implemented for long haul transmission in WDM. This research puts both the traditional RZ and NRZ modulation format in long haul optical fibre transmission the next generation high data rate of 40GB/s with and without WDM and the performance was compared accordingly.

2. Literature Review

IM or Intensity Modulation is a special form of 'Amplitude Shift Keying' (ASK) in which there is no carrier wavelength to be present when transmitting a '0'. It can simply be applied by switching the optical source off and on which is direct modulation. However, it has few drawbacks such as causing chirp as well as causing variation in source's amplitude and frequency. This leads us to use an external modulator which is known to be as Mach-Zehnder Modulator (e.g. [7-9]). Where A is the amplitude which is '0' when the optical source is off and 'A' when the device is on. In terms of duty cycle, there are two kinds of intensity modulation which are Non Return to Zero (NRZ) OOK and Return to Zero (RZ) OOK. When the source is turned on for the full period of its 'On Time' meaning 100% duty cycle, it refers to RZ and on the contrary when it is on for the fraction of the period for example 1/2 or 1/3 of its period causing duty cycle to be 50% or 30% respectively, it is referred to RZ [10-12].

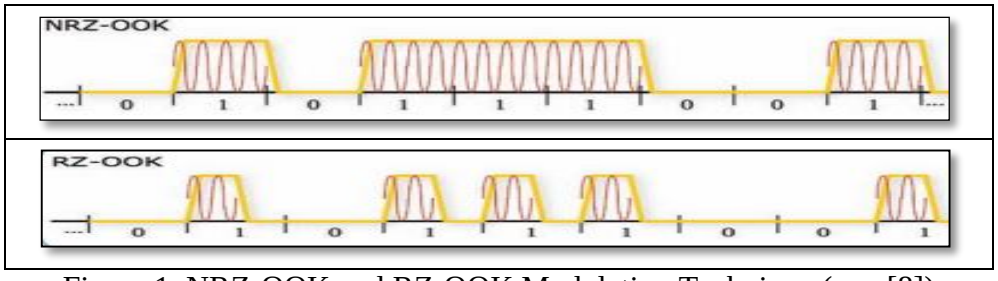


Figure 1. NRZ-OOK and RZ-OOK Modulation Technique (e.g. [8])

3. Methodology

Information in a form of random bit of streams was generated by Bit generator which then went through Pulse Generator to form a square pulse. Next, it was passed through RZ and NRZ modulation schemes with the carrier laser wave. Thereafter it was sent to the fibre optics through WDM and after pre and post amplifying process, the optical signal would be received by the receiver consisting of a Demultiplxer, photodiode and filter. Simulation was done in order to test the optical system in Optsim. After implementing the design parameter, the performance parameter (Eye diagram and Bit Error Rate, BER) were evaluated to get the impairment parameter and the data was compared.

4. Simulation Operation

Table 1 shows the parameter specification for the simulation model. The designs, modeling were constructed and simulated in the industrial level software "OptSim", version 5. 'CW Lorentzian Laser' was used as the optical source and its "Centre Emission Wavelength" was fixed at ~1550 nm. The power was fixed at ~0db. Three types of optical links were used which are Single Mode Fibre (SMF), Dispersion Compensated Fibre (DCF) and EDFA (Erbium Doped Fibre Amplifier). The total length of SMF was divided into three stages-90km, 180km and 270km. The fibre was selected to be the minimum which was 0.2 decibel (db) per kilometre.

Table 1: Parameter Description for Optsim Simulation

Design Parameter	Performance parameter
Optical Link (Standard Single Mode Fibre)	BER (Bit Error rate)
Optical Source (Laser of 1550 nm & 1310 nm)	Eye Diagram
Bit Rate (40 B/S)	
Duty Cycle (Laser of 1550 nm & 1310 nm)	
Modulation Format (RZ, NRZ)	

In accordance with minimum loss, high dispersion was introduced to 'SMF' which was fixed at '17 ps/nm/km'. Fibre non-linear coefficient was selected to be ~1.36811 1/w/k. '-100ps/nm/km' of dispersion was introduced to DCF. The length of it was calculated in such a way where the total dispersion in a transmission to be 0. "Flat Gain" EDFA was used throughout the entire period with a gain of 30db.

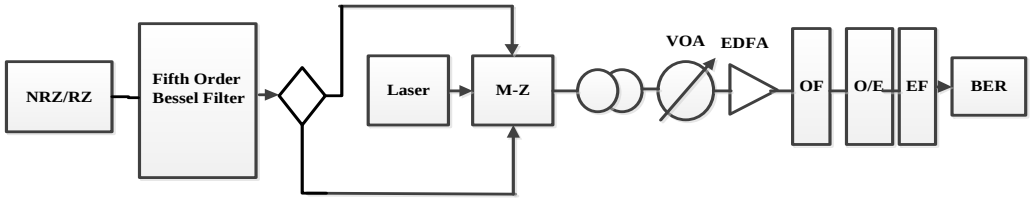


Figure 2. NRZ-OOK and RZ-OOK Simulation Set-up

"The Flat Noise Figure" was kept as 5db. Figure 2 and 3 are the simulation and transmission line set-up whereas figure 4 and 5 indicate the NRZ and RZ modulation format built in Optsim. Finally, figure 6 shows the entire 16 Chanel WDM optical fibre communication network by NRZ modulation.

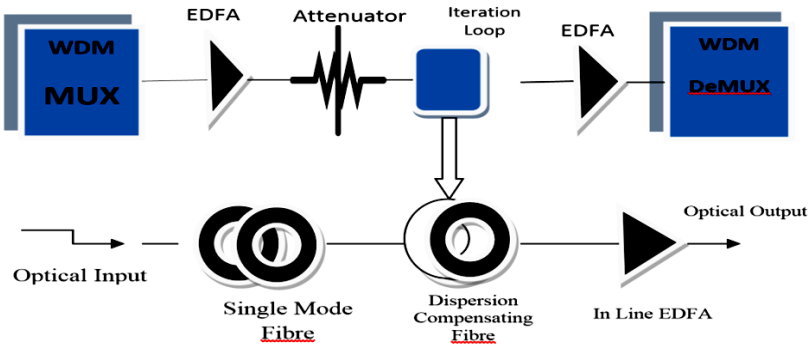


Figure 3. Transmission Link Set-up.

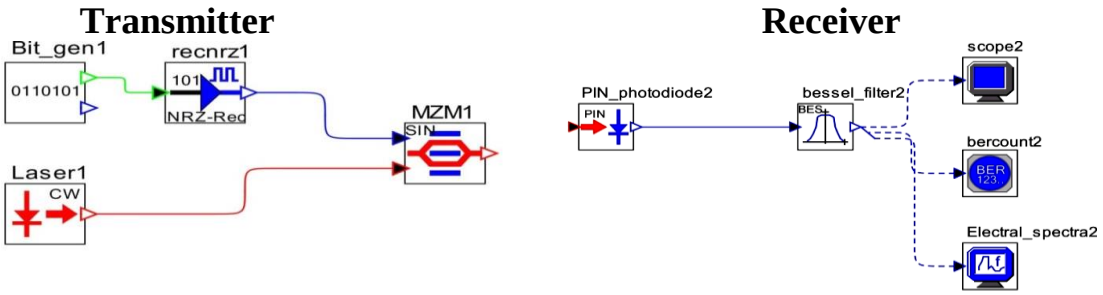


Figure 4. NRZ Modulation format.

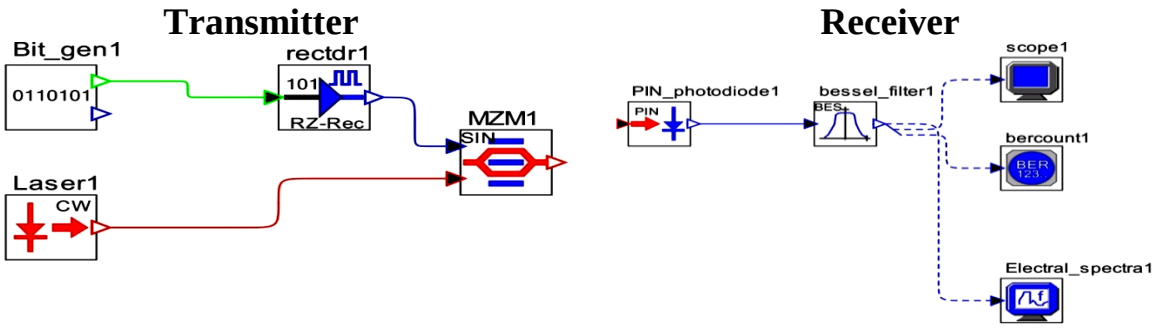


Figure 5. RZ Modulation format

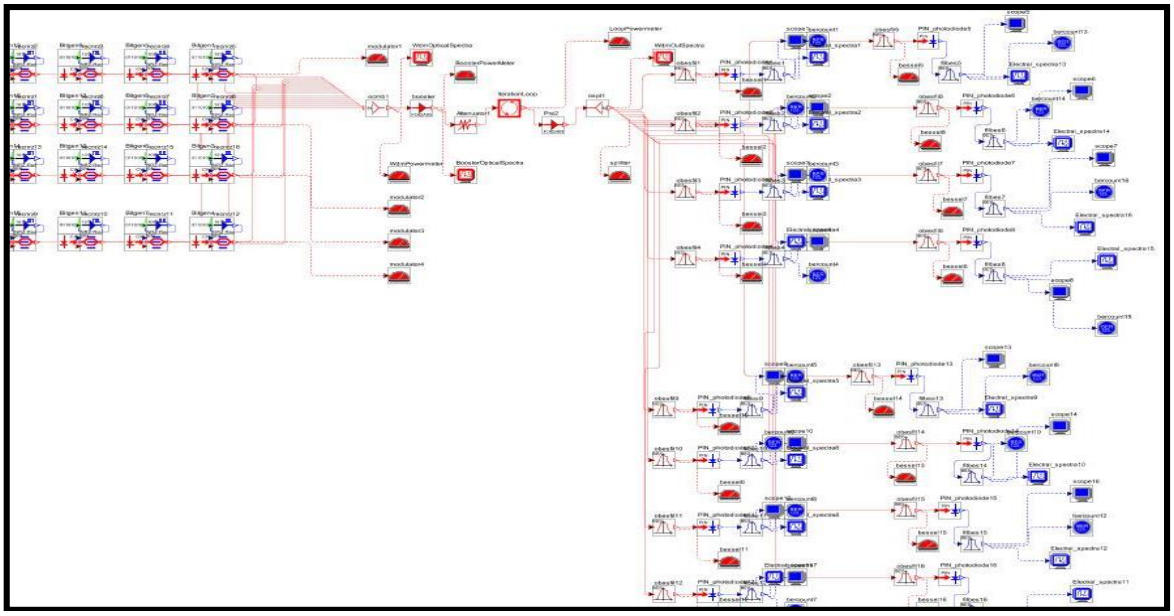
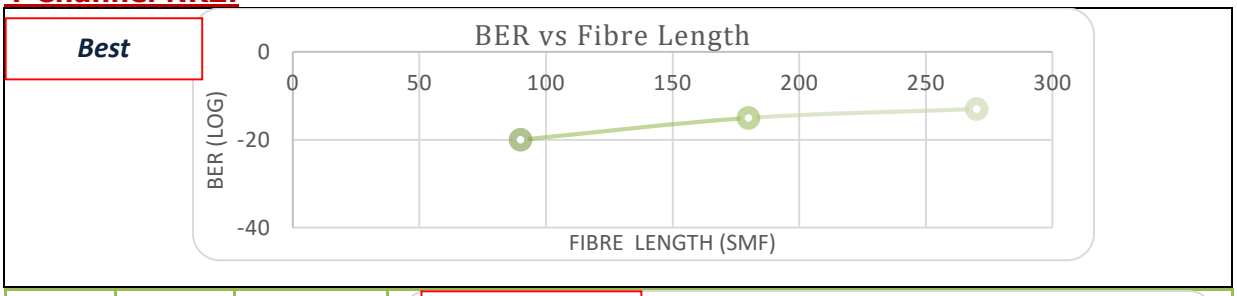


Figure 6. 16 Channel WDM Schematic Diagram (NRZ)

5. Result Analysis

Three SMF spans were used in order to measure the BER, those were 90km, 180km and 270km. Inline EDFA was used for the last two distances which were 180 km and 270 km. Since the 1st span consist of SMF having a distance less than 90 km, no inline amplifier was needed. Simulation had been completed for 2 different channels starting from 4, followed by 16. For NRZ modulation, referring to figure 7 and 8, it was clearly noticeable for '16 Channel WDM' that BER increased significantly for the distance of 180 km and 270 km. Due to the increase of the span and as well as number of channel, worst channel performance kept getting poorer. But it was logical since cross talk and non- linearity affect in the centred channel of WDM extensively. Overall NRZ showed standard performance for short distance transmission and became moderate with the increase of number of channel as well as fibre length.

4-Channel NRZ:



Fibre Length (km)	Worst channel (BER)	Best Channel (BER)
90	10^{-11}	10^{-20}
180	10^{-10}	10^{-15}
270	10^{-8}	10^{-13}

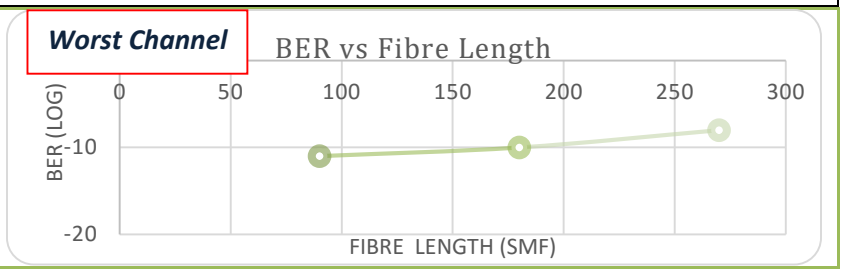
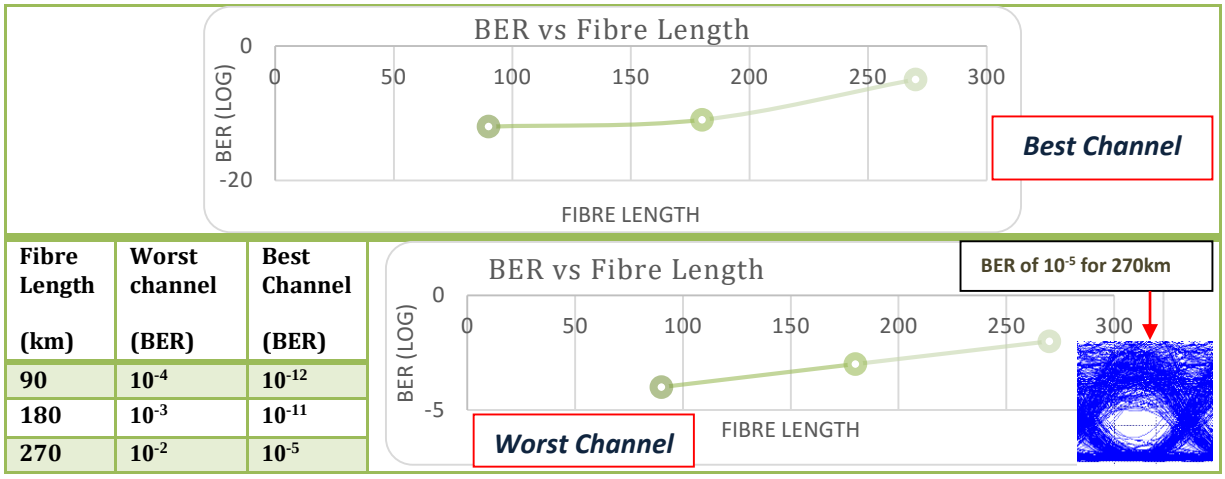


Figure 7. BER values for 4 Channel WDM NRZ-OOK (Bit Rate~ 40 Gb/s)

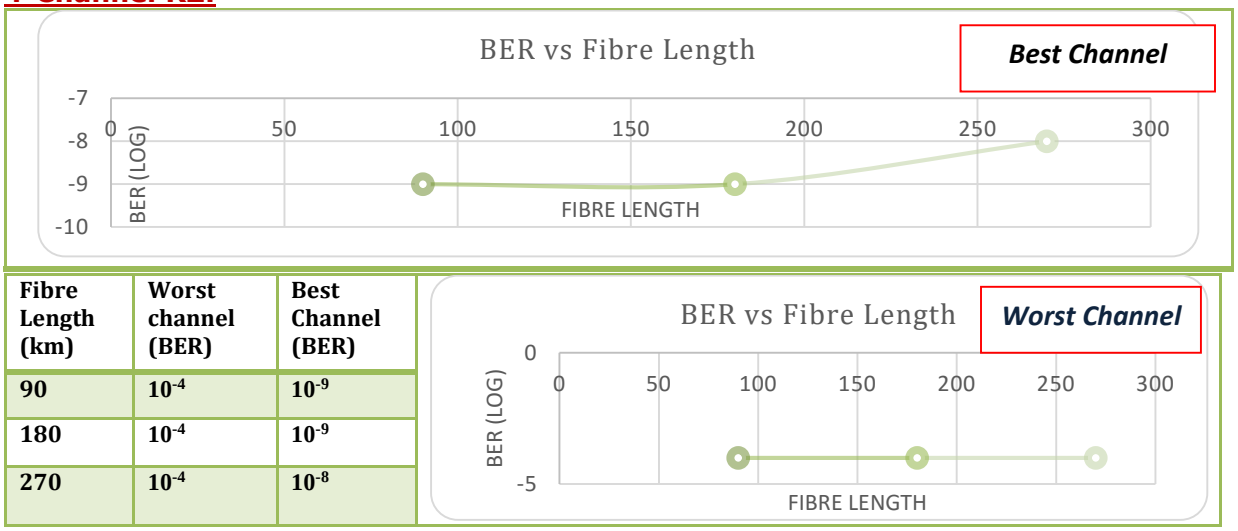
16 channel NRZ:



Fibre Length (km)	Worst channel (BER)	Best Channel (BER)
90	10^{-4}	10^{-12}
180	10^{-3}	10^{-11}
270	10^{-2}	10^{-5}

Figure 8. BER values for 16 Channel WDM NRZ-OOK (Bit Rate: 40 Gb/s)

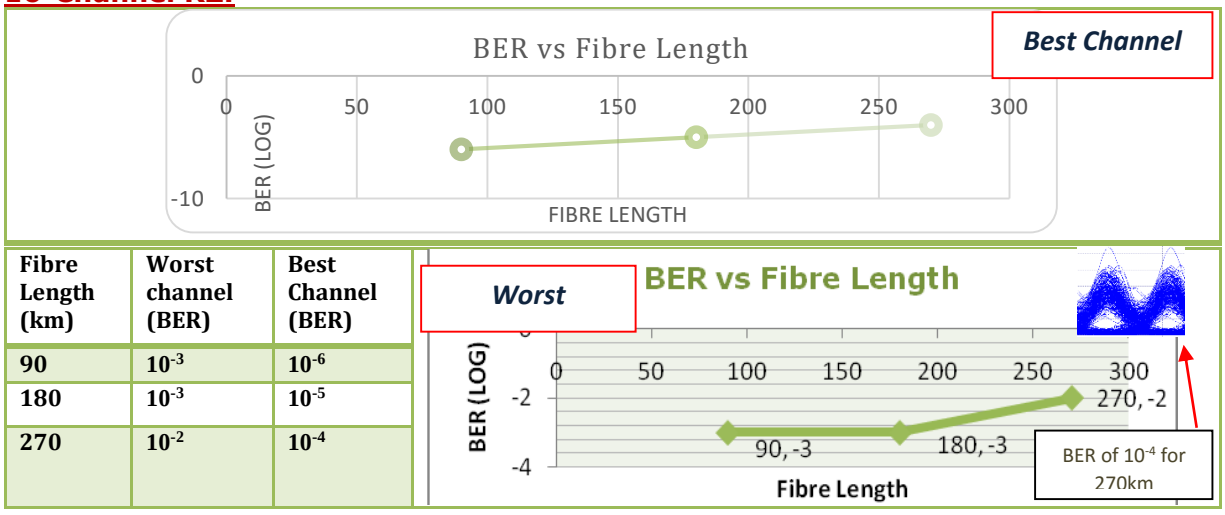
4-Channel RZ:



Fibre Length (km)	Worst channel (BER)	Best Channel (BER)
90	10^{-4}	10^{-9}
180	10^{-4}	10^{-9}
270	10^{-4}	10^{-8}

Figure 9. BER values for 4 Channel WDM RZ-OOK (Bit Rate~ 40 Gb/s)

16-Channel RZ:



Fibre Length (km)	Worst channel (BER)	Best Channel (BER)
90	10^{-3}	10^{-6}
180	10^{-3}	10^{-5}
270	10^{-2}	10^{-4}

Figure 10. BER values for 16 Channel WDM RZ-OOK (Bit Rate~ 40 Gb/s).

As far as RZ concerns, BER fell down drastically with the increase of fibre length (Figure 9 and 10). With the increase of number of channel, BER became even worse. To analyse the reason behind it, it was figured out that due to the wide optical spectra of RZ, while transmitting through WDM, the signal got affected severely by the other channels and cross talk and non-linearity took place. Considering '4 Channel WDM' RZ showed poor performance for best channel in terms of fibre length for all the 3 spans than NRZ as the BER increased from 10^{-9} to 10^{-8}.

Lastly, while investigating '16 Channel WDM', BER increased for both the modulation formats. "NRZ-OOK" showed moderate performance for 90km fibre span but BER increased as the fibre span increased and for a span of 270 km, it came up with a high BER of 10^{-5}. "RZ-OOK" showed the worst as the BER increased from 10^{-6} to 10^{-4}. Figure 8 and figure 10 shows the eye diagram from the simulation result the value of which is provided in tabularised form.

6. Conclusion

To recapitulate, it should be mentioned that the objectives of this research were successfully accomplished. NRZ-OOK modulation showed standard performance overall but went down at the end while performing for 16 Channel WDM. On the contrary RZ-OOK performed the worst in terms of all categories making it unworthy for long haul transmission. To sum it up, this research has a significant importance in terms of optical fibre communication. The two of the most widely used technique were compared in WDM system for next generation data rate in long haul transmission. A wide range of future work scope including addition of Duobinary, DQPSK and more advanced modulation can be included for further research. Lastly, it greatly enhanced the knowledge and understanding of transmitting information of high data rate in WDM system which will further benefit the researchers to go forward and take necessary step.

References

[1] Amin Malekmohammadi, A. F. Abas, M. K. Abdullah, G. A. Mahdiraji, M. Mokhtar, M. Fadlee.A. Rasid, (2009). *"Absolute Polar Duty Cycle Division Multiplexing Technique over Wave Length Division Multiplexing system"*, Optics Communications, vol 282, PP. 4233-4241.

[2] A. Malekmohammadi, M. K. Abdullah, A. F. Abas, G. A. Mahdiraji, M. Mokhtar, (2009). *"Analysis of RZ-OOK over Absolute Polar Duty Cycle Division Multiplexing in Dispersive Transmission Medium"*, IET Optoelectron. Vol. 3, no.4, pp. 197-206,

[3] W. Idler, A. Klekamp, R. Dischler, J. Lazaro, A. Konczykowska, (2003). *"System performance and tolerances of 43-Gb/s ASK and DPSK modulation formats"* Proceedings of the ECOC, Rimini, Italy.

[4] P. Winzer, R. Essiambre, (2009). "*Advance modulation formats for high-capacity optical transport networks*", J. Lightwave Technol. 24 4711–4728.

[5] X. Zheng, F. Liu, P. Jeppesen, (2001). "*Receiver optimization for 40-Gb/s optical duobinary signal"*, IEEE Photonic Technol. Lett. 13 744–746.

[6] L. Christen, S.R. Nuccio, X. Wu., A.E. Willner, (2007). "*Polarization-Based 43 Gb/s RZDQPSK Receiver Design Employing a Single Delay-Line Interferometer"*, Proceedings Conference on Lasers and Electro-Optics, CLEO, Baltimore, pp.1–2.

[7] Dr. Ilya Lyubomirsky, "*Advanced modulation format for ultra-dense wavelength division multiplexing"*, University of California, Riverside, CA 92521.

[8] NorizanBinti Mohamed Nawawi, (2008). "*Investigation of Stimulated Brillouin Scattering for the generation of Millimeter Wave for radio over fibre*", MEng, *UniversitiTeknologi Malaysia, Malaysia,* Faculty of Electrical Engineering.

[9] Ildefonso M. Pol. (2009) "*Optical Modulation for High Bit Rate Transport Technologie*", Technology Note. [Online]. Available: http://www.sunrisetelecom.com/support/Intro_optical_Modulation.pdf

[10] M. Asif, H. Ali, H.M. Afzal, T.A. Siddiqui. (2015). "*Comparative analysis and power optimization for return to zero and non-return to zero coded transmission in 40Gbps fibre optics system*", 7th International Congress on Image and Signal processing (CISP), IEEE, China.

[11] S. Yao, S. Fu, H. Wang, M. Tang, (2014). "*Performance comparison for NRZ, RZ and CSRZ modulation formats in RS-DBS Nyquist WDM system*", IEEE Journal of Optical Communications and Networking, V-6, 355-361.

[12] J. Latal, J. Vitasek, P. Koudelka, P. Siska, (2014). *"Simulation of Modulation formats for Optical Access Network based on WDM-PON"*, 16th International IEEE Conference on Transparent Optical Networks (ICTON), IEEE, Austria.

eureca 2017 – Conference Paper
Paper Number EUG20

Design of a Fully Automated Ventilation System for Vehicles Subjected to direct sunlight

Ahmed Medani Mohamed[1], Ahmed Abdalla Omer[1], Obai Younis[2,1,*], Dania Ahmed[1]

[1]*University of Khartoum, faculty of engineering, Khartoum, Sudan*

[2] *Prince Sattam Bin Abdulaziz University, Faculty of Engineering -Wadi Addwasir, KSA*

[*]oubeytaha@hotmail.com

Abstract

The heat trap phenomenon inside a vehicle's compartment produced by hot weather caused the car's compartment to gain heat from the sunlight radiation, inside the cabin will have higher temperature compared to the outside surroundings. The heat trapped in the enclosed compartment will bring uncomfortable feeling and suffocation for the driver and passengers when they enter the parked car. Let alone that children and pets left inside can be exposed to major health risks. Higher air conditioning power is necessary to cope with this phenomenon however it only functions when the engine is operating. This research is intended to invent a ventilation system to eliminate the dangers of excessive heat inside the compartment by the use of CFD analysis to determine the best position to install a fan and to optimize the air distribution. The project studied three different cases. And a temperature drop of 26°C was achieved.

Keywords: Heat trap phenomenon, sunlight radiation, ventilation, CFD.

1. Introduction

Generally, in countries like Sudan where the temperature rises up to 45°C in summer, re-entering a car parked directly under the sunlight can cause uncomfortable feeling and suffocation. There are also major health risks attributed to this temperature rise as a result of breathing contaminated air inside the vehicle produced by the plastic accessories inside. Also a phenomenon called the heat stroke in an adult can occur when body temperature increases by 5°C, children can reach dangerous body temperatures at much faster rate. Studies indicate that each year children die from Hyperthermia (an acute condition that occurs when the body absorbs more heat that it can dissipate) as a result of being left in a parked car. [1]

This extreme rise in the temperature levels inside the parked car cabin is caused due to the heat transferred by a combination of conduction, convection and radiation. Conduction occurred in the stagnant volume of air inside the car cabin, while convection takes place as the air inside the cabin contacts the cabin material itself. Moreover, heat is being radiated form the glass and body of the car, however, in this case radiated heat is the most influencing factor. The temperature variation inside the car depends on the thermal radiation exchanged between the environment and body of the car and also the radiation absorbed and emitted by the interiors of the cabin. In order to address this problem various approaches have been adopted. For instance, an improved ventilator system that comprises of a high volumetric capacity fan and motor powered by solar panel was proposed by Innovage Company [2]. The disadvantage in this research is that a small portion of the glass will be left open which may endanger the vehicle and leave it vulnerable to theft and robbery. Another study adopted an automatic ceiling fan using PIR sensor by Mohd Rasidi and Md Radzi (2009). This research was quite a good solution to this issue but in a country like Sudan where sand storms can occur frequently, a ceiling fan may leave the vehicle dusty and uncomfortable. Other researches and ideas that address this issue were presented.

This study aims to design and employ a ventilation system that is completely independent from the vehicles power systems. An internal system which means that no parts of it are exposed to ambient so the vehicle's security would not be threatened. A low priced system that can be produced in a closed package and installed easily. This system proposed an axial cooling fan which will be located in the surface where the back speakers' area is mounted behind the rear seat. This system is to be controlled by an Arduino board based circuit that functions according to the analog signals received from type LM35 temperature sensors and getting its power supply from a separated and dedicated battery. The microcontroller based circuit senses the temperature difference between inside and outside of the car, with the help of LM35 sensors, and depending on the temperature difference switches the fan on or off. To determine the specifications of the fan and its placement, temperature variation of a parked car directly under the sun was observed and flow simulation and analysis were performed in ANSYS R15.0 FLUENT workbench where a model of a 2012 Hyundai Accent was tested in different conditions. After the simulation was completed experiment was performed on a prototype, fabricated based on the findings of simulation, to observe the performance of the smart ventilation system.

2. Theory of heat analysis in vehicles

The Heat Balance Method (HBM) was used for the determination of the cooling load inside the compartment [3]. The variation of temperature inside a car was taken from a previous study conducted by Nuha ElBadawi and Zenab Elhadi in 2014 [4] in which they found that the average temperature inside the compartment can reach up to 78°C while the outside temperature in summer can be as high as 46°C. These values were used in the cooling load formulas to determine the ambient load, Direct Radiation load, Diffuse Radiation load and Reflected Radiation load. All these values were added together to obtain the total cooling load of the vehicle which was 2.31KW. The heat flux was calculated for each glass and 25% of each value was assumed to be absorbed by the front and rear seats, these values is shown in table (1).

4. Table 57. Heat flux values for each glass

Boundary Surface	Heat flux (W/m^2)
*Front Glass	739.30
*Front Passenger Glass/glass	555.90
Front Seats	616.98
**Rear Passenger Glass/glass	494.80
**Rear Glass	736.39
**Rear Seat	616.56

(*) front passenger glass above refers to the pair of glasses mounted on the front doors of the vehicle. and the heat flux values shown in table 1 refer to each glass separately. Also the front glass refers to the front windshield glass of the vehicle.
(**) the rear passenger glass refers to the pair of glasses mounted in the rear passenger doors of the vehicle, and the rear glass refers to the rear windshield glass of the vehicle. And the rear seat refers to the rear bench seat of the vehicle.

As an assumption was made for the above values that heat is transmitted to the vehicle through the glass only and all other surfaces are insulated. These values were verified using a solar power meter which is an instrument used to measure the heat flux from solar radiation for a unit surface area. The details of the device are as follows:

- **Model**: ISM 410
- **Manufacturer**: ISO-Tech
- **Range**: 2000 W/m^2
- **Accuracy**: Typically within $\pm$ 10 W/m^2 or $\pm$ 5%, whichever is greater in sunlight. Additional temperature induced error $\pm$0.38 $W/m^2/$°C.
- **Angular Accuracy**: Cosine corrected < 5% for angles <60^o.
- **Spectral Response**: 400~1100 Nm.

2.1 Boundary Conditions and Setup

After calculating the cooling load requirements, the flow rate was calculated and found to be a minimum of 137 CFM (cubic feet per minute). Catalogs from PELONIS TECHNOLOGIES Co. Ltd. were used for the selection of the fan, the closet standard was found to be and axial fan 12V fan with 150 CFM which discharges air with a velocity of 6.288 m/s. This value was considered as a boundary condition later on in ANSYS.

The geometry used is shown in figure (1). The turbulence model used for solution is SST-Kω which was found suitable for this situation due to the combination of internal and external flow inside the compartment. The discretization scheme used was QUICK. QUICK-type schemes are based on a weighted average of second-order-upwind and central interpolations of the variable. The QUICK scheme will typically be more accurate on structured meshes aligned with the flow direction.

According to HBM cooling load calculations, the mass flow rate had been calculated and the Selection of the fan was done by choosing a suitable fan from fans manufacturers. Companies produce fans in standard flow rates. Thus the fan was chosen as a standard fan from PELONIS Technologies company with a flow rate of 150 CFM and a diameter of 120 mm. The inlet fan velocity was then calculated and found to be 6.288m/s and the air outlet was chosen to be the natural installed outlet vents located under the front passenger seats. This outlet was chosen after a short survey in local workshops specialized in air conditioning maintenance. The two holes under the front seats can be located in various types of vehicles and automobiles. Then it was considered as Outflow in the boundary conditions selection, for it was a natural outlet in inside the vehicle.

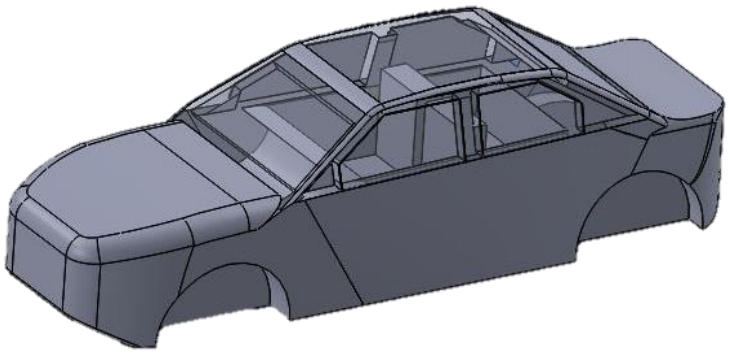


Figure 96. Model of the vehicle

2.2 Mesh Generation

Due to the sensitivity of the case and complexity of the geometry it was decided to use ICEM software to generate the mesh. The advantage of ICEM is the ability to control the mesh quality aspects manually resulting in a mesh with quality over 90%. Figure (2) below shows the quality of the mesh specified by color, red color represents poor mesh quality and blue color represents high mesh quality.

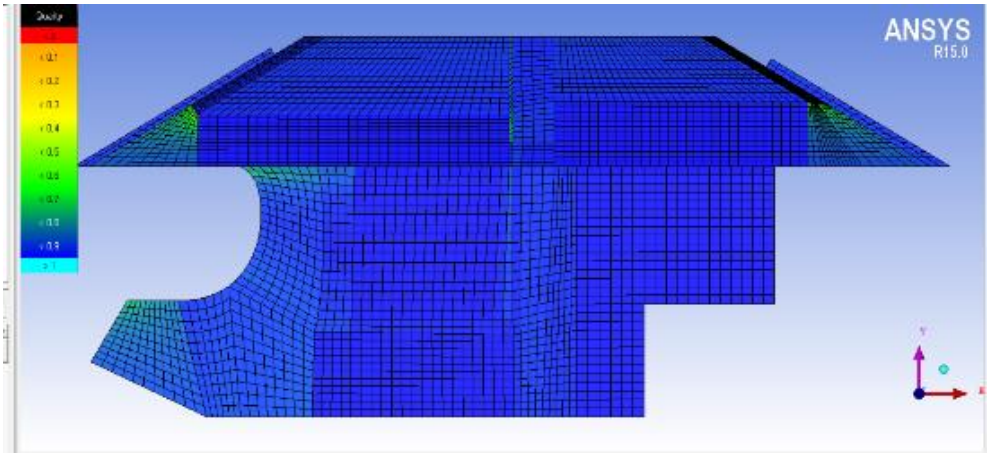


Figure 97a. Mesh Quality specified by color

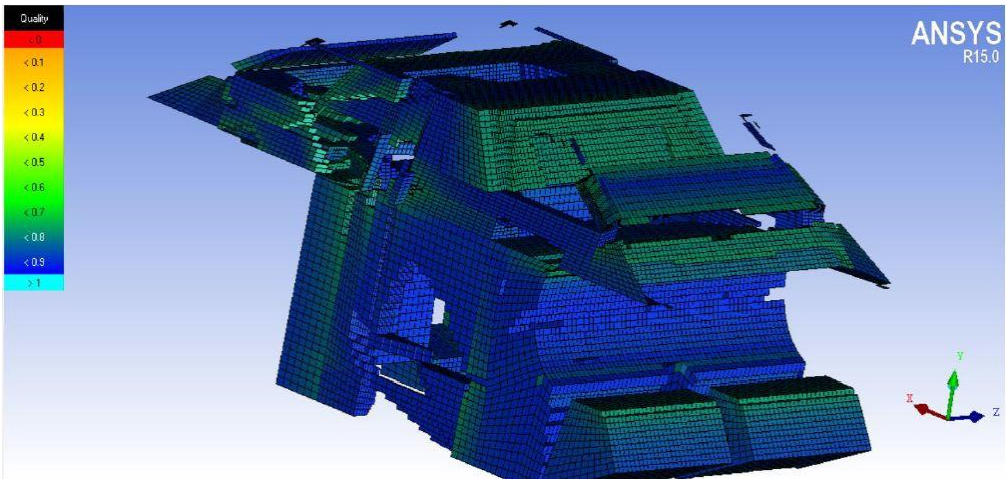


Figure 98b. Mesh Quality specified by color

As can be seen above the processing of the mesh resulted in a high quality fine mesh indicated by the blue color.

Four mesh sizes were chosen for the mesh independency study which are concluded in the table (2).

5. Table 58. Mesh Sizes

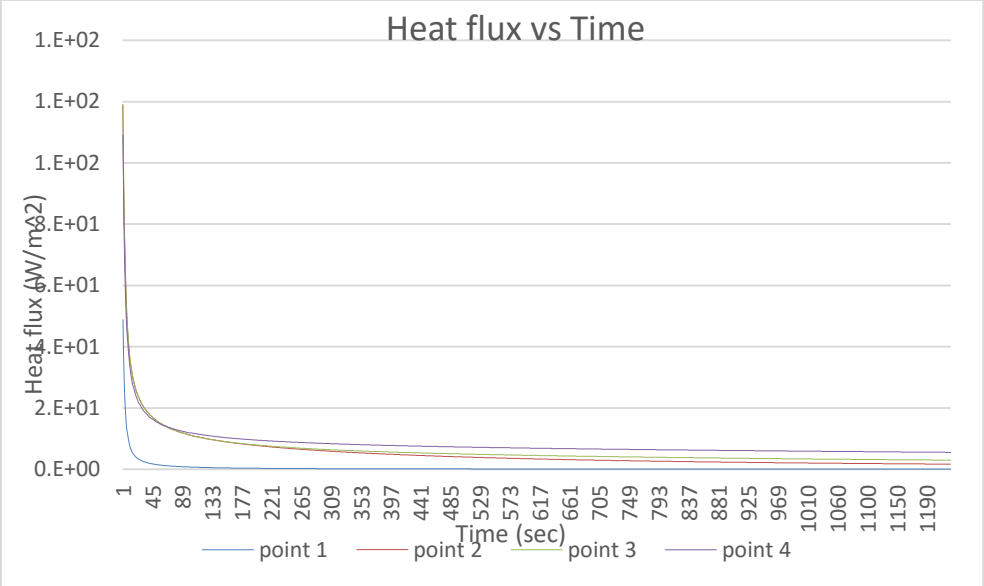
Mesh No.	**No. of nodes**	**Min. volume (m)**	**Max volume (m)**
Mesh 1	144842	6.272E-8	6.72E-5
Mesh 2	381616	1.500E-8	1.90E-5
Mesh 3	205651	3.100E-8	4.60E-5
Mesh 4	256553	2.170E-8	4.34E-5

Since the study is a transient case also three-time step sizes were specified to check for the optimum time step in order to minimize the computational power. Which were 0.1 sec, 0.5 sec and 1.0 sec.

Then two cases were studied and observed. The first study used a constant heat flux calculated from the cooling load formulas, the second study used a constant surface temperature which was taken from a previous study by K.MU [5] to be 81°C. The purpose of this study was to analyze the effects of transient heat flux and difference

between constant and transient heat flux on the glass. And indeed, the constant heat flux case yielded unrealistic results.

In terms of temperature, it is obvious that the heat flux will decay to a point near zero as shown in the figure (3).



6. Figure 99. Decay rate of heat flux

The 4 points shown in figure (3) were specified in the front glass of the model. Thus, the constant temperature approach was used to carry on with the simulation procedure.

2.3. Air Induction Methods

The method, how air is being induced in the car cabin is essential for air distribution and consequently the rate of cooling inside the car cabin. Thus, it was decided to further modify it and run several cases to check for the best distribution of air and ventilation performance for the fan previously selected. Three cases were considered where the inlet port was changed in terms of orientation and number of fans, the three cases are:

1. Plain fan. (in Palin fans the axis of the fan is perpendicular to the surface mounted in it)
2. 30° tilted fan.
3. Two plain fans with half the flow rate for each fan. (assuming more air distribution).

The first case was the first design proposal using the fan selected previously and was not subject to any modifications.

3. Results of the three cases

After conducting the mesh independency study for both constant heat flux and constant surface temperature, the optimum mesh was found to be the same which is mesh 4 with 256,553. The comparison was made on a line that contains 50 sample

points and starts from the front glass and passes through the axis of the fan in the middle. The physical property used for comparison was temperature as it is the most important parameter in this study. Using error bars with ±5% percentage error in the smallest mesh (mesh 2). The time Independency study was made also with the same technique above but using different location, which were 4 points located inside the cabin, as shown in figure (4). These 4 points were used later on as the position of the four sensors in the prototype. Which are:

1. Above front passenger head and near the front glass.
2. Near the driver head and next to the front passenger glass.
3. Near the front passenger seat
4. In the back seat

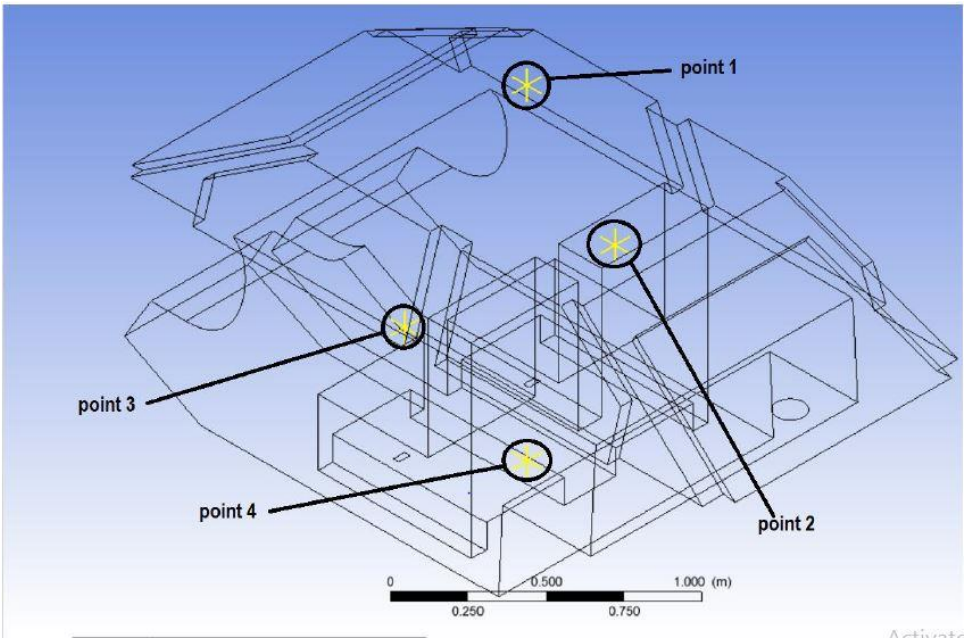


Figure 100. Positions of sensors in ANSYS Fluent

These four spots where considered because they represent the targeted area in which passengers will experience the heat rise when entering the vehicle. The optimum time step size among the three for both, the constant heat flux and constant surface temperature, was found to be 0.5 second.

After specifying the optimum time step and mesh size the 3 inlet cases were simulated to check for the best air distribution and ventilation efficiency and results of these 3 cases were taken at 5 seconds, 10 seconds and 150 seconds for two different cases which are.

Heating the cabin for 10 minutes then operating the fan, which can be considered the worst-case scenario the fan would have to face.

Operating the fan after 3°C difference between the inside and outside is reached, which is the way the prototype later on is programmed to.

The difference between these two above cases was not considerable and whether heating the cabin, or operating the cabin after difference reaches 3°C between inside and out, the temperature inside the compartment would not differ very much for the 3 inlet cases mentioned above as shown in figures (5-7) for each inlet case in the cooling period only.

As observed from above figures, it would not make much of a difference if the cabin is heated up for 10 minutes then the fan operates in the three inlet cases.

Thus, the system will be designed based on the 2nd case of cooling after 3°C for the purpose of pertaining the fan life time, and reducing the operation time it would take to cool down the vehicle.

The contours of temperature for the three inlet cases in the second approach of constant surface temperature are taken at different time intervals to monitor the distribution of air in the three cases. The results are displayed in a vertical plane passing through the axis of the plain fan as shown in figure (8).

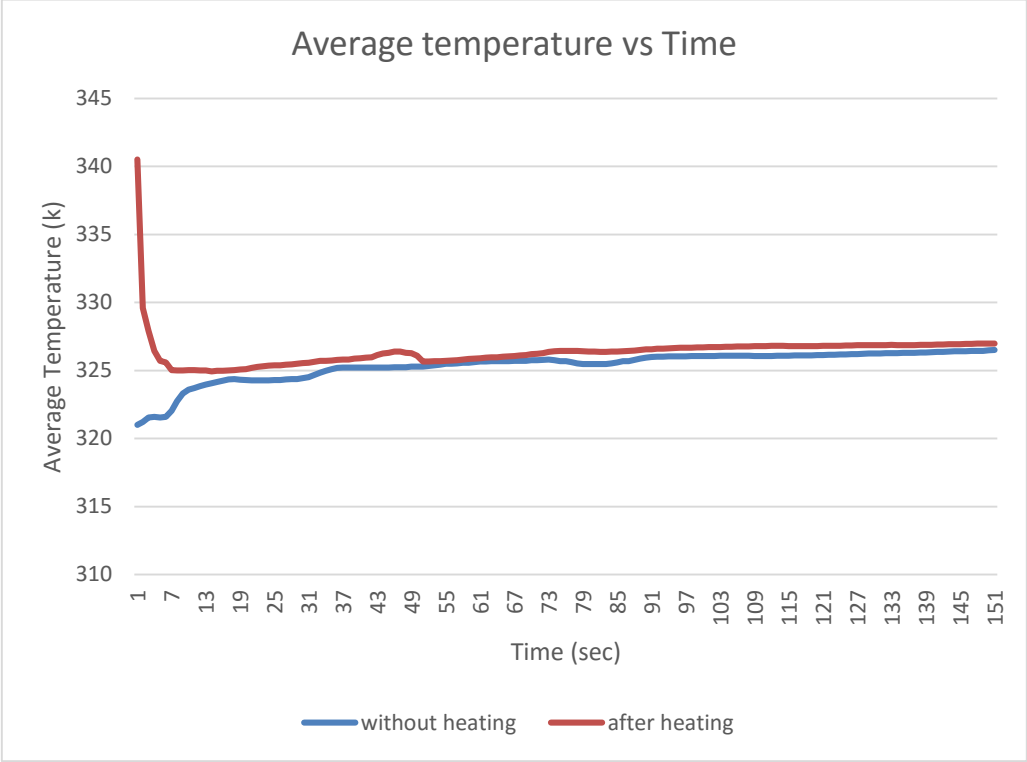


Figure 101. Plain fan in case of heating then cooling and cooling after 3° difference

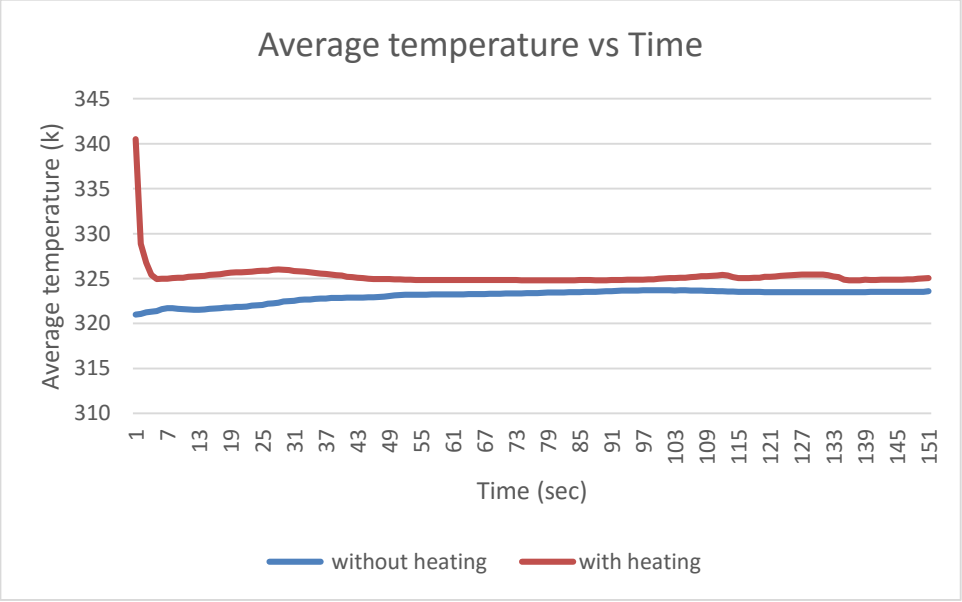


Figure 102. Two fans in case of heating then cooling and cooling after 3° difference

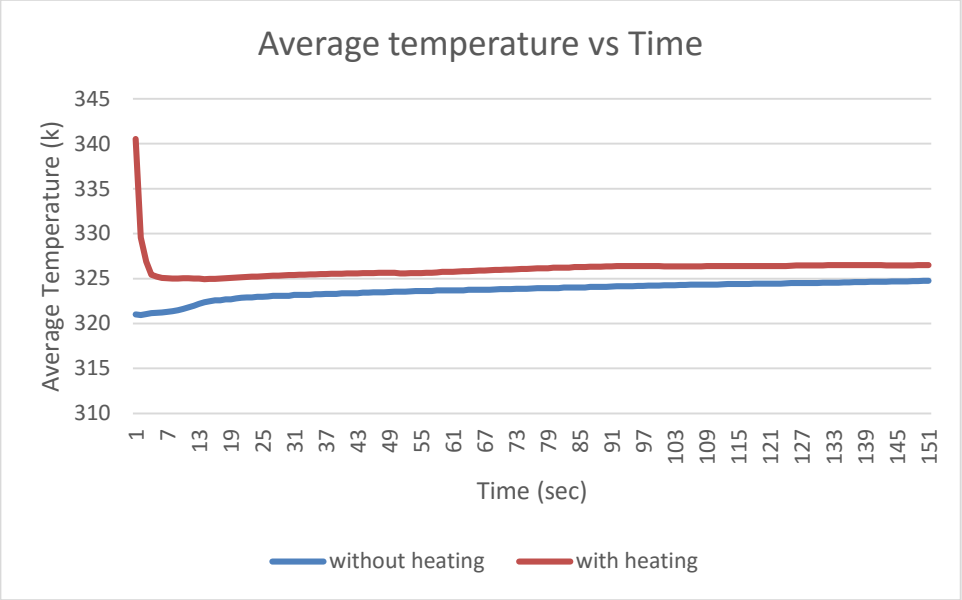


Figure 103. 30deg tilted fan in case of heating then cooling and cooling after 3° difference

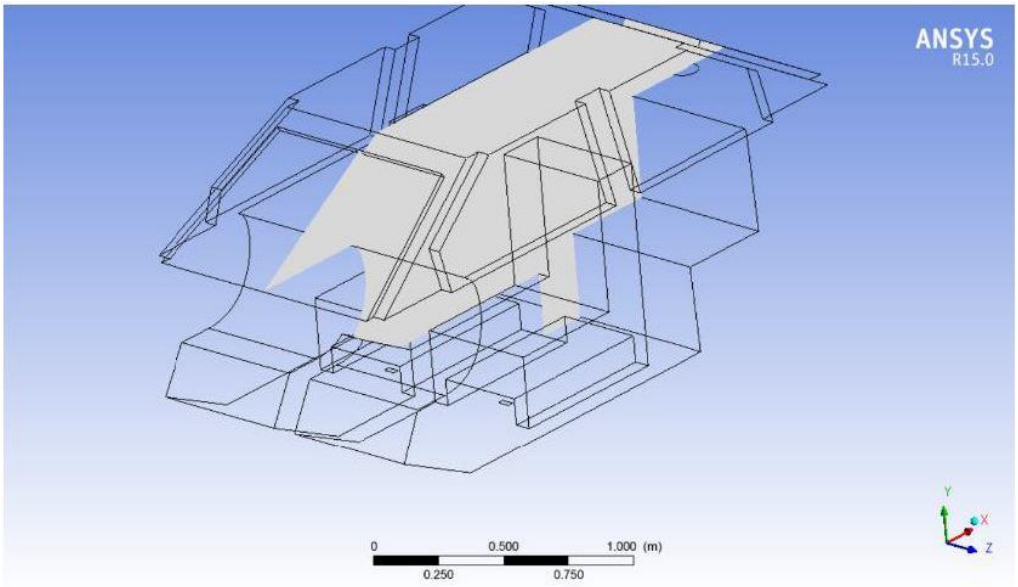


Figure 104. Vertical plane used to display results

7. The system-regardless of the case used- in general achieved a very convenient temperature drop as shown in the figures (9-11) for 150 seconds operation time.

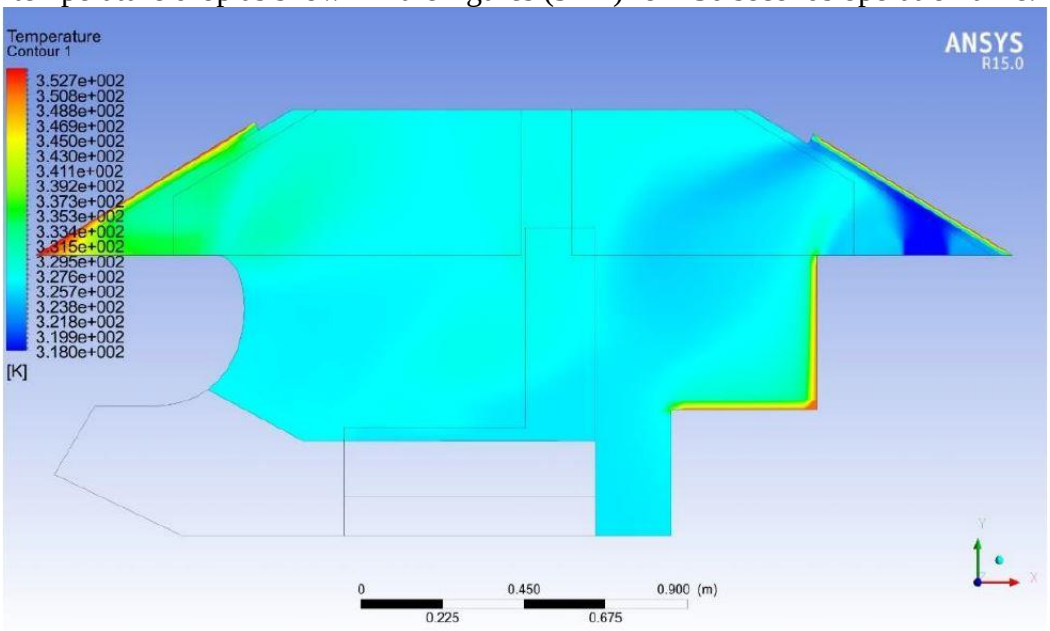


Figure 105. Plain fan temperature Distribution at 150seconds

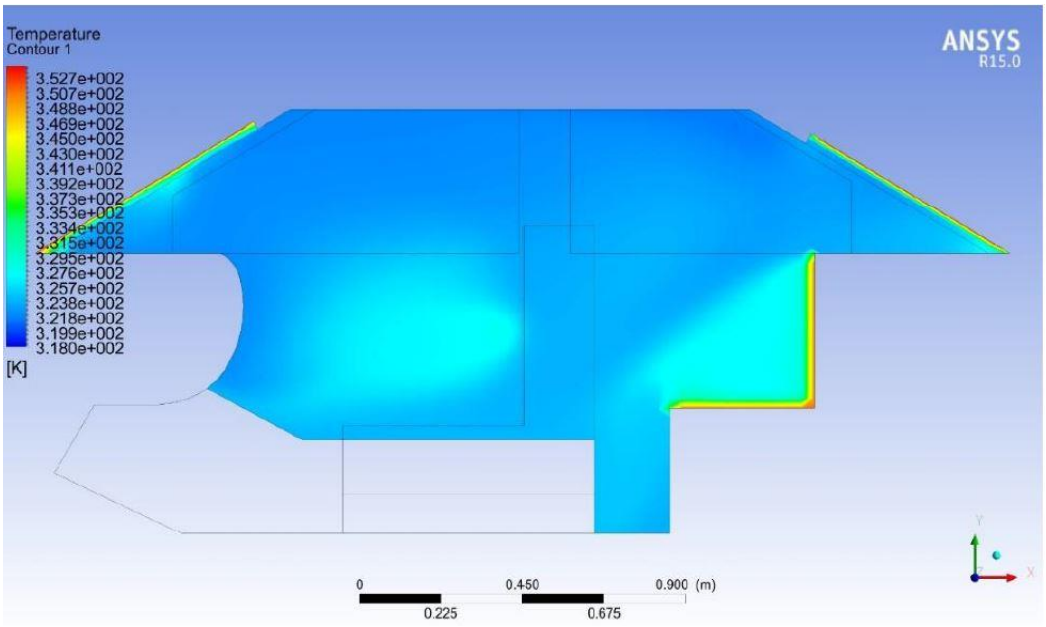


Figure 106. Two plain fans temperature distribution at 150 seconds

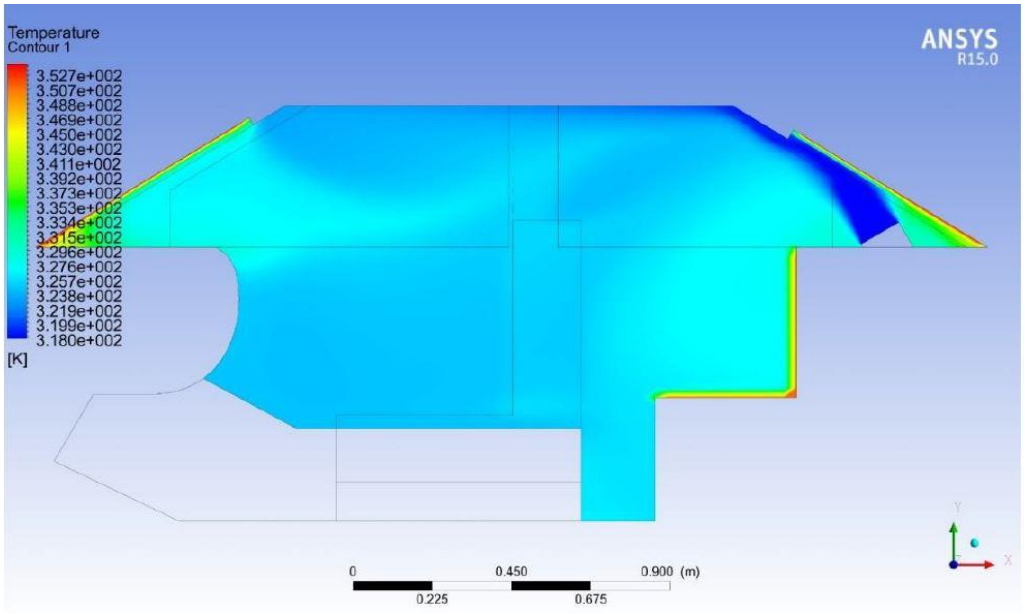


Figure 107. 30° tilted fan temperature distribution at 150 seconds

From the figures (9-14), the following justification can be noticed:

- The temperature distribution of the two plain fans is better and the temperature drop is higher than the other two cases proving that ventilation is best served using two fans.
- The effect of the rear glass on air streamlines in the case of a plain fan causes air to move to the middle of the cabin which can be considered a targeted area, however, it lacks the efficiency of ventilation and heat removal due to the major losses kinetic energy of air caused by the stagnation of the air streamlines by the rear glass.
- In the 30° tilted fan the air moves parallel to the roof of the cabin and when the streamlines reach the front glass area it pushes the high temperature streamlines to the front targeted area (driver seat). Also, the rear passenger seats heated up even more due to the poor air distribution in rear cabin part.

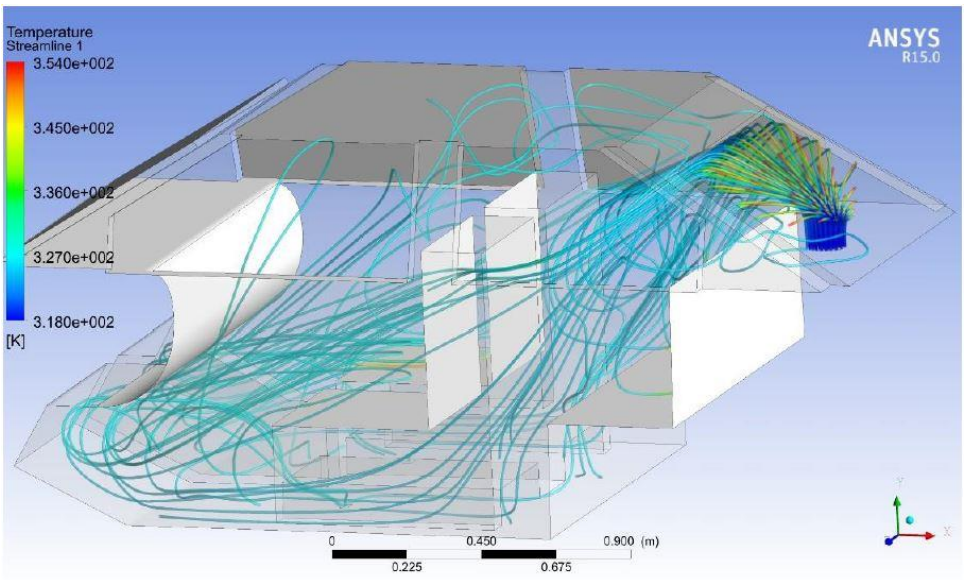


Figure 108. 3D streamlines of air distribution in plain fan case

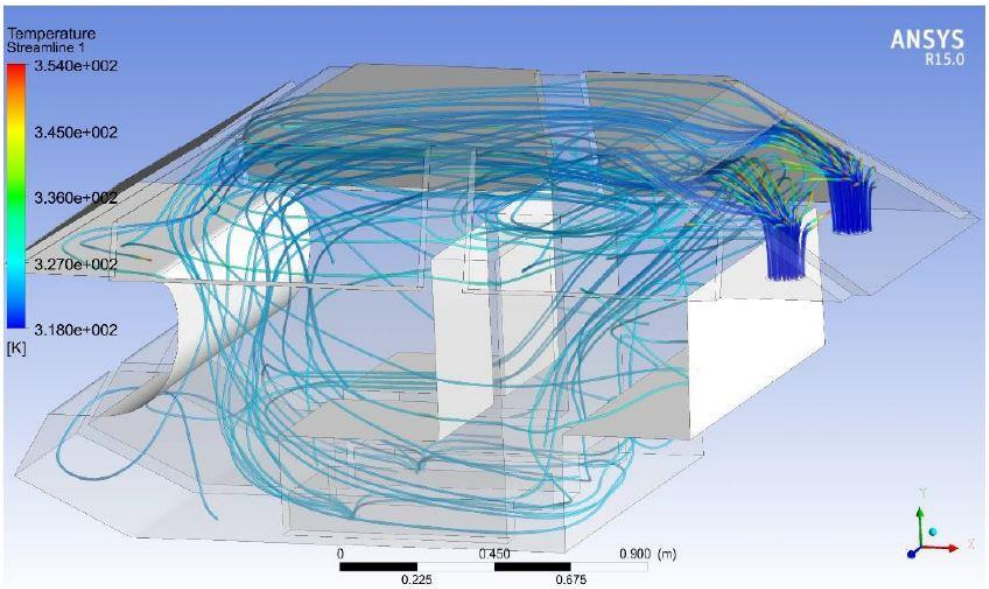


Figure 109. 3D streamlines of air distribution in two plain fans case

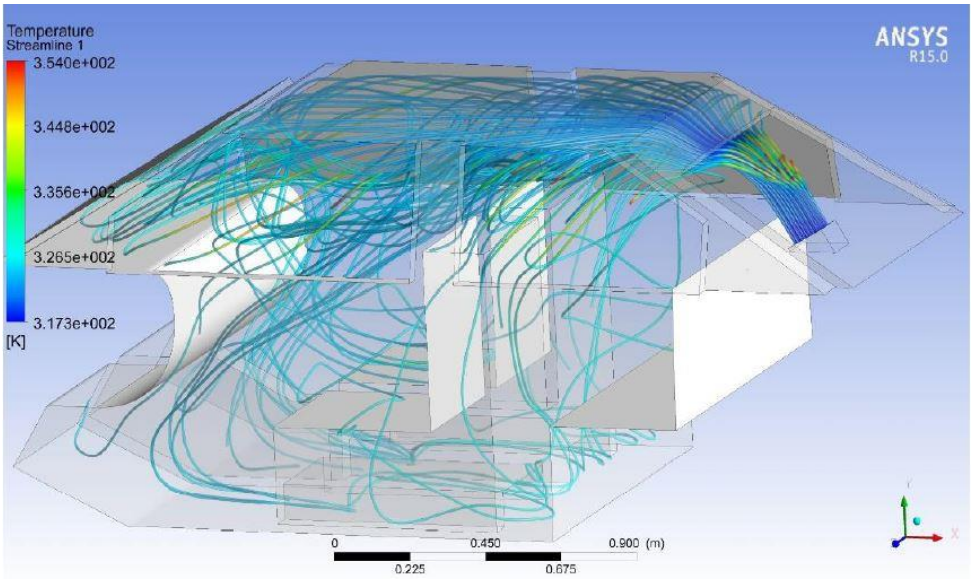


Figure 110. 3D streamlines of air distribution in 30deg tilted fan case

The average temperature was calculated from the same 4 sensors points, mentioned before. Figure (15), is showing the difference of temperature distribution between the three cases.

As observed, the average temperature was initially increasing; due to the heat distribution that occurs initially inside the compartment when the fans are operating. Though, the two plain fans achieved the highest efficiency of ventilation and heat removal. The average temperature of the compartment after 150 seconds in the three cases are:

- For Plain fan: 53°C
- For two plain fans: 51°C
- For the 30deg tilted fan: 52°C

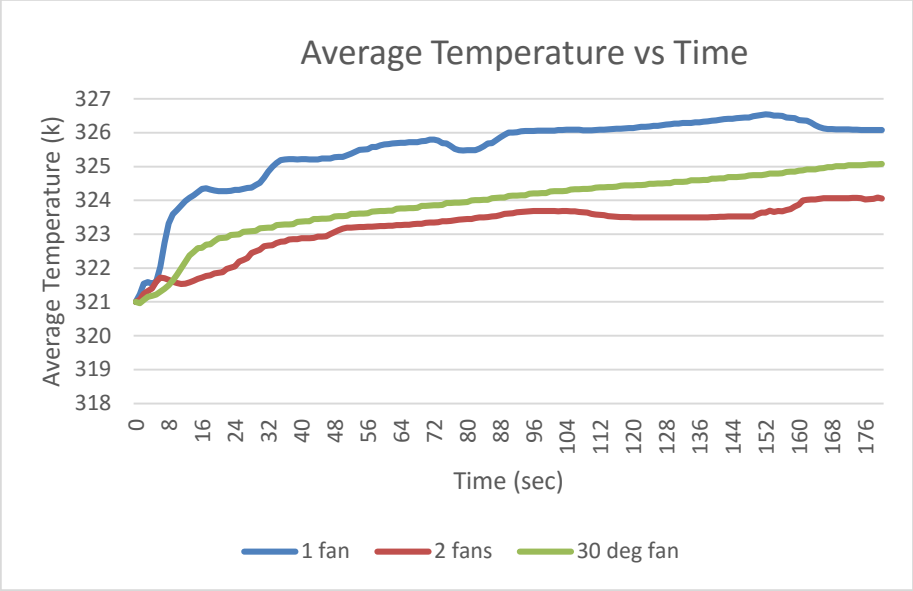


Figure 111. Average temperature for the 3 cases vs time

It may be noted that the difference between the three cases did not exceed 2°C. Which- to the driver and passenger- would not be noticeable. Thus, for economic concerns, the plain fan was used to fabricate the prototype. and it will be used as the proposed option for this system.

5. Experimental Setup

The first step to fabricate and manufacture the prototype was to scale down the actual model into a smaller prototype for the purpose of minimizing the total cost of manufacturing. A scale of 1:3 was used and 2D drawings was prepared with the necessary dimensions for the manufacturing procedure. It may be noted that all the circular sections of the actual model were removed and replaced with sharp squared edges in order to simplify the procedure. Then the cooling load was calculated for the prototype to determine the required fan flow rate. Which is found to be 14.77 CFM.

The heat flux calculations were not necessary at this stage because the prototype was manufactured for the purpose of testing the system reliability and performance.

The process used L-angle steel to make a skeleton of the prototype then this skeleton was covered using mild steel sheets, as shown in figure (16), due its availability and low price in market. The sheet metal was attached by means of welding. After the process if finished. The two outlet holes were drilled.



Figure 112. Manufacturing process of the prototype

After finishing the manufacturing process, the prototype was covered with black paint to enhance the heat transfer in order for the sensors later on to heat up in a much faster rate. Then this prototype shown in figure (17), was covered internally with Aluminum foil-EPE foam insulator mats with thickness of 5mm. the insulator was installed in order to achieve the assumption of restricting the heat from the glass only.

Then a 5mm SGG ANTELIO clear glass was installed produced by Saint-Gobain Co.Ltd [6]. With a solar factor of 0.81 which expresses the transmissivity of the glass.



Figure 113. Glass and insulation installed in the prototype

The electronic system used in the prototype consist of the following:

- Arduino Uno Board
- LCD shield
- Type LM35 temperature sensors
- 12V battery
- Type ULN2003 transistor array driver IC
- 5x7 cm PCB board
- 50x50x20 mm axial cooling fan.

The above components represent the complete electronic control system, where the Arduino board is programmed by means of a computer code (C/C++) to read the

temperature from 4 sensors located in the four points specified above and take their average then subtract that value from the outside temperature and based on that difference the Arduino board will send a 5V signal to the ULN2003 driver which will convert it into a 12V signal to feed the cooling fan. The function of the LCD shield is only to display the average temperature and outside temperature of the prototype.

The 12V battery is directly connected to the ULN driver which feeds the fan. The axial fan (figure (18)) used was found in local market with a flow rate of 20 CFM, 0.4A supply current and equipped with PWM ball bearings.



Figure 114. AVC axial fan used in experiment

After writing the code for the Arduino board and connecting all these components together using jumper wires then a test was conducted to ensure the system is operating correctly. As shown in the figure (19).

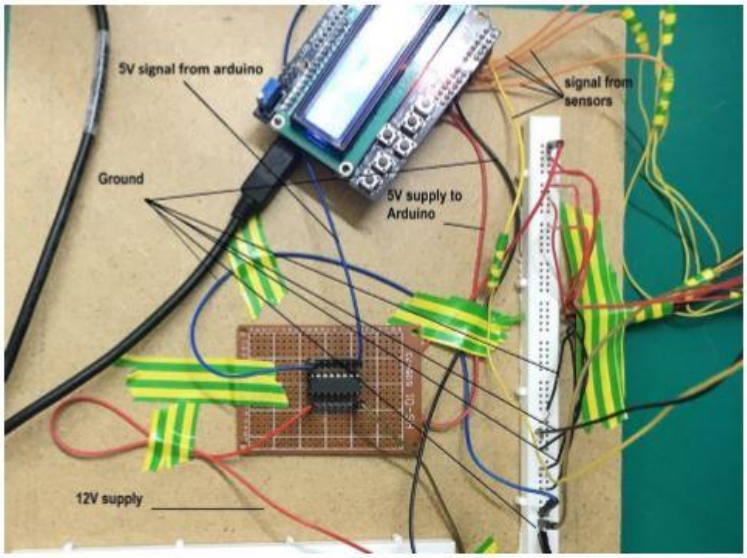


Figure 115. Electronic control system

8. 5.1 Experimental Results

The results above were taken from the prototype after several experiments, and they vary from the numerical results because the readings were taken manually by the use of a stop watch. The fan operates based on a code written to discharge air when the temperature exceeds 3°C.

When the fan is observed during operation it fluctuates as the signal amplitude fluctuates (figure (20)), in order to maintain the difference between the inside and outside below 3°C.

The other reasons for the difference between the experimental and numerical can be concluded in points.

1. There was no heat sink (front and rear seat) that convert into heat sources and emit heat to the compartment.
2. The insulation used in the prototype did not express the real case scenario. It was only installed to restrict heat from glass only as assumed in the cooling load calculation.
3. Other than that, the material used to manufacture the prototype has different thermal conductivity and absorptivity than assumed.
4. The fan used in the experiment was purchased from the local market and did not match the fan selected for the simulations.

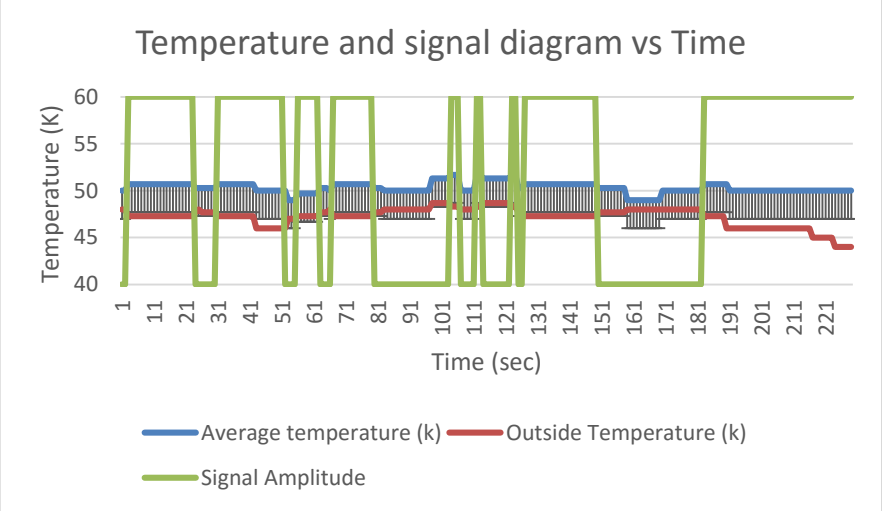


Figure 20. Temperature and signal diagram

9. 6. System Commercialization

For this system to be commercialized in the future the total cost of the system to be calculated, and from order placement bills it's found to be $65 USD. Divided as shown in table (3).

Table 59. Total cost of the System

Component	**Cost (USD)**
Arduino board	15
LCD Shield	09
LM35 sensors x5	10
ULN2003 Driver	02
12V Battery	12
Jumper wires	02
PCB board	02
31 pins needed	02
The axial cooling fan for the actual model	11

If the system is to be designed and produced in a production line the capital cost would be less because components ordered in large quantities have less setup, carrying

and purchasing costs. And this cost will be the same for the actual model as the model and prototype have different fans only. All other components are the same.

7. Conclusion and Discussion

Two approaches were utilized and used to address the problem of high temperature rise inside a vehicle's compartment which may cause severe health problems. A numerical approach to simulate a solution to this problem and resulted in a temperature drop of over 20℃, using an axial flow fan with air velocity of 6.28 m/s. the simulation was executed on three different cases for the fan. The most convenient case technically and economically was used a plain horizontal fan. Further than that an experiment was done on a scaled down prototype.

The experiment was executed to demonstrate the working principle of the ventilation system, and to show that it can be fully automated without any human interactions.

According to observations and analysis, there are two reasons explaining why the ventilation system as a whole could not reach the ambient temperature. The first one is the transient Heat flux; when the temperature inside the compartment increase, the heat flux decreases to a point near zero, this would be also true in the case of cooling when the temperature decreases the heat flux will increase to make up for the heat loss due ventilation. Thus, the ventilation system will stop in a point where it cannot drop below it. The second reason is the Air Capacity; the inlet of the vehicle is relatively small resulting in a stagnant air stream in some areas, when the air consumes all of its heat capacity, it will not be able to draw any more heat out of the car. Thus, to maintain an internal temperature similar to the ambient there are three possible choices to decide from. Increasing the outlet size, cooling air to a temperature below the ambient before it enters the compartment or reducing the distance between the fans and targeted areas to minimize the losses in kinetic energy.

Acknowledgments

We Acknowledge the department of mechanical engineering at the university of Khartoum for funding this projects, we are also thankful for Eng. Hussam Hassan for assisting us with the electronic matters of this project.

References

[1] "*Heat Trapped inside cars a greater health risk than infectious diseases*," May 2007. [Online, accessed December2015]. Available: http://www.vaccinationinformationnetwork.com/heat- trappedinside-cars-a-greater-health-risk-than-infectious-diseases/.

[2] Innovage, "*Innovage Company Solar Ventilator*," Innovage Company, [Online]. Available: http://www.innovage.com/SolarVentilator. [Accessed January 2016].

[3] M.A.Fayazbakhsh and M. Brahami, (2013). *Comprehensive Modeling of Vehicle Air Conditioning Loads Using Heat Balance Method*, vol. I, pp. 3-5, SAE International

[4] N. Elbadawi,Z. Elhadi and Z. Noureldeen. (2014).*Car Solar Ventilation System to Avoid Glass Overheating,* Final Year Project Report, University of Khartoum, Sudan.

[5] K. M.U, (1999). *Development of a Ventilation technique to limit the car cabin temperature under a blazing sun*, vol. Japan, p. University of Toyama.

[6] S. Gobain, "*SGG Antelio clear glass*," Saint Gobain, [Online, accessed December 2015]. Available:http://uk.saint-gobain-glass.com/trade-customers/glass-and-solar-radiation.

eureca 2017 – Conference Paper
Paper Number EUG21

PCM Based Thermal Energy Storage System Integrated with Solar Parabolic Through Collector

S.Raja[1*], S.Prakash[1], R.Gokulnath[1], A.Krishnamoorthy[1], J.Lillymercy[1]
[1]*School of Mechanical engineering, Sathyabama University, Chennai, India*

**Corresponding author: rajha93@gmail.com*

Abstract

In thermal systems such as solar thermal and waste heat recovery systems, the available energy supply does not usually coincide in time with the process demand. Hence some form of thermal energy storage (TES) is necessary for the most effective utilization of the energy source. TES is the temporary storage of high or low-temperature energy for later use. Among the available technologies for the thermal storage systems, latent heat storage (LHS) systems, using phase change material (PCM) as storage medium, are attractive due to their advantages such as high heat storage capacity and isothermal behavior during charging and discharging processes. The objective of this research work is to study the performance of a TES unit which stores heat energy from available heat sources such as solar heater. For experimental purpose, a solar parabolic trough collector is used as a heat source. A TES unit of 10MJ capacity is designed and fabricated for storing heat and supply hot water for family of 5 to 6 persons. The TES unit contains paraffin as PCM filled in spherical capsules, packed in an insulated storage tank. Water and HP Hytherm 600 are used as Heat Transfer Fluids (HTFs) to transfer heat from the solar parabolic trough collector to the storage tank and also they act as a sensible heat storage material. For different mass flow rates of heat transfer fluid, charging experiments were carried out to verify functioning of the TES unit. It is observed that heat is stored in PCM and water up to a temperature of 65^{o}C when TES unit is connected with heat source (solar parabolic trough collector) and it is also observed that charging time is less when Hytherm 600 is used as HTF compared to that of water.

Keywords: PCM, Thermal energy storage, parabolic trough collector, Hytherm 600.

1. Introduction

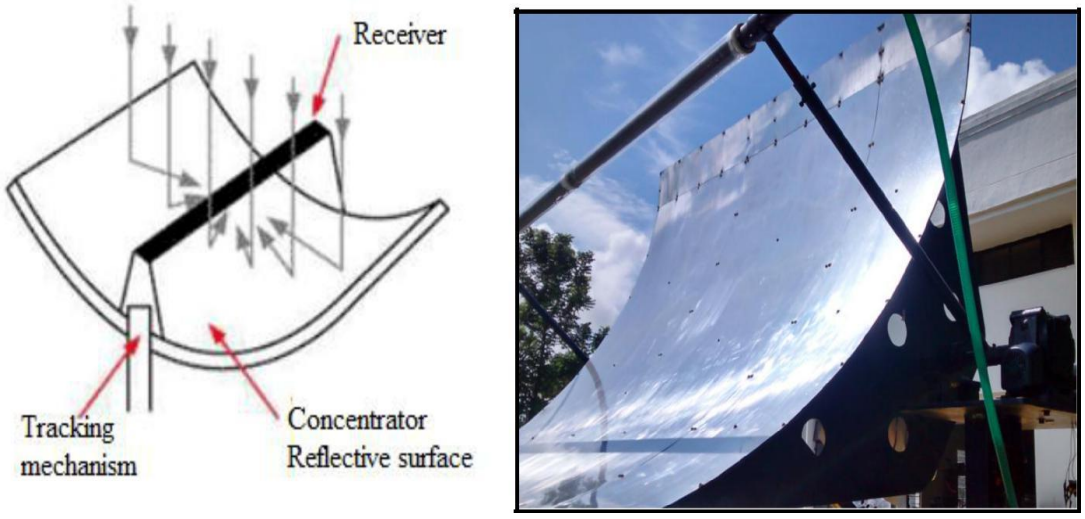
The energy demands in the commercial, industrial and utility sectors vary on daily, weekly and seasonal basis. Energy storage units can be used with energy management systems to reduce energy consumption in commercial and industrial establishments by using available waste heat or alternate energy sources (solar energy). Thermal Energy Storage (TES) is one of the key technologies for energy conservation and has recently been developed to a point where it can have a significant impact on modern technologies. TES is the temporary storage of high or low-temperature energy for later use and it appears to be the most appropriate method for correcting the mismatch that occurs between the supply and demand of energy. Increasing societal energy demands, shortages of fossil fuels, and concerns over environmental impact are providing impetus to the development of renewable energy sources such as solar, biomass and wind technologies [1,2]. Because of their intermittent nature, effective utilization of these and other energy sources is in part dependent on the availability of efficient and effective energy storage systems. In particular, solar energy, being non-polluting, clean and inexhaustible, has received wide attention among scientists and engineers. Mazloumi et al. [3] proposed that the collector mass flow rate has negligible effect on minimum collector area and has significant effect on optimal capacity of storage tank. The high efficiency of the PTC and high flux density of the heat pipe results in lightness when compared to flat plate and evacuated tube collector systems [4,5]. A Saade et al. [6] suggested that by using fiber reinforced material as parabolic trough material and coated with Aluminium foil then the instantaneous efficiency gets increased. The heat transfer analysis and numerical modeling of the PTC is essential to optimize and to understand its performance effectively. The collector efficiency will be better when the absorber tube is coated with black chrome, but it is less significant when compared to cermet coating on absorber material [7-10]. Vellaisamy Kumaresan et al. [11] noted the effect of carbon nanotubes in enhancing the thermal transport properties of PCM during solidification. They have found that enhancement in the thermal conductivity of 30–45% is achieved both in the liquid and solid states of the Nano fluid phase change material compared to that of pure PCM. They have also found that the presence of carbon nanotubes in the PCM at the interior locations suppresses the higher conductive resistance offered by the solidified PCM, and the sub cooling of the PCM that occurs near the wall surface. Though there are many advantages, an important factor is that solar energy is time dependent energy source with an intermittent character. The energy needs for a wide variety of applications are also time dependent, but in a different pattern and phase from the solar energy supply. This implies that solar energy based device or utility must be matched dynamically both at the source point and the application point. Once the characteristics of end-use demand and the nature of energy source option are known, the total demand and supply in the time domain have to be brought together through integration of an efficient energy storage and distribution network. Hence the commercial acceptance and economics of solar thermal systems are tied to the design and development of efficient thermal energy storage (TES) systems. Among non-concentrating collectors, the PVT solar collectors show the best overall performance and the molten salts with excellent properties are considered to be the ideal materials for high-temperature thermal storage applications [12-15].There are many applications where there is a time mismatch between energy availability and demand. In such applications TES systems are of great importance. The other applications of TES are the storage of solar energy for overnight heating, the storage of summer heat for winter use, the storage of winter ice for space cooling in the summer, and the storage

of heat or coolness generated electrically during off-peak hours for use during subsequent peak hours. TES systems have enormous potential to facilitate more effective use of thermal energy equipment and large-scale energy substitutions in the economic perspective. It is therefore a very attractive technology for meeting society's needs and desires for more efficient and environmentally benign energy use. The use of TES systems for thermal applications such as heating and cooling has recently received much attention. In various energy sectors the potential benefits of TES for heating and cooling applications have been fully realized. Although these systems provide energy at a higher cost than fossil fuels, the major advantages are their limited impact on the environment and sustainability of the energy source [16-19].

2. Materials and methods

2.1 Parabolic Trough Collector (PTC)

The PTC system uses mirrored surfaces of a linear parabolic reflector to focus direct solar radiation onto a tubular solar receiver. The receiver is positioned along the focal line of the parabola, and it mainly consists of an absorber tube and a glass cover. The concentrated solar radiation is absorbed and converted into thermal energy by the heat transfer fluid (HTF) flowing through the absorber tube, while the protecting evacuated glass cover is used to reduce the convection heat loss from the absorber. Figure 1(a) shows the schematic view of the parabolic trough collector. In this work a solar PTC of 7.5 m^2 area is used for collecting solar energy. The Photographic view of parabolic trough collector is shown in Figure 1(b). Table 1 shows the specifications of PTC used in this experiment.



(a) (b)

Figure 1. (a) Schematic view of Parabolic trough collector (b) Photographic view of Parabolic trough collector

2.2 Tracking mechanism

A tracking mechanism must be reliable and able to follow the sun with a certain degree of accuracy, return the collector to its original position at the end of the day or during the night, and also track during periods of intermittent cloud cover. Additionally, tracking mechanisms are used for the protection of collectors, i.e. they turn the collector out of focus to protect it from the hazardous environmental and working conditions, like wind dust, overheating and failure of the thermal fluid flow mechanism. It is sufficient to use a single axis tracking of the sun and thus long collector modules are produced. The collector can be orientated in an east–west direction, tracking the sun from north to south, or orientated in a north–south direction and tracking the sun from east to west. The advantages of the former tracking mode is that very little collector adjustment is required during the day and the full aperture always faces the sun at noon time but the collector performance during the early and late hours of the day is greatly reduced due to large incidence angles (cosine loss). North–south orientated troughs have their highest cosine loss at noon and the lowest in the mornings and evenings when the sun is due east or due west. Over the period of one year, a horizontal north–south trough field usually collects slightly more energy than a horizontal east–west one. However, the north–south field collects a lot of energy in summer and much less in winter. Therefore, the choice of orientation usually depends on the application and whether more energy is needed during summer or during winter. Figure 2 shows the tracking control unit.

Table 1. Specifications of parabolic trough collector

S.No	Parameters	Value	Units
1	Aperture area of the PT reflector	7.5	m^2
2	Aperture width.	2.5	m
3	Aperture length	3	m
4	Rim angle	70	Deg.
5	Focal length of PTC	0.9	m
6	Length of glass envelope	3	m
7	Length of absorber tube	4	m
8	Absorber tube	D_o=0.06 D_i=0.052	m
9	Glass envelope	D_o=0.085 D_i=0.08	m
10	Collector material	Al sheet(mirror polished)	mm
11	Absorber tube material	Stainless steel coated with heat resistant black paint	
12	Support structure	Mild steel	

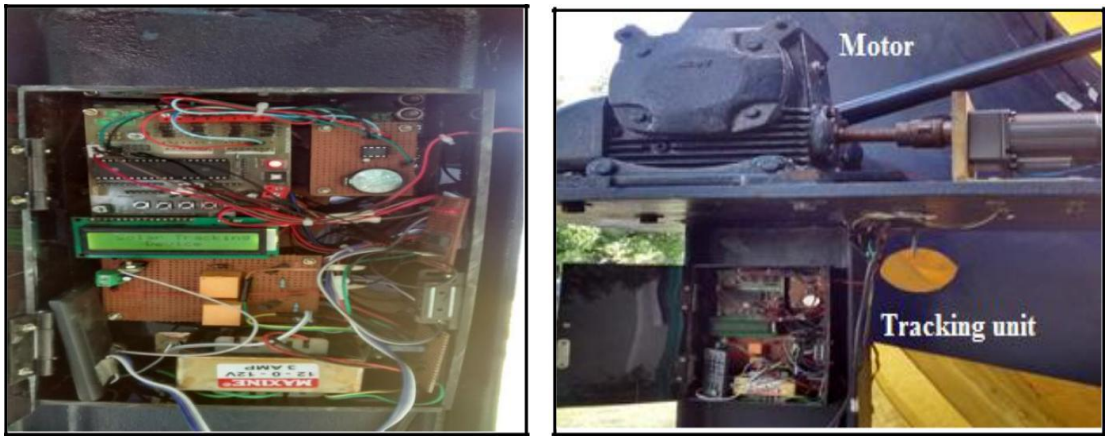


Figure 2. Tracking control unit

2.3 Heat transfer fluids

Water and HP Hytherm 600 are used as Heat Transfer Fluids (HTFs) to transfer heat from the solar parabolic trough collector to the storage tank and also they act as a sensible heat storage material. Water act as excellent heat transfer fluid in low temperature applications (< 90^{o}C) such as domestic heating, hospital sterilization purposes etc. Hytherm 600 is recommended in services where bulk operating temperatures go up to 305°C even replacing some synthetic products. This product finds extensive application in textile, pharmaceuticals, chemical and processing industries. The physiochemical properties of water and HP Hytherm 600 are compared in Table 2.

Table 2. Physiochemical properties of water and HP Hytherm 600

PARAMETERS	WATER	HP HYTHERM 600
Boiling Point (^{o}C)	100	305
Density (kg/m^{3})	997.1	828.57
Thermal conductivity(W/m K)	0.611	0.12
Specific heat (kJ/kg k)	4.187	3.102

2.4 Experimental setup

A schematic diagram of the experimental set-up is shown in Figure 3. Figure 4 shows the photographic view of the experimental set up. It consists of an insulated cylindrical TES tank, which contains PCM encapsulated spherical capsules, constant temperature bath, solar PTC, storage tank, flow meter, and circulating pump. The cylindrical TES tank is made of stainless steel and has a capacity of 60 litres with a diameter of 370 mm and height of 530 mm. There are two plenum chambers on the top and the bottom of the tank and a flow distributor is provided on the top of the tank to make the HTF flow uniform.

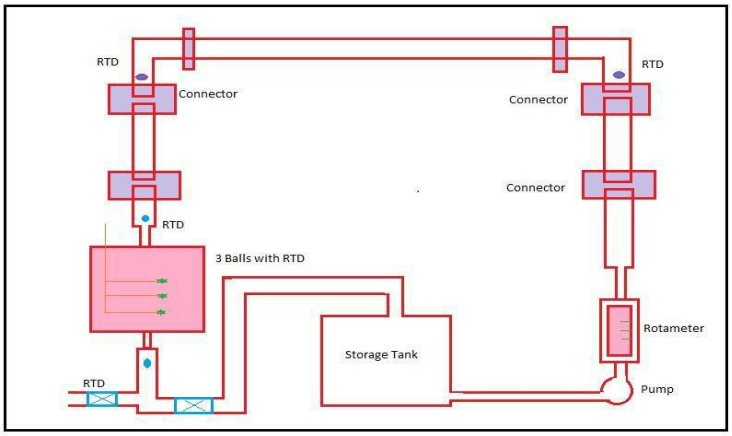


Figure 3. Schematic view of experimental set-up

The storage tank is insulated with asbestos material of 8 mm thick and provided with aluminium cladding. Spherical capsules made of high-density polyethylene (HDPE) are used as PCM containers as spherical shape gives the best performance among the various types of containers. The outer diameter of spherical capsule is 60 mm and its wall thickness is 0.8 mm. The total number of capsules in the TES tank is 196. The spherical capsules are uniformly packed in seven rows and a wire mesh supports each row. In the analysis two rows of spherical capsules are considered as one segment. The PCM capsules occupy 67% of the total volume (test section) of storage tank and the remaining volume is occupied by SHS material i.e. water in the present work. The TES tank is divided into three segments along its axial direction and the RTDs (resistance temperature detectors, type Pt. 100) with an accuracy of 0.1^{o}C are placed at the inlet, outlet and three segments of the TES tank to measure the temperatures of HTF. Another three numbers of RTDs are inserted into the PCM capsules and they are placed at three segments of the TES tank to measure the temperatures of PCM. The position and number of RTDs are also designated in Figure 2. The RTDs are connected to a temperature indicator, which provides instantaneous digital outputs.

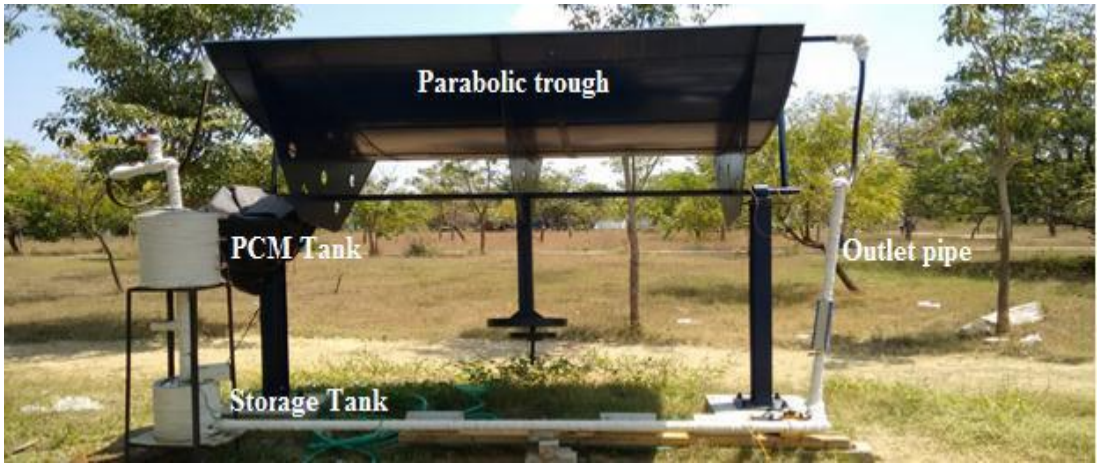


Figure 4. Photographic view of Experimental Setup

2.4 Experimental procedure

The experiments were conducted for six different days in the month of March at Chennai. The Solar Radiation values for six different days are shown in Table 3. The charging experiments are carried out on the storage system with a varying inlet heat source (solar parabolic trough collector). The HTF inlet temperature varies in accordance with the solar radiation. During the charging process, the HTF is circulated through the TES tank continuously and it exchanges its energy to PCM capsules. In the beginning of the charging process, the temperature of the PCM inside the packed bed capsules is in between 30^{o}C and 32^{o}C, which is lower than the melting temperature. Initially the energy is stored inside the capsules as sensible heat until the PCM reaches its melting temperature. As the charging process proceeds, energy storage is achieved by melting the PCM at a constant temperature. Finally the PCM becomes superheated. The energy is then stored as sensible heat in liquid PCM. Temperature of the PCM and HTF at different locations of the TES tank, as shown is recorded at an interval of 20 minutes. The charging process is continued until the thermal equilibrium is attained between HTF and PCM temperatures.

Table 3. Solar Radiation values for six different days

Day	Solar Radiation (MJ/m^2/day)
1	23.24
2	22.56
3	23.72
4	23.30
5	22.84
6	23.42

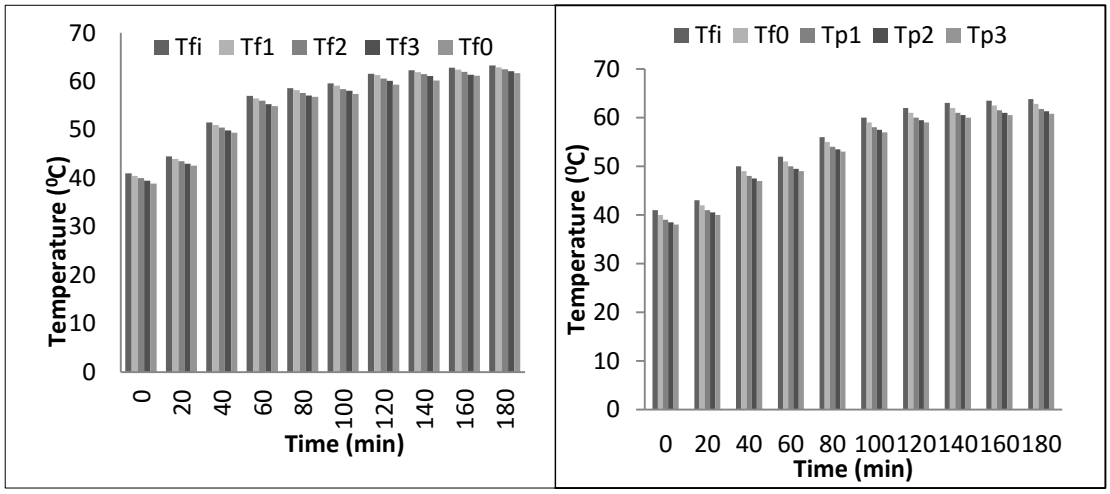
3. Results and discussions

In this experimental work, water and HP Hytherm 600 are used as heat transfer fluids (HTFs) to transfer the heat from solar parabolic trough collector to the storage tank. The temperature distribution of HTFs and PCM in the TES tank, for various mass flow rates are reported and compared during the charging process. Various parameters like Total energy stored in TES tank, useful heat gain, collector efficiency are reported in detail. The charging processes are conducted for the combination of various parameters of mass flow rates for two different heat transfer fluids (Water and HP Hytherm 600) by varying the flow rates in the range of 2, 4 and 6 liters per minute.

3.1 Water and PCM temperatures

The variation of HTF and PCM temperatures at three segments of the TES tank, that is at x/L = 0.3, 0.6 and 0.9 are shown in figures when the storage tank is connected to the solar PTC. Tfi and Tf0 denote the inlet and outlet temperatures of heat transfer fluid respectively whereas Tf1, Tf2 and Tf3 represent the HTF temperatures at three segments of the tank respectively. Tp1, Tp2 and Tf3 represent the PCM temperatures at three segments of the tank respectively. The graphs are drawn for the charging

duration, which represents the time from the beginning of the charging process till the last segment (x/L = 0.9) attains thermal equilibrium with the inlet HTF. The inlet temperature of HTF from the solar PTC increases continuously with time at a uniform rate till the PCM in the storage tank attains the phase change temperature. The water temperature in the storage tank increases gradually in accordance with the inlet temperature of HTF supplied from the solar collector and the PCM temperature also increases gradually along with the HTF temperature.



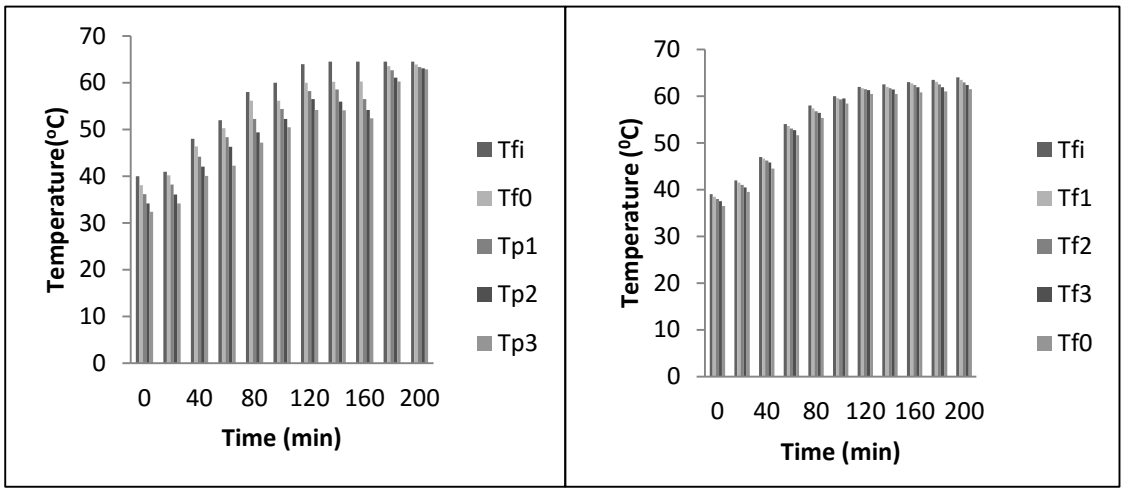
(a) (b)

Figure 5: (a) Variation of HTF temperature (Water) with time for a flow rate of 2 lpm (b) variation of PCM temperature with time for a flow rate of 2 lpm

Figure 5(a) represents the variation of HTF temperature inside the storage tank for a flow rate of 2 lpm. It is observed from the figure that the temperature of the HTF at all the segments increases at a faster rate until it reaches the melting temperature of PCM. However, the rise in temperature of HTF in the first segment is very fast as the hot water enters at the top of the storage tank. For this segment the temperature increases up to 65^{o}C in 120 minutes and thereafter remains uniform until the PCM melts completely. It is also observed that a constant temperature difference exist between the segments from top to bottom of the storage tank throughout the period of melting. The temperature of the second segment attains the temperature of the first segment only after the melting process is completed in the first segment. The same trend is observed in the successive segments. This is due to the fact that, after complete melting of the PCM in the first segment, the rate of heat absorbed in the first segment decreases as the local temperature difference between the inlet fluid and PCM in the first segment decreases. Hence the heat transfer in the second segment increases and the temperature also increases.

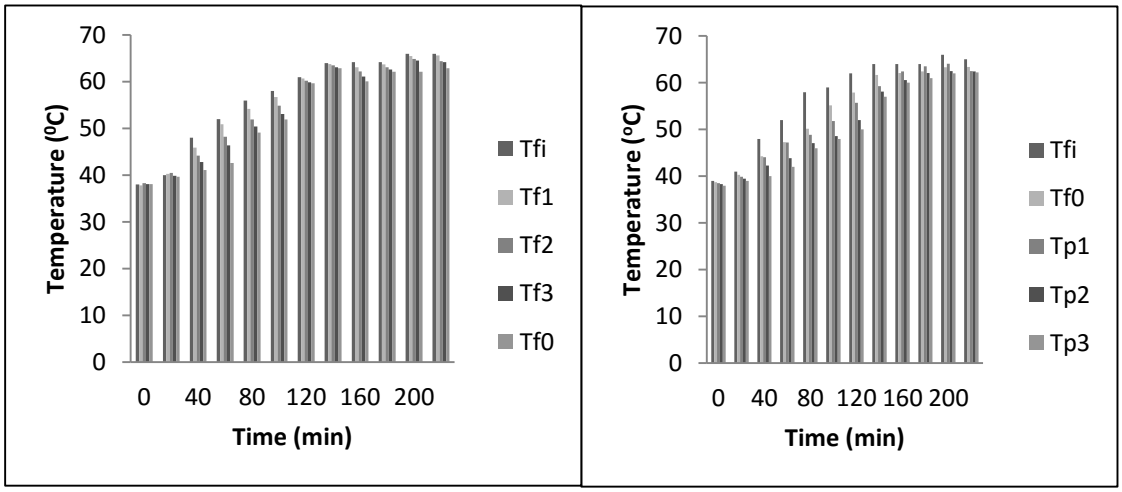
Figure 5(b) represents the variation of PCM temperature for a flow rate of 2 lpm. It is seen from the figure that the PCM temperature increases gradually at the beginning of the charging period and remains nearly constant (58 to 62^{o}C) during melting process and increases rapidly during heating of liquid PCM. Also, it is noted from the figure that the PCM in the first segment is completely charged within 65% of the total charging time of 180 minutes. Figure 6(a) and 7(a) shows the variation of HTF (water)

temperature with time inside the storage tank for a flow rate of 4 and 6 lpm respectively whereas variation of PCM temperature with time for a flow rate of 4 and 6 lpm is shown in Figure 6(b) and 7(b) respectively.



(a) (b)

Figure 6: (a) Variation of HTF temperature (Water) with time for a flow rate of 4 lpm (b) variation of PCM temperature with time for a flow rate of 4 lpm



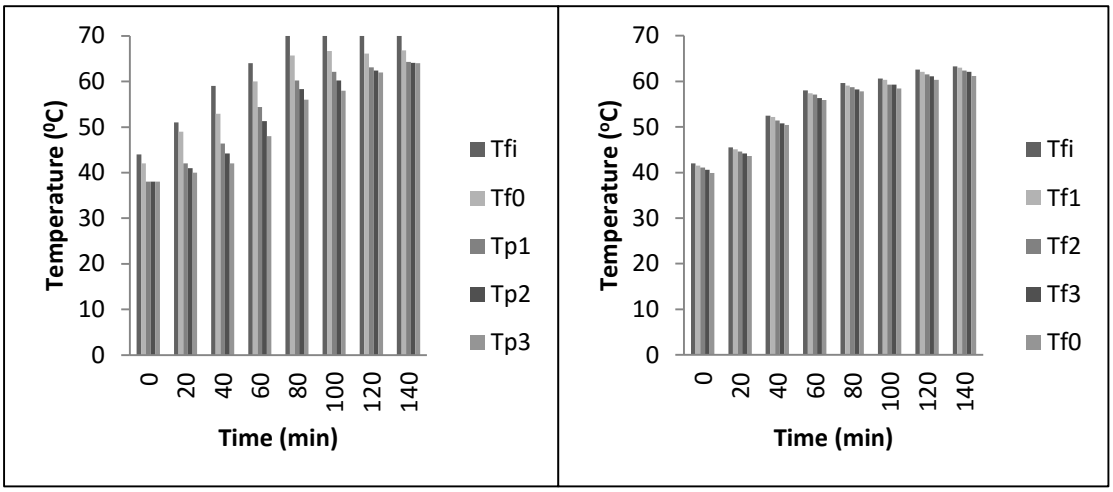
(a) (b)

Figure 7: (a) Variation of HTF temperature (Water) with time for a flow rate of 6 lpm (b) variation of PCM temperature with time for a flow rate of 6 lpm

3.2 HP HYTHERM 600 and PCM temperatures

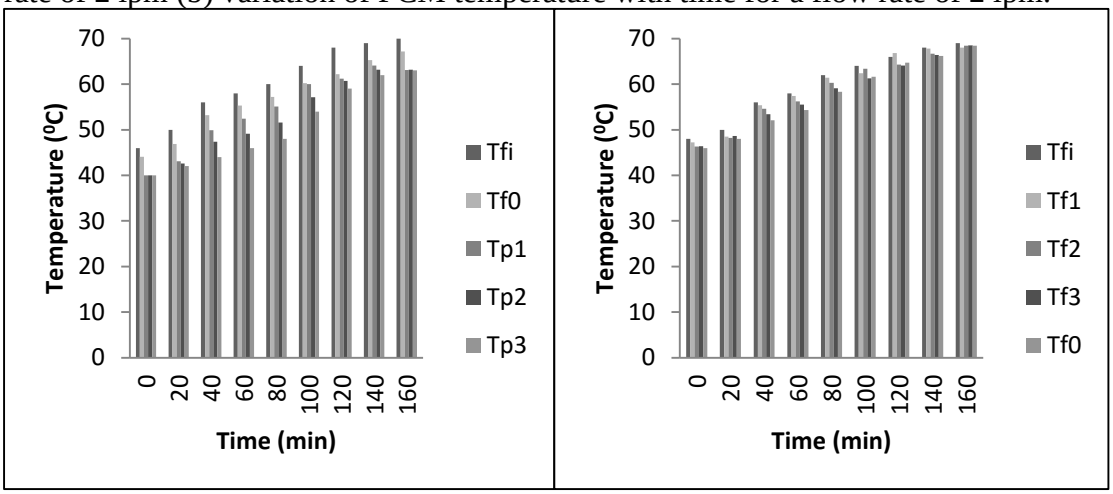
The charging process is repeated for the same mass flow rate with Hytherm 600 as the Heat transfer fluid. The corresponding graphs are drawn and the variations of HTF and PCM temperatures at the segments of the TES tank for Hytherm 600 are shown in Figures 7, 8 and 9. The charging time of heat storage in PCM for water as HTF is 180,

200 and 220 minutes at flow rates of 2, 4 and 6 lpm respectively, whereas for Hytherm 600 the charging time is 140, 160 and 180 minutes at flow rates of 2, 4 and 6 lpm respectively.



(a) (b)

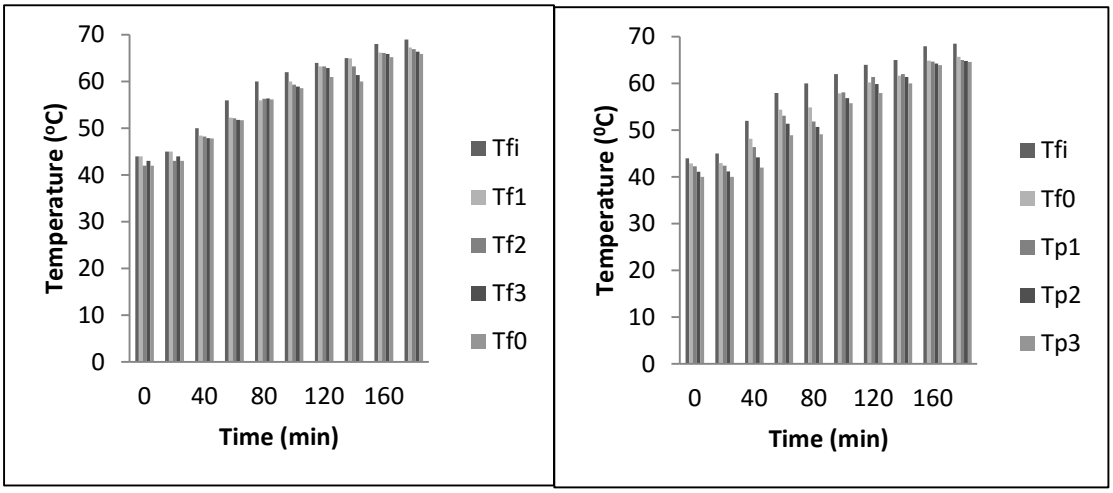
Figure 8: (a) Variation of HTF (HYTHERM 600) temperature with time for a flow rate of 2 lpm (b) variation of PCM temperature with time for a flow rate of 2 lpm.



(a) (b)

Figure 9: (a) Variation of HTF (HYTHERM 600) temperature with time for a flow rate of 4 lpm (b) variation of PCM temperature with time for a flow rate of 4 lpm

Figure 8(a), 9(a) and 10(a) shows the variation of HTF (HYTHERM 600) temperature with time inside the storage tank for a flow rate of 2, 4 and 6 lpm respectively whereas variation of PCM temperature with time for a flow rate of 2, 4 and 6 lpm is shown in Figure 8(b), 9(b) and 10(b) respectively. From the above graphs it is observed that the charging time for HP Hytherm 600 as HTF is less compared to water. This is due to the fact that Thermal diffusivity for HP Hytherm 600 is more compared to that of water.



(a) (b)

Figure 10: (a) Variation of HTF (HYTHERM 600) temperature with time for a flow rate of 6 lpm (b) variation of PCM temperature with time for a flow rate of 6 lpm

3.3 Performance parameters

The various performance parameters like collector's useful heat gain, collector efficiency, total energy stored in TES unit, and overall efficiency are calculated for both the heat transfer fluids (water and HP Hytherm 600) with flow rate of 4 lpm and compared. Table 3 shows the comparison of performance parameters for both the heat transfer fluids (water and HP Hytherm 600).

Table 3. Performance parameters for water and HP Hytherm 600

Parameters	Units	Water	Hytherm 600
Useful heat gain	W	3344	2056
Useful heat gain	%	49.5	30.45
Total energy stored in TES tank	kJ	6752.083	5278.97
Overall efficiency	%	27.90	21.72

The above parameters indicate that water is proven effective heat transfer fluid for low temperature applications such as domestic water heating, hospital sterilizations and chemical laboratories etc. where the temperature requirement is less than 90°C.

4. Conclusion

A thermal energy storage system using combined sensible and latent storage concept was developed for storing heat energy from solar PTC and use the hot water at an average temperature of 45°C for domestic applications. A series of charging experiments were conducted on the TES unit to study its performance by integrating it with solar parabolic trough collector. The significance of time wise variation of

HTF inlet temperature and mass flow rate on the system performance was reported. The following conclusions are summarized as follows

- In the Analysis of the temperature distribution of the HTF in the storage tank during melting process, it is found that the temperature of the bottom segment attains the temperature of the previous segment, only after the melting process is completed in the top segment. This is due to the fact that, after the complete melting of the PCM in the top segment, the rate of heat absorbed in the top segment decreases as the local temperature difference between the HTF and PCM in the top segment decreases. Hence the heat transfer in the bottom segment increases and the temperature also increases.
- The existence of thermal stratification in the combined storage tank improves the collector efficiency and hence the system efficiency.
- The charging time duration for water at a flow rate of 2 lpm is 180 minutes and for HP Hytherm 600 it is 140 minutes. This is due to the higher thermal diffusivity of Hytherm 600 when compared with water.
- In the present analysis, water and paraffin are selected as sensible heat and latent heat storage materials respectively. Such systems can be adopted, where the requirement of heat is within the temperature range of 50-80^{o}C. For higher temperature applications, Hytherm 600 is more suitable. Many applications are possible with the combined sensible and latent heat storage system like waste heat recovery utilization, food preservation and air conditioning applications, electronic cooling etc. Each application requires careful attention in the selection of PCM materials and the design of the storage system.

References

[1] Govindaraj Kumaresan, Rahulram Sridhar, Ramalingom velraj. (2012) ‘Performance studies of a solar parabolic trough collector with a thermal energy storage system’, Energy Vol.47, pp.395-402.

[2] Giorgio Cau, Daniele Cocco. (2014) ‘Comparison of medium-size concentrating solar power plants based on parabolic trough and linear Fresnel collectors’, Energy Procedia 45, 101 – 110.

[3] Mazloumi, Kalogirou. (2008), ‘Simulation of solar lithium bromide-water absorption cooling system with parabolic trough collector’, Energy Conservation and Management 49, 2820-2832.

[4] El Fadar, A. Mimet a, M. Perez-Garcıa. (2009) ‘Study of an adsorption refrigeration system powered by parabolic trough collector and coupled with a heat pipe’, Renewable Energy 34, 2271–2279.

[5] O.A. Jaramillo, E. Venegas-Reyes, J.O. Aguilar , R. Castrejón-García , F. Sosa Montemayor. (2013) ‘Parabolic trough concentrators for low enthalpy processes’, Renewable Energy 60, 529-539.

[6] Atul A Saade, Sadiq, B. (2013) ‘Performance evaluation of low cost FRP parabolic trough reflector with mild steel receiver’, International journal of energy and environmental engineering.

[7] Vasquez Padilla, Gokmen Demirkaya, D. Yogi Goswami, Elias Stefanakos, (2011) 'Heat transfer analysis of a parabolic trough solar receiver', Applied Energy 88, 5097-5110.

[8] Soteris Kalogirous. (1996), 'Parabolic trough collector system for low temperature steam generation Design and performance characteristics', Applied energy, Vol. 55, Issue 1, pp.1-19.

[9] Sarada Kuravi, Jamie Trahan, Yogi Goswami, D. Muhammad Rahman, M, and Elias stefanakos, K. (2013), 'Thermal energy storage technologies and systems for concentrating solar power plants', Progress in energy and combustion scince 39, pp.285- 319.

[10] Govindaraj kumaresan, Rahulram Sridhar,and Ramalingam velraj. (2012) 'Performance studies of a solar parabolic trough collector with a thermal energy storage system', Energy Vol.47, issue 1, pp.395-402.

[11] Vellaisamy kumaresan, ramalingam velraj. (2012) 'The effect of carbon Nanotubes in enhacing the thermal transport properties of PCM during solidification', Heat mass transfer Vol 48, pp.1345-1355.

[12] Soteris kalogirou, A. (2004) 'Solar thermal collectors and applications', Progress in Energy and combustion science Vol 30, pp.231-295.

[13] Tian, Y. and Zhao, C.Y. (2013) ' A review of solar collectors and thermal energy in solar thermal applications', Applied energy 104, pp.538-553.

[14] Pei Gang, Ji Jie, and Li jing. (2011) ' Design and analysis of a novel low-temperature solar thermal electric system with two stages collectors and heat storage units', Renewable Energy 36, pp.2324-2333.

[15] Kody powell, M. and Thomas Edgar, F.(2012) ' Modeling and control of a solar Thermal power plant with thermal solar energy storage', Chemical engineering science 71, pp.138-145.

[16] Reddy, K.S, Ravi kumar, K, and Ajay,C.S. (2015) ' Experimental investigation of porous disc enhanced receiver for solar parabolic through collector', Renewable energy 77, pp.308-319.

[17] Mohammed Zadeh, P, Sokhansefan, T, Kasaeian, A.B, Kowsary, F, and Akbarzadeh, A. (2015) ' Hybrid optimization algorithm for thermal analysis in a solar parabolic trough collector based on nanofluid', Energy vol.82, pp.857-864.

[18] Sharma, R.K, Ganesan, P, Tyagi, V.V, Metselaar, H.S.C, and Sandaran, S.C. (2015) ' Developments in organic solid-liquid phase materials and their applications in thermal energy storage', Energy conversion and management Vol 95, pp.193-228.

[19] Qian Xu, Longlong Li, Huairui Li, Weidong Huang, Yongping Li. (2014) 'performance comparision of solar parabolic trough system with glass and film reflector', Energy conversion and management Vol 85, pp.581-590.

eureca 2017 – Conference Paper
Paper Number EUG22

Analysis of Carbon Reinforced Metal Matrix Composite for IC Engine Valves

P. Sivashankari[1*], A. Krishnamoorthy[2**], S. Prakash[3], S. Raja[4], S. Venkatesh[5]
[1*,2,3,4,5] *School of Mechanical Engineering, Sathyabama University, Chennai, TN, India*

*jsrshank1981@gmail.com, **akrish61@gmail.com

Abstract
The automotive industry is driven by the need of building fuel-efficient engines with lighter weight, which has recognized the need for material substitution with outstanding properties. The volumetric efficiency of the engine can influenced to a certain level by designing the valve train, which controls the gas flow, valve timing, size and overlapping. The objective of this analysis is to combine metal matrix composite with a polymer for increasing the tensile strength as well as to reduce the wear and tear, thereby enhancing the mechanical and thermal properties and improving the performance of valve in commercial vehicles. Recent Research shows a better result with metal matrix composite than the existing material. The elemental analysis of the engine valve guides done by using ANSYS software. The results obtained showed the increase in mechanical and thermal properties.

Keywords: Metal matrix composites, Carbon fiber, Reinforcement, Mechanical properties, Thermal properties.

1. Introduction

Composite materials are finding its way into the industry as it adds more weightage and performance to the material property[1]. The start of the technological period has brought the need for new materials to tackle everyday challenges of current materials for different applications[2]. In the way of finding new advanced materials, researchers have innovated various material systems. One of the most promising material systems in the past few decades is Metal Matrix Composite (MMC), where two or more constituents combined to fabricate a new material[3] . By formulating a composite, it is possible to use the unique advantages of different constituents in a harmonizing manner to restrain the limitations of each constituent[1]. The need for lightweight structural material for the applications in the automotive industry and aerospace industry is a need these days. This is partially due to the enforcement of new emission regulations and the rising of fuel expenditure[4]. Traditional materials such as aluminium and titanium are failing to overcome current challenges of ordinary materials that are facing today[5]. The property of materials significantly deteriorates at a relatively low temperature and in turn limits their usability in decisive components[6]. However, by combining intrinsic ductility of matrix and toughness with high stiffness and high specific strength materials, such as ceramic filaments and carbon fibers[7]. The inclusion of such reinforcements into metal matrix composite considerably improves the hardness, tensile strength, compressive strength and other mechanical and thermal properties[8]. Applications of aluminium metal matrix composites include industries such as automotive aerospace and hold the greatest promise for future growth[9].“The Inorganic polymer matrix composite Strength Related to Interference Condition” states that polymer matrix resulted in improvements in both mechanical and thermal properties when compared to existing material[8]. The input parameters were standard and the results obtained showed better improvements than the existing material. “Carbon Fibers Reinforced Metal Matrix Composites” states that carbon fiber reinforced metal matrix composites possess a great potential to replace existing unreinforced metals[10] and alloys in automobiles and it is essential to consider the properties of the materials used in such applications through which the failure can be analyzed[11]. Due to the enhanced wear resistance and reduced coefficient of friction, they are promising materials for a variety of engineering applications[12]. “Comparative Study of Different Materials with Al-Sic for Engine Valve Guide by Using FEM” stated that Al-Sic composites are suitable to high temperature and pressures such as racing cars, turbo-charged engines, loco aircraft engines where cost isn’t a major factor[13]. “Tribological and mechanical behavior of particulate Aluminium matrix composites” states that mechanical and Tribological properties were better for single reinforcement than pure aluminium and furthermore it was observed that hybrid matrix composites possess a better mechanical and Tribological properties compared to single reinforcement composites[14]. The existing materials used in IC engine valves are include carbon steel alloys, stainless steels, high-strength nickel-chromium-iron alloys and titanium alloys[15]. The temperature, principle strain and stress distribution over the entire surface of the engine valve were acquired[16], [15], [16]. The main importance to choose this material is because of cost reduction and its availability. Since the work concentrates on the automobile industry, it is essential to consider the properties of the materials used in such applications through which the failure can be analyzed. Apart from this, properties such as high strength, corrosion performance, high impact strength and high modulus, ductility and distortion after

machining also play an important part in material selection. However, the exact set of properties and their importance is heavily dependent on the specific component or part and properties like tensile and compressive strength, Young's modulus, corrosion.In this Paper analyzes the mechanical Properties with Aluminium reinforced composite material (MMC) with polymer (CF) for the application of valves. The ANSYS software is used to carry out the finite element analysis of the (MMC) engine valve guide.

2. Methodology

The following process is carried out under utmost safety precaution and care to the samples. The apparatus used for testing purposes that is both mechanical and metallurgy were under ASTM standards. Furthermore the microscopic structure analysis was conducted.

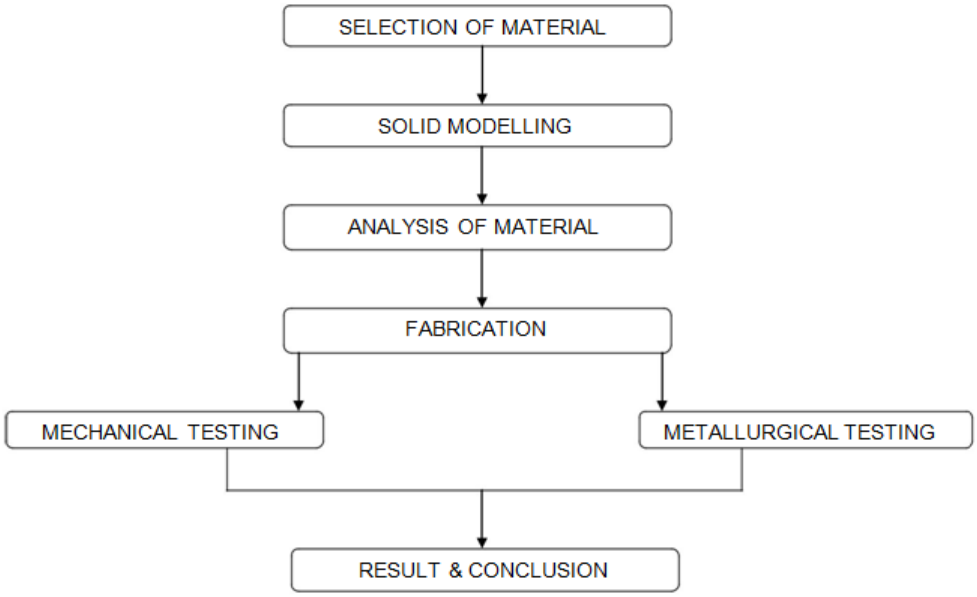


Figure 3.1. Flowchart of the Process

The sample compositions were 83% of aluminium and 7% of Silicon carbide and 10% carbon fibers and for the second sample 82% of aluminium 6% of Silicon carbide and 12% of carbon fibers. Solid model was done using modeling software and later the material was analyzed using ANSYS software under standard input properties of the materials[15]. The fabrication process followed here was stir casting[16], Aluminium powder was poured into the cast at a temperature above 600 ˚C. And allowed to melt completely, simultaneously Silicon Carbide and Carbon fiber powder were taken in the correct proportions and stirred well.



(a) Mixing of CF and Sic with aluminium cast



(b) Cast being poured onto the mould

Figure 3.2. Fabrication Process of the Material

The stirred mixture was preheated up to a certain temperature in order to bond with the Aluminium metal. Stir casting method was followed as it is cost effective and quite simple in terms of getting the weight of the final product [17]–[19]and the most important advantage in this is that, the time processing which is far less compared to other process.

The total elapsed time for the entire process was 90 min and it was noted that amount of Sic present in the mixture resulted in increase in the amount of slack. The cast was poured into the mold with 20mm diameter and 200mm in length after 90 minutes. The mold was left over to cool for almost 30 minutes. The above procedure was performed with almost care.



(a) Tensile test



(b) Compression test.

Figure 3.3. Tensile and Compression test of the Material

Figures show the fabrication process of the material. Fig 1 (a) shows the CF and Sic poured into an aluminium cast (b) cast being poured onto the mold Fig 2 (a) the sample milled for tensile test (b) the sample milled for the compression test.The solid cylinder obtained was machined to desire shape for further testing[17], [20]. The solid cylinder was machined into four different moulds for tensile test, compression test, impact test and thermal conductivity test. Further a 5mm piece from the solid mould was observed for metallurgical testing. Testing was performed with the help of experts and the machines used were under ASTM standards.

3. Experimental Analysis

A hollow cylinder was constructed using the modeling software Creo Parametric and this model was analyzed in the analyzing software ansys under standard input

parameters. The results obtained were positive and matched the existing material. The above image shows the meshed FEM of engine valve guide used for analysis. A hollow cylinder was considered in place of valve and further test were performed. The input values that were given during FEA analysis were as follows. Temperature 35°C-250°C, tensile strength for the material was given as 3100 MPa and the compressive strength 400 GPa.

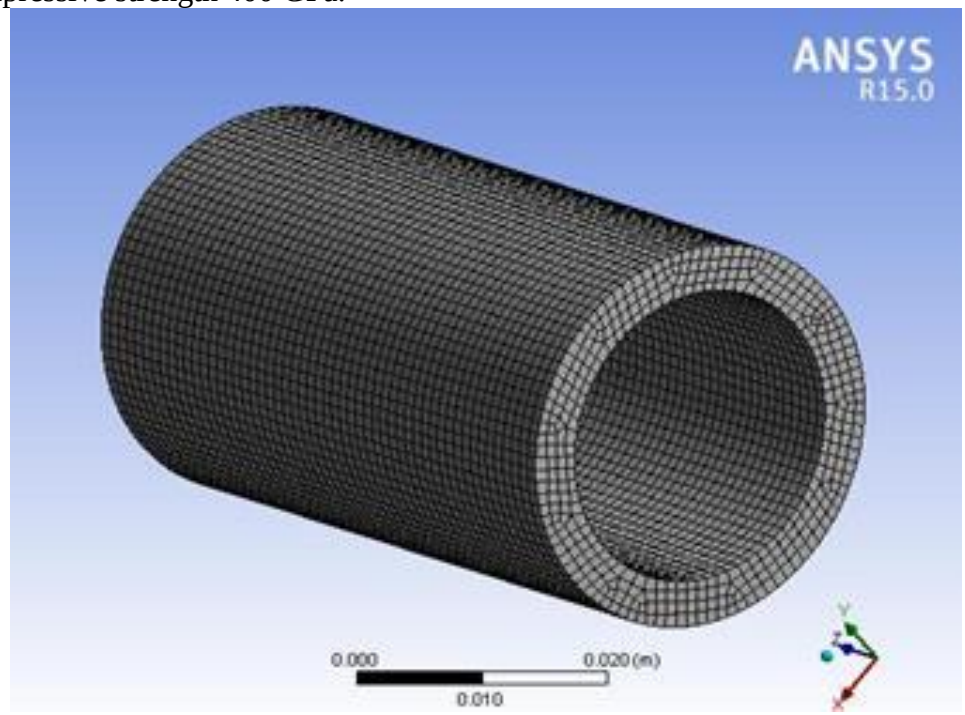
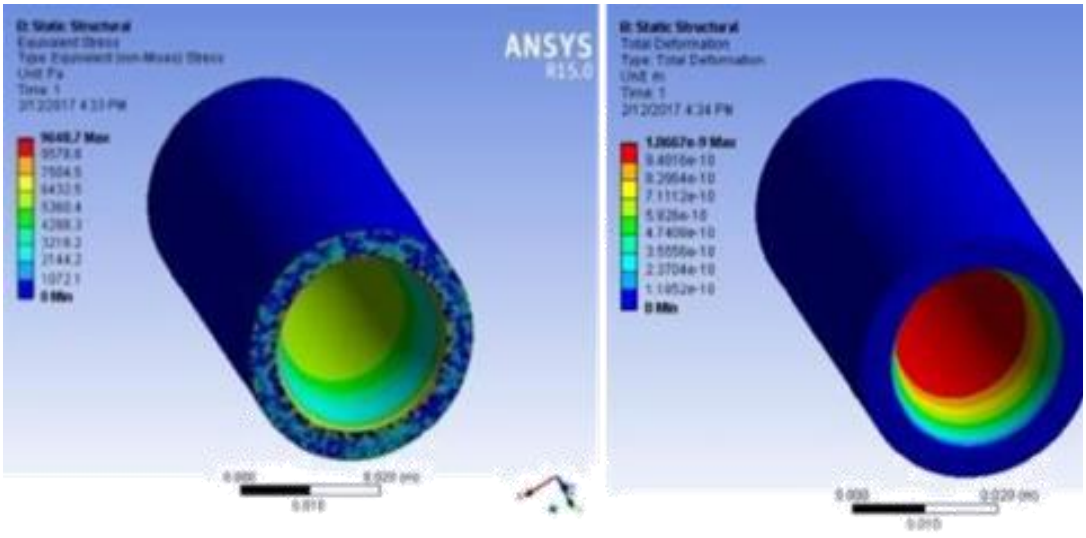
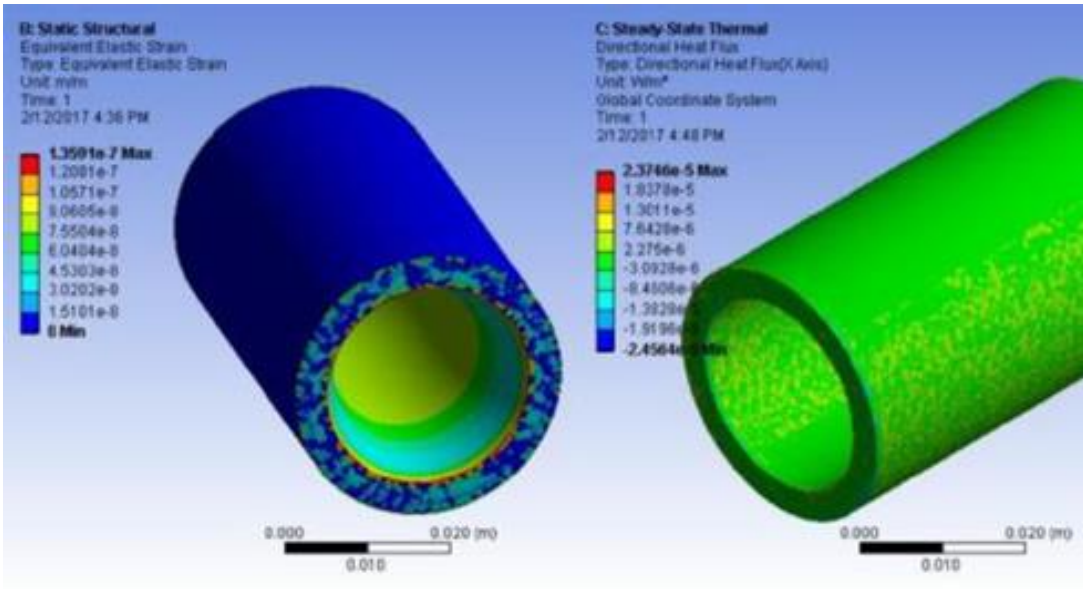


Fig: 4.1: FEM of Engine Valve Guide used for the Analysis

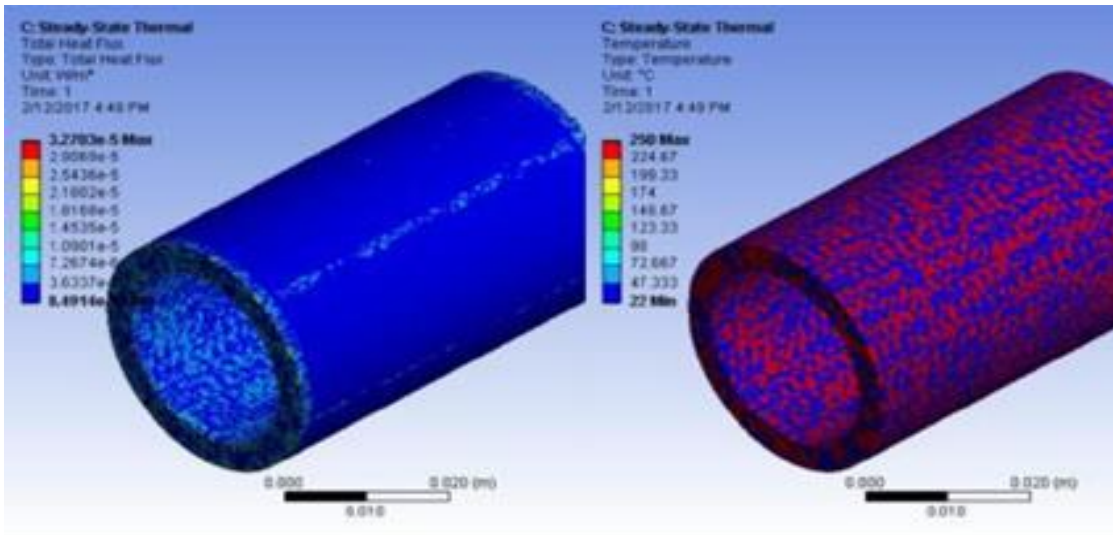


(A) Von Misses Stress On The Surface

(B) Total Deformation On The Surface



(C) Equivalent Elastic Strain On The Surface (D) Directional Heat Flux On The Surface

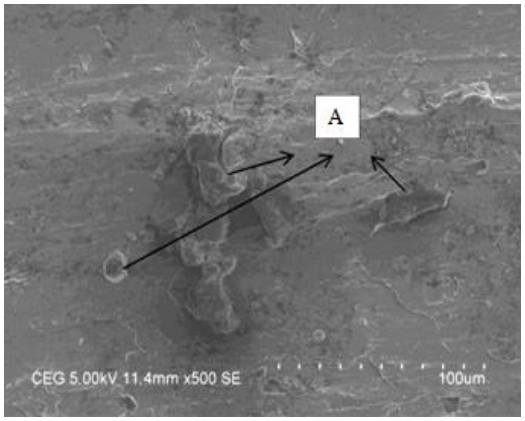


(E) Total Heat Flux On The Surface (F) Temperature Distribution On The Surface.

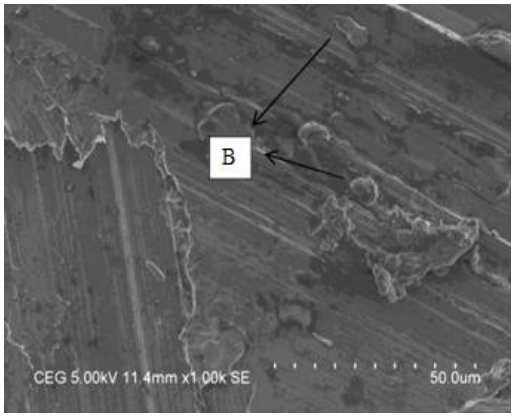
Figure 3. FEA Evaluation

The Figure 3 shows the Von Misses Stress distribution, Total Deformation on the Surface, Equivalent Elastic Strain, directional heat flux and total heat flux along with the temperature distribution on the surface. The experimental analysis was conducted using the analytical software ANSYS and the results obtained for static structural such as Von-Misses stress on the surface, total deformation on the Surface, Equivalent elastic strain on the surface and for steady state thermal analysis such as directional heat flux on the surface, temperature on the surface, total heat flux on the surface are mentioned below in Figure. The governing equation for the simulation are as follows. $k = 7.789 + 0.0223\Lambda T - 4.388E - .006\Lambda T^2$.

Metallurgy is a domain of materials science and engineering that studies the physical and chemical behavior of metallic elements, their intermetallic compounds, and their mixtures. Metallurgy is subdivided into ferrous metallurgy (sometimes also known as black metallurgy) and non-ferrous metallurgy or colored metallurgy. Ferrous metallurgy involves processes and alloys based on iron while non-ferrous metallurgy involves processes and alloys based on other metals.



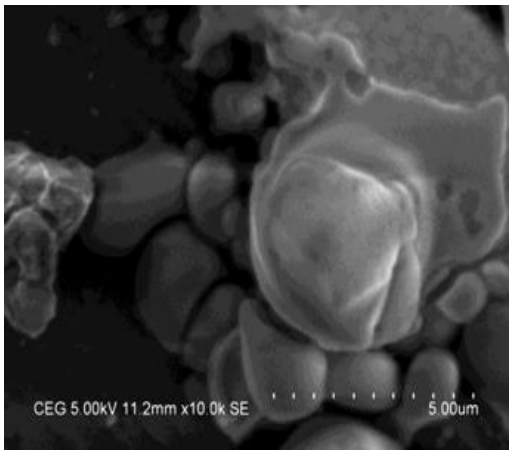
(a)SEM of MMC with 10%CF



(b) SEM of MMC with 12%CF



(c) SEM of MMC with 12%CF



(d) SEM of MMC with 12%CF

Figure 4. Metallurgical testing results

Fig 4 shows the metallurgical testing results (SEM analysis) of the material which was conducted at various scales to determine the fibre structure on the surface of the material (a) SEM of MMC with 10%CF (b) SEM of MMC with 10% CF (c) SEM of MMC with 12% CF (d) SEM of MMC with 12% CF. Further mechanical properties and thermal properties obtained for the material was obtained and the results were found to be matching the existing material as shown in table 1

Table 1. Mechanical and thermal properties of test materials.

Properties	MMC with CF 10%	MMC with CF 12%
Rockwell Hardness Test	54.66	62.06
Impact Test(J)	7	9
Ult. Tensile Strength(N/mm^2)	340.203	304.218
Ult.CompressiveStrength(N/mm^2)	336.464	298.568
Conductivity(W/mK)	121.63	124.31

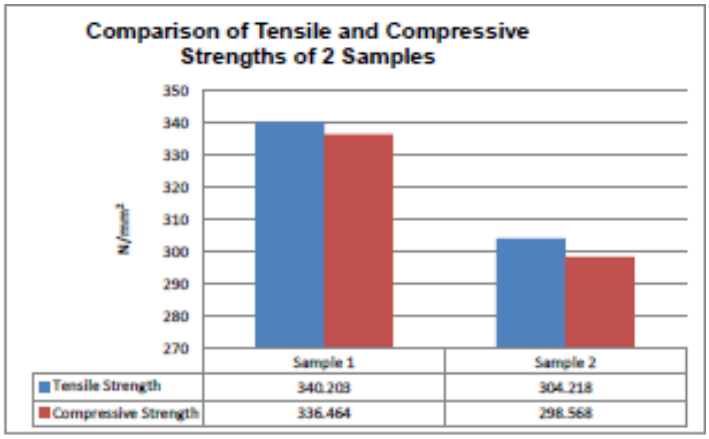


Fig: 4.8: Comparison of Tensile and Compressive Strengths of 2 samples

4. Conclusion

The FEA analysis results were positive and the maximum and minimum Von-Misses stress values found in the engine valve guide were 0 Pa and 9648.7 Pa respectively. The maximum and minimum Total Deformation values found in the engine valve guide were 0 m and 1.0667E-09 m respectively. The maximum and minimum Equivalent elastic strain values found in the engine valve guide were 0m/m and 1.3591E-07 m/m respectively. It was observed that steady state mechanical properties matched the existing material. The Directional heat flux decreases from the cylinder side to the outer side. The Directional heat flux values are -2.4564E-05 W/m^2 and 2.3746E-05 W/m^2. The temperature distribution was observed and found to be safe. The Total heat flux decreases from the cylinder side to the outer side. The respective Total heat flux values are -8.4914E-06 W/m^2 and 3.2703E-05 W/m^2. It was observed that steady state thermal properties of the material proved to be safe under normal working conditions. The Microstructure image clearly shows the fiber structure in spherodized form in both the samples. It was further observed that Sample 1 showed higher physical properties when compared to existing material by 21% in tensile and 29% in compressive strength. The impact strength when compared to existing material showed an increase of 3J and the hardness of the material showed to be almost the same. The thermal properties of the sample showed an improvement of 26%.It was further observed that Sample 2 showed

higher physical properties when compared to existing material by 11% in tensile and 15% in compressive strength. The impact strength when compared to existing material showed an increase of 5J and the hardness of the material showed a 17%. The thermal properties of the sample showed an improvementof 29%. When compared between both the samples, Sample 1 showed a higher percentage is stresses by 22% and showed a reduction in thermal and impact properties by 7%. The hardness of sample 2 showed a 9% higher than sample 2. But further research is required in order to find more optimized results and other materials can be used as a substitute which may produce a better result.

References

[1] N. Chawla, Y.-L. Shen, O. Perez, G. Patriarche, M. Lancin, O. Perez, G. Patriarche, M. Lancin, B. V. Ramnath, C. Elanchezhian, M. Jaivignesh, S. Rajesh, C. Parswajinan, A. S. A. Ghias, T. Shalu, E. Abhilash, M. A. Joseph, and M. Section, "Particulate reinforced metal matrix composites - a review," *J. Mater. Process. Technol.*, vol. 58, no. 10, pp. 4809–4813, 1991.

[2] O. Perez, G. Patriarche, M. Lancin, O. Perez, G. Patriarche, and M. Lancin, "Interphases and mechanical properties in carbon fibres / Al matrix composites To cite this version :," 1993.

[3] B. V. Ramnath, C. Elanchezhian, M. Jaivignesh, S. Rajesh, C. Parswajinan, and A. S. A. Ghias, "Evaluation of Mechanical Properties of Aluminium Alloy- Alumina-Boron Carbide Metal Matrix Composites," *J. Mater.*, vol. 58, pp. 332–338, 2014.

[4] N. Chawla and Y.-L. Shen, "Mechanical Behavior of Particle Reinforced Metal Matrix Composites," *Adv. Eng. Mater.*, vol. 3, no. 6, pp. 357–370, 2001.

[5] T. Shalu, E. Abhilash, and M. A. Joseph, "Development and characterization of liquid carbon fibre reinforced aluminium matrix composite," *J. Mater. Process. Technol.*, vol. 209, no. 10, pp. 4809–4813, 2009.

[6] M. G. McKimpson and T. E. Scott, "Processing and properties of metal matrix composites containing discontinuous reinforcement," *Mater. Sci. Eng. A*, vol. 107, pp. 93–106, 1989.

[7] M. M. Dave and K. D. Kothariengineering, "CompositeMaterial-AluminiumSiliconAlloy:A Review."

[8] D. W. Radford, A. Grabher, and J. Bridge, "Inorganic Polymer Matrix Composite Strength Related to Interface Condition," *Materials (Basel).*, vol. 2, no. 4, pp. 2216–2227, Dec. 2009.

[9] D. Kotecki, "Welding stainless steel," *Adv. Mater. Process.*, vol. 155, no. 5, pp. 41–44, 1999.

[10] K. Shirvanimoghaddam, S. U. Hamim, M. Karbalaei Akbari, S. M. Fakhrhoseini, H. Khayyam, A. H. Pakseresht, E. Ghasali, M. Zabet, K. S. Munir, S. Jia, J. P. Davim, and M. Naebe, "Carbon fiber reinforced metal matrix composites: Fabrication processes and properties," *Compos. Part A Appl. Sci. Manuf.*, vol. 92, pp. 70–96, Jan. 2017.

[11] J. G. Kaufman, J. G. Kaufman, and J. Gilbert, "Introduction to Aluminum Alloys and Tempers Library of Congress Cataloging-in-Publication Data."

[12] T. Characteristics, A. Rod, and M. Ma, "Tribological Characteristics of Innovative Al6061-Carbon fibre Rod Metal Matrix Composites," *J. Mater.*, vol. 50, pp. 597–605, 2013.

[13] H. Kumar Srivastva, A. Singh Chauhan, M. Kushwaha, A. Raza, P. Bhardwaj,

and V. Raj, “Comparative Study of Different Materials with Al-Sic for Engine Valve Guide by Using FEM,” *World J. Eng. Technol.*, vol. 4, pp. 238–251, 2016.

[14] P. Sharma, D. Khanduja, and S. Sharma, “Tribological and mechanical behavior of particulate aluminum matrix composites,” *J. Reinf. Plast. Compos.*, vol. 33, no. 23, pp. 2192–2202, Dec. 2014.

[15] N. H. Babu and G. S. Naidu, “FEA of Al-SiC composite in engine valve guides,” in *2016 International Conference on Electrical, Electronics, and Optimization Techniques (ICEEOT)*, 2016, pp. 3836–3838.

[16] R. Gangaram Bhandare Ȧ and P. M. Sonawane Ḃ, “Preparation of Aluminium Matrix Composite by using Stir Casting Method & it’s Characterization,” 2014.

[17] C. S. Ramesh and T. B. Prasad, “Friction and Wear Behavior of Graphite-Carbon Short Fiber Reinforced Al–17%Si Alloy Hybrid Composites,” *J. Tribol.*, vol. 131, no. 1, p. 14501, 2009.

[18] M. K. Surappa, “Aluminium matrix composites: Challenges and opportunities,” *Sadhana*, vol. 28, no. 1–2, pp. 319–334, Feb. 2003.

[19] K. Shirvanimoghaddam, H. Khayyam, H. Abdizadeh, M. Karbalaei Akbari, A. H. Pakseresht, E. Ghasali, and M. Naebe, “Boron carbide reinforced aluminium matrix composite: Physical, mechanical characterization and mathematical modelling,” *Mater. Sci. Eng. A*, vol. 658, pp. 135–149, Mar. 2016.

[20] J. Wang, Z. Li, G. Fan, H. Pan, Z. Chen, and D. Zhang, “Reinforcement with graphene nanosheets in aluminum matrix composites,” *Scr. Mater.*, vol. 66, no. 8, pp. 594–597, Apr. 2012.

eureca 2017 – Conference Paper
Paper Number EUG23

X-ray Diffraction Analysis of *Scomberomorus Guttatus*-derived hydroxyapatite and montmorillonite on polylactic acid biocomposite

Hon-Meng Ng[1], Soo-Tueen Bee[1]*, Lee Tin Sin[1]*, Ratnam, C. T.[2], A. R. Rahmat[3]
[1] Department of Chemical Engineering, Lee Kong Chian Faculty of Engineering and Science, Universiti Tunku Abdul Rahman, Bandar Sungai Long, Jalan Sungai Long, 43000 Kajang, Selangor, Malaysia
[2] Radiation Processing Technology Division, Malaysian Nuclear Agency, Bangi, 43000 Kajang, Selangor, Malaysia.
[3] Department of Polymer Engineering, Faculty of Chemical Engineering, Universiti Teknologi Malaysia, 81310 UTM Skudai, Johor, Malaysia.

*Soo-Tueen Bee (direct.beest@gmail.com) and Lee Tin Sin (direct.tinsin@gmail.com)

Abstract
Up to date, the hydroxyapatite (HAp) as synthesized by chemical approaches has been widely investigated to provide reinforcement and bioactive sites for polylactic acid (PLA) as potential for application in bone grafting/regeneration field. However, the effect of HAp as derived from biogenic resources (e.g. fish bone) on polylactic acid has still not been well explored. Moreover, the further addition of HAp into PLA for better reinforcement is usually limited to low amount by its brittle ceramic nature. With an attempt to compensate for insufficient reinforcing effect of limited amount HAp on PLA, the addition of montmorillonite (MMT) as secondary reinforcing agent into PLA/HAp composite is thus proposed in this study. In order to prepare HAp for the synthesis of PLA/HAp/MMT composite, the collected fish bone waste of Mackerel fish (*Scomberomorus Guttatus* spp.) was mainly subjected to water boiling treatment and thermal calcination. The extracted HAp was then identified by several characterization techniques (FTIR, EDX, XRD, TGA) and melt blended with PLA and MMT at various composition using Brabender mixer. To evaluate the incorporation effect of biogenic HAp and MMT on fundamental properties of PLA biocomposites, the crystallographic structure of compounded PLA/HAp/MMT blends was investigated by XRD analysis. Results indicated the good effectiveness of HAp to promote PLA crystallization by the increased crystallinity of neat PLA. Meanwhile, this effect could be further enhanced after the addition of MMT by making the adjacent polymer chains to become closer. As calculated by using relevant XRD data, the increased value of *d*-spacing of MMT with an increase of HAp loading level also revealed the good ability of HAp to promote the intercalation of MMT into PLA matrix. Based on these findings, one can conclude that the fish bone waste derived-HAp and MMT could generate promising synergistic effect on improving the crystallographic structure of PLA.

Keywords: Hydroxyapatite, Biocomposites, Biomedical, Bone, Physical properties.

1. Introduction

Biodegradable polymer, poly (lactic acid) (PLA) which is derived from renewable resources found a favorable niche for application as bone fracture fixation materials in bone regeneration field mainly due to its biodegradation over time; therefore avoiding the second surgery for removal of an implant [1, 2]. The increasing role of PLA in the bone tissue engineering (BTE) also could be due to its degradation at a controlled rate, good processability and availability to produce in various shapes [3, 4]. However, the mechanical properties and thermal stability of PLA are often insufficient for load bearing and industrial applications in BTE [5, 6]. Note that the mechanical strength of biopolymer as candidate for load bearing bone implant should be high enough to match with those of human bone providing mechanical support during initial stage of bone formation [7, 8]. Meanwhile, the high thermal stability is necessary against the thermal degradation during industrial production since the toxic thermal decomposition product of PLA would be harmful to the living cells by trapping in polymer matrix [2, 7, 9]. Nevertheless, inorganic fillers in micro- and nanosizes such as hydroxyapatite (HAp) and nanoclay have been found to tackle above limitations through a small amount of addition, creating PLA composites with enhanced thermo-mechanical properties [2, 5, 10].

The incorporation of HAp ($Ca_{10}(PO_4)_6(OH)_2$) schematically presented in Fig. 1) can improve the mechanical and thermal properties of PLA composite via favorable organic-inorganic interaction between polymer-HAp to restrict polymer chains' mobility and the non-thermal degradable behaviour of HAp in the high temperatures range of 900-1200 °C [11-15]. As a major inorganic component of natural bone, the presence of HAp is also responsible for bone regeneration of composite implant by its promising bioactivity and osteoconductivity [1, 16]. It also makes directly bonds to the regenerated bones without mediatory tissues by the good bone binding ability [1, 17]. These behaviors could compensate for the lack of ability of pure PLA to induce osteogenesis or regeneration function of surrounding bone tissues due to its poor cellular attachment by the hydrophobic nature and absence of cell recognition sites [7, 17, 18]. More importantly, pH buffering effect of basic calcium phosphates ions released from the dissolution of HAp could neutralize the acidic molecules as decomposed from hydrolysis of PLA ester bonds that could induce unfavorable inflammatory response of the in-contact tissue and catalysis of the hydrolytic degradation [2, 9, 19-22]. However, it is common that the mechanical properties of prepared PLA/HAp composite are still lower than that of human bone unless the loading of a larger amount of HAp particles [23, 24]. In real application, however, it is considered impossible to load higher particles amount of HAp for PLA due to its high brittleness as would be aggravated by the increasing content of brittle ceramic filler (%elongation < 1 for HAp), which could result in improper plastic deformation that is necessary to withstand the stresses as imposed from patient's normal activity [25-27]. Thus, an additional reinforcement is necessary to assure the competitive mechanical properties of PLA-based bone graft implant, making the montmorillonite (MMT) to be proposed as the secondary enhancement element on PLA/HAp composite for present research work. As one of the most frequently studied nanoclay in PLA polymer systems, MMT is the most familiar species of smectide group, which consists of two fused tetrahedral silica thin layers sandwiching an edge-shared octahedral sheet of either magnesium or aluminum hydroxide [1, 3, 6, 28, 29]. The enhancement effect of MMT

on mechanical and thermal properties of organic polymer can be attributed to the nano-reinforcement effect of the intercalated/exfoliated layered silicates within polymer matrix and the high heat resistance of clay material [2, 6, 30, 31]. Moreover, the biocompatibility and safety of clays in medical application is widely supported in literature especially their same alkali nature with HAp that is important to neutralize the unfavorable acidic effect of PLA degradation product [3, 20, 32, 33].

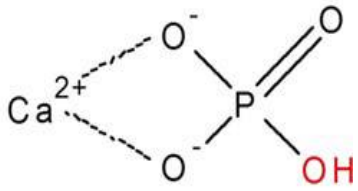


Figure 1. Structural formula of hydroxyapatite.

Under above-mentioned backgrounds, the objective of present investigation is to develop new class of biodegradable material with much better performance, being potentially interesting for bone tissue engineering by adding HAp and MMT as secondary enhancement element into PLA composite. In order to achieve the established goal, it is of interest to study with as much detail as possible the synergistic effect of HAp and MMT on the structure and properties of PLA/HAp/MMT composite through characterizations on crystallographic structure by carrying out the XRD analysis. From the point of view of biomedical application, the present studied HAp filler is proposed to be derived from biogenic resources without involving any chemical precursors as traditionally used for in situ precipitation of HAp considering the health-risk problem of residual chemicals remaining on chemically-synthetic HAp [26, 34-36]. The other problems associated with chemical synthesis also include the high cost laborious process and difficulty to be scaled-up for industrial production [1, 13, 36-38]. More importantly, the reinforcing effect of biogenic HAp on PLA has still not been well explored to the best of our knowledge. Therefore, fish bone of Mackerel fish (*Scomberomorus Guttatus* spp.) was selected as biogenic resource to derive HAp, which is coded as MHAp for current research work. Meanwhile, the behind motivation of present research is also to convert fish bone waste into valuable product seeing the increasing disposal of fish bone from the food processing industry as waste currently that would cause serious environmental problem by the lack of appropriate waste management [39, 40]. As is well known, the easy occurrence of agglomeration of nanosize-filler (such as MMT) in polymer during melt processing was always to be questioned [41]. Thus, the loading level of present studied MMT was maximally bound to 4 phr by referring to the previous studies related to melt compounding of PLA/MMT composite as carried out by Shayan et al., 2015 [42] and Zaidi et al., 2009 [43] which found that the mechanical strength of PLA/MMT nanocomposites increased with an increase of MMT concentration up to 4 wt% but started to agglomerate at 5wt% that would cause the deterioration in properties of PLA composites.

2. Experimental

2.1 Materials

The polylactic acid pellets with injection grade of REVODE 101 (ρ = 1.31 g/cm^3 and MFI = 10–11 g/10 min) was purchased from Zhejiang Hisun Biomaterials Co., Ltd. This PLA was used as the base polymer in this study. The trimethylopropane trimethacrylate (TMPTMA) with industrial-grade containing 175 ppm monomethyl ether hydroquinone was supplied by Sigma–Aldrich (M) Sdn Bhd and was used as the cross-linking promoter in this study. The fish bone waste of Mackerel fish was collected from local restaurant and was used to derive MHAp as primary reinforcement in present study. The commercial grade of montmorillonite (MMT), Nanomer 1.3P was purchased from Nanocor, Arlington Height and was used as secondary reinforcement in PLA/HAp composite.

2.2 Preparation of Hydroxyapatite

The MHAp was obtained from fish bone waste of Mackerel fish after several crucible processes. Importantly, a fish bone without flesh or tissue remnants was necessary to be prepared first from the collected fish bone waste by subjecting to water boiling treatment for 4 hours. Next, the pretreated fish bone was continuously flushed with H_2O to ensure complete tissue removal followed by oven drying until constant weight is obtained. These dried fish bones then underwent thermal calcination process at 800°C for 4 hours in furnace. Afterwards, the calcined fish bones were crunched into HAp powder by using pestle and mortar. The successful extraction of MHAp was be confirmed by characterization techniques: Fourier transform infrared (FTIR) spectroscopy, scanning electron microscopy/energy dispersive X-ray spectroscopy (SEM/EDX), X-ray diffraction (XRD) test and Thermogravimetric analysis (TGA).

2.3 Preparation of Samples

PLA were compounded with MHAp, MMT and TMPTMA using a Brabender mixer at the heating temperature of 135 °C and rotor speed of 50 rpm for a mixing time of 8 min. The loading levels of PLA, MMT and TMPTMA were fixed at 100 phr, 0/2/4 phr and 3 phr, respectively while the loading levels of MHAp were varied from 2 to 10 phr.

2.3 X-ray Diffraction (XRD) Test

The compounded PLA/HAp/MMT blends were further characterized by XRD analysis by using a Shimadzu XRD 6000 diffractometer with CuKα radiation (λ = 1.542 Å) for a range of scattering angles 2θ (3°< 2θ <40°) at a scan rate of 2°/min. The test was performed at 30 kV and 30 mA with a thin-film attachment rotating at a speed of 50 rpm.

3. Results and Discussion

3.1 Characterizations of prepared MHAp

The HAp powder derived from fish bone waste of Mackerel fish (*Scomberomorus Guttatus* spp.) has been characterized by the FTIR, SEM/EDX, XRD and thermogravimetric analysis as shown in Fig. 2 (a)-(d).

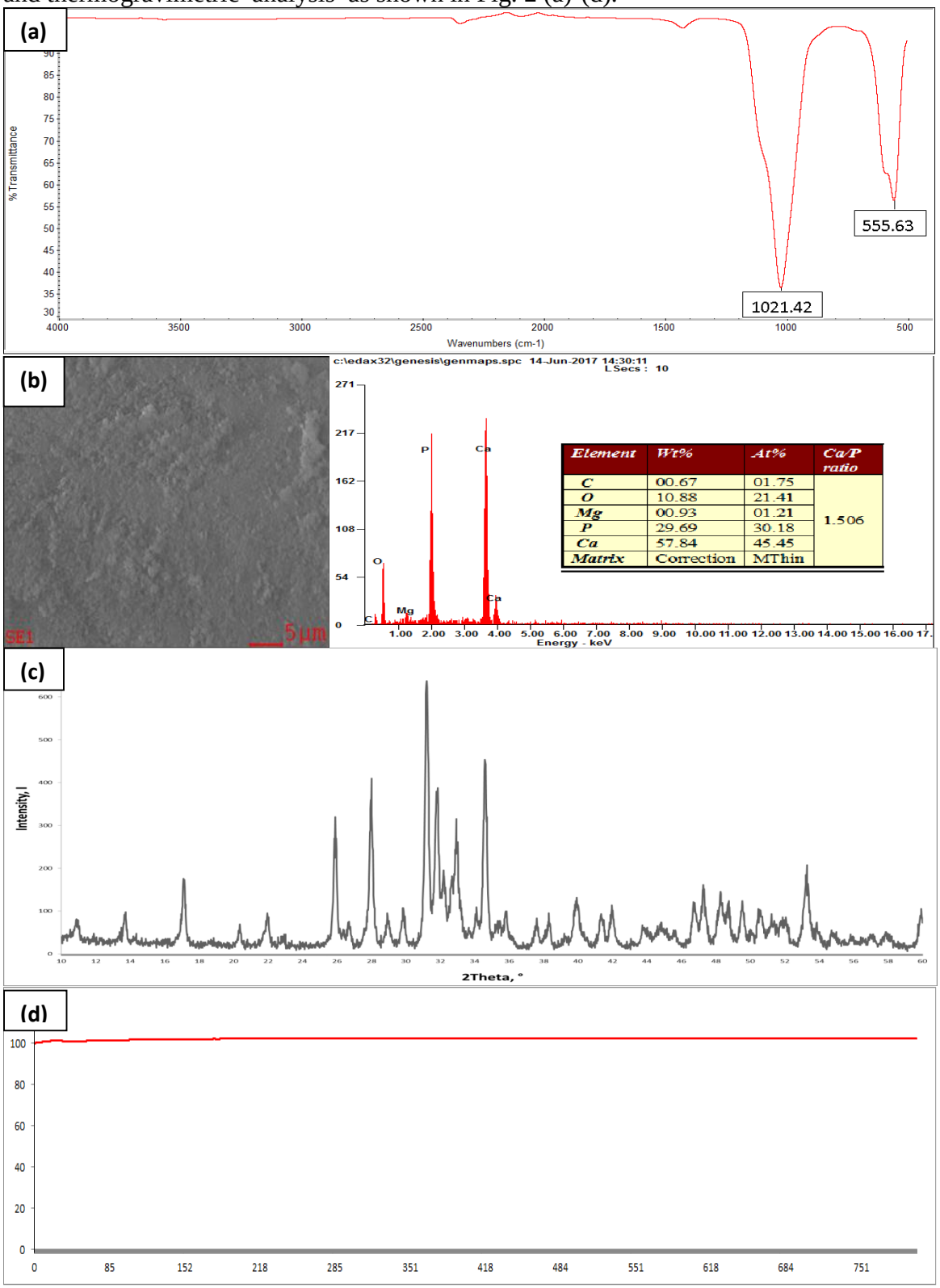


Figure 2. FTIR spectrum, (b) SEM imaging with EDX (energy dispersive X-ray), (c) XRD pattern and (d) TGA spectrum of HAp extracted from fish bone waste of *Scomberomorus Guttatus* species.

The successful extraction of hydroxyapatite from Mackerel fish bone can be identified by chemical and elemental composition analysis of the MHAp samples using FTIR and EDX techniques, respectively. The presence of phosphate groups in MHAp can be evidenced by: (1) two prominent absorption peaks located at 1021.42 cm^{-1} and 555.63 cm^{-1} (Fig. 2a), corresponding to the stretching modes and the bending modes (O-P-O bonds) of PO_4^{3-} vibration, respectively [1, 16, 44], (2) the presence of phosphorus and oxygen peak in EDX spectrum (Fig. 2b). Another main element, calcium, which constitutes the HAp also has been proved by the presence of Ca peak in EDX. Moreover, the XRD pattern of MHAp also showed the presence of the major HAp peaks at 27.975°, 31.201°, 34.592° 2θ angles as shown in Fig. 2c. Meanwhile, the appearance of strongest XRD peak at 31.201° also matches with the strongest HAp peak in the 2theta range of 31°~32° for a standard hydroxyapatite as reported elsewhere [11].

It is also important to examine whether the secondary phases (Tricalcium phosphate, CaO etc.) and organic impurities occurred or not in the HAp after being extracted by calcination, however, their absence can be verified by: (1) lower Ca/P ratio in MHAp than in HAp associated with CaO, (2) no evolution of peaks corresponding to Tricalcium phosphate (TCP) was observed from the XRD analysis, (3) absence of mass loss in TGA graph (Fig. 2d) or any characteristic band (e.g C-H bonding) in FTIR spectrum corresponding to organic matter. For the statement (1), the Ca/P ratio of MHAp was calculated as 1.506 from EDX analysis, which is indicative of the absence of CaO as secondary phase since the EDX result would give to higher Ca/P ratio (~2.13) for the HAp attached by CaO phase [45]. Such CaO phase is usually decomposed from the calcinations (beyond 650 °C) of fish bone according to the decomposition reaction of HAp: $Ca_{10}(PO_4)_6(OH)_2$------>$Ca_3(PO_4)_2 + CaO + H_2O$, where $Ca_3(PO_4)_2$ is referred to tricalcium phosphate (TCP) [11, 46]. Implicitly, TCP phase also would not be liberated as secondary phase in MHAp under the absence of CaO phase, which is in agreement with the beforementioned statement (2). Without the presence of any secondary phases and organic impurities, the as-prepared MHAp is thus in form having high phase purity [13, 17, 47], meaning that the good interfacial interaction between MHAp and PLA matrix can be expected. The absence of secondary phase also represents the formation of stoichiometric structure of HAp [46], however the obtained Ca/P ratio (1.506) is slightly lower than but close to the stoichiometric value of 1.67, and hence nearly stoichiometric MHAp was successfully produced with this sample. A little of discrepancy is attributed to the disturbance from trace amounts of substituting ions such as cations (Mg^{2+}) as indicated in EDX spectrum that would affect the Ca/P ratio of HAp [13, 37]. Favorably, presence of Mg ions is additional advantage as Mg is a vital element required for enhancement in bone regeneration process [7, 13]. Meanwhile, since there is lack of any secondary phase or organic impurities as additional components in nearly stoichiometric MHAp, its consequently excellent compositional homogeneity can be used to stabilize it against decomposition at elevated temperatures, contributing to higher thermal stability during composite processing [11].

For HAp being hydrophilic in nature, It is supposed that –OH stretching and vibrational band exist at around 3500-3700 cm^{-1} as broad peak and 600-650 cm^{-1} respectively in the FTIR spectrum of lamellar MHAp, however, they cannot be observed because of their low severity in HAp [48]. The poor hydrophilicity of MHAp as resulted from its lack of surface hydroxyl groups can be further proved by: (1) the

absence of a broad peak in the range of 3000–3600 cm^{-1} as assigned to adsorbed H_2O in the HAp powder [16, 48], (2) the absence of initial mass loss (at temperature around 100°C) related to the removal of adsorbed water molecules as indicated in TGA graph [21, 49]. It is believed that the OH groups have been mostly displaced by carbonate (CO_3^{2-}) ions, resulting in the formation A-type carbonated apatite as typically occurred in biological system [13, 50]. This can be further supported by several evidences from: (1) FTIR spectrum which exhibits a very weak $\nu_3CO_3^{2-}$ band at around 1450-1500 cm^{-1} [10, 21, 44], (2) the presence of carbon peak in EDX spectrum that should not be belonged to the organic impurities. Moreover, the presence of carbonate (CO_3^{2-}) ions also can be used to explain the lower Ca/P ratio in MHAp. Beneficially, the lower occurrence of HAp filler agglomeration in composite can be expected in the present study by the decreased surface charge energy on MHAp as the amount of surface OH-groups have been reduced by the A-type carbonate ions substitution. Moreover, the carbonated apatite is closely related to the mineral component of human bone, it is advantageous for enhancement in osteoconductivity contributing to aid bone formation during implantation [50].

3.2 XRD study of prepared composite samples

The X-ray diffraction analysis is usually conducted to evaluate the crystallography structure, dispersion state of filler and degree of crystallinity of polymer matrix. The XRD patterns of pristine PLA and PLA composite filled with various content of MHAp and MMT are shown in Fig. 3 (a)-(c). The XRD patterns are characterized in the 2θ range of 3°–40°. All related XRD data are summarized in Table 1. The degree of crystallinity (%Xc) was calculated as the percentage of the scattered intensity of the crystalline phase over the scattered intensity of the crystalline and amorphous phase. Based on the obtained angle and FWHM of the diffraction peak, the crystallite size (*L*) and d-spacing (*d*) can be calculated using the Scherrer and Bragg's formula respectively, which are given in Eq. (1) and (2):

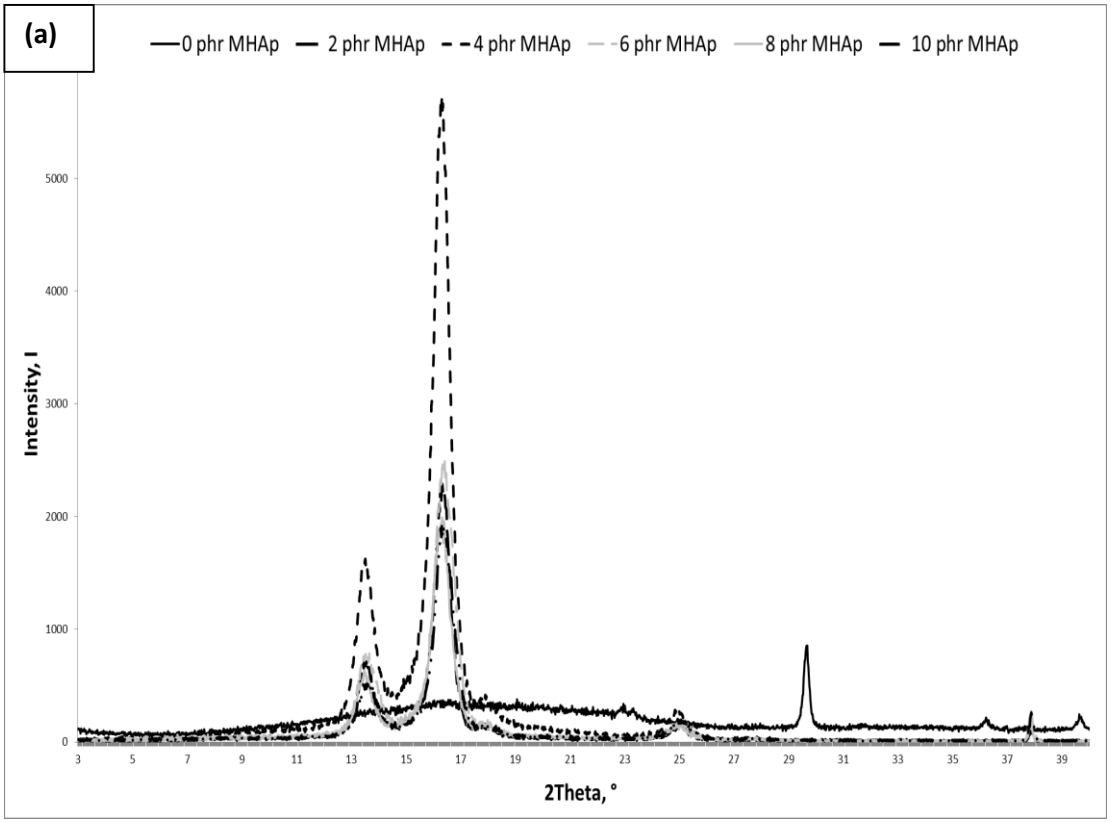
$$L = \frac{k\lambda}{\beta cos\theta} \quad (1)$$

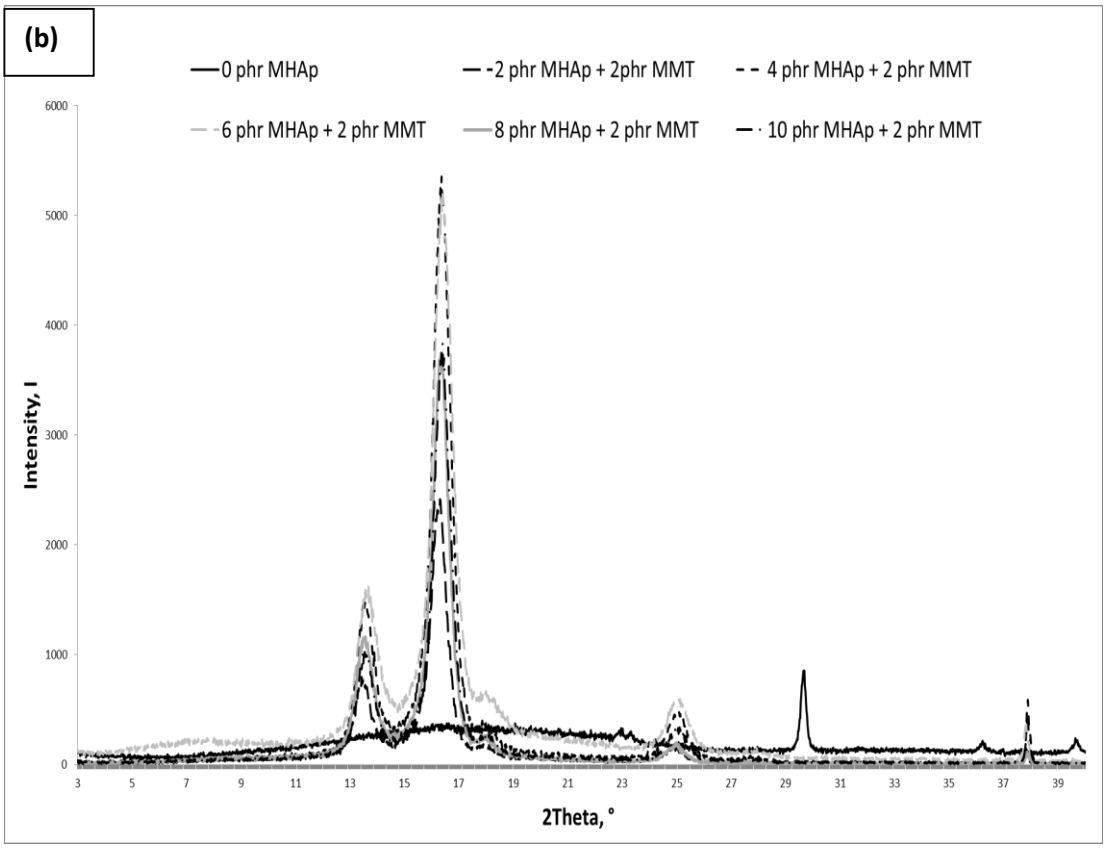
$$d = \frac{\lambda}{2sin\theta} \quad (2)$$

where λ = 1.542 Å is the wavelength of the Cu-Kα X-ray radiation used, *B* (in radians) is the full width at half maximum (FWHM) of the diffraction peak, θ is the Bragg angle (in radians), *k* is the Scherrer constant (taken to be 0.9).

The XRD patterns of all PLA composites added with increasing of loading level of MHAp are shown in Fig. 3a. Accordingly, five significant diffraction peaks occur at 2θ range of 13.5°-13.6° (Peak A), 16.3°-16.4° (Peak B), 17.8°-17.9° (Peak C), 24.9°-25.0° (Peak D), 37.8°-37.9° (Peak E). However, these five diffraction peaks were absent on XRD curve of neat PLA instead of replacing the original PLA diffraction peak as located at 22.91°, 29.64°, 36.21°, 39.64°, bringing about higher crystallinity (~35-39%) than that of pristine PLA (14.38 %) as shown in Table 1. This implies that the dispersed MHAp particle has fully ruptured the highly ordered chain arrangement structure in crystallite of original PLA peaks into random chain arrangement structure during melt processing and facilitated the recrystallization process throughout the PLA amorphous phase for new crystal structural arrangement at numerous locations. Thus, one can conclude that the MHAp fillers have high tendency to act as heterogeneous nucleating

agents effective for promoting the crystallization for PLA by providing preferential nucleation sites, thus favoring a higher %Xc of composite as compared to that of unfilled PLA [9, 51]. By the





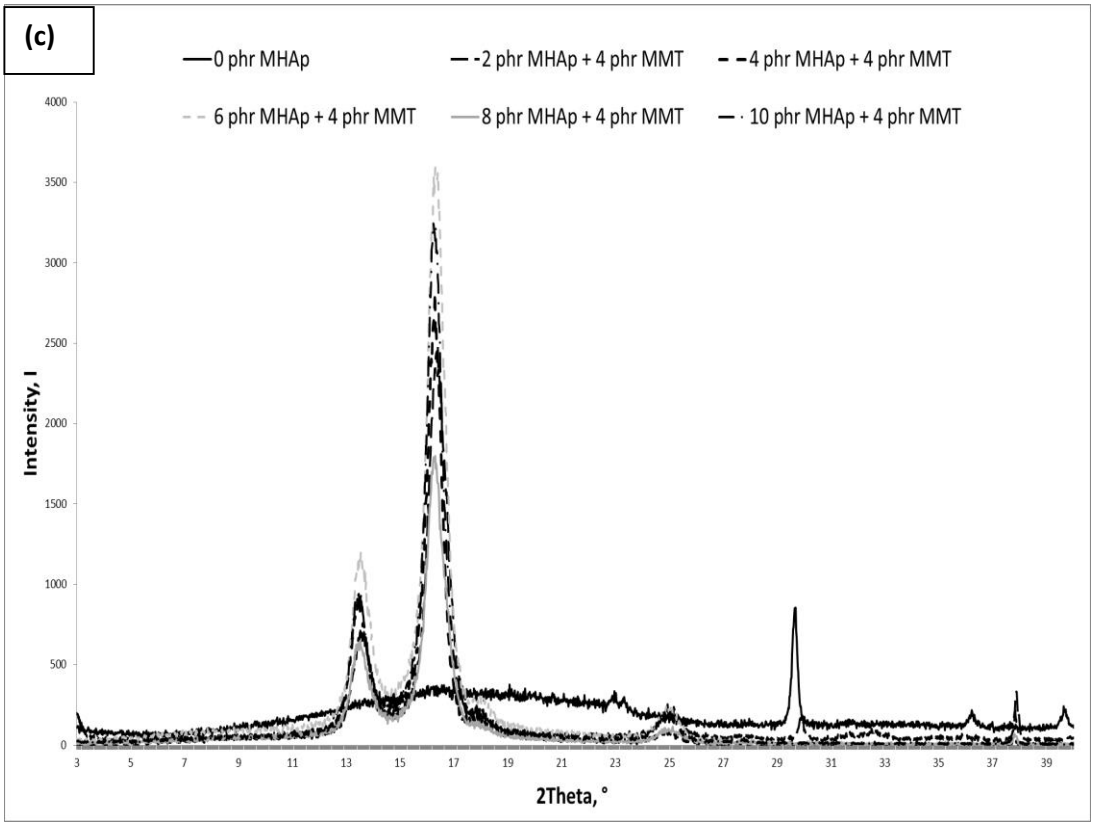


Figure 3. XRD pattern curves for PLA/MHAp composites added with (a) 0 phr MMT, (b) 2 phr MMT and (c) 4 phr MMT under increasing of MHAp loading level from 0 phr to 10 phr.

existence of nucleating agent in free space between polymer chains in amorphous phase, the minimization of free space between polymer chains could be achieved under the presence of interfacial interaction between HAp-polymer [25, 48]. Indeed, a good interfacial interaction is essential for the nucleating agent (HAp) driving the adjacent polymer chains to initiate the nucleation of crystallites during polymer crystallization process [48, 52]. In general, the formation of favorable inorganic-organic interaction between HAp and PLA in form of chemical bonding can be achieved via: (1) the hydrogen bonding between oxygen atom of PO_4^{3-} and hydrogen atom of polymer COOH group [53], (2) the hydrogen bonding between the =O sites of polymer carbonyl groups and -OH group of HAp [1, 10, 11] and (3) chemical linkage between oxygen atom in the ester group double bond of PLA and Ca^{2+} in the HAp in form of weak ionic bond namely chelation [24, 53]. However, the organic-inorganic interaction as stated in case (2) can be excluded from the present study since there is lack of –OH groups in MHAp as discussed before. But the lack of surface –OH groups is contributable to avoid the occurrence of HAp filler aggregation by the lower particle surface energy and thus ensure the good interfacial interaction between MHAp-PLA even at higher loading level. This can be proved by the fact that PLA composites filled with 6/8/10 phr of MHAp still keep high crystallinity even their peak intensity and crystallite size for peak A, B and C is significantly decreased following after the incorporation of 4 phr MHAp, which is mainly compensated by the appearance of extra peak E (formation of relatively large size crystallite) that is absent for composites filled with 2 and 4 phr MHAp. Regarding to the calculated d- spacing as tabulated in Table 1, the increasing of MHAp portion from 2 phr to 10 phr did not exhibit a significant effect on d-spacing of all diffraction peaks (peaks A, B, C, D and E). This implies that the close packing of polymeric macromolecular chains arrangement happens in all developed crystalline regions (crystallites), while the same reason as that for the PLA composites filled with 2 or 4 phr MMT could be applied. This shows that the addition of either MHAp and/or MMT particles did not affect the compactness of macromolecular chain in all the crystalline regions.

After the addition of 2 phr MMT in PLA/MHAp composite, the peak intensity of A, B, C and D is significantly increased with respect to that of all composite without MMT, which is also accompanied by the appearance of extra peak E (Fig. 3b) for composite filled with 2/4 phr MHAp that is absent in Fig. 3a. This can be due to the successful intercalation of MMT into PLA matrix as proved by the enhanced d-spacing of silicate layer (relative to its original spacing) according to Table 2, subsequently making the adjacent polymer chains to become closer. Therefore, the minimization of the free space between polymer chains by the presence of MHAp could be further decreased by MMT, enabling surrounding polymer chains to crystallizing more in a higher efficiency under the nucleation effect of MHAp. Moreover, Table 2 also presents the inter-chain separation (*R*) for MMT and MMT added PLA/MHAp composite which was determined from Klug and Alexander equation as shown in Eq. (3):

$$R = \frac{5\lambda}{8sin\theta} \quad (3)$$

It is found that the *d*, change of d-spacing (Δd) and *R* of MMT in polymer matrix is enhanced by an increasing MHAp content from 2/4 phr to 8 phr, indicating the improved dispersion and intercalation state of MMT by the presence of MHAp. The possible explanation could be the high tendency of repulsive interaction occurred

Table 1. The 2θ, crystallite size (*L*) and *d*-spacing for deflection peaks A, B, C, D and E on XRD pattern curves (in Fig. 5.2a-c) of PLA composites added with various loading levels of MHAp and MMT.

Loading level, phr (MHAp/MMT)	Deflection peak A			Deflection peak B			Deflection peak C			Deflection peak D			Deflection peak E			%Xc
	2θ,°	*L*, Å	*d*,Å	2θ,°	*L*, Å	*d*,Å	2θ,°	*L*, Å	*d*,Å	2θ,°	*L*, Å	*d*,Å	2θ,°	*L*, Å	*d*,Å	
0/0	Nil	Nil	Nil	Nil	Nil	Nil	Nil	Nil	Nil	Nil	Nil	Nil	Nil	Nil	Nil	14.38
2/0	13.519	125.94	6.54	16.316	124.48	5.43	17.840	99.24	4.97	24.973	116.61	3.56	Nil	Nil	Nil	39.49
4/0	13.514	113.07	6.54	16.286	119.85	5.44	17.860	94.62	4.96	24.892	119.19	3.57	Nil	Nil	Nil	35.38
6/0	13.592	99.21	6.51	16.393	102.41	5.40	Nil	Nil	Nil	25.057	97.54	3.55	37.868	207.43	2.37	35.10
8/0	13.487	120.00	6.56	16.292	114.01	5.43	17.820	80.71	4.97	24.890	110.19	3.57	37.801	213.37	2.38	36.87
10/0	13.607	100.65	6.50	16.391	106.40	5.40	17.940	85.89	4.94	25.021	106.24	3.55	37.858	205.19	2.37	37.27
2/2	13.466	120.36	6.57	16.249	123.02	5.45	17.700	72.02	5.00	24.882	121.56	3.57	37.800	228.98	2.38	35.59
4/2	13.570	110.93	6.52	16.357	113.66	5.41	17.940	92.41	4.94	24.998	110.41	3.56	37.875	213.81	2.37	36.77
6/2	13.656	94.99	6.48	16.398	102.80	5.40	18.000	67.94	4.92	25.027	101.04	3.55	37.793	200.26	2.38	36.68
8/2	13.540	110.42	6.53	16.316	117.49	5.43	17.920	104.67	4.94	24.912	112.49	3.57	Nil	Nil	Nil	36.28
10/2	13.570	116.86	6.52	16.370	119.05	5.41	17.920	88.62	4.94	25.010	112.83	3.56	37.870	223.06	2.37	37.03
2/4	13.594	101.58	6.51	16.384	104.46	5.40	17.900	83.75	4.95	25.021	99.51	3.55	37.857	198.34	2.37	31.92
4/4	13.469	121.36	6.57	16.256	128.10	5.45	17.820	97.08	4.97	Nil	Nil	Nil	Nil	Nil	Nil	36.86
6/4	13.546	107.03	6.53	16.321	110.03	5.42	17.920	89.33	4.94	24.948	98.76	3.56	Nil	Nil	Nil	32.19
8/4	13.517	104.94	6.54	16.306	103.86	5.43	18.200	144.13	4.87	25.017	86.35	3.56	Nil	Nil	Nil	30.70
10/4	13.470	118.83	6.56	16.270	122.25	5.44	17.760	82.69	4.99	24.900	113.52	3.57	37.810	234.33	2.38	35.19

Remarks: Nil = No peak detected

between PO_4^{3-} groups of MHAp and the negative sites in MMT clay structure [54, 55] to facilitate the melt intercalation of PLA into the MMT galleries during melt blending under homogeneous distribution of MHAp. As certain amount of PLA chains are introduced into the MMT galleries, the available free space to the polymer chains is thus decreased by MHAp in an easier way, contributing to facilitate the crystal structural arrangement consequently. This can be verified by the increased crystallite size for major deflection peaks of PLA/MHAp composite, development of small crystalline region (as peak E) and the increased %Xc of PLA composite filled with 4/6 phr MHAp after the addition of 2 phr MMT, as referred to Table 2.

Table 2. The angle, *d*-spacing, change of *d*-spacing and inter-chain separation of 2 and 4 phr MMT added PLA composites filled with increasing of amount MHAp

Loading level, phr (MHAp/MMT)	2θ,°	*d*, Å	Δd, Å	*R*, Å
MMT	1.049	84.13	-	105.16
2/2	0.827	106.73	22.60	133.42
4/2	0.847	104.19	20.06	130.23
8/2	0.788	111.95	27.82	139.93
2/4	0.746	118.28	34.15	147.85
4/4	0.749	117.88	33.75	147.35
8/4	0.740	119.24	35.11	149.05

Notes: these data were obtained upon XRD analysis in the 2θ range from 0° to 3°.

As compared to Fig. 3b, the increasing addition of MMT from 2 to 4 phr has decreased the peak intensity of major diffraction peaks of PLA/MHAp composite especially filled with 4/6/8 phr MHAp. This fact can be further supported by the reduction in %Xc or crystallite size of mostly all of 2 phr MMT added composites and disappearance of peak E of 2 phr MMT added composites filled with 4/6/8 phr MHAp after further addition of MMT content up to 4 phr. The possible explanation is the existence of higher degree of intercalated structure for MMT as indicated by the larger value of *d*, change of d-spacing (Δ*d*) and *R* of silicate layer (referred to Table 2), enabling the more extensive PLA chains to be intercalated into clay galleries [55]. Such a higher degree of intercalated structure for 4 phr MMT might be due to the more prominent occurence of repulsive interaction between MMT and MHAp at higher MMT loading level during compounding, which further facilitating the intercalation of MMT into PLA matrix. By the restriction effect of large surface area silicate layer on the extensive intercalated polymer chains, the movement of surrounding polymer chains (amorphous phase) is inhibited for folding and arranging crystallization under nucleating effect of MHAp [6]. In other words, as more polymer chains introduced into MMT gallaries, less polymer chains participate in PLA crystallization as promoted by MHAp, explaining the reduced peak intensities, %Xc and crystallite size of PLA/MHAp composite when added with higher MMT loading level. However, even the peak densities of major diffraction peaks decreased by the addition of MMT from 2 to 4 phr, almost peak intensities and crystallite siz still keep higher than that of composities without MMT especially when filled with 4/10 phr MHAp, indicating the promising synergistic effect of MHAp and MMT on improving the crystallographic structure of PLA.

4. Conclusions

Overall, the hydroxyapatite in form of A-type-carbonated-apatite without any secondary phase or organic impurities has been successfully extracted from fish bone waste of Mackerel fish, as verified by the characterization techniques of FTIR, EDX, XRD and TGA. With high phase purity of extracted MHAp surface, it could effectively interact with PLA by favorable organic-inorganic interaction between their functional groups, hence effectively driving the adjacent polymer chains to initiate nucleation of PLA crystallites and even recrystallization throughout amorphous phase based on XRD analysis. Such nucleating effect of MHAp on improving crystallinity of PLA by minimizing the free space between polymer chains can be further enhanced under the presence of MMT which could improve the efficiency of nucleation of crystallites during crystallization process by the melt intercalation of PLA into clay galleries. The good intercalation state of MMT in PLA matrix has been confirmed by the higher interlayer spacing than that of pure MMT and also could be further improved by the increasing of MHAp loading level due to the high tendency of repulsive interaction between phosphate groups of MHAp and the negative sites in MMT to facilitate the delamination of MMT in PLA matrix. Eventhough there would be more extensive PLA chains to be intercalated into clay galleries at higher MMT loading level by the more prominent occurrence of repulsive interaction between MMT and MHAp, however, this also implied that more polymer chains would be inhibited in movement for participating in the PLA crystallization process as promoted by the nucleating effect of MHAp. Therefore, further increment in MMT loading level from 2 phr to 4 phr has caused the reduction in crystallinity and crystallinite size of PLA matrix.

References

[1] Wan, Y. Z., Wu, C. Q., Xiong, G. Y., Zuo, G. F., Jin, J., Ren, K. J., Zhu, Y., Wang, Z. R., Luo, H.L. (2015). Mechanical properties and cytotoxicity of nanoplate-like hydroxyapatite/polylactide nanocomposites prepared by intercalation technique. *Journal of the Mechanical Behavior of Biomedical Materials*, 47, 29-37.

[2] Castro-Aguirre, E., Iñiguez-Franco, F., Samsudin, H., Fang, X., Auras, R. (2016). Poly(lactic acid)—Mass production, processing, industrial applications, and end of life. *Advanced Drug Delivery Reviews*, xxx, xxx–xxx.

[3] Nieddu, E., Mazzucco, L., Gentile, P., Benko, T., Balbo, V., Mandrile, R., Ciardelli, G. (2009). Preparation and biodegradation of clay composites of PLA. *Reactive and Functional Polymers*, 69, 371–379.

[4] Malwela, T., Ray, S.S. (2015). Enzymatic degradation behavior of nanoclay reinforced biodegradable PLA/PBSA blend composites. *International Journal of Biological Macromolecules*, 77,131–142.

[5] Fukushima, K., Tabuani, D., Arena, M., Gennari, M., Camino, G. (2013). Effect of clay type and loading on thermal, mechanical properties and biodegradation of poly(lactic acid) nanocomposites. *Reactive and Functional Polymers*, 73, 540–549.

[6] Sermsantiwanit, K., Phattanarudee, S. (2012). Preparation of bio-based nanocomposite emulsions: Effect of clay type. *Progress in Organic Coatings*, 74, 660–666.

[7] Lijuan, X., Liuyun, J., Chengdong, X., Lixin, J., Ye, L. (2014). Study on a novel double-layered composite membrane of Mg-substituted nano-

hydroxyapatite/poly(L-lactide-co-ε-caprolactone): Effect of different L-lactide/ε-caprolactone ratios. *Materials Science and Engineering: A*, 615, 361-366.

[8] Hong, Z., Zhang, P. B., He, C. L., Qiu, X. Y., Liu, A. X., Chen, L., Chen, X. S., Jing, X. B. (2005). Nano-composite of poly(L-lactide) and surface grafted hydroxyapatite: Mechanical properties and biocompatibility. *Biomaterials*, 26, 6296-6304.

[9] Mathieu, L. M., Bourban, P. E., Ma˚nson, J. A. E. (2006). Processing of homogeneous ceramic/polymer blends for bioresorbable composites. *Composites Science and Technology*, 66, 1606–1614.

[10] Dadbin, S., Kheirkhah, Y. (2014). Gamma irradiation of melt processed biomedical PDLLA/HAP nanocomposites. *Radiation Physics and Chemistry*, 97, 270-274.

[11] Choi, D., Marra, K. G., Kumta, P. N. (2004). Chemical synthesis of hydroxyapatite/poly(ε-caprolactone) composites. *Materials Research Bulletin,* 39, 417–432.

[12] Yuan, Q. H., Qin, C. P., Wu, J. B., Xu, A. P., Zhang, Z. Q., Liao, J. Q., Lin, S. X., Ren, X. Z., Zhang, P. X. (2016). Synthesis and characterization of Cerium-doped hydroxyapatite/polylactic acid composite coatings on metal substrates. *Materials Chemistry and Physics*, 182, 365-371.

[13] Akram, M., Ahmed, R., Shakir, I., Ibrahim, W. A. W., Hussain, R. (2013). Extracting hydroxyapatite and its precursors from natural resources. *Journal of Materials Science*, 49(4), 1461–1475.

[14] Li, J., Zheng, W., Li, L., Zheng, Y. F., Lou, X. (2009). Thermal degradation kinetics of g-HA/PLA composite. *Thermochimica Acta*, 493, 90–95.

[15] Chung, E. J., Sugimoto, M. J., Ameer, G. A. (2011). The role of hydroxyapatite in citric acid-based nanocomposites: Surface characteristics, degradation, and osteogenicity in vitro. *Acta Biomaterialia*, 7, 4057–4063.

[16] Nga, N. K., Giang, L. T., Huy, T. Q., Viet, P. H., Migliaresi, C. (2014). Surfactant-assisted size control of hydroxyapatite nanorods for bone tissue engineering. *Colloids and Surfaces B: Biointerfaces*, 116, 666–673.

[17] Torabinejad, B., Mohammadi-Rovshandeh, J., Davachi, S. M., Zamanian, A. (2014). Synthesis and characterization of nanocomposite scaffolds based on triblock copolymer of L-lactide, ε-caprolactone and nano-hydroxyapatite for bone tissue engineering. *Materials Science and Engineering: C*, 42, 199–210.

[18] Chlopek, J., Rosol, P., Morawska-Chochol, A. (2006). Durability of polymer-ceramics composite implants determined in creep tests. *Composites Science and Technology*, 66, 1615-1622.

[19] Simpson, R. L., Nazhat, S. N., Blaker, J. J., Bismarck, A., Hill, R., Boccaccini, A. R., Hansen, U. N., Amis, A. A. (2015). A comparative study of the effects of different bioactive fillers in PLGA matrix composites and their suitability as bone substitute materials: A thermo-mechanical and in vitro investigation. *Journal of the Mechanical Behavior of Biomedical Materials*, 50, 277-289.

[20] Mkhabela, V., Ray, S. S. (2015). Biodegradation and bioresorption of poly(ε-caprolactone) nanocomposite scaffolds. *International Journal of Biological Macromolecules*, 79, 186-192.

[21] Li, X. M., Feng, Q. L., Cui, F. Z. (2006). In vitro degradation of porous nano-hydroxyapatite/collagen/PLLA scaffold reinforced by chitin fibres. *Materials Science and Engineering: C*, 26, 716-720.

[22] Gigli, M., Fabbri, M., Lotti, N., Gamberini, R., Rimini, B., Munari, A. (2016). Poly(butylene succinate)-based polyesters for biomedical applications: A review. *European Polymer Journal*, 75, 431-460.
[23] Zou, B., Li, X. H., Zhuang, H. H., Cui, W. G., Zou, J., Chen, J. G. (2011). Degradation behaviors of electrospun fibrous composites of hydroxyapatite and chemically modified poly(DL-lactide). *Polymer Degradation and Stability*, 96, 114-122.
[24] Kasuga, T., Ota, Y., Nogami, M., Abe, Y. (2001). Preparation and mechanical properties of polylactic acid composites containing hydroxyapatite fibers. *Biomaterials*, 22, 19-23.
[25] Liuyun, J., Chengdong, X., Lixin, J., Lijuan, X. Effect of hydroxyapatite with different morphology on the crystallization behavior, mechanical property and in vitro degradation of hydroxyapatite/poly(lactic-co-glycolic) composite. *Composites Science and Technology*, 93, 61-67.
[26] Petricca, S. E., Marra, K. G., Kumta, P. N. (2006). Chemical synthesis of poly(lactic-co-glycolic acid)/hydroxyapatite composites for orthopaedic applications. *Acta Biomaterialia*, 2, 277-286.
[27] Eftekhari, S., Sawi, I. E., Bagheri, Z. S., Turcotte, G., Bougherara, H. Fabrication and characterization of novel biomimetic PLLA/cellulose/hydroxyapatite nanocomposite for bone repair applications. *Materials Science and Engineering: C*, 39, 120-125.
[28] Lee, Y. H., Lee, J. H, An, I. G., Kim, C., Lee, D. S., Lee, K. W., Nam, J. D. (2014). Electrospun dual-porosity structure and biodegradation morphology of Montmorillonite reinforced PLLA nanocomposite scaffolds. *Biomaterials*, 26, 3165-3172.
[29] Stloukal, P., Kalendova, A., Mattausch, H., Laske, S., Holzer, C., Koutny, M. (2015). The influence of a hydrolysis-inhibiting additive on the degradation and biodegradation of PLA and its nanocomposites. *Polymer Testing*, 41, 124-132.
[30] Rapacz-Kmita, A., Stodolak-Zych, E., Szaraniec, B., Gajek, M., Dudek, P. (2015). Effect of clay mineral on the accelerated hydrolytic degradation of polylactide in the polymer/clay nanocomposites. *Material Letters*, 146, 73–76.
[31] Jiang, L., Zhang, J. W., Wolcott, Michael. P. (2007). Comparison of polylactide/nano-sized calcium carbonate and polylactide/montmorillonite composites: Reinforcing effects and toughening mechanisms. *Polymer*, 48, 7632-7644.
[32] Ruiz-Hitzky, E., Darder, M., Fernandes, F. M., Wicklein, B., Alcântara, A. C. S., Aranda, P. (2013). Fibrous clays based bionanocomposites. *Progress in Polymer Science*, 38, 1392–1414.
[33] Michael, F. M., Khalid, M., Walvekar, R., Ratnam, C. T., Ramarad, S., Siddiqui, H., Hoque, M. E. (2016). Effect of nanofillers on the physico-mechanical properties of load bearing bone implants. *Materials Science and Engineering: C*, 67, 792–806.
[34] Cai, X., Tong, H., Shen, X. Y., Chen, W. X., Yan, J., Hu, J. M. (2009). Preparation and characterization of homogeneous chitosan–polylactic acid/hydroxyapatite nanocomposite for bone tissue engineering and evaluation of its mechanical properties. *Acta Biomaterialia*, 5, 2693–2703.
[35] Mostafa, A. A., Oudadesse, H., Mohamed, M. B., Foad, E.S., Gal, Y. L., Cathelineau, G. (2009). Convenient approach of nanohydroxyapatite polymeric matrix composites. *Chemical Engineering Journal*, 153, 187–192.

[36] Babaei, Z., Jahanshahi, M., Rabiee, S. M. The fabrication of nanocomposites via calcium phosphate formation on gelatin–chitosan network and the gelatin influence on the properties of biphasic composites. *Materials Science and Engineering: C*, 33, 370–375.
[37] Jing, X., Mi, H. Y., Turng, L. S. (2017). Comparison between PCL/hydroxyapatite (HA) and PCL/halloysite nanotube (HNT) composite scaffolds prepared by co-extrusion and gas foaming. *Materials Science and Engineering: C*, 72, 53–61.
[38] Basha, R. Y., Kumar, T. S. S., Doble, M. (2015). Design of biocomposite materials for bone tissue regeneration. *Materials Science and Engineering: C*, 57, 452–463.
[39] Sunil, B. R., Jagannatham, M. (2016). Producing hydroxyapatite from fish bones by heat treatment. *Material Letters*, 185, 411–414.
[40] Ferraro, V., Carvalho, A. P., Piccirillo, C., Santos, M. M., Castro, P. M. L., Pintado, M. E. (2013). Extraction of high added value biological compounds from sardine, sardine-type fish and mackerel canning residues — A review. *Materials Science and Engineering: C*, 33, 3111–3120.
[41] Mohammadi, M., Ziaie, F., Majdabadi, A., Akhavan, A., Shafaei, M. (2017). Improvement of mechanical and thermal properties of high energy electron beam irradiated HDPE/hydroxyapatite nano-composite. *Radiation Physics and Chemistry*, 130, 229–235.
[42] Shayan, M., Azizi, H., Ghasemi, I., Karrabi, M. (2015). Effect of modified starch and nanoclay particles on biodegradability and mechanical properties of cross-linked poly lactic acid. *Carbohydrate Polymers*, 124, 237–344.
[43] Zaidi, L., Bruzaud, S., Bourmaud, A., Me´de´ric, P., Kaci, M., Grohens, Y. Relationship Between Structure and Rheological, Mechanical and Thermal Properties of Polylactide/Cloisite 30B Nanocomposites. Journal of Applied Polymer Science, 116, 1357–1365.
[44] Suljovrujic´, E., Ignjatovic´, N., Uskokovic´, D., Mitric´, M., Mitrovic´, M., Tomic´, S. (2007). Radiation-induced degradation of hydroxyapatite/polyL-lactide composite biomaterial. *Radiation Physics and Chemistry*, 76, 722–728.
[45] Chen, D. Z., Tang, C. Y., Chan, K. C., Tsui, C. P., Yu, Peter. H. F., Leung, Mason. C. P., Uskokovic, P. S. (2007). Dynamic mechanical properties and in vitro bioactivity of PHBHV/HA nanocomposite. *Composites Science and Technology*, 67, 1617–1626.
[46] Sheikh, Z. S., Najeeb, S., Khurshid, Z., Verma, V., Rashid, H., Glogauer, M. (2015). Biodegradable Materials for Bone Repair and Tissue Engineering Applications. *Materials*, 8, 5744-5794.
[47] Berger, S., Müller, E., Schnabelrauch, M. (2009). Influence of methacrylate-containing surface modifiers on the mechanical properties of nano-hydroxyapatite/polylactide network composites. *Material Letters*, 63, 2714-2717.
[48] Davachi, S. M., Heidari, B. S., Hejazi, I., Seyfi, J., Oliaei, E., Farzaneh, A., Rashedi, H. (2017). Interface modified polylactic acid/starch/polyε-caprolactone antibacterial nanocomposite blends for medical applications. *Carbohydrate Polymers*, 155, 336-344.
[49] Markoˇciˇc, E., Skerget, M., ˇKnez, Z. (2011). Solubility and diffusivity of CO_2 in poly(L-lactide)–hydroxyapatite and poly(D,L-lactide-co-glycolide)–hydroxyapatite composite biomaterials. *Journal of Supercritical Fluids*, 55, 1046-1051.
[50] Neuendorf, R. E., Saiz, E., Tomsia, A. P., Ritchie, R. O. (2008). Adhesion between biodegradable polymers and hydroxyapatite: Relevance to synthetic bone-like materials and tissue engineering scaffolds. *Acta Biomaterialia*, 4, 1288-1296.

[51] Chen, L. J., Wang, M. (2002). Production and evaluation of biodegradable composites based on PHB–PHV copolymer. *Biomaterials*, 23, 2631-2639.
[52] Neto, W. A. R., Pereira, I. H. L., Ayres, E., de-Paula, A. C. C., Averous, L., Góes, A. M., Oréfice, R. L., Bretas, R. E. S. (2012). Influence of the microstructure and mechanical strength of nanofibers of biodegradable polymers with hydroxyapatite in stem cells growth. Electrospinning, characterization and cell viability. *Polymer Degradation and Stability*, 97, 2037-2051.
[53] Bhowmik, R., Katti, K. S., Katti, D. (2007). Molecular dynamics simulation of hydroxyapatiteepolyacrylic acid interfaces. *Polymer*, 48, 664-674.
[54] Depan, D., Kumar, A. P., Singh, R. P. (2009). Cell proliferation and controlled drug release studies of nanohybrids based on chitosan-g-lactic acid and montmorillonite. *Acta Biomaterialia*, 5, 93–100.
[55] Payne, S. A., Katti, D. R., Katti, K. S. (2016). Probing electronic structure of biomineralized hydroxyapatite insidenanoclay galleries. *Micron*, 90, 78–86.

eureca 2017 – Conference Paper
Paper Number EUG24

Performance Analysis of Duobinary Modulation for 40gb/s N-channel WDM in EDFA Based Standard Single Mode Fibre

MD Shahrukh Adnan khan[1], Md. Moshiur Rahman[1,*], Manobendu Sarker[1], Aravind CV[2]
[1]*Department of Electrical and Electronic Engineering,*
University of Asia Pacific, Dhaka, Bangladesh
[2]*School of Engineering, Taylor's University. Subang jaya, Malaysia.*

[*]sourov.eee@uap-bd.edu

Abstract
In this paper, performance of Duobinary modulation format is investigated in Wavelength Division Multiplexing System for a next generation high data rate of 40 Gb/s per channel. The main objective is to simulate and review the optical spectra, efficiency and Bit Error Rate (BER) for standard single mode fibre with Duobinary modulation. With variation of fibre length from 90km to 270km and WDM channel capacity from 4 to 16, simulation shows impressive performance in BER, bandwidth reduction, spectral efficiency and channel capacity. But with increase of fiber length, BER starts to fall apart showing the incapability of the modulation over long haul transmission. Studying all the cases, "Duobiray" is considered to be a promising modulation technique for short distance transmission only. For long haul, it is incapable of performing efficiently. Lastly, further scope of research is discussed and future work has been recommended.

Keywords: Index Terms— Duobinary, EDFA, SMF, WDM, OptSym, BER, Performance Analysis.

1. Introduction

Remarkable developments have been obtained in the field of optical fiber communication system in recent years because of higher data transmission rate, lower system cost and bandwidth efficiency. According to researchers' opinion, increase in data rate as well as decrease in channel spacing may be the two probable solutions in order to escalate system capacity. Wavelength division multiplexing (WDM) has recently shown its capacity to support high bandwidth data transmission [1], [2]. The new generation light wave system has facilitated higher data rate per channel (40 Gb/s and above) [3] and dense wavelength division multiplexing technique (DWDM). For addressing these matters, a new advanced modulation format [4], [5] is needed which will operate within less bandwidth, have less sensitivity to self-phase and cross phase effects and finally able to carry multiple bits per symbol and transmit large amount of information. Also a modulation technique less susceptible to this noise can bring major improvement in transmission efficiency. Furthermore, in long distance high bit-rate optical transmission, chromatic dispersion (CD), attenuation and non-linear effects are responsible for limiting transmission distance. Erbium-doped fiber amplifiers (EDFA) can balance the fiber [3], [6]. The dispersion influence can be overcome by utilizing periodic dispersion compensation with the help of dispersion compensation fiber (DCF) [7].

In early 90's of 20th century, 'Intensity Modulation' or 'On-Off Keying' format is mostly used which worked fine with a data rate of ~10 Gb/s. But now, at 21st century, data rate is escalated to ~40, ~80 or ~100 Gb/s together with a narrow channel spacing of ~100GHz [3] for which 'On-Off Keying' is no longer suitable modulation format for new generation communication. Various researches have been conducted and still a lot of studies have been being carried out regarding the advanced modulation technique. Among them, the 'Duobinary' modulation format has been taken into consideration for its less susceptibility to dispersion as well as non- linearity. Its receiver and transmitter are cost effective and less complicated compared with other advanced formats such as 'Differential Binary Phase Shift Keying' (DBPSK) [8], 'Differential Quadrature Phase Shift Keying' (DQPSK) [9], '8DPSK' and so on.

There are numerous researches on Duobinary modulation over different transmission channel along with different parameters. Chuanbowen et al. in [10] try to maximize the power budgets by using Duobinary transmission systems based on 1.55-μm directly modulated lasers (DML) for optical access networks of 28 Gb/s per wavelength while skipping the use of optical amplifiers over 40-km long SSMF. Authors in [11] present BER characteristics according to optical received power utilizing Duobinary direct modulation operated at 40 Gb/s over 2 km non-zero dispersion shifted fiber (NZ-DSF) with a dispersion coefficient of 4.5 ps/nm*km with wavelength 1.55 μm. Performance comparison between low-pass filter or delay-and-add circuit to produce 3-level electrical Duobinary signals over 45-km SSMF at 28-Gb/s is presented in [12] and they claim from their experimental results that low pass filter performs better than the delay-and-add circuit. Tianjian et al. in [13], they propose a novel external DSP 112-Gbps system for the first time with SFP form factor and Duobinary 4-PAM signalling where the nonlinear Volterra pre-equalizer works as compensation for non-linarites, can cover 10 km. They conclude that this promising system can greatly enhance the capacity of single slot line card and become a prominent candidate for next generation mobile back-haul and datacenter interconnection. Authors

in [14] also present a novel approach by employing direct duobinary aiming up to 10 km SMF with 56 Gbps total bit rate using direct detection which will responsible for reducing latency. An impressive wavelength division multiplexed passive optical networks (TWDMPON) system, using 25-Gb/s Duobinary modulation is demonstrated over 20-km SSMF in [15]. They have experimental results for both upstream and downstream separately and manifest significant performance improvement. But a research gap has been observed in terms of specific comparison of the Duobinary technique with and without WDM both for long and short haul transmission for high data rate. This paper tries to fill up the gap observed in the research industry.

The main objective of the paper is to simulate Duobinary Modulation format in a wavelength division multiplexing system for a given data rate of ~40 gigabit per second. Both SMF and DCF were utilized in the transmission link. Therefore, calculation was made to get a fully dispersion compensated system. Investigation of performance factors such as Bit Error Rate, Quality Factor was undertaken with variation of WDM channel and optical fiber length.

2. Duobinary modulation

Duobinary or Phase Shaped Binary Modulation format was carried out first in 1960's by a person name Adam Lender. In intensity Modulation, '1' and '0' represent the switch on and off of a LASER source. After modulation, the electrical bit stream converts into optical signal and as a result the amplitude changes. On the contrary, in Duobinary modulation, there are 3 states of signal levels instead of two which are '0', '1' and '2'. Each symbol here is the addition of the current and previous state. If the current state is assumed to be 'Kn' and the previous state to be 'Kn-1', the formation of symbol levels are as follows (table 1) [11-15]:

Table 1: Duobinary Modulation States

Current bit (K_n)	**Previous Bit(K_{n-1})**	**State**
1	1	2
1	0	1
0	1	1
0	0	0

The bias voltage can easily be changed in order to revalue the three levels to be 1, 0 and -1 instead of 2,1 and 0. The phase difference between the upper level and lower level is ~π. In a 'Duobinary' modulation format, if R bits are being transmitted per second, the bandwidth of the signal will be R/2 which is the 'Nyquist Rate' of a transmission making duo binary format to be bandwidth efficient twice of Non Return to Zero On-Off Keying (NRZ OOK).

3. Simulation model

The designs and modeling were both constructed and simulated in the industrial level software OptSim [16]. 'CW Lorentzian Laser' was used as the optical source with the Centre Emission Wavelength of ~1550 nm. The power was fixed at ~0 dB. Two types of optical links were used which are SMF and DCF. For SMF the fiber attenuation was 0.2 dB per kilometer and the dispersion was fixed at '17 ps/nm/km'. Fiber non-linear coefficient was selected to be ~1.36811 l/w/k. For DCF the dispersion was fixed at '-100ps/nm/km' and the length was calculated in such a way where the total dispersion in a transmission to be 0 ps/nm. The EDFA used in the setup had gain of 30

dB and noise figure (NF) of 5 dB. Figure 1 given below represents the Duobinary transmitter set-up.

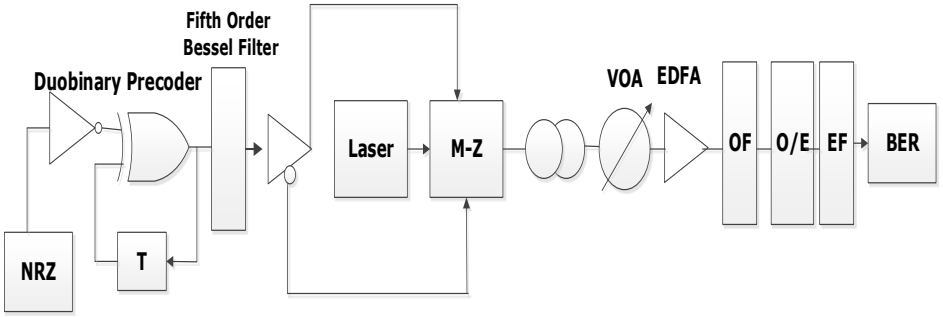


Figure 1-Transmitter set-up of Duobinary Modulation

3.1 Transmitter and Receiver Complexity

Here, Table 2 indicates the transmitter and receiver set-up elements for our simulation.

Table 2: Transmitter and Receiver simulation set-up.

Modulation Format	Transmitter Complexity	Receiver Complexity
Duobinary	10. (a) 1 Dual Arm Mach Zehnder Modulator (b)Driver Amplifier for each modulation arm (c)Duobinary filter	1 Photodiode

3.1.1 Transmitter Link:

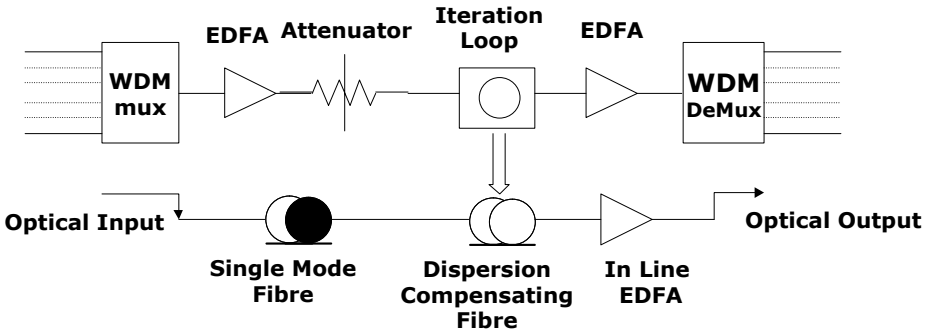


Figure 2.1- Transmission Link

Transmission link comprises with a multiplexer and a Demultiplexer at the starting and end respectively (Fig. 2.1). In VBS, “Combiner” and “Splitter” had been used for multiplexer and Demultiplexer respectively. A “Fixed Gain EDFA Booster” was added after the combiner followed by “SMF” and “DCF”. Inline amplifier was used to strengthen the signal after fiber span. A post amplifier was included after the loop followed by the splitter. The gain of all EDFA was fixed at 30db with a noise figure of 5db. The “Attenuator” was put into the circuit to kill the gain of the “Booster”.

3.1.2 Simulation Set-up

Following figure 2.2 is the 8 channel WDM simulation diagram built in Optsim for Duobinary modulation in Single Mode Fibre.

Information in a form of random bit of streams was generated by Bit generator which then went through Pulse Generator to form a square pulse. Next, it was passed through RZ and NRZ modulation schemes with the carrier laser wave. Thereafter it was

sent to the fibre optics through WDM and after pre and post amplifying process, the optical signal would be received by the receiver consisting of a Demultiplxer, photodiode and filter. Simulation was done in order to test the optical system in Optsim. After implementing the design parameter, the performance parameter (Eye diagram and Bit Error Rate- BER) were evaluated to get the impairment parameter and the data was compared with the published values in order to get the suitable modulation format.

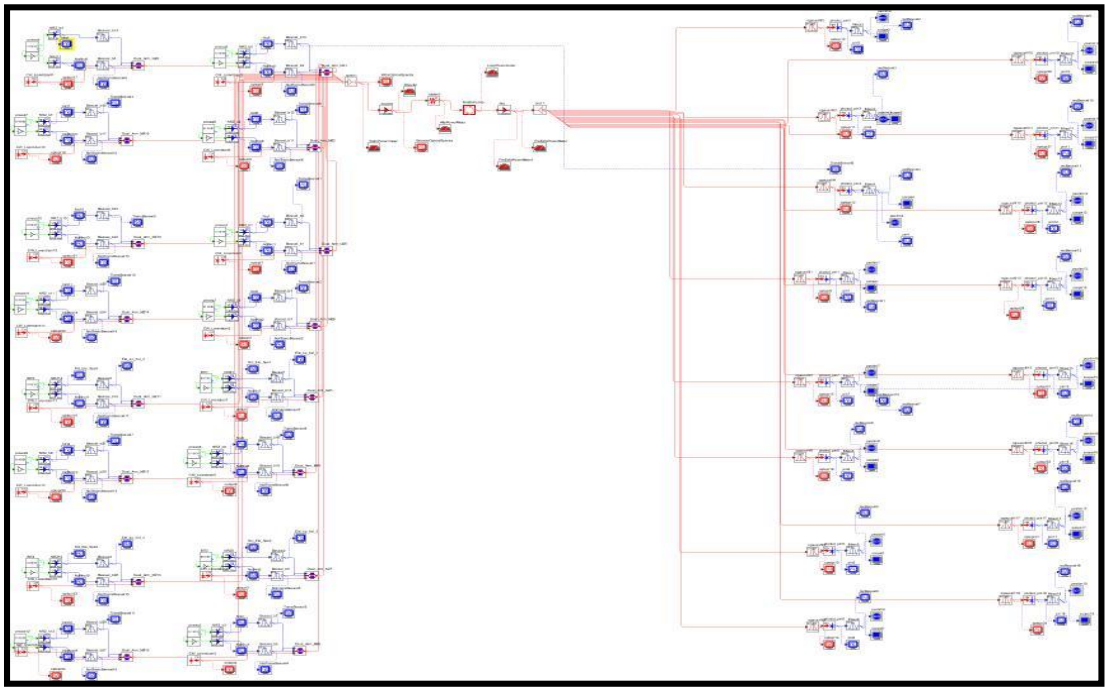


Figure 2.2: Schematic Diagram for 8 Channel WDM Duobinary simulation in SMF for 40Gb/S bit rate

3.2 Design Parameters:

Table 3 states the design parameters used in our simulation

Table 3: Simulation parameters descriptions.

<table>
<tr><td colspan="2">Bit Rate</td><td>40 Gb/s</td></tr>
<tr><td colspan="2">Optical Source</td><td>CW Lorentzian LASER</td></tr>
<tr><td rowspan="2">Optical Link</td><td>SMF</td><td>Total length of SMF was divided into three stages- 90km, 180km and 270km. Operating Wavelength: 1550nm, Fiber loss: 0.2(db)/km. Fiber no-linear coefficient ~ 1.36811 1/w/k.</td></tr>
<tr><td>DCF</td><td>DCF introduces negative dispersion to the fiber in order to make the total dispersion in a transmission to be 0. ‘-100ps/nm/km’ of dispersion was introduced to DCF. The calculated length of DCF for the compensation of dispersion is described as follows:
$\text{Length of SMF(km)} = \frac{D_{SMF}}{\text{Dispersion Introduced by DCF}}$
Here, D_{SMF} indicates the total dispersion introduced by SMF
<table>
<tr><td>SMF length</td><td>90 km</td><td>180 km</td><td>270 km</td></tr>
<tr><td>D_{SMF}</td><td>1530 ps/nm</td><td>3060 ps/nm</td><td>4590 ps/nm</td></tr>
<tr><td>Length of D_{SMF}</td><td>15.3 km</td><td>30.6 km</td><td>45.9 km</td></tr>
</table>
</td></tr>
<tr><td colspan="2">EDFA</td><td>“Flat Gain” EDFA was used throughout the entire period with a gain of 30dB. “The Flat Noise Figure” was kept as 5dB.</td></tr>
<tr><td colspan="3">Modulation format- Duobinary</td></tr>
</table>

4. Results

Spectral Bandwidth (3db): From the above diagram provided by the Optical Spectral Analyzer, the bandwidth of 'Duobinary' optical spectra was found to be ~40 GHz (3db). In figure 3, the value was expressed in THz.

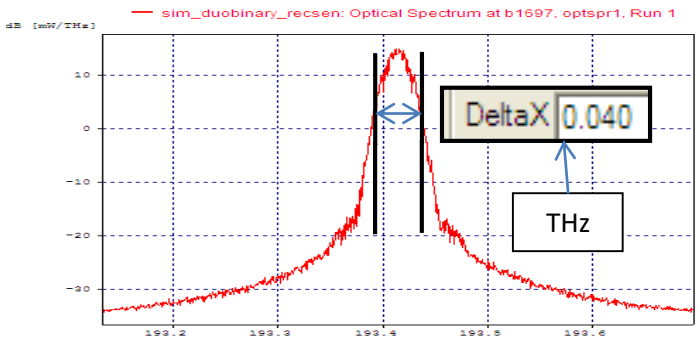


Figure 3- Optical Spectrum for RZ-OOK (Bit Rate~ 40 Gb/s).

4.1 Spectral Efficiency:

According to the formula of Spectral Efficiency [17]

$$Spectral\ Efficiency = \frac{Bit\ rate}{Spectral\ Bandwidth}$$

$$Spectral\ Efficiency_{Duobinary} = \frac{40}{40}\ \text{Bit/s/Hz} \sim 1\ \text{bit/s/Hz}$$

4.2 Filter Cut-off frequency:

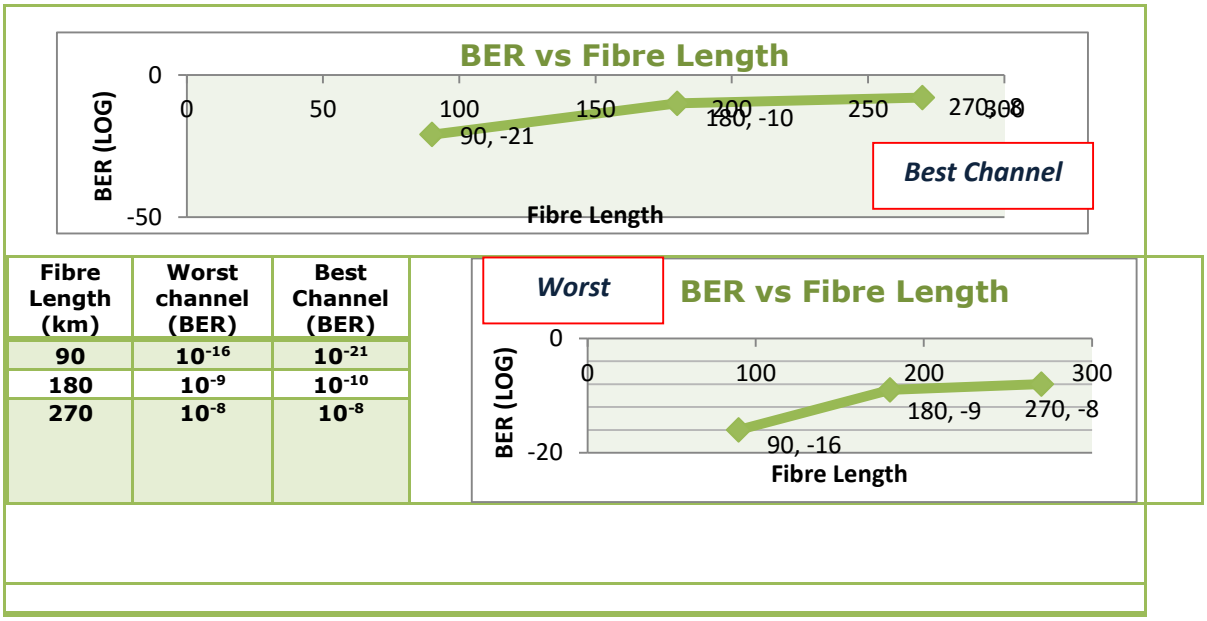
Receiver filter 3db frequency [17][18][19] = (0.75 x Spectral Bandwidth)

$$\text{Receiver Filter 3db frequency}_{\text{Duobinary}} = (0.75 \times \text{Spectral Bandwidth}) = 30\ \text{GHz}$$

But it was found that at the cut-off frequency of 28 GHz, the receiver filter was working properly. This 2 db decrease of the filter bandwidth made 'Duobinary' to be superior to NRZ in terms of filter bandwidth.

4.3 Bit Error Rate:

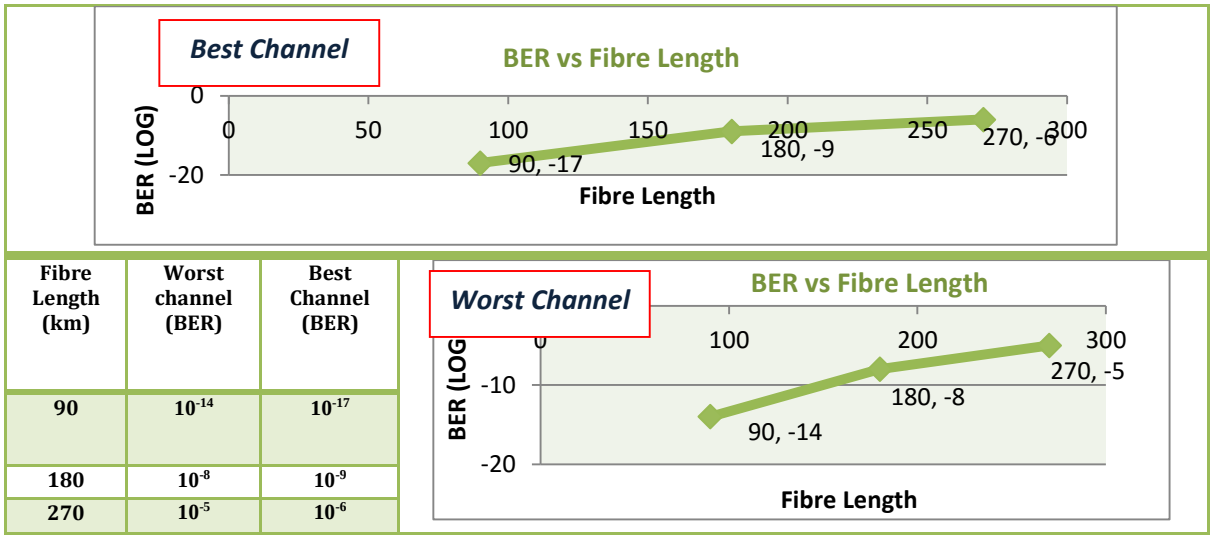
4.3.1 4 Channel



Fibre Length (km)	Worst channel (BER)	Best Channel (BER)
90	10^{-16}	10^{-21}
180	10^{-9}	10^{-10}
270	10^{-8}	10^{-8}

Figure 4 - BER Values of 4 Channel Duobinary (Bit rate~ 40 Gb/s)

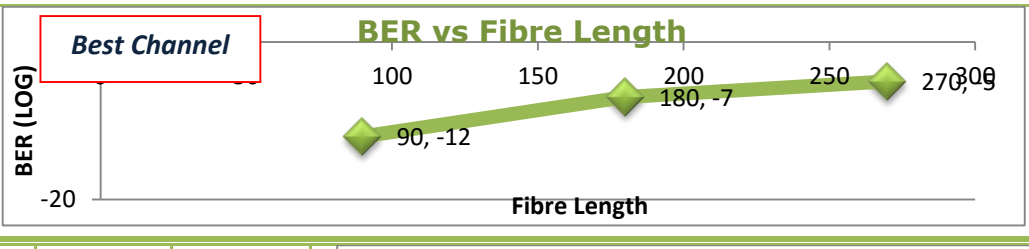
4.3.2 8 Channel



Fibre Length (km)	Worst channel (BER)	Best Channel (BER)
90	10^{-14}	10^{-17}
180	10^{-8}	10^{-9}
270	10^{-5}	10^{-6}

Figure 5 - BER Values of 8 Channel Duobinary (Bit rate~ 40 Gb/s)

4.3.3 16 Channel



Fibre Length (km)	Worst channel (BER)	Best Channel (BER)
90	10^{-8}	10^{-12}
180	10^{-6}	10^{-7}
270	10^{-4}	10^{-5}

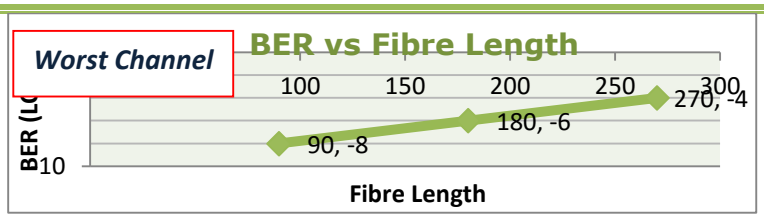


Figure 6 - BER Values of 16 Channel Duobinary (Bit rate~ 40 Gb/s).

4.4 Eye Diagram Analysis

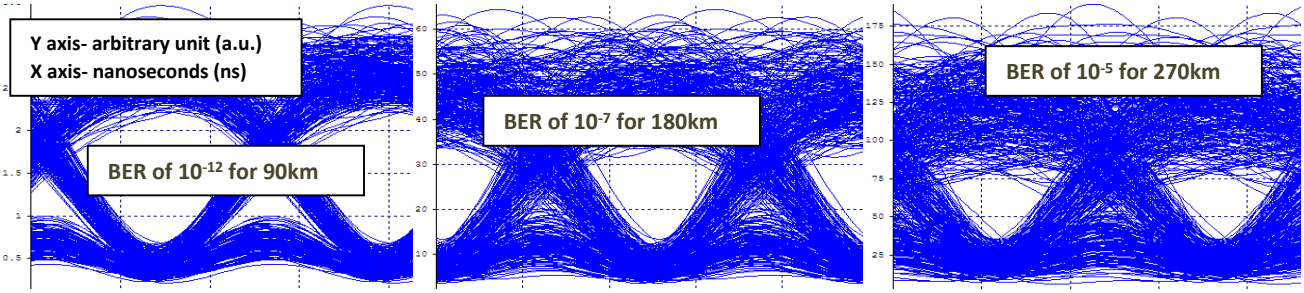


Figure 7- Eye diagrams for 16 Channel WDM of Duobinary Modulation Format.

The "Eye Diagram" for 16 channels is provided in figure 6 for each span (Best Channel). Key thing to notice here that with the increase of fiber length, BER decreased radically making it unsuitable for long distance transmission. On the other hand, it showed solid performance with the increasing number of channels. Unlike the previous two modulation formats, BER did not fall down significantly with the increase of channel number.

'Duobinary' showed outstanding performance in terms of bandwidth reduction. J. Jhang, A. Yin [20] worked with the same configuration with RZ-OOK and measured its spectra as 160 GHz. Comparing to RZ-OOK, its optical spectra squeezed to one fourth of 'RZ-OOK'. It also had spectral efficiency of approximately ~1bit/s/Hz where as traditional modulation format "Return to Zero OOK" showed approximately ~0.25 bit/s/Hz with the same configuration [20]. In 4 Channel WDM, while varying the fiber length, it was interesting to observe that although "Duobinary" started off with solid performance of BER ~10^{-21} for 90km, the performance radically fell apart with increase of fiber span. For 180 km of SMF, the BER of it increased by ~10^{-11} whereas for 270 km it showed a value of ~ 10^{-8}.Analyzing '8 Channel WDM', in spite of having an excellent BER of ~10^{-17} at the beginning, "Duobinary" again fell apart along the way with the increase of fiber length. For a length of 180km, BER of it increased to 10^{-9} and for a length of 270 km, it ended up having a poor BER of ~10^{-6}. Lastly, while investigating '16 Channel WDM', "Duobinary" as usual started with a low BER of ~10^{-}

^{12} (for 90km), with the increase of fiber span it went high dramatically as it ended up with poor BER of ~10^{-5}. Studying all the cases, "Duobiray" however starting off with a low BER every time but failed to maintain it and finally ending up having poor BER as the fiber length increased every time for all the 3 different number of channels. Therefore, "Duobinary" was decided not to be suitable long haul transmission. Analyzing the WDM Channel Capacity, it can be concluded that "Duobinary" gave good performance in terms of "WDM Channel Capacity" as it managed to show low BER despite of the increase in channel number. Referring to L. Li and A. M. Mohammadi's work [20]-[22],traditional modulation format RZ-OOK showed poor performance in terms WDM for; all the 3 different number of channels as the BER increased from 10^{-9} to 10^{-6} for a channel number of 4 and 16 respectively. However, in our case, while increasing the fiber span, "Duobinary" fell apart and was no longer able to provide better BER performance.

5. Conclusion

To recapitulate, it should be mentioned that the objectives of this experiment were successfully achieved. The main task was to observe the performance of Duobinary Modulation for a WDM network with a data rate of ~40 Gb/s. Although Duobinary showed some outstanding performance in bandwidth reduction, spectral efficiency and channel capacity; however, the poor performance with an increase of fiber length was the limitation of it. There are several other ways for the implementation of Duobinary. Our experiment and results recommends future research on advanced techniques such as RZ-Duobinary and CSRZ-Duobinary (Carrier suppressed Return to Zero). This paper also recommends conduct simulation by varying polarization mode dispersion, refractive index and some other factors which were fixed or deactivated throughout our research.

Acknowledgment

The authors would like to acknowledge University of Nottingham (UK, Malaysia, China) to give a platform to conduct this research.

References

V. K. Chaubey, S. Abirami, and G. Peres, "Performance evaluation of an intelligent routed WDM mesh network: An analytical approach," *Optical Fiber Technology*, vol. 13, no. 2, pp. 129–134, Apr. 2007.

L. Guo, X. Wang, W. Ji, W. Hou, and T. Yang, "A new waveband switching method for reducing the number of ports in wavelength-division-multiplexing optical networks," *Optical Fiber Technology*, vol. 15, no. 1, pp. 5–9, Jan. 2009.

V. S. Rao, I. B. Djordjevic, and B. Vasic, "Advanced detection and coding techniques for nonlinear intersymbol interference cancellation in 40 Gb/s systems," *IEE Proceedings - Optoelectronics*, vol. 153, no. 4, pp. 174–178, Aug. 2006.

N. Chi, W. Fang, Y. Shao, J. Zhang, B. Huang, J. Zhu, and L. Tao, "High speed optical transmission utilizing constant envelope modulation based on frequency shift keying and minimum-shift keying (Invited Paper)," *Chinese Optics Letters*, Sep. 2010.

P. J. Winzer and R.-J. Essiambre, "Advanced Modulation Formats for High-Capacity Optical Transport Networks," *Journal of Lightwave Technology*, Dec. 2006.

I.-T. Lu and R. C. Qiu, “Dispersion in chiral optical fibres,” *IEE Proceedings - Optoelectronics*, vol. 145, no. 3, pp. 155–158, Jun. 1998.

G. Bellotti, A. Bertaina, and S. Bigo, “Dependence of self-phase modulation impairments on residual dispersion in 10-Gb/s-based terrestrial transmissions using standard fiber,” *IEEE Photonics Technology Letters*, vol. 11, no. 7, pp. 824–826, Jul. 1999.

N. Badhan and N. Sharma, “Comparative analysis of CSRZ, DB and DPSK modulation formats for single channel 40Gb/s system,” in *2014 International Conference on Medical Imaging, m-Health and Emerging Communication Systems (MedCom)*, pp. 95–100, 2014.

Lujiao Li, Yaojun Qiao, and Yuefeng Ji, “Performance analysis of 40 Gb/s RZ-DQPSK transmission system with alternate polarization formats,” in *2010 3rd IEEE International Conference on Broadband Network and Multimedia Technology (IC-BNMT)*, pp. 388–391, 2010.

C. Sun, S. Bae, and H. Kim, “Transmission of 28-Gb/s Duobinary and PAM-4 Signals Using DML for Optical Access Network,” *IEEE Photonics Technology Letters*, pp. 1–1, 2016.

A. Abbasi, C. Spatharakis, G. Kanakis, N. M. Andre, H. Louchet, A. Katumba, J. Verbist, X. Yin, J. Bauwelinck, H. Avramopoulos, G. Roelkens, and G. Morthier, “PAM-4 and Duobinary Direct Modulation of a Hybrid InP/SOI DFB Laser for 40 Gb/s Transmission over 2 km Single Mode Fiber,” in *Optical Fiber Communication Conference*, Washington, D.C., 2016, p. M2C.6.

“Transmission of 28-Gb/s duobinary signals over 45-km SSMF Using 1.55-μm directly modulated laser - IEEE Xplore Document.” [Online]. Available: http://ieeexplore.ieee.org/document/7718268/. [Accessed: 25-Nov-2016].

T. Zuo, L. Zhang, zhang qiang, J. Zhou, E. Zhou, and G. N. Liu, “Single Lane 112-Gbps Analog Small Form-factor Pluggable Module with Only 4-GHz End-to-end 3-dB Bandwidth Employing Duobinary 4-PAM,” in *Optical Fiber Communication Conference*, Washington, D.C., p. Th1G.5, 2016.

L. Suhr, J. J. Vegas Olmos, B. Mao, xiaogeng xu, G. N. Liu, and I. Tafur Monroy, “Direct modulation of 56 Gbps duobinary-4-PAM,” in *Optical Fiber Communication Conference*, Washington, D.C, p. Th1E.7., 2015.

Z. Ye, S. Li, N. Cheng, and X. Liu, “Demonstration of high-performance cost-effective 100-Gb/s TWDM-PON using 4×25-Gb/s optical duobinary channels with 16-GHz APD and receiver-side post-equalization,” in *2015 European Conference on Optical Communication (ECOC)*, pp. 1–3, 2015.

https://optics.synopsys.com/rsoft/rsoft-system-network-optsim.html

M. K. Abdullah, A. M. Mohammadi, "Absolute Polar Duty Cycle Division Multiplexing: An economical and spectral efficient multiplexing technique", *5th International IEEE Conference on Wireless and Optical Communications Networks*, 2008.

M. Saqlain, U. Illahi, J. Iqbal, "Comprehensive Study Analysis of Novel Mapping Multiplexing Technique for Long Haul Optical Fibre Transmission Systems", *Europian Scientific Journal*, vol- 9, 2013.

G. A. Mahdiraji, M. K. Abdullah, M. Mokhter, A. M. Mohammadi, "70-GB/s amplitude-shift-keyed system with 10GHZ clock recovery circuit using duty cycle division multiplexing", *Photonic Network Communications Springer*, vol- 19, pp 233-239, 2010.

L. Li, J. Zhang, A. Yin, "Analysis the Speciality of Modulation Format in WDM-PON System", *Journal of Computers*, vol- 6, 2011.

Amin Malekmohammadi, M.K.Abdullah, A.F.Abas, G.A.Mahdiraji, " Effect of Guard Band on the Performance of APDCDM Technique in 40 Gb/s Optical Fibre Communication system", *ICP*, 2010.

A. Malekmohammadi, M.K. Abdullah, G.A. Mahdiraji,"Analysis of return-to-zero-on-off-keying over absolute polar duty cycle division multiplexing in dispersive transmission medium" *IET Optoelectron*, Vol. 3, Iss. 4, pp. 197–206., 2009

eureca 2017 – Conference Paper
Paper Number EUG25

The ORPOC Star: Five Characteristics that Define an Optimal Motorcycling Riding Posture

S. Suresh[1], M. I. N. Ma'arof[1], H. Husain[2] and N. Senin[3],
[1] Mechanical Engineering Department, Faculty of Engineering & Q uantity Surveying, INTI International University, Persiaran Perdana BBN, Putra Nilai, 71800 Nilai, Negeri Sembilan, Malaysia
[2]Faculty of Mechanical Engineering, Universiti Teknologi MARA, 40450 Shah Alam, Selangor, Malaysia
[3]Mechanical and Human Factor Department (MHFD), MIMOS Berhad, Technology Park Malaysia, 57000 Bukit Jalil Kuala Lumpur.

[*]I14007178@student.newinti.edu.my,

Abstract
Literary evidences have shown that vehicular comfort has been continuously studied for decades. The study ranges for a variety of vehicles such as cars, trucks and sometimes motorcycles. A renowned motorcycle ergonomics expert noted that the characteristics of a comfortable motorcycling riding posture are determined via the: (i) type of motorcycling activity performed, (ii) motorcycle design, and (iii) human operator's body built. However, it is emphasized that a comfortable riding posture is not necessarily the best option for real world motorcycling. It is strongly suggested that it is best for a motorcyclist to aim for an optimal riding posture instead. This is because an optimal riding posture could best suits various types of motorcycling conditions, challenges and work demand while simultaneously does not sacrifice on comfort. Henceforth, in considering the complexity given by motorcycling, it is anticipated that it is inadequate to achieve an optimal riding posture by only considering to the three aforementioned characteristics noted by the expert. The objective of this study was to identify the characteristics that define an optimal riding posture for motorcycling. Literature assessment and non-structured observation were used in identifying the characteristics, while, survey study was used to validate the findings. The findings show that there are five (5) characteristics that upon unification would define an optimal riding posture. The five (5) characteristics are (i) the human operator's anthropometric characteristic and body mass, (ii) the motorcycle cockpit designs (the handlebar, seat and the foot-pegs), (iii) the capability in performing motorcycling duties, (iv) the overall real world motorcycling comfort over time, and (v) the overall real world motorcycling safety. Collectively, these five (5) characteristics were named the Optimal Riding Posture Characteristics (ORPOC) Star. Conclusively, it is recommended that for motorcycling, it is best to aim for an optimal riding posture. This is because a comfortable motorcycling riding posture does not necessarily be optimal; yet, an optimal riding posture is almost always comfortable.

Keywords**:** Motorcycle, Riding Posture, Ergonomics, Optimal, Comfort

1. Introduction

1.1 Motorcycle Ergonomics

Motorcycle is a two or three wheeled motor vehicle that is mainly used globally due to its versatility and being economical. For many years, motorcycle has been the most preferable, convenient and affordable mode of transport (Sarani et al., 2011). In term of motorcycle ownership within European countries, Greece ranks the highest with 101 motorcycles per 1000 inhabitants, while, Netherlands ranks about average with 33 motorcycles per 1000 inhabitants while Slovenia has the lowest with 7 motorcycles per 1000 inhabitants (Hagenzieker, 2010). Manan and Várhelyi (2012) noted that motorization in Asian countries is growing fast and the motorcycle is the dominating transport mode. The same study further added that the number of motorcycles per thousand people averaged over several major Asian cities is approximately 196, which is 7 times the average of the rest of the world. For example, the number of registered motorcycles in Taiwan comprises 50% of the total number of registered vehicles; in Thailand it is 63%, in Cambodia 84%, in Vietnam 95%, in Laos 79% and in Indonesia 73%. Malaysia, with a population of more than 27.6 million, is not an exception. According to The Road Transport Department of Malaysia, the total number of motorcycles in 2009 was 8,940,230 (47% of all motorised vehicles), which was 5% more than passenger cars.

Conclusively, these statistics proven that motorcycle is indeed a globally popular mode of transportation. Even so, in retrospect to research on motorcycle, it was found that the literature on motorcycle ergonomics is rather lacking. Most vehicle related ergonomics focused on four-wheeled vehicles – most notably cars, and other heavy machineries such as busses, tractors and cranes. This study gives a highlight on motorcycle ergonomics due to the immense opportunity for research and exploration in this field of study. The objective of this study was to identify the characteristics that define an optimal riding posture for motorcycling.

1.2 Comfortable vs. Optimal Riding Posture

Chappells and E. Shove (2004) defined comfort as a feeling of contentment, a sense of cosiness or a state of physical and mental well-being. The study further added that with considerable implications for indoor environmental management and energy demand meanings of comfort have changed dramatically over the last century. In another study, Suzuki (1998) highlighted that riding comfort and other requirements relating to comfort have become factors as important as safety and speed in evaluating the characteristics of transport. This is indeed a good argument, since as Kyung and M. A. Nussbaum (2008a) noted: a low degree of riding comfort (or increase in discomfort) will speed up the level of muscle fatigue. It is interesting to note that there are several factors that contribute to riding comfort such as the vibration, noise, temperature, humidity, seat design, and riding postures. Short- and long-term sitting comfort/discomfort need to be distinguished (Kyung and M. A. Nussbaum, 2008a). Sitting discomfort increases over time while sitting comfort tends to remain constant.

In short, due to the significance made by comfort, this scope of ergonomics has been continuously studied.

As opposed to the conventional 3 types of riding postures noted by Robertson and Minter (1996) – which is very closely associated with the one highlighted by Graf et al., (1995); Ma'arof and Ahmad (2012) introduced 4 types of riding postures via the Riding Posture Classification (RIPOC) system. Even so, from a general ergonomics perspective, the motorcycling riding posture could still be treated as sitting posture. A sitting posture was regarded by Kyung and M. A. Nussbaum (2008b) as potentially unhealthy working posture and considered as one of the major contributing factors for several musculoskeletal disorders such as pain in the lower back, neck and shoulder – and this is the case for a car where a full-back support is available. Therefore, for a riding posture where the human operator would seat without the availability of a full-back support, the subject of comfort is even more profound.

Stedmon (2010) noted that the characteristics of a comfortable motorcycling riding posture are determined via: (i) type of motorcycling activity performed (ii) the motorcycle design, and (iii) human operator's body built. This study partially agrees with this statement. However, it is stressed that it is inadequate to achieve an optimal riding posture by only considering/addressing these three characteristics. Furthermore, by only aiming at acquiring a comfortable riding posture would result in various ergonomics issues.

Firstly, the type of motorcycling activity performed. This study suggests that it is very difficult to relate comfortable riding posture with the type motorcycling activity performed. This is because, certain type of motorcycling activity could not be effectively performed in a comfortable riding posture. In the light of this argument, let's take a motorcycling activity that involves high speed of travelling and requiring the need for utmost control over the motorcycle and work (motorcycling duties) efficiencies as an example. For this type of motorcycling activity, the "RIPOC Type 1" riding posture (Ma'arof and Ismail, 2012) is arguably the best riding posture. The spinal flexion practiced aids in streamlining during motion, whilst, the human operator's forwarded center of mass and the ability to utilize the whole body at the utmost extent due to superiority in the range of motion for the upper body and greater leverage for the lower body facilitates in performing the motorcycling duties. However, in referring to the literature, this particular riding posture could be labelled as an ergonomically risky riding posture. The beyond 20 degrees spinal flexion practiced via this riding posture was the main risk factor that contributes to the highest risk. Chen et al., (2009), Eger et al., (2008), Okunribido et al., (2007 and 2006), O'Sullivan et al., (2006), Gallagher (2005), Cho and Yoon (2001); Neuman et al., (2001b), Mehta and Tewari (2000), Harrison et al., (1999), Magnusson and Pope (1998) and Gustafson-Soderman (1987) have all emphasized that such postural demands is potentially to results in adverse health effects to the human operator from high muscular and joint forces and spinal disc pressure for instances. Telemeterized implants on the spinal column already shows the average of 48% increment of the resultant implant force for at 15 degree flexion alone (Rohlmann et al., 2011), while this riding posture is designated with over 20 degree spinal flexion. Therefore, at beyond the 20 degree mark; the theoretical implant force at the spinal column would be at 64% (with 3.2% increment with additional 1 degree flexion). This justifies the hazard experienced by the human operator upon practicing this riding posture. Henceforth, it is arguably not a comfortable riding posture.

Therefore, it is very difficult to relate comfortable riding posture with the type of motorcycling activity performed.

Secondly, is with respect to motorcycle design. This study agrees that motorcycle design could greatly influence the human operator's riding posture's comfort characteristics. A thick seat with a lumbar support, along with high handlebar placement (though, not beyond shoulder level) could provide comfort to the human operator. Indeed, creature comfort is always a plus in motorcycling. However, certain level of caution needs to be address. Code (2010) stressed that human error will always be the key factor in the occurrence of motorcycle road accident. Hence, in order to minimize the occurrence of this type of error, the human operator has to be constantly at ready and alert during motorcycling. It is greatly anticipated that a too comfortable riding posture would impede the human operator to be in such physical and psychological working state due to being at lax. This was the issue highlighted in the study by Ma'arof et al., (2014) in justifying the need to have certain level of discomforts during motorcycling in order to ride safely. Henceforth, based on this notion, it is stressed that it is better to aim for an optimal riding posture instead of only focusing in reaching extensive comfort during motorcycling.

Finally, with respect to the human operator's body built. It is completely undeniable that the human operator's body built has a major influence in determining comfort level – suggestively that Stedmon (2010) was referring to the human operator's anthropometric characteristics and physical size. Hence, the 'one size fits all' is not the best design principle for motorcycle fabrication. In retrospect to the statement made by Robertson and Minter (1996), Stedmon (2010) noted that only recently that motorcycle manufacturers have integrated adjustability into their motorcycle designs. For example, the 2014 Ducati Monster 1200 series come with adjustability compatibility in term of ergonomics. Such change in the landscape of motorcycle manufacturing is a great welcome. However, due to the differences in anthropometric characteristics and physical built, it is expected to be extremely difficult for the motorcycle manufacturers to cater adjustability in their motorcycle designs which targeted mainly in reaching comfort. Therefore, it is suggested that the aim for optimal riding posture is much less complex instead.

In short, by only aiming to achieve a comfortable riding posture, several ergonomics issues are foreseen. Thus, it is best to shift the design perspective that aims towards in achieving an optimal riding posture. The three characteristics highlighted by Stedmon (2010) in determining a comfortable riding posture are great. However, it is inadequate to achieve an optimal riding posture by only considering/addressing these three characteristics. It was believed that there are several other factors that have to be considered for an optimal riding posture.

2. Research Methodology

The research methodology was divided into: (i) research design, (ii) establishment methods, and (iii) validation method. The details are as follow:

2.1 Research Design

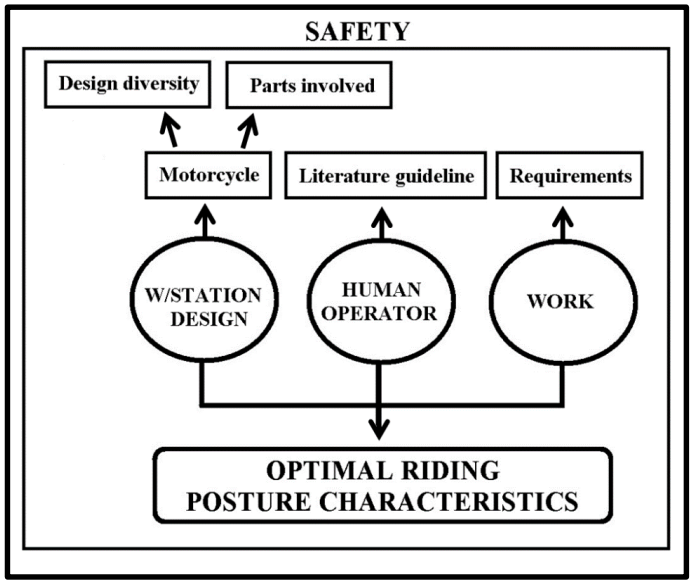


Figure 1: Research design

Figure 1 shows the research design for this study. In identifying the characteristics that define an optimal riding posture, the assessments were performed from three (3) different perspectives. Accuracy in findings was insured by tackling the study from three (3) different perspectives. The perspectives were: (i) workstation design, (ii) human operator, and finally (iii) the work perform.

Firstly, with respect to the workstation design, the workstation is the motorcycle. The motorcycle as a workstation concept was documented in both Robertson and Minter (1996) and Robertson et al., (2013). In treating motorcycle as a workstation, the component assessed were the issue in the diverse motorcycle design. Motorcycles are manufactured with different designs and engineered with diverse functionality purposes. Even so, it is anticipated that although the designs may vary, motorcycles still share common parts that is in direct contact (physical contact or work-wise contact) with the human operator. There is the need to address these parts in identifying the characteristics that define an optimal riding posture. Hence, the assessments were also made from the perspective of the workstation design.

Secondly, the human operator is the component that completes the motorcycling ergonomics system. Furthermore, it is the fundamental of ergonomics where the workstation and work are designed to suits the human operator. This is especially with respect to the guidelines given by literature in ensuring the workstation and work to 'fit' the human operator. Therefore, in identifying the characteristics that define an optimal riding posture, it was vital to view the issue from the standpoint of the human operator. The requirements for a human operator to work in a challenging working environment have to be always taken into account.

Finally, motorcycling presents a complex and special type of vehicular operation in contrast to other four-wheeled vehicles. Motorcycle is a non-enclosed vehicle and due to this, the vehicular operation performed (motorcycling duties such as throttle control and manoeuvring the motorcycle) by the human operator is different. For example, due to not being enclosed, the human operator has to resist the challenges

that come from the external environment such as windblast, climate and weather conditions. Furthermore, due to being a single-line-two-wheeled vehicle, the human operator has to simultaneously balance themselves independently while manoeuvring the motorcycle via their whole body – noted as the "Uno-Body Motion" (Ma'arof et al., 2012). Due to such complex working condition, it is best to identify the characteristics that define an optimal riding posture from the perspective of motorcycling work. The requirements for the work to be performed were taken into considerations.

All of these perspectives represent different needs and requirements of motorcycling with respect to ergonomics. Even so, collectively, these three perspectives were viewed under the scrutiny of safety. This is because motorcycling activity is already generally hazardous since the human operator is not operating an enclosed vehicle and literally exposed to the environment which may possess various types of threats. Thus, any judgment or recommendations on any ergonomics issue, the human operator's safety is always the main priority.

2.2 Establishment Methods

The following were the methods used in identifying the characteristics that define an optimal riding posture.

2.2.1 Literature Assessment

Literature assessments were made in reviewing studies related to vehicular comfort/discomforts. Literatures were gathered via Universiti Teknologi MARA (UiTM) library online database including ScienceDirect, SCOPUS, Scientific.net, and ergonomics books.

2.2.2 Field Study: Non-structured observation

Given that most of the authors are avid motorcyclists, motorcycling activities were performed to grasp better appreciation and understanding on the activity. In addition, minor ethnographic observation was also performed to have better perspective on motorcycling from the standpoint of the public/non-researcher motorcycling committee.

2.3 Validation Methods

The following was the method used in validating the findings from method 2.1.

2.3.1 Survey Study

A descriptive survey study was performed. The experimental procedure was also approved by Ethics Committee of the Research Management Institute (RMI) of the Universiti Teknologi MARA, Shah Alam, Selangor, Malaysia. The objective of the questionnaire was to identify the key characteristics that define an optimal riding posture. The data collection tool was a set of questionnaire specifically developed with respect to the research objective. By measuring the score level given by the respondents via the Likert's scale, the level of significance/importance of the characteristics could be quantified. The language used for the questionnaire was "Bahasa Melayu".

The respondents were a group of male undergraduate students (n = 139) from the Faculty of Mechanical Engineering, Universiti Teknologi MARA, Malaysia. All respondents fulfilled the inclusive criteria. The inclusion criteria for the survey study are as follow:

i. Respondents are male student with more than 1 year motorcycling experience (motorcycle of any engine capacity).
ii. Age between 18 – 25 years old.
iii. The respondents are healthy while answering the questionnaire.
iv. The respondents have no history of accident or physical trauma in the past one year.

The survey was performed in a voluntary basis. Prior to answering the questionnaire, the following were performed:

i. The respondents were briefed on the nature and answering method of the survey.
ii. The respondents were informed that they could withdraw at any moment with no penalty and their personal information will be kept confidential.
iii. Upon agreement to participate in the survey study, the respondents were required to fill the consent form prior to participate in the survey

3. Result

3.1 Identification of Optimal Riding Posture Characteristics

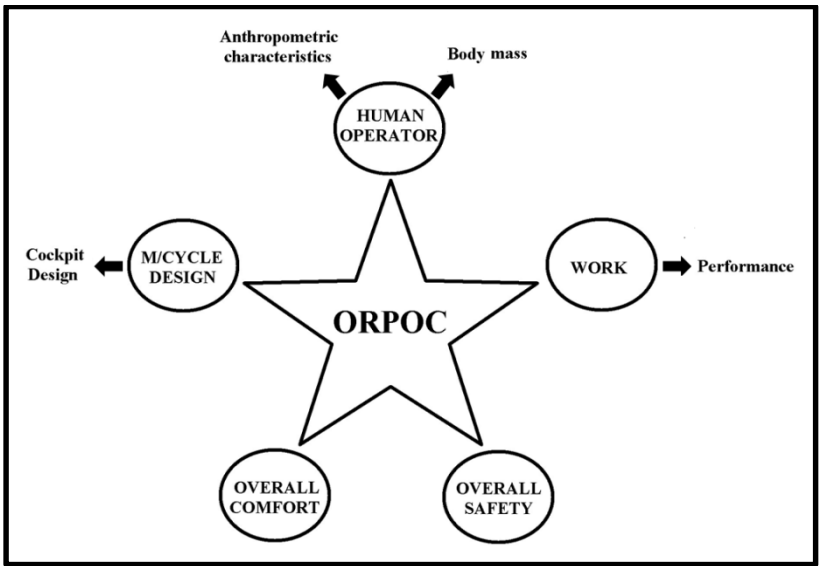


Figure 2: The Optimal Riding Posture Characteristics (ORPOC) Star

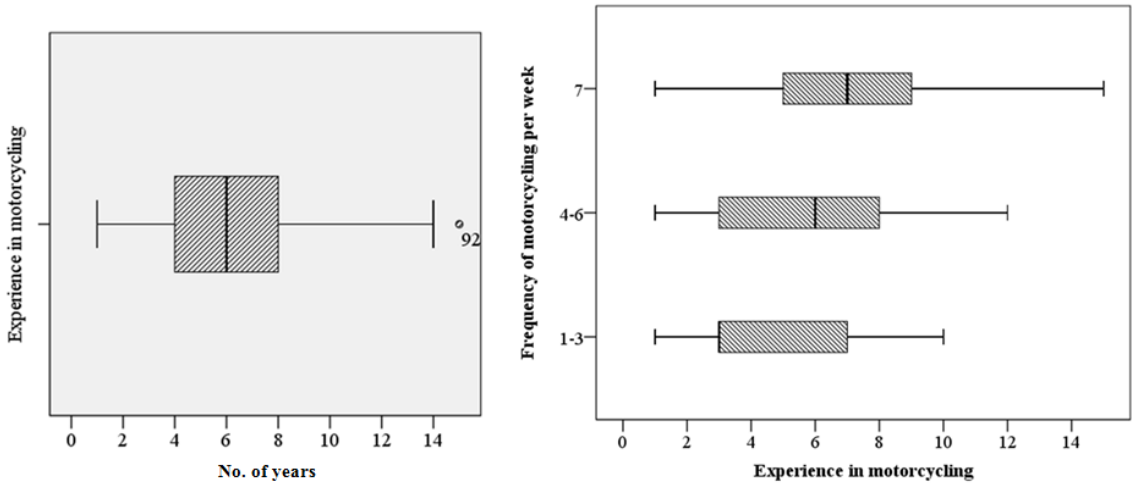
From the literature assessment and field study, it was summarized that there are five (5) characteristics that define an optimal riding posture. These five (5) characteristics are united as the Optimal Riding Posture Characteristics (ORPOC) Star (see Figure 2). The five (5) characteristics are:

i. Human operator's anthropometric characteristic and body mass
ii. Motorcycle cockpit designs (the handlebar, seat and the foot-pegs)
iii. Capability in performing motorcycling duties

iv. Overall real world motorcycling comfort over time
v. Overall real world motorcycling safety

3.2 Validation Result

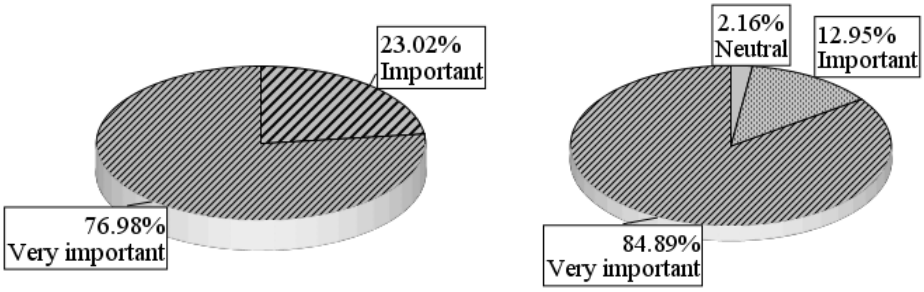
From the survey study it was seen that, most of the respondents were 23 years old. The height class of 1.61-1.70m and the weight class of 61-70kg showed the highest mode with respect to the respondents.



(a) (b)

Figure 3: Box and whisker plot of (a) respondents' motorcycling experience, and (b) respondents' frequency of motorcycling per week versus motorcycling experience

From Figure 3, about 25% (32) of the respondents have up to 4 years of experience in motorcycling. It was found that the respondents' frequency of motorcycling per week showed increment with increasing motorcycling experience. This was already anticipated since a more experienced motorcyclist would tend to perform motorcycling activity more frequently.



(a) (b)

Figure 4: Pie charts showing the result for (a) the importance of comfort during motorcycling, and (b) the importance of safety during motorcycling

From Figure 4, the result showed that generally 100% of the respondents agree that comfort is important for motorcycling activity (76.98% respondents selected 'very important', whilst, the remaining 23.02% selected 'important'). Almost similarly, with 84.89% and 12.95% of the respondents had selected 'very important' and 'important', whilst, only merely above 2% (at 2.16%) chosen 'neutral', it is agreed that the element of safety is generally important for motorcycling. In summary, the respondents were not divided in the importance of comfort and safety during motorcycling. Interestingly, that was however not the case for the other characteristics.

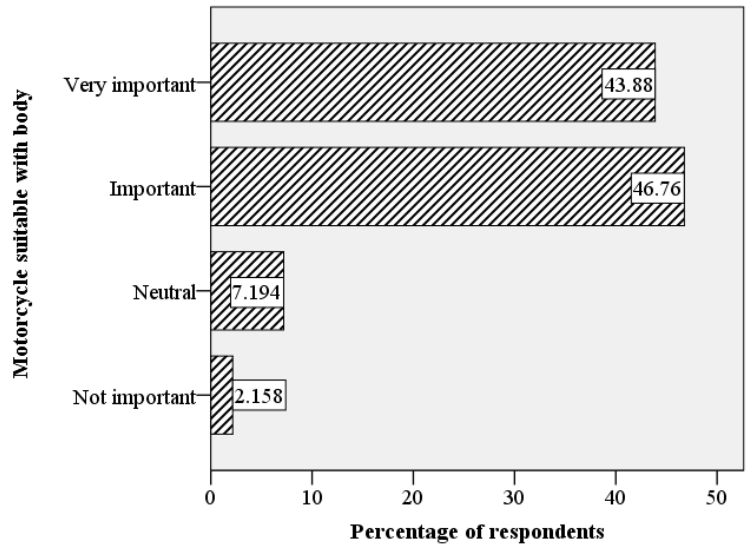


Figure 5: Likert's scale for question on the importance of having a motorcycle that suits the human operator

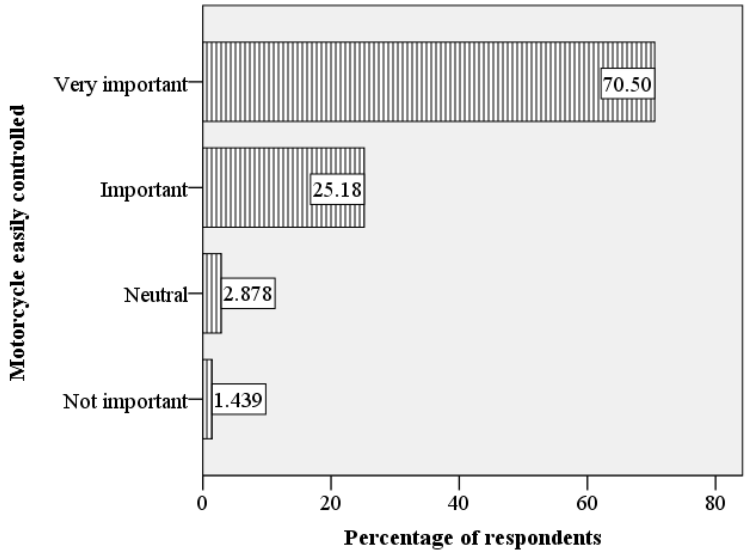


Figure 6: Likert's scale for question on having a motorcycle that is easy to manoeuvre and control

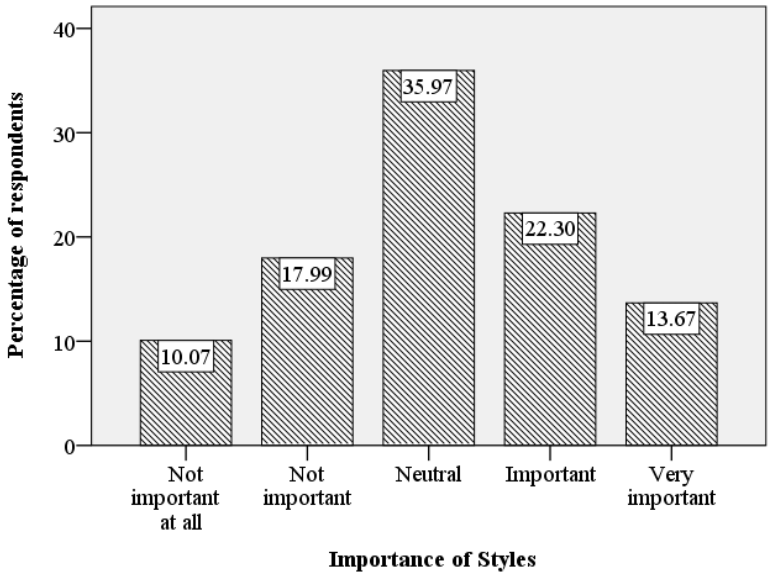


Figure 7: Likert's scale for question on the importance of styles while motorcycling

As shown in Figure 5 on the importance of having a motorcycle that suits the human operator, it was found that although vast majority the respondents selected 'important' and 'very important' (46.76% and 43.88%), 7.194% selected 'neutral', whilst, 2.158% chosen 'not important'. This shows that personal preferences are also a key factor in motorcycling. Certain motorcyclists who prefer certain types or designs of motorcycle might not take into consideration on their design 'fit' on the motorcycle. Nevertheless, given that the percentage given by the survey study, it was still concluded that having a motorcycle that suits the human operator's physical built and size is generally important.

Also showing a similar pattern as the question on the importance of having a motorcycle that suits the human operator (see Figure 5), the respondents seems to be a little divided in term of having a motorcycle that is easy to manoeuvre and control for motorcycling (see Figure 6). A majority of 70.50% and 25.18% of the respondents selected 'very important' and 'important', whilst, only a 2.878% and 1.439% selected 'neutral' and 'not important'. Nevertheless, it could also be said that this may come again to personal preferences and based on the survey study it was concluded that having a motorcycle that is easy to manoeuvre and control is important for motorcycling.

Finally, only with respect to style during motorcycling that the result was rather divided (see Figure 7). 22.30%, 17.99%, 13.67% and 10.07% have all selected 'important', 'not important', 'very important' and 'not important at all' respectively. Even so, with the majority of 35.97% stood for 'neutral' regarding this issue, it was concluded that 'style' is not a major importance in motorcycling.

4. Discussion

The aim of this study was to identify the characteristics of an optimal riding posture for motorcycling. The findings were then validated via a survey study. From the literature assessment and field study, it was summarized that there are five (5) characteristics that define an optimal riding posture.

Firstly, is with respect to the human operator's anthropometric characteristic and body mass. An optimal riding posture has to take the human operator's anthropometric characteristics and body mass into consideration in 'fitting' into the workstation (the motorcycle). This is crucial since these two independent characteristics would determine the amount of static loading (on the spinal column and body joints) and muscular activation needed to perform and maintained the riding posture. This is supported by literature such as Hamilton et al., (2013), Na et al., (2005), Nanthavanij (1996 and 1994). These literatures emphasized the strong connection between anthropometric characteristics and body mass with the overall human operator's comfort level.

Secondly, is regarding the motorcycle cockpit design. The motorcycle cockpit is made up of (i) handlebar (along with its components such as the triple clamps and top yoke), (ii) body (commonly houses the fuel tank), and (iii) seat/seating platform. The issue with motorcycle cockpit designs is with respect to ergonomically accommodate the human operator on the workstation (the motorcycle). Furthermore, changes or modifications are recommended to be performed to better 'fit' the human operator in performing the work (Okunribido et al., 2007, Magnusson and Pope, 1998). The motorcycle's cockpit design needs to be considered since it provides the contact point and platform where the human operator would be positioned to perform the work. Such workstation design consideration for human operator is strongly highlighted by studies such as Thariq et al., (2010) and Park et al., (2000).

Thirdly, the capability in performing motorcycling duties is defined as the riding posture could provide the human operator the capability to effectively, efficiently and safely perform the complex real world motorcycling duties. This is with respect to provide the necessary physical range of motion, the advantage of leverage and other aspects (dependent on the human operator's personal preferences) that aids in manoeuvring and controlling the motorcycle. As acknowledged by Codes (2010), human error will always be the main reason for the occurrence of road accidents involving motorcyclist. Therefore, having a premise that could minimize the occurrence of human error during real world motorcycling is absolutely crucial.

Fourthly, the overall real world motorcycling comfort is defined as the capability of the riding posture to provide a comfortable working condition for the human operator to perform real world motorcycling activities. This is in the sense that upon practicing and maintaining the riding posture, the human operator does not experience any awkwardness and significant physical stress and/or strain. Such awkwardness and physical stress and/or strain maybe originated from excessive muscular activities and uneven static loading distributions (e.g. high accumulation of static loading on small body joints). Another important aspect of motorcycling comfort is for the human operator to vary the riding posture with time. Duration of time is very crucial in the development of any work related disorders (Peeters et al., 2013; Brink et al., 2012; Rohlmann et al., 2011; Chen et al., 2009; Mehta and Tewari, 2000; Magnusson and

Pope, 1998). Chen et al., (2009) have noted that even for 1 hour of daily motorcycling could significantly increases the probability of adverse effects on the human operator. The optimal riding posture would ultimately provide minimal physical and physiological hazard to the human operator over time (Gallagher, 2005).

Finally, the overall safety reflects a condition where the riding posture could provide the overall safety to the human operator in performing real world motorcycling duties. The safety aspects comprise the human operator's physical, physiological and psychological well-being. The riding posture could ensure that the human operator could perform real world motorcycling in a safe and healthy manner in involving all the Human-Machine-Environment Interface (HMEI) elements.

In short, an optimally riding posture could provide the human operator with a safe working/motorcycling experience for the human operator with respect to practice and control the riding posture for longer duration of time in contrast to a non-'optimally' riding posture. From the perspective of this study, comfortable does not always illustrates optimal, yet, optimal is almost always comfortable. Hence, it is best to aim for an optimal riding posture for motorcycling.

5. Conclusion

Conclusively, there are five (5) characteristics that define an optimal riding posture. These five (5) characteristics are united as the ORPOC Star. The characteristics are: (i) the human operator's anthropometric characteristic and body mass, (ii) the motorcycle cockpit designs (the handlebar, seat and the foot-pegs), (iii) the capability in performing motorcycling duties, (iv) the overall real world motorcycling comfort over time, and (v) the overall real world motorcycling safety. It is strongly recommended that it is best to aim for an optimal working posture for any types of workstations and works. An optimal riding posture could best suits various types of motorcycling conditions, challenges and work demand while simultaneously does not sacrifice on comfort. This is even more crucial for real world motorcycling where the human operator is exposed to various hazards.

Acknowledgement

The authors would like to acknowledge the Ministry of Education (MOE) Malaysia for funding this research through the Fundamental Research Grant Scheme (FRGS/1/2014/TK01/UITM/02/3). The authors would also like to express their utmost gratitude to all members of the Motorcycle Engineering Test Lab (METAL), the staffs of the Faculty of Mechanical Engineering and the Institute of Graduate Studies in Universiti Teknologi MARA and the Human Factors and Ergonomics Society Malaysia (HFEM) who have, directly or indirectly, contributed to this research.

References

[1] Allen, P. H., Wadsworth, E. J. K. and Smith, A. P. 2006, The relationship between recorded hours of work and fatigue in seafarers. In P. D. Bust. (ed.) *Contemporary Ergonomics 2006*, (Taylor and Francis, London), 546-548
[2] Chen H-C., Chen W-C., Liu Y-P., Chen C-Y., & Pan Y-T. (2009). Whole-body vibration exposure experienced by motorcycle riders – an evaluation according to ISO 2631-1 and ISO 2631-5 standards. International Journal of Industrial Ergonomics, Volume 39, Issue 5, 708-718.
[3] Code, K., (2010). Code break – electronic rider aids. How a chip can save your bacon. Motorcyclist July 2010, Retrieved August 22, 2013 From Sport Rider Official Website: Http://Goo.Gl/Hvixs8.
[4] G. Kyung and M. A. Nussbaum, "Driver sitting comfort and discomfort (part II): Relationships with and prediction from interface pressure," International Journal of Industrial Ergonomics, vol. 38, pp. 526-538, 2008a.
[5] G. Kyung, M. A. Nussbaum, and K. Babski-Reeves, "Driver sitting comfort and discomfort (part I): Use of subjective ratings in discriminating car seats and correspondence among ratings," International Journal of Industrial Ergonomics, vol. 38, pp. 516-525, 2008b.
[6] Gallagher S. (2005). Physical limitation and musculoskeletal complaints associated with work in unusual or restricted postures: a literature review. Journal of Safety Research, Volume 36, Issue 1, 51-61.
[7] H. Chappells and E. Shove, "COMFORT: A review of philosophies and paradigms," March 2004.
[8] H. Suzuki, "Research trends on riding comfort evaluation in Japan," Proceedings of the Institution of Mechanical Engineers. Part F, Journal of rail and rapid transit, vol. 212, pp. 61-72, 1998.
[9] Hamilton M. A., Strawderman L., Babski-Reeves K., & Hale B. (2013). Effects of BMI and task parameters on joint angles during simulated small parts assembly. International Journal of Industrial Ergonomics, Volume 43, Issue 5, 417-424.
[10] M. Hagenzieker, "SWOV Fach Sheet: Motorcyclists," SWOV Institute for Road Safety Research, Leidschendam, Netherlands, December 2010.
[11] M. I. N. Ma'arof and I. N. Ahmad, "Proposed standard method for motorcycle nomenclature system," in Network of Ergonomics Societies Conference (SEANES), 2012 Southeast Asian, 2012, pp. 1-6.
[12] M. M. Abdul Manan and A. Várhelyi, "Motorcycle fatalities in Malaysia," IATSS Research, vol. 36, pp. 30-39, 2012.
[13] Ma'arof, M. I. N., Ahmad, I. N., Abdullah, N. R., Karim, S. A. (2012), "*Motorcycling Riding Issues: Understanding the Phenomenon and Development of Ergonomics Intervention in Improving Perceived Comfort for Prolonged Riding*", *iDECON*, 2012.
[14] Magnusson M. L., & Pope M. H. (1998). A review of the biomechanics and epidemiology of working postures (it isn't always vibration which is to blame!). Journal Of Sound And Vibration, Volume 215, Issue 4, 965-976.
[15] Mehta C. R., & Tewari V. K. (2000). Seating discomfort for tractor operators – a critical review. nternational Journal of Industrial Ergonomics, Volume 25, Issue 6, 661-674.
[16] Mohamed Thariq M.G., Munasinghe H.P., & Abeysekara J.D. (2010). Designing chairs with mounted desktop for university students: ergonomics and comfort. International Journal of Industrial Ergonomics, Volume 40, Issue 1, 8–18.

[17] Na S., Lim S., Choi H-S., & Chung M. K. (2005). Evaluation of driver's discomfort and postural change using dynamic body pressure distribution. nternational Journal of Industrial Ergonomics, Volume 35, Issue 12, 1085-1096.
[18] Nanthavanij S. (1994). An Ergonomie Assessment Of Fixed-Height, Partially Adjustable, And Fully Adjustable VDT Workstations By IntelAd. Computers & Industrial Engineering, Volume 27, Issues 1–4, 361-364.
[19] Okunribido O. O., Shimbles S. J., Magnusson M., & Pope M. (2007). City bus driving and low back pain: a study of the exposure to posture demands, manual materials handlings and whole-body vibration. Applied Ergonomics, Volume 38, Issue 1, 29-38.
[20] Park M-Y., Kim J-Y., & Shin J-H. (2000). Ergonomic design and evaluation of a new VDT workstation chair with keyboard-mouse support. International Journal of Industrial Ergonomics, Volume 26, Issue 5, 537-548.
[21] Peeters, G.M., Burton, N. W., & Brown, W. J. (2013), Associations between sitting time and a range of symptoms in mid-age women. Preventive Medicine 56, Issue 2, 135-141.
[22] R. Sarani, A. Roslan, and N. Saniran, "Motorcycle," MALAYSIAN INSTITUTE OF ROAD SAFETY RESEARCH (MIROS), May 2011.
[23] Rohlmann A., Zander T., Graichen F., Dreischarf M., & Bergmann G. (2011). Measured loads on vertebral body replacement during sitting. The Spine Journal, Volume 11, Issue 9, 870-875.
[24] Stedmon, A. (2010). HMI: Human-Motorcycle Interaction. Centre For Motorcycle Ergonomics & Rider Human Factors, Department Of Mechanical, Materials, Manufacturing Engineering (M3), University Of Nottingham, 1-18.

eureca 2017 – Conference Paper
Paper Number EUG26

Investigation of Ethylene Octene Copolymer Effects on Polypropylene Wood Composite

Chun Ming Ng[1], Soo Tueen Bee[1] , Chong-Yu Low[2] , Lee Tin Sin[1]

[1]*Department of Chemical Engineering, Lee Kong Chian Faculty of Engineering and Science, Universiti Tunku Abdul Rahman, Bandar Sungai Long, Jalan Sg Long, 43300 Cheras, Kajang, Selangor.*

[2]*Department of Petrochemical Engineering, Faculty of Engineering and Green Technology, Universiti Tunku Abdul Rahman, Jalan Universiti, Bandar Barat, 31900 Kampar, Perak.*

[*]direct.beest@gmail.com (Soo-Tueen Bee)

Abstract
PP-wood composite has been studied for its reinforcing properties and durability against humidity compared to conventional wood products, and PP-wood composite commonly commercialized as green plastic composite as it can be recycled easily by melting it and remold into a new product. Ethylene-octene copolymer (EOC) addition into PP improved its impact properties by reducing PP stiffness. In this study, the effect of adding EOC on mechanical properties into PP-wood composite was investigated. From the tensile analysis, the increasing of EOC amounts has gradually reduced the tensile strength of PP-wood composite from 14.57 MPa to 10.59 MPa before irradiation. However, the increasing of maleic anhydride grafted EOC loading level from 0.5 phr to 2 phr has decreased the tensile strength of all PP-wood composites except 1.5 phr.

Keywords: Polypropylene-wood composite, Ethylene-octene copolymer, Maleic Anhydride.

1. Introduction

Wood Plastic Composite (WPC) been introduced to the vast market used in furniture and household application due to its good weathering properties against UV and ozone inherited from plastic and rigidity from wood. This combination enabled WPC becomes the choice for applications which required to have plastic durability with wood surface finishing. In this research, the focus mainly on the study of the ethylene-octene copolymer (EOC) addition to polypropylene WPC for impact improvement and followed by crosslinked with electron beam irradiation method to further enhance its mechanical, thermal and weathering properties while further reduced the cost [1].

Alternatively, Incorporation of natural fiber in thermoplastic such as polypropylene started gaining the attention of multiple researchers around the globe as it serves as ability in improving strength and modifying thermal properties of the original composite. At this moment, the latest cost-effective way in the modification of polypropylene's mechanical properties is using renewable resources namely wood fiber, kenaf, flax, and lignin [2]–[4]. Previous published works gaining positive feedback on the enhancement of PP natural fiber composite typically on wood PP composite.

Another point of view, incorporation of coupling agent acting as adhesives between PP and wood fiber somehow exhibited slight improvement in mechanical properties as it improved the natural incompatibility of the two species and subsequently enhanced their stress distribution model within the polymer matrix and fiber. Typical coupling agents like silane, acrylic, and maleic anhydride were used to overcome the polymer-fiber weak interaction by connecting both species as mutual bonding with the strength of lower than permanent bonding like covalent formed from crosslinking process, particularly maleic anhydride became an emerging agent been used due to its market availability and ease of grafting to thermoplastic for mass production [5]–[10].

In addition, MA incorporated polymer-natural fiber composite exhibited positive feedbacks with its excellent reactivity toward both of the PP and wood fiber by forming a bridge between them, bond formation such as covalent bond and secondary bonds (Van der Waals force interaction and hydrogen bonds) were observed by incorporating MA into the composite [11].

On the contrary, EOC acts as an impact modifier and EOC commonly blended with PP to achieve better processability and desired mechanical properties such as tensile strength, Young modulus, and impact strength [12]. With its thermoplastic-like and thermoset-like properties made it a polymer compatibilizer in enhancing PP elasticity for better crack resistance when used in PP-wood composite due to reinforced effects from wood fiber. EOC dispersion capability in the polymer matrix made it an ideal choice to add into PP-wood composite to enhance its impact strength [13].

In this study, the EOC and maleic anhydride grafted ethylene octane (MA-g-EOC) used to measure their effects at various level of loadings toward the PP wood composite. Maleic anhydride grafted polymer functioned as coupling agent had been characterized by previous researchers eg. [14]–[16].

2. Methodology

2.1 Materials

Ethylene-octene copolymer was purchased from The Dow Chemical Company LLC, Engage 8100 (EOC) and Amplify GR 216 (EOC-g-MA) both with a specific gravity of 0.87 and MFI of 1 g/10 minutes. The polypropylene (PP) was used as polymer base in this study and it was manufactured by Lotte Titan Chemical, Titanpro PD943. The purchased PP resin has a specific gravity of 0.91 and MFI of 11 g/10 min. The wood flour was purchased from System Three wood flour which is filtered fine sawdust. Wood flour was used as filler in this study.

2.2 Experimental

2.2.1 Samples Preparation

Melt mixing method was utilized to compound the PP-wood composites according to Table 1 by using Brabender® Mixer 50 EHT GmbH internal mixer. PP and EOC/MA-g-EOC were firstly melted for 3 minutes and then followed by the addition of wood flour. The mixture compound was allowed to mix thoroughly for another 3 minutes. During compounding process, the mixing temperature was set at 170 °C and torque fixed at 60 rpm[17], [18],[19]. This is to maximize the mixing of polymer with the fiber and avoid losses of wood flour during the process and retard the possibility wood degradation due to prolonged exposure to the high processing temperature. The compounded PP-wood composites were hot press into 3 mm thickness sheet by using a hot press machine at a temperature of 175 ^{o}C for 8 min. The pressure load of the machine was set at 25 tonnes. The 3 mm thick sheets of PP-wood composites were then cut into required shapes.

Table 1: Experimental Formulations

Sample	Polypropylene	Wood Flour	EOC	EOC-g-MA
PW1502			0.5 phr	0.2 phr
PW1506				0.6 phr
PW1501				1.0 phr
PW1512			1.0 phr	0.2 phr
PW1516				0.6 phr
PW1511	100 phr	50 phr		1.0 phr
PW15A2			1.5 phr	0.2 phr
PW15A6				0.6 phr
PW15A1				1.0 phr
PW1522			2.0 phr	0.2 phr
PW1526				0.6 phr
PW1521				1.0 phr

2.2.2 Tensile test

The 3 mm thick sheet of PP-wood composites were cut into dumbbell shape in according to ASTM D639 type IV as shown in Fig. 1 and Table 2. The dumbbell-shaped

specimens were tested using an Instron Tensile Microtester with straining rate of 50mm/min. The width and thickness of each specimen were measured using a vernier caliper before the testing. The tensile strength, elongation at break and Young's modulus were recorded as an average value of 5 specimens.

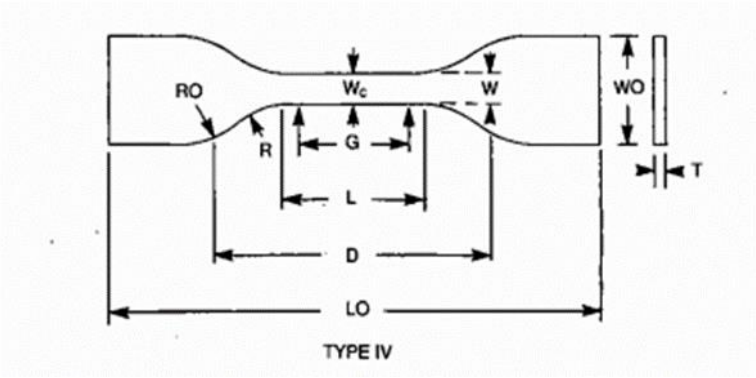


Figure 1: Label of Section for ASTM D638 Type IV Tensile Specimen[20]

Table 2: Dimensions for ASTM D638 Type IV Tensile Test Specimen [20]

Dimensions (see Drawings)	Type IV	Tolerances
W-Width of narrow section	6	±0.5
L-Length of narrow Section	33	±0.5
WO-Width Overall	19	+ 6.4
LO-Length Overall	115	No max
G-Gage length	25	±0.13
D-Distance between grips	65	±5
R-Radius of fillet	14	±1
RO-Outer Radius	25	±1
T-Thickness	4 or under	-

3. Results and Discussions

3.1 Tensile Strength of Composite

All tensile data collected and tested under constant room temperature at 25 °C to ensure consistency of result during mechanical testing. Figure 2 illustrates the effect of loading level of EOC and loading level of maleic anhydride grafted on EOC on the tensile strength of PP wood composite by varying the concentration of MA-g-EOC at 0.2, 0.6 and 1.0 phr and EOC concentration at 0.5 phr, 1.0 phr, 1.5 phr and 2.0 phr as tabulated in Table 1.

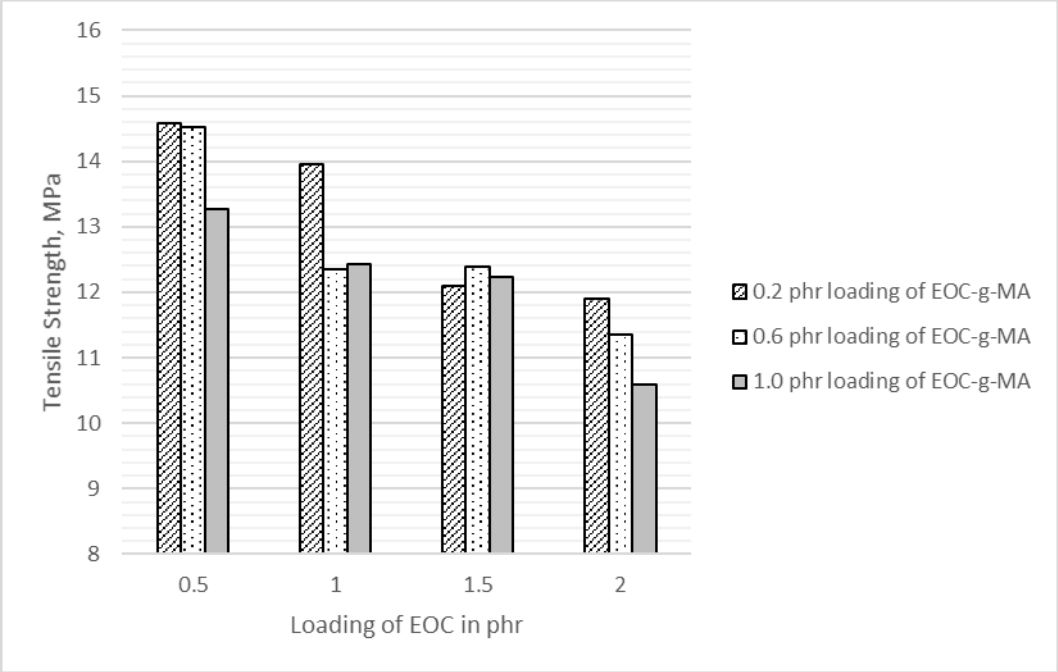


Figure 2: Tensile Strength of PP-Wood Composite with Various Loading Levels of EOC and MA-g-EOC.

From the result of tensile strength, the increasing of EOC loading level was found to gradually decrease the tensile strength of PP-wood composites. The indicates that the incorporation of EOC in PP-wood composites has caused an inferior effect on tensile strength of PP-wood composites. This might be due to the hydrophobic behaviour of EOC unable to improve the interaction effect between the PP and wood flour in the polymer matrix. According to the Fig. 2, it was observed that the tensile strength of all EOC amount added PP-wood composites (except 1.5 phr EOC) was observed to decrease when the loading level of maleic anhydride grafted on EOC increased from 0.2 phr to 1 phr. This observation has suggested that increasing of maleic anhydride amounts grafted on EOC would cause a reduction in tensile strength as a result of increased EOC species been occupied into the PP matrix caused a reduction in tensile strength [13]. In addition, adhesion of PP and wood fibre might be absent due to the natural incompatibility of the two species where PP existed as hydrophobic species while wood fibre as hydrophilic species, without any polymer-fibre binder or compatibilizer, could result in weak or non-existence of interfacial interaction between the two species, similar result could be found in [19], [21]–[23]. The result showed that EOC contents increased caused a reduction in tensile strength of the PP wood composite from a high at 14.57 MPa to a low at 10.59 MPa in overall.

Referred to the low loading of EOC at 0.5 phr, changes in tensile strength was not significantly observed for sample with 0.2 and 0.6 phr MA-g-EOC loading, but when the loading of MA-g-EOC reached 1 phr caused the sample's tensile dropped about 8.5 - 8.9 % compared to the previous loading of MA-g-EOC. This might due to increasing amount of EOC presence in PP matrix and increased its rubbery phase of the composite. A similar result was observed at both 1.0 and 2.0 phr loading of EOC might explain that EOC presence dominated the effect of MA, a coupling agent between polymer with fiber and downplayed the role of the coupling agent in this three EOC concentration samples.

However, a different result was observed for sample with 1.5 phr loading of EOC where the changes in tensile strength were not significant and gradually constant across the changes in MA-g-EOC concentration. With a slight increase in tensile for 0.6 phr loading of MA-g-EOC, at this loading of MA might translate in overcoming shortly the EOC weakening effects toward the tensile strength of the composite. MA commonly added or grafted to PP-fibre composite for enhancement effect in term of interfacial interaction between PP and wood or other fiber referred here with previous studies conducted in [8], [9].

Although as EOC's concentration increased reduced the tensile strength with an exception for the composite with 1.5 phr loading of EOC, but the changes are kept at a minimum with differences in between 0.2 to 0.3 MPa according to the result obtained. This might due to crystal arrangement changes by the presence of EOC in the matrix. From the result, it was suggested that incorporation of EOC into the PP matrix affects tensile strength rather than Young's modulus of the composite, this might cause by the weak adhesion between wood particles and EOC due to the incompatibility of the two species [9].

Apart from that, tensile strength weakening effects induced by incorporation of wood fiber that distorted the PP matrix creating low interfacial interaction in the matrix phase induced lower tensile strength, as the ratio of PP to wood was kept at 2:1 across all the formulations. 50 phr loading of wood flour as used in this study might create chances for slip in PP matrix phase consequently caused mechanical failure at lower stress applied [24]. At 2.0 phr loading of EOC, saw a consistent reduction in tensile strength with the increase in MA-g-EOC loading into the composite suggested that higher EOC loading caused loss in tensile strength from 11.9 MPa to 10.59 MPa.

3.2 Young's Modulus

The Young's modulus of the composite trending behaves differently compared to tensile strength for EOC increment in composition as showed in Fig. 3.

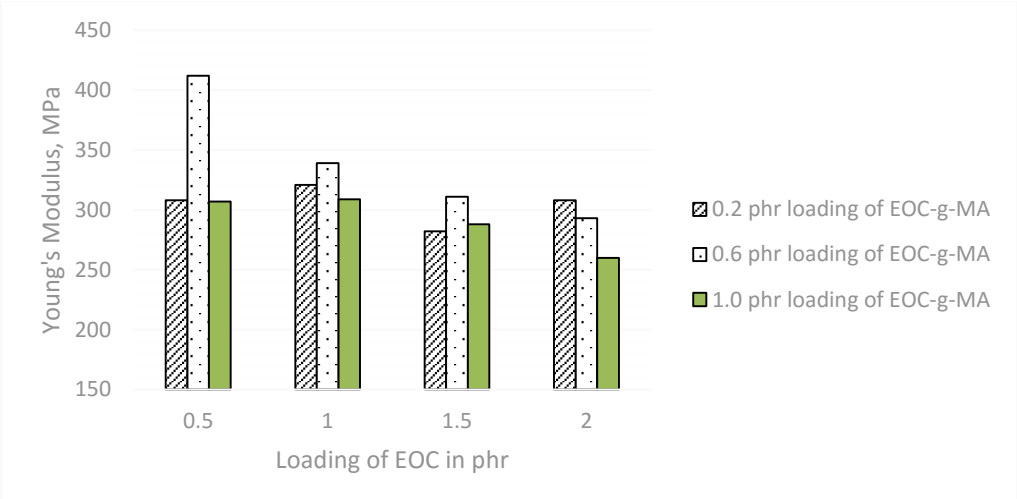


Figure 3: Young's Modulus of PP-Wood Composite with Various Loading of EOC and MA-g-EOC before Electron Beam Irradiation

At 0.5 phr loading of EOC and 0.6 phr loading of MA-g-EOC, Young's modulus increased to 412 MPa from 308 MPa, which behaved opposite compared to tensile strength behavior in previous section. From the result of Young's modulus reflected that higher modulus produced by the 0.6 phr MA-g-EOC loaded samples except 2 phr EOC loaded sample, this result suggested that MA-g-EOC loading at 0.6 phr created better rigidity compared to the rest, while lost in tensile strength does not caused lost in modulus in huge margin.

Similar trending was observed across the result for the composite with 0.6 phr of MA-g-EOC loaded sample showed an increased peak from the bar chart in Fig. 3. This suggested that with 0.6 phr of EOC-g-MA effectively reduced the composite percent elongation might suggest that the composite is much stiffer than its counterpart. Thus, incorporation of MA-g-EOC at 0.6 phr into PP-wood composite made the composite become more rigid and less elastic compared to other except for 2.0 phr EOC loaded composite. However, further investigation after electron beam irradiation should result in better elongation of the specimen and better elasticity compared to the non-irradiated samples as referred to the previous study in [17], [13], [12], [25], [26].

From the trending for 0.6 phr MA-g-EOC loaded sample demonstrated constant dropping in modulus across the EOC loading increment from 0.5 to 2 phr loading. Decrease in modulus trending showed that EOC increases started to distort the PP-EOC matrix as the two species was not miscible to each other in the sense of interaction importance when compared.

3.3 Elongation at Break

From the result of tensile strength and Young's modulus above, both revealed an opposite trend. Percent elongation at break for PP-wood composite with various loading of EOC and MA-g-EOC result were obtained and plotted in bar chart Fig. 4 below for comparison.

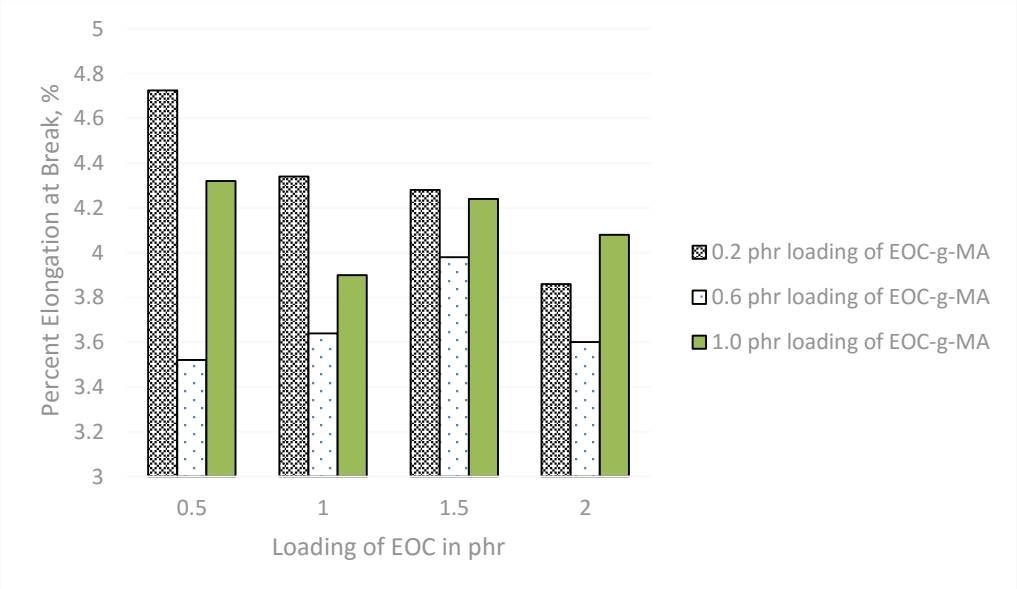


Figure 4: Percent Elongation at Break of PP-Wood Composite with Various Loading of EOC and MA-g-EOC before Electron Beam Irradiation

The percent elongation at break in overall view demonstrated that each formulation possessed different trending compared to both tensile and modulus result above. At low loading of EOC gives better elongation result compared to the other EOC loading, possibly due to complexity in compact PP-wood composite as the loading was much lower compared to other study with high loading of EOC and low loading of fiber done in [9].

Referred to Fig. 4, samples with 0.2 phr loading of MA-g-EOC overall demonstrated a consistent dropped in elongation as EOC loading increased from 0.5 to 2 phr. The result revealed that EOC presence across this PP-wood composite caused the composite to elasticity loss and low tensile, might induced by the EOC in PP matrix does not interact well by weak interfacial interaction. As described by [26], interfacial interaction of composite between PP-EOC, PP-EOC-MA-g-EOC, PP-wood, EOC-wood and MA-g-EOC-PP-wood is important in forming bonding to ensure mechanical properties does not degrade or weaken when forming a composite. Such weak interfacial interaction destructed the composite resistance against stress and hardly comparable with other composite which is adhered perfectly. Due to absence of electron beam modifications and low loading of MA presence in composite (< 0.5 wt %), adhesion between PP and wood, and EOC hardly achieve and created different phase within the composite's microstructure.

By comparing the 0.6 phr MA-g-EOC loaded samples demonstrated better trending in term of increasing in elongation percent at break from 0.5 to 1.5 phr loading of EOC in PP-wood composite. As described and observed in previous result of tensile strength and modulus, the result obtained for 0.6 phr MA-g-EOC loaded sample tends to perform better comparing to 0.2 and 1 phr MA-g-EOC loading samples. However, the improvement in percent elongation result observed was not significantly changed as compared to the weakening effect of other loading.

However, comparing the sample of 1 phr MA-g-EOC loaded with various loading of EOC revealed a fluctuation in percent elongation at break value when compared. This phenomenon might cause by the inconsistency in stress distribution when EOC concentration increased in PP matrix while MA effects remained less prevalent toward the mechanical properties. Further explanation on this, lack of effective bonding formation within the polymer matrix could be result in poor elongation while caused failure when excessive stress been applied to the composite and comparable to previous study in [27], [15].

4. Conclusion

In this study, it found that the increased in EOC loading level has reduced the tensile strength of PP-wood composites where at 0.5 phr loading of EOC with tensile strength of 14.57 MPa dropped to a low of 10.59 MPa at 2.0 phr of EOC loading. This also indicated that Ma-g-EOC does not have prominent effect at this low concentration in adhering wood fiber with PP. In other hand, Young's modulus which demonstrated an opposite result compared to tensile properties in which 0.6 phr of Ma-g-EOC possessed better result compared to other loading of Ma-g-EOC resulted in better

rigidity and less elastic. Further investigation on electron beam irradiation effects on the composite could reflect in enhancement in both tensile strength and interaction between wood and PP. While the percent elongation at break result the best at 0.5 phr EOC loading with 0.2 phr MA-g-EOC loaded PP-wood composite. In following work in study using electron beam irradiation might improve the mechanical properties discussed above which does not irradiated as reported by previous researchers.

References

[1] Kirk Hanawalt, "Wood-Plastics Composites Done Right : Plastics Technology." [Online]. Available: https://www.ptonline.com/articles/wood-plastics-composites-done-right. [Accessed: 09-Nov-2017].

[2] T. Schnabel, H. Huber, T. A. Grünewald, and A. Petutschnigg, "Changes in mechanical and chemical wood properties by electron beam irradiation," *Appl. Surf. Sci.*, vol. 332, pp. 704–709, 2015.

[3] S. W. Kim, S. Oh, and K. Lee, "Variation of mechanical and thermal properties of the thermoplastics reinforced with natural fibers by electron beam processing," *Radiat. Phys. Chem.*, vol. 76, no. 11–12, pp. 1711–1714, 2007.

[4] T. Huber, U. Biedermann, and J. Müssig, "Enhancing the Fibre Matrix Adhesion of Natural Fibre Reinforced Polypropylene by Electron Radiation Analyzed with the Single Fibre Fragmentation Test," *Compos. Interfaces*, vol. 17, no. 4, pp. 371–381, Jan. 2010.

[5] H. A. A. Youssef, M. R. R. Ismail, M. A. M. A. M. Ali, and A. H. H. Zahran, "Effect of the various coupling agents on the mechanical and physical properties of thermoplastic-bagasse fiber composites," *Polym. Compos.*, vol. 29, no. 9, pp. 1057–1065, Sep. 2008.

[6] J. Sharif, S. F. Mohamad, N. A. Fatimah Othman, N. A. Bakaruddin, H. N. Osman, and O. Güven, "Graft copolymerization of glycidyl methacrylate onto delignified kenaf fibers through pre-irradiation technique," *Radiat. Phys. Chem.*, vol. 91, pp. 125–131, 2013.

[7] J. Harun, K. Abdan, and K. Zaman, "Rheological behaviour of injection moulded oil palm empty fruit bunch fibre - Polypropylene composites: Effects of electron beam processing versus maleated polypropylene," *Mol. Cryst. Liq. Cryst.*, vol. 484, no. October 2014, pp. 500–508, Apr. 2008.

[8] A. Sudár, C. Burgstaller, K. Renner, J. Móczó, and B. Pukánszky, "Wood fiber reinforced multicomponent, multiphase PP composites: Structure, properties, failure mechanism," *Compos. Sci. Technol.*, vol. 103, pp. 106–112, 2014.

[9] S. Bagheri-Kazemabad *et al.*, "Morphology, rheology and mechanical properties of polypropylene/ethylene-octene copolymer/clay nanocomposites: Effects of the compatibilizer," *Compos. Sci. Technol.*, vol. 72, no. 14, pp. 1697–1704, 2012.

[10] C. T. Ratnam, G. Raju, and W. M. Z. W. Yunus, "Oil palm empty fruit bunch (OPEFB) fiber reinforced PVC/ENR blend-electron beam irradiation," *Nucl. Instruments Methods Phys. Res. Sect. B Beam Interact. with Mater. Atoms*, vol. 265, no. 2, pp. 510–514, 2007.

[11] S. M. B. Nachtigall, G. S. Cerveira, and S. M. L. Rosa, "New polymeric-coupling agent for polypropylene/wood-flour composites," *Polym. Test.*, vol. 26, no. 5, pp. 619–628, Aug. 2007.

[12] S. Poongavalappil, P. Svoboda, R. Theravalappil, D. Svobodova, M. Danek, and M. Zatloukal, "Study on the influence of electron beam irradiation on the

thermal, mechanical, and rheological properties of ethylene-octene copolymer with high comonomer content," *J. Appl. Polym. Sci.*, vol. 128, no. 5, pp. 3026–3033, 2013.

[13] J. R. Kumar, P. S. Gopala Krishnan, and S. K. Sharma, "Studies on natural fiber reinforced isotactic polypropylene-ethylene-octene copolymer blend composites," *J. Thermoplast. Compos. Mater.*, vol. 25, no. 7, pp. 865–878, 2012.

[14] H. Gao, Y. Xie, R. Ou, and Q. Wang, "Grafting effects of polypropylene/polyethylene blends with maleic anhydride on the properties of the resulting wood-plastic composites," *Compos. Part A Appl. Sci. Manuf.*, vol. 43, no. 1, pp. 150–157, Jan. 2012.

[15] A. Hassan, N. Othman, M. U. Wahit, L. J. Wei, A. R. Rahmat, and Z. A. Mohd Ishak, "Maleic anhydride polyethylene octene elastomer toughened polyamide 6/polypropylene nanocomposites: Mechanical and morphological properties," in *Macromolecular Symposia*, 2006, vol. 239, pp. 182–191.

[16] N. Sombatsompop, C. Yotinwattanakumtorn, and C. Thongpin, "Influence of type and concentration of maleic anhydride grafted polypropylene and impact modifiers on mechanical properties of PP/wood sawdust composites," *J. Appl. Polym. Sci.*, vol. 97, no. 2, pp. 475–484, Jul. 2005.

[17] R. Rajeshbabu, U. Gohs, K. Naskar, V. Thakur, U. Wagenknecht, and G. Heinrich, "Preparation of polypropylene (PP)/ethylene octene copolymer (EOC) thermoplastic vulcanizates (TPVs) by high energy electron reactive processing," *Radiat. Phys. Chem.*, vol. 80, no. 12, pp. 1398–1405, 2011.

[18] A. Almaslow, C. T. Ratnam, M. J. Ghazali, R. J. Talib, and C. H. Azhari, "Effects of electron-beam and sulfur crosslinking of epoxidized natural rubber on the friction performance of semimetallic friction materials," *Compos. Part B Eng.*, vol. 54, no. 1, pp. 377–382, 2013.

[19] C. E. Lane, I. Ahmad, D. H. Mohd, and I. Abdullah, "Effects of Rice Husk Modification with Liquid Natural Rubber and Exposure to Electron Beam Radiation on the Mechanical Properties of NR/HDPE/Rice Husk Composites," *Sains Malaysiana*, vol. 40, no. 9, pp. 985–992, 2011.

[20] "ASTM D638 - 14 Standard Test Method for Tensile Properties of Plastics." [Online]. Available: https://www.astm.org/Standards/D638.htm. [Accessed: 05-Sep-2017].

[21] M. M. Younes *et al.*, "Effect of electron beam irradiation on physico-mechanical properties of wood flour-polyethylene composites," *Polym. Compos.*, vol. 29, no. 7, pp. 768–772, 2008.

[22] I. S. Aji, E. S. Zinudin, M. Z. Khairul, K. Abdan, and S. M. Sapuan, "Induced tensile properties with EB- cross linking of hybridized kenaf/palf reinforced HDPE composite," *Pertanika J. Sci. Technol.*, vol. 21, no. 1, pp. 135–140, 2013.

[23] I. Ahmad, C. E. Lane, D. H. Mohd, and I. Abdullah, "Electron-beam-irradiated rice husk powder as reinforcing filler in natural rubber/high-density polyethylene (NR/HDPE) composites," *Compos. Part B Eng.*, vol. 43, no. 8, pp. 3069–3075, 2012.

[24] a. El-Sabbagh and A. El-Sabbagh, "Effect of coupling agent on natural fibre in natural fibre / polypropylene composites on mechanical and thermal behaviour," *Compos. Part B Eng.*, vol. 57, pp. 126–135, Feb. 2014.

[25] R. Rajeshbabu, U. Gohs, K. Naskar, M. Mondal, U. Wagenknecht, and G. Heinrich, "Electron-induced reactive processing of poly(propylene)/ethylene-octene copolymer blends: A novel route to prepare thermoplastic vulcanizates," *Macromol. Mater. Eng.*, vol. 297, no. 7, pp. 659–669, 2012.

[26] T. Czvikovszky, "Electron-beam processing of wood fiber reinforced polypropylene," *Radiat. Phys. Chem.*, vol. 47, no. 3, pp. 425–430, 1996.
[27] M. R. Ismail, A. A. M. Yassen, and M. S. Afify, "Mechanical properties of rice straw fiber-reinforced polymer composites," *Fibers Polym.*, vol. 12, no. 5, pp. 648–656, Aug. 2011.

eureca 2017 – Conference Paper
Paper Number EUG27

A Numerical Investigation on the Performance of Wind Turbine Airfoils with Gurney Flaps and Airfoil Shape Alteration

Abubker Fadl[1], Mohammed Abbasher [1], Obai Younis Taha[2,1,*], Ali El Seory[1]

[1] *University of Khartoum, Faculty of engineering, Department of Mechanical Engineering Khartoum, Sudan*
[2] *Prince Sattam Bin Abdulaziz University, Faculty of engineering at Wadi Aldwaser, Department of Mechanical Engineering, KSA*

[*] *Oubeytaha@hotmail.com*

Abstract
1. A two-dimensional numerical investigation was conducted to determine the effect of a modified gurney flap configuration on S823 and S822 airfoils (from the NREL airfoil families). The device used consists of a flap (flat plate) on the order of 1-3% of the airfoil chord in length, oriented perpendicular to the chord line and located on the pressure side at 96%c from the leading edge, whilst the remaining 4%c was eliminated similarly to the structure of blunt trailing edge airfoils, for the purpose of drag reduction and structure stability. The flow field around the airfoil was numerically predicted using the commercial package ANSYS Fluent 15.0, an incompressible Navier—Stokes solver, and the two-equation turbulence model k – ε at different Reynolds numbers. The numerical results show that the flaps increase the airfoil lift coefficient and slightly decrease the drag coefficient. The obtained data also show that flaps with high length increase the drag significantly. It was found that using a flap length of 2%c at angles of attack ranging from 4 to 6 increases the lift to drag ratio to reach its maximum value (increases by 97% and the lift coefficient by 138%).

Keywords: Numerical investigation, airfoil, Gurney flap, blunt airfoil.

1. Introduction

Flow control is a major, rapidly evolving field of fluid dynamics. It implies a small change of a configuration serving an ideally large engineering benefit, like drag reduction and lift increase. This benefit could really affect the aerodynamic performance of airfoils used in different aerodynamic devices.

Gurney flap is a passive control method (does not require adding energy) consisting of a small tab located at the trailing edge of the airfoil [1]. The device provides a significant increase in lift with a small drag penalty for tab lengths less than 3%c.

Liebeck [1] stated that racing car tests conducted by Dan Gurney showed that when the flap was installed on the rear wing, the vehicle had increased turning speeds. The increased cornering speeds were attributed to the increased downward force applied by the rear wing. It was also noticed, that increasing the flap size above 2% of the wing chord length noticeably increased the drag, even though there was a continuing increase in downward force.

Myose et. al [2] conducted low speed wind tunnel tests on NACA 0011 airfoil with Gurney flap heights ranging from 1% to 4% of the chord. They noticed that Gurney flap increases the upper surface suction and lower surface pressure thereby resulting in lift increment. They also reported increase in nose-down pitching moment due to Gurney flap. The wake velocity profiles plotted by them indicate downward turning of the flow behind the airfoil due to presence of Gurney flap. They concluded that Gurney flap works by increasing the effective camber of airfoil.

Jang et al [3] conducted a two-dimensional numerical investigation to determine the effect of a Gurney flap on a NACA 4412 airfoil. The flow field around the airfoil was numerically predicted using INS2D, and the one-equation turbulence model of Baldwin and Barth. Six Gurney flap sizes between 0.5% and 3.0% of the airfoil chord were studied. The results showed that Gurney flaps increase the airfoil lift coefficient with only a slight increase in drag coefficient. It also showed that the use of a 1.5% chord length Gurney flap increases the airfoil lift coefficient by 0.3 and decreases the angle of attack required to obtain a given lift coefficient by 3°.

Baker et al [4] preformed wind tunnel experimentation and Reynolds-averaged Navier-Stokes simulations to analyze simple, static trailing-edge devices applied to an FB-3500-1750 blunt airfoil. The drag reduction devices investigated include splitter plates, base cavities, and offset cavities, splitter plate lengths between 50% and 150% of the trailing-edge thickness and plate angles (+ 10°). Drag reductions on the order of up to 50% were achieved with the addition of a splitter plate, but caused drastic changes to lift, primarily due to the method of device implementation.

This study tests a combined configuration between blunt airfoils and gurney flaps. It involves removing the trailing part of the airfoil downstream the flap, which is perpendicular to the chord line. The length to be removed is 4%c and the flap to be studied is 1%c wide. The primary objective is to study the Navier-Stokes analysis of the flow past NREL's S822 and S823 airfoils with this flap configuration of different heights using Ansys's CFD Fluent 15 and to compare the results obtained against clean airfoil configuration results. IT also aim to select the flap length and the range of angle of attacks, AoAs that give the maximum lift to drag ratio, C_l/C_d.

This configuration (shown in Figures 1, 2, 3, 4 and 5) is expected to minimize the drag penalty accompanied with gurney flaps while addressing the need for thick airfoil sections necessary to meet the structural and volume requirements of various aerodynamic systems [4].

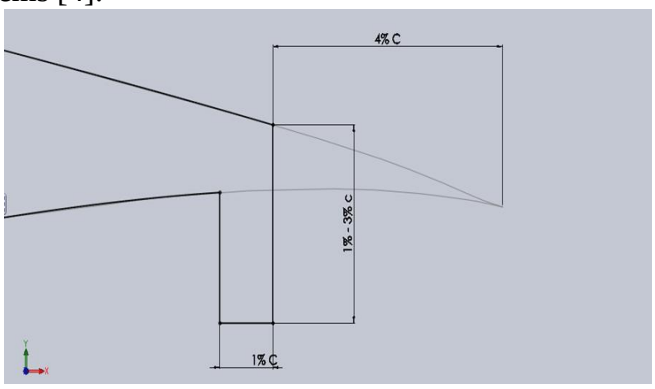


Figure 116. Trailing edge flow structure of the airfoil with the Gurney flap

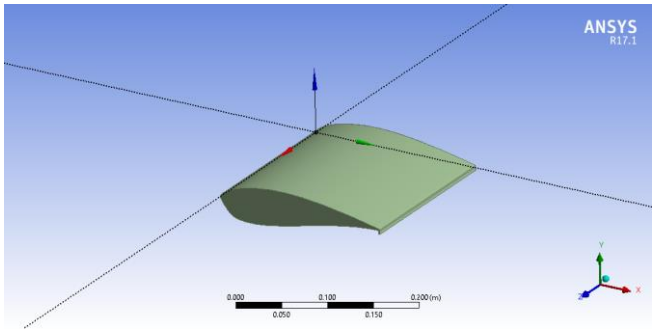


Figure 117. A 3D view of a the blade section equipped with the flap

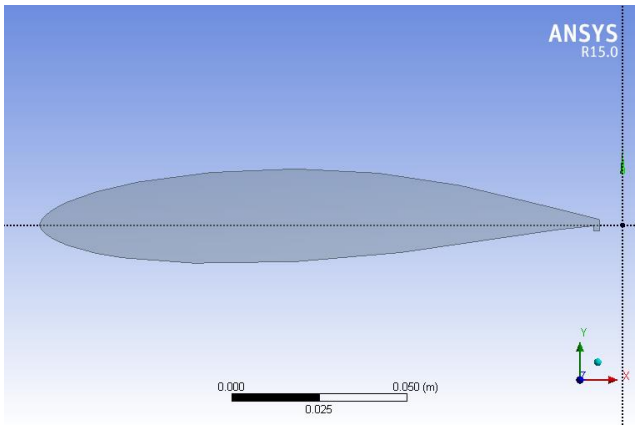


Figure 118. The airfoil equipped with flap1

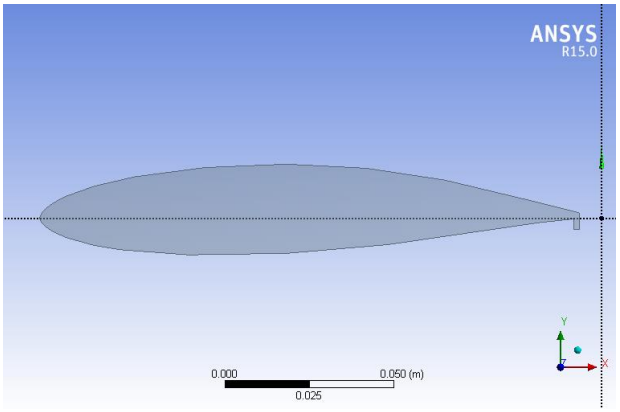


Figure 119 The airfoil equipped with flap2

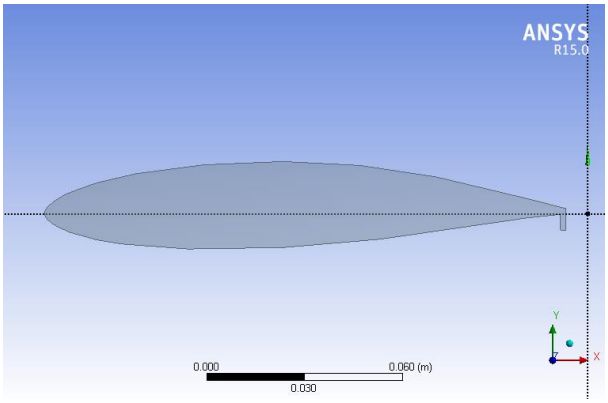


Figure 120 The airfoil equipped with flap3

2. Governing Equations

The system of equations known as the Navier–Stokes equations takes account of the full three-dimensional, viscous nature of fluid motion and is equally valid in laminar and turbulent flows.

The equation of continuity expresses the principle of conversation of matter. The differential form of the equation is obtained by considering the flow into and out of an elementary control volume. For the rectangular Cartesian coordinate system, with coordinates x, y, z measured relative to a stationary frame of reference, and corresponding velocity components u, v and w the continuity equation is:

$$\frac{\delta\rho}{\delta t} + \frac{\delta(\rho u)}{\delta x} + \frac{\delta(\rho v)}{\delta y} + \frac{\delta(\rho w)}{\delta z} = 0 \qquad (1)$$

where ρ is the fluid density.

The x, y and z components of the momentum equation are obtained by applying Newton's second law to an elementary volume of fluid. The resulting three equations for the rectangular Cartesian coordinate system are:

$$\frac{\delta(\rho u)}{\delta t}+\frac{\delta(\rho u^2)}{\delta x}+\frac{\delta(\rho uv)}{\delta y}+\frac{\delta(\rho uw)}{\delta z}=\rho X-\frac{\delta P}{\delta x}+\frac{\delta}{\delta x}\left[\mu\left(2\frac{\delta u}{\delta x}-\frac{2}{3}\left(\frac{\delta u}{\delta x}+\frac{\delta v}{\delta y}+\frac{\delta w}{\delta z}\right)\right)\right]+$$
$$\frac{\delta}{\delta y}\left[\mu\left(\frac{\delta u}{\delta y}+\frac{\delta v}{\delta x}\right)\right]+\frac{\delta}{\delta z}\left[\mu\left(\frac{\delta w}{\delta x}+\frac{\delta u}{\delta z}\right)\right] \quad (2)$$

$$\frac{\delta(\rho v)}{\delta t}+\frac{\delta(\rho v^2)}{\delta x}+\frac{\delta(\rho vu)}{\delta y}+\frac{\delta(\rho vw)}{\delta z}=\rho Y-\frac{\delta P}{\delta y}+\frac{\delta}{\delta y}\left[\mu\left(2\frac{\delta v}{\delta y}-\frac{2}{3}\left(\frac{\delta u}{\delta x}+\frac{\delta v}{\delta y}+\frac{\delta w}{\delta z}\right)\right)\right]+$$
$$\frac{\delta}{\delta z}\left[\mu\left(\frac{\delta v}{\delta z}+\frac{\delta w}{\delta y}\right)\right]+\frac{\delta}{\delta x}\left[\mu\left(\frac{\delta u}{\delta y}+\frac{\delta v}{\delta x}\right)\right] \quad (3)$$

$$\frac{\delta(\rho w)}{\delta t}+\frac{\delta(\rho w^2)}{\delta x}+\frac{\delta(\rho wu)}{\delta y}+\frac{\delta(\rho wv)}{\delta z}=\rho Z-\frac{\delta P}{\delta z}+\frac{\delta}{\delta z}\left[\mu\left(2\frac{\delta w}{\delta z}-\frac{2}{3}\left(\frac{\delta u}{\delta x}+\frac{\delta v}{\delta y}+\frac{\delta w}{\delta z}\right)\right)\right]+$$
$$\frac{\delta}{\delta x}\left[\mu\left(\frac{\delta w}{\delta x}+\frac{\delta u}{\delta z}\right)\right]+\frac{\delta}{\delta y}\left[\mu\left(\frac{\delta v}{\delta z}+\frac{\delta w}{\delta y}\right)\right] \quad (4)$$

Equations (2-4) in which the symbols x, y, z represent the components of a body force, were first derived, independently, by Sir George Stokes and the French engineer, Louis Navier in 1822, and consequently the equations are known collectively as the Navier–Stokes equations[5].

$k-\varepsilon$ Turbulence model

The model used in this study is the turbulence model $k-\varepsilon$, which uses the following two equations, one for turbulent kinetic energy, k and the other for the dissipation of turbulent kinetic energy, :

$$\frac{\delta(\rho k)}{\delta t}+\ \mathrm{div}(\rho kU)=\mathrm{div}\left[\frac{\mu_t}{\sigma_k}\ \mathrm{grad}\ k\right]+\ 2\mu_t E_{ij}\ .\ E_{ij}-\ \rho\varepsilon \quad (5)$$

$$\frac{\delta(\rho\varepsilon)}{\delta t}+\ \mathrm{div}(\rho\varepsilon U)=\mathrm{div}\left[\frac{\mu_t}{\sigma_\varepsilon}\ \mathrm{grad}\ \varepsilon\right]\ +C_{1\varepsilon}\frac{\varepsilon}{k}\ 2\mu_t E_{ij}\ .\ E_{ij}-C_{2\varepsilon}\ \rho\varepsilon\ \frac{\varepsilon^2}{k} \quad (6)$$

where μ_t is the eddy viscosity,

$$\mu_t=\ \rho\ C_\mu\frac{k^2}{\varepsilon} \quad (7)$$

where σ_k,E_{ij},$C_{1\varepsilon}$,$C_{2\varepsilon}$,C_μ, σ_ε are dimensionless constants.

3. Methodology

In this numerical study, an incompressible Navier—Stokes solver and the turbulent model $k-\varepsilon$ were used to calculate the flow field around the airfoil. The meshing type used in this simulation is a 2D, C-type grid. The meshing software used was ANSYS ICEM. The first step in the meshing process is to import the curves that constitute the bottom and top airfoil surfaces. The curves are made up from a set of points.

The computational domain is a C-type far filed expanding 12 chord lengths from the airfoil in all directions as shown in Figure 6 and 7. The domain consists of four edges, a curved edge in front of the airfoil leading edge, top and bottom edges that are parallel to the airfoil chord line, and a vertical edge to the rear of the airfoil trailing edge. A fluid surface overlaps the airfoil curves created in between the domain edges [6].

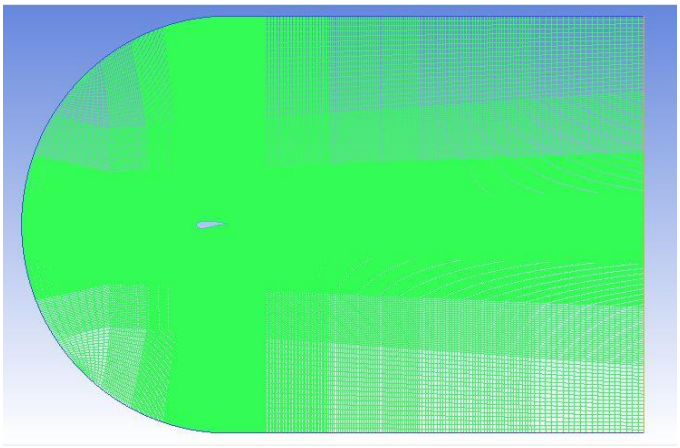


Figure 121. Far- field mesh

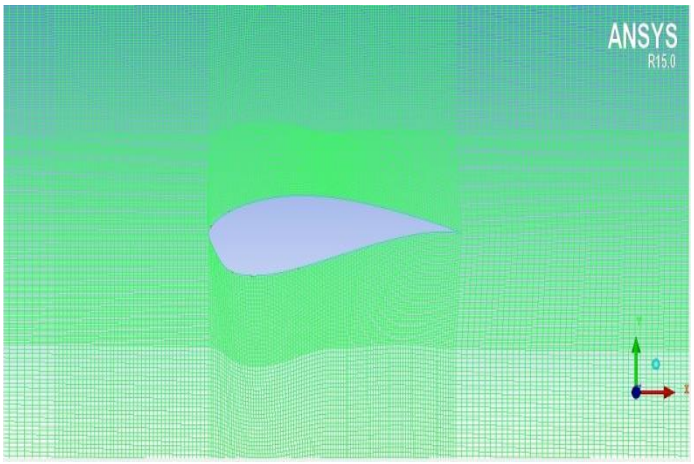


Figure 122. Near airfoil mesh

4. Results and Discussions

The wind turbine used in this study is designed by Ashraf [7]. The turbine rotor blade consists of seven sections, the sections are made of airfoils S822 and S823, with seven different Re numbers (shown in Table 1). To determine the flap effect along the blade, the flow around each section was studied separately for various angles of attack, AoAs.
The flaps have heights of 1%c, 2%c, and 3%c, located at the airfoil trailing edge. The calculations were performed applying the k-ε turbulence model.

Table 1. Re number for each case

Case	Re	Airfoil
1	160000	S823
2	70000	S823
3	60000	S823
4	65000	S822
5	45000	S822
6	40000	S822
7	20000	S822

4.1 Experimental Validation

The wind tunnel experimental results of the S822 clean airfoil at Re=100 000 obtained by Somers [8] were compared against numerical results (Figures 8 and 9), to validate the turbulent model selection and the mesh accuracy, the lift and drag coefficients were taken as comparison parameters.

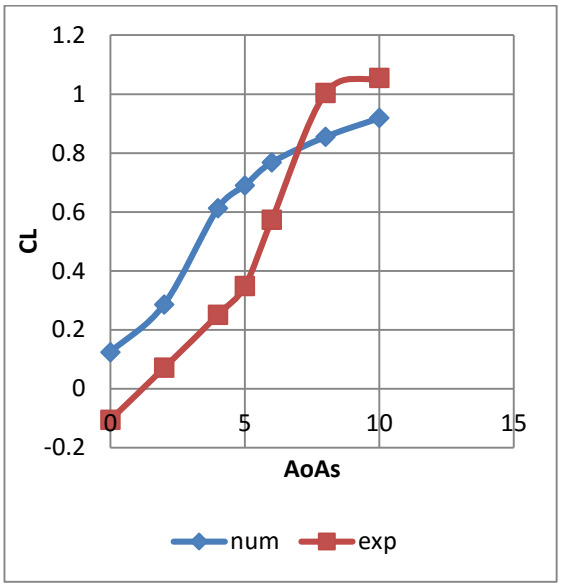


Figure 123. Lift coefficient experimental and numerical results

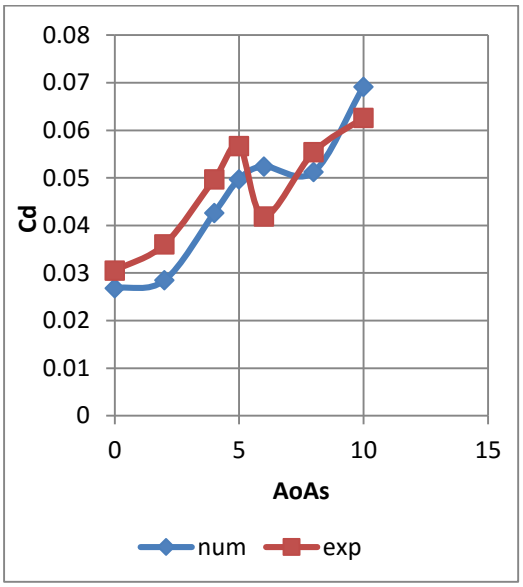


Figure 124. Drag coefficient experimental and numerical results3

The difference between the two results arises from the fact that the numerical study was executed with a 2D model, while the experimental with a 3D model.

The performance assessment of gurney flaps in each case was done by comparing the following parameters:

a. The main aerodynamic coefficients (lift (C_l), drag (C_d) and lift to drag ratio (C_l/C_d)).
b. Pressure distribution.
c. Coefficient of friction.

These parameters are presented in comparison between the three flaps and the clean airfoil.

4.2 Aerodynamic Coefficients

Figures 10 to 16 show lift coefficient for airfoil S823 and S822 with different sizes of gurney flaps at various angles of attack. In general, for a given angle of attack, C_l increases as long as the height of the gurney flap increases.
According to Liebeck [1], the drag of airfoils equipped with Gurney flaps is higher than the drag of clean airfoils. Figures 17 to 23 show similar behavior to results obtained by Liebeck at low AoAs. On the contrary, at higher AoAs flaps of 1%c and 2%c heights produce less drag when compared to clean airfoil. This decrease in drag is due to the

fact that blunt airfoils delay separation at low Re numbers [9], opposed to high Re, as blunt airfoils generate more drag [10]. It was also noticed that for a particular angle of attack C_d increases as the flap height increases (the flap with 3%c height produces more drag penalty than the flap with height of 2%c). At low AoAs, It was noticed that the drag of flap 1%c is higher than that of the clean airfoil, this changes at AoAs above 6 degree as the drag of the flap drops below the clean airfoil's drag.

These changes in lift and drag are translated into C_l/C_d (Figures 24 to 30). Although flap 3%c has the maximum lift values, flap 2%c was found to have the maximum value of C_l/C_d, this is mainly attributed to the high drag values that flap 3%c generate. For this reason lift to drag ratio is considered as one of the most vital parameters in assessing the performance of aerodynamic devices.

eureca 2017 – Conference Paper
Paper Number PG01

Analysis of Taper Width Variations in Linear Reluctance Machine

Aminath Saadha[1], Aravind CV[1,*], Preshant Krishna[1], F.Azhar[2]
[1]*School of Engineering, Taylor's University, Selangor, Malaysia*
[2]*Faculty of Engineering, Universiti Teknikal Malaysia, Melaka Malaysia*

*aravindcv@ieee.org

Abstract
Linear motors are being used in different application with a huge popularity in the use of transport industry. With the invention of maglev trains and other high speed trains, linear motors are being used for the translation and braking applications for these systems. However, a huge drawback for the linear motor design is the cogging force, low thrust values, and voltage ripples. This paper aims to study the force analysis with change in taper/teeth width of the motor stator and mover to understand the best teeth ratio to obtain a high flux density and a high thrust. The analysis is conducted through JMAG software and it is found that the optimum teeth ratio for both the stator and mover gives an increase of 94.4% increases compared to the 0.5mm stator and mover width.

Keywords: Linear Reluctance Motor, Taper, Teeth, Force

1. Introduction

Electric motors are devices that convert the electrical energy to magnetic energy and ultimately into mechanical energy. Electromagnetism is the basis of motor operation in order to produce the magnetic forces required for production of rotational or linear motion[1]. As one of the fastest growing industries, electrical motor manufacturing represents a major industry worldwide, where electric motor driven systems account for approximately 45% of total global electricity consumption and is expected to rise to 13,360 terawatt hour (TWh) by 2030[2].

Recent developments in the industry have brought forth linear machines that provides mechanical translation without intermediate gears, screws or crank shafts. In a linear motor either the moving or stationary member must extend over the entire range of motion of the moving member[3]. The motion occurs because of the electromagnetic force developed in the actuator. All types of motor configurations and topologies can be produced in the linear fashion, i.e. dc, induction, synchronous and reluctance[4]. Linear electric machines are associated with long linear progressive motion, such as transportation and other similar applications.

The most prominent application of linear motors is the utilization of these motors in transport systems, specifically railway system in the use of train thrust and in braking [5]. Linear reluctance motors are popularly used in electrodynamic braking of high speed trains. These brakes operate on the principle of converting the traction motors of the train to a generator that convert the kinetic energy of the train into electrical power [6].

To overcome the problem of adhesion between the wheel tread and the rail, the braking force in electromagnetic brakes are achieved through strong magnetic forces that are induced with large electromagnets attached to the vehicle over the top of the rails [7]. In Electromagnetic rail brakes, the frictional forces are produced between the electromagnets and the rail [8]. If the electromagnetic fields generate eddy currents in the rails, creating forces acting in the opposite direction of the movement of the train, it is a linear eddy current brake system.

However, these brake systems are still susceptible to the cogging effects of the permanent magnets due to the magnetic retention, which greatly reduces the efficiency of the motor [9]. A linear reluctance motor that does not utilize permanent magnets have been introduced, thus minimizing the cogging force and decreasing the weight of the linear motor. The objective of this paper is to study the different teeth ratios of the linear reluctance motor and to propose a ratio for the best thrust/force characteristic.

2. Literature Review

Linear Electric Machines are in general three-phase machines fed through power electronic controllers and taking advantage of regenerative electric braking for fast, robust, and precise thrust, speed, or position control. The topology of a linear switched reluctance motor is similar to that of a stepping motor with variable reluctance platen. In addition, it is equipped with position sensors [10]. The turn-on and turn-off instant of the input current is synchronized with the position of the moving part. The thrust is very sensitive to the turn-on and turn-off instant. In these type of motors, the rotor tends to move to a position where the inductance of the excited winding is maximized or the reluctance is minimized.

In the case of a linear stepping or linear switched reluctance motor, the speed υ of the moving part is as in Equation (1).

$$v = v_s = f_{sw}\tau \quad (1)$$

Where f_{sw} is the fundamental switching frequency in one armature phase winding and τ is the pole pitch of the reaction rail. For a rotary stepping or switched reluctance motor $f_{sw} = 2p_r n$ where $2p_r$ is the number of rotor poles and n is rotational speed in rev/s. The fundamental energy conversion equation for linear electric machines is as in Equation (2).

$$F\dot{x} = vi \quad (2)$$

Where F is mechanical force (N), $\dot{x}$ is mechanical velocity (m/s), v is the Voltage (V), and i is current (A). It is assumed that F and $\dot{x}$ are in the same direction. Numerous studies have been conducted into increasing the thrust of these linear motors such as, [11] where slots are used to decrease harmonic components of the thrust force. These slots can be in the form of skewed or fractional slot [12]. This allows the analysis of rated performance calculation and effects such as cogging torque, ripple torque, back-emf form prediction. Analysis which combines the orthogonal optimization algorithm for tooth shifting and pole shifting of a double-sided slotted permanent magnet synchronous linear motor are carried out in [13].

This study achieves a model with a suppressed thrust ripple which in turn increased the efficiency. A 9-pole 10-slot structure of a short primary permanent magnet LSM is proposed in N. Bataar et.al, which is focused on reducing the cogging force through detent force minimization by optimizing the length of armature core and shape of the exterior teeth simultaneously by using (1+lambda) evolution strategy coupled with response surface method using multi-quadric radial basis function [14].

Other studies are focused on establishing a platform for the analysis and test of characteristics such as thrust ripples and detent force of the permanent magnet linear motor [15]. It is predicted that thrust ripples are generated by the distortion of the stator flux linkage distribution, reluctance force due to the relative position between the mover and stator, Y. Zhu et.al, aims to rectify this through the utilization of predictive control algorithm [16], which will result in the minimization of the voltage ripple by high precision control. The same result is obtained through moving node techniques in research conducted by Ki-Chae et.al [17].

Linear Motor Systems which has electromechanical multi-parameter, and strong coupling is difficult to control. W. Ai et.al proposes an analysis of relative weights of various factors for thrust fluctuations in permanent magnet LM [18], using the fuzzy analytic hierarchy process to reduce these fluctuations in the thrust. It can be seen through these research that the cogging force deteriorates the performance and even excite the mechanical resonance thus decreasing the efficiency and also the life span of the motor [19]. This paper will look into the teeth size variation for obtaining the highest force in the mover and the stator of the linear motor [20]. The paper will first outline the method of analysis and then propose the results of the study, finally discussing the results and propose a ratio for the best stator and mover teeth gap for a linear reluctance motor based on the results of the study.

3. Methodology

The main structure of the linear reluctance motor studied in this paper consists of three basic structures; the stator, which is the stationary nonmoving part, the mover, which consists the coil and is the linear translation component. Figure 1 below shows the arrangement of the structure.

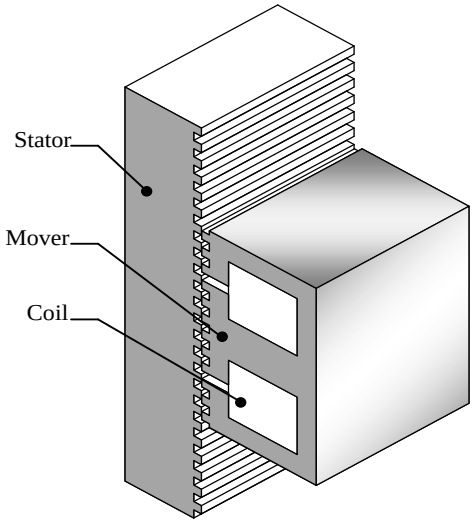


Figure 1: The Linear Reluctance Motor.

The parameter that is to be studied is the teeth gap of both the stator and mover to show which is the best ratio of teeth width gap for obtaining the highest thrust from the linear motor. Figure 2 below shows the parameter to be studied while figure 3 gives an in depth analysis for obtaining the ratio.

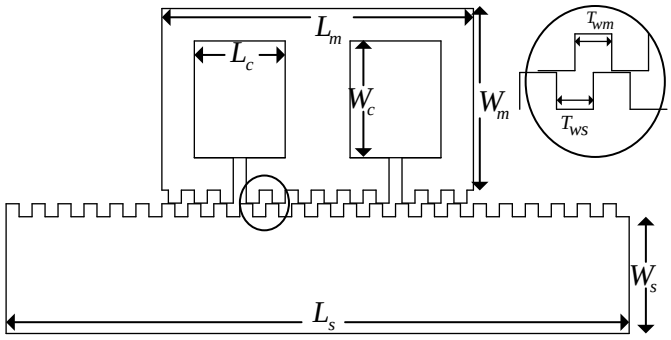


Figure 2: Parameter to be studied

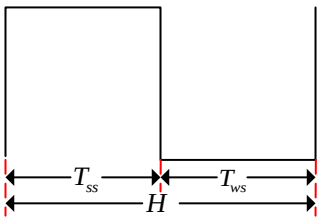


Figure 3: Teeth ratio

As seen from figure 3, the total pole width of the motor is to be kept constant at 4mm therefore, the teeth gap for the stator is denoted in equation 3.

$$H_s = T_{ss} + T_{ws} \quad (3)$$

Where, H_s is the total width of the pole and T_{ss} is the gap where the tooth protrudes and T_{ws} is the dip in the teeth. The parameter T_{ws} is then changed while keeping H_s constant.

The same parameter for the mover teeth are also varied to obtain the best ratio for the teeth and the combination of the ratio of the teeth in both stator and mover to obtain the highest thrust.

The dimensions of the stator and mover are summarized in Table 1 below:

Table 1: Parameter List

Parameter			Value
Length of stator	$\boldsymbol{L_s}$	(mm)	96
Width of stator	$\boldsymbol{W_s}$	(mm)	18
Teeth height of stator		(mm)	2
Length of mover	$\boldsymbol{L_m}$	(mm)	48
Width of mover	$\boldsymbol{W_m}$	(mm)	28
Teeth height of mover		(mm)	2
Length of coil	$\boldsymbol{L_c}$	(mm)	14
Width of coil	$\boldsymbol{W_c}$	(mm)	18
Number of turns in coil			330
Resistance of coil		Ω	4.6

The simulations are run on FEM software JMAG. The parameters used for the coil is 330 turns with a total resistance of 4.6Ω. The material, and circuit parameters are kept constant for the whole analysis. A total of 49 simulations are carried out with different combinations of T_{ws} and T_{wm}

4. Results and Discussion

The analysis was run using JMAG software, in order to obtain the flux lines, magnetic flux density, absolute force of translations and other parameters. For this study the force in Y direction of the motor is considered, since increase in the force shows the decrease in cogging force which shows an increase in the efficiency of motor.

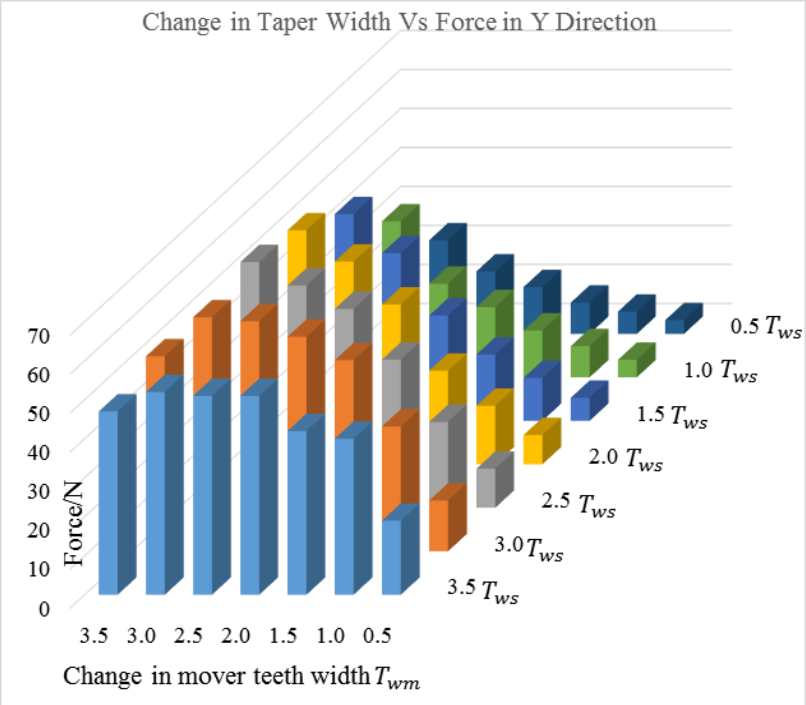


Figure 4: Analysis of the taper width of stator and mover based on absolute force

As seen in figure 4, an increase in the teeth width of both the stator and the mover, increases the absolute force to a certain point, however further increase shows a decrease in the force that is generated. This can be seen in all of the stator teeth width measurements from $0.5T_{ws}$ to $3.5T_{ws}$. The force in Y direction of $0.5T_{ws}$ increases from 24N to 63N at $2.5T_{ws}$ and then decreases to 52N at $3.5T_{ws}$. This effect is better illustrated in Figure 5.

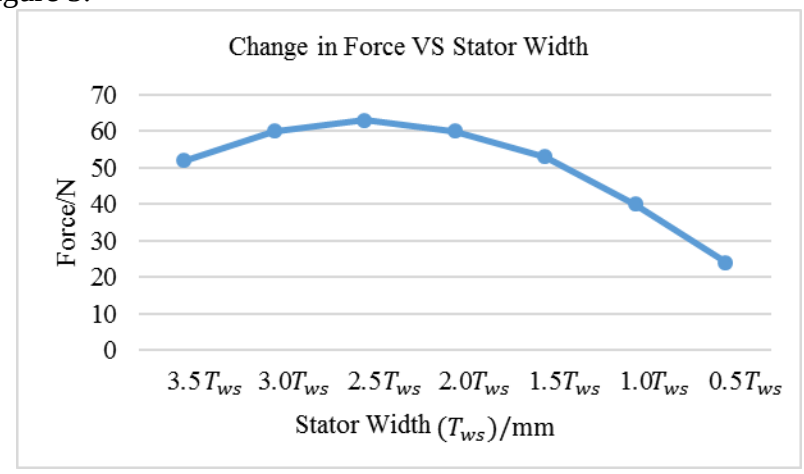


Figure 5: Change in Force with Change in Teeth Width

As seen the force increases with an increase in the teeth gap showing that that the magnetic flux density increases. This is because as the teeth gap T_{ws} increases the, extruded part of the teeth which is the T_{ss} decreases, since total teeth width H_s is kept constant. This decrease in T_{ss} decreases the surface area of extrusion, thus forcing the magnetic flux to be concentrated, increasing the density and hence increasing the force. However, a further increase of the gap from $3.0T_{ws}$ decreases the force since the extruded part of the teeth T_{ss}, is too small and the magnetic flux leaks from the teeth gap as shown in figure 6. This leakage decreases the density of the magnetic flux thus decreasing the force of the motor.

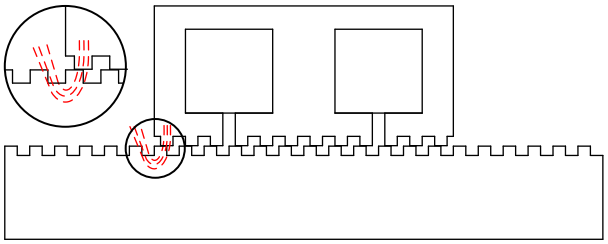


Figure 6: Leakage of magnetic flux

The same effect can be seen for the mover teeth width T_{wm}, for which the force increases from 47N at 3.5 T_{wm} to 52N at 3.0 T_{wm} and then decreases to 19N at 0.5T_{wm} at a constant stator teeth width of 3.5 T_{ws}. Based on these results it is best to identify which ratio of teeth width for both the stator and the mover provides the highest force, thus increasing the efficiency of the motor. The highest force obtained for each stator width is illustrated in figure 7.

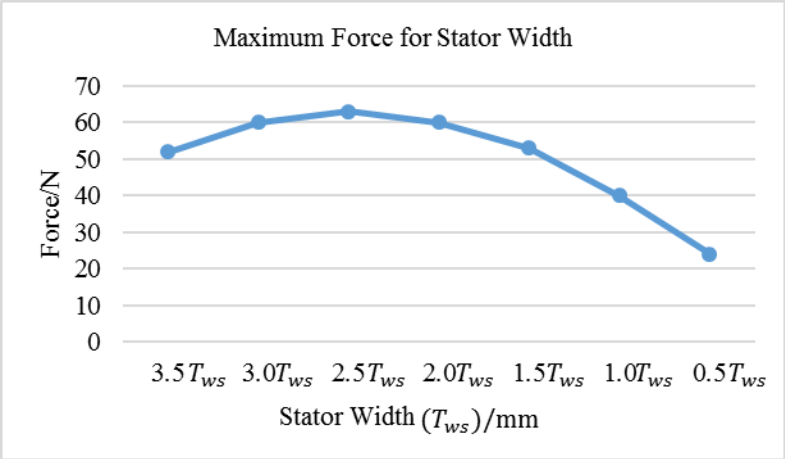
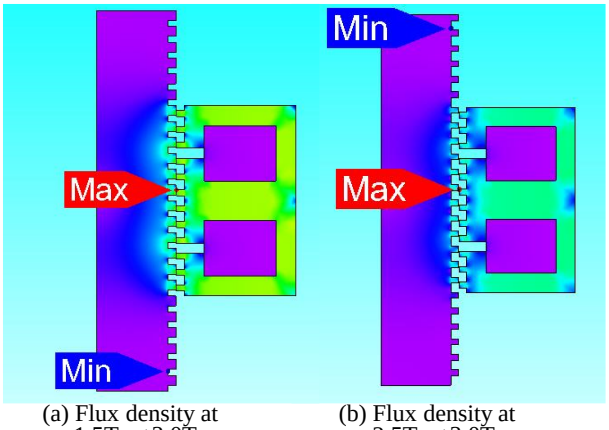


Figure 7: Maximum force for each stator width.

As shown by the curve in figure 7, the highest absolute force for the motor design is at 463N which is achieved at 2.5T_{ws}. The graph also shows that the best teeth width for the mover is at 3.0 T_{wm}, since all of the maximum force for the stator is achieved at this teeth width. However, motor design should also take into consideration the manufacturing process and the materials required. The 2.5mm teeth width is better since this will decrease the material costs for the motor production. The flux density for this size is also the best since there the distribution is more uniform and the motor shows areas of lower flux concentration which shows that continuous operation of the motor will not result in excessive heat buildup in the body which will result in a lower life span for the motor. The comparison of the flux density for the motor is shown in figure 8.



(a) Flux density at $1.5T_{ws}$ at $3.0T_{wm}$ (b) Flux density at $2.5T_{ws}$ at $3.0T_{wm}$

Figure 8: Flux Distribution for 1.5 T_{ws} and 2.5 T_{ws}

Based on these results it can be seen that the best stator tooth width is 2.5mm for T_{ws} and the mover teeth width is 3.0mm for T_{wm}. Both of these ratios provide an increase in 94.4% force compared to 0.5mm for both the stator and mover, and a 25.4% increase compared to 3.5 mm teeth width for both the stator and mover.

5. Conclusion

Linear motors are used for different applications and is gaining popularity in the transport industry mainly in railway systems. The main disadvantage of the current motor types is the cogging force by the use of permanent magnets, and voltage ripple which decreases the thrust force of the linear motor. This study aims to analyse the effects of the linear reluctance motor's taper width of both the stator and mover to identify the best ratio of teeth gap to obtain the highest force values.

The analysis was done through the software JMAG, by changing the parameters of the teeth gap while keeping the other parameters such as motor dimensions, materials, circuit, coil resistance and number of turns constant. The teeth gap of stator T_{ws} and mover T_{wm} is changed to obtain the results.

As seen from the analysis the best results for the teeth gap can be found at $2.5T_{ws}$ and 3.0 T_{wm} which gives an increase of in 94.4% force compared to 0.5mm for both which is the lowest teeth width that both the stator and mover can achieve.

Further analysis and studies can be conducted by changing the teeth shape and obtaining the optimum teeth shape for increased thrust, decrease in cogging force, and higher efficiency.

Acknowledgment

This work was supported by Taylor's University through its TAYLOR'S RESEARCH SCHOLARSHIP programme. The authors wish to express financial support of the project through the Taylor's Research Grant Scheme TRGS/MFS/1/2016/SOE/005

References

[1] L. jing Jin Mei-shan, Chen Da-chuan, Li Jing, Qiu Chang-li, "Emulated Analysis in the Performance of Linear Introduction Motor," *Energy Procedia*, vol. 17, pp. 79–83, Jan. 2012.

[2] M. H. A. Babak Ganji, "Analysis and modeling of different topologies for linear

switched reluctance motor using finite element method," *Alexandria Eng. J.*, vol. 55, no. 3, pp. 2531–2538, Sep. 2016.

[3] Y. L. Huisheng Liang, Zongxia Jiao, Liang Yan, Longfei Zhao, Shuai Wu, "Design and analysis of a tubular linear oscillating motor for directly-driven EHA pump," *Sensors Actuators A Phys.*, vol. 210, pp. 107–118, Apr. 2014.

[4] X. L. Qibao Lv, Zhiyuan Yao, "Contact analysis and experimental investigation of a linear ultrasonic motor," *Ultrasonics*, vol. 81, pp. 32–38, Nov. 2017.

[5] J. O. Andrzej Milecki, "Electrohydraulic linear actuator with two stepping motors controlled by overshoot-free algorithm," *Mech. Syst. Signal Process.*, vol. 96, pp. 45–57, Nov. 2017.

[6] Q. Z. Xiangyu Zhou, Yi Zhang, "A novel linear ultrasonic motor with characteristic of variable mode excitation," *Ceram. Int.*, vol. 43, pp. S64–S69, Aug. 2017.

[7] J.-H. Jeong, J. Lim, C.-W. Ha, C.-H. Kim, and J.-Y. Choi, "Thrust and efficiency analysis of linear induction motors for semi-high-speed Maglev trains using 2D finite element models," in *2016 IEEE Conference on Electromagnetic Field Computation (CEFC)*, 2016, pp. 1–1.

[8] P. Z. A.R. Albrecht, P.G. Howlett, P.J. Pudney, X. Vu, "Energy-efficient train control: The two-train separation problem on level track," *J. Rail Transp. Plan. Manag.*, vol. 5, no. 3, pp. 163–182, Nov. 2015.

[9] S. K. Satoshi Oto, Tadashi Hirayama, "Study on Thrust Improvement and Ripple Suppression of HTS Linear Switched Reluctance Motor with Coreless HTS Excitation Windings," *Phys. Procedia*, vol. 81, pp. 178–181, Jan. 2016.

[10] B. P. Tianwen Li, Qingdong Yang, "Research on Permanent Magnet Linear Synchronous Motor Control System Simulation," *AASRI Procedia*, vol. 3, pp. 262–269, Jan. 2012.

[11] W. Z. Xiaojun Yang, Dun Lu, Chengfang Ma, Jun Zhang, "Analysis on the multi-dimensional spectrum of the thrust force for the linear motor feed drive system in machine tools," *Mech. Syst. Signal Process.*, vol. 82, pp. 68–79, Jan. 2017.

[12] R. Y. Mingyi Wang, Liyi Li, "Overview of thrust ripple suppression technique for linear motors - CMP Journals & Magazine," *Chinese J. Electr. Eng.*, vol. 2, no. 1, pp. 77–84, 2016.

[13] IEEE Staff, *Thrust optimization of permanent magnet synchronous linear motor based on tooth-shifting of double sides*. IEEE, 2016.

[14] N. Baatar, Hee Sung Yoon, Minh Trien Pham, Pan Seok Shin, and Chang Seop Koh, "Shape Optimal Design of a 9-pole 10-slot PMLSM for Detent Force Reduction Using Adaptive Response Surface Method," *IEEE Trans. Magn.*, vol. 45, no. 10, pp. 4562–4565, Oct. 2009.

[15] L. Zhang, B. Kou, Y. Zhang, and Y. Jin, "Thrust characteristic analysis and test of the synchronous permanent magnet linear motor," in *2014 17th International Conference on Electrical Machines and Systems (ICEMS)*, 2014, pp. 1733–1737.

[16] Y. Zhu and Y.-H. Cho, "Thrust Ripples Suppression of Permanent Magnet Linear Synchronous Motor," *IEEE Trans. Magn.*, vol. 43, no. 6, pp. 2537–2539, Jun. 2007.

[17] Ki-Chae Lim, Joon-Keun Woo, Gyu-Hong Kang, Jung-Pyo Hong, and Gyu-Tak Kim, "Detent force minimization techniques in permanent magnet linear synchronous motors," *IEEE Trans. Magn.*, vol. 38, no. 2, pp. 1157–1160, Mar. 2002.

[18] W. Ai, G. Yan, B. Chen, Y. Xiao, and Q. Li, "Analysis of Weight for Thrust

Fluctuations of Linear Motor System Based on FAHP," in *2010 International Conference on Manufacturing Automation*, 2010, pp. 217–223.

[19] S. K. Tadashi Hirayama, Satoshi Oto, Atsushi Higashijima, "Experimental Manufacture and Performance Evaluation of Linear Switched Reluctance Motor with HTS Excitation Windings," *Phys. Procedia*, vol. 81, pp. 174–177, Jan. 2016.

[20] A. S. Nariman Roshandel Tavana, "Pole-shape optimization of permanent-magnet linear synchronous motor for reduction of thrust ripple," *Energy Convers. Manag.*, vol. 52, no. 1, pp. 349–354, Jan. 2011.

eureca 2017 – Conference Paper
Paper Number PG02

Proposed Framework of Hybrid Photovoltaic Thermal Systems to Ecotourism in Malaysia

Mohammad Taghi Hajibeigy*[1], Aravind CV[1], Rashmi W[2]
Electrical and Electronic Engineering, School of Engineering, Taylor's University, 47500 Subang Jaya, Selangor, Malaysia

Abstract
Ecotourism is widely recognized for its positive impacts to the environment. Ecotourism is defined as nature-based tourist experiences, which visitors travel to regions for the purpose of appreciating their natural beauty, relaxation and being harmonious with Mother Nature. Ecotourism probably had its foundations in the ethics of conservation, which can help maintain what's left of nature and fosters environmental education. Employing the sustainable energy, paying more attention to the natural resources and developing existing natural resources will have a direct impact to healthier sustainable environment for the inhabitant. If not all, most of the ecotourism sites are located in the remote area in which to utilize electrical energy from the normal grid is difficult or very costly. On the irony, utilizing the conventional non-renewable energy have negative effect and ruins the ecotourism sites. Therefore, utilizing Hybrid Photovoltaic Thermal (PVT) systems is a fit alternative energy source to serve the limited energy demands of ecotourists sites. The amount of the energy production depends on the visitors' capacity of the site. Since the rural area enjoys the cheap and large field, it is easier to plan and assemble the PVT systems to suffice the needed energy. In this research the sustainability of local environment along with the sustainable usage of energy were considered. This paper presents the sustainable energy usage of tourism in Malaysia and aims to address the impact of sustainable and non-sustainable on the rural area of ecotourism. This paper also addresses some of the emission, carbon reduction and climate change issues that the world is expected to meet soon.

Keywords: Ecotourism, Sustainable, Environmental Impacts, Hybrid, Sustainable energy

Abbreviations

CO_2	Carbone dioxide
IUCN	International Union for Conservation of Nature
PVT	Photovoltaic Thermal

1. Introduction

Tourism is a potential matter in environmental, social and economic levels of many government agendas. Government sees tourism as a tool of development giving priority to protect the environments and traditions with minimum negative impacts [1]. Malaysia being the major attraction for the tourist destination in this part of the world enjoys a bigger share of tourist in the entire year [2]. Among the tourism, ecotourism is one of the rapid growing movements in the worldwide tourism industry. Ecotourism is a method of unconventional tourism that aims to achieve economic gain locally by development through natural resource protection. The environment has an inherent value which prevails its value as a tourism asset. Ecotourism relays to the quality of the environment which must be carefully safeguarded from the effect of the activity and type of energy utilizations in its vicinity. The International Union for Conservation of Nature (IUCN) defined ecotourism as "environmentally responsible travel and visitation to relatively undisturbed natural areas in order to enjoy and appreciate nature (and any accompany in cultural features-both past and present) that promotes conservation, has low negative visitor impact and provides for beneficially active socioeconomic involvement of local populations"[3]. World Commission on Environment and Development define sustainable as "Development that meets the needs of the present without compromising the ability of future generations to meet their own needs" [4]. The above definition implies that the important aspect of the definition is to appreciate and protect the nature at the same time an instrument for conservation and sustainable development. In order to comply with the above definition and guard the nature, the source of energy usage must be carefully considered and prohibit the usage of any source of energy which produces environmentally hazard gasses such as carbon dioxide (CO_2), carbon monoxide (CO), nitrogen dioxide (NO_2) and phosgene (PO_4).

Renewable energy resource such as sun is an extremely important part of generating energy needed in the natural rural area since Sun is the most abundance, sustainable and exist everywhere without any cost. It aims to assist in the reduction of the emission of greenhouse gases which are produced by non-renewable energy sources such as fossil fuel. However, the newly designed hybrid PVT systems can produce both electrical energy and the same time high thermal energy. Since the heat accumulated on the PV reduces the PV efficiency, the removal of the large amount of thermal energy from the PV not only help to maintain the PV electrical efficiency but also to serve as the useful thermal energy needed in the rural area. The aims of this paper is to investigate environmental impacts of energy source usage in relation to ecotourism and focuses on environmental impact of the energy source usage on ecotourism in Malaysia.

1.1 Ecotourism in Malaysia

Malaysia is an exceptional country in terms of its tourist attractions and rich natural resources. The utmost important characteristics of the country are its ethical and cultural

diversity, ecotourism attractions, and diverse natural resources. The Belum Temengor Forest Complex is reputed to be more than 130 million years old. This is the oldest in the world, and even older than the Amazon forest and Congo basin. Ten top attractions for Malaysian ecotourism which have outstanding natural assets and present opportunities for local people to involve in ecotourism development are shown in table 1in rough order of priority [5].

Table1. Ten Top Attractions for Malaysian Ecotourism and their Natural Assets [5].

No.	Place	Natural assets
1	Lower Kinabatangan River, Sabah	Proboscis monkeys, river, wildlife
2	Wang Kelian, Perlis	Limestone, caves and forest
3	Kenong Forest Park, Pahang	Elephants, caves, streams
4	Belum / Temenggor, Perak	Wildlife, forest and lake
5	GunungStong, Kelantan	Mountain,waterfall, rockfaces
6	Ulu Muda, Kedah	Forest, lake and sandstone
7	TasikBera, Pahang	Lake, culture, fish
8	Hose Mountains, Sarawak	Forest, trekking, birdwatching
9	TasikKenyir\, Terengganu	Lake, boating, trekking, fishing
10	PulauKuku, Johor	Mangroves, wildlife, seafood

1.2 Environmental impact of ecotourism

Ecotourism differs from conventional tourism because it mainly concerns the perceptions and values of individuals which influenced a great portion appreciation of environment. Therefore, it reduced the scale of exploitation of these natural resources [6]. In comparison to other type of tourism, manners, such as the proper management of waste at the sites and recycling are stressed in ecotourism. Ecotourism is specific in nature and it impacts the environment as well as the changes in people's attitudes in a positive sense. Hence, it is distinguished from other tourism forms owing to its natural area surroundings [7]. On the other hand, sustainable ecotourism objective is to address the needs of to sustain the visited environments, help to educate the local communities in regards to their natural surrounding and to preserve the virginity of the nature [8]. However, the impact of the tourism on the destination could be negative. Among the negative impact is the generating Carbon dioxide (CO_2) which is produced by using non-renewable energy source such as fossil fuel.

1.3 Carbon dioxide (CO_2) damage

Carbon emissions, most particularly CO_2, are part of a group of gases that harmfully impact the quality of our air and raise the greenhouse effect. Real world activities such as energy consumption, waste disposal and transportation contribute towards carbon footprint as these activities contribute towards CO_2 Ecological Footprint is a common baseline for Carbon Footprint - emission of gases contributing to climate change, associated with human production or consumption activities. In a rural tourism setting, all service providers to tourists may contribute to the deterioration of the environment in the course of their tourism activities. When consumption (operational practices and

activities of tourists) supersedes carbon offset initiatives, mitigation approaches are needed [9].

1.4 Carbon Offset Plan

In order to have an effective offset plan, the true measures are vital to evaluate proper offset methods.
A carbon tax on aviation fuel would particularly affect long-haul flights, because of high emissions, and short-haul flights and the emission during take-off and landing [10].Taxation should be in accordance with the amount of pollution they generate and use the fund to reverse the pollution by implanting trees, promote a healthier environment, promote sustainable energy, and other forms of contribution to the Mother Nature on the location sites. The plan should be able to calculate the carbon emission for all the activities and offer offset price that is tied to a chosen project before the payment method is determined. The mentioned process is shown in the Figure 1.

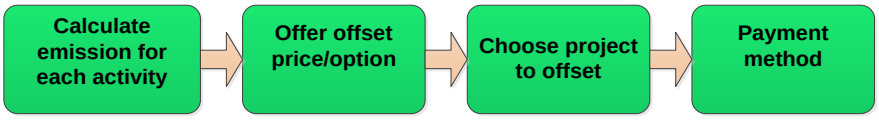


Figure 1:Offset carbon mission plan [9].

It is recommended that the vehicle operates on the site will be battery operated and the energy for using to recharge battery comes from the PVT source. The usage of renewable energy source without proper plan hinder and cause limitation on the growth of the area. The limitation in any aspect prevents growth in any form and manner such as financial impact on the local residence as well as on a national level and impact on the development of natural resources. The fund generated from the tourists can help the local community's living standard, physical, economic and social environments of destinations which solely depend on the quantity and the quality of the ecotourists. There are several ways to minimize the limitations for ecotourism. One approach is to plan for the usage of sustainable energy in place of the pollution sources energy such as fossil fuels that is non-renewable, hazardous and unnatural phenomenon in the earth's atmosphere like Global warming. Most clean, natural and renewable energy comes either directly or indirectly from the Sun. Therefore, the best answer that could be uttered out lies in the Sun. The Sun stands as a reliable renewable source of energy.

1.4 Energy Demands at the ecotourists Site

As the number of ecotourists increases the energy demand proportionally will increase as well. The PVT systems can be used to supply the demands and replaces the existing fossil fuel energy. The eco sites normally located in the rural areas and are not comfortable to transfer the energy from the normal conventional source via grid to these areas. Besides, the conventional method is not in line with the concept of ecotourism and in fact is hazardous to the Mother Nature which will ruins the eco-system. The fit alternative method is the solar energy. The solar energy is present everywhere, renewable, the most abundant, free and environmentally friendly [11]. Solar energy can cover a significant percentage of tourism infrastructures. The PVT systems can cover both heat demand and electrical demand. The proposed systems include a PV array, enhanced solar

collectors, solar charger for optimized energy harvesting, and a converter-inverter module to supply ac and dc electrical energy. The PVT systems deliver both electrical energy to suffice the electrical energy need while the thermal system produces thermal energy which can heat water to be used for shower, pool or to be used in radiator to warm the rooms and offices. The application of PVT systems in the industry is suggested as a reliable solution for a wider use of solar energy systems [12]. Globally the usage of sustainable and renewable energy source has been increased. Figure 2 shows the renewable energy consumption by region in the word.

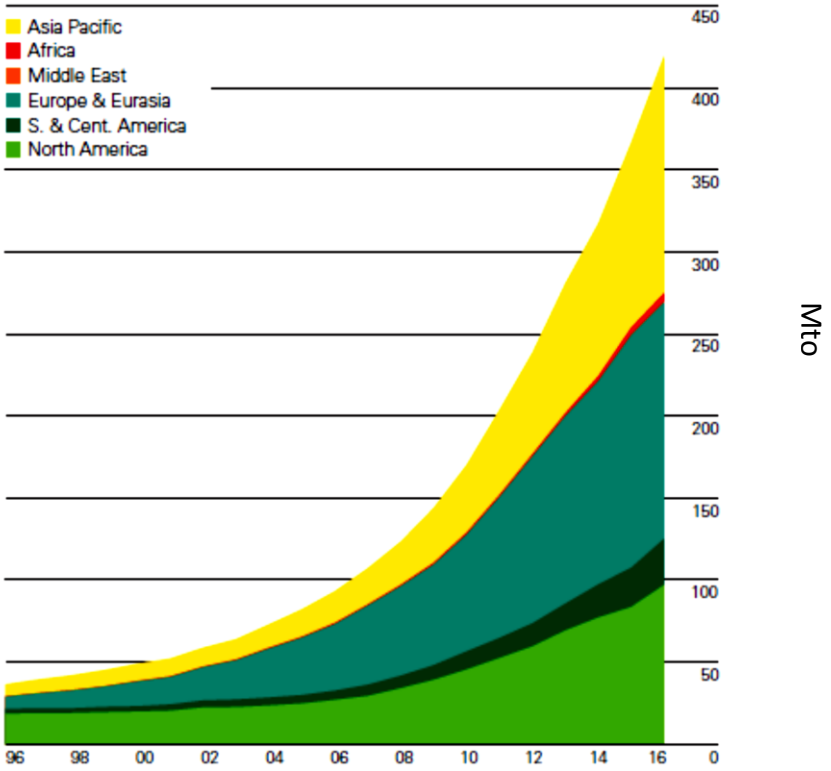


Figure 2: Renewable energy consumption by region, year 1996 – 2016 vs. Million tonnes oil equivalent (Mtoe) [13].

The graph shows the exponential increase of renewable energy consumption in different continent. This is in favour of the natural area and better sustain the eco system from ecological effect caused by CO_2 which is generated by producing energy from non-renewable energy fossil fuel. Implementing PVT systems in rural area will boost the total renewable energy consumption of Malaysia which in turn help the ecological and sustain the ecotourists area. Generating 1kW electrical energy by PV system producing 150 kWh each month prevents 75 kg of fossil fuel from being extracted. It avoids 150 kg of CO_2 from entering the atmosphere and keeps 473 L of water from being consumed [14]. Figure 3 shows Malaysia energy consumption for the past 26 years. The graph shows a steady increase on the yearly energy consumption of Malaysia. This trend is alarming to the ecological system which put more pressure to use alternative method to non-renewable energy source to protect ecological infrastructure.

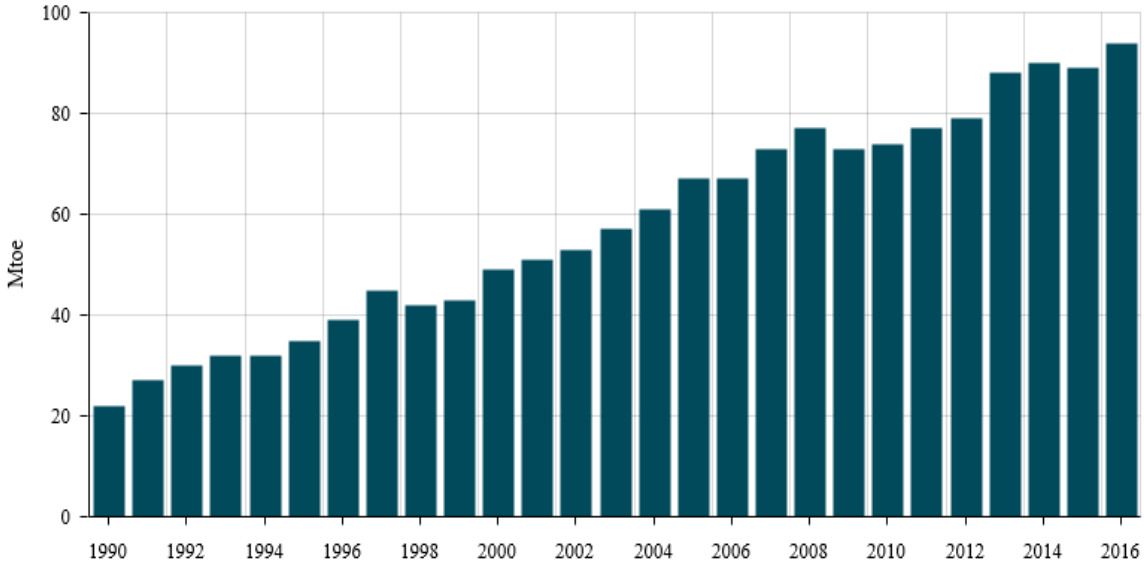


Figure 3: Malaysian energy consumption, year 1996 – 2016 vs. million tonnes oil equivalent (Mtoe) [13].

2. Energy Requirement at the Ecotourists Site

It is highly important and critical to calculate and analyse the energy required for the ecotourism sites.
Malaysia being a tropical country average sun insolation ranges about 4.8 kWh/m^2/day – 5.8 kWh/m^2/day. Photovoltaic (PV) system is well recognized and widely utilized to convert the solar radiation to electric energy. The normal factor influence the energy management is the active energy utilization (KWh), the reactive energy consumption (KVARh) and the peak demand (KW). Conventionally the utility system put their effort on the reduction of KWh consumption and on addressing the required reactive energy to improvise the power factor [15]. Nadarajan and Aravind [2] use the below procedure for the demand analysis and the net KW demand.

Let the contracted power be (PC), the maximum demand be (PD) the power used in excess (PE) computed as

$$PE = PC - PD \quad (1)$$

$$PD = PDm\ x\ KD \quad (2)$$

where *PDm* is the actual peak demand value from the maximum demand meter and *KD* is the demand factor.

The penalty by the supplier to the utility is computed as:

$$PP = (PC - PD)\ x\ KP \quad (3)$$

where *KP* is the penalty factor. Therefore the actual KW value (*PA*) computed is given by

$$PA = [(PC - PD)\ x\ KP] + [PDm\ x\ KD] \quad (4)$$

2.1 **Energy production by utilizing P**V

The generation of electrical energy solely relies on the solar radiation, the total surface area of the PV being utilized and the efficiency of the PV itself. Figure 4 shows annual average solar radiation energy for different

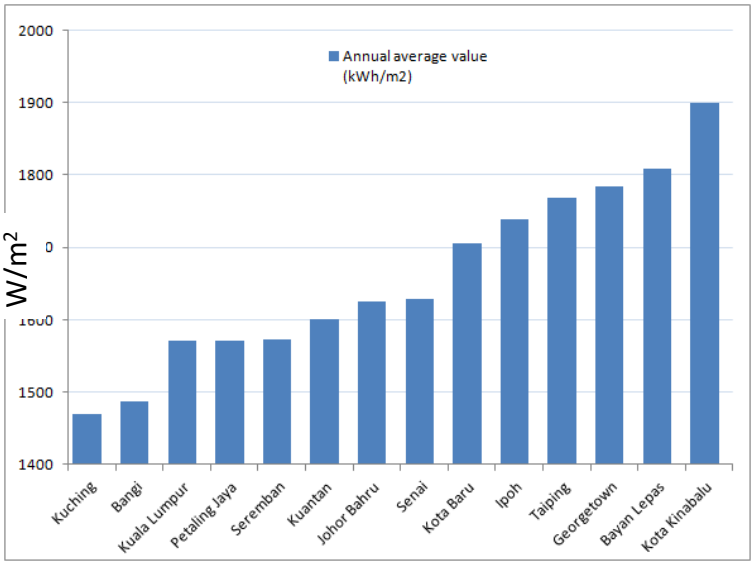


Figure 4: Aannual average sun radiation energy watt (W/m^2) for different city in Malaysia [16].

Figure 4 above shows that for every square meter (1m^2) of PV produces 1900 W of energy per hour in Kota Kinabalu, compared to only 1571 W/h in Kuala Lumpur; assuming 100% solar cell efficiency. The electrical energy (Watt) obtained can be calculate from equation (5).

$$KWh = H\ x\ G\ x\ \eta\ x\ S \quad (5)$$

Where H is the total hours of sun light, G is the sun radiation (W/m^2), η is the efficiency of PV module and S is the total surface area of the PV. Using equation (5) a solar panel with efficiency of 15% only produces 285 Wh in Kota Kinabalu and 235 Wh in Kuala Lumpur. With 5 hours of total solar radiation per day, and with an installation of 10 m^2 of solar PV can produce 1.425 kWh in Kota Kinabalu, and 1.178 kWh in Kuala Lumpur daily [16]. Table 2 shows the estimated total electrical power generation by different PV surface area coverage with the efficiency of 15% for a full day assuming 5 hours of full solar radiation without cloud. The table was generated based on the equation (5) and the yearly average solar radiation on each location.

Table 2. Electrical Energy generated by the PV for one day for different PV surface area in different locations in Malaysia .

Locations in Malaysia	(10 m^2) KWh/Day	(50 m^2) KWh/Day	(200 m^2) KWh/Day	(500 m^2) KWh/Day	(1000 m^2) KWh/Day	(5000 m^2) KWh/Day
Kota Kinabalu	14.25	71.25	285.00	712.50	1425.00	7125.00
Bayan Lepass	13.58	67.88	271.50	678.75	1357.50	6787.50
Georgetown	13.35	66.75	267.00	667.50	1335.00	6675.00
Ipoh	13.05	65.25	261.00	652.50	1305.00	6525.00
Kota Baru	12.83	64.13	256.50	641.25	1282.50	6412.50
Johor Baru	12.23	61.13	244.50	611.25	1222.50	6112.50
Kuantan	12.00	60.00	240.00	600.00	1200.00	6000.00
Seremban	11.78	58.88	235.50	588.75	1177.50	5887.50
Bangi	11.10	55.50	222.00	555.00	1110.00	5550.00
Kuching	10.95	54.75	219.00	547.50	1095.00	5475.00

The electrical and thermal efficiencies of the PVT systems are independent of location. However, the solar radiation and also, to a lesser extent, ambient conditions such as temperature and wind speed will strongly influence the total energy generation. The electrical and thus thermal efficiencies are considered to vary in the ranges 18.0–15.3% and 60–50%, respectively, for operating temperatures between 25 Cº and 85 Cº [17]. With the thermal efficiency given above the total energy of the PVT systems can be higher than given calculated value. For a PV module in air, the total convective energy (q_{conv}) exchange from a module surface is shown in Equation (6).

$$q_{conv} = h_c . A. (T_{module} - T_{ambient}) \quad (6)$$

where hc is the convective heat transfer coefficient, A is the surface area of the PV module, T_{module} is the temperature of the module and $T_{ambient}$ is the ambient temperature surrounding the systems [18].

3. Modelling Framework and Methodology

3.1 PVT Hybrid Systems Design

PVT hybrid systems consisted of two main parts, electrical system and thermal system. The PV module conventionally produces electrical energy while the thermal unit produces thermal energy. The electrical system consisted of PV module, charge controller, battery, convertor and invertor for ac and dc voltage usage. The thermal system consisted of aluminium plate, heatsinks, thermal container, thermal transfer fluid, heat exchanger, thermal storage tank and pump. The control unit regulate the speed and operation of pump based on the temperature difference of thermal fluid in the thermal container and the water in the thermal storage tank. The proposed entire structure of the hybrid PVT systems is shown in Figure 5.

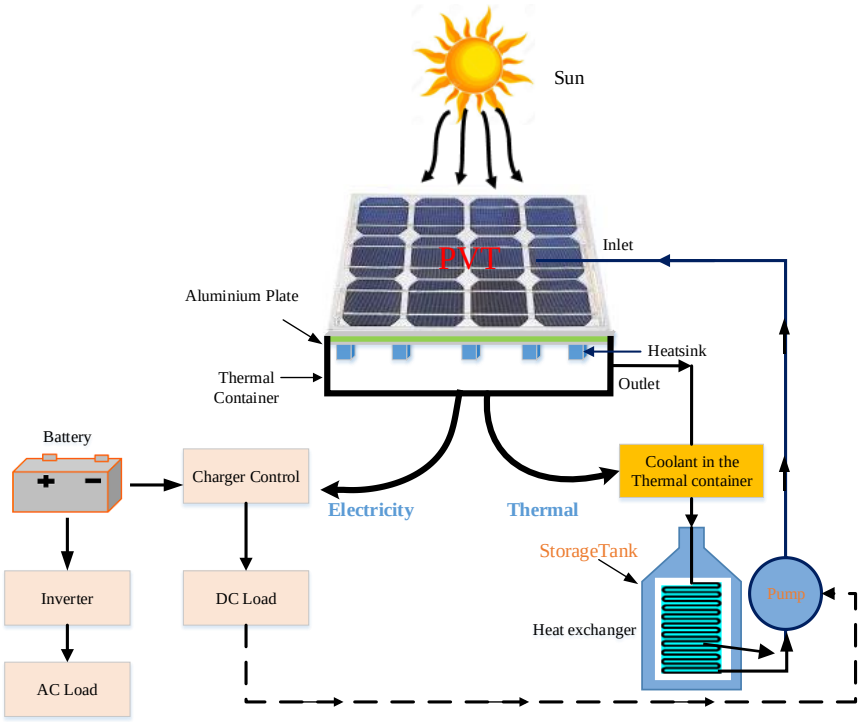
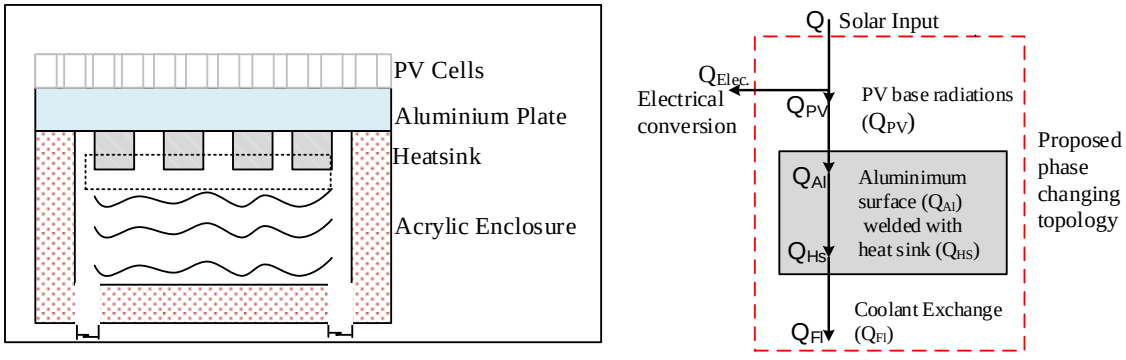


Figure 5: Photovoltaic Thermal Hybrid PVT Systems.

3.2 Systems Configurations

The designed hybrid PVT systems consisted PV module, aluminum plate, heatsinks and thermal container. The aluminum plate is directly attached below the PV module via thermal glue to absorb the thermal energy from the PV module. The heatsinks are welded on the bottom layer of the aluminum plate to further remove the heat from the aluminum plate. The thermal container is made of acrylic which holds coolant. The coolant used as the transfer medium. The assembled unit is placed inside a thermal container, which the unit sat on the top of the thermal container. The heatsinks also fit inside the container which is immersed in the coolant. Each layer of the Hybrid PVT systems is shown in Figure 6.



(a) Phase layered system setup (b) Stage changing topology

Figure 6: Hybrid PVT Systems with thermal container [19].

4. Conclusion

It is evident that ecotourism has positive impacts on the environment and economy of the local and the country as whole. The development of ecotourism can support both in preservation and conservation and of the environment at the destination while the negative effect cannot be ignored. The negative effect of ecotourism mostly comes from creating CO_2 by using fossil fuel energy source. However, there are advanced technologies and designs available for hybrid PVT systems to meet the specific demands and characteristics of the tourism facilities. In order to develop the harness and the abundant amount of solar energy radiation by PVT, the systems with the hybrid controller is suggested. In order to effectively examine the sustainable development of the tourism destination in Malaysia a system to assess sustainability from the integrated perspective need to be in placed in order to evaluate the existing effect of the energy source usage.

Acknowledgement:
This research was supported by Taylor's SoE Research Budget scheme towards the measurement and testing equipment.

References

[1] A. Liu and G. Wall, "Planning tourism employment: a developing country perspective," *Tourism Management*, vol. 27, pp. 159-170, 2006.
[2] Aravind, C.V., M. AL-Atabi, J. Ravishankar, A. Malik, and E. T. Ambikarajah, "Eco-Tourism Sustainability Through PV Technology: A Comprehensive Review," *Journal of Engineering Science and Technology*, vol. 8, pp. 654-669, 2013.
[3] C. Lascurain. (1996). *World Conservation Union*. Available: http://www.iucnworldconservationcongress.org/
[4] NGO and C. o. Education, "Our Common Future," U. Nations, Ed., ed. U.S.A.: WCED, 1987.
[5] I. Louis, G. Davison, J. Payne, W. Yap, P. Fletcher, and E. Lina, "Malaysian National Ecotourism Plan," vol. Excecutive Summary, M. o. Culture, Ed., ed. Malaysia, 1996, pp. 41-48.
[6] I. Thomas, "Defining Tourism," *USA:Rosen Publishing Group Inc*, 2004.
[7] D. N. Ravens, *The Natural and Human Environment Combined*. New York: Children's Press, 1996.
[8] M. Briffa, &Le,G. (2004) Conventional Links to Sustainable Development *Nerd Press*
[9] V. Nair, "Conceptualising Carbon Footprint and Offset Measures for Rural Tourism Destinations: A Possible Plan for Himalaya? ," Leh, LadakhJune 2014 June 2014.
[10] R. S. J. Tol, "The impact of a carbon tax on international tourism," *Transport and Environment*, vol. 12, pp. 129-142, 2007.
[11] B. K. Maskey, "Development Governance. Agenda for Action. Centre for Development and Governance,," ed. Kathmandu, 2000.
[12] G. Peterson and L. D., "People and their behavior: A challenge for recreation management," *Journal of Forestry*, vol. 77, pp. 343-346, 1979.

[13] (4 November 2017). *Global Energy Statisctical Yearbook*. Available: https://yearbook.enerdata.net/total-energy/world-consumption-statistics.html
[14] Leung, D. Y. C, Yang, and Y., "Wind energy development and its environmental impact: A review," *Renewable and sustainable energy review*, vol. 16, pp. 1031-1039, 2012.
[15] Nadarajan and C. Aravind, "Peak Demand Analysis for the Look-ahead Energy Management System," presented at the eureca, Taylor's University, 2013.
[16] (2017, 5 November). *Sustainable Energy and Environment Forum*. Available: http://www.thegreenmechanics.com/2013/08/annual-solar-radiations-in-different.html
[17] A. Ramos, M. A. Chatzopoulou, I. Guarracino, J. Freeman, and C. N. Markides, "Hybrid photovoltaic-thermal solar systems for combined heating, cooling and power provision in the urban environment," *Energy Conversion and Management*, vol. 150, pp. 838-850, 15 October 2017.
[18] J. AD and U. CP, "Thermal Model For Photovoltaic Systems," *Solar Energy*, vol. 70, pp. 349-359, 2001.
[19] M. T. Hajibeigy, C. Aravind, M. Al-Atabi, and P. Hoole, "Heat Response Model for Phase Layered Topology in a Photovoltaic Thermal System,"*Indonesian Journalof Electrical Engineering and Computer Science*, vol. 7, pp. 52-60, July 2017.

4.3 Pressure Distribution

The pressure distribution around the airfoils is shown in Figure 31 and 32 below. It's clearly seen that flaps have the ability to increase pressure significantly in the pressure side and slightly in the suction side around the flap, which substantially boost the lift.
On the other hand, it is noticed that increasing the flap size above 2% of the wing chord length noticeably increases the drag making it impractical to use.

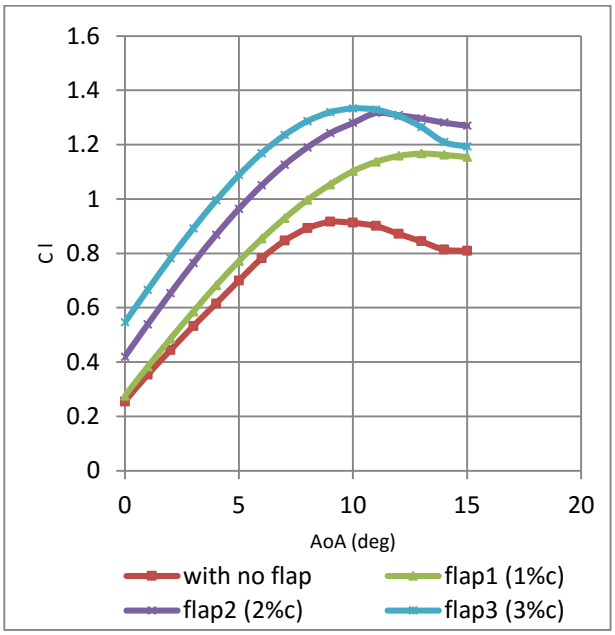


Figure 10. C_l variation case (1) with/without a gurney flap

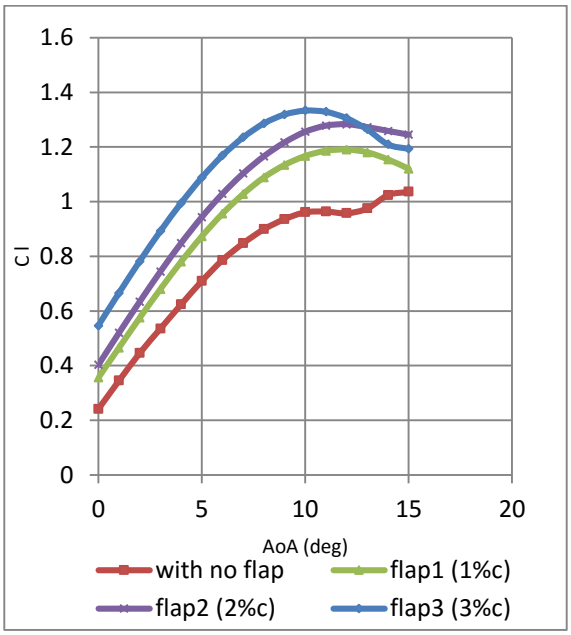


Figure 11. $C_l$variation for case (2) with/without a gurney flap

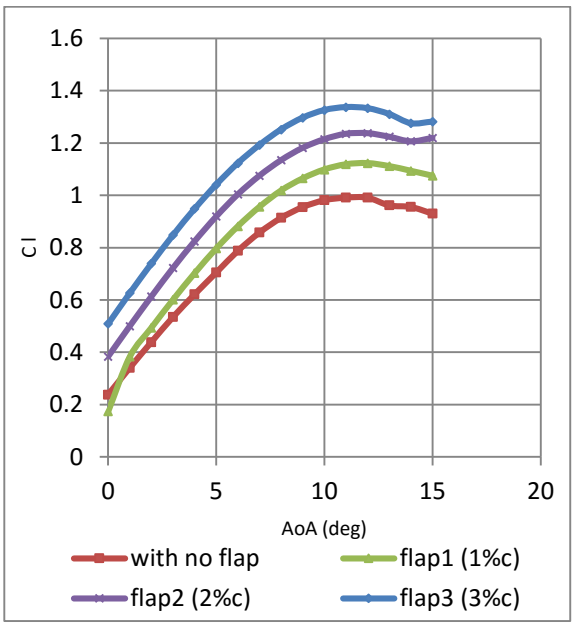


Figure 12. C_l variation for case (3) with/without a gurney flap

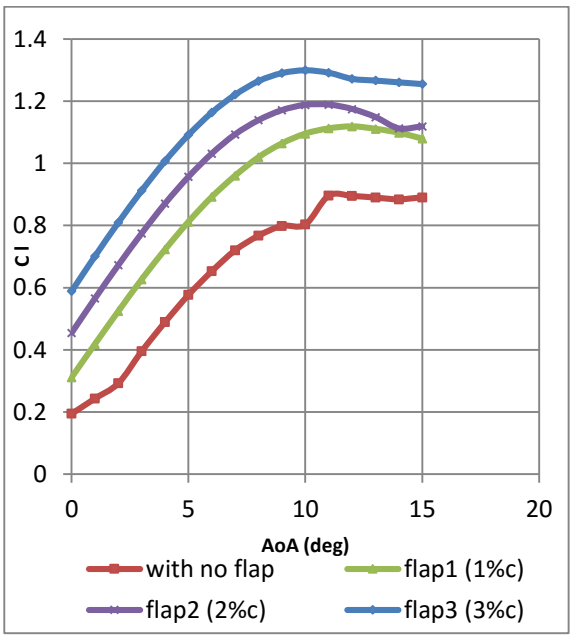


Figure 13. C_l variation for case (4) with/without a gurney flap

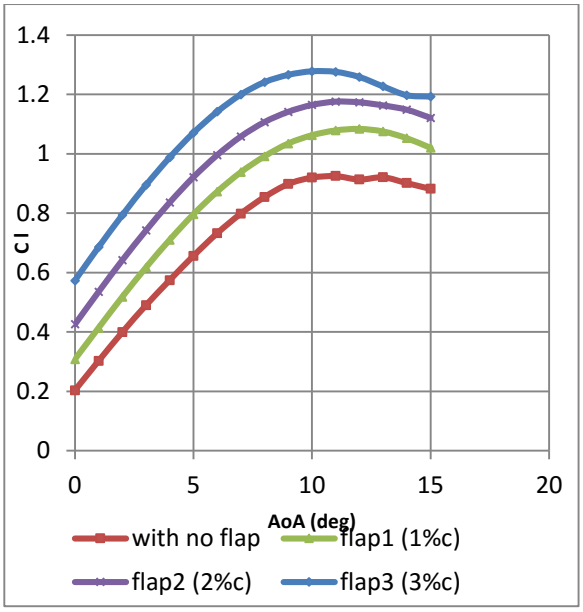


Figure 14. C_l variation for case (5) with/without a gurney flap

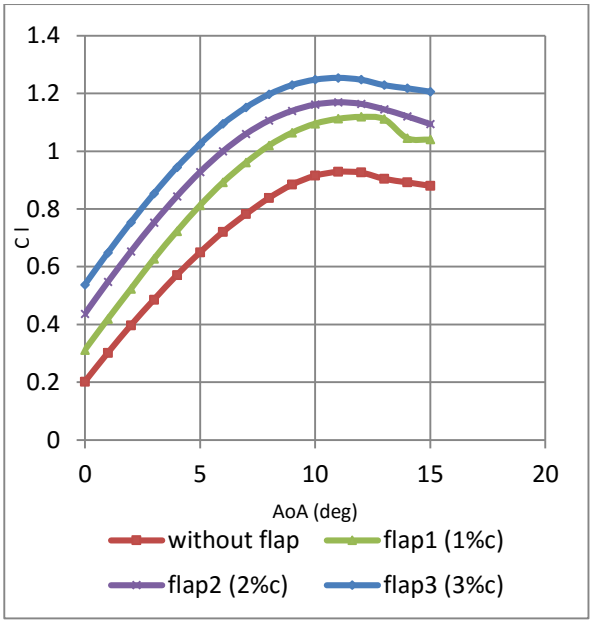


Figure 15. C_l variation for case (6) with/without a gurney flap

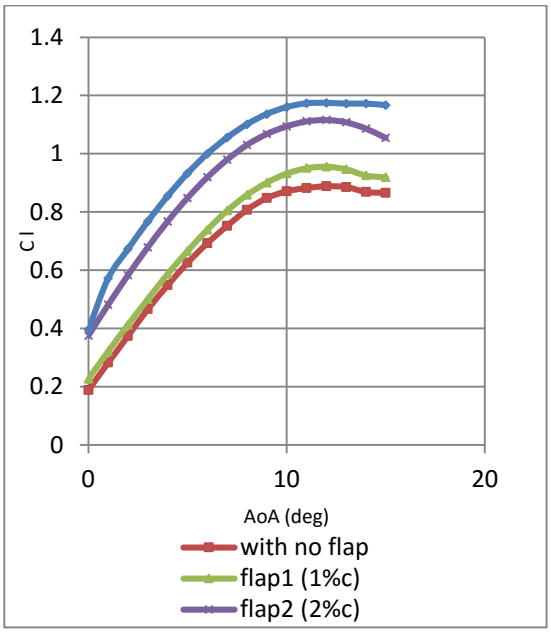


Figure 16. C_l variation for case (7) with/without a gurney flap

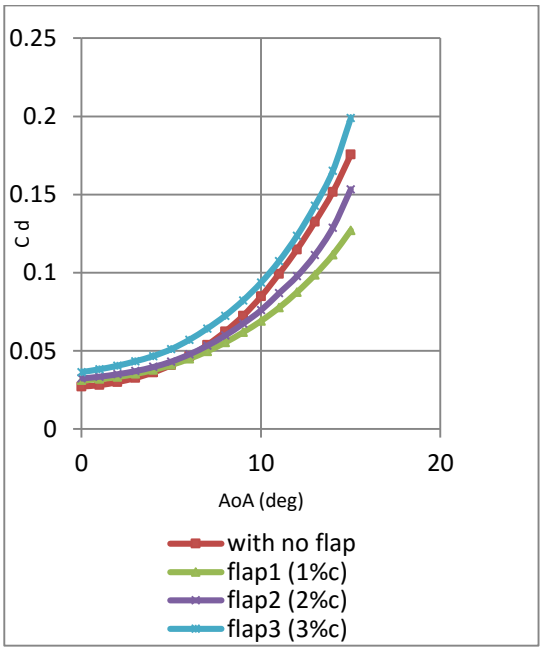


Figure 17 C_d variation for case (1) with/without a gurney flap

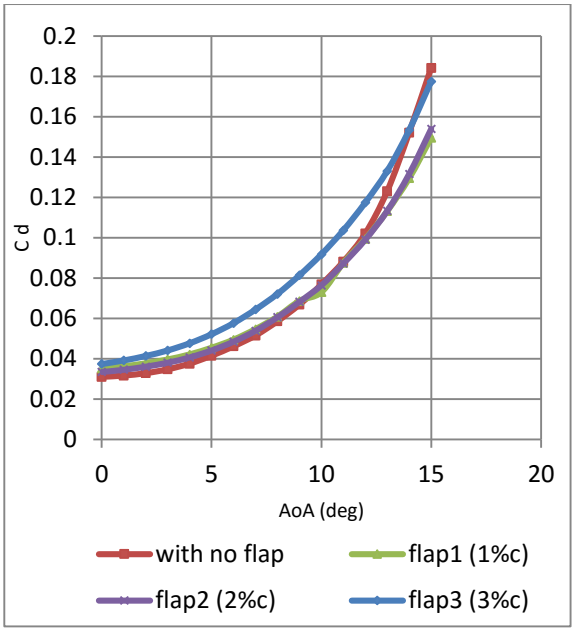


Figure 18. C_d variation for case (2) with/without a gurney flap

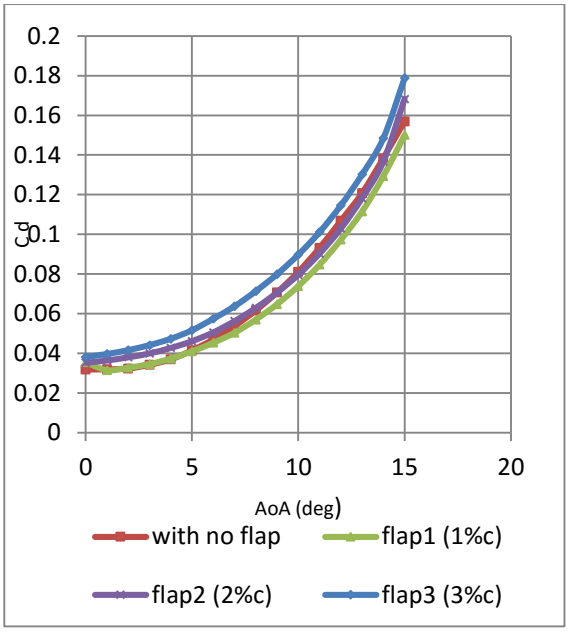


Figure 19. C_d variation for case (3) with/without a gurney flap

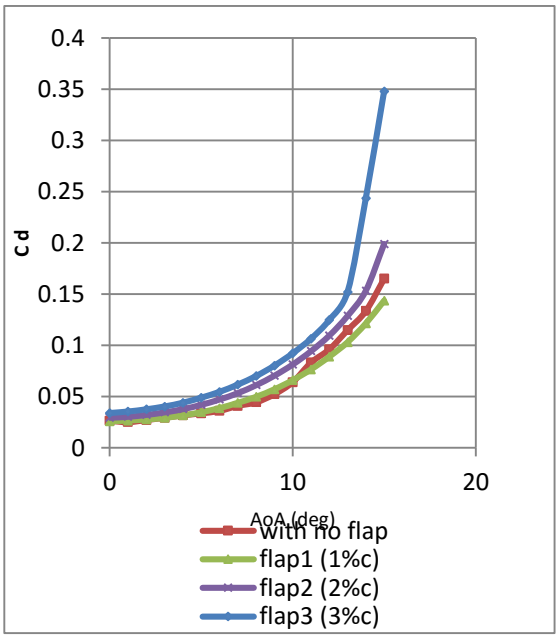


Figure 20. C_d variation for case (4) with/without a gurney flap

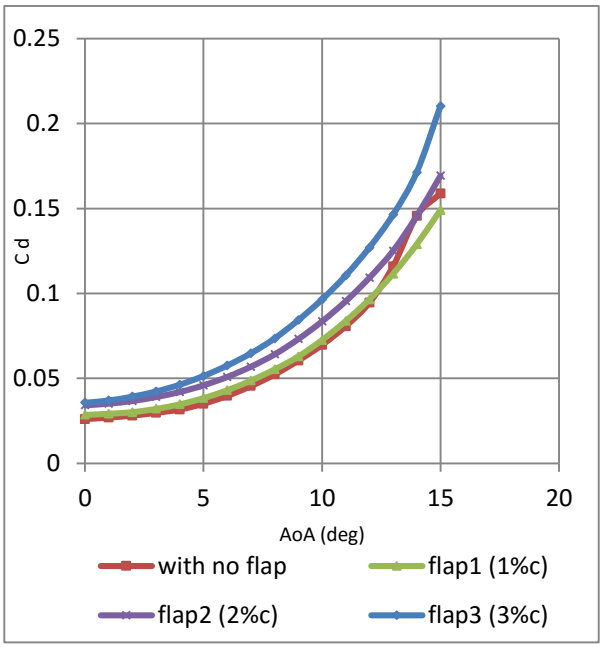


Figure 21. C_d variation for case (5) with/without a gurney flap

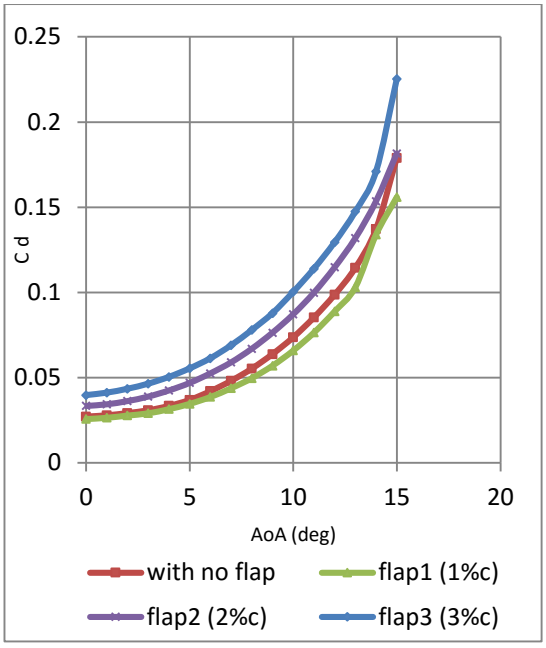


Figure 22. C_d variation for case (6) with/without a gurney flap

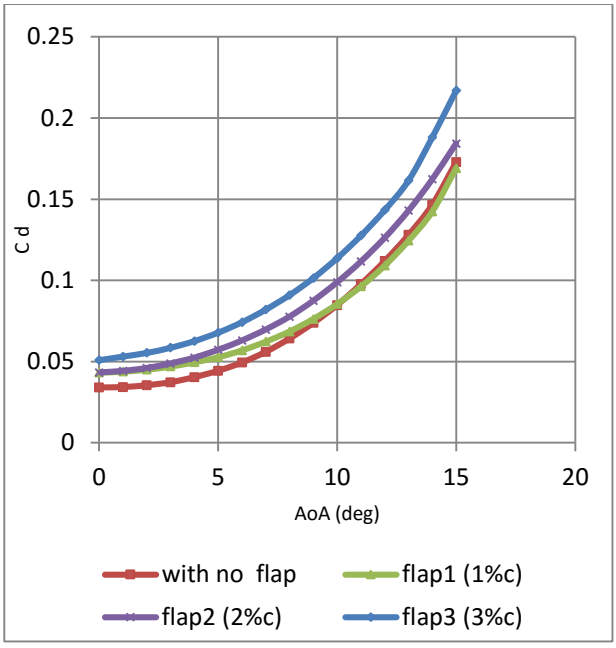


Figure 23. C_d variation for case (7) with/without a gurney flap

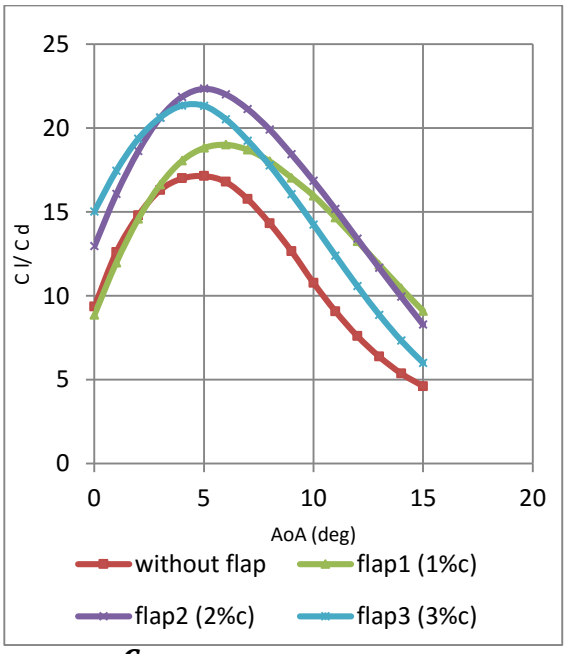


Figure 24. C_l/C_d variation for case (1) with/without a gurney flap

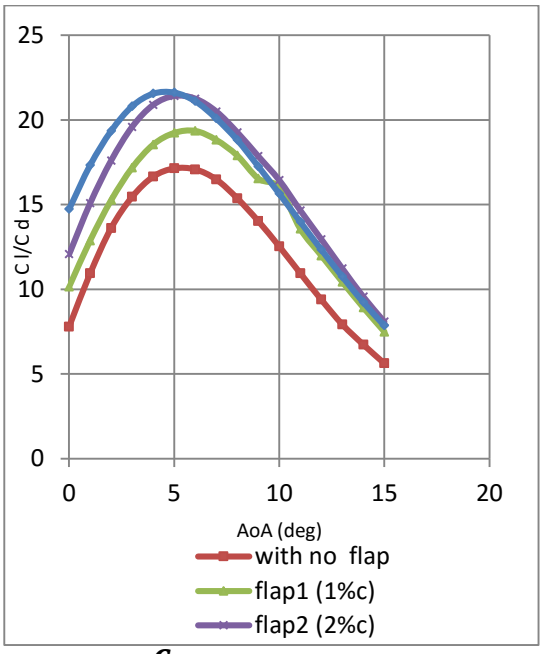


Figure 25. C_l/C_d variation for case (2) with/without a gurney flap

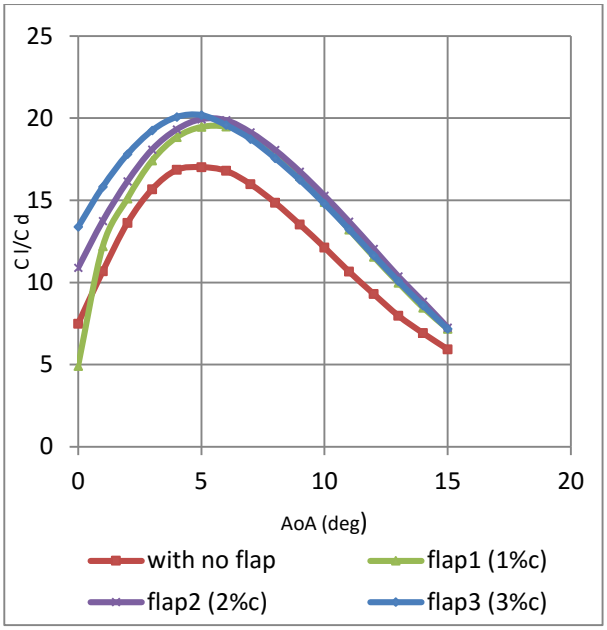


Figure 26. C_l/C_d variation for case (3) with/without a gurney flap

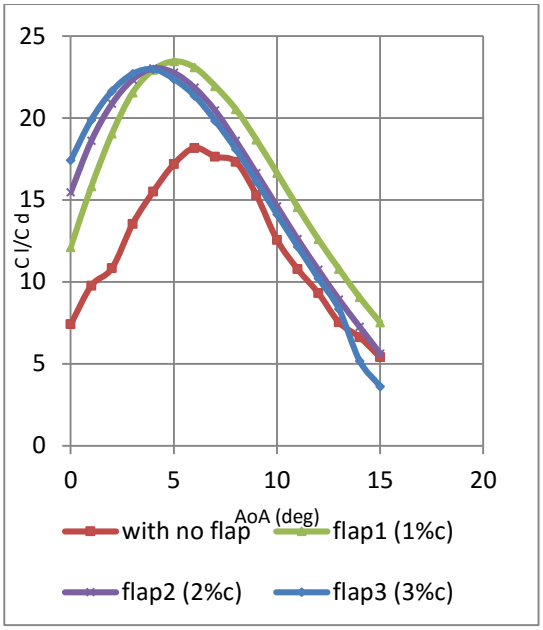


Figure 27. C_l/C_d variation for case (4) with/without a gurney flap

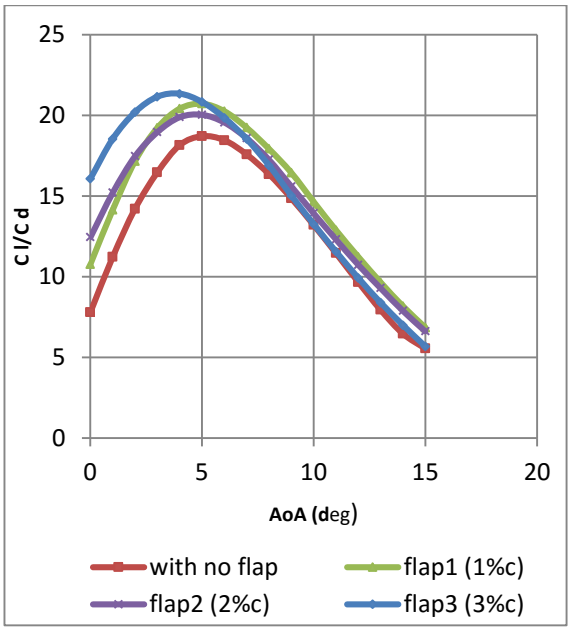


Figure 28. C_l/C_d variation for case (5) with/without a gurney flap

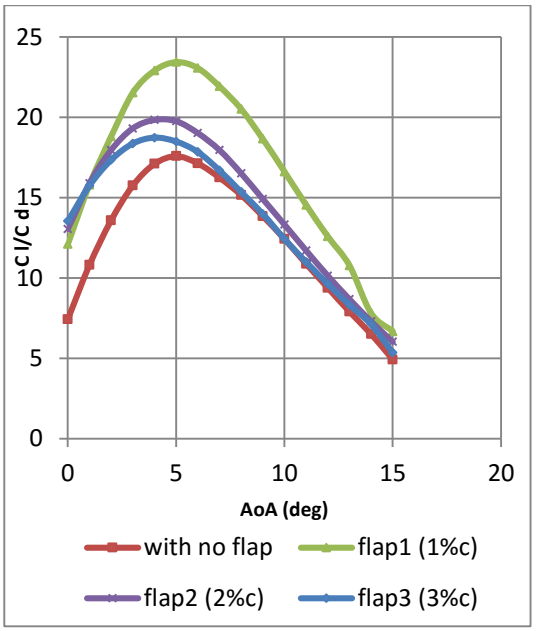


Figure 29. C_l/C_d variation for case (6) with/without a gurney flap

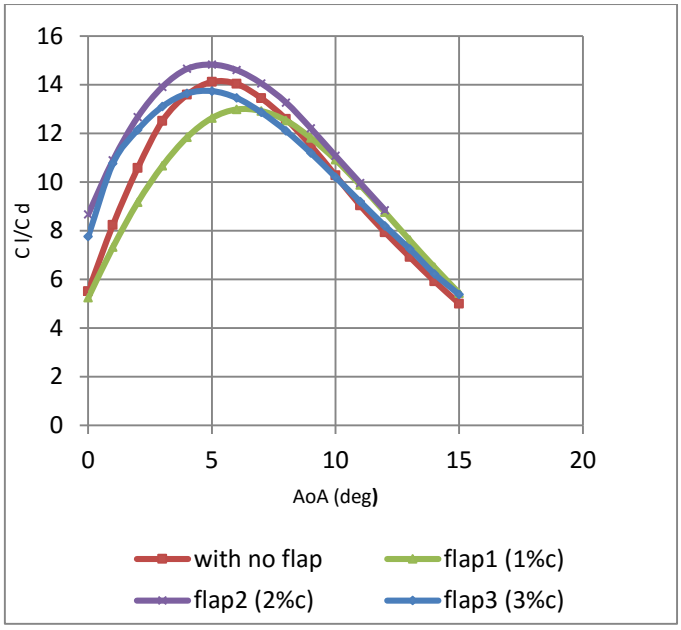


Figure 30. C_l/C_d variation for case (7) with/without a gurney flap

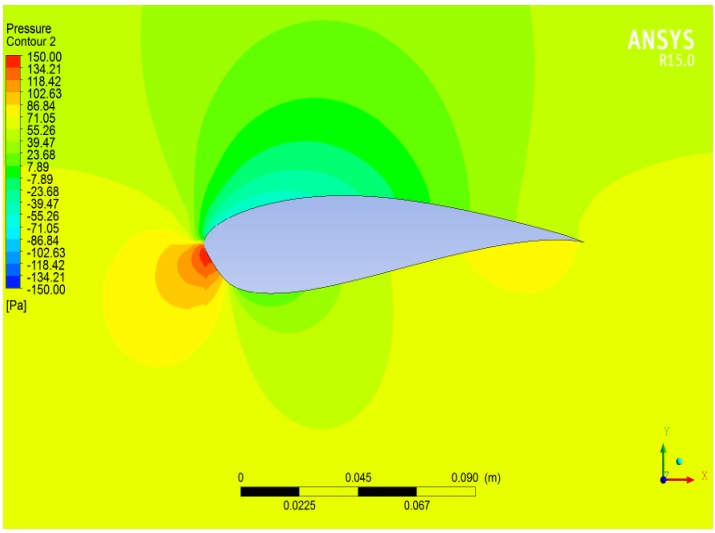


Figure 31. Pressure distribution for clean airfoil at AoA=5°

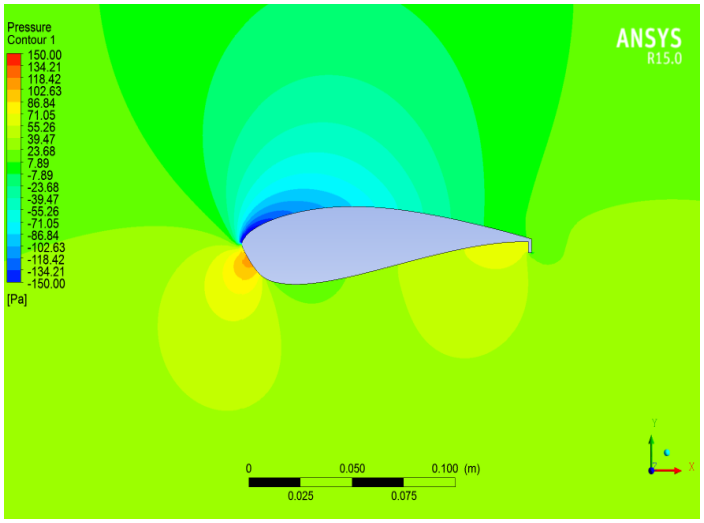


Figure 32. Pressure distribution with a gurney flap of height=3%c at AoA=5°

4.4 Separation

Velocity vectors are illustrated in Figures 30 and 31 below; which describe the velocity magnitude and direction of the flow at AoA 10°, at this angle separation is clearly visible, hence the comparison between the two cases of clean airfoil and airfoils equipped with flaps can be easily made. Here it is clear that the boundary layer separation zone developed (Figure 33) on the suction side is delayed when the gurney flap is deployed (Figure 34). The separation is caused by the adverse pressure gradient, in other words the increase of fluid pressure in the flow direction. This increment decelerates the flow as the kinetic energy decreases which subsequently raise drag.

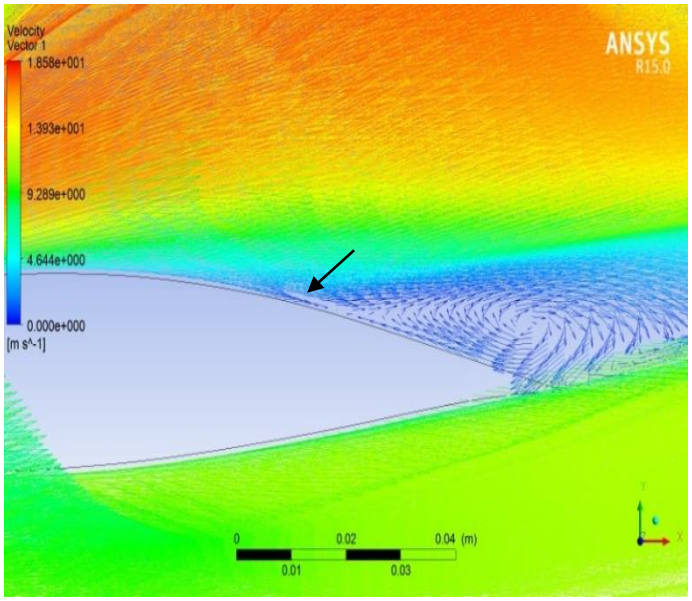


Figure 33. Velocity vectors without gurney flap at AoA=10°

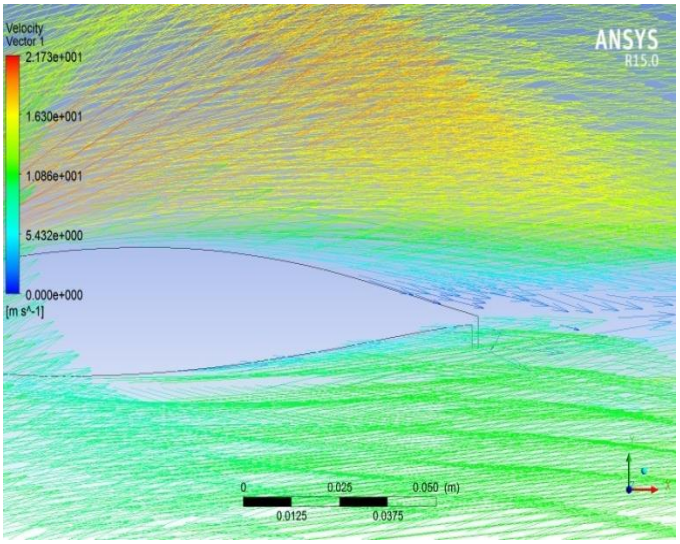


Figure 34. Velocity vectors with gurney flap of height=3%c at AoA= 10°

4.5 Friction Coefficient

The friction coefficient values around the airfoil give a more precise indicator to the position where separation occurs than velocity vectors do. Figure 35 shows that when no flap is deployed, the adverse pressure gradient becomes large and separation develops at a distance equal 70%c from the leading edge, which is the distance where shear stress reaches zero. On the other hand, it is obviously seen that there is no boundary layer separation in the cases where flaps are used and as a result the pressure drag decreases.

From Figures 17 to 23 it can be seen that drag values decrease as Re number increases, for example, at Re=160 000 the C_d values at different AoAs are lower than those of

Re=70 000. This decrease is due to the fact that the high Reynolds values prevent separation from occurrence.

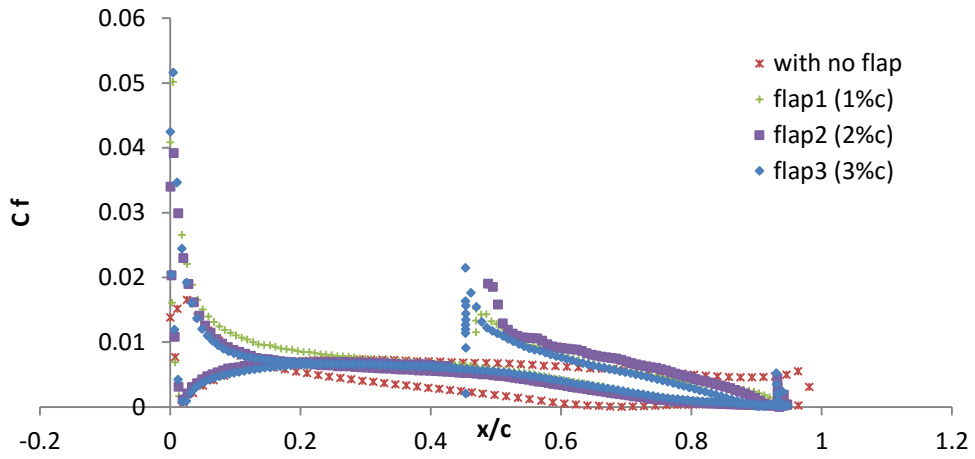


Figure 35. Change in C_f with relative chord with/without a gurney flap at AoA=10°

5. Conclusion

The 2D numerical investigation on airfoils S822 and S823 with gurney flaps was conducted using ANSYS's FLUENT 15 and turbulence model k-ε at seven different Reynolds numbers. The numerical results showed with the flap extended, the wing generates more lift at all AoAs below stall (It has reached 138% in some cases). It was remarked that a slight decrease in Cd in flap length 1%c due to separation delay, and slightly increases in flap length 2%c, yet increases noticeably at higher lengths. Also flap lengths of 3%c and higher are inefficient due to the very low values of C_l/C_d ratio. The reason behind the increase of C_l and C_d is the pressure rise in the pressure side around the flap area. It was found that the best operating range of AoAs for S822 and S823 equipped with flap is 4 to 6 degrees. Also K-ε turbulence model failed to simulate flows at AoAs over 15° due to the high turbulent flows and vortices created around the airfoil [11].

Acknowledgment

We would like to thank the Department of Mechanical Engineering, University of Khartoum for providing us with the tools necessary to accomplish this project.

References

[1] Liebeck R.H,"Design of subsonic airfoils for high lift". Journal of Aircraft, 1978;15(9): 547–561.
[2] Jang C.S., Ross J. C., Cummings R.M," Computational evaluation of an airfoil with a gurney flap," AIAA Paper 92-2708. June 1992.
[3] J. P. Baker, C.P. van Dam "Drag reduction of blunt trailing-edge airfoils," Department of Mechanical and AeronauticalUniversity of California; 2008.

[4] Myose R, Papadakis M, Heron, I. Gurney Flap Experiments on Airfoils, Wings, and Reaction Plane Model. Journal of Aircraft. 1998; 35(2):206–211.
[5] Anderson J.D, Computational fluid dynamics the basics with applications, New York: McGraw-Hill, 1995.Chapter 2, The governing equations of fluid dynamics: their derivation, a discussion of their physical meaning and a presentation of forms particularly suitable to CFD, P 37-48.
[6] Ryne Derrick Radermacher. Computational analysis of a wing oscillator. Western Michigan University; 2012.
[7] Ashraf Kamal Shams-Eldin. Wind turbine blade design and optimization. Department of mechanical engineering: University of Khartoum; 2015.
[8] Somers D.M. "The S822 and S823 Airfoils". Midwest Research Institute. U.S. Department of Energy Office of Energy Efficiency and Renewable Energy, Pennsylvania, NREL/SR-500-36342, 1993.
[9] Sato J, Sunada Y," Experimental Research on Blunt Trailing-Edge Airfoil Sections at Low Reynolds Numbers". AIAA Journal, 1995; 33(11).
[10] Loftin.L, Smith.H. Aerodynamic Characteristics of 15 NACA Airfoil Section at Seven Reynolds Numbers from 0.7×106 to 9×106. National Advisory Committee for Aeronautics: 1945.
[11] K Ren et al. Validation of Turbulence Models in STAR-CCM+ by N.A.C.A. 23012 Airfoil Characteristics. Deperterment of Mechanical Engineering: University of Bridgeport; 2009.

eureca 2017 – Conference Paper
Paper Number PG03

Linking Liberatory Pedagogy to Engineering and Sustainable Development

Jayasubamani Arvi S.Moganakrishnan[1*],Satesh Narayana Namasivayam[2]

[1,2,] *Taylor's School of Engineering Taylor's University (Lakeside Campus)*
No. 1, Jalan Taylor's, 47500 Subang Jaya
Selangor Darul Ehsan, Malaysia

[*]jayasubamani@gmail.com

Abstract
This paper is written to reflect liberatory pedagogy as a relevant pedagogy to be used in link with engineering education and sustainable development. Critical pedagogy is introduced in terms of its historical origin in educational approaches with regards to its operating paradigm and its intended outcome for education. Its influences as a new pedagogy for engineering education is discussed to iterate the importance of its pedagogical approach for the development of our diverse engineering education young aspirants. It is further discussed in alignment with the values proposed for Education for Sustainable Development and its potential significance for Engineering Education for Sustainable Development (EESD). Its application to specifically, design education is explored through deconstructing of engineering student narratives to place understanding of power and privilege in learning settings which educators could consider critical pedagogy as a potential pedagogy to address posing of problems within the praxis. The use of liberatory pedagogy for design education would allow us to understand how current assumptions on learning outcomes for design education can be interpreted as simple minded and fails to represent the complexity of construction which informs certain low tech community design projects. This in turn, undermines other knowledge forms, knowledge content and views which are dismissed in its importance amidst expertise and technical knowledge which are seen as that which is valid. This paper attempts to show from liberatory constructivists' perspective how such undermining results in dictating a fixed image of the engineer as the expert but not one who learns among the other learning selves within the lived experience.

Keywords: Liberatory pedagogy, critical pedagogy, design education, engineering education, engineering education for sustainable development

1. Introduction

Engineering education and sustainable development (SD) are linked by many pedagogies which has brought possibilities for development of young engineers to acknowledge the agenda as imperative for engineering and society in the future. These pedagogies have been highlighted in its benefit in bringing understanding of concepts, practice and values in relation to SD which stems from the educational efforts within Educational research undertaken particularly, from Environmental Education and Education for Sustainable Development (ESD)[1]–[3]. University curricula for engineering has contributed to the development as well, framed under the Engineering Education for Sustainable Development initiative following the Barcelona Declaration and the Decade of Education for Sustainable Development (2005-2014) for implementation of educational programs in link with SD [4], [5].

In terms of engineering education, incorporation of sustainability within the curriculum has led to exploration of relevant module to discuss sustainability as well as unsustainability as that which needs to be addressed particularly for professional development[4]. Within engineering education, design education has received specific attention in its potential to be a constructive activity for the application of highly cognitive skills for learning of design[4], [6]–[8]. A trend of changes to design education is noted within the literature which emphasizes on embracing of multidisciplinary towards transdisciplinary approaches which involves a more comprehensive approaches towards understanding of problems solving particularly the problems raised as affecting human well-being and environment[9]–[11].

On the other hand, as SD becomes understood as development practices which involves problem solving and decision making which are multidimensional, diverse and complex. This is due to involvement of people, culture and environment, pedagogies which are in support of transformative approaches are seen as relevant with critical implementation of ESD[2], [12], [13]. Transformative approaches are approaches which deals with changing of perspectives, particularly relevant with regards to understanding how people, culture and environment interact in resulting sustainability and unsustainability and our changing roles in addressing them. One area of such transformation is working across discipline, being transgressive towards addressing of complexity in problem solving[14]. Such transformation is detailed by many literature seeking transdisciplinary imagination as a way to build our capacity towards addressing complex problems in a collective[15], [16]. Transdisciplinary initiatives would require us to open our design space in a synergistic approach in which we could understand how we could understand contributing as part to the fresh new ‘whole’. With relevance to engineering design education, bringing design into the societal domain with the current mainstream construction for such transdisciplinary endeavours may be problematic in terms of the ideals and mechanistic pathways of simplified education we prescribe to.

Reflection of such critical experiences within engineering education brings test to assumption that educational process which are constructed can be neutral, performed in positivic tradition of achieving outcomes as conceptualized without understanding society. A pedagogy which can support critical study of educational implementations for the students is critical pedagogy, aimed at deconstructing power and priviledges

within the narratives which inform the learning process and become dominating pathways which eliminates others and their knowledge[17], [18].

This paper aims to construct the liberatory pedagogy as concept, its origin as well as its worth to problematize current prevailing ideology for design education for EESD. It hopes to address the needed changes to bring possibilities for engineering students to take active roles in society with understanding of power and privileges which leads to oppression and unsustainability.

2. What is liberatory pedagogy?

Liberatory pedagogy or critical pedagogy was introduced by Paulo Friere through his seminal work, Pedagogy of the Oppressed[12], [19]–[21]. It is thus, a teaching approach inspired by his work as well as other radical philosophies in effort to help students question and challenge posited "domination" and to undermine the beliefs and practices that are alleged to dominate. Given these premises, it becomes an approach to help students achieve "critical consciousness." which relates to critical thinking in reflexivity of their social and cultural positions amidst current professional roles[22].

In this tradition the educator channels efforts towards directing the learners to ‘question ideologies and practices considered oppressive (including those at school), and encourage "liberatory" collective and individual responses to the actual conditions of their own lives’

Within the classroom setting, students learning begins to critically study the process in which they can begin to view that a practice in society deeply problematic. For example, in the way we perceive aboriginal groups as incompetent, unruly and uncivilized or women as incapable of technicalities or provide significant idea in equal to men. Upon presenting these views, they attempt to change the perceived oppression through constructive methods which allows them to act in direction of a collective response, in respect of those who have been oppressed by the system.

Liberatory pedagogy has been explored mainly through the post formal educational thinking which champions education which emancipates the thinking of the unrepresented. This includes gender, religion, Eastern culture as well different abilities in challenged individuals which remain unaddressed in a education system which is mainly colonial, western, abled and male oriented[17], [18], [23].

Within engineering education, it remains rare although recent call from the engineering education research has highlighted the need to look in specific towards critical experiences in learning[24], [25]. Given the attention, certain perspectives through liberatory pedagogy has been explored. Using femisnism in a objectivised, Western,male oriented subject such as thermodynamics is an eye opener towards use of the pedagogy in representing meaningful engineering education for women [17], [23].Although, the author, Riley notes the ongoing nature of this process of understanding critical pedagogy, she denotes through her experience the changing of her power relationship as student faciltator than the lecturer and how she directs the class in the form of dialogue as opposed to controlling the class. The use of introducing

sustainable technologies not only from the Western male society but also the Eastern as well as from women inventors such as the bain -marie (double boiler) which has failed to be mentioned in most thermodynamic courses[17].

Within sustainable development, such dialogue oriented platforms have been identified as pertinent in bringing a more democratic and inclusive approach to education[20], [26]. Dialogues are important communicative platforms in which we could address our differences constructively and reflexively in effort to build a collective response[27]–[29]. Critical pedagogy aims at providing such dialogue oriented platforms within the curriculum that is usually diversified and currently, globalised. As a critical approach, it allows educators to bring changes in building collective response in addressing issues found problematic in society particularly sustainability which is informed both socially and culturally in an overlap with environment[22].

The following section will depict how critical pedagogy could be explored within the context of design education for engineers and sustainable development.

3. Liberatory Pedagogy for Design

Design education is an important element of the education of engineers which has link to development of expertise as well as identity as designers[30]. Through design education, they learn the trajectory of responding to client requirement and explore the meaning of client-designer relationship through team work of a number of students in a team.[6], [7] However, with regards to SD and education which works on building of capacity to address complex problems, incorporation of more comprehensive approaches towards inquiry of problems are used. This includes multidisciplinary, interdisciplinary and transdisciplinary approaches which are implemented towards transforming the disciplinary mindset, working away from silos towards a transgressive mindset of crossing boundaries in view of the common problem which affects the interest of various parties [11], [31], [32].

However, mainstream design education for sustainable development continues to promote a neutral perspective to a product oriented design learning process even for projects intended for a social or environmental need of communities. This process in turn creates unhealthy power relationship [12], [18] □□between student and potential community of address as well as cognitive dissonance [27] with regards to the outcome which are reduced to a product which is not aligned to complex intersubjective experience [22] of learning about people, space and technology through design and the issues of unsustainability.

Engineering design is a process of proceeding from problem defining based on the problems identified or explained by the client towards problem solving in the form of producing technical solution [30]. As education, it does not allow us to understand intersubjectivity of the experience which involves people, space and technology. The values considered within the objectives of the process is depicted as static references to a social or environmental problem which may seems to correspond to a social need or environmental need. These values are not considered in a way which allows us to understand our views as intervening designers with the intention that our act of designing a physical product may solve a social or environmental problem in the living.

As students who enters the intersubjective realm of complex relationships to a social and environmental problem, it does not allow us to see ourselves as emerging learning selves. The outcome which become simplified, reduced to a product that either satisfies the requirements of client or create a niche technology suggesting a technical perspective to a much more complex, multidimensional problem.

Student experience within involves projection of language which shows no reflexivity of priviledge and power within the conversation which will obstruct the potential for these projects to reflect a partnership with community that they are addressing.

Within a project for the aboriginal community that was intended for providing access to clean water, discussion with educator reveals his views with dialogue entry from the educator. Students within this project have been able to conceptualise a rain water harvesting project proposal to provide access of water. However, when discussing questions to be asked to villagers on the details on the living of the aborigin and how the project would intervene with their lifestyle, this conversation was noted

Educator : With regards to the project, we are going to visit the kampung (village) for you to talk to the villagers. Before we proceed, I would like to know what do you know about our Orang Asli (aborigin)?

Student : They are uneducated, and live in uncivilized manner.

Educator : Why do you think so?

Student : Showing a disapproving body language (They don't have much facilities around them. Therefore, they are fine with living in the poor way)

Educator : What about the rest, what do you think?

Student : (Silent a while)... They don't have much knowledge

Educator : Do you need more knowledge to live here or to live within the forest?

Student : Silent….wondering...showing facial expressions reflecting the irrelevance of the question

The depiction of conversation above is an insight to into the conversations between an educator involved in constructing education linking designing to sustainable development and engineering design students working on a project for the aboriginals. The conversation depicts the thinking of engineering student who is unaware of his views coming from a priviledged background to understand the difficult sociohistorical conditions of the aboriginal which results in a discriminatory stance against the aboriginals they are intending to design for. The educator questioning is intended to reflect on the educational practice which incorporates the aboriginals as clients requiring a solution for clean water provision As the current design pedagogy only requires input of problem definition without understanding sociohistoric conditions and its impact towards community deriving solutions put the engineering students in an

unhealthy relationship towards building of partnership between the community they work for and themselves.

The aboriginal living conditions around the world have become a focus particularly within sustainable development agenda where these communities are fighting back for their priviledge towards an education that does not marginalise and access to their deprived land. Within Malaysia, the aboriginal community condition has become a political focus in the recent within the National Transformational Plan. The aboriginals living conditions have become focus particularly with regards to their education as dignified native citizens of Malaysia who have been marginalized by the current mainstream education [33]. The lack of access to resources like water resulting in a socio environmental problem is also reflected within their community. The aboriginals identification with these resources through their lifestyle such as catching fish and diving reflects a closer relationship but have been limited due to development of the mountains and hills where these resources are found. Despite having profound knowledge of the forest, their conditions which in turn has led them to reservation lands has made it difficult to access of water and fulfilled, dignified living.

Our position as designers are to be considered in terms of understanding of our power relationships when working with these communities. In partnership, a designer is sharing his or her knowledge and in turn is informed of other kind of knowledge within a process of collective inquiry [15]. Our lending of expertise is among others who also contribute content through personal experiences, mutual place based experience as well as holistic knowledge such as art and indigenous technology [15]. We also recognizes our knowledge among others in a synoptic process which in turns builds the bigger picture, the picture of the whole in relevance to a collective response to a condition of unsustainability[15].

The use of liberative pedagogy within this context would challenge the mainstream design education which simplifies the design process as that which involves technicalities as outcome. Liberative pedagogues help students to pose questions in view of the domination of practices that does not permit learning in a critical and reflexive way. The use of liberative pedagogy in design would involve reflexive process of the intersubjective experience in understanding knowledge of the people in informing the unsustainability in the living. For example, understanding of the wells and streams used by the aboriginals to gain water and their introspective experience of how it might be changing and affecting their lives. With regards to access to clean water, with the knowledge shared, we might be able to decide if the critical condition is to be solved with what kind of social environmental intervention. For example, do we have a problem of water availability or water treatment which provide a more socially robust knowledge from our understanding informed of socio-environmental knowledge as well as technical knowledge.

Liberative pedagogy could also help to build our understanding on the emerging our new,learning selves from the intersubjective process of being affected by the situation resulting in an empathic stance instead of technicality. Other than our technical selves, our social and cultural roles which emerges as a result of the interaction between people, technology and space results in a more compassionate engineers who values learning as part of the development process. Vare and Scott [34] emphasizes such outcomes in their reference within ESD as that which helps towards building of our capacity to deal

with unsustainability, in reference towards learning as the main component of sustainable development. McKenzie [35] relates to the intersubjectivity as a critical pathway towards participation for social action, a bottoms up approach rather than the top down technological implementation approach. With relevance to these perspectives is Ekins [36] view of sustainable development efforts within developing countries which would involve technology transfer as its main phase of change which mainly involves changes in the field and not in the top level of planning and management.

Potential criticism of this perspective could stem from the deviation of building expertise , resulting in dilution of competency as well as subjectivity which introduces uncertainty within the philosiphical tradition of objectivity and functionality. Molinga [37] denotes with regards water professionals fear of dilution of expertise in the progressive change being highlighted for engineers to become more transdiscipliuary, crossing boundaries in order to solve problems in taking various other roles. However, Brown [16] asserts through her work on the development of the collective mind, the need to understand the self among the collective and how individuals contribute. Thus, with these arguments, liberative pedagogy is seen relevant in broadening the image of the engineer designer as one who is not limited to technicalities but is in the present as emerging in their learning as part of the collective response towards sustainability in society.

4. Conclusion

Thus, with linking liberatory pedagogy to design and sustainable development has been a constructionists approach in the critical way for engineering education. This paper was written to be an eye opener of educational approaches within the critical pathways focusing on student experience of learning. As education have become a foremost proponent targeted with regards to sustainable development and building of our future, the engineer as the technical expert is limiting of an image in a rather complex platform requiring the play of their role.

Within this paper, liberatory pedagogy has been discussed in its use and its particular relevance to the engineering field based on efforts by educational pedagogues exploring opportunities to include them within engineering education. In light of this, the potential use of liberatory pedagogy was discussed within design education with arguments provided for challenging of the mainstream design education. Student narrative was used to discuss the context of delivering these approaches and its useful relevance in building the capacity of he engineer more than technical expert but in reflexive of their emerging social and cultural role when learning with others.

Potential criticism of taking such perspectives for design education was also discussed with iteration of the pedagogy as that which emancipates and not that limits the identity of the engineer.

References

[1] D. Ferrer-Balas, J. Bruno, M. De Mingo, and R. Sans, “Advances in education transformation towards sustainable development at the Technical University of Catalonia, Barcelona,” Int. J. Sustain. High. Educ., vol. 5, no. 3, pp. 251–266, Sep. 2004.

[2] M. Pavlova, “Towards using transformative education as a benchmark for clarifying differences and similarities between Environmental Education and Education for Sustainable Development,” Environ. Educ. Res., vol. 19, no. 5, pp. 656–672, Nov. 2012.

[3] M. Leerberg, V. Riisberg, and J. Boutrup, “Design responsibility and sustainable design as reflective practice: An educational challenge,” Sustain. Dev., vol. 18, no. 5, pp. 306–317, 2010.

[4] K. Kastenhofer, A. Lansu, R. van Dam-Mieras, and M. Sotoudeh, “The Contribution of University Curricula to Engineer ing Education for Sustainable Development,” GAIA-Ecological Perspect. Sci. Soc., vol. 19(1), pp. 44–51, 2010.

[5] C. Hopkins and R. McKeown, “Education for Sustainable Development: past experience., present action and future prospects,” Educ. Philos. Theory, vol. 33, no. 2, pp. 231–244, 2001.

[6] V. M. Novak, “Design management of sustainability values: a learning organization perspective.,” Archit. Eng. Des. Manag., vol. 10, no. 3/4, pp. 218–232, 2014.

[7] D. Sobek and C. Plumb, “Using The Engineering Design Process To Re Envision Multidisciplinary Educational Experiences For Engineering Students,” in 2007 Annual Conference & Exposition, 2007, pp. 12.1570.1–12.1570.14.

[8] M. Wolcott, S. Brown, M. King, D. Ascher-Barnstone, T. Beyreuther, and K. Olsen, “Model for Faculty, Student, and Practitioner Development in Sustainability Engineering through an Integrated Design Experience,” J. Prof. Issues Eng. Educ. Pract., vol. 137, no. 2, pp. 94–101, 2011.

[9] J.-Y. Park, “Transitioning toward Transdisciplinary Learning in a Multidisciplinary Environment,” Int. J. Pedagog. Learn., vol. 6, no. 1, pp. 82–93, 2010.

[10] A. ERTAS and K. M. . T. FRIAS, “Shifting Engineering Education from Disciplinary to Transdisciplinary Practice.,” Int. J. Eng. Educ., vol. 31, no. 1A, pp. 94 – 105, 2015.

[11] A. Ertas, T. Maxwell, V. P. Rainey, and M. M. Tanik, “Transformation of higher education: the transdisciplinary approach in engineering,” IEEE Trans. Educ., vol. 46, no. 2, pp. 289–295, 2003.

[12] I. Thomas, “Critical Thinking, Transformative Learning, Sustainable Education, and Problem-Based Learning in Universities,” J. Transform. Educ., vol. 7, no. 3, pp. 245–264, Jul. 2009.

[13] Y. Sipos, B. Battisti, and K. Grimm, “Achieving transformative sustainability learning: engaging head, hands and heart,” Int. J. Sustain. High. Educ., vol. 9, no. 1, pp. 68–86, Jan. 2008.

[14] C. Mitchell, D. Cordell, and D. Fam, “Beginning at the end: The outcome spaces framework to guide purposive transdisciplinary research,” Futures, vol. 65, pp. 86–96, Jan. 2015.

[15] V. A. Brown, “Collective inquiry and its wicked problems,” Tackling wicked Probl. through Transdiscipl. Imagin., pp. 61–83, 2010.

[16] V. A. Brown, “Utopian thinking and the collective mind: Beyond transdisciplinarity,” Futures, vol. 65, pp. 209–216, 2015.

[17] D. Riley, “Employing liberative pedagogies in engineering education,” J. Women Minor. Sci. Eng., vol. 9, no. 2, 2003.

[18] L. Claris and D. Riley, “Situation critical: critical theory and critical thinking in engineering education,” Eng. Stud., vol. 4, no. 2, pp. 101–120, 2012.

[19] J. Asghar, “Critical Paradigm: A Preamble for Novice Researchers,” Life Sci., vol. 10, no. 4, pp. 3121–3127, 2013.

[20] E. Frydaki and E. Katsarou, “The dialogic practices of educational action

research participants as a means of supporting or undermining its critical orientation," Action Res. Educ., vol. 4, 2013.

[21] E. Ellsworth, "Why doesn't this feel empowering? Working through the repressive myths of critical pedagogy," Harv. Educ. Rev., 1989.

[22] M. McKenzie, "The places of pedagogy: or, what we can do with culture through intersubjective experiences," Environ. Educ. Res., 2008.

[23] D. Riley, A. L. Pawley, J. Tucker, and G. D. Catalano, "Feminisms in engineering education: Transformative possibilities," NWSA J., vol. 21, no. 2, pp. 21–40, 2009.

[24] J. M. Case and G. Light, "Emerging Research Methodologies in Engineering Education Research," J. Eng. Educ., vol. 100, no. 1, pp. 186–210, Jan. 2011.

[25] A. Johri and B. M. Olds, "Situated Engineering Learning : Bridging Engineering Education Research and the Learning Sciences," J. Eng. Educ., vol. 100, no. 1, pp. 151–185, 2011.

[26] T. Meppem and R. Gill, "Planning for sustainability as a learning concept," Ecol. Econ., vol. 26, no. 2, pp. 121–137, Aug. 1998.

[27] N. Chabrak and R. Craig, "Student imaginings, cognitive dissonance and critical thinking," Crit. Perspect. Account., vol. 24, no. 2, pp. 91–104, 2013.

[28] K. McPhail, "The dialectic of accounting education: from role identity to ego identity," Crit. Perspect. Account., vol. 12, no. 4, pp. 471–499, 2001.

[29] P. Vare and W. Scott, "Learning for a Change: Exploring the Relationship Between Education and Sustainable Development OPINION ESSAY," vol. 1, no. 2, pp. 191–198, 2015.

[30] C. L. Dym, A. M. Agogino, O. Eris, D. D. Frey, and L. J. Leifer, "Engineering design thinking, teaching, and learning," J. Eng. Educ., vol. 94, no. 1, pp. 103–120, 2005.

[31] N. a. Ashford, “Major challenges to engineering education for sustainable development: What has to change to make it creative, effective, and acceptable to the established disciplines?,” Int. J. Sustain. High. Educ., vol. 5, no. 3, pp. 239–250, 2004.

[32] G. Tejedor and J. Segalàs, “TRANSDISCIPLINARITY IN ENGINEERING EDUCATION. A MUST FOR SUSTAINABLE DEVELOPMENT IN TECHNOLOGY EDUCATION,” EDULEARN15 Proceedings. IATED, pp. 7083–7090, 06-Jul-2015.

[33] G. P. Means, “The Orang Asli: Aboriginal Policies in Malaysia,” Pac. Aff., vol. 58, no. 4, pp. 637–652, 1985.

[34] P. Vare and W. Scott, “Learning for a Change: Exploring the Relationship Between Education and Sustainable Development,” J. Educ. Sustain. Dev., vol. 1, no. 2, pp. 191–198, Sep. 2007.

[35] M. McKenzie, “The places of pedagogy: Or, what we can do with culture through intersubjective experiences,” Environ. Educ. Res., vol. 14, no. 3, pp. 361–373, 2008.

[36] P. Ekins, “Making development sustainable,” Glob. Ecol. A new arena Polit. Confl., pp. 91–103, 1993.

[37] P. P. Mollinga, “Towards the transdisciplinary engineer: Incorporating ecology, equity and democracy concerns into water professionals’ attitudes, skills and knowledge,” Irrig. Drain., vol. 58, no. S2, pp. 195–204, 2009.